12th International Corrosion Congress

PRECEEDINGS

September 19-24, 1993

Volume 3A

Houston, Texas USA

CORROSION: SPECIFIC ISSUES

NACE International

CORROSION CONTROL FOR LOW-COST RELIABILITY

12th International Corrosion Congress

PRECEEDINGS

VOLUME 3A

CORROSION: SPECIFIC ISSUES

The manuscripts in this volume have been printed from camera-ready copy and have been accepted without editing by NACE International.

Neither NACE International, its officers, directors, members thereof, nor instructors accept any responsibility for the use of the methods and materials discussed herein.

Any goods, products, and/or services mentioned are mentioned as items of information only. Such mention does not constitute an endorsement by NACE International.

The information is advisory only, and use of the materials and methods is solely at the risk of the user.

ISBN: 1-877914-65-7

Published by

NACE International
P.O. Box 218340
Houston, TX 77218-8340

NACE International

PRECEEDINGS CONTENTS

NON-METALLIC COATINGS ON STEEL SUBSTRATES

VOLUME 2

ATMOSPHERIC CORROSION

CHEMICAL PROCESS INDUSTRY WORKSHOP

HIGH TEMPERATURE CORROSION

VOLUME 3B

INHIBITORS

Paper # Page #

LOCALIZED CORROSION/CREVICES

LOCALIZED CORROSION/PITTING

PASSIVITY AND BREAKDOWN

VOLUME 4

CATHODIC PROTECTION

HYDROGEN EFFECTS

PIPELINE CORROSION

RELIABILITY AND CORROSION CONTROL OF WELDMENTS/CORROSION RESISTANT ALLOYS

VOLUME 5A

AIRCRAFT

AUTOMOTIVE/ACCELERATED TESTING

CORROSION IN CONCRETE

ELECTRONICS

EXPERT SYSTEMS

SURFACE ANALYSIS TECHNIQUES

NUCLEAR ENERGY AND WASTE STORAGE

Corrosion-Resistant Amorphous Chromium-Valve Metal Alloys

K. Hashimoto, J. H. Kim, E. Akiyama, H. Habazaki, A. Kawashima and K. Asami
Institute for Materials Research
Tohoku University
Sendai, 980 Japan

Abstract

New alloys, that is, Cr-Ta, Cr-Nb, Cr-Zr and Cr-Ti alloys with a single amorphous phase were prepared by a sputter deposition method in wide composition ranges. Their corrosion resistance in concentrated hydrochloric acids was significantly high due to spontaneous passivation and higher than that of alloy constituents. In particular, amorphous Cr-Ta alloys were immune to corrosion in 12 M HCl at 30°C. XPS analysis revealed that the formation of double oxyhydroxide passive films consisting of chromic ions and valve metal cations seems responsible for the high corrosion resistance.

Key terms: amorphous Cr-valve metal alloys, high corrosion resistance in 12 M HCl, passivity in 12 M HCl

Introduction

Sputter deposition is a quite effective method to produce amorphous alloys. In particular, sputtering does not require melting for alloy formation, and hence sputtering enables us to produce alloys even when the melting point of an alloy constituent far exceeds the boiling point of another alloy constituent. By utilizing this advantage of sputtering some of the present authors succeeded to tailor corrosion-resistant new amorphous alloys, such as Cu-Ta[1], Cu-Nb[1], Al-Ta[2], Al-Nb[2], Al-W[3], Al-Mo[3], Al-Zr[3-5], and Al-Ti[3-7]. The amorphous copper valve metal alloys were extremely corrosion-resistant even in 12 M HCl. The amorphous aluminum alloys were also corrosion-resistant in 1 N HCl, due to formation of passive oxyhydroxide films consisting of cation mixtures of aluminum and alloying elements.

On the other hand, chromium is the most effective alloying element in enhancing the corrosion resistance of amorphous metal-metalloid alloys in strong acids but suffers transpassive dissolution at high potentials. In contrast, as mentioned above, the addition of valve metals such as titanium, zirconium, niobium and tantalum is necessary in imparting the high corrosion resistance to amorphous metal-metal alloys in strong acids, and their anodic oxide films are stable at high potentials, being thickened by anodic polarization. Accordingly, when single phase solid solution alloys composed of chromium and valve metals are formed, they would

be ideally corrosion-resistant in strong acids.

We succeeded to prepare various amorphous chromium-valve metals alloys by a sputter-deposition technique and examined their corrosion behavior. This paper reports that their corrosion resistance is much higher than that of chromium and alloy constituting valve metals.

Experimental Procedures

D. C. Magnetron sputtering was used for preparation of chromium-valve metal alloys. The target was composed of 99.99% pure chromium disc of 100 mm in diameter and 6 mm in thickness, on the sputter-erosion of which 99.95% pure tantalum, niobium, zirconium, titanium or aluminum discs of 20 mm in diameter were placed. The composition of sputter-deposits was controlled by changing numbers of valve metal discs on the chromium disc. Cu-Ta alloys were also prepared by using the target composed of tantalum-placed copper discs. Glass plates were used as substrates which were rinsed by immersion in water containing a commercial detergent for cleaning of aluminum metal at about 75°C. Sputtering apparatus and conditions were the same as those described elsewhere[2].

The composition of sputtered alloys was determined by the electron probe micro-analysis. The structure of sputter-deposited alloys was identified by X-ray diffraction with Cu K_α radiation at θ-2θ mode.

Corrosion and electrochemical experiments were carried out in 6 M and 12M HCl at 30°C open to air. The corrosion rates of alloys were estimated by the inductively coupled plasma emission spectrometry for dissolved elements in the hydrochloric acids after immersion tests. Potentiostatic polarization and open circuit immersion for 1 h were carried out to analyze the specimen surface by X-ray photoelectron spectroscopy. X-ray photoelectron spectra were measured by means of an SSI SSX-100 photoelectron spectrometer with Al K_α radiation. Binding energies were calibrated by a method described elesewhere[8,9], binding energies of the Au $4f_{7/2}$ and $4f_{5/2}$ electrons of gold metal and the Cu $2p_{3/2}$ and $2p_{1/2}$ electrons of copper metal were taken as 84.07, 87.74, 932.53 and 952.35 eV, respectively and the kinetic energy of the Cu $L_3M_{4,5}M_{4,5}$ Auger electrons of copper metal as 918.67 eV.

The composition and thickness of the surface film and the composition of the alloy surface immediately under the surface film were quantitatively determined by a previously proposed method using integrated intensities of photo-electrons, under the assumption of a three-layer model of the outermost contaminated hydrocarbon layer of uniform thickness, the surface film with uniform thickness and the underlying alloy with X-ray photoelectron spectroscopically infinite thickness[10]. It was also assumed that constituents of the layers distribute homogeneously in each layer.

The photoionization cross-sections of Cr $2p_{3/2}$, Ti $2p$, Zr $3d$, Nb $3d$, Ta $4f$ and Cl $2p$ electrons relative to the photoionization cross-section of the O $1s$ electrons used were 1.71[9], 1.277[11], 2.561[12], 2.982[13], 2.617[14], and 1.017[15], respectively. The sensitivity factor of the Cu $L_3M_{4,5}M_{4,5}$ Auger electrons relative to the photoionization cross-section of the O $1s$ electrons used was 1.638[13].

Results and Discussion

Figure 1 shows structures identified by X-ray diffraction for sputter-deposited binary alloys. They were composed of an amorphous single phase in wide composition ranges. It has been generally known for the amorphizable conditions of binary alloys by rapid quenching from the liquid state that the atomic radius ratio of alloy constituents is smaller than 0.85 and that groups of two elements in the periodic table are well separated. The atomic radius of chromium is not largely different from atomic radii of niobium and tantalum and hence the atomic radius ratios of Cr/Nb and Cr/Ta are larger than 0.85. Furthermore, they belong to the neighbor groups in the periodic table. Nevertheless, these alloys form an amorphous single phase structure by sputter deposition. Accordingly, the sputter deposition technique is a quite effective method in preparing new amorphous alloys.

Figure 2 shows change in corrosion rates of Cr-Ti and Cr-Zr alloys measured in 6 M HCl at 30°C with increasing valve metal contents. Chromium metal dissolves actively in this aggressive solution, exhibiting the corrosion rate of 48 mm/y. The corrosion rates of titanium and zirconium metals were 1.7×10^{-1} and 2.9×10^{-4} mm/y, respectively. The corrosion rates of amorphous single phase Cr-Ti alloys are lower than those of chromium and titanium metals. Similarly the corrosion rates of amorphous single phase Cr-Zr alloys are lower than those of chromium and zirconium metals, and tend to decrease with increasing alloy chromium content.

Figure 3 shows corrosion rates of Cr-Nb, Cu-Ta and Cr-Ta alloys in 12 M HCl at 30°C as a function of the valve metal content of the alloy. Corrosion rates of chromium, niobium and tantalum metals were 360, 3.1×10^{-2} and 9.8×10^{-5} mm/y, respectively. When Cu-Ta alloys are amorphized, their corrosion resistance cannot exceed that of tantalum metal, because their corrosion resistance is due to the addition of passivating tantalum to less corrosion resistant copper[14]. In contrast, similarly to amorphous Cr-Ti and Cr-Zr alloys, the corrosion rates of amorphous Cr-Nb and Cr-Ta alloys are lower than those of metals which constitute the amorphous alloys. The corrosion resistance of amorphous Cr-Nb alloys increases with increasing the alloy chromium content. In particular, the amorphous Cr-Ta alloys are extremely corrosion-resistant, being immune to corrosion even in the quite aggressive 12 M HCl.

As an example, potentiostatic polarization curves of amorphous Cr-Nb alloys and sputter-deposited niobium metal measured in 12 M HCl are shown in Figure 4. The number written in front of the symbol of the element denotes the concentration of the alloying element in atomic percent. Amorphous Cr-Ti and Cr-Zr alloys in 6 M HCl and amorphous Cr-Nb and Cr-Ta alloys in 12 M HCl were all spontaneously passive and the alloys with higher chromium contents exhibited a higher cathodic current density and a lower anodic current density with a consequent higher open circuit potential. Consequently, the chromium-containing film seems more active for oxygen reduction and more protective in comparison with the films formed on the valve metals. The cathodic polarization of high valve metal alloys led to monotonous increase in the cathodic current density, whereas the cathodic polarization of high chromium alloys resulted in passivity breakdown showing a high anodic dissolution current due to active dissolution of chromium. Accordingly, unless cathodic polarization was carried out, the passivity is maintained for high chromium alloys, and the high corrosion resistance of these alloys can be attributed to the fact that the air-formed oxide films on these alloys are quite stable and protective in these aggressive environments.

In order to confirm this fact X-ray photoelectron spectroscopic analysis of the alloy surfaces was performed. Figure 5 shows cationic fractions in the films formed on amorphous Cr-Nb alloys in 12 M HCl. Cationic compositions of the air-formed films on as-sputtered alloys are almost the same as bulk alloy compositions. Immersion or anodic polarization in the passive region for the amorphous Cr-29Nb alloy results in no significant change in cationic fractions from those in the air-formed film. The cathodic polarization of this alloy in the active region of chromium leads to an increase in the niobium content in the film due to slight dissolution of chromium. Immersion of the amorphous Cr-63Nb alloy gives rise to a slight increase in the niobium content of the film, because a lower chromium content in the air-formed film is not sufficient to ennoble the open circuit potential to the passive region of chromium by accelerating the cathodic oxygen reduction. Similar analytical results were obtained for amorphous Cr-Ti, Cr-Zr and Cr-Ta alloys, although cations of the latter three valve metals tend to be slightly concentrated in the passive films as well as in the air-formed films. The analysis of the underlying alloy surfaces revealed that the enrichment of the valve metal cations in the films resulted from preferential oxidation of valve metals since the valve metals were slightly deficient in the underlying alloy surfaces.

Major anions constituting the passive film were O^{2-} and OH^- and the concentration of chloride ions included in the film was very low. Figure 6 shows change in concentrations of O^{2-} and OH^- in the passive films formed on amorphous Cr-Nb alloys. The film composition changes continuously from $CrO_{1+0.u}(OH)_{1-0.2u}$ on chromium metal to $NbO_{2+0.v}(OH)_{1-0.2v}$ on niobium metal. Consequently the passive

films formed on the Cr-Nb alloys consist of a double oxyhydroxide such as $(Cr,Nb)O_x(OH)_y$.

Another interesting result is an electronic interaction between chromium ions and valve metal cations in the film. Figure 7 shows an example of the change in the binding energies of the inner shell electrons of cations in the films formed on the amorphous Cr-Ta alloys. In comparison with the film formed on chromium metal, the binding energies of the Cr $2p_{3/2}$ electrons of Cr^{3+} ions in the passive film on the alloys are higher, while the binding energies of the Ta $4f_{7/2}$ electrons of Ta^{5+} ions in the passive films on the alloys are lower than the binding energy of the Ta $4f_{7/2}$ electrons of Ta^{5+} ions in the film on tantalum metal. This indicates that charge transfer occurs from chromic ions to pentavalent tantalum cations in the passive film. Although alloying of chromium with tantalum leads to the charge transfer from tantalum atoms to chromium atoms in the alloys due to the alloying effect because of a larger electronegativity of chromium than tantalum, the direction of the charge transfer between cations in the film is reverse. The similar charge transfer from chromic ions to valve metal cations were found for all passive oxyhydroxide films formed on amorphous Cr-Ti, Cr-Zr, Cr-Nb alloys. Consequently, the passive films formed on the chromium-valve metal alloys in HCl were not simple mixtures of chromium oxyhydroxide and valve metal oxyhydroxides but double oxyhydroxides consisting of chromic ions and valve metal cations, both of which distribute homogeneously in the films so as to show the electronic interaction between chromic ions and valve metal cations. This seems responsible for the fact that the corrosion resistance of the amorphous chromium-valve metal alloys is higher than the corrosion resistance of alloy constituting elements.

Conclusions

Novel amorphous alloys consisting of chromium and valve metals were prepared by magnetron sputtering. Cr-Ta, Cr-Nb, Cr-Zr and Cr-Ti alloys with a single amorphous phase structure were formed in wide composition ranges.

In spite of the fact that chromium dissolved actively, these amorphous alloys were spontaneously passive in concentrated hydrochloric acids, showing a very high corrosion resistance which is higher than that of alloy constituting valve metals. In particular, the amorphous Cr-Ta alloys were immune to corrosion in 12 M HCl. Since the chromium-containing film enhanced cathodic oxygen reduction and decreased the anodic current density, the open circuit potentials of the alloys were higher than those of alloy-constituting valve metals. According to XPS analysis the passive films formed on the alloys consist of double oxyhydroxides of chromic ions and valve metal cations. The charge transfer between these two cations was found from the change in the binding energy of the inner shell electrons of these cations. This kind of electronic interaction indicates that the passive film is not the simple mixture of chromic oxyhydroxide and valve metal oxyhydroxide,

but consists of a double oxyhydroxide such as $(Cr,M)O_x(OH)_y$ where M is a valve metal cation. The formation of double oxyhydroxides seems responsible for the high corrosion resistance of the alloys, which is higher than that of alloy-constituting valve metals.

References

1. K. Shimamura, K. Miura, A. Kawashima, K. Asami and K. Hashimoto, "Corrosion, Electrochemistry and Catalysis of Metallic Glasses, R. B. Diegle and K. Hashimoto, Eds., The Electrochemical Society, Princeton, (1988): p.232.
2. H. Yoshioka, A. Kawashima, K. Asami and K. Hashimoto, "Corrosion, Electrochemistry and Catalysis of Metallic Glasses, R. B. Diegle and K. Hashimoto, Eds., The Electrochemical Society, Princeton, (1988): p.242.
3. H. Yoshioka, A. Kawashima, K. Asami and K. Hashimoto, Corros. Sci., 31 (1990): p.349.
4. H. Yoshioka, A. Kawashima, K. Asami and K. Hashimoto, Electrochim. Acta, 36 (1991): p.1227.
5. H. Yoshioka, A. Kawashima, K. Asami and K. Hashimoto, Corros. Sci., 33 (1992): p.425.
6. Q. Yan, H. Yoshioka, A. Kawashima, K. Asami and K. Hashimoto, Corros. Sci., 31 (1990): p.401.
7. Q. Yan, H. Yoshioka, A. Kawashima, K. Asami and K. Hashimoto, Corros. Sci., 32 (1991): p.327.
8. K. Asami, J. Electron Spectrosc., 9 (1976): p.469.
9. K. Asami and K. Hashimoto, Corros. Sci., 17 (1977): p.599.
10 K. Asami, K. Hashimoto and S. Shimodaira, Corros. Sci., 17 (1977): p.713.
11 H. Yoshioka, S. Yoshida, A. Kawashima, K. Asami and K. Hashimoto, Corros. Sci., 26 (1986): p.795.
12 J. H. Scofield, J. Electron Spectrosc., 8 (1976): p.129.
13 E. Hirota, H. Yoshioka, A. Kawashima, K. Asami and K. Hashimoto, Corros. Sci., 32 (1991): p.1213.
14 J. H. Kim, H. Habazaki, H. Yoshioka, A. Kawashima, K. Asami and K. Hashimoto, Corros. Sci., 33 (1992): p.1507.
15 K. Hashimoto, K. Asami and K. Teramoto, Corros. Sci., 19 (1979): p.3.

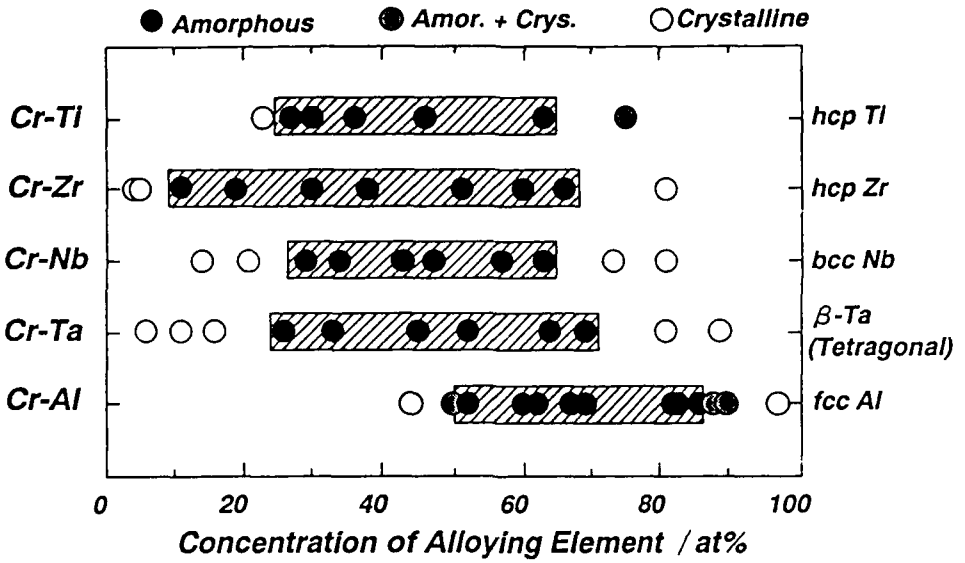

Fig. 1. Structures of sputter-deposited Cr-valve metal alloys identified by X-ray diffraction.

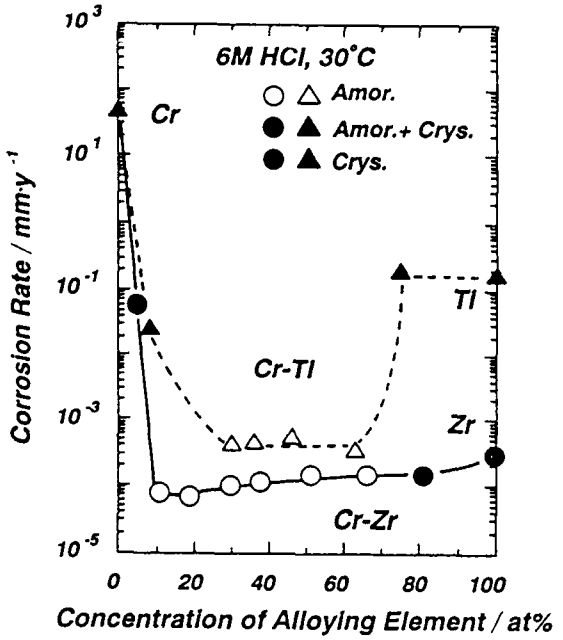

Fig. 2. Corrosion rates of sputter-deposited Cr-Ti and Cr-Zr alloys and chromium, titanium and zirconium metals measured in 6 M HCl at 30°C.

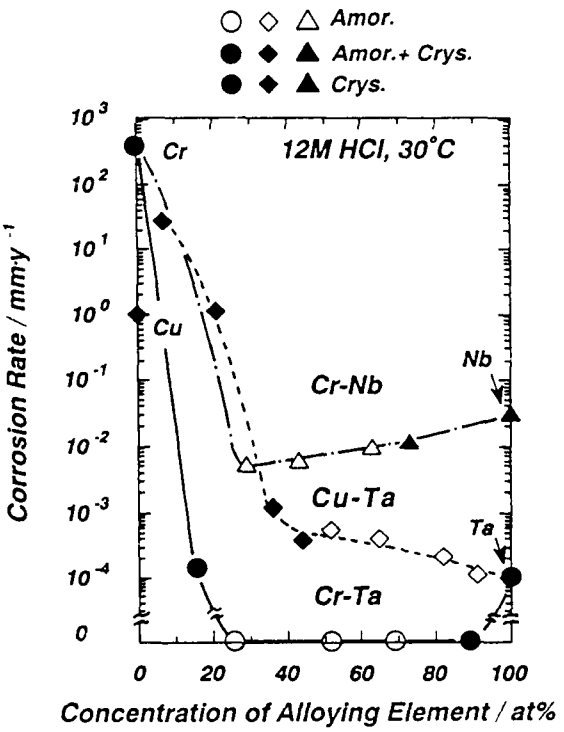

Fig. 3. Corrosion rates of sputter-deposited Cr-Nb, Cu-Ta and Cr-Ta alloys and chromium, copper, niobium and tantalum metals measured in 12 M HCl at 30°C.

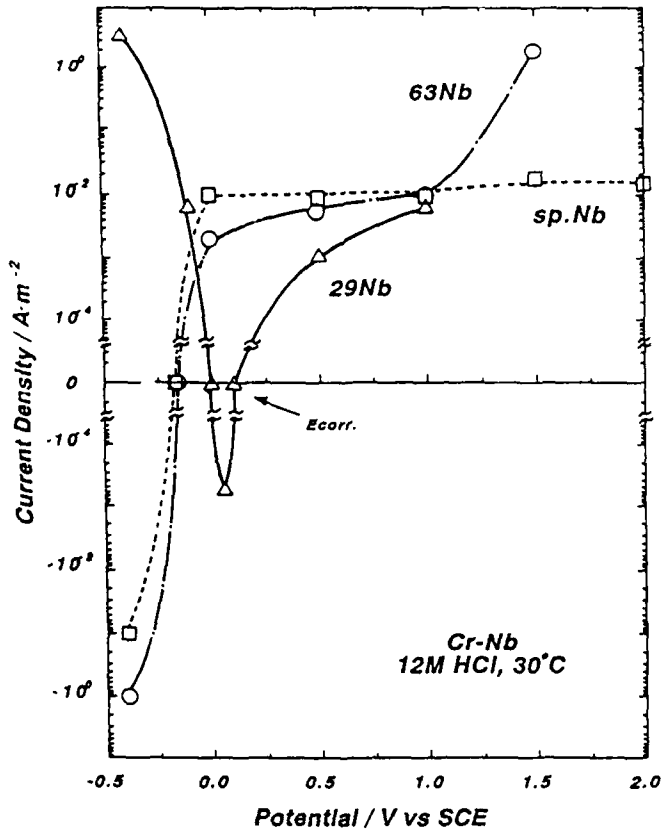

Fig. 4. Potentiostatic polarization curves measured after polarization for 1 h for sputter-deposited Cr-29Nb and Cr-63Nb alloys and niobium metal measured in 12 M HCl at 30°C.

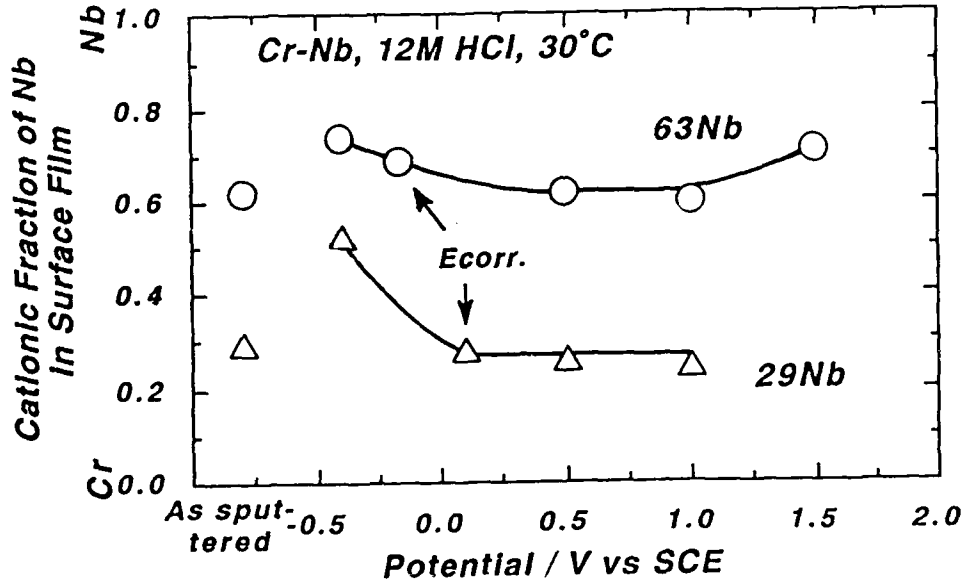

Fig. 5. Cationic fractions in the air-formed films on as-sputtered Cr-29Nb and Cr-63Nb alloys and in the films formed on these alloys by immersion or potentiostatic polarization for 1 h in 12 M HCl at 30°C.

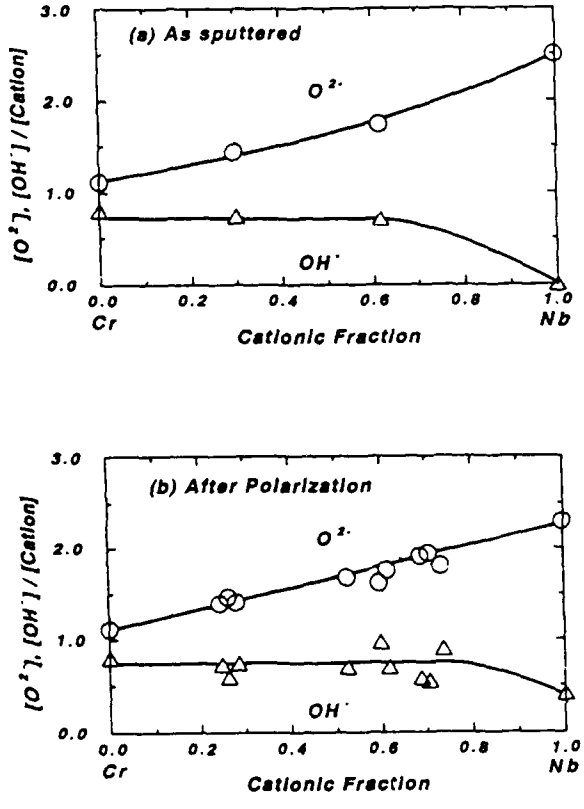

Fig. 6. Numbers of O^{2-} and OH^- linked to a cation in the passive films formed under various potentials on amorphous Cr-Nb alloys in 12 M HCl at 30°C as a function of niobium content in the film.

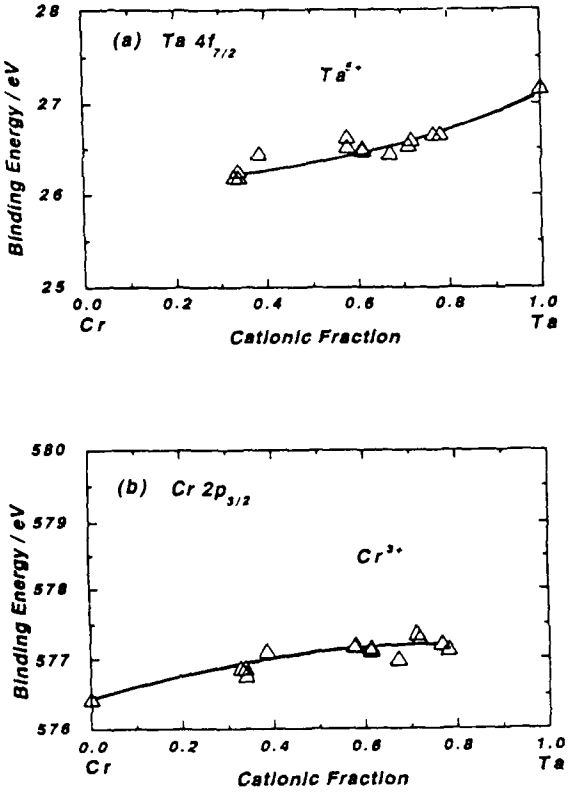

Fig. 7 Binding energies of Ta $4f_{7/2}$ and Cr $2p_{3/2}$ electrons of the cations in the passive film formed on amorphous Cr-Ta alloys as a function of tantalum ion content of the film.

A New Ni-Mo Alloy with Improved Thermal Stability

D. L. Klarstrom
Haynes International, Inc.
1020 West Park Avenue
P. O. Box 9013
Kokomo, IN 46904-9013

Abstract

The limitations of alloy B-2 are described in terms of phase transformations that occur in the Ni-Mo and Ni-Mo-Fe systems. The development of B-3 alloy, a new alloy with improved thermal stability is presented. The time-temperature-transformation characteristics, including the effects of coldwork, are described and discussed. Comparative data is given on uniform corrosion resistance, corrosion of weldments and stress corrosion cracking. Correlations between 700°C tensile ductility and thermal stability, and between 700°C tensile ductility and susceptibility to stress corrosion cracking are also presented and discussed.

Key Words: Ni-Mo alloys, thermal stability, corrosion of weldments, stress corrosion cracking, 700°C tensile ductility

Introduction

Nickel-molybdenum alloys have been used commercially for over sixty years because of their exceptional resistance to non-oxidizing corrosive media such as hydrochloric, sulfuric and phosphoric acids. One of the first alloys, HASTELLOY® alloy B, was used successfully for many years, but it suffered the serious drawback of requiring the solution heat treatment of fabricated components in order to eliminate carbide precipitation in weld heat-affected zones. Some experimental work performed by Flint[1] indicated that the problem could be solved by lowering the carbon content of the alloy to very low levels. Subsequent work by Flint[2] indicated that further improvements in corrosion resistance could be achieved by reducing iron and silicon levels. The achievement of low carbon levels on a routine basis for large size commercial heats eventually became a reality through the development of the argon-oxygen decarburization (AOD) melting process[3]. This enabled the commercialization of an improved alloy known as HASTELLOY alloy B-2[4].

Although the new alloy lived up to expectations for superior corrosion resistance in the as-welded condition, it soon became apparent that the thermal stability of the alloy had been adversely impacted by the reduction of residual alloying elements, especially iron levels. This resulted in the susceptibility of alloy B-2 to the Ni_4Mo transformation, which occurred quite rapidly when the alloy was exposed to the 650-750°C temperature range[5]. This

transformation was often responsible for cracking experienced during alloy manufacturing operations as well as during customer component fabrication. In addition to these problems, a number of cases of in-service environmental cracking were reported. These cracks were invariably associated with weld heat-affected zones.

In order to resolve the problem issues of alloy B-2, a research program was undertaken at Haynes International, Inc. to identify an alloy with improved thermal stability without sacrificing the excellent corrosion resistance of alloy B-2. This paper will report on the results of this program which has led to the development of a new alloy known as HASTELLOY B-3™ alloy. The new alloy employs a balanced composition of Ni, Mo, and specific residual alloying elements such that the Ni_3Mo transformation is favored in equilibrium. Compared to Ni_4Mo, this transformation is quite sluggish, requiring many hours rather than minutes for initiation and completion. The superiority of the new alloy will be illustrated through the comparison of mechanical properties, resistance to stress corrosion cracking, and general corrosion resistance.

Transformation Characteristics of Ni-Mo Alloys

The nominal compositions of the B-family of alloys discussed in this paper are given in Table 1. Although they are really multi-component alloys, some insight to their phase equilibria can be obtained by examining the available binary and ternary phase diagrams. The nickel-rich portion of the Ni-Mo system[6] is shown in Figure 1. This diagram indicates that an alloy of composition Ni-28%Mo would exist as α, a face-centered cubic (fcc) solid solution, at temperatures of about 860°C and above. Below that temperature, the composition lies within the $\alpha + \beta$ phase field. The β-phase corresponds to Ni_4Mo, an ordered intermetallic compound having a body-centered tetragonal (bct) crystal structure. Because of the limited number of slip systems available in the bct structure, high strength and low ductility values are associated with the β-transformation [7,8]. Studies of the time-temperature-transformation characteristics of the β-phase indicate that it exhibits a C-shape curve with the transformation occurring in less than two minutes at a temperature of 750°C[5].

A portion of the Ni-Mo-Fe system at 700°C[5] is shown in Figure 2. The diagram indicates that for alloys with molybdenum levels of commercial interest (26-30%), the equilibrium phases present can be significantly altered from those of the binary Ni-Mo system with relatively modest additions of iron. This involves the transition from the $\alpha + \beta$ phase field to the $\alpha + \gamma$ phase field. The γ-phase corresponds to Ni_3Mo, which is an ordered intermetallic compound having an orthorhombic crystal structure. The γ-phase transformation is quite complex and involves a number of transition metastable phases such as DO_{22}, an ordered tetragonal phase which is chemically Ni_3Mo, Ni_2Mo, a body-centered orthorhombic compound, and a metastable Ni_4Mo phase[9,10]. Because of its complex nature, the γ-transformation is sluggish compared to the β-transformation[9].

®HASTELLOY and B-3 are trademarks of Haynes International, Inc.

Considering the foregoing and the compositional ranges given in Table 1, it is clear that alloy B-2 is subject to the β-transformation which has rapid kinetics. Alloy B, on the other hand, is subject to the γ-transformation which has sluggish kinetics.

Alloy Development

From the preceding phase equilibria, it is apparent that it is not possible to develop an alloy containing 26-30%Mo which is free from any phase transformation. The best that can be hoped for is an alloy which displays sluggish reaction kinetics like alloy B. Such an alloy would, in effect, buy time so that cracking could be avoided during standard alloy manufacturing and fabrication procedures. One would also like to accomplish this without sacrificing the excellent corrosion resistance of alloy B-2. These were precisely the objectives that were adopted for the alloy development program.

In designing the new alloy chemistry, the carbon and silicon levels were kept as low as possible in line with alloy B-2 to ensure good as-welded corrosion resistance. The effects of various alloying elements on thermal stability were determined through the evaluation of laboratory produced heats. Initially, attention was focused on the effects of 0-24 hour exposures at 700°C on hardness, room temperature mechanical properties and corrosion resistance. The 700°C exposure temperature was selected because it was known that the transformation kinetics for alloy B-2 were fairly rapid at that temperature. It was discovered later, however, that the tensile properties at 700°C, especially ductility, determined for annealed material held at temperature for 1 hour prior to testing were excellent indicators of thermal stability. Alloy chemistries possessing poor thermal stability exhibited very low tensile elongations. Sample failure occurred by brittle intergranular fracture, and there were numerous secondary cracks along the gage length. Alloy chemistries possessing excellent thermal stability had high elongation values. Sample failure occurred by a ductile shearing mechanism, and there were few secondary cracks in the gage length. With such data, it was possible to derive a relationship between 700°C tensile ductility and alloy chemistry using multiple linear regression analysis techniques which described maximum thermal stability with minimum alloying content. This permitted the dual objectives of the program to be achieved. This relationship, which took into account both intentional and residual alloying elements, was subsequently used to define the compositional range shown in Table 1.

Thermal Stability

Time-Temperature-Transformation Characteristics

A comparison of the time-temperature-transformation (T-T-T) characteristics of alloy B-2 versus B-3 alloy is presented in Figure 3. The diagram was determined on the basis of hardness changes using a paired t-test and a significance level of 0.05 as the distinguishing criterion. The lines shown, therefore, are conservative in the sense that the transformations are just beginning and minimal changes could be expected in mechanical and corrosion resistant properties. The effect of coldwork was also determined using samples that had

been cold rolled 30%.

For alloy B-2, the transformation involved Ni_4Mo or a combination of Ni_4Mo + Ni_3Mo. It occurred within 12 minutes in the 700-750°C temperature range for material in the annealed condition. A typical microstructure exhibiting the striations which characterize the transformation is shown in Figure 4 for a sample aged at 700°C/24 hours. The presence of 30% coldwork accelerated the start of the transformation to 6 minutes and shifted the nose to approximately 750°C.

The transformation characteristics of B-3 alloy are markedly different. The curve consists of a lower portion at temperatures of 700°C and below in which the metastable phases DO_{22}, Ni_2Mo and Ni_4Mo were found to occur. The lower curve exhibited a nose located at approximately 4-1/2 hours at 650°C. These reactions occurred on a very fine scale which required TEM examination for phase identification. The upper portion of the curve involved the Ni_3Mo transformation. As shown in Figure 5 for a sample aged at 750°C/100 hours, the Ni_3Mo transformation is typified by striations and the occurrence of a lamellar reaction product that initiates on grain boundaries. The presence of 30% coldwork accelerated the beginning of the transformation reactions, and the nose of the lower curve was shifted to approximately 2 hours at 625°C.

Comparison of the data in Figure 5 clearly shows that B-3 alloy has a 20:1 advantage over alloy B-2 in the time for the start of any phase transformation for either the annealed or coldworked condition. Further, B-3 alloy in the coldworked condition enjoys a 10:1 advantage over alloy B-2 in the annealed condition. This advantage in transformation kinetics provides much greater ease in the heating of coldworked B-3 components during solution annealing treatments. Currently, it is recommended that alloy B-2 components be heated very rapidly to avoid the transformation in the 600-800°C temperature range which could cause cracking if residual tensile stresses are present[11].

Tensile Properties

Earlier it was indicated that 700°C tensile elongation was found to be a good indicator of thermal stability. A comparison of the results obtained for samples of alloy B-2 and B-3 alloy sheet is given in Figure 6. The samples were held at temperature for 1 hour prior to testing. The results clearly confirm the differences between the two alloys as indicated in Figure 3. The data also underscore the fact that elevated temperature tensile ductility can be severely degraded by the phase transformations. This is very important to realize since room temperature data generated on material exposed to elevated temperatures may not show such a precipitous change as illustrated in Table 2. The mechanism for the ductility loss at elevated temperatures has not yet been elucidated. However, the fracture mode is intergranular which strongly suggests that grain boundary phase transformations, perhaps induced by plastic deformation during the tensile test, are involved. This phenomenon certainly helps to explain the susceptibility of alloy B-2 to cracking during thermal treatments, especially when room temperature data generated on exposed samples would

indicate that no problem exists.

Corrosion Resistance

Uniform Corrosion

A comparison of the uniform corrosion resistance of B-3 alloy and alloy B-2 in a variety of boiling acid mixtures is presented in Table 3. Considering the normal scatter in the data, it is reasonable to conclude the B-3 alloy offers the same good corrosion resistance to these media as alloy B-2. Although only a limited amount of testing has been done to evaluate the effects of contaminant species, the results to date would indicate that the corrosion rate of B-3 alloy is increased by the presence of oxidizing ions as is the case for alloy B-2.

Corrosion of Weldments

To assure that the alloy possesses good corrosion resistance in the as-welded condition, samples of sheet and plate up to 12.5mm (0.5-inch) thick were welded with matching filler metal and tested in 20% HCl at 149°C for 96 hours in an autoclave per the standard test used for alloy B-2. After testing, a metallographic section through the weldment was prepared and examined for corrosion attack along the weld fusion zone. A reading of 0.18mm (7 mils) or less is considered acceptable. To date, all of the samples tested have shown a depth of attack of 0.09mm (3.5 mils) or less with an average of 0.05mm (2 mils). Thus, the as-welded corrosion resistance of B-3 alloy can be considered to be as good as that of alloy B-2.

With respect to the corrosion resistance of weld heat-affected zones, the improved thermal stability of B-3 alloy has been shown to provide definite benefits. In one test, autogenous weldments produced in 3mm (0.125-inch) thick sheet samples were tested in a boiling mixture of 60% H_2SO_4 + 8% HCl for 96 hours. As illustrated in Figure 7, the alloy B-2 sample experienced intergranular corrosion attack to a depth of approximately 0.10mm (4 mils) in the weld heat-affected zone while no such attack was observed in the B-3 sample. Results confirming this behavior were also obtained in field test samples exposed to 20-30% H_2SO_4 + ferrous sulfate at 110°C for 96 days[12].

Stress Corrosion Cracking

As indicated earlier, there were a number of cases in which alloy B-2 experienced in-service cracking that appeared to be environmentally related. Most of these cases involved cracking which initiated in weld heat-affected zones. A link to the phase transformations that occur in the alloy was suspected, but no hard evidence of this was found. However, in the alloy development program, it was found that test samples of alloy B-2 and many of the experimental heats showed cracking at stamped identification markings when aged for various periods of time at 700°C and tested in boiling 20% HCl. Subsequently, it was found that U-bend samples of alloy B-2 which had been aged at 700°C/1 hour would undergo

intergranular stress corrosion cracking (SCC) in boiling 20% HCl. Some additional testing was done in boiling solutions of 5% and 60% H_2SO_4, and intergranular SCC was found in both cases. No cracking was encountered in any of the test solutions when the samples were in the annealed condition. Thus, it would appear that the presence of some phase transformation product, perhaps a metastable one considering the short time period involved, is necessary to impart SCC susceptibility. Also, because of the independence of the acid type or concentration on the susceptibility of alloy B-2 in the aged condition, it is strongly suspected that hydrogen is involved in the cracking mechanism. Tests conducted on samples of B-3 alloy in the annealed or aged condition in boiling 5% and 60% H_2SO_4 acid mixtures revealed that the alloy is not susceptible to stress corrosion cracking in these solutions. Earlier tests in the alloy development program had indicated no susceptibility of the alloy to SCC in boiling 20% HCl.

Given the apparent link between thermal stability and susceptibility to SCC, it was logical to expect that there should be a correlation between 700°C tensile elongation and SCC susceptibility. To test this hypothesis, several heats of alloy B-2 sheet displaying different levels of 700°C tensile ductility were tested in boiling 5% H_2SO_4 using U-bend samples prepared from materials aged at 700°C/1 hour. A summary of the results obtained along with those for B-3 alloy is presented in Table 4. It can be seen from the data that all of the alloy B-2 heats exhibited susceptibility to SCC, but, clearly, the time to failure increased in direct proportion to the 700°C ductility. The B-3 samples did not crack. Therefore, it would appear that ductility levels on the order of 50% elongation are required to ensure immunity to SCC.

Concluding Remarks

A new Ni-Mo alloy has been developed with improved thermal stability over alloy B-2. Based in terms of T-T-T characteristics, this advantage is on the order of 20:1 in either the annealed or coldworked condition. The improved thermal stability was achieved with no sacrifice in uniform corrosion resistance, and, in fact, the corrosion resistance of weld heat-affected zones also appears to be improved. The alloy development program established a useful correlation between 700°C tensile ductility and thermal stability. During the program it was also discovered that alloy B-2 is susceptible to SCC in boiling 20% HCl, 5%H_2SO_4 and 60%H_2SO_4 when aged at 700°C/1 hour. No such SCC susceptibility was found for B-3 alloy. A correlation was shown between 700°C tensile ductility and time to cracking in boiling 5%H_2SO_4 for alloy B-2. From the results for B-3 alloy, it would appear that a level of ductility on the order of 50% elongation is required to ensure immunity to SCC.

References

1. G. N. Flint, J. Inst. Metals, 87 (1958/59), p. 303.

2. G. N. Flint, Metallurgia, 62 (1960), p. 195.

3. W. A. Krivsky, U.S. Patent 3,252,790, May 24, 1966.

4. F. G. Hodge and R. W. Kirchner, Materials Performance, 15 (1976), p. 40.

5. C. R. Brooks, J. E. Sprinell and E. E. Stansbury, Intl. Metals Reviews, 29 (1984), p. 210.

6. P. V. Gutherie and E. E. Stansbury, "X-ray and Metallographic Study of the Nickel-Rich Alloys of the Nickel-Molybdenum-II, "Report ORNL - 3079, 1961.

7. B. Chakravarti, E. A. Starke, Jr. and B. G. Lefevre, J. Mat. Sci., 5 (1970), p. 394.

8. J. E. Sprinell, L. M. Ruch and C. R. Brooks, Met. Trans. A,6A (1975), p. 1301.

9. G. von Tendeloo, R. DeRidder and S. Amelinckx, Phys. Stat. Sol., 27 (1975), p. 457.

10. D. Schryvers, G. von Tendeloo and S. Amelinckx, Phys. Stat. Sol., 87 (1985), p. 401.

11. Haynes International, Inc., Brochure H-2010D.

12. Haynes International, Inc., Brochure H-2101.

Table 1

Nominal Compositions of Commercial Ni-Mo Alloys

Alloy	Ni	Co	Fe	Cr	Mo	W	Mn	Si	C	Al	Cu	V
B	67	2.5*	5	1*	28	-	1*	1*	0.05*	-	0.5*	0.3
B-2	69	1*	2*	1*	28	-	1*	0.1*	0.01*	-	-	-
B-3	65[a]	3*	1.5	1.5	28.5	3*	3*	0.1*	0.01*	0.5*	0.2*	0.2*

*maximum [a]minimum

Table 2

The Effect of Test Temperature on the Tensile Ductility of alloy B-2 Sheet Exposed at 700°C

Test Temp °C	Time at 700°C, Hrs	% El
25	None	57
25	1	53
700	1	1

Table 3

A Comparison of Uniform Corrosion Resistance in Various Boiling Acids

	Average Corrosion Rate, mm/y (mils/y)	
Acid Medium	B-3	B-2
50% Acetic Acid	<0.01 (0.1)	0.01 (0.3)
40% Formic Acid	0.01 (0.5)	0.02 (0.6)
50% Phosphoric Acid	0.03 (1.2)	0.07 (2.6)
50% Sulfuric Acid	0.04 (1.7)	0.04 (1.4)
20% Hydrochoric Acid	0.31 (12.1)	0.40 (15.6)

Table 4

Correlation between 700°C Tensile Elongation and Susceptibility to SCC in Boiling 5%H_2SO_4 for Samples Aged at 700°C/1 Hour

Material	700°C % EL*	Time to SCC,* Days
alloy B-2, Heat A	1	2
alloy B-2, Heat B	12	10
alloy B-2, Heat C	34	20
B-3 alloy	50	NC**
* Average of duplicate tests		
**NC = No Cracking in 91 days		

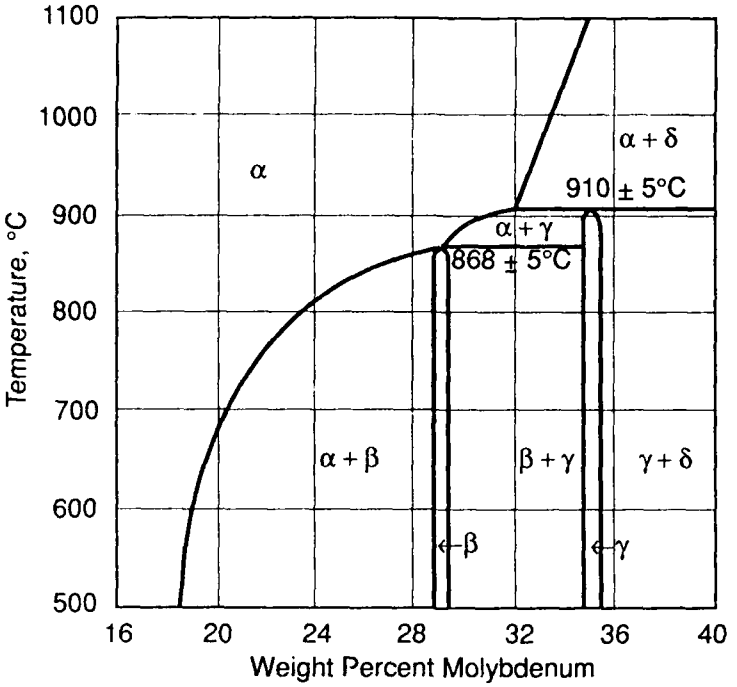

Figure 1: The nickel-rich portion of the Ni-Mo binary system[6].

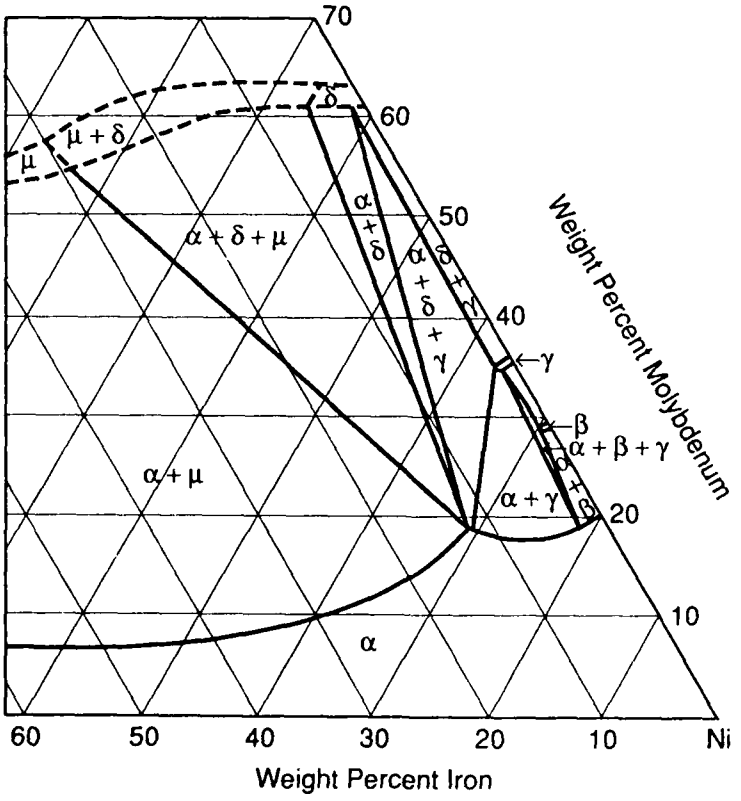

Figure 2: A portion of the proposed isothermal section of the Ni-Mo-Fe system at 700°C[5].

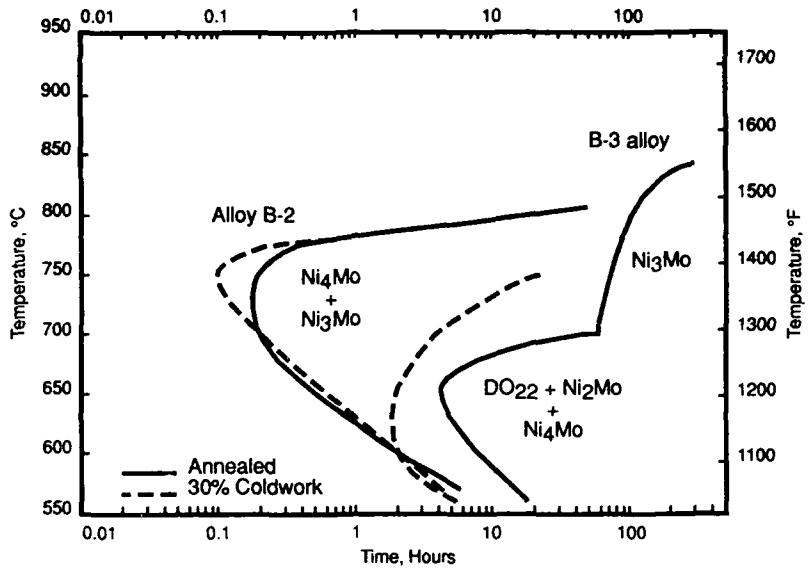

Figure 3: Comparison of T-T-T Characteristics of Alloy B-2 vs B-3 alloy

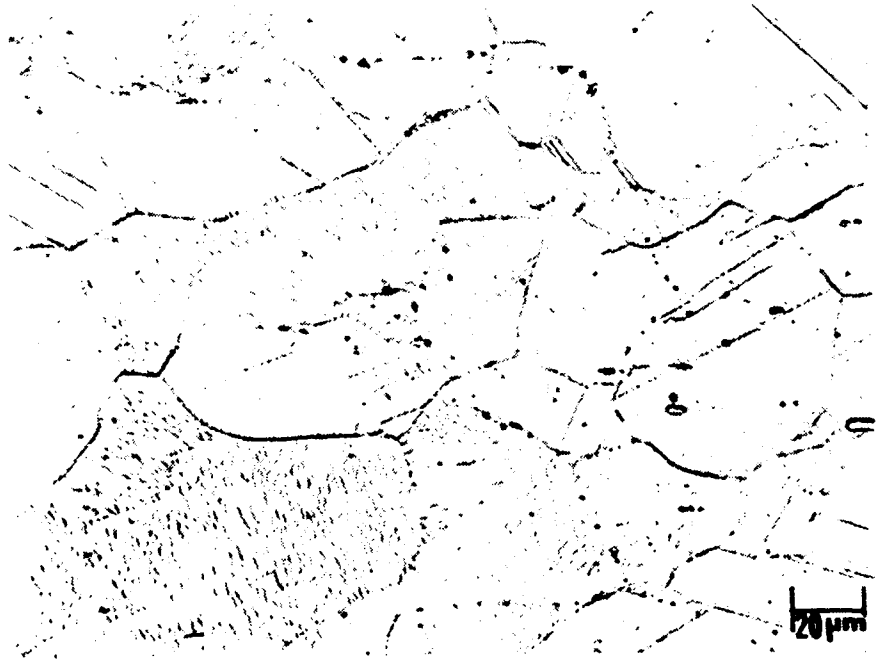

Figure 4: Microstructure of alloy B-2 aged at 700°C/24 hours.

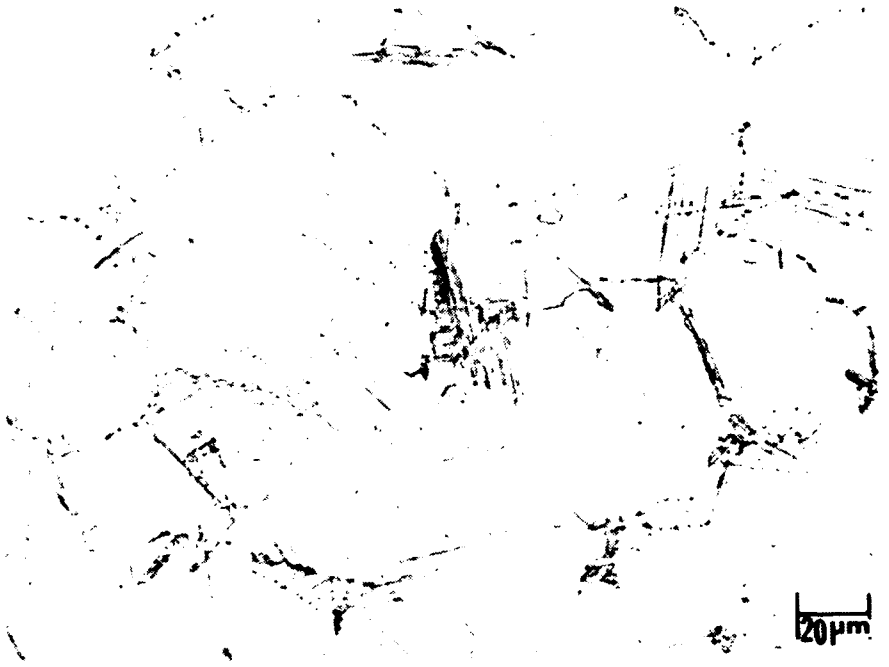

Figure 5: Microstructure of B-3 alloy aged at 750°C/100 hours.

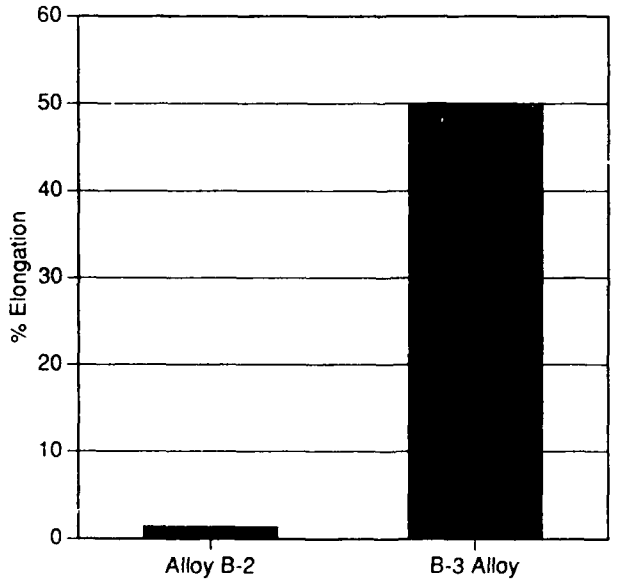

Figure 6: 700°C Tensile Elongations: Alloy B-2 vs B-3 alloy

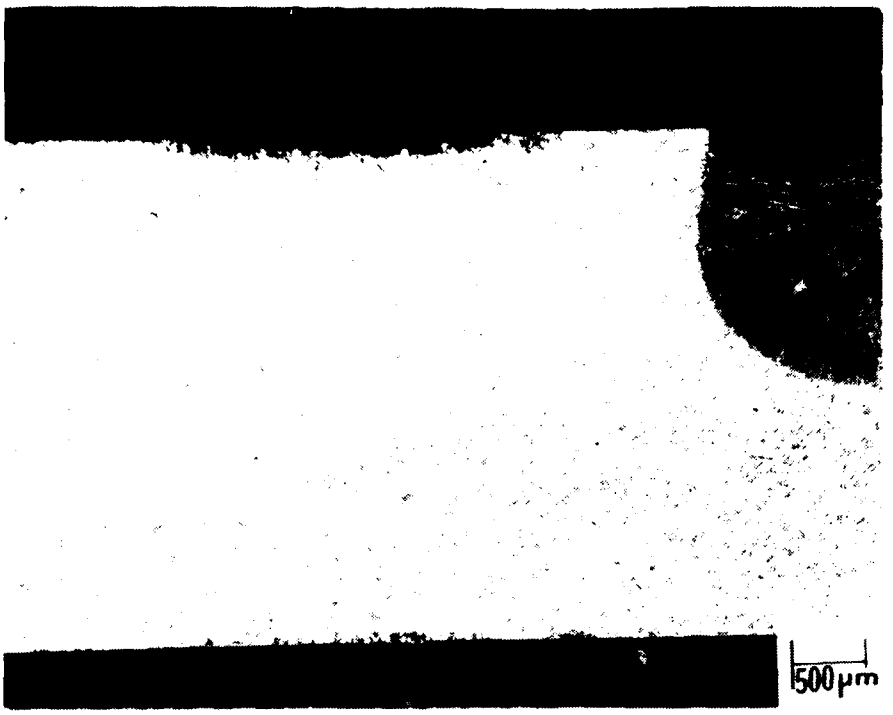

a) alloy B-2

b) B-3 alloy

Figure 7: Autogenously welded samples corrosion tested in boiling 60% H_2SO_4 + 8% HCl for 96 hours.

Corrosion behaviour of stainless maraging steel in acidic chloride solutions.

Marikkannu Viswanathan,
Central Electrochemical Research Institute,
Karaikudi - 623 006,
India.

K.Balakrishnan,
Central Electrochemical Researach Institute,
Karaikudi - 623 006,
India.

Abstract

Corrosion behaviour of stainless maraging steel in acidic chloride solutions has been investigated by electrochemical techniques. Polarization behaviour of the alloy steel in 'solution annealed' and 'maraged' condition differed considerably. In the solution annealed condition, active-passive transition was observed in acidic chloride solution whereas in maraged condition only active dissolution was observed. Both $[H^+]$ and $[Cl^-]$ were found to have a considerable effect on the dissolution mechanism of maraged alloy. The anodic reaction order with respect to $[H^+]$ and $[Cl^-]$ were found to be -0.51 and +0.509 respectively. A reaction mechanism sequence has been proposed for the observed experimental results.

Key terms : Maraging steel,acidic chloride,corrosion mechanism.

Introduction

The advent of high speed aircrafts and missiles has had a great impact on steel industries. The need for reduction in weight for effective fuel saving has led to the emergence of a series of special steels in 1950's. These are very low carbon content steels having very high yield strength and could be further strengthened by age-hardening or maraging. However these steels are sensitive to environments and stress corrosion cracking. Though the mechanical properties of these alloys have been studied in great detail much information is not avilable on the general corrosion behaviour of these steels in different environments. Some investigations have, however been reported on SCC of 18% Nickel maraging steel [1-4]. It would be of both scientific and technological interest to investigate the corrosion behaviour of these special grade steels in chloride solutions.

The present investigation aims at analysing the role of pH and chloride ion on the corrosion behaviour of the alloy in 'solution annealed' and 'maraged' conditions.

Experimental method

Electrode:
The stainless maraging steel was received in the form of sheet in the solution annealed condition and had the composition 0.02% Carbon, 12% Chromium, 12% Cobalt, 4% Nickel, 4% Molybdenium, 0.5% Titanium, 0.05% Aluminium, 0.1% Silicon and balance iron. Test electrodes of size 1 cm x 5cm were cut from the solution-annealed sheet and maraged at 450^{o}C for 4 hrs. After maraging, the samples were mechanically polished, degreased in acetone and then throughly washed in distilled water. Samples were lacquered so as to expose 1 cm^{2} area and were stored in a dessicator until used.

Electrolyte:
Electrolytes were prepared from A.R grade acids and double distilled water.

Technique:
Electrochemical polarisation measurements were made by using EG&G Princeton, NJ, model 273 potentiostat/galvanostat in conjunction with PAR universal programmer and X-Y recorder. Experiments were performed in a standard three electrode polarisation cell (saturated colomel electrode (SCE) as reference, platinum foil as the counter electrode and the sample as the working electrode). Polarization was performed with a scan rate of 1 mVs^{-1}.

Results and Discussion

Maraged condition:
Electrodissolution of stainless maraging steel was studied by anodic polarisation in 1M acidic chloride solution of various [H^{+}] and [Cl^{-}] at constant ionic strength.

Effect of pH: The polarisation behaviour of the alloy in solutions of various hydrogen ion concentrations are shown in Fig.1 and the results are summarised in Table.1. Anodic Tafel slope, b_a, is found to be 65 + 5 mV / decade.

The plot of log.anodic current at constant potential Vs. log. hydrogen ion concentration (Fig.2) shows that the anodic reaction order with respect to [H^{+}] is -0.5.

Effect of chloride ion : Electrodissolution of stainless maraging steel in 1 M acidic chloride solution of pH 0 with various chloride ion concentrations are shown in Fig.3 and the summary of the results in Table.2. The anodic Tafel slope, b_a, is 80 + 10 mV/decade. The anodic Tafel slope in chloride-perchlorate mixture is slightly higher than the value of 65 + 5 mV decade^{-1} obtained for 1 M chloride solution. Corrosion potential shifts cathodically as concentrations of chloride ion is increased.

The anodic reaction order with respect to chloride ion in solution of pH 0, [illegible] potential is + 0.5. (Fig.4)

The results presented indicate that the kinetics of dissolution of stainless maraging steel depend on both $[H^+]$ and $[Cl^-]$ and follows the empherical relationship

$$i_a = K [Cl^-]^{+0.5} [H^+]^{-0.5} \exp FE/RT \quad (1)$$

These experimental results can be interpreted by a mechanism analogous to the chloride accelerated mechanism for iron[5] and nickel[6] electrodissolution.

$$M + H_2O \rightleftharpoons M.H_2O_{ad} \quad (i)$$

$$M.H_2O_{ad} + Cl^- \rightleftharpoons M Cl_{ad} + H_2O \quad (ii)$$

$$M Cl_{ad} + H_2O \rightleftharpoons M ClOH^-_{ad} + H^+ + e \quad (iii)$$

$$M ClOH^-_{ad} \longrightarrow M ClOH + e \quad (iv)$$

$$M ClOH + H^+ \rightleftharpoons M^{++} + Cl^- + H_2O \quad (v)$$

It is assumed that step (iv) is the rate controlling and steps (i) to (iii) are in quasi-equilibrium and $M ClOH^-$ follows Temkin adsorption behaviour with its surface converage, θ, ranging between 0.2 and 0.8. Similar to analysis by Chin[7] the surface coverage can be determined as

$$f(\theta) = -\ln \frac{k_i k_{ii} k_{iii}}{k_{-i} k_{-ii} k_{-iii}} [Cl^-] [OH^-] \exp FE/RT \quad (2)$$

The rate of step (iv) is

$$r_{(iv)} = k_{(iv)} \exp \beta FE/RT \exp \gamma f(\theta) \quad (3)$$

for intermediate surface coverage ($0.2 < \theta < 0.8$). Equations (2) and (3) give

$$r_{(iv)} = K [Cl^-] [OH^-] \exp (\beta + \gamma) FE/RT \quad (4)$$

if γ and β are assumed equal to 0.5, the rate of metal dissolution can be determined from equation (4) as

$$i_a = K_a [Cl^-]^{+0.5} [OH^-]^{+0.5} \exp FE/RT \quad (5)$$

which is in accord with the empherical representation in equation (1).

A salient feature of the mechanisms is the direct participation of hydroxyl ions in the dissolution process in which the bulk electrolyte is acidic. The involvement of OH^- ions at the metal / acid interface was first suggested by Bonhoeffer and Heusler[8]. The generation of OH^- ions in acid solutions is presumed to occur by dissociation of water molecules at the electrode surface. In

presence of chloride ion, simultaneous or competative adsorption is possible depending upon the ionic strength of individual ion. In the present case both OH^- as well as Cl^- ions are getting adsorbed.

Solution annealed Steel:
The effect of pH on the polarization behaviour of the alloy in solution annealed condition is shown in Fig.5. The anodic curve shows the passive behaviour of the alloy steel under solution annealed condition in acidic chloride solutions. Increase in pH of the solution widens the passive region of the curve and lowers the passivation current. (Table 2)

On the other hand in solution of zero pH with varying chloride ion concentration (Fig.6 and Table 2), the dissolution rate is independent of chloride ion concentration.

Conclusion

In summary, the results of the present work indicate that the kinetics of dissolution of stainless maraging steel (maraged) in 1M acidic chloride solution strongly depends on the concentration of both H^+ and Cl^- ions and proceeds in a manner similar to iron dissolution through the formation of metal chloro complex as the reaction intermediate.

Solution annealed steel shows passive behaviour in acidic chloride solution and the characteristics of polarisation curve depend on the pH of the soultion.

Acknowledgement

The authors would like to acknowledge Prof.G.V.Subba Rao, Director, CECRI, Karaikudi for his kind permission to publish this paper.

Reference

1. J.A.S.Green and F.G.Haney, Corrosion, 23 1 (1957) p.5

2. E.H.Phenlps and A.W.Loginow, Corrosion 16 3 (1960) p.97

3. R.B.Setterlund, Mat.Prot. 4 12 (1965) p.27

4. S.W.Dean and H.R.Copson, Corrosion 21 3 (1965): p.95

5. R.J.Chin and K.Nobe,J.Electrochem.Soc.119 (1972): p.1457

6. A.Bengali and K.Nobe,J.Electrochem.Soc.126 7 (1979): p.1118

7. K.F.Bonhoeffer and K.E.Heusler, Z.Electrochem 61 (1957): p.122

TABLE 2

SUMMARY OF ANODIC POLARIZATION DATA FOR STAINLESS MARAGING STEEL (SOLUTION ANNEALED CONDITION) IN 1 M ACIDIC CHLORIDE SOLUTIONS.

S.No.	Electrolyte	$[H^+]$, M	$[Cl^-]$	E_{corr} mV/SCE	Passivation characteristics	
					Passivation current $\mu A/cm^2$	Passive range mV Vs. SCE
1.	0.001 M HCl + 0.999 M NaCl	10^{-3}	1	-80 ± 10	0.4	−40 to + 100
2.	0.01 M HCl + 0.99 M NaCl	10^{-2}	1	-70 ± 10	0.4	0 to + 70
3.	0.1 M HCl + 0.9 M NaCl	10^{-1}	1	- 60 ± 10	0.8	+ 20 to + 60
4.	1 M HCl	1	1	-240 ± 10	12.0	−200 to + 40
5.	0.1 M HCl + 0.9 M NaCl	1	10^{-1}	-235 ± 10	9.0	—
6.	0.01 M HCl + 0.99 M NaCl	1	10^{-2}	-225 ± 10	7.0	—
7.	0.001 M HCl + 0.999 M NaCl	1	10^{-3}	-220 ± 10	5.0	—

TABLE 1
SUMMARY OF ANODIC POLARIZATION RESULTS FOR STAINLESS STEEL (MARAGED CONDITION) IN 1 M ACIDIC CHLORIDE SOLUTIONS

S.No.	Electrolyte	$[H^+]$,M	$[Cl^-]$	E_{corr} mV/SCE	b_a mV/dec	Anodic Current at constant anodic potential *	Anodic Current at constant anodic potential **
1.	0.0001 M HCl + 0.9999 M $HClO_4$	1	10^{-4}	-265 ± 5	5	0.12	0.30
2.	0.001 M HCl + 0.999 M $HClO_4$	1	10^{-3}	-275 ± 5	75	0.30	0.65
3.	0.01 M HCl + 0.99 M $HClO_4$	1	10^{-2}	285 ± 5	75	1.00	1.60
4.	0.1 M HCl + 0.9 M $HClO_4$	1	10^{-1}	-295 ± 5	80	2.00	4.00
5.	1 M HCl	1	1	300 ± 10		4.50	10.00
6.	1 M HCl	1	1	-300 ± 10	70	0.08	0.25
7.	0.1 M HCl + 0.9 M NaCl	10^{-1}	1	-320 ± 10	65	0.30	0.80
8.	0.01 M HCl + 0.99 M NaCl	10^{-2}	1	-350 ± 10	60	1.00	2.50
9.	0.001 M HCl + 0.999 M NaCl	10^{-3}	1	-380 ± 10	60	3.50	8.00
10.	0.0001 M HCl + 0.9999 M NaCl	10^{-4}	1	-400 ± 10	60	8.00	27.00

* for 1 to 5 E_a = -125 and 6 to 10 E_a 250mV respectively

** for 1 to 5 E_a = 100 and 6 to 10 E_a 225mV

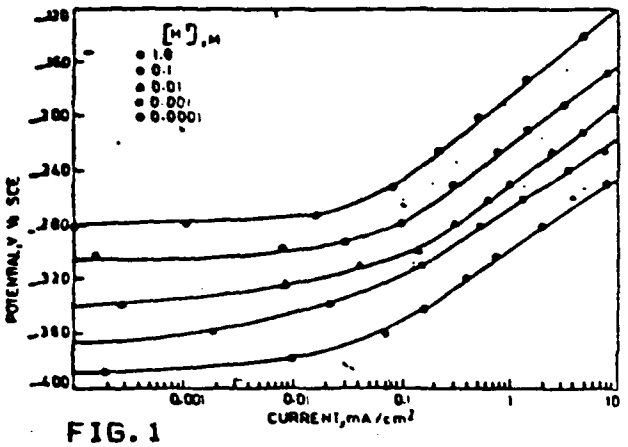

FIG. 1

ANODIC POLARISATION CURVES OF MARAGED STEEL IN xM HCl + yM NaCl, x+y = 1M SOLUTIONS.

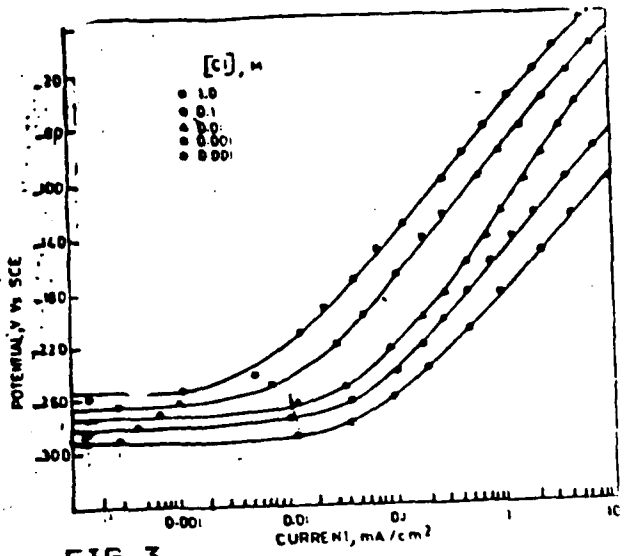

FIG. 3

ANODIC POLARISATION PLOT FOR MARAGED STEEL IN xM HCl + yM HClO, (x+y) = 1M SOLUTIONS

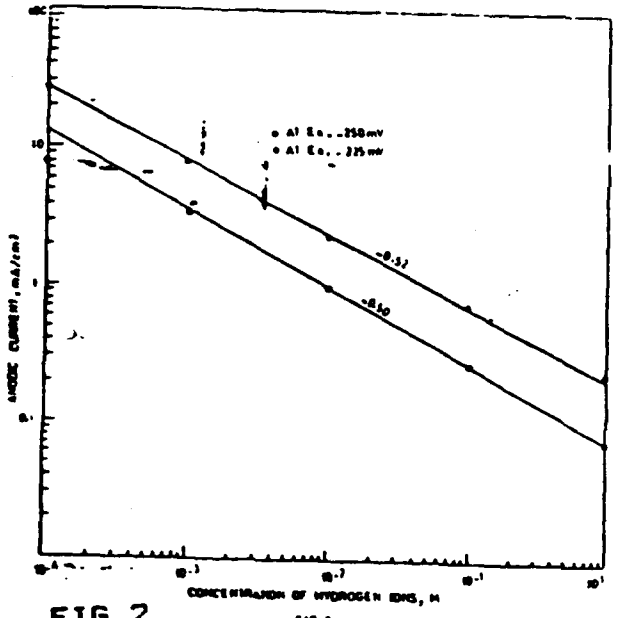

FIG. 2

ANODIC REACTION ORDER PLOT FOR MARAGED STEEL - EFFECT OF [H⁺]

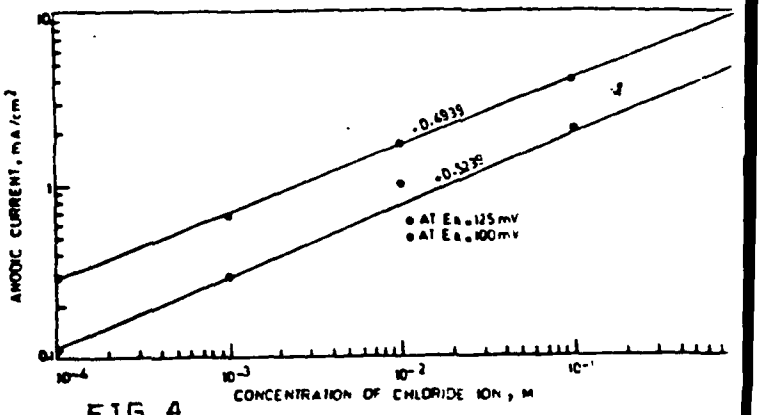

FIG. 4

ANODIC REACTION ORDER PLOT FOR MARAGED STEEL - EFFECT OF [Cl⁻]

FIG. 1 ANODIC POLARISATION CURVES OF MARAGED STEEL IN x M HCl + y M NaCl, x + y = 1M SOLUTIONS.

FIG. 2 ANODIC REACTION ORDER PLOT FOR MARAGED STEEL - EFFECT OF [H^+]

FIG. 3 ANODIC POLARISATION PLOTS FOR MARAGED STEEL IN x M HCl + y M $HClO_4$ (x + y) = 1M SOLUTIONS.

FIG. 4 ANODIC REACTION ORDER PLOT FOR MARAGED STEEL-EFFECT [Cl^-]

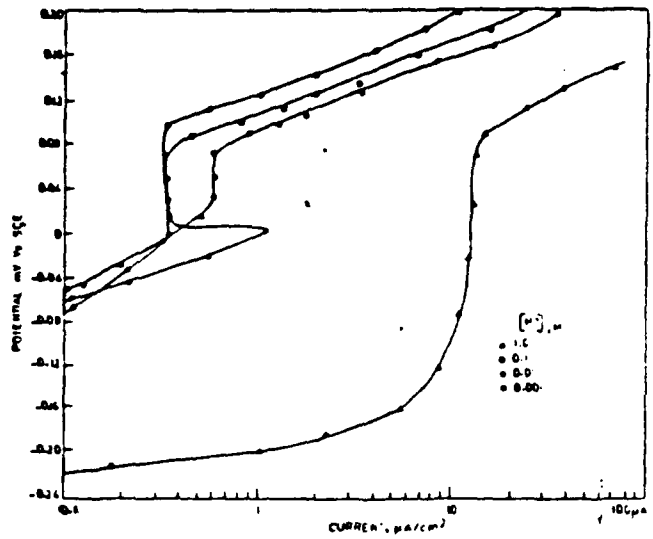

FIG 5
ANODIC POLARISATION CURVES OF SOLUTION
ANNEALED STEEL IN xM HCl + yM NaCl, x+y = 1M.

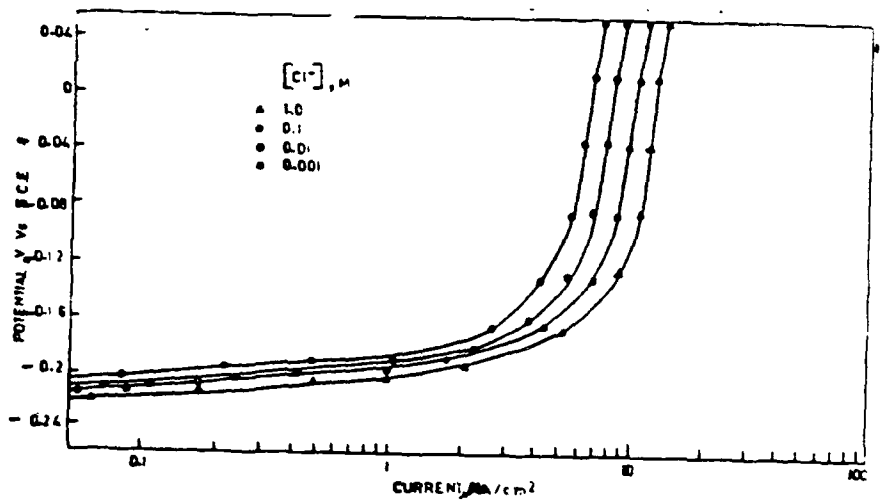

FIG 6
ANODIC POLARISATION CURVES OF SOLUTION
ANNEALED STEEL IN xM HCl + yM $HClO_4$, x+y = 1M.

FIG.5 ANODIC POLARISATION CURVES OF SOLUTION ANNEALED STEEL IN x M HCl + y M NaCl, x + y = 1 M SOLUTIONS.

FIG.6 ANODIC POLARISATION CURVES OF SOLUTION ANNEALED STEEL IN x M HCl + y M $HClO_4$ x + y = 1 M SOLUTIONS.

Electrochemical Characterization of Ni-based Soft Magnetic Alloys

Gaii R. Ball
Department of Materials Science and Engineering
The Case School of Engineering
Case Western Reserve University
Cleveland OH 44106

J. H. Payer
Department of Materials Science and Engineering
The Case School of Engineering
Case Western Reserve University
Cleveland OH 44106

Abstract

The results of an investigation of the passive behavior of bulk soft magnetic alloys as influenced by electrolyte pH, chloride content and alloy composition are described A series of Ni-Co alloys and a single Ni-Fe alloy were evaluated by potentiodynamic anodic polarization in 0.5 M Na_2SO_4 solutions of pH 3, 7, and 10 at chloride concentrations of 0, 10^{-3}M, and 10^{-2}M. The Ni-Co alloys showed active-passive behavior in all solutions with the exception of the $Ni_{0.20}Co_{0.80}$ which was active in all solutions. Possible explanations for this active behavior are discussed. For a given electrolyte condition, the polarization curves for the Ni-Co alloys which showed active-passive behavior were indistinguishable. The $Ni_{0.40}Fe_{0.60}$ alloy showed considerable pitting upon exposure to chloride (10^{-2}M). The Ni-Co alloys which showed active-passive behavior were less susceptible to pitting than the Ni-Fe alloy.

Key terms: nickel, cobalt, soft magnetic alloys, anodic polarization, chloride effects

Introduction

Electrochemical characterization of Ni-Co and Ni-Fe alloys is of considerable interest, as these soft magnetic materials are frequently used in magnetic recording heads. The investigation reported here is a characterization study of the corrosion behavior of these alloys in a variety of pH and chloride concentration conditions.

These studies will provide a basis for predicting in-service corrosion behavior as well as corrosion or etching behavior during the manufacturing process. The Ni-Fe system has been studied.[1, 2, 3] However, little work has been done on the Ni-Co system.

The corrosion behavior of a range of Ni-Co ($Ni_{0.2}Co_{0.8}$, $Ni_{0.4}Co_{0.6}$, $Ni_{0.6}Co_{0.4}$, and $Ni_{0.8}Co_{0.2}$) alloys and one Ni-Fe ($Ni_{0.4}Fe_{0.6}$) alloy was studied using potentiodynamic anodic polarization. This technique was used to determine the characteristic

potentials and current densities for each alloy over a range of pH. The effect of chloride ion on the corrosion behavior was also examined. Metallographic and structural (X-ray diffraction) studies of these alloys were also conducted to determine the effect of microstructure on corrosion behavior.

Experimental

The bulk alloys listed in Table I were acquired from Materials Research Corporation (Orangeburg, NY) through P. Peterson at IBM/ San Jose and were subsequently analyzed by X-ray fluorescence (XRF). Ni 200 (99.74%) was supplied by Metal Samples, (Munford, AL) and Co (99.9%) was supplied by Goodefellow Corp. (Malvern, PA). Immediately prior to electrochemical testing, the samples were polished to an 800 grit (FEPA) finish, rinsed in acetone, methanol, and distilled water.

Anodic polarization measurements were made using a standard three electrode cell[4], with the alloy sample as the working electrode (2.54 cm^2 electrode area). The electrolyte was a 0.5 M Na_2SO_4 solution prepared from distilled water and reagent grade chemicals and the pH was adjusted by NaOH and H_2SO_4 titration. The pH measurements were taken with an Orion Ross glass electrode and measured on an Orion 901 Ion analyzer. All tests were conducted at 30.0 ± 0.2°C. The chloride content was set at 0, 10^{-3}, and 10^{-2} M concentrations by the addition of NaCl. The solutions were deaerated by bubbling N_2 through the cell for 1 hour prior to testing. During the test, the N_2 flowed over the electrolyte, and mild agitation was accomplished by use of a magnetic stir bar and plate.

Electrochemical potentials were measured with respect to a saturated calomel electrode (SCE) via a Luggin capillary salt bridge tube that was placed less then 3 mm from the surface of the working electrode. A Pt mesh counterelectrode was used. The electrochemical cell was controlled by an EG&G-PAR model 173 potentiostat and model 175 universal programmer. Data were gathered via PC-based data acquisition hardware and software. The potentiodynamic scan rate was 2 mv/sec for all reported curves. Upon insertion into the cell, a measurement of the free corrosion potential was taken after the working electrode was immersed in the cell for approximately 30 seconds. The working electrode was subjected to a pretreatment approximately 250 mV below this free corrosion potential for 1 minute. In the case of an active metal, the sweep started at this potential and increased anodically through the free corrosion potential and into the active regime until the current was greater than 10^{-1} amps. If a metal showed an active-passive transition, the sweep continued through this transition and the passive region until the transpassive region was observed by a steady increase in current of several orders of magnitude. The sweep direction was then reversed, and data collection continued until the current density crossed over the passive curve observed during the anodic sweep.

Structural analysis of the alloy and pure metal samples were done by X-ray diffraction of polycrystalline bulk samples using Cu-Kα (λ = 1.5418Å) radiation. Scans were measured from 2θ = 40° to 55° at a scan rate of 0.025°/sec. Diffraction data was gathered via PC-based data acquisition software and hardware.

Results

Overview

The objective of this study was to determine by anodic polarization measurements the corrosion behavior as a function of solution pH and chloride level of five alloys: $Ni_{0.2}Co_{0.8}$, $Ni_{0.4}Co_{0.6}$, $Ni_{0.6}Co_{0.4}$, $Ni_{0.8}Co_{0.2}$ and $Ni_{0.4}Fe_{0.6}$. In addition, the corrosion behavior of Ni200 and 99.9% cobalt were also studied under the same conditions. Below are the results of the studies on the effect of pH, chloride concentration and alloy composition on the corrosion behavior.

In general, the $Ni_{0.2}Co_{0.8}$ alloy exhibited active behavior and did not passivate in any of the electrolytes, as seen in Figure 1. In the curve for the pH3 electrolyte, the free corrosion potential, E_{corr}, was observed at -410mV-SCE. The current increased with increasing potential until the test was stopped at 0.0V-SCE. The pure cobalt also did not passivate under any of the conditions tested. This result is consistent with the reported critical current density for passivation for cobalt in 1*N* H_2SO_4 is 500 mA/cm^2, well beyond the range of current densities examined here.[5] All of the alloys except $Ni_{0.2}Co_{0.8}$ exhibited classic active-passive-transpassive behavior at all 3 pH levels, as seen in Figures 2-4. For example, the behavior of $Ni_{0.6}Co_{0.4}$, shown in Figure 2, had a free corrosion potential, E_{corr}, at -410 mV-SCE. As the potential was increased, the metal entered the active corrosion regime, as seen by the increasing current with potential. At the passivation potential, -30 mV-SCE, the alloy has reached the critical current density for passivation, 17.7 mA/cm^2, and passivation occurs. In the passive regime, the passive current density is 0.27 mA/cm^2. This passive behavior continues to the pitting potential, E_{pit}, +750 mV-SCE, at which point the current once again begins to increase with increasing potential in the transpassive region. The potential is reversed at +1.83V-SCE and the current once again decreases along the same curve as the increasing potential curve.

Effect of pH

The effect of electrolyte pH on the polarization behavior was consistent for all of the alloys tested. Decreasing the pH shifted the entire polarization curve to more anodic potentials and increased the critical current density for passivation. The average anodic shift was -52 mV/pH unit.

For the passivating Ni-Co alloys, ($Ni_{0.4}Co_{0.6}$, $Ni_{0.6}Co_{0.4}$, and $Ni_{0.8}Co_{0.2}$) the anodic polarization curves all show typical active/passive/transpassive behavior. The observed increase in the critical current density for passivation is typical for an active/passive metal.[5, 6] The critical current density for passivation, i_{cp},varied over three orders of magnitude with pH. For example, in chloride-free solutions, i_{cp} for the Ni0.6Co0.4 alloy in the pH3 electrolyte was 17.8 mA/cm^2 whereas the critical current density for passivation in the pH7 solution was 1.91 mA/cm^2 and i_{cp} at pH10 was 11μA/cm^2.

The $Ni_{0.4}Fe_{0.6}$ alloy also showed typical active/passive/transpassive behavior and the influence of pH on corrosion behavior was similar to the passivating Ni-Co alloys. The anodic shift with pH was linear with a slope of -51mV/pH unit, and the critical current density (in chloride-free solutions) decreased from 66.1 mA/cm^2 at pH3 to 0.78 mA/cm^2 at pH10.

Effect of Alloy Composition

In the Ni-Co system, all of the alloys examined showed similar active behavior, with free corrosion potentials near that of nickel, as shown in figure 5. At pH3, nickel had an E_{corr} of -410mV-SCE, E_{corr} of cobalt was -510mV-SCE and the E_{corr} of the alloys ranged from -380 to -430mV-SCE. The Ni-Fe alloy also had a free corrosion potential near that of nickel, -430mV-SCE at pH3.

Although all of the Ni-Co alloys showed similar active behavior, one of the alloys, $Ni_{0.2}Co_{0.8}$, did not passivate under any of the conditions studied. The remaining Ni-Co alloys, ($Ni_{0.4}Co_{0.6}$, $Ni_{0.6}Co_{0.4}$, and $Ni_{0.8}Co_{0.2}$) showed essentially identical anodic polarization behavior, as seen in figures 2-4.

The lack of passivity of the $Ni_{0.2}Co_{0.8}$ alloy merited further attention. The microstructure of the alloys was examined by metallurgical analysis and by X-ray diffraction to determine if there was any microstructural differences between the different alloy compositions. In addition, the effects of microstructure on the corrosion behavior were observed by microscopic examination of the metal surface after anodic dissolution.

Metallographic analysis of polished alloy specimens revealed that the microstructure of the $Ni_{0.2}Co_{0.8}$ alloy was different than that of the other alloys. Where the higher Ni alloys showed an equiaxed single phase structure (Figure 6), the $Ni_{0.2}Co_{0.8}$ alloy showed a banded microstructure, as seen in Figure 7. Based on the Ni-Co phase diagram[7], this structure is an allotropic hexagonal close-packed (HCP) phase for alloys with X_{Ni}<~35%. The $Ni_{0.2}Co_{0.8}$ alloy is within this ε-Co phase field, The martinsitic transformation $\alpha\text{-}Ni_{(FCC)} \rightarrow \varepsilon\text{-}Co_{(HCP)}$ occurs around 300°C. The banded structure observed is consistent with this type of diffusionless transformation.

X-ray diffraction spectra of Ni, Co, and the Ni-Co alloys are shown in Figure 8. Peaks were seen near $2\theta = 44.4°$ and 51.6°. These peaks correspond to FCC reflections for Ni or Co.[8,9] In addition, a small peak was also seen in the spectrum of the $Ni_{0.2}Co_{0.8}$ alloy at $2\theta = 47.2°$, which corresponds to the strongest cobalt HCP reflection.[9]

Examination of the $Ni_{0.2}Co_{0.8}$ metal surface after anodic dissolution showed general corrosion with some grain etching. This etching is probably due to variations in crystallographic orientation of the individual grains, and not the phases (FCC or HCP) within the grain, as these are both close-packed phases. There is no evidence of microstructural effects causing the observed active behavior in the $Ni_{0.2}Co_{0.8}$ alloy.

Effect of Chloride Concentration

The effect of chloride concentration on the passivation behavior depended upon alloy composition. In general, the passivation behavior of the Ni-Co alloys was not greatly affected by the chloride levels tested, and the non-passivating $Ni_{0.2}Co_{0.8}$ alloy was not affected by the chloride levels used. On the other hand, the $Ni_{0.4}Fe_{0.6}$ alloy was strongly affected by the higher (10^{-2}M) chloride levels, and pitting was observed in the alloy exposed to this chloride level.

The Ni-Co alloys were not affected by the lower (10^{-3} M) chloride concentration, but at higher chloride levels (10^{-2} M), changes in the anodic polarization were observed, as seen in Figure 9. For the $Ni_{0.4}Co_{0.6}$ alloy in pH3 electrolyte, the critical current density increased from 15mA/cm2 at 0 and 1mM chloride to 30mA/cm2 at 10mM. Some changes were evident in the passive current suggesting degradation of the passive film as the transpassive region was approached, as seen in $Ni_{0.4}Co_{0.6}$ at pH3 (Figure 9) The free corrosion potential was unaffected by chloride concentration, which is consistent with the observation that the non-passivating $Ni_{0.2}Co_{0.8}$ alloy was unchanged in the chloride-containing electrolytes.

The Ni-Fe alloy was affected more strongly by chloride in the electrolyte than the Ni-Co alloys. This was most apparent in the pH3, 10 mM chloride solutions as seen in Figure 10; the critical current density for passivation increased from 25 mA/cm2 for 0 and 1 mM chloride concentrations to 83mA/cm2 at 10mM chloride. The passivation current was not affected, but the pitting potential dropped from 1.29 to 1.18 to 0.51V-SCE for the 0, 1mM and 10 mM chloride levels, respectively. The Ni-Fe alloy was severely pitted at the higher chloride levels, as indicated by the hysteresis in the anodic polarization curve and also by visual observation of pits on the sample after testing. A pitting hysteresis loop was observed in the 10 mM chloride electrolyte for all three pH conditions The range of stable passivation (between E_{pass} and E_{prot}) increased from 0.33 V at pH3 to 0.51 V at pH10 whereas the range of stable passivation (between Epass and Epit) ranged from 1.39 V at pH3 to 1.37 V at pH7 and 0.98 V at pH10.

Discussion

Tendency to Passivate

Active Alloys. The lack of passivity of the $Ni_{0.2}Co_{0.8}$ alloy was studied. Microstructural characterization revealed that the $Ni_{0.2}Co_{0.8}$ alloy differed from the other Ni-Co alloys. Where metallurgical examination showed a single phase solid solution for the high Ni alloys, the $Ni_{0.2}Co_{0.8}$ alloy showed a typical martensitic structure. Structural analysis by X-ray diffraction revealed that the pure metals and high Ni-Co alloys had FCC structures, but the $Ni_{0.2}Co_{0.8}$ alloy was indeed composed of two allotropic phases, FCC and HCP. However, this microctructural difference between the $Ni_{0.2}Co_{0.8}$ alloy and the higher Ni alloys is *not* the cause of the active behavior, in that there is no preferential attack of either phase, but only general corrosion is observed on the $Ni_{0.2}Co_{0.8}$ alloy.

A possible explanation for the active behavior is based on Newman and Sieradzki's geometric approach to the passivation of Fe-Cr alloys based on percolation theory.[10,11] By considering the arrangement of a minority species in a random binary solid solution, (Cr in a Fe-Cr alloy) they have suggested that incomplete passivation in Fe-Cr alloys occurs when there is not a sufficient amount of Cr on the surface to form a continuous passive film. Once a critical "threshold concentration" of the minority species is reached, a continuous passive film is formed and stable passivation occurs; once the minority species concentration exceeds the threshold value, the passive behavior does not depend on the minority species concentration.

A similar argument is applicable to the Ni-Co system. Between 20 and 40wt% Ni, complete passivation occurs. Based upon the indistinguishable passivation behavior of higher Ni alloys, and the similarity of their behaviors to that of pure nickel, the nickel appears to dominate the anodic polarization behavior. The $Ni_{0.2}Co_{0.8}$ alloy may not be able to completely passivate because there is insufficient nickel to form and maintain a continuous passive film on the surface.

Passivating Alloys. The critical current density of passivation (a measure of the ease of passivation) among passivating alloys (Ni-Co where $X_{Ni} \geq 0.4$ and Ni-Fe) varies with both electrolyte pH and chloride content. An increase in critical current density indicates that the alloy is not able to form a passive film as easily as when the critical current density is lower. As reported earlier, i_{cp} increased with decreasing pH from 0.1 mA/cm^2 at pH10 to ~1 mA/cm^2 at pH7 to ~10 mA/cm^2 at pH3. This increase in critical current density is related to the ability of the metal to form the passive film on its surface. If this film is a hydroxide species, and it forms by the following type of reaction:

$$Me^{n+} + nOH^- \rightarrow Me(OH)_n \qquad [1]$$

then the solubility product of that reaction would be $K_{sp} = [Me^+][OH^-]^n$. As the pH decreases, the hydroxyl concentration decreases, and the metal ion concentration must be larger before K_{sp} is reached and formation of the passive film occurs; this higher metal ion concentration correlates to reaching a higher critical current density before the onset of passivation.

In comparing the critical current densities for the Ni-Co alloys ($i_{cp} \approx 10$ mA/cm^2 at pH3) and the Ni-Fe alloy ($i_{cp} \approx 25$ mA/cm^2 at pH3), the solubility product correlates with this behavior. In Table II, the solubility products of a number of metal hydroxides are listed.[12] At a given pH (constant hydroxyl concentration), the concentration of metal ions necessary for the formation of a passive film is inversely proportional to the solubility product of the film species. Since K_{sp} for ferrous hydroxide, $Fe[OH]_2$ is orders of magnitude lower than the K_{sp} of either nickel(II) or cobalt(II) hydroxide, a higher metal ion concentration is necessary for ferrous hydroxide formation, and a higher current density is reached before the onset of passivation of the Ni-Fe alloy than a Ni-Co alloy.

The effect of chloride concentration on critical current density for passivation is indicative of the observation that chloride interferes in the formation of passive films. The observation in these studies was that the critical current density was not affected by the 1 mM chloride solution, but increased current density was seen along with other signs of passive film degradation at $[Cl^-]$ = 10 mM, as shown in Figures 9 and 10.

Stability and Breakdown of Passivity

An explanation for the greater pitting susceptibility of the Ni-Fe alloy is based upon the solubility properties of constituent metal hydroxides. In the case of Ni-Co alloys, there is little difference between the solubility of nickel(II) and cobalt(II) hydroxides, as seen in Table II.

However, in the case of a Ni-Fe alloy, there are considerable differences between the nickel(II) and the ferric hydroxides. Consider the following hydrolysis reactions:

$$Ni^{2+} + H_2O \longrightarrow Ni(OH)_2 + 2H^+ \quad [2]$$

$$Co^{2+} + H_2O \longrightarrow Co(OH)_2 + 2H^+ \quad [3]$$

$$Fe^{2+} + H_2O \longrightarrow Fe(OH)_2 + 2H^+ \quad [4]$$

$$Fe^{3+} + 3\,H_2O \longrightarrow Fe(OH)_3 + 3H^+ \quad [5]$$

In these reactions, the hydrolysis of 2^+ cations yields 2 H^+ ions whereas the ferric hydrolysis yields 3 H^+ ions and is, on a per metal ion basis, more acidifying. In addition, the solubility product of ferric hydroxide is 18 orders of magnitude smaller than that of nickel(II) or cobalt (II) hydroxide. Once localized passive film breakdown begins (in the transpassive regime), fewer ferric ions than nickel or cobalt ions must enter the solution before the hydrolysis reaction is triggered. Once the acidifying hydrolysis reactions begin, the metal is more difficult to repassivate in those localized areas, and auto-catalytic pitting begins.

Summary

Based upon this study, the following comments may be made:

1. The effect of pH on these alloys is consistent with traditional active and active-passive-transpassive metals. In general, the corrosion resistance of the alloys increase with increasing pH; i.e. the alloys passivate more readily and the critical current density for passivation decreases with increasing pH.

2. The effect of alloy constitution was marked in the Ni-Co system. There appears to be a minimum nickel concentration between 20 and 40 wt.% required for complete passivation. Above this threshold value, anodic polarization behavior has no alloy composition dependence, based on the indistinguishable anodic behavior of the Ni-Co alloys with $X_{Ni} \geq 40$ wt.%. Below the threshold value, active corrosion and no passivity is observed.

3. The Ni-Fe alloy was more susceptible to chloride pitting than the Ni-Co alloys. These Ni-Co alloys showed minor effects at high [Cl^-] levels (10mM NaCl) whereas the Ni-Fe alloy was severely pitted.

Future work

Additional characterization of these alloys is warranted. Electrolytes with higher chloride concentrations (5×10^{-2} to 10^{-1} M) will be used to further examine the pitting behavior of Ni-Co alloys. The passive films formed on these alloys by anodic polarization will also be analyzed and compared to the bulk alloys; the similarity of the corrosion behavior in the passivating Ni-Co films suggests a similar protective film, despite compositional variations among the alloys themselves.

Acknowledgments

The authors would like to acknowledge the support of this research by IBM (Shared University Program grant #1314) and the National Science Foundation, Division of Materials Research (Grant DMR-901475; sponsor, Dr. Bruce A. MacDonald).

References

1 Lee, C. H., Stevenson, D. A., Lee, L. C., Bunch, R. D., Walmsley, R. G., Juanitas, M. D., Murdock, E., and Opfer, J. E., "Electrochemical and Structural Characterization of Permalloy," *Corrosion of Electronic and Magnetic Materials, ASTM STP 1148,* P. J. Peterson, Ed., American Society for Testing and Materials, Philadelphia, 1992, pp. 102-114.

2 Lee, W. Y., Seigmann, Hans C., Eldridge, Jerome M., *Journal of the Electrochemical Society,* **124**, 1744-51 (1977).

3 Dagan, G., Tomkiewicz, M., *Journal of the Electrochemical Society,* **139**, 461-6 (1992).

4 ASTM Standard G5-82, "Standard Reference Method for Making Potentiostatic and Potentiodynamic Anodic Polarization Measurements", American Society for Testing and Materials, Philadelphia, 1982.

5 Uhlig, H. H., Corrosion and Corrosion Control, 3d ed., p 371, Wiley-Interscience, New York, (1985).

6 Fontana, Mars, Corrosion Engineering, 3d ed., p. 471, McGraw-Hill Book Company, New York, (1986).

7 Nishizawa, T and Ishida, K., *Bulletin of Alloy Phase Diagrams,* **4**, 390, (1983).

8 Swanson, Tatge, *National Bureau of Standards (U.S.),* Circ. **539**, 13, (1953).

9 Troiano and Tokich, *Trans. AIME,* **175**, 728 (1948).

10 Newman, R.C., Meng, F.T., Sieradzki, K., *Corrosion Sciencse,* **28**, 523-7 (1988).

11 Qian, S., Newman, R.C., Cottis, R.A., *Journal of the Electrochemical Society,* **137**, 435-9 (1990).

12 CRC Handbook of Chemistry and Physics, 60th ed. CRC Press, 1985-86.

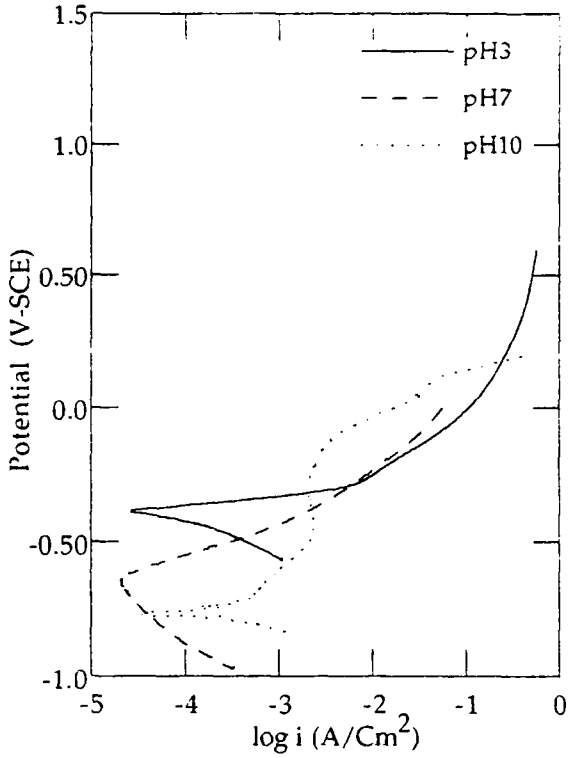

Figure 1: Polarization Curves of $Ni_{0.2}Co_{0.8}$ alloy

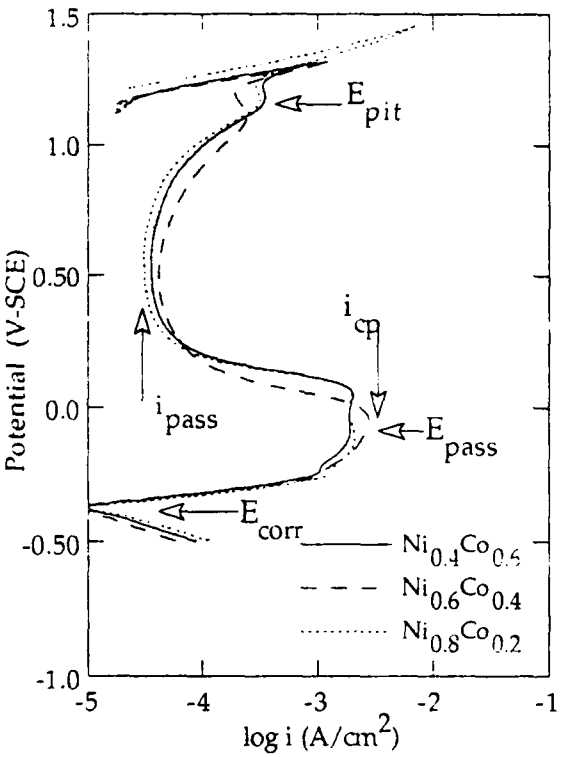

Figure 2: Polarization Curves for Ni-Co alloys at pH3

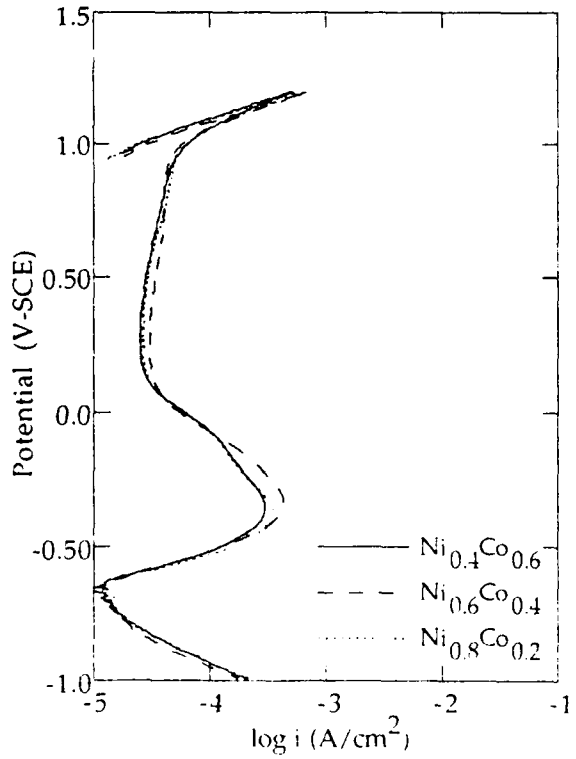

Figure 3: Polarization Curves for Ni-Co alloys at pH7

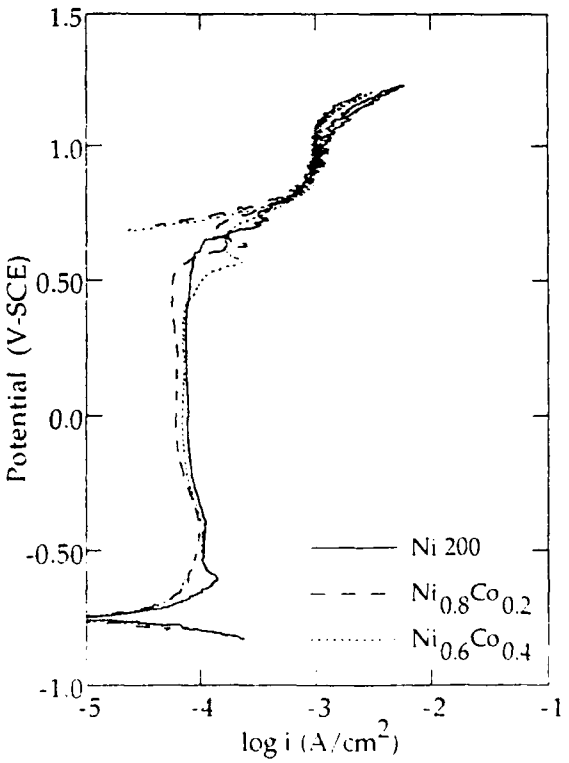

Figure 4: Polarization Curves for Ni-Co alloys at pH10

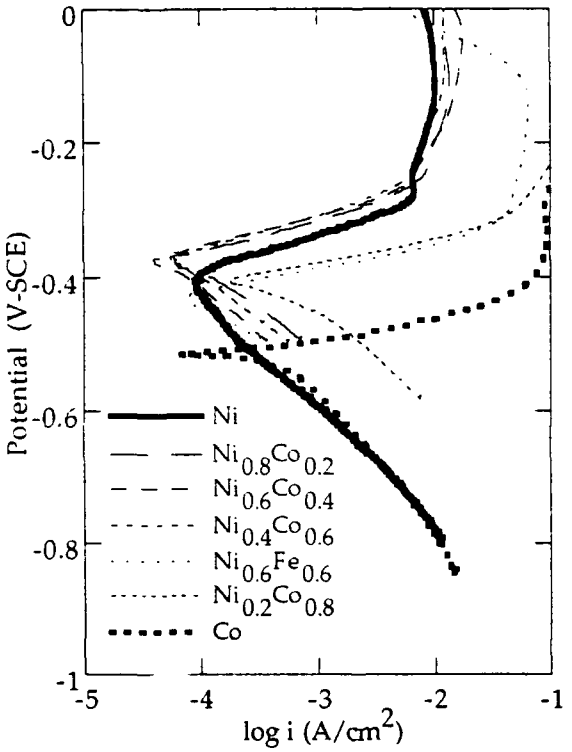

Figure 5: Active behavior at pH3

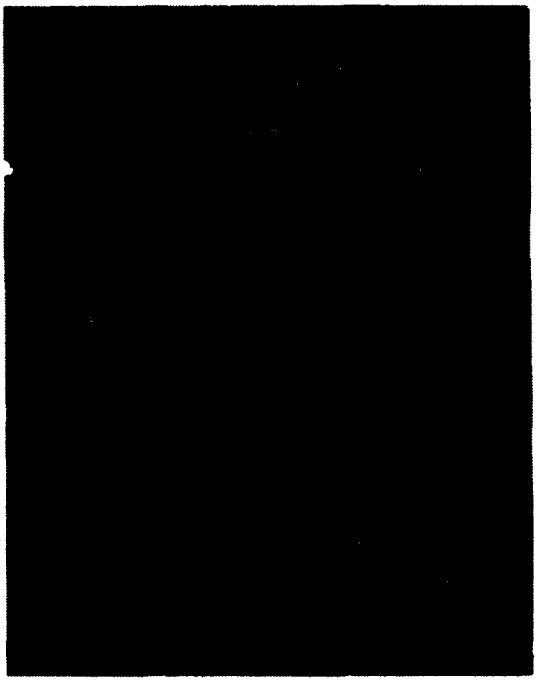

Figure 6: Photomicrograph of $Ni_{0.4}Co_{0.6}$ alloy; single phase microstructure is typical of higher Ni alloys (50 X)

Figure 7: Photomicrograph of $Ni_{0.2}Co_{0.8}$ alloy; banded microstructure is indicative of diffusionless transformation (50 X)

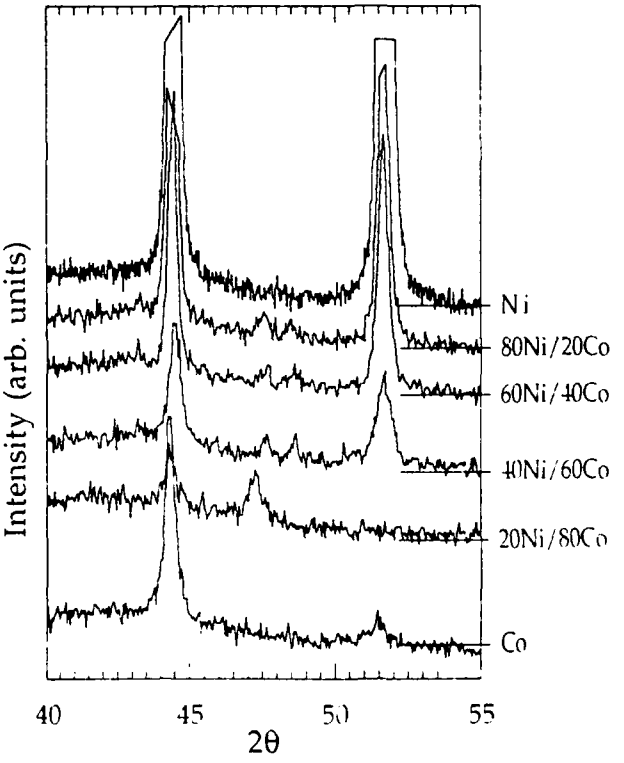

Figure 8: X-Ray Diffraction Spectra of pure metals and alloys.

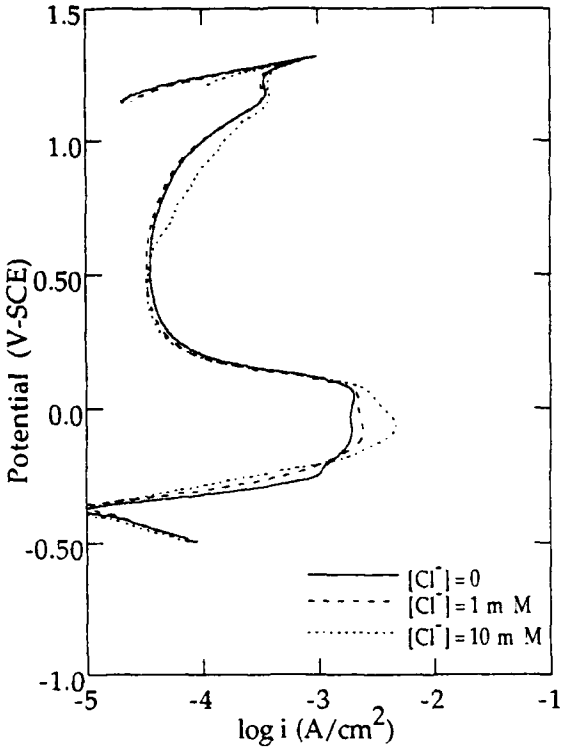

Figure 9: Polarization of $Ni_{0.4}Co_{0.6}$ alloy: effect of chloride concentration, pH3.

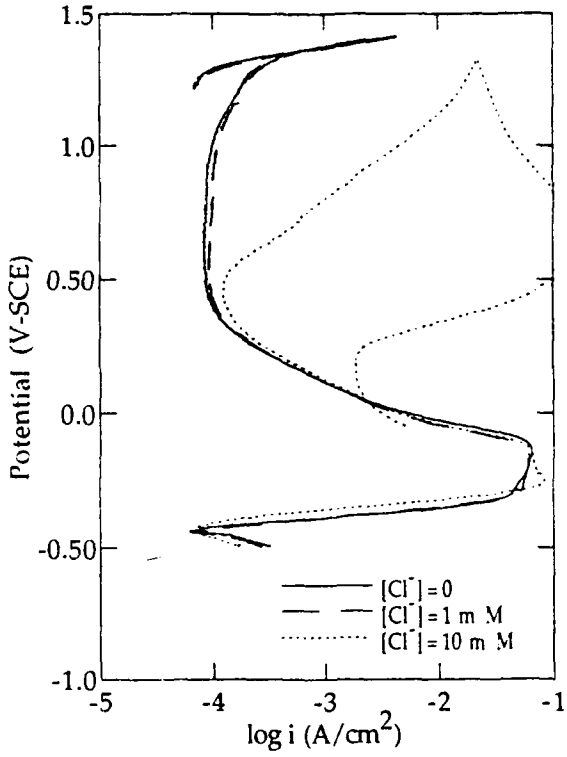

Figure 10: Polarization of Ni-Fe alloy: effect of chloride concentration, pH 3

Table I

Chemical Analysis by X-ray Fluorescence (XRF)

Nominal Comp.	%Ni	%Co	%Fe	%other
$Ni_{0.8}Co_{0.2}$	78.6	21.4	<0.1	<0.1
$Ni_{0.6}Co_{0.4}$	59.0	41.0	<0.1	<0.1
$Ni_{0.4}Co_{0.6}$	39.2	61.8	<0.1	<0.1
$Ni_{0.2}Co_{0.8}$	18.2	81.8	<0.1	<0.1
$Ni_{0.4}Fe_{0.6}$	40.0	<0.1	60.0	<0.1

Table II

Solubility Products of Metal Hydroxides[12]

Metal Hydroxide	K_{sp}
$Fe(OH)_2$	1.64×10^{-14}
$Fe(OH)_3$	1.10×10^{-36}
$Ni(OH)_2$	1.45×10^{-18}
$Co(OH)_2$	1.09×10^{-18}

Evaluation and application of the EPR-double loop test to assess the degree of sensitisation in stainless steels

R.F.A. Jargelius-Pettersson and P. Szakalos
Swedish Institute for Metals Research
Drottning Kristinas väg 48
S-114 28 Stockholm, Sweden

Abstract

The Electrochemical Potentiokinetic Reactivation (EPR) double loop method has been used to measure the degree of sensitisation of a type 304 stainless steel after various sensitisation times at 620°C. Results from testing in a field cell and a laboratory cell are compared and the dependence of evaluated parameters on test temperature is quantified.

Key terms: stainless steel, sensitisation, EPR, DOS, test method

Introduction

The Electrochemical Potentiokinetic Reactivation (EPR) technique is an electrochemical test to assess the degree of sensitisation in stainless steels. It has proved particularly useful for field testing in that it is both quantifiable and non-destructive. The original method, termed the single loop test, was proposed by Cihal et al.[1] and now standardised as ASTM G108-92. In this form the EPR technique has however the dual disadvantages, from the point of view of field testing, of requiring careful surface preparation and a metallographic evaluation of grain size. The double loop method, proposed later by Akashi et al.[2] and standardised in JIS G0580-1986, eliminates both these difficulties.

In double loop testing (Fig. 1) the material to be tested is first polarised in the anodic direction, this causes general dissolution to occur so the anodic peak i_a is directly related to the tested surface area. After passivation a corresponding potential scan is performed in the reverse direction. As is the case with the single loop test this produces dissolution only at sensitised grain boundaries so the cathodic peak i_r, or more specifically the ratio i_r/i_a gives a measure of the degree of sensitisation.

The single loop test involves only the reverse scan and is normally evaluated in terms of the reactivation charge passed, i.e. the area under the curve, rather than the maximum current. This evaluation method is clearly also applicable to the double loop technique and previous work[3] has indicated relatively good agreement between the single and double loop techniques if compared in this way.

The EPR test is normally performed at 30°C±1°C but this degree of temperature control can seldom be achieved in field measurements. In order to be able to compare and evaluate results an understanding of the effect of temperature variations on EPR results is thus of central importance. In a previous work[4] the effect of temperature in the range 10-40°C on the charge passed during the single loop test was evaluated, yielding an activation energy of 67 ± 9 kJmol^{-1} and the equation:

$$Q^{30} = Q\exp 26.4\frac{(30-T)}{(273+T)} \quad (1)$$

which may be used to convert the charge Q at temperature T to a charge Q^{30} at 30°C.

The aim of the present work is threefold: to compare the results of EPR double loop testing in a field cell to those from testing in a conventional laboratory cell, to assess the temperature dependence of the double loop test and to compare the results of double loop testing to previous single loop evaluation[4].

Experimental

The material employed was a type 304 (Sandvik charge 4-31009) stainless steel pipe of 10mm wall thickness and composition (in wt %) 0.052C,0.55Si,1.23Mn,0.017P,0.011S,18.7Cr,9.5Ni, 0.39Mo, and 0.039N. In order to produce a wide variation in the degree of sensitization, specimens were heat treated at 620°C for times of 3, 6, 9.5, 16 and 24 hours and then water quenched. The specimens were in the form of cylinders with diameter 11mm cut from the wall of the tube. These were spot welded to copper wires and the entire assemblies mounted in Technovit 4004 cold-setting plastic so as to expose only the circle corresponding to the outer surface of the pipe.

EPR measurements were performed according to the double loop technique, as described by Majidi and Streicher[5]. The solution used was $0.5M H_2SO_4 + 0.01M KSCN$ made from analytical grade chemicals and distilled water. A limited amount of testing was performed in a laboratory cell of volume 3 litres and in this case the test solution was dearated before and during the test with argon gas. The majority of the testing was however performed in a field cell of volume 70 ml and no deaeration was performed. In order to achieve the desired temperature control the entire field cell was immersed in a thermostatted water bath.

In both cases testing followed the same procedure. The corrosion (rest) potential was first measured for two minutes, this was found in all cases to lie in the acceptable range of -350 to -450 mVSCE so no cathodic charging was performed. The potential was then increased from the rest potential to +200mVSCE at 6V/hour (1.67mV/s) and then immediately returned to the rest potential at the same rate to produce the reversed scan. Measurements were performed at 20°C, 30°C and 40°C and in the majority of cases duplicate tests were performed to check reproducibility.

Results and Discussion

Comparison between field cell and laboratory cell

The results of all tests are summarised in Table 1 in terms of the peak anodic and reversed scan currents, i_a and i_r respectively, the current ratio i_r/i_a and the charge Q. The latter may be converted to P_a values using the measured ASTM grain size of 6.0[4] or to Q_L values using a mean linear intercept l of 40μm (see appendix for definitions and equations). No significant difference was observed between the results from the field cell or from the laboratory cell so both were used for the evaluation of the temperature dependence.

It was noted that for both the field cell and the laboratory cell a large scatter in i_r and Q were observed for the most sensitised specimens at 40°C.This was associated with the appearance of a black deposit on the specimen surface which dissolved with time if the specimen was left in the testing solution or could readily be rinsed off with water. This is probably a sparingly soluble dissolution product which cannot be removed from the surface at a sufficient rate during the reversed scan but instead partially blocks dissolution. No such deposit was however observed in connection with the anodic scan or noted with the single loop testing of the same specimens[4]. The results from the 16 hour and 24 hour specimens tested at 40°C were for this reason not included in the evaluation of the temperature dependence of i_r and Q. On this basis it is also suggested that the double loop EPR method should be used with caution when measuring large degrees of sensitisation at high temperatures.

Evaluation of temperature dependence

Figs.2-4 show i_a, i_r and Q respectively, plotted as a function of the logarithm of the sensitisation time and the reciprocal of the absolute temperature. This illustrates the expected result that the anodic current is independent of the degree of sensitisation, but nevertheless weakly dependent on temperature, while i_r and Q are both strongly dependent on temperature and the degree of sensitisation. The latter phenomenon is also illustrated qualitatively by the micrographs in Fig.5 which show the dependence of the amount of grain boundary dissolution on sensitisation time. An evaluation of the Arrhenius plots for the three parameters yields values of 40 ± 7, 58 ± 9 and 66 ± 11 kJmol^{-1} for the activation energies for i_a, i_r and Q respectively. Thus in order to convert a value at a temperature T in the given interval to that at 30°C the following equations may be used:

$$i_a^{30} = i_a \exp 15.7 \frac{(30-T)}{(273+T)} \qquad (2)$$

$$i_r^{30} = i_r \exp 23.2 \frac{(30-T)}{(273+T)} \qquad (3)$$

$$\left(\frac{i_r}{i_a}\right)^{30} = \left(\frac{i_r}{i_a}\right) \exp 7.5 \frac{(30-T)}{(273+T)} \qquad (4)$$

$$Q^{30} = Q \exp 26.4 \frac{(30-T)}{(273+T)} \qquad (5)$$

It is apparent from the above equations that only a weak temperature dependence is encountered when the current peak ratio i_r/i_a is used for evaluation. This is illustrated in Fig.6 in which the correction equations above have been applied to both Q and i_r/i_a values. The effect of correction is marked for Q values and its applications indicates sensitisation to follow the dependence

$$Q_{DL} = 1.2 \log_{10}(t-t_o) \text{ where } t_o = 1.7 \text{ hours (error coefficient, } r^2 = 0.96) \qquad (6)$$

Similar analysis of i_r/i_a yields

$$i_r/i_a = 0.3 \log_{10}(t-t_o) \text{ where } t_o = 0.9 \text{ hours. } (r^2 = 0.87) \qquad (7)$$

these may be compared to previous single loop results[4] which are shown in Fig 7a and yield:

$$Q_{SL} = 0.6 \log_{10}(t-t_o) \text{ where } t_o = 0.6 \text{ hours } (r^2 = 0.73) \quad (8)$$

t_o, the onset of measurable sensitisation, should be identical in all cases; the observed deviation is attributable to scatter.

Comparison to single loop measurements

The above equation for temperature correction of the double loop charge, Q_{DL}, is very similar to that obtained from analysis of single loop data on the same specimens[4] which indicates the good agreement between the two methods if evaluated in the same manner. This is also indicated by Fig. 7b which compares uncorrected values of Q_{DL} and Q_{SL} performed at 20°C, 30°C and 40°C. The correlation coefficient for measurements at 30°C is 0.90 and for all measurements 0.95. If the double loop data is instead evaluated in terms of i_r/i_a the correlation is poor if all temperatures are compared (Fig 8), but reasonable (correlation coefficient 0.88) for the measurements at 30°C. This is a logical consequence of the diffing temperature dependence of Q and i_r/i_a. Applying the temperature correction to both Q_{SL} and i_r/i_a gives however much better correlation (coefficient = 0.87).

Conclusions

1. The EPR double loop technique may be satisfactorily used to perform field measurements of the degree of sensitisation of type 304 stainless steel. There is no significant difference between the results of testing performed in a field cell of volume 70 ml and in a 3 litre laboratory cell.

2. The measurement of high levels of sensitisation at 40°C is not recommended in view of the occurrence of surface deposition which causes a large scatter in results.

3. There is excellent agreement between the single loop and double loop tests if both are evaluated in terms of the charge Q passed under the reactivation scan (or a conventional P_a or Q_L value which includes area and grain size normalisation). The equation:

$$Q^{30} = Q \exp 26.4 \frac{(30-T)}{(273+T)}$$

may be used to convert the charge Q at temperature T to a charge Q^{30} at 30°C. There is also good correlation if the double loop data is evaluated in terms of the peak current ratio i_r/i_a.

4. The peak currents recorded on the anodic and reversed potential scans in the double loop method show a different dependence on testing temperature, the two processes yielding activation energies for dissolution of 40 and 58 kJmol^{-1} respectively. Using these values for the activation energies, the equation:

$$\left(\frac{i_r}{i_a}\right)^{30} = \left(\frac{i_r}{i_a}\right) \exp 7.5 \frac{(30-T)}{(273+T)}$$

may be derived to convert i_r/i_a values obtained at temperature T to i_r/i_a^{30} values at 30°C for purposes of comparison. This is a much weaker temperature dependence than for Q values.

5. For the 0.052%C steel investigated, the evolution of sensitisation in terms of the charge Q measured in single and double loop EPR tests may be approximately described by the equation:

$Q = 1.2 \log_{10}(t-t_o)$ where $t_o = 1.7$ hours

Acknowledgements

The financial support of the Swedish Nuclear Power Inspectorate (SKI) for this work is gratefully acknowledged.

References

1. V. Cihal, A. Desestret, 5th European Corrosion Congress (Paris, France, Soc. de Chem Ind. 1973)
2. M. Akashi, T. Kawamota, F. Umemura, Boshoku Gijutsu 29(1989) p163
3. R. F. A. Jargelius, E. Symniotis-Barrdahl, P. Aaltonen, H. Hänninen, T. Berglund, 11th Scandinavian Corrosion Congress (Stavanger, Norway, Högskolesenteret i Rogaland, June 1989) F-4
4. R. F. A. Jargelius, S. Hertzman, E. Symniotis, H. Hänninen, P. Aaltonen, Corrosion 47:6(1991)429-435
5. A.P Majidi, M.A.Streicher: Corrosion 40:11 (1984) 584-593
6. W.L.Clarke: Report NUREG/CR-1005 GEAP-2488 (1981)
7. E.E.Underwood: Quantitative Stereology. Addison Wesley, 1970

Appendix: Calculation of P_a and Q_L values

l = mean linear intercept in mm (measured at 1x enlargement)
X = ASTM grain size
A = EPR test area
L_A = length of grain boundary per unit specimen area (in mm/mm²)
P_a = EPR charge per unit grain boundary area (GBA)
Q_L = EPR charge per unit grain boundary length (GBL)
w = grain boundary width (assumed to be 10^{-3}mm)[6]

The expression[6] for P_a is derived assuming a grain boundary width of 1μm:

$P_a = Q / GBA$ [1][6]

$GBA = A (5.09544 \times 10^{-3} \exp(0.34696X))$ [2][6]
$X = -3.2877 - 6.6439(\log_{10} l)$ [3][6]

Hence:

$GBA = A(5.09544 \times 10^{-3} \exp(-1.1407)\exp(-2.3\log_{10} l))$

$= A \times 0.00163 \times 1/l = 1.63Aw/l$ assuming $w = 10^{-3}$mm [4]

P_a $= Ql/0.00163A$ if l is expressed in mm [5]

Using the expression:

$L_A = \pi/2l$ [6][7]

the grain boundary area can be rigorously calculated from first principles as:

GBA $= L_A Aw$ [7]

$= \pi Aw/2l$

$= 1.57Aw/l$ [8]

The numerical discrepancy between [4] and [8] is due to the assumption of a circular grain shape in the former but no such assumption in the latter.

In view of the fact that w has no physical significance, it inclusion in the evaluation equation is questionable. The EPR charge may thus instead be normalised to the grain boundary length:

GBL $= L_A A$

$= \pi A/2l$ [9]

Q_L $= Q/GBL$ [10]

$= 2Ql/\pi A$ [11]

$= 0.00163P_a \times 2/\pi$ [12]

If however the accepted units of C/cm^2 are used for P_a this leads to units of Q_L in [12] of Cmm/cm^2. Using SI units and expressing Q_L in C/m yields the following conversion relation:

$Q_L(C/m) = 0.0104P_a(C/cm^2)$ [13]

Table 1. Results of EPR double loop tests. Those marked with an asterisk were performed in the 3 litre laboratory cell

Sens.time (hours)	Test temp. (°C)	i_a (mA/cm²)	i_r (mA/cm²)	Q (C/cm²)
3	20	37.7* 32.8 34.4 33.0	2.8* 2.1 2.8 2.9	0.158* 0.086 0.136 0.114
6	20	30.0 29.0 30.0 40.0 28.3	4.4 4.4 2.2 5.7 4.7	0.240 0.108 0.162 0.319 0.248
9.5	20	35.4	7.8	0.408
16	20	29.0	8.4	0.482
24	20	33.6 35.5 33	8.2 10.7 10.7	0.466 0.622 0.605
3	30	51.8 54.0 49.2	6.8 7.2 12.6	0.348 0.407 0.749
6	30	49.2 54.0 48.2	12.6 13.2 16.2	0.749 0.752 0.886
9.5	30	52.8 51.0	16.2 16.2	0.886 0.972
16	30	58.4 68.5	22.9 14.1	1.384 0.903
24	30	61.2 67.2 70.4	27.6 18.0 22.4	1.873 1.127 1.433
3	40	91.0* 68.4 129*	11.1* 13.4 14.8*	0.628* 0.733 0.822*
6	40	87.6 108 71.4 97.2	20.0 25.2 15.6 28.8	1.044 1.536 1.782 -
9.5	40	76.8 98.6*	32.4 22.1*	2.228 1.415*
16	40	92.0 99.5*	25.0 26.8*	1.636 1.771*
24	40	87.6 99.0*	42.0 15.5*	2.748 1.140*

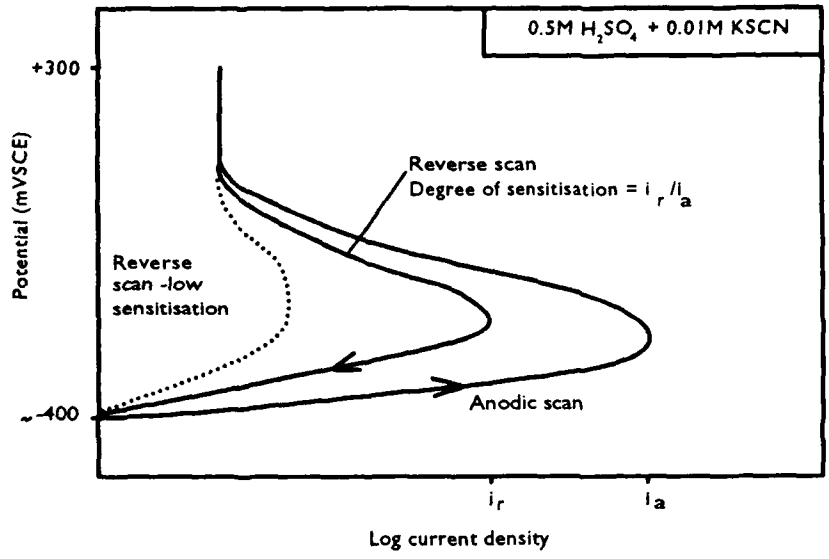

Fig. 1 Schematic illustration of the EPR double loop technique

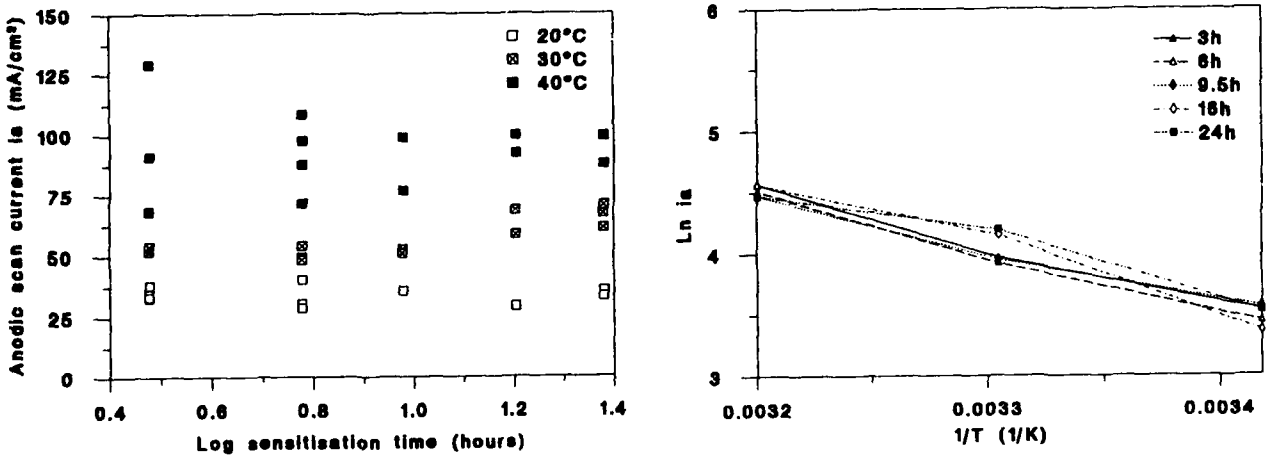

Fig. 2 Dependence of the maximum current on the anodic scan (i_a) on sensitisation time and test temperature.

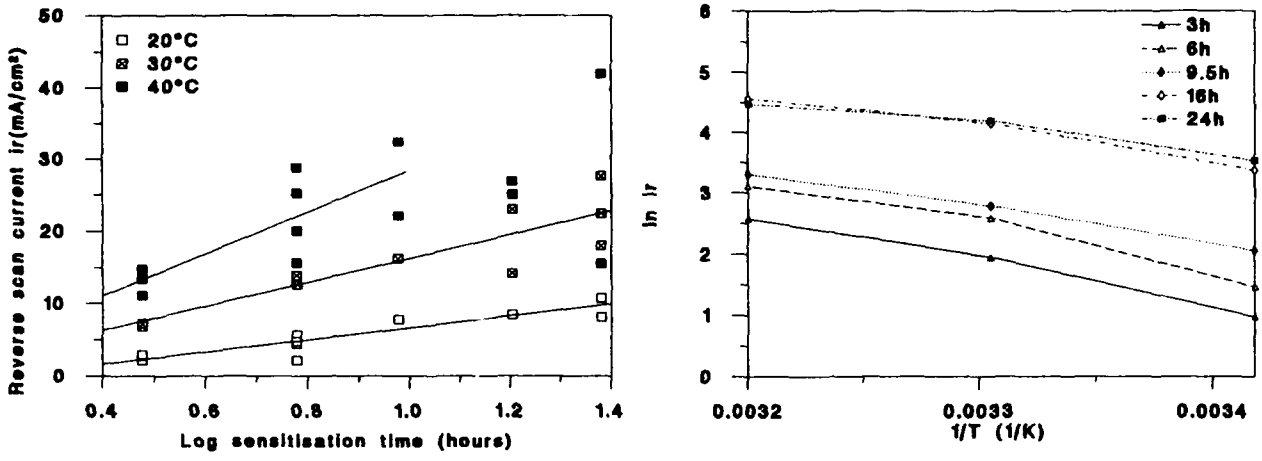

Fig. 3 Dependence of the maximum current on the reverse scan (i_r) on sensitisation time and test temperature.

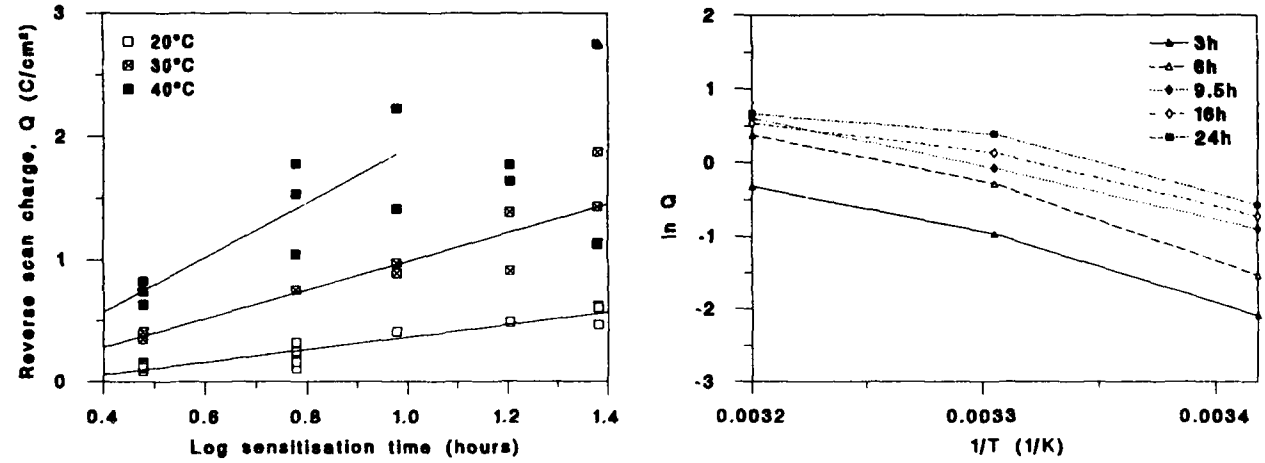

Fig. 4 Dependence of the charge passed during the reverse scan (Q) on sensitisation time and test temperature.

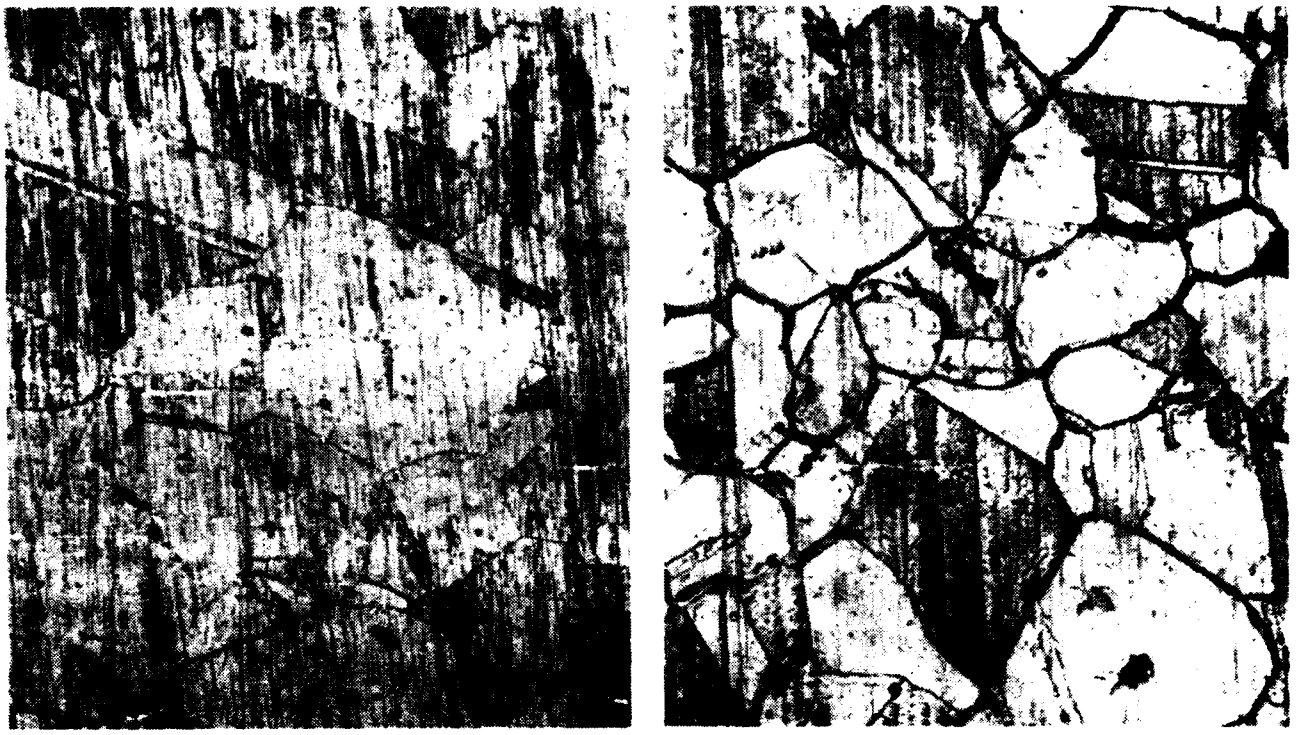

Fig. 5 Microstructures of specimens 3 hours and 16 hours after EPR testing at 30°C showing varying amount of grain boundary attack (400x)

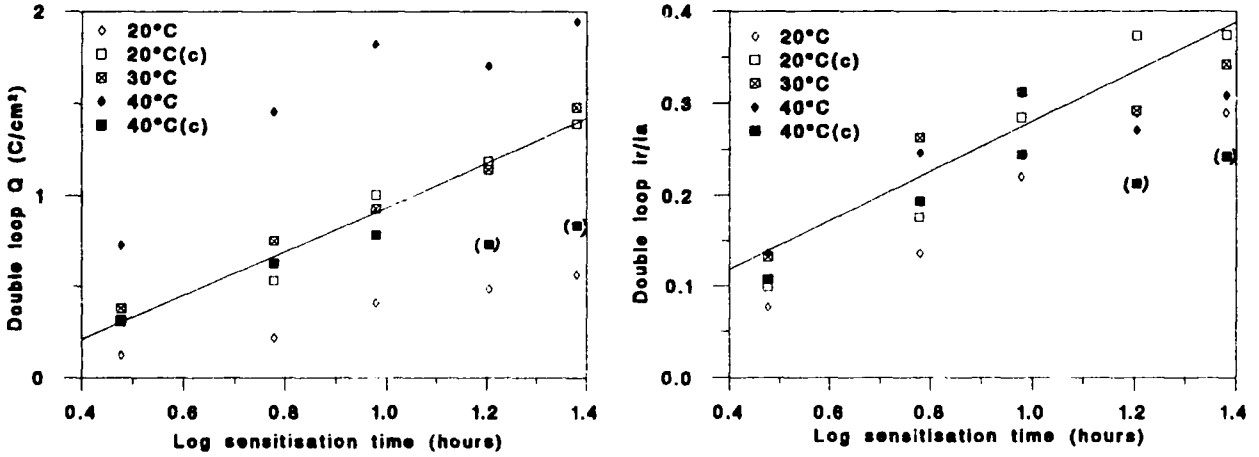

Fig. 6 Effect of temperature correction on Q_{DL} and i_r/i_a values. The diamond points show the original measurements, the square points show the corrected values. Use of all values except the two in parentheses yields the relations:
$Q_{DL} = 1.2 \log_{10}(t\text{-}t_o)$ where $t_o = 1.7$ hours (error coefficient $r^2 = 0.96$)
$i_r/i_a = 0.3 \log_{10}(t\text{-}t_o)$ where $t_o = 0.9$ hours ($r^2 = 0.87$)

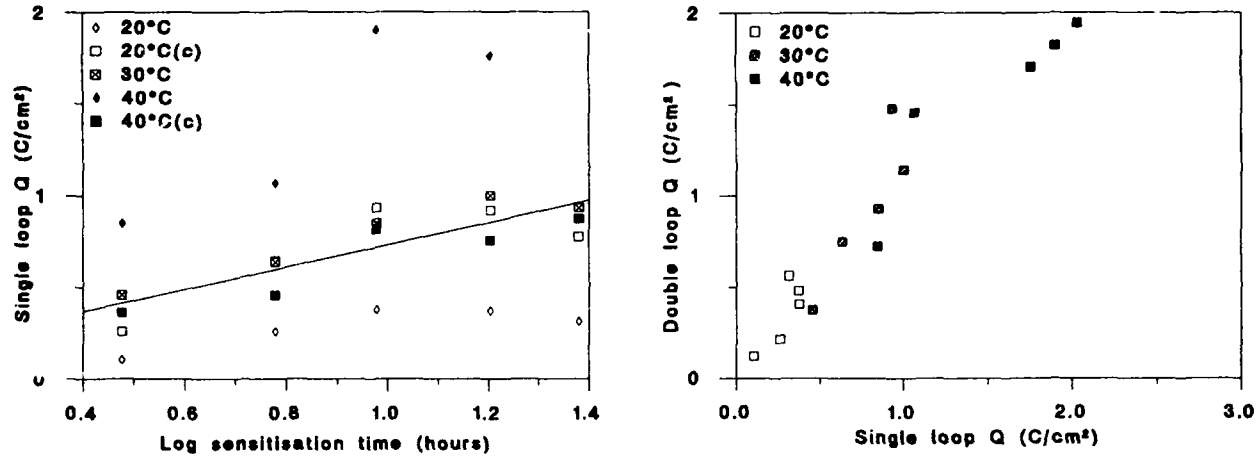

Fig. 7 (a) Effect of temperature correction on single loop data[4]. Corrected data show relation:
$Q_{SL} = 0.6 \log_{10}(t\text{-}t_o)$ where $t_o = 0.6$ hours ($r^2 = 0.73$)
(b) Comparison between double loop and single loop charges Q measured on the same series of specimens at the same temperature. Correlation coefficient is 0.95 for all temperatures together and 0.90 for 30°C alone.

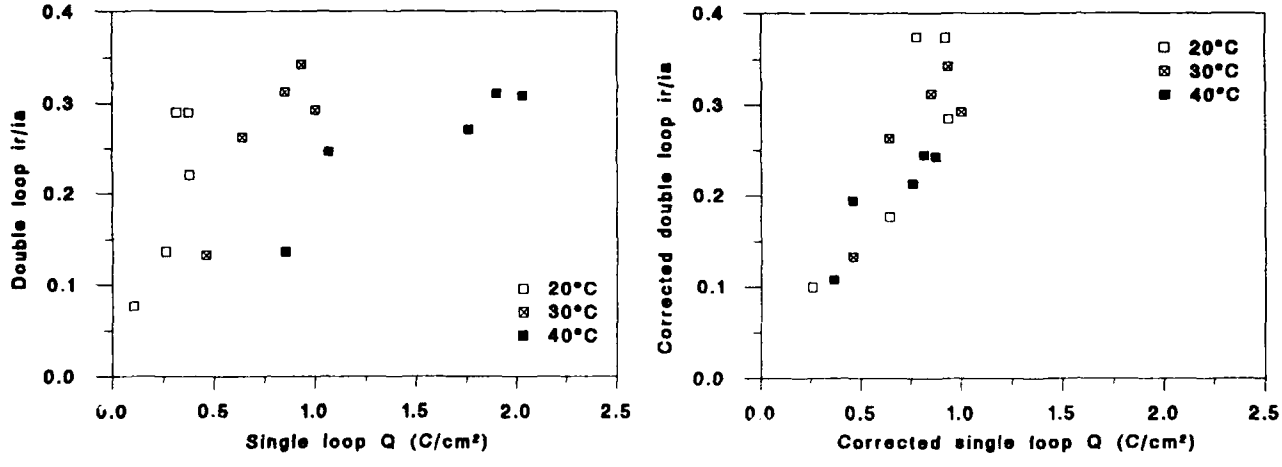

Fig. 8 Comparison between double loop i_r/i_a and single loop Q without (left) and with temperature correction. Correlation coefficient is 0.88 at 30°C and 0.87 for all values after temperature corrrection.

Corrosion Behaviour of Sintered Austenitic Stainless Steels in Sulphate and Chloride Media

E.Angelini
Dept.Mat.Sci.Chem.Eng., Polythecnical University of Torino,
Corso Duca degli Abruzzi 24
I10129 Torino, Italy

P.Bianco
Chemical Laboratory of the Chamber of Commerce,
Via Ventimiglia 165
I10165 Torino, Italy

F.Rosalbino
Dept.Mat.Sci.Chem.Eng., Polythecnical University of Torino,
Corso Duca degli Abruzzi 24
I10129 Torino, Italy

M.Rosso
Dept.Mat.Sci.Chem.Eng., Polythecnical University of Torino,
Corso Duca degli Abruzzi 24
I10129 Torino, Italy

G.Scavino
Dept.Mat.Sci.Chem.Eng., Polythecnical University of Torino,
Corso Duca degli Abruzzi 24
I10129 Torino,Italy

Abstract

Electrochemical investigations (polarization curves, polarization resistance measurements), together with weight loss measurements and analysis of the solutions after permanence of the samples were used to evaluate the corrosion behaviour of type 304L and 316L sintered austenitic stainless steels in sulphate and chloride containing solutions.

The samples were sintered in nitrogen based atmophere, at 1120 and 1190°C, and in vacuum at 1200°C and submitted to X-ray diffraction analysis and SEM observation together with EDS microanalysis before and after the corrosion tests.

A correlation is tempted between the corrosion behaviour and the mechanical properties of samples as rockwell hardness, shrinkage, unnotched impact strenght, ultimate tensile strenght.

Key terms: sintered steels, corrosion, thermochemical treatments

Introduction

An increasing interest towards the application of sintered stainless steels may be noted in the area of mechanical components manufacturers, in the tentative of obtaining materials with good corrosion resistance, good mechanical properties, excellent reliability at low production costs.
Consequently a constant search for the optimization of industrial sintering processes is carried out by changing sintering temperatures and atmospheres, and by adding specific alloying elements.
The corrosion behaviour in particular is simultaneously affected by several parameters of complex identification. Various Authors have tried to found inferences between sintering density, temperature and atmospheres, total and interconnected porosity, interstitial content of C, O, N, presence of noble alloying elements,etc. and corrosion behaviour in different aggressive media.
Itzhak et al.[1] suggested that the main mechanism affecting the low corrosion resistance of hot-pressed austenitic stainless steels in sulphuric acid solution is the evolution of hydrogen concentration cells due to electrolytic stagnation in the interconnected open pores; moreover the local intergranular sensitivity to the corrosive environment is increased due to carbide precipitation [2].
The addition of elements as Sn,Cu and Ni (up to 10% wt) increase the corrosion resistance of hot-pressed sintered stainless steels, essentially by improving the passivation processes [3-5]. Also the pore morphology has a crucial role in the environmental behaviour of sintered steels: the double pressing, double sintering processes, resulting in a closed, round pore morphology, allow to obtain a corrosion behaviour similar to wrought stainless steels [6].
Raghu et al.[7,8] too attribute the inferior corrosion resistance of sintered stainless steels filters to the formation of hydrogen ion concentration cells following entrapment of the sulphuric acid solution in the pores, and underline that the pore morphology, more than porosity itself is responsible for the corrosion mechanism.
A lack of sensitivity to the density changes and a strong dependence on the sintering conditions has been found by Ahlberg [9] for the corrosion behaviour of sintered ferritic and austenitic stainless steels in sulphuric acid.
Media of lower aggressivity have been taken into account by Fedrizzi et al.[10]; they characterized from an electrochemical point of view type 316L austenitic stainless steels, sintered with addition of copper in dissociated ammonia atmosphere, in borate solutions with and without chloride ions. The chromium nitrides precipitation affects to a low extent the passivation curves, while the interconnected porosity shape and amount seem to be more important parameters; furthermore in chloride containing solutions copper seems to

favor the localized attack resistance, probably as a consequence of the formation of protective corrosion products; in sulphuric acid solution too the beneficial effect of Cu addition is observed[11].
In earlier studies [12-14] we tried to relate the sintering atmospheres and temperatures of type 304L and 316L austenitic stainless steels to their mechanical and electrochemical properties in different media, it was concluded that austenitic stainless steels sintered in nitrogen based atmosphere show better mechanical properties but lower corrosion resistance with respect to samples sintered in vacuums because of the precipitation of chromium nitrides.
In order to clarify the corrosion mechanism in this paper the effect of morphological changes induced by the sintering process in different atmospheres on the corrosion behaviour of sintered AISI 304L and AISI 316L samples has been evaluated in sulphate and chloride containing solutions, and preferential dissolution reactions have been identified by means of the chemical analysis of the solutions after immersion tests.

Experimental

The studies were carried out on samples (bars or bushings) produced by compacting BSA powders of type 304L and 316L stainless steels, whose composition is shown in Table I, with lithium stearate (0.7% wt) as lubricant. The compacted samples were sintered in industrial plants in nitrogen-based atmosphere (62.5%vol N_2, 37.5%vol H_2, -35°C dew point), obtained by adding nitrogen to dissociated ammonia. Sintering was performed at 1120 and 1190°C for 1h, with a step at 500°C for the lubricant elimination, for an overall cycle time of 8 h, these samples will be indicated respectively as N1120 and N1190. For comparison sake, a series of specimens was also sintered in vacuums at 1200°C for 1 h, with pre-heating steps, for an overall cycle time of 6 h, these samples will be indicated as V1200.
The microstructural analysis was performed by means of a diffractometer Philips mod. 1380/70; the porosity and pore size distribution were evaluated by means of a mercury porosimeter Carlo Erba.
The specimens were tested in 0.5M H_2SO_4, 0.5M K_2SO_4 and 0.1M NaCl solutions, at room temperature.
The corrosion rates were determined by weight loss measurements after increasing immersion period, 7, 14 and 21 days. In order to point out possible preferential dissolution reactions of the single elements occurring during the immersion tests, a quantitative analysis of the solutions was performed, after increasing immersion times, by means of optical emission spectrometry (ICP-OES, Perkin Elmer Plasma 40). In order to determine the total amount of the elements dissolved, before the removal from the electrolytes, the samples were ultrasonically treated and the removed solid

corrosion products were successively dissolved by acidification of the solutions with nitric acid.
The data are expressed as wt % of each element with respect to the total weight of the corrosion products.
Before and after the immersion tests, the samples were examined by SEM observation, employing a SEM Jeol Mod. 6400, equipped with an energy dispersion microprobe EDS, Tracor Z-Max.
The samples submitted to the electrochemical investigations were polished up to 600 Grit, ultrasonically degreased in acetone and dried at 150°C for 2 h to prevent any liquid segregation in the pores.
The polarization measurements were carried out potentiodinamically at a scanning rate of 1mV/s, starting from a potential of -0.9 V(SCE), by means of an electrochemical interface Solartron mod.1286, deareating the electrolyte by nitrogen bubbling for 30 min.
The polarization resistance measurements were performed in deareated solutions, by superimposing to the free corrosion potential of the sintered sample a triangular wave (10mV in amplitude and 25 mHz in frequency) and recording the corresponding current density.

Results and discussion

The sintered samples were first characterized by determining the properties listed in Table II. A slight decrease in the values of volume mass is observed for samples sintered in nitrogen-based atmosphere with respect to samples sintered in vacuum. A similar trend is found for the total porosity, which ranges, for example for AISI 304L, between 12% and 10.9% respectively for V1200 and N1190 samples; contemporarily a decrease in the average pore size is observed, this factor may be important in the context of localized attacks during the corrosion process.
An increase of hardness is found on samples sintered in nitrogen-based atmosphere, due to the precipitation of nitrided phases as shown below: on AISI 304L samples sintered in vacuum a hardness value of 44 is measured, while N1120 and N1190 have respectively values of 72 and 78.
Among the other mechanical properties considered, the ultimate tensile strength is higher on samples sintered in nitrogen-based atmosphere, while shrinkage and unnotched impact strength show an opposite trend, and higher values are measured on samples sintered in vacuum.
The sintering atmosphere influences to a great extent the microstructure of samples as shown by the X-ray diffractograms of Fig.1. The specimens of both the alloys sintered in vacuum maintain a monophasic austenitic structure, while on samples sintered in nitrogen-based atmosphere the precipitation of chromium nitrides (Cr_2N type) is evident, and is accompanied, in the case of AISI 316L by the formation of ferrite, as already noticed in previous papers[15-16].

The formation of nitride phases beneficially affects several mechanical properties of sintered steels but lowers their corrosion resistance as shown by weight loss measurements and electrochemical characterizations performed in different aggressive media.

In Fig.2 the results of the immersion tests in 0.5 M H_2SO_4 solution at increasing immersion periods are shown: as expected the corrosion rates of wrought alloys, reported for comparison sake, are one order of magnitude lower than sintered samples. Moreover among sintered samples, the best behaviour is observed for specimens sintered in vacuum : for type 304L the corrosion rate for the first immersion period ranges from 0.20 g dm^2 day for V1200 to 0.75 and 1.40 g dm^2 day, respectively, for N1120 and N1190. In the second immersion period the occlusion of pores caused by corrosion products induces a general decrease of the corrosion rate, which increases again during the third week. Furthermore the corrosion resistance of type 316L samples sintered in nitrogen-based atmosphere is lower than the one of type 304L specimens.

Let us examine now the results of the quantitative analysis for Fe, Cr and Ni, of the solutions after the immersion tests, reported in Fig.3. They may help in clarifying the corrosion process, allowing the identification of possible preferential dissolution reactions.

For both alloys iron dissolves preferentially with respect to the other elements: for samples sintered in vacuum the values of iron in solution are 1-2% larger than the stoichiometric value, for N1120 and N1190 samples the increase ranges from 7 to 10%.

Chromium shows an opposite trend: this element dissolves to a lesser extent with respect to the stoichiometric value. For example for AISI 304L specimens sintered in vacuum only 17% of Cr dissolves with respect to the stoichiometric 18.6%, while with N1190 samples the amount of Cr dissolved is only 10-12%.

The behaviour of nickel is similar; the concentration of this element in the solutions deriving from the corrosion of N1190 samples type 304L is 7.5% with respect to the stoichiometric 10.3%.

A good agreement may be pointed out between the values of the total mass dissolved because of the corrosive attack as evaluated by means of weight loss measurements and by means of the multielemental analysis of the solutions. As an example N1190 type 304L samples after 7 days of immersion in the sulphuric acid solution lost 729.2 mg, and the sum of the amounts of Fe, Cr and Ni determined in the solution was 728.1 mg.

The preferential dissolution of iron is confirmed by SEM observations of samples after the corrosion tests; an increase of Cr and Ni concentration has been detected by means of EDS microanalysis on the corroded areas.

Fig.4 and 5 show the BSE micrographs of the cross sections of samples after corrosion tests in 0.5 M H_2SO_4 solution. The

dramatic decrease in the corrosion resistance of N1120 and N1190 samples is well evidenced. On AISI 304L the corrosive attack penetrates for approximately 400 microns and 800 microns on N1120 and N1190 samples; the situation is even worse on AISI 316L samples where the depth of penetration is 800-990 microns on N1120 samples and interests approximately the total thickness of N1190 samples, leading to a disintegration of the specimen.
An observation of the corroded zones at higher magnification allows to confirm the previous findings.
In Fig.6 the SEM micrograph of the corroded layer of sample N1190 (a particular of Fig. 4(c)) is shown, together with the X-ray concentration maps for Fe, Cr and S. The penetration of the sulphuric acid causes a preferential attack in the zones sourronding the Cr_2N precipitates, the EDS microanalysis reveals a noteworthy enrichment of chromium, that reaches concentrations ranging from 32 to 46 % wt.
The phenomenon is stressed on AISI 316L samples, where again phases with high Cr content remain unattacked. In Fig.7 the surface of a corroded N1190 sample may be observed, together with the X-ray concentration profile for Fe and Cr of the linescan indicated on the micrograph: the Cr content increases when the microprobe spot scans the unattacked particle of nitrided phase.
These findings indicate that the behaviour of AISI 304L and 316L sintered samples in sulphuric acid solution is firstly affected by chromium nitrides precipitation: in both cases samples sintered in vacuum show a higher corrosion resistance with respect to samples sintered in nitrogen-based atmosphere, furthermore the corrosion rates increase with the increase of the treatment temperature. However in order to explain the higher corrosion rate of AISI 316L samples sintered in nitrogen-based atmosphere with respect to the AISI 304L specimens, we have to take into account other morfological and physical factors. A detrimental effect on the corrosion resistance of N1120 and N1190 AISI 316L samples is displayed by the observed formation of ferrite and by the porosity: the total porosity is higher than AISI 304L, while the average pore size is lower, leading to the exposition to the aggressive environment of a higher specific area.
The potassium sulphate solution, because of its lower aggressivity did not succeed in differentiating the behaviour of the two alloys.
With the chloride-containing environment, the typical localized corrosive attack prevents from the evaluation of the corrosion rates by means of weight loss measurements; notwithstanding this, the morphology of the attack is similar for AISI 304L and AISI 316L, but the depth of penetration of the electrolyte is higher on samples sintered in nitrogen-based atmosphere.
Fig.8a shows the cross-section of a sample of AISI 304L sintered in nitrogen-based atmosphere after immersion in 0.1M NaCl solution, together with the X-ray concentration maps for Fe, Cr and Cl. The entity of corrosion is low and

the penetration is limited to 30 microns, an increase of chromium content is revealed by EDS analysis in the corroded zones, the concentration ranges from 25 to 30%.
A similar situation is observed in Fig.8b for a sample of AISI 316L sintered in nitrogen-based atmosphere after immersion in 0.1M NaCl solution, in the attacked zone an increase of chromium is detected.
The multielemental analysis of the chloride-containing solutions, not reported for brevity, indicates less stressed phenomena of preferential dissolution, probably due both to the less aggressivity of the solution and to a different kind of corrosive attack.
The electrochemical tests are in good accordance with the results obtained from the immersion tests.
The polarization resistance values confirm that the corrosion rates evaluated after short immersion periods have the same trend that the ones obtained with longer immersion tests. The R_p evaluated in sulphuric acid solution and expressed in ohm cm^2 are the following :for AISI 304L as expected the larger value is for wrought samples, 1460, while the values for sintered samples are respectively 457 for V1200, 411 for N1120 and 383 for N1190; similarly for AISI 316L, wrought samples show values of 6960, and the R_p are lower on sintered samples, V1200 samples give values of 407, N1120 of 390 and finally N1190 of 308.
The polarization curves recorded on AISI 304L in 0.5 M H_2SO_4 solution, Fig.9, show a tendency to passivation only on wrought samples, while on sintered samples the anodic current densities are three order of magnitude higher, and increase from samples sintered in vacuum to samples sintered in nitrogen-based atmosphere.
In NaCl 0.1M the pitting potential may be determined only for wrought samples, sintered samples do not passivate because of interstitial corrosion phenomena.
The behaviour of AISI 316L samples is rather similar, except for a tentative passivation of samples sintered in vacuum, visible on the polarization curves recorded in H_2SO_4 0.5M.

Conclusions

Austenitic type 304L and 316L stainless steels sintered in nitrogen-based atmosphere and in vacuum have been studied in order to evaluate their electrochemical behaviour in sulphate and chloride containing media of different pH, and their mechanical properties.

The corrosion resistance of the sintered specimens depend on the material microstructure (chromium-rich phases precipitation, ferrite formation, porosity, average pore size) and the effect of microstructure varies with the test environment.

The chromium nitride precipitation, taking place on samples

sintered in nitrogen based atmosphere, lowers the corrosion resistance of these samples with respect to the ones sintered in vacuum; this phenomenon is particularly evident in the sulphuric acid solution, where a preferential dissolution reaction of iron occurs. The presence of ferrite and a wide pore distribution,related to a higher surface area, could explain the poorer corrosion resistance of AISI 316L samples sintered in nitrogen-base atmosphere with respect to AISI 304L samples.

For both alloys, samples sintered in nitrogen-based atmosphere show better hardness and strength characteristics.

References

1. D.Itzhak, E .Aghion, Corr. Sci., 23 (1983): p.1085.
2. D.Itzhak, E.Aghion, Corr. Sci., 24 (1984): p.145.
3. D.Itzhak, S.Harush, Corr. Sci., 25 (1985): p.883.
4. D.Itzhak, P.Peled, Corr.Sci., 65 (1986): p.49.
5. P.Peled, D. Itzhak, S.Harush, Corr.Sci., 28 (1988): p.327.
6. P.Peled, D.Itzhak, Corr. Sci., 30 (1990): p.59.
7. T.Raghu, S.N.Malhotra, P.Ramakrishnan, Br. Corr. J., 23 (1988): p.109.
8. T.Raghu, S.N.Malhotra, P.Ramakrishnan, Corrosion, 45 (1989): p.698.
9. E.Ahlberg, P.Engdahl, R.Johansson, Electrochimica Acta, 34 (1989): p.100.
10. L.Fedrizzi, A.Molinari, F.Deflorian, L.Ciaghi, P.L.Bonora, Corrosion, 46 (1990): p.672.
11. L.Fedrizzi, A.Molinari, F.Deflorian, A.Tiziani, P.L.Bonora, Br.Corr.Journal, 26 (1991): p.46.
12. M.Rosso, G.Scavino, E.Galetto, G.Pesce, Modern Developments in Powder Metallurgy. Metal Powder Industries Federation, Princeton, N.J., 1988, Vol.18-21, pp.779-785.
13. E.Angelini, F.Rosalbino, M.Rosso, G.Scavino, Giornate Nazionali Corrosione Protezione, Milano october 1992, Ext. Abs. pp.217-226.
14. G.Scavino, E.Angelini, M.Rosso, F.Rosalbino, Comparison of the corrosion resistance properties of PM steels, Surface Treatment '93, April 1993, Southampton, Ext.abs. in press.
15. B.DeBenedetti, E.Angelini, XXII International Metallurgy Congress Innovation for quality, AIM, Bologna, 1988, Proc. Part I, pp. 439-453
16. B.DeBenedetti, E.Angelini, Metallurgia Italiana, 78 (1986): p.31

Table I - Chemical composition of stainless steels (wt %)

AISI	C	Si	Ni	Cr	Mo	Mn	S	P
304L	0.015	0.67	10.28	18.65	-	0.11	0.007	0.002
316L	0.012	0.86	12.90	17.85	2.22	0.17	0.006	0.015

Table II - Properties of sintered steels: Volume mass (V.M.), Total porosity (P.T.), Porosity size average (P.S.A.), Rockwell hardness (HRB), Shrinkage (SR.), Unnotched impact strength (UIS), Ultimate tensile strength (UTS).

Code	V.M. (Kg/m^3)	P.T. (%)	P.S.A. (microns)	HRB	SR. (%)	UIS (J/cm^2)	UTS (MPa)
AISI 304L							
V1200^	$6.52\ 10^3$	12.0	1.99	44	1.13	91	465
N1120°	$6.39\ 10^3$	11.7	1.25	72	0.94	38	505
N1190'	$6.43\ 10^3$	10.9	0.79	78	0.82	36	574
AISI 316L							
V1200^	$6.43\ 10^3$	10.4	0.98	38	1.27	88	476
N1120°	$6.34\ 10^3$	12.7	0.98	63	0.87	41	470
N1190'	$6.36\ 10^3$	11.4	0.79	69	0.51	40	527

^V1200 : sintered in vacuum at 1200°C
°N1120 : sintered in nitrogen-based atmosphere at 1120°C
'N1190 : sintered in nitrogen-based atmosphere at 1190°C

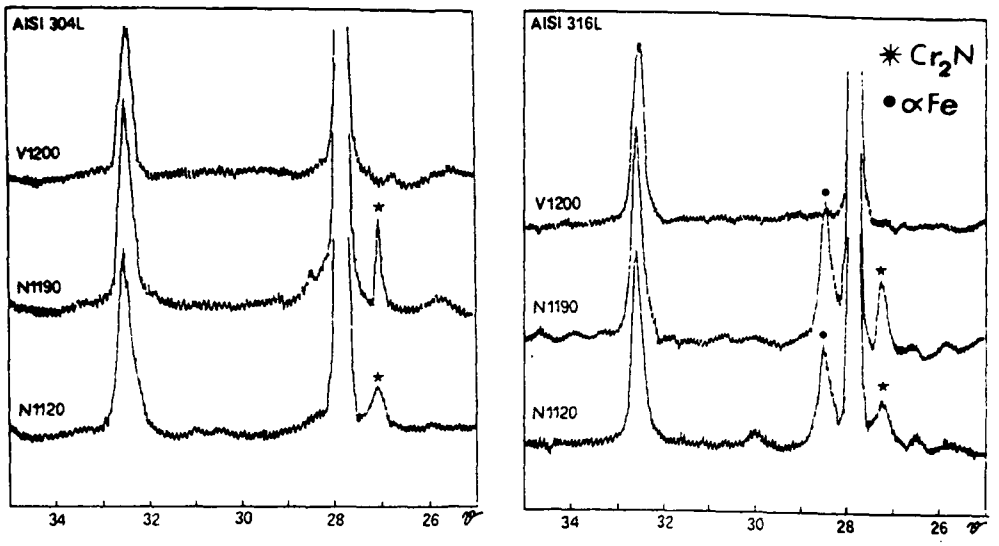

Fig.1 - X-ray diffractograms of sintered samples (see Table II for codes).

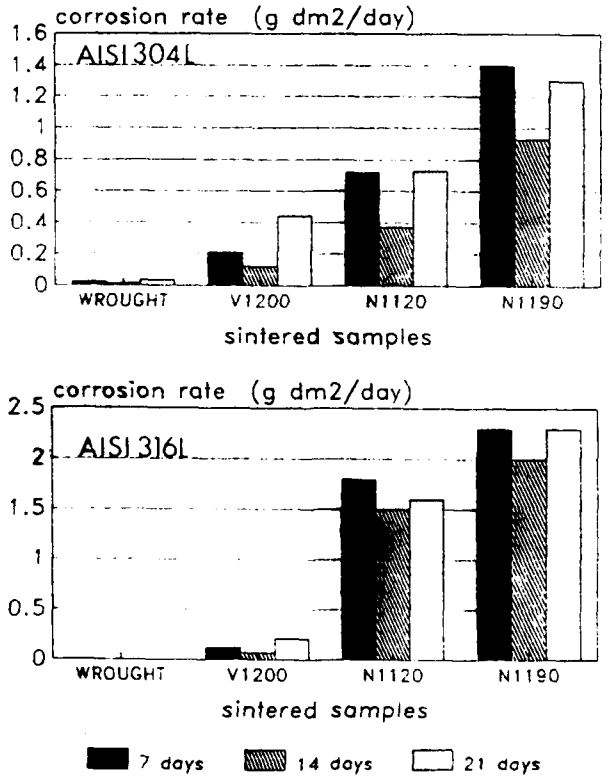

Fig.2 - Corrosion rates ($g/dm^2 \cdot day$) in 0.5M H_2SO_4 solution, T=25°C, of wrought and sintered samples (see Tab.II for codes).

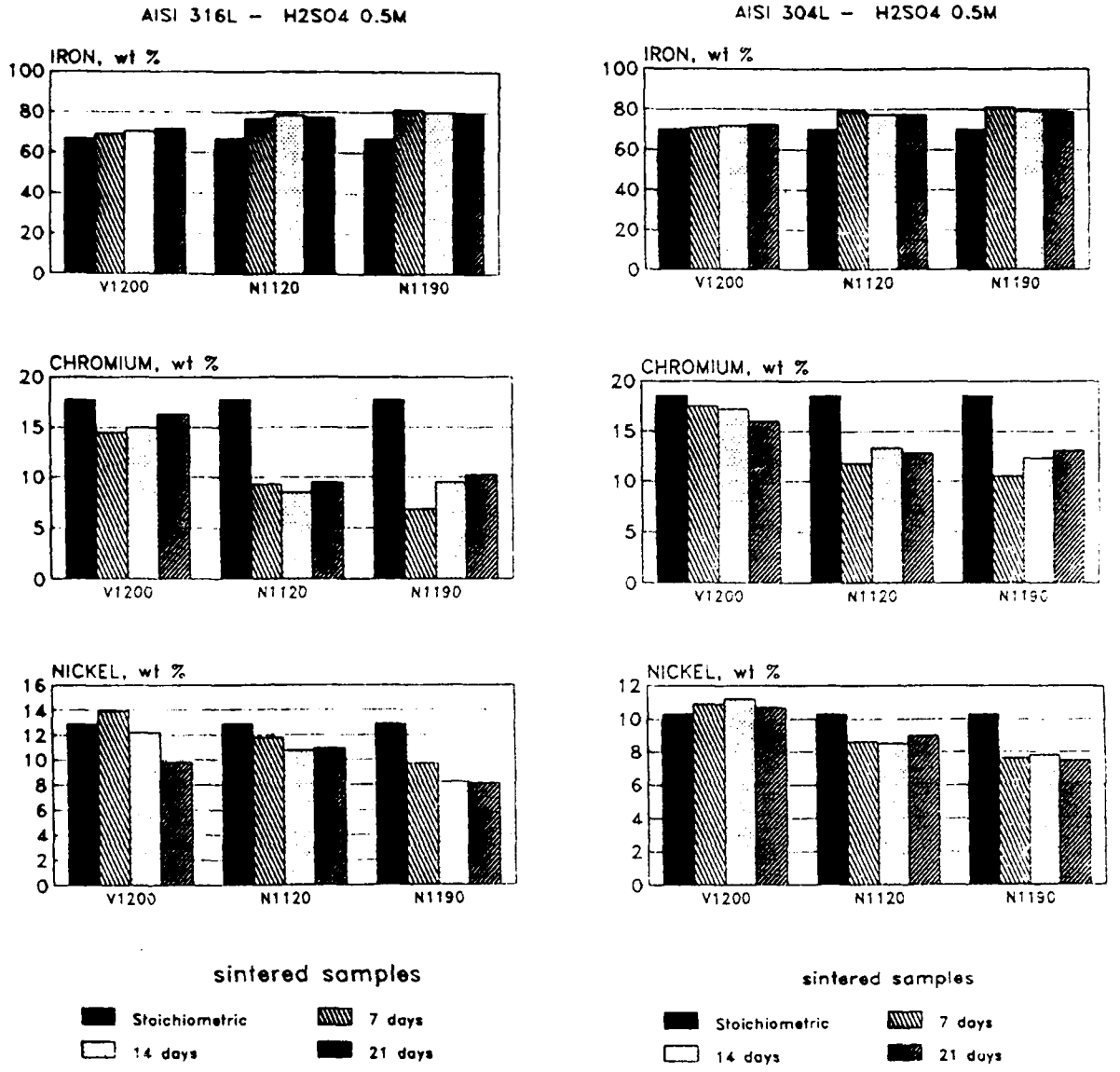

Fig.3 - Amounts of Fe, Cr and Ni dissolved in the 0.5 M H_2SO_4 solution during the corrosion tests of sintered samples (see Tab.II for codes). The contents are expressed as wt % of each element relative to the total weight of the corrosion products revealed by the ICP-OES analysis of each solution.

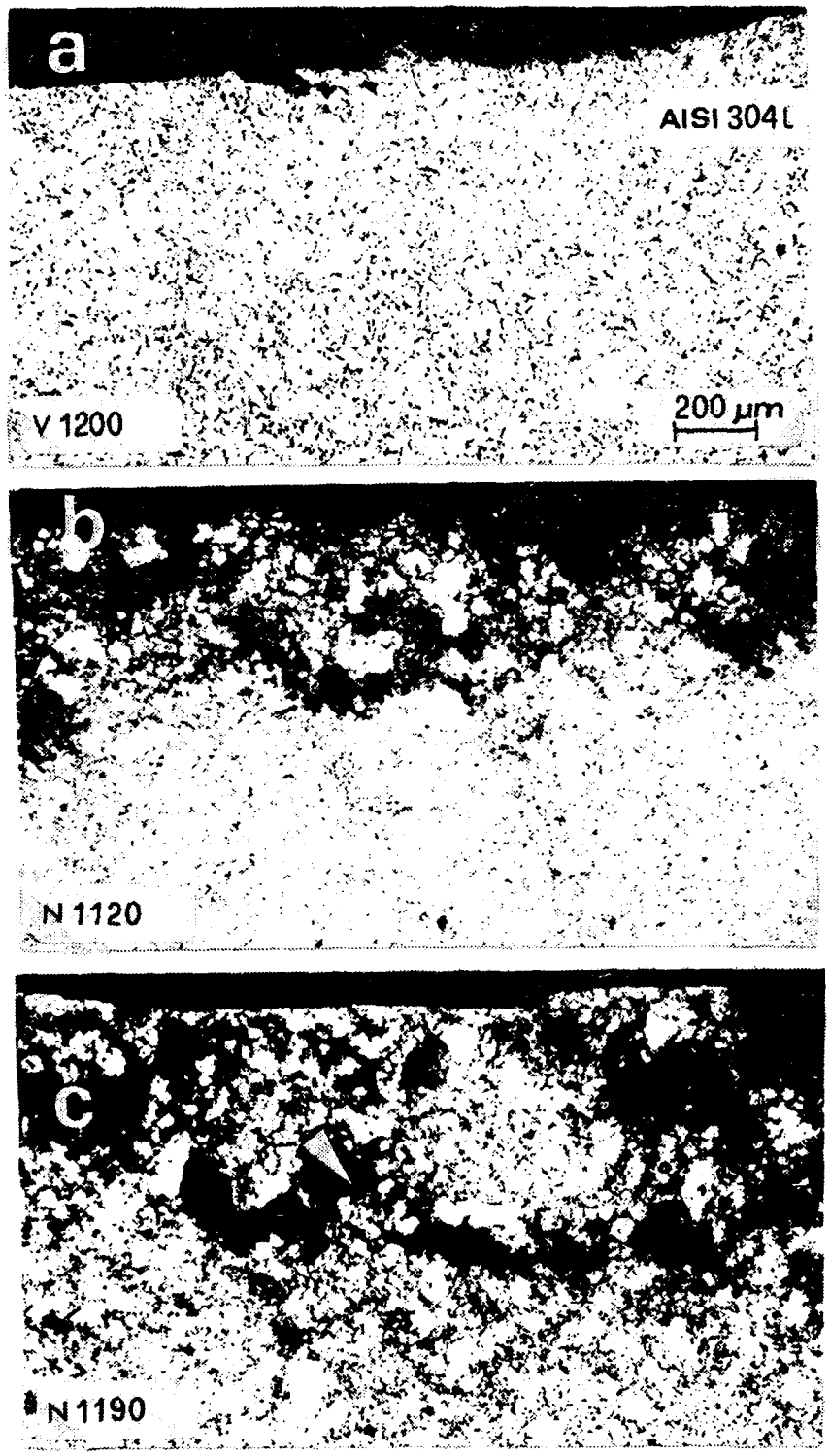

Fig.4 - Cross- sections of samples of AISI 304L after 21 days of immersion in 0.5M H_2SO_4 solution, T=25°C (see Tab.II for codes).

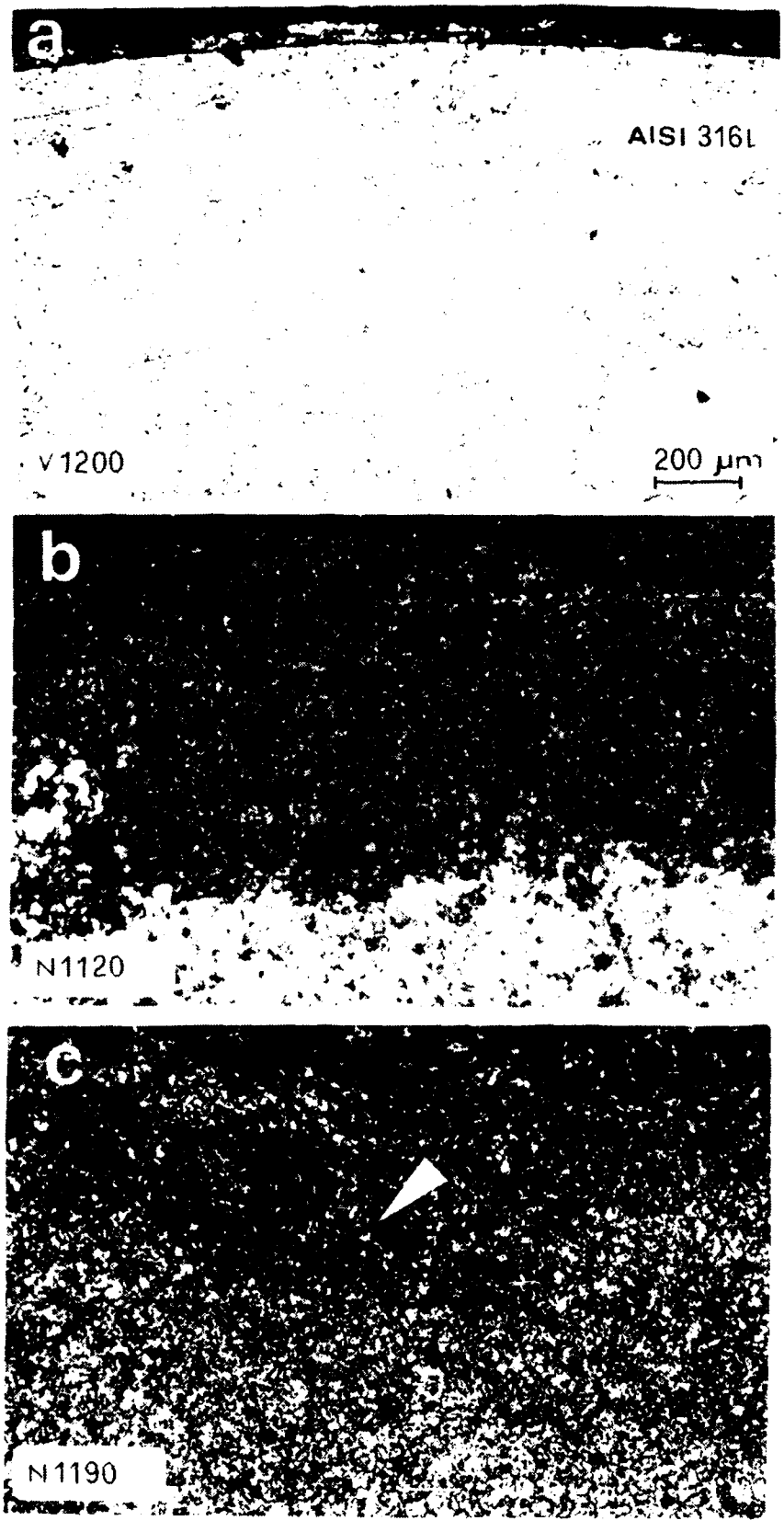

Fig.5 - BSE micrographs of the cross- sections of samples of AISI 316L after 21 days of immersion in 0.5M H_2SO_4 solution, T=25°C (see Tab.II for codes).

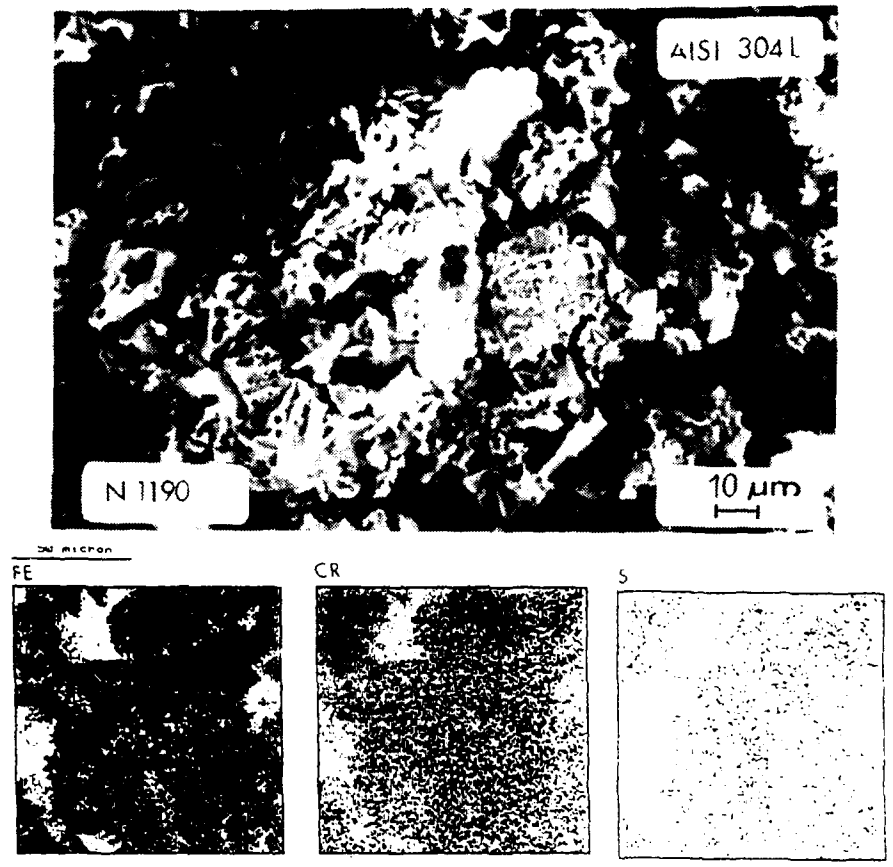

Fig.6 - SEM micrograph of the area indicated in Fig.4(c); Fe, Cr and S X-ray concentration maps.

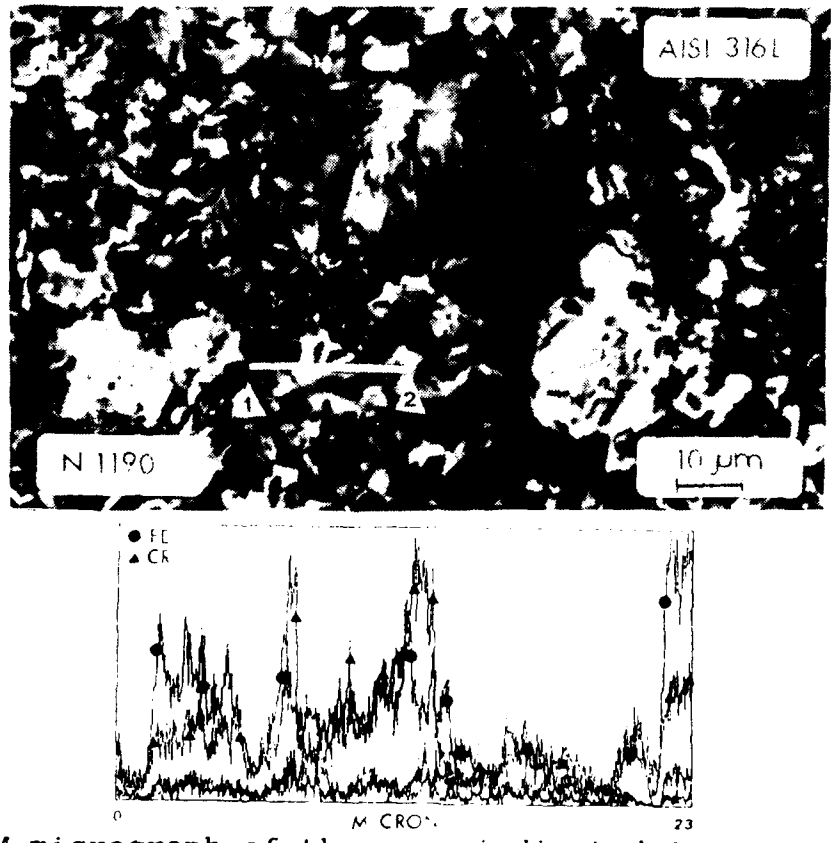

Fig.7 - SEM micrograph of the area indicated in Fig.5(c); Fe and Cr X-ray concentration profiles for the line 1-2.

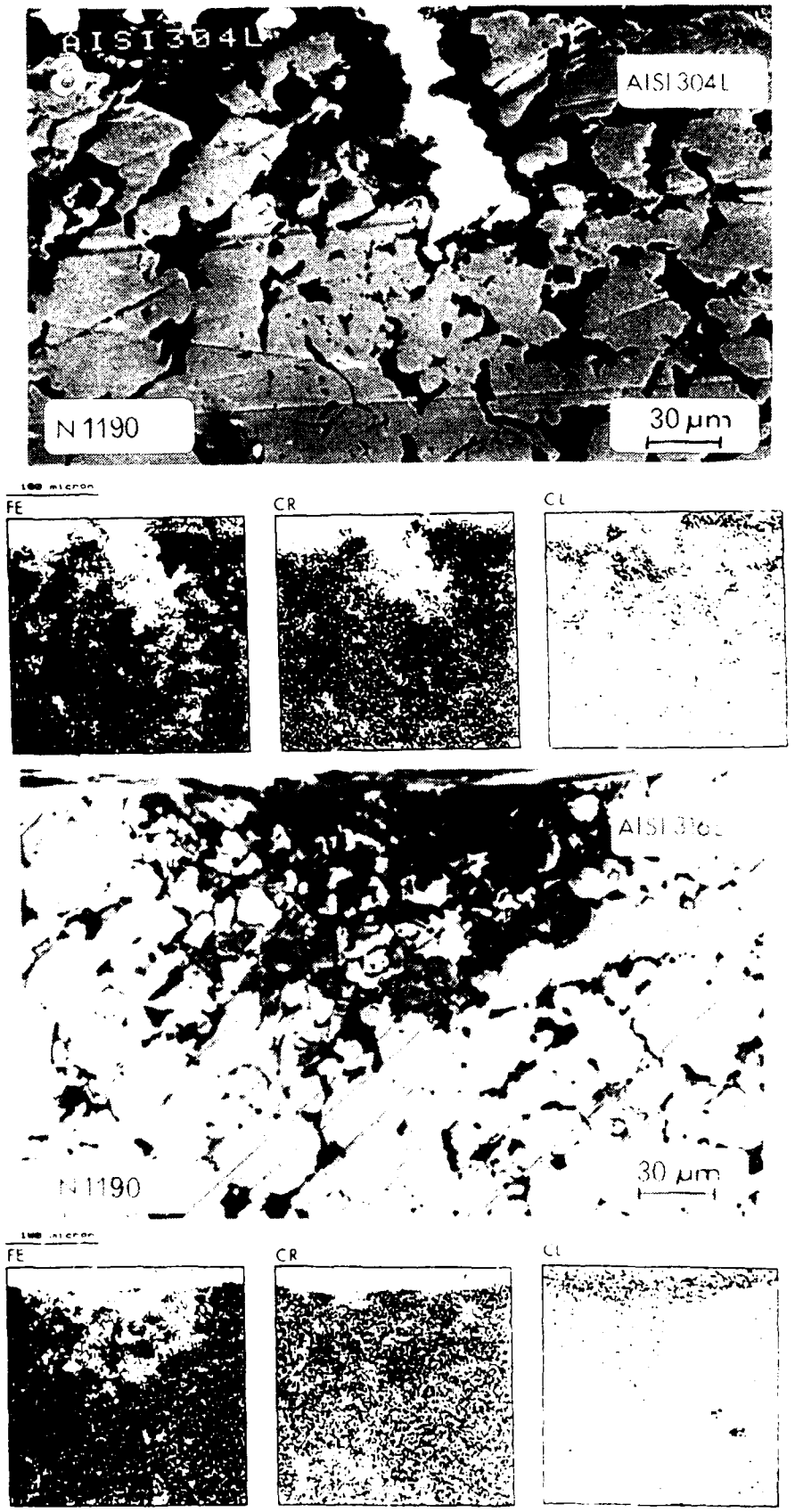

Fig.8 - SEM micrographs of the cross- sections of samples of AISI 304L (a) and AISI 316L (b) after 21 days of immersion in 0.1M NaCl solution, T=25°C; X-ray concentration maps for Fe, Cr and Cl (see Tab.II for codes)

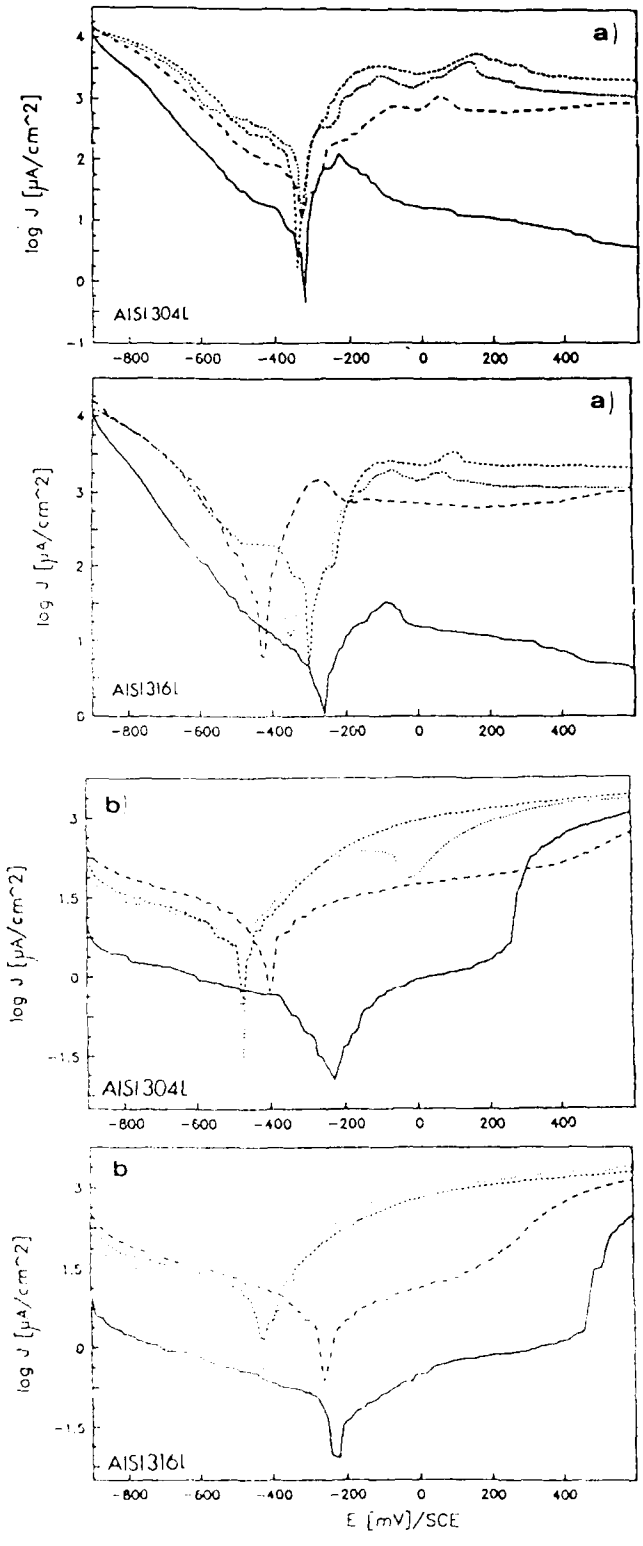

Fig.9 - Polarization curves in 0.5 M H_2SO_4 (a) and 0.1 M NaCl (b) solutions, T=25°C, recorded on wrought and sintered samples: (——) wrought, (— — —) V1200, (- - - -) N1120, (····) N1190, (see Tab.II for codes). Potential scan rate: 1 mV/s.

Advances in Technology Produce New Materials for Challenging Applications

Norman B. Schmidt
Product Application Manager
Carpenter Technology Corporation
PO Box 14662
Reading, PA 19612-4662

Terry A. DeBold
Specialist, Stainless Alloy R&D
Carpenter Technology Corporation
PO Box 14662
Reading, PA 19612-4662

Abstract

Advances in the technology of melting and hot deformation have made new alloys and products available. New stainless and nickel-base alloys have found application as valves, fasteners and specialized equipment in the oil field, and in various industrial and chemical environments. This paper provides a review of the technology behind new materials and provides specific examples of service applications.

Key terms: arc melting, argon-oxygen decarburization, vacuum-arc remelting, electroslag remelting, vacuum induction melting, rotary forging, corrosion resistance, pitting, strength, sour service, stainless steel, nickel-base alloy

Introduction

More than eighty years ago, August 20, 1913, the first successful cast of stainless steel was made, in Sheffield, England. This martensitic alloy of iron and chromium was soon followed by the production of an iron-chromium-nickel composition in Germany, which was the first austenitic stainless to be developed. Over the next several decades, near variants of the original compositions were provided to expand the range of useful properties and enhance fabricability. As researchers explored the attributes of more and more alloying elements, the contribution of these attributes focused on two somewhat divergent regimes. The first looked at corrosion resistance in increasingly harsh chemical environments at near ambient temperatures, and the second was concerned with strength and oxidation resistance at very elevated temperatures. By the 1930's and early 1940's, minor additions of elements such as titanium and aluminum to nickel-chromium-iron alloys provided properties needed in the newly emerging gas turbine/jet engine equipment. As more complex compositions were invented, manufacturing became more challenging, and a greater understanding of metallurgical characteristics in conjunction with greater processing controls was necessary for a reliable end result. The two families of alloys, corrosion resisting and heat resisting, because of the commonality of elements such as chromium, nickel and molybdenum, frequently crossed the boundaries of use with super 12% chromium alloys being used for turbine applications, and iron and nickel based superalloys being employed to resist corrosive attack.

With increasing challenges related to manufacturing came significant advances in melting and hot working techniques that mitigated the problems One of the most important was the development of vacuum induction melting and vacuum arc remelting around 1950. This technique, and later modifications and advances, controlled undesirable impurities and optimized desirable properties. It allowed increases in beneficial alloy elements, without the formation of deleterious phases and permitted broadened hot working ranges. In turn, new and more versatile hot working equipment

expanded the types of alloys that could be made in wrought form.

This paper will discuss a number of unique alloys developed in the recent past that have benefited from technology advances. Some planned and unanticipated applications will be used to illustrate how these alloys are expanding the capability of metallic materials to handle increasingly critical requirements. The first section will briefly review current melting procedures and a unit of hot working equipment, known as the rotary forge. The second section will explore alloys which owe their properties to the latest understanding of the combining of composition and processing.

Melting Techniques

Arc Melting

Most stainless alloys are produced by melting techniques performed in an air environment. Initially, stainless steel scrap of known composition, along with charge chrome and some alloying elements are melted in the electric arc furnace (see Figure 1). When the total charge is completely melted, it is transferred via ladle to the argon-oxygen decarburization (AOD) vessel for refining.

AOD Processing

The AOD vessel is a pear shaped refractory lined steel shell, through which oxygen, argon and nitrogen are blown into the molten metal bath to achieve decarburization (see Figure 2). After the desired aim carbon is achieved, alloys, lime and ferro-silicon or aluminum are added to reduce chromium and other metallic elements that were oxidized. One of the primary benefits of the AOD process is the ability to obtain very low levels of sulfur (S). Volatile residual elements can be removed due to their high vapor pressures. The injection of inert gas into the bath provides a means for removing unwanted gas impurities. However, some pick-up in hydrogen and nitrogen occurs during vessel tap and ingot teeming. Trim additions of alloy elements bring the composition within desired limits.

When compared to straight electric furnace product, AOD processed steels offer improved cleanness, due to lower non-metallic inclusions. Because the molten metal is in intimate contact with furnace refractory, slag, and ambient atmospheres there are unavoidable levels of randomly distributed non-metallics in the ingots.

Vacuum Induction Melting

Vacuum induction melting (VIM) provides a melt with reduced gas content and good chemistry control. A disadvantage is contact of the molten metal with the furnace refractory. VIM is frequently used to cast electrodes to be remelted in the vacuum arc remelting or electroslag remelting processes discussed below.

The vacuum induction process uses an airtight vessel or vacuum chamber which completely encloses the melting equipment. Mechanical vacuum systems, in conjunction with an oil diffusion system, are used to evacuate the chamber. A water cooled copper coil surrounds the furnace and heating is accomplished by sending an electric current through the coil. This current sets up a magnetic field that interacts with the charge material, creating frictional heat between the atoms. The charge materials must be of the composition desired - only relatively small quantities of late alloy additions are made via a recharge system. When the metal is molten the furnace is tilted enabling the heat to be poured over a spout and into an awaiting mold, as shown in Figure 3. A mold turntable is used to position empty molds under the pouring spout.

Vacuum Arc Remelting

Vacuum Arc Remelting (VAR), shown in Figure 4, is a popular operation frequently used for stainless and nickel-base alloys. The feedstock for remelting often consists of consumable electrodes produced by conventional air melting techniques or vacuum induction melting, discussed above. In the VAR furnace electric current is passed through the electrode and the electrical power produces the heat necessary for the remelting through the formation of an electric arc. It is the melting of the electrode and subsequent resolidification (another definition of "R") of the ingot that gives the remelted material its superior properties. The controlled solidification virtually eliminates ingot macrosegregation and significantly reduces microsegregation. The number and size of non-metallic inclusions is reduced and the remaining inclusions are smaller and distributed more evenly. The removal of gases and volatile elements is enhanced by the remelting process. The melting, performed in water cooled copper crucibles, eliminates undesirable metal/refractory reactions. Many chemical reactions are favored at the low pressures and high temperatures obtained during vacuum arc remelting, such as (1) dissociation of oxides, carbides, hydrides, sulfides and nitrides, (2) deoxidation, and (3) degasification. One drawback of VAR is the lack of any effective form of sulfur removal, but this can be overcome by use of low sulfur electrodes. Inclusion removal is facilitated by flotation to the molten pool surface where they are pushed to the edge of the pool by ripple action. The water-cooled copper crucible quickly cools the molten metal resulting in uniform alloying element and inclusion distributions.

Electroslag Remelting

The electroslag remelting process (ESR), shown in Figure 5, is similar in many respects to VAR. The process combines fully controlled melting conditions with fully controlled freezing conditions, but remelting occurs through a chemically active slag as opposed to melting under a vacuum. Single phase AC power is applied to the electrode, which is aligned above the water-cooled mold. The electrode is immersed in the slag, and droplets of molten metal form on the bottom of the electrode and fall through the slag to the metal pool. The slag is the heating component of the system; it acts as a solvent for non-metallics, protects the molten metal from contamination and acts as a mold lining. The water-cooled mold promotes a shallow molten pool which reduces microsegregation, increases chemical homogeneity, improves inclusion distribution and increases ingot soundness.

Processing via Rotary Forging

To extend the technical capabilities for producing difficult-to-work alloys or developing special properties, processing can be directed to the relatively new rotary forging facility. See Figure 6. The basic concept uses four mechanically driven hammers to rapidly exert force simultaneously on four sides of the workpiece. This causes spreading to occur in the longitudinal direction. The equipment can make rounds, flats, squares, rectangles, hollows and multiple outside diameter bars up to 39 ft. in length. Advantages over conventional 2-die forging presses include:

- Four-point contact as opposed to two point.
- Force exerted on all sides, limited to longitudinal spreading.
- Surface tears and center bursts minimized.
- Uses approximately 50% less energy than a conventional system.
- Centerline of workpiece is constant, providing better straightness.
- Rapid forging speed allows a proper temperature to be maintained. Work can be completed without numerous reheats, which may be necessary in a conventional system.
- Precise size control and close tolerances.
- Opportunity for different cooling or quenching methods.

As an example, it is possible to take a 17-inch diameter ESR ingot of a nitrogen strengthened stainless drill collar alloy and in one heating forge it into an 8 1/2" diameter, 422-inch long section in 15 minutes.

Alloy Development and Application

General-Purpose Corrosion Resistance.

Beginning with the first stainless steels, which were essentially Type 420 and Type 304, more complex alloys evolved as the ramifications of increased alloy content on structure, phases, workability, and heat treatment were understood and overcome. It is instructive to consider the development and optimization of a classic alloy, Carpenter 20 stainless, to contrast the pace and philosophy of alloy development "then" vs. "now". This alloy is probably the best recognized proprietary stainless steel and the closest to the "ultimate" stainless steel in the decades of the 50's, 60's and 70's.

It started as a cast alloy, which was commercialized as "Alloy 20" by Duriron in 1940. The nominal composition was 29% Ni, 20% Cr, 2.5% Mo and 3.5% Cu, and it was designed to handle sulfuric acid. It is made today as ACI designation CN-7M (UNS J95150). The original casting grade, with greater than 55% alloy content, was too difficult to produce in wrought form because of hot working problems. When Carpenter solved these problems in 1951 via a special treatment with rare earth elements, Carpenter 20 stainless was born.

Because of its excellent corrosion resistance in a wide variety of oxidizing environments, beyond sulfuric acid, and because wrought components such as tubing, plate and sheet were being welded, it was necessary to stabilize the alloy against intergranular carbide precipitation. The addition of columbium to the analysis produced Carpenter 20Cb stainless. Over the years extensive research was conducted to understand the influence of various alloy elements on corrosion resistance, such as manganese, silicon, columbium, carbon, and nickel. In 1965 sufficient information had been developed on the beneficial effect of increased nickel on stress-corrosion cracking resistance in chlorides and in sulfuric acid to allow the introduction of the third iteration of the alloy, which became known as 20Cb-3® stainless (UNS N08020). This end result has been a material having the resistance shown in Figure 7, with improved fabricability and optimum utility of the fabricated product in a wide variety of applications. A common example is shown in Figure 8.

Another development allowing the use of high deposition rate welding practices such as gas metal arc and submerged arc with essential freedom from weld hot cracking is designated by the American Welding Society as E320LR (covered electrodes) or ER320LR (bare wire) filler metal. The improvement in hot cracking resistance is shown in Figure 9. Residual elements in these filler metal products are carefully controlled using melting know-how.

Pitting Resistance and Strength

Historically, stainless steels have been susceptible to pitting and crevice corrosion in environments containing high levels of chlorides, in both chemical as well as marine applications. The beneficial influence of nitrogen on pitting resistance was utilized with the nitrogen strengthened alloy 22Cr-13Ni-5Mn (UNS S20910). Also, major improvements were offered by increasing the molybdenum content to the vicinity of 6 percent, as in AL-6XN* stainless (UNS N08367).

*Registered trademark Allegheny Ludlum Corp.

To improve the pitting resistance offered by UNS N08020, at some sacrifice in resistance to sulfuric acid, 20Mo-6® stainless (UNS N08026) was developed. Most of these types of alloys are very effectively ranked by their Pitting Resistance Equivalent Index (PRE = Cr + 3.3% Mo + 16% N). Many have found application as sheet or plate for fabrications in the chemical process industry.

One very specialized application has been developed in drilling of oil and gas wells and in resisting the corrosion of geothermal environments. Here armored cable and wire line are used to insert and remove instruments and tools from the wells. Some environments can be very corrosive, containing CO_2, NaCl and H_2S at high temperatures. Because wells extend to depths of 20,000-25,000 feet, high strength is required to withstand the tensile loads involved. A modification of UNS N08026, called 20Mo-6®HS stainless (UNS N08036) has been developed. The nominal composition is as follows:

C	Cr	Ni	Mo	Cu	N	Fe
0.05	23.6	36.4	5.7	1.1	0.32	Bal

The HS grade achieves high strength through cold work, not by heat treatment. In the cold worked condition UNS N08036 retains excellent resistance to environmental cracking and chloride-induced pitting and crevice corrosion while remaining non-magnetic. Tensile strength capability reaches 270 ksi (1862 MPa), with good ductility demonstrated by the wrap test in Figure 10. Despite its leaner alloy content, it can be substituted for MP35N (UNS R30035) where that alloy represents technical overkill.

The corrosion resistance of UNS N08036 in sour and simulated drilling environments is shown in Table 1. High strength U-bends resisted ambient temperature sulfide stress cracking in the NACE TM0177 environment. Good resistance was also demonstrated at elevated temperatures in simulated drilling environments.

Another demanding application, born of the harsh environments encountered in the directional drilling of some oil and gas wells, is the stainless non-magnetic drill collar. Drilling muds employed to protect the formations can be very high in compounds such as $MgCl_2$ and $BaCl_2$, which can promote stress-corrosion cracking. Drill collars provide the weight on the drill bit to facilitate penetration. They range from about 4 inches to 10 inches outside diameter, around 3 inches inside diameter, and are usually about 30 feet long. They must have about 100 ksi minimum yield strength, and where used with measurement while drilling systems must be fully non-magnetic to avoid interference with telemetry from the instruments near the bottom of the hole.

The 15-15LC™ stainless (UNS S21300) was developed as a candidate to meet the requirements for a chromium-manganese stainless drill collar. An example of this product is shown in Figure 11. The nominal composition of this material is:

C	Cr	Mn	Ni	Mo	N	Fe
0.04	17.5	17.5	1.0	1.0	0.5	Bal

The best way to achieve the maximum nitrogen solubility and the homogeneity of alloying elements necessary to a fully austenitic structure free from magnetic "hot spots" is to cast electrodes from the AOD vessel and use electroslag remelting to make the ingots. These ingots must subsequently be forged into the drill collar form, and the temperature of the final passes must be carefully controlled to impart the correct amount of "warm working" to achieve the strength required. Mechanical properties vary with product size, but typically have been as shown in Table 2. High strength, along with excellent ductility and impact values have been obtained with this non-magnetic material.

After the O.D. is turned to the desired dimensions and the I.D. is trepanned, a compressive treatment

is applied to the I.D. surface to prevent the initiation of stress-corrosion cracks. Stress-corrosion cracking resistance of I.D. treated drill collar sections has been confirmed in the laboratory. A simulated drilling mud solution (26% sodium chloride with 2.5% ammonium bisulfite) was boiled in the bore using an immersion heater. After 1,000 hours, absence of stress-corrosion cracking was confirmed using metallographic techniques.

Highly-Alloyed Compositions for Severe Environments

Because the length of exposure to down hole environments is of limited duration for armored cable, wire line, and drill collars, it is possible to use the stainless alloys already mentioned. But where formations are being produced, and oil and gas containing high levels of chlorides and H_2S must be contained within critical components, alloys with far better resistance to environmental cracking at elevated temperatures must be employed. For a number of years Pyromet® 718 alloy (UNS N07718) was employed for sub-surface and surface components handling sour gas. This alloy was selected from among the nickel-base precipitation hardenable gas turbine alloys because its composition provided a level of strength and corrosion resistance superior to the cold worked austenitic stainless steels and the duplex stainless steels. With the development of fields in Mobile Bay, a more corrosion resistant hardenable alloy was needed for the more severe conditions. Alloy development research began in 1983; progress was reported in papers given at previous NACE conferences (references 1 to 3) and today Custom Age 625 PLUS® alloy (UNS N07716) has become a widely used material. An example of one application for which this alloy has been tested, a sub-surface safety valve, is shown in Figure 12.

The composition of this grade is nominally:

C	Cr	Ni	Mo	Ti	Cb	Fe	Al
0.01	21.0	60.75	8.0	1.3	3.4	5.0	0.2

It is vacuum induction melted followed by vacuum arc remelting. Many of the larger sizes have been produced on the rotary forge. After hot working, bars are heat treated at the mill using a double aging treatment to produce the mechanical properties desired in the component produced from the bar stock. Typically the mechanical properties for oil field applications are 130 ksi (896 MPa) 0.2% Y.S., 181 ksi (1248 MPa) U.T.S., 32% elongation (4D), 54% reduction in area and 38 HRC.

Table 3 provides examples of a few of the tests performed to demonstrate the resistance of UNS N07716 to both ambient and elevated temperature environmental cracking. Establishing resistance to NACE TM0177 at room temperature is an important first step for materials used in sour service. UNS N07716 was resistant when coupled to steel, which increases the severity of the test for more noble materials by stimulating hydrogen formation. For qualification purposes, slow strain rate tests (SSRT) in environments designed to simulate down hole conditions have demonstrated excellent resistance to the test environment. Results of SSRT tests in one of these environments at 300° F are shown in Table 3. The table also shows that UNS N07716 resisted hydrogen sulfide and elemental sulfur (S°) in deaerated brine when tested at 350 and 400°F (177 and 204°C).

With today's increased emphasis on avoiding unexpected failure or costly repair of equipment operating in severe environments containing chlorides, UNS N07716 is being selected for applications beyond the oil patch. It is a primary candidate for fasteners in marine and chemical environments and has been used for critical components in the pulp and paper industry. Direct aged material and cold worked plus aged material with strengths higher than those evaluated for inclusion in NACE MR0175 are being evaluated for drill collars and automotive engine fasteners.

Strength, Toughness and Corrosion Resistance

In some cases the magnitude of general corrosion resistance needed for a critical application does not require the level of chromium associated with even the leanest of stainless steels. Occasionally, a combination of properties, such as strength, fracture toughness and resistance to fatigue and stress corrosion cracking delineates a unique new alloy. Such is the case for Aermet® 100 alloy (UNS K92580) which was originally developed as a high strength, high fracture toughness grade as a candidate for aircraft landing gear. Its nominal composition is

C	Cr	Ni	Mo	Co	Fe
0.23	3.1	11.1	1.2	13.4	Bal

It is melted using vacuum processes.

Other alloys which have been used or considered include HY 180 with 200 ksi tensile strength and its derivative AF 1410 (UNS K92571) with 235 ksi (1620 MPa) tensile strength. These alloys have excellent fracture toughness but not enough strength for the latest designs. Alloys with tensile strength exceeding 250 ksi (1724 MPa), such as H11 tool steel (UNS T20811), 300M alloy (UNS K44220) and Marage 250 lack either stress-corrosion cracking resistance or sufficient fatigue strength and fracture toughness.

UNS K92580 was developed using a computer model of the properties and interactions in the Fe-Co-Ni-Mo-Cr-C system. The effect of impurity elements such as P, S, O, and N were also taken into consideration. Mechanical working (hot and cold) was optimized with a primary and secondary forging operation designed to produce a grain size of nominally ASTM 9. The heat treatment includes solution treating, refrigerating and aging. The result is the alloy described in Table 4, with an exceptional combination of strength and fracture toughness and fatigue strength superior to that of other high strength alloys.

Table 4 also demonstrates the resistance to stress-corrosion cracking in sodium chloride, a property necessary for materials exposed to marine environments. Resistance to stress-corrosion cracking was also evaluated using a U-bend sample alternately immersed in a 3.5% NaCl solution and withdrawn and allowed to dry, then re-immersed. The cycle calls for 10-minute immersion and 50 minutes to dry. Results showed alloys H-11 and 300M to be highly susceptible to stress corrosion cracking, with both alloys showing a mean time-to-fail of one day or less. UNS K92580 while not immune, was significantly more resistant, with a mean time-to-fail of 25 days.

Because UNS K92580 has such high fracture toughness and improved resistance to stress-corrosion cracking, it has been selected as a candidate for landing gear on the F/A-18 E/F carrier-based aircraft, Figure 13, where the marine environment and possible overstressing from a hard landing could present potential problems. The alloy is also being evaluated as a candidate for main jet engine shafts, fasteners, and welded tube for bicycle frames.

Regardless of the degree of corrosion resistance needed, alloy development is focused more narrowly today on niche applications than was the case when corrosion resistant alloys and high temperature alloys tended to be employed within simpler regimes of service. Newly developed alloys are now subjected to more sophisticated evaluations, such as fracture toughness tests, corrosion fatigue tests, and slow strain rate tests mentioned in this paper. Engineers are interested in defining the "envelope" of service conditions where predictable performance can be achieved. To insure reliability, the producers must take advantage of more controllable processing and strict conformance to manufacturing guidelines. A good example of this is the large quantities of different sizes of UNS N07716 which have been purchased in the fully heat treated condition, tested and certified prior to

service in critical components in Mobile Bay.

It seems a long way from the cutlery steel produced in 1913, but is undoubtedly just a milepost on the road to materials for the future.

References

1. R. B. Frank, T. A. DeBold, "Properties of an Age-Hardenable, Corrosion-Resistant, Nickel-Base Alloy," CORROSION/88, paper no. 75 (Houston TX: National Association of Corrosion Engineers, 1988).

2. R. B. Frank, T. A. DeBold, "Heat Treatment of an Age Hardenable, Corrosion-Resistant Alloy - UNS N07716," CORROSION/90, paper no. 59, (Houston, TX: National Association of Corrosion Engineers, 1990).

3. T. A. DeBold, N. B. Schmidt, M. F. Bluem, S. R. Herman, "Evaluation and Qualification of a Precipitation-Hardened Material for Deep, Hot Sour Environments," CORROSION/92, paper no. 49, (Houston, TX: National Association of Corrosion Engineers, 1992).

Table 1 - Resistance of UNS N08036 U-Bends to Environmental Cracking

U. T. S.		Wire Diameter			
ksi	MPa	in	mm	Environment	Result
275	1896	0.092	2.34	5% NaCl + 0.5% acetic acid + H_2S purge (NACE TM0177 solution) at room temperature	No cracks in 42 days, with and without steel couple
275	1896	0.092	2.34	Saturated NaCl + 2.5% NH_4HSO_3 at 228°F (109°C)	No cracks in 42 days
275	1896	0.092	2.34	23.5% $MgCl_2$ + 6% KCl + 0.3% CaO at 235°F (113°C)	No cracks in 42 days
274	1889	0.031	0.79	Saturated NaCl + 5% $MgCl_2$ + 5% H_2S at 350F (177°C) and 5000 psi (34.5 MPa)	No cracks in 14 days

0.031" diameter wire cold drawn 72%; 0.092" diameter cold drawn 77%.

Table 2 - Typical Room Temperature Mechanical Property Range for UNS S21300 Warm Worked Bar

Property	Value
0.2% Y.S.	105-118 ksi (723-813 MPa)
U.T.S.	129-138 ksi (887-949 MPa)
% Elong (4D)	38-42
% R.A.	72-74
Charpy V-Notch	178-202 ft-lb (241-274 J)
Brinell Hardness	269-302

Table 3 - Environmental Cracking Resistance of UNS N07716 Bars

Solution treated plus aged at 1350F (732C)/8h, furnace cool to 1150F (621C)/8h/AC

0.2% Y. S. ksi	0.2% Y. S. MPa	Sample Style	Environment	Temp. (°F)	Result
130	896	Transverse U-Bends[a]	NACE TM0177[b] (steel couples)	75°F 24°C	No cracks; 1000h
129.5	893	Longitudinal SSRT[c]	25% NaCl + 0.5% acetic acid + 100 psi H_2S, (added at room temperature)	300°F 149°C	Time to fail ratios[d] of 0.93 to 1.07
126.5	872	Longitudinal SSRT[c]	16.5% NaCl + 150 psi H_2S, 150 psi CO_2 (added at room temperature), 10 g/l S°	350°F 177°C	Time to fail ratios[d] of 0.99 and 1.03
130	896	Transverse U-Bends[a] and C-Rings[a,e]	25% NaCl + 0.5 g/l S° + 1400 psi H_2S	400°F 204°C	No cracks; 28 days

Two or more specimens per test from approximately mid-radius location.
1400 psi = 9653 kPa; 150 psi = 1034 kPa; 100 psi = 689 kPa.

a Well aged at 500F (260C) for 720 hours after heat treatment.
b 5% NaCl + 0.5% acetic acid, purged with H_2S.
c Slow strain rate tensile specimen.
d Time to fail in corrosive environment vs. inert environment.
e C-rings stressed at 100% of 0.2% Y. S.

Table 4 - Typical Mechanical Properties and Environmental Cracking Resistance of UNS K92580

Heat Treatment: [1625°F (855°C), 1 hour, AC] + [-100°F (-73°C), 1 hour] + [900°F (482°C), 5 hours]

Property	Longitudinal Orientation	Transverse Orientaton
0.2% Y.S.	250 ksi (1724 MPa)	250 ksi (1724 MPa)
U.T.S.	285 ksi (1965 MPa)	285 ksi (1965 MPa)
% Elong.	14	13
% R.A.	65	55
Charpy V-Notch	30 ft-lb (41J)	25 ft-lb (34J)
Frac. Tough. K_{Ic}	115 ksi√in (126 MPa√m)	100 ksi√in (110 MPa√m)
K_{Iscc} in 3.5% NaCl	35 ksi√in (38.5 MPa√m)[a]	Not tested

a K_{Iscc} based on 1000 hour exposure in 3.5% NaCl at room temperature with a L-T specimen orientation.

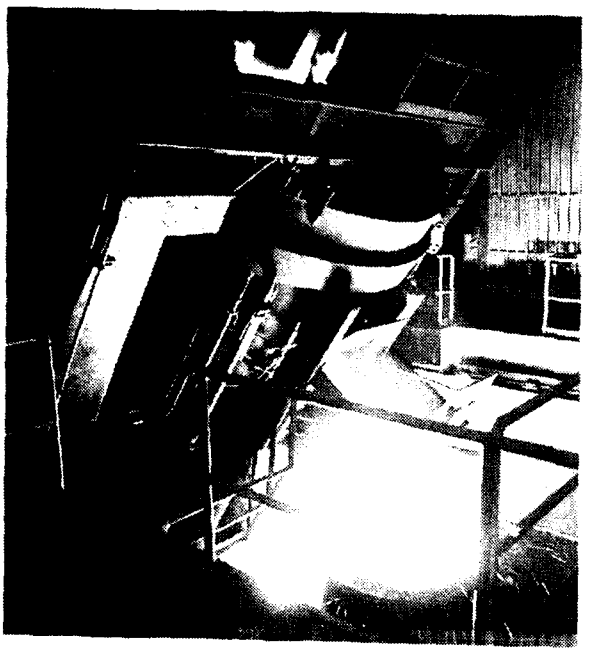

Figure 1 - Tapping 30-ton electric arc furnace.

Figure 2 - Argon-oxygen decarburization is useful in removing carbon and controlling the chemistry of stainless steels.

Figure 3 - Heats processed in vacuum induction furnaces are melted and poured in the absence of atmospheric comtaminants.

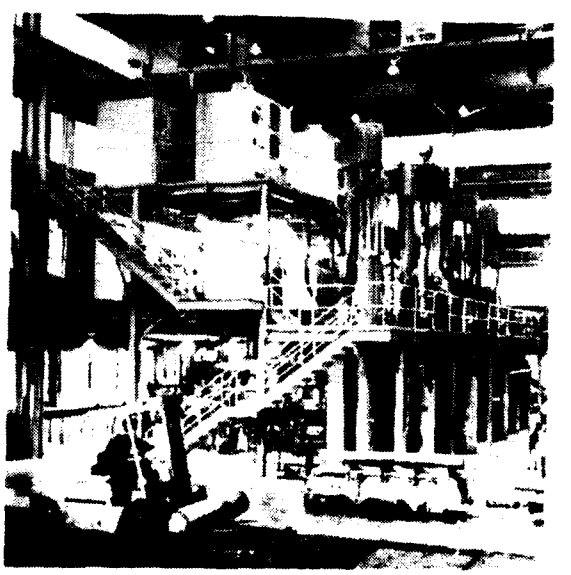

Figure 4 - Refinement in vacuum arc remelting furnaces creates a finer, more uniform grain structure in the resulting ingot.

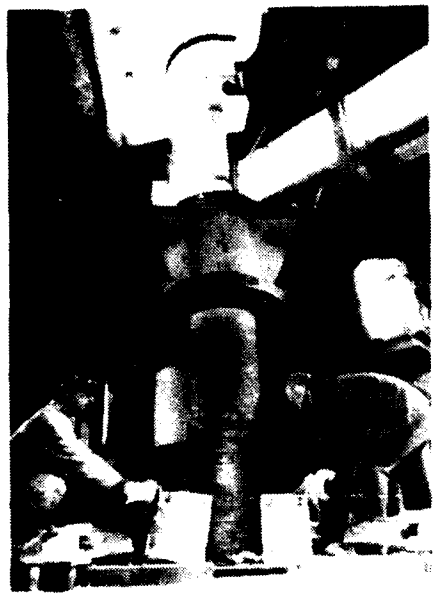

Figure 5 - Electroslag remelting (ESR) results in metals of higher purity with fewer inclusions, more uniform grain structure and improved mechanical properties.

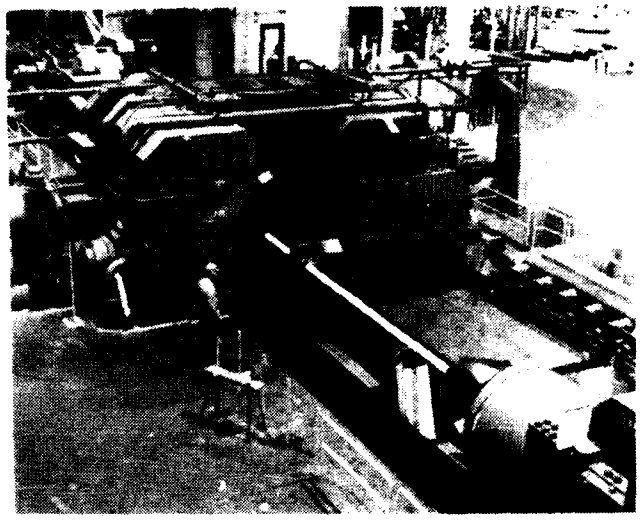

Figure 6 - Rotary forge readily produces materials difficult to work with conventional forging practices.

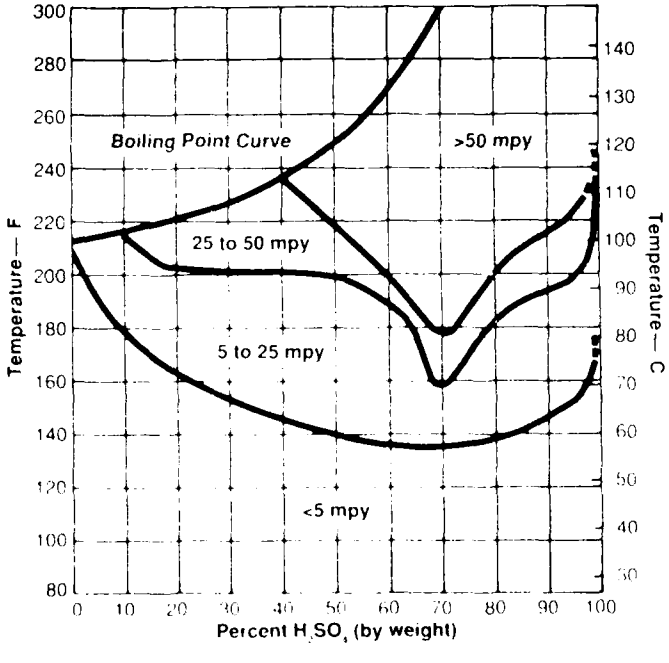

Figure 7 - Typical iso-corrosion properties of UNS N08020 in sulfuric acid.

Figure 8 - Type 316 stainless (left) and UNS N08020 (right) after exposure to hot sulfuric acid for identical periods.

Figure 9 - Gas metal arc weld bend test specimens showing improvement of ER320LR filler metal over conventional ER320 filler metal.

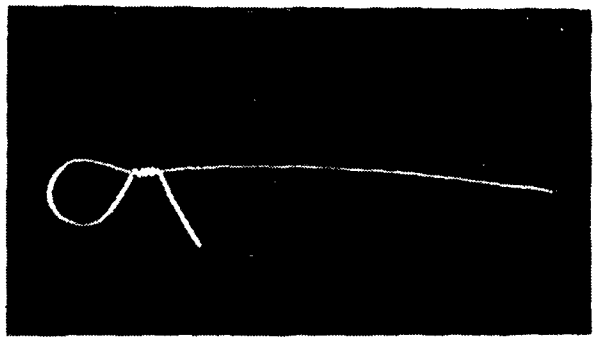

Figure 10 - Ductility of high-strength UNS N08036 wire permits severe bending.

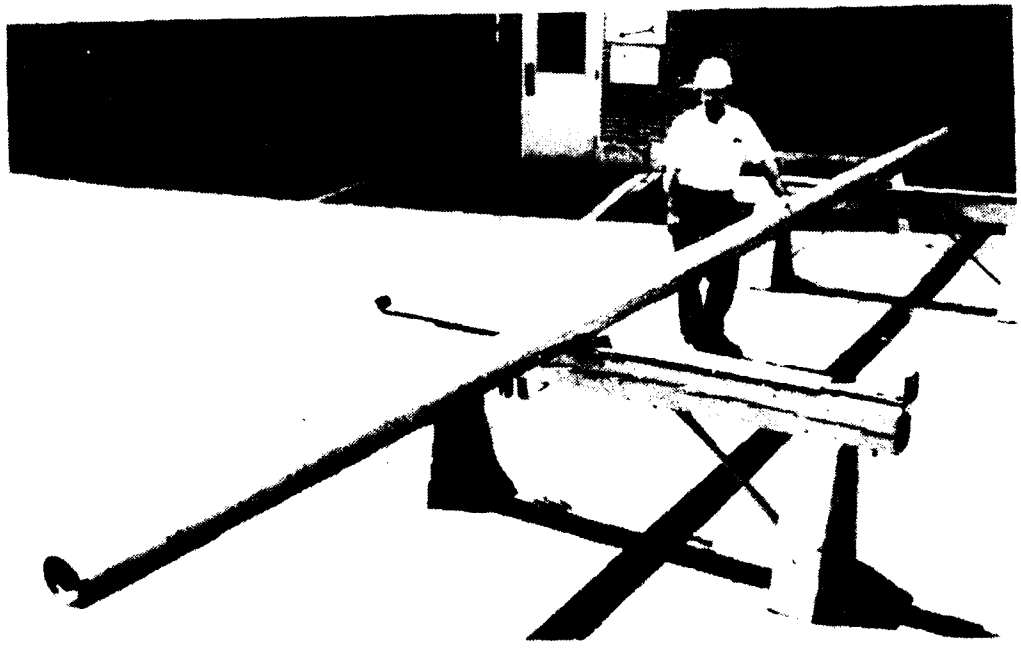

Figure 11 - UNS S21300 drill collar.

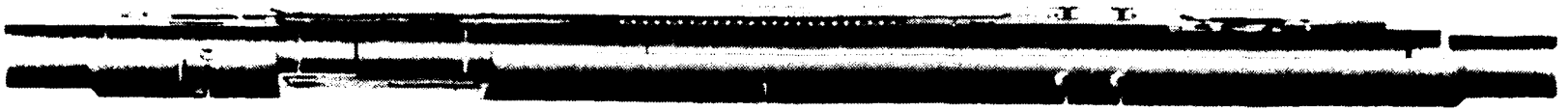

Figure 12 - Sub-surface safety valve (courtesy Camco).

Figure 13 - UNS K92580 is designed into the landing gear of the new carrier-based McDonnel Douglas F/A-18 E/F because of the alloy's high strength, high fracture toughness and stress-corrosion cracking resistance.

Passive Behavior of Niobium and Niobium-Titanium Alloys in Sulfuric Acid Solutions.

Luis-Otavio S. Bulhões
Laboratório Interdisciplinar de Eletroquímica e Cerâmica
Departamento de Química Universidade Federal de São Carlos
Caixa Postal 676 - 13560 São Carlos SP Brazil

Délcio Rehfeld*
Laboratório Interdisciplinar de Eletroquimica e Cerâmica
Departamento de Química Universidade Federal de São Carlos
Caixa Postal 676 - 13560 São Carlos SP Brazil

Abstract

The electrochemical behavior of niobium and niobium-titanium alloys has been investigated in dearated aqueous 0.1 mol/L H_2SO_4 solutions, at 25 °C. The studies were carried out through cyclic voltammetry, potentiostatic technique and electrochemical impedance spectroscopy. The analyses of cyclic voltammograms indicate that the metals and alloys behave like valve metals and a passivating film grows on the metal surface during the anodic polarization. The corrosion current density for Nb and Nb-47 % Ti alloy decreases as the potential increases. With Nb-2 % Ti alloy an increase in steady-state current density with the potential is observed. The passivating film resistance for Nb and alloys varies between 5 and 50 MΩ, depending on the final potential for the formation of oxide film. From the impedance data it was possible to propose the existence of a duplex film on Nb-2 % Ti surface.

Key terms: niobium, niobium-titanium alloys, passivation.

* Present address Departamento de Biologia e Química-Universidade de Ijuí Ijuí RS Brazil

I. Introduction

Niobium (Nb) and Nb alloys are considered corrosion resistant materials and have been widely applied in diversified systems in the chemical industry [1-2]. The corrosion resistance of niobium results from the formation of a thin homogeneous oxide film on the metal surface. However, Nb is susceptible to different forms of corrosion exhibiting intensive corrosion rates in acid solutions at high temperatures [3-4].

At room temperature niobium is passivated in a most of inorganic acids, except in HF. The use of niobium in chemical industry depends on its purity, since for example traces of carbon decrease its resistance to corrosive agents [5]. Despite of the interest in passivation of niobium in sulfuric acid [6-8] and chloride media [7-9], there is a lack of information on the behavior of niobium-titanium alloys.

In this paper the effects of Ti on the corrosion resistance of niobium in dearated, 0.1 mol/L sulfuric acid were evaluated by dc polarization curves and electrochemical impedance spectroscopy.

II. Experimental

Sulphuric acid (Merck, p.a.) was used without purification. The solutions were prepared by using distilled water, purified by passing through a four cartridge Milli-Q system.

The working electrodes were made from niobium (99.9 % m/m-CBMM-Brazil), titanium (99.7 % m/m-Aldrich) and from Nb-Ti alloys with 47 % m/m and 2 % m/m in Ti respectively. Before the use in the electrochemical experiments these metallic specimens were machined into circular disks and annealed in vacuum. These disks were further embeded in a glass tube by using an epoxy resin (Ciba-Geigy). The geometrical surface area of Nb and Ti exposed to the electrolyte was 0.28 cm^2 and for the alloys was 0.20 cm^2. A platinum plate served as a counter electrode. All potentials were measured against a hydrogen electrode in the same solution (HESS; Pt/H_2, 0.1M H_2SO_4), where the hydrogen was formed by the application of 300 mC of cathodic charge.

The electrochemical behavior of Nb, Ti and alloys in sulphuric acid was evaluated by using cyclic voltammetry, potentiostatic and impedance

technique. An EG&G PARC model 273 potentiostat/galvanostat and an EG&G PARC model 5208 lock-in amplifier were used for these measurements. Electrochemical impedance spectroscopy (EIS) was performed using a sinusoidal ac potential perturbation of 10 mV, superimposed to the dc signal in the frequency (f) range 75 KHz - 1 mHz. The experiments were controlled by a managing software (M378 from EG&G PARC) run in an IBM type microcomputer from SID.

III. Results and Discussion

The cyclic voltammograms for Nb and alloys in sulfuric acid solutions are shown in Figures 1 to 3. During the potential sweep at more positive potentials, a plateau is observed which is a typical behavior for valve metals. The current density in the plateau region increases with the potential sweep rate (v). The fact that the current is constant is an indication that the electric field across the film is constant and the increase with the potential sweep rate implies that the electric field also increases.

The chronopotentiograms were obtained at more positive potentials than the anodic peak potentials observed in the cyclic voltammograms. These potentials are in the passive region, ranging between 0.5V and 1.5 V. These measurements were performed by applying a linear potential sweep from -0.5 V up to the desidered potential waiting for the steady-state current. The results are shown in Figure 4 where niobium and Nb- 47 % Ti alloy exhibits a decrease in the dissolution current up to 1.3 V. This decrease in the steady-state current density with the increase in potential can be explained by the thickening of the oxide film inhibiting the dissolution that occurs by the transport of cations through the film. At higher potentials an increase in the corrosion current is observed for the Nb and can be related to structural changes in the film that increases the metal dissolution. In the Nb- 2 % Ti alloy the increase in the corrosion current is observed at more negative potentials (0.9 V).

From these results one can conclude that the addition of 2 % m/m of Ti to Nb shifts the dissolution potential to more negative values. While the increase of Ti in the alloy decreases the corrosion current giving values smaller than 0.1 $\mu A/cm^2$ up to 1.5 V. In general noibium and niobium - titanium alloys exhibt a higher corrosion resistance than pure titanium in similar conditions [11].

The impedance data of Nb and Nb-Ti alloys in sulfuric acid solutions are shown in Figures 5 to 7. These data were obtained in the passive region

with the current density lower than 0.1 $\mu A/cm^2$. A typical Bode plot of Nb and alloys electrodes are shown in Figures 5 to 7. The impedance data display one maximun phase lag, regardless of the applied potential in the passive region.

In order to analyse this response, a complex non-linear least squares fit procedure for impedance data was performed [12]. This impedance spectra can be described by a resistor in series with a parallel resistor-constant phase element (CPE) combination. The series resistance is associated with the solution resistance that remains constant close to 20 Ω. The parallel CPE and the resistance are associated with the frequency dependent capacitance and with the film resistance (R_f) respectively; values of these parameters are shown in Table I.

The film resistance is related to the resistance to ionic transport across the oxide film. This resistance increases with the potential for Nb and Nb-47 % Ti alloy. For the Nb-2 % Ti alloy a maximum value in R_f is observed at 0.7 V.

The n values showed in Table I are close to 0.9 indicating that the CPE behaves like a capacitor. The decrease in CPE with the increase in potential is associated with the increase in the defects density in the oxide film.

From the chronopotentiometric data for Nb and Nb-Ti alloys in aqueous acid solutions one observes that the corrosion current density shows a linear variation with the potential, giving values smaller than 0.1 $\mu A/\mu A/cm^2$. For Nb and Nb- 47% m/m Ti alloy the corrosion current density decreases with increasing potential to more positive values. At potentials higher than 1.5 V a structural change in the oxide film occurs increasing the corrosion current density in most of studied systems.

The electrochemical impedance spectroscopy measurements indicates that the resistance to the charge transport across the oxide film for Nb and niobium - titanium alloys are between 5×10^5 and 7×10^7 Ω . The higher values on film resistance are observed in films formed on niobium and on Nb - 47 % m/m Ti alloy.

The film resistances obtained in films formed on Nb - 2 % m/m Ti alloy exhibits a maximum value at 0.7 V. From the analysis of the behavior of phase angle at high frequencies in the Bode diagram, for the Nb - 2 % m/m alloy (Fig. 6), one can propose the existence of a duplex film, with different structures.

The defect density in the films formed on different materials decreases with the increase in potential.

In general the corrosion resistance of niobium and aniobium - titanium alloys in sulfuric acid solutions at ambient temperature are similar but shows a better perfrormance than the titanium in the same condition.

Acknowledgement- This research work was financially supported by the CNPq.

References

1. L. O. S. Bulhões, M. A. B. Gomes, A. A. Huss, R. Guimarães, C. R. Sanches, Proc. of 10th International Congress on Metallic Corrosion, Madras, India, paper 12.15 (1987), p. 2575.
2. J. Vehlow, Proc. of 8th International Congress on Metallic Corrosion, Mainz, RFA, (1987), p. 1436.
3. C. R. Bishop, Corrosion, 19(1963) 308.
4. L. O. S. Bulhões, E. Joanni, Proc. of 9th International Congress on Metallic Corrosion, Toronto, Canada, (1984), p. 437.
5. J. Pagetti, J. T. Talbot, Corrosion, 15(1967)171.
6. D. L. MacLlary, Corrosion, 18(1962)67.
7. C. A. Hampel, Corrosion, 14(1958)557.
8. B. S. Covino, C. P. Carter, S. D. Cramer, Corrosion, 36(1980)554.
9. F. Di Quarto, S. Piazza, R. D'Agostino, C. Sunseri, Electrochim. Acta, 34 (1989)321.
10. T. Hurlen, H. Bentzen, S. Hornkjol, Electrochim. Acta, 32(1987)1613.
11. D. L. Arsov, Electrochim. Acta, 30(1985) 1645.
12. B. A. Boukamp, Sol. State Ionics, 20(1986)31.

Table I. Electrochemical parameters determined from EIS data in 0.1 mol/L H_2SO_4 at 25 °C.

System	E/V	R_f/ M	$Q \times 10^6/\Omega\ Hz^n$	n
Nb	0.7	13.8	15.4	0.93
	1.1	20.2	9.2	0.94
	1.3	50.4	8.6	0.94
Nb - 2% m/m Ti	0.5	16.1	18.9	0.89
	0.7	30.8	16.5	0.88
	0.9	17.2	14.1	0.89
	1.1	18.8	12.6	0.88
	1.3	6.9	12.1	0.88
Nb - 47% m/m Ti	0.5	6.5	16.7	0.92
	0.7	7.7	12.0	0.93
	0.9	9.6	9.3	0.94
	1.1	15.1	7.7	0.94
	1.3	18.7	6.3	0.94

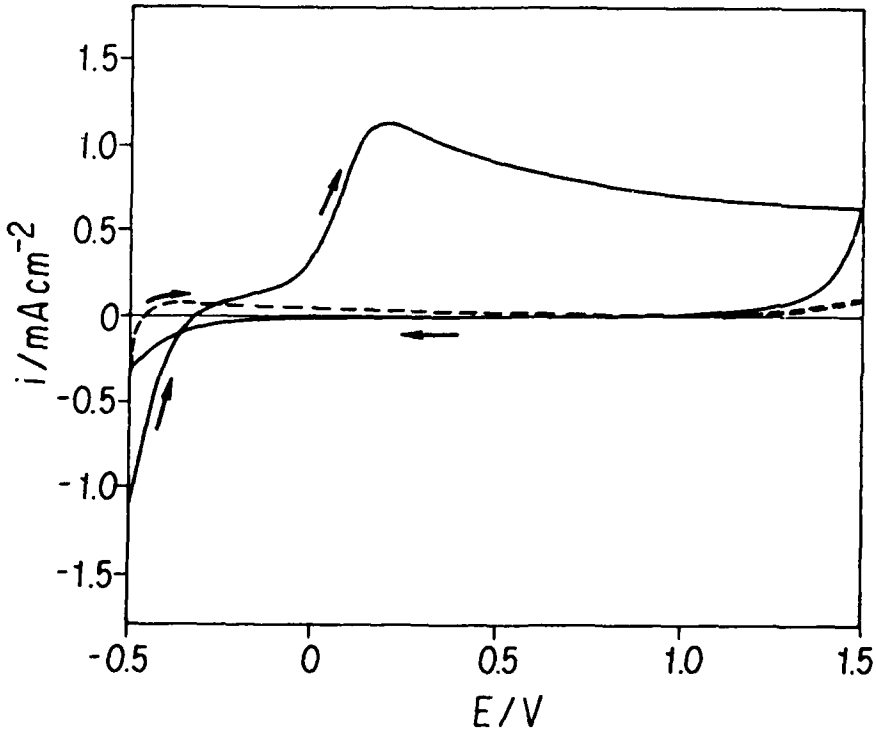

Figure 1. Cyclic voltammogram for niobium electrode in 0.1 mol/L H_2SO_4 at 25 °C, v= 0.05 V/s.

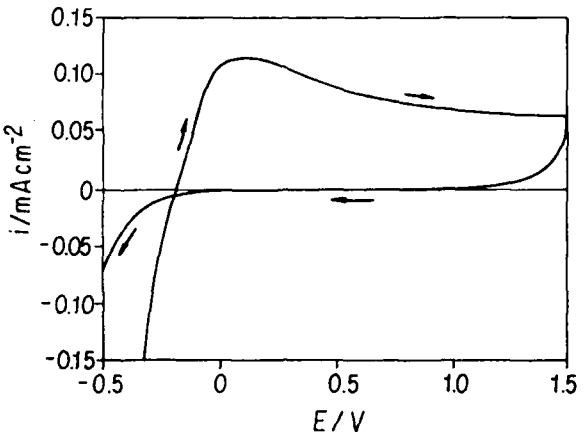

Figure 2. Cyclic voltammogram for niobium- 2 % m/m titanium electrode in 0.1 mol/L H_2SO_4 at 25 °C, v= 0.05 V/s.

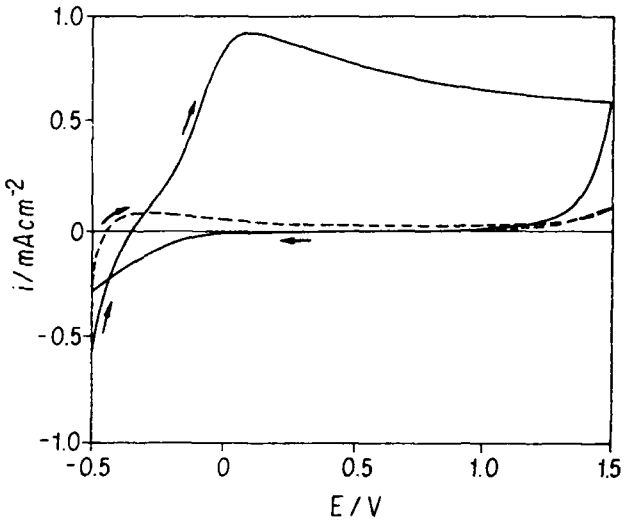

Figure 3. Cyclic voltammogram for niobium- 47 % m/m titanium electrode in 0.1 mol/L H_2SO_4 at 25 °C, v= 0.05 V/s, dashed line second cycle.

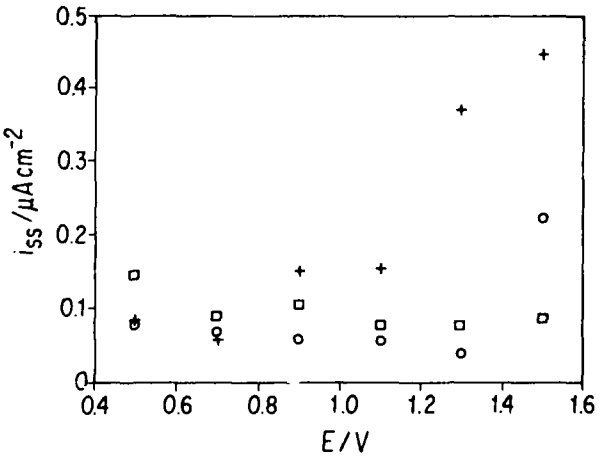

Figure 4. Corrosion current density as function of potential of (O) Nb; (+) Nb- 2 % m/m Ti; (□) Nb - 47 % m/m Ti; in 0.1 mol/L H_2SO_4 at 25 °C.

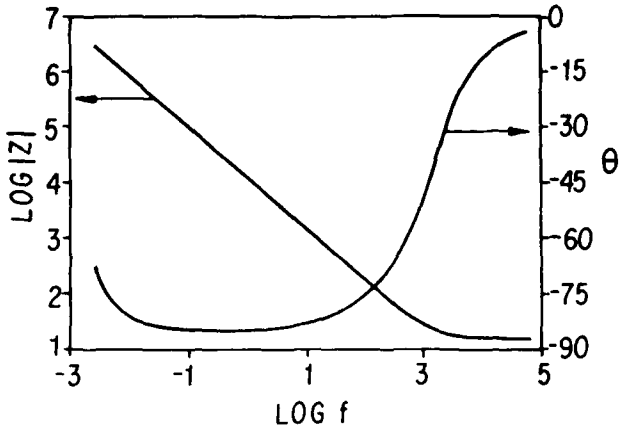

Figure 5. Dependence of the impedance and the phase angle on frequency for the oxide film obtained on Nb at E = 0.7 V; in 0.1 mol/L H_2SO_4 at 25 °C.

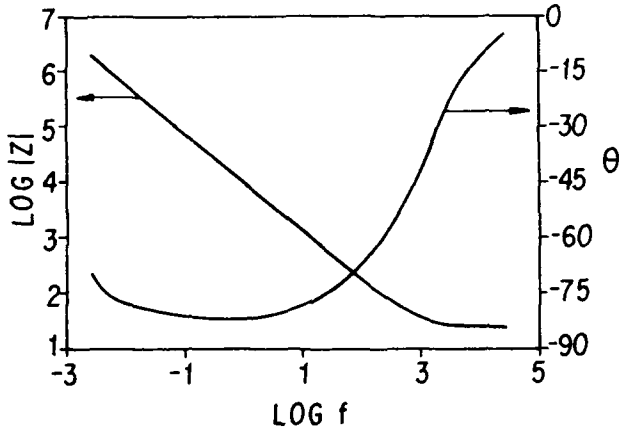

Figure 6. Dependence of the impedance and the phase angle on frequency for the oxide film obtained on Nb- 2 % m/m Ti at E = 0.5 V; in 0.1 mol/L H_2SO_4 at 25 °C.

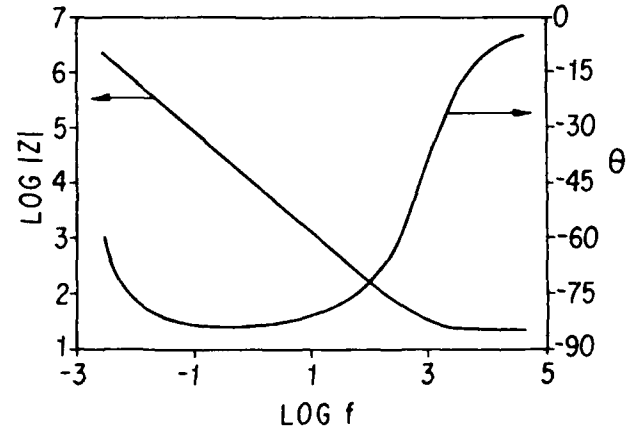

Figure 7. Dependence of the impedance and the phase angle on frequency for the oxide film obtained on Nb- 47 % m/m Ti at E = 0.5 V ; in 0.1 mol/L H_2SO_4 at 25 °C.

The Effects Of Microstructure (Cast versus Wrought) on the Wear and Corrosion Properties of a Cobalt-Based Alloy

T. H. Meyer
Robert Zapp Werkstofftechnik GmbH & Co. KG
Goltsteinstrasse 28
4000 Düsseldorf 1, Germany

P. Crook
Haynes International, Inc.
P. O. Box 9013
Kokomo, IN 46904-9013 USA

Abstract

Cobalt-based alloys have been used for many years to resist various forms of wear. In particular, they possess outstanding resistance to cavitation erosion, liquid droplet impingement erosion, slurry erosion, and galling. Most of these alloys, however, contain an abundance of carbide precipitates, which preclude (due to their influence on ductility) the manufacture of wrought products, such as plate and sheet. Notable exceptions are UNS R30006 (carbide-containing) and UNS R31233 (carbide-free); these are available in both wrought and cast forms.

UNS R30006 has been studied by many workers, the emphasis being on the role of the carbides. UNS R31233, which is relatively new, has been the subject of only a few previous studies, yet offers the opportunity to determine the effects of the large microstructural differences between wrought and cast products, in the absence of carbides (i.e. the effects of compositional homogeneity within the solid solution).

To evaluate the wear behaviour of wrought and cast versions of UNS R31233, three room temperature tests were chosen. These were the vibratory cavitation erosion test (ASTM G 32), the dry sand/rubber wheel abrasion test (ASTM G 65), and a modification of the ASTM G 98 galling test. Surprisingly, a cast microstructure was found to be beneficial to abrasion and galling resistance, and despite its considerably lower yield strength, the cast version was almost equal to the wrought version under cavitation conditions.

To assess the influence of microstructure upon corrosion resistance, several oxidizing and non-oxidizing acid media were used. The effects of a cast versus wrought microstructure were greatest in environments which promote localized attack.

Introduction

Since their development at the turn of the century, alloys based on the ternaries Co-Cr-W and Co-Cr-Mo have been widely used to combat abrasion, erosion, and sliding wear, particularly under corrosive conditions and at high temperatures. Most contain significant quantities of carbon, to promote the formation of carbides within their microstructures during alloy solidification. The predominant carbide in these alloys is chromium-rich M_7C_3; tungsten-rich M_6C is also found in those alloys with a high tungsten content.

These microstructural carbides benefit resistance to low-stress abrasion[1] and increase hardness, but reduce corrosion resistance, and severely limit ductility, to the point where most compositions cannot be processed into wrought products. The advantages of wrought processing include higher corrosion resistance (by virtue of increased compositional homogeneity), enhanced resistance to low-stress abrasion (due to the changes in size and shape of the carbides), and wider industrial usage. Two cobalt-based, wear-resistant alloys are available in wrought product form, as well as castings and weld overlays. These are UNS R30006 (with a carbon content of 1 wt.%) and R31233 (the carbon level of which, 0.06 wt.%, is in the soluble range). The compositions of these two alloys are presented in Table 1.

Although the resistance of the Co-Cr-W and Co-Cr-Mo alloys to low-stress abrasion is dependent upon the volume fraction, size, and shape of the microstructural carbides, the resistance of these alloys to most other forms of wear stems from the unusual crystallographic characteristics imparted by cobalt to the solid solution (i.e. the carbides are superfluous to performance in most cases).

Cobalt itself exists in two crystallographic forms, hexagonal close packed (at temperatures below 417°C) and face centered cubic (at higher temperatures). In practice, the hcp form is difficult to generate upon cooling, and the room temperature structure usually takes a metastable (ultra-low stacking fault energy) fcc form. Alloying elements in cobalt shift the transformation temperature (up or down, depending on whether they promote the hcp or fcc form). Typical hcp stabilizers are chromium, molybdenum, and tungsten; commonly used fcc stabilizers are nickel, iron, and carbon (within its soluble range)[2].

As with pure cobalt, most of the wear-resistant Co-Cr-W and Co-Cr-Mo alloys exhibit a metastable fcc structure at room temperature. Under the action of mechanical stress this influences the deformation and fracture characteristics as follows:

1. The alloys exhibit high yield strengths due to restricted, planar flow of the stacking faults.

2. Macroscopic hcp platelets are formed by the coalescence of stacking faults, thus reducing internal strain.

3. Deformation twinning is prevalent, again reducing internal strain.

4. Work hardening rates are extremely high, as a result of stacking fault interactions.

Stabilizers of the hcp structure generally improve the wear properties of these alloys (even at high temperatures, through their influence on the stacking fault energy of the fcc form). Conversely, fcc stabilizers tend to reduce resistance to wear. From a wrought processing standpoint, however, fcc stabilizers are of benefit, and hcp stabilizers are detrimental.

In alloys such as R30006 and R31233, the fcc and hcp stabilizers are carefully balanced to allow ease of wrought processing, yet provide extraordinary wear characteristics. The hcp stabilizers chromium, molybdenum, and tungsten are necessary for resistance to aqueous corrosion.

Excluding the work done in the biomedical field regarding the influence of wrought processing on the fatigue properties of Co-Cr-Mo alloys, previous comparisons between wrought and cast versions of these alloys have been concerned mostly with R30006, and mostly the effects of carbide morphology. In this work, R31233 was chosen for study to allow the effects of inhomogeneity (in the cast microstructure) to be evaluated separately.

Experimental Considerations

To evaluate the wear and corrosion properties of the wrought and cast versions of R31233, three room temperature wear tests and seven corrosive media were employed. In selecting the three wear tests, consideration was given to those conditions under which cobalt-based alloys normally excel (and therefore conditions under which microstructural inhomogeneity might be most influential). It was also considered appropriate to cover each of the three main wear categories, i.e. abrasion, erosion, and sliding wear.

To study the effects of microstructure on abrasion, the ASTM G 65 (dry sand/rubber wheel) low-stress abrasion test was used. The test apparatus is depicted in Figure 1. The procedure involved forcing a surface ground test block (of dimensions 76.2 x 25.4 x 12.7 mm) against a chlorobutyl rubber wheel, while feeding rounded, quartz grain sand (212 to 300 microns diameter) to the interface at 390 g/min. Each test involved a load of 13.6 kg, a rotational speed of 200 revolutions per minute, and 2000 revolutions of the rubber wheel, which was 228.6 mm in diameter.

From the erosion category, the ASTM G 32 cavitation erosion test was selected. A schematic of the test apparatus is presented in Figure 2. This apparatus comprises a transducer (a source of vibrations), a tapered cylindrical member (to amplify the oscillations), and a container, in which the test liquid (distilled water) is held. The specimens, which were shaped as cylindrical buttons of diameter 14.0 mm, with a 6.4 mm threaded shank, were screwed into a threaded hole in the end of the tapered cylinder for test purposes. Samples were tested for 96 hours, at a frequency of 20 kHz and an amplitude of 0.05 mm.

The samples were weighed at intervals of 24 hours, and throughout the test the distilled water was maintained at 16°C. The test surfaces were prepared by polishing on silicon carbide papers, to a grain size of 26 microns.

The third test employed was a modification of the ASTM G 98 (pin-on-block) galling test. The sample configuration is shown in Figure 3. The procedure involved:

a. Cyclic motion of the test pin through an arc of 120°.
b. Application of the load by means of a Riehle mechanical tester, in the load holding mode.
c. Quantitative interpretation of the test scars by surface profilometry.

The cylindrical pins (of diameter 15.9 mm) and the counterface blocks (of dimensions 76.2 x 25.4 x 12.7 mm) were surface ground prior to test. During test, the pins were subjected to five rotational cycles (i.e. they were turned back and forth through ten arcs of 120°) by means of a wrench, at loads of 1361, 2722, and 4082 kg.

In visual terms, the cylindrical pins and counterface blocks appeared to suffer the same degree of damage for a given test. The blocks, therefore, were used in the quantitative determination of damage, since they were more amenable to profilometry, allowing travel of the stylus to and beyond the circumference of the scar. For accuracy, the stylus was passed twice over each scar (one pass along the diameter parallel to the sides of the block; the other along the diameter perpendicular to it). Measurement involved appreciable overlap of the adjacent unworn regions, to enable calculation of the initial peak-to-valley amplitude.

By considering each radius as a distinct region of the scar, four values of final peak-to-valley amplitude were measured per scar. The average of these four values was used to determine the degree of damage incurred, by subtracting the average of four values of initial peak-to-valley amplitude.

With regard to corrosion testing, the following media were chosen as appropriate:

1. 10% Hydrochloric Acid, 66°C
2. 10% Sulphuric Acid, Boiling
3. 30% Sulphuric Acid, Boiling
4. 54% Commercial Phosphoric Acid, 116°C
5. 65% Nitric Acid, Boiling
6. 50% Sulphuric Acid + 42 g/l Ferric Sulphate, Boiling (ASTM G 28A Test)
7. 23% Sulphuric Acid + 1.2% Hydrochloric Acid + 1% Ferric Chloride + 1% Cupric Chloride (ASTM G 28B Test)

In commercial phosphoric acid, nitric acid and the ASTM G 28A solution, the chromium content of iron-, nickel-, and cobalt-based alloys is known to be very important, through its influence on passive film formation. The G 28B solution was included to determine the influence of inhomogeneity upon resistance to localized attack. In this environment, the chloride ions can cause breakdown of the passive film, leading to pitting, or in the

presence of a crevice, crevice corrosion.

The wrought R31233 samples for wear testing were prepared from solution annealed plates of thickness 12.7 to 19.1 mm. The corrosion test samples were prepared from solution annealed sheet of thickness 3.2 mm. The solution annealing treatment involved a temperature of 1121°C and water quenching. The composition of the heat of material used is given in Table 1. The cast R31233 samples were prepared from bars of diameter 25.4 to 38.1 mm, made by the investment casting process. These bars were tested in the as-cast condition. The composition of the cast heat is given in Table 1.

All tests, except the galling test, involved duplicate samples. The results presented are average values.

Results and Discussion

In the dry sand/rubber wheel abrasion test, wrought R31233 gave an average volume loss of 90.4 cu mm, as compared with 83.4 cu mm for the as-cast material. This result was somewhat surprising, given that the yield strength and hardness of wrought plate are considerably higher than those of cast bar. Typical tensile properties of the wrought and cast versions and the actual hardnesses of the abrasion test blocks are given in Table 2. A possible explanation of the higher resistance to low stress abrasion of the cast material is that elemental segregation leads to regions of very high strength as well as weak regions, and that these play a significant role in the abrasion process.

The cavitation erosion test results are presented in Table 3, and graphically in Figure 4. From these, it is evident that the wrought and cast materials exhibit almost equal resistance to this form of degradation. For perspective, the austenitic stainless steel S31603 exhibits an erosion depth of 0.1802 mm after just 24 hours, under the same test conditions.

Given that the cavitation properties of the cobalt-based alloys have been attributed to elastic resilience, transformation tendencies, and their low stacking fault energies[3,4] this work suggests that local variations in these properties (due to inhomogeneity in the cast structure) do not affect cavitation resistance, even though they markedly affect mechanical properties, particularly tensile strength.

Sectioning and metallographic examination of the tested cavitation samples (Figures 5 and 6) revealed that the surface degradation mechanism was generally independent of microstructural features, such as grain boundaries and precipitates (in the case of the cast sample). These figures also reveal that the grain size of the wrought structure of R31233 is very fine relative to the grain size of the investment cast structure. The dark angular particles in the cast structure are believed to be inclusions, and the lighter precipitates were analysed as primary M_7C_3 carbides (by x-ray diffraction). Also of importance is the cross-hatched, near-surface microstructure (in both samples). This cross-hatching is attributed to hcp platelet formation, under the action of mechanical stress.

The galling test results are presented in Table 4. For the purpose of this work, R31233 was tested against itself (i.e. both the pin and block were made from R31233) and against a popular nickel-based alloy, N10276 (the block being made from 12.7 mm thick plate of this alloy). As discussed in the previous section, the values in Table 4 represent averages of four readings from a single scar.

Review of these data reveals that, generally, the wrought and cast versions of R31233 behave in a similar manner under conditions conducive to galling. Not only are they both more resistant under self-mated conditions than against a nickel-based alloy, but also, neither exhibits a strong load dependency.

At two loads under self-mated conditions, and at two loads versus N10276, the cast version exhibited significantly less damage than the wrought version. This suggests that elemental segregation can be beneficial, as it appears to be for low stress abrasion. Again the presence of stronger regions may be important, in this case by virtue of their low stacking fault energies. Stacking fault energy has been shown to be an effective monitor of the galling resistance of fcc alloys, under self-mated conditions[5].

The corrosion test results are presented in Table 5. From these it is evident that, in certain media the cast version is essentially equivalent to the wrought version, but in others it is significantly less corrosion resistant. The media in which the cast version is equivalent are those for which chromium is important. The strong negative effect of the cast microstructure in the other media is attributed to the variations in molybdenum and tungsten contents. Of particular importance is the higher corrosion rate of the cast material in the ASTM G 28B solution. Since this environment promotes localized (pitting) attack, the corrosion rate, averaged over the whole surface, is misleading. The corrosion rate differential indicates that the cast version is much more prone to pitting than the wrought version.

Annealing experiments have shown that the susceptibility of the cast product to pitting can be reduced by heat treatment in the temperature range 1177 to 1232°C, followed by water quenching.

Conclusions

1. The wear properties of UNS R31233 are not significantly degraded in moving from a homogeneous, wrought microstructure to a segregated, investment casting microstructure; in fact, the resistance to low-stress abrasion and the resistance to galling are enhanced in the case of the cast microstructure.

2. Segregation in the cast microstructure is detrimental to corrosion resistance in those media which promote localized attack.

References

1. W. L. Silence, Wear of Materials, (1977), ASME, p. 77.
2. C. T. Sims, The Superalloys, John Wiley & Sons, (1972), p. 145.
3. K. C. Antony, and W. L. Silence, Proceedings of ELSI 5, Cambridge Univ. Press, (1979) p. 671.
4. C. J. Heathcock, B. E. Protheroe, and A. Ball, Proceedings of ELSI 5, Cambridge Univ. Press (1979), p. 631.
5. K. J. Bhansali, and A. E. Miller, Wear of Materials, (1981), ASME, p. 179.

TABLE 1

UNS Compositional Ranges & Compositions Tested*

	UNS Ranges		R31233 Compositions Tested	
	R30006	R31233	Wrought	Cast
Co	Bal	Bal	54.51	Bal
Fe	3.0 max	1.0-5.0	3.06	3.16
C	0.9-1.4	0.02-0.10	0.05	0.06
Mn	1.0 max	0.1-1.5	0.72	0.73
P	-	0.030 max	0.006	< 0.020
S	-	0.020 max	<0.002	< 0.005
Cr	27.0-31.0	23.5-27.5	24.89	26.70
Mo	1.5 max	4.0-6.0	4.70	4.92
Ni	3.0 max	7.0-11.0	8.96	8.76
Si	1.5 max	0.05-1.00	0.38	0.30
B	-	0.015 max	<0.002	< 0.005
N	-	0.03-0.12	0.07	0.10
W	3.5-5.5	1.0-3.0	1.81	2.04

*All values in wt. %

TABLE 2

R.T. Tensile Properties and Hardnesses of Wrought & Cast Versions of R31233

	Wrought Plate	As-Investment-Cast
0.2% Offset Yield Strength (MPa)	547	392
Ultimate Tensile Strength (MPa)	1019	773
Elongation (%)	36.0	34.7
Hardness	36 HRC	93 HRB

TABLE 3

Comparative Cavitation Erosion Test Data

	Erosion Depth mm			
	24 hr	48 hr	72 hr	96 hr
Wrought	0.0068	0.0229	0.0402	0.0574
Cast	0.0075	0.0243	0.0427	0.0597

TABLE 4

Comparative Galling Test Data

	Degree of Damage (microns)		
	1361 kg load	2722 kg load	4082 kg load
Self-Mated			
Cast	1.5	1.3	1.9
Wrought	2.9	2.7	2.0
Versus N10276			
Cast	12.7	10.4	10.9
Wrought	11.4	14.6	17.6

TABLE 5

Comparative Corrosion Data

Media	Corrosion Rate (mm/y)	
	Cast	Wrought
10% HCl, 66°C	6.2	1.7
10% H_2SO_4, Boiling	2.1	1.9
30% H_2SO_4, Boiling	18.8	10.5
54% P_2O_5, 116°C	0.2	0.2
65% HNO_3, Boiling	0.2	0.2
ASTM G28A Test	0.3	0.2
ASTM G28B Test	1.0	0.0

FIGURE 1

Dry Sand/Rubber Wheel Test Apparatus

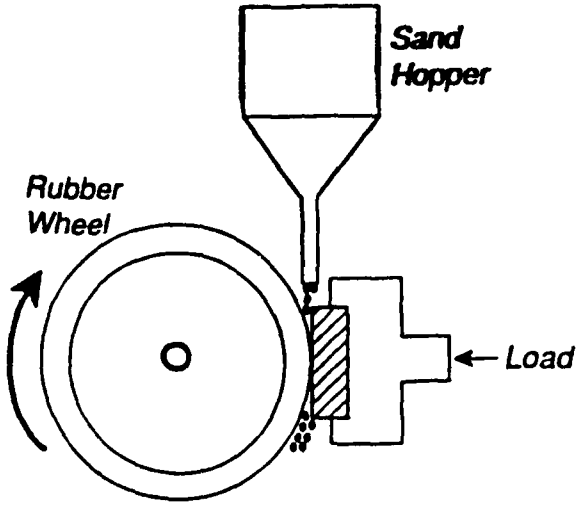

FIGURE 2

Vibratory Cavitation Erosion Test Apparatus

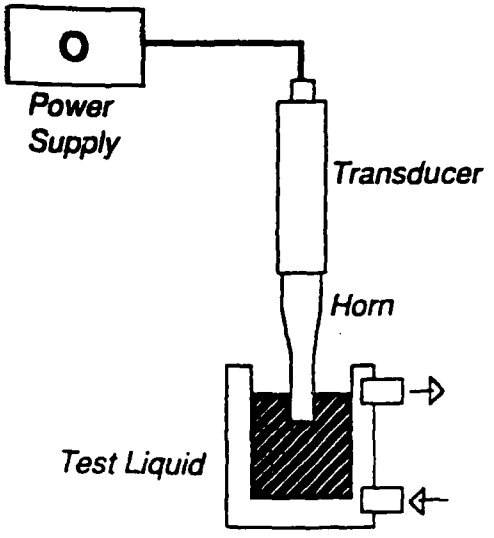

FIGURE 3

Pin-On-Block Galling Test Apparatus

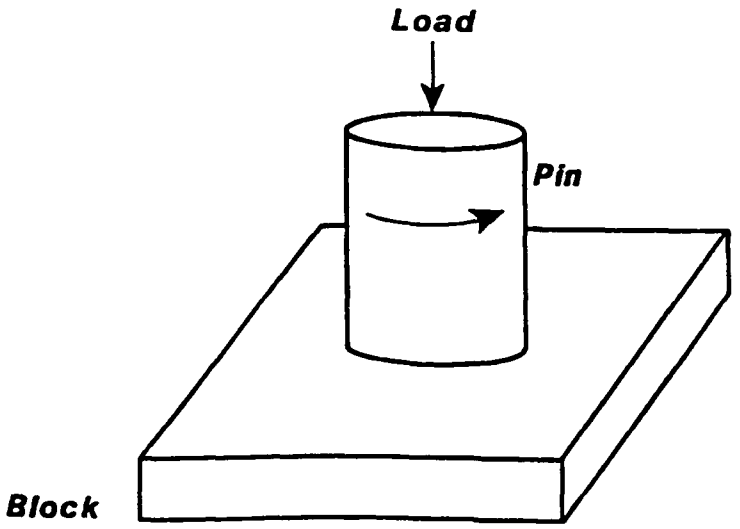

FIGURE 4

Comparative Cavitation Erosion Plots

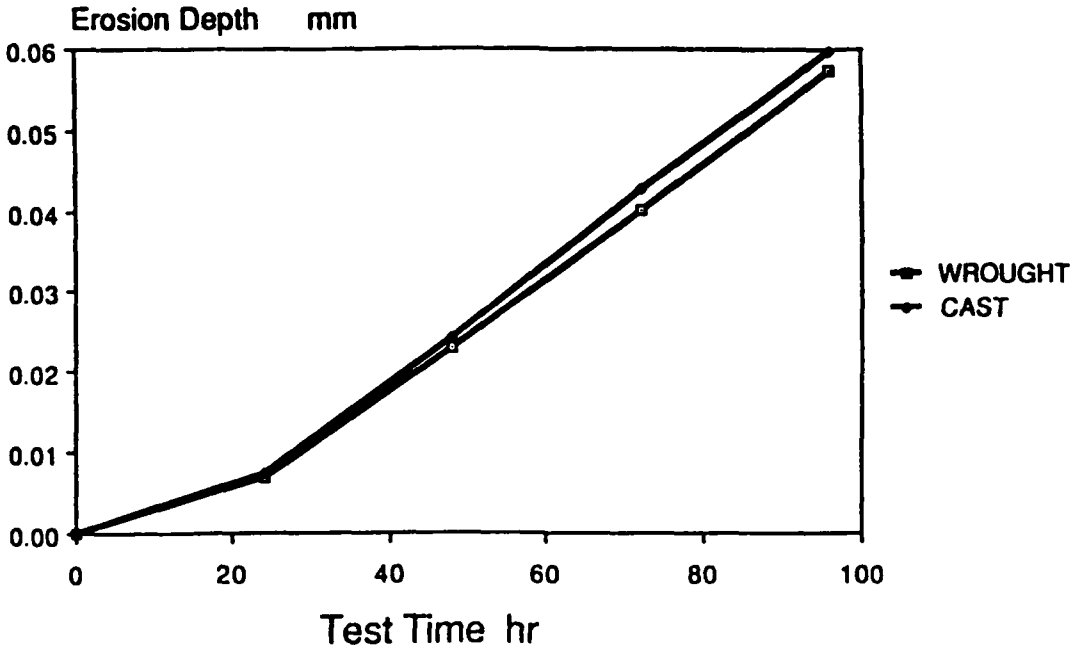

FIGURE 5

Wrought Cavitation Erosion Sample
200X Hydrochloric/Oxalic Acid Etch

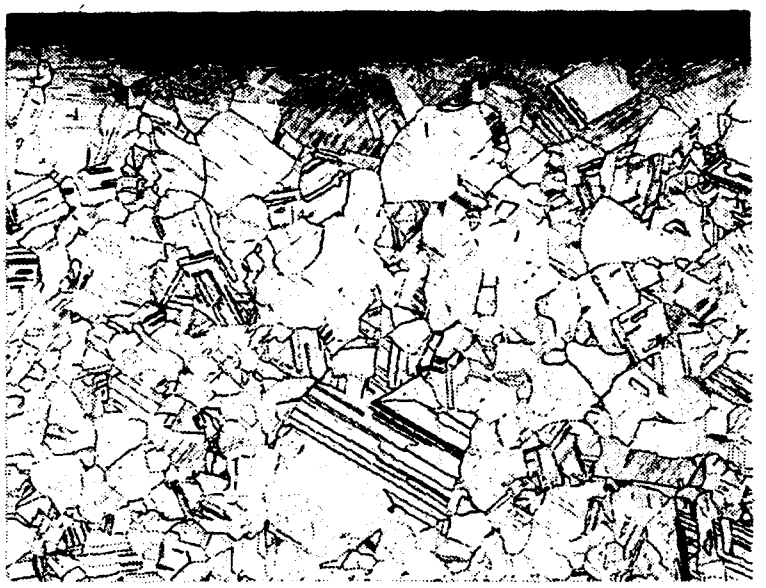

FIGURE 6

Cast Cavitation Erosion Sample
200X Hydrochloric/Oxalic Acid Etch

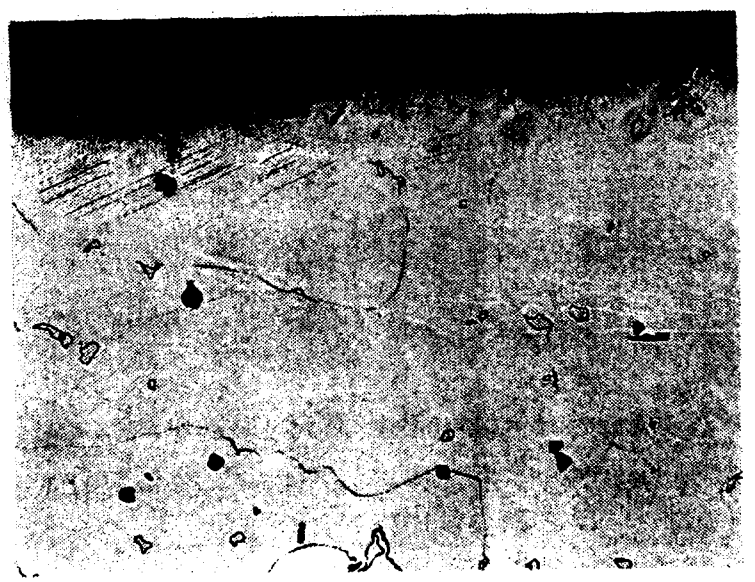

Effect of Aging Treatments on the Intergranular Corrosion of 22Cr-5Ni Duplex Stainless Steel

K. Ravindranath
Dept. of Metallurgical Engineering
Indian Institute of Technology
Powai, Bombay 400 076, India
(Present Address: PSL Pipe Coaters Pvt. Ltd.
Gandhidham 370 201, India)

S.N. Malhotra
Dept. of Metallurgical Engineering
Indian Institute of Technology
Powai, Bombay 400 076, India

Abstract

Duplex stainless steels have better corrosion resistance and mechanical properties and these make them suitable for several critical applications. The main problem associated with this class of stainless steels is the precipitation of secondary phases during heat treatments and welding. These precipitated phases and the accompanying chemical inhomogeneities can deteriorate their corrosion resistance. The present investigation was aimed to study the precipitation characteristics in a commercial high alloy duplex stainless steel and the effect of precipitation on the intergranular corrosion of this stainless steel. Duplex stainless steel was given aging treatments at 873 K and 973 K. Optical microscopy and XRD was carried out on the aged duplex stainless steel for the microstructural study. The aged samples were evaluated for intergranular corrosion (IGC) susceptibility with the ASTM standard A262 practices B and F. Results indicated that the IGC resistance of duplex stainless steel is strongly affected by the precipitation of secondary phases and the sigma precipitate influenced the IGC to a greater extent than the grain boundary attack due to the chromium rich carbide precipitation.

Key terms: intergranular corrosion, duplex stainless steel, sigma

Introduction

Duplex stainless steels are Iron-Nickel-Chromium alloys with an austenite-ferrite microstructure at room temperature. These steels provide combination of properties not readily attainable by conventional single phase ferritic or austenitic stainless steels. Compared to ferritic stainless steels they can offer greater toughness and better weldability; compared to austenitic stainless steels higher strength, better corrosion resistance and improved resistance to stress corrosion cracking [1-5]. Studies on the welded parts of some duplex stainless steels have shown that they are inferior to the base metal for corrosion resistance due to microstructural changes. There are reports on the heat treatment effects on the first generation duplex stainless steels [6-8]. Even though the nature of precipitation and their effect on second generation duplex stainless steels is limited, it can be inferred from the chemical composition and microstructure that a variety of phases can precipitate in this class of stainless steels too. Most of these phases will be rich in chromium and molybdenum and their precipitation in turn will affect the corrosion resistance of this class of stainless steels. So the present investigation was undertaken to study the nature of precipitates during aging at 873 K and 973 K and their effect on the intergranular corrosion (IGC) of a 22 chromium - 5 nickel duplex stainless steel.

Experimental

Experimental investigation was carried out on a commercial grade duplex stainless steel, viz 2205. Chemical composition of the stainless steel is given in table 1. Figure 1(a) shows the microstructure of the mill annealed sample. The stainless steel was given aging treatments at 873 K and 973 K for time durations 6 minutes, 1 hour, 10 hours and 100 hours. After the heat treatment, samples were quenched in water to facilitate fast cooling. Microstructure of the aged samples were examined under optical microscope. X-ray diffraction study was conducted on the heat treated samples for the phase identification. X-ray diffractometry was carried out on Philips PW 1820 with iron as target.

The aged samples were evaluated for intergranular corrosion as per the ASTM standard A262 practices B and F [9]. Samples were exposed to the boiling solution of ferric sulphate - sulphuric acid (A262-B practice) and copper - copper sulphate - sulphuric acid (A262-F practice) for 48 hours. After the test period the weight loss observed for

the samples was converted into corrosion rate. To study the nature of attack, tested samples were observed under scanning electron microscope.

Results and Discussion

I. Microstructural Study

Samples aged at 873 K for up to 10 hours did not give evidence of any precipitation when examined under optical microscope. Microstructure of the sample aged at 873 K for 100 hours showed fine sigma precipitate in the ferrite phase as shown in figure 1(b). This precipitate is observed at ferrite-ferrite, austenite-ferrite boundaries and also inside the ferrite phase as islands. Sigma precipitate is not observed in the austenite phase.

Aging at 973 K for 6 minutes did not result in the formation of any precipitate in the sample. But, precipitates were observed at isolated ferrite grain boundaries in the sample aged for 1 hour at this temperature. Prolonged aging for 10 and 100 hours at 973 K resulted in extensive sigma precipitation in the sample. Microstructure of the samples are shown in figure 2. On aging for 100 hours, the sigma precipitate was found to coarsen and in some areas whole of the ferrite phase was transformed into sigma. After aging for 100 hours, fine precipitates were observed at austenite grain boundaries also.

X-ray diffractogram of the samples aged at 873 K showed peaks for austenite and ferrite phase only. Even though microstructural study indicated sigma precipitate in the sample aged for 100 hours at 873 K, XRD spectra did not indicate its presence, probably the volume fraction of the precipitated sigma is very low.

Samples aged at 973 K for 10 and 100 hours showed peaks for the sigma phase. X-ray diffractogram of the samples are given in figure 3. It is seen from the figure that as the sigma phase precipitates, the peak intensity of the ferrite phase decreases. This shows that sigma phase is forming at the expense of the ferrite phase. For the sample aged for 100 hours, austenite peak appeared to be the most intense peak confirming that sigma precipitates in duplex stainless steel by the transformation of ferrite into sigma and austenite.

The secondary phase that precipitated in the stainless steel is found to be the sigma phase. There are reports on

the precipitation of sigma phase in duplex stainless steels [8,10-13]. In the initial stages, sigma nucleates as fine precipitates at the grain boundary, and as the aging time increase, the precipitate coarsens and occupy majority of the prior ferrite area by eutectoid decomposition of ferrite into sigma and austenite [10,13].

II Corrosion Study

Corrosion rate of the mill annealed and heat treated samples are given in table 2. Mill annealed sample exhibited a corrosion rate of 19 mpy in both the test solutions. Aging of the stainless steel at 873 K for 6 minutes did not affect the corrosion resistance. In ferric sulphate-sulphuric acid solution, influence of aging was noticeable after aging for 1 hour and prolonged aging for 10 hours increased the corrosion rate to 184 mpy. Corrosion rate further increased to 355 mpy after aging for 100 hours.

After aging treatments at this temperature, microstructure of the sample aged for 100 hours had shown fine sigma precipitate in the ferrite phase. The precipitation of chromium rich sigma precipitate result in the formation of an area which are poorer in chromium and richer in nickel. This phenomenon will lead to the precipitation of secondary austenite in the ferrite phase. As this secondary austenite is poorer in chromium, they will dissolve out actively in acid solution [7,8,14]. Even though microstructure of the sample aged for 10 hours did not show any precipitate, corrosion rate indicate that very fine sigma might have precipitated in the sample which are not resolvable under optical microscope. There are reports that sigma affects the corrosion behavior even before they are optically visible [15,16]. The increased corrosion rate observed in ferric sulphate-sulphuric acid solution can then be said to be due to the dissolution of this submicroscopic sigma and low chromium secondary austenite.

When aged at 973 K for 1 hour and 10 hours, in ferric sulphate-sulphuric acid solution, the corrosion rate increased to 233 and 335 mpy respectively indicating that samples after these treatments are highly susceptible to intergranular corrosion. Interestingly, corrosion rate show a reduction for the sample aged for 100 hours. Figure 4 shows SEM photomicrograph of the samples after exposure to the ferric sulphate-sulphuric acid solution. Photomicrograph gives evidence of severe grain boundary attack. Ferrite area of the samples show tendency for general dissolution as a result of sigma precipitation.

Reason for the drastic increase in corrosion rate on aging is the dissolution of the precipitated sigma phase in the ferric sulphate-sulphuric acid solution. This corrosion attack is likely to have been initiated at the chromium depleted zone around the sigma precipitate and finally attack results in the undermining and dropping out of the fine sigma precipitate. This type of attack could be seen in the ferrite phase of the samples. Longer aging resulted in the formation of sigma precipitate at the austenite grain boundaries also. This led to the attack on grain boundaries in the austenite region, in addition to the attack in the ferrite phase. Aging for 100 hours may be leading to the healing of some grain boundaries and area around the precipitates by the diffusion of chromium and molybdenum from the interior of the grains. This will reduce the IGC susceptibility of the samples. Another reason for the reduced corrosion rate for the sample aged for 100 hours could be the coarsening of the sigma precipitate. It is reported that fine sigma particles are more dangerous than the coarse precipitates with regard to corrosion resistance [16]. Even if the area around the coarse precipitates are attacked, it will not lead to dropping of the precipitate.

When tested in copper - copper sulphate - sulphuric acid solution, the duplex stainless steel was found to be quite resistant to intergranular corrosion. At the aging temperature of 873 K, only aging for 100 hours sensitized the material. After all other aging treatments, the stainless steel was found to be immune to intergranular corrosion. Scanning electron micrograph of the sample aged for 100 hours after exposure to the boiling copper - copper sulphate - sulphuric acid solution indicate the attack on ferrite - ferrite and ferrite - austenite grain boundaries and the general dissolution of the ferrite phase as shown in figure 5. The general dissolution of ferrite phase after aging at this temperature could be due the dissolution of low chromium area around the sigma precipitate.

Samples aged at 973 K for durations up to 10 hours showed good resistance to intergranular corrosion. Sample aged for 100 hours showed a corrosion rate of 69 mpy indicating susceptibility to intergranular corrosion. Figure 6 shows the surface appearance of the sample aged for 100 hours after exposure to the copper - copper sulphate - sulphuric acid solution. Micrograph shows corrosion attack on austenite grain boundaries also.

Intergranular corrosion characteristics of the samples aged at 973 K clearly indicate the formation of chromium depleted zone as a result of the sigma precipitation. The

scanning electron micrographs confirm that chromium depleted area first forms along austenite - ferrite grain boundaries and this result in the attack on austenite - ferrite boundaries. Further aging of the stainless steel for 100 hours results in the precipitation of sigma along austenite - austenite grain boundaries with accompanying chromium depletion along the boundary.

The tests indicated varying degree of IGC susceptibility as per ferric sulphate - sulphuric acid and copper - copper sulphate - sulphuric acid tests. Samples, in general, exhibited a higher IGC susceptibility in ferric sulphate - sulphuric acid solution. The difference in intergranular corrosion susceptibility observed for the samples in A262 B and F test solutions could be due to the different electrochemical potentials where the tests are operating. The ferric sulphate - sulphuric acid test operates at 600 mV (SCE), where as in the copper - copper sulphate - sulphuric acid test the potential is 100 mV (SCE) [17]. Because of this different operating potentials, sensitivity of the test will also be different. Ferric sulphate - sulphuric acid test detects the presence of sigma phase also along with chromium depleted zone in stainless steels. Results indicate that the IGC in the duplex stainless steel is controlled to a great extent by the sigma phase precipitation. The IGC due to carbide precipitation in the stainless steel will be remote as the carbon content of the stainless steel is very low.

Conclusions

1. Aging of the duplex stainless steel at 873 K and 973 K precipitated sigma phase in the stainless steel.

2. The sigma precipitates at first in ferrite phase, but on prolonged aging it is observed even in austenite phase.

3. In the duplex stainless steel IGC is controlled to great extent by the sigma phase precipitation at grain boundaries.

4. The duplex stainless steel has good resistance to IGC in copper - copper sulphate - sulphuric acid solution.

Acknowledgements

The authors gratefully acknowledge Dr. S. Bernhardsson, Sandvik Steel, Sweden for providing the duplex stainless steel and M/s PSL Pipe Coaters Pvt. Ltd. for the co-operation and support.

References

1. H.D. Solomon, T.M. Devine, Duplex Stainless Steels, R.A. Lula (Ed.), ASM (1983), p. 693.

2. T.G. Gooch, Duplex Stainless Steels, R.A. Lula (Ed.), ASM (1983), p. 573.

3. S.Azuma, H. Tsuge, T. Kudo, T. Moroishi, Corrosion, 45 (1989), p. 235.

4. S. Bernhardsson, R. Mellstrom, J. Oredsson, CORROSION/81 paper no.124 (National Association of Corrosion Engineers, Houston, TX)

5. B.D. Craig, J. Materials for Energy Systems, 5 (1983), p. 53.

6. T.M. Devine, Acta Metall., 36 (1988), p. 1491.

7. T.M. Devine, J. Electrochem. Soc., 126 (1979), p. 374.

8. H.D. Solomon, T.M. Devine, ASTM STP 672 (1979), p. 430.

9. ASTM Standard A262, Annual Book of ASTM Standards, Vol. 03-02 (1989).

10. Y. Maehara, Y. Ohmori, J. Murayama, N. Fujino, T. Kunitake, Metal Science, 17 (1983), p. 541.

11. G. Herbsleb, P. Schwaab, Duplex Stainless Steels, R.A. Lula (Ed.), ASM (1983), p. 15.

12. T.A. De Bold, JOM, 41 3 (1989), p. 12.

13. M.E. Wilms, V.J. Gadgil, J.M. Krougman, B.H. Kolster, Materials at High Temperatures, 9 (1991), p. 160.

14. J-S Chen, T.M. Devine, Corrosion, 45 (1989), p. 62.

15. D. Warren, Corrosion, 15 (1959), p. 213.

16. R.F. Steigerwald, Corrosion, 33 (1977), p. 338.

17. M.A. Streicher, ASTM STP 656 (1978), p. 3.

Table 1: Chemical Composition of Duplex Stainless Steel

Cr	Ni	Mo	Mn	C	N	Fe
21.75	5.46	2.96	1.44	0.016	0.15	Balance

Table 2: Corrosion Rate of 2205 Stainless Steel

Aging Treatments		Corrosion Rate (mpy)	
Temperature K	Time (Hour)	A262-B Test	A262-F Test
Mill Annealed		18.79	19.26
873	0.1	15.83	22.76
873	1	35.34	22.32
873	10	183.83	23.99
873	100	354.75	52.68
973	0.1	23.08	20.33
973	1	233.31	26.21
973	10	334.81	35.08
973	100	135.38	69.33

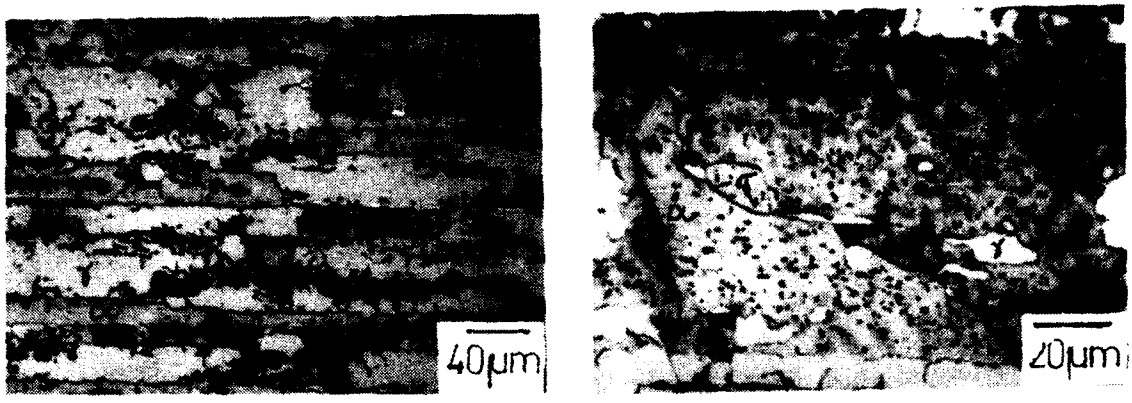

(a) (b)

Fig. 1: Optical photomicrograph of 2205 stainless steel (a) Mill Annealed Sample (b) Sample aged at 873 K for 100 hours (Etchant: 10M KOH).

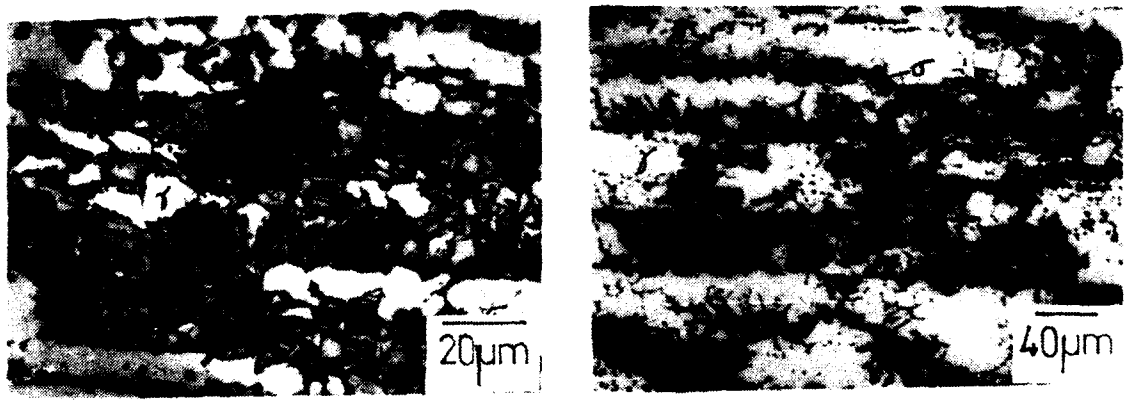

(a) (b)

Fig. 2: Optical photomicrograph of 2205 samples aged at 973 K and etched with 10M KOH (a) aged for 10 hours (b) aged for 100 hours.

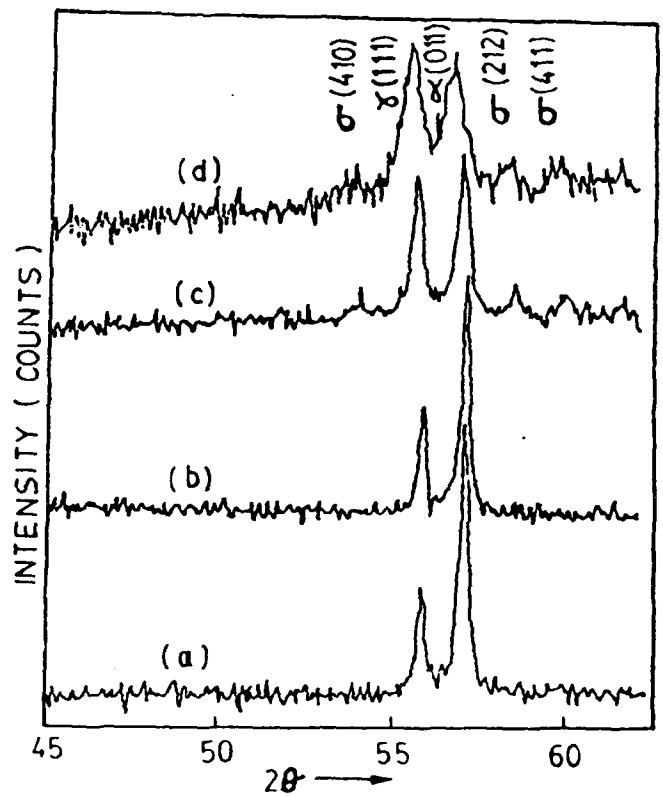

Fig. 3: XRD spectra of 2205 aged at 973 K for (a) 0.1 hour, (b) 1 hour, (c) 10 hours, (d) 100 hours.

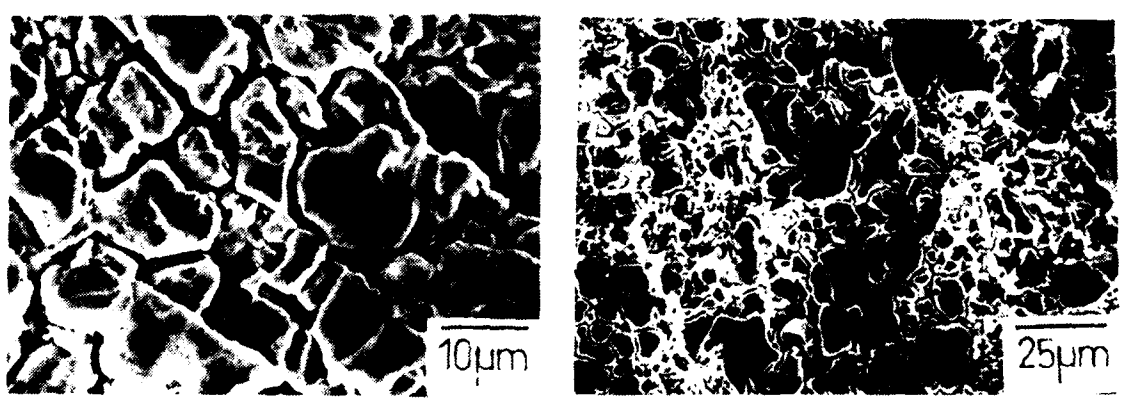

Fig. 4: Surface appearance of aged 2205 samples after the ferric sulphate-sulphuric acid test: Aging treatments; (a) 973 K for 1 hour, (b) 973 K for 100 hours.

Fig. 5: Scanning electron micrograph of 2205 aged at 873 K for 100 hours after A262-F test.

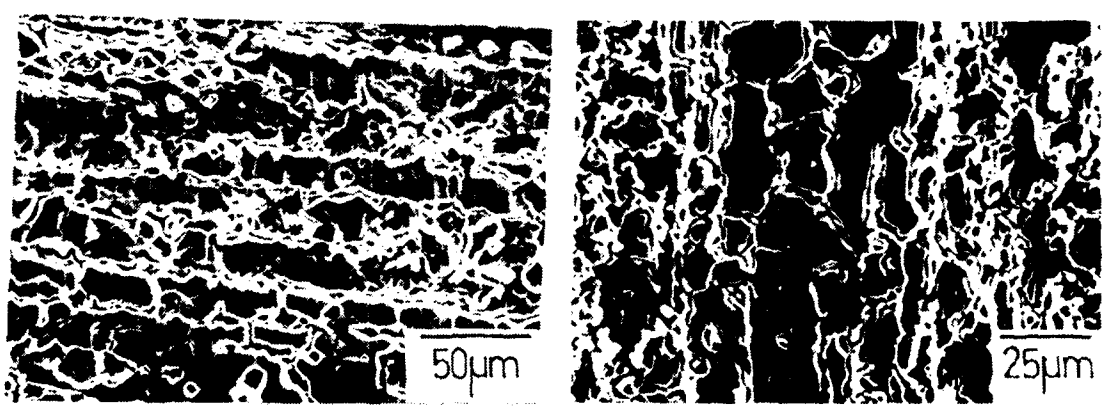

Fig. 6: Surface appearance of aged 2205 samples after A262-F test; Aging treatments (a) 973 K for 1 hour (b) 973 K for 100 hours

Optimized Lean-Pd Titanium Alloys for Aggressive Reducing Acid and Halide Service Environments

R. W. Schutz
RMI Titanium Company
1000 Warren Avenue
Niles, Ohio 44446 USA

Ming Xiao
RMI Titanium Company
1000 Warren Avenue
Niles, Ohio 44446 USA

Abstract

A corrosion database derived from weight-loss, electrochemical characterization, crevice, and stress corrosion laboratory testing has been established for the optimized Pd-lean titanium alloys: Ti Grades 16 and 18, and Ti Gr. 5/Pd. Results indicate nearly equivalent resistance for the Gr. 16 and 7 alloys to dilute reducing acids and acidic halide crevice attack, offering a cost-attractive alternative to Ti Gr. 7 and Ni-Cr-Mo alloys in aggressive industrial service. The medium and high strength Ti Gr. 18 and Gr. 5/Pd alloys are shown to resist hot chloride stress corrosion, and offer reducing acid and crevice corrosion resistance approaching that of Ti Gr. 7 and superior to Ti Gr. 12. This combination of traits makes them attractive candidates for pressure vessels/piping handling high pressure/high temperature halide or brine service, and for sweet or sour geothermal brine well and deep sour oil or gas well production equipment and components.

Introduction

The Grade 7 (Ti-0.15% Pd) titanium alloy has traditionally been the alloy of choice when conventional titanium alloys and Ni-Cr-Mo alloys exhibit susceptibility to attack in hot reducing acids or oxidizing acidic halide media. As the most resistant commercial titanium alloy, Grade 7 titanium uniquely resists crevice and pitting corrosion in chlorine-saturated brines, acidic metal chloride solutions (i.e., $FeCl_3$, $ZnCl_2$, $AlCl_3$), and to hydrolyzable concentrated brines ($MgCl_2$, $CaCl_2$) to high temperatures. Superior resistance to hot dilute reducing inorganic and organic acids is also recognized. Unfortunately, the utilization of this alloy has been severely limited and stifled by its high relative cost to the unalloyed grades, stemming from the alloy's Pd content. This price issue has been alleviated by reducing nominal alloy Pd content to 0.05 wt.%, thereby reducing alloy cost on the order of 20-25% with little influence on corrosion performance. This optimized Ti-Pd alloy has recently been incorporated into ASTM product specifications as titanium Grade 16 (and Gr. 17 as Pd-lean version of Ti Gr. 11).

Increased demand for more design-efficient alloys possessing medium to high strength along with superior corrosion resistance has fueled increased consideration of Ti Grade 9 (Ti-3Al-2.5V) and Ti Grade 5 (Ti-6Al-4V) for industrial, marine, and downhole service. However, since many of these applications involve chlorides or other halides at higher temperatures, these alloys may be limited by their susceptibility to crevice corrosion. In the case of the Grade 5 alloy, stress corrosion cracking susceptibility must also be considered. These shortcomings are addressed through a minor nominal addition of 0.05 wt.% Pd to each alloy, with minimal impact on alloy cost.

Since all these optimized Pd-containing alloys represent more recent developments, little service or laboratory corrosion performance has been established on these improved alloys. This paper aims to provide such a relevant database based on extensive laboratory corrosion testing by the authors and that published by other researchers. Comparative alloy corrosion behavior is assessed via weight loss, electrochemical, crevice, and stress corrosion tests in reducing acids and acidic chloride brines. Candidate applications for each new alloy are proposed based on these results.

Experimental

Test Materials - The titanium alloys evaluated in this paper are defined in Table 1. Corrosion testing was conducted on annealed 1.5 mm thick sheet stock produced from 27 kg ingots of Ti Grades 16 and 18, and Ti Gr. 5/Pd. Ti Gr. 2, 7 and 5 sheet samples were as mill-produced and annealed. Sheet coupons were wet ground (200 grit) and lightly pickled in HF-HNO_3 solution.

Test Methods and Media - General corrosion testing consisted of simple weight loss immersion exposures (1-3 days) of sheet coupons in naturally-aerated test solutions. Coupon weight measurement accuracy was ±0.0001 gm.

Anodic/cathodic polarization characteristics of alloy samples were determined in deaerated (argon-sparged) 20% NaCl (pH 0.5) at 90°C via potentiodynamic scanning at 0.5 mV/sec. The anodic repassivation pitting potential of sheet samples was measured in boiling 5% NaCl (pH 3.5) via the galvanostatic method utilizing a constant current density of +200 mA/cm^2.

Crevice corrosion resistance was evaluated using bolted assemblies of metal sheet coupons (38 mm x 38 mm x 1.5 mm) interspaced with 1 mm virgin PTFE sheet spacers, bolted together with a torque of 30-50 mm·kg. Each assembly incorporated four metal coupons and created twelve metal-to-PTFE sheet crevices (1). Exposures in these nonagitated solutions were all 30 days. Post-exposure coupon evaluation included surface cleaning via glass bead blasting (if required to remove corrosion deposits) and visual examination at 1-40X.

The Ti Grade 18 alloy was evaluated via two stress-corrosion cracking (SCC) test methods: stressed U-bends and slow strain rate (SSR) tests. The U-bend SCC tests were conducted by Zimpro Passavant Environmental Systems (2), and involved autogenously TIG-welded sheet U-bends of Ti Grades 2, 9, 12, and 18 stressed to >100% yield strength. Each U-bend specimen incorporated PTFE sheet spacers at bolt/nut to U-bend sample contact surfaces, thereby creating severe PTFE sheet to metal test crevices as well. Long term (360, 770 hr.) exposures were conducted at 280°C and 300°C in shaking autoclaves containing the synthetic acidic chloride industrial waste solutions described in Table 6.

The SSR tests were conducted on Ti Gr. 18 and Ti Gr. 5/Pd plate (smooth) tensile samples strained at a rate of 4×10^{-6} $sec.^{-1}$ in actual hypersaline (sat. NaCl) brine samples obtained from a Salton Sea geothermal brine well. These tests were conducted at 180°C and 288°C with brine pH's adjusted to 3.5 and 5.0, respectively. The Ti Gr. 5/Pd samples were also SSR-tested in a worst-case deep sour gas well brine fluid described in Table 9. Time to failure and reduction in area of samples strained to failure in the brine versus an inert helium gas were compared by ratio, along with SEM examination of sample fracture faces.

Results

Reducing Acid Resistance - Figures 1 and 2 reveal the dramatic enhancement in alloy resistance hot dilute HCl solutions obtained with minor (~0.05 wt.%) additions of Pd to Ti Grades 2, 5, and 9 The "lean-Pd" Ti Gr. 16 alloy exhibits resistance essentially the same as the richer Ti Gr. 7 alloy

over most of the acid concentration range tested. It is only under the more aggressive, active-corrosion conditions (where rates are >0.1 mm/y) where the Grade 16 alloy displays slightly inferior resistance compared to Gr. 7. Figure 2 also reveals that the leaner alloy content (i.e., Al and V) of Ti Gr. 18 results in measurably improved reducing acid resistance over the Ti Gr. 5/Pd alloy despite equivalent alloy Pd levels.

Figure 3 shows that the weld metal of these Pd-containing alloys exhibits essentially equivalent corrosion resistance to corresponding base metal in dilute reducing acids. No detrimental influence on adjacent heat affected metal zones is noted either. This was evaluated in detail for the Ti Gr. 7 and 16 alloys, in which thermal treatments of 593-982°C-10Min-AC were imposed on base metal samples prior to acid exposure. Figure 4 results indicate no significant influence of the thermal treatments or welding on corrosion rate of Gr. 7 or 16 in boiling HCl media.

The obvious enhancement in titanium alloy reducing acid resistance by Pd addition is also evident in the boiling concentrated formic acid solution data shown in Table 2. The Pd-containing alloys are fully resistant in the 10% acid, and significantly inhibit Gr. 2, 5, and 9 alloy attack in the 50% acid. High temperature dilute sulfuric acid exposures also reveal similar resistance between Grades 7 and 16 at lower acid concentrations, with deviations noted under more aggressive conditions at higher acid strengths (see Table 3).

Oxidizing Acid Resistance - Table 2 data from boiling $FeCl_3$ solutions suggests that the addition of Pd has no negative influence on titanium alloy resistance in mildly oxidizing acid environments. In fact, the lean-Pd Gr. 16 alloy can be expected to exhibit corrosion behavior more akin to C.P. titanium in severely oxidizing acid media (i.e., boiling HNO_3), where the "richer-Pd" Gr. 7 alloy is known to be slightly inferior (3).

Electrochemical Behavior - The electrochemical characteristics of Pd and non-Pd-containing titanium alloys in hot acidic brine media are compared in Table 4. It is evident that the Pd addition consistently shifts the alloy's corrosion potential (E_{CORR}) in the noble (positive) direction, where oxide film stability/formation (i.e., passivation) are favored. The significant decrease in cathodic Tafel slope measured, along with the insignificant effect on anodic passive current, suggests that the Pd addition primarily acts to depolarize the cathodic reduction process (i.e., facilitate H_2O^+ reduction in reducing acids). This well known "reduced hydrogen overvoltage" mechanism for titanium alloys (3-5) also involves surface enrichment of Pd within the titanium oxide film (5) in reducing acids. This phenomenon enhances the ability of Pd to cathodically depolarize and enable the alloy even when alloy Pd levels are as low as 0.04 wt.%. It is interesting to note that the relative degree of ennoblement (and Tafel slope reduction) by Pd addition diminishes somewhat as alloy content increases (i.e., increasing Al content), which correlates with alloy corrosion rate profiles in HCl (Figures 1 and 2).

The anodic repassivation potential values outlined in Table 4 suggest that alloy Pd addition has little or no influence on anodic pitting potential in halide brines.

Crevice Corrosion Resistance - Tables 5 and 6 present crevice corrosion data on Pd-containing titanium alloys in aggressive oxidizing acid-chloride solutions at high temperatures. The Grade 7 and 16 alloys proved to be fully resistant in all chlorinated and non-chlorinated brines, which included pH levels as low as 1.0. Similarly, the Gr. 18 and Gr. 5/Pd alloys resisted attack down to pH 2 in non-chlorinated brines. In the more aggressive chlorinated brines, crevice attack was initiated on Gr. 5/Pd alloy coupons at pH 2, which represented a borderline, incipient attack condition for the more resistant Gr. 18 alloy. On the other hand, Ti Gr. 18 was found to resist crevice attack to pH's as low as 1.5 in aerated or oxygenated aqueous chloride media to temperatures as high as 300°C, as indicated in Table 6 data (2). These particular test conditions represent those prevalent in wet oxidation processes for treating municipal and industrial sludge waste streams (6).

Prior corrosion studies by Kitayama, et. al. (5) confirm the crevice resistance of Ti Gr. 7 and 16 alloys in high temperature concentrated NaCl brines. The results of these studies, presented in Tables 7 and 8, demonstrate the resistance of these alloys to PTFE and other common gasket material-to-metal crevices to temperatures of 200°C and pH's as low as 2.

The crevice resistance of the higher strength Gr. 18 and Ti Gr. 5/Pd alloys in high temperature sour brines, representing worst-case produced fluids from deep sour gas wells, has also been demonstrated (7, 8). In these 500 hour tests, no stress or crevice corrosion was indicated up to 250°C in an environment consisting of 25% NaCl, 1 MPa H_2S, 1 MPa CO_2, and 1 gpl elemental sulfur.

Stress Corrosion Resistance - Since it is generally known and accepted that the Ti Gr. 7 and 16 alloys are immune to SCC in aqueous halide media, SCC tests have focused on the higher strength Pd-containing titanium alloys. The Gr. 18 alloy appears to resist base and weld metal cracking in long term U-bend tests in the oxidizing acidic chloride environments described in Table 6 (2). The highly discriminating slow strain rate (SSR) tests on both Gr. 18 and Gr. 5/Pd alloys in saturated NaCl geothermal brine fluids similarly reveal total SCC resistance up to ~300°C, as shown in Table 9.

SCC resistance of the Ti Gr. 18 and Gr. 5/Pd alloys in hot brines is not compromised by the presence of sulfides or elemental sulfur either. Recent work by Ueda (8) and Kitayama (7) and co-workers which included four-point beam, C-ring, and SSR tests show that these two alloys fully resist cracking under the worst-case sour brine environment, described in the prior section, up to 260°C. Compatibility with acidic sour brine conditions specified for NACE TM-01-77 Standard tests was demonstrated as well. SCC resistance of Ti Gr. 5/Pd in high temperature worst-case sour brine is also confirmed by Table 9 SSR test data.

Practical Implications

The corrosion database for Pd-containing titanium alloys developed and reviewed in this paper provides the basis for several improved, optimized titanium alloys for industrial service. The results on the Ti Gr. 16 alloy demonstrate that a leaner Pd formulation (~0.05Pd) offers corrosion performance essentially the same as the Ti Gr. 7 Alloy (~0.15Pd) when halide crevice corrosion and reducing acid corrosion resistance are limiting considerations. This Gr. 16 alloy alternative offers a means to significantly reduce mill product cost below that of the traditional Gr. 7 alloy, and becomes much more competitive with the Ni-Cr-Mo alloys for hot aggressive industrial applications. The reduction in Pd level does not influence alloy mechanical or physical properties, so that the ASME or ANSI pressure vessel code design allowables for Ti Gr. 7 apply to Ti Gr. 16. It may also be assumed that a similar replacement of Ti Gr. 11 with Ti Gr. 17 for cost benefits may also be substantiated by the corrosion database developed for Ti Grades 7 and 16. Candidate areas for Ti Gr. 16 and 17 alloy application are presented in Table 10.

The corrosion database for the Ti Gr. 18 and Ti Gr. 5/Pd alloys indicate that these alloys offer a unique combination of medium to high strength (515 - 900 MPa YS) and halide crevice corrosion and reducing acid resistance approaching that of Ti Gr. 7, and exceeding that of Ti Gr. 12. This combination of properties make these alloys ideal for equipment/components handling high temperature/high pressure aqueous halides and/or dilute acid process streams. Examples of candidate applications are also outlined in Table 10. Note that the Gr. 18 alloy may be designed under the ASME Pressure Code Vessel Code based on design allowables for the Ti Gr. 9 alloy, since the Pd addition does not influence alloy metallurgy and mechanical properties.

Conclusions

1. A corrosion database has been established for the optimized lean-Pd alloys: Ti Gr. 16, 18 and Gr. 5/Pd.

2. Ti Gr. 16 offers nearly equivalent resistance to dilute reducing acids and halide crevice corrosion as the "Pd-rich" Ti Gr. 7 alloy, and is recommended as a more cost attractive alternative for aggressive service.

3. Ti Gr. 18 and Gr. 5/Pd represent medium to high strength alloys with reducing acid and halide crevice corrosion resistance approaching that of Ti Gr. 7, and superior to Ti Gr. 12. This makes them suitable for pressure vessels, piping, and other components in hot halide process streams, geothermal brine wells, and deep sour gas well service.

4. The Ti Gr. 18 and Gr. 5/Pd alloys are resistant to stress corrosion cracking in hot sweet and sour chloride brines.

References

1. R. W. Schutz and L. C. Covington, "Guidelines for Corrosion Testing of Titanium," ASTM STP 728, ASTM, 1981, pp. 59-70.

2. T. P. Oettinger, "Summary of Corrosion Test Results on an Experimental Titanium Grade 9 Alloy Containing Palladium," Zimpro Passavant Environmental Systems, Inc., interoffice memo dated 10/24/91.

3. Metals Handbook, 9th Edition, Vol. 13 - Corrosion, ASM International, 1987, p. 669.

4. N. D. Tomashov, et. al., "Corrosion and Passivity of the Cathode-Modified Titanium Alloys," Titanium and Titanium Alloys - Scientific and Technological Aspects, Vol. 2, Plenum Press, NY, pp. 915-924, 1982.

5. S. Kitayama, Y. Shida, and M. Oshiyama, Sumitomo Search, Jan. 1990, (41), pp. 23-32, Sumitomo Metals, Japan.

6. T. Oettinger, et. al., "Use of Titanium for Treatment of Toxic and Hazardous Wastes," ASTM STP 917, ASTM, 1986, pp. 14-29.

7. S. Kitayama, et. al., "Effect of Small Pd Addition on the Corrosion Resistance of Ti and Ti Alloys in Severe Gas and Oil Environment," Paper No. 52, NACE Corrosion '92 Annual Conference, NACE, Houston, TX, March 1992.

8. M. Ueda, et. al., "Corrosion Behavior of Titanium Alloys in a Sulfur-Containing H_2S-CO_2-Cl-Environment," Paper No. 271, NACE Corrosion '90 Annual Conference, NACE, Houston, TX, April 1990.

Table 1. Titanium Alloys Evaluated

ASTM GRADE	NOMINAL COMPOSITION (wt.%)
Gr. 2	Unalloyed (C.P.)
Gr. 16	Ti-0.05Pd
Gr. 7	Ti-0.15Pd
Gr. 9	Ti-3Al-2.5V
Gr. 18	Ti-3Al-2.5V-0.05Pd
Gr. 5	Ti-6Al-4V
Gr.5/Pd	Ti-6Al-4V-0.05Pd

Table 2. Corrosion Rates Titanium Alloys in Boiling Acid Solutions

ALLOY	10 wt.% FORMIC ACID (mm/y)	50 wt.% FORMIC ACID (mm/y)	10 wt.% $FeCl_3$ (mm/y)
Ti Gr. 2	1.68	3.36	0.02
Ti Gr. 16	0.00	0.01	0.00
Ti Gr. 7	0.00	0.02	0.00
Ti Gr. 9	3.32	7.11	0.00
Ti Gr. 18	0.00	3.38	0.00
Ti Gr. 5	3.53	8.08	0.02
Ti Gr. 5/Pd	0.00	5.71	0.00

Table 4. Comparative Electrochemical Characteristics of Various Pd-containing Titanium Alloys in Hot Acidic Brines

ALLOY	CORROSION POT'L (E_{CORR})* (volts vs. Ag/Cl)	PASSIVE CURRENT** (mA/cm^2)	CATHODIC TAFEL SLOPE* (volts)	REPASSIVATION POT'L (E_{PROT})*** Volts vs. Ag/AgCl)
Gr. 2	-0.59	14	0.17	7.7
Gr. 16	-0.31	24	0.10	7.1
Gr. 7	-0.30	24	0.08	7.1
Gr. 9	-0.68	27	0.19	2.7
Gr. 18	-0.40	35	0.14	2.8
Gr. 5	-0.68	27	0.13	2.4
Gr. 5/Pd	-0.48	23	0.11	2.5

* in 20% NaCl/pH 0.5/90°C
** at -0.1V vs. Ag/AgCl in 20% NaCl/pH 0.5/90°C
*** in boiling nat. aerated 5% NaCl/pH 3.5

Table 3. Corrosion Resistance of Pd-containing Titanium Alloys in High Temperature Dilute Sulfuric Acid Solutions (1 day exposure)

TEST CONDITION	ALLOY	CORROSION RATE (mm/y)
3 wt.% H_2SO_4 at 240°C (naturally-aerated)	Ti Gr. 7	0.025
	Ti Gr. 16	0.00
	Ti Gr. 18	0.08
5 wt.% H_2SO_4 at 240°C (naturally-aerated)	Ti Gr. 7	0.028
	Ti Gr. 16	0.70
	Ti Gr. 18	3.01

Table 5. Crevice Corrosion Test Data for Pd-containing Titanium Alloys in Acidic Oxidizing NaCl Brines
(30 day exposures)

TEST ENVIRONMENT	ALLOY	CREVICE ATTACK FREQUENCY	COMMENTS
20% NaCl/pH2/ 260°C (naturally-aerated)	Ti Gr. 16	0/12	No attack
	Ti Gr. 7	0/12	
	Ti Gr. 18	0/12	
	Ti Gr. 5/Pd	0/12	
20% NaCl/pH2/90°C (Cl_2 gas-sat.)	Ti Gr. 16	0/12	No attack
	Ti Gr. 7	0/12	
	Ti Gr. 9	4/4	Significant attack
	Ti Gr. 18	2/12	Borderline/incipient
	Ti Gr. 5	12/12	Severe attack
	Ti Gr. 5/Pd	8/12	Mild/shallow attack
20% NaCl/pH1/90°C (Cl_2 gas-sat.)	Ti Gr. 2	12/12	Severe attack
	Ti Gr. 16	0/12	No attack
	Ti Gr. 7	0/12	
	Ti Gr. 18	6/12	Shallow attack
	Ti Gr. 5/Pd	12/12	Significant attack
Boiling 10% $FeCl_3$ (pH 1.0-0.3) 102°C	Ti Gr. 2	12/12	Severe attack
	Ti Gr. 16	0/12	No attack
	Ti Gr. 7	0/12	
	Ti Gr. 18	6/6	Significant attack
	Ti Gr. 5/Pd	6/6	

Table 6. Stress and Crevice Corrosion Resistance of Titanium Alloys Exposed to High Temperature Oxidizing, Acidic-Chloride Waste Solutions

Source: T. P. Oettinger, Zimpro Passavant Environmental Systems (2)

TEST ENVIRONMENT	ALLOY	SCC?*	CREVICE ATTACK?**
Industrial waste soln. with 20 gpl Cl^-, pH 3-4, 5 vol.% excess O_2 gas over soln., 280°C, 360 hrs.	Ti Gr. 2	No	Yes
	Ti Gr. 12	No	No
	Ti Gr. 9	No	Yes
	Ti Gr. 18	No	No
Industrial waste soln. with 20 gpl Cl^-, pH 1.5, 5 vol.% excess O_2 gas over soln., 280°C, 360 hrs.	Ti Gr. 2	No	Yes
	Ti Gr. 12	No	No
	Ti Gr. 9	No	Yes
	Ti Gr. 18	No	No
Synthetic waste soln. with 20 gpl Cl^-, pH 1.8, 20 vol.% excess O_2 gas over soln., 300°C, 770 hrs.	Ti Gr. 2	No	Yes
	Ti Gr. 12	No	No
	Ti Gr. 9	No	Yes
	Ti Gr. 18	No	No

* welded sheet - U-bend SCC tests

** PTFE sheet - sample sheet crevices

Table 7. Incidence of Crevice Corrosion on Titanium Alloys in Aerated Saturated-NaCl Solutions (pH 6) with Various Gasket-Metal Crevices

Source: S. Kitayama, et. al. (5) (500 hour exposures)

TEMP.	150°C			200°C	
Gasket Material	PTFE	Asbestos	Neoprene Rubber	PTFE	Asbestos
Ti Gr. 2	4/4	2/2	2/2	4/4	4/4
Ti Gr. 16 (0.05Pd)	0/4	0/2	0/2	0/4	0/2
Ti Gr. 7 (0.14Pd)	0/4	0/2	0/2	0/4	0/2

Table 8. Incidence of Crevice Corrosion on Titanium Alloys in Aerated Saturated-NaCl Solutions (PTFE gasket/metal crevices)

Source: S. Kitayama, et. al. (5)

TEMP.	100°C				200°C			
pH	2		6		2		6	
TEST TIME	500 Hr.	1000 Hr.	500 Hr.	1000 Hr.	500 Hr.	1000 Hr.	500 Hr.	1000 Hr.
Ti Gr. 2	4/4*	4/4	4/4	4/4	4/4	--	4/4	--
Ti Gr. 16 (0.05Pd)	0/4	0/4	0/4	0/4	0/4	0/8	0/4	0/8
Ti Gr. 7 (0.14Pd)	0/4	0/4	0/4	0/4	0/4	0/8	0/4	0/8
Ti Gr. 12	4/4	--	4/4	--	4/4	--	4/4	--

* Number of creviced surfaces attacked out of total creviced surfaces tested.

Table 9. Slow Strain Rate Test Data for Ti Gr. 18 and Ti Gr. 5/Pd in High Temperature Well Fluid Brine Environments

ALLOY	TEST TEMP.	BRINE pH	RA RATIO	TTF RATIO	SCC?
Ti Gr. 18	180°C*	3.5	1.0	1.0	No
	288°C*	5.0	1.0	1.0	No
Ti Gr. 5/Pd	180°C*	3.5	1.0	0.98	No
	288°C*	5.0	1.0	1.0	No
Ti Gr. 5/Pd	246°C**	~3.5	0.96	1.0	No
	272°C**	~3.5	1.0	1.0	No

* Salton Sea geothermal brine

** 20% NaCl/6.9 MPa H_2S/3.4 MPa CO_2/1 gpl S^o

Table 10. Candidate Industrial Applications for Optimized Pd-containing Titanium Alloys

CANDIDATE SERVICE OR EQUIPMENT	PROSPECTIVE ALLOY
chlor-alkali, chlorate cell components	Ti Gr. 16, 17
hot seawater/brine plate exchangers	Ti Gr. 17
hot Ca, Mg salt brines	Ti Gr. 16
hot acidic metal halides ($FeCl_3$, $CuCl_2$, $AlCl_3$, $NiCl_2$, $ZnCl_2$)	Ti Gr. 16
hot aqueous Cl_2/Br_2	Ti Gr. 16
hot dilute organic/inorganic acids	Ti Gr. 16, 17
MnO_2 anodes	Ti Gr. 16
FGD scrubber inlets/prescrubbers	Ti Gr. 16
tubesheet/vessel explosive cladding	Ti Gr. 17
wet oxidation processes	Ti Gr. 18, Ti Gr. 5/Pd
Other waste treatment processes	Ti Gr. 18
high temp. organic synthesis	Ti Gr. 18
hydrometallurgical ore leaching processes	Ti Gr. 18
deep sour gas well tubulars/components	Ti Gr. 5/Pd
offshore flow/export lines, coiled tubing	Ti Gr. 18
pressure vessels, piping	Ti Gr. 18
valves, pumps, shafting, agitators, fasteners	Ti Gr. 18, Ti Gr. 5/Pd

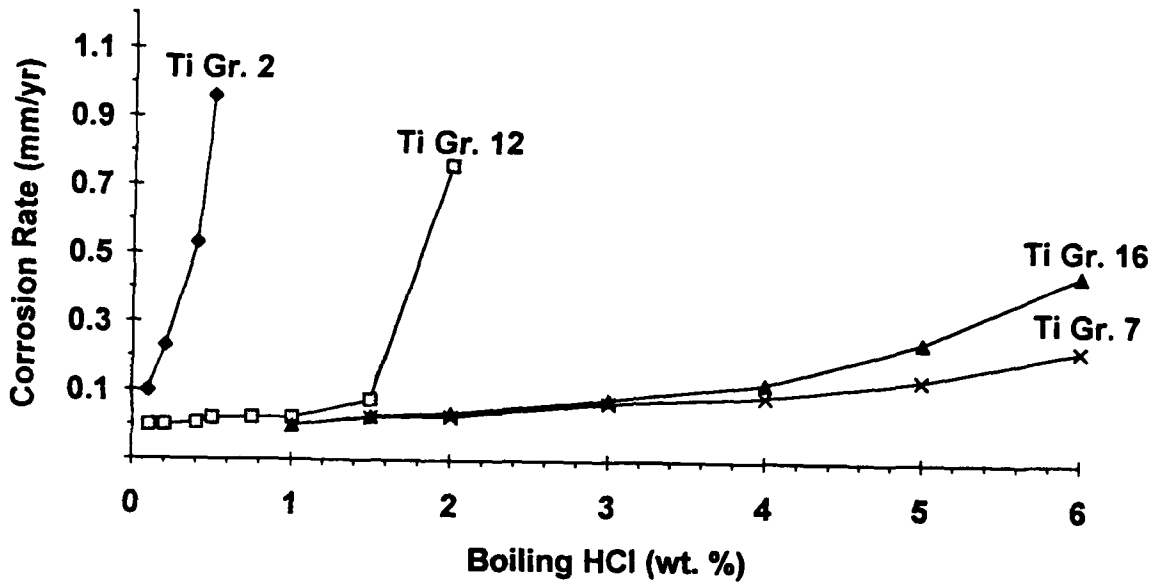

Figure 1. Corrosion rate profiles for Ti Gr. 7 and 16 alloys in boiling HCl solutions.

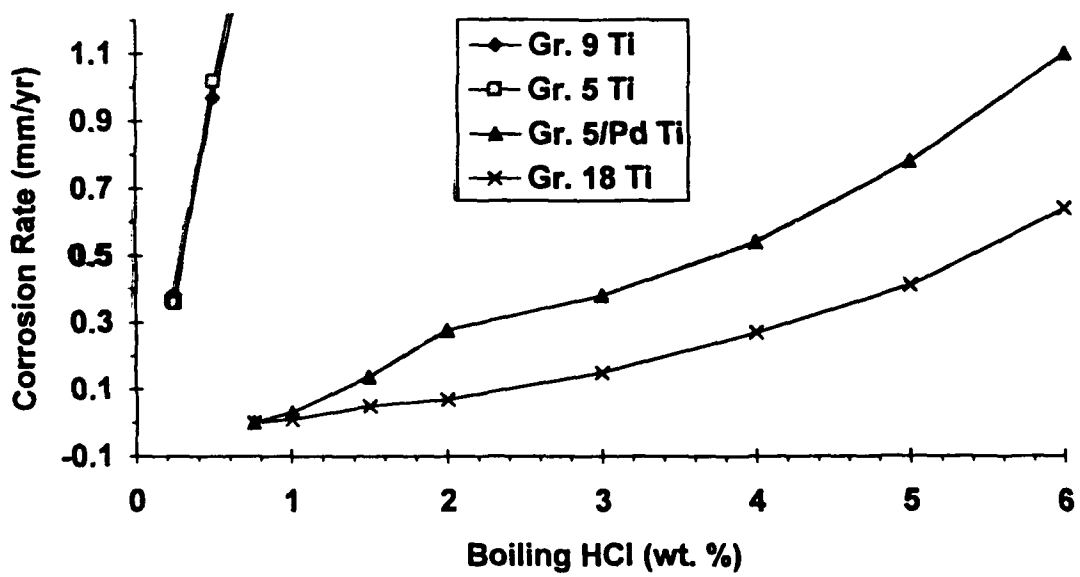

Figure 2. Corrosion rate profiles for the Pd-enhanced elevated strength titanium alloys in boiling HCl solutions.

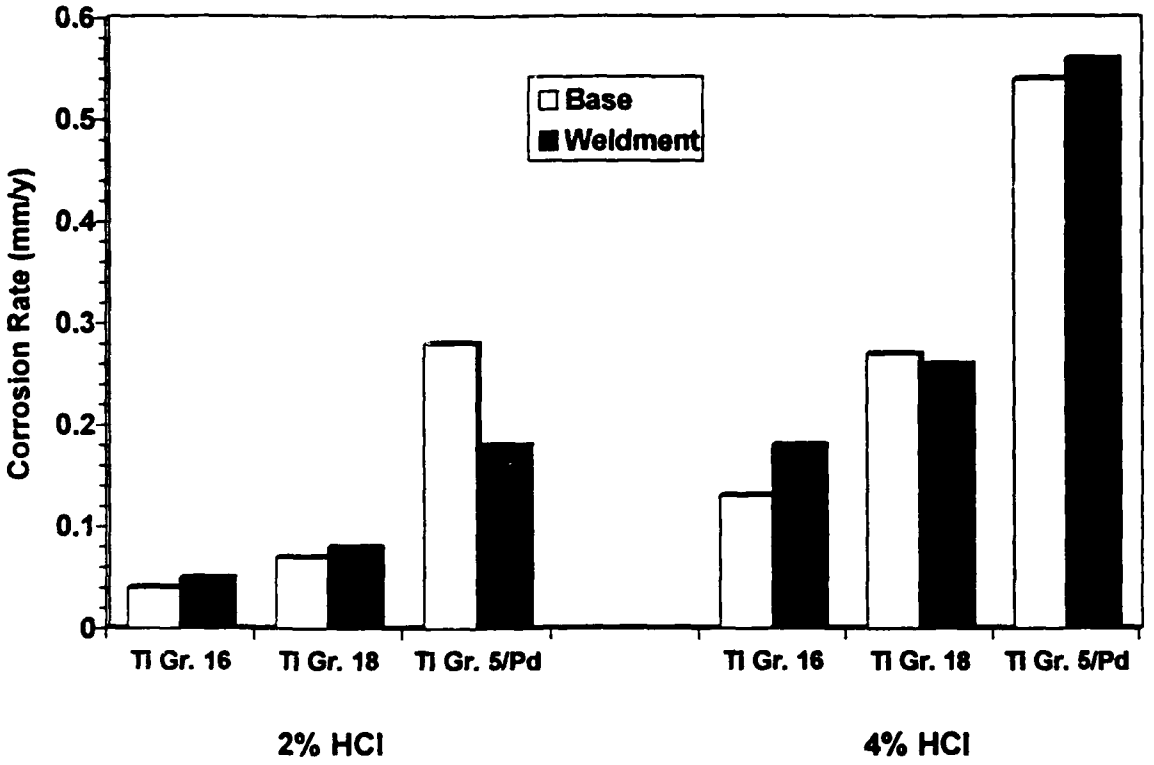

Figure 3. Comparative corrosion rates for base and weld metal for Pd-containing titanium alloys in boiling HCl.

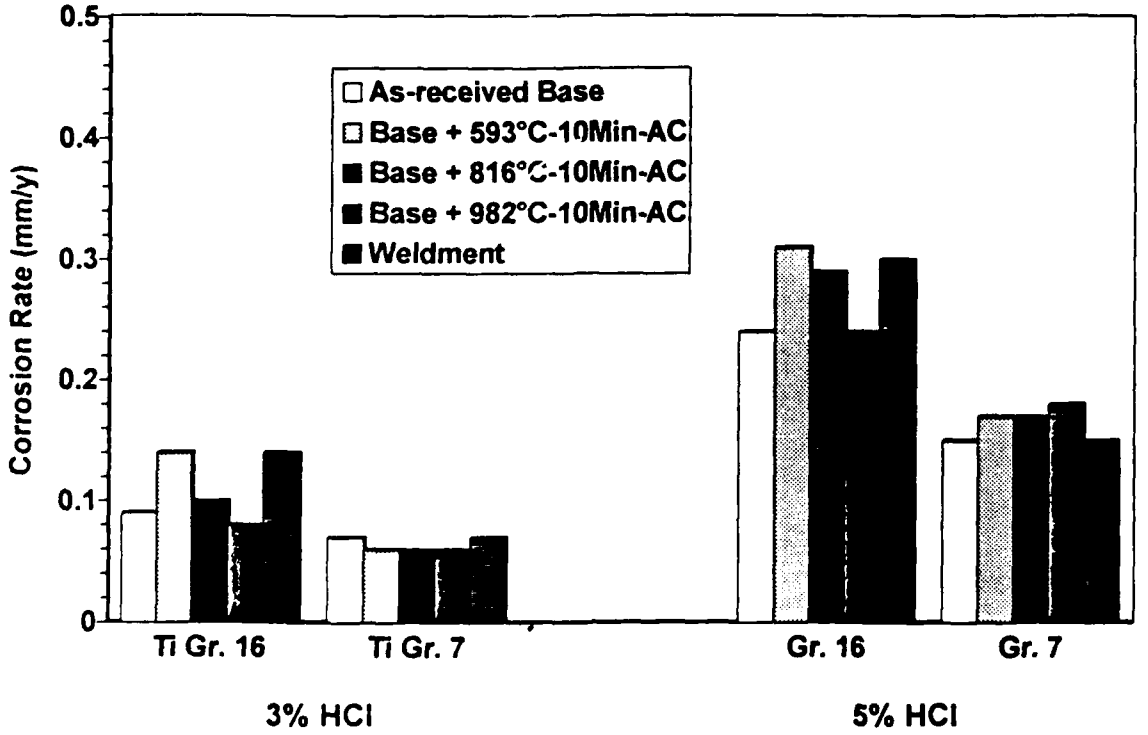

Figure 4. Effect of thermal treatments on corrosion resistance of Ti Grades 7 and 16 in boiling HCl.

Corrosion Characteristics and Applications of Newer High and Low Nickel Containing Ni-Cr-Mo Alloys

D.C. Agarwal
VDM-T
11210 Steeplecrest Drive, # 120
Houston, Tx 77065-4939

U. Heubner/W. Herda
Krupp VDM GmbH
Plettenberger Str. 2
P.O. Box 1820
5980 Werdohl
Germany

Abstract

The materials of construction for the modern chemical process industries not only have to resist uniform corrosion caused by various corrodents but must have sufficient localized corrosion and stress corrosion cracking resistance. The commonly used metals span a wide spectrum, starting at carbon steel on the very low end to high performance nickel base alloys of the Ni-Cr-Mo family on the other end.

Even though the standard austenitic stainless steels (Alloy 304L and 316L) have been and continue to be the workhorse of many industries, their vulnerability to localized corrosion and chloride stress corrosion cracking has been a major problem in certain processes. The knowledge that chromium and molybdenum improved the localized corrosion resistance and increased nickel enhanced the chloride SCC resistance led to different alloys with varying nickel, chromium, molybdenum and iron contents. The knowledge that in certain low nickel containing alloys nitrogen could be added to impart certain unique mechanical, metallurgical and corrosion characteristics was used to come up with a completely new 6% Mo alloy class which were very cost effective and in certain cases approached or equaled the corrosion resistance of the more expensive high nickel containing alloys. Two alloys of this 6 Mo stainless steel class, with varying chromium and nickel contents were developed to bridge the performance gap between the standard austenitic stainless steel and the very high performance nickel based alloy of the Ni-Cr-Mo family such as alloy C-276, alloy 22, alloy C-4 and the most recent development, alloy 59.

This paper presents the various metallurgical, thermal stability and corrosion characteristics of the 2 alloys of the 6 Mo family known as Alloy 1925hMo - alloy 926 - UNS # N08926, Alloy 3127hMo - alloy 31 - UNS # N08031 and the most recent development of alloy 5923hMo - alloy 59 - UNS # N06059. Some actual case histories where these alloys have solved some specific problems in the industry are also presented.

Key words: 6Mo Stainless Steels, Alloy 31, Alloy 926, Alloy 59, UNS # N08031, UNS #N08926, UNS #N06059, 1925hMo, 3127hMo, 5923hMo, localized corrosion, stress corrosion cracking, mineral acids

Introduction

The increased severity of corrosion environments of modern chemical process industries created as a result of the need to comply with rigid environmental regulations and the need to increase production efficiency (use of higher temperatures, pressures, more effective catalysts) and versatility by being able to utilize the same piece of equipment under varying operating conditions (oxidizing, reducing, others), has placed a greater burden on corrosion engineers to find the right alloy.

At one time one of the major factors in any material selection used to be initial cost with little thought given to maintenance and costs associated with lost production due to unscheduled equipment downtime. In today's economic environment increased maintenance costs and downtime have placed a greater emphasis on the need for reliable, safe and versatile performance of process equipment. The "C" family of the Ni-Cr-Mo alloys over the last 60 years has had many variations starting with Alloy C in the 1930's, Alloy C-276 in the 1960's, Alloy C-4 in the 1970's, Alloy 22 in the 1980's and the most recent and versatile development of alloy 59 in the 1990's. This alloy 59 is in its true sense a pure alloy of the Ni-Cr-Mo family.

The cost effective bridging of the performance gap between the standard austenitic stainless steels, their various upgraded versions (alloy 904L, alloy 28, alloy 20, others) and the high performance "C" family of alloys was

accomplished by the development of two alloys within the 6Mo family, with different nickel and chromium contents. These alloys not only bridged the corrosion performance gap but also provided a cost effective alternative to some of the higher nickel containing alloys of the Ni-Cr-Mo family such as alloy G-3, G-30 and alloy 625. These 6Mo alloys are alloy 926 (UNS # N08926) and alloy 31 (UNS # N08031). Table 1 gives the typical chemistry of these alloys in comparison to some other existing and well known corrosion resistant alloys.

The following sections briefly highlight the metallurgical, mechanical, corrosion, thermal stability and fabricability characteristics of alloy 59, alloy 926 and alloy 31 and provide various literature references for obtaining further information.

Alloy 59 - Highlights

The historical development of the various "C" family of alloys and their corrosion behavior is adequately described elsewhere [1-8]. The design of alloy 59 increased the chromium and chromium plus molybdenum contents to the highest level possible in a nickel matrix, omitted tungsten and reduced iron content to typically less than 1%. This combination created a significantly improved corrosion resistant and thermally stable alloy in comparison to alloy C-276 and alloy 22, both of which contain tungsten [9-10]. Further evidence of the detrimental effects of tungsten on thermal stability behavior is shown in Table 2, which shows the tungsten containing alloy 22 to have 2 orders of magnitude higher corrosion rate and heavy localized pitting attack when tested in ASTM G-28B solution after a 1600°F sensitization heat treatment. Alloy 59 had low corrosion rates and no localized attack when tested under similar conditions.

Alloy 59 Corrosion Resistance

ASTM G-28 Method A. Uniform corrosion rates are shown in Figure 1. Alloy 59 with 0.6 mm/year (24 mpy) is clearly superior to Alloy 22 with 0.9mm/year (36 mpy). Alloy C-4 and Alloy C-276 due to their lower chromium content exhibit much higher uniform corrosion rates in this highly oxidizing solution of boiling 50% H_2SO_4 + 42 g/l of $Fe_2(SO_4)_3 * 9H_2O$

ASTM G-28 Method B. This test was designed to detect susceptibility to intercrystalline or intergranular attack more accurately than the above mentioned ASTM G-28, Method A. Due to the lower sulfuric acid concentration of this solution (23% H_2SO_4 vs. 50% H_2SO_4) and subsequently lower boiling temperatures, the uniform corrosion rates are significantly lower, (Fig. 1). Again, Alloy 59 shows the best performance in this test.

"Green Death Solution". This environment is a non-standard media in an attempt to simulate severe oxidizing chloride acid conditions in flue gas streams. However, it does not have any relevancy to real world environments. Table 3 shows the localized corrosion behavior of this alloy in comparison to others. As is shown, Alloy 59 has the highest pitting resistance equivalent when calculated by PRE = %CR + 3.3% Mo. Alloy 59 also has the highest critical pitting temperature and the lowest depth of attack under crevice corrosion conditions in both green death and modified green death test solutions when tested at 105°C. Another significant analysis is that the higher molybdenum containing alloys (Alloy 59 and Alloy C-276) have 10 times lower crevice corrosion depth of attack than the lower molybdenum containing Alloy 22. In real world situations crevice corrosion conditions are more critical than pure pitting conditions.

Mineral Acids/Acid Mixtures. Most standardized corrosion tests relate to oxidizing conditions, where Alloy 59 has been demonstrated to be superior to other Ni-Cr-Mo alloys as shown above. However, the superior behavior of Alloy 59 in some reducing media is shown in table 4. In boiling 10% sulfuric acid, Alloy 59 exhibits a more than 3 times lower corrosion rate than the other well established Ni-Cr-Mo alloys, and the corrosion rate of only 0.18 mm/year in boiling 1.5% hydrochloric acid, more than 3.5 times lower than that of Alloy 22. Other data and iso-corrosion curves in hydrochloric and sulfuric acid are presented elsewhere[11].

Welding and Corrosion Behavior. Welding of Alloy 59 follows the general rules established for welding of high alloyed nickel base materials where cleanliness is of great importance and heat-input should be kept low[12, 13]. The use of a matching filler metal is recommended. Preheating is not required and the interpass temperature should not exceed 150°C (300°F). Its sensitivity to hot cracking is low and even smaller than that observed in case of Alloy C-276[14]. Further details on weldability and fabricability are described elsewhere[10].

The influence of welding on corrosion resistance has been tested on GTAW weldments using a matching filler and on Gas Plasma Arc Weldments (GPAW) made as square butt welds without filler metal. The test samples consisted of about 15-20% of their surface of the weldment, the remainder being base metal with heat affected zone. As evident from Table 5 in the boiling ASTM G28, Method A test solution no degradation of corrosion resistance occurred and the intergranular penetration in base metal and heat affected zone did not exceed the 0.05 mm criterion even after 120 hours. In the ASTM G28, Method B test solution the corrosion rate of the welded samples

is increased with preferential weld and heat affected zone attack but without any intergranular penetration in the heat affected zone. In sulfuric acid with very high chloride concentration as shown in table 5, Alloy 59 has very low corrosion resistance even in the welded condition. Also, welding does not impair the resistance to pitting either.

Application of Alloy 59

Alloy 59 has been successfully used in a number of commercial applications , details of which are provided elsewhere[10-12]. Some major applications including test programs have been in flue gas desulfurization systems of coal fired power plants, air pollution control systems of hazardous and municipal waste incinerators, citric acid production, eletrolytic purification of gold, production of special chemicals utilizing halogenic organics, conductor rolls for electrolyctic galvanizing, waste acid recovery systems, pharmaceutical industry, chlorine driers and many others.

Alloy 1925hMo - Alloy 926 - Highlights

This alloy was derived from Alloy 904L by increasing its molybdenum content from 4.8% to 6.5% and stabilizing the alloy by fortifying it with 0.2% nitrogen, an austenitic stabilizer. This addition of nitrogen not only alleviated the need to add more expensive nickel, but provided other benefits of improving localized corrosion resistance, increasing mechanical strength, and improving its stress corrosion cracking behavior. Table 6 shows its localized corrosion resistance in an ASTM G-48 test in comparison to other alloys. This test consists of immersing a sample in 10% solution of hydrated ferric chloride solution for 24 hours and then examining it visually for pitting and crevice corrosion. The temperature, known as critical pitting or critical crevice corrosion temperature, has been found to have a direct relationship to the pitting resistance equivalent, which is defined as: PRE = %CR + 3.3% Mo + 30x%N. As is evident from Table 6, this alloy shows a marked improvement over many alloys.

Resistance to chloride stress cracking is likewise improved significantly. Table 7 shows the data according to NaCl drop evaporation method. It is quite clear that this alloy is even superior to the high nickel containing Alloy 825. This apparent anomaly can be explained by the fact that in many cases stress corrosion cracking initiates at the bottom of the pit, and since the pitting corrosion resistance of Alloy 926 is far superior to Alloy 825, fewer sites favorable for crack initiation can form in this alloy.

Its good behavior in chloride media means that not only it can be used to resistance attack in process media containing halogens, but also in contact with corrodents such as seawater and brackish water. Figure 2 shows the pitting potential of this alloy in aerated stirred artificial seawater in comparison to an advanced 6Mo Alloy 31 and 317L stainless steel.

Table 8 and Table 9 shows the uniform corrosion resistance behavior of this alloy in various concentrations of sulfuric acid.

Table 10 gives a comparison of its mechanical properties in comparison to other alloys. This alloy is readily weldable and is recommended to be welded with an over-alloyed filler metal to compensate for the segregation of chromium, and more particularly molybdenum, which occurs in the interdentritic weld zones. Suitable welding products for this alloy are Alloy 625, Alloy C-276, or Alloy 59. Further details on its weldability, fabricability and other properties are documented elsewhere[15, 16].

Alloy 3127hMo - Alloy 31 - Highlights

This is a new alloy, recently introduced. Its chemistry (Table 1) shows this alloy to have a relatively low nickel content, when compared to Alloy 625, with a very high chromium content, and a significant addition of molybdenum, with nitrogen fortification and copper additions. As would be expected form its chemical composition, the alloy has a high pitting resistance equivalent of over 50, similar to that of Alloy 625. Its localized corrosion resistance is similar to, or in certain tests, superior to Alloy 625 in the scatterband of the ASTM G-48 test data points (Table 6). This alloy's resistance to sulfuric acid (Table 8) is excellent and even better than that of alloy C-276.

The pitting potential of Alloy 31, as determined in artificial seawater, is maintained over a wide temperature range (Fig. 2). This high resistance to corrosion in chloride containing media together with its resistance to a wide range of chemicals makes this alloy a suitable candidate for service in heat exchangers using seawater or brackish water as a coolant. Its high chromium content with increased Mo and N has allowed this alloy to give even better performance in the wet phosphoric acid industry over the existing Alloy 28.

One particular oxidizing media in the pulp and paper industry (chlorine dioxide bleach washer) holds significant promise for this alloy. Wensley and others[17, 18] have shown that in chloride contaminated solutions of chlorine-

dioxide the high nickel alloys resist local attack but show high uniform corrosion. The standard stainless steels, though good from uniform corrosion viewpoint, suffer from localized attack. Wensley's work showed alloy 31 resistant to both forms of corrosion. This work is of significant importance due to the recent trend of chlorine dioxide substitution for chlorine as a bleaching agent in the pulp and paper industry.

The mechanical properties (Table 10) compare favorably with those of other high alloyed stainless steels and some nickel base alloys. Like Alloy 1925hMo, Alloy 31 should be usually welded with over alloyed filler metals such as Alloy 625, Alloy C-276 and Alloy 59. This alloy has a high degree of metallurgical stability. Interganular corrosion tests on welded specimens and determination of pitting and crevice corrosion temperatures of welded samples did not show any degradation as a result of standard welding procedures. More details on the development of this alloy and its corrosion behavior is presented elsewhere[19, 20].

Applications of 6Mo Alloys

Alloy 926 has found wide usage in various industries as shown in Table 11. Major applications of over 2500 tons have been in the Saga Snorre Offshore Platform, pulp and paper mills and air pollution control industry. Details are documented elsewhere[16, 21, 22].

Alloy 31 - The high resistance of this alloy to corrosion in chloride contaminated water at high temperatures, together with its resistance to a wide range of chemical media has led this alloy to be considered for service in heat exchangers using seawater or brackish water as a coolant. This alloy has already been selected or recommended for use in bleach washers and pulp lines in chlorine dioxide stages of pulp and paper plants, agitators/stirrers, and heat exchanges in phosphoric acid production, seawater cooled sulfuric acid coolers, high temperature heat exchangers and spinning baths in viscose rayon production, heat exchangers handling high chloride, low pH media in fine chemical production, and heat exchangers for sulfuric acid pickling baths.

Specifications

Alloy 59, Alloy 926 and Alloy 31 are covered under the appropriate ASTM and international specifications. Furthermore all these alloys are also covered under the ASME code case for construction of pressure vessels.

Conclusions

The advanced Ni-Cr-Mo Alloy 59 has been designed to withstand the most severe corrosive conditions of the modern chemical process industry and today's environmental pollution control systems where other alloys are at the end of their usefulness limits. This alloy's excellent thermal stability, fabricability, and equivalent corrosion resistance in both welded and unwelded condition in a wide variety of corrosive media makes this alloy a suitable candidate to meet the eve increasing challenges of the modern chemical process industry of the 1990's and the 21st century.

The special 6Mo super-austenitic stainless steel Alloy 926 and Alloy 31 are providing cost effective alternatives to some of the higher and more expensive alloys currently used in the process industry. They demonstrate excellent corrosion resistance in a wide varied range of media, have good strength and ductility and can be readily fabricated by conventional techniques. They are natural candidates for applications where the standard stainless steels are inadequate or marginal and where economic conditions rule out the use of more expensive nickel base alloys.

References

1. F.T. McCurdy, Proc. Am. Soc. Testing Material, Vol. 39, P. 698, (1939)
2. E.D. Weisert, Corrosion, Vol. 13, p. 659, (1957)
3. W.A. Luce, Chem . Engg., Vol. 61, No. 3, p. 254, (1954)
4. Wayne Z. Friend, Corrosion of Nickel and Nickel Base Alloys, John Wiley & Sons, Inc., New York - Chichester - Brisbane - Toronto, pp. 292-367, (1980)
5. I. Class, H. Grafen & E. Scheil, Z. Metallkunde, Vol. 53, p. 283 (1962)
6. M.A. Streicher, Corrosion, Vol. 19, p. 272 (1963) ibid Vol. 32, p. 79 (1976)
7. R.B. Leonard, Corrosion, Vol. 25, p. 222 (1969)
8. F.G. Hodge & R.W. Kirchner, Corrosion, Vol. 32, p. 332 (1976)

9. R. Kirchheiner, M. Koehler, U. Heubner, A New Highly Corrosion Resistant Material for the Chemical Process Industry, Flue Gas Desulfurization and Related Applications, Corrosion/90, Paper No. 90, National Association of Corrosion Engineers, Houston, Texas, (1990).

10. D.C. Agarwal, et al, "Cost Effective Solution to CPI Corrosion Problems with a New Ni-Cr-Mo Alloy: Corrosion/91. Paper # 179, (Houston, Tx: National Association of Corrosion Engineers, 1991)

11. D.C. Agarwal, et al, "Recent Alloy Development in the Ni-Cr-Mo Alloy System" Proceedings 1st Pan-American Corrosion and Protection Congress, Mar del Plata, Argentina, 25-30 Oct., 1992, Vol. 1, pp. 83-101

12. U. Heubner et al., Nickel Alloys and High Alloy Special Stainless Steels, expert-Verlag, Sindelfingen, p. 78 (1987)

13. Metals Handbook, 9th Edition, Vol. 6, Welding, Brazing and Soldering, American Society for Metals, Metals Park, Ohio, 1983.

14. U. Brill, T. Hoffman and K. Wilken, "Solidification Cracking: Super Stainless Steels and Nickel Base Alloys", Materials Weldability Symposium, Materials Week 90, SM International, materials Park, Ohio, 1990.

15. D.C. Agarwal, "The New Nitrogen Fortified 6% Mo Super-austenitic Stainless Steels: Their Weldability and Corrosion Resistance", Weldability of Material Symposium, Materials Week, Detroit, Oct. 8-12, 1990

16. D.C. Agarwal, M.R. Jasner, M.B. Rockel, 1991 OTC, Paper # 6598, (Houston, Tx: Offshore Technology Conference 1991)

17. Wensley, A., and Reid, Craig, Corrosion/91, Paper #193, (Houston, Tx: National Association of Corrosion Engineers, 1991)

18. Wensley, A., et al., "Corrosion of Stainless Alloys in a Chlorine Dioxide Bleach Pulp Washer", 1991, Tappi Engineering, Conference Proceedings, pp. 499-509.

19. U. Heubner, M. Rockel, F. Wallis, Werkstoffe und Korrosion. Vol. 40, pp. 459-466, 1989

20. Heubner U., et al., Corrosion/91, Paper #321, (Houston, Tx: National Association of Corrosion Engineers, 1991)

21. D.C. Agarwal & F. White, Corrosion/92, Paper #324, (Houston, Tx: National Assocation of Corrosion Engineers, 1992)

22. D.C. Agarwal, et al., "The 6% Mo Superaustenitics. The Cost-Effective Alternative to Nickel Alloys", *Proceedings 1st Pan American Corrosion and Protection Congress, Mar del Plata, Argentina, 25-30,*. 1992, Vol 1, pp. 103-114.

TABLE 1

NOMINAL CHEMICAL COMPOSITION OF NEW AND SOME EXISTING ALLOYS TO RESIST AQUEOUS CORROSION

Alloys	UNS#	Ni	Cr	Mo	Fe	N	Others	PRE*
Alloy 926 (1925hMo)	N08926	25	21	6.5	46	0.2	Cu	48
Alloy 31 (3127hMo)	N08031	31	27	6.5	31	0.2	Cu	54
Alloy 59 (5923hMo)	N06059	59	23	16	1	-	-	76
316L	S31603	12	17	2.3	66	-	-	24
904L	N08904	25	21	4.8	46	-	Cu	32
Alloy 20	N08020	37	20	2.4	34	-	Cu, Cb	29
825	N08825	40	22	3.2	31	-	Cu	32
G-3	N06985	48	23	7	19	-	Cu, Cb	45
625	N06625	62	22	9	3	-	Cb	52
22	N06022	58	22	13	3	-	W	65
C-276	N10276	57	16	16	5	-	W	69

*PRE = Pitting Resistance Equivalent = % Cr + 3.3% Mo + 30 N

TABLE 2

THERMAL STABILITY AS MEASURED IN ASTM G28B SOLUTION AFTER SENSITIZATION TREATMENT

Sensitization Treatment at 1600°F	Corrosion rate (mpy) Alloy 22*	Alloy 59**
1 hr.	339	4
3 hrs.	313	4
5 hrs.	1606	17

* Alloy 22 - Heavy pitting attack over entire surface
** Alloy 59 - No pitting attack

TABLE 3

LOCALIZED CORROSION RESISTANCE IN GREEN DEATH AND MODIFIED GREEN DEATH SOLUTION

A. Green Death Solution
11.5% H_2SO_4 + 1.2% HCl + 1% $CuCl_2$ + 1% $FeCl_3$

	Alloy 59	Alloy 22	Alloy C-276	Alloy C-4
■ Pitting Resistance Equivalent PRE = % Cr + 3.3% Mo	76	65	69	69
■ Critical Pitting Temperature	>120°C	120°C	115-120°C	100°C
■ Critical Crevice Temperatures	110°C	110°C	105°C	85-95°C

B. Modified Green Death - Test Solution with Lower Oxidizing Species of Cupric & Ferric Ions
11.5% H_2SO_4 + 1.2% HCl + 0.7% $CuCl_2$ + 0.7% $FeCl_3$

	Alloy 59	Alloy C-276	Alloy 22
■ At 105°C - Pitting	No Attack	No Attack	No Attack
■ At 105°C - Crevice Depth of Attack			
a) Green Death	0.025 mm	0.035 mm	0.35 mm
b) Modified G.D.	<0.025 mm	0.025 mm	0.25 mm

TABLE 4

CORROSION RESISTANCE OF ALLOY 59 IN VARIOUS ACID ENVIRONMENTS

		Corrosion rate (mm / y)**				
Media	Temp. °C	59	22	C-276	C-4	625
10% H_2SO_4	Boiling	.14	.46	.58	.79	1.2
20% H_2SO_4 + 1.5% HCl	50	0	0	0	-	0
	80	.003	.004	.007	-	.003
50% H_2SO_4 + 1.5% HCl	50	.38	.45	.42	-	.75
98.5 % H_2SO_4	150	.28				
	175	.19				
	200	.14				
1.5% HCl	Boiling	.18	.68	-	-	-

*To convert to mpy, multiply by 40

TABLE 5

INFLUENCE OF WELDING ON CORROSION RESISTANCE OF ALLOY 59

		Corrosion Rate (mm/y)		
Test Media	Temperature (Time)	Unwelded	GTAW	GPAW
ASTM G-28A	Boiling (120 hours)	0.60	0.48	0.62
ASTM G-28B	Boiling (24 hours)	0.11	0.63	0.81
H_2SO_4 - pH1 + 7% Chloride ions	Boiling (21 days)	0.003	0.007	0.003

TABLE 6
CRITICAL PITTING/CREVICE CORROSION TEMPERATURE
10% $FeCl_3$, SOLUTION (ASTM G-48)

New Alloys	PRE*	CPT(°C)*	CCT(°C)*	Cost Ratio to 316L
926	48	70	40	2.3
31	54	>85**	65	2.6
59	76	>85**	>85**	4.1
Existing Alloys				
316L	24	15	>0	1.0
304L	32	45	25	2.2
20	29	15	<10	2.3
825	32	30	<5	2.8
G-3	45	70	40	3.2
625	52	77.5	57.5	4.1
C-276	69	>85**	>85**	4.1

*PRE - Pitting Resistance Equivalent = % Cr + 3.3% Mo + 30N
*CPT - Critical Pitting Corrosion Temperature in 10% $FeCl_3$ Solution
*CCT - Critical Crevice Corrosion Temperature in 10% $FeCl_3$ Solution

** It has been postulated that when temperature of 10% $FeCl_3$ solution exceeds 85°C, a chemical breakdown of the solution occurs

TABLE 7

STRESS CORROSION CRACKING BEHAVIOR ACCORDING TO NaCl DROP EVAPORATION METHOD

Alloy	Time to Failure
304	< 10 hours
316	< 25 hours
317	100 hours
904L	>500 hours
926 (1925hMo)	>1000 hours - no failure*
28	250 hours
825	275 hours

*Test stopped after 1000 hours

TABLE 8

UNIFORM CORROSION RESISTANCE OF THE NEWER 6MoSS ALLOYS IN DILUTE SULFURIC ACID MEDIA IN COMPARISON TO ALLOY C-276

Corrosion Rate (mpy)

% H_2SO_4	60°C Alloy 926	60°C Alloy 31	60°C Alloy C-276	80°C Alloy 926	80°C Alloy 31	80°C Alloy C-276	100°C Alloy 926	100°C Alloy 31	100°C Alloy C-276
20	<0.1	<0.1	<1	0.2	<0.1	4	130	<0.3	7
40	<.15	<0.1	<1.5	<.5	<0.2	3.2	124	<1	10
60	<0.25	<0.1	<1.5	<1.0	<0.5	3.5	47	1	11
80	<0.5	<0.2	<1	160	<1	15	>500	240	240

TABLE 9

UNIFORM CORROSION RATE OF ALLOY 1925hMo (ALLOY 926) IN CONCENTRATED H_2So_4 MEDIA

Temperature °C	98% H_2SO_4	99% H_2SO_4
80	2	<1.5
100	8	5
120	8	4.5
150	11	6
100 (Plant Test)	98.5% Concentration	1.5 mpy

TABLE 10

TYPICAL ROOM TEMPERATURE MECHANICAL PROPERTIES OF VARIOUS ALLOYS

ALLOY	UNS NO	UTS N/mm^2	0.2% YIELD N/mm	% ELONGATION
316L	S31603	538	241	55
904L	N08904	586	283	50
926	N08926	655	310	50
31	N08031	717	352	50
G-3	N06985	676	310	50
625	N06625	862	448	45
C-276	N10276	759	365	60
22	N06022	731	359	60
59	N06059	772	379	60

TABLE 11

SOME TYPICAL INDUSTRIAL APPLICATIONS FOR ALLOY 926

Offshore and Marine:
- Seawater Lines
- Product Coolers
- Reverse Osmosis Desalination Plants

Pulp and Paper:
- Bleach Washers
- Pulp Lines
- Recovery Boiler Scrubbers

FGD:
- Scrubbers
- Fans
- Ducts
- Dampers

Chemical Process Industry:

Inorganics:
- o H_2SO_4 distribution systems (sulphur route)
- o Metasilicate production
- o Sodium perchlorate crystallizers
- o Hydrofluoric acid production (scrubber)
- o Ammonium chloride evaporators
- o Catalyst strippers
- o Wet exhaust fans
- o Phosphoric acid digestion systems
- o Many others

Organics:
- o Ethyl acetate production
- o Thermoplastic rubber (catalyst strippers)
- o TDI and MDI production
- o Organic intermediates (chloride catalysts)
- o Fine chemicals (pharmaceuticals, agrichemicals, etc., numerous applications in the acid chloride media)
- o Many others

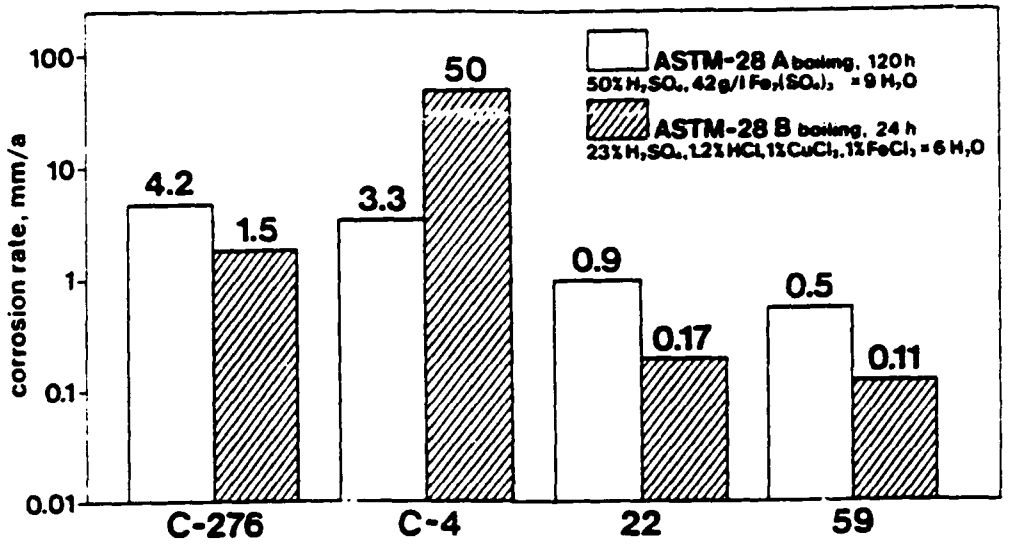

Fig. 1: ASTM G-28A and ASTM G-28B Test Data for Various Alloys

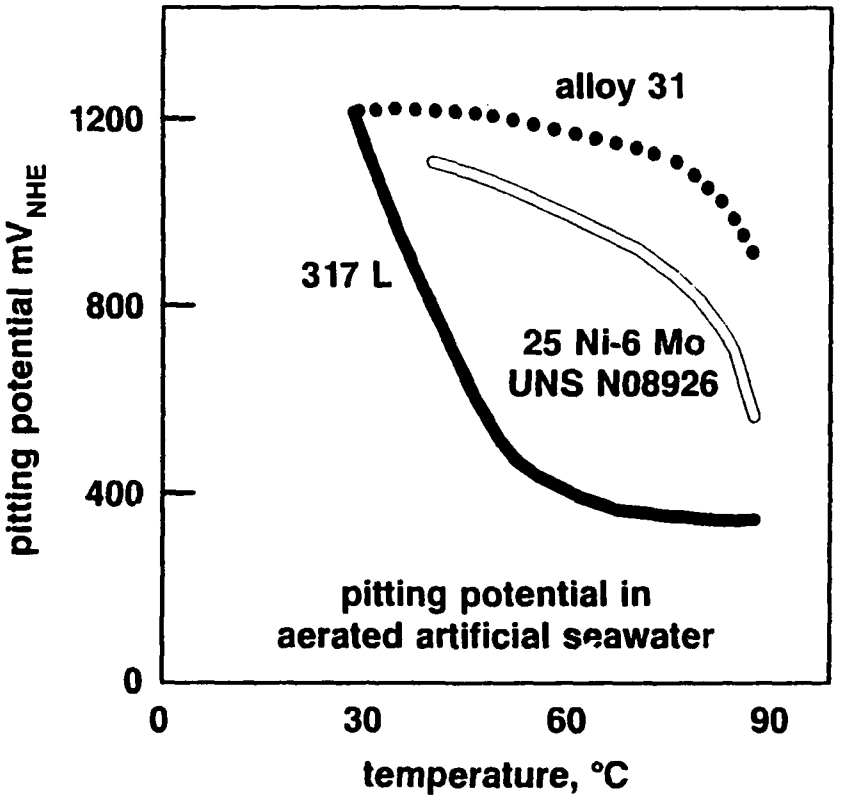

Fig. 2: Temperature dependence of pitting potential in aerated and stirred artificial seawater

Duplex Stainless Steels for Demanding Applications

J. Michael Nicholls
R & D Centre
AB SANDVIK STEEL
S-811 81 Sandviken, Sweden

Abstract

The properties of three highly corrosion resistant duplex stainless steels are discussed, and the particular advantages and applicability of these steels are illustrated by a number of laboratory tests and by case experiences. The duplex grades are compared to carbon steel and austenitic steels in several corrosive environments testing pitting and crevice corrosion, stress corrosion cracking and general corrosion.

Several examples from practical experience of successful installations of duplex steels are given. Life cycle cost calculations illustrate that significant savings can be made when not only the acquisition costs are compared but also the estimated life time, down time costs, material savings etc.

Introduction

Duplex or ferritic-austenitic stainless steels have been in general use for several decades due to their unique mechanical and corrosion properties. However, in many industrial applications where these steels would give definite advantages, carbon steels and austenitic standard and special grades are still being used to a very high extent. The high strength and fatigue resistance of duplex steels together with a low thermal expansion may in many cases allow for considerable design advantages, in that less material is needed and that they can be implemented in existing carbon steel equipment.

With the wide variety of conditions present in industrial environments such as oil and gas, refinery, chemical process, pulp and paper, sea water handling and waste management, the selection of proper materials for every application is of crucial importance for a problem-free operation. In the past, carbon steels and standard austenitic steels (e. g. AISI 304L, AISI 316L) have been widely used in more or less aggressive environments, and in many cases these steels have suffered from corrosive attacks, which in turn have led to serious shutdowns.

In this paper the properties of three highly corrosion resistant **duplex** stainless steels are discussed[1]. In many cases these steels have improved operational conditions as well as the overall cost by replacing low-alloyed steels, that have previously failed in service. The more corrosion resistant alloys presented here are also considered alternatives to highly alloyed austenitic stainless steels, nickel base alloys and titanium.

For early generations of duplex steels several problems have been reported concerning the weldability. Due to very low nitrogen contents high ferrite levels were obtained in the welds which resulted in bad impact strength and impaired corrosion resistance. Unfortunately, this may have given the duplex steels a bad reputation, persisting even today, although since many years nitrogen alloyed base materials as well as overalloyed welding materials are available to the market.

General Description of the Duplex Alloys

SAF 2304 [1] (UNS S32304, referred to here as **23-4-0**) is a new low cost duplex steel intended mainly for construction purposes and other applications where high strength and a general corrosion resistance at least as good as for 316L steels are specified. The pitting resistance in chloride solutions is similar to that of 316L, while the stress corrosion cracking resistance is much higher, allowing this duplex alloy to be used at elevated temperatures and chloride concentrations.

2205 (UNS S31803, referred to here as **22-5-3**) is the traditional duplex steel that during the years has found a large number of applications, especially where a high pitting and stress corrosion cracking resistance is essential. The Sandvik **SAF 2205** [1] is produced with a high nitrogen content, giving the steel an optimal balance between the two phases. This improves the mechanical and corrosion properties significantly.

SAF 2507 [1] (UNS S32750, referred to here as **25-7-4**) is the latest development of the Sandvik duplex grades (super duplex class), designed for very severe conditions, and for chloride containing environments in particular. The high contents of chromium, molybdenum and nitrogen have been balanced to give this steel its extremely high resistance to stress corrosion cracking, pitting and crevice corrosion. Very low corrosion rates are also observed for organic acids, as well as for inorganic acids in some concentration ranges.

Alloy Compositions and Microstructure

The nominal chemical composition of the duplex stainless steels discussed here are presented in Table 1. The microstructure of all these alloys consists of a ferritic matrix (35-55 %) with the austenite embedded in it, see Figure 1. The basic design principle of these duplex steels is a carefully controlled balance of the different alloying elements stabilising the two phases in the quench-annealed as well as in the welded condition. The result of this is a very strong fine-grained structure in which both phases possess a high resistance against corrosion. This is of fundamental importance, especially in chloride containing environments in which pitting is otherwise likely to be initiated in the weaker phase. Further, a well controlled low level of impurity elements provides for a very good resistance against intergranular corrosion.

Mechanical and Physical Properties

Numerous papers have been published on the basic properties of duplex steels[1] and only a few examples of the characteristic properties are discussed here. The fine grained dual-phased structure of the duplex steels results in higher tensile strengths than for austenitic stainless steels, see Figure 2 and Table 2. The range of values presented (400-550 N/mm^2) are typical values, whereas for the wrought material, e. g. seamless tubes with thin wall thicknesses, considerably higher yield strengths are obtained. The higher strength of the duplex materials will in many cases allow for substantial reductions in e. g. wall thickness in tubes, lowering the weight and total cost of the installation. In spite of the high strength, the ductility still remains at a high level, and fabrication procedures such as bending and widening can be performed in the same way as for austenitic steels.

---

[1] Trademark of Sandvik AB

The impact strength of the duplex steels is maintained at low temperatures and the ductile to brittle transition temperatures are below -50°C (-58°F). As duplex steels are often used for construction purposes due to their high strength, the fatigue properties are often considered. The stress fatigue limit at cyclic load is approximately equal to the yield stress, which allow these steels to be utilised in non stationary high stress applications such as hydraulic subsea cables.

The thermal expansion coefficients of the duplex steels are all close to that of carbon steel, see Figure 3. This gives them design advantages over the austenitic steels, especially in cases where the steel is exposed to large variations in temperature during the operation and where parts of the equipment is designed in carbon steel.

Corrosion Properties

Pitting and Crevice Corrosion

Local forms of corrosion are generally of much concern since they are often difficult to detect and may rapidly lead to a complete breakdown of a system. Duplex stainless steels are often recognised for their property of withstanding aggressive chloride containing environments, where the dominating form of attack appears in the form of pitting or crevice corrosion[2]. The main factor behind the high resistance to local attacks in this case is the ability to form a strong protective passive-layer on the surface, or if this layer is damaged to quickly repassivate the surface again.

It is well known that the compositional elements governing the pitting corrosion properties are mainly chromium, molybdenum and nitrogen. An internationally adopted system of ranking steels from the compositions only, with respect to their resistivity to pitting corrosion, is that of calculating a pitting resistance equivalent[3], PRE. The PRE is generally defined by the regression formula

$$PRE = \%\,Cr + 3{,}3 \times \%\,Mo + 16 \times \%\,N \qquad \text{(weight-\%)}$$

The PREs of the duplex steels discussed here are presented in Table 3 together with the values for some austenitic steels. Relatively often a minimum PRE value is specified for a particular application, such as for tough sea water service where a value of 40 or above can be required.

In evaluating the pitting corrosion properties of a duplex steel it is necessary to consider the partitioning of the alloying elements to the ferrite and austenite phases respectively. For the early generations of duplex steels the ferrite phase had the highest corrosion resistance due to the enrichment of chromium and molybdenum to that phase. The modern duplex steels have much higher alloying levels of nitrogen, an element which is enriched almost entirely in the austenitic phase. The PRE formula above was derived originally for austenitic steels[3] and is clearly not valid for duplex steels, should the partitioning of the alloying elements not be balanced to yield equal PREs for the two phases. If this is not the case it is obviously the resistance of the weaker phase that defines the properties. Within the development of the duplex steels at Sandvik, phase diagram calculations[4] have been used in the design. Figure 4 illustrates the case of the super duplex steel **25-7-4** with 25 % Cr and 4 % Mo, where the Ni content is varied to keep the ferrite level constant The PRE of the separate phases is shown as a function of the N-level and the quench-annealing temperature. It is clear that in order to obtain a balance in the PRE for N-levels below approximately 0.25 % unrealistically high quenching temperatures would have to be used and that a lower PRE would be obtained. The chemical

compositions and PRE numbers of the individual phases of the **25-7-4** steel are shown in Table 4, illustrating the balancing of alloying elements in this grade.

A common practice of evaluating the pitting and crevice corrosion properties of the more highly alloyed stainless steels is the 72 h immersion test in $FeCl_3$ according to the ASTM G48A and B standards. The standard specifies only two temperatures (22°C and 50°C), but mostly the test is modified and the temperature is increased in steps of 2,5 or 5°C every 24 h until pitting is observed, starting from an appropriate temperature. The method is used mainly to rank different steel or as an acceptance criteria, and is less useful in predicting the performance in a specific process.

In Figure 5 critical pitting temperatures (CPT) and critical crevice temperatures (CCT) in the $FeCl_3$ test are compared for duplex and austenitic stainless steels. The austenitic 6Mo+N steel has the composition 20 % Cr, 18 % Ni, 6 % Mo and 0,20 % N and the 904L 20 % Cr, 25 % Ni, 4,5 % Mo and 1,5 % Cu. The $FeCl_3$ solution is a very aggressive environment, comparable to chlorinated sea water.

In Figures 6 and 7 electrochemical determinations of CPT are presented for neutral aqueous chloride solutions at potentials of +300 mV SCE and +600 mV SCE respectively. In Figure 8 the acidity is varied for a 3 % NaCl solution at a potential of +600 mV SCE. The comparison for the low alloyed steels in Figure 6 shows that the duplex **23-4-0** has similar or superior pitting resistance as the 304L and 316L steels. Figures 7 and 8 illustrate the very high pitting corrosion resistance of the **22-5-3** and **25-7-4** duplex steels. It should be noted that the fixed potential of +600 mV SCE is a very high potential not often encountered in practice and in most applications corrosion will not occur even at much higher temperatures.

Numerous publications have reported corrosion test results from comparisons of duplex and austenitic stainless steels for a variety of chloride containing media, where pitting and crevice corrosion may occur[2]. It can be concluded from the accumulated data of independent laboratory tests as well as from many years of practical service experience that the duplex steels have pitting and crevice corrosion resistance as good as or better than austenitic standard and special grades.

Stress Corrosion Cracking

Stress corrosion cracking (SCC) is perhaps the most serious form of corrosion encountered in industrial processes. In particular where water is used for the process cooling this is a very common problem for the standard austenitic grades. The risk of SCC can be eliminated with the use of more resistant materials such as high nickel alloys or duplex stainless steels. While the austenitic steels in many cases become resistant at Ni levels above 25 % the duplex alloys will have the same or higher resistance at much lower alloying levels due to the dual-phase structure[2].

A number of methods have been developed to evaluate the SCC resistance of steels and Ni-base alloys under accelerated conditions. Methods like slow strain rate testing (SSRT) and some types of constant load testing in concentrated chloride solutions expose the samples to extremely tough conditions, and does not always give the correct ranking of alloys as compared to field experience. The probable reason for this is that in well designed stainless steel equipment the material will be exposed to conditions similar to constant strain where the material may be able to relax. In this case the passivation process will not be constantly disrupted and the stress remains at sound levels.

In Figure 9 a compilation of test results from autoclave SCC test and practical experience is presented. The samples are loaded to the 0,2 % yield strength level. The pressure is approximately 100 bar and the oxygen content 8 ppm. Fresh NaCl solution is constantly pumped into the chamber and the duration of the test is 1000 h (6 weeks). The curves in the diagram illustrate the limit below which SCC does not occur. Comparing the curve for the lower alloyed austenitic steels (practical experience) it is obvious that the duplex **23-4-0** has far better properties than the 304L and 316L in that it can withstand higher temperatures as well as higher chloride levels. The higher alloyed duplex steels **22-5-3** and **25-7-4** have comparable or higher resistance than the 904L (25 % Ni) and the austenitic UNS N08028 (31 % Ni). The curves for the autoclave tests have been found to correspond rather well to practical experience, although they may be somewhat conservative.

Figure 10 shows the results of SCC tests according to the well-known NACE TM 0177 norm (5 % NaCl, 0,5 % acetic acid saturated with hydrogen sulphide). No cracking was observed for the **25-7-4** duplex steel for up to 90 % of the tensile stress. The test has been repeated at 90°C without any sign of cracking. The **25-7-4** duplex is included in the NACE MR0175 for use at temperatures up to 232°C (450°F) in sour environments (partial pressures of H_2S below 1,5 psi).

General Corrosion

The duplex stainless steels are mainly known for their high resistance against local corrosion but have also found a widespread use in applications where protection against general corrosion is needed (e.g. organic and inorganic acids and caustics)[2].

In Figures 11-16 several examples of iso-corrosion curves (0,1 mm/year) are shown for various acids. All three duplex steels are resistant toward acetic acid (<0,1 mm/year corrosion rate) up to the boiling point, whereas the 304L is resistant only at lower temperatures (Figure 11). In formic acid, the most aggressive (pure) organic acid existing, the curves are more spread out, with the super duplex **25-7-4** resistant almost to the boiling point for all concentrations (Figure 12). Note also that the low-alloyed **23-4-0** performs better than 304L and 316L. Figure 13 describes the results from tests in boiling mixtures of acetic and formic acid, compared with some austenitic grades. Also for hydrochloric and sulphuric acids the duplex steels have good properties, Figures 14-16, although the application range is more limited in these cases.

Mechanically Induced Corrosion

Research by Sandvik as well as independent studies have shown that the duplex steels have very good erosion-corrosion[5] and corrosion-fatigue properties[2, 6]. This will allow these steels to be utilized in transport of sand-containing sea water, in pumps or other mechanical constructions where the material is subject to varying high stresses and a corrosive environment simultaneously.

Weldability

A major concern in the evaluation of the applicability of duplex steels is of course the weldability. The duplex steels discussed here are all welded with duplex filler metals, designed to preserve optimal properties of the welded joints. The chemical composition of the weld materials are carefully developed to produce a high austenite content and a rapid austenite reformation of the weld metal. This will provide for very good toughness and corrosion properties,

not only for the weld itself but for the heat affected zone as well. The welding consumables developed for the duplex steels discussed here are presented in Table 5.

The **22.8.3.L** and **25.10.4.L** are TIG-welding wires and the **25.10.4** and **22.9.3.LR** and **LB** variants are rutile-basic and basic covered electrodes respectively for the **25-7-4** and **22-5-3** steels. The basic electrodes are intended mainly for applications where higher impact properties are required as compared to the rutile-basic electrodes.

The **23-4-0** alloy is normally welded with the **22.8.3.L and 22.9.3.LR, LB** consumables, which will give a very corrosion resistant weld joint. Similarly, for the highest corrosion resistance in very aggressive environments the **22-5-3** alloy can be welded with the super duplex consumables **25.10.4.L, LR, LB**. Detailed recommendations regarding welding parameters, gas shielding, post-weld treatment and so on have been developed. Following given practices, welding of duplex steels can be performed just as easily as for austenitic standard or special grades.

Practical Experience - Examples

Amine Reclaimer. Tube side: steam, shell side: organic salts, oxalic acid, thiosulphates, thiocyanates, 18-22 % MEA, glycerine, sulphur residuals, T=140°C (285°F). Previously carbon steel, Monel 400 and AISI 321 were used but all failed. The change to **23-4-0** duplex in 1987 has been successful and no corrosion is reported.

Fermentation of Hydrocarbons. T=40°C (104°F), T=120°C (248°F) 0,5 h/day, Cl^-=200-500 ppm, pH=3,5-4,5. 316Ti has been tested but failed due to corrosion fatigue. **23-4-0** duplex was installed following excellent test results.

Train Seat Frames, Bottom Cross-Member Seat Support. Rail cars for Hong-Kong, where local conditions are hot, humid and marine. 30 years guarantee. Originally AISI 316 was specified but did not meet strength requirements. **23-4-0** duplex was chosen due to higher strength, good corrosion resistance to a lower overall cost.

Refinery - Distillation. Tube side: water 28-45°C (82-113°F). Shell side: dichlorethane and dichlormethane condensing at 120°C (118°F), inlet 200°C (392°F)-outlet 100°C (212°F). Carbon steel lasted one year and 321 failed due to pitting and SCC after 0,5 year. **22-5-3** duplex in service since 1985.

Chemical Industry - Soda Ash. Tube side: sea water 12-60°C (54-140°F). Shell side: 57 % NH_3, 33 % CO_2, 10 % H_2O, H_2S present but no oxygen. Outlet 66-70°C (150-158°F). Welded and seamless titanium failed and 316 baffle plate eroded very quickly. **22-5-3** in service since 1983 without failure.

Subsea Control Tubing. Instrumentation tubing in **25-7-4** duplex steel for remote hydraulic control and transportation of service fluids to subsea templates in the North Sea Ten parallel tubing lines are entwined with electric control cables The combination of high strength and corrosion resistance gave considerably lower total cost than austenitic 6Mo+N grades Approx. 1 000 000 metres delivered so far.

Chemical Industry 20 % NaOH, 6 % Amine (1/3 EDA 1/3 DETA 1/3 MS), 21 % NaCl, 0.2 % NH_3, 52 % H_2O, T=120-140 C (248-284 F). Previously Inconel 600 and Nickel 200

failed due to general corrosion. **25-7-4** duplex with its high resistance to chlorides and good properties in NaOH at moderate concentrations has solved the corrosion problem.

Refinery - Heat Exchanger. Tube side: Sea water. Shell side: Butane (T_{in}=80°C, T_{out}=30°C (176-86°F)). Titanium failed regularly after three months due to small amounts of fluorides in the butane. Duplex **25-7-4** was installed and the process temperature could be raised from 40 to 80°C. The mantel piece is made in carbon steel and the use of duplex gives no problems with thermal expansion. The life time of the process has increased dramatically and no corrosion problems have been reported after three years.

Several hundreds of documented references are available on the duplex steels discussed here.[7]

Life Cycle Cost Calculations

In evaluating the compatibility of different steels for a given application a number of technical aspects will of course be considered, although in the end, the financial aspects may have a decisive role. Naturally, the more advanced duplex steels are more expensive than carbon steel or the 304L and 316L steels, and to estimate the overall operating cost of an application it is necessary to consider not only the investment cost but the properties/cost ratio, expected service lifetime, maintenance cost, reliability/safety, possible reductions in materials consumption, reduction in use of inhibitors, etc. Realistic life-cycle cost calculations demonstrate the economical advantages that can be found for duplex steels in many industrial applications[8].

LCC - example 1: Refinery tube condenser.
In table 6 the real costs over a five-year period have been calculated for carbon steel (CS), 316L, and three duplex grades for various corrosion conditions (from Ref. 8). Although the initial installation cost is lower for the carbon steel, the total cost after the five-year period is much higher than for the duplex grades, due to the high corrosion rate of the carbon steel.

LCC - example 2: High pressure piping-system on offshore platforms.
In table 7 a total-cost comparison is made for a high pressure system (from Ref. 8). Comparison is made between CuNi90/10, austenitic 6Mo+N, carbon steel + concrete, and super duplex **25-7-4**. The lower cost of the duplex **25-7-4** is due to high strength (reduction of wall thickness), high resistance to erosion corrosion (higher flow rate with reduction of pipe diameter) and very low down time costs.

Conclusion

Duplex stainless steels have found a widespread use in many industrial applications due to their versatility. Modern duplex steels are characterized by very high strength and fatigue resistance, pitting, crevice and stress corrosion properties as good as or better than for austenitic grades. Duplex welding consumables have been developed, to provide very good toughness and corrosion properties, and the welding of duplex steels can be performed just as easily as for austenitic grades. In many cases the properties of the duplex steels will allow for considerable design advantages and cost savings.

This paper is published with the approval of AB Sandvik Steel

References

1. For a general introduction and history of the development, properties, and use of duplex steels see e. g. H. D. Solomon and T. M. Devine Jr: Duplex Stainless Steels, Conference Proceedings, Ed. R. A. Lula, ASM 1983, p. 693-756, and the Duplex Stainless Steels '91, Oct. 1991, Beaune, France, Conference Proceedings, Vol. 1,2, Ed. J. Charles and S. Bernhardsson, (Les Editions de Physique): J. Charles Duplex Stainless Steels - Structure and properties, p 4; J. Charles, Super Duplex Steels: Structure and properties, p 151; S. Bernhardsson: Low Alloyed Duplex Stainless Steels: Alloy design and properties, p 137; L. van Nassau, H. Meelker and J. Hilkes: Welding Duplex and Super-Duplex Stainless Steels, p 303, and J.-O. Nilsson, Super Duplex Stainless Steels, Materials Science and Technology, Vol. 8 (1992) 685.

2. For a review on the corrosion properties of duplex steels see e. g. S. Bernhardsson, The Corrosion Resistance of Duplex Stainless Steels, and Refs therein. Duplex Stainless Steels '91 Conference, p 185.

3. K. Lorenz, G. Medawar, Thyssen Forschung 1 (1969), p. 97.

4. M. Hillert et al Dept of Metallurgy, Royal Inst. of Tech., Stockholm, Sweden. Software for phase diagram calculations.

5. SINTEF Corrosion Centre Report: Erosion-corrosion testing of stainless steels, STF34 F93017, 1993.

6. Internal Report, AB Sandvik Steel, and R. E. Johansson and H. L. Groth, Corrosion fatigue and fatigue data for duplex stainless steels, Duplex Stainless Steels '91 Conference, p. 283.

7. Reference lists for SAF 2304, SAF 2205 and SAF 2507, AB SANDVIK STEEL.

8. R. Kiessling, S. Bernhardsson, LCC Calculations and Design Examples for Duplex Stainless Steels, Duplex Stainless Steels '91 Conference, p. 605, and R&D Centre Report, AB Sandvik Steel, S-33-38-ENG, February 1992.

Table 1.
Nominal chemical compositions of the duplex steels (wt-%)

Steel grade	C max.	Si	Mn	P max.	S max.	Cr	Ni	Mo	N
23-4-0 (S 32304)	0,03	0,5	1,2	0,040	0,04	23	4	-	0,1
22-5-3 (S 31803)	0,03	≤1,0	≤2,0	0,030	0,02	22	5,5	3,1	0,18
25-7-4 (S 32750)	0,03	≤0,8	≤1,2	0,035	0,02	25	7	4	0,3

Table 2.
Mechanical properties of duplex stainless steels. Minimal values for up to 20 mm wall thickness of tubes. Considerably higher values are obtained for thinner wall thicknesses.

Tube and pipe with wall thickness max. 20 mm (0,79 inch)

Steel grade		Yield strength 0,2% offset		1,0% offset		Tensile strength		Elong. A5	Hardness Vickers
		N/mm^2 min.	ksi min.	N/mm^2 min.	ksi min.	N/mm^2	ksi	% min.	approx.
UNS S32304	23-4-0	400	58	450	65	600-820	87-119	25	230
UNS S31803	22-5-3	450	65	500	73	680-880	99-128	25	260
UNS S32750	25-7-4	550	80	640	93	800-1000	116-145	25	290

Table 3.
PRE calculated for different steels.
PRE = % Cr + 3,3 x % Mo + 16 x % N

Alloy	% Cr	% Mo	% N	PRE
25-7-4	25	4	0,3	43
6Mo+N	20	6	0,2	43
Sanicro 28[1]	27	3,5	-	39
25Cr-duplex	25	3	0,2	38
22-5-3	22	3,1	0,2	35
AISI 904L	20	4,5	-	35
23-4-0	23	-	0,1	25
AISI 316L	17	2,2	-	24

Table 4.
Chemical compositions and PRE numbers of individual phases of 25-7-4 quench-annealed at 1075°C.

	Cr	Ni	Mo	N	PRE
Ferrite	26,5	5,8	4,5	0,06	42,5
Austenite	23,5	8,2	3,5	0,48	42,5

(PRE = % Cr + 3,3 x % Mo + 16 x % N)

[1] Trademark of Sandvik.

Table 5.
Nominal Chemical Composition of duplex welding consumables (weight-%)

Sandvik grade	C_{max}	Si	Mn	P_{max}	S_{max}	Cr	Ni	Mo	Others	Application
22.8.3.L	0,020	0,5	1,6	0,020	0,015	22,5	9	3,2	N=0,16	Sandvik 22-5-3, 23-4-0 and similar grades
22.9.3.LR	0,025	1,0	0,8	0,03	0,025	22	9	3,0	N=0,14	- " -
22.9.3.LB	0,04	<0,9	0,8	0,03	0,025	22	9	3,0	N=0,15	- " -
25.10.4.L	0,020	0,3	0,4	0,020	0,020	25	9,5	4,0	N=0,25	Sandvik 25-7-4, 22-5-3 and similar grades
25.10.4.LR	0,03	0,5	0,7	0,030	0,025	25	9,5	4,0	N=0,25	- " -
25.10.4.LB	0,04	0,5	1,0	0,030	0,025	25	9,5	4,0	N=0,25	- " -

Table 6
LCC-calculations for a refinery tube condenser. The carbon steel is subjected to general corrosion.

	CS	316L	23-4-0	22-5-3	25-7-4
Tube cost/set	1	6,5	5,5	7	9,5
Fabrication and installation, cost/set	3	3,5	3,5	3,5	4
Total installed cost	4	10	9	10,5	13,5
Life time room temp.	10 mo	>5 y	>5 y	>5 y	>5 y
in Cl^-, up to 150°C	<10 mo	<1 y	>5 y	>5 y	>5 y
in Cl^-, up to 180°C	<10 mo	<1 y	<1 y	>5 y	>5 y
in Cl^-, up to 300°C	<10 mo	<1 y	<1 y	<1 y	>5 y
No. of changes/5 y, no Cl^-	6	<1	<1	<1	<1
No. of changes/5 y, Cl^- (SCC)	6	5	<1,T<150°C	<1,T<180°C	<1,T<300°C
Costs/5 y, no Cl^-	28	10	9	10,5	13,5
Costs/5 y, Cl^- (SCC)	28	60	9,<150°C	10,5 <180°C	13,5 <300°C

Table 7
LCC-calculations for high-pressure piping systems on offshore platforms.

	CuNi 90/10	Austenitic 6MoN	Carbon steel + concrete	25-7-4
Density, g/cm^3	8,9	8,0	7,9	7,8
Modulus of elast. kN/mm^2	132	200	203	200
0,2 Y.S., 20°C, N/mm^2	90	300	241	550
UTS, 20°C, N/mm^2	290	650	414	800
0,2 Y.S./weight	10,1:1	37,5:1	30,5:1	70,5:1
Erosion resistant	No	Yes	No	Yes
Replacements, 20 year period	1	-	4	-
Installed cost/m, high pressure system	4,0	1,5	1	1,1
Total cost comparison	3	0,75	1	0,50

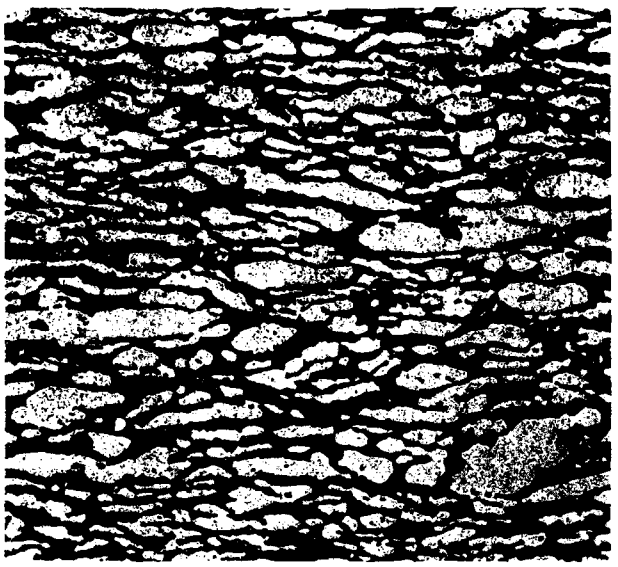

Figure 1. Duplex microstructure of the 22-5-3 alloy. Dark phase - ferrite, light phase - austenite. Magnification 320X.

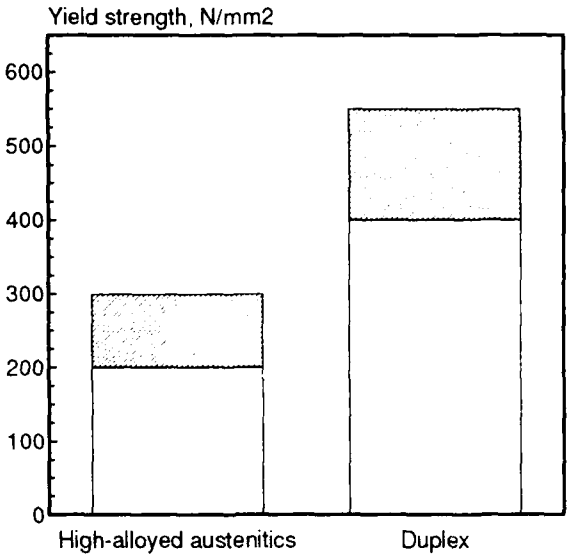

Figure 2. Comparison of minimum yield strength, 0,2 % offset, of duplex and high alloy austenitic grades, for material in the quench-annealed condition.

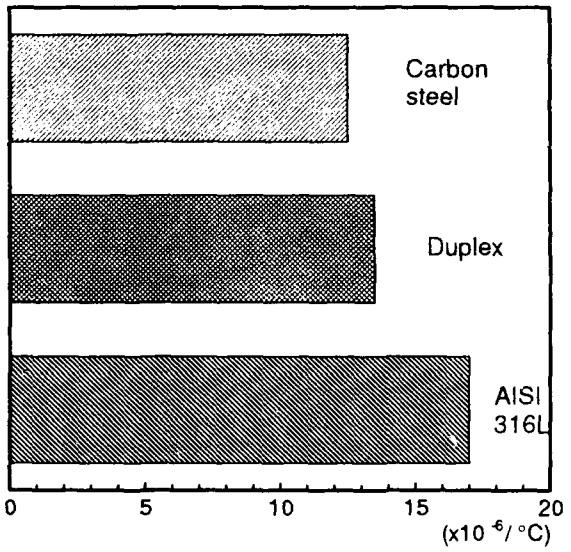

Figure 3. Thermal expansion coefficients of different steels (20-100°C, 68-200°F)

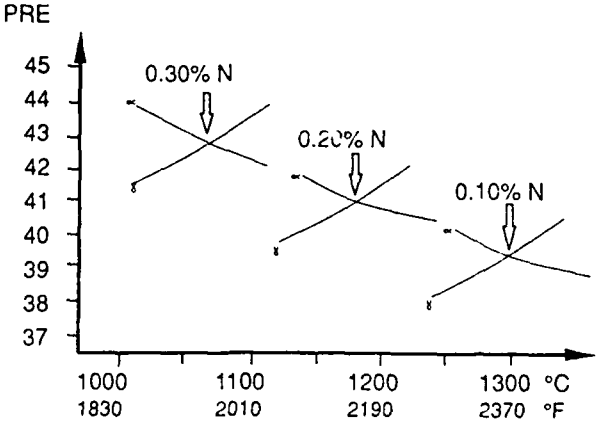

Figure 4. Theoretical phase diagram calculations based on alloys with 25 % Cr and 4 % Mo. Ni was varied to keep a constant ferrite content. PRE=Cr+3,3Mo+16N.

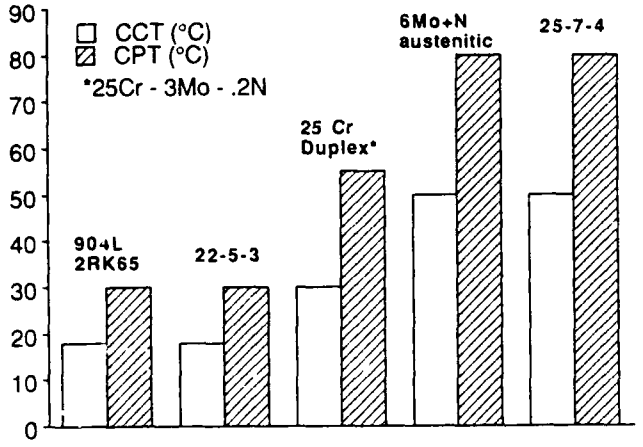

Figure 5. Critical pitting and crevice temperatures in 6 % $FeCl_3$, 24 h (similar to ASTM G48).

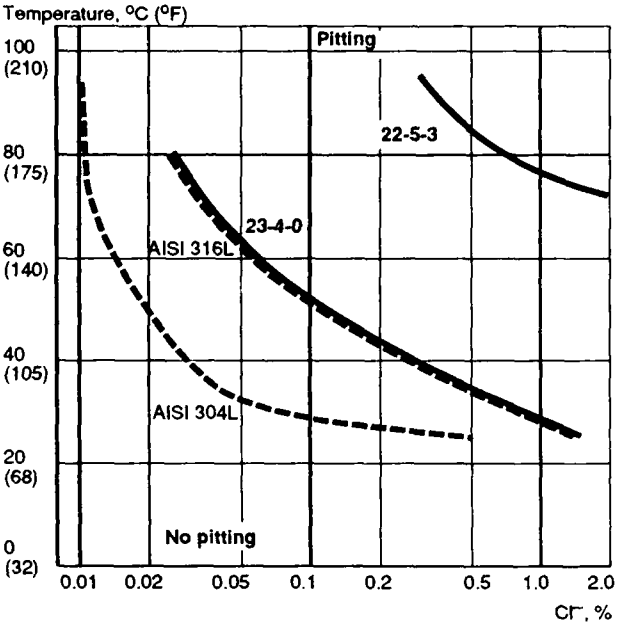

Figure 6. Critical Pitting Temperatures (CPT) in neutral aqueous chloride solutions. Potential = +300 mV SCE.

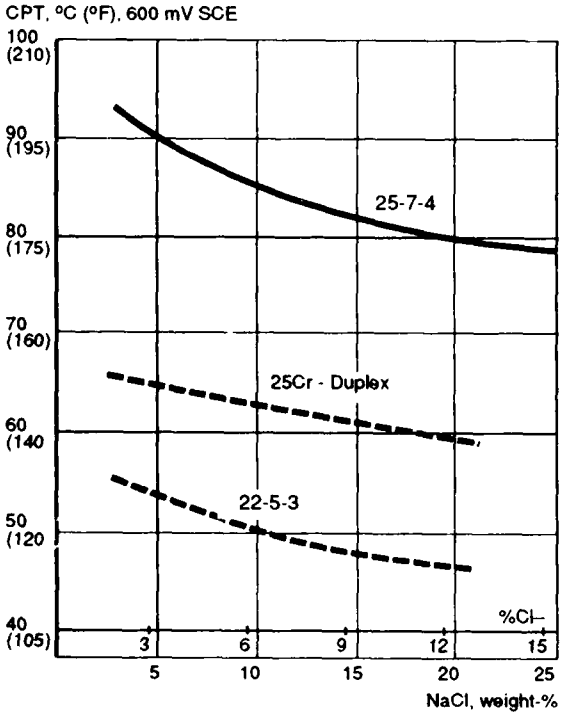

Figure 7. Critical pitting temperatures (CPT) for varying concentrations of sodium chloride, from 3 to 25 % (potentiostatic determination at +600 mV SCE.

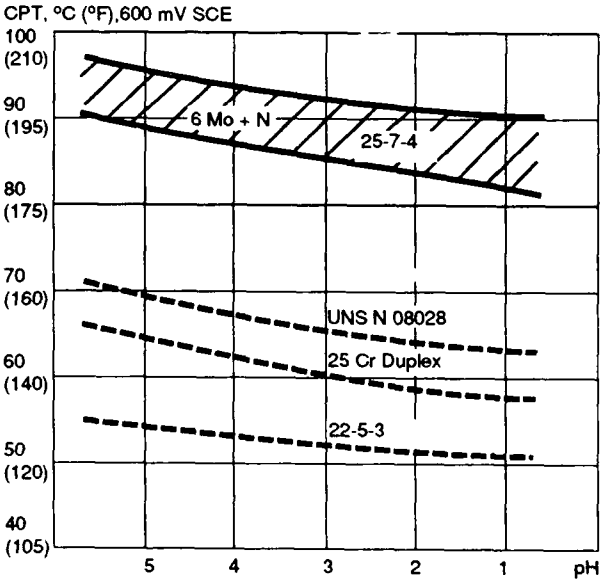

Figure 8. Critical pitting temperatures (CPT) in 3 % NaCl for various pH (potentiostatic determination at +600 mV SCE).

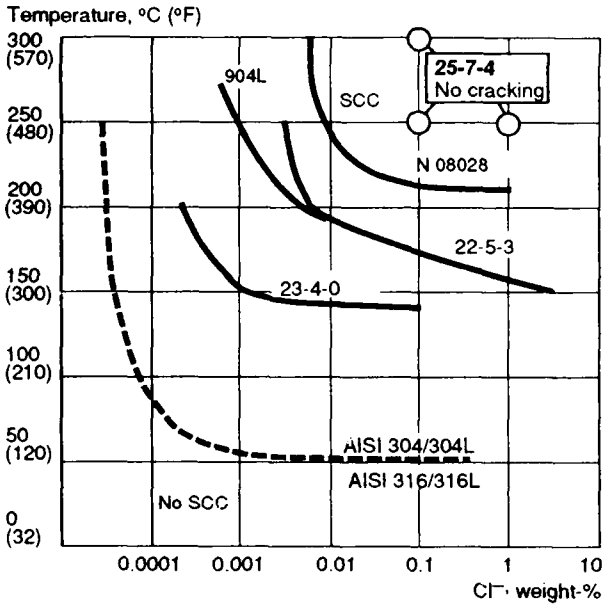

Figure 9. **SCC resistance in oxygen-bearing (abt. 8 ppm) neutral chloride solutions. Testing time 1000 hours. Applied stress equal to yield strength at testing temperature.**

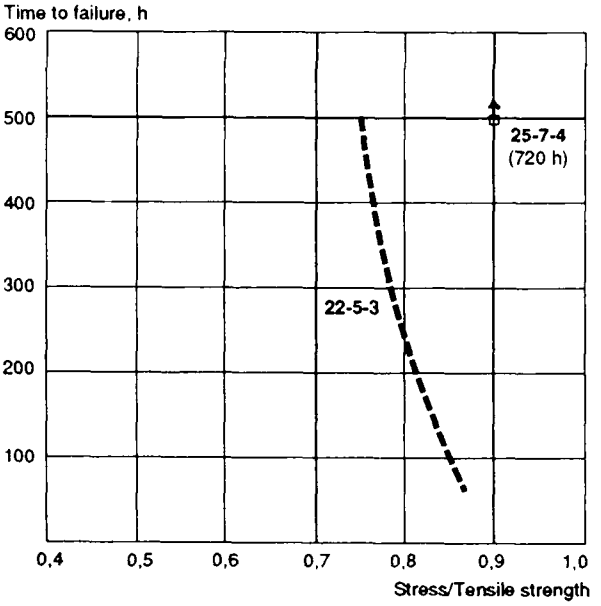

Figure 10. **Constant-load SCC tests in NACE-solution at room temperature (NACE TM 0177).**

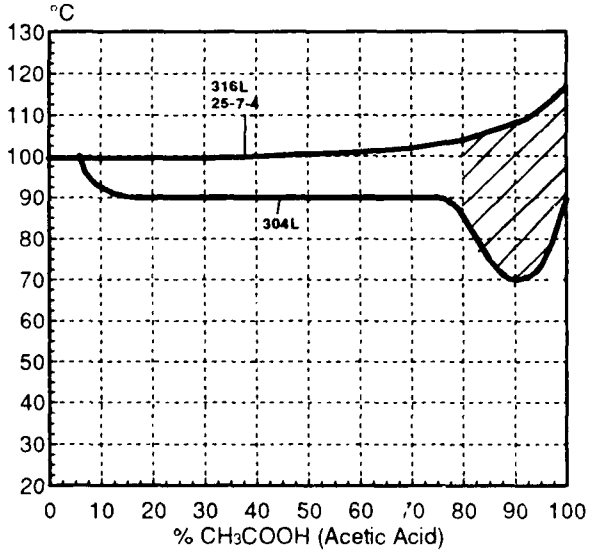

Figure 11.
Isocorrosion diagram, 0,1 mm/year, in acetic acid.
Shaded area represents risk of localized attacks on 304L steel. The curve for the higher alloyed steels coincides with the boiling point curve.

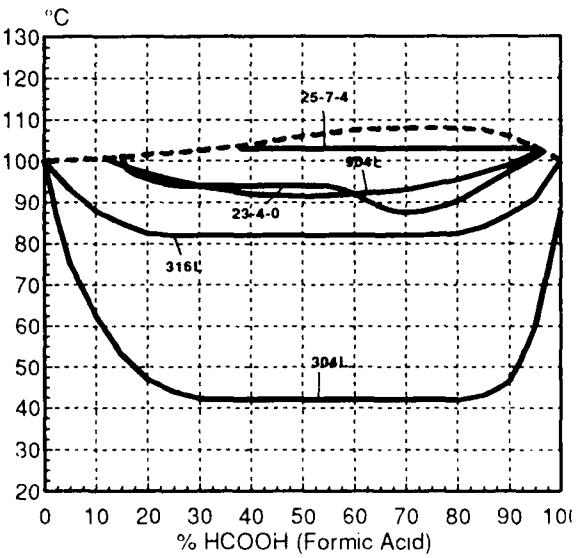

Figure 12.
Isocorrosion diagram, 0,1 mm/year, for stainless steels in formic acid.
Broken line curve represents the boiling point.

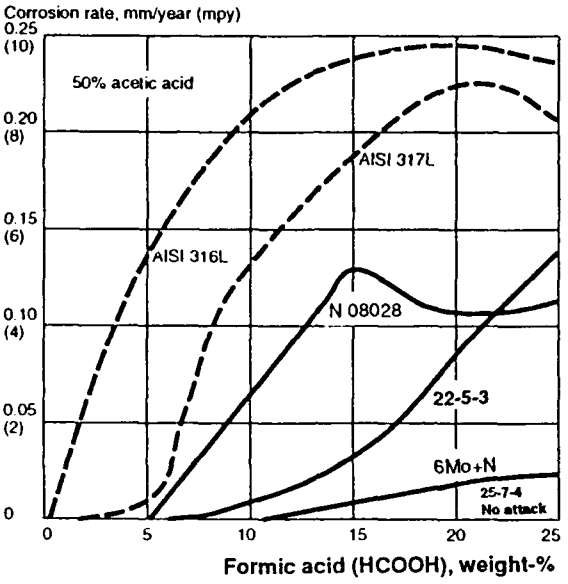

Figure 13.
Corrosion rate of 25-7-4, 22-5-3, UNS S 08028 (27% Cr, 31 Ni, 3,5 Mo, 1% Cu) and 6Mo+N, 316L and 317L in boiling mixtures of acetic and formic acids.

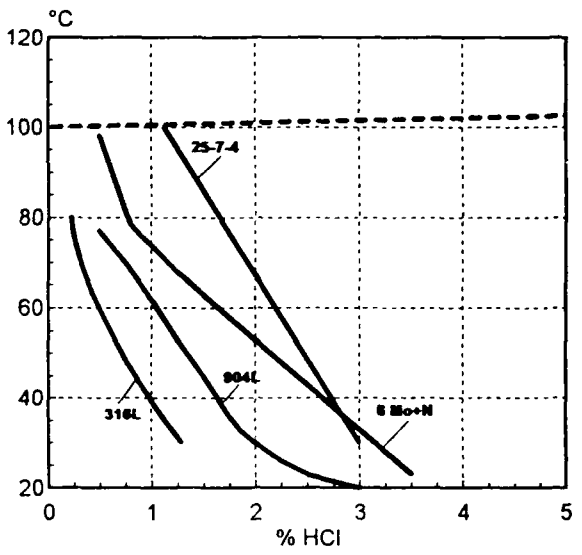

Figure 14.
Isocorrosion diagram, 0,1 mm/year, in hydrochloric acid.
Broken-line curve represents the boiling point.

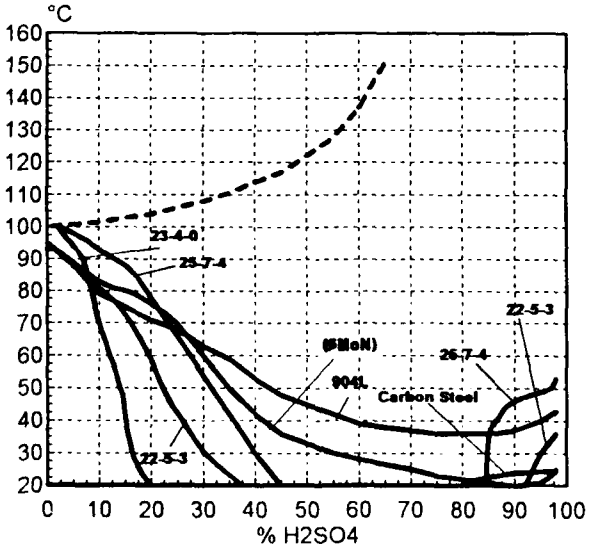

Figure 15.
Isocorrosion diagram, 0,1 mm/year, for some stainless steels and carbon steel in naturally aerated sulphuric acid of chemical purity.
Broken-line curve represents the boiling point

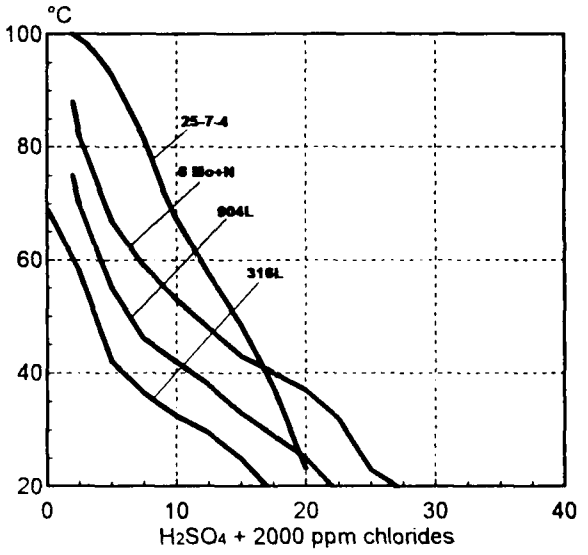

Figure 16.
Isocorrosion diagram, 0,1 mm/year, in sulphuric acid with an addition of 2000 ppm chlorides.

Investigation of Modified Schiff Bases For High Temperature Applications in the Area of Tribology

K. S. Rajan, P. K. Sen and A. Snelson
IIT Research Institute
10 West 35th Street
Chicago, Illinois 60616

V. S. Agarwala and A. A. Conte, Jr.
Naval Air Warfare Center
Aircraft Division Warminster
P. O. Box 5152
Warminster, Pennsylvania 18974-0591

Abstract

With the objective of developing high temperature stable compounds for tribological applications in Naval Aircraft Systems, studies are in progress on the design, synthesis and characterization of chemically modified Schiff bases. A number of fluorine-substituted as well as polyaromatic ring-based Schiff bases have been prepared and characterized by Infrared spectral and differential scanning calorimetric methods. Some among the Schiff base components are (i) fluoroanilines, diaminonaphthalenes, and diaminoanthraquinones and (ii) fluorobenzaldehydes and fluorosalicylaldehyde. Results of wear tests on perfluoro-polyalkylether-based lubricants containing the candidate Schiff bases as additives are presented and discussed in terms of their chemical structure-stability characteristics and wear protection properties at elevated temperatures. [Supported by Naval Air Warfare Center under Contract No. N62269-91-0227].

Introduction

Recent studies[1-4] aimed at investigating macrocyclic compounds for their application to high-temperature lubrication have indicated the promising nature of the Schiff base class of compounds. Lubricant formulations containing Schiff base additives were found to exhibit a rather unique duality of wear-resistance and corrosion protection characteristics. The Schiff bases are prepared by the condensation of an organic amine compound and an aldehyde component. By virtue of their planar structure and metal binding affinities, they tend to attach to the surfaces of metals through chemical bonds and thereby afford corrosion protection and wear resistance. Further, they exhibit satisfactory thermal stability. Results of our earlier studies have indicated that the Schiff base compound derived from salicyl-aldehyde and 4,4'benzidine was found to exhibit several-fold improved wear-protection characteristics when compared to the standard MILSPEC high-temperature lubricant.[5]

It is entirely possible that through the substitution of fluorine into the component units one could obtain modified Schiff bases with improved thermal stability. By the inclusion of such modified Schiff bases, grease formulations with substantially improved lubricant and corrosion protection properties at elevated temperatures could be obtained. Results of studies undertaken along these lines are presented in this paper.

Experimental Methods and Results

A number of fluorine-substituted Schiff base compounds were designed and synthesized. The aldehydic compounds used in the preparation were (1) benzaldehyde (**B**), (2) Salicylaldehyde (**S**) and, (3) fluorobenzaldehyde (**FB**). The primary amines used for derivatizing the Schiff bases consisted of the following: (1) aniline (**AN**), (2,3-fluoroaniline (**3-FA**), (3) 4-fluoroaniline (**4-FA**), (4) ethylenediamine (**ED**), (5) 1,2-phenylenediamine (**1,2-PD**), (6) 1,4-phenylenediamine (**1,4-PD**), (7) 4,4'-benzidine (**BNZ**), (8) 2,6-diaminoanthraquinone (**2,6-DA**), (9) 2,3-diaminonaphthalene (**2,3-DN**), (10) 1,8-diaminonaphthalene (**1,8-DN**), (11) 1,2-diaminocyclohexane (**1,2-DC**), (12) 1,5-dihydroxy-4,8-diaminoanthraquinone (**1,5-DH-4,8-DA**). All the aldehydes and the primary amines listed above were obtained from commercial sources in the United States.

Synthesis of Schiff Bases

All the Schiff bases investigated in this study were prepared by the condensation of each of the aldehyde components with the amine component under anhydrous conditions. The procedure developed by us (which is generally applicable to each one of the Schiff base compounds) is described below.

A three-necked flask of suitable capacity is fitted with a condenser and a pressure-equalizing separatory funnel. The third neck is fitted with a calcium chloride guard tube. A known quantity of the aldehyde component is taken in the flask to which required amounts of dimethylformamide (DMF) is added and stirred. Calculated quantity of the diamine (2 moles of aldehyde per mole of the diamine) is dissolved in DMF separately and is added dropwise to the agitated (using magnetic stirrer) aldehyde in the reaction flask at room temperature. At the end of the addition, the reaction mixture is warmed to 60°C and maintained at this temperature overnight. The reaction mixture is allowed to come to room temperature and the resulting solid (Schiff base) is filtered into a Buchner funnel. The solid product is washed with small amounts of ether and dried under vacuum.

The molecular structures of the different Schiff bases synthesized in this research along with those of their component aldehydes and amines are illustrated in Figure 1.

Thermal Stability

The thermal stability characteristics of a number of Schiff bases prepared in this research were determined by means of the differential scanning calorimetric (DSC) method using Perkin Elmer DSC-1B unit. Experiments were conducted under the following operating conditions: Sample Size = 1 to 2 mg; temperature range = 40 to 320°C;

Sensitivity Range = 16 m. cal/sec; scan speed = 10° min; Recorder Range = 10 mv, full scale; chart speed = 10 mm/sec.

Ten Schiff base compounds were selected for the DSC analyses. Duplicate runs were made of each of the ten materials. Each sample was sealed in a vented pan and placed in the DSC head. Gas (either N_2 or air) was passed through the DSC head at a constant rate of 20 mL/min. The basic thermal stability of each material was determined by testing it under nitrogen. The thermal trace of the sample exposed to air was compared with the corresponding sample run under nitrogen in order to characterize possible oxidative exothermic behavior. Each sample was weighed before and after each DSC run and the weight loss during the analysis was determined. The performance of the instrument was checked daily by running an indium calibration standard. The results of the DSC analysis on the ten samples are summarized in Table 1. An examination of the thermograms indicates that the thermal behavior of all the compounds vary similarly when exposed to atmospheres of nitrogen and air, indicating that in the temperature range studied (i.e., ambient to 320°C) they did not undergo any oxidation. However, the sharp endotherms shown by samples (#21, #22, #23, #24, #25, #28 and #30) at the temperatures indicated in Table 1 probably correspond to the materials melting phase transition. In Figure 2 are presented the DSC-thermograms of samples #21 and #22 to illustrate the sharp endotherms obtained. All of the samples showed some evidence of weight loss during the heating cycle. Samples #25 and #30 showed relatively low melting points, i.e., approximately 78°C and 48°C, respectively, compared to the other samples, i.e., melting points in excess of 200°C. Samples #26 and #27 did not show any well-defined sharp endotherm characteristic of a simple melting point, but did show rather broad endotherms indicative of possible simultaneous melting and sublimation/evaporation. Sample #29 did not exhibit any sharp or broad endotherm and its melting point would appear to be above 320°C.

Preparation of Greases with Schiff Base Additives

A perfluoroalkylpolyether grease conforming to MIL-G-27617D, Type III was used to prepare the Schiff base grease which we have designated as Bensalox-K (5% 4,4' Benz). In particular, a Krytox 240 AC grease, which contains a perfluoroalkylpolyether fluid (Krytox 143) thickened with fluorocarbon telomer solids (Vydax 1000) was used. The Schiff base compound was added to the "as-received" grease and thoroughly mixed by hand for approximately 0.5 hours. It was then passed through a three-roll mill (3 times) and recovered. Other brand name greases meeting the specification could have been used.

Instrument Bearing and Wear Tests

R-4 instrument bearing tests were performed on the perfluoropolyalkylether grease preparations containing the Schiff bases as additives. These tests were conducted in accordance with ASTM Method, D-3337 under the test conditions given below.

Bearing Size: R-4 (6.35 mm bore diam.) stainless steel; Load: 2.2N radial, 22 N axial; Speed: 12,000 rpm; Temperature: 204°C; Grease weight: 75 mg.

Results of the bearing tests carried on grease samples containing each one of five different Schiff base preparations are summarized in Table 2. A consideration of the data indicated the promising nature of all the salicylidene Schiff base-containing grease samples.

Four ball wear tests were carried out on a number of grease preparations containing Schiff bases with and without fluoride substitution into their molecular structures. These tests were performed in accordance with ASTM Method D-2266 under the conditions given below.

Ball composition: A1S1 52100 Steel; Load: 40 Kg; Speed: 1,200 rpm; Temperature: 75°C.

Results of the four ball wear tests are summarized in Table 3 and the data plotted in Figure 3. A consideration of the data presented in Table 3 and Figure 3 indicates that the inclusion of 4-fluorobenzaldehyde-based Schiff bases into the grease preparations has resulted in considerable improvement in their wear characteristics. Significant reductions in the wear scar diameters of the four balls were observed in the cases of the greases which contained the fluorinated Schiff bases as the additives (see Figure 3 and Table 3).

Thin Films of Schiff Bases on Metal Surfaces and Infrared Spectral Characterization

Results of the differential scanning calorimetric analyses of Schiff base compounds have indicated the stability of these compounds up to 300°C. This finding suggests the possible deposition of thin films of the Schiff bases onto metal surfaces. Infrared spectroscopic examination of such films was conducted in order to gain an insight into the mechanistic basis for the high temperature lubricant properties of the Schiff-base-included greases. By using a matrix isolation cryostat (set up at IIT Research Institute), their films of the Schiff base derived from 4,4'-benzidine and 3-fluorosalicylaldehyde were deposited on a cesium iodide (CsI) optical window (as the matrix) and on a steel coupon held at 10K. A KBr pellet of the Schiff base was also made separately. The infrared (IR) spectra of the Schiff base (1) deposited on the CsI matrix and (ii) in KBr pellet were recorded in the transmission mode at 10K on a Perkin Elmer Model 283 Spectrophotometer in the wavelength range 2.5 to 50 μm (Figures 4-6). The steel coupon containing the Schiff base film was brought to ambient temperature and the IR spectra recorded in the reflectance mode using a Perkin Elmer reflectance attachment (Figure 7). A comparison of the IR Spectra of Figure 4 and 5 (taken at a temperature of 10 K) with those of Figure 6 taken at ambient temperature indicates the stability of the Schiff base film. The reflectance IR Spectra of the Schiff base film on steel surface (Figure 7) did not change when subsequently recorded after heating at 110-120°C for 14 days indicating the oxidative stability of the film.

Summary

A number of modified Schiff bases have been designed and prepared in which fluorine has been substituted into the molecular structures of either the aldehydic or the amine component. Results of the differential scanning calorimetric (DSC) analysis have

indicated enhanced thermal stability for the fluorine-substituted Schiff bases. Infrared spectral analyses have indicated the stable film forming characteristics and the enhanced thermal stability of the fluorine-substituted Schiff bases. Further, surface-binding of the Schiff bases through their nitrogen and hydroxyl functionalities appears to be taking place. R-4 instrument bearing tests (at 204°C) on Schiff base-containing greases have shown bearing performance life of 277 to 864 hours. This amounted to an improvement factor of 4.2 to 13.3 over the baseline grease. Further, test data from the four ball wear tests on greases containing fluorine-substituted Schiff bases in accordance with ASTM Method D-2266 have shown that the effect of the fluorinated Schiff bases on reducing wear scar diameters is dramatic. On the basis of the results obtained in this research, it may be stated that in addition to an effective surface coverage by the planar-structured Schiff bases, substitution of fluorine into their molecular structure appears to have helped in enhancing their thermal stability and wear protection characteristics.

References

1. K. S. Rajan, P. K. Sen, E. J. Vesely, Jr., S. K. Verma, V. S. Agarwala and A. A. Conte, CORROSION/90, paper no. 444, pp. 1-13, 1990.

2. K. S. Rajan, "Study of Wear-Preventive Properties of Macrocyclic Compounds for High Temperature Application," Final Report of Contract No. N62269-88-C-0234-P0002, 1992.

3. K. S. Rajan, P. K. Sen, E. J. Vesely, Jr., S. K. Verma, V. S. Agarwala and A. A. Conte, "Lamellar Structure Organics As Wear-Corrosion Inhibitors," presented at the 1989 TMS Fall Meeting, Indianapolis, Indiana, October, 1989.

4. K. S. Rajan, P. K. Sen, V. S. Agarwala, and A. A. Conte, "Schiff Base Lubricants," Corrosion and Wear Technology Review, Naval Air Development Center, Warminster, Pennsylvania, August, 1990.

5. "Synthetic Lubricating Oil Greases," Navy Case No. 72943; Patent Application Filed (1991).

TABLE 1. SUMMARY OF DSC ANALYSIS OF SELECTED SCHIFF BASES

Schiff Base	Material No.	Test No.	DSC N_2	Atm Air	Sample Remaining N_2 (Wt%)	Sample Remaining Air (Wt%)	DSC Peak ENDO[a] (°C)
4,4'-Benzidine with benzaldehyde	21 21	21-02 21-03	X	 X	95.3	 97.3	243 244
4,4'-Benzidine with salicylaldehyde	22 22	22-02 22-03	X	 X	96.6	 100.0	268 267
4,4'-Benzidine with fluorobenzaldehyde	23 23	23-01 23-03	X	 X	96.0	 97.8	255 256
4,4'-Benzidine with fluorosalicylaldehyde	24 24	24-01 24-03	X	 X	96.8	 95.8	278,285 278,285
4-Fluoroaniline with salicylaldehyde	25 25	25-11 25-03	X	 X	0.0	 0.0	78,286 77,271
Aniline with salicylaldehyde	26 26	26-11 26-03	X	 X	0.0	 0.0	274 257
Fluoroaniline with salicylaldehyde	27 27	27-11 27-03	X	 X	1.9	 0.6	269 273
2,3-Diaminonaphthalene with 4-fluorobenzaldehyde	28 28	28-01 28-03	X	 X	77.8	 91.5	201 202
1,2-Diaminonaphthalene with salicylaldehyde	29 29	29-01 29-03	X	 X	79.3	 88.5	- -
4-Fluoroaniline with benzaldehyde	30 30	30-01 30-03	X	 X	0.0	 0.0	48,256 49,253

[a]Temperature at which maximum in endotherm occurred.

TABLE 2. INSTRUMENT BEARING TESTS ON SCHIFF BASE-CONTAINING GREASES

Schiff Base Additive (5% by wt)	Bearing Performance Life, hrs. Test Unit No. 1	2	3	Overall Avg.	Improvement Factor
Baseline	87 71	58 47	85 44		
Avg.	79	52	65	65	–
4,4'Benzidine with Salicylaldehyde	420+ 360	400+ 728	425+ 590	(560)	8.6
Avg.	390+	564+	508+	481+	7.4+
Three Roll Milled (0.75 lb Batch)		894*	834*	864*	13.3*
Cu 4,4'Benzidine with Salicylaldehyde	33	44	47	41	0.6
Ethylenediamine with 4-Fluorobenzaldehyde	85 –	84 79	78 81		
Avg.	85	82	80	81	1.2
4,4'Benzidine with 4-Fluorobenzaldehyde	297 377	122 420	134 104		
Avg.	337	346 296	328 189	277	4.2
2,6 Diamino-anthraquinone with Salicylaldehyde	418 –	359 440+	213 408+	(330)	5.1
Avg.	418	400+	311+	368+	5.6+

+ = Test stopped before failure occurred.
* = Test still in progress.
Base grease = Perfluoropolyalkylether grease.
Temperature = 204°C.

TABLE 3. FOUR-BALL WEAR TESTS ON SCHIFF BASE-CONTAINING GREASES

Aldehyde / Amine	4-Fluorobenzaldehyde	Benzaldehyde	Salicylaldehyde
Aniline (AN)	# 0.53	• 0.69	• 0.91
3-Fluoroaniline (3-FA)			# 0.51
4-Fluoroaniline (4-FA)	# 0.58	# 0.59	
Ethylenediamine (ED)	# 0.54	• 0.67	• 0.77
1,2-Phenylenediamine (1,2-PD)	# 0.60	* 0.64	• 0.66
1,4-Phenylenediamine (1,4-PD)	# 0.56	• 0.84	• 0.79
4,4'Benzidine (BNZ)	# 0.56	• 0.69	• 0.68
2,6-Diaminoanthraquinone (2,6-DA)	• 0.67	* 0.64	• 0.66
2,3-Diaminonaphthalene (2,3-DN)	# 0.58		# 0.55
1,8-Diaminonaphthalene (1,8-DN)		* 0.61	• 0.81
1,2-Diaminocyclohexane (1,2-DC)	# 0.55		• 0.69
1,5-Dihydroxy 4,8-diamino-anthraquinone (1,5-DH-4,8-DA)		• 0.68	

= Significant reduction in wear scar diameter.
* = Moderate reduction in wear scar diameter.
• = No significant reduction in wear scar diameter.
Base line wear scar diameter for mineral oil grease = 0.72.
Schiff base in grease = 5% (by wt).

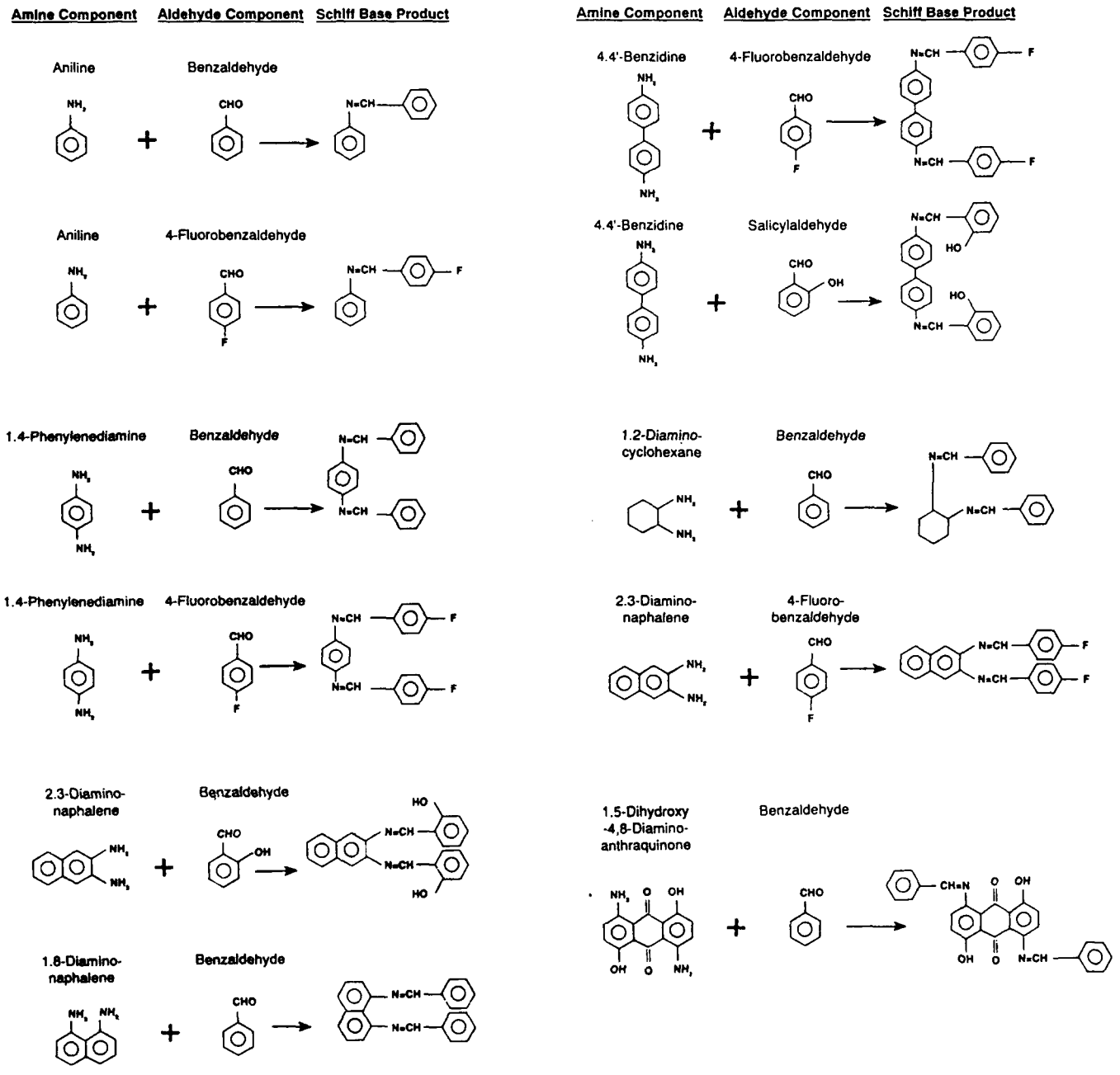

Figure 1. Molecular Structures of Aldehydes, amines and schiff bases

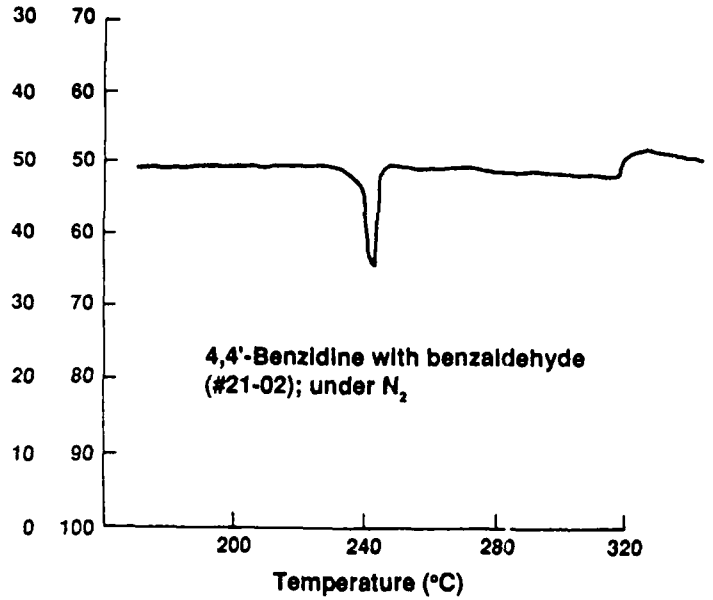

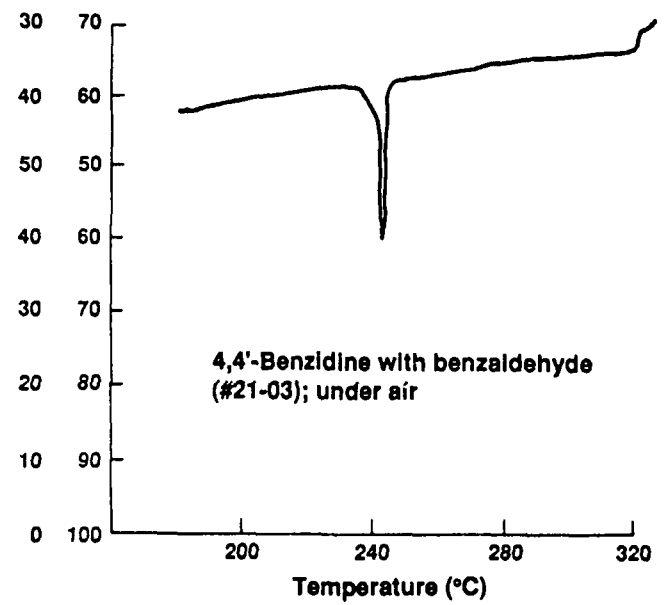

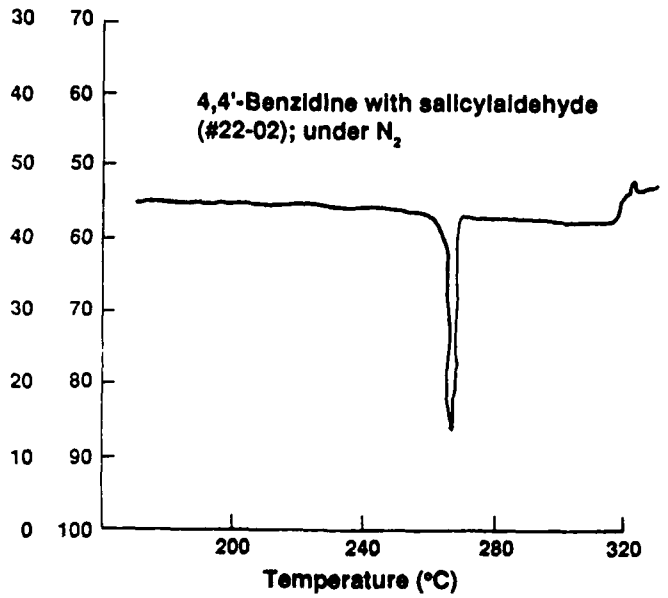

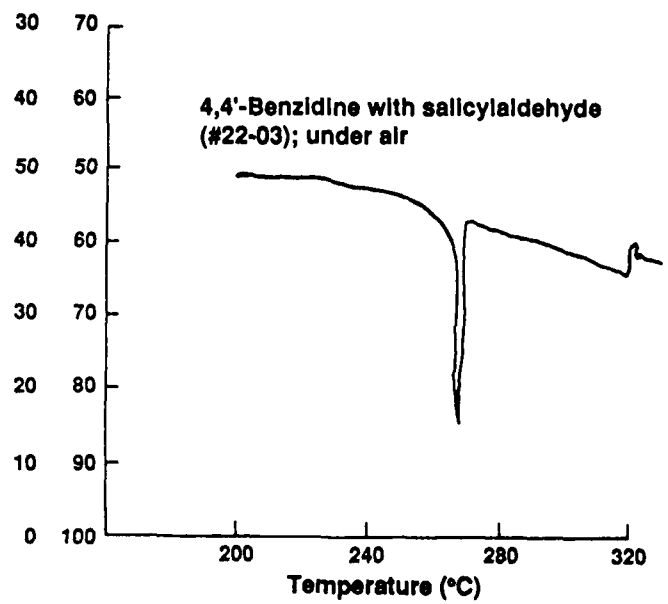

Figure 2. DSC - Thermograms of Schiff bases.

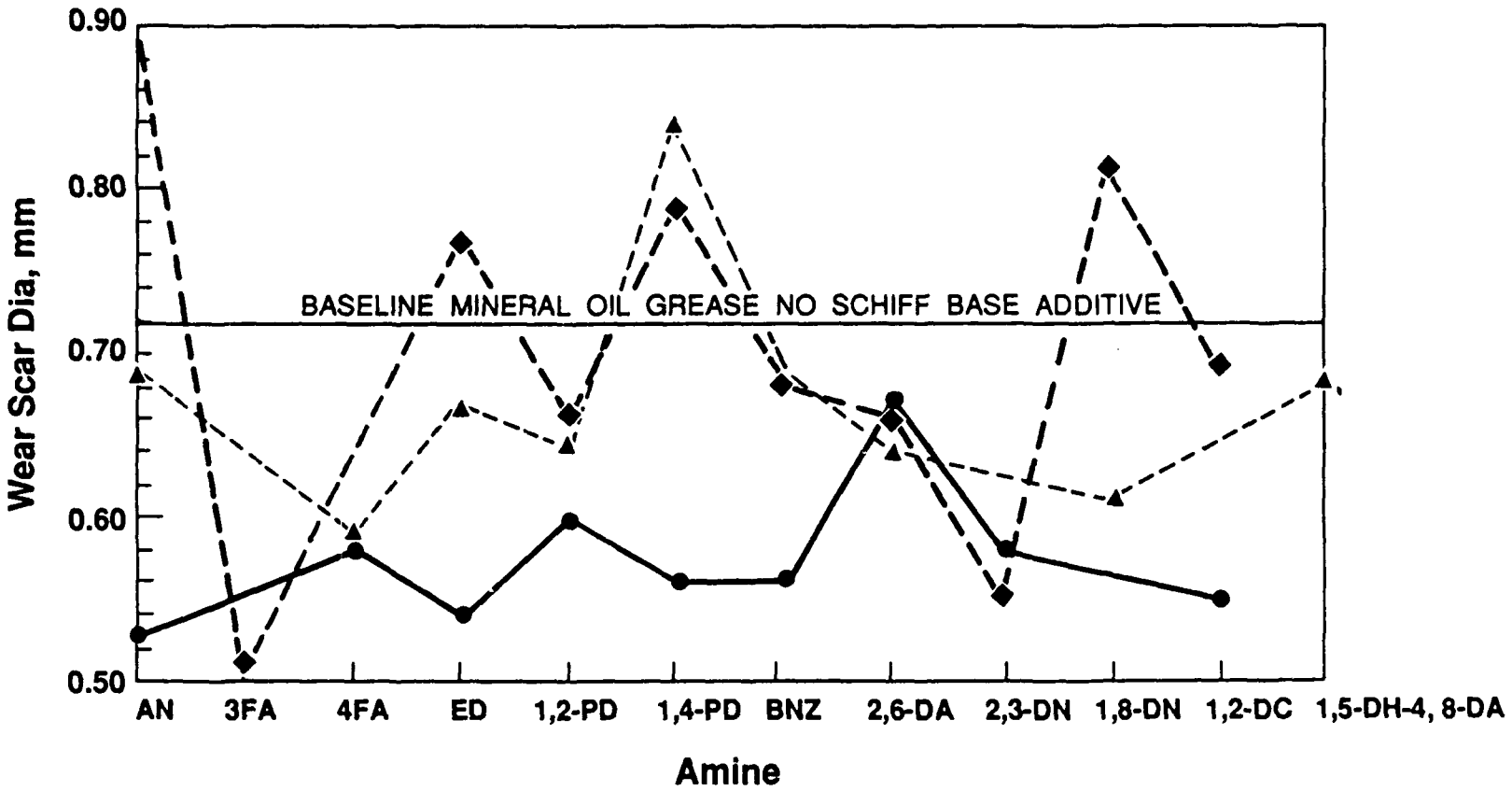

Figure 3. Four-ball wear tests on (5%) Schiff base greases.

Aldehyde —●— 4-Fluoro Benzaldehyde --▲-- Benzaldehyde —◆— Salicylaldehyde

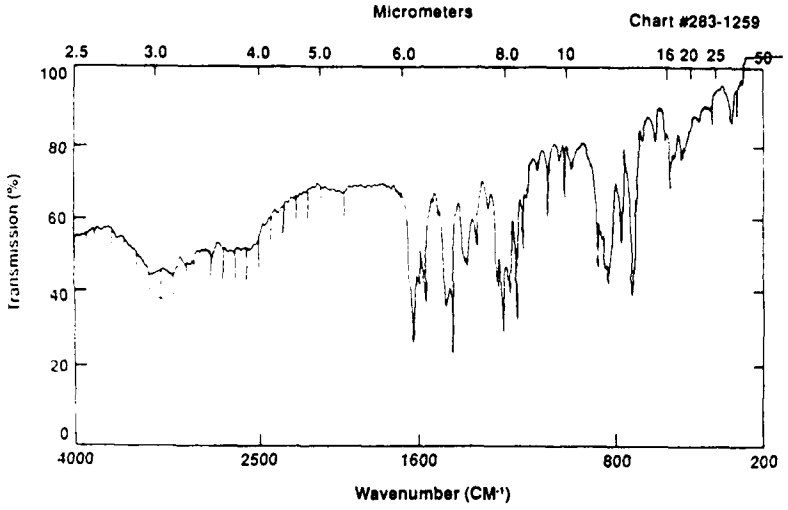

Figure 4. IR spectrum of Schiff base of 4,4'-Benzidine + 3-Fluorosalicylaldehyde. Sample vaporized at 270-275°C for 4 hours, deposited on a Cesium Iodide flat at 10K and spectrum recorded at 10K.

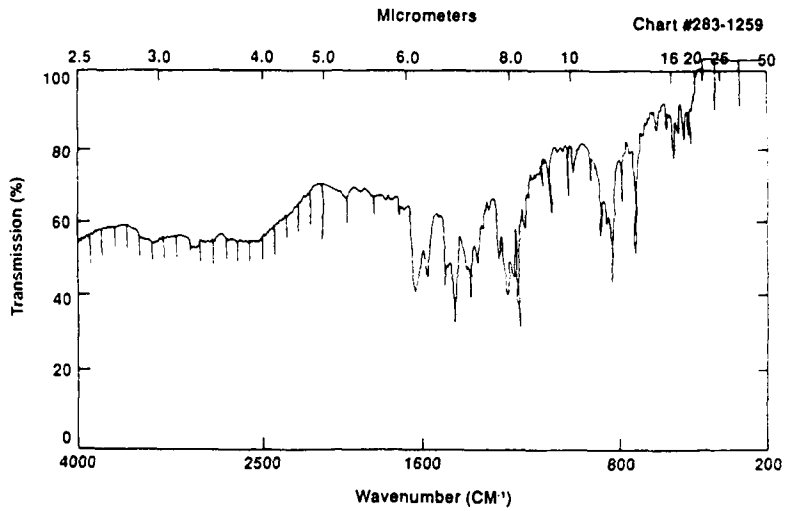

Figure 5. IR spectrum of Schiff base of 4,4'-Benzidine + 3-Fluorosalicylaldehyde. Sample vaporized at 270-275°C for 4 hours, deposited in a Cesium Iodide flat at 10K and spectrum recorded at 298K.

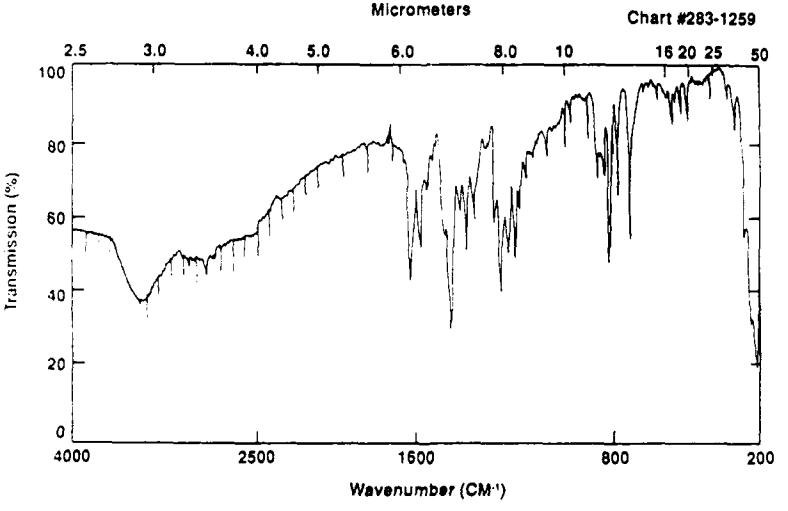

Figure 6. IR spectrum of Schiff base of 4,4'-Benzidine + 3-Fluorosalicylaldehyde contained in a KBr pellet at 298K.

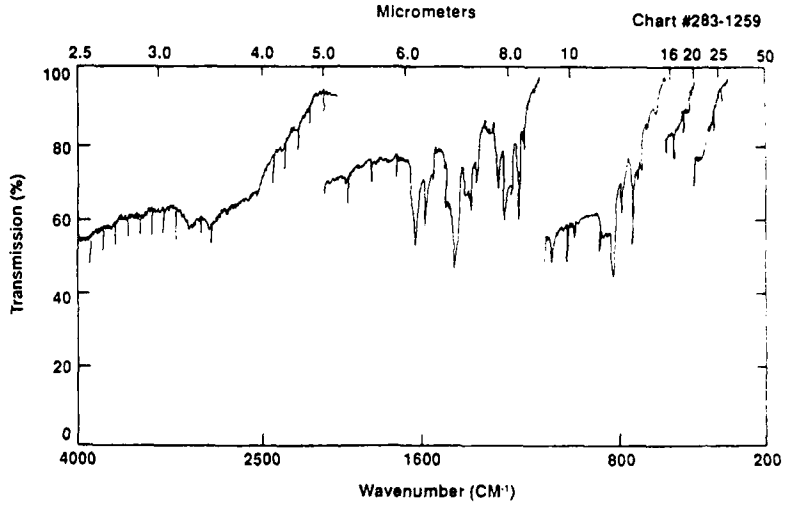

Figure 7. IR spectrum of Schiff base of 4,4'-Benzidine + 3-Fluorosalicylaldehyde. Sample vaporized at 270-275°C for 4 hours, deposited on a steel coupon at 10K and spectrum recorded at 298K.

Corrosion Inhibition of Calcium Chloride Brines

Kaveh Sotoudeh
Nalco Chemical Company
Naperville, Illinois

Paul R. Cote
Eastman Kodak Company
Rochester, NY

Abstract

Today's requirement for low-temperature industrial process cooling utilizes a number of brines. They include aqueous solution of inorganic salts, aqueous solution of organic compounds and, chlorinated or fluorinated hydrocarbons. The most popular of the brines, calcium chloride ($CaCl_2$) is the most economical. Furthermore, it is low on toxicity and easy to handle. The corrosive nature of this brine has traditionally been managed using chromate. The ever increasing environmental constraints on the use of chromate, has encouraged a search for non-chromate alternatives.

This paper details development of a calcium chloride corrosion inhibitor formulation free of chromate and all other heavy metals. It also discusses some intermediate formulations which ultimately led us to the final version. Within the temperature range of -30°F to 180°F, the final product is compatible with 0 to 35 wt% (specific gravity 1.00 to 1.35) brine. Its flexible operating pH (6.5-11), eliminates the need for frequent caustic addition. This inhibitor is designed to protect mild steel, copper and, to eliminate fouling within the above operating parameters.

Key terms: brine, calcium chloride, corrosion inhibition, chromate, phosphate, molybdate, zinc

Introduction

The requirement for low temperature industrial process cooling media has led to development of a number of brines. In refrigeration terminology, a brine is any liquid-cooled refrigerant which is circulated as a heat-transfer fluid. Operating temperature of the cool-side of these brines range from 32° to -90° F[1]. The brines may be:

1. An aqueous solution of inorganic salts, such as sodium chloride and calcium chloride.

2. An aqueous solution of organic compounds, such as alcohols (methanol or ethanol) or glycols (ethylene or propylene).

3. Chlorinated or Fluorinated hydrocarbons which include methylene chloride and trichloroethylene.

The selection of a brine for a given application depends on factors such as:

Corrosiveness: For proper operations, the construction material of the system requires protection against brine.

Cost: Cost of the initial charge and its makeup requirements should be reasonable.

Freeze-Point: The brine must have a freeze-point sufficiently below that of the lowest operating temperature of the system.

Safety: Toxicity and flammability are two important considerations in the brine application.

Thermal Performance: The heat-transfer properties of the brine are crucial to the performance of the evaporators and process heat-exchangers.

The availability, low cost, and low toxicity of calcium chloride has made it the most popular brine. At high concentrations, this water soluble inorganic salt can lower the freeze-point to about -35°F. Use of salt brines for freeze protection (freeze-point depression) was once prevalent. The technique was even used in the cooling systems of diesel and gasoline engines[2]. It was only later when corrosion forced many such systems to switch away to the less corrosive alcohol/water [3], then to glycol/water compositions. Systems that continue to use salt solutions have managed to control corrosion by using the low cost chromates[4].

Traditionally, chromates have been used to curtail the corrosiveness of the salt brines. A potential problem associated with the use of chromate is its tendency to induce pitting when present below the threshold concentration[4,5]. Keeping chromate above the threshold concentration in the brine (800 ppm chromium), has been the way to minimize this shortfall. However, this high concentration has contributed to the current difficulty, namely its toxicity[6,7]. In the past, many chromate users managed the toxicity issue by reducing the hexavalent chromium. Before disposing, the hexavalent chromium containing solution was reduced to Cr^{+3} using ferric chloride. Since efficiency of this technique is less than complete, environmental restrictions have increased disposal costs of the incompletely reduced sludge. This along with the potential for brine leakage into the process or surrounding plant environment, has encouraged users to turn away from chromate as the choice corrosion inhibitor of salt brines.

A search of commercial literature revealed a number of water-treatment companies claiming to possess chromate-free technology for brines. All of which are based on one or two of the following: nitrite, phosphate, molybdate or zinc. A search of the scientific literature revealed much the same as the commercial literature. A few newer inhibitors were identified namely alkanolamine (substituted), benzotriazole, citric acid, maleic acid, polyacrylates, saccharate, silicate, thiocyanate, and triethanolamine.

This paper describes our attempt in developing an effective non-chromate inhibitor program for $CaCl_2$ brines. It also reports on performance of conventional water-treatment programs relative to a brine-specific, novel inhibitor program.

Experimental

Electrochemical approach was the first screening method utilized. This was decided solely based on the fact that such methods are faster and less laborious than the conventional gravimetric methods. Promising candidates identified electrochemically, were then reexamined using gravimetric techniques.

Electrochemical Test

For the most part we relied on the linear polarization technique. The perturbation wave chosen started at -20 mV and ended at +20 mV of the open-circuit potential; scan rate was 0.1 mV/sec. Because the linear polarization technique can be considered nondestructive, the same sample and test solution were used to determine the Tafel slopes. The Tafel test started at -110 mV of the open-circuit potential and ended at +110 mV. The calculated slopes replaced the default values in the linear polarization program, allowing a more accurate reporting of the corrosion rates.

Gravimetric Test

The glassware test was a modified version of the ASTM D-1384 used to evaluate coolant corrosiveness[8]. The metals varied between two mild steel coupons or one mild steel and one copper coupon. Copper coupons were CDA 110. The test solution consisted of a given concentration of calcium chloride to which the experimental additive was added. The brine was maintained at 125°F ± 4°F for two weeks while stirring it at about 1.5 feet/sec.

Mild steel and copper coupons were precleaned by grinding to 600 grit. Post cleaning consisted of scrubbing mild steel coupons with a Nylon abrasive pad until all corrosion products were removed. Copper was cleaned by rinsing under running DI-water. The non-corrosive nature of the post cleaning procedures eliminated the need for correction factors.

Candidate Inhibitor Selection

Utilizing the scientific literature, a number of corrosion inhibitors were identified as potential $CaCl_2$ corrosion inhibitors. A closer examination raised questions on viability of some of the reported inhibitors; the most notable question was on calcium tolerance. To ensure $CaCl_2$ compatibility of the final formulation, we ran the following test on each candidate prior to the corrosion testing. The candidate inhibitor was added to a 25% $CaCl_2$ solution at 80°F and stirring for two hours. In absence of cloudiness, the brine was then heated to 110°F for 30 minutes. Complete solubility and absence of precipitation/cloudiness was the criterion for acceptance of the candidate for further testing.

Calcium Incompatible Candidate Inhibitors

Inorganic Phosphates-have long been recognized as effective ferrous metal corrosion inhibitors[9]. They have been used widely in both closed and open recirculating systems[10]. The mechanism of protection can be anodic[11] or cathodic[12] depending on the phosphate. The cathodic mechanism involves formation of insoluble calcium phosphate at cathodic sites where hydroxyl anion is formed. This affinity for calcium became the major hindrance for its use in calcium brines as, precipitation formed upon addition of ortho and polyphosphates to the brine.

Phosphonates-are commonly referred to as the organic phosphates. Many phosphonates can function as both corrosion inhibitors and sequestrant agents. Many others are also scale inhibitors. The mechanism of corrosion inhibition by phosphonate is cathodic[13,14]; it forms insoluble calcium phosphonate[15]. The sensitivity to calcium led to drop out of some phosphonates in the compatibility test, e.g. 1-phosphono glycolic acid. One such phenomenon has previously been reported[16]. HEDP (hydroxyethylidene-diphosphonic acid) and, PBTC (phosphonobutane tricarboxylic acid) were the only phosphonates compatible with the brine.

Citrate-is a ferrous corrosion inhibitor[29,30] and has widely been used for cleaning boilers and cooling towers[31]. It has also been shown to protect other metals[32]. Citrate was compatible with room temperature brine. However, the brine turned hazy at 110°F and did not clear up when cooled.

Molybdate-is the least toxic of the metal-inhibitors. The most prominent members of this class of inhibitors are chromates[17], dichromate[18,19], arsenites[20,21] and, zinc. In calcium brines however, molybdate formed an insoluble calcium molybdate.

Synthetic Polymers-with acrylic backbone were also investigated for their compatibility with the brine. Irrespective of their molecular weight and their branching, they were not soluble in the brine.

Promising Candidate Inhibitors

Borate-is a buffer[24] suited for closed system applications where pH control is important[25,26]. To a lesser degree it can protect ferrous metals in aerated[27] and deaerated conditions[28].

Mercaptobenzothiazole and tolyltriazole-are both known for their excellent protection of copper and its alloys. Their synergism gives protection to high lead solder[33] and, to a lesser degree, to steel and gray cast iron[34,35].

Nitrite-has been extensively used as a ferrous corrosion inhibitor[36]. It is almost always the first candidate of choice to replace phosphate. Aside from being economical, nitrite is an effective corrosion inhibitor. It can be added to most non-chromate inhibitors including phosphate[37]. It has demonstrated ability to inhibit corrosion of other metals[38].

Tricthanolamine-is a recognized ferrous corrosion inhibitor[39,40]. It is also an aluminum corrosion inhibitor[41] and is compatible with other inhibitors[42,43,44]. Because of its buffering capability it is used with phosphate in many closed system formulations[45].

Zinc-a metal-inhibitor has long been recognized as an effective mild steel corrosion inhibitor. It has been used as sacrificial anode[22], coating on steel[23], or as soluble zinc[15]. The mechanism of protection is by cathodic inhibition. At cathodic sites were oxygen reduction produces hydroxyl ions, zinc reacts with the hydroxyl anion to form insoluble zinc hydroxide which blocks and deactivates the site.

Results And Discussion

Calcium Chloride Corrosiveness

Prior to evaluation of the candidate inhibitors, the corrosive nature of the brine was determined. The data is shown in Table 1-I,II,III. As expected, our test showed inverse relationsnip between brine corrosiveness and its concentration. However, the overall magnitude of mild steel corrosion was smaller than anticipated. We believe the low corrosion rate is due to the limited solubility of oxygen. Oxygen solubility is continuously reduced as brine concentration is increased, lowering the corrosion rate. The authors believe this is the same phenomenon reported first by H.H. Uhlig[46] and later by Trivedi et.al[47]. Even at 70°F calcium chloride brine remained very corrosive and caused significant fouling (Table 1-VII,VIII,IX). Production of insoluble corrosion products are highly undesirable because when settled in low flow areas or attaching to the heat-exchangers, they will lead to underdeposit corrosion. Settled insolubles will also insulate the metallic substrate from coming in contact with corrosion inhibitors. The corrosiveness of the brine toward copper is shown in Table 1-IV,V,VI. However, the dissolution of the copper appears to be independent of brine concentration in the range of 20 to 30%. Presence of soluble copper in brine leads to increased mild steel corrosion and needs to be addressed. The information obtained from testing the uninhibited brine provided the baseline from which we determined effectiveness of the candidate inhibitor programs.

Chromate

Chromate inhibited brines have traditionally been the least corrosive brines. Therefore before seeking a suitable non-chromate formulation, we evaluated performance of a chromate inhibited brine. It was used to benchmark optimum inhibitor performance. The data is shown in Table 2-I,II,III. At 800 ppm chromium greater than 95% of the coupon surfaces were protected. The remaining area was covered with adherent corrosion products. After removal of the corrosion product, mild steel penetration was measured at ~6 mpy by an optical micrometer. Because of the localized nature of corrosion, we abandoned the general corrosion method (weight loss technique) for the more appropriate direct measurement technique (optical micrometer). For more information on corrosion rate measurements consult NACE Standard RP0775-91, item No. 53031. Despite localized penetration, chromate performed well on steel by totally eliminating fouling. This characteristic was highly desirable since, upon accumulation of corrosion products new modes of corrosion would appear (e.g. underdeposit corrosion, erosion corrosion and, cavitation).

Nitrite

After quantifying the chromate performance on steel, the first non-chromate formulation was then tested. Nitrite was added at 4000 ppm to two brine solutions. Unlike the uninhibited brine which resulted in general-type corrosion, the mild steel loss turned intensely localized (Table 2, IV,V). Furthermore, unlike the chromate inhibited brine, fouling was significant.

Since nitrite has been recommended for this application, the poor performance of nitrite was unexpected. To eliminate trace copper as the culprit, another formulation consisting of nitrite and tolyltriazole was tested. Dissolved copper is a trace element common to commercial grade calcium chloride brines and, tolyltriazole is capable of curbing its adverse effect on

ferrous metals. Intensification of mild steel corrosion persisted in presence of TT (Table 2-VI). Variations in type and concentration of the copper inhibitor did not alter nitrite's undesirable performance. In a final attempt to make nitrite work, we increased its concentration by 25% and added nitrate to the formulation. Protection of mild steel by nitrate in ferric chloride brines is an arcane prior art[48]. This final attempt was also unsuccessful (Table 2-VII). From the above results we unequivocally concluded that nitrite is to be avoided as calcium chloride brine inhibitor. Mercer[49] has eluded to this phenomenon in passing, however, until now no experimental evidence has been offered in its support.

Phosphonate Treatments

Incompatibility of inorganic phosphates and the ineffectiveness of nitrite to inhibit calcium chloride corrosion led us to evaluate organic phosphates. The only two which passed the compatibility test were HEDP and, PBTC. By themselves they showed no corrosion inhibition (Table 3-I,II). Failure of the organic phosphates to protect steel by themselves did not come as a surprise. In practice phosphonates are always used in combination with other inhibitors. Such combinations include inorganic phosphate[12], molybdate[13] or zinc[14]. In an attempt to enhance the effectiveness of HEDP and PBTC, we formulated them with each of the following: molybdate, orthophosphate, polyphosphate and zinc. Although all but zinc had failed the brine compatibility test, we hoped the calcium sequestering capability of phosphonates would increase their calcium tolerance thus, preventing precipitation. The ortho and pyrophosphate formulations once again dropped out of solution. The molybdate formulation also resulted in a precipitate but, it redissolved after 15 minutes of continuous stirring. This precipitation did not redissolve when brine concentration was >28%. In light of this handicap, we still tested the HEDP/molybdate formulation in 25% brine. Not only was the corrosion inhibition of steel nonexistent (Table 3-III), but a voluminous solid deposit had also accumulated by the end of the test. This testified to inadequacy of molybdate-based formulation as $CaCl_2$ brine inhibitor.

The final test of phosphonates were done with zinc. They were fully compatible with $CaCl_2$ brines so long as the pH was maintained below 8. Zinc/phosphonate formulations began to turn hazy at pH=8.0. Indeed, we detected a buffer region which started at pH=8 where haziness first appeared, to 8.4 where haziness reached maximum. We postulate that the buffering capacity was due to Zn^{+2} transformation to zinc hydroxide. Because of the pH handicap we evaluated the zinc/phosphonate formulations at 8. Corrosion inhibition was nonexistence (Table 3-VI,VII) and fouling increased due to zinc hydroxide formation.

A Novel Calcium Chloride Brine Inhibitor

To develop a viable calcium chloride inhibitor treatment we screened a host of potential inhibitors. Several multicomponent corrosion inhibitor treatments were identified. Amongst them only one could be prepared in a concentrated form. Stability of the concentrate exceeded three-month storage at 0°, 20°, 40° and 120°F, eliminating shelf-life concerns. To ensure that the concentrate preparation did not adversely effect performance, the treatment was tested gravimetrically using the concentrate (Table 4-I). Having confirmed excellent metallic protection without fouling, the next step became stress testing of the formulation. The following tests were designed to simulate scenarios common to actual field operations.

Dependence of Performance on pH

The previous test showed satisfactory performance within a narrow pH range (9.0 to 9.5). To determine effect of pH, intermittent pH adjustments during the test were halted allowing a gradual drop in pH. The natural drop in pH was induced by continuous forced aeration. Even when pH dropped down to 6.4, copper and steel protection were undisturbed (Table 4-II,III). In another test we simulated a pre-acidified brine. Although pH of most commercially available brines are basic, there are some exceptions. To simulate two such cases, pH was adjusted to a lower value with concentrated HCl. No adverse effect was observed (Table 4-IV,V). Yet to simulate an acid process leak, pH of two inhibited brines were adjusted to 2. The first brine housed two mild steel samples. After 12 hours, pH of both brines were adjusted using 50% caustic. At this time two mild steel coupons were immersed in the second brine. Once again performance remained unaffected (Table 3-VI,VII). The above demonstrated the formulation's ability to give protection in acidified brine and, to completely recover from a pH shock.

Exposure to Chlorine

To investigate the susceptibility of the inhibitor ingredients to formation of chlorohydrocarbons, a literature search was conducted. Not finding any corroborating evidence, a chlorine leak was simulated by adding 5 wt% household bleach to an inhibited brine. The brine was heated to 140°F for 2 hours and then cooled. No FT-IR detectable chlorohydrocarbon species were identified.

Oxygen Dependence

Performance dependence of some corrosion inhibitors on availability of oxygen has been documented[50,51]. Since all the results reported here have been in aerated conditions, an electrochemical attempt was made to ensure proper performance in absence of oxygen. Utilizing linear polarization, mild steel corrosion in argon saturated brine was measured at 1.4 mpy. A potentiodynamic scan of the same electrode exposed a passive region. This passive region was the only one observed amongst the inhibited and uninhibited brines (Figure 1).

Reducing Nitrite Aggression

Two gravimetric tests evaluated performance of the final formulation in nitrite contaminated brines. In the first test nitrite was added to an inhibited brine and in the second test, a field sample actually containing nitrite was used. As can be seen in Table 5, at recommended concentration, the adverse effect of nitrite on mild steel was significantly reduced. To gain insight in the above phenomenon, two anodic cyclic polarization scans were run, the results of which are presented in Figure 2. Addition of nitrite caused 190 mV noble shift in corrosion potential. This coupled with the gravimetric results indicated that nitrite shifted the rest-potential of mild steel to above the critical pitting potential. The scan also revealed pit-repassivation tendency on the part of the formulation. The pits formed on the anodic scan repassivated as the scan changed direction by, descending line crossing over the ascending line. This tendency is absent when nitrite is added.

"Long-Term" Corrosion Rate and Chromate compatibility

The gravimetric data reported above were the result of 2-week tests. Such a relatively short experimental time would require a fast acting inhibitor treatment. However, a 2-week test is not necessarily indicative of a durable protection[52]. To ensure lasting protection, the formulation was tested at 130 F for 2 months. Result showed even a smaller loss as the inhibitor established itself more firmly on the surface (Table 6-I,II). Finally, to ensure that the formulation was fully chromate compatible, it was tested with four chromate inhibited brines. Such a compatibility would allow chromate treated units to gradually deplete the chrome in the system without resorting to direct disposal of the laced brine. Test results were favorable (Table 6-III,IV,V,VI). Indeed, there existed a synergistic interaction between chromate and the formulation. The few localized sites on the coupons were measured significantly shallower than those exposed to chromate inhibited brine.

CONCLUSION

An effective non-chromate brine corrosion inhibitor has been formulated. This multicomponent corrosion inhibitor formulation is capable of protecting carbon steel and copper in calcium chloride brines with wide concentration and pH range. It is immune to extreme pH, chlorine exposure and, is fully compatible with chromate.

ACKNOWLEDGEMENT

The authors wish to thank Cooling the Water Department for supporting this effort and Nalco Chemical Company and Eastman Kodak Company for allowing the work to be published. The individuals who made particularly valuable contributions were Fred L. Harlan, Daniel A. Meier, Emelito P. Rivera and Michael G. Trulear.

GLOSSARY

ASTM	American Society for Testing and Materials
MBT	Sodium Mercaptobenzothiazole
HEDP	Hydroxyethylidene-Diphosphonic Acid
PBTC	Phosphonobutane Tricarboxylic Acid
Na-TT	Tolyltriazole (sodium salt)
TT	Tolyltriazole
mV	Millivolt
Sec	Second

REFERENCES

1. Perry Handbook of Chemical Engineering, Chapter 12, Page 45, 1988.

2. Harpers Weekly, "Comparative Value of Non-Freezing Solutions," Harper & Brothers, New York, N.Y., 1909.

3. L.C. Rowe, "Automotive Engine Coolants: A Review of Their Requirements and Methods of Evaluation," Engine Coolant Testing: State of The Art, STP705, 1980.

6. A. Von Koeppen; G.A. Emerle; K. Nishio; B.A. Metz, "Pollution Control Technology Applied to Cooling Water Treatment", Material Performance, 12(7), 1973: p.23-8.

7. D.R. Robitaille, "Sodium Molybdate As a Corrosion Inhibitor in Cooling Tower", Material Performance, 15(11), 1976: p. 40-4.

4. J.I. Bregman, "Corrosion Inhibitors", Chapter 4, MaCmillan company, New York, Collier-MaCmillan Limited, London 1963.

5. K.M. El-Sobki; A.A. Ismail; S. Ashour; A.A. Khedr; L.A. Shalaby, "Corrosion Behavior of Aluminum in Neutral and Alkaline Chloride Solution Containing Some Anions", Corrosion Prevention and Control, 28(6), 32A, 1981: p. 7-12.

8. Annual Book of ASTM Standards, "Corrosion Test for Engine Coolants in Glassware (ASTM D-1384)", American Society for Testing and Materials, Philadelphia, Pennsylvania, Volume 15.05, 1987: p. 42.

9. Mars G. Fontana, "Corrosion Engineering", Chemical Publishing Company, New York 1986.

10. L.C. Rowe, R.L. Chance and M.S. Walker, "Antifreeze Coolant for Aluminum and Cast Iron Engines", Material Performance, 1983: p. 17.

11. J.G.N. Thomas, "The Adsorption of Anions on Iron During Anodic Passivation in Neutral Solution", British Corrosion J., 1966: p. 156.

12. B.E. Moriarty, "Surface Studies of Corrosion Inhibitors in Cooling Water Systems", Material Performance, Jan 1990: p. 68.

13. A. Ashcraft, G. Bohnsack, "The Mechanism of Corrosion Inhibition and Transition to Underdeposit Corrosion", Material Performance, February 1988: p. 31.

14. G. Bohnsack, K.H. Lee, D.A. Johnson, E. Buss. "Investigations of the Mechanisms of Organic Compounds Used in Cooling Water Corrosion Control", Corrosion 85 paper number 379.

15. R.H. Ashcraft, Gerhard Bohnsack, "The Influence of Typical Cooling Water Parameters on the Corrosion Inhibiting Effect of 2-phosphonobutane-1,2,4-tricarboxylic Acid (PBTC)", Corrosion 86 Paper 401.

16. P. Thevissen, W. Cleuren, A. De Crom, I. Colman and S. Kerremans; "Development of An All Organic Program for Open Evaporative Cooling Water Systems Based on a New Copolymer", Proceedings of the 7th European Symposium on Corrosion Inhibitors, 1990: P. 485.

17. General Motors Corporation, "Coolant For Detroit Diesel Engines", 7SE-298, August 1984.

18. J.I. Bregman, "Corrosion Inhibitors", Chapter 4 "Cooling Water, Other Systems", The MaCmillan Company, New York, Collier-Macmillan Limited, London 1963.

19. R.D. Hudgens and R.D. Hercamp, "Test Methods For The Development of Supplemental Additives For Heavy-Duty Diesel Engine Coolants", Engine Coolant Testing: Second Symposium, ASTM STP-887, Roy E. Beal, Ed., American Society For Testing and Materials, Philadelphia, 1986: p. 189.

20. U.S. Patent 3,228,884, L.G. Daignault, F.W. Moore, M. E. Antalek (Assigned to Texaco Inc.), "Method For Producing A Corrosion Inhibited Antifreeze Composition", January 11, 1966.

21. M.S. Walker, "The Effect of Inhibitors in Antifreeze on Corrosion of Heat Rejecting Surface" Material Performance, July 1973: p. 29.

22. R. Juchniewicz, J. Jankowski, J, Szukalski; "Electrochemical Protection of Domestic Hot and Cold Water System"; Material Performance, January 1991: p. 22.

23. F. Santagata; "New Horizons for The Use of Zinc in The Protection of Steel, Cold-Laminar Galvanizing: A New Anti-Corrosion Technology"; Corrosion Prevention and Control, June 1988: p. 58.

24. D. Bijimi, D.R. Gabe, "Passivation Studies Using Group Via Anions I. Anodic Treatment of Tin", British Corrosion J., No. 3, 1983: p. 88.

25. U.S. Patent 4684475, A. Matulewicz, N. William (assigned to First Brands Corp.), "Organophosphate and Silicate Containing Antifreeze." August 4, 1987.

26. V. Jovancicevic, J. OM. Bockris, J.L. Carbajal, P. Zelenay, "Adsorption and Absorption of Chloride Ions on Passive Iron Systems", Journal of Electrochemical Society, Vol 133, No. 11, 1986: p. 2219.

27. M.S. Walker, "The Effect of Inhibitors in Antifreeze on Corrosion of Heat Rejecting Surface", Material Performance, July 1973: p. 29.

28. C. Xuzun, C. Zhenjia and Ma. Renchuan, "Inhibition mechanism of borate as a corrosion inhibitor of carbon steel", Proceedings of the 7th European Symposium on corrosion inhibitors, 1990: p. 561.

29. A.A. Aksut and Uneri Saadet, Chim. Acta Turc., 12(2), 279-97, 1984: p. 279-297.

30. J.P.G. Farr; M. Saremi, Surface Technology, 17(1), 1982: p. 19-27.

31. J.W. McCoy, "The Chemical Treatment of Cooling Water", Chemical Publishing Company, New York (1974).

32. B.W. Samuels, K. Sotoudeh and R.T. Foley, Corrosion, 1981: p. 358.

33. L.C. Rowe, R.L. Chance and M.S. Walker, Material Performance, Vol. 22, No. 6, June 1983: p. 17.

34. M.S. Vukasovich, F.J. Sullivan, Material Performance, 22(8), 1983: p. 25-33.

35. M. Iovchev, British Corrosion Journal, Vol. 18, No. 3, 1983; p. 148.

36. D.M. Brasher and D. Reichenberg, "Comparative Study of Factors Influencing the Action of Corrosion Inhibitors for Mild Steel in Neutral Solution IV. Mechanism of Action of Mixed Inhibitive and Aggressive Anions", British Corrosion Journal, 1968: p. 144.

37. Japanese Patent Kokai Tokyo Koho JP 61/21176 A2 [86/21176]. Nakaya, Fumio; Wakita, Shinichi; Murakami, Hisatoshi (assigned to Tatsuta Electric Wire and Cable Co.), "Antifreeze Compositions." January 29, 1986.

38. M.Y. Mourad, S.M. Abd El-Wahaab, S.A. Soliman, A.S. El-Gaber, "Inhibitory Effect of Sodium Nitrite on Corrosion of Lead in O.1 M Sodium Hydroxide Solution", Indian J. Technology, 26(10), 511-13, 1988: p. 511- 13.

39. A.I. Khentov; T.M. Kal'varskaya; N.I. Trofimov; A.F. Kazankina; N.G. Semenova; E.P. Popovskaya, "Inhibiting Effect of Promhydrol Hydraulic Fluid Additives", Zh. Prikl. Khim. (Leningrad), 58(8), 1908-11, 1985: p. 1908-11.

40. Japanese Patent Kokai Tokyo Koho JP 59/208082 A2 [84/208082]. Tatsuta Electric Wire and Cable Co., Ltd., "Corrosion Inhibitors for Water Cooling Systems." November 26, 1984.

41. Japanese Patent Kokai Tokyo Koho JP 59/100271 A2 [84/100271]. Mitsubishi Aluminum Co., Ltd., "Aluminum and Aluminum Alloy Surface Treatment." June 9, 1984.

42. Czechoslovakian Patent CS 227447 B. Nemcova, Jitka, Bartonicek, Robert, Vosta, Jan, Sverepa, Otakar, Panacek, Frantisek, Svoboda, Miroslav, Jizba, Josef, Kulhavy, Teofil, "Agent With Dispersion-Sequestrative and Corrosion-Inhibitive Effects." June 1, 1984.

43. U.S. Patent 4452758. A.C. Wilson; S.T. Hirozawa; S.E. Eisenstein; Maxwell, Jerrold F. (assigned to BASF Wyandotte Corp.), "Compositions and Process for Inhibiting Corrosion of Aluminum." June 5, 1984.

44. P. N. S. Yadav; R.S. Chaudhary; C.V. Agarwal, "Aliphatic Amines as Corrosion Inhibitors for Aluminum Alloys in Acidic Chloride Solution Containing Tungstate Ions", Corrosion Prevention and Control, 30(5), 1983: p. 9-13.

45. R.G. Bates, Determination of pH Theory and Practice. New York: John Wiley and Sons, 1964.

46. H.H. Uhlig, "Corrosion Handbook", John Wiley and Sons. New York (1948).

47. Kavita Trivedi, S.K. Srivastava and N.P. Shukla, "Corrosion in Saline and Sea Water," Corrosion Prevention and Control, 99, August 1992: p. 99.

48. F. Beniere and D. Laouali; "Inhibition of Corrosion of The Aluminum Heat Exchangers and Radiator In Central Heating"; Proceedings of the 7th European Symposium on corrosion inhibitors, 1990: p. 535.

49. A.D. Mercer, "Types of Inhibitors Used in Neutral Aqueous Solutions", Proceedings of The 7th European Symposium on Corrosion Inhibitors, 1990: p. 449.

50. T.R. Weber, M.A. Stranick, M.S. Vukasovich, "Molybdate Corrosion Inhibition in Deaerated and Low Oxygen Water", Corrosion 85, Paper 122, 1985.

51. R.H. Ashcraft, Gerhard Bohnsack, "The Influence of Typical Cooling Water Parameters on The Corrosion Inhibiting Effect of 2-Phosphonobutane-1,2,4-Tricarboxylic Acid (PBTC)", Corrosion 86, Paper 401, 1986.

52. A. Weisstuch and C.E. Schell, "An Electrochemical Study of Heteropoly Molybdates as Cooling Water Corrosion Inhibitors", Corrosion, 1972: p. 299.

Table 1. Calcium Chloride Corrosiveness

	% Calcium Chloride Concentration								
	30	25	20	30	25	20	30	25	20
	Temperature								
	120°F						70°F		
	I	II	III	IV	V	VI	VII	VIII	IX
Test Metal	Weight Loss (MPY)								
Copper (CDA 110)	-	-	-	6.5	6.9	6.1	-	-	-
Mild Steel Corrosion									
General	6.2	10.1	19.6	-	-	-	5.1	9.5	15.1
Localized	-	-	-	-	-	-	-	-	-
Fouling	H	H	H	S	S	S	H	H	H
pH	8.2	8.1	7.9	8.0	7.9	8.1	7.8	8.0	8.0

Table 2. Effect of Chromate and Nitrite (120°F)

	% Calcium Chloride Concentration						
	30	25	20	25	20	25	25
Inhibitor	Inhibitor Concentration (ppm)						
	I	II	III	IV	V	VI	VII
Chromium (Cr)	800	800	800	-	-	-	-
Nitrite	-	-	-	4000	4000	4000	4984
Tolyltriazole	-	-	-	-	-	20	20
Nitrate	-	-	-	-	-	-	360
Test Metal	Weight Loss (MPY)						
Mild Steel Corrosion							
General	-	-	-	-	-	-	-
Localized	5.3	7.2	6.8	70	100	65	50
# of Sites	1	2	2	11	17	13	9
Fouling	N	N	N	H	H	H	H
pH	8.4	8.7	8.8	9.5	9.4	9.6	9.5

H= Heavy, M= Moderate, S= Slight, N= None

Table 3. Phosphonate Inhibition (120°F)

	% Calcium Chloride Concentration				
	25	25	24	25	25
Inhibitor	Inhibitor Concentration (ppm)				
	I	II	III	IV	V
HEDP	150	-	150	150	-
PBTC	-	150	-	-	150
Molybdate	-	-	500	-	-
Zinc	-	-	-	300	300
Test Metal	Weight Loss (MPY)				
Mild Steel					
General	20.4	12.1	14.4	18.9	16.6
Localized	-	-	-	-	-
Fouling	H	H	H	H	H
pH	8.8	8.9	8.8	8.0	8.0

Table 4. Effect of pH On Performance (120°F)

	% Calcium Chloride Concentration						
	25	25	25	25	25	25	25
	I	II	III	IV	V	VI	VII
Test Metal	Weight Loss (MPY)						
Copper (CDA 110)	0.25	-	0.20	0.21	0.23	0.41	0.3
Mild Steel Corrosion							
General	1.3	1.5	-	1.7	1.6	1.6	1.3
Localized	-	-	-	-	-	-	-
Fouling	N	N	N	N	N	N	N
Initial pH	9.5	9.0	9.2	8.0	7.1	2.0[1]	2.0[2]
Final pH	9.0	6.4	6.7	6.2	5.9	6.2	6.3

[1]. Readjust pH to 9 after 12 hours, samples already immersed.

[2]. Readjust pH to 9 after 12 hours, samples to be immersed.

Table 5. Effectiveness on Nitrite Contamination (120°F)

	% Calcium Chloride Concentration			
	25	25	25	25
	Lab Samples		Field Samples	
	I	II	III	IV
Nitrite (ppm)	4500	4500	~1800	~1800
Formulation (ppm)	-	15200	-	15200
Test Metal	Weight Loss (MPY)			
Copper (CDA 110)	-	-	1.4	0.5
Mild Steel Corrosion				
General	12.7	11.8	13.3	5.0
Localized	70	20	78	18
Fouling	M	M	M	M
Initial pH	8.4	9.1	9.1	9.5
Final pH	9.7	5.4	9.3	8.8

Table 6. Long-Term Performance and Chromate Compatibility (120°F)

	% Inhibited Calcium Chloride Concentration					
	25	20	25	20	25	20
	I	II	III	IV	V	VI
Chromate as Cr (ppm)	-	-	400	400	800	800
Test Metal	Weight Loss (MPY)					
Copper (CDA 110)	0.12	0.2	-	0.2	0.19	-
Mild Steel Corrosion						
General	0.7	1.3	-	-	-	-
Localize	-	-	3.0	3.2	2.9	3.0
Fouling	N	N	N	N	N	N
Initial pH	8.7	9.1	8.9	9.0	9.0	9.1
Final pH	6.0	6.2	6.9	7.1	7.0	6.9

H= Heavy, M= Moderate, S= Slight, N= None

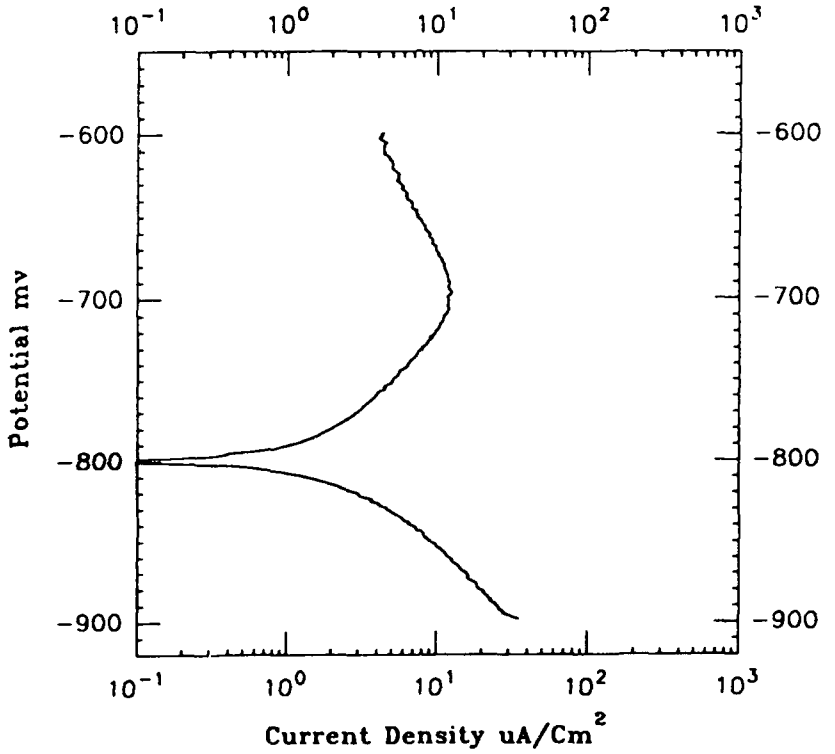

Figure 1. Potentiodynamic Polarization of Mild Steel in Deaerated $CaCl_2$

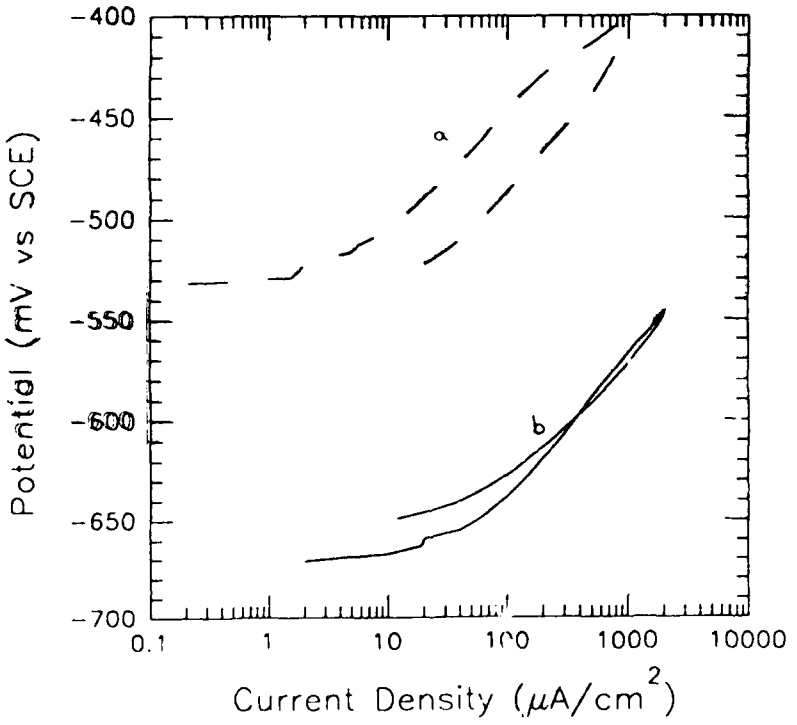

Figure 2. Cyclic Polarization of Mild Steel in Inhibited $CaCl_2$ Solution
a) In Presence of Nitrite, b) In Absence of Nitrite

The Effect of Temperature and Chloride Concentration on Stainless Steels in Ammonium Chloride Solutions

Olof Forsén
Helsinki University of Technology
Laboratory of Corrosion and Material Chemistry
Vuorimiehentie 2
02150 Espoo, Finland

Jorma Virtanen
Helsinki University of Technology
Laboratory of Corrosion and Material Chemistry
Vuorimiehentie 2
02150 Espoo, Finland

Jari Aromaa
Outokumpu Research Oy
PO Box 60
28101 Pori, Finland

Markku Tavi
Neste Oil
PO Box 310
06101 Porvoo, Finland

ABSTRACT

Ammonium chloride precipitation is a serious problem in many oil refining processes. The precipitation of ammonium chloride deposits is possible in every hydrocarbon stream where nitrogen, hydrogen and chloride are present. The normal practice to avoid or to remove ammonium chloride deposits is to add water into process stream. This may result to acid chloride solutions and severe corrosion problems if the equipment are not constructed of proper materials. In this paper the pitting corrosion resistance of different stainless steels in ammonium chloride environment is studied. The pitting resistance equivalent (PRE) values based on the nominal analysis of the material are compared to the electrochemical behaviour of these materials.

Key terms: ammonium chloride, pitting corrosion, austenitic and duplex stainless steels, oil refining.

I. Introduction

Fouling caused by ammonium chloride is a very common phenomenon in many processes in oil refining and petrochemicals industry. The precipitation of ammonium chloride is possible in every hydrocarbon stream where nitrogen, hydrogen and chloride are present. This precipitation can cause problems in process equipments, for example clogging of heat exchangers and column trays or vibrations of turbines or erosion in high turbulent flow etc. Being very soluble in water but almost insoluble in almost all of the hydrocarbons, the ammonium chloride deposition is a problem, even if there is only little water in the process stream. In the presence of moisture, ammonium chloride can form hydrochloric acid causing pitting or underdeposit corrosion of alloy steels or rapid general corrosion of carbon steel.

Ammonium chloride precipitates usually with decreasing temperature. The temperature where the precipitation starts can be easily estimated, when the dissociation constant of ammonium chloride is known[1]. The temperature dependence of solid ammonium chloride formation is shown in Figure 1.

The normal practice to avoid precipitation of ammonium chloride or to remove these deposits, is to add water into process stream. The amount of the water has to be high enough to avoid low pH in the water and/or the water has to be pretreated with neutralizing agents. If the amount of added water is too low or if it exists only as moisture or as impurity in the process stream, the pH of the water can be very low.

The chloride content in a process stream after a debutanizer of a reforming unit is normally between 100 and 1000 ppm[2]. During the normal operation also some salt deposits are formed inside the process units causing operational problems. When these deposits are washed during operation, the chloride content of draw-off water may rise to as high as 100 000 ppm. Continuing the washing procedure decreases the chloride content after a couple of days back to the hundred ppm level. Typical iron and chloride contents and pH of draw-off water during the washing procedure are presented in Figure 2.

As stated above, the addition of water is a good solution to remove ammonium chloride scales. This simple solution is not possible in process units, where draining system is not designed to handle excess water or in units, where water is considered as an impurity element. Furthermore, when using impure or chemically treated water, extra attention must be paid, so that this water will not cause any other problems, like caustic embrittlement or stress corrosion cracking of copper based alloys by ammonia or stress corrosion cracking of stainless steels with oxygen etc. Water which is warmed and cooled with process stream causes also loss of energy. Therefore, selection of a material that will withstand also the corrosive environment outside normal operation is sometimes the most economical solution.

The aim of this work was to help materials selection in a gasoline reforming unit. Process description and corrosion problems of this unit are presented in earlier papers[2,3]. In this investigation some guidelines are given to materials selection to ammonium chloride environment with different chloride contents and temperatures.

II. Experimental

This investigation was made in order to compare the corrosion rates of different materials by electrochemical methods and give some guidelines for the materials selection. The corrosion behaviour was also compared to the PRE-value of various materials: The PRE-values were calculated by using equation (1), where element symbols Cr, Mo and N refer to the nominal alloy composition in wt-%. Nitrogen is commonly known to improve the localized corrosion resistance of austenite phase and the constant for the effect of nitrogen on PRE varies between 13 to 30[4,5,6]. In this investigation the most usual value for N content (16) was used.

$$PRE = Cr + 3.3*Mo + 16*N \quad (1)$$

The compositions of experimental materials are given in table 1. The criteria for selecting the materials to laboratory tests is that they have to have reasonably good resistance not only to general corrosion but also to localized and stress corrosion.

The pH of the solution was kept constant and only chloride content and temperature were varied. As known, the chloride content and temperature of the solution affect mainly to the pitting corrosion and pH to the general corrosion of stainless steels. The pitting corrosion behavior of material will also give some approximation on the crevice corrosion resistance, although one has to remember that crevice corrosion will begin already at 20 - 80 °C lower temperatures than pitting.

According to analysis made of deposits of one process heat exchanger, the ammonium salt precipitates consists of 99.5 % of ammonium chloride and less than 0.01 % iron. The test solutions of electrochemical tests were thus prepared of pro analysis pure ammonium chloride and distilled water. pH of the test solutions was approximately 6. The tests were carried at temperature range of 25 to 85 °C and with chloride contents 100-35000 ppm. The test solution was purged with nitrogen gas for at least 45 minutes before start of the experiment and purging was continued during the experiment.

Electrochemical tests were made with EG&G PARC 273 potentiostat and M342 SoftCorr software. The test cell was a so called Avesta-cell, which has been developed to improve the reliability of pitting corrosion tests by eliminating possible crevice effects[7]. For that reason the increase of current density at high potentials indicates either transpassive dissolution or pit propagation and growth. To avoid local concentration variations near the specimen the test solution was also circulated during the test. Prior to electrochemical tests the materials were first polarized cathodically at -1000 mV vs. SCE for 5 minutes. After this cathodic cleaning the test materials were left unpolarized until the change of free corrosion potential was less than 0.2 mV/s. When this steady state was reached the cyclic polarization curve tests were started. The iR-drop was corrected after the experiment by using solution resistance measured with EIS. Corrosion potential, pitting potential and repassivation potential of test materials were estimated from these curves.

III. Results

The experiments were made to determine the pitting resistance of a material by polarization curves. The presence of a hysteresis loop on the polarisation curves indicates possible pitting corrosion. Examples of both kind of polarisation curves are shown in Figure 3. When the pitting resistance of a material was determined not only the repassivation potential but also the shape of the hysteresis loop and the difference between pitting and repassivation potentials were used. After the tests all the test samples were investigated with optical microscope to ensure the pitting and absence of possible crevice effect.

The results of polarization measurements were used to construct pass-fail charts for the tested materials with different temperatures and chloride contents. Examples of these charts are shown in figures 4 and 5. Solid marks in the charts indicate no pitting (pass) and open marks indicate pitting corrrosion (fail).

Figure 6 shows a combined result of pass-fail charts for test materials Polarit 757 (UNS S31603), Polarit 772, SAF 2304 (UNS S32304) and SAF 2205 (UNS S31803). The pitting corrosion behavior at different temperatures with different chloride concentrations is estimated by fitting a log(T) vs. log[Cl^-] curve to the border points of pass and fail areas. The fitted curves in figure 6 present the maximum temperature for a chloride content where the material showed no pitting in our experiments. The safe area for each material is thus located below these curves. The PRE values of different materials are also presented in figure 6. The pitting resistance of materials with different microstructure and with same PRE values differs in the areas of low chloride content. But when the chloride content of the electrolyte increases, the difference in pitting resistance of austenitic and duplex steels with same PRE values decreases. This might be due to the different corrosion resistances of ferrite and austenite phases. The ferrite is enriched in chromium and molybdenum and the austenite is enriched in nickel and nitrogen[8]. However, this unequal distribution of alloying elements is not so strong, so that at high chloride contents also ferrite will show pitting despite the higher chromium and molybdenum content in it.

The highly alloyed materials 254 SMO (UNS S31254), 654 SMO and SAF 2507 (UNS S32750) did not show pitting corrosion at 80 °C and 35 000 ppm chlorides. When the temperature was increased to 85°C in the same solution all these materials had a clear hysteresis loop in the polarization curves. However, when studying these samples with microscope after the experiment, it was not possible to say, if the hysteresis loop was a result of pitting or general corrosion.

IV. Discussion

Process equipment are generally fabricated of low cost carbon steel and, depending on the corrosive environment, with extra corrosion allowance. In ammonium chloride environment carbon steel apparatus have typically a corrosion allowance of 6 mm. For example in heat exchanger tubes this extra corrosion allowance is not possible or economical. Therefore the corrosion resistance is most critical in components with small wall thicknesses.

Because the precipitation of ammonia salts causes different problems in the process equipment they have to be removed. The most effective way of doing this during operation, is to wash them off with water addition to process stream. In this case proper materials selection is the only effective way to keep the equipment operational. According to the laboratory tests made in near neutral ammonium chloride solutions, only highly alloyed austenitic and duplex stainless steels are resistant enough to pitting corrosion. The PRE value is a useful approximation on the corrosion resistance of a material, although the pitting resistance of duplex stainless steels was a little better at low chloride contents than that of austenitic stainless steels with same PRE values. On the other hand, the scatter of duplex stainless steel results was significantly higher, so the border of the safe area is not so sharp as for pure austenitic steels.

Although the aim of this study was to evaluate the pitting corrosion resistance of different materials, the pitting corrosion resistance is not the only factor that has to be taken on account in materials selection. When choosing the material for an equipment in a complicated process environment, also the possibilities of crevice corrosion and stress corrosion cracking must be estimated. Materials may fail due to crevice corrosion at temperatures remarkably lower than the critical pitting temperature. When there is a possibility to stress corrosion cracking it is also much safer to select duplex stainless steels instead of pure austenitic stainless steels with same nominal composition.

V. Acknowledgements

Ms. Tarja Kaitale, Plant Superintendent,Neste Oil, is greatly acknowledged for technical help in field tests and her fruitful comments. The authors would also thank Ms. Elisabeth Alfonsson, Avesta AB, Mr. Bengt Wallen, Avesta AB, Mr. Mikko Nieminen, Suomen Sandvik and Mr. Arto Pahkala, Outokumpu Polarit, for precious information and experimental materials

VI. Literature

1. R.R. Williamson, Naphta Hydrotreating unit chloride concentration. Technical Service Department CCR Platforming Symposium 1988.

2. O. Forsén, J. Aromaa, U. Vilanti, M. Tavi, Materials Selection to Combat Chloride Corrosion in Oil Refining, (Helsinki, Finland: 12th Scandinavian Corrosion Congress & Eurocorr '92), pp. 321 - 326.

3. O. Forsén, J. Aromaa, M. Tavi, Corrosion Resistance of Different Materials in Dilute Ammonium Chloride Bearing Environment. Accepted for publication in Corrosion Science.

4. R.D. Reed, Nitrogen in Austenitic Stainless Steels, Journal of Metals, 36 3 (1989): pp. 16 - 21.

5. M.R. Watts, Material Development to Meet Today's Demand. Anti-Corrosion, 36 2 (1989): pp. 4 - 10.

6. E. Alfonsson, R. Qvarfort, Investigation of the Applicability of Some PRE Expressions for Austenitic Stainless Steels, (Materials Science Forum vol 111 -112, 1992), pp. 483 - 492.

7. R. Qvarfort, New Electrochemical Cell for Pitting Corrosion Testing, Corrosion Science, 28 (1988): pp. 135 - 140.

8. G. Tither, New developments in stainless steels for resistance to corrosion in sea water, (Corrosion in seawater systems, London, Ellis Horwood ltd, 1990), pp. 11-23.

Table 1. Nominal composition of test materials, wt-%.

Material	PRE	Type	C_{max}	Ni	Cr	Mo	Others
Polarit 757 (UNS S31603)	27	austenitic	0.03	13	17.5	2-3	
Polarit 772	34.5	austenitic	0.03	13.5	17.5	4.5	0.17 N
Avesta 254 SMO (UNS S31254)	43	austenitic	0.019	18	20	6	0.7 Cu, 0.2 N
Avesta 654 SMO	54	austenitic	0.02	22	24	7	0.4 Cu, 0.45 N
SAF 2304 (UNS S32304)	25	duplex	0.03	4	23		0.1 N
SAF 2205 (UNS S31803)	38	duplex	0.03	5.5	22	3	0.14 N
SAF 2507 (UNS S32750)	43	duplex	0.019	7	25	4	0.27 N

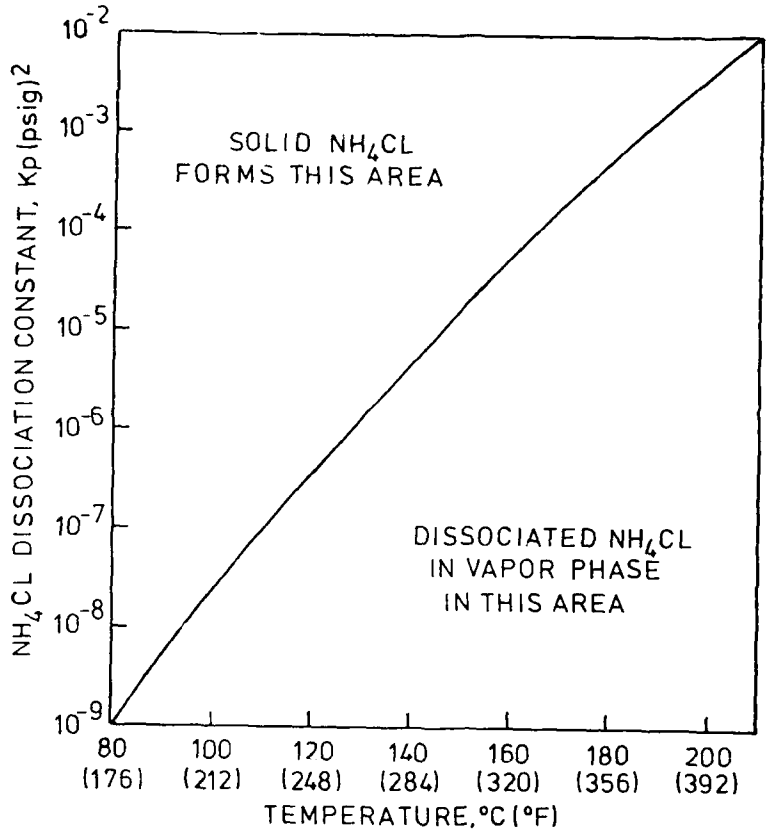

Figure 1. The temperature dependence of NH_4Cl precipitation.

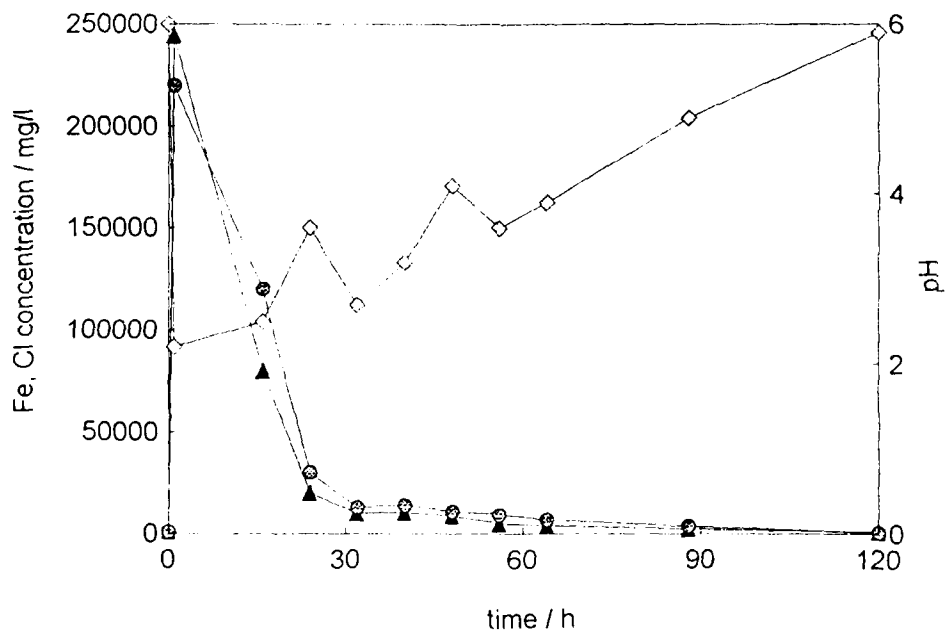

Figure 2. The effect of washing procedure on water pH, iron and chloride concentrations.

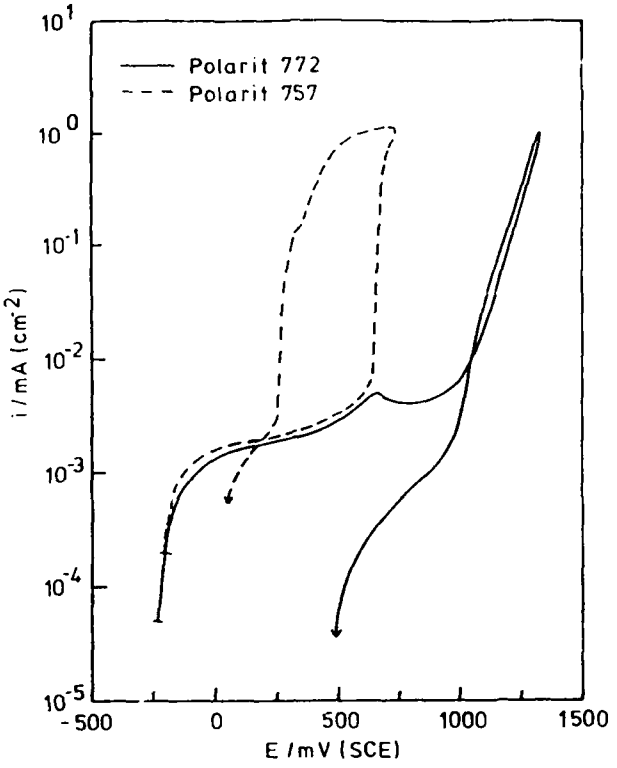

Figure 3. Cyclic polarization diagrams for Polarit 757 (UNS S31603) (failed) and Polarit 772 (passed) stainless steels. 1000 ppm NH_4Cl solution, T = 40 °C.

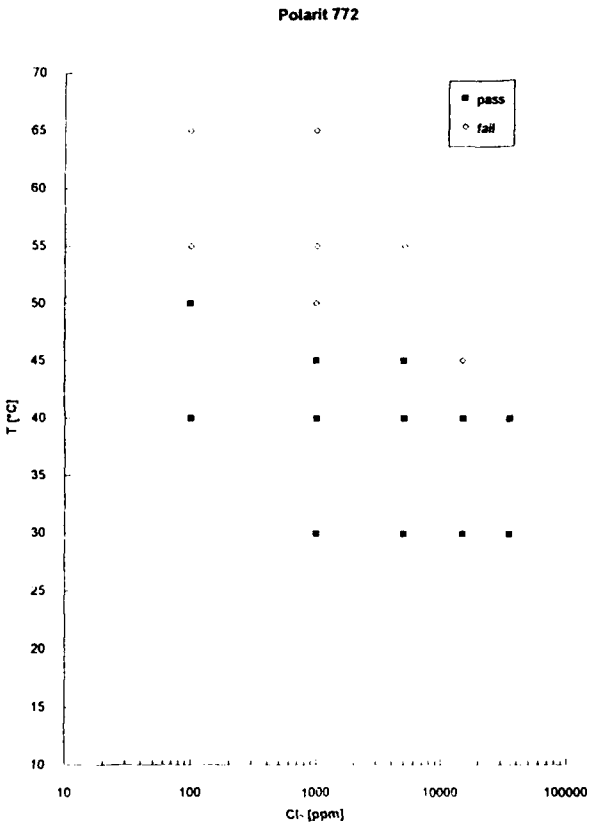

Figure 4. The pass and fail chart for Polarit 772 stainless steel.

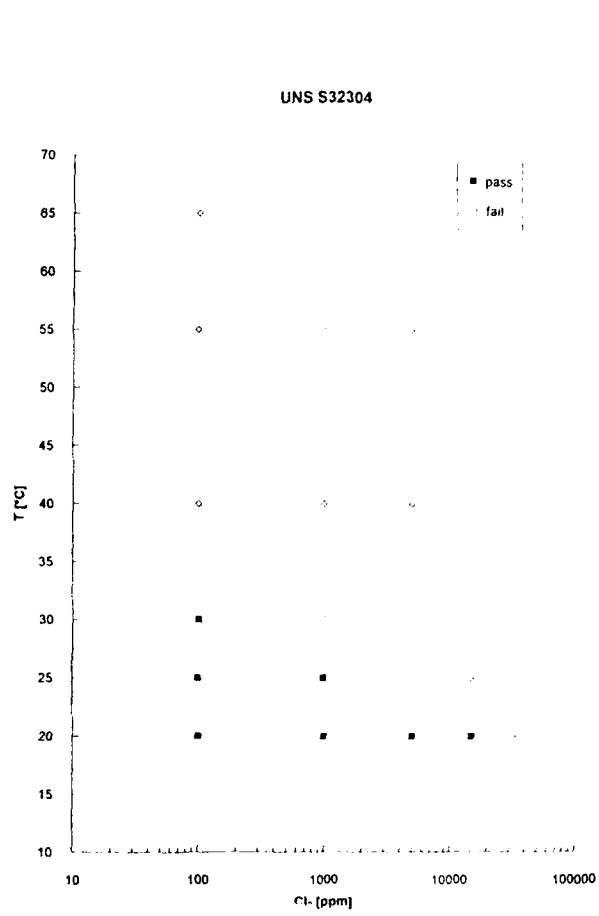

Figure 5. The pass and fail chart for SAF 2304 (UNS S32304) duplex stainless steel.

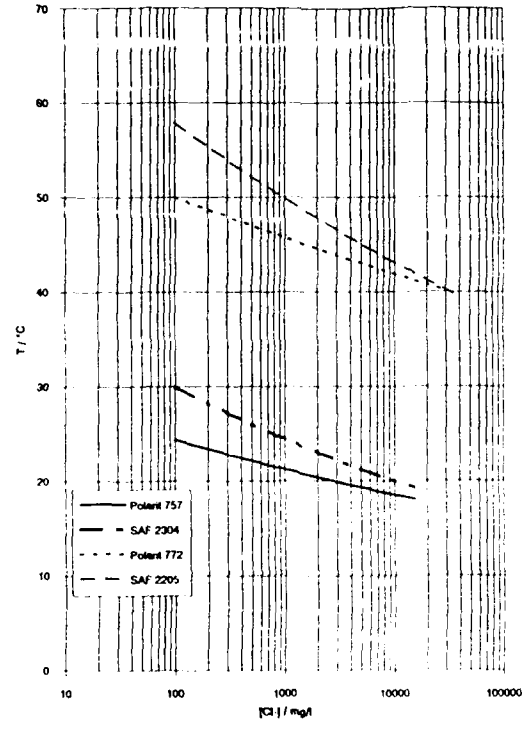

Figure 6. Combined results from pass-fail charts. The lines show the temperatures below which the materials did not show pitting in the electrochemical tests.

Rest Potential Measurements for Stainless and Low-Alloy Steels in High Temperature Water

Alasdair Charles,
Materials Division,
Department of Mechanical, Materials
and Manufacturing Engineering,
University of Newcastle upon Tyne,
Newcastle upon Tyne, NE1 7RU,
U.K.

John Congleton,
Materials Division,
Department of Mechanical, Materials
and Manufacturing Engineering,
University of Newcastle upon Tyne,
Newcastle upon Tyne, NE1 7RU,
U.K.

Abstract

Quasi-equilibrium potentials have been measured for an AISI 316L stainless, an AISI 309 weld butter and a low-alloy steel in deareated, phosphate / hydrogen phosphate / sulphite / sulphate doped water. Measurements have been made from room temperature up to 250°C under static and flowing solution conditions. The rest potentials observed under flowing conditions were cathodic to those observed in a static solution.

The result of galvanic coupling of AISI 316L and low alloy steels was to produce a rest potential value similar to that of the low-alloy steel alone under the same conditions.

The effect of 1 ppm copper contamination upon the rest potential of the stainless steel was to shift it anodically by up to 200 mV. A much smaller anodic potential shift was observed for the low-alloy steel.

Key terms: rest potential, stainless steel, low alloy steel, refreshed loop

Introduction

One method of oxygen scavenging in steam generating systems is to use sodium sulphite and this leads to a significant sulphate burden in the water over a period of service. The water can also be maintained at a high pH for corrosion control by phosphate/hydrogen phosphate pH buffering. It is now becoming accepted that a major factor in mitigating stress corrosion cracking of steels in high temperature water is to ensure that the materials have an adequately cathodic electrochemical potential, ECP, during their life. Thus, the measurement of electrode potentials is emerging as a necessary adjunct to plant operation.

Although the water chemistry used in the power generating industry is carefully monitored and controlled, there are occasions such as during shut-down and start-up when the water chemistry may alter and induce a change in the ECP of the materials exposed to the environment. Thus, the effect of variations in electrolyte composition upon ECP are of interest with respect to the life span and integrity of high temperature pressurised systems.

It is also known that environment assisted cracking of alloys, particularly in connection with weldments, can occur in high purity water systems [1,2] and that such corrosion is highly potential dependant [3]. The present research was aimed at measuring the rest potentials of alloys, or alloy couples, in water chemistries relevant to power generating systems.

There are a variety of problems inherent in measuring rest potentials for stainless steels and other alloys in high temperature water. These are related to the low reactivity of the alloys in the electrolyte, film formation upon the alloys and the magnitude of the solution resistance. Further difficulties arise in trying to control the oxygen content of the electrolyte, which has a significant effect upon the potentials being measured [2]. The existing data exhibits some degree of scatter arising from variations in the experimental methods used and to the long equilibration time required to establish stable potential conditions in such systems [4].

We have examined the requirements for achieving stable, reliable, electrode potentials over the temperature range 20°C to 250°C. Measurements have been made on a wrought austenitic 316L stainless steel, a AISI 309 stainless steel weld butter and a ferritic chromium/molybdenum, CrMo, low alloy steel taken from a weldment.

Experiments have been performed to assess the effect of solution flow upon the ECP's of the alloys by comparing data from a refreshed loop and static autoclaves. To determine the potentials likely to be found close to weldments, where environment assisted cracking may occur, the effect of galvanic coupling of the steels has also been examined.

It is possible that contamination of the electrolyte by copper is likely in high temperature water systems and we have examined the affect of such off-water chemistry conditions and compared the rest potentials observed with those found in a 'good' chemistry environment.

Experimental

The compositions of the three alloys, as determined by EDAX, are shown in table 1. It may be noted that the composition of the 309 weldment exhibits signs of alloy depletion, caused by the welding, when compared with the nominal composition, also given in the table.

The alloys were examined as solid cylindrical specimens, of 2 sq.cm surface area, drilled and tapped at one end to allow electrical contact via a steel rod which was isolated from the electrolyte by PTFE shrink wrap. The specimens were polished to a 4/0 emery finish, degreased and rinsed with deionised water just before use.

For experiments below 100°C, saturated mercury/mercury sulphate reference electrodes were used and temperature corrections were made to convert values to the SHE scale [5]. These electrodes were selected because the bulk solution contained sulphate so any leakage of electrolyte from the reference electrode would be of little consequence.

For tests conducted above 100°C, silver/silver chloride (0.1 M KCl) electrodes were used which are basically of the Andresen design [6]. The silver/silver chloride junction of the electrode was external to the autoclave and was kept at ambient temperature. Correction for the thermal liquid junction potential generated between the internal and external portions of the electrode was performed using data from Macdonald et al.[7].

Potential measurements have been reported in the literature in a variety of water chemistries and at quite high temperatures but it is acknowledged that the stability and life span of the reference electrodes used can be unsatisfactory. Autoclaves with large chambers require reference electrode probes of a sufficient length for the electrode tip to reach into the vicinity of the specimen, particularly if potential control is to be applied. Such electrodes have a tendency to fail due to gas bubble formation inside the probe which breaks the electrical contact between the silver chloride/electrolyte junction and the porous frit junction. To help mitigate this effect, silica or zirconia grit was used as a filler material within the probe. In later experiments a carbon fibre thread was inserted into the electrode as an alternative safe-guard, so that even if a large gas bubble did form across the diameter of the probe, the conductive nature of the carbon fibres would help to prevent loss of electrical contact between the electrolyte on either side of the cavity.

All potential measurements were made using high input impedance digital voltmeters or with buffer amplifiers linked to pen chart recorders. The reference electrodes were checked before and after each test. The pH, conductivity, oxygen concentration and chloride content of the solutions were also monitored before and after each experiment.

Table 2 shows the composition of the electrolyte. The solutions were prepared using "Analar" grade chemicals and distilled and deionised water. The solution was purged with "white spot" nitrogen to deoxygenate the electrolyte before the sodium sulphite was added. The electrolyte oxygen concentration was monitored using a Clarke cell probe [8] and purging with nitrogen was maintained throughout each test. The electrolyte was deemed suitable for use if the oxygen concentration was < 5 ppb.

'Off water' chemistries containing copper ions were prepared by the addition of copper sulphate to the electrolyte.

Static solution experiments below 100°C were performed in glass cells which were placed in thermostatically controlled water, or oil, baths. The cells contained three ports in the neck through which the electrodes and the gas bubbler were sealed. A small vent allowed gas to leave the cell via a condenser tube.

Static solution experiments above 100°C were performed in 1.5 litre autoclaves. Three separate test specimens could be inserted into the chamber along with the thermocouple and reference electrode probes. The chamber was purged with nitrogen before the head was tightened down at the start of each test. The potential of the chamber body was monitored during the experiments to identify any fault due to shorting-out of the specimens to the body.

Refreshed loop experiments were performed in a 75 ml autoclave which could be used with two alloy samples and two reference electrodes, as illustrated in figure 1. The tests were performed using a flow rate of approximately 10 ml per minute and an operating pressure of 500 psi (3.45 MPa). The autoclave temperature was only increased incrementally when the electrode potential had stabilised at the previous temperature.

At the end of each experiment the test specimens were examined optically. In some cases the specimen film and substrate were then examined by scanning electron microscopy. The oxide film and other crystalline deposits could be removed from samples, with minimum damage to the substrate, by cathodic stripping in an alkaline "de-rusting" solution. Energy dispersive analysis by x-rays was performed on some samples of bulk material and on some oxide films generated during the tests.

Results

Static Solution Data

Figure 2 illustrates typical trends in open circuit potential with time for the steels at room temperature. The alloys initially exhibit large changes in open circuit potential and then tend to some quasi-equilibrium value, or rest potential, after several days of exposure to the environment.

The initial changes in potential for each steel may be explained by considering the surface reactivity of the alloys. The 316L stainless steel has a protective chromium oxide coating which is not affected to any extent by immersion in the electrolyte and thus does not show an initial potential minimum. The CrMo steel has a thin, air-formed, oxide layer which is readily broken down causing a cathodic potential shift. The alkaline electrolyte then stimulates film growth and the potential of the CrMo specimen returns to a more noble value associated with the equilibrium between iron (II) and iron (III) oxyhydroxides [9]. The 309 stainless steel samples exhibited an initial film break-down, probably due to the alloy depletion effect mentioned previously, then re-passivated. The final potentials of the stainless steels are likely to be associated with the equilibria between chromium oxide and oxyhydroxide species. The rest potentials observed become less cathodic across the range from CrMo to 309 to 316L.

Figure 3 shows the data from the first 100 hours of testing in a static autoclave experiment at 150°C. The alloys exhibit an initial potential minima associated with break-down of the surface oxide layer followed by re-passivation. The effect of

increased temperature upon the specimens is thus to decrease the stability of their air-formed oxide layers, which is in agreement with thermodynamic considerations, and to reduce the time taken for equilibration to occur, which is reasonable in terms of the reaction kinetics. The 316L and 309 specimens were found to be tarnished at the end of test while, at temperatures of 75°C and above, the CrMo specimens were coated with a thick, black, film of magnetite and phosphate salts. The formation of magnetite at temperatures above 75°C upon CrMo steel may be explained by examining the potential/pH diagrams for the iron - water system [9] which show that a region of mixed oxyhydroxide stability develops in alkaline environments near to this temperature.

The effect of temperature upon the quasi-equilibrium electrode potentials of the alloys is shown in figure 4. The data in this figure was obtained by averaging at least three results at each temperature for each steel. The typical scatter band for a potential measurement under a particular set of conditions was approximately 50 mV. The scatter band for the stainless steels was larger than that for the CrMo steel under all conditions examined and the scatter was observed to decrease with increasing temperature. From figure 4 it can be seen that the 316L material passivates in the electrolyte and shows a nearly linear potential / temperature relationship of approximately 3 mV/°C. The 309 specimens show a similar trend although there is a slight change in slope at about 70°C indicating a change in the nature of the surface film. The CrMo material maintains a fairly constant potential at temperatures up to 75°C and then generates increasingly cathodic potentials as the temperature rises. The change in gradient arises from the formation of a predominantly magnetite film on the surface at temperatures above 75°C. The potential versus temperature lines for the three alloys can be seen to converge with increasing temperature. All the data lies within the region of water stability, ie. between the oxygen and hydrogen evolution lines, which are shown as dashed lines in figure 4. The rest potential gradients observed are of similar value to the gradient of the oxygen evolution line (approximately 2.4 mV/°C) and it is probable that they are related to metal/oxide/hydrated oxide equilibrium reactions.

The effect on potential of galvanic linking a CrMo specimen to a 316L specimen is shown in the figure 5. The open circuit potentials observed across the temperature range are similar to those for a single CrMo sample and thus indicate that the potential of the 316L steel has been moved cathodically by coupling. The observed potentials may be explained by the application of "mixed potential" theory [10]. The CrMo dissolution is the major anodic process and as such its tafel line intersection with the cathodic reduction of oxygen line dominates the mixed potential of the galvanic couple.

Figure 6 shows the averaged free corrosion potentials obtained in both copper free and 1 ppm copper environments. It can be seen that Cu^{2+} addition has no consistent effect upon the potential of CrMo steel but that it does cause an anodic potential shift in both the 316L and 309 data, particularly at the lower temperatures where shifts of approximately 250 mV were observed. The magnitude of the potential shift was found to decrease with decreasing copper ion concentration. Thus, at 10 ppb Cu^{2+}, an anodic shift of approximately 100 mV was observed for 316L steel. Stainless steel specimens were found to be

slightly tarnished after test while the CrMo samples were observed to have copper deposited upon then as well as an inner layer of magnetite at temperatures above 70°C. The copper film was found to be approximately 0.75 um thick.

Refreshed Loop Data

Figure 7 shows the averaged free corrosion potentials for the three alloys under refreshed and static solution conditions. It can be seen from figure 7 that the general effect of solution flow is to cause a cathodic shift in the free corrosion potentials observed for the alloys.

The time required to generate stable rest potential values was considerably shorter in the refreshed autoclave than under stagnant solution conditions. For example, at 150°C equilibration of the potential of a 316L specimen occurred in about 10 hours in the refreshed loop but after approximately 50 hours under static conditions. Niedrach and Stoddard [12] have previously reported an equilibration time of 8 to 16 hours for 304 stainless steel under refreshed conditions in simulated BWR electrolyte.

Figure 8 shows the quasi-equilibrium potentials of the alloys in 1ppm copper poisoned electrolyte across the temeprature range. The effect of the Cu^{2+} addition is to cause an anodic shift in the free corrosion potentials and this shift was greatest for the stainless steels. The general behaviour is similar to that observed under static solution conditions, if allowance is made for the cathodic shift in the results obtained in the refreshed autoclave. After testing, the low alloy steel specimens were observed to have a thin magnetite film with areas of a copper coloured hue, while 309 and 316 specimens were slightly tarnished with some discolouration due to copper deposition. The quasi-equilibrium potential of a solid copper specimen was determined from 25°C to 250°C, for comparison with the copper-filmed steel values, and this data is also presented in figure 8. The specimen was coated in a thin black film after test, probably a mixed copper oxide under these potential/pH conditions [13]. The rest potential values of the copper sample suggest that the film formed on CrMo steel specimens is porous and that the resultant potential observed for the steel in copper poisoned solution is a "mixed-potential" arising from the cathodic reaction rate for copper deposition and the anodic reaction rate for corrosion of the steel. The shift in potential of the stainless steels with copper addition is more difficult to explain [11] and may be related to the formation of copper complexes.

Discussion

The experiments performed have established the free corrosion potential behaviour of the three steels in doped water over the temperature range 25°C to 250°C. The results are consistent and show trends which are essentially complementary to results in the known literature.

Lin [11] has examined the effects of copper contamination in BWR water on the free corrosion potentials of 304 and 316 stainless steels. Although BWR water chemistry is quite different from that used in the present study the trends in behaviour with copper addition were similar, allowing for the 600 to 700 mV potential off-set in the relatively high oxygen, and low conductivity, BWR environment.

The effect of solution flow upon rest potentials of stainless steels has been discussed in the literature in connection with

BWR systems [11,14,15,16]. The results indicate that solution flow will increase the magnitude of any potential shift caused by chemical additives, for example copper, and that the film formed under flowing electrolyte will be thinner, more homogeneous and more protective than that formed in stagnant water. There are no reports of cathodic shifts in potential with solution flow, as seen in this work, but this may be related to the changes in electrolyte pH. Initially, BWR simulant solutions are approximately neutral while the water used for the present tests was quite alkaline. During static solution tests the electrolyte became less alkaline while the literature indicates that the BWR water became slightly more alkaline. The rest potential shift caused by change in static solution pH, as determined from the Nernst equation, could be as much as 100 mV in the positive direction in our experiments. Thus, if a correction for pH change is made to the present results, the effect of solution flow on the rest potentials is less significant.

The potential changes observed in the experiments are related to film formation or removal and the changes in the film properties with temperature. The extent of the change in potential was most significant for the relatively un-reactive stainless alloys. The CrMo steel oxidised during the high temperature tests and a layer of magnetite mixed with the phosphate inhibitor was generated on the steel surface.

Conclusions

1. The test duration required to obtain reliable rest potential measurements for stainless and low alloy steels was of the order of 10 hours in a refreshed water loop and 100 hours in a static autoclave. Some scatter exists in the results but averaging not less than three experiment data points allows consistent trends in the data to be revealed.

2. The rest potentials determined in flowing electrolyte were cathodic to those found under static conditions, but this is considered to be partially related to the maintenance of a more alkaline pH in the flowing system than in stagnant water.

3. Copper ion contamination of the electrolyte causes an anodic shift in the rest potentials, which in the case of the low alloy steel is consistent with mixed-potential theory.

References

1. J.Congleton and R.N.Parkins, Corrosion Vol.44 No.5 (1988) p.290.

2. M.E.Indig, J.E.Weber and D.Weinstein, "Environmental aspects of carbon steel stress corrosion in high purity water" Reviews on coatings and corrosion V, No.1-4 (1982) p.173.

3. R.N.Parkins, Corrosion Science Vol.20 (1980) p.147.

Table 1. Approximate Alloy Compositions, wt%, as determined by EDAX; the balance iron.

ELEMENT	316L	309(nominal)	309(welded)	Cr/Mo
% Cr	16.9	22 - 24	20.9	1.1
% Ni	11.5	12 - 15	10.7	-
% Mo	1.9	-	0	0.5
% Mn	1.4	-	1.9	0.6
% Si	0.6	1.0 max	0.9	-

Table 2. Electrolyte composition and properties.

Chemical	Quantity g/l	Concentration ppm
Sodium Phosphate	0.220	55
Sodium Hydrogen Phosphate	0.164	110
Sodium Sulphite	0.128	81
Sodium Sulphate	0.740	500

Resultant pH = 10.6 due to phosphate/hydrogen phosphate buffering, oxygen concentration < 5 ppb
and
conductivity = 1400 uS/cm.

4. W.R.Kassen and D.Cubicciotti, "Proposed guidelines for implementing ecp measurements in boiling water reactors" Corrosion/90, paper no.485, (NACE 1990).

5. D.Dobos, "Electrochemical Data" Elsevier (1975) p.265.

6. P.L.Andresen, "Innovations in experimental techniques for testing in high temperature aqueous environments", GEC report No. 81CRD088 (1981).

7. D.D.Macdonald, A.C.Scott and P.Wentrcek, J.Elecrochem.Soc. 117 (1979) p.908.

8. J.K.Fowler and K.B.Oldham, "Voltammetric membrane cell used in equilibrium mode for dissolved oxygen assey" Electrochem.Soc. symposium, Canada, Edited by W.A.Adams et al. (1975).

9. R.J.Biernat and R.G.Robins, Electrochim. Acta. (1972) p.261.

10. M.G.Fontana, "Corrosion engineering", McGraw-Hill (1987) p.462.

11. C.C.Lin, F.R.Smith, N.Ichikawa and M.Itow, Corrosion Vol.48 No.1 (1992) p.16.

12. L.W.Niedrach and W.H.Stoddard, Corrosion Vol.42 No.12 (1986) p.696.

13. M.M.Laz, R.M.Souto, S.Gonzalez, R.C.Salvarezza and A.J.Arvia, Electrochim. Acta. Vol.37 No.4 (1992) p.655.

14. D.D.Macdonald, H.Song, K.Makela and K.Yoshida, Corrosion Vol.49 No.1 (1993) p.8.

15. H.Choi, F.H.Beck, Z.Szklarska-Smialowska and D.D.Macdonald, Corrosion Vol.38 No.2 (1982) p.76.

16. S.H.Shim and Z.Szklarska-Smialowska, Corrosion Vol.43 No.5 (1987) p.280.

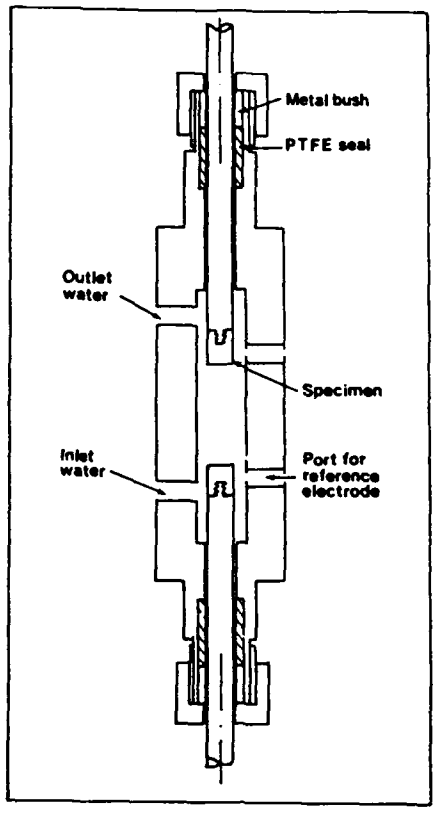

Figure 1. Cross-section of the refreshed autoclave used for rest potential measurements

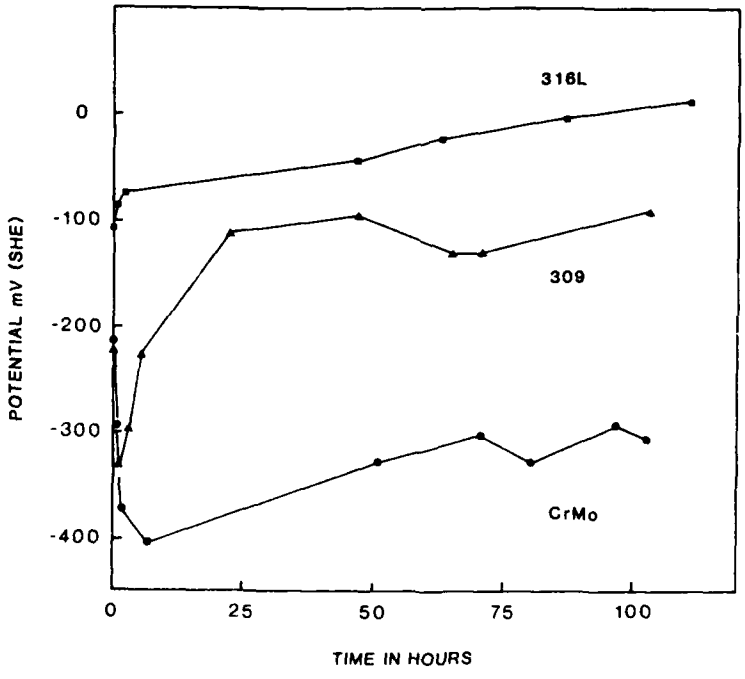

Figure 2. Graph showing the typical potential/time behaviour of the alloys in doped water with < 5ppb oxygen and at 20°C.
Where ■ = 316L, ▲ = 309 and ● = CrMo.

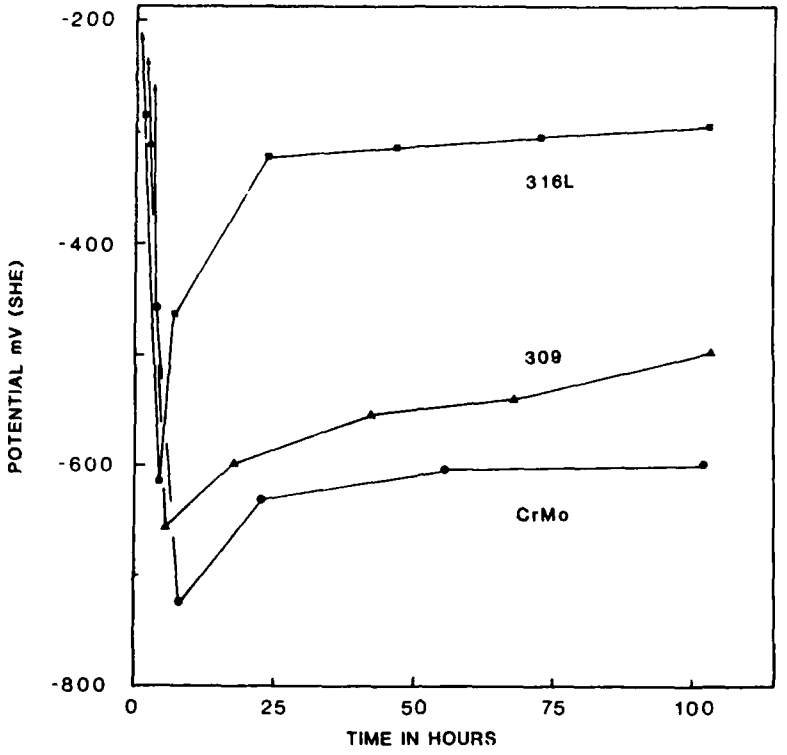

Figure 3. Graph showing the typical potential/time behaviour of the alloys in doped water with < 5ppb oxygen and at 150°C.
Where ■ = 316L, ▲ = 309 and ● = CrMo.

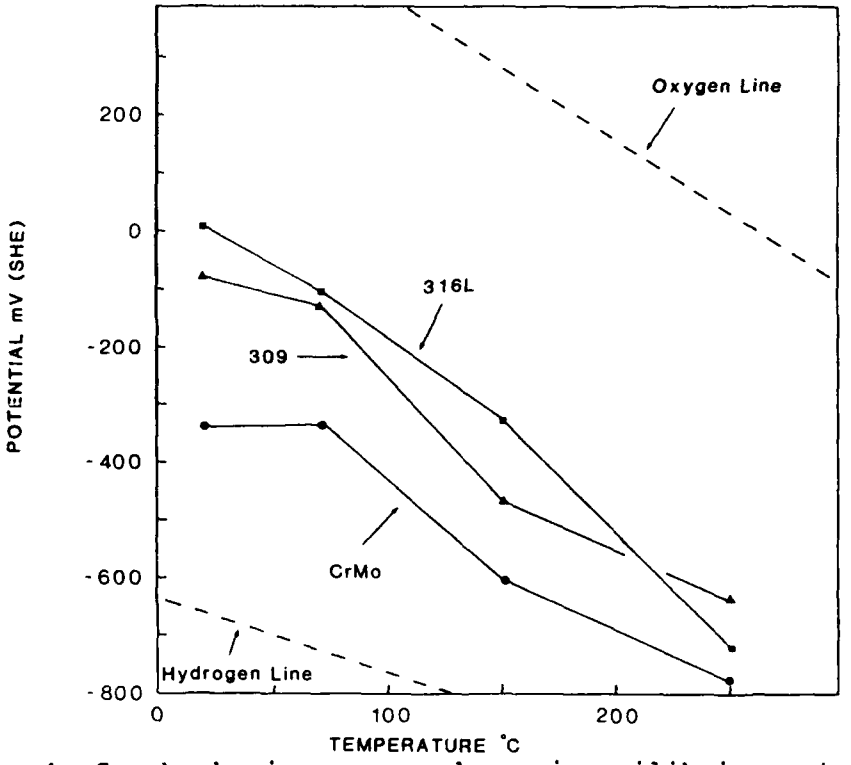

Figure 4. Graph showing averaged quasi-equilibrium potentials versus temperature for the alloys in doped water with < 5ppb oxygen and under static conditions.
Where ■ = 316L, ▲ = 309 and ● = CrMo,
the oxygen line corresponds to
$4\ OH^- = O_2 + 2\ H_2O + 4\ e^-$
and the hydrogen line corresponds to
$2\ H_2O + 2\ e^- = H_2 + 2\ OH^-$.

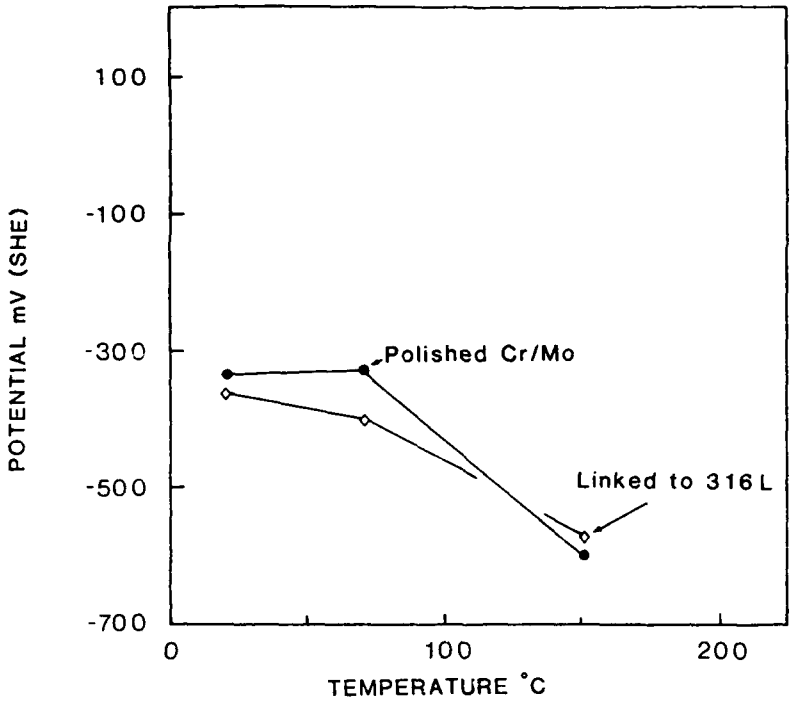

Figure 5. Graph showing the changes in quasi-equilibrium potential with temperature for a CrMo sample and a galvanic link of 316L and CrMo steel in doped water with < 5ppb oxygen.

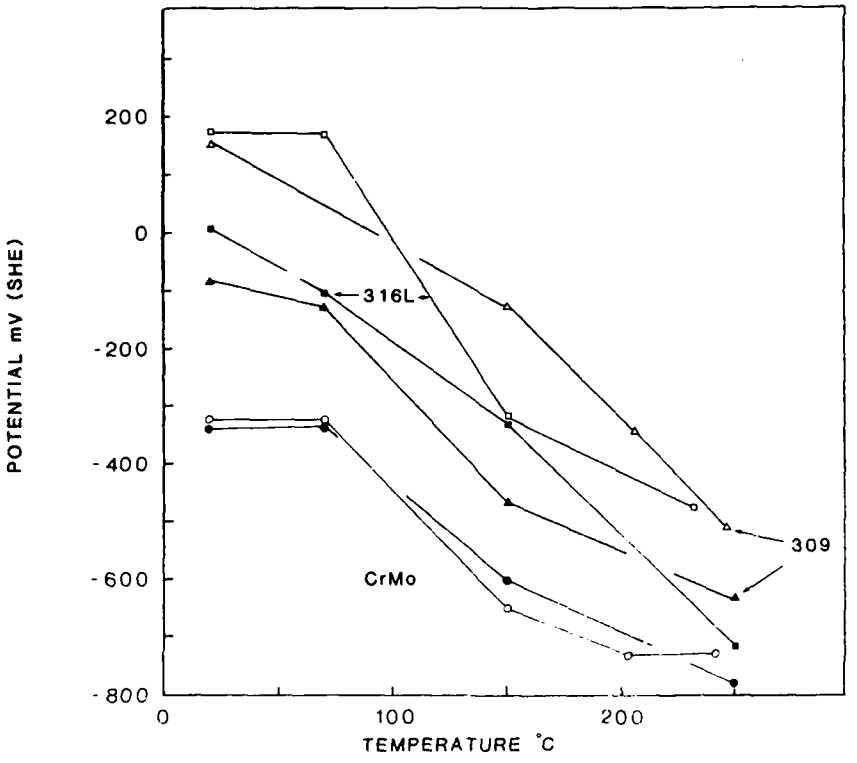

Figure 6. Graph showing the averaged quasi-equilibrium potentials for the alloys in 'copper free' (closed symbols) and 1ppm copper doped (open symbols) water with < 5ppb oxygen and under static conditions. Where □ ■ = 316L △ ▲ = 309 ○ ● = CrMo.

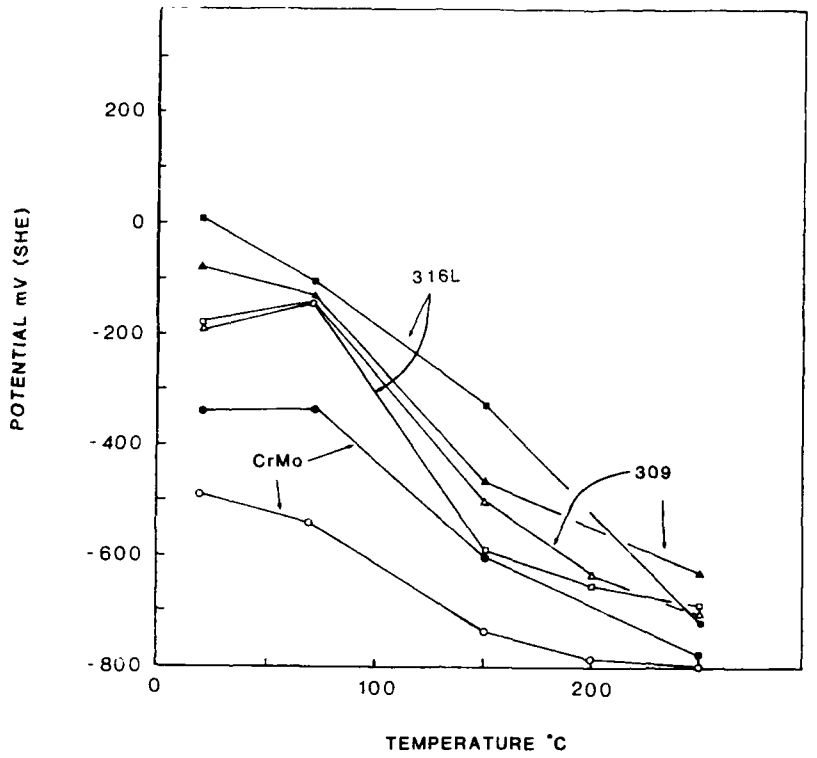

Figure 7. Graph showing the averaged quasi-equilibrium potentials for the alloys under static (closed symbols) and refreshed (open symbols) conditions in doped water with < 5ppb oxygen.
Where □ ■ = 316L, △ ▲ = 309 and ○ ● = CrMo.

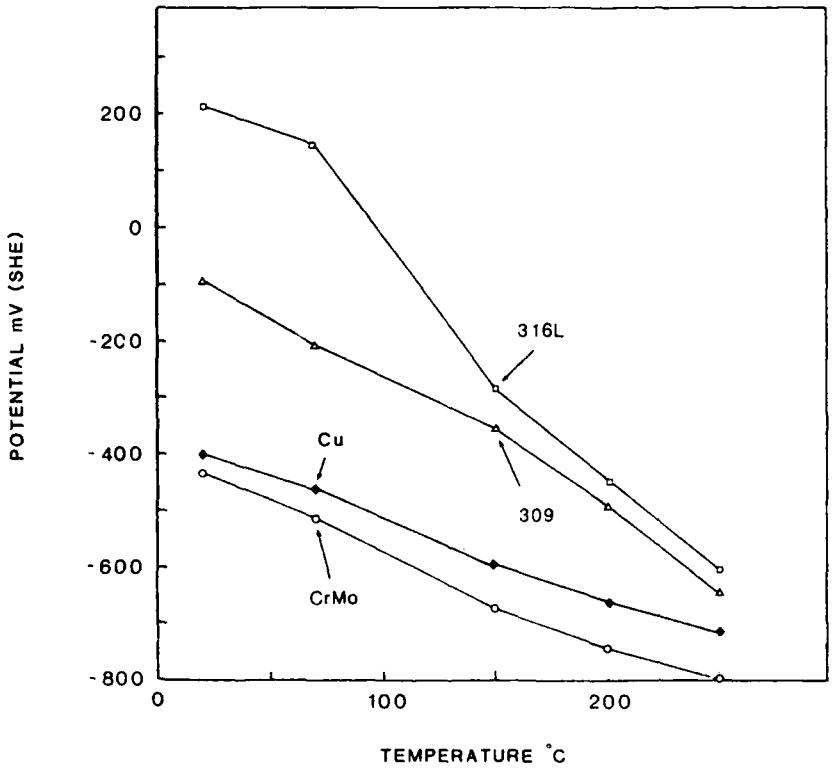

Figure 8. Graph showing the averaged quasi-equilibrium potentials for the alloys in 1ppm copper doped (open symbols) water with < 5ppb oxygen and under refreshed conditions. Data for a solid copper specimen is shown for comparison.
Where □ = 316L, △ = 309, ○ = CrMo and ◆ = Cu.

Managing Galvanic Corrosion In Waters

Arthur H. Tuthill P.E.
Tuthill Associates, Inc.
PO Box 204
Blacksburg, Virginia 24060

Abstract

This paper summarizes 30 case history solutions to severe galvanic corrosion problems the author has encountered in heat exchangers, condensers, valves, pumps, steel and copper alloy welds, fasteners, coated hulls, ballast tanks, electrical connectors, propellers, and partially lined tanks. Guidelines are developed to assist engineers in managing galvanic corrosion problems they may encounter.

Galvanic Corrosion

When two different materials are welded, bolted or otherwise joined together in an electrolyte, the uncoupled corrosion rate of the least noble (anodic) is increased, and the uncoupled corrosion rate of the more noble (cathodic) is decreased. Inco's familiar galvanic series, Figure 1, shows which material of a couple in seawater is anodic and which is cathodic. Wesley and Brown's chapter in Uhlig's Corrosion Handbook provides an excellent description of the various reactions that can occur within a galvanic couple, ([1]). For the purpose of understanding the reactions occurring in these 30, cases the following provides sufficient background.

Anodic Reaction

The oxidation (corrosion) which occurs at the anode is represented thusly:

$$M^{o} \rightarrow M^{+} + e$$

Where M^{o} is a metal atom, Fe, Cu, Ni, Cr etc.
M^{+} is the metal ion in the electrolyte.
e is the electron from the metal atom.

Cathodic Reactions

In the vast majority of situations the cathodic reaction occurring in galvanic corrosion is oxygen reduction or hydrogen evolution or both.

The hydrogen evolution reaction is represented by $2H^{+} + 2e = H_2$
The reduction of oxygen occurs as follows

$O_2 + 4H^{+} + 4e = 2H_2O$ (acid solutions)
$O_2 + 2H_2O + 4e = 4OH^{-}$ (alkaline solutions)

In oxygen containing waters at near neutral pH the oxygen reduction is of primary importance. The extend of corrsion is frequently controlled by the area of the cathode and the rate at which oxygen can reach its surface (mass transfer). However, under certain conditions the hydrogen evolution reaction can become important. This is primarily when the potential becomes cathodic such as in the case of CP being applied or very active metals such as aluminium or zinc being involved. Figure 2 shows the anodic and cathodic reactions

([1])Uhlig, H.H., "Corrosion Handbook", John Wiley and Sons, 1947.

inside surface for as much as 40 feet from the inlet end was effective cathodic surface. This meant the cathode to anode ratio could approach a 1000 to 1, not 3 to 4 to 1 as originally supposed. ([2])

Figure 3 shows a half section of a copper alloy condenser or heat exchanger with titanium tubes. The differences in potentials for the various tubesheet materials coupled to titanium are shown. The potential difference between nickel copper alloy 400 and titanium is about 25% of the potential difference between naval brass or aluminum bronze and titanium suggesting nickel copper alloy 400 might perform better. However the effective cathodic area of the titanium is so large that it tends to overwhelmthe lower difference in potential. All tubesheet materials shown have suffered accelerated corrosion when coupled to titanium tubes.

Solutions: The principal solution to corrosion of copper alloy tube sheets in power plant condensers tubed with titanium, 6% Mo austentic or superferritic stainless steel has been installation of a well designed impressed current cathodic protection system in the waterbox. The potential and the potential distribution must be controlled so as to prevent hydryding of titanium or hydrogen embrittlement of superferritic tubing.

Iron anodes ar also used for this purpose. Many of the Middle East MSF unit reject sections have titanium tubes, CA 614 or 630 tubesheets with copper alloy waterboxes (sometimes 90/10CuNi or cast nickel aluminium bronze) with orin anodes to protect the copper alloys.

4) Problem: Waterboxes and Tubing: The early nuclear submarines were fitted with nickel copper alloy 400 waterboxes (the higher strength allowed a weight saving) and C71500 copper nickel tube sheets and tubes. The copper nickel tubing was anodic to and corroded preferentially to the nickel copper, alloy 400 waterboxes.

Solution: The cathodic surface area was reduced by solder wiping the nickel copper waterboxes with a 50:50 lead tin solder. Later the nickel copper waterboxes were redesigned and changed to C71500 accepting a slight weight penalty.

5) Problem: Waterboxes and tubing: Maintenance forces at one of the Office of Saline Water's desalination plants observed that there was considerable general corrosion of the bare steel waterboxes facing the copper nickel tube sheet and tubes. It was decided to epoxy coat the steel waterboxes. Figure 4 shows the deep pitting that occurred after the next 6 months operation. The coating failed locally at surface irregularities exposing the substrate steel to deep localized corrosion in saline water.

Since most of the coating was still intact all of the oxidation reaction, corrosion, had to occur in the very small area of steel exposed.

Solutions:

1 Epoxy coat the tubesheet and tube ends to reduce the cathodic area. This was the option chosen.
2 Install supplemental cathodic protection.
3 Increase anodic area by removing the coating from the waterbox allowing corrosion of the steel waterbox to continue over the whle surface area rather than at the localized areas where coating breakdown occurs. This is a last resort option as the steel corrosion products can, and have, of and failure to copper alloy tubing.

6) Problem: Waterbox waster plates: One shipowner outfitted his vessel with a complete C70600 copper nickel cooling water system and found that biofouling growth in the waterboxes was quite heavy despite the antifouling characteristics of copper nickel. Investigation revealed that the shipowner hadretained

([2]) Gehring, G.A. Jr., Kuester, C.K. and Maurer, J.R. "Effective Tube Length - A Consideration on Galvanic Corrosion of Marine Heat Exchanger Materials" NACE Corrosion/80 Paper No. 32, 1980

and the electron flow from the anodic to the cathodic site (Ti tubes) for a copper alloy heat exchanger with titanium tubes. Superferritic and 6% austenitic stainless steel tubes would behave as titanium in this arrangement.

Uhlig states that the penetration (corrosion) follows this equation:

$P = P_0 (1 + B/A)$

Where P is the penetration (corrosion) of the anodic metal of area A coupled to the cathodic metal of area B.

P_0 is penetration of the anodic metal without coupling

From these basic reactions, it can be seen that the amount of dissolved oxygen available at the cathode, the surface area of the anode and the surface area of the cathode can have a major influence on the extent of galvanic corrosion that will occur. A small anodic surface will suffer much deeper corrosion than a large anodic surface. The lack of dissolved oxygen, as in deaerated solutions, will limit the reduction reaction to the formation of hydrogen which tends to be adsorbed on the cathodic surface thus reducing the cathodic area. A large cathodic area will result in more corrosion of the anodic metal than a small cathodic area. The engineer can reduce the cathodic area by painting the cathodic metal.

These are the principal factors on which solutions to the following 30 case histories were based.

Case History Solutions To Galvanic Corrosion Problems

Condensers And Heat Exchangers

1) Tube to Tubesheet Copper Alloy Systems: The common copper alloy tubing, admiralty, aluminum brass and copper nickel are cathodic to naval brass, muntz metal and aluminum bronze, the common copper alloy tube sheet alloys. The galvanic effect is not large but is in the desired direction - protection of the more critical component, the tubing. For copper nickel , C71500 tubing can be used with C70600 or C71500 tubesheets, with a beneficial or neutral galvanic effect. C70600 tubing should be used with C70600, naval brass, muntz metal or aluminum bronze tubesheets where the galvanic effect is neutral or beneficial. Were C70600 tubes to be used with C71500 tubesheets, the galvanic effect would tend to accelerate corrosion of the inlet end. This combination is generally avoided. The author's experience has been that the galvanic effect is small, does not significantly affect performance and is generally neglected for all these copper alloy combinations except for C70600 tubes in C71500 tubesheets which is best avoided.

2) Problem: Copper Nickel Plate Type Heat Exchangers: A naval flat plate type heat exchanger of C71500 was subject to inlet end erosion-corrosion due to the turbulence pattern at the inlet end. The inlet end of the plates eroded-corroded down to a knife edge.

Solution: Plates were redesigned in a C70600-C71500-C70600 roll bonded clad plate configuration. As the C70600 eroded-corroded, the C71500 was galvanically protected achieving the desired life.

3) Problem: Stainless steel and titanium tubes; copper alloy tubesheets: When copper alloy condensers were first retubed with 6% Mo and titanium tubes, it was thought the effective cathode area would extend only a few diameters down the tubes. Surprisingly severe corrosion of copper alloy tube sheets occurred. Several studies revealed that titanium and 6% Mo tubing were so easy to polarize that the whole

the steel waster plates which had been required in his former coated waterbox - aluminum brass tubed systems. The galvanic protection afforded the copper alloy waterbox negated its inherent antifouling characteristics allowing the waterboxes to foul.

Solution: Removal of the steel waster plates allowed C70600 to regain and retain its natural antifouling characteristics.

Valves

7) Problem: Stainless steel valves in copper alloy piping: The question of how stainless steel valves in a copper nickel piping system will perform frequently is asked. One answer has been supplied by the long term performance of alloy 20 (CN7M/Carpenter 20C63) valves installed in C70600 piping on a Gulf Coast cargo vessel.

Solution: The copper nickel piping adjacent to the stainless steel valves was inspected after several years in service. Slightly more pipe wall metal loss occurred adjacent to the stainless steel valve than several diameters from the alloy valve. The galvanic effect was spread over such a large area of pipe that no threat to the 20 year life of the piping system was indicated. Refer to Figure 5.

In a controlled test, May and Weldon, found the weight loss for C70600 pipe coupled to a CN7M valve was 3.2x as great as for C70600 pipe insulated from a CN7M valve in a 2 year controlled experiment. Flow rate was 3.7fps (1.1ms) ([3])

8) Problem: Butterfly valves: The crude oil - ballast copper nickel piping system on a large tanker was fitted with a style of butterfly valves where the rubber seat was held in place with stainless steel keeper rings and did not cover the full carbon steel face of the valve. While this construction was appropriate for crude oil service, when the ballast tanks were filled with sea water the copper nickel, to steel area ratio was >20:1. Galvanic corrosion undermined the keeper rings, leading to failure and leakage.

Solution: The corroded area was machined out and rebuilt with alloy 625 filler metal which is cathodic to the copper nickel piping. After one year the rebuilt valves were in pristine condition and no increase in copper nickel piping corrosion could be detected.

Pumps

9) Problem: Saline water intake pumps: Stainless steel internals in vertical turbine intake pumps are quite resistant to the severe erosion - corrosion conditions when the pumps are operating but are vunerable to under deposit corrosion and microbial influenced corrosion when these pumps are placed on extended standby as is normal practice.

Solution: The inlet and diffuser sections, sometime the case, are made of austenitic nickel grey or dictule iron which provides sufficient galvanic protection to prevent corrosion of the stainless steel impeller and shaft while on standby.

In several cases where the inlet bell and diffuser section had been made of stainless steel depriving the impeller and shaft or protection, severe impeller and shaft corrosion occurred within the first year. Such

([3]) May, T.P. and Weldon, B.A., "Copper-nickel alloys for service in seawater" 24th International Congress on Fouling and Marine Corrosion, Cannes, France June 8-13 1964.

corrosion could have been prevented by replacing the inlet section with austenitic nickel iron. The users elected to use steel anodes in the stainless steel inlet section which were effective, but required periodic renewal.

Welds

10) Problem: Icebreaker hull welds: Welds on steel hulls and offshore oil structures are normally coated and/or cathodically protected. When coated and/or protected, little difference in the corrosion behavior of the weld metal and the base metal has been reported. Icebreakers however, abrade off coatings and strip off anodes, as they move through the ice. In the early 1960's severe weld corrosion of icebreaker hulls was reported. Investigation by International Nickel's marine corrosion laboratory indicated the matching composition filler metal normally used was anodic to and corroded preferentially to the hull plate, Figure 6.

Solution: The weld metal was changed to one contining 1% Ni insuring that the weld metal would be cathodic to the hull.

11) Problem: Rudder welds: In the 1980's the author encountered weld metal corrosion of a large steel rudder where the coating and cathodic protection were ineffective apparently due to highly turbulent conditions around the rudder.

Solution: In this case the shipowner elected to use an even more cathodic filler metal, alloy 625, to provide greater insurance of good performance under the highly turbulent conditions surrounding this particular rudder.

12) Problem: Filler metal for copper nickel: Standard practice is designed to avoid most galvanic corrosion problems. The higher nickel content alloy, 70-30 copper nickel, C71500 is welded with a near matching composition filler metal which has a slightly higher alloy content making it cathodic to the C71500 base metal. Monel filler metal which is strongly cathodic to C71500 is also used as a filler metal for C71500 and for copper nickel to steel welds.

The lower nickel content alloy, 90-10 copper nickel, C70600, is welded with C71500 filler metal which is quite cathodic to the lower nickel content alloy. Most welding rod suppliers do not offer a matching composition filler metal for the leaner C70600 alloy fearing it might inadvertently be used on C71500 with catastrophic results.

13) Problem: Filler metal for aluminum bronze: C63000 and C954000, 8% aluminum bronzes, are welded with a higher aluminum content to weld metal to prevent stress corrosion cracking. The higher aluminum content weld metal in slightly anodic to the base metal. Experience has shown the slightly anodic weld metal performs well in fabricated waterboxes, pumps and column pipes. However, some fabricators advocate using a matching composition filler metal for the final bead. While it is desirable to have the weld metal cathodic to the base metal, it is not always possible to do so as in the case of aluminium bronze. Experience is the best guide.

14) Problem: Filler metal for other copper alloys: Silicon and phosphor bronze alloys are generally welded with a matching composition filler metal. Preferential corrosion of such welds, when it occurs, is an indication that a more noble filler metal, such as copper nickel or nickel copper should be used.

15) Problem: Filler metal for stainless steels: Stainless steels do not exhibit the tendency towards galvanic corrosion of the weld metal found in steels and copper alloys. Stainless steels can be sensitized to intergrannular corrosion (IGA) if the older 0.07 or 0.08% carbon max. grades are selected for welded fabrication in lieu of the more common 0.03% carbon max. grades. The 4 1/2% and 6% Mo grades are fabricated using a higher Mo content filler metal to avoid weld metal corrosion that can occur with a matching

composition filler metal. The reduction in corrosion that occurs when matching composition filler metals are used in welding the higher molybdenum filler metals is due to segregation of molybdenum in the cast weld metal structure. Solution annealing (SA) at 2150F (C) will homogenize molybdenum. When SA is impractical a higher molybdenum content filler metals such as 625, C276 or C22 are used. Neither IGA or molybdenum segregation are due to galvanic factors, however.

Fasteners

16) Problem: Stainless steel fasteners were used to secure the aluminum awning to the store front of a building in a coastal city. The aluminum bolt holes were enlarged by galvanic corrosion allowing the awning to drop, Figure 7.

Solution: Pack the bolt holes with a lubricant that will adhere to and displace moisture from metallic surfaces at assembly. Inspect and repack as necessary. An adherent lubricant insulates the dissimilar metals, not completely, but sufficiently to markedly reduce the aluminum hole enlargement. Most lubricants are not adherent and may promote rather than mitigate such galvanic corrosion.

17) Problem: The steel stuffing box bolts in the bilge of a copper nickel hulled work boat were covered by sea water and failed by galvanic corrosion allowing water to enter nearly sinking the vessel.

Solution: The steel bolts were replaced with nickel copper alloy 400 bolts which are cathodic to copper nickel as originally specified.

18) Problem: Stainless steel fasteners in FRP hulls below the waterline fail by crevice corrosion for lack of the galvanic protection a steel or aluminum hull would have provide.

Solutions: 1) Enbed the fasteners more securely in resin so sea water will not wick into the fastener recess.
2) Use nickel copper alloy 400 bolts.

19) Problem: Brass screws holding a steel port hole fitting on a steel hulled boat failed by dezincification in heavy seas flooding the head and nearly sinking the boat before the port hole opening could be closed.

Solution: Use nickel copper alloy 400 screws.

20) Problem: Nickel copper alloy K500 and other high strength fasteners have failed in cathodically protected strucutres in sea water from the hydrogen released by the cathodic protection system on cathodic surfaces.

Solution: Avoid fasteners with > 100,000 psi tensile strength in cathodically protected structures. Use nickel copper alloy 400 fasteners.

The following guidelines are helpful in selecting fasteners

1 Select fastener material that is cathodic to all other metals in the assembly.

2 Avoid use of fasteners with >100,000 psi tensile strength in structures that are, or may be, cathodically protected at sometime in their useful life.

3 Avoid brass screws that are subject to dezincification. Although steel will galvanically protect copper and bronze, steel is not alway effective in preventing dezincification of high zinc brasses.

4 Good performance of stainless steel fastener materials is dependent upon galvanic coupling with steel or similar anodic substrates to prevent crevice corrosion.

5 In the atmospheres or low conductivity fluids such as fresh water where galvanic effects are limited to the immediate area of the junction between the fastener and substrate, failure by hole enlargement can be just as serious as failure of the bolt itself.

Hull Related Cases

21) Problem: Deep corrosion occurred in the steel hull adjacent to the weld joining the nickel copper alloy valve body to the hull in the bell shaped inlet of an older type submarine hull cooling water intake, Figure 8. The hull cathodic protection system was not effective in preventing localized corrosion in this deep recess and could not easily be modified to do so.

Solution: The coating was removed from the bell mouth by sandblasting, enlarging the anodic area and spreading the corrosion over a larger area thus reducing the depth of attack.

22) Problem: A nickel copper alloy pipe passed through a well coated steel ballast tank on an older type submarine. Deep corrosion of the steel bulkhead occurred adjacent to the nickel copper pipe to steel weld where the coating tended to fail over the rough pipe to bulkhead weld. Rewelding and recoating of the repaired area only moved the problem to the area just beyond the repair weld, Figure 9.

Solution: Coating the nickel copper alloy pipe reduced the cathodic area and extended the yearly inspection for repairs to a more acceptable 5 plus, year period. This is a classic case of coating the more durable cathodic material to reduce galvanic corrosion.

Note: The 1981 Edition of the Naval Technical Manual "Preservation of Ships" Chapter 631 Section 7.107 now requires "Monel, copper nickel and other alloy pipes to be coated so as to minimize galvanic corrosion of steel at alloy pipe to steel bulkhead welds."

23) Problem: Electrical connectors: Electrical connectors are required to supply power to the winches and other equipment external to the hull and under the shroud of submarines. This equipment operates in sea water. Type 316 through hull connectors are standard for this service. Each is welded to the hull to maintain hull tightness and integrity. The steel hull and its cathodic protection system prevent crevice corrosion of the type 316 electrical connectors that would occur in the absence of protection.

24) Problem: Stainless steel propellers: Stainless steel is subject to crevice and under biofouling corrosion in coastal waters. Type CF3 propellers have, nevertheless, been used successfully since 1952 and are standard for coastal tugboats, towboats and workboats in the U.S. Blades are straightened and weld repaired routinely. Stainless steel is quite resistant to velocity and turbulence while these work boats are in operation. The steel hull and its cathodic protection system provide sufficient galvanic protection to prevent crevice corrosion of the stainless steel propellers while these craft are in port and idle. The low carbon permits weld repair without sensitization.

Partial Linings

Partial stainless steel linings are installed in steel tanks and vessels by weld overlay, metal spray or sheet lining. The author has encountered galvanic corrosion at the termination of the lining and at piping that passes through the lined area. The nature of the electrolyte modifies the galvanic effect.

Galvanic corrosion has occurred at

I The termination of lining above the liquid in the vapor zone.

II The termination of lining below the liquid level.

III Carbon steel piping passing through the stainless steel lined section of tank. Refer to Figure 10 and sections A, B & C.

25) Problem: I Vapor Zone: Termination of lining above the liquid in the vapor zone. Galvanic corrosion results in a groove in the steel adjacent to the alloy termination weld, Figure 10 Section A. The anode to cathode area is approximately 1:1. The groove deepens slowly with time.

Solution: Yearly monitoring and rewelding when the depth of groove warrants is the normal remedial measure.

26) Problem: III Liquid zone: Carbon steel pipe penetrating the lined portion of the tank wall.

Galvanic corrosion leads to corrosion of the steel pipe at the junction with the alloy lining. Figure 10 Section B.

Solutions: 1) Replace with stainless steel piping.
2) Coat the stainless steel liner to reduce the cathodic surface and minimize corrosion of the steel piping.

27) Problem: II A.1 Liquid zone: Termination of lining below the liquid level in a poorly conducting electrolyte such as fresh water. Tank uncoated below lining.

A deep groove forms in the steel just below the alloy to steel weld, Figure 10 Section C-A.

Solution: Yearly rewelding of the groove is often necessary. The groove reforms just below the rewelded area if alloy filler metal is used; in the rewelded area if carbon steel filler metal is used.

28) Problem: II A.2 Liquid zone: Termination of lining below liquid level in alkaline paper mill liquor.
Tank wall coated below partial lining.

Deep localized corrosion can occur in areas where the coating may be scratched, damaged or where localized coating failure occurs over weld metal or surface irregularities. Through wall corrosion and leakage can be anticipated at breaks in the coating within a year or so. Figure 10 Section C-B.

Solution: 1) Supplemental cathodic protection in the lower portion of the tank will prevent corrosion at breaks in the coating.
2) Coat the cathodic surface, the stainless steel liner, to reduce the cathodic surface and minimize corrosion at breaks in the coating.

29) Problem: II A3 Liquid zone: Termination of lining below the liquid level in an alkaline paper mill liquor, a highly conductive electrolyte. Tank uncoated below the partial lining.

Metal loss is spread out over a large area of the carbon steel. It is difficult to measure the slightly greater metal loss adjacent to the lining, Figure 10 Section C-C.

Solution: Yearly monitoring is normally all that is required.

Carbon - Graphite

30) Problem: Graphite or carbon filled gaskets and packing: Severe pitting corrosion of stainless steel and copper alloy valve stems, pumps shafts and flange faces in contact with graphite/carbon filled non metallic

packing, gaskets and lubricants.

Most black or dark packings, gaskets and lubricants contain graphite/carbon which is quite noble (cathodic) to copper alloys and stainless steels. In saline waters severe pitting corrosion has occurred where such materials come in contact with copper alloy or stainless steel valve stems, pump shafts or flange faces.

Solution: Ban graphite filled non metallic packing and gaskets in brackish and saline waters. Only occasional problems have been reported in fresh waters.

Summary

1) When two dissimilar metals are in contact, corrosion of one will be increased and corrosion of the other will be retarded. Galvanic corrosion can be successfully managed and made to works towards, rather than against, durability of the assembly by understanding and utilizing the principles that govern galvanic corrosion.

2) Increasing the anodic area (by removing any coating) will allow the corrosion to be spread over a larger area below the liquid level in a conductive fluid. Increasing the anodic area in a poorly conductive fluid or above the liquid level is ineffective.

3) Painting the cathodic area will reduce the effective cathodic area and reduce corrosion of the anode in a conductive fluid.

4) Selecting cathodic materials, often highly cathodic materials, for fasteners, for weld filler metals and for the critical component of an assembly such as a pump or valve will take advantage of the galvanic effect, making the assembly more durable.

5) The cathodic member of a couple can initiate damaging corrosion of bolt holes, tubesheets and coated anodic surfaces.

6) The cathodic member can be damaged by the hyrodgen released on cathodic surfaces in cathodically protected structures and in some galvanic couples.

7) Avoid use of graphite filled packing and gaskets in brackish and saline waters.

Acknowledgement

The author wishes to express appreciation for the support of the Nickel Development Institute in preparation of this paper.

References

1. Uhlig, H.H., "Corrosion Handbook" John Wiley and Sons, 1947

2. Gehring, G.A. Jr., Kuester, C.K. and Maurer, J.R. "Effective Tube Length - A Consideration on Galvanic Corrosion of Marine Heat Exchanger Materials" NACE Corrosion/80 Paper No. 32, March 1980

3. May, T.P. and Weldon, B.A., "Copper-nickel alloys for service in seawater" 24th International Congress on Fouling and Marine Corrosion, Cannes, France June 8-13, 1964

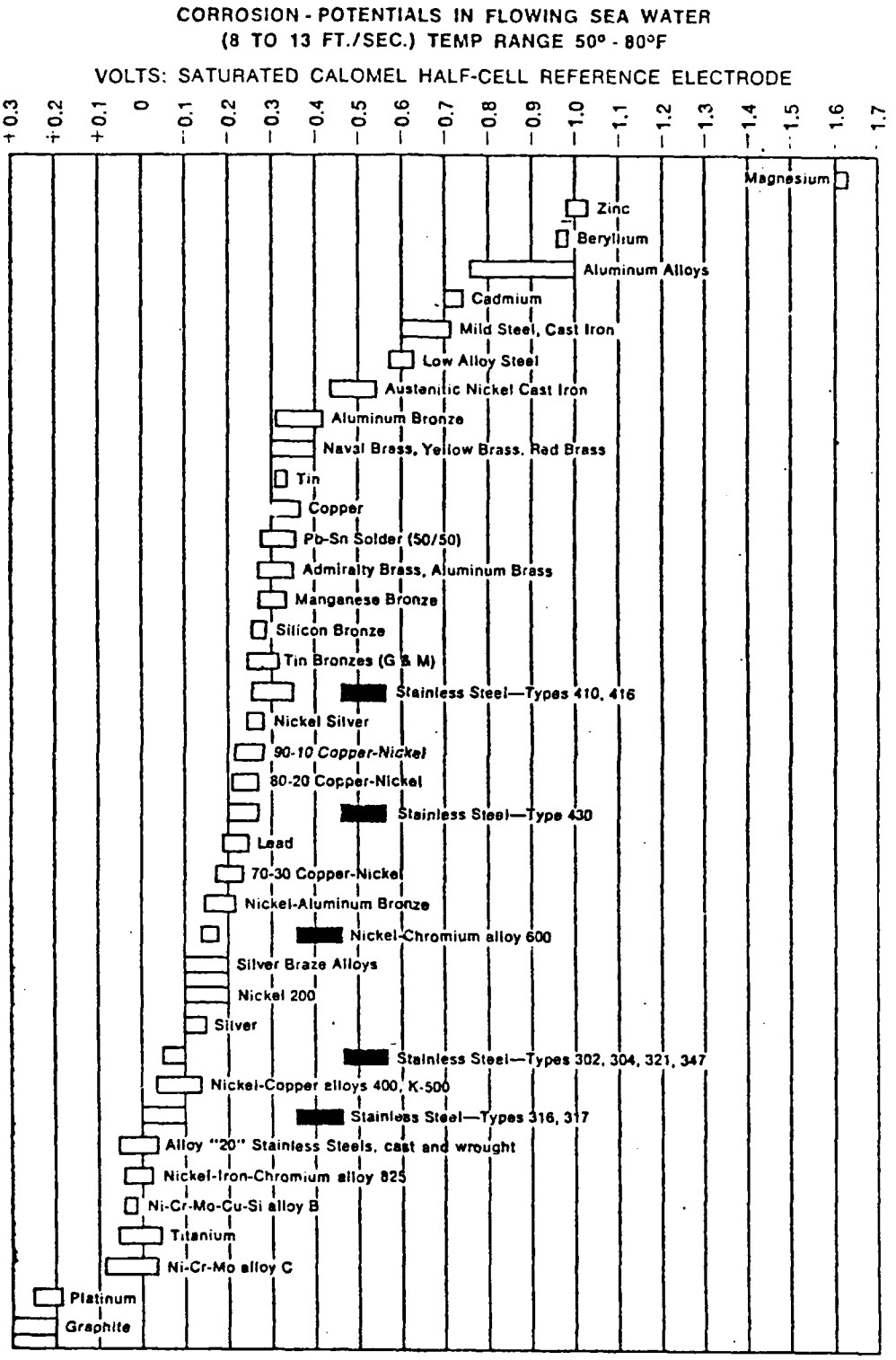

Alloys are listed in the order of the potential they exhibit in flowing sea water. Certain alloys indicated by the symbol: ▬ in low-velocity of poorly aerated water, and at shielded areas, may become active and exhibit a potential near -0.5 volts

Figure 1 Galvanic Series - Flowing Seawater (INCO)

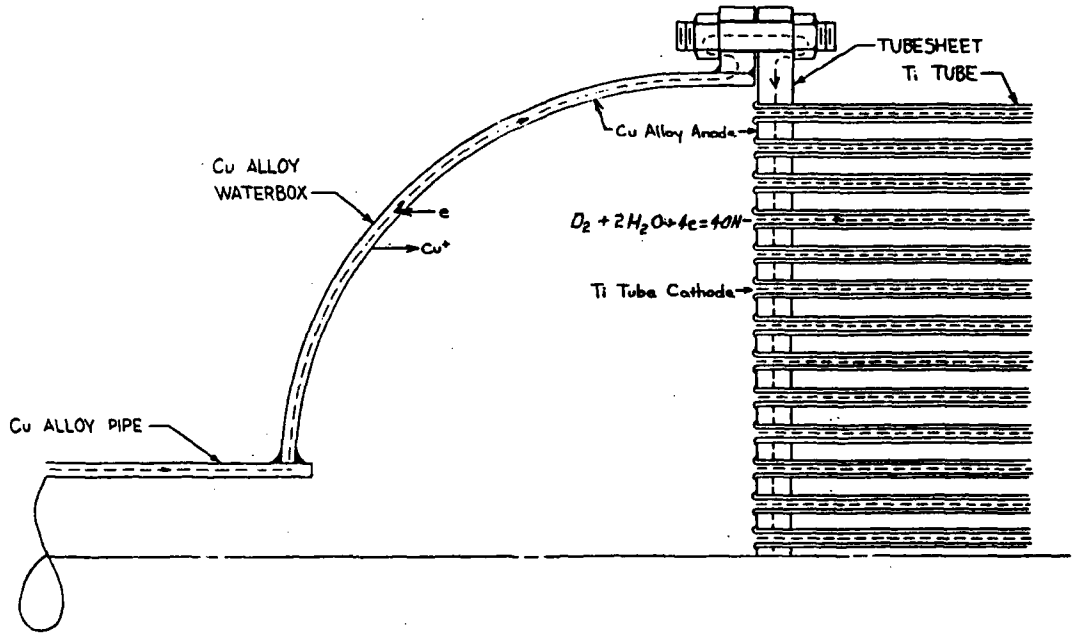

Figure 2 Upper half of waterbox and inlet end of a condenser or heat exchanger

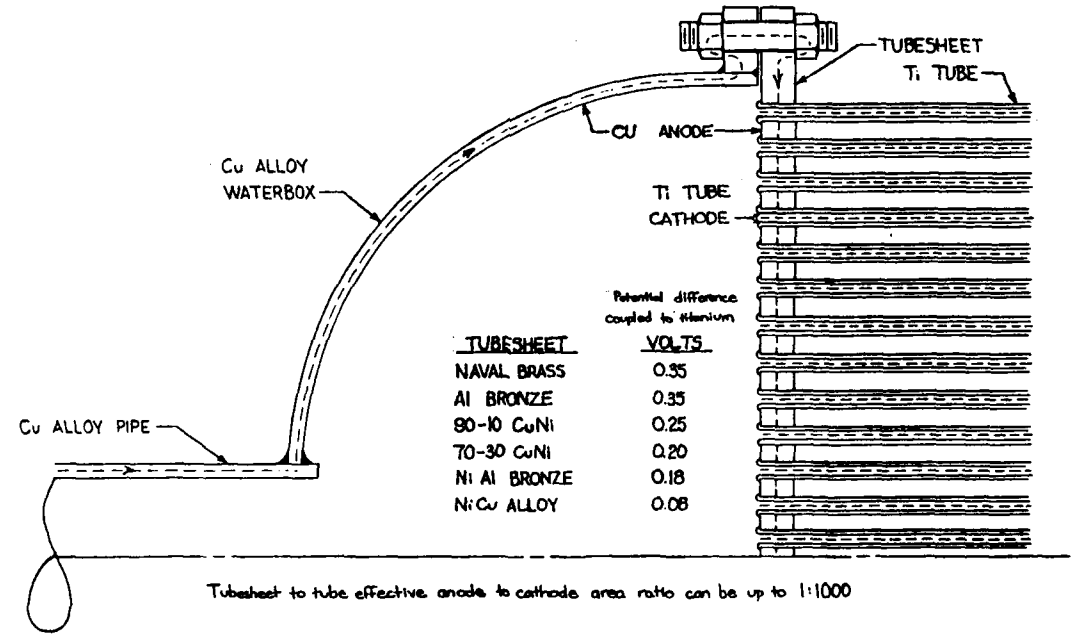

Figure 3 Upper half of waterbox and inlet end of a titanium tubed copper alloy condenser of heat exchanger. The adverse area ratio overwhelms the differences in potential.

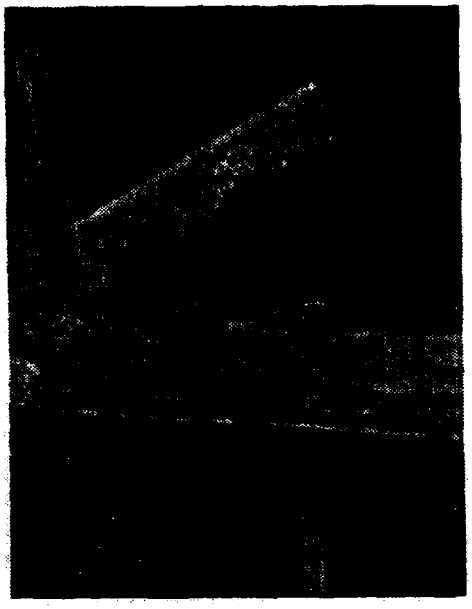

Figure 4 Deep pitting in coated steel waterbox in a desalintion heat exchanger with C70600 tube sheet and tubes - 6 months

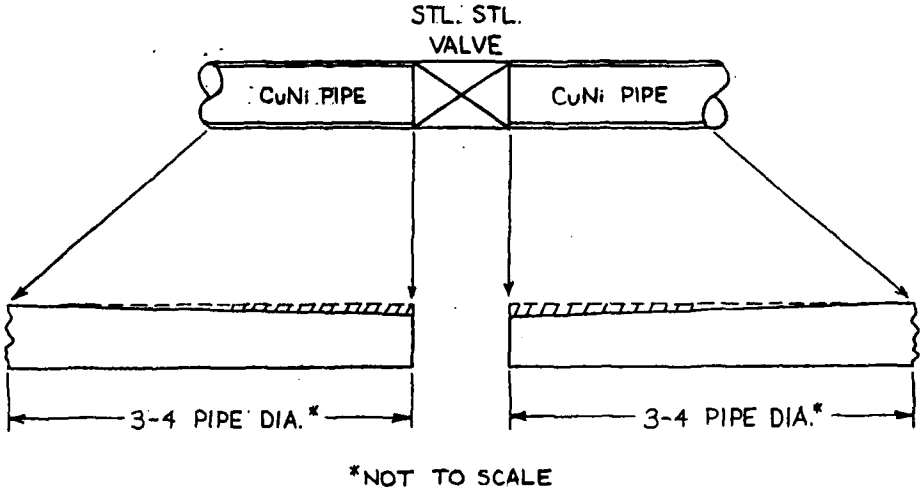

Figure 5 Metal loss patgtern in CuNi pipe adjacent to SH. SH. valve (seawater)

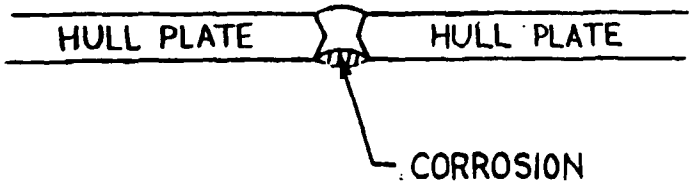

Figure 6 Corrosion of hull plate weld with CP (seawater)

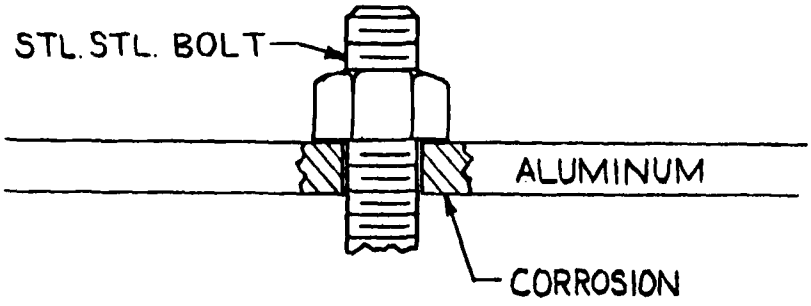

Figure 7 Corrosion enlarges aluminum bolt hole
(Marine atmosphere)

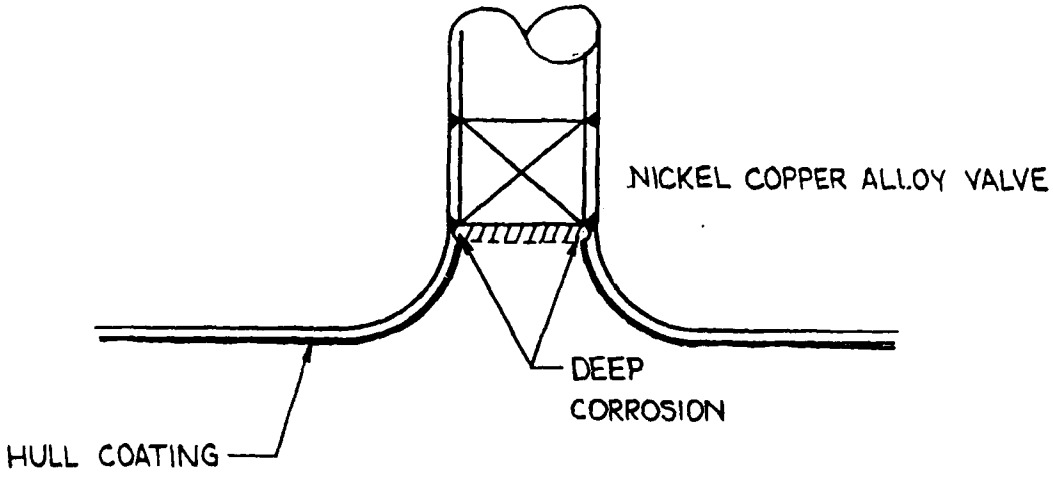

Figure 8 Deep corrosion in hull adjacent to nickel copper alloy to steel hull weld (seawater)

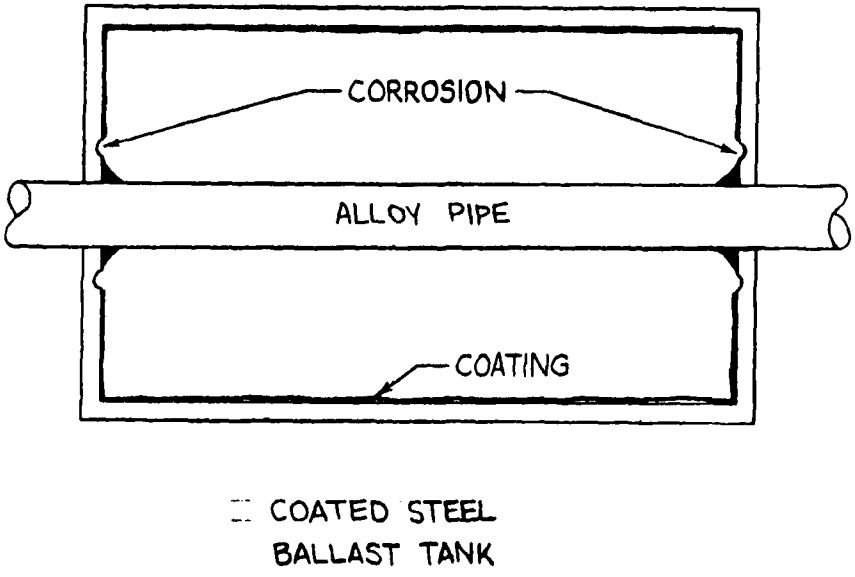

Figure 9 Corrosion of steel bulkhead adjacent to alloy pipe to bulkhead weld

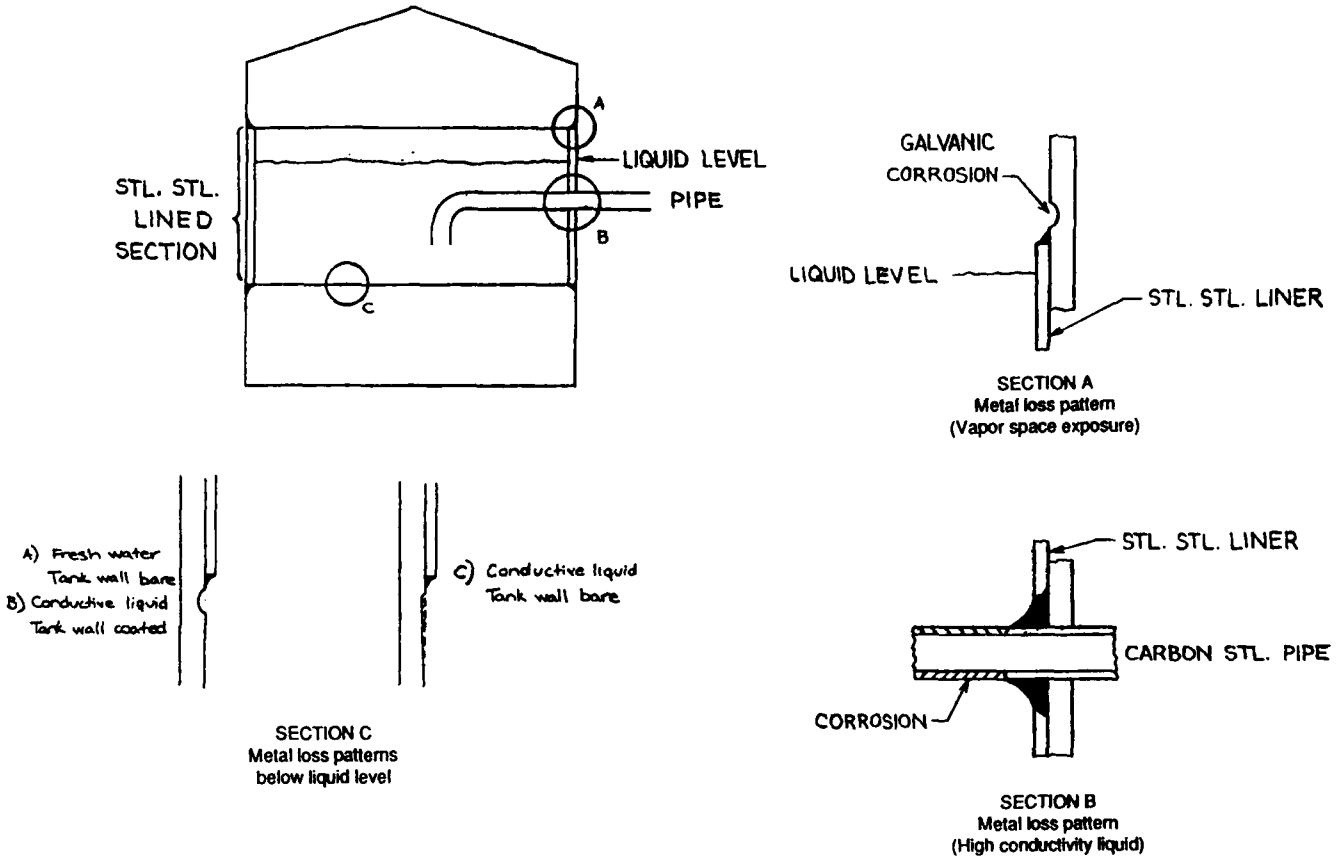

Figure 10 General arrangement of a tank with a partial SH. SH. liner in the area of the liquid level

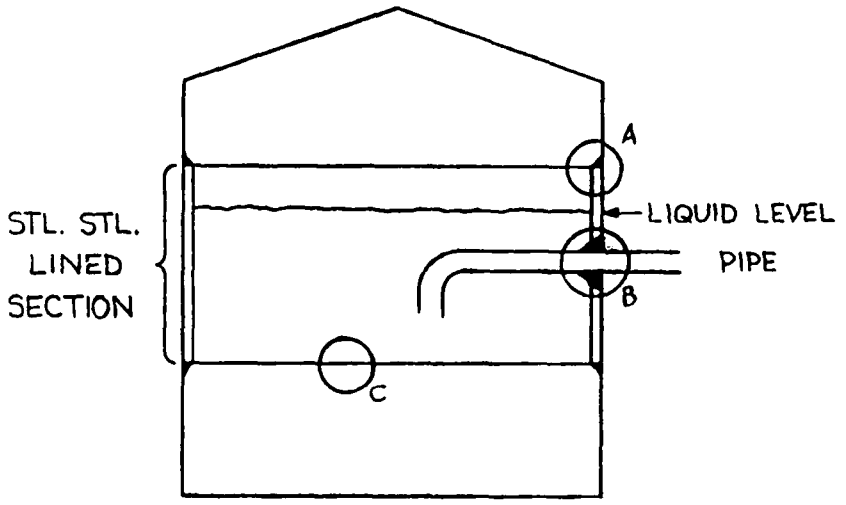

Figure 10 General arrangement of tank with a partial stainless steel liner in the area of the liquid level

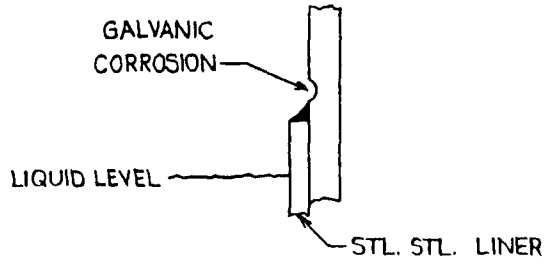

SECTION A OF FIG. 10
Metal loss pattern above liquid level
(Vapor space exposure)

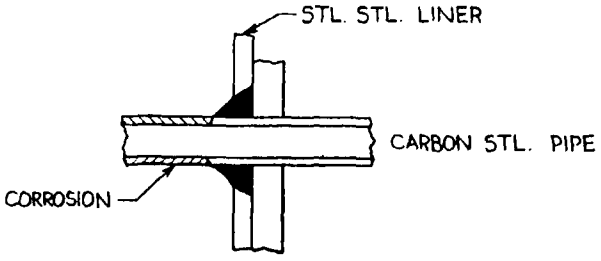

SECTION B OF FIG. 10
Metal loss pattern - carbon steel pipe passing
through stainles steel liner below liquid level
(High conductivity liquid)

A) Fresh water
Tank wall bare

B) Conductive liquid
Tank wall coated

Conductive liquid
Tank wall bare

SECTION C OF FIG. 10
Metal loss patterns
below liquid level

Combination of acoustic emission and electrochemical techniques in erosion-corrosion studies of passive stainless steels in acidic media.

L. RENAUD
Creusot-Loire Industrie, BP 56
71200 LE CREUSOT- FRANCE

B. CHAPEY, R. OLTRA
URA CNRS 23 Réactivité des Solides
BP 138 21004 DIJON- FRANCE

Abstract

This study has been conducted to investigate the ability of acoustic emission techniques (AE) to measure the frequency of the mechanical impacts of slurries flowing in aqueous solution, their distribution in energy and the total mechanical wear.The mean idea is to be able (during erosion-corrosion experiments) to separate the two individual contributions.
RMS AE signals are used to obtain the integrated value of the mechanical wear and the instantaneous rate of abrasion. The integrated RMS AE signals give an estimation of the total mechanical wear during the abrasion experiments in corrosion media and enable to study the synergy between the corrosive damage and abrasive wear. It can be concluded that RMS AE signals provide a new tool to measure the rate of mechanical abrasion in a slurry jet test apparatus. The experimental results concern the behavior of passive stainless steels in acidic media (sulfuric acid).
Concerning materials behaviour, it is shown that :
- an austenitic, a superaustenitic and a duplex grade have almost the same pure erosion rate.
- corrosion rate is directly dependant on erosion rate
- corrosion resistance of stainless steels is mainly due to corrosion resistance i.e. the ability for a material to repassivate after high impact fluxes and subsequent local depassivations.

Key terms : erosion-corrosion, stainless steels, acoustic emission, sulfuric acid.

INTRODUCTION

Degradation of the materials due to the combined effects of erosion by particles and corrosion, has an enormous economical impact. There are indeed a great number of industries that are subjected to this type of degradation. For example : hydrometallurgy and phosphoric acid production plants which necessitate an attack step where ores are dissolved in hot concentrated sulfuric acid, mining industries, oil and marine industries and also all the chemical industries which are handling corrosive fluids containing abrasive particles coming either from the reactants or from a precipitation due to chemical reactions.

A lot of equipement are subjected to erosion-corrosion such as : vessels, agitators, pumps, impellers and all the pipes and tubes that handle these fluids. Product forms are also of various types such as plates, tubes and forged or cast pieces.

It has to be mentionned that erosion-corrosion phenomena are not well understood today. As a consequence, most of the people have the tendancy to choose a "hard" material as resistant material. It will be shown in fact that, under erosion-corrosion, the higher the corrosion resistance, the higher the resistance to erosion + corrosion. Another consequence of this misunderstanding of erosion-corrosion phenomena is the great difficulty to choose the right material for a given application. This leads to the fact that these equipments are considered as "consumable equipments". A lot of money could be saved by an adequate selection of the materials.

These behaviors are to be attributed to the high complexity, of erosion-corrosion phenomena which falls itself from the great number of parameters governing hydrodynamic, mechanical, metallurgical, chemical and electrochemical aspects of erosion-corrosion.

In previous works, it could be shown that the corrosion of a given material is governed by the erosion rate (1,2). This can be easily understood if one considers that the resistance of a material under erosion and corrosion is mainly related to the ability of its passive film to be restored after local breakdowns.
Two important parameters arise from this approch : the frequency of impacts which influences the depassivation rate and the energy of the impacts which controls the volume of matter affected by each impact. The knowledge of the erosion regime is then very important but not easy to achieve. This paper presents the development of a new technique based on Acoustic Emission (AE) which allows the quantification of the erosion regime through the measurement of the kinetic energy fluxes of particles in a flowing corrosive fluid.

EXPERIMENTAL

Erosion setup

The slurry jet apparatus used in this study is based on an "impinging jet" device.The flow velocity of the corrosion electrolyte (9 m.s-1) is controlled by the pressure in the loop.The impinging jet is designed so that the main impact angle of the abrading particle (SiC 500 µm) is 90°.
The mechanical damage is estimated in a non-aggresive environment : Na_2SO_4 0.1 M under cathodic protection (-1900 mV/SSE). The mechanical damage is a function of various physical characteristics of the slurry-jet as determined by the frequency of the impacts and the energy distribution of the particles.

Materials

The erosion experiments were performed on various stainless steels : a classical 316L

austenitic grade, an economical duplex grades (UNS S32304) containing 23 % Cr-4 % Ni and superaustenitic grades : the reference one 904L (UNS N08904) and a high corrosion resistant grade (UNS N08932). The chemical compositions are given in table 1. All the erosion experiments in corrosive environment were conducted in a Na_2SO_4 1M solution at 25°C.

Development of an acoustic emission device

The use of an acoustic sensor is not largely widespread for abrasion experiments with a flowing slurry suspension. Some attempts have been proposed to characterize the abrasive wear in lubricated sliding contacts (4).
Acoustic emission (AE) was also previously proposed as a method of monitoring hard particle impact on metallic surfaces by analysing AE signals (burst emissions) with a broad bandwith piezoelectric transducer positioned on the opposite face of the target. Quantitative analysis of the AE signals allowed to size the particles (5).
This study deals with the measurement and the subsequent signal analysis of acoustic emission from impinged metallic target in aqueous corrosive environment.
It has been assumed that mechanical stresses induced by the impact of a particle in suspension in the flowing fluid, generates an ultrasonic wave. Then for each particles impact, the AE signal consists of a single burst emission. During erosion experiments, the summation of the counts, which is achieved by counting the number of times the AE signal crosses a preset trigger level voltage, can be correlated the erosion rate.

Fig.1 summarizes all the possibilities offered by this technique. Fig. 1a shows two particles impact AE signals and Fig. 1b shows the corresponding electrochemical response of the material (current density under polarization).
By recording these signals during all the experiments, we should be able to quantify the erosion regime (frequence of the impacts, energy of the impacts) and the "harmfulness" of the impacts (corrosion current).

As the erosion can also be considered as a pseudo-continuous phenomenon, the RMS AE signal might be expected to provide information about the total mechanical erosion.
A Europhysical Acoustic (bandwidth 350-1200 kHz) sensor is coupled with PTFE grease to the stainless steel target (Fig. 2a). The output signals can be amplified if necessary. The signal is transmitted directly to a digital oscilloscope to trigger the electrochemical transient response. On the other hand it is transformed by a RMS device the output of which is connected to a Digital Audio Tape recorder (sampling rate 48 kHz).
After recording (maximum 2 hours duration), the RMS AE signal is computed by a 486 computer in order to calculate an integrated value and to count the events. This device is presented in Fig. 2b. Its main advantages are the possibility of long duration recordings allowing the detection of all possible modification in the erosion or corrosion regimes and the possibility to easily transport the device on industrial sites for in-situ measurements owing to its compacity (no nead of the computer for recording).

EXPERIMENTAL RESULTS

Acoustic emission

Acoustic emission transients arise from each particle impact. The AE response can be processed in two ways :

* burst emission : the AE response can be used as a trigger for the electrochemical records

* RMS signal : the RMS AE signal allows to quantify the mechanical erosion, i.e., its amplitude and its rate (after calibration).

AE burst emission

The AE signal has been recorded for single impact. As shown in Fig. 1, the acoustic signal can trigger the record of the electrochemical response. This experiment permits the definition of the threshold of the time interval between two consecutive impacts.
On the other hand experimental studies were conducted to establish a correlation between the electrochemical response and the acoustic burst emissions for various kinds of abrading particles (SiC, glass beads...). From these results it was concluded that the acoustic response is correlated to the nature of the mechanical damage and that the corresponding electrochemical response is correlated to the shpe of the particle (6).

RMS AE signal

The frequency range of each acoustic burst is in the domain of 1 MHz, the continuous emission of the AE signals during continuous erosion was then not possible to record.
The RMS value of the initial AE signal is a conventional technical solution falling in the range of 10KHz for the continuous recording of the individual bursts. Compared to previous applications of AE techniques (4), the time constant of the RMS component was reduced to 140 ms. The Fig.3 shows a characteristic fluctuating RMS AE signal due to the accumulation of consecutive impacts.
To check the validity of the RMS measurement which is assumed to give a value proportional to the energy of the mechanical impact, the RMS AE signal variation was studied as function of a well-controlled mechanical damage. For impacts due to glass beads, the peak value of the RMS signal is proportional to the square root of the kinetic energy of the particle (6).

Relation between RMS AE signal and pure mechanical removal

Erosion tests (1 hour duration) were conducted in the following conditions :

* abrading particles : SiC 500 µm
* electrolyte : non-agressive environment.

Then the pure mechanical removal is correlated to the RMS AE signal. As shown by other authors for abrasive wear (4), the total integrated RMS signal can be plotted as function of the mass loss measured after the erosion test conducted with various concentrations (g/l) of abrading particles. Results for the tested duplex stainless steel are shown in Fig. 4. The total wear is defined at the end of the erosion experiment by measuring the mass-loss.
This type of diagram is important since it definies the relation between the erosion conditions (kinetic energy flux) and the corresponding mass loss. It should be noted that this curve is plotted for a given particles nature and size distribution. By varying these parameters, series of curves could be plotted and usable after in-situ AE recording.

Fig. 5 shows once more the interest of the AE device. If the mass-loss due to erosion is plotted versus particles concentration, one can note the diminution of mass-losses when particles concentrations increases. This is due to the interactions between the particles in front of the materials surface. Now if this mass-loss is plotted versus AE signal (i.e kinetic energy fluxes) one can note a linear relationship. This means that the A.E. sensor indicates what the material actually received as energy, taking into account all the modifications that can arise in a circuit (thickening of particles, great amount of particles...). This method is then much more powerfull than methods quantifying the fluid itself.

Fig. 6 presents the integrated value for various particle concentrations versus mass-loss for three stainless steels : a 316 L austenitic, a super austenitic grade (UNS N08904) and a duplex grade (UNS S32304). It can be seen that in a large erosion domain (from 5 to 50 g/l of 500 µm dia. SiC particles), the 3 grades are quite similar.

Determination of the impact frequency

During experiments conducted for various concentrations of abrading particles (3g/l to 40g/l), RMS AE signals are transmitted to DAT recorder. They are counted by computing the RMS signals peaks to define the mean rate of impacts. Assuming the mechanical wear proportional to the mean rate of impacts, the variation of the mechanical wear can be plotted as function of the computered number of RMS peaks per time unit (Fig.7).

At concentrations of abrading particles higher than a given value in the flowing fluid, a limit is reached for the speration in time of two RMS peaks (see Fig.7 : limit of RMS) while the relation between the wear and the integrated RMS signal (Fig.4) remains valid for this high value of the concentration of abrading particles. It confirms that only the integrated RMS value can be correlated to the mechanical wear for high level of the abrading rate (impacts per time unit).

Corrosion experiments

During erosion tests in corrosive media the main problem is the definition of the balance between, respectively, the mass-loss due to corrosion and the mass-loss due to mechanical damage. To illustrate this phenomenon, erosion experiments in corrosive environment were carried on a duplex stainless steel target instrumented with the AE sensor. During the test, the sample is under potentiostatic control at +0.2 V/SSE (in the passive range) in H_2SO_4 1M.

After measuring the total mass-loss during the erosion+corrosion test, it is possible through the curve plotted in Fig. 4, to estimate the mass-loss due to mechanical abrasion. Then by difference between the total mass-loss at the end of the erosion test and the mechanical wear, the mass-loss due to corrosion can be directly calculated as shown in Table II.

For the aforementioned experiments, the abrading conditions fall in a range for which an acceptable correlation is found between the faradaic estimation and the corrosion mass-loss allowing the comparison of different materials behaviours. These results are in agreement with results obtained on various metal-electrolyte systems as shown in a previous paper (1).

For high level of erosion (high value of the mechanical wear) the corrosive mass-loss can no more be estimated by calculating the electrical charge found during the abrasion test. This typical behavior of passive materials was explained by taking into account the role of the electrical couplings between the impinged areas and surrounding areas (1).

In this case the comparison of different stainless steels is not easy. One possible way is to perform polarization resistance measurements under erosion with quantified erosion rates. By this approach, the corrosion rate cannot be calculated, but a ranking of the materials is possible since in first approximation polarization resistance gives the overall resistance of the passive film under erosion. Fig. 8 presents the results obtained on 316 L austenitic, UNS N 08932 superaustenitic and UNS S32304 duplex grades stainless steels. It can be seen that for all the grades, increasing the erosion rate decreases the overall stability of the passive film. It can also be seen that a highly corrosion resistant grade (UNS N 08932 25 Cr - 25 N - 5 Mo - 0.2 N - 1.6 Cu) has a higher resistance to erosion/corrosion than that of a 316 L grade at each erosion rate (polarization resistance almost 10 times higher). This is to be compared to the behavior under pure erosion where austenitic, superaustenitic and the duplex grade have approximately the same behavior. This underlines the role of alloying elements for a given corrosive medium.

We have already obtained similar results which allowed to classify some stainless steel grades (7).

DISCUSSION

The main applications of the AE technique in erosion experiments conducted with an impinging slurry-jet apparatus can be summarized as follows :

i) real-time evaluation of the abrading conditions,

ii) calculation of the mechanical wear.

Regarding the first application, the record of the RMS AE signals during the erosion test can be used to follow any change in the abrading conditions (6). This later point was not presented in this paper. On the other hand the continuous recording of the integrated RMS signal allow to establish the influence of the erosion rate upon the synergy between the mechanical and corrosive damages.
For passive materials, two conclusions, related to the influence of the rate of erosion can be formulated :

i) firstly for the same total mechanical wear on two separated samples, the level of corrosive damage is a function of the rate of abrasion,

ii) secondly is has been show (especially in free corroding conditions) that the repassivating kinetics of the corrosion system in connection with the duration of subsequent particle impact determine the corrosion rate (1,2). In the case of a continuous abrasion in free potential conditions (3), the controlling parameter is the overlapping of the individual potential transients. This overlapping depends on the ratio between the frequency of the impacts and the time constant of the slower electrochemical step.
For a high impact frequency the potential of the metallic surface falls to the "corrosion potential". In other words the system can move (or not) from the passive state to the active state as function of the erosion rate, consequently inducing a large change in the corrosive rate().
The measurement of the RMS AE signal could enable the validation of these empirical assumptions.
In the present study the second one was checked by coupling an acoustic sensor to the target during erosion experiments conducted in free potential corrosion conditions. As shown in Fig.9 the change in the electrochemical potentiel from the passive range (steady-state in absence of erosion) to the active range is directly connected to erosion rate determined by its integrated value (integrated value of the RMS).
Work is in progress to correlate the time evolution of the potential transients and the instantaneous erosion rate measured by counting the peaks of the RMS AE signals. So that it will be possible to confirm the control of the erosion rate upon the corrosion rate, related to the ratio between the impact frequency and the repassivation rate.

CONCLUSION

Erosion-corrosion is a great economical problem since it renders useless a lot of costly equipments. The study of erosion-corrosion is not easy due to the number of parameters involved and due to the difficulty in separating the two contributions : erosion and corrosion. It is nevertheless necessary to do this separation of stainless steels since corrosion in acidic media is governed by the erosion rate due to particules. A nrew technique based on A.E was then developed which allows the quantification of the erosion rate. This device would be easily used for in-situ measurements.
The main problem encountered in the use of AE in erosion experiments was related to the accumulation of the individual burst emissions at a high frequency rate. This problem has been solved by processing the RMS value of the AE signals recorded during all the erosion experiment, i.e., an average time of two hours.
Preliminary results have been obtained for the counting of the mechanical events from time evolution of the RMS signal. These experimental resuits confirm that the fluctuations of potential of an abraded passive surface, in connection with the repassivating kinetics, are related to the frequency of the impacts.
The most important result of this study concerns the measure of the mechanical wear during erosion experiments in corrosive media. RMS AE signals are due to the mechanical impacts of slurries and the peak value of RMS signal is directly proportional to the root square of kinetic energy of the particle.
There is a direct linear relation between integrated RMS and wear of material. This

integrated RMS AE signal gives an estimation of the total mechanical wear during the erosion experiments in corrosive media and allows to study the synergy between the corrosive damage and abrasive wear. It can be concluded that RMS AE signals provide a new tool to measure the rate of mechanical abrasion in a slurry jet test apparatus.
One more important result concerns the materials. It was shown that under the tested erosion-corrosion conditions the resistance of a material is mainly due to the stability of the passive film i.e to the chemical composition of both materials and medium. At either low or high erosion rates, in corrosive media, superaustenitic grades perform better than a 316 L grade even if the pure erosion rates are similar.

Aknowledgement
Tis work has been financialy supported by the "Conseil Régional de Bourgogne".

References

(1) R. OLTRA, "Electrochemical aspects of localized corrosion during abrasion of passive iron-based alloys in acidic media", Wear-Corrosion Interactions in Liquid Media, Edq. A.A. Sagues and E.I. Meletis, T.M.S, p.3-18, 1991
(2) U. LOTZ, M. SCHOLLMAIER, E. HEITZ, Werkstoffe und Korrosion, 36, 163 (1985)
(3) J.C. BOSSON "Etude des phénomènes d'abrasion-corrosion sur les aciers inoxydables", thèse de doctorat, mention chimie-physique, université de Bourgogne, 1992.
(4) R.J. BONNESS, S.L. McBRIDE, "Adhesive and abrasive wear studies using acoustic emission techniques", Wear, 149, 41 (1991)
(5) D.J. BUTTLE, C.B. SCRUBY, " Characterisation of particle impact by quantitative A.E", Wear, 137, 63 (1990)
(6) R. OLTRA, B. CHAPEY in preparation.
(7) L. RENAUD, B. CHAPEY, J.C BOSSON, R. OLTRA, "Erosion-corrosion properties of stainless steels", Duplex Stainless Steels 91, Vol 2, p 939-946.

grade	structure	C	Cr	Ni	Mo	N	Cu
AISI 316 L	austenitic	<0,03	16/18	10/13	2/2.5	-	-
UNS N08904	super austenitic	<0,02	20	25	4,3	-	1,5
UNS N08932	super austenitic	<0,02	25	25	5	0,2	1,5
UNS S32304	austeno ferritic	<0,03	23	4	-	0,09	-

Table 1 : Chemecal composition of the different stainless steels (weight %)

concentration SIC (g/l)	integrated RMS (V.s)	mechanical wear (mg) calculated from RMS	total mass-loss (mg)	corrosive mass-loss (mg)	corrosive mass-loss calculated from Faraday's law (mg)
3	27	2,20 ± 0,01	2,32 ± 0,01	0,12 ± 0,01	0,10
4,5	47	3,65 ± 0,01	3,85 ± 0,01	0,20 ± 0,01	0,17

Table 2 : Experimental results for an abrasion experiment in a corrosive media (abrasion of the tested duplex stainless steel (UNS S32304) in H2SO4 1M, at imposed potential E= + 0,2 V/SSE)

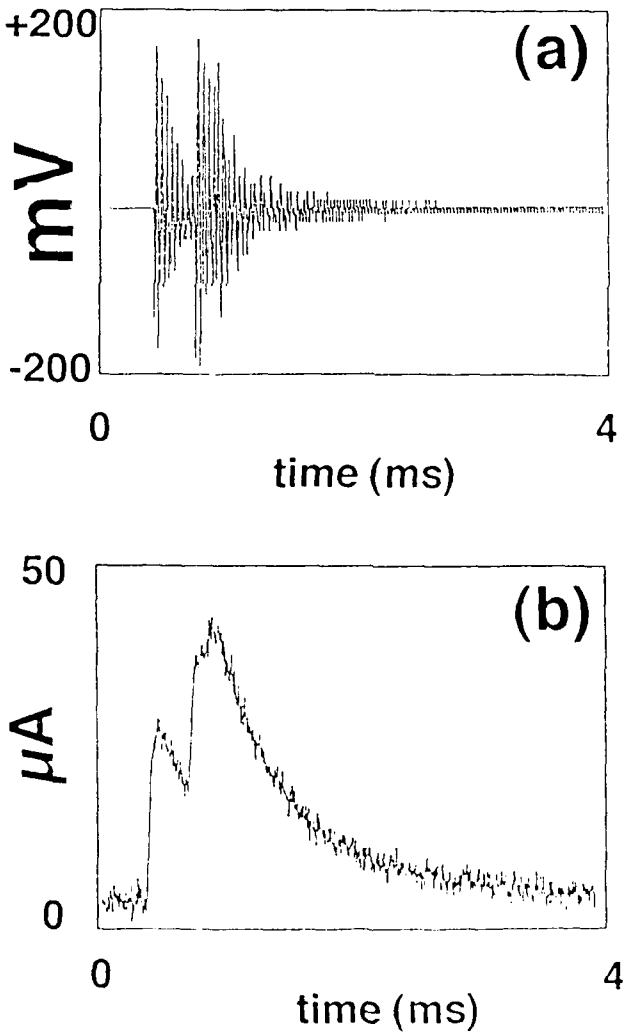

Fig. 1 : Comparison between the burst acoustic emission and electrochemical transients for two consecutive impacts

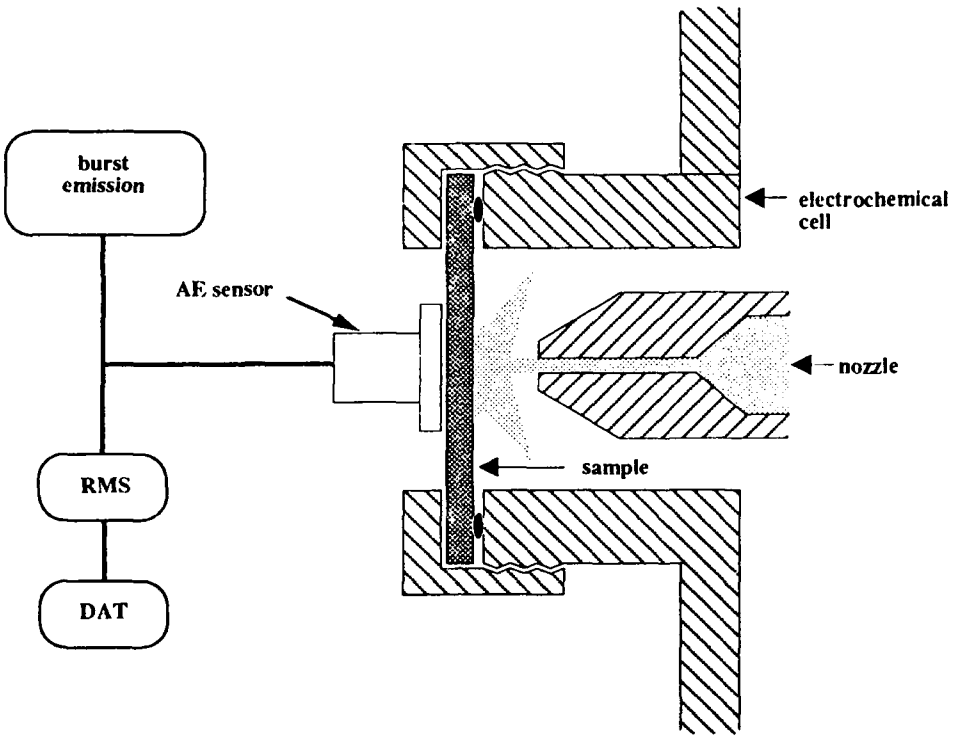

Fig. 2a : Experir ntal coupling of acoustic emission sensor with the sample

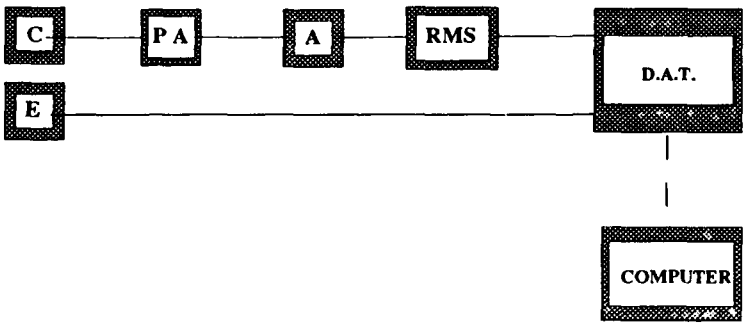

C : Acoustic emission Sensor
P.A : Pre-amplifier
A : Amplifier
E : Electrochimical measurements
D.A.T : Digital Audio Tape

---- : can be disconnected during experiments

Fig. 2b : Acquisition and signal treatment device

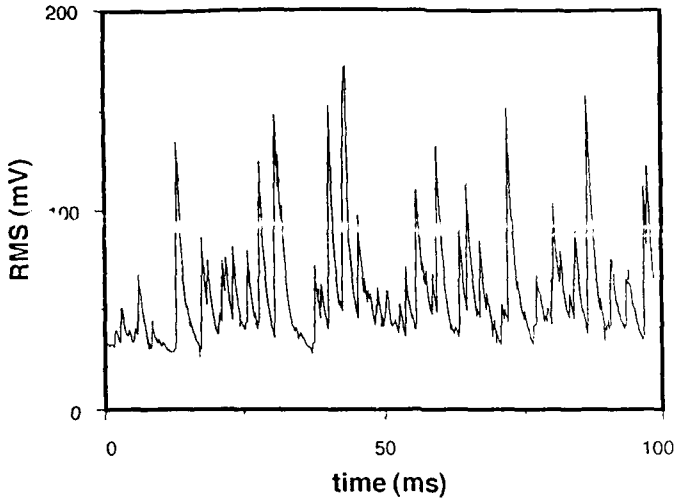

Fig. 3 : RMS signals as function of time for a continuous abrasion (record on DAT)

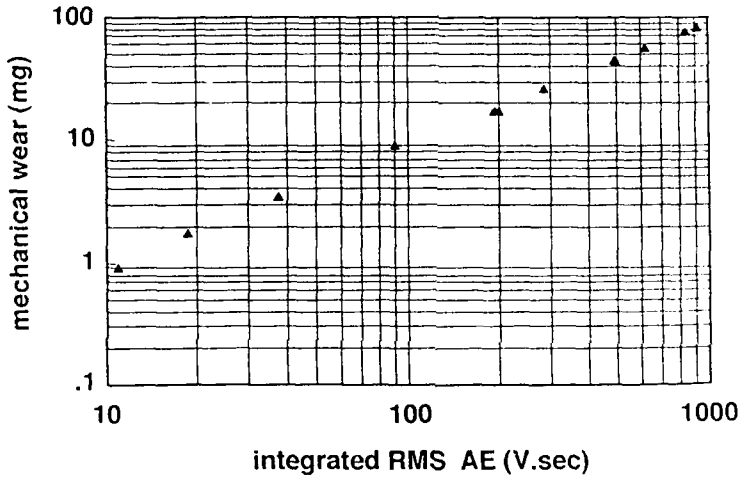

Fig. 4 : Integrated RMS A.E value as function of the mechanical wear for a continuous abrasion

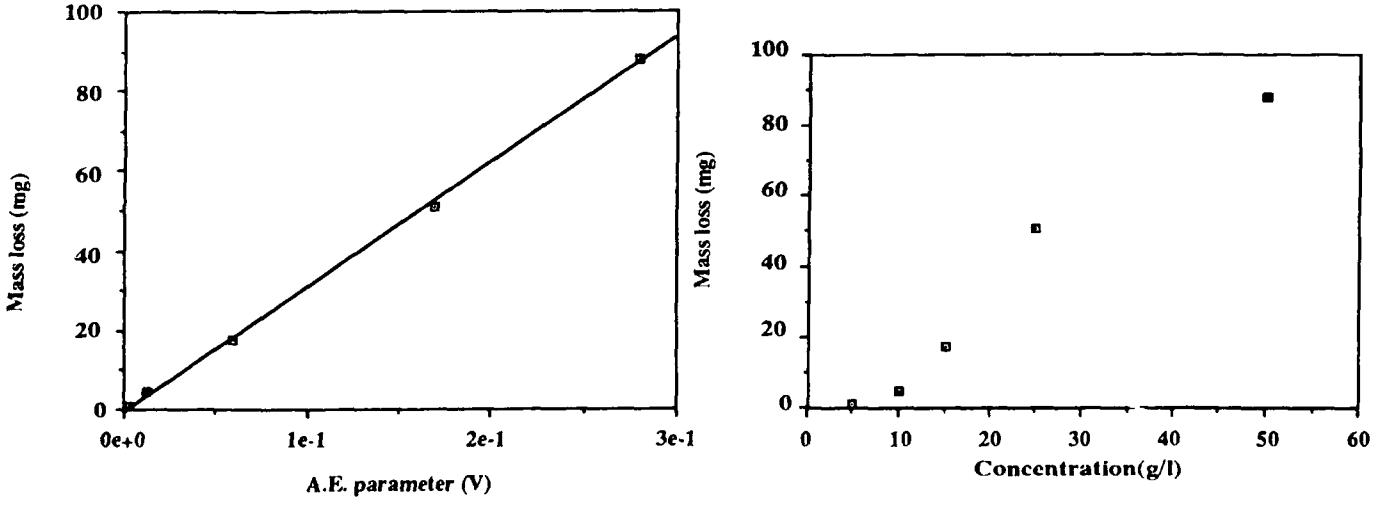

Fig. 5 : Quantification of mass loss using acoustic emission

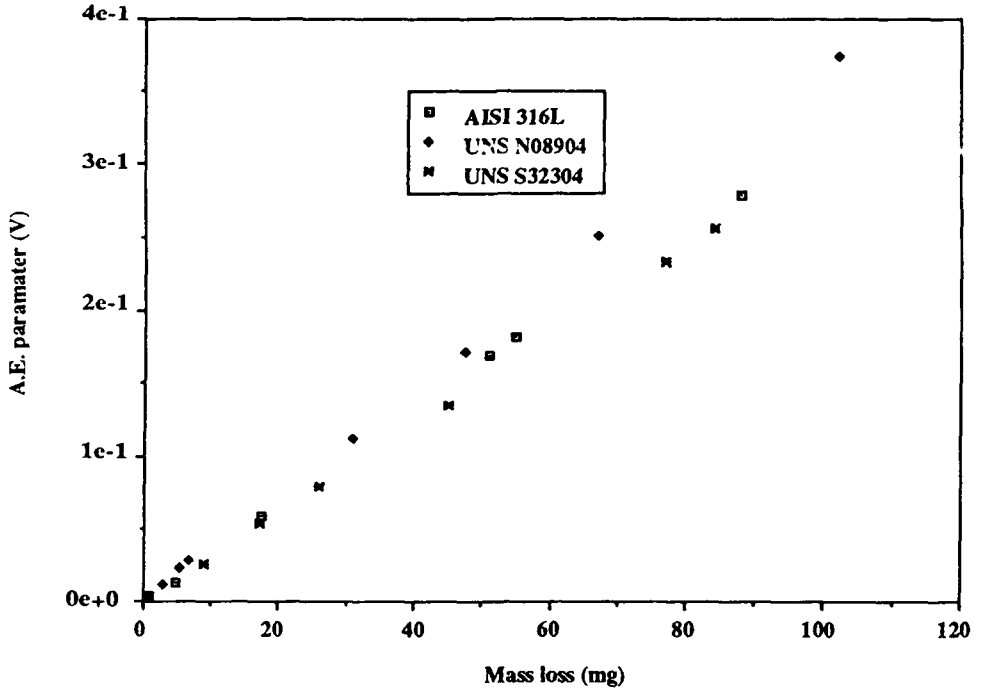

Fig. 6 : Standard mass loss curves for 3 different materials
(Medium Na2SO4 0,1M, 500 microns dia. SiC particles, v = 9,4 m/s)

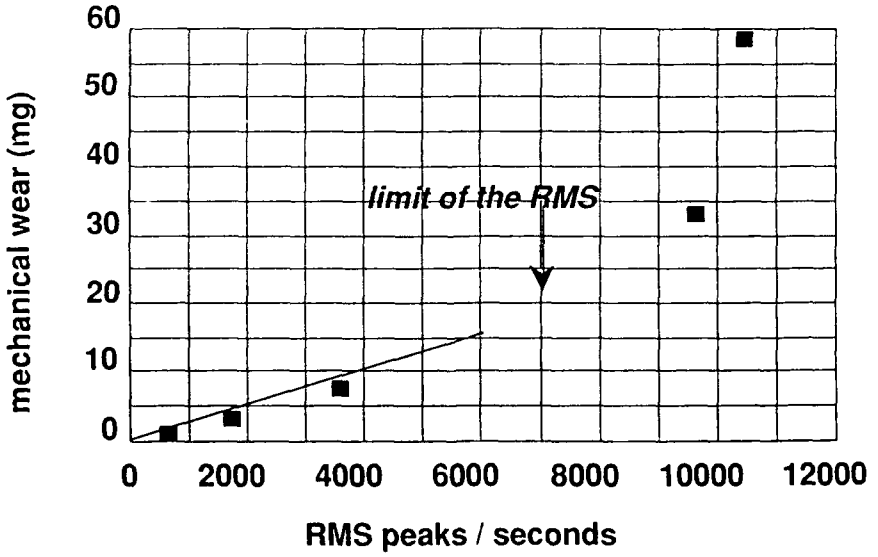

Fig. 7 : Variation of the mechanical wear as fonction of the mean rate of impacts

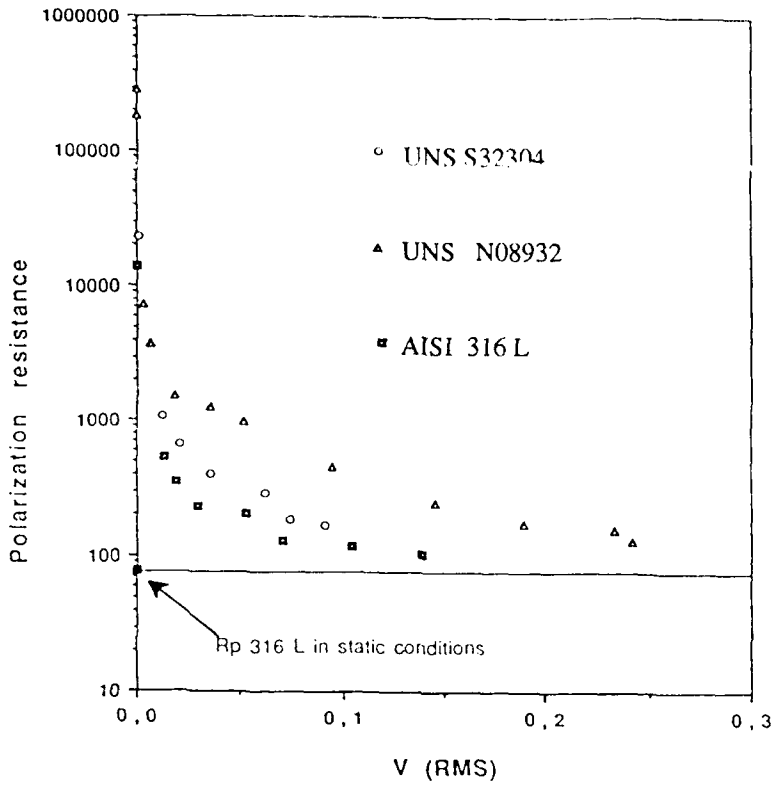

Fig. 8 : Influence of erosion conditions on polarization resistance of different stainless steels in 1M sulfuric acid at ambiant temperature.

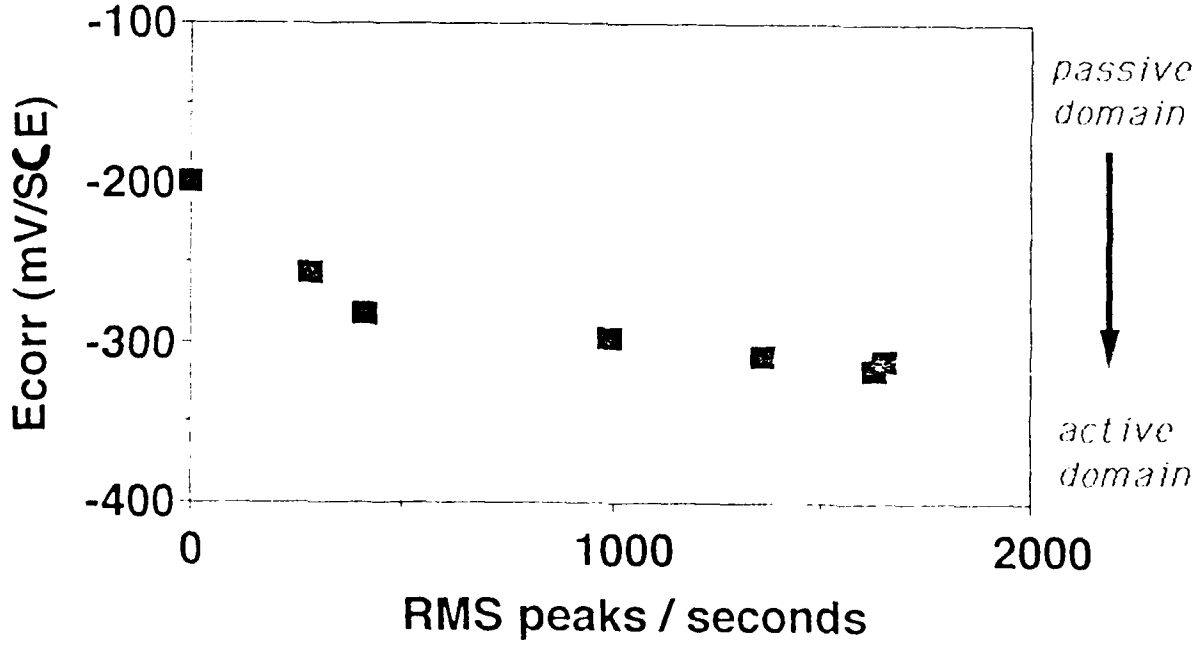

Fig.9 : Change of the mean electrochemical potential as function of the rate of abrasion (AISI 316L)

Accelerated Corrosion Testing of CrNi Stainless Steels in Nitric Acid by Electrochemical Methods

Gerhard Schanz
Nuclear Research Center Karlsruhe
Institute for Material Research III
P.O. Box 3640
7500 Karlsruhe, Germany

Siegfried Leistikow
Nuclear Research Center Karlsruhe
Institute for Material Research III
P.O. Box 3640
7500 Karlsruhe, Germany

Abstract

An electrochemical corrosion study of the austenitic CrNi stainless steel W.Nr. 1.4306 (AISI 304L = UNS S30403) in three different grades of quality was performed in 7N HNO_3, at 90 °C, and during ≤ 48 h by means of potentiostatic and potentiodynamic tests in the transient potential from passivity to transpassivity.

The experimental results prove that the applied methods are reliably able to accelerate corrosion testing (when compared to the ASTM standard Huey test) either by potentiodynamic screening over the above mentioned potential range, or by potentiostatic testing at +1200 mV_H as standard test potential. A variety of steels of different grades and product forms were tested that way, generally in respect to their applicability in nitric acid, but especially to differentiate them according to their chemical composition and microstructural homogeneity, both closely related to their state of heat treatment and sampling position from cast and forged steel blocks.

Key terms: CrNi stainless steel, nitric acid, intercrystalline corrosion, electrochemical tests

Introduction

As contributions to the International Conference on Localized Corrosion (Orlando, 1987)[1] and the Eurocorr' Conference (Budapest, 1991)[2] we presented papers about the potentiality of electrochemical testing methods to qualify CrNi stainless steels for application in nitric acid media.

It was pointed out that - in contrast to chemical solution testing methods - electrochemical potentiostatic test conditions have the advantage to keep the most important test parameter - the corrosion potential - strictly constant, while by measurement of the corrosion current the corrosion reaction can be followed up from the beginning specimen surface attack to the formation of a final corroded surface microstructure. Relating the gravimetrically measured total metal loss to the current flow an efficiency factor gives additional informations about the corrosion mechanism, i.e. material quality.

We have shown[3], that by chemical and electrochemical corrosion testing in the potential range from +1000 to +1350 mV_{H} (ASTM standard Huey testing in boiling aceotropic nitric acid takes place at +1150 ±50 mV_{H}) three austenitic CrNi steels of the nominal designation DIN W.Nr. 1.4306 (AISI Type 304L = UNS S30403) could be qualified in the solution annealed condition in respect to their corrosion originating from different chemical compositions, e.g. their content in minor element components, and homogeneity. More qualitative indications of different sensitivity to intercrystalline corrosion could be detected that way - already after one hour of testing[4].

Quantitatively evaluable results could be achieved by tests of longer durations. When the results of these tests were plotted as measured current density versus applied corrosion potential three composition (grade)-dependent curves could be drawn. They are suitable to give predictions of the steel corrosion behavior in nitric acid over a wide range of potentials, equally shown by chemical tests of AISI 310Nb stainless steel by M. Okubo et al.[5] This fact made us curious whether potentio-dynamic measurements in the same system would allow to further accelerate the corrosion test procedure without lack of accuracy and deliver similar curves.

Another effort to extend the applicability of electrochemical methods was directed towards specimens of cast and forged steel blocks of equal quality of composition to identify influences of processing, (laboratory) heat treatment, and sampling position. Needless to say that all testing work was done in parallel and compared to the results of our ASTM standard Huey testing, which is - because of its lower potential - considerably more time-consuming without being able to lay claim on higher precision.

Experimental

Material Composition, Specimen Shape, and Pretreatment

Three austenitic CrNi steels W.Nr. 1.4306 (AISI 304L = UNS S30403) of commercial (n), nitric acid grade (s), and nitric acid grade electroslag remelted (s(ESU)) quality were delivered as solution annealed plates. Two other steels of nominal same designation and grade were delivered as cast or forged materials, specimens from both were taken of blocks at the outside and the inside sampling positions. The chemical compositions of all steels are given in Table 1.

For electrochemical testing cylindrical specimens (29,5 mm ∅) were machined from the plates and blocks. Tests were performed after the specimens got the following heat treatments

- solution annealing (as received or laboratory, 3 min 1050 °C/W),
- sensitization annealing (laboratory, 30 or 60 min 700 °C/W).

The wrought and cast material was sensitized for 30 min, the forged steel for 60 min at 700 °C. Before mounting the specimens in the test holder, their surfaces - exposed to the corroding acid - were wet polished by 1000 mesh emery paper, degreased, rinsed, and weighed.

Chemical Environment

Initially, all our tests were performed in boiling aceotropic 14.4N HNO_3 (121 °C) and according to the ASTM standard Huey test procedure by immersion of steel specimens during 5 - 15 periods (240 - 720 h). After each period the acid was renewed, nevertheless the corrosion potential of W.Nr. 1.4306 steel specimens was not constant during each run. As an average value $+1150 \pm 50$ mV_{H} was measured.

Our task to simulate as close as possible reprocessing conditions of nuclear fuel has led us to nitric acid of lower concentration (7N) and temperature (90 °C). Such acid containing oxidizing ionic species, which again showed - because of their quick reduction - no constant redox/corrosion test potentials.

This was the reason to use - instead of strong acids and/or solutions containing oxidizing ion additions - the electrochemical way to oxidize the test specimen by polarization at all desired corrosion potentials and to measure the resulting current density as indicator of metal dissolution as described below.

Electrochemical Testing: Method and Performance

To perform electrochemical tests in nitric acid a special electrochemical cell (Figure 1) was built which showed the following characteristics:

- A nitric acid-resistant specimen holder exposing the disc-shaped specimen to the corroding acid which was contained in
- a thermostatically heated 1,5 L reaction flask,
- a Luggin capillary which connected the cell by a KNO_3-solution filled salt bridge to the $Hg/Hg_2SO_4/K_2SO_4$ reference electrode, positioned in a separate small glass container,
- a Pt counter electrode.

Otherwise the usual pheripherical electrochemical instruments, as potentiostat and recorder, were used.

Potentiostatic polarisation tests were performed at +1350, +1300, +1250 and +1200 mV_{H} during 1 to 48 h test duration. Tests at +1150 mV_{H}, in which weight loss was not reliably measurable, were started after specimen precorrosion during 1 h at +1350 mV_{H}. Potentiodynamic tests were performed with a scan rate of - 10 mV/h starting from +1350 mV_{H} and ending in the range between +1150 and +1100 mV_{H} at the free corrosion potential of the respective specimen.

Test Evaluation

The gravimetrically measured weight losses of the specimens were used to calculate the average metal loss $\Delta\ell$ [µm] and the average rate of metal loss w [mm/a]. The current I [mA], which was measured during the corrosion reaction, was calculated as maximum and average value to give the current density [mA/cm^2] as function of time. The average current efficiency factor η was calculated by relating the registered charge transfer during the corrosion reaction to the total metal loss; the latter included the proportion of the metal not being dissolved by charge transfer, but fallen out because of intercrystalline desintegration.

Experimental Results

Differentiation of DIN W.Nr. 1.4306 Sheet Specimens of Various Grades

Introductory remarks. A preceding program had demonstrated that potentiostatic tests of only 1 h duration in nitric acid solutions are providing indications on the susceptibility of stainless steels against intergranular corrosion, if the current densities are recorded and the specimens are metallographically examined [4]. This procedure was resumed with extended test durations, supplemented by gravimetric mass loss measurements and analyzed by calculation of time-averaged current efficiency factors. With these improvements the current density signal can be converted to the actual corrosion rate with adequate precision.

As-received condition. It was reproduced and confirmed that as deduced from the corrosion behavior and quantitatively measurable by current density curves a quality ranking in respect to composition and homogeneity of the three steel grades in the solution annealed condition is generally possible within one hour of testing and a potential range of +1150 to +1350 mV_{H}. However, for lower test potentials this period is too short to obtain reliable and reproducible averages of the fluctuating current density values, and the gravimetrically measured mass losses are below or close to the detection limit. Corresponding errors in the calculated current efficiency factors prevent their detailed interpretation.

Considerable improvements were reached by choice of the still practicable test duration of 48 h at +1150, +1200 and +1250 mV_{H}. At +1300 mV_{H} the tests were terminated after ca. 7 to 10 h and at +1350 mV_{H} after ca. 1 to 4 h, using the current integrals, measured at +1250 mV_{H}, as stop criteria, in order to keep constant the total extent of corrosion for those three potentials. Table 2 indicates the quality ranking for the three steel grades in terms of their time-averaged corrosion rates, as calculated from the gravimetric results. The current density curves for +1200 mV_{H} are still typical for the corrosive attack and resulting modification of the mechanically prepared fresh specimen surfaces (Figure 2): A steady surface roughening takes place. At +1250 mV_{H} the two lower qualities are approaching already a steady state surface of considerable roughness during intergranular and localized material dissolution, combined with grain undercutting and decohesion of undissolved grain residues.

Figure 3 summarizes the current density measurements as a plot of the corrosion potential dependence of the maximum values observed during the test periods. Showing comparable slopes of roughly one order of magnitude per 50 mV, the curves of the three steel grades are considerably separated. From a closer look it is obvious that grade s is behaving similar to the s(ESU)-version at low potential and to the n-version at high potential. This means that its benefit as against n is lost with increasing potential and before that of the s(ESU)-grade.

Sensitized condition. Laboratory heat treatments, 30 min 700 °C /W for the grades n and s, 3 min 1050 °C solution annealing followed by 1 h 700 °C/W sensitizing for the grade s(ESU) were used to prepare the specimens for a similar test series as the above described one, in which the test durations were 1 h at +1350 mV_{H}, 5 h at +1300 mV_{H} and 48 h at the other potentials. The gravimetric results are found included in Table 2, reproducing the quality ranking of the as received materials condition. The current densities registered in the tests at +1200 mV_{H} pronounce the lower quality of the grade n (Figure 4), whereas the advantages of the s and finally of the s(ESU) grade are diminishing with increasing test potential. This is also drastically shown in the plot of the current density maxima versus the corrosion potential (Figure 3).

Potentiodynamic results of solution annealed and sensitized material tests. This less time-consuming test procedure might be used for the characterization of steel grades instead of individual potentiostatic tests, if more detailed information deduced from microstructural specimen evaluation and gravimetry are not required.

The potentiostatic results are essentially confirmed by plots of the same kind according to single potentiodynamic tests with the three 1.4306 grades (Figure 3). The slow scanning rate of -10 mV/h applied in the tests and the high start potential of +1350 mV_{H} obviously were conditions, under which stationary corrosion proceeded, because steady state surface microstructures must have quickly developed. Compared to the solution-annealed microstructure the grade n suffers most from the sensitization treatment at potentials up to +1200 mV_{H}, whereas at higher potentials the influence is smaller and the quality spectrum narrow (Figure 3). Sensitization in its strict sense causing increased susceptibility against intercrystalline corrosion, is thus found restricted to a narrow potential range. Above this range similar kinds of intercrystalline and localized attack are unavoidable, irrespective of the heat treatment.

Current efficiency factors. Each of the above reported potentiostatic tests allowed to calculate a time-averaged current efficiency from the current integral and the mass loss of the specimen. Table 3 indicates the most important parameters influencing these values namely the grade quality, the corrosion potential and, indirectly, the test duration. The lower grade material will earlier or more pronounced develop grain undercutting and disintegration, by which the efficiency increases. This effect explains values clearly above one, if the time and the potential are high enough for the development of this microstructure. This was not yet provided at +1200 mV_{H}. A comparison of the three grades in the solution-annealed condition for +1250 to +1350 mV_{H} shows that - at equal values of the corrosion current integral - the microstructural desintegration is most pronounced at +1250 mV_{H}. At +1300 and +1350 mV_{H} the uniform corrosion is proceeding fast enough to diminish the importance of grain desintegration by grain boundary attack. Surprisingly, the corrosion of sensitized specimens is not proceeding selectively enough to show higher and remarkably different efficiency values compared to the solution annealed condition.

Quality Differentiation of Cast and Forged W.Nr. 1.4306 Steel Samples

The chemical composition of the same grade materials, but produced by casting or use of forging, which were chosen for comparison purposes, is presented in Table 1. They belonged to a variety of wrought (sheet or forged) or cast W.Nr. 1.4306 steel samples, for which sampling position and heat treatment were varied for tests under indentical potentiostatic corrosion conditions in 7N HNO_3 at 90 °C and at +1200 mV_{H} for 48 h. This test procedure was chosen in order to quantify the specimen susceptibility to intercrystalline corrosion according to a compromise between acceptable acceleration of the degradation mechanisms, practicable test duration and depth of surface attack.

According to the gravimetric results of Table 4 the cast and the forged material are typical for the lower quality range of their respective grades, so that no special influence of the mode of manufacturing can be distinguished. These results were fully confirmed and supplemented by the current density curves and the microstructural specimen evaluation as presented in Figure 5 for the example of the interior samples. The cast material, which was especially coarse-grained in the interior of the block, showed here a considerably lower quality compared to the outside. At the interior the forged material behaved slightly better than at its surface.

For both materials the as-received - or in one case the sensitized - condition resulted in the highest corrosion rates, the laboratory solution annealed condition gave much better results. This might indicate difficulties in the solution annealing process on production basis or in a larger scale, compared to a better temperature-controlled laboratory procedure. In the same sense the microstructural observation of residual deformation of the forged material in the as-received condition is mentioned.

Discussion and Conclusions

In the context of the reprocessing of spent nuclear fuel the applicability of low carbon CrNi stainless steels as candidate material for the plant construction (dissolver, evaporator, tubing etc.) in half concentrated nitric acid solutions at elevated temperatures was investigated initially by the ASTM standard Huey test and similar tests in nitric acid solutions with single or combined additions of corrosion enhancing oxidizing ionic species.

Later on these tests were accompanied by electrochemical measurements of the redox potential of the solutions and the free corrosion potential of the exposed steels, to confirm the relevance of the corrosion potential range, thus covered. The other aspect, electrochemical corrosion testing by anodic polarization, has to be considered here as a complementary procedure of remarkable advantage.

The corrosion potential, the main parameter, determining the corrosion rate and its local degrading effectiveness, is held strictly constant in potentiostatic tests. According to Figure 3, in which the current densities are summarized in potential dependence, a potential change of 50 mV changes the corrosion rate by roughly one order of magnitude. The quality or acceptability of a certain steel or vice versa the aggressivity against this steel of a given nitric acid solution, here presented by three individual curves for different grades of DIN W.Nr. 1.4306 in the solution annealed condition can be judged on this basis. It was found that different material processing, heat treatments and even sampling positions will lead to deviations from these "master curves" and finally to individual ones (Figure 3).

Parameters of comparatively lower importance, not mentioned so far, are corrosion temperature and acid concentration.

The corrosion rate is primarily understood as the instantaneous or the time-averaged rate of mass loss. An independent and continuously available measurement is that of the total current flow density, which - related to the total weight loss - provides the knowledge of the current efficiency factor. It was shown that time-averaged potential dependent values of this factor provide more detailed information on the corrosion mechanism and material quality.

A highly important factor is the duration of test exposure, since the fresh material is developing a rough surface, characterized by general corrosion, localized attack in form of pits and tunnels, wedge-formed attack of grain and twin boundaries precipitates and inclusions by intergranular corrosion. These features have been studied systematically in the microstructural specimen evaluation.

The total extent and depth of metal loss is especially important if the corrosion behavior of the material exposed to a special medium is to be quantified or even extrapolated. As determined by the combination of various potentials and durations of exposure, an adequate pessimistic[1] choice of those parameters (here + 1200 mV_{H}, 48 h) is essential for the test procedure. It has been shown that - compared to the Huey test - the moderate degree of rate acceleration by anodic polarization is permissible, whereas at higher transpassive potentials the

corrosion mechanisms and phenomena are changeing. In this range, where the corrosion rates grew - because of an unspecific metal dissolution - unacceptably high, and the chances for differentiation of material quality were found to disappear, no advantage from material optimization can be expected.

Acknowledgement

The authors gratefully acknowledge the contributions of Messrs. E. Pott, P. Graf and H. Zimmermann to the experiments and evaluations.

References

1. S. Leistikow, R. Simon
Advances in Localized Corrosion
(Houston, TX: National Association of Corrosion Engineers, 1992) p. 283.

2. G. Schanz, S. Leistikow
Proc. Eurocorr '91, Budapest 1991, Vol. II, 1991, p. 619.

3. S. Leistikow, R. Kraft, G. Schanz
Proc. Ann. Meeting on Nuclear Technology '92,
Karlsruhe, Germany (1992) p. 237

4. R. Simon
Berichte Kernforschungszentrum Karlsruhe, Germany, KfK 4372 (1988).

5. M. Okubo et al.
Proc. Recod '87, Paris 1987, Vol. 3, 1987, p. 1181.

1) A pessimistic choice is always necessary since deviations from nominal conditions of application have to be considered, a side effect, the acceleration of the corrosion test procedure, is highly welcome as long as it does not change the corrosion mechanism

Table 1: Chemical Composition of Tested CrNi Stainless Steel, Designation. DIN W.Nr. 1.4306 (UNS S30403 – AISI Type 304L), Various Grades

1. Sheet Material

DIN W.Nr., Grade*)	Chemical Composition [wt %]							
	C	Si	Mn	P	S	Cr	Mo	Ni
1.4306n	0,024	0,60	1,44	0,025	0,003	18,00	0,17	10,23
1.4306s	0,015	0,02	1,70	0,022	0,007	19,11	0,02	12,50
1.4306s(ESU)	0,007	0,02	1,59	0,022	0,005	19,13	-	12,40

2. Cast Material

1.4306s	0,024	0,17	1,54	0,018	0,009	19,13	0,063	12,01

3. Forged Material

1.4306s(ESU)	0,013	0,02	1,65	0,024	0.005	19,02	-	12,44

*) Different Grades:
1.4306n = Low Carbon Commercial Product
1.4306s = Nitric Acid Grade (NAG)
1.4306s (ESU) = NAG, Electroslag Remelted

Table 2: Test Results of W.Nr. 1.4306 Sheet Specimens of Different Grades and Heat Treatments:
Comparison of Corrosion Rates in 7N HNO_3, 90°C under Potentiostatic Test Conditions

W.Nr. 1.4306 [Grade]	Test Potential [mV_H]	Average Corrosion Rate	
		Sol. Annealed [mm/a]	Sensitized [mm/a]
n	1200	1,90	2,31
s		0,82	0,64
s(ESU)		0,53	0,56
n	1250	48,9	48,2
s		35,3	36,4
s(ESU)		9,5	25,6
n	1300	225	210
s		149	169
s(ESU)		72	148
n	1350	546	512
s		444	466
s(ESU)		346	466

Table 3: Test Results of W.Nr. 1.4306 Sheet Specimens of Different Grades and Heat Treatments:
Comparison of Current Efficiency Factors under Potentiostatic Conditions in 7N HNO_3, 90°C

W.Nr. 1.4306 [Grade]	Test Potential [mV_H]	Current Efficiency (η)	
		Sol. Annealed	Sensitized
n	1200	0,91	0,95
s		0,87	0,88
s(ESU)		0,85	0,85
n	1250	1,24	1,25
s		1,17	1,00
s(ESU		0,88	0,94
n	1300	1,21	1,07
s		1,02	0,92
s(ESU)		0,88	0,92
n	1350	1,14	0,94
s		0,92	0,89
s(ESU)		0,88	0,94

Table 4: Test Results of W.Nr. 1.4306 Specimens of Different Products, Grades, Sampling Positions, and Heat Treatments:
Comparison of Corrosion Rates in 7N HNO_3, 90°C under Potentiostatic Test Conditions

W.Nr. 1.4306 [Grade]	Test Potential [mV_H]	Heat Treatment	Average Corrosion Rate	
			Outside [mm/a]	Inside [mm/a]
Cast/s	1200	as received	1,42	2,37
		solution annealed	1,03	1,17
		sol. ann. + sensitized	1,35	2,70
Forged/ s(ESU)	1200	as received	1,64	1,48
		solution annealed	1,04	0,89
		sol. ann. + sensitized	1,29	1,23

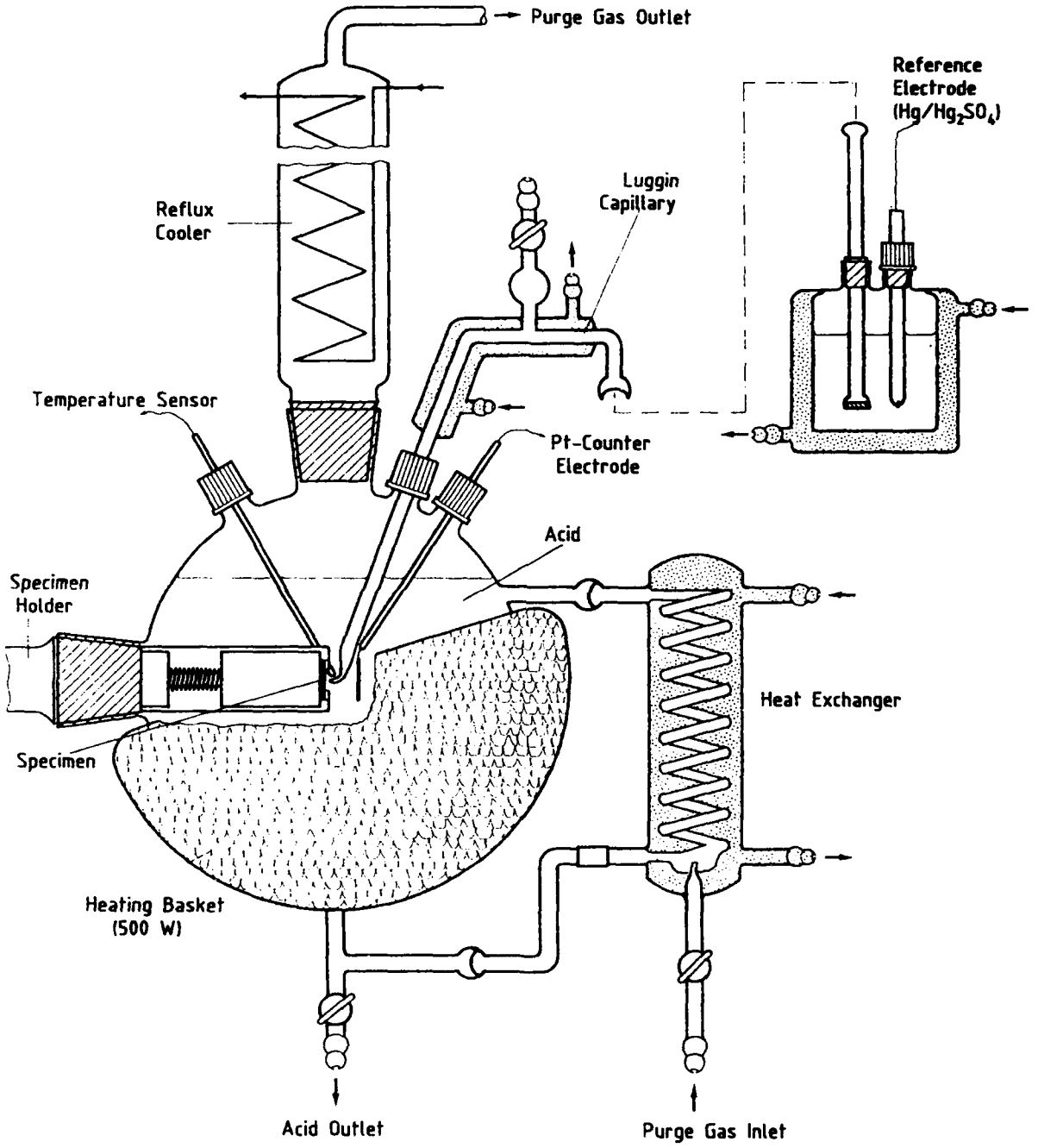

Figure 1: Electrochemical Cell for Corrosion Tests in Nitric Acid

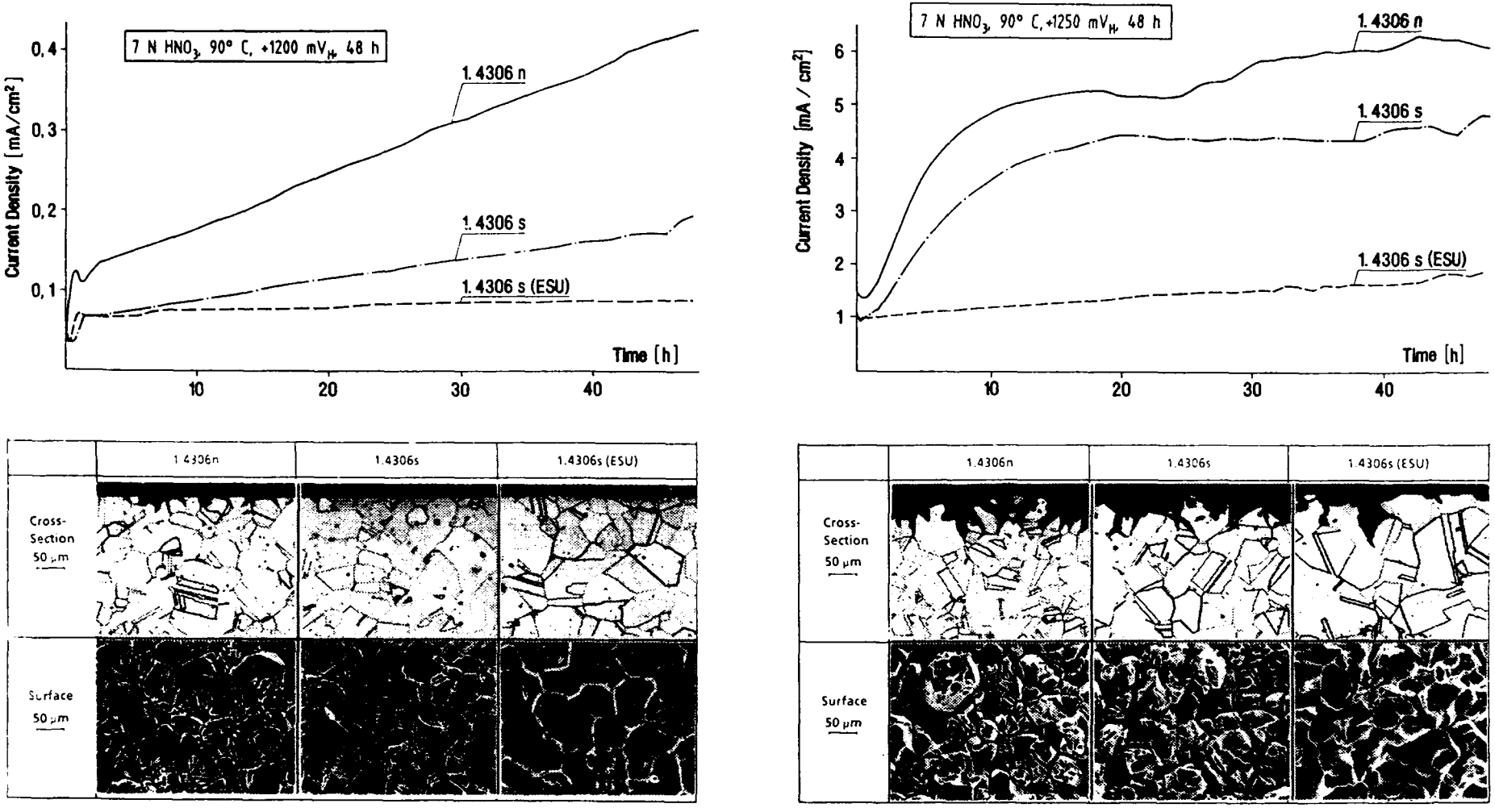

Figure 2: Potentiostatic Electrochemical Measurements of W.Nr. 1.4306 As-received Steel Sheet Exposed to 7N HNO_3, 90 °C at +1200 and +1250 mV_H for 48 h

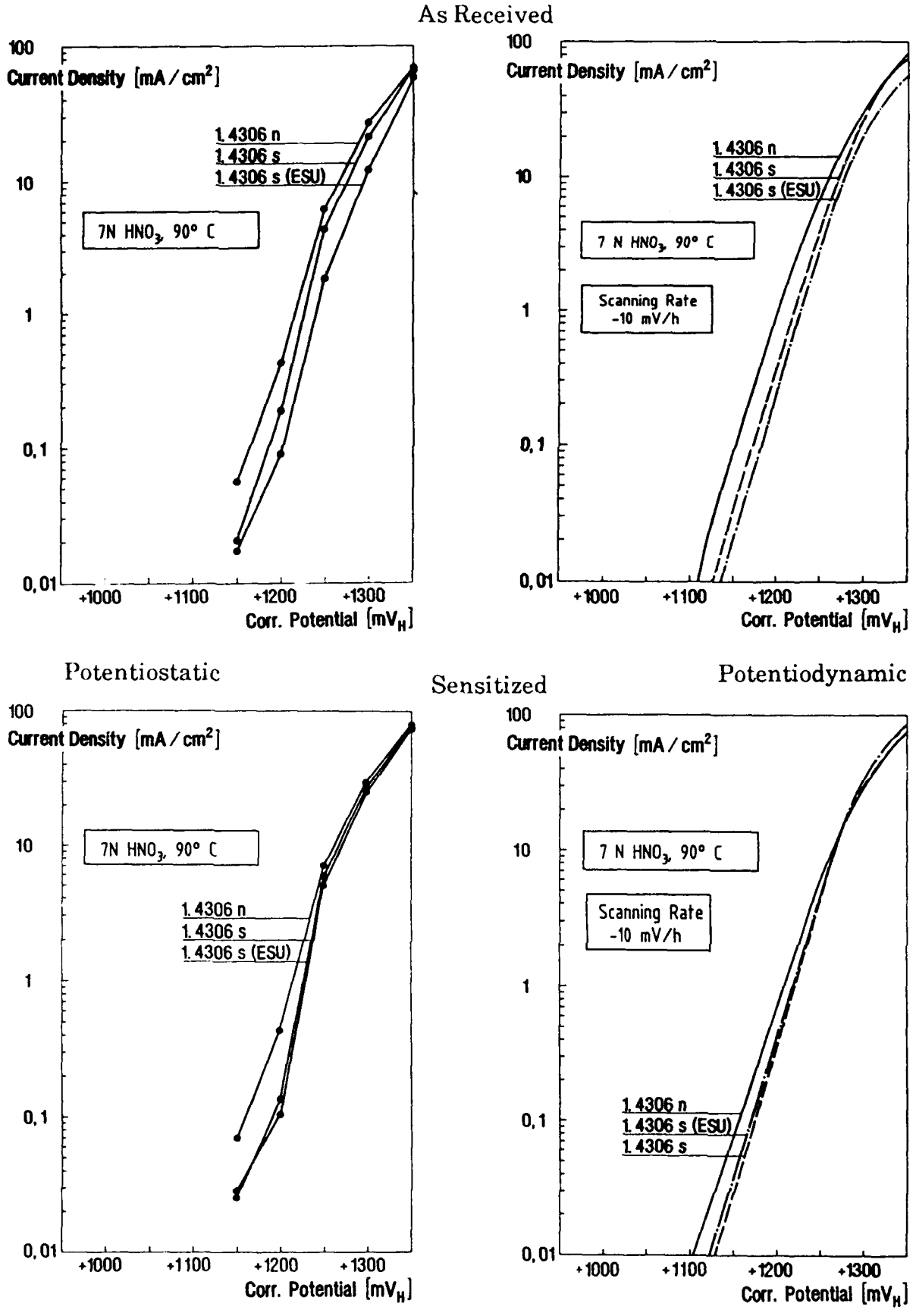

Figure 3: Potentiostatic and Potentiodynamic Measurements of Current Density/Corr. Potential Curves by Exposure of W.Nr. 1.4306 in 7N HNO_3, 90 °C

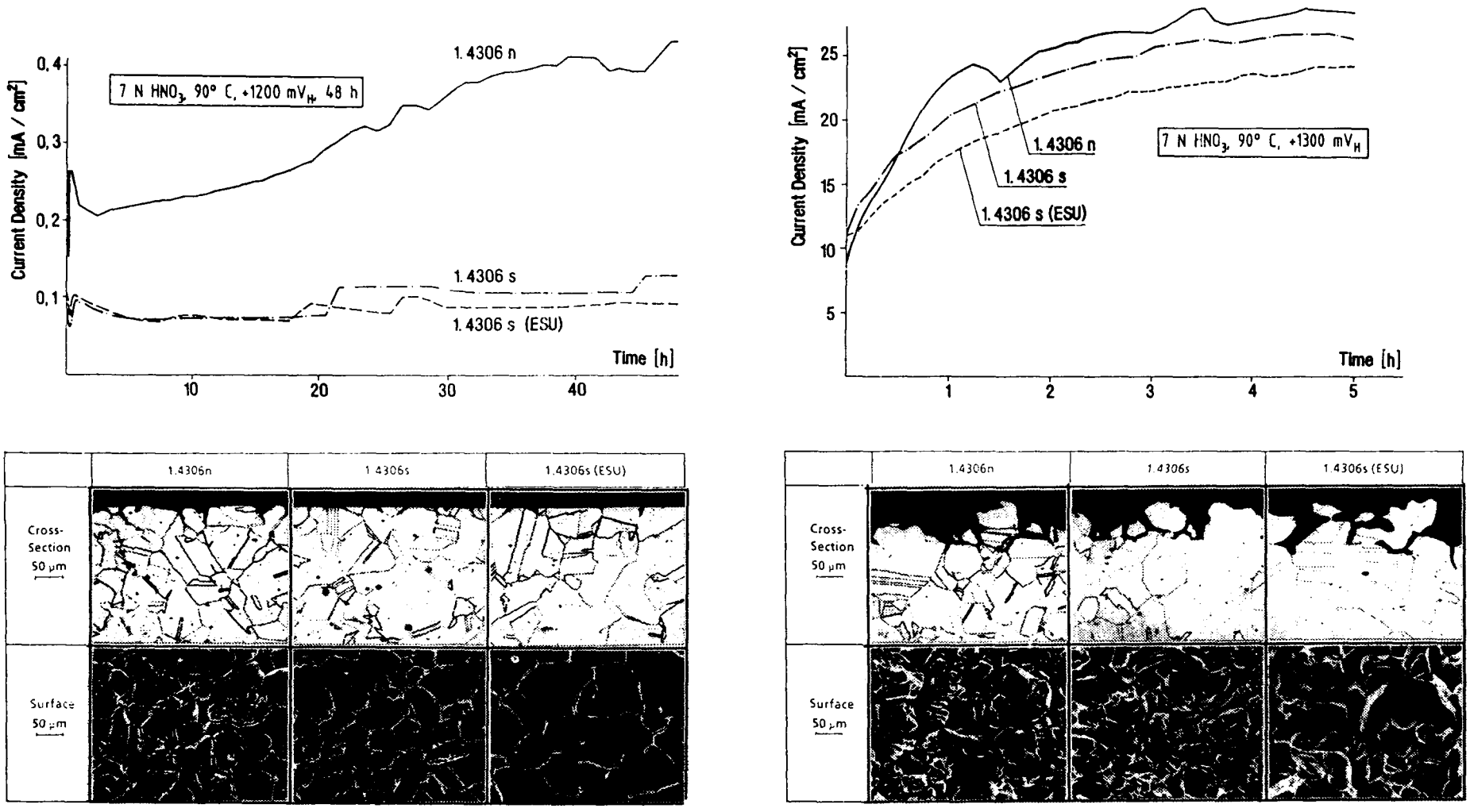

Figure 4: Potentiostatic Electrochemical Measurements of W.Nr. 1.4306 Sensitized Steel Sheet Exposed to 7N HNO_3, 90 °C at +1200 mV_H for 48 h and +1300 mV_H for 5 h

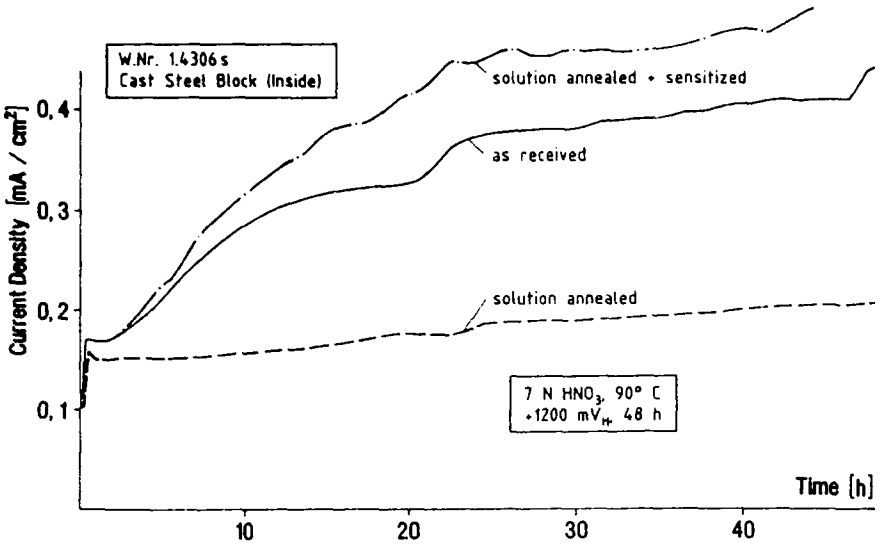

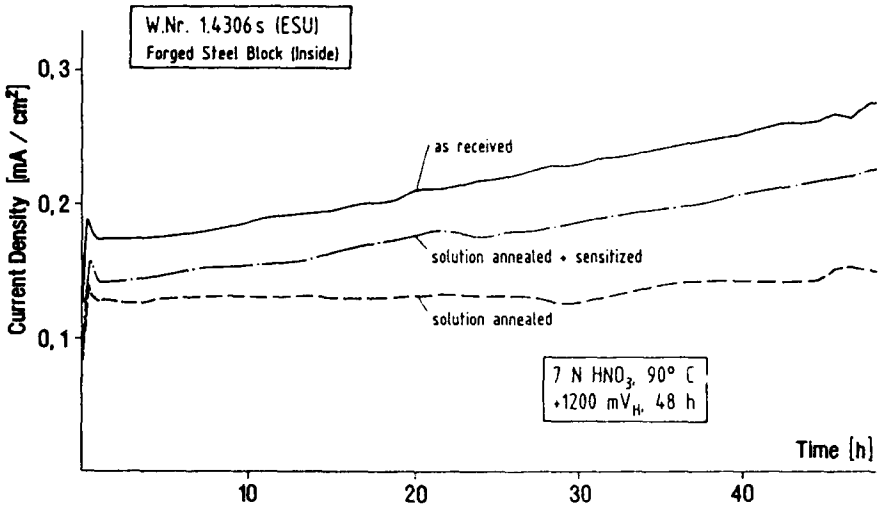

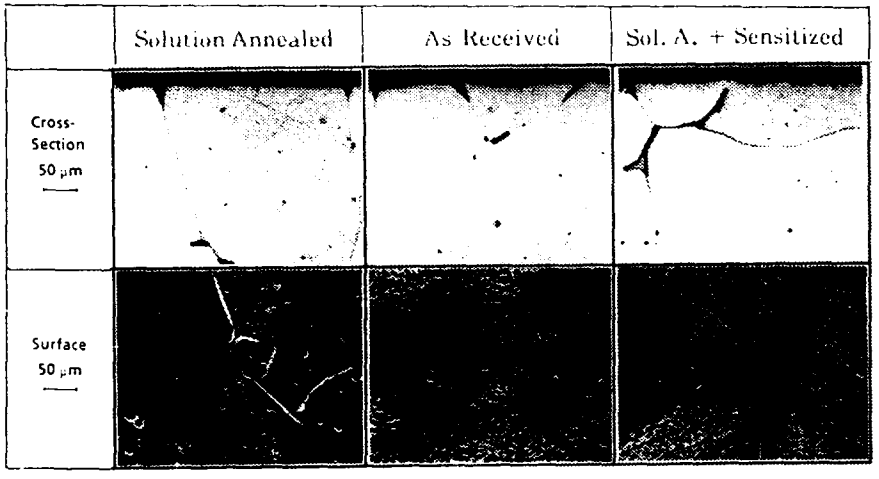

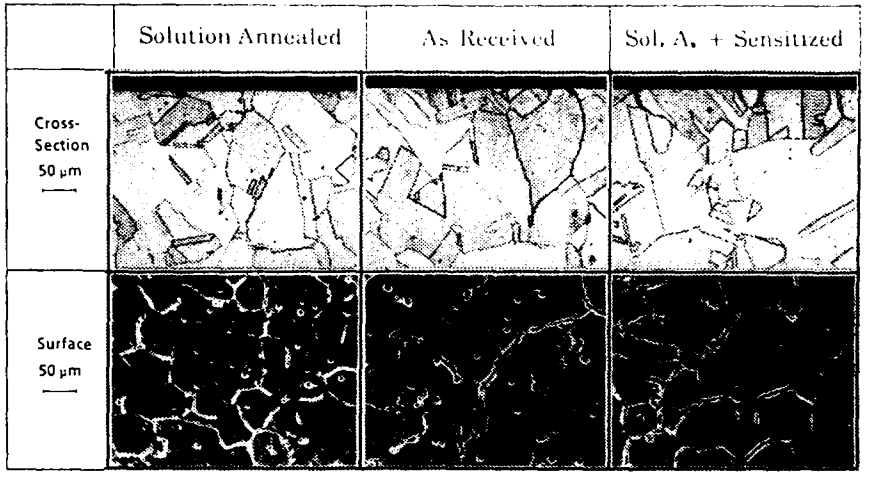

Figure 5: Potentiostatic Electrochemical Measurements of W.Nr. 1.4306 Cast and Forged Steel Blocks Exposed to 7N HNO_3, 90 °C at + 1200 mV_H for 48 h

Tunneling Corrosion Mechanism of the Hot Forged Austenitic Stainless Steel in Highly Oxidizing Nitric Acid

Hiroo Nagano
Research and Development Center
Sumitomo Metal Industries Ltd.
1-8, Fusoh-cho, Amagasaki, 660, Japan

Haruhiko Kajimura
Research and Development Center
Sumitomo Metal Industries Ltd.
1-8, Fusoh-cho, Amagasaki, 600, Japan

Abstract

Austenitic Stainless Steels have been used for reprocessing plants where spent nuclear fuels are dealt with in hot nitric acid. Conventional stainless steels are resistant enough to nitric acid. However, they are prone to localized corrosion when nitric acid becomes highly oxidizing with birth of oxidants such as Ce^{4+} or Cr^{6+} ion during the reprocessing. Pitting type corrosion, so-called tunneling or end-grain corrosion occurred on the forgings of 25%-20%-Nb stainless steel (310Nb stainless steel) in such nitric acid solutions because of transpassive corrosion. It has well been known that metal surfaces of steel products casted, forged or rolled are susceptible to the tunneling corrosion in aggressive corrosion media. Nevertheless, neither clear explanations of the mechanism nor definite countermeasures have been proposed yet.

This paper describes the mechanism and countermeasures on the tunneling corrosion of stainless steels in nitric acid relevant to spent nuclear fuel reprocessing. The results obtained are as follows:

Both general and intergranular corrosion occur on austenitic stainless steels in boiling 8N HNO_3 with Cr^{6+} ions. Tunneling corrosion is initiated and propagates at the metal surfaces of 310Nb stainless steel forgings along chromium depleted areas vertical to metal flows. The grooves due to the tunneling corrosion are of diameters of 0.5 to 2 mm with a maximum depth of 6mm depending on exposure time and Cr^{6+} concentration in nitric acid.

Tunneling corrosion proceeds by build up of galvanic corrosion cells with Cr depleted parts as anodes and their neighborhoods as cathodes.The Cr depleted parts are formed during solidification of ingots and still retained parallel to the metal flow even after forging. The ESR (Electro Slag Remelting) is one of the useful preventive methods to tunneling corrosion from the view point of steel homogenization.

Key items: reprocessing, nitric acid, pitting, tunniling corrosion, stainless steel, segregation

Introduction

It is well known that austenitic stainless steels has high corrosion resistance in nitric acid by forming passive films on them. Therefore, they have widely been used as materials for spent nuclear fuel reprocessing plants dealing with nitric acid. However, they were susceptible to severe corrosion in nitric acid solutions containing such oxidizing species as Cr^{6+} or Ce^{4+} which were prevalent in dissolvers and acid recovery tanks. The corrosion pattern was of a combination of general and intergranular corrosion.

In addition to that, a peculiar type of corrosion, so-called tunneling corrosion or end-grain corrosion occurred along the metal flows of stainless steel forgings. The flanges and joints

fabricated from forgings constitute important parts of reprocessing plants. It has been reported that tunneling corrosion was preferentially initiated at the sites of intermetallic compounds of stainless steel forgings[1-4]. On the other hand, it has also been described that segregation of constituents of alloys was associated with tunneling corrosion[5].

This paper is aimed at clarifying the tunneling corrosion mechanism and innovating countermeasures against it.

Experimental

I. Field Tests

A. Materials Used

Several charges of 310Nb stainless steel were melted by an electric furnace, and their chemical compositions are given in Table 1. They were made to plates, tubing and forgings which were put into field tests for evaluation of corrosion performance of this alloy.

B. Mock up Test Equipment

An evaporator simulating the acid recovery tank of a reprocessing plant was constructed by use of 310Nb products such as plates, tubing and forgings. The evaporator was equipped with a tank of 1,000mm in diameter and 5,000mm in height, and a reboiler of 1,050mm in diameter and 6,000 mm in height, respectively.

C. Operation Conditions

First run: operation with boiling 8N HNO_3 for 1,400h

Second run: operation with boiling 8N HNO_3 with 0.5g/lCr^{6+}ions for 11,000h

II. Simulated Tunneling Corrosion Tests

A. Measurements of segregation of alloying elements

A mapping electron probe micro analysis (EPMA) technique was used for investigating segregation of alloying elements such as Cr, P, S, Mn and Mo in the matrix of 310Nb stainless forging. The analyzer used was the Seikou Electron's SMA/850. The electron beam with a spot of 10μm square was scanned on a rectangle of 4 and 8mm in length.

B. Corrosion Tests

1. Materials Used. The chemical compositions of the materials used are shown in Table1. There are several charges of 310Nb stainless steel of 3 or 3.5 ton in weight which were melted by the Argon Oxygen Decarburization (AOD) process or AOD plus the Electro Slag Remelting (ESR) process. They were forged by the forging ratio of 18 to 60 according to the product size, and then heat treated at 1373K followed by water quenching. Corrosion specimens were cut off from the forgings in the way so as to make the metal surface of a specimen perpendicular to the longitudinal metal flow.

Clad steel specimens were made according to the procedure as shown in Figure 1 to investigate the effect of Cr segregation on the tunneling corrosion.The plates of charges H (310 Nb) and I (304L) were contacted to each other and then hot rolled at 1,473K, followed by the solution treatment at 1,373K.

2. Corrosion Tests. (1) Immersion corrosion tests were carried out in 8N HNO_3 with various concentrations of Cr^{6+} up to 10 g/l at the boiling point. The test solution was exchanged every 24 h or 48h. (2) Electrochemical measurements of corrosion potentials or anodic polarization curves for the alloys were also undertaken.

Results

I. Occurrence of Tunneling Corrosion in the Field Tests

Tunneling corrosion occurred on the surfaces of flanges exposed consecutively to boiling 8N HNO_3 for 1,400 h and then to boiling 8N HNO_3 with 0.5g/l of Cr^{6+} ions for 1,1000 h (Figure 2). There are two types of tunneling corrosion appearance with its distribution. One is a uniform distribution popular with large diameter forgings, and the other is a localized one popular with smaller diameter forgings as schematically shown in Fig.3.

Figure 4 shows an example of the microstructure of tunneling corrosion. Figure 5 depicts the relationship between depths and diameters of tunneling corrosion pits.The depths are dispersed up to 10 mm with 1 mm as the majority depth of pits.

II. Tests Results of Simulated Tunneling Corrosion

A. Relationship between Segregation of Alloying Elements and Tunneling corrosion

As the tunneling corrosion penetrated along metal flows, segregation of some alloying elements seemed to be associated with this corrosion. A specimen for mapping EPMA was cut off parallel to the metal flows as shown in Figure 6 from the portion where tunneling corrosion pits appeared. Table 2 is the mapping EPMA results, elucidating that just Cr solely segregates in the 310 Nb stainless steel forging among several elements analyzed. Figure 7 shows the segregation of Cr content on the surface parallel to the metal flow. A tunneling corrosion pit is located at the upper left portion, below the bottom of which a Cr depleted zone elongates downward. Figure 8 is the qualitative data for the distribution of Cr content on the longitudinal surface parallel to the metal flows of a forging.

B. Growth of Tunneling Corrosion Pits

Figure 9 shows how tunneling corrosion pits grow on 310Nb stainless steel with time in boiling 8N HNO_3 bearing 0.5 g/l Cr^+ ions. The longer the immersion time is, the bigger a pit grows.

C. Effect of the Chromium Content on Tunneling Corrosion

It has already been reported in the papers that Cr is beneficial for the corrosion resistance of stainless steels in nitric acid[2], and it seems to be valid in both the passive and transpassive potential regions up to 1.4 V vs.SHE or 1.16 V vs.SCE[6]. Cr is segregated in the forgings and influences corrosion resistance in hot nitric acid with oxidants, therefore, primary concern was focused on its effect on the occurrence of tunneling corrosion.

Figure 10 shows the potentiodynamic polarization curves for a 310Nb plate representative of the matrix bearing the nominal Cr concentration of 25% and a 304L plate representative of the Cr depleted zone bearing 19 % Cr. Both alloys enter into the transpassive state at the potential above around 800 mV vs. SCE where anodic currents increase with potential. Arrows in the figure point to the corrosion potentials of alloys immersed in nitric acid with a specific Cr^{6+}ion concentration, respectively. Corrosion potential increases in hot nitric acid containing Cr^{6+} ions as its concentration goes up, approaching a maximum potential of 1000 mVvs.SCE.

As it was understood that tunneling corrosion occurred at the potential between 800 and 1000 mVvs.SCE at the laboratory test condition as well as presumably in reprocessing plants, potentiostatic corrosion tests were undertaken on 310 Nb and 304L stainless steels in 8N HNO_3 at 100C. Higher anodic current flows on the material with lower Cr content at this potentiostatic condition as given in Figure 11, distinctly different from the behavior obtained at the potentiodynamic one. Therefore, it is understandable that a Cr depleted part in 310Nb stainless steel is susceptible in oxidizing nitric acid to more corrosion than a part with the nominal Cr content.

D. Galvanic Corrosion due to Difference in Chromium Concentration

The galvanic corrosion test result is depicted in Figure 12. Corrosion of 304L stainless steel coupled with 310 Nb stainless steel is accelerated in boiling 3N HNO_3 bearing Cr^{6+} ions with the area ratio of 310 Nb to 304L. 304L is attacked up to 3 times at the area ratio of 100 as much as isolated 304L as a reference. On the other hand, 310Nb shows no corrosion acceleration.

E. Simulation of Tunneling Corrosion

310Nb-304L clad steel specimens simulating Cr negative segregation in forgings (Figure 1) were put into test in boiling 8N HNO_3 with 5g/l Cr^{6+} ions. 304L representative of a lower Cr part was attacked severely in accordance with the area ratio, which is observed in Figure 13. This phenomenon could lead to the conclusion that galvanic action is one of the most important factors for tunneling corrosion mechanism.

III. Countermeasures of Tunneling Corrosion

Homogenization of steel quality by special melting methods or heat treatments were considered to improve corrosion resistance against tunneling corrosion. As described in Table 3, materials melted solely by the AOD method incurred tunneling corrosion, i.e., the longer the test duration or the higher the Cr^{6+} concentration was, the more severely the materials C and D were attacked. As for the effect of homogenization by heat treatment, even the isothermal heat treatment on the forgings at 1573K for 30h did not improve tunneling corrosion resistance at all.

On the other hand, 310Nb forgings melted by the consecutive AOD and ESR process showed no tunneling corrosion at all the test conditions tested. This beneficial effect has been supported by the fact that no continuation of negative Cr segregation was detected in the forgings produced by the consecutive AOD and ESR process.

Discussion

I. Relationship between Tunneling Corrosion and Negative Segregation in 310Nb Stainless Steel

In general, concerning distribution of alloying elements in the matrix of forgings are not so homogeneous as rolled products. The mapping EPMA result has found out that tunneling corrosion penetrated the Cr depleted zones formed longitudinally along the metal flows.

The present data has illustrated that negative Cr segregation is closely related with tunneling corrosion. This tunneling corrosion of austenitic stainless steels is a combination of dominant intergranular corrosion with general corrosion occurring in the transpassive potential region which is encountered in laboratory corrosion tests as well as in the reprocessing process dealing with spent nuclear fuels.

Text books of corrosion describes that passive films on stainless steels break away in the transpassive state, beginning to dissolve Cr from the metal surface into solution as CR^{6+} ions. Consequently, the higher Cr content an alloy bears, the severer corrosion it has. However, the tunneling corrosion in question here occurs in the specific transpassive potential region, i.e., between 800 and 1000 mV vs. SCE at the highest, close to the passivity - transpassivity boundary potential, where a stainless steel with less Cr content is attacked more than one with higher Cr content. For example, the corrosion rate for the 19% Cr material (304L) is 3.4 times and 2.5 times that of the 25% Cr material (310Nb) at 920 and 1000 mV in nitric acid, respectively.

II Formation of Chromium Depleted Zones Elongated parallel to Metal Flows

Some papers have reported the cases of negative Cr segregation in steels. Cr concentration in dendrite arms decreased down to about 21% in a 25%Cr-20%Ni stainless steel ingot [7]. Another similar phenomenon was also described with a 18%Cr-8%Ni stainless steel ingot [8].

Dendrite arms solidified at the early stage from molten metal are generally poor in Cr content. The efficient solidification partition coefficient for Cr, K_e is described as :

$$K_e = C^*/C_O \qquad (1)$$

where, C^*: the Cr concentration at the center of dendrite arms
Co: the mean Cr concentration

K_e is between 0.84 and 0.87, explaining Cr depletion in stainless steels at the early solidification stage.

Furthermore, there are some other causes of Cr depletion coming from solidification processes of ingots. After the completion of solidification of dendrite arms, equiaxed crystals begin to solidify, which fall down through the liquid and precipitate at the bottom of an ingot. This phenomenon is one of the origins of negative Cr segregation. The equiaxed crystals gather each other, leading to form a channel pattern of Cr poor zones. The discrepancy of Cr concentration

between the Cr depleted zone and the other nominal part is too large to be canceled by homogenization heat treatments.[9]

It may be concluded from the above mentioned findings that any conventional ingot larger than a few tons has semi-micro or micro inhomogeneity longitudinally or transversely to the axis of an ingot , e.g., Cr depletion etc. Therefore, 310Nb forgings made of such commercially available size ingots still remain longitudinal Cr depleted zones parallel to metal flows.

III. Tunneling Corrosion Mechanism

Tunneling corrosion occurs on metal surfaces of 310Nb stainless forgings in highly oxidizing nitric acid, initiated on the metal surface vertical to metal flows and penetrating longitudinally parallel to the metal flows. This peculiar type of corrosion popular with the forgings is closely associated with negative Cr segregation, because Cr depleted parts are prone to tunneling corrosion.

Electrochemical explanation for tunneling corrosion is given in Figure 14, showing enlargement of polarization curves affected by Cr concentration at the potential region around the boundary between passivity and transpassivity. Austenitic stainless steels, in general, have attacks of both intergranular and general corrosion regardless of Cr content in hot nitric acid containing oxidants with high standard potential.

However, the Cr depleted zone of a stainless steel is more severely attacked at the potential range compared with other parts without any Cr deficiency. Furthermore, corrosion of the Cr deficient portion is accelerated by galvanic action with its neighborhood.

Tunneling corrosion current density I_{tunnel} for a fixed area ratio of a Cr depleted portion to that of higher Cr is described as:

$$I_{tunnel} = I_g + (I_{corr,\,L} - I_{corr,\,H}) \qquad (2)$$

where, I_g is the galvanic current density between lower Cr and higher Cr portions
$I_{corr,\,L}$ is the current density for a Cr depleted portion
$I_{corr,\,H}$ is the current density for a higher Cr portion

$I_{corr,\,L}$ and $I_{corr,\,H}$ are the anodic current densities intrinsic to Cr concentration, respectively, therefore the difference in the current densities of $I_{corr,\,L}$ and $I_{corr,\,H}$ is almost determined by the corrosion condition. On the other hand, as for I_g the smaller the area ratio of a Cr deficient part is, the larger I_g becomes. For example, as the area ratio of the galvanic couple between 19% Cr and 25% Cr steels was changed down to 1/100, the corrosion of 19% Cr steel increased about three times as much as that of isolated 19% Cr.

Figure 15 describes the mechanism of tunneling corrosion encountered on 310Nb stainless steel forgings in highly oxidizing nitric acid. Negative Cr segregation is formed in ingot making and forging processes longitudinally parallel to metal flows, still remaining continuous micro or semi-micro Cr depleted zones. The sites of tunneling corrosion are Cr depleted areas, and the penetration by tunneling corrosion is basically understood to be the corrosion difference between Cr depleted and Cr not depleted portions. To say more precisely, the tunneling corrosion rate is the superimposition of the intrinsic corrosion rate difference and galvanically accelerated corrosion rate.

Conclusions

Study was undertaken on mechanism of tunneling corrosion and its prevention for 310Nb stainless steel (25% Cr-20%Ni-Nb) in highly oxidizing nitric acid. The results obtained are summarized as follows:

1. Tunneling corrosion appearing on metal surfaces of austenitic stainless steel forgings is a typ of pitting corrosion combined with general corrosion which is initiated on a surface vertical to metal flows and then proceeds longitudinally along them.The size of tunneling corrosion changed up to 2 mm in diameter and 6 mm in depth dependent on the corrosiveness of nitric acid and immersion time of materials.
2. 310Nb stainless steel has general corrosion on its entire surface in highly oxidizing nitric acid because its corrosion potential remains at the transpassive potential region due to the high oxidation reduction potentials of oxidants in the acid. Tunneling corrosion is added to general corrosion in the total corrosion loss and grows 3 to 13 times as deep in penetration as general corrosion.
3. Tunneling corrosion is caused by micro or semi- micro negative segregation of chromium parallel to the metal flows of working. Corrosion occurs preferentially on Cr depleted zones, accelerated galvanically with Cr deficient parts as anodes and their neighborhoods as cathodes.
4. Metallurgical homogenization is useful as preventive measures to tunneling corrosion. The electro slag remelting process has completely resolved this problem by making ingots free from negative chromium segregation. On the other hand, the long term isothermal heat treatment has not shown any beneficial effect on reducing tunneling corrosion.

Acknowledgement

The authors deeply appreciate Mr. M. Ohkubo, Dr. T. Okada and Mr. M. Harada for their enthusiastic cooperation through entire study, and also Dr. T. Ikeda for his advise and comments.

References

1. U. Blom and B. Kvarnback, Materials Performance, 14 (1975): p. 43.
2. E. - M. Horn and H. Kohl, Werk. und Korr., 37 (1986): p. 57.
3. J. A. Beavers, W. E. Berry, J. C. Griess and R. R. White, US DOE Rep. ORNL-SUB 7327-13, 1982.
4. A. Desestret, G. Gay and P. Soulignac, " Colloque de Metallurgie 25th" (Inst. Natl. Sci. Tech. Nucl., 1983), p. 121.
5. R. D. Shaw and D. Elliott, Stainless Steel ' 84", (1985), p. 395.
6. G. Herbsleb, K. - J. Westerfeld, Werk. und Korr., 27 (1976): p. 404.
7. M. Sugiyanma, T. Umeda and H. Matsuyama, Tetsu-to-Hagane (The Iron and Sreel institute of Japan), 60 (1974): p. 32.
8. H. Mizukami, Y. Nagakura, S. Izumi and T. Kusakawa, Testu-to-Hagane, 76 (1990): p. 722.
9. S. F. Pugh. Defect and Structure, (USA: Martinus Ni Jhoff Publ, 1982),p.241.

Table 1 Chemical composition of materials used (mass%)

Product	Material	Melting* method	Chemical composition (mass %)							
			C	Si	Mn	P	S	Ni	Cr	Nb
Forging	A (310Nb)	AOD	0.013	0.29	0.63	0.015	0.001	20.29	25.51	0.24
	B (310Nb)	AOD	0.010	0.23	0.70	0.015	0.001	20.30	25.35	0.24
	C (310Nb)	AOD	0.009	0.22	0.71	0.016	0.001	20.40	25.65	0.24
	D (310Nb)	AOD	0.010	0.25	0.68	0.019	0.001	20.70	25.65	0.25
	E (310Nb)	AOD + ESR	0.008	0.21	0.68	0.007	0.001	20.80	24.90	0.28
	F (310Nb)	AOD + ESR	0.012	0.17	0.66	0.009	0.001	21.05	24.90	0.23
	G (310Nb)	AOD + ESR	0.009	0.18	0.65	0.008	<0.001	20.97	24.43	0.25
Plate	H (310Nb)	AOD	0.010	0.27	0.64	0.013	0.001	20.18	25.10	0.24
	I (304L)	AOD	0.028	0.75	1.15	0.028	0.010	10.52	19.03	—

* Melting method {AOD : Argon Oxygen Decarburization
ESR : Electro Slag Remelting

Table 2 Analysis of alloying elements and impurities in the 310Nb forging by the mapping EPMA

Melting method	AOD					AOD +ESR
Material	A		C		D	E
Element	L*	T**	L	T	L	L
Cr	Yes	Yes	Yes	Yes	Yes	No
Mn	No	No	No	No	—	—
P	No	—	—	—	—	—
S	No	No	—	—	—	—
Cu	No	—	—	—	—	—
Mo	No	—	—	—	—	—

Yes: Segregated
No : No segregation
- : No measurement
* L: Longitudinal surface to the metal flow
**T: Transverse surface to the metal flow

Table 3 Immersion test results in tunneling corrosion

Melting method	Material	Forging ratio	Cr^{6+} concentration in 8N HNO_3 (g/ℓ)	Immersion time (h)					Corrosion rate (g/m² h)
				48	96	144	192	240	
AOD	C	27	0.1	○	○	○	○	○	—
		27	0.5	○	○	○	○	○	—
		27	1.0	○	○	○	○	○	—
		27	5.0	○	○	○	×* (0.6)	×	16
		27	10.0	○	×* (0.5)	×* (0.8)	×* (0.9)	×	44
		60	10.0	—	—	—	×* (0.9)	—	—
	D	4	1.0	—	—	—	—	△	—
		4	10.0	○	×	×	×	×	—
		7	10.0	△	×	×	×	×	46
		15	1.0	—	—	—	—	△	—
		15	10.0	△	×	×	×	×	—
AOD + ESR	E	6	10.0	○	○	○	○	○	—
		27	10.0	○	○	○	○	○	—
		60	10.0	○	○	○	○	○	—
	F	6	5.0	○	○	○	○	○	14
		6	10.0	○	○	○	○	○	—
		60	10.0	○	○	○	○	○	—
	G	6	5.0	○	○	○	○	○	16
		6	10.0	○	○	○	○	○	45
		60	10.0	○	○	○	○	○	—

Tunneling corrosion { ○: No occurrance
△: Slight occurrance
×: Occurred
*: Tunneling corrosion depth (mm)
—: No test

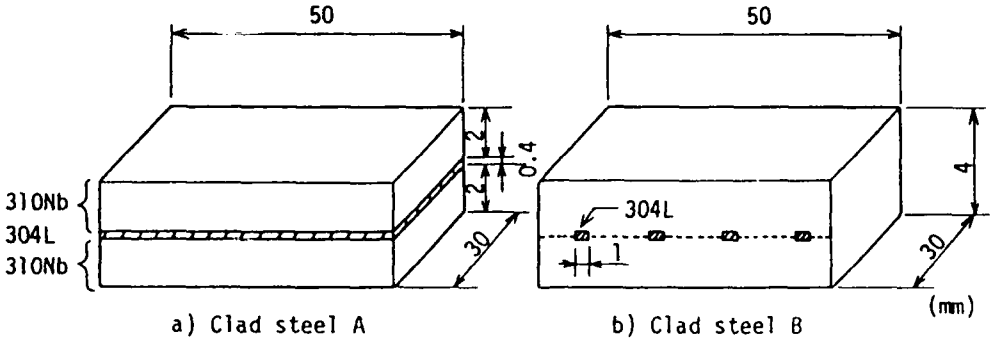

Figure 1. 310Nb-304L clad steels

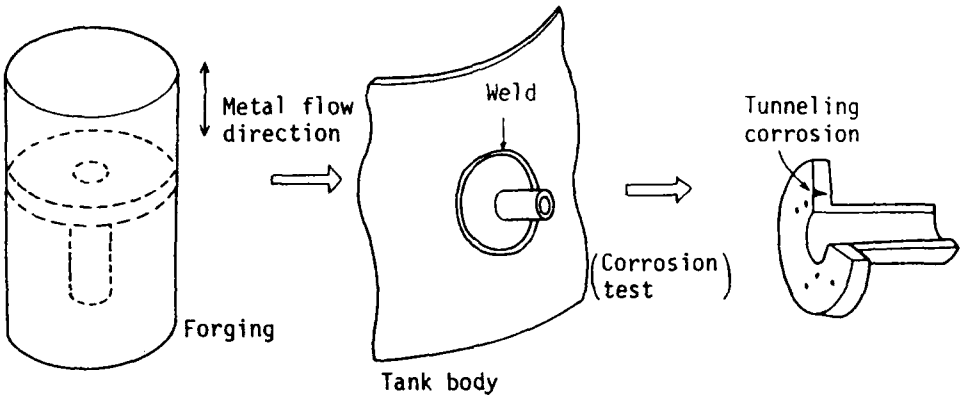

(a) Nozzle fabricated from forging (b) Mounting a flange on to a tank body by welding (c) Tunneling corrosion

Figure 2. Tunneling corrosion occurrence on the nozzle fabricated from a forging.

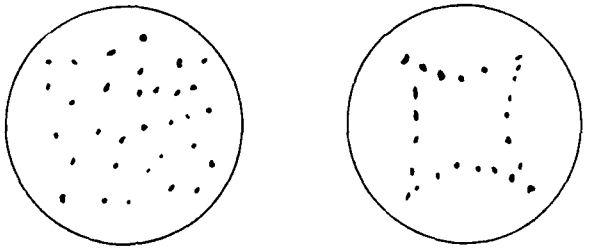

(a) Uniform distribution of tunneling corrosion (A large diameter forging)

(b) Localized distribution of tunneling corrosion (A small diameter forging)

Figure 3. Two types of tunneling corrosion distribution.

Figure 4. Microstructure of tunneling corrosion.

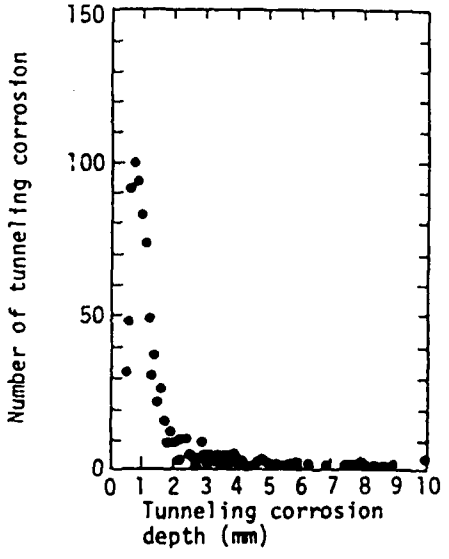

Figure 5. Relationship between depths and numbers in tunneling corrosion.

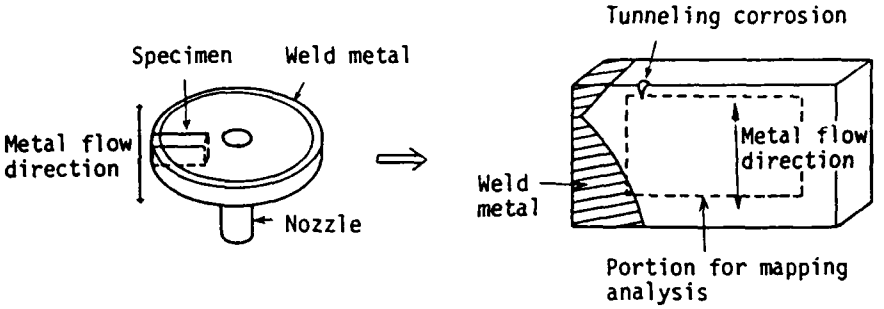

Figure 6. Portion for the mapping EPMA analysis on the specimen cut off from the nozzle where tunneling corrosion occurred.

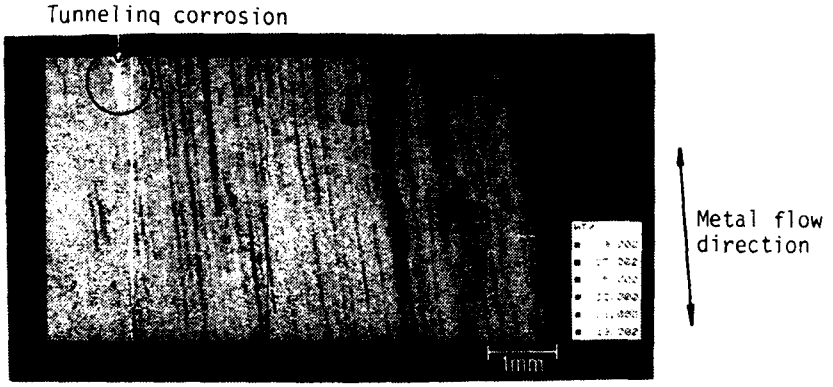

Figure 7. Mapping EPMA analysis of Cr content on the longitudinal surface to the metal flow in the 310Nb forging melted by the AOD process.

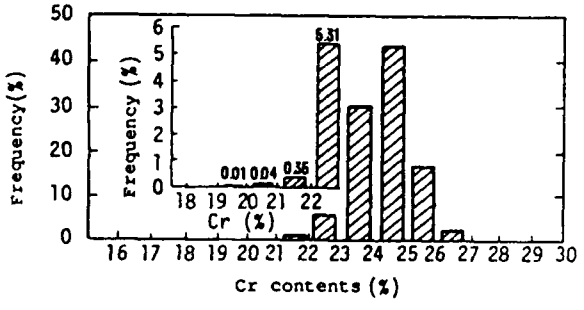

Figure 8. Histogram of Cr content on the longitudinal surface of a 310Nb forging.

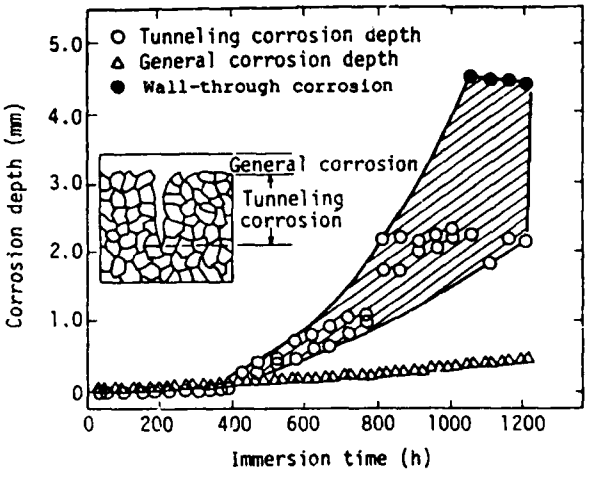

Figure 9. Dependence of tunneling corrosion growth on the immersion time in boiling 8NHNO$_3$+0.5g/lCr^{6+}.

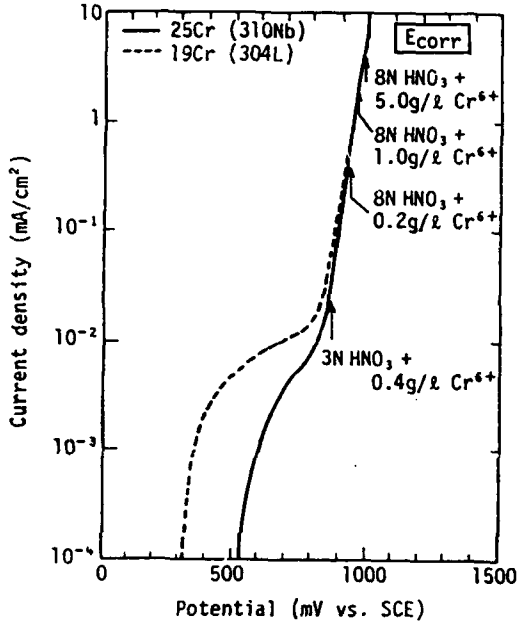

Figure 10. Polarization curves for 310Nb and 304L in 3N HNO_3 at 373K.

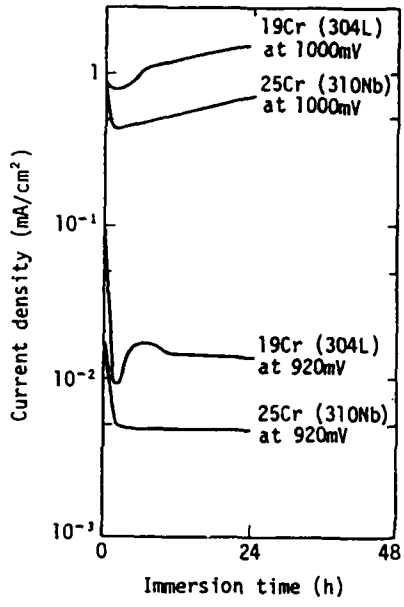

Figure 11. Corrosion current densities for 304L and 310Nb in 8N HNO_3.

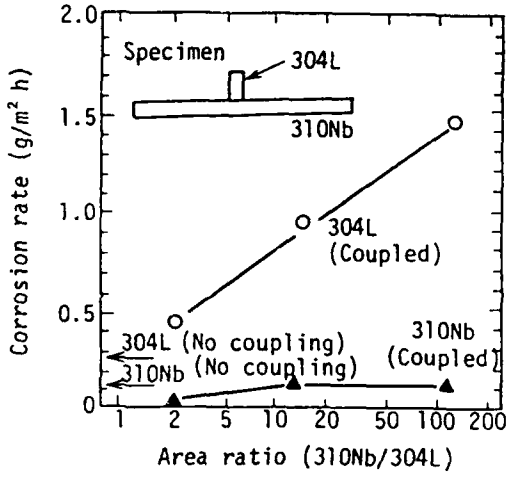

Figure 12. Galvanically accelerated corrosion for 304L with the area ratio of 310Nb to 304L in boiling 3N HNO_3+0.4g/lCr^{6+}.

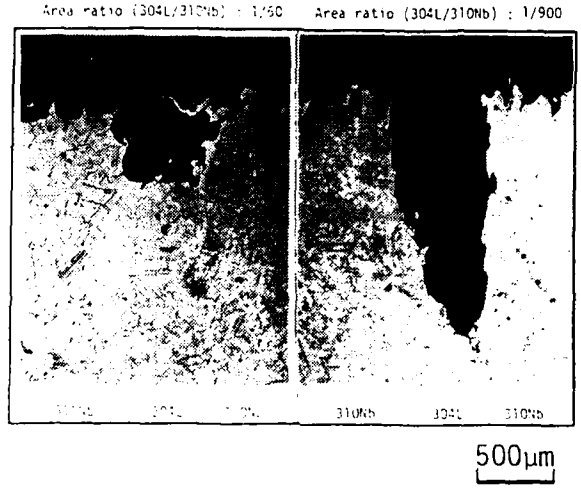

Figure 13. Post-test micrographs of 304L-310Nb clad steels (Boiling 8N HNO_3+5g/lCr^{6+}, 2 periods of 24h immersion test).

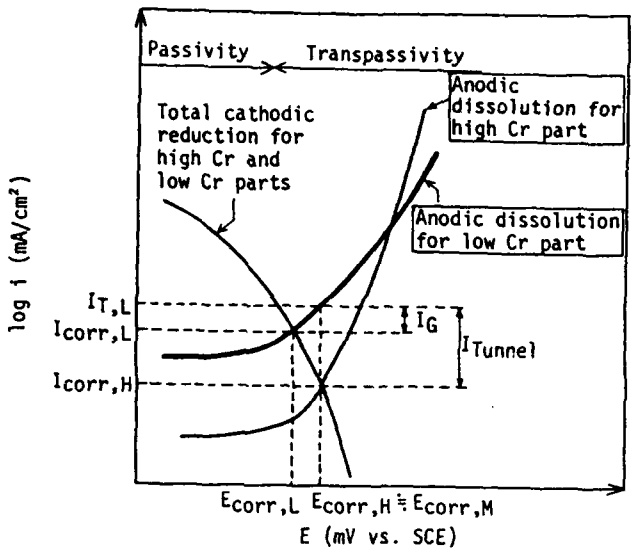

Figure 14. Electrochemical explanation for tunneling corrosion kinetics

($E_{corr,L}$: Corrosion potential of small part with low Cr when it is isolated (mV)
$E_{corr,H}$: Corrosion potential of large part with high Cr (mV)
$E_{corr,M}$: Corrosion potential of specimen where low Cr and high Cr part are coexistent (mV)
$I_{corr,L}$: Corrosion current density of small part with low Cr when it is isolated (mA/cm²)
$I_{corr,H}$: Corrosion current density of high Cr part (mA/cm²)
I_G : Galvanic current density between small part with low Cr and large part with high Cr (mA/cm²)
$I_{T,L}$: Total corrosion current density of low Cr part (mA/cm²)
I_{Tunnel} : Current density of tunneling corrosion (mA/cm²))

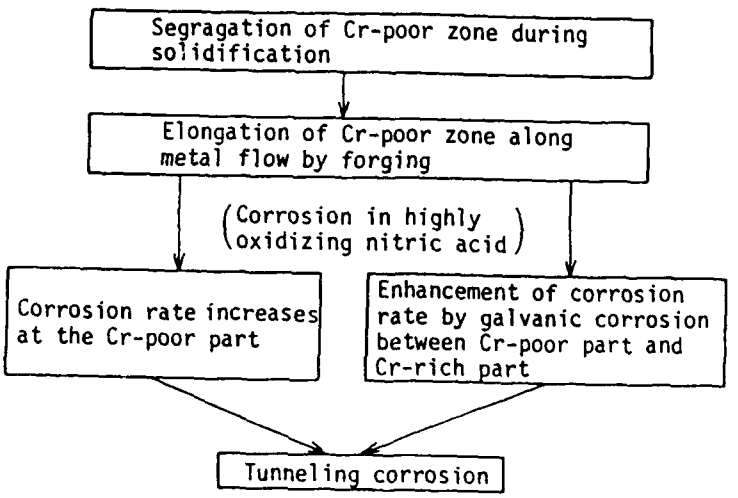

Figure 15. Mechanism of tunneling corrosion

Corrosion and Wear in White Cast Irons

S. W. Watson
Albany Research Center, U. S. Bureau of Mines
1450 Queen Avenue, Albany, OR 97321

S. D. Cramer
Albany Research Center, U. S. Bureau of Mines
1450 Queen Avenue, Albany, OR 97321

B. W. Madsen
U. S. Bureau of Mines
Mail Stop 6204
810 7th St., NW
Washington, DC 20241

Abstract

White cast irons and hardfacings are used in the mining and mineral processing industry to combat corrosion and wear. They are part of a broad class of modern materials with unique structural properties increasingly utilized in severe industrial environments. The mining and mineral processing industries crush over 1 billion tons of ore annually. Metal wear losses in wet grinding increase manyfold over those in dry grinding. A fundamental understanding of wear/corrosion synergism in white cast irons is the object of research at the Bureau of Mines to provide a basis for modeling wear/corrosion interactions in the general class of metal-matrix composites.

Samples of the individual phases found in white cast iron were fabricated for study of the chemical and mechanical processes occurring on each phase during corrosive wear. The samples included the mixed carbides $(Cr,Fe)_7C_3$ and $(Cr,Fe)_3C$, the pure carbides Cr_7C_3 and Cr_3C, the matrix and the Cr-depleted alloy surrounding the carbides. The initial studies described here examined corrosion and wear processes separately to establish baseline measurements for the samples.

Dry wear rates were measured using the pin-on-drum technique with garnet, alumina, and silicon carbide abrasives used to rank the performance of the samples. Several carbides of intermediate hardness exhibited brittle fracture. The hardest carbides exhibited no wear with garnet except in locally soft areas where second phases were present.

Corrosion in the absence of wear was characterized by potentiodynamic polarization measurements in oxygen- and nitrogen-saturated acid sulfate solutions. These measurements provide a general description of monolith electrochemical behavior and were used to pinpoint effects that could be important in galvanic and localized corrosion. No evidence of uniform corrosion was observed. Galvanic effects are possible between the carbides and the matrix.

Key terms: corrosion, wear, white-cast-iron, synergism

Introduction

Corrosion and wear damage to structural materials directly and indirectly costs the Nation hundreds of

billions of dollars annually. In 1989, corrosion damage alone was estimated to be $200 billion or about 4 pct of the gross national product[1]. An additional $100 billion of costs results from corrosion damage to the infrastructure (bridges, pipelines, etc.) and to storage tanks containing toxic, hazardous and radioactive wastes. Annual grinding media costs frequently approach or exceed energy costs in some processes[2]. Corrosion and wear damage arising from comminution is equivalent to 12 pct of the more than 30 billion Kwh annually consumed by U.S. industry for crushing and grinding[3]. Wear debris and corrosion products formed during comminution affect product quality and can adversely affect subsequent beneficiation by altering the chemical and electrochemical properties of the mineral system [2,4-5]. Metal wear loss in wet grinding is 8 to 10 times that in dry grinding[3]. Corrosion may account for 40-60 pct of the total consumption of grinding media in wet grinding of sulfide ores[6]. Wear and corrosion processes involve many mechanical and chemical mechanisms and the combined action of these mechanisms can result in significant mutual reinforcement of these processes. Dunn[7] proposes seventeen synergistic relationships (summarized in Figure 1) between abrasion, impact and corrosion that could significantly increase wear damage in wet and aqueous environments beyond the individual contributions of wear and corrosion. Any strategy for minimizing the effects of these relationships requires a fundamental understanding of the mechanisms involved, the way in which they interact, and their importance in specific mineral-metal environments.

Research on wear/corrosion synergism has been limited largely to studies on mild steel, high-carbon low-alloy steel, and stainless steels [4-6,8-12]. Hard-phase metal-matrix composites represent a broad class of modern materials with unique structural properties increasingly utilized to varying degrees in corrosive and wear environments and susceptible to wear/corrosion synergism. White cast irons and hardfacings, containing large quantities of strategic and critical metals, are a subclass of these materials used in the mining and mineral processing industry to combat corrosion and wear. A fundamental understanding of wear/corrosion synergism in white cast irons should define the important quantitative principles involved in wear/corrosion interactions for hard-phase metal-matrix composites and should provide the basis for a general physicochemical model describing these interactions.

Samples representing single phases in white cast iron (matrix, Cr-depleted region, carbide hard phases) were fabricated and characterized in terms of mechanical and chemical properties. Baseline wear rates were measured for each of the samples by standard dry wear technique of pin-on-drum. Two- body wear rates were measured in the absence of corrosion, corrosion rates in the absence of wear, as well as the wear/corrosion synergism in a specially designed wear/corrosion apparatus called a cylinder-anvil apparatus depicted in Figure 2.

Equipment and Experimental Procedures

A. Samples Preparation

The original intent was to make monoliths of the individual phases found in white cast iron (from G. Laird's studies [13]) for study of the chemical and mechanical processes occurring on each phase during corrosive wear. The samples included the mixed carbides $(Cr,Fe)_7C_3$ and $(Cr,Fe)_3C$, the pure carbides Cr_7C_3 and Cr_3C, the matrix and the Cr-depleted alloy surrounding the carbides. The exact composition for the mixed carbides was chosen from the metastable phase diagram for carbon-chromium-iron system shown in Figure 3 (composed by combining phase diagrams of V. G. Rivlin[14], R. S. Jackson[15] and R. P. Thorpe and B. Chicco[16]). These samples were prepared by hot pressing commercially available pre-mixed powders of the correct composition according to a modified procedure described by T. Nasu, et al.[17] and T. Ogasawara et al.[18] The carbides were hot-pressed at 1130-1200°C at pressures up to 5000

psi for at least 1 hour; the matrix and Cr- depleted matrix specimens were hot pressed at 1080-1100°C at pressures up to 1900 psi for at least 1 hour. After hot-pressing into cylindrical shapes, the samples were glass-encapsulated and HIPed (Hot Isostatic Pressed). The carbides were HIPed at 1130-1200°C at pressures of 30,000 psi with Ar gas for at least 2 hours; the matrix and Cr-depleted matrix were HIPed at 1080-1100°C at pressures of 20,000 psi with Ar gas for at least 2 hours. The samples were then machined into the appropriate shapes for the experimental studies.

B. Corrosion Studies

Baseline corrosion studies were conducted in a 1-liter, modified Greene-type polarization cell equipped with a nitrogen gas bubbler, a 5-by 1-cm, platinum counter electrode, and a saturated calomel electrode as the reference electrode connected to the polarization cell via a Luggin probe assembly. The working electrodes consisted of the fabricated samples. The specimens were mounted in a Lexan[1] compression mounting holder that uses a Viton-A O-ring to seal the exposed area of 1.37 cm^2. The working electrode specimens were prepared by abrading them on wet SiC papers down to 400 grit. The specimens were ultrasonically cleaned in ethanol, rinsed with Type 1[2] water, and dried with N_2 gas. The measurements were conducted in 1N sulfuric acid as well as 1N sodium sulfate saturated with both oxygen and nitrogen.

C. Wear Studies

Dry wear rates were measured using the pin-on-drum technique developed at the Bureau[19,20]. The pin-on-drum abrasive-wear testing machine is shown in Figure 4. This machine consists of a head that rotates the pin test specimen while traversing the length of a rotating cylinder that is covered with abrasive paper. The cylindrical pin specimens of 1/4 inch were made from the fabricated samples and a standard pin made of Type A514 steel. The standard pin specimen was used as a quality control standard. The abrasive cloth was of 150 grit SiC, Al_2O_3, or garnet.

D. Cylinder-Anvil Studies

The rotating cylinder-anvil apparatus has been used at the University of Utah[11] to measure concurrent corrosion and abrasive wear processes. A schematic drawing of the rotating-cylinder-anvil apparatus is shown in Figure 2[11]. The apparatus consists of a rotating cylinder specimen (1)[3] 2.5 cm diameter and .5 cm high. The specimens of samples or white cast iron samples are polished to 600 grit with SiC paper, ultrasonically cleaned in acetone, ethanol, and Type 1 water, and dried with N_2 gas. The rate of rotation (30 to 200 rpm) is controlled by a variable speed motor (2) through a rotating shaft(3) and bevel gear box(4). The rotating specimen is fixed by a phenolic nut(5) for ready removal and weighing after each experiment. Contact pressure is applied to the rotating specimen through two opposing anvils(7) composed of commercially available SiC rod 0.84 cm in diameter. The anvils are mounted in phenolic holders on Teflon coated steel rods(8) and contact the specimen with constant or intermittent loading (up to 37 kg) by hydraulic cylinders(9). The hydraulic system consists of a pump, oil reservoir, directional

---

[1]Reference to specific products does not imply endorsement by the U.S. Bureau of Mines.

[2]This refers to ASTM D1193-77 Standard for reagent grade water.

[3]Numbers refer to elements of cylinder-anvil apparatus denoted in Figure 2.

control valve, flow control valve, pressure gages, and a pressure regulator.

The apparatus also includes a polarization cell to conduct electrochemical experiments. This cell consists of a plastic cylinder container (10) equipped with o-ring gaskets around rods(8) to make an air tight seal, carbon brush electrical contact(11) to specimen (1), two platinum counter electrodes(12), a Luggin-probe assembly (13) to the SSE (saturated sulfate electrode) reference electrode, a stirrer(14), a controller(16) and a gas bubbler inlet(15). A 1N Na_2SO_4 solution (pH 6.4) saturated with N_2 was used as the electrolyte.

E. Electrochemical Measurements

All of the electrochemical experiments were conducted with a computer-controlled potentiostat-galvanostat. The potentiodynamic polarization curves were acquired at a scan rate of 20 mV/min using a 3 electrode configuration of working electrode (sample), counter electrode (platinum) and various reference electrodes of saturated calomel electrode, silver-silver chloride, and mercury-mercury sulfate. For the corrosion studies, a N_2 or O_2 saturated 1N H_2SO_4 or 1N Na_2SO_4 was used, for the cylinder anvil studies 1N Na_2SO_4 electrolyte was used.

The polarization resistance, R_p, was obtained by fitting the linear approximation to the Butler-Volmer equation for activation-controlled electrochemical reactions to the data within $\pm$ 30 mV of E_{corr}.

The corrosion currents were found from the intersection current obtained from extending the Tafel fits of the cathodic and anodic branches of the potentiodynamic polarization curves.

The proposed galvanic coupling for figure 9 was obtained by plotting the current vs potential for (the cathode sample 1, $Cr_{4.8}Fe_{2.2}C_3$), and the anode (Cr-depleted matrix) on the same graph. The point at which these data cross is the current for the galvanic coupling. For a cathode to anode ratio of 10, the current for the cathode ($Cr_{4.8}Fe_{2.2}C_3$) is multiplied by 10.

Results and Discussion

A. Characterization of Samples

The sample formulas and chemical composition, as determined by X-ray diffraction and electron microprobe analysis, are tabulated in Table 1. X-ray diffraction (XRD) and electron microprobe analysis both indicate there are trace amounts of second phases present in the samples. Electron microprobe scans on the first set of fabricated samples indicate that there are some chemical inhomogeneities from incomplete reaction and dispersal of the powder reactants. The original intent was to make monolithic samples of the components of the white cast iron. These research samples are improving with refinement of fabrication. It is hoped that the research samples may evolve into monoliths. The information in Table 1 is for the last fabricated samples. The Cr_3C is a mixture of $Cr_{23}C_6$ and Cr_7C_3. The stable forms of M_3C must contain considerable Fe[21]. This fact is quite clear from the metastable phase diagram of C-Cr-Fe in Figure 3. The densities of the samples (tabulated in Table 1) were determined by weighing and measuring the dimensions of the quite precise cylindrical shapes after HIPing as well as by a liquid displacement technique. The percentage of theoretical density subtracted from 100% gives some indication of porosity of the samples. Unfortunately, there are no literature density values for the mixed carbides. The theoretical densities for Cr_7C_3 and $Cr_{23}C_6$ are 6.9-6.92. It was a assumed that the theoretical densities of the mixed carbides were greater than 7 g/cc. The densities of the matrix samples

are 7.6 g/cc. Sample 4 was purchased as a pure compound not a mixture of elemental powders. This sample has the lowest percent of theoretical density (94%). This sample may require a refinement in fabrication technique. The matrix samples also require further processing to render them austenitic, fcc structure like the white cast irons.

B. Corrosion Tests

1. Samples. Typical potentiodynamic polarization curves are shown in Figures 5, 6, and 7 for M_7C_3's , M_3C's and matrix materials, respectively. In general the M_7C_3's are passive, exhibit no tendency to pit, have similar corrosion potentials (E_{corr}), and cathodic regions. Their behavior is not linked simply to the fraction of iron present. The sample with the intermediate iron concentration, $Cr_{4.8}Fe_{2.2}C_3$, has the highest corrosion current at E_{corr} of all the M_7C_3's.

The M_3C's (displayed in Figure 6) have similar E_{corr}, exhibit no tendency to pit, and with the exception of an oxidation peak in the passive region for $Cr_{0.2}Fe_{2.8}C$, have low passive currents, very low for Cr_3C ($Cr_{23}C_6$ and Cr_7C_3). The high concentration of iron in the $Cr_{0.2}Fe_{2.8}C$ leads to an iron oxidation peak at around +0.3 V with the formation of a passive film at higher potentials. Passive currents for the $Cr_3C(Cr_{23}C_6)$ are 100 times lower than for $Cr_{0.2}Fe_{2.8}C$.

Figure 7 includes the potentiodynamic curve for a white cast iron sample containing 40% carbides for comparison with the matrix and samples. The polarization curves for the matrix and Cr-depleted matrix are similar with the Cr-depleted matrix exhibiting slightly higher corrosion currents in the active and passive regions. Both exhibit instability near E_{crit} where the surface passivates with a 100-fold drop in current. The white cast iron sample displayed some of the same features as the matrix (peak at +.8 V vs NHE) and the Cr-depleted matrix (hump at +.2 V vs NHE); the white cast iron exhibited a more positive E_{corr} and slightly lower current rates in the active and passive regions. The corrosion currents for the matrix, Cr-depleted matrix, and white cast irons are 10 to 100 times higher than those of the carbides.

Electrochemical parameters obtained from the polarization curves are summarized in Table 2. Values of R_p are reported in Table 2 along with E_{corr} and I_{corr} (the corrosion rate). The corrosion currents of the mixed (Cr,Fe)-carbides are 10 times or more higher than the pure Cr-carbides. The corrosion current of the matrix is 3 to 100 times higher than the carbides. The Cr-depleted material corrodes at slightly higher rates than the matrix.

Polarization measurements on sample 1 ,$Cr_{4.8}Fe_{2.2}C_3$, at various pH's (electrolytes of 1N H_2SO_4 of pH = 0.3 and 1N Na_2SO_4 of pH = 6.4 were used) and with saturation by both O_2 and N_2 (shown in Figure 8) indicate the principal effect of dissolved oxygen and of H^+ is on the cathodic reaction current. The increase in corrosion rate and E_{corr} with decrease in pH, comparing sodium sulfate - N_2 and sulfuric acid - N_2, agrees with the shifts predicted by the Butler-Volmer model when the cathodic reaction controls corrosion. The shifts result from the increased availability of H^+ at the metal surface for the sulfuric acid - N_2 solution. The two to fourfold increase in corrosion rate that results when oxygen is added to the solution represents the increased flux of reducible species to the carbide surface. The shifts in corrosion rate and E_{corr} again are consistent with cathodic control of the corrosion process. However, the relatively small amplitude of the corrosion rate increase for an increase in oxygen concentration suggests concentration polarization for the oxygen reduction reaction produced by relatively slow diffusion of O_2 through the laminar boundary layer at the carbide surface. Thus, cathodic control and concentration

polarization appear to affect the corrosion rate of the carbides in acid solutions containing dissolved oxygen.

Galvanic effects are possible between the carbides and the matrix. These couples will involve anodic dissolution of the matrix or, more likely, the Cr-depleted matrix surrounding the carbides and reduction of hydrogen ion or oxygen on the carbides. Galvanic couples may also exist within the carbides between regions of different composition. A galvanic couple of as much as a 0.1 V is possible between the matrix and the carbides. Figure 9 depicts the galvanic couple between $Cr_{4.8}Fe_{2.2}C_3$ and the Cr-depleted matrix. Galvanic couples between the matrix and the carbides (cathode/anode area ratio of 1) are shown to increase matrix corrosion rates 4-fold. When cathode areas are substantially higher, as would occur with large carbides surrounded by a thin zone of chromium-depleted matrix, corrosion rates would increase further. For example, a cathode/anode area ratio of 10 leads to an 6-fold increase in the corrosion rate.

The corroded surfaces of the samples from the electrochemical experiments were examined by SEM. No evidence of uniform corrosion was observed.

C. Dry Wear Tests

Pin-on-drum dry wear rates were quantified using a dimensionless measure that varies linearly with the pressure of the abrasive on the material,

$$w = \Delta m/LA\rho$$

where Δm is the pin mass loss, L is the length of the pin path over the abrasive, A is the cross-sectional area of the pin, and ρ is the density of the pin material. Modelling of competing wear and corrosion processes requires expressing damage rates in similar units. For corrosion this is typically a penetration rate, r. The above wear rate is expressed as a penetration rate multiplying w by the linear velocity of the drum, v, i.e., $r = wv$.

The mechanical properties of the samples are given in Table 3. The data for steel Type A514 used as the standard for the wear tests are also included in Table 3; the reproducibility of the standard was within one standard deviation. The mixed $(Cr,Fe)_7C_3$ wears much less than the pure Cr_7C_3 on all abrasives. (These results are preliminary as the Cr_7C_3 was not as dense a sample as the mixed $(Cr,Fe)_7C_3$.) The mixed $(Cr,Fe)_3C$ wears more than the Cr_3C ($Cr_{23}C_6$ and Cr_7C_3) on garnet but less than the ($Cr_{23}C_6$ and Cr_7C_3) on SiC and Al_2O_3. The wear rates for the matrix and Cr-depleted matrix are similar on all abrasives. Wear rates of the matrix and Cr-depleted matrix are 50 times greater than the carbides on garnet.

A dry wear test using SiC as abrasive for the anvils was conducted in the rotating-cylinder-anvil apparatus with a white cast iron specimen of 13.5% Cr (84.1% Fe) quite comparable in chemical composition to the matrix. SEM examination was performed on the dry wear test debris. Large flakes of white cast iron fractured off the wear surface. The examination found the wear surface to be worn smooth and have numerous fine cracks with pull outs of material. The fracture surface of the wear flakes exhibited fatigue striations as well as areas that are worn smooth from the flexing of the flake before it fractured (fatigued) off. The wear rate was 0.059 expressed in dimensionless units as the results in Table 3. A direct wear rate comparison between the tests using the pin-on-drum apparatus and the cylinder-anvil apparatus can not be made. Each apparatus has different forces on the sample. Separate experiments need to be completed to determine the contact area for the cylinder-anvil apparatus. Also sets of experiments need to be performed using standards with the cylinder-anvil apparatus to develop an equation similar to the

dimensionless wear rate developed for the pin-on-drum apparatus.

D. Cylinder-Anvil Synergism Experiments

The study of two-body wear/corrosion synergism was conducted with the rotating cylinder-anvil apparatus. These studies were conducted on a 13.5% Cr white cast iron and the matrix sample 6. The wear/corrosion synergism studies consisted of four tests; a potentiodynamic corrosion test with and without anvil pressure (28 kg force on anvils) and sample rotation at 50 rpm and a wear test with anvil pressure and sample rotation with and without cathodic protection as described by B. W. Madsen[22]. The potentiodynamic corrosion tests for the white cast iron and the matrix are shown in Figures 10 and 11, respectively. The synergism of wear on corrosion is quite evident for both the white cast iron and matrix from the potentiodynamic scans displayed in Figures 10 and 11. The active currents around E_{corr} with anvils were at least 3 orders of magnitude larger for the white cast iron sample and 1 order of magnitude larger for the matrix material. For both samples the formation of a corrosion protective film at high anodic potentials was retarded with the application of anvil pressure. The corrosive wear rates for the white cast iron in the 1N Na_2SO_4 electrolyte without galvanic protection was .022 expressed in dimensionless units as the data in Table 3. The wet wear was less than one-half the dry wear rate of .059.

Conclusions

- Samples of seven different compositions representing single phases in white cast irons were fabricated. Pre-blended powders were hot pressed into cylinders, glass encapsulated, and then HIPed. The samples were characterized by chemical and physical property measurements.

- Electrochemical measurements on the samples in the absence of wear were completed. The corrosion rate of the matrix material was 3 to 100 times greater than that of the carbides. The corrosion rates of the mixed (Cr,Fe)-carbides were 10 times or more higher than the pure Cr-carbides. No evidence of uniform corrosion was observed.

- As much as a 0.1 V galvanic couple is possible between the matrix and the carbides.

- Sample dry wear measurements using garnet, Al_2O_3, and SiC abrasives were completed on the pin-on-drum apparatus. Wear rates of the matrix were as much as 50 times those of the carbides with the garnet.

- Two-body wear/corrosion synergism studies were conducted on a white cast iron and the matrix. The effect of abrasion on corrosion was shown to exist for both the white cast iron and matrix.

References

1. Personal Communication, Dale Miller, Director, Public Affairs, National Association of Corrosion Engineers (NACE), Houston, TX, available from S. D. Cramer (ALRC).
2. Pozzo, R. L. and I. Iwasaki. Pyrite-Pyrrhotite Grinding Media Interactions and Their Effects on Media Wear and Flotation, *J. Electrochem. Soc.*, 136(6), 1989, pp. 1734-1740.
3. National Materials Advisory Board, Comminution and Energy Consumption, NMAB-364, National Academy Press, Washington, DC, 1981, 283 pp.
4. Pozzo, R. L., and I. Iwasaki. Effect of Pyrite and Pyrrhotite on the Corrosive Wear of Grinding

Media, *Minerals and Metallurgical Processing,* August 1987, pp. 166-171.
5. Pozzo, R. L., and I. Iwasaki. An Electrochemical Study of Pyrrhotite-Grinding Media Interaction Under Abrasive Conditions, *Corrosion,* 43(3), 1987, pp. 159-169.
6. Jang, J. W., I. Iwasaki and J. J. Moore. The Effect of Galvanic Interaction Between Martensite and Ferrite In Grinding Media Wear, *Corrosion,* 45(5), 1989, pp. 402-407.
7. Dunn, D. J. Metal Removal Mechanisms Comprising Wear In Mineral Processing, in Wear of Materials 1985, ed. by K. C. Ludema, Am. Soc. Mech. Engr., New York, NY, 1985, pp. 501-508.
8. Hoey, G. R., W. Dingley, and C. Freeman. Corrosion Inhibitors Reduce Ball Wear in Grinding Sulfide Ore, CIM Bull., 68, 1975, 120.
9. Pitt, C. H., and Y. M. Chang, Corrosive-Erosive Wear of Grinding Ball Metals at High Jet Velocities, *Corrosion,* 43(10), 1987, pp. 599-605.
10. Lin, H., and Z. Qingde. The Behavior of 28% Chromium White Cast Iron in Abrasion and Corrosion-Abrasion Wear, in Wear of Materials 1987, ed. by
K. C. Ludema, Am. Soc. Mech. Eng., New York, NY, 1987, pp. 653-659.
11. Kotlyar, D., C. H. Pitt, and M. E. Wadsworth. Simultaneous Corrosion and Abrasion Measurements Under Grinding Conditions, *Corrosion,* 44(5), 1988, pp. 221-228.
12. Natarajan, K. A., S. C. Riemer, and I. Iwasaki. Influence of Pyrrhotite on the Corrosive Wear of Grinding Balls in Magnetite Ore Grinding, *Intl. J. Mineral Processing,* 13, 1984, pp. 73-81.
13. Laird II, G., G. L. F. Powell, R. R. Brown, and R. E. Nielsen. Some Comments on the Eutectic Solidification of Cr-Ni(-Si-Mn) White Cast Irons
(To be published).
14. Rivlin, V. G., Critical Review of Constitution of C-Cr-Fe and C-Fe-Mn Systems, Intl. Metals Review, 29, 1984, pp. 299-327.
15. Jackson, R. S., The Austenite Liquidus Surface and Constitutional Diagram for the Fe-Cr-C Metastable System, J. Iron and Steel Institute, 208, 1970. pp. 163-167.
16. Thorpe, W. R., B. Chicco, The Fe-Rich Corner of the Metastable C-Cr-Fe Liquidus Surface, *Metall. Trans. A,* 16A, 1985, p. 1541.
17. Nasu, T., C.C. Koch, K. Nagaoka, N. Itoh, M. Sakurai, and K. Suzuki , EXAFS Study of the Solid State Amorphization Process, *Materials Science and Engineering,* A124,1991, pp. 1385-1388.
18. Ogasawara, T., A. Inoue, and T. Maumoto , Amorphization in Fe-metalloid Systems by Mechanical Alloying, *Materials Science and Engineering,* A124,1991, pp. 1338-1341.
19. Blickensderfer, R., J. H. Tylczak, and B. W. Madsen. Laboratory Wear Testing Capabilities of the Bureau of Mines, BuMines IC 9001, 1985, 36 pp.
20. Blickensderfer, R., B. W. Madsen, and J. H. Tylczak. "Comparison of Several Types of Abrasive Wear Tests", in Wear of Materials 1985, ed. by K. C. Ludema, Am. Soc. Mech. Eng., New York, NY, 1985, pp. 313-323.
21. Kudielka, H. and J. Moller, The Stability of Chromium in (Fe-Cr)C, Zeitschrift fur Kristallographie 118, 1963, pp. 213-222.
22. Madsen, B.W. , Corrosive wear, chapter for 10th edition of ASM Metals Handbook:Friction, Lubrication and Wear Technology, 18, 1992, pp. 271-279.

Table 1. Monoliths fabricated for wear/corrosion studies.

Samples	Formula	XRD[1]	Electron microprobe	Density g/cm^3	Percent Theoretical Density
2	$Cr_{3.7}Fe_{3.3}C_3$	$(Cr,Fe)_7C_3$ Cr_2O_3(t)	$Cr_{3.2}Fe_{3.9}C_3$	7.23	100
1	$Cr_{4.8}Fe_{2.2}C_3$	$(Cr,Fe)_7C_3$	$Cr_{4.4}Fe_{2.8}C_3$ graphite (t)	6.94	100
4	Cr_7C_3	Cr_7C_3 Cr_3C_2(t)	Cr_7C_3	6.56	94
3	$Cr_{.2}Fe_{2.8}C$	Fe_3C	$Cr_{0.2}Fe_{2.8}C$ various comp $(Cr,Fe)_3C$ Cr-rich particle(t) graphite(t)	7.32	100
5	Cr_3C	$Cr_{23}C_6$ Cr_7C_3(t)	$(Cr,Fe)_{23}C_6$ $(Cr,Fe)_7C_3$	6.58	100
6	Matrix (13Cr87Fe)	ferrite, $(Cr,Fe)_{23}C_6$(t) $(Cr,Fe)_7C_3$(t)	11Cr89Fe $(Cr,Fe)_{23}C_3$(t) $(Cr,Fe)_7C_3$(t) $(Cr,Fe)_3C_2$(t)	7.61	100
7	Cr-depleted matrix (5Cr95Fe)	same as matrix	5Cr95Fe same as matrix	7.57	100

[1](t) = trace

Table 2. Electrochemical parameter summary for monoliths and minerals exposed to N_2-saturated 1N sulfuric acid.

Samples	Formula	R_p (ohm-cm^2)	E_{corr} V vs NHE	I_{corr} a/cm^2
2	$Cr_{3.7}Fe_{3.3}C_3$	13685.	-0.094	1.1e-6
1	$Cr_{4.8}Fe_{2.2}C_3$	233	-0.179	7.1e-5
4	Cr_7C_3	32000	-0.106	4.6e-7
3	$Cr_{.2}Fe_{2.8}C$	266	-0.117	4.5e-5
5	Cr_3C ($Cr_{23}C_6$ and Cr_7C_3)	7633.	-0.145	1.1e-6
6	Matrix (13Cr87Fe)	15.9	-0.252	1.2e-3
7	Cr-depleted matrix (5Cr95Fe)	11.7	-0.226	1.2e-3
W215	White cast iron	13.5	-0.193	1.6e-3

Table 3. Pin-on-drum Dry wear Rates[1]

Samples	Formula	Hardness KHN_{1000}	Wear rate, w x 10^6		
			Garnet	Al_2O_3	SiC
2	$Cr_{3.7}Fe_{3.3}C_3$	1319	1.13	6.79	36.3
1	$Cr_{4.8}Fe_{2.2}C_3$	1078	0.32	4.98	36.5
4	Cr_7C_3	938	4.65	26.95	106.0
3	$Cr_{.2}Fe_{2.8}C$	908	7.54	18.27	46.7
5	Cr_3C	1461	0.48	3.85	51.9
6	Matrix (13Cr87Fe)	300	24.7	29.03	35.7
7	Cr-depleted	224	27.0	27.57	34.4
Std. steel	Type A514	296	46.3 ± 1.3	39.4 ± 0.6	40.6 ± 0.8

[1] 150 grit abrasive, 6.8 kg load, 12.8 m track.

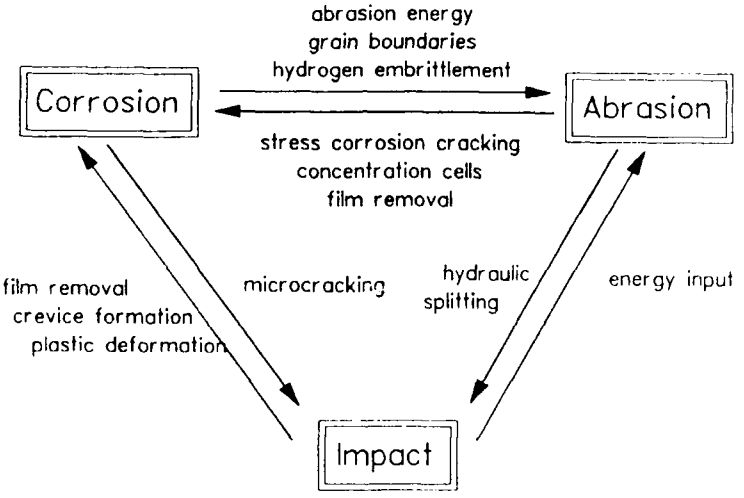

Figure 1. - Dunn's synergistic relationships.

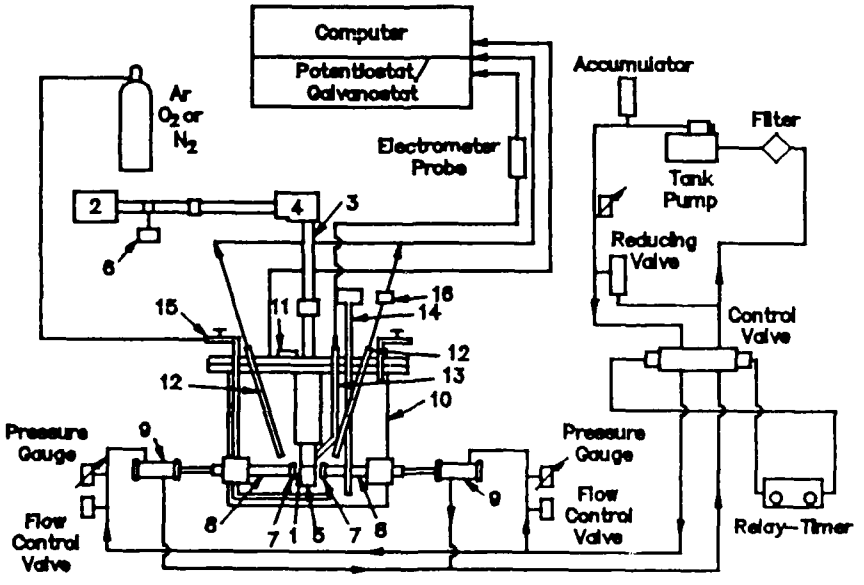

Figure 2. - Cylinder anvil apparatus

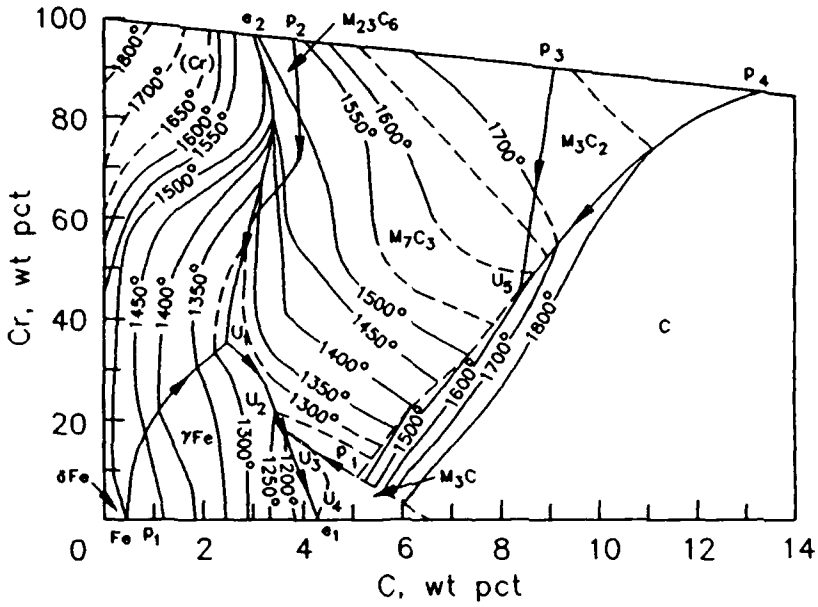

Figure 3. - Phase diagram C-Cr-Fe system.

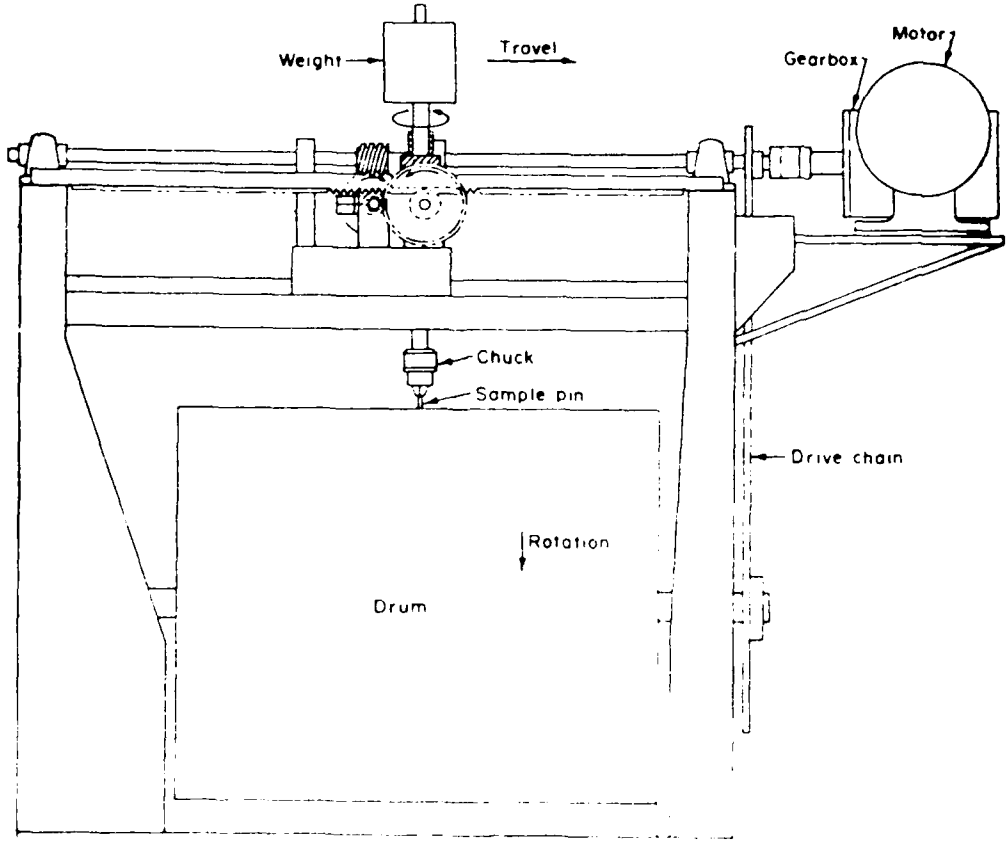

Figure 4. Pin-on-drum wear test apparatus.

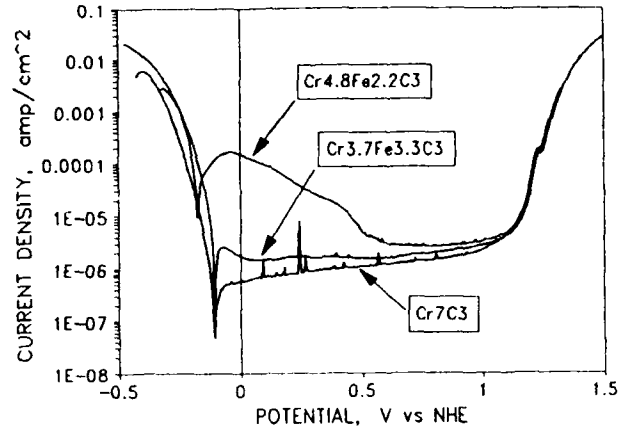

Figure 5. - Potentiodynamic polarization of M_7C_3's in N_2-saturated 1N sulfuric acid.

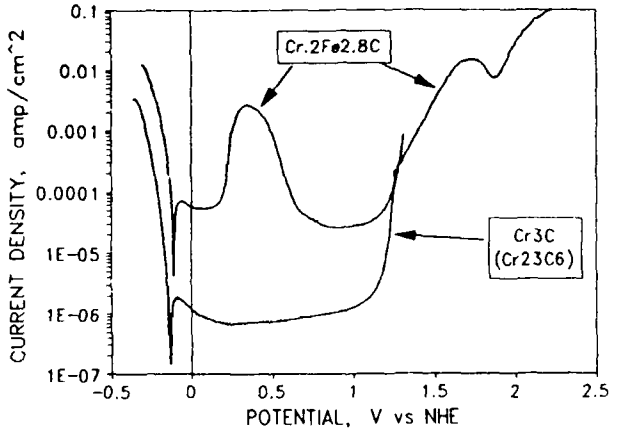

Figure 6. - Potentiodynamic polarization of M_3C's in N_2-saturated 1N sulfuric acid.

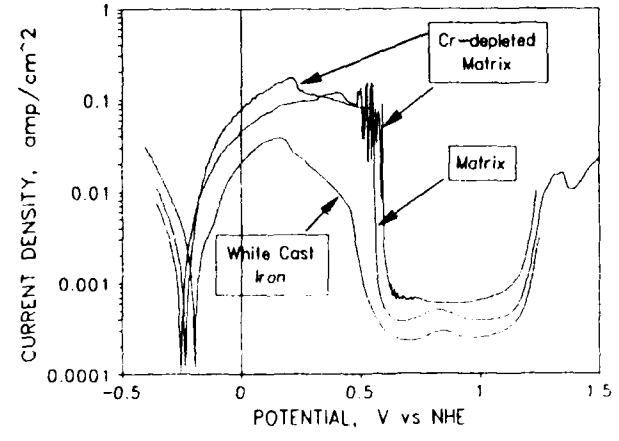

Figure 7. - Potentiodynamic polarization of matrix, Cr-depleted matrix, and white cast iron in N_2-saturated 1N sulfuric acid.

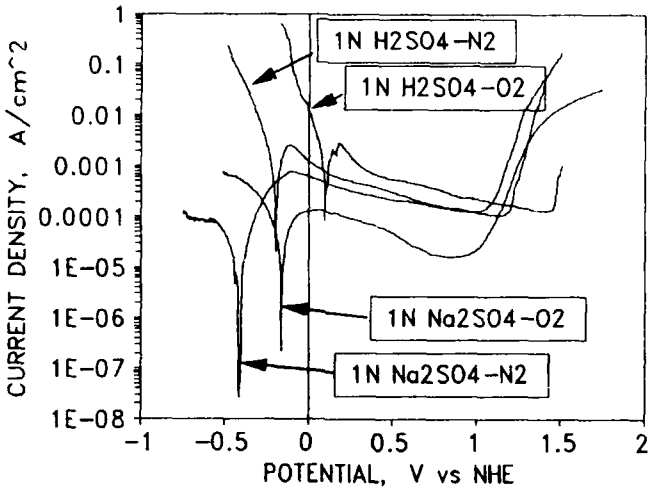

Figure 8. - Potentiodynamic polarization of $Cr_{4.8}Fe_{2.2}C_3$ in N_2- and O_2-saturated 1N sulfuric acid and 1N sodium sulfate.

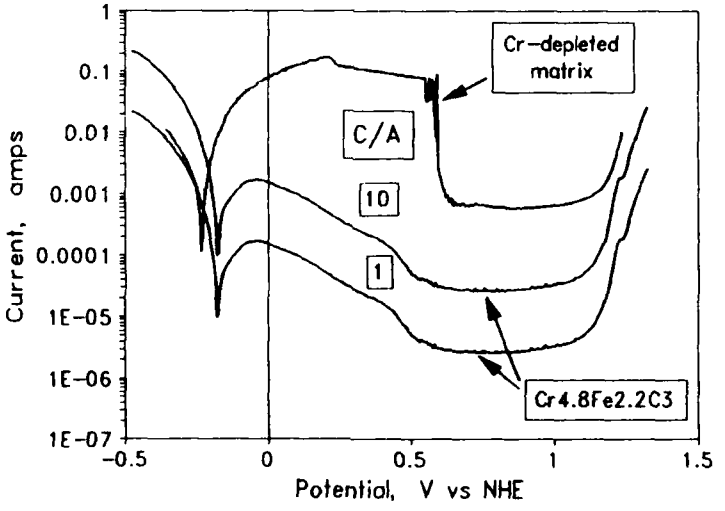

Figure 9. - Proposed galvanic coupling between Cr-depleted matrix and $Cr_{4.8}Fe_{2.2}C_3$.

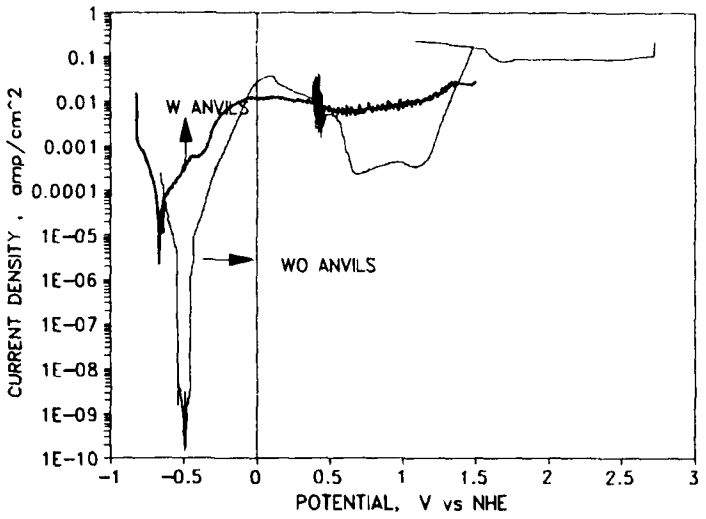

Figure 10. - Potentiodynamic polarization of white cast iron sample in N_2-saturated 1N sodium sulfate showing the effect of abrasion on corrosion.

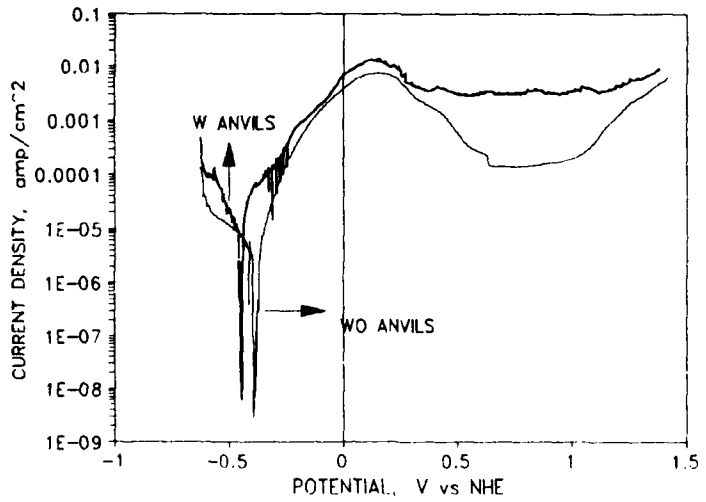

Figure 11. - Potentiodynamic polarization of matrix sample in N_2-saturated 1N sodium sulfate showing the effect of abrasion on corrosion.

Microelectrochemical Methods for Corrosion Studies

T. Suter and H. Böhni

Institute of Materials Chemistry and Corrosion

Swiss Federal Institute of Technology

ETH-Hönggerberg, CH-8093 Zürich, Switzerland

Abstract

By performing electrochemical measurements on surfaces in the micrometer range the background noise can drastically be reduced.Therefore by applying an equipment with high current resolution, events can be detected where the amplitude is far below the noise level of traditional electrochemistry (1-2nA). Using an experimental setup for detecting currents as low as 100fA, local potentiodynamic polarization curves were measured. At samples of stainless steel DIN 1.4301 with areas of 150µm in diameter exposed to a 1M Na_2SO_4 solution, current transients in the range of pA (**"microtransients"**) were detected. The microtransient's behaviour of various stainless steels was examined in solutions with and without chloride under potentiostatic conditions. Surprisingly all kinds of steel show microtransient activity even in solutions free of chlorides. The number of microtransients is strongly related to the content of manganese sulfide. In solutions containing chorides the number and the magnitude of the microtransients increase, whereas their life-time decreases.

Key words: Microelectrochemistry, corrosion, stainless steel, transient measurement, high resolution current measurement, microtransients, manganese sulfide inclusions

Introduction

Nowadays, corrosion and passivation mechanisms of metals are mainly investigated using electrochemical techniques. Most of the electrochemical methods only give information about the behaviour of a relatively large surface. Usual test areas are in the mm^2-cm^2 range. In the case of pitting and crevice corrosion activation and passivation are very local processes. Concerning the initiation mechanism of such local attacks various models were proposed [1]. However, all of these models are almost exclusively based on the examination of large samples. Therefore they are not yet able to describe all the different phenomenas of local corrosion with a coherent theory.

During the last few years instruments of high resolution and new measuring methods (e.g. STM) were developed. Therefore both the local and the current resolution could be improved to a high degree.

Considering the spatial resolution, electrochemistry may be divided into three areas:

area	position resolution	used measuring method
Macroelectrochemistry	1m - 10^{-3}m	i/E-curves, impedance spectroscopy, photo electrochemistry
Microelectrochemistry	10^{-3}m - 10^{-6}m	Potential and current density mapping, Laser-spot-scanning, local i/E-curves
Nanoelectrochemistry	10^{-6} - 10^{-9}m	STM

In the area of nanoelectrochemistry the development of the scanning tunneling microscope (STM) allowed the study of metallic surfaces down to the nm-range [2, 3]. However it has to be considered that not ionic charge carriers but tunneling currents are measured. Thanks to commercially available STM's being easy to use this area is now intensively investigated.

The microelectrochemistry may be understood as the link between macro- and nanoelectrochemistry. It can be divided into two areas:

1) Samples in the mm - cm range are scanned by using microelectrodes and focused laser beams [4 - 7]. By that way information about the local nature of processes can be retrieved.
2) By decreasing the size of the sample surface area the noise can be decreased as well. Using measurement equipment with a high enough current resolution, processes can be detected being hidden in the noise otherwise.

   Some methods of the macroelectrochemistry already yield information about events in the µm-range (e.g. metastable pits) [8 - 10].

   The currents in microelectrochemistry can detect events which correspond to the nm range.

In microelectrochemistry methods are traditionally used where the sample surface is scanned. Analysis of small areas is restricted to the current resolution of the potentiostat being used [11].

In this report it will be shown how the current resolution is improved down to 100fA.

Experiments

Materials

The electrochemical investigations were carried out on four different stainless steels. The composition of these plate materials is listed in Table 1. The samples were mechanically ground with diamond paste (6µm) and rinsed with distilled water and ethanol. All solutions were prepared from reagent grade chemicals and distilled water.

Electrochemical micro-cell

In order to perform electrochemical experiments within the micrometer range it is necessary to reduce the sample surface area. One possibility is, to use a mounted wire [12,13]. The disadvantage of this method is, that only from a few steels wires can be obtained commercially. A second possibility is to cover part of the sample's surface with a photolacquer [11]. Problems arise with this method when cathodic prepolarisation is applied (detachment of photolacquer). Beside this, only one measurement per sample is possible.

Because of the above mentioned problems not the sample itself was modified but the size of the electrochemical cell has been reduced. Fig. 1 shows schematically the electrochemical micro-cell used. Basically it consists of a glass capillary filled with an electrolyte, similar to the one used in chromatography. The outside diameter is 400µm, the inside diameter 50-230µm. As seal a 10-20µm strong layer of silicone rubber (specific resistivity = $10^{15}\Omega$/cm) has been used for the front end. To stabilise the glass capillary it was glued into a micropipette. The counter electrode consists of a 0.5mm strong platinum wire. A calomel-electrode was used as reference electrode. It was connected to the glass capillary by an electrolyte bridge.

Experimental arrangement

Fig 2. shows a schematic diagram of the whole experimental setup. Both the glass capillary (electrochemical cell) and the sample were fixed on movable stages (Newport 462 XYZ). The

sample stage could be controlled by an interface card (Newport PMC 300). After each experiment the sample was lowered and moved in x-y direction. It was adjusted to a new location after the glass capillary has been rinsed with new electrolyte. The first positioning of the glass capillary was done by a microscope inclined by 45°. This setup allows to carry out a series of experiments on one sample and to evaluate them statistically.

The currents in electrochemical experiments at this micrometer scale are not anymore in the range of $\mu A(10^{-6})$ and $nA(10^{-9})$ but rather in the range of $pA(10^{-12})$ and $fA(10^{-15})$. To detect those extremely small low currents, several precautions are necessary:

1. Good shielding

A good shielding against electromagnetically interferences has to be used:

To suppress the electrical component the equipment was set up within a Faraday cage of 3mm thick copper. Due to a consequent use of wires that were protected against magnetic interferences and by keeping them as short as possible, magnetic interference could be reduced to a minimum. During an experiment all electrical wires were kept about 2-3m away from the experimental equipment.

2. High-resolution Potentiostat

Use of a low noise potentiostat running on battery which is able to detect currents down to the fA-range:

A modified, battery operated Jaissle potentiostat (type 1002T-NC-3) has been used. Thanks to the modification of the original apparatus (1002T-NC) the current detection limit could be improved from 50pA down to better than 100fA. It contains a special parallel operation amplifier which is also used for measuring electrochemical noise. Thus the detection limit was improved by a factor of 1000. In combination with a double impedance converter (Jaissle Typ 1003) an input resistance of $10^{15}\Omega$ and an input current of 20fA resulted. As input signal for the potentiostat a low noise signal generator (Prodis Typ 1/16-I) was used.

3. Reduction of signal noise

The remaining noise (mostly 50Hz) of the measured signal (direct voltage signal proportional to the flowing current) has to be reduced furthermore:

With available DC-filters a good treatment of the direct voltage signal in the µV range has not been possible. The lock-in technique allows to filter and amplify alternating voltages of certain frequences out of a noisy signal. The output signal is a direct voltage proportional to the amplitude and averaged over a certain time. Hence the signal had to be modified to alternating current by a selfmade chopper. The chopper frequency (2033Hz) was fed to the lock-in amplifier (EG&G 5210) as reference-signal. By choosing that relatively high frequency and a time constant of 300ms, events - like transients – with a lifetime shorter than 1s can be detected.

Checking the current detection limit of a potentiostat one has to consider not just the noise of the potentiostat but also the thermic noise (Johnson noise) of the test resistors. There is:

$$U(RMS) = \sqrt{4kTR\Delta\nu} \quad (1)$$

$$U(RMS) \sim \sqrt{R} \quad (2)$$

$$i(RMS) \sim 1/\sqrt{R} \quad (3)$$

with

k	Boltzman constant	T	temperature
$\Delta\nu$	frequency band width	R	universal gas constant

With increasing resistance the noise in the voltage increases by the square root of the resistance, while the current noise decreases by the same factor. Therefore especially manufactured 10GΩ (10^{10}) resistors were used for the experiment. Fig. 3.a shows the shape of the nominal voltage curve, fig. 3.b the measured current. The potential increase of both ramps represents with 0.2 mV/s the same value that has been used to measure the potentiodynamic polarization curves. The resulting current increase proofs that the detection limit is not reached at 100 fA. The noise of the current curve corresponds well with the expected noise of the 10GΩ resistors. This means that the own noise of the potentiostat is not higher than 20fA. In order to do more exact test measurements, resistors in the TΩ (10^{12}) range would be necessary.

Results / Discussion

Local potentiodynamic polarization curves

Fig. 4 shows both a macroscopic potentiodynamic polarization curve (MPPC) and a microscopic potentiodynamic polarization curve (μPPC) of the stainless steel DIN 1.4301 in 1M Na_2SO_4. There aren't shown current densities but measured currents. The proportion of the macroscopic to the microscopic area was about 4500. After a waiting time of five minutes under open circuit conditions, the sample was cathodically prepolarized for 1 min. at -500mV before the potential was scanned with an increment of 0.2mV/s.

Considering that from large area measurements in 1M Na_2SO_4 both the potential under open circuit conditions and the begin of the transpassive range vary within a potential range of 200mV, the two curves are in good agreement. Differences occur in the Chromium peak between 500 and 900mV (Chromium oxidation from Cr^{3+} to Cr^{6+}) [7] which can generally be of different size but is tendencially smaller than in microscopic measurements. Unexpected and in strong contrast to the MPPC the μPPC shows current transients ("**microtransients**"). The first hypothesis could be that these transients are noise. However noise was found to have a different shape and repeated measurements exhibit the same behaviour. Fig.4 shows that the size of the microtransients vary from a few pA to around 300pA. These microtransients can no longer be seen in large area measurements because they are hidden in the noise or they may be part of it. Calculating the total number of transients per cm^2 in a potential range of 100-1000mV a number of 50'000 to 300'000 microtransients results.

Potentiostatic Microtransient measurements

Influence of materials

Figures 5 a-d show the microtransient characteristics of the stainless steels 1.4305, 1.4301, 1.4439, 1.4529 at 1M Na_2SO_4. After 5 minutes under open circuit conditions they were cathodically prepolarized for 1 minute at -500mV and after another 5 minutes a potential step to +300mV was performed. Each experiment lasted 90 minutes. The measured current density consists of several partial current densities:

$$i = i_L + i_C + i_O + i_{Redox} \qquad (4)$$

with

i_L current density of oxide formation
i_C corrosion current density
i_O current density of the O_2 development
i_{redox} current density of other redox reactions

i_{redox} and i_O can be neglected because of the measurement conditions used. During the formation of the passive film is $i_L >> i_C$, which means that (4) can be reduced to $i = i_L$. In the case of a high field mechanism i_L is given by:

$$i_L = k \cdot t^{-n} \qquad (5)$$

For the formation of a thin homogenous oxide film $n \approx 1$.

Except steel DIN 1.4305 the values plotted on double logarithmic paper yielded a straight line behaviour. This kind of graph hardly shows any current transients. Therefore a linear scaling was chosen for the time axis and hence the curves show an exponential decay. Where the microtransients were small compared to the current level, the underground level was subtracted according to formula 5.

Concerning the microtransients characteristics the steel DIN 1.4305 obviously differs from the three other steels. This steel shows a high number of transients whereas for the other steels only a few transients can be detected. When comparing the corrosion characteristics of the different materials the following order for the pitting corrosion susceptibility is obtained:

$$1.4305 >> 1.4301 > 1.4439 > 1.4529$$

Concerning the number of microtransients (fig. 5) the following order is obtained:

$$1.4305 >> 1.4439 > 1.4301 > 1.4529$$

Steel DIN 1.4301 apparently does not fit to the expected sequence.

Because of the small area measured one does not obtain mean values anymore as in the case of large area measurements. Single measurement will never show the real behaviour. Therefore a statistically reliable evaluation requires the evaluation of a sufficient number of transients summarised in table 2.

It is interesting to note that the manganese and sulfur contents of the four alloys decrease in the same sequence as the microtransients activity. If one assumes that steel DIN 1.4439 contains more but smaller manganese sulfide inclusions the exponential behaviour could easily be explained.

Evidently further work has to be carried out in order to correlate content as well size of inclusions to the number of microtransients.

Influence of Chloride

By sealing the glass capillary with a silicon layer, crevice corrosion may occur when measuring in chloride containing electrolytes. Therefore only chloride concentrations were chosen which are so low, that even under strong crevice conditions (O-ring-cell) crevice corrosion has never been observed [14]. Fig. 6 a-d show the microtransient characteristics of the steel DIN 1.4529 in three different electrolytes containing chlorides. The measurements were performed potentiostatically at +300mV. By adding 0.1M NaCl to a 1M Na_2SO_4 solution the number of transients increases from about 10 to about 20 transients. By adding 1M NaCl, however, the number of transients raises to about 250. In a pure 0.1M NaCl solution about 120 transients can be detected. Sodium sulfate lowers the number of transients by a factor of six, which means that it exhibits an inhibitive effect.

When chloride is present also the shape of the transients changes. The transients become clearly shorter and higher.

The microtransient characteristic of the steel DIN 1.4439 in a solution of 0.1M NaCl + 1M Na_2SO_4 is shown in fig. 6. There are about four times as many transients as for the steel DIN 1.4529. Caused by the presence of chloride both steels show a different behaviour than in pure 1M Na_2SO_4. The presence of chlorides even cause a much better differentiation concerning the microtransient chararacteristics.

Comparison with macrotransient measurements

Because macrotransient measurements have been used now for many years to characterise stainless steels, it is possible to make some statements based on statistical considerations. By examining the microtransients obtained so far during this project it has to be taken into account that the results have a preliminary character.

Size of transients and size of pits

As for "macrotransient measurements" the minimal size of transients is determined by the resolution of the potentiostat or by the noise of 2-3nA. The maximum detectable size is determined to a high degree by the parameters applied to the experiment. It may be in the range of 100µm.

The magnitude of the measured microtransients is in the range of a few 100fA to about 1nA. Therefore the currents for the microtransients are 1000-10'000 times lower.

When assuming hemispherically growing holes as cause for the transients, the following formula can be used to calculate the pit radius:

$$r^3 = \frac{QM6}{\rho\pi zF4} \qquad (6)$$

with

Q	amount of charge
M	molecular weight
ρ	density
z	number of changed electrons
F	Faraday constant

When applying values for ρ, z, M for average steels, one obtains pit radii of 100nm to 10µm for the macrotransients, whereas for the microtransients the pit radii are smaller by about a factor of 10.

Whether the microtransients are caused by growing pits is still uncertain. A slow current increase with a fast repassivation as in the case of most of the macrotransients was hardly ever observed. Much more often microtransients show a fast current increase followed by a relatively slow decrease. This behaviour may indicate that only inclusions are dissolved and that the repassivation of the new surfaces is the main cause for the microtransients [13]. Whether there are any other processes causing also microtransients has still to be investigated.

Noise

If the noise characteristic of the passive film corresponds to that of the resistor (thermal noise is determinant) a reduction of the area by a factor of 4500 would reduce the noise from 1-2nA to 15-30pA. (The reduction is proportional to the square root of the area.)

The Lock-In-Technique eliminates noise to a high extent. In order to obtain the real value of the noise, measurements using a digital volt meter (Keithley 197 Microvolt DMM) were performed. Even without Lock-In-Technique the noise was about ten times lower than calculated above. Therefore it can be assumed, that the noise consists to a large extent of microtransients.

Sensitivity

The best differentiation between macro- and microtransient measurements can be obtained by looking at the number of transients for low chloride concentrations. At the present time it is not possible to make predictions for the behaviour in higher concentrated soltuions of chloride. Traditional transient measurements for the steel DIN 1.4529 in a 0.1M NaCl solution at +300mV show 0-2 transients/cm^2 (time of measurement = 24h) [15], whereas microtransient measurements result in 250'000-500'000 microtransients/cm^2 (time of measurement = 2h).

Conclusions

- The reduction of noise is a big advantage of electrochemical measurements in the micrometer range. Therefore small events can be detected which are otherwise covered by the noise. The passive currents are in the pA-fA range. The detection of such low currents requires especially adapted equipment. By measures providing a good shielding and by the use of low-noise high-resolution instruments it could be shown that a resolution better than 100fA was achieved.
- Measurements in the micrometer range can be done relatively easy and quick by the use of a movable electrochemical micro-cell.
- Analogous to the traditional transient characteristic stainless steels also show a "microtransient characteristic". The amplitude of these transients is lower than that of the usual noise (1-2nA). Noise measurements lead to the conclusion, that the noise mostly consists of microtransients.
- The microtransient characteristics of the 4 stainless steels DIN 1.4305, DIN 1.4301, DIN 1.4439, DIN 1.4529 in a 1M Na_2SO_4 solution relate to the content of manganese sulfide.
- Chlorides cause an increase in the number of microtransients, an increase of their size and a decrease of their life-time. Furthermore the examined steels may more clearly be distinguished in presence of chloride than in pure 1M Na_2SO_4 solution.
- Thanks to the high resolution of the applied method even at low chloride concentrations numerous events can be detected which are just part of the noise in large area measurements.

References

1. H. Böhni, Corrosion Mechanisms, p.285, Marcel Dekker Inc., New York, 1987
2. H.Siegenthaler, R.Christoph: Scanning tunneling microscopy and related methods, p. 315, Kluwer Academic Publishers, Netherlands, 1990
3. R. Sonnenfeld, J. Schneir, P.K. Hansma: Modern Aspects of Electrochemistry, p. 1, Plenum Press, NewYork, 1990
4. H.S. Isaacs: J.Electrochem. Soc. Vol.135(1988), p.2180
5. M.J. Franklin, D.C. White, H.S. Isaacs, Corrosion Science Vol. 33 (1992),p. 251
6. D. Shukla, T. Wines, U. Stimming: J.Electrochem. Soc. Vol.134(1987), p. 2086
7. P.Schmuki, H.Böhni, Oxide Films on Metals and Alloys, Proc.-Vol. 92-22, (Pennington, NJ:The Electrochemical Society, 1992):p.326
8. P. Corboz, Electrochem. Soc.Vol.128(1981), p. 92
9. G.S. Frankel, L. Stockert, F. Hunkeler, H. Böhni, Corrosion, Vol. 43 (1987), p.432
10. P.C. Pistorius, G.T. Burstein, Proc. 5 th Int. Conference of the South African Corrosion Institute, Johannesburg (South Africa), 1990
11. W. Brandle, Dechema Symposium "Mikro-Elektrochemie", Vortragszusammenfassungen, Thüringen (BRD) 1992
12. P.C. Pistorius, G.T. Burstein, Electrochmical Methods in Corrosion Research Proc. 4th Int. Symposium, Espoo (Finland), 1991
13. A.M. Riley, D. B. Wells, D.E. Williams, Corrosion Science Vol. 32 (1991), p. 1307
14. A. Allwardt, Diploma Thesis, ETH Zürich, 1992
15. R. Morach, P. Schmuki, H. Böhni, Electrochemical Methods in Corrosion Research Proc. 4th Int. Symposium, Espoo (Finland), 1991

Table 1: Nominal chemical composition of the examined materials.

DIN	AISI	C	Cr	Ni	Mo	Mn	S
1.4305	303	0.045	17-19	8-10	-	<2	0.15-0.35
1.4301	304	0.045	18.1	8.7	0.06	1.3	0.003
1.4439	317LN	0.027	17.26	12.72	4.3	1.04	0.004
1.4529	-	0.012	20.8	24.9	6.42	0.82	0.002

Table 2: Influence of material on number and size of microtransients

Material (Steel DIN)	Number of microtransients	Size of microtransients
1.4305	extremely many	big
1.4301	few	usually small, in rare cases high
1.4439	relatively many	small to medium
1.4529	few	small to medium

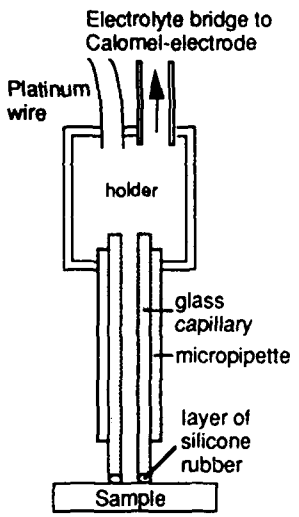

Fig. 1 : Electrochemical micro-cell

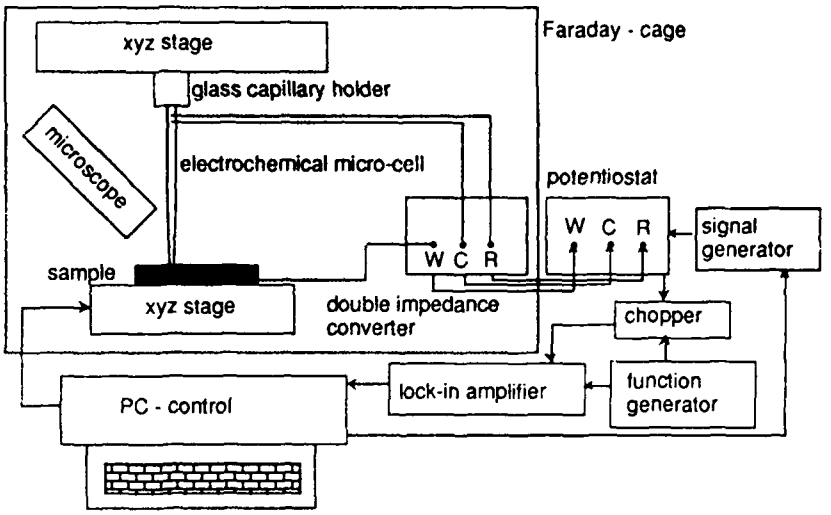

Fig. 2: Experimental set-up for Microtransient measurements

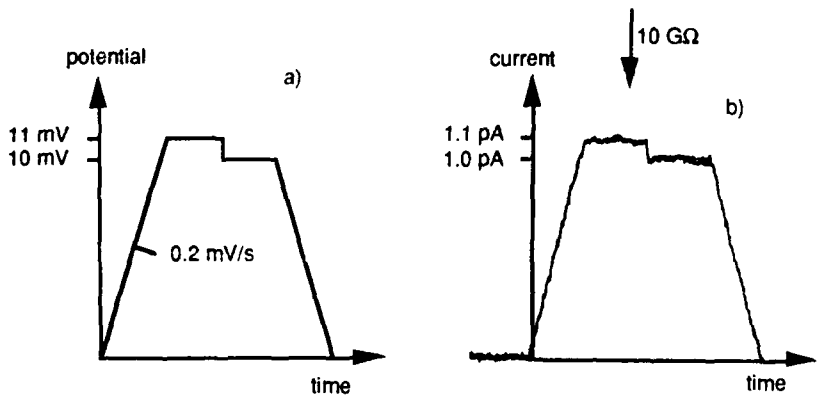

Fig. 3: Current resolution of the potentiostat:
a) nominal potential
b) measured current (using 10 GΩ resistors)

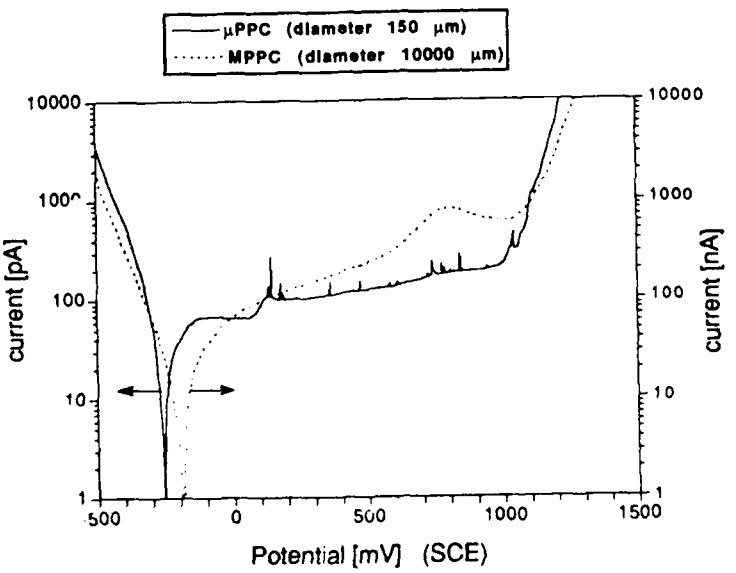

Fig. 4: Macroscopic and microscopic potentiodynamic polarisation curves of the DIN 1.4301 stainless steel in 1M Na_2SO_4 ($\Delta\varepsilon/dt$ = 0.2 mV/s)

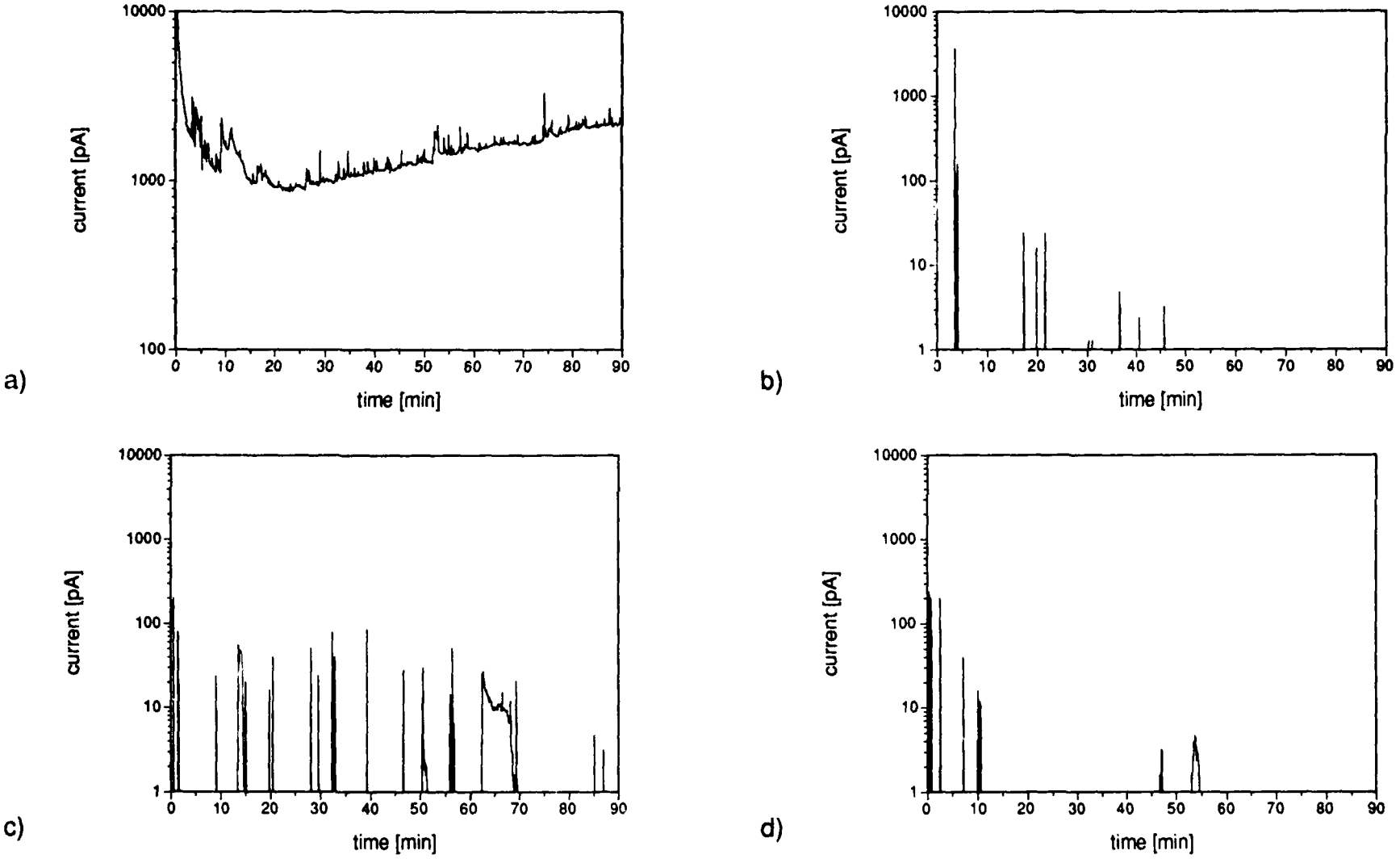

Fig. 5 : Current microtransients observed on different stainless steels in 1M Na_2SO_4 at a potential of +300 mV (SCE):
a) DIN 1.4305
b) DIN 1.4301 (after underground subtraction)
c) DIN 1.4439 (after underground subtraction)
d) DIN 1.4529 (after underground subtraction)

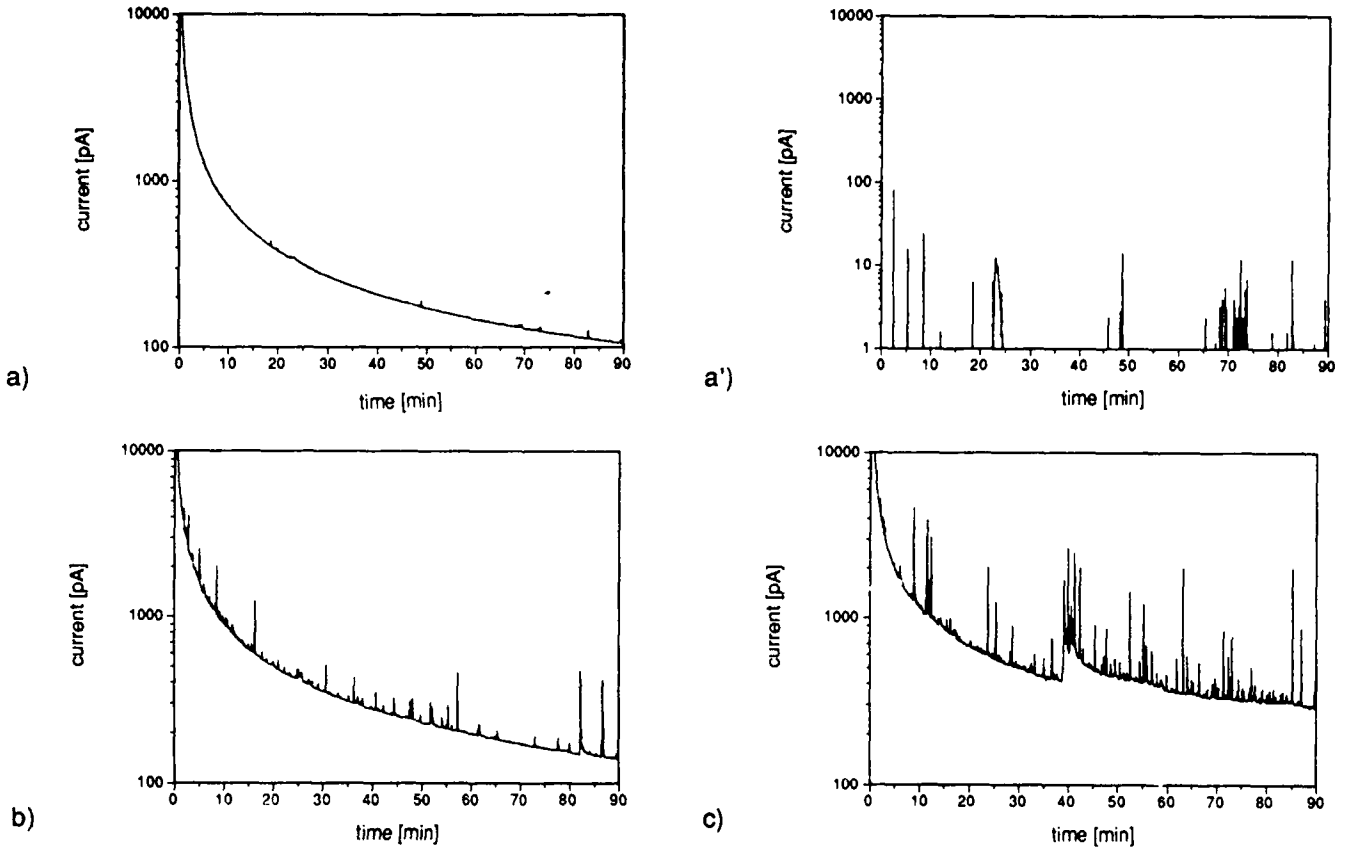

Fig. 6 : Current microtransients observed on a DIN 1.4529 stainless steel in different electrolytes containing chlorides at a potential of +300 mV (SCE):
a) 1M Na_2SO_4 + 0.1M NaCl
a') 1M Na_2SO_4 + 0.1M NaCl (after underground subtraction)
b) 0.1M NaCl
c) 1M Na_2SO_4 + 1M NaCl

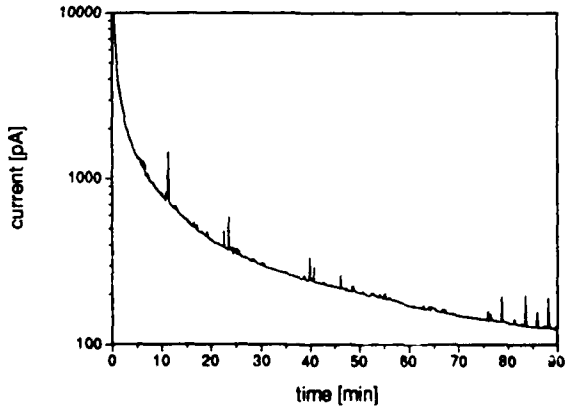

Fig. 7: Current microtransients observed on a DIN 1.4439 stainless steel in 1M Na_2SO_4 + 0.1 M NaCl at a potential of +300 mV (SCE)

PVC Film-Modified Electrodes Studied by EHD Impedance

Célia Regina Sousa da Silva
Lab.de Corrosão "Prof.Manoel de Castro"
PEMM/COPPE/UFRJ
Cx.Postal 68505
CEP:21949-900 Rio de Janeiro-Brasil

Oswaldo Esteves Barcia
Departamento de Físico-Química
Instituto de Química - UFRJ
CEP:21949-900 Rio de Janeiro-Brasil

Oscar Rosa Mattos
Lab.de Corrosão "Prof.Manoel de Castro"
PEMM/COPPE/UFRJ
Cx.Postal 68505
CEP:21949-900 Rio de Janeiro-Brasil

Claude Deslouis
UPR15 du CNRS
Physique des Liquides et Electrochimie
4 place Jussieu
75252 Paris Cedex 05 - France

Abstract

A glassy carbon electrode was coated with a PVC film obtained under different conditions of polimerization. By Electrohydrodynamic Impedance (EHD) it was possible to characterize the surface as a partially blocked electrode. The behaviour of the PVC film was correctly simulated by a regular array of microelectrodes.

A nickel electrode was coated with a PVC film and the porous structure of the film was determined by EHD impedance and optical metallography. An excellent agreement was found between both techniques.

Key terms: EHD impedance, partially blocked electrode, modified surface.

Introduction

Surface modification has been extensively studied with the aim to changing the interface reactivity for a better control of electrochemical processes such as: Electroanalytical Chemistry, Electrocatalysis, Corrosion and Corrosion Protection (see for example the references [1-3]).

Modified surfaces by polymer films is an important part of this field of research [1,4-5]. In this case, mass transport can play a major role in the electrochemical process. Two situations are normally encountered when a polymer film is present on the electrode surface:

-(i) The reaction area between the metal and the film is not significantly reduced with respect to the free area in the absence of film. Thus, the concentration gradient depends only on the normal coordinate and two concentration profiles are established, one within the film itself depends on molecular diffusion and another outside the film is imposed by convection-diffusion.

-(ii) Mass transport occurs only in pores of the polymer and no reaction exists anywhere else. This means that the film blocks the electrode surface except at the pores ends, giving rise to a so-called blocked electrode [6].

Following the above remarks, one important point dealing with surfaces covered by polymer films is to know the film structure itself. For partially blocked electrodes, it has beeen shown that a quantitative analysis of the phenomenon can be done by use of the electrohydrodinamic impedance (EHD), allowing one, in particular, the possibility of measuring experimentally the average dimension of the active site [7]. When the blocked fraction has a moderate value, the EHD impedance presents in general two time constants: One at low frequencies is related to the disk response where the inhomogeneities due to the blocked surface are not seen because the pores are mutually interacting from the standpoint of diffusion. In the high frequency domain, the response corresponds to the sum of the individual contributions of the pores [7,8].

Very recently, by using an experimental model of partially blocked electrode consisting of an array of active sites devised by photolithography, we showed that the analysis presented by Caprani et *al* [7] can be extended to an homogeneous distribution of active sites [8]. In particular, it has been shown that the EHD impedance can be used for experimentally characterizing a partially blocked electrode by two parameters: the average dimension of the active sites and the active fraction of the interface.

In the present paper, preliminary results are presented for a partially blocked electrode where both above parameters are unkown. Calculation of these parameters from EHD results are discussed on some examples.

Experimental

Nickel (99.99%, 0.28 cm^2) and glassy carbon (0.2 cm^2) rods covered with a PVC polymerized film on their cross-section, were used so as to elaborate a porous electrode. The lateral part of the electrodes were isolated by a molding epoxy resin. All PVC films were prepared from a well-defined mixture of TOPO (tri-n-octylphosphinoxide) and PVC in cyclohexanone as solvent. One base solution was prepared with 1.25 g of PVC and 1.025 g of TOPO in 6 ml of cyclohexanone. Samples were taken from this solution and dissolved in cyclohexanone for preparing less concentrated solutions. For example, a solution of 20% V/V means that 20 ml of this base solution was added to 80 ml of cyclohexanone.

The fast redox reaction:

$$Fe(CN)_{\sigma}^{3-} + e^{-} \underset{\longleftarrow}{\longrightarrow} Fe(CN)_{\sigma}^{4-}$$

was performed on the active sites of the electrode. Two solutions were used according to the electrode nature: $K_3Fe(CN)_6$ (10^{-2}M) in KCl (M) for glassy carbon and $K_3Fe(CN)_6$ (5 10^{-3}M) in NaOH (2M) for nickel. In both cases, a saturated calomel electrode was used as reference.

An experimental model of a partially blocked electrode covering the glassy carbon with a thin photosensitive film (thickness 1 μm) was also used. A photographic mask realized by the reduction by 40 of an original design of a regular array of identical circular sites (see Fig. 1) was placed against the resin and UV illumination was performed. Different diameters of active circles were used, but 141 μm was the most appropriate for the purpose of this work.

The experimental device described elsewhere [6] was composed of a rotating disk electrode drive, by a very low inertia motor, the angular velocity of which, Ω, was controled by a servo-system. A small sine wave modulation of the angular velocity was superimposed at a frequency ω by means of a Frequency Response Analyser (FRA Schlumberger 1250) such that the instantaneous velocity was:

$$\Omega(t) = \bar{\Omega}\ (1 + \Delta\Omega \cos\omega t)$$

The fluctuating componenet of the current $\Delta i\cos(\omega t + \phi)$ was sent to the channel 1 input of the FRA while the output voltage of a tachometer, mechanically fastened to the motor, and proportional to $\Omega(t)$, was sent to the channel 2. The transfer function $\tilde{I}/\tilde{\Omega}$ representing the ratio of the complex amplitudes of the current and the angular velocity was then proportional to the ratio CH1/CH2. This transfer function is the electrohydrodinamic impedance (EHD impedance) and is normally presented in Bode coordinates: phase shift vs p and reduced amplitude A(p)/A(0) vs p, where p is the dimensionless frequency, $p = \omega/\Omega$.

Results and Discussion

Glassy Carbon

In Fig.2 are presented the Koûtecky-Levich plots (I_L^{-1} vs $\Omega^{-1/2}$) for the glassy carbon electrode without any PVC film covering the electrode. A straight line crossing the origin of the coordinates was found. In Fig. 3 are shown the EHD impedance diagrams measured on the same electrode. The curves were obtained for different mean angular velocities and are displayed vs the dimensionless frequency p. The data fall on a single curve and this result shows that the glassy carbon electrode is an uniform acessible surface from the viewpoint of diffusion as predicted by the theory of the EHD impedance [6,9].

In Fig. 4 are presented the I_L^{-1} vs $\Omega^{-1/2}$ plots for the electrode covered with TOPO/PVC films of 20% and 40% (see the experimental section) polymerized at 25 °C and 20% polymerized at 70 °C. The steady-state current clearly depends on the PVC film structure. Indeed, for the 20% film, the temperature change from 25 to 70 °C increases the solvent evaporation, thus inducing the formation of a more compact film which give rise to a lower current. In the same way, a 40% solution is expected to generate a less porous structure.

In Figs. 5 (A, B and C) are shown the reduced amplitudes of the EHD impedances relative to the same three films analyzed in the previous figure. The diagram presented in Figure 5A is typical of a partially blocked electrode as described in the introduction of this paper. Two time constants are clearly visible, one in low frequencies representing the response of the disk electrode assumed as totally active and another in high frequencies due to the sum of the response of the sites assumed as independent from the viewpoint of diffusion. The physical effects in the region of intermediate frequencies cannot be so clearly analyzed.

In Fig. 5B, corresponding to a higher polymerization temperature, a qualitative effect of the change in the PVC film structure on the EHD impedance is observed: The low frequency region is not so characteristic of the fully active disk response, which means that the different active sites have only weak interactions from the viewpoint of diffusion in steady-state conditions. This hypothesis is still more justified for the 40% film as shown in Fig. 5C. In this latter case, the response of the fully active disk has now disappeared and there only remains the response of the individual active sites as was recently demonstrated in our study with model electrodes [8]. In the same figure is also plotted in dashed line the average curve corresponding to the experimental data obtained with the model electrode presented in Fig. 1 when the active sites have a mean diameter d=141 μm. It can be concluded that a regular array of microelectrodes reproduces very well the structure of the PVC films. However, this point could not be directly verified on the PVC structure because metalographic measurements cannot be easily performed with very thin films as those used here. Such results with the nickel electrode are now presented.

Nickel

As previously done for the glassy carbon electrode, prelimirary measurements were performed on the bare nickel electrode. The I_L^{-1} vs $\Omega^{-1/2}$ plots and the EHD impedance diagrams respectively reported in Figs. 6 and 7, lead to the same conclusion that the bare nickel electrode behaves as a uniformly accessible surface from the viewpoint of diffusion.

In Fig. 8 are shown the I_L^{-1} vs $\Omega^{-1/2}$ plots for two PVC films obtained in the same conditions, which gives an idea of the good reproductibility of the conditions of elaboration of those films. In Fig. 9 the EHD impedance corresponding to the same electrode as that of Fig. 8 is given. A well-marked behaviour of a partially blocked electrode is found where the two time constants can be observed. As already mentioned, the high frequency part of this diagram can be used to evaluate the characteristic dimension of the active sites. For a single site, the formula given in ref. [7] provides the diameter to the site, supposed located at a distance R from the rotation center:

$$d = 3.0432\ R\ (p_c/p_d)^{-3/2} \qquad (1)$$

p_c and p_d are the respective cut-off frequencies (reciprocal of the time constants) of the high and low frequencies domains which represent the response of the isolated microelectrode or that of the disk electrode. This result was extended in ref. [11] to a homogeneous distribution of identical sites of diameter d on a disk of radius R. In this case, application of Eq. (1) provides an apparent diameter d, (substitute d_a for d in Eq. (1)) from which d can be obtained as $d=2/3\ d_a$.

With the present experimental conditions (R=3000 μm, p_d=0.2 and p_c=5) one finds d_a=73 μm then d=48μm.

In order to visualize the porous structure of the PVC film, nickel was electrodeposited from a classical Watts bath by a galvanostatic current of $3.5\ 10^{-3}$ A during five minutes on the electrode covered by the PVC film as cathode. By this procedure, nickel was only deposited on the active sites of the surface thus filling the pores of the film. In Fig. 10 is shown a photograph of the electrode surface after the electrodeposition. By optical metallography, the mean diameter of the pores was determined as d=40 $\pm$ 10 μm, a value in excellent agreement with the 48 μm determined by EHD impedance measurements. The aspect of Fig. 10 also confirms that the sites distribution is uniform with a identical sites dimension.

A work is in progress [10] to precise the accuracy and reproducibility in determining the site diameter, and also the active fraction of the surface which can be deduced from those measurements [8]. Further developments will also involve the analysis of multimodal distribution of site sizes or inhomogeneous distributions.

Conclusion

In this paper, it has been shown by the EHD impedance measurements that it is possible to follow the changes occurring in the structure of a PVC film and in particular to determine with a good accuracy the average dimension of the pores of the film.

Acknowledgements

This paper was developed by Contract No. 115/90 CAPES (Brazil) - COFECUB (France).

References

1. H.D.Abruna, Coord.Chem.Reviews, 86 (1988), p. 135.

2. R.W.Murray, A.G.Ewing and R.A.Durst, Anal.Chem., 59 (1987), p. 379A.

3. M.S.Weighton, Science, 231 (1986), p.32.

4. C.P.Andrieux, J.M.Saveant, J. Electroanal.Chem., 93 (1978), p. 163.

5. K.Doblhofer, R.D.Armstrong, Electroch.Acta, 33 (1988), p. 453.

6. C.Deslouis, B.Tribollet, "Flow Modulation Techniques in Electrochemistry", VCH series, Advance inElectrochem. Sci, and Eng., Eds. GERISCHER/TOBIAS Vol.2 (1991) pp 205-264.

7. A.Caprani, C.Deslouis, S.Robin and B. Tribollet,J.Electroan.Chem., 238 (1987), p. 67.

8. C.R.S.Silva, O.E.Barcia, O.R.Mattos and C. Deslouis, J.Electroanal. Chem., submitted.

9. B.Tribollet, J. Newmann, J.Electrochem. Soc., 130 10 (1983), p. 2016.

10. C.R.S.Silva - Doctorat Thesis.

11. C.Deslo , G.Maurin, N.Pébère and B.Tribollet, Electrochimica Acta, 34 8 (1989), pp. 1229-1236.

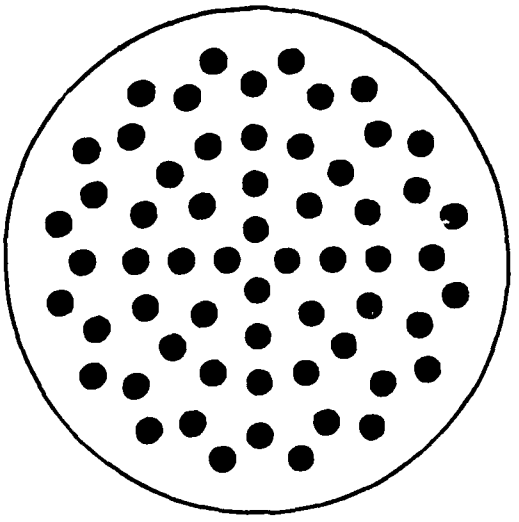

Fig.1 - Pattern of the photographic mask used for devising the active sites on the surface of the disk electrode (d = 141 μm).

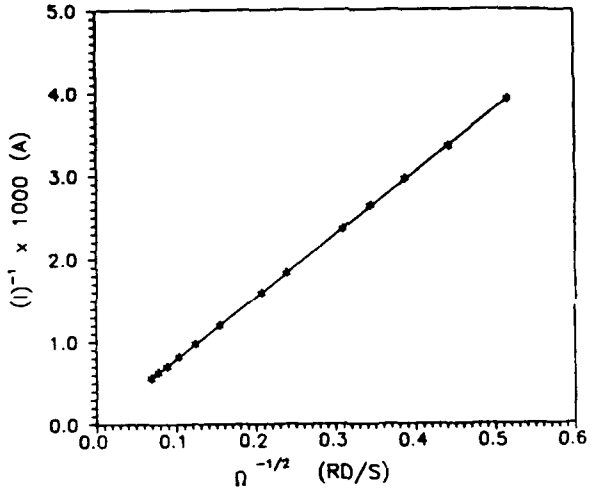

Fig.2 - Koutecky-Levich plots (I_L^{-1} vs $\Omega^{-1/2}$) for glassy carbon. Reduction plateau of the Ferri/ferrocyanide system (10^{-2} M) in 1M KCl.

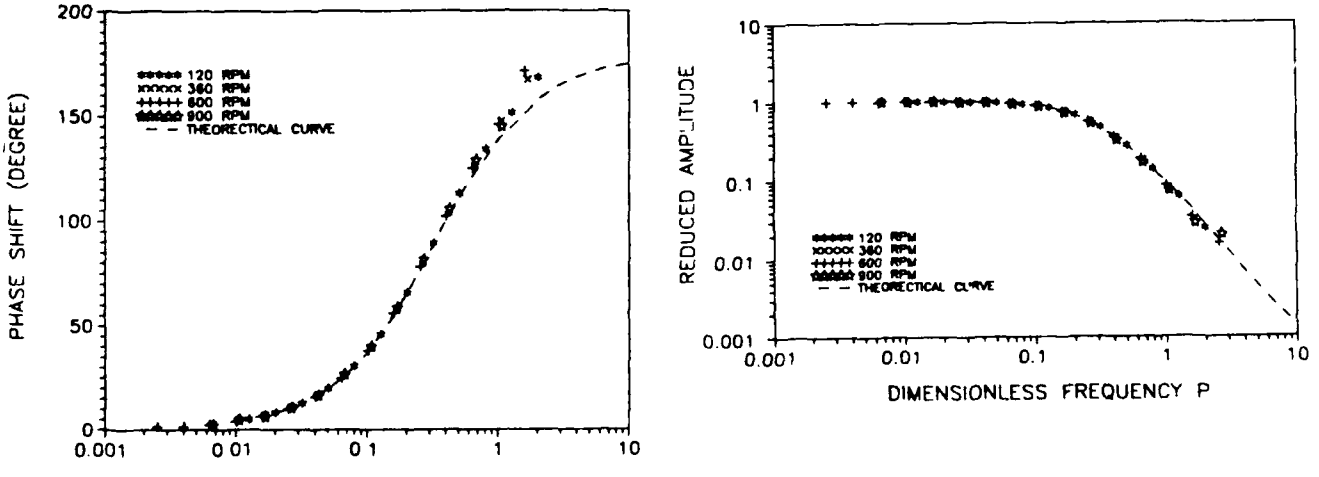

Fig.3 - EHD impedance for glassy carbon. Dashed line corresponds to a Schmidt number of 1000.

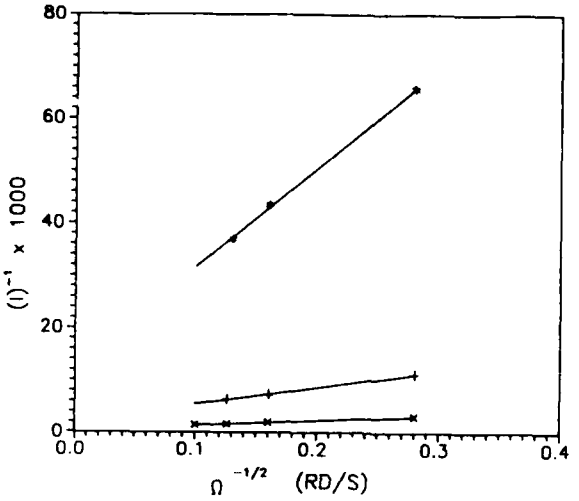

Fig.4 - Koutecky-Levich plots (I_L^{-1} vs $\Omega^{-1/2}$) for glassy carbon covered with differents PVC films. (*) 40%; (+) 20% at 70°C; (×) 20% at 25 °C.

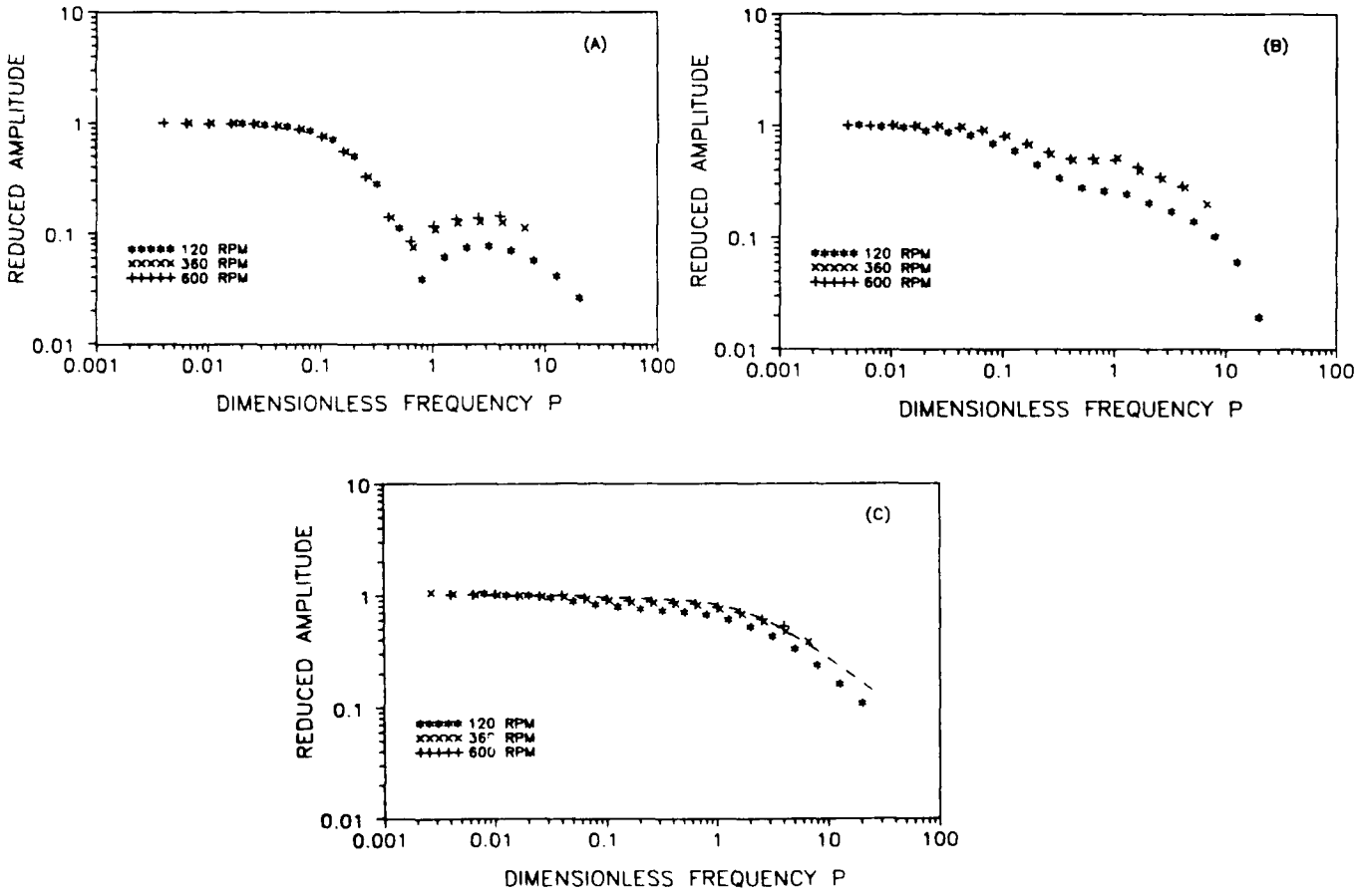

Fig.5 - Reduced amplitude of the EHD impedance for the same PVC films shown in Fig.4. (A) - 20%. (B) - 20% polymerized at 70 °C. (C) - 40%. Dashed line corresponds to an array of circular active sites (d=141 μm) defined by the pattern of Fig. 1.

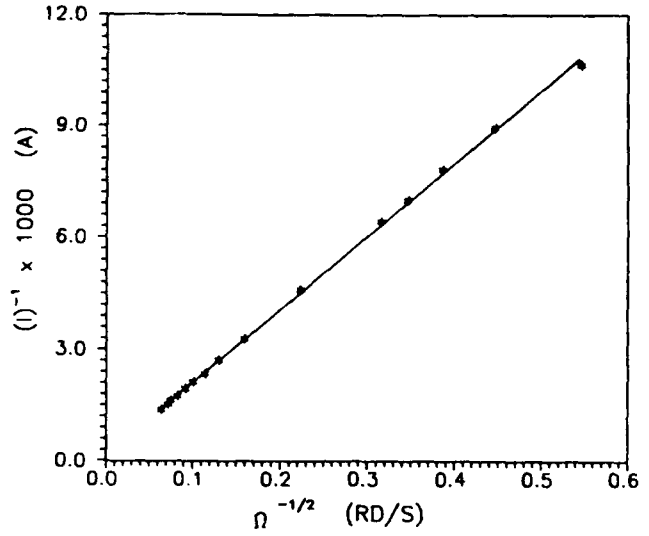

Fig.6 - Koutecky-Levich plots (I_L^{-1} vs $\Omega^{-1/2}$) for nickel electrode. Reduction plateau of the ferri/ferrocyanide system ($5\ 10^{-3}$ M) in NaOH 2M.

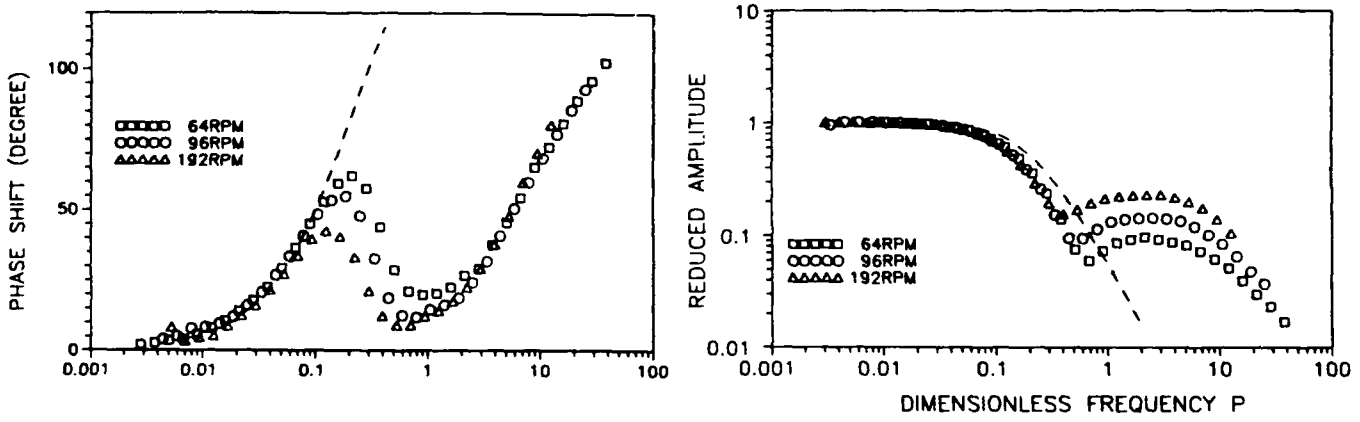

Fig.7 - EHD impedance for nickel electrode. Dashed line corresponds to a Schmidt number of 3000.

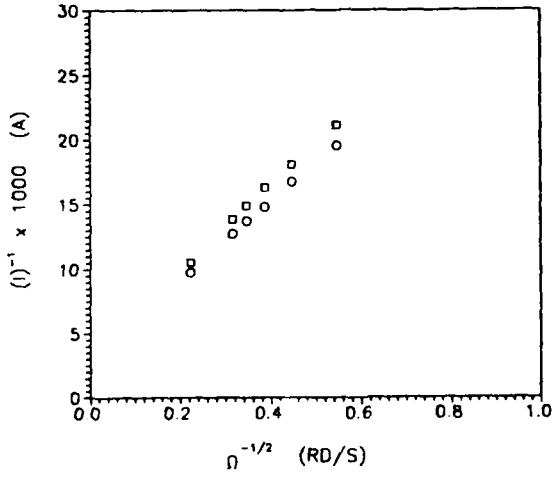

Fig.8 - Koutecky-Levich plots (I_L^{-1} vs $\Omega^{-1/2}$) for nickel electrode covered with two PVC films prepared in the same experimental conditions.

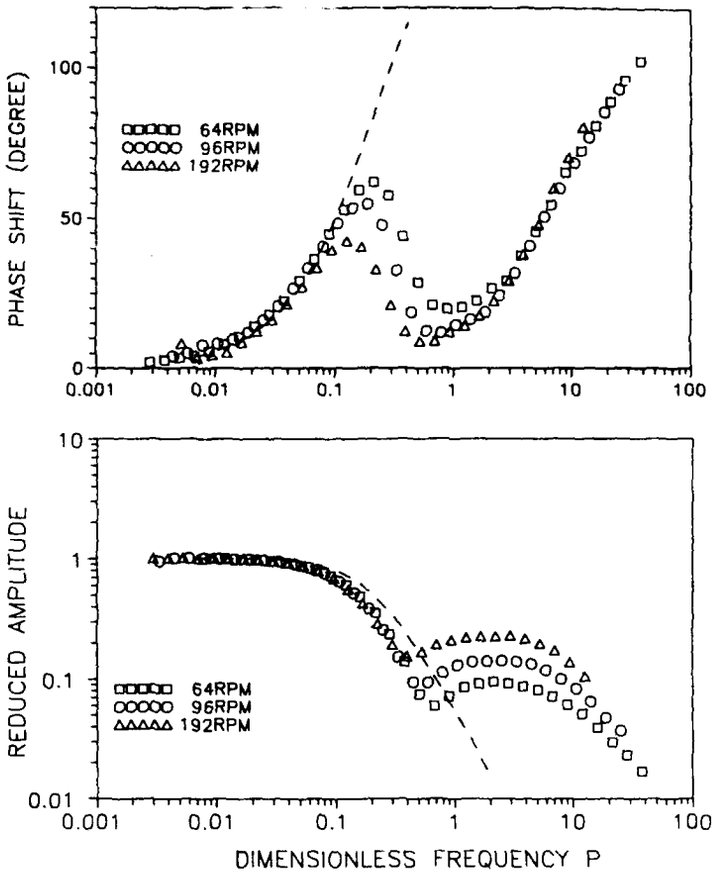

Fig.9 - EHD impedance for the same electrode used in Fig.8. Dashed line corresponds to a Schmidt number of 3000.

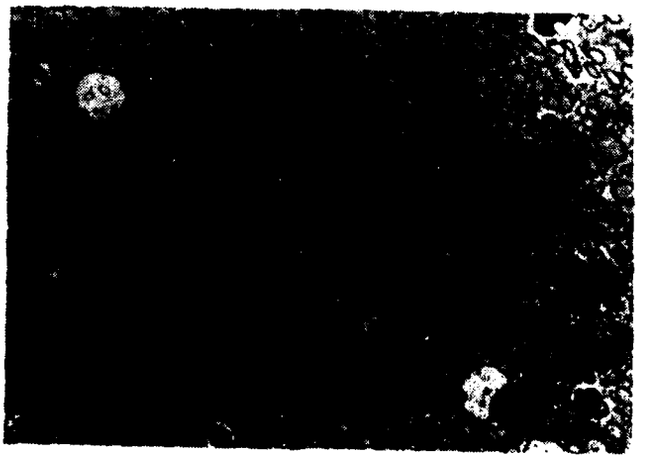

Fig. 10 - Nickel electrodeposited on the pores of nickel electrode covered with a PVC film. Pore diameter determined as d=40 ± 10 μm.

Electrochemical Noise Analysis of Iron Exposed to NaCl Solutions of Different Corrosivity

F. Mansfeld
Corrosion and Environmental Effects Laboratory (CEEL)
Department of Materials Science and Engineering
University of Southern California
Los Angeles, CA 90089-0241, USA

H. Xiao
Corrosion and Environmental Effects Laboratory (CEEL)
Department of Materials Science and Engineering
University of Southern California
Los Angeles, CA 90089-0241, USA

Abstract

Potential and current noise data have been collected for pure iron foils which were exposed to 0.5 N NaCl which was aerated, deaerated or aerated with $NaNO_2$ added as inhibitor. Potential and current noise data were obtained at the beginning of each hour over a 24 h period either sequentially or simultaneously. Statistical and spectral analyses were performed resulting in noise resistance values. For the noise resistance $R_n = \delta V/\delta I$, where δV and δI are the rms values of potential and current, respectively, similar values as for the polarization resistance R_p determined with EIS at the end of the tests were obtained. Another type of noise resistance R_{sn} obtained from spectral analysis of simultaneously collected data was compared with R_p and R_n for aerated and inhibited solutions. The pit index defined as $PI = \delta I/I_{mean}$, where I_{mean} is the mean current in a noise measurement, did not provide meaningful information.

Key terms: electrochemical noise, noise resistance, spectral noise response, spectral noise resistance, polarization resistance, pit index

Introduction

Electrochemical noise analysis (ENA) is unique among all electrochemical techniques used in corrosion research since no external signal needs to be applied for the collection of experimental data. Therefore ENA is of great interest for corrosion studies especially if one considers the additional benefit that the costs of instrumentation are greatly reduced in comparison with other popular techniques. In general, a ZRA and one or two voltmeters under computer control are sufficient. It is obvious that ENA has great promise not only for basic laboratory studies, but also - perhaps even more so - for corrosion monitoring. It is therefore not too surprising that a number of research groups have reported results obtained mainly with the measurement of potential noise. There has been a tendency to relate all electrochemical noise data to localized corrosion, however recently the present authors have found [1-4] that potential noise can be

misleading in cases where small fluctuations in mass transport control can produce large changes in the corrosion potential E_{corr}. Such is the case for metals and alloys which are immune to corrosion such as Pt or are passive such as stainless steels in neutral, aerated environments. Mansfeld and Xiao [1 - 4] have shown that potential noise as analyzed with the use of power spectral density (PSD) plots is similar for Pt and for an Al/SiC metal matrix composite, which pits severely in aerated 0.5 N NaCl. However the current noise PSD-plots were very different for the two materials. In order to obtain more information about experimental and theoretical details of ENA, the well-know system Fe/NaCl has been investigated in three solutions of different corrosivity. Data analysis has been carried out using both spectral and statistical analysis. The system Fe/NaCl was also of interest since Lumsden et al [5] had reported data for this system which showed poor agreement between the noise resistance R_n obtained with ENA and the polarization resistance R_p obtained with electrochemical impedance spectroscopy (EIS).

Experimental Approach

Pure Fe foils (99.999%, 0.1 mm thickness) were exposed to 0.5 N NaCl which was open to air or deaerated. Samples were polished to 1200 grade, then degreased in 50°C hexane for 20 minutes. The experimental arrangement for the measurement of potential and current noise is shown schematically in Fig.1. Two pieces of the Fe foils with 5 cm^2 exposed area each were used as working electrodes. These two samples were placed vertically and parallel to each other in a specially designed test cell [3,4]. A SCE reference electrode was placed between the two test electrodes. The two identical samples were connected to a Schlumberger model 1286 potentiostat which was used as a ZRA to apply zero potential between the two electrodes. The current output of the potentiostat was connected to the rear channel of a computer controlled HP3457A multimeter providing the current noise record. Two ultra-accurate metal resistors (100 kohm each) were connected in series between the two electrodes. This arrangement provided an average potential point for the two samples. Since the resistance of these two resistors (200 kohm) was much larger than the solution resistance (about 100 ohm), no measurable disturbance would be introduced to the system by the potential and current measurements. The potential between this average point and the reference electrode was sampled as potential noise through the front channel of the multimeter.

The electrochemical potential and current noise were initially recorded sequentially during a 24-hour period. The two test electrodes were kept at zero potential difference from the start of immersion until the end of the test. At the beginning of every hour of immersion time, the potential noise was recorded first, immediately followed by the coupling current noise measurement. For both the potential and current measurement a 2 points/second sampling rate was used for 500 seconds in each measurement. The timing and measuring mode switching were controlled by an IBM-AT compatible computer. A computer program was developed to read and store the noise data as well as to remotely control the experiment through the GPIB (IEEE-488) interface [1 - 4].

In order to determine the noise behavior of iron in solutions of different corrosivity and at different potentials, three solutions were used: 0.5 N NaCl open to air; 0.5 N NaCl

deaerated with N_2; 0.5 N NaCl + 0.01 M $NaNO_2$ as inhibitor, open to air. After recording the electrochemical noise for 24 hours, the impedances of the samples were measured using a two-electrode arrangement. The experimental noise data were further processed using statistical analysis.

In addition to the sequentially collected data, potential and current noise were recorded simultaneously for the aerated and inhibited solutions, using a slightly different two-voltmeter arrangement and a more advanced control program. The sampling rate was 2 points per second and each test was carried out for 1024 seconds.

Data Analysis and Experimental Results

For all tests carried out with iron in NaCl, the mean value and the standard deviation (rms) of the potential and current noise were determined. From these data the noise resistance R_n defined as:

$$R_n = \delta V/\delta I \qquad (1)$$

was calculated, where δV is the rms of the corrosion potential fluctuation and δI is the rms of the current fluctuations [5,7,8]. Experimental values of R_n for carbon steel in NaCl have recently been reported by Lumsden et. al. [5], who tried to correlate R_n with the polarization resistance R_p as determined from EIS. Finally, the pit index PI, which has been defined as the ratio of the rms current noise δI and the mean coupling current I_{mean} [7,8], has been calculated:

$$PI = \delta I/I_{mean} \qquad (2).$$

In addition to the statistical analysis, the noise data obtained by simultaneous collection of potential and current noise were analyzed in the frequency domain using FFT. The spectral noise response $R_{sn}(f)$ is calculated at each frequency f by:

$$R(f) = V(f)/I(f) \qquad (3)$$

and

$$R_{sn}(f) = |R(f)| = [R(f)_{re}^2 + R(f)_{Im}^2]^{1/2} \qquad (4),$$

where V(f) and I(f) are complex numbers obtained from FFT. The spectral noise resistance R^o_{sn} is defined as the value of $R_{sn}(f)$ at $f = 0$:

$$R^o_{sn} = \lim_{f \to 0} \{R_{sn}(f)\} \qquad (5).$$

The experimental results obtained with sequential collection of potential and current noise data and the results of the data analysis are displayed in Fig. 2 - 8. Fig. 2 shows

experimental potential and current noise data after exposure for one hour to the deaerated NaCl solution. For the example in Fig. 2, E_{corr} decreased by about 10 mV in 500 sec. For the current, fairly rapid fluctuations of low amplitude (< 0.3 μA) were observed. The mean values of E_{corr} for iron exposed to NaCl, which was open to air, deaerated or open to air with an addition of 0.01 M $NaNO_2$, are shown in Fig. 3, while Fig. 4 presents the mean values of the coupling current. E_{corr} in the aerated solution decreased slowly with time as the rust layer is formed. In the deaerated solution E_{corr} was more negative and fairly constant after a few hours of immersion. In the aerated solution containing $NaNO_2$ the positive potentials typical for this type of inhibitor were observed. The mean coupling current was very small for the deaerated and the inhibited solution, while both positive and negative current peaks occurred in the aerated solution. The data shown in Fig. 4 are different from those reported by Lumsden et al [5], in which a very large dc current of 700 to 750 μA occurred indicating large differences in the corrosion kinetics of the two steel samples. There is also an interesting difference in the potential - time behavior for the deaerated solution in Fig. 3 and the results reported by Lumsden et al [5], where deaeration was started about 3 hours after immersion in the aerated solution. The increase of E_{corr} after about 6 hours (Fig. 7 c in [5]) must be due to the reduction of previously formed iron oxides which polarizes the sample towards positive potentials after deaeration.

Fig. 5 and 6 show the rms values of potential and current, respectively. The largest rms potential values in the range between 1 and 10 mV are observed for the inhibited solution, where iron is in the passive state and the fluctuations of E_{corr} are larger similar to the results reported previously for Pt [1-4]. For the deaerated solution the potential fluctuations are very small and fairly constant (about 0.1 mV). These observations are consistent with earlier findings [1 - 4] that mass transport of oxygen can play a large role in potential noise. The rms current values are the largest and show the highest variations with time for the aerated solution in which significant corrosion occurs (Fig. 6). For the deaerated and the inhibited solutions much smaller values of the rms current are observed with larger fluctuations for the inhibited solution. In these solutions the sample surfaces remained shiny during the 24-h test.

The noise resistance R_n, which is derived from the data in Fig. 3 - 6 according to Eq. 1, is shown in Fig. 7 for the three test solutions. The highest values of R_n (10 - 100 kohm) are observed for the inhibited solution. For the deaerated solution a very stable time behavior is observed with R_n slowly increasing from about 1 kohm to about 10 kohm after 24 h. The sample exposed to NaCl/air has the lowest R_n values with the largest fluctuations between 10 ohm and 5 kohm.

The pit index PI, which has been proposed as a tool for determining the nature of the corrosion mechanism [8], did not give meaningful information for the system iron/NaCl studied here. Very similar values of PI were observed in Fig. 8 for the three solutions of different corrosivity. For the inhibited solution PI exceeded 1.0 several times in the first 6 h, which in the proposed approach [8] would indicate initiation of pits. During the same time the PI for iron in NaCl/air was quite low despite the observed formation of rust. For $NaCl/N_2$ the PI was between 0.1 and 1 (Fig. 8), which supposedly indicates the

occurrence of localized corrosion. However, localized corrosion was not observed in the deaerated and the inhibited solution. In fact, corrosion rates in these solutions were very low.

Fig. 9 shows the impedance spectra for the Fe samples after exposure in the three solutions for 24 hours. The spectra have been fitted to a one-time-constant model to obtain R_p, which is listed in Table 1 for comparison with R_n determined for 24 hours of exposure. Fairly good agreement between these two parameters is observed. Lumsden et al reported much larger values of R_n than R_p for carbon steel in NaCl [5]. Some of these differences might be due to the dissimilar nature of the steel samples used by these authors [5].

The results of the analysis of simultaneously recorded potential and current noise data are presented in Fig.10 - 12 for the aerated NaCl solution with and without $NaNO_2$. Similar R_n-values were determined (Fig. 10) as in the experiments with sequential recording of potential and current noise (Fig. 7). This results demonstrates that for relatively short sampling times sequential and simultaneous recording of noise data will provide the same results in terms of statistical analysis. However for spectral analysis, in which potential and current fluctuations are correlated in the frequency domain, simultaneous recording of potential and current noise data is necessary. Fig. 11 shows the spectral noise response R_{sn} calculated from Eq. 3 and 4 as a function of frequency for the first (Fig. 11 a) and last hour (Fig. 11 b) of exposure. The frequency independent low values of R_{sn} (Fig. 11) for the aerated solution indicate uniform corrosion at high rates in contrast to the curves with higher and frequency- dependent R_{sn}-values for the inhibited solution which show larger scatters (Fig. 11). From curves obtained for each hour of exposure such as those shown in Fig. 11 a and b the spectral noise resistance $R°_{sn}$ was determined by extrapolation to $f = 0$ according to Eq. 5. These $R°_{sn}$-values are plotted in Fig. 12 as a function of exposure time for both solutions. A comparison of the results in Fig. 10 and Fig. 12 shows that the noise resistance R_n as defined in Eq.1 (Fig. 10) and the spectral noise resistance $R°_{sn}$ as defined in Eq. 5 (Fig.12) have very similar values at each exposure time. Fig. 13 shows the impedances spectra for both solutions obtained at the end of the 24 hour exposure period. The impedance data were fitted to one time-constant-model to obtain R_p. A comparison between the 24 hour-values of R_n, $R°_{sn}$ and R_p is given in Table 2 for the two test solutions. Very good agreement is observed between the noise resistances R_n and $R°_{sn}$ obtained with two different experimental and analysis techniques and R_p determined with EIS.

Summary and Conclusions

For pure iron in 0.5 N NaCl, which was aerated, deaerated or aerated containing $NaNO_2$ as inhibitor, the mean and the rms values of E_{corr} and of the coupling current between two electrodes of the same material have been determined on an hourly basis for a 24 h period. From these data the noise resistances R_n and $R°_{sn}$ has been determined as a function of exposure time. Satisfactory agreement between the polarization resistance R_p, $R°_{sn}$ and R_n has been observed. However, the Pit Index (PI), which has been proposed as a tool for determining the type of corrosion, provided misleading results.

The latter result is perhaps not too surprising considering that in Eq. 2, I_{mean} should be close to zero for all cases of uniform corrosion. PI can therefore show large fluctuations independent of the actual corrosion mechanism.

Statistical analysis of noise data has several advantages over other analysis techniques. It does not require expensive equipment and/or complicated analysis programs such as software based on FFT or the maximum entropy method (MEM) for spectral analysis. A theoretical analysis of the relationship between the noise resistance R_n as defined in Eq.1 with the polarization resistance R_p, which is defined as the limit of the impedance at zero frequency, has apparently not been carried out be those who advocate the use of R_n [5,7,8]. Experimentally, it has been shown in the present study for the Fe/NaCl system that R_n and R_p have similar values and trends. The establishment of a theoretical relationship of R_n and R_p is part of present investigations carried by the authors.

The significance of the statistical analysis leading to experimental values of R_n occurs in corrosion monitoring applications, where only qualitative results are needed in a fast, simple and inexpensive way. The electrochemical noise method applied in this manner will therefore be extremely useful in large scale corrosion monitoring and field testing.

The manner in which the potential and current noise data are acquired (sequentially or simultaneously) has not been important in the determination of R_n in the experiments discussed in this report. The 500 seconds data acquisition period is short enough to assume that the average properties of the surface did not change during this time. Since in statistical analysis one is interested only in average effects, sequential data collection will not produce significant differences with the simultaneous data collection. However for advanced spectral analysis leading to the determination of the spectral noise resistance $R°_{sn}$, simultaneous data acquisition is essential for obtaining accurate results. Very strong correlations between R_n and $R°_{sn}$ and R_p and $R°_{sn}$ have been obtained, which is also consistent with the results of the sequential recording experiments. A quantitative understanding of electrochemical noise and its relationship to (localized) corrosion phenomena can only be achieved through spectral analysis of noise data. A theoretical model is being developed at present to explain the correlation between the polarization resistance R_p determined from dc or ac data and the noise resistance R_n or $R°_{sn}$ determined from electrochemical noise data.

Acknowledgement

This project has been funded by Montana State University under subcontract No. 291435-01. The simultaneously collected noise data have been displayed and analyzed by Dennis Han, who is graduate student at CEEL.

References

1. F. Mansfeld and H. Xiao, "Evaluation of Electrochemical Techniques for the Study of Localized Corrosion Phenomena in MIC", NSF-CONICET Workshop on Biocorrosion and Biofouling, Mar del Plata, Argentina, Oct.1992

2. F. Mansfeld and H. Xiao, "Electrochemical Techniques for the Detection of Localized Corrosion Phenomena in MIC", ASTM Symp. "Microbiologically Influenced Corrosion (MIC) Testing", Miami, Florida, Nov.1992

3. F. Mansfeld and H. Xiao, "Development of Electrochemical Test Methods for the Study of Localized Corrosion Phenomena in Biocorrosion", ACS Symp., Washington D.C., Aug.1992

4. F. Mansfeld and H. Xiao, "Electrochemical Noise Analysis of Iron Exposed to NaCl Solutions of Different Corrosivity", submitted to J. Electrochem. Soc.

5. J.B. Lumsden, M. Kendig and S. Jeanjaquet, CORROSION '92, Paper No. 224, 1992

6. M. Kendig, S. Jeanjaquet and M. Mahoney, CORROSION '88, Paper No. 383, 1988

7. A.N. Rothwell and D.A. Eden, CORROSION '92, Paper No.223, 1992

8. D.A. Eden, D.G. John and J.L. Dawson, International Patent No. 87/07022

9. K. Hladky, United States Patent No. 4575678

10. D.A. Eden, A.N. Rothwell and J.L. Dawson, CORROSION '91, Paper No.444, 1991

11. C-T. Chen and B.S. Skerry, Corrosion 47, 598 (1991)

12. C. Gabrielli, F. Huet, M. Keddam and R. Oltra, Corrosion 46, 266, (1990)

13. F. Carassiti, R. Cigna, G. Gusmano and R. Goolamallee, Materials Science Forum, 44&45, 271 (1989)

14. R.G. Hardon, P. Lambert and C.L. Page, Br. Corros. J., 23, (4), 225, (1988)

15. P. Searson and J. L. Dawson, J. Electrochem. Soc. 135, 1908 (1988)

TABLE 1--Comparison of R_n and R_p for three different test environments

environment	open to air	deaerated(N_2)	inhibited($NaNO_2$)
R_n(KΩ)	0.8	8.3	54.7
R_p(KΩ)	1.6	15.9	22.1

TABLE 2--Comparison of R_n, $R°_{sn}$ and R_p for simultaneously recorded data in two solution environments

environment	open to air	inhibited($NaNO_2$)
R_n(KΩ)	0.4	195.8
$R°_{sn}$(KΩ)	0.4	79.1
R_p(KΩ)	1.4	220.0

The exposed area of each sample is 5 cm^2;
The values of R_n and $R°_{sn}$ were recorded at 24h exposure time.

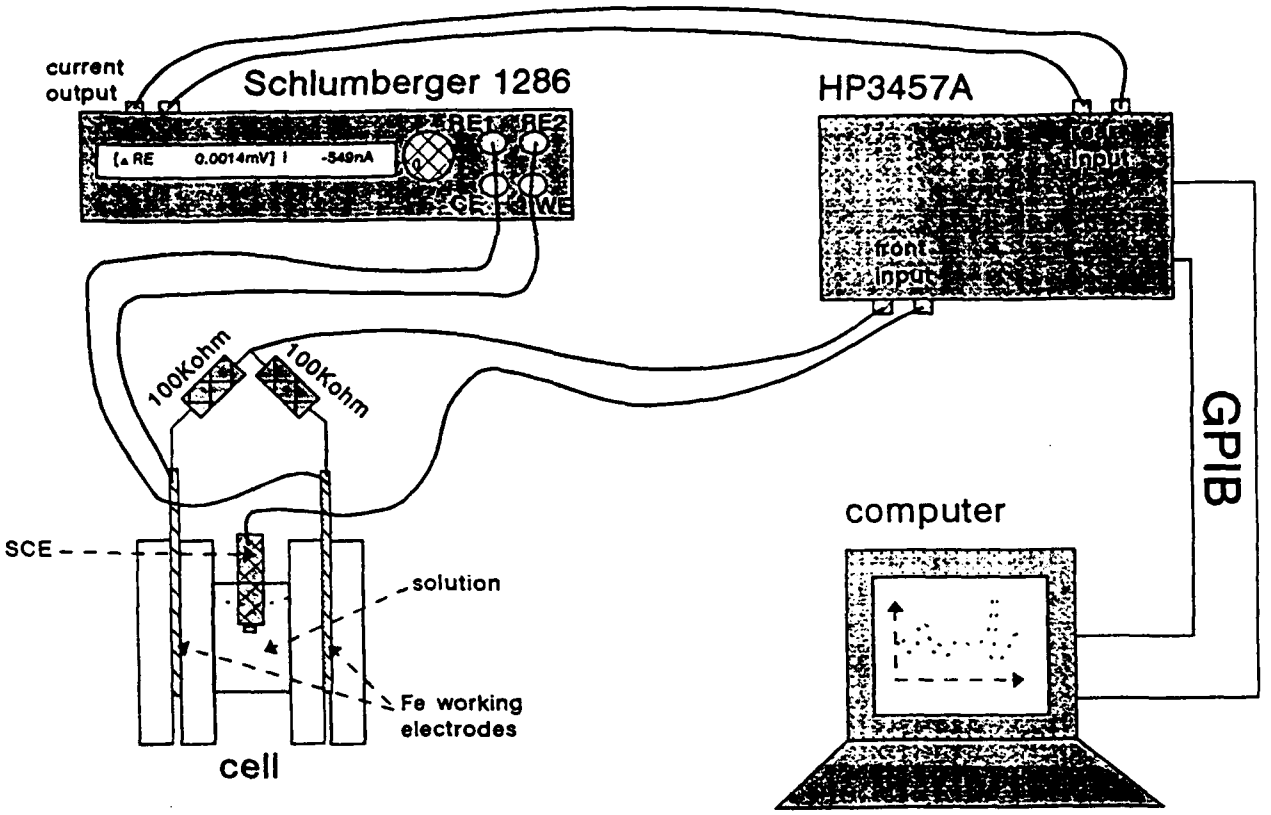

Fig.1 Experimental arrangement for potential and current noise measurements

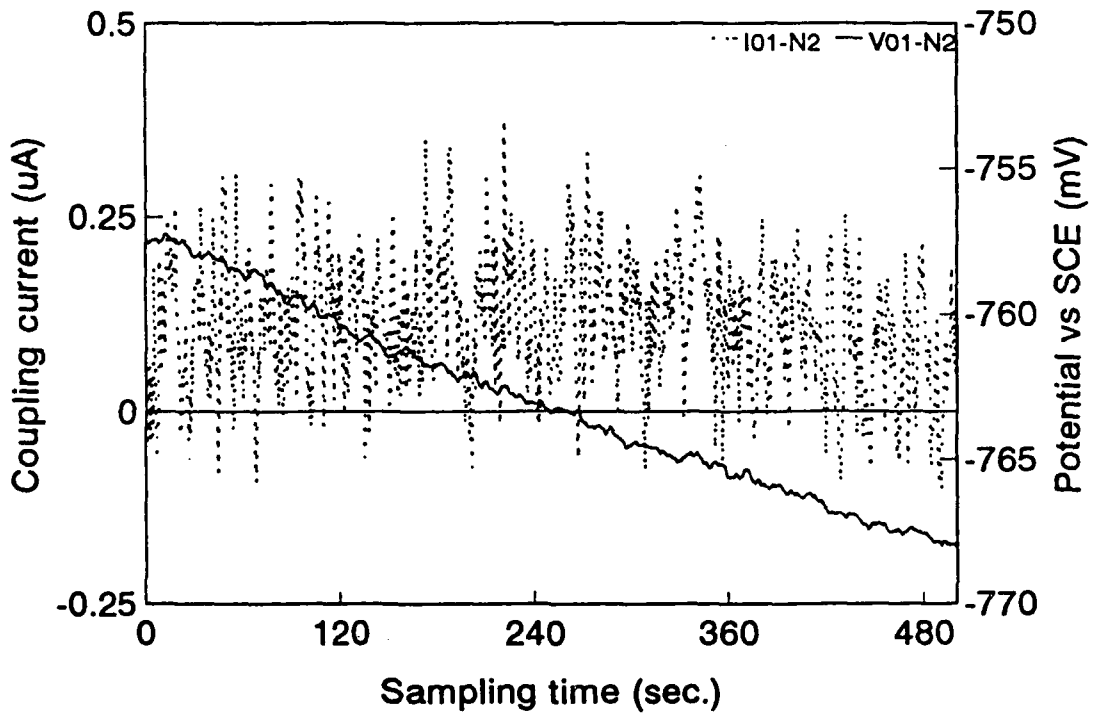

Fig.2 Potential and current noise recorded for iron in 0.5 N NaCl (deaerated) after exposure for one hour.

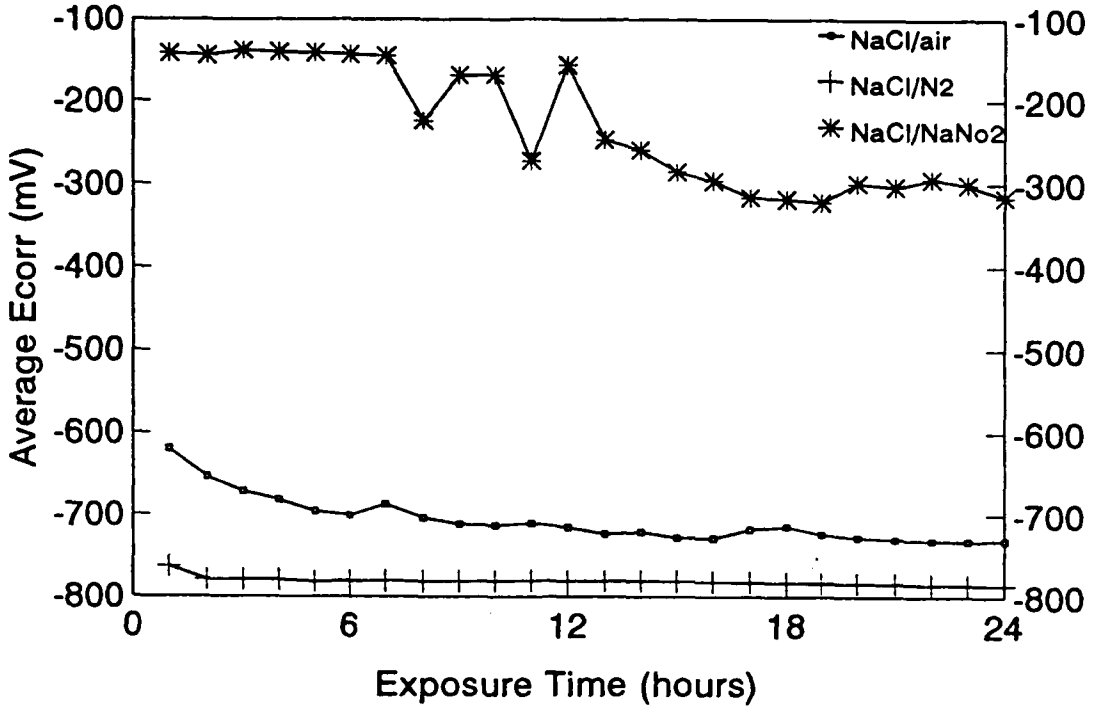

Fig.3 Time dependence of the mean E_{corr} for iron in three solutions

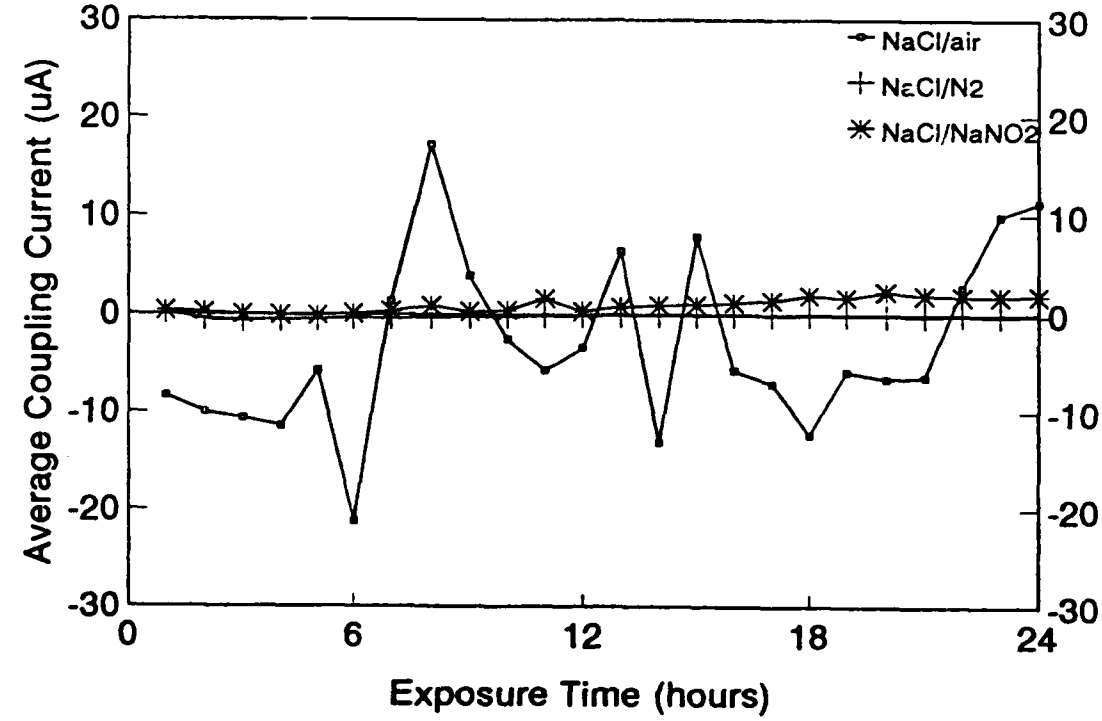

Fig.4 Time dependence of the mean coupling current I_{mean} for iron in three solutions

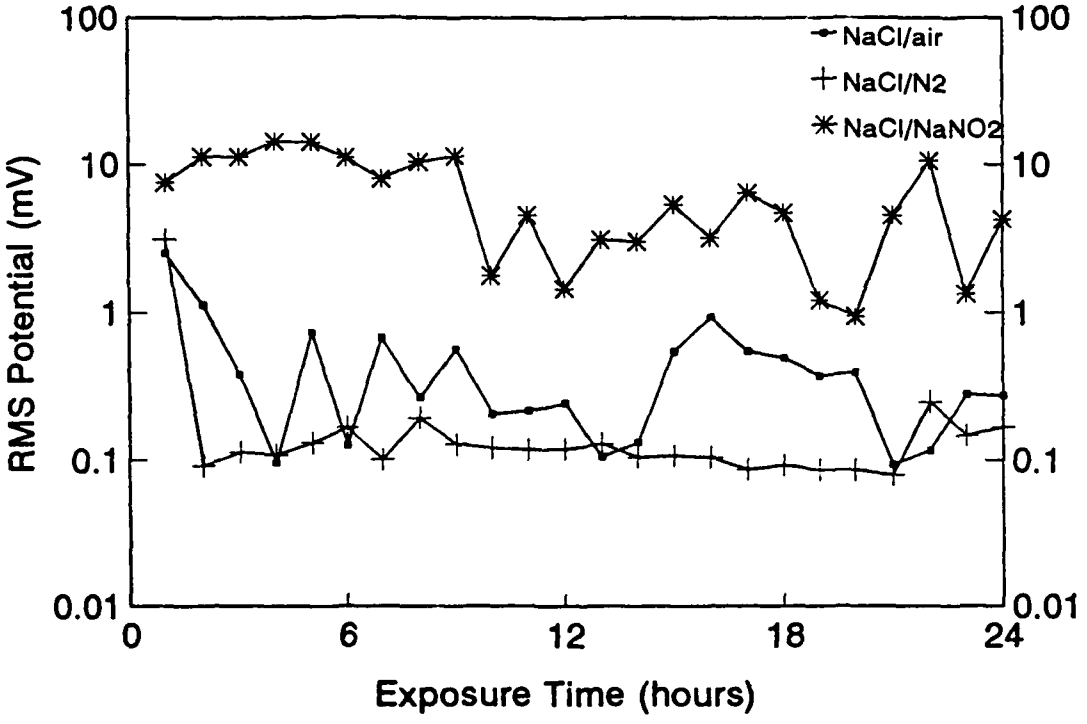

Fig.5 Rms potential values δV for iron in three solutions

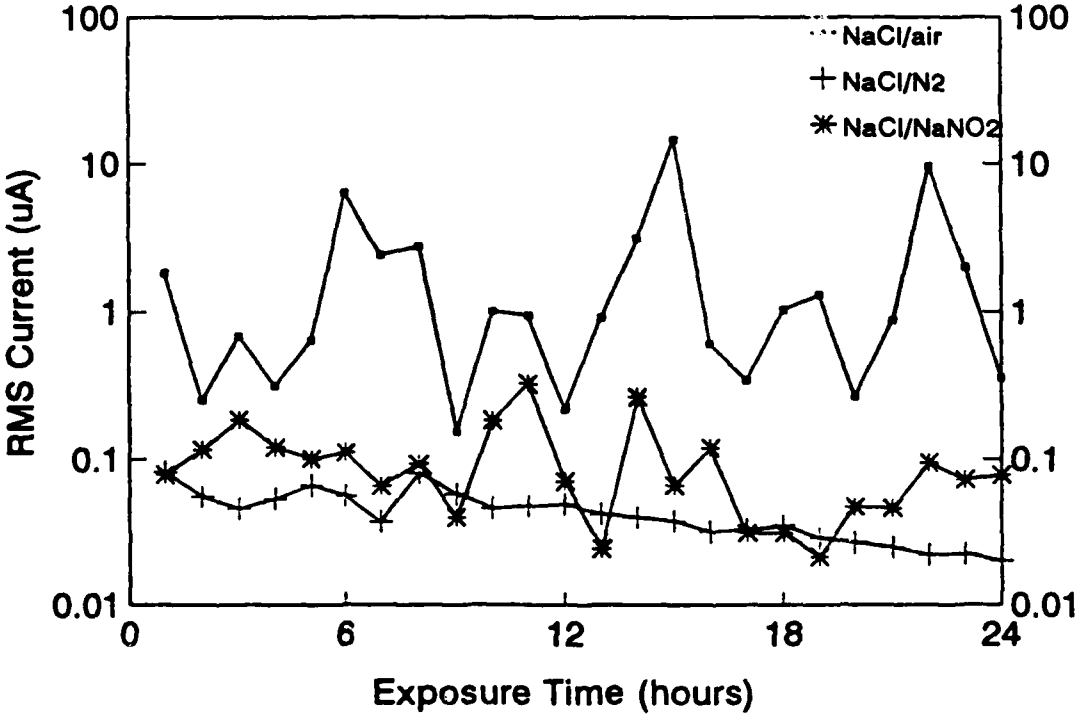

Fig.6 Rms current values δI for iron in three solutions

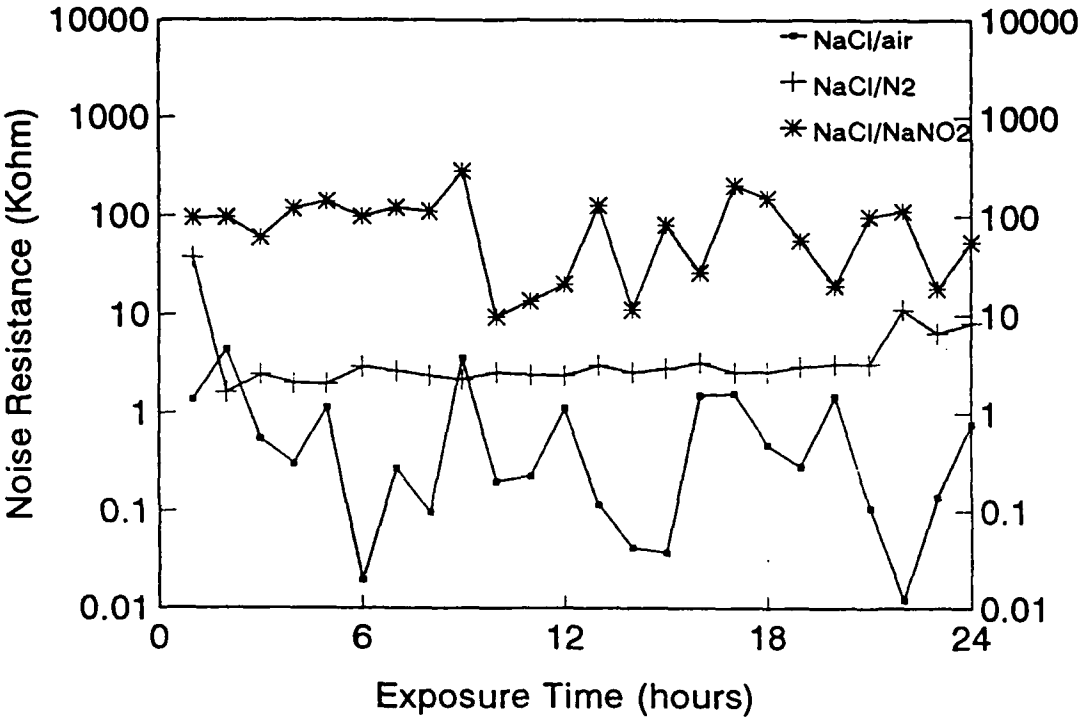

Fig.7 Noise resistance R_n for iron in three solutions

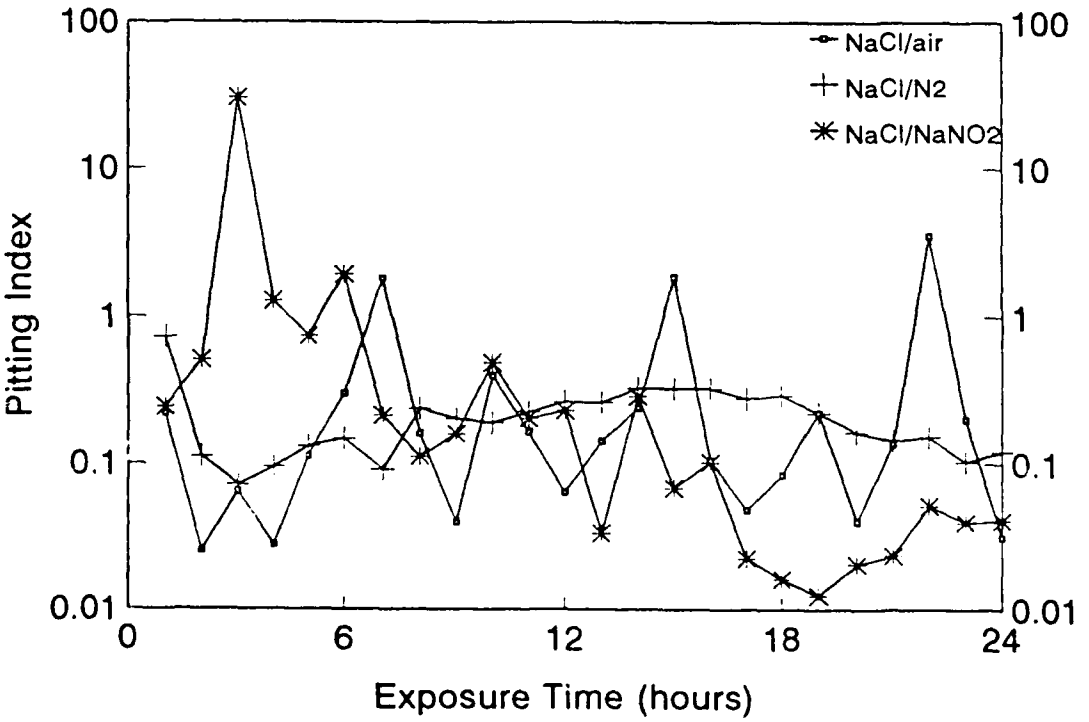

Fig.8 Pit index PI for iron in three solutions

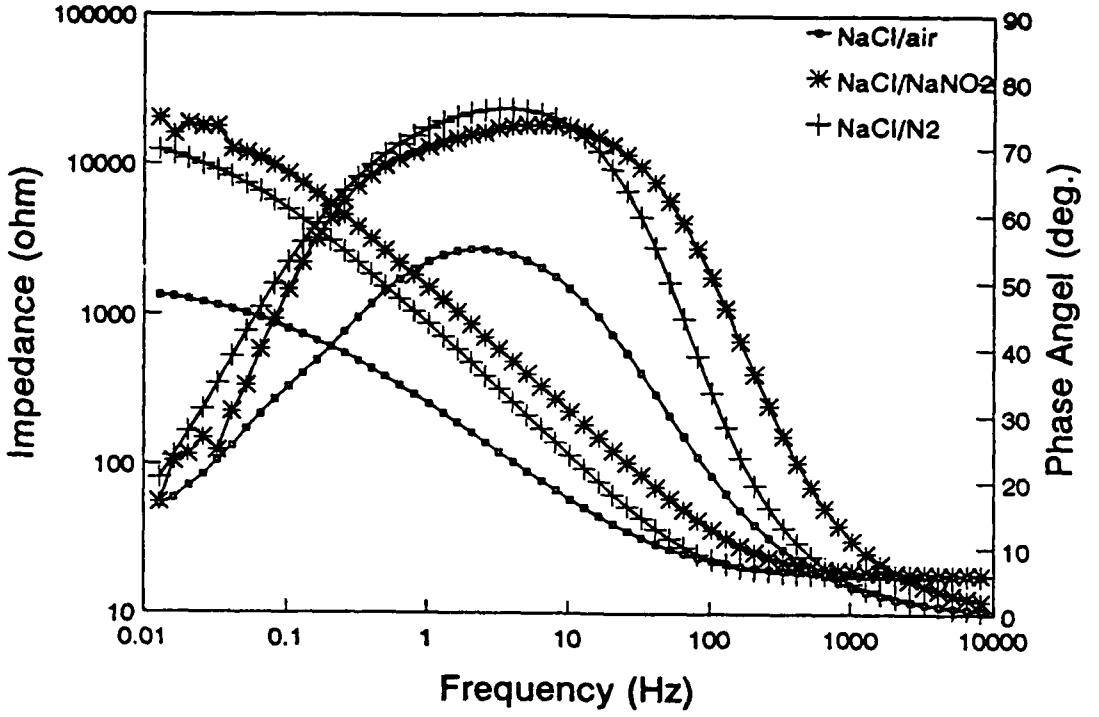

Fig.9 Bode-plots for iron after immersion in three different solutions for 24 hours

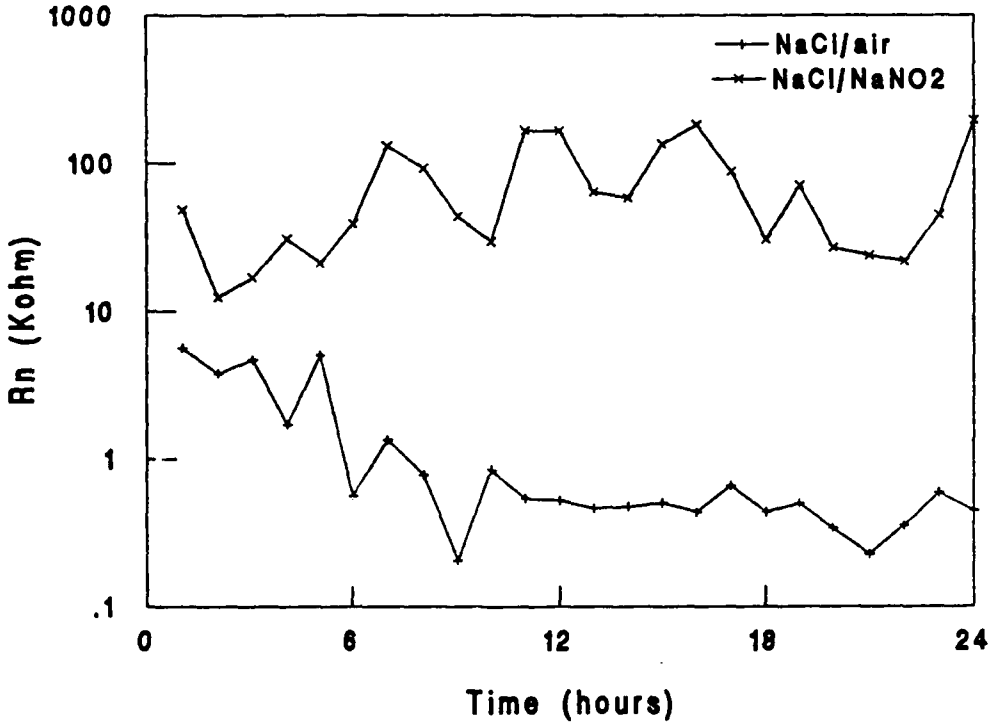

Fig.10 Noise resistance R_n determined from simultaneously recorded potential and current noise data for iron in aerated and in aerated inhibited 0.5 N NaCl

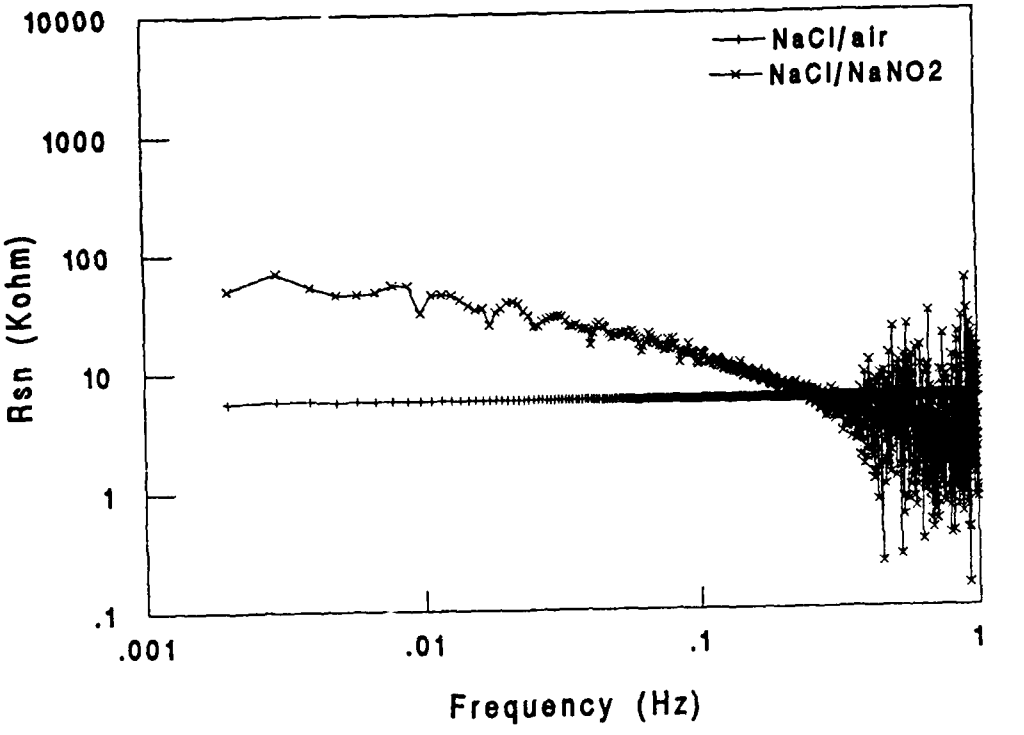

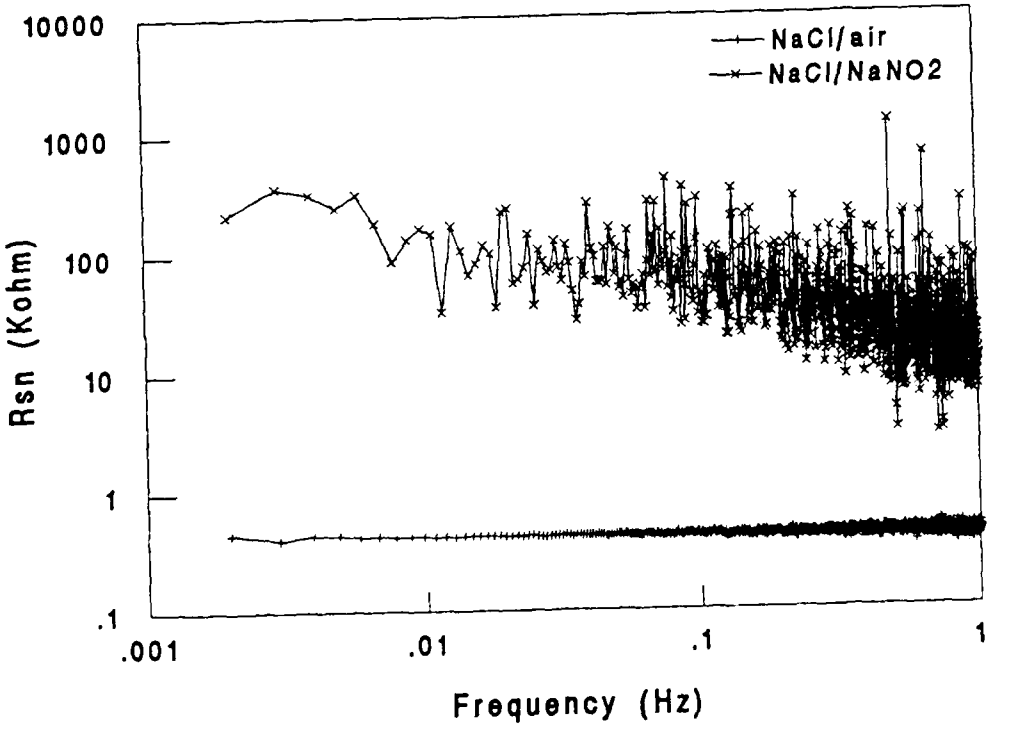

Fig.11 Frequency dependence of spectral noise resistance R_{sn} for aerated and for aerated inhibited 0.5 N NaCl after exposure for one hour (Fig.11a) and 24 hours (Fig.11b)

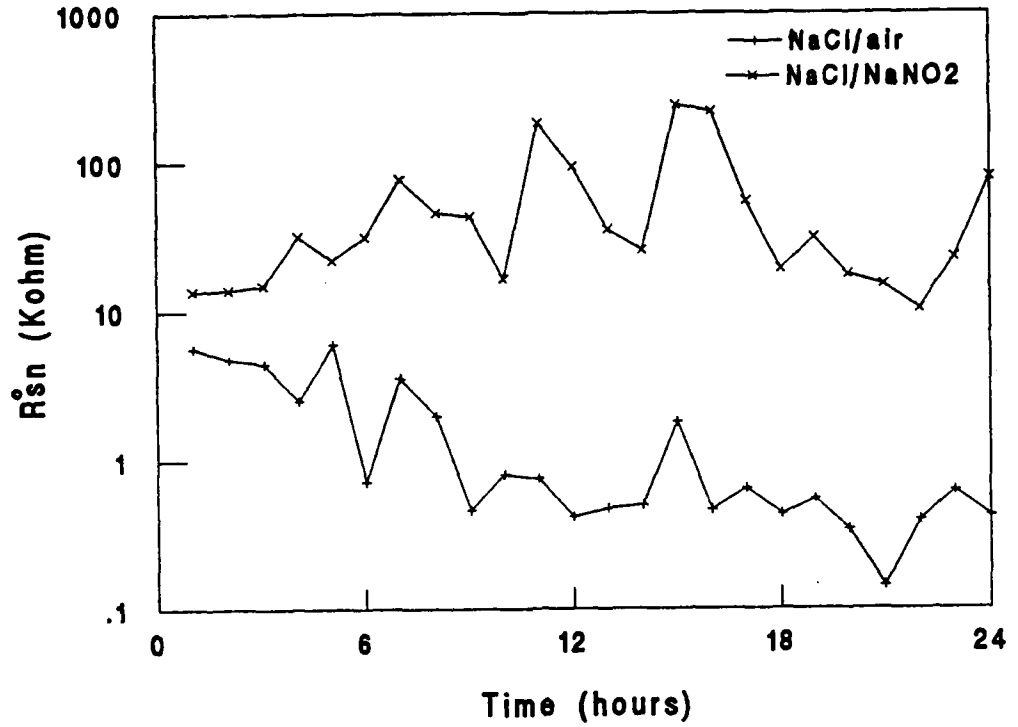

Fig.12 $R°_{sn}$-values as a function of exposure time for aerated and for aerated inhibited 0.5 N NaCl

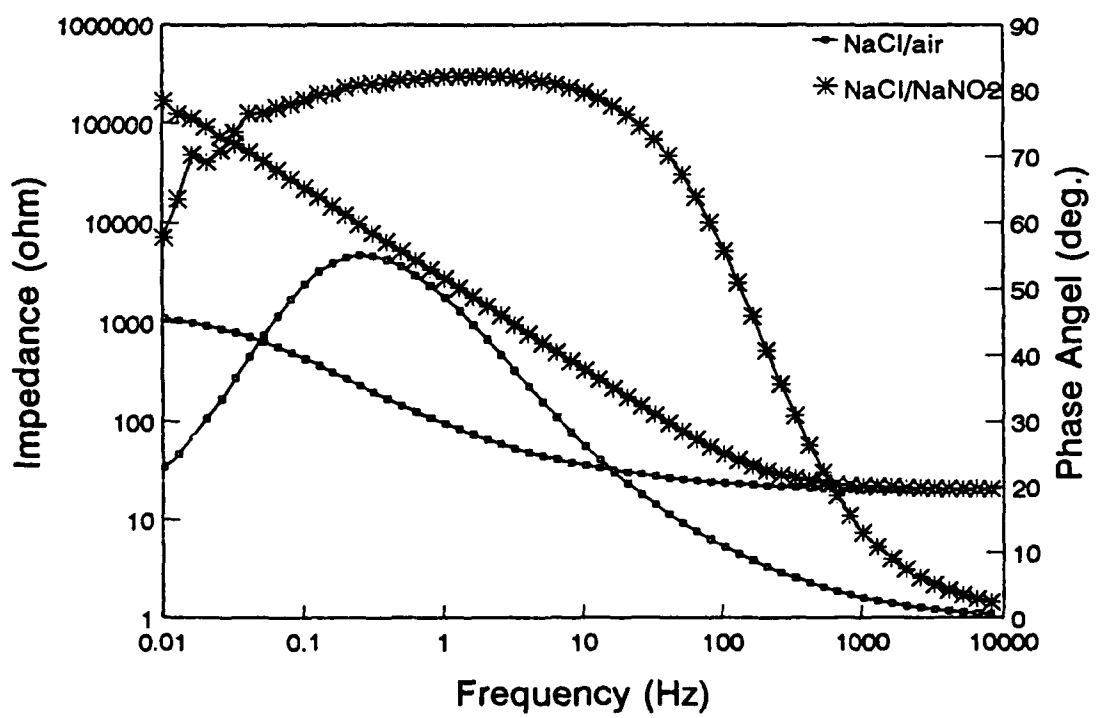

Fig.13 Bode-plots for iron in aerated and in aerated inhibited 0.5 N NaCl after 24 hour immersion

Characteristics of electrochemical noise generation during pitting corrosion.

S.Muralidharan
Central Electrochemical Research Institute
Karaikudi - 623 006
India

G.Venkatachari
Central Electrochemical Research Institute
Karaikudi - 623 006
India

K.Balakrishnan
Central Electrochemical Research Institute
Karaikudi - 623 006
India

Abstract

During pitting corrosion of metals, voltage fluctuations take place due to film breakdown. Due to this fact, the measurement of voltage noise can be used for detecting the initiation of pitting corrosion. Studies on the measurement of voltage noise have been made for steel in 500 ppm of inhibitor solutions such as potassium chromate, sodium nitrite, and sodium benzoate containing various amounts of chloride concentrations. It has been found that the voltage noise is less than $10^{-8}, \bar{V}^2$ in the absence of pitting corrosion. Also the PSD data are similar to the characteristic white noise generated due to the presence of passive film. During pitting corrosion the voltage noise is increased to the range of 10^{-7} to 10^{-6} $\bar{V}^2$. The PSD data show low frequency spectral components for frequencies less than 0.1 Hz.

Key terms : Noise power, Pitting Corrosion, Inhibitors, Power spectral density.

Introduction

During pitting corrosion of metals, voltage/current fluctuations, take place due to film breakdown. Earlier studies [1-7] have shown that there is an increase in the magnitude of electrochemical voltage/current noise during pitting corrosion. In most of the cases, a low frequency noise or flicker type of noise has been observed during pitting corrosion. Measurement of voltage noise power $\bar{V}^2$ from autocorrelation spectra of voltage - time data has been found to be useful for studying the pitting corrosion of aluminium and stainless steel in chloride solutions [8] and for the evaluation of corrosion inhibitors [9,10]. In this paper the results of voltage noise measurements during pitting corrosion of steel at initial stages in 500 ppm of potassium chromate, sodium nitrite and sodium benzoate containing sodium chloride are reported.

EXPERIMENTAL DETAILS

The structural steel (0.2% C) specimens of 1 Sq.cm with stem were embedded in araldite, polished on 1/0 to 3/0 emery papers and degreased with trichloroethylene. Two identical electrodes were immersed in 500 ppm of inhibitors containing different amounts of NaCl. The electrodes were fixed vertically facing each other in the cell and the cell assembly was put in the faraday cage. The voltage fluctations with sampling period for 5 minutes of the two electrodes, the autocorrelation functions and the autopower spectra of the voltage - time data were measured with a signal processor (1200, Solartron, UK) in the band width of 20mHz to 1Hz. The noise power ($\bar{V}^2$) is obtained at $\tau = 0$ from the auto correlation function which is defined by the equation

$$\phi_{xx}(\tau) = \lim_{T \to \infty} \frac{1}{T} \int_0^{\infty} x(t) \cdot x(t+\tau)\, d\tau$$

Where T is the total duration of measurement and τ is the delay time. The noise power ($\bar{V}^2$), is the measure of noise level. All the experiments were carried out at 298 $\pm$ 1 K, after 1 hour immersion in the respective solutions for the period of 5 hours.

RESULTS

The noise power $\bar{V}^2$ values for steel in 500 ppm of inhibitor containing NaCl have been obtained from the auto correlation spectra of voltage-time data. Fig.1 gives the typical auto correlation spectra for steel in 500 ppm K_2CrO_4 with and without 500 ppm NaCl. The frequency distribution of voltage noise data is analysed through the PSD plots and figure 2 gives the PSD spectra for the same system. Similar type of auto correlation and autopower spectra have been observed for other systems examined in this paper.

The variation of noise power ($\bar{V}^2$) with time for steel in 500 ppm of K_2CrO_4 solutions containing different amounts of NaCl is shown in Fig.3. The noise power is very low and is of the order of 10^{-8} $\bar{V}^2$ for 500 ppm K_2CrO_4, and chromate solutions containing 100 and 250 ppm NaCl. On visual inspection, the specimens were found to be unaffected in these solutions. For solutions of 500 ppm K_2CrO_4 containing 500 ppm and 1000 ppm NaCl, the noise power is in the range of 10^{-6} $\bar{V}^2$ which is about 1000 times higher than in the other solutions. It has also been visually observed that one or two pits are formed on the surface in K_2CrO_4 solutions containing 500 and 1000 ppm of NaCl after 1 hour of immersion.

The change in the noise power with time for steel in 500 ppm $NaNO_2$ containing 0 to 400 ppm NaCl is shown in Fig.4. The noise power for 500 ppm $NaNO_2$ containing 200 to 400 ppm of NaCl is in the range of 10^{-7} V^2. In these systems a number of minute dotlike pits have been observed on the surface. In solutions of $NaNO_2$ containing less than 100 ppm NaCl the noise power is of the order of 10^{-9} V^2 and in these solutions, pitting corrosion was not noted.

The influence of chloride ions on the noise power for steel in 500 ppm sodium benzoate is shown in Fig.5. Upto 50 ppm NaCl the values of noise power are the same as that of the pure sodium benzoate solution and the surface has been found to be unaffected. For NaCl concentrations of 100 ppm and above, the noise power values are in the range of 10^{-7} to 10^{-6} V^2. It is observed that a number of dot like pits are formed on the surface in benzoate solutions containing more than 100 ppm NaCl.

DISCUSSION

The analysis of noise power data shows that the values of noise power are less than 10^{-8} V^2 for solutions in the absence of pitting corrosion. However, during pitting corrosion the noise power values are increased to 10^{-7} to 10^{-6} V^2. Moreover these values decrease with time in the absence of pitting corrosion. Similar observation has been reported for aluminium in inhibited solutions containing NaCl [10]. But in solutions which can cause pitting corrosion, the noise power mostly tends to increase with time due to the occurrence of several processes like higher corrosion rate, hydrogen evolution from pits and formation of new film cracking sites (4).

The psd values of steel in the inhibitor solutions containing NaCl in the absence of pitting corrosion show that the noise generated is of white noise type, which is characteristic of a metal covered with passive film. Such type of psd behaviour has been reported during passivation [11-13]. But during pitting corrosion the psd values have been found to contain low frequency components for frequencies less than 0.1 Hz. Such type of behaviour has been reported by earlier workers [7,11,12,14]. Non stationarity has been invoked as an explanation for low frequency noise during pitting corrosion[3]. Thus from the magnitude of noise power and from the psd behaviour it is possible to assess the pitting corrosion tendency of steel in inhibitor solution containing chloride ions.

The magnitude of noise power increase for steel during pitting corrosion in chromate containing NaCl is nearly 1000 times. But during pitting corrosion in nitrite and benzoate solutions containing NaCl the noise power increase is only 10 to 100 times. The large increase of noise power in chromate containing NaCl during pitting is due to the formation of one or two active pits on the surface. But in the case of pitting corrosion in solutions

of nitrite and benzoate containing NaCl, the formation of number of minute dot like pits results in a smaller increase in noise power values. Earlier galvanostatic polarisation studies [15] have also indicated that one or two active pits are formed in chromate solutuions containing NaCl whereas a number of minute dot like pits are formed in nitrite or benzoate solutions containing NaCl.

CONCLUSIONS

The measurement of noise power and auto power spectra has been found to be useful for assessing the pitting tendency of chloride ions in the presence of inhibitor. During pitting corrosion low frequency noise is generated. The noise power of steel during pitting corrosion by chloride ions in the presence of inhibitor is found to be increased by 100 to 1000 times higher than in the absence of pitting corrosion.

ACKNOWLEDGEMENT

The authors thank the Director, CECRI, for his permission to present this paper.

REFERENCES

1. K.Hladky and J.C.Dawson, Corr.Sci,21 (1981) p.317
2. K.Hladky and J.C.Dawson, Corr.Sci,22 (1982) p.231
3. U.Betrocci and Y.Yang-Xiang, J.Electrochem Soc.131 (1984) p.1011
4. J.Uruchurtu and J.C.Dawson, Electrochemical methods in corr.Res.Ed.M.Duprat, Materials Science Forum Vol.8 (1986) p.113.
5. C.Bataillon and C.Fiaud, 8th Eur.Congr.Corr.Vol.2 (Nov.1985) p.39.
6. P.R.Roberge, R.Beaudoin and V.S.Sastri Corr.Sci.29(1989) p.1231.
7. M.Hashimoto, S.Miyajima and T.Hurato, Corr.Sci.33,(6) 1992 p.865, p.905
8. SP.Manoharan, S.Muralidharan, G.Venkatachari and K.Balakrishnan Procd.11th ICC, Italy, Vol.1 (1990) p.541.
9. S.Muralidharan, SP.Manoharan, G.Venkatachari and K.Balakrishnan, B.Electrochem. 6 (1) 1990 p.41
10. C.Marticelli, G.Brunoro, A.Frignani and G.Trabanelli, J.Electrochem. Soc 139 3, (1992) p.706.
11. K.Naachstedt and K.E.Heusler, Electrochim. Acta 33,3 (1988) p.311.
12. F.Flis, J.L.Dawson, J.Gill and G.C.Wood Corr. Sci32,8 (1991) p.877.
13. Chin Nan Cao, Qingrong Shi and H.Lin, B.Electrochem 6 8 (1990) p.710.
14. C.A.Loto and R.A.Cottis, B.Electrochem 4 12 (1988) p.1001
15. K.S.Rajagopalan, K.Venu and G.Venkatachari, Procd.3rd Eu. Symp on Corrosion Inhibitors, Ferrara, Italy (1970)p.711.

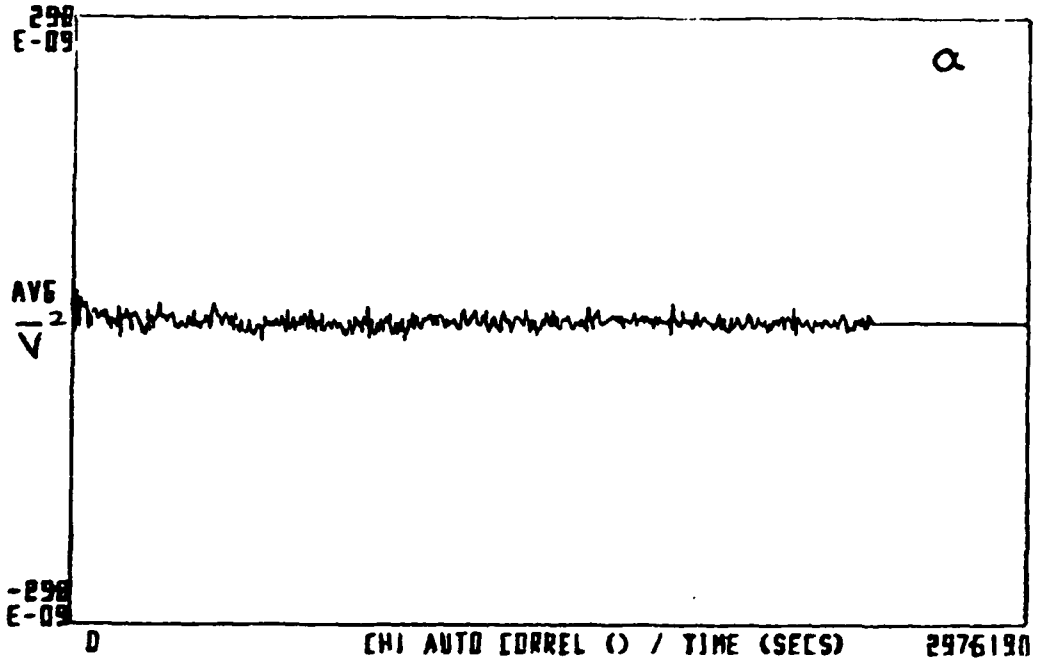

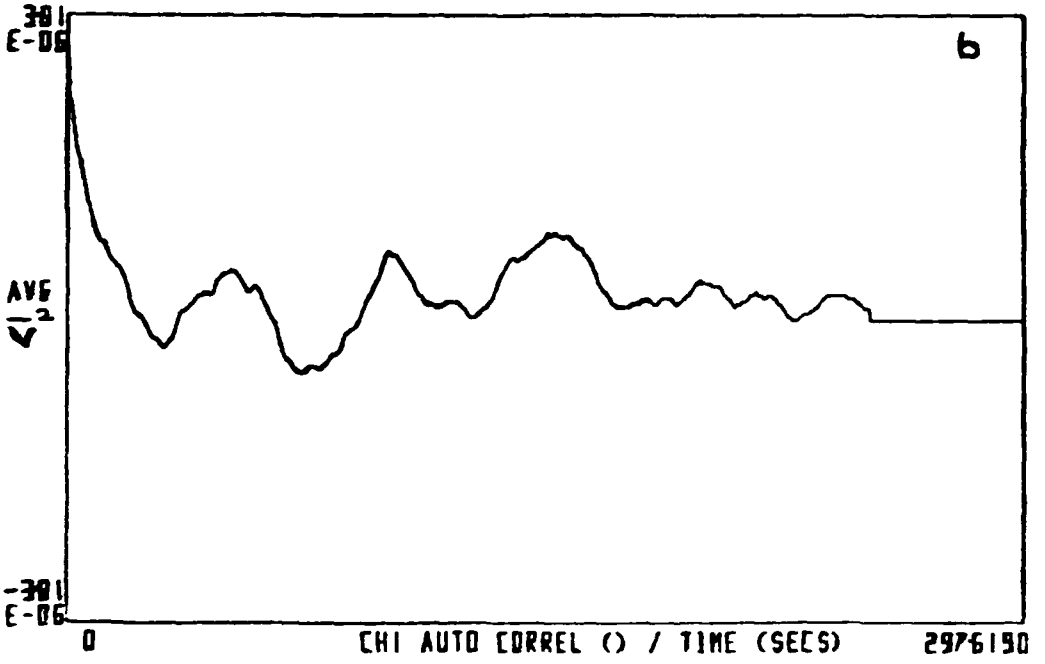

Fig.1 AUTO CORRELATION SPECTRA FOR STEEL IN 500 ppm K_2CrO_4 CONTAINING NaCl
(a) 0 ppm NaCl
(b) 500 ppm NaCl

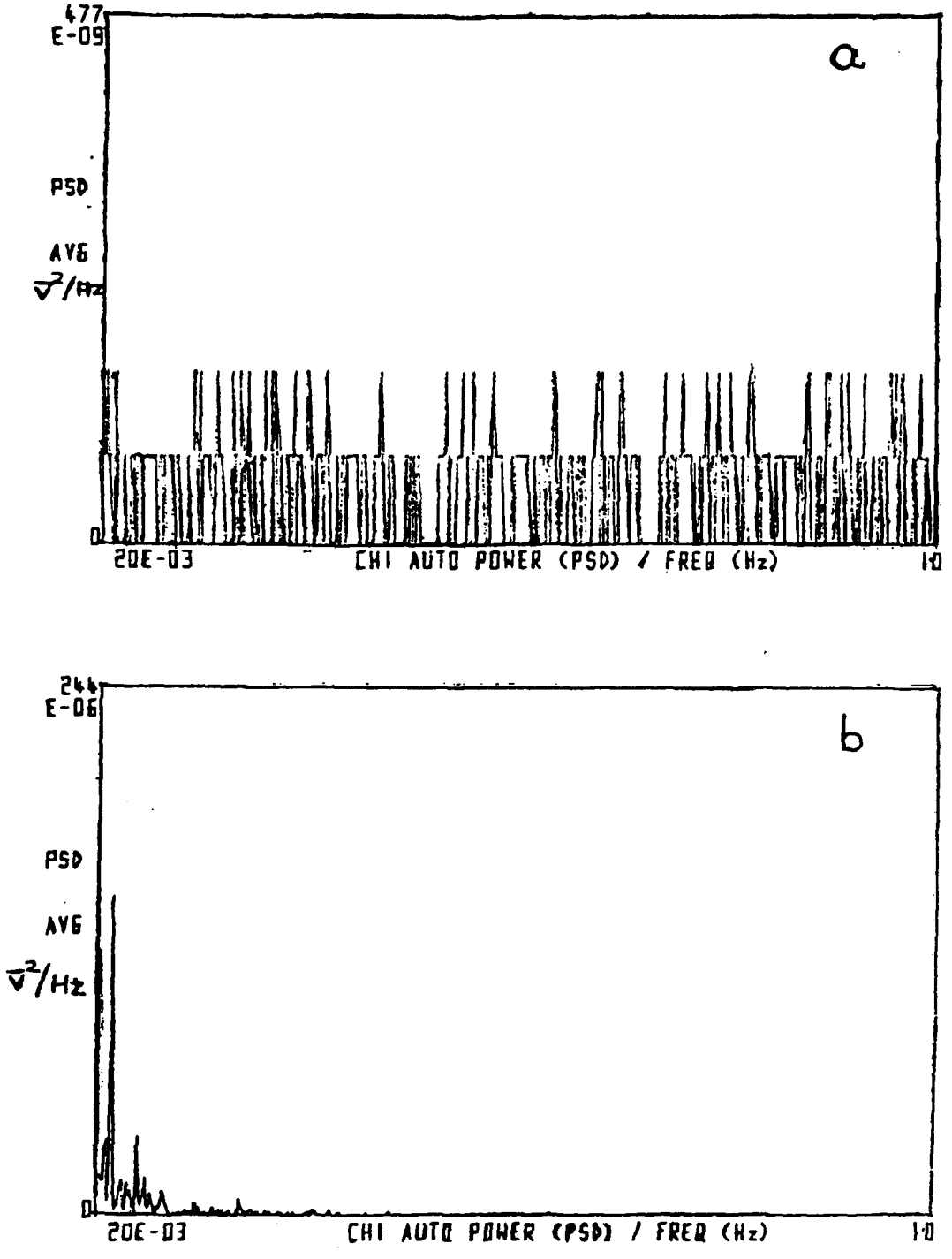

Fig.2 *AUTO POWER SPECTRA FOR STEEL IN 500 ppm K_2CrO_4 CONTAINING NaCl*
(a) 0 ppm NaCl
(b) 500 ppm NaCl

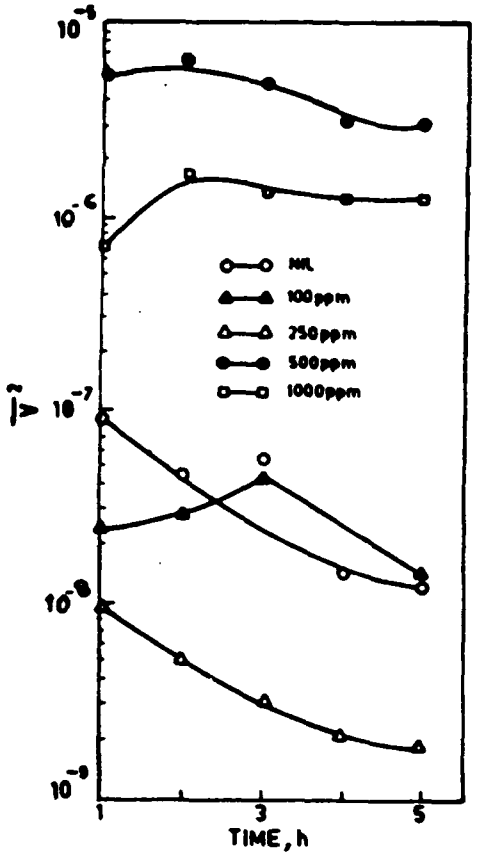

Fig.3 Variation of Noise power with time for steel in 500ppm K_2CrO_4 containing NaCl.

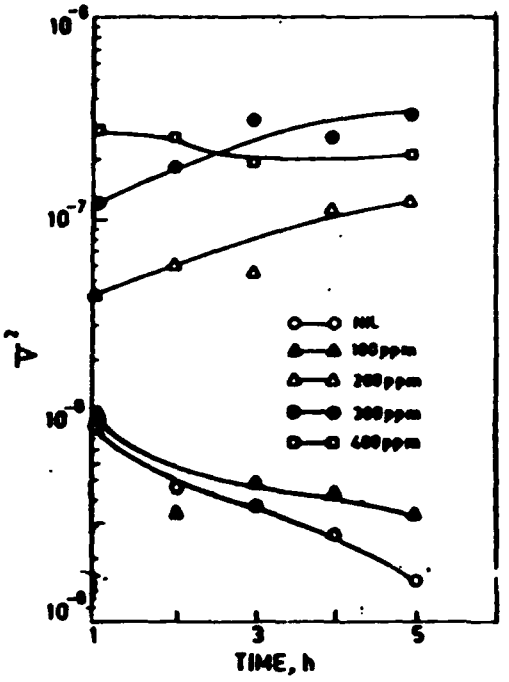

Fig.4 Variation of Noise power with time for steel in 500 ppm $NaNO_2$ containing NaCl.

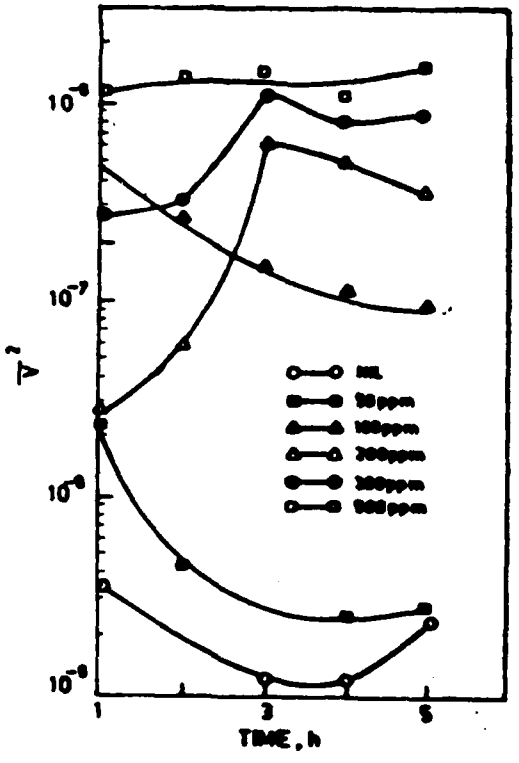

Fig.5 Variation of Noise power with time for steel in 500 ppm Sodium Benzoate containing NaCl.

ELECTROCHEMICAL NOISE AS THE BASIS OF CORROSION MONITORING

A.Legat

"J.Stefan" Institute, University of Ljubljana, P.O.BOX 100, 61111 Ljubljana, Slovenia

ABSTRACT

A method of corrosion monitoring based on electrochemical noise is described. Electrochemical noise was measured in a freely corroding system containing three identical metal electrodes. One pair of electrodes formed a voltage source, while the other pair formed a current source. The results of the electrochemical noise measurements were compared with the results of corrosion measurements from various reference methods.

Tests of the corrosion monitoring system were performed on steel and copper alloys in the pilot equipment under simulated conditions similar to those in heat exchangers. Measured values of electrochemical voltage and current were transformed to frequency area, and power spectrum densities were calculated. An additional mathematical treatment enabled estimation of the corrosion rate and the distinction between uniform and local corrosion.

Keywords: Corrosion Monitoring, Electrochemical Noise, Power-Spectrum Density, *I vs E* curves, Uniform Corrosion, Local Corrosion, Galvanic Corrosion

INTRODUCTION

Several methods of corrosion measurement are known: however, not all of them are able to distinguish between different types of corrosion. Moreover, only few are suitable for on-line corrosion monitoring. Stochastic fluctuations of the corrosion potential and the current generated by corrosion reactions are known as electrochemical noise. These fluctuations can be measured in freely corroding systems, where corrosion processes are not disturbed by any external voltage or current. The characteristics of electrochemical noise are determined only by the type and rate of corrosion, and therefore the use of electrochemical noise as a possible corrosion monitoring method has received considerable attention in recent years (1-11). Some of the studies dealt only with potential fluctuations (1-3,6,7), but most of them performed potential and current electrochemical noise measurements (4,5,8-11). Two principal techniques for the monitoring of electrochemical noise signals have been used: digital (2-7) and analogue signal processing (8,9). The digital signal processing technique involves the acquisition of raw data and their subsequent numerical analysis, while the analog processing method produces an output signal proportional to the root mean square of the noise using electronic filters and amplifiers. Field applications of electrochemical noise are mostly based on the second technique (8,9). Analysis of electrochemical noise for various metals have been performed; however, only a few studies distinguished strictly between different corrosion types (8,10,11). The aim of the present work was to develop a corrosion monitoring system based on measurements and analysis of electrochemical noise, and to prove its applicability in the field.

EXPERIMENTAL METHOD

Electrochemical potential and current-noise were measured in a freely corroding system containing three identical metal electrodes. A voltage signal generated by one pair of electrodes and a current signal generated by the other pair were amplified, digitized and fed into a personal computer. Preamplifiers were galvanically isolated from the computer in order to eliminate ground loops. Resolution was 1 nA for current and 1 μV for voltage measurements. Input impedances were 2 Ω for current input

and 10^9 Ω for voltage input. The sampling rate was 250 mHz. In one test period, 1024 voltage and current values were collected.

The corrosion monitoring system was tested in the Šoštanj Thermal Power Plant. All process units of the plant have cooling tower water systems. The quality of cooling water (from the river Paka) changes due to meteorological and operating conditions. In a period of two months it covered a wide range of pH and anion activity between two extreme cases (Table 1). The output temperature of the cooling water was approximately 38°C.

Steam condenser tubes are critical elements in the operation of most process plants. The tubes in the condensers in Šoštanj Thermal Power Plant are made of Admiralty brass and they are fixed to walls of mild steel. In order to study corrosion processes in the condensers and to achieve optimal chemical treatment of the cooling water, the corrosion monitoring system was tested on the pilot equipment under simulated conditions similar to those in heat exchangers.

Electrochemical noise measurements were made with three different types of probes using cooling water of various quality. Two types of probes contained three identical metal electrodes: rods of mild steel were encapsulated in an epoxy tube (Fig.1a); rings of Admiralty brass were inserted as part of a steam condenser tube (Fig.1b). One type of probe was constructed to measure galvanic corrosion: electrodes of copper and platinum formed a voltage source and electrodes of mild steel and copper formed a current source (Fig.1c). The corrosion monitoring system was verified using various reference methods (visual inspection, SEM analysis, I *vs* E polarization curves).

RESULTS AND DISCUSSION

Some methods which may be used to correlate electrochemical noise to different types and rates of corrosion have been described elsewhere (1-11). The electrochemical current-noise power-spectrum density ($PSD(I)$) at higher frequencies can be a measure of general corrosion, while the shape and repetition rate of transients of electrochemical potential and current-noise determine the type of corrosion (11). The slope

of the power-spectrum density of the electrochemical voltage-noise relationashiop ($PSD(U)$) after linear trend removal was recognized as a significant parameter for distinguishing between uniform and local corrosion. The electrochemical noise generated by uniform corrosion is white noise, and therefore the slope is close to zero. Localized corrosion generated electrochemical noise consisted of exponentially decreasing transients and the slope of the PSD(U) curve is higher ($> \quad 12 \quad dB(V^2Hz^{-1})\, decade^{-1}$).

The electrochemical noise measured for mild steel in cooling water 1 (CW1) and cooling water 2 (CW2) after linear trend removal can be seen in Fig.2 and 3. The electrochemical noise in CW1 (Fig.2) consisted of very frequent voltage and current spikes. The amplitudes of the noise measured in CW2 were lower; however, some nearly exponentially decreasing transients were present in addition to the noise of higher frequencies (Fig.3). It was found that the periodical fluctuations of current at approximately 0.85 mHz were influenced by the temperature control system within an interval of 2°C.

Electrochemical noise measurements indicated that in CW1 mild steel corroded uniformly ($k = \quad 6.3 \quad dB(V^2Hz^{-1})\, decade^{-1}$); however in CW2 the uniform type changed to localized corrosion ($k = \quad 15.3 \quad dB(V^2Hz^{-1})\, decade^{-1}$) with a lower average corrosion rate. The ratio between $PSD(I)$ obtained for CW1 (Fig.2) and $PSD(I)$ obtained for CW2 (Fig.3) was approximately 18 (in the frequency interval from 10 mHz to 125 mHz). Visual inspection and I *vs* E polarization curves (Fig.4) confirmed the results of electrochemical noise analysis. The values of the corrosion current densities obtained by Tafel extrapolation of I *vs* E curves measured at the end of 10 days exposure were: 80 $\mu A\, cm^{-2}$ in CW1 and 20 $\mu A\, cm^{-2}$ in CW2. The ratio of j_{corr} in CW1 to j_{corr} in CW2 was lower than the ratio of $PSD(I)$ in CW1 to $PSD(I)$ in CW2. Namely both methods measured the instantaneous corrosion rate; however, they could not be performed simultaneously. Additional methods should be used for more accurate determination of the corrosion rate.

Reference methods and the analysis of electrochemical noise measurements (Fig.5,6) showed that Admiralty brass corroded in CW1 and in CW2 only locally with a very low average corrosion current density ($< 1\mu A\, cm^{-2}$). It was evident from the potential-noise function that the initiation rate of pits was higher in CW2 (Fig.6), while the measured current-noise was close to the instrumental limit. Periodical fluctuations at lower frequency (0.85 mHz) were influenced by oscillation of temperature.

I vs E polarization curve measured in CW2 confirmed the tendency to localized corrosion (Fig.7), while *I* measured in CW1 was lower and scattered due to instrumental noise (PAAR Potentiostat M273).

The direct current (mild steel/copper) measured by the galvanic probe proved that the corrosion rate of mild steel was higher in CW1 ($I = 32\mu A$) than in CW2 ($I = 16\mu A$). Pitting corrosion of copper could be recognized from the measured electrochemical voltage (copper/platinum - Fig.8, 9). However, for a detailed analysis of measurements with this type of probe other configurations of the measuring system and more tests should be performed.

CONCLUSIONS

A corrosion monitoring system based on electrochemical noise was succesfully tested in pilot equipment under simulated conditions similar to those in heat exchangers with mild steel and Admirality brass. The electrochemical current-noise power-spectrum density ($PSD(I)$) at higher frequencies was confirmed as a measure for general corrosion and the slope of the power-spectrum density of the electrochemical voltage-noise relation after linear trend removal was found to be a significant parameter for distinguishing between uniform and local corrosion.

As expected, the electrochemical noise measurements proved that the rate of uniform corrosion of mild steel changed as a function of the pH of the cooling water; however, local corrosion of mild steel and Admirality brass was influenced by its anion activity. Periodic fluctuations of electrochemical voltage and current at approximately 0.85 mHz were generated by condunctivity oscillations caused by the regulation of the temperature over the interval of 2°C.

Electrochemical noise was confirmed as very suitable method for corrosion monitoring; however, classical spectral analysis (FFT) might not be the optimal mathematical description beacuse the chaotic behaviour of corrosion processes requires a different mathematical treatment.

REFERENCES

1. **K. Hladky and J.L. Dawson**, *Corros. Sci.* **21**, 317 (1981)
2. **K. Hladky and J.L. Dawson**, *Corros. Sci.* **22**, 231 (1982)
3. **J. Uruchurtu and J.L. Dawson**, *Electrochemical Methods in Corrosion Research* (ed. M. Duprat), p. 113, Material Science Forum **8**, (1986)
4. **I. Al-Zanki, J. S. Gill and J.L. Dawson**, *Electrochemical Methods in Corrosion Research* (ed. M. Duprat), p. 463, Material Science Forum **8**, (1986)
5. **A.M.P. Simoes and M.G.S. Ferreira**, *Br. Corros. J.***22**, 21 (1987)
6. **P.C. Searson, J.L. Dawson**, *J. Electrochem. Soc.***135**, 1908 (1988)
7. **C. Monticelli, G. Brunoro, A. Frignani, G. Trabanelli**, *J. Electrochem. Soc.***139**, 706 (1992)
8. **J.L. Dawson, W.M. Cox, D.A. Eden, K.Hladky and D.G. John**, *Proc. On-Line Surveillance and Monitoring*, Venice, p.531 (1986)
9. **P.E. Doherty, D.C.A. Moore, W.M. Cox, J.L. Dawson**, *Proc. Environmental Degradation of Materials in Nuclear Power Systems - Water Reactors*, Jekyll Island, Georgia, p.13-65, (1989)
10. **D.A. Eden, A.N. Rothwell**, *Proc. Corrosion/92*, No. 292, Nashville (1992)
11. **A. Legat, C. Zevnik**, *Advances in Corrosion and Protection*, Manchester (1992), *in press*

TABLE 1

PHYSICAL CHARACTERISTICS AND CONCENTRATION OF ANIONS IN COOLING WATER IN THE ŠOŠTANJ THERMAL POWER PLANT

	pH	conductivity [mS cm^{-1}]	$C_{(Cl^-)}$ [mg l^{-1}]	$C_{(NO_3^-)}$ [mg l^{-1}]	$C_{(SO_4^{2-})}$ [mg l^{-1}]
cooling water 1 (CW1)	8.1	1.9 - 2.2	32.5	22.1	588
cooling water 2 (CW2)	8.4	6.4 - 7.2	58.0	30.2	1120

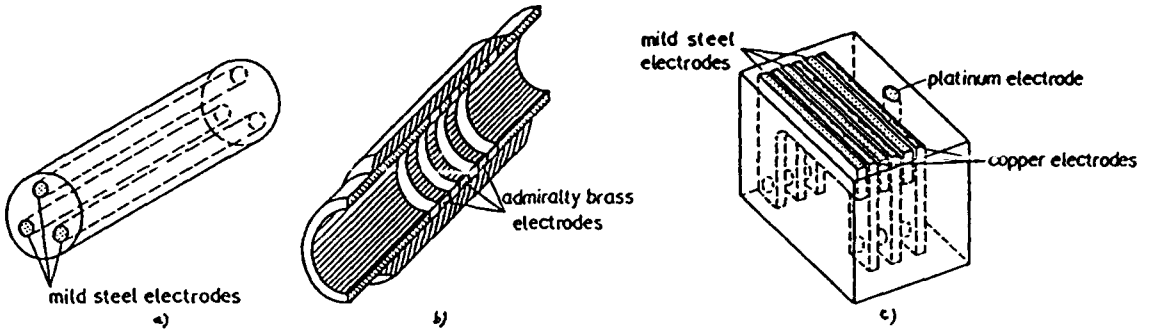

FIGURE 1 - Design/scheme of electrochemical noise probes: a) mild steel probe; b) cross-section of Admiralty brass probe; c) galvanic probe

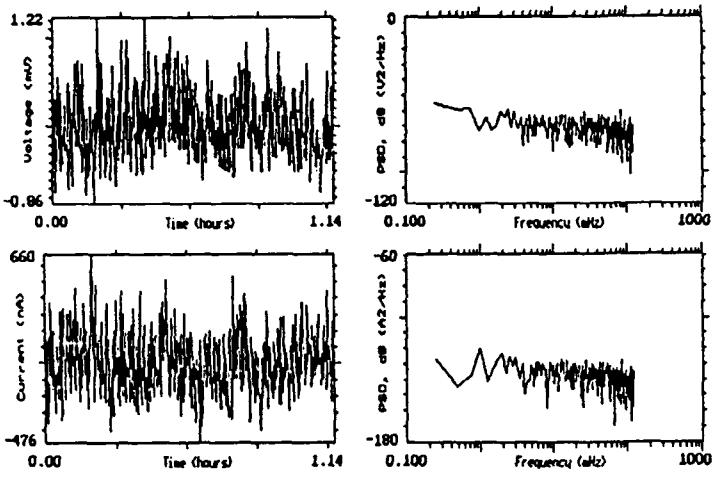

$\overline{PSD(U)} = -73.8 \;\; dB(V^2Hz^{-1})$
$\overline{PSD(U)} = -140.1 \;\; dB(A^2Hz^{-1})$
$k(PSD(U)) = 6.3 \;\; dB(V^2Hz^{-1})\, decade^{-1}$
$k(PSD(I)) = 8.2 \;\; dB(A^2Hz^{-1})\, decade^{-1}$

FIGURE 2 - Electrochemical noise for mild steel in CW1 (cooling water 1) after linear-trend removal

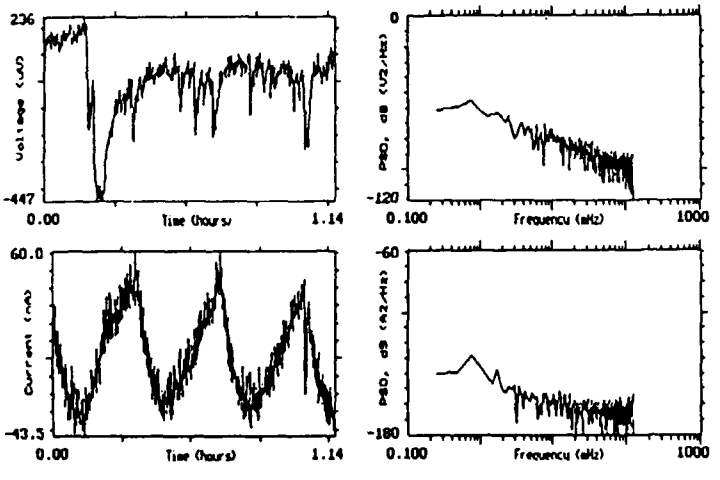

$\overline{PSD(U)} = -94.8 \;\; dB(V^2Hz^{-1})$
$\overline{PSD(U)} = -164.9 \;\; dB(A^2Hz^{-1})$
$k(PSD(U)) = 15.3 \;\; dB(V^2Hz^{-1})\, decade^{-1}$
$k(PSD(I)) = 3.1 \;\; dB(A^2Hz^{-1})\, decade^{-1}$

FIGURE 3 - Electrochemical noise for mild steel in CW2 (cooling water 2) after linear-trend removal

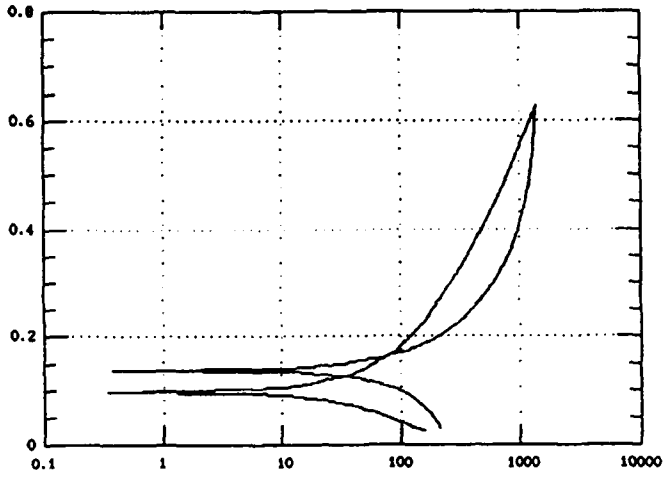

FIGURE 4 - Linear polarization *(I vs E)* curve for mild steel in CW2 after 1 week's immersion

$$\overline{PSD(U)} = -102.8 \;\; dB(V^2Hz^{-1})$$
$$\overline{PSD(U)} = -176.7 \;\; dB(A^2Hz^{-1})$$
$$k(PSD(U)) = 15.1 \;\; dB(V^2Hz^{-1})\, decade^{-1}$$
$$k(PSD(I)) = 0.5 \;\; dB(A^2Hz^{-1})\, decade^{-1}$$

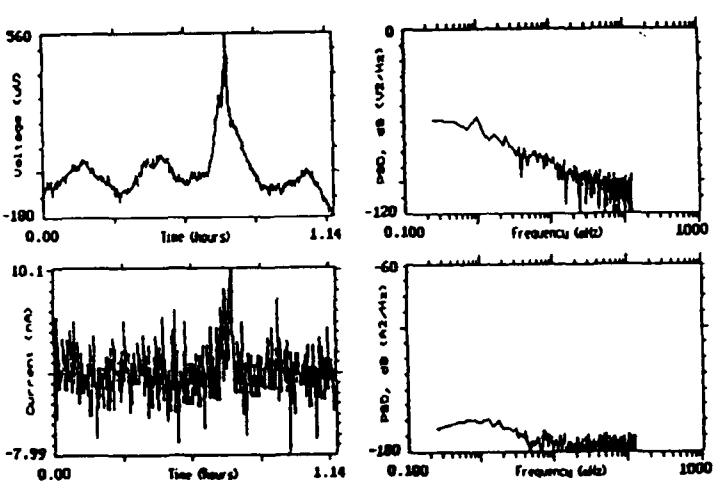

FIGURE 5 - Electrochemical noise for Admiralty brass in CW1 (cooling water 1) after linear-trend removal

$$\overline{PSD(U)} = -97.9 \;\; dB(V^2Hz^{-1})$$
$$\overline{PSD(U)} = -176.9 \;\; dB(A^2Hz^{-1})$$
$$k(PSD(U)) = 29.0 \;\; dB(V^2Hz^{-1})\, decade^{-1}$$
$$k(PSD(I)) = 0.8 \;\; dB(A^2Hz^{-1})\, decade^{-1}$$

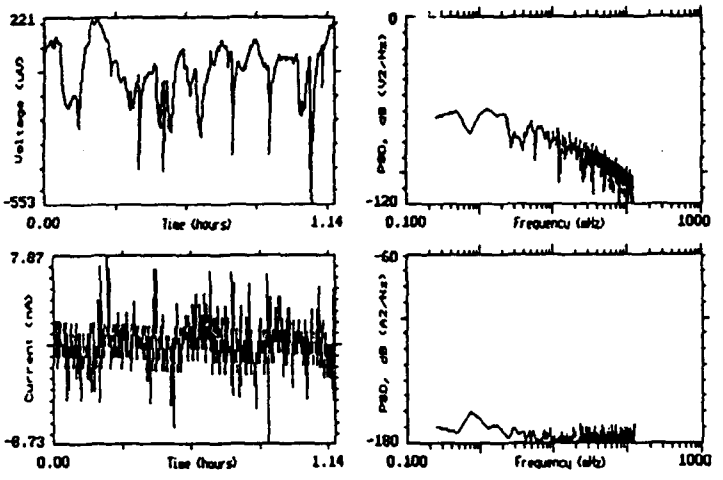

FIGURE 6 - Electrochemical noise for Admiralty brass in CW2 (cooling water 2) after linear-trend removal

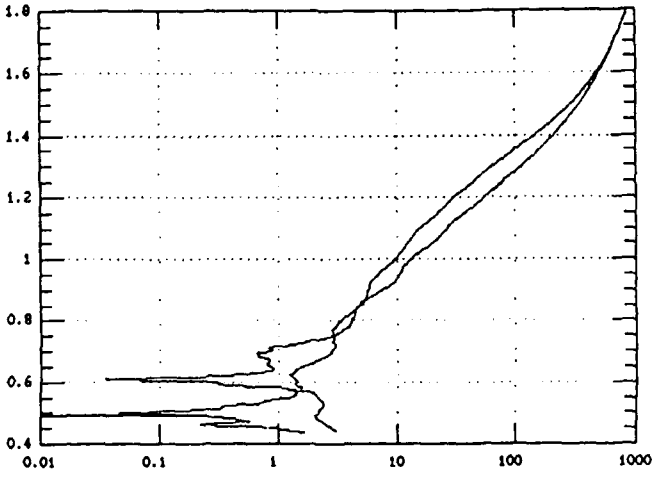

FIGURE 7 - Linear polarization *(I vs E)* curve for Admiralty brass in CW2 after 1 week's immersion

$$\overline{PSD(U)} = -81.8 \;\; dB(V^2Hz^{-1})$$
$$\overline{PSD(U)} = -147.8 \;\; dB(A^2Hz^{-1})$$
$$k(PSD(U)) = 22.1 \;\; dB(V^2Hz^{-1})\, decade^{-1}$$
$$k(PSD(I)) = 4.8 \;\; dB(A^2Hz^{-1})\, decade^{-1}$$

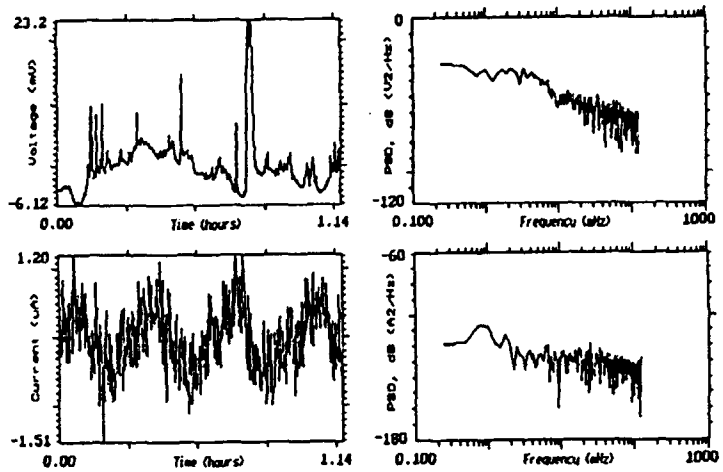

FIGURE 8 - Electrochemical noise for galvanic (copper/mild steel/platinum) probe in CW2 after linear-trend removal

$$\overline{PSD(U)} = -63.1 \;\; dB(V^2Hz^{-1})$$
$$\overline{PSD(U)} = -134.6 \;\; dB(A^2Hz^{-1})$$
$$k(PSD(U)) = 16.7 \;\; dB(V^2Hz^{-1})\, decade^{-1}$$
$$k(PSD(I)) = 10.5 \;\; dB(A^2Hz^{-1})\, decade^{-1}$$

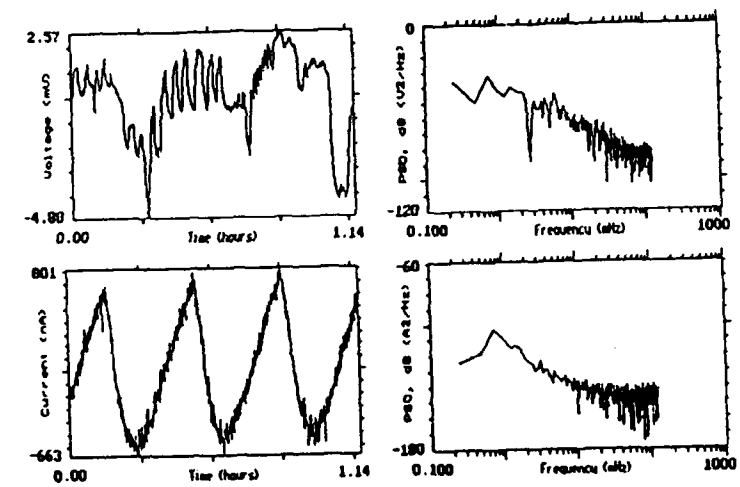

FIGURE 8 - Electrochemical noise for galvanic (copper/mild steel/platinum) probe in CW1 after linear-trend removal

Electrochemical relaxation techniques for the measurement of instantaneous corrosion rates

V. Lakshminarayanan
Raman Research Institute
Bangalore 560080, India

S.R.Rajagopalan
Materials Science Division
National Aeronautical Laboratory
Bangalore 560017, India

Abstract

The electrochemical relaxation techniques described in this paper offer several advantages including the ability to provide information on interfacial capacitance and kinetic parameters of corrosion systems.

The two techniques developed in this work are (a) programmed pulse relaxation, and (b) sinusoidal ac relaxation. In the former technique, a programmed current pulse is applied and the resulting potential-time transient is analysed. All the corrosion kinetic parameters, in addition to double layer capacitance can be obtained for corrosion systems.

An analysis of the ac harmonic current when a small amplitude potential perturbation is applied to the corrosion system provides information on corrosion rate of the system. In this work, a suitable technique for correcting the double layer charging current for the first harmonic has been developed. Using this data as well as the second harmonic current, corrosion rates for a few systems have been determined.

Key terms: exponential relaxation, ac harmonic, double layer capacitance

I. INTRODUCTION

Classical steady state techniques are still being mostly used for measurement of instantaneous corrosion rates. The popularity of these DC techniques, viz., polarisation resistance measurement and Tafel extrapolation technique arise from the fact that their instrumentation is simple and data analysis quite straightforward. These advantages largely overshadow the problems inherent in these methods. Since these methods involve perturbing the systems for considerable duration, any drift in corrosion potential between the beginning and end of polarisation will adversely affect the measured corrosion rates.[1] The polarisation for longer duration also affects the electrode surface by increasing the surface roughness during the anodic polarisation and reduction of passive film, if any, during cathodic polarisation resulting in

changes of surface microstructure during measurement. The problem is aggravated when there is a large drift in corrosion potential due to the formation of corrosion product film on the surface.[1]

The electrochemical relaxation techniques largely overcome these problems as the perturbation is applied only for a short duration. In addition to this, they provide information on the interfacial capacitance of the electrode/solution phase boundary. It is no longer true that the instrumentation and data analysis involved in relaxation techniques are complex. This is made possible by the advent of digital computers which at once provides the necessary excitation waveform and also acquires the data for subsequent data analysis.

The authors have developed a class of transient relaxation techniques and been using them routinely in the laboratory for corrosion rate measurements. These techniques consist of two current controlled techniques, viz., exponential relaxation technique and decreasing current ramp technique.[2,3] The methods, instrumentation and data analysis procedure were all described in detail. However, in this paper, it will be shown that using a personal computer with interphase hardware many of the problems associated with the earlier instrumentation are overcome. In addition to this, it will be shown that ac harmonic current measurements can be used for corrosion rate measurement provided the double layer changing current is accounted for in the measured response.[4,5] A simple method for charging current correction is described and it is shown that the ac harmonic technique can be used for reliable corrosion rate measurement,provided proper frequency range is chosen for measurement.

II. METHODS

(A) Exponential Relaxation Technique

This employs a current input which decays exponentially with time constant τ. The input $i = f(t, \Delta I, \tau) = \Delta I \exp(-t/\tau)$ is applied to the electrochemical system and resulting potential-time transients have been shown to provide kinetic parameters of electrochemical systems. Depending upon whether the amplitude of ΔI is small or large, the technique is called small amplitude exponential or large amplitude exponential relaxation technique respectively.

When the amplitude of ΔI is small, and when the system is under activation control, the potential response to the current perturbation is given by,

$$\eta = \frac{\Delta I \, R_p \, \tau_d}{(\tau_d - 1)} \left[\exp(-t/\tau) - \exp(-\tau_d \, t/\tau)\right] \qquad (1)$$

where $R_p = \dfrac{RT}{(\alpha_c + \beta_a) \, nF I_{corr}}$ and $\tau_d = \tau / R_p C_d$.

The potential profile exhibits a maximum, where charging current is zero. A

typical potential response is shown in Fig .(1). Since at the maximum,

$$T_{max} = \frac{t_{max}}{\tau} = \frac{ln\,\tau_d}{(\tau_d - 1)} \tag{2}$$

and

$$\eta_{max} = \Delta I\, R_p \exp(-T_{max}) \tag{3}$$

it is easy to calculate R_p and τ_d and hence C_d from (2) and (3). One can use these values as starting points for curve fitting of the equation (1) to get precise values of R_p and C_d.

The potential response can also be used for obtaining corrosion rate and Tafel slopes as follows:

$$\Delta I \exp(-t/\tau) = -C_d(d\eta/dt) + I_{corr}\,[\exp(-2.3\eta/b_c) - \exp(2.3\eta/b_a)] \tag{4}$$

where $b_a = 2.3RT/\beta_a nF$ and $b_c = 2.3RT/\alpha_c nF$.

Eqn.(4) can be rearranged to get

$$\begin{aligned}(d\eta/dt) = {} & 1/C_d[(b_a\, b_c/(2.3(b_a + b_c)R_p)(\exp(-2.3\eta/b_c) \\ & - \exp(2.3\eta/b_a)) - \Delta I \exp(-t/\tau)]\end{aligned} \tag{5}$$

When the polarisation is within say, 5 mV, the double layer capacitance can be considered constant with potential.

In eqn. (5), only unknown parameters are b_a and b_c as R_p and C_d can be evaluated from (2) and (3). b_a and b_c are varied in steps of 1 or 2 mV and eqn. (5) is solved numerically using 4th order RK method to obtain a set of $\eta - t$ data points at each step. These data points are fitted with the experimentally obtained values from the $\eta - t$ transients and the best fit values of b_a and b_c are found. Corrosion rate can be calculated from R_p, b_a and b_c from the expression:

$$R_p = [b_a\, b_c/(2.3(b_a + b_c)I_{corr})] \tag{6}$$

when $b_c \rightarrow \infty$ as it happens when the cathodic conjugate reaction is mass transfer controlled or when $b_a \rightarrow \infty$ during passive dissolution. it is obvious that the method involves determining only one unknown parameter.

The above method offers the advantage of obtaining corrosion rate, Tafel slopes and double layer capacity of the corrosion system from a single transient polarised to a small potential.

In the large amplitude technique, the potential is polarised to the Tafel region by applying a current pulse of suitable amplitude. The slopes at several η values which occurs both at rising and falling portion of the curve are measured. It is possible to show,

$$(C_d)_\eta = (i_2 - i_1)/(S_1 - S_2) \tag{7}$$

and

$$(i_F)_\eta = i_1 + (C_d)_\eta S_1 \quad (8)$$

where i_2 and i_1 are the total currents at times t_2 and t_1 at any particular potential η. S_2 and S_1 are the slopes at these points and $(i_F)_\eta$ is the faradaic current at any potential η. Using (7) and (8), the faradaic current i_F can be obtained at several η values. A plot of i_F *vs.* η is obtained from a single transient from which I_{corr} can be obtained as the intercept. Incidentally, C_d is obtained as a function of potential. A similar relaxation technique is the decreasing current ramp technique (dcrt) which uses a linearly decreasing current ramp of the form

$$i = \Delta I(1 - t/\tau)$$

The detailed methodology and instrumentation were described elsewhere[3] and will not be discussed here.

(B) AC Harmonic Method of Measurement of Corrosion Rate

Due to non-linear nature of the current-potential relationship in an electrochemical system, harmonics are generated when a small amplitude ac potential is applied. The first harmonic ac current can be separated into faradaic and non-faradaic components.

$$I_t \cos\phi = -I_{corr} E_p[(\alpha + \beta) - (\alpha^2 - \beta^2)\eta] \quad (9)$$

where $\alpha = 2.3/b_c$ and $\beta = 2.3/b_a$, and

$$I_t \sin\phi = 2\pi f C_d E_p \quad (10)$$

where ϕ is the phase shift between the applied potential and current resonse, E_p is the amplitude of the potential input, f is the frequency of the input signal and I_t is the total current amplitude. If the faradaic impedance is assumed to be resistive, the faradaic current will be inphase with the applied voltage. In that case, eqn. (9) represents the pure faradaic component.

The expression for the second harmonic current is given by,

$$I_2 = \frac{I_{corr}}{4} E_p^2 [(\alpha^2 - \beta^2) - (\alpha^3 + \beta^3)\eta] \quad (11)$$

when I_2 is measured at various η values and plotted,

$$\frac{Slope}{Intercept} = \frac{(\alpha^3 + \beta^3)}{(\alpha^2 - \beta^2)} = -\frac{(\alpha - \beta)^2 + \alpha\beta}{(\alpha - \beta)} \quad (12)$$

From (9), $(\alpha + \beta)$ can be obtained at $\eta = 0$, i.e.,

$$i_1 \cos\phi = I_{corr} E_p(\alpha + \beta) \quad (13)$$

and second harmonic current I_2 at $\eta = 0$ is

$$I_2 = \frac{I_{corr}}{4} E_p^2 (\alpha^2 - \beta^2) \quad (14)$$

From (13) and (14) α and β can be obtained by a simple arithmetic. I_{corr} can, of course, be obtained from (13).

III. INSTRUMENTATION

The methods described above involve (a) generation of suitable excitation waveform, (b) galvanostat/potentiostat, (c) data acquisition system, (d) data analysis.

(A) Generation of the Waveform

The excitation signal is generated through a digital to analog converter interphased to a PC (IBM 386). The data acquisition system consists of two D/A converters and 8 differential input A/D converters. The signal is generated using a BASIC programme with a CALL routine. A/D generated interrupt routines are used to transfer previously generated integer array variables to a 12 bit D/A to generate an analog O/P signal.

The following parameters are controlled by entering the respective values:

(i) Amplitude and Duration of excitation signal

(ii) Number of steps

(iii) Number of cycles

(B) Galvanostat/Potentiostat

A home made potentiostat is used in galvanostat mode. The op-amps used in the circuit have large bandwidth and high slew rate. A high current op-amp OPA 512 is used as a booster amplifier. The potential response is obtained through an instrumentation amplifier fabricated by conventional three op-amp design.

(C) Data Acquisition

The potential response data are acquired through a 12 bit analog to digital converter. The number of A/D conversions is the same as the number of steps in the excitation signal. The A/D is operated on a pacer triggerred mode. The acquired data are displayed on the graphics screen. The data are also analysed using a software developed for measuring the derivative of the potential response. The derivatives are obtained at each point using four point fit. The values for corrosion rate, Tafel slopes, double layer capacitance as a function of potential are computed using this software.

(D) AC Harmonic Technique

For the potential controlled ac technique, a small amplitude ac potential from a low distortion oscillator is applied to the corrosion system through a potentiostat. The cell current is converted to voltage with a op-amp C-V converter. The resulting ac voltage is filtered using a state variable tuned filter fabricated for this purpose. The first and second harmonic responses were filtered and rectified using an absolute value circuit. The DC voltage is applied through a separate input for the potentiostat.

Since at the instance of peak of the applied voltage the measured current is purely faradaic as the charging current represented by,

$$\omega C_d E_p \sin \omega t = 0, \quad \text{when} \quad \omega t = 0$$

i.e., when the applied potential is a cosine wave. Hence a measurement of the inphase component of the first harmonic current w.r.t. the applied ac voltage represents the purely faradaic component.[6] In other words the measured peak sampled current $I_1 \cos \phi$ is the pure faradaic component of the total current. This, of course, assumes that the faradaic impedance is purely resistive. This assumption is valid for corrosion systems where the corrosion reaction exhibits activation control. Again the measured current can be considered purely faradaic only when the uncompensated resistance R_u is zero. This can be usually achieved by positive feedback technique[7] where a fraction of the output voltage is fed back to the potentiostat by monitoring the onset of oscillation.

(E) Corrosion Cell

The system consists of a corrosion cell containing the electrolyte with a Teflon stopper. There is a provision for two symmetrical counter electrodes of platinum a reference electrode (usually SCE) and an inlet and outlet for purging with oxygen free nitrogen in the case of acid electrolytes. The specimen metal strip with an area of 1 cm^2 is exposed to the electrolyte with the rest masked off with araldite, an epoxy resin. The specimens were polished in the usual manner of preparation for corrosion systems. The solution is kept well stirred for an hour before making measurements.

IV. RESULTS AND DISCUSSION

(A) Exponential Relaxation Technique

The results obtained for various corrosion systems using exponential relaxation technique had been presented and discussed earlier.[2,5]

Table I shows R_p and C_d obtained for three different corrosion systems using small amplitude relaxation technique.

Table II presents the I_{corr} and Tafel slopes obtained using the small amplitude relaxation technique from eqn. (5) and (6) using 4th order R.K. method for curve fitting. The steady state polarisation experiments were also conducted. The corrosion rates and Tafel slopes obtained for the three systems are also presented for comparison. The good agreement of the values obtained using the relaxation technique with the steady state polarisation values show that the methods described here can be used for reliable measurement of corrosion rate.

Fig. (2) shows the plots of $I_1 \cos \phi$ against polarising dc potential at $f = 1$ Hz for the system of MS in 0.5 MH_2SO_4. The linearity confirms eqn. (4).

It can be seen that the first harmonic current response decreases with increasing cathodic polarisation, whereas it increases with increasing anodic polarisation. This shows $\alpha < \beta$ for this system.

The second harmonic current response of the system is measured using a tuned filter at different frequencies. Measurement of I_2 was carried out as a function of cathodic and anodic overpotentials. A plot of I_2 vs. η at $f = 1$ Hz is shown in Fig. (3). It can be noticed that I_2 decreases with increasing cathodic polarisation while opposite is the case for anodic polarisation, confirming that $\alpha < \beta$.

The corrosion rates for the following three systems have been measured using the above method:

(i) Mild steel in 0.5 M H_2SO_4

(ii) Armco iron in 0.5 M H_2SO_4

(iii) Mild steel in 1 M HCl.

The results obtained for the above systems are shown in Table III along with the values obtained using steady state polarisation technique.

It has been observed that the first harmonic faradaic current response $I_1 \cos \phi$ is almost constant at low frequencies and begins to increase at higher frequencies as can be seen from Fig. (4). At large frequencies the double layer capacitance acts as a shunt path, such that most of the current passes through it than R_p. This observation can be compared with the faradaic impedance measurement[8] where the lower limit of rate constant that can be determined is limited by the condition $R_{ct} \leq 1/C_d\omega$. In other words, the change transfer resistance should not be so large that all the current takes the path through C_d. If a similar condition is applied with regard to R_p, then for reliable measurement of corrosion rate, R_p should be lower than $1/C_d\omega$. Substituting reasonable values of R_p and C_d ($R_p = 15\ \Omega cm^2$ and $C_d = 100\ \mu F/cm^2$), the condition is fulfilled when the frequency is less than 100 Hz. It can be seen from the figure that a similar trend is observed in the case of MS in 0.5 M H_2SO_4.

In the equivalent circuit, generally assumed for the system, the ohmic resistance R_u and double layer capacitance C_d are nearly ideal circuit elements while the components of faradaic impedance are not ideal and change with frequency. Hence care has to be exercised in selecting a particular frequency at which measurement should be made. As a rule of thumb, it is possible to adopt the phase shift between the applied voltage and the total current as a criterion for selecting the frequency range. It is inferred that the frequency range at which phase shift (ϕ) is less than 4° to 10° will give reliable values of I_{corr}.

References

[1] N.Azzerri, *J. Appl. Electrochem.*, 6 (1976), 139

[2] V.Lakshminarayanan and S.R.Rajagopalan, *J. Electroanal. Chem.*, 215 (1986), 393

[3] V.Lakshminarayanan and S.R.Rajagopalan, *Proceedings of the 10th International Congress on Metallic Corrosion*, (1987), p.4075.

[4] J.Devay and L.Meszaros, *Acta Chim. Acad. Sci. Hung.*, 100 (1979), 183

[5] V.Lakshminarayanan, *Ph. D. Thesis* (1987)

[6] A.Poojary and S.R.Rajagopalan, *Proc. Indian Acad. Sci., (Chem. Sci.)*, 97 (1986), 437.

[7] M.C.H.McKubre and D.D.MacDonald, *Comprehensive treatise of electrochemistry*, Ed. R.E.White, J.O'M Bockris, B.E.Corway and E.Yeager, Plenum Press (1984)

[8] A.J.Bard and L.R.Faulkner, *Electrochemical Methods, Fundamentals and Applications*, John. Wiley and Sons (1980), p.573.

Table I

R_p and C_d values obtained by the small amplitude exponential relaxation technique

System	τ (mS)	R_p (Oh m.cm^2)	C_d (μF cm^{-2})
MS/0.5 M H_2SO_4	10	14.8	98.5
Armco Iron/0.5 M H_2SO_4	100	248	90.5
Cu/1M NaCl	500	348	790

Table II

Corrosion parameters obtained by the small amplitude exponential relaxation technique

System	τ (mS)	I_{corr} (mA/cm^2)	b_a (mV)	b_c (mV)
MS/0.5 M H_2SO_4	10	1.28	77	104
	log.pol	1.20	73	96
Armco Iron/0.5 M H_2SO_4	100	0.072	68	96
	log.pol	0.074	70	96
Cu/1M NaCl	500	0.063	51	-
	log.pol	0.064	55	-

Table III

Corrosion Rate and Tafel slopes for different systems by AC potential perturbation technique (values in parenthesis are steady state logarithmic polarisation values)

System	I_{corr}	b_c	b_a
MS/0.5 M H_2SO_4	1.30	95	82
	(1.30)	(93)	(83)
Armco Iron/0.5 M H_2SO_4	0.085	105	85
	(0.084)	(105)	(83)
MS/1M HCl	0.742	104	83
	(0.700)	(93)	(86)

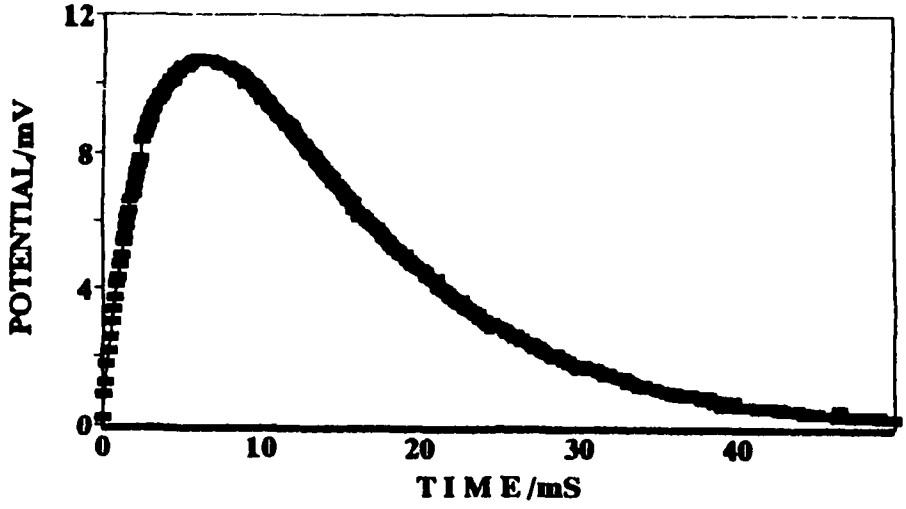

FIG 1: A typical potential response to an exponentially decaying current input.

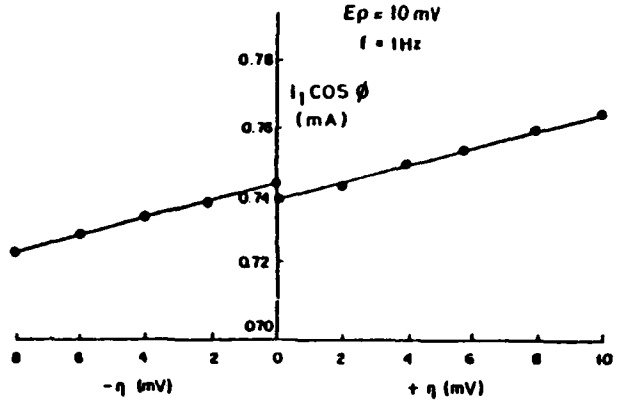

FIG 2: A plot of peak sampled first harmonic current against applied dc potential

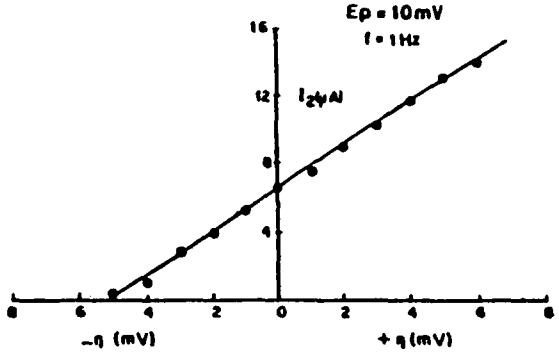

FIG 3: A Plot of second harmonic current against applied dc potential

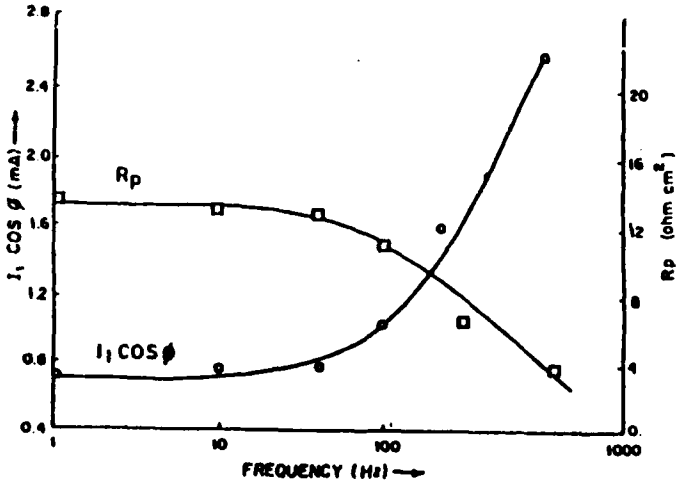

FIG 4: Variation of peak sampled first harmonic current and Polarisation resistance Rp with frequency of the applied ac potential

Rapid Evaluation of Corrosion Behavior Using Random Potential Pulse Method

Y. Sugie
Himeji Institute of Technology
2167 Shosha, Himeji, Hyogo 671-22, Japan

S. Fujii
Himeji Institute of Technology
2167 Shosha, Himeji, Hyogo 671-22, Japan

Abstract

Corrosion behavior of metallic materials could be visually recognized using FWT images. In addition, by using a pattern recognition technique, we could define the corrosion state of the steel materials.

The current density, i, obtained by the random pulse method had a good correlation with the observed polarization curve. Therefore, a relative corrosion rate can be estimated by the change in i. The random pulse test required only a few minutes, which includes data treatment. The corrosion state and rate can be determined in a short time.

Key terms: pattern recognition, pitting corrosion, intergranular corrosion, stainless steel

Introduction

Since C. Wagner and W. Traud[1)] indicated that the corrosion behavior was caused by an electrochemical reaction, an electrochemical measurement and understanding were used in corrosion studies. Moreover, accompanied by the development and improvement in electronics, many electrochemical instruments are used as essential experimental processes in the determination and prevention of corrosion. Presently, the electrochemical measurement methods applied to corrosion measurement are the polarization resistance method, which was developed by M. Stern[2)], and the potentiodynamic method to investigate the characteristics due to protection films on a steel surface. These characteristics include the repassivation potential for pitting corrosion and the EPR test for intergranular corrosion, etc. However, the monitoring of corrosion of metals and alloys is still time consuming. We proposed a new experimental method, called the

random potential pulse method, for corrosion monitoring; The electrode process is assumed to be composed of two processes, a solution process which has a dynamic characteristic due to the accumulation of material in solution, and a surface process which has a non-linear characteristic similar to the Butler's relation, etc. It should be pointed out that the metal dissolution processes non-linear characteristics are nearly static due to the absence of material accumulation along the direction normal to the surface at the metal electrode surface. The random potential pulse method was developed by Ichise et al[3]. for electrochemical analysis. The random potential pulse method features extraction due to the non-linear characteristics of the electrode process. We applied this method to the measurement of corrosion behavior, i.e., active, passive and transpassive dissolution or localized corrosion and the corrosion rate of steels in various environments.

We also tried to develop a rapid evaluation method of the degree of sensitization and observation of pitting corrosion for stainless steels.

Experimental procedure

I. Random potential pulse method

A. Materials

The materials used for this study were 13Cr steel, type 304, 304L, 316 and 316L stainless steels. The specimen's dimensions were 10 mm x 10 mm and 2mm in thickness. Table 1 lists the chemical composition of these materials. They were solution annealed at 1323 K in an argon atmosphere for 30 min and then water quenched. Specimens used for the degree of sensitization measurement were heat-treated at 923 K for 1.8~86.4 ks to provoke grain boundary sensitization. The specimen's surface was mechanically polished with 600 grit SiC paper before testing. They were then degreased in acetone, rinsed with pure water, and covered with silicon resin except for a $1cm^2$ exposed area.

B. Test Solutions

The test solutions are 0.1N H_2SO_4 for measuring corrosion behavior of 13Cr steel, the 0.5M H_2SO_4+0.01M KSCN for measuring the degree of sensitization of the type 304 and 316 steels, and 3.5 % NaCl + 0.6 % $FeCl_3$ solution for the evaluation of pitting corrosion.

C. Experimental Instruments

Figure 1 shows a schematic diagram of the instruments used for the measurements. The resolution of analog-to-digital (A/D) and digital-to-analog (D/A) converter was 12 bit. The attenuator (ATT) factor was

-20 db. A Low-pass filter (LPF) with a cutoff frequency at 30 kHz was used. The random potential pulse signal generated from the D/A was applied to a potentiostat through the ATT. The response current filtered through the LPF, and the potential was sampled using a computer, which was capable of periodic triggering and control. The data were sampled at 50 ms intervals. Figure 2 shows the electrolytic cell used to measure pitting corrosion behavior.

D. Prepararion of Random Pulse Signal

Figure 3 shows the random potential pulse waveforms used in this work. The random potential pulse signal consists of 512 continuous pulses, ranging from 0 to 7. In this signal, the combination of potential (E_0, E_1), 64 ways, appears eight times and the combination of potential (E_0, E_1, E_2), 512 ways, appears once.

E. Pretreatment of Data

The set of the sampled currents was arranged as follows. Current is a two-dimensional function of applied potential. Thus, it is expressed as $I = f(E_0, E_1)$. Figure 4 shows a set of currents pretreated; this is a matrix consisting of 8 by 8 elements. If the potential level E_0 for a sampled datum was 5 and that of E_1 was 3, the datum was then restored in the slashed part X(5, 3) in Figure 3. For one measurement, each of 64 elements of matrix X stores current eight times.

F. Feature Extraction

In order to compress the data and extract features, the fast two-dimensional Walsh transform, which is used as an image compression technique, was performed on matrix X. The random potential signals generated from the D/A converter were applied to the potentiostat. The response current was sampled by the computer.

G. Walsh Transform

The Walsh functions look like infinitely clipped Fourier functions. Fourier functions are continuous sines and cosines, while the Walsh functions are complete orthogonal square-wave functions. Calculation of the fast Walsh transform (FWT) requires only addition and subtraction, wheres calculation of the fast Fourier transform (FFT) is composed of complex multiplication, addition, and subtraction.

Figure 5 shows the two-dimensional Walsh transform waveforms (4 by 4). If the X(n,k) matrix represents the intensity of the sample over an array on N by N points, the two-dimensional Walsh transform, Y(m, l), is expressed by the following Equation (1).

$$Y(m,l) = 1/N/K\sum_{n=0}^{N-1}\sum_{k=0}^{N-1} X(n,k)W_{ml}(n,k) \qquad (1)$$

where the X(n,k) matrix represents the intensity, and the Y(m,l) matrix is the power of each image element over a sample array of N by N points. In matrix notation, the transform is expressed as Equation (2).

$$Y = [W_{nn}] \times X \qquad (2)$$

where $[W_{nn}]$ is the Walsh matrix of order N by N.

In this paper, each element in the X(n, k) matrix corresponds to the magnitude of the current. Table 2 shows the reduction of the power in each sequence band. The value of each element in the sample matrix is reduced by one- and two-dimensional FWTs, and the two-dimensional FWT is a more effective technique for the information compression than the one-dimensional FWT. Extraction of the features from the image pattern has been conducted using the two-dimensional FWT coding. The principle of information compression by FWT is based on the fact that the power of high-sequency component of an image is small compared with the power of the low-sequency component. The low-sequency components of the transformed data contain most of the fundamental image information, while the high-sequency components can be regarded as noise. By omitting the components with small power in the transformed image, the information compression can be achieved and the images can be distinguished using retention of the image details while discriminating against backgroud noise.

H. Experiment of Random Pulse Method

Table 3 lists the experimental conditions for the random pulse method. Each specimen was kept at the rest potential for 10 min. before the test began. The process of the spectra, taken by the method already described, was executed under computer control and was accomplished for a set of currents. Plots and printouts were immediately produced.

II. Measurement of Degree of Sensitization (DOS)

This is a combination of the electrochemical potentio-kinetic reactivation (EPR) method and the random potential pulse method. It is a new method for evaluation of DOS called multi-EPR (M-EPR).

A schematic illustration for the M-EPR method is shown in Figure 3. The procedure is followed according to the number shown in Figure 6 : 1) a specimen is held at this corrosion potential in a test solution for 120 s, about -400 mV vs. a Ag/AgCl reference electrode containing 4.0 N KCl as the internal solution; 2) the potential is held at -190 mV for 120 s to obtain an active dissolution current, i_a; 3) the potential is kept at 240 mV for 120 s to

passivate the specimen; and 4) the specimen is polarized by using a random potential pulse in its active region for one hundred sec. The current is sampled at 0.195 s after a random pulse is applied. During the polarization, the current is stored in an 8 by 8 current matrix which is composed of the random pulse and is saved 8 times for each component of the matrix. The DOS is evaluated with the current ratio of i_a to i_r, where i_a is the maximum current obtained by anodic electrolysis and i_r is the normalized value which is obtained by dividing the maximum component of the 8 by 8 current matrix by 8. The ratio is used as an indicator of DOS.

III. Observation of Pitting Corrosion

An observation of the corrosion state for the stable, initiation and propagation state of pitting corrosion on the steel surface was performed by appling the random potential pulse signal. Conditions for the applied potential signal are listed in Table 4.

Results and Discussion

I. Randon Potential Pulse Method

A. Corrosion behavior

Figure 7 shows the voltammogram, which should be called a random pulse voltammogram (RPVs), and its transformed images. In these transformed images, the left side is the low-sequency part and the right side is the high-sequency part. The data set was represented by a value of 100. Figure 6 shows the effect of FWT. A feature of the original sample image is visibly extracted.

Table 5 gives the characteristics of the spectra parameter in various regions. In the active region, the relative intensity of the component Y_{00} was 100 and the other component is nearly 0. In the passive and transpassive regions, that of Y_{10} instead of Y_{00} was 100. This seems to be the reason for the significant anodic current flows with a change in potential and the response of the currents to the potentials is at the same level in many cases. In the passive and transpassive region, the currents flow by formation and breakdown of the passive film. The relative intensity of component Y_{00} is around 15 in the passive region and 30 in the transpassive region, and its value is increased with current density. The specific spectra element to distinguish the passive and transpassive state was component Y_{20}. In the passive and transpassive states, these are around 0 and -10, respectively. These results show that the relation between current and potential does not clearly change in the passive state. But a difference does appear by

changing the small current response because of the breakdown of the protective film in the transpassive state.

B. Corrosion Rate

The corrosion rate was evaluated from the current density, i.e., the average value of the current matrix. Each current data element saved eight current values. The average current (i) was defined:

$$i = X_{mean}/8A \qquad (3)$$

where X_{mean} is the average value of 64 elements of matrix X, and A is the specimen's surface area.

Table 5 gives the value of current densities obtained by Equation (3).

The current densities obtained by random pulse method have a good correlation with that of polarization curve of Figure 2.

II. Evaluation of DOS

Figure 8 shows the voltammograms and contour maps obtained using the M-EPR method for Type 304 and 316 stainless steels with various heat treatments. The ordinate in this map is current and the maximum element of the current matrix is 100. Different sensitizing times produces different voltammograms. The voltammograms of Type 304 with and without sensitization are a dome shaped. These shapes have no relation to sensitizing time. The magnitude of the current is increased with sensitizing time. For Type 316, the non-treated specimen has a shad roof shape voltammogram. Its shape changed to a gable roof shape with treatment time. The specimen surface appeared to have an etch pit or continuous pit along the grain boundary in which the voltammogram was gable roof shaped. The specimen seems to be susceptible to intergranular corrosion. On the other hand, the specimen with a shad roof shape was due to general corrosion and did not have a susceptibility to intergranular corrosion.

Figure 9 shows the correlation between the reactivation ratio for EPR tests and that of M-EPR measurements. On both tests, reactivation ratios increased with sensitization time. The coefficient of correlation to both tests was 0.986. Reproducibility of the M-EPR tests was investigated using the sensitized specimen at 923 K for 28.8 ks. This result is shown in Table 6 The data obtained from the EPR tests had a similar coefficient of variation to those from the M-EPR tests.

From the above results, it is concluded that the M-EPR test is applicable as a rapid test to detect the DOS of Type 304 and 316 stainless steels.

III. Observation of Pitting Corrosion

A. Three dimensional voltammograms

Three dimensional voltammograms for various corrosion states is shown

in Figures 10a~10d. For the passive state in Figure 10a, the potential of the E_1 array is linearly increased with each increment of E_1. The current density varied between -0.25 and 0.25 $nAcm^{-2}$ at 121 mV as the center potential of the pulse signals. But the slope ($\Delta i/\Delta E$) of the voltammogram plane did not change and its value was 5/7 x $10^{-5}\Omega^{-1}$ cm^{-1}. Therefore, the passive film that formed on the steel surface seems to be stable due to its generally flat plateau in the voltammogram. For the repassive state in Figure 10b, the voltammogram showed almost the same shape as the passive state, but variation in the current density was two times larger than that of the passive state. The voltammogram plane showed distortion because the film formed by repassivation did not have a higher resistivity than the film formed by passive treatment. For the propagation state in Figure 10c, the current density is linearly increased with each increment of E_1 but does not change to the values of E_0. The voltammogram in the propagation state is not affected by the past potential E_0 but is affected by the present potential E_1. For the initiation state in Figure 10d, the current response and potential change has a non-linear relationship to each other during the initiation state. The past and present potential has a complicated influence on the current response. The anodic current from pit initiation and cathodic current from repassivation flow complicates the reaction system. The voltammogram resembles a wavy form and is almost susceptible to the influence of the outer environment because it is extremely changable due to be very shallow pit in the initiation state.

B. Calculation of polarization resistance

Polarization resistance (Rp) was calculated using the slope of E_1 in the voltammogram. The results are shown in Table 8. Rp in the pit initiation state is 100 Ωcm^2 and its value is three orders smaller than that of the passive and repassive states. From these results, Rp indicates a susceptibility to pitting corrosion.

Conclusions

The random pulse method as a rapid corrosion test method was applied to evaluate the corrosion behavior of stainless steels in corrosive environments. The results obtained are summarized as follows:

1) The corrosion states of steels could be recognized by FWT spectra Y. In the active corrosion region, the relative intensity of the Y_{00} component was 100, whereas in the passive and transpassive regions, the relative intensity of Y_{10} was 100. The corrosion state could be visually recognized from FWT

images. The random pulse test required only a few minutes which included data treatment. The corrosion state and rate can be determined in a short time.

The average current density or the corrosion rate agreed with the result of the polarization measurement.

2) The evaluation of the DOS for sensitized stainless steels.

The M-EPR test method to evaluate the DOS of types 304, 304L, 316 and 316L stainless steels has been developed. The reactivation ratio obtained by the M-EPR method was proportional to that using the EPR one, and the coefficient of correlation between the two methods was 0.986. The coefficient of variation of the M-EPR was 0.18, indicating the same degree of reproducibility as that of the EPR. The shape of the voltammogram obtained by the M-EPR changed with dissolution behavior and corrosion forms by pattern recognition.

3) The three dimensional voltammogram of pitting corrosion showed characteristic shapes depending on the corrosion state of the steel surfaces. The slope of the voltammogram and polarization resistance reflected the corrosion susceptibility of the materials. The variation in the voltammogram with time corresponds to a change in the corrosion state.

The random pulse method could be recognized as a useful tool to monitor the corrosion states and rates of the steel alloys.

References

1. C. Wagner and W. Traud, Z. Electrochem., **44** (1938): p.391.
2. M. Stern and A. Geary, J. Electrochem. Soc., **104** (1957): p. 56.
3. M. Ichise and T.Kojima,Bunseki, **4** (1988): p. 102.

Table 1. *Chemical Composition of Stainless Steels*

	Element (wt%)								
Steels	C	Si	Mn	P	S	Ni	Cr	Mo	Cu
13Cr	0.05	0.27	0.77	0.021	0.018	0.78	12.51	0.35	----
SUS304	0.066	0.58	0.82	0.029	0.002	8.75	18.29	0.14	0.14
SUS304L	0.023	0.63	0.99	0.027	0.006	9.37	18.18	----	----
SUS316	0.054	0.67	1.38	0.030	0.005	11.16	17.21	2.21	0.33
SUS316L	0.023	0.52	0.92	0.031	0.001	12.31	17.51	2.06	----

Table 2. *FWT and inverse FWT of the sample matrix*

Sample Values				One-Dimensional FWT Values			
127	127	127	127	108	0	0	0
108	110	111	102	110	1	−3	2
98	100	101	102	100	−1	0	−1
93	94	96	97	95	−2	0	−1
Two-Dimensional FWT Values				**Inverse FWT Values**			
108	0	−1	0	127	127	127	127
10	1	−1	1	108	110	111	102
4	0	1	0	98	100	101	102
6	0	1	−1	93	94	96	97

Table 3. *Experimental conditions of the random pulse method in 0.1 N H_2SO_4*

Corrosion region	Initial potential (mV vs Ag/AgCl)	Pulse period (ms)
Active	-300	25
Passive	500	25
Transpassive	900	25

Table 4. *Conditions of the applied signal.*

Maximum pulse amplitude (ΔEp)	70
Minimum pulse amplitude (ΔE)	ΔEp/7
Pulse interval (Tp)	200ms
Initial potential (Ei)	Corrosion potential

Table 5. *Charcteristics of the spectra parameters in various regions.*

Spectra parameter	Active region	Passive region	Transpassive region
Y_{00}	100	21	27
Y_{10}	5	100	100
Y_{20}	8	2	-12
Y_{01}	-85	-170	-210
Y_{02}	20	-6	21

Table 6. *Relation between the current densities obtained by the polarization curve and those by random pulse method.*

Corrosion Region	Polarization Curve ($\mu A/cm^2$)	RPV Method ($\mu A/cm^2$)
Active	290	260
Passive	1.5	1.4
Transpassive	4.2	3.9

Table 7. *Reproducibility of the reactivation ratios obtained by M-EPR and EPR test with SUS 304 sensitized at 923 K for 28.8 ks.*

	μ (%)	σ (%)	σ/μ
M-EPR	32.3	5.85	0.18
EPR	20.2	2.76	0.14

Table 8. *Polarization resisitance caluculated from random pulse voltammograms.*

States	Polarization resistance Rp(Ωcm^2)
Passive	1.4×10^5
Repassive	0.7×10^5
Pit propagation	1.4×10^2

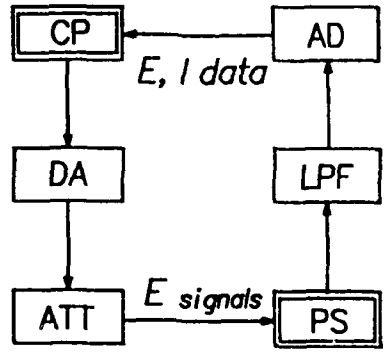

Figure 1. *Schematic diagram of the instruments for measurements. A/D : Analog-to-digital converter; ATT : Attenuator; CP : Computer; D/A : Digital-to-analog converter; LPF : Low-pass filter; PS : Potentiostat.*

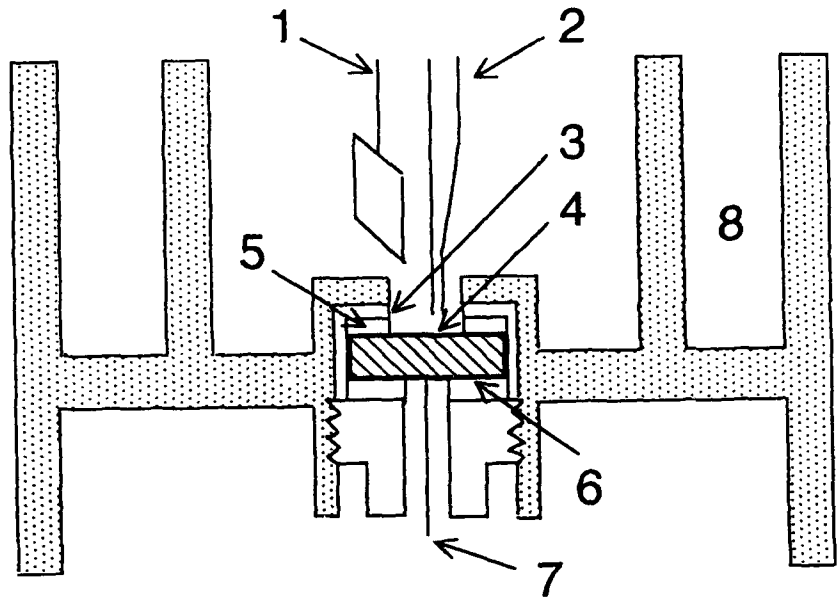

Figure 2. *Schematic illustration of electrolytic cell for pitting corrosion.*

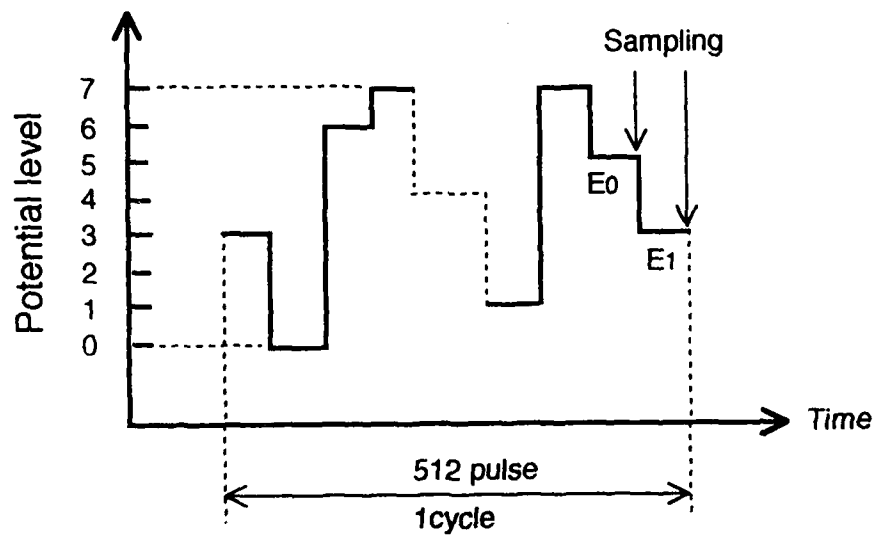

Figure 3. *Profile of the random potential pulse.*

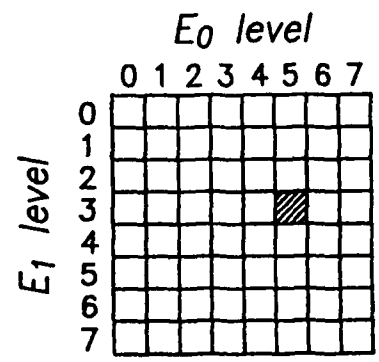

Figure 4. *Current matrix as a function of the potential, E_0 and E_1.*

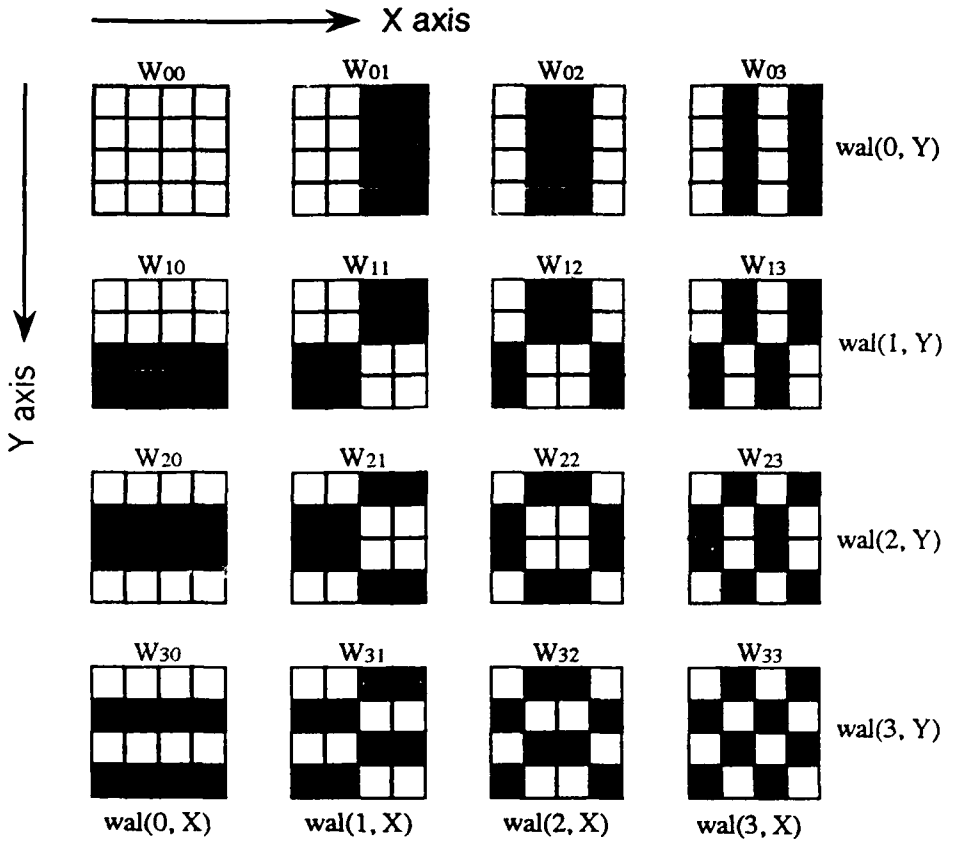

Figure 5. *Sequency-ordered two dimensional Walsh functions (4 by 4).*

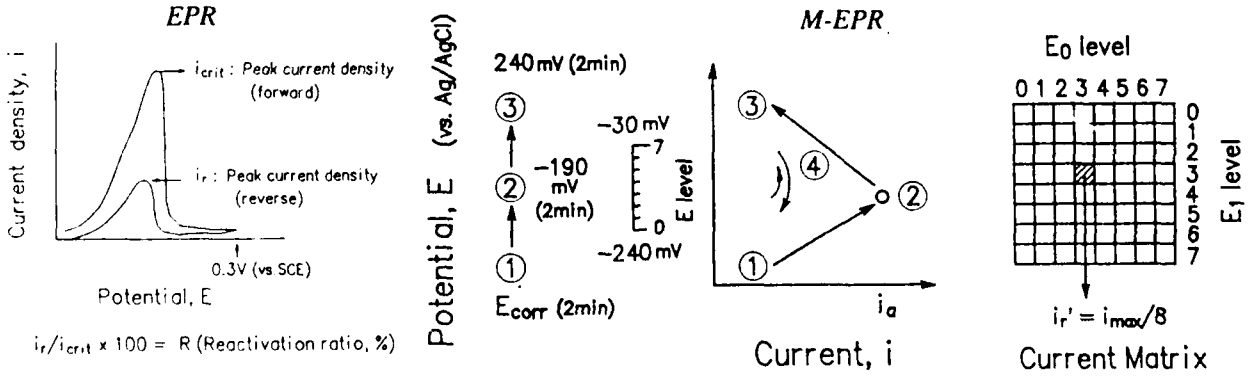

Figure 6. *Schematic illustration of the EPR and the M-EPR method for the degree of sensitization.*
i_a : Peak current of active dissolution; i_{max} : Maximum component of current Matrix
i_r : i_{max} / 8 (Average of i_{max}); i_r/i_a : Reactivation ratio
E_0 : Present potential; E_1 : Past potential; E_{corr} : Corrosion potential.

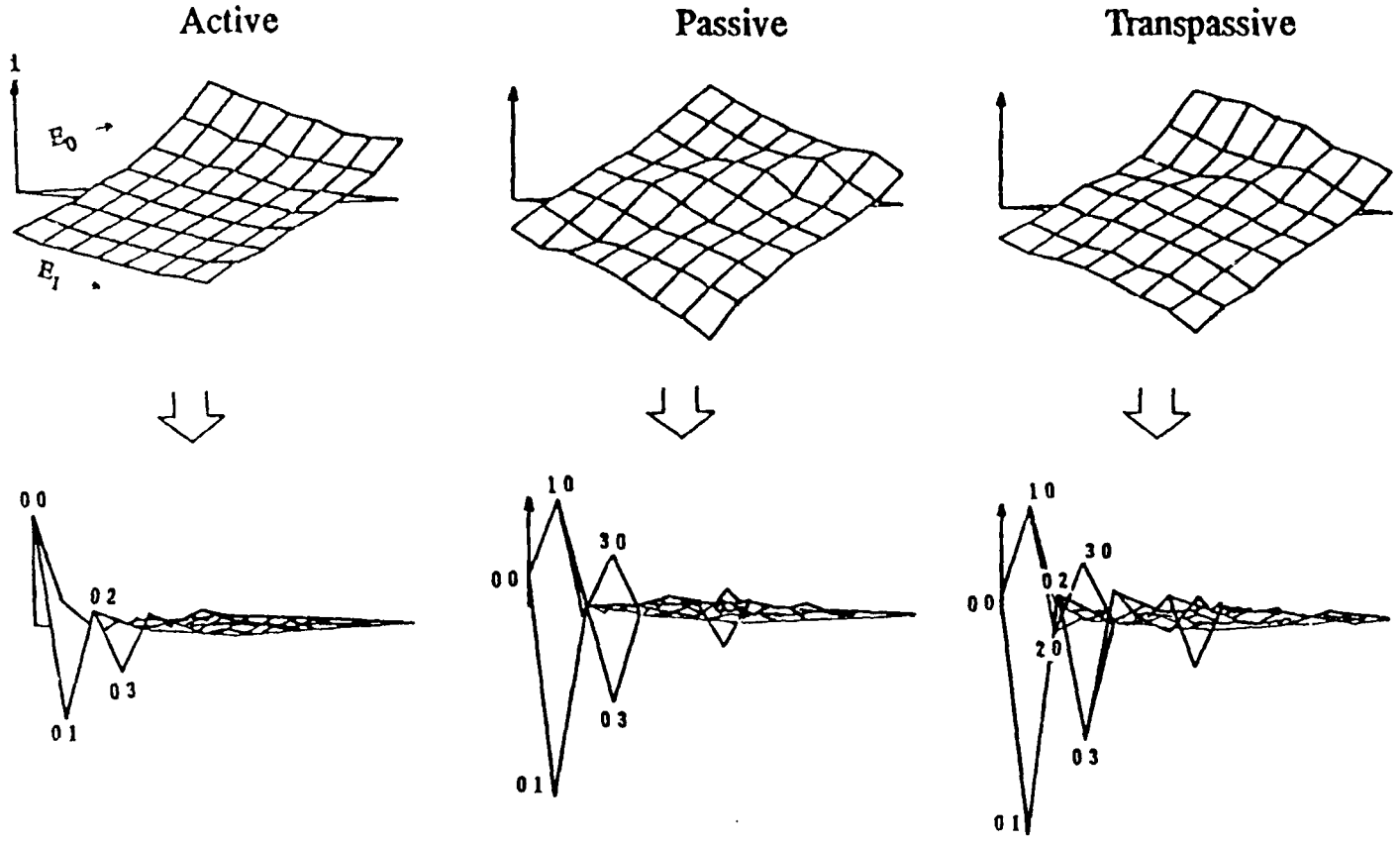

Figure 7. *Random pulse voltammograms and the Walsh transformed images.*

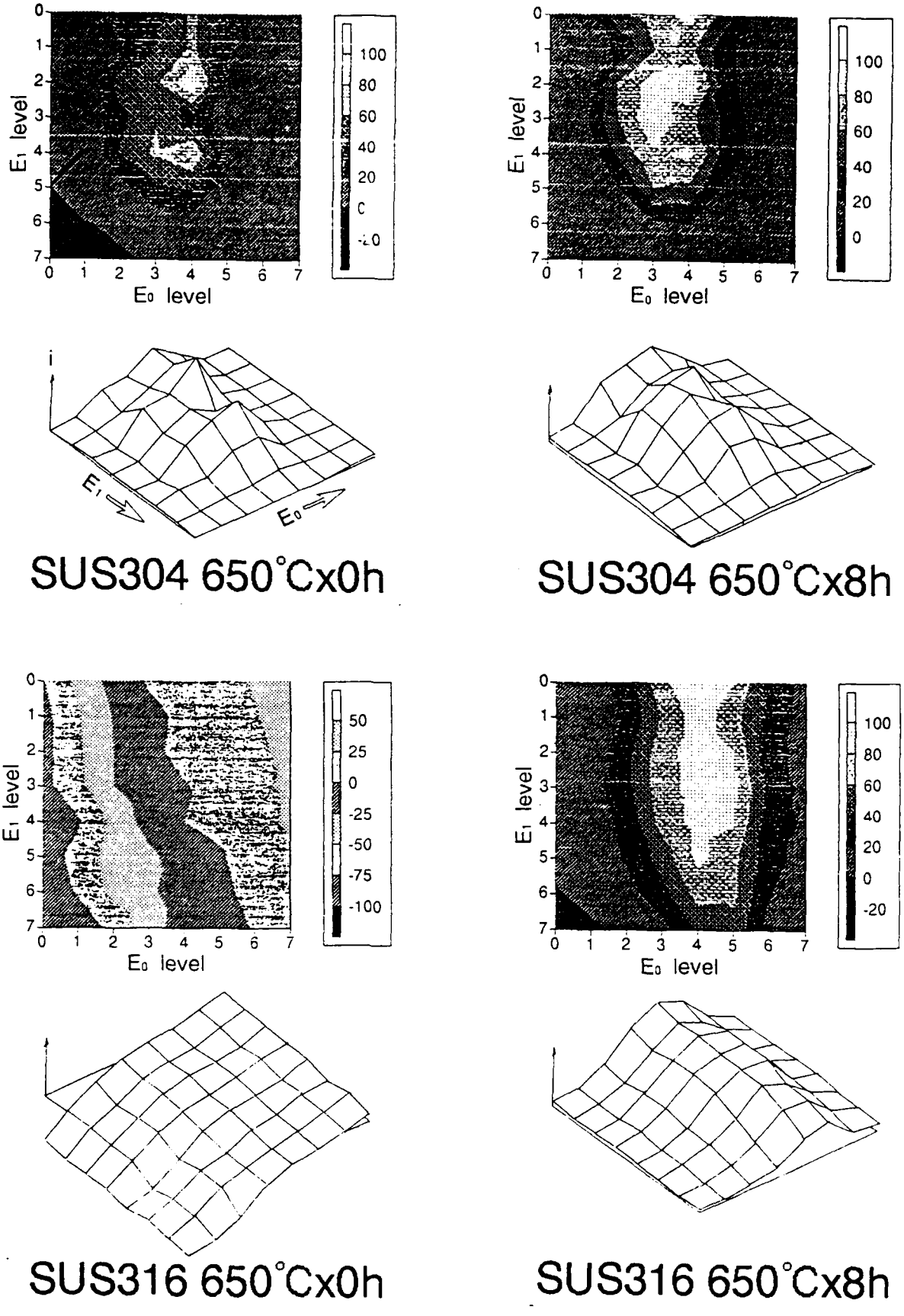

Figure 8. *Random pulse voltammogram of SUS 304 and 316 by M-EPR.*

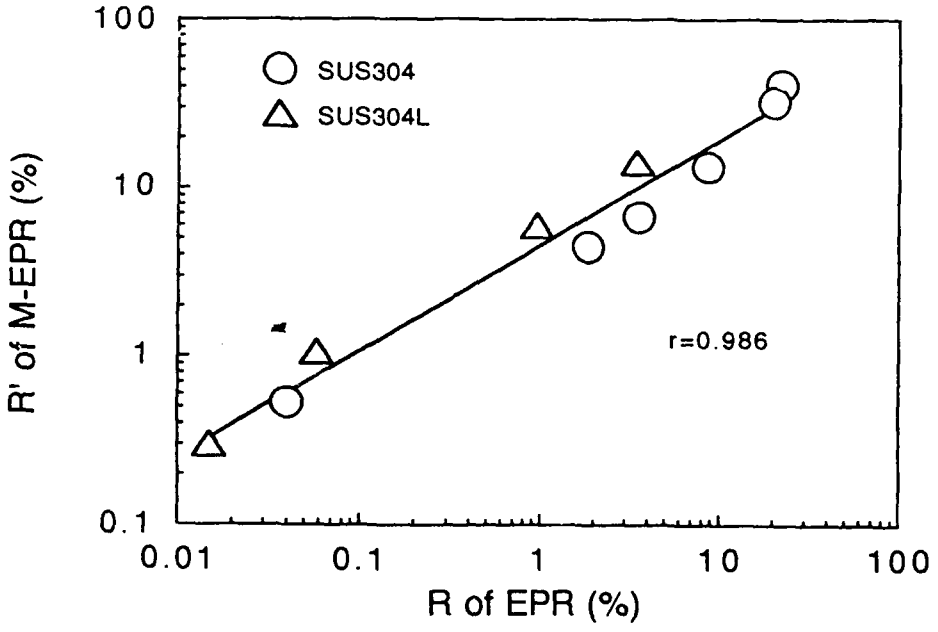

Figure 9. *Relationship between R of EPR and R' of M-EPR for SUS304 and 304L with various degree of sensitization.*

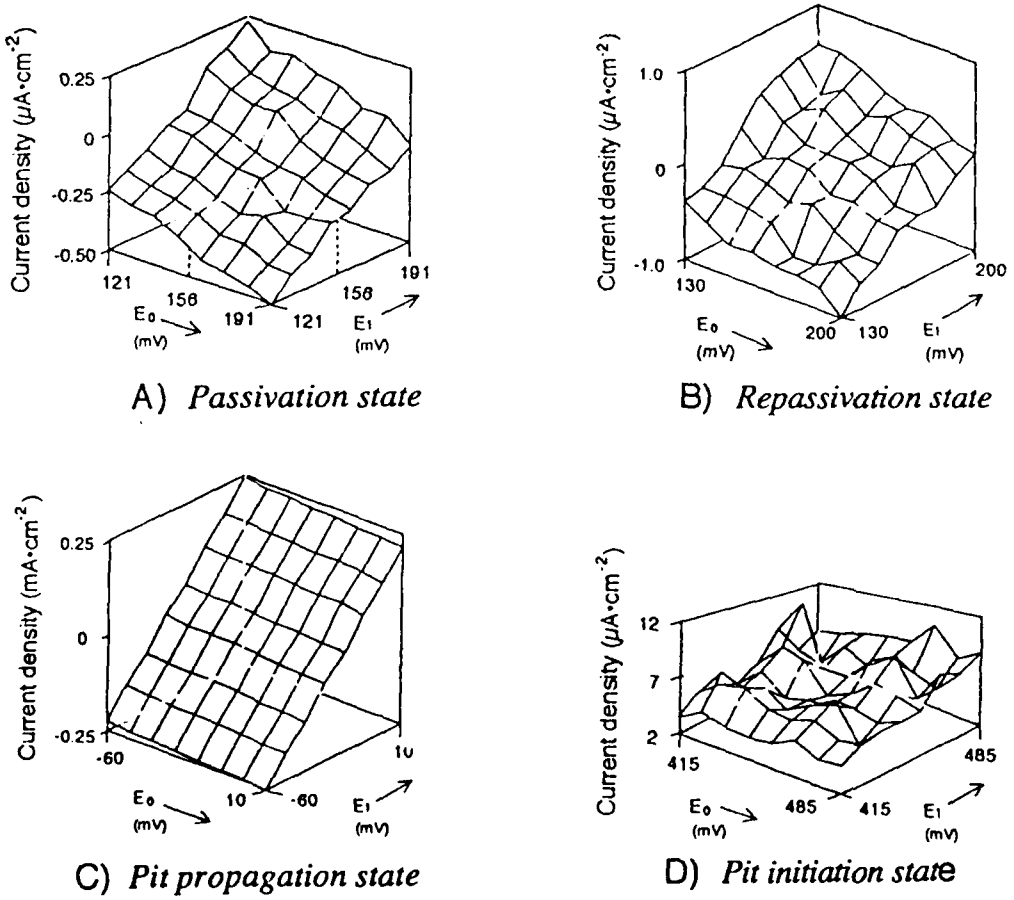

Figure 10. *Three dimensional voltammograms for pitting corrosion of SUS 304.*

Application of Modern Electronic Technique in Corrosion

Furong QIU
Fujian Institute of Research on the Structure of Matter
Chinese Academy of Sciences
PO Box 1287
Xiamen 361012, China

Abstract

Modern electronic techniques play an important role both in corrosion science and in corrosion control engineering. From the point of view of electrochemical behavior of metallic corrosion and with his own experience of practice, the author has briefly reviewed some typical applications of the technique, such as measuring, calculation, controlling and designing, including the use of microcomputers mainly in China.

Key items: corrosion, electronic technique, microcomputer

Introduction

Electrochemical corrosion is the most commom form of metallic corrosion. Based on the electrochemical nature of metallic corrosion[1] , numerous eletrochemical testing techniques have been developed since the 70's for studying the mechanism of occurrence and development on corrosion, in which the modern electronic techniques play an important role for laboratory investigations and industrial engineering. The technique is helpful in the case of materials selection, inhibitor evaluation, assessment of surface treatments, and controlling and monitoring of cathodic protection. Since the 80's, microcomputers have become more widely and commonly used. Because the advantages of microcomputer in low cost, high performance, multifunctions, and ease of use, it is now a necessary part of routine work in data acquisition, calculation, modeling, controlling, monitoring and managing[2].

It is well recognized that morden electronic techniques are an extremely powerful tool for raising efficiency, improving accuracy, saving time, minimizing human labor, and collection data and information.

In this paper, the author has outlined some applications of electronics in corrosion mentioned in the previous papers[1,2] and emphasized the application of microcomputer in Mainland China, including his own practice in this field.

Typical Applications

1. Measuring

For use in the laboratory, potentiostats, logarithm to linear convertors and impedance convertors, galvanic corrosion (zero resistace) current meters, and linear polarization resistance measurement system were developed with transistors first and then with integrated circuits and silicon controlled rectifiers in the 70's.

Since the 80's, microprocessors and microcomputers, such as TRS-80, Apple II plus, DJS-033, Macintosh, and IBM PC, have been employed to set up corrosion measurement systems and eletrochemical AC impedance measurement systems.

For example, Zhou Xiandong et al.[3], established an apparatus controlled by microcomputer for measuring potential distribution on metal surfaces immersed in an electrolyte. It is very useful for measuring the electrochemical inhomogenities on metal surfaces and for monitoring localized corrosion. Almost at the same time, Shi Xiaoyen et al.[4] used a similar system to investigate the electrochemical behavior of low alloy steels in chloride solutions.

2. Calculation

In general, from the data of weight loss of coupons, resistance increment of a resistance probe, solved quantities of metallic ions, or one or more of electrochemical parameters determined, the corrosion rate can be calculated by means of microcomputer and automatically tabulated and plotted according to units or forms required by users.

Ellipsometer is of useful tools for surface science with high sensitivity, the feature that it can be used in in-situ measurements, and much lower price than other modern spectroscopes. But it is necessary to use a computer to obtain an experimental result by calculation the experimental data with series complex equations. In 1980, the author and his colleagues began using microcomputer to perform the calculations[5]. They transferred mathematically the equations, developed an ellipsometic software using BASIC to calculate the theoretical curves for surface films on metals both nonabsorbent and absorbent. Examples were given for 304 stainless steel in HCl solutions. Fitting the values of Δ and ψ gathered from experiments on the theoretical curves, the optical constants and thickness of the film can be obtained. They indicate the growth dynamics of surface film and, furthermore, explain the passivity of metals.

3. Designing

In corrosion control engineering, the current distribution of cathodic protection system in internal surface of pipeline as well as in sea water must to be designed carefully before installation.

Guo Rungsheng et al.[6] reported a design method for sacrificial anode cathodic protection system of plate pile piers. By means of execution a software namely Chinese SuperCalc on an IBM PC computer, the service life of anodes can be calculated exactly and verified.

4. Controlling

Nowadays, potentiostats and rectifiers are widely applied to protect underground pipelines, ships, and docks in coastal area from corrosion in Mainland China. Most of the potentiostats for industry have the performance of output current limiting, over or under protection alarm, potential indication, and automatic operation. Some of them have AC interference resistant unit, lightning draining unit and other special units such as data recording and printing units.

Yang Jinwei et al.[7] developed a computerized cathodic protection system for multi-anode control. In this system, each anode is driven by its own DC power module, the output of which is controlled independently. During the interval between the successive control of the same anode channel, the computer can control over other anode channels. Laboratory tests have verified these considerations through computerized 103 channel control system.

The author and his colleagues recently have developed a multi-function power apparatus for cathodic protection of steel reinforced concrete structures in marine enviroments, in which the operating mode in terms of constant potential, constant current and constant voltage can be selected individually and the IR drop due to the high resistivity of concrete can be eliminated during actual protection potential measuring[8].

5. Inspection

Electronic techniques have begun to be used in ocean engineering since the 80's in China. Fu Chuao et al. developed a cathodic protection status detector for inspection of offshore platforms[9]. This computerized apparatus can be used to indicate the protection level, full protected or over/under protected at the critical zone such as underwater nodes of steel jackets.

Xu Bin et al.[10] set up a remote potential survey instrument for subsea pipelines.

A cathodic protection monitoring system has been serving on HZ26-1 platform over a year in the South China Sea.

6. Management and Data Base

Recently, a 240 channel cathodic protection data system has been installed in a nuclear power plant. The system displays in Chinese and prints out the managing parameters of 8 potentiostats, for instances, reference potentials, protection current, and anodic voltage, with a total of 96 channels. In addition, the microcomputer controls the power switch of the printer such that the power will not be turned on until start of printing, resulting in prolonged the service life of the printer[2].

Li Hongxi et al established an Atmospheric Corrosion Data Base using dBASE III with microcomputer[11]. Afterwards, the atmospheric corrosion map of Shenyang area was completed.

Summary

As briefly reviewed above, modern electronic techniques have been gradually and widely applied in corrosion research and corrosion engineering in China. It is hoped that more reliable electronic instruments will be made to meet the needs in laboratory and in industrial corrosion monitoring and control.

References

[1] QIU Furong, Electronic Technique(in Chinese), 17 9 (1990): p. 10.

[2] QIU Furong, Application of Microcomputers in Corrosion, to be published.

[3] ZHOU Xiandong, LIN Chanjian and TIAN Zhaowu, Journal of Chinese Society of Corrosion and Protection(in Chinese), 5 4 (1985): p. 283.

[4] SHI Xiaoyen, XU Shili, XU Chuanbi, CAI Changshou and QIU Furong, Corrosion and Protection(in Chinese), 12 1(1991): p. 10.

[5] QIU Furong, LIU Zhiping and DING Xuedi, Journal of Chinese Society of Corrosion and Protection(in Chinese), 2 2 (1982): p. 48.

[6] GUO Rungsheng, CHEN Guangzhang, CHEN Renxin and ZHU Xiaoxin, Corrosion and Corrosion Control for Offshore and Marine Construction, (Oxford, U.K.:Pergamon Press, 1988), p. 357.

[7] YANG Jinwei, XU Naixin and ZHANG Chengdian, Journal of Chinese Society of Corrosion and Protection(in Chinese), 10 3 (1990): p. 216.

[8] QIU Furong, YOU Qingqian, KE Chaozong, ZHUANG Changqi, ZHENG Zhongli and ZHOU Shaoying, Corrosion Science and Protection Tecnology(in Chinese), in press.

[9] FU Chao et al., Materials Protection(in Chinese), 25 12 (1992): p.13.

[10] XU Bin et al., Ocean Science, 2 3 (1990): p. 48.

[11] LI Hongxi, ZHANG Shuqin and LIU Shourong, Corrosion Science and Protection Technique(in Chinese), 4 3 (1992): p. 200.

Improvement of Mansfeld's Method for Computing Electrochemical Parameters from Polarization Data

Gabriele Rocchini
ENEL – Thermal and Nuclear Research Center
Via Rubattino 54, 20134 Milan, Italy

Abstract

A theory aimed at improving the Mansfeld's method through the introduction of a convergence criterion and giving an objective significance to the determination of the Tafel slopes has been developed. Examination of some theoretical curves has shown that the convergence of the actual method depends on the corrosion current density, for when the value of I_c is lower than a given bound a decrease can be observed in the convergence radius. This difficulty, which requires a suitable choice of the initial values of B_a and B_c, can be overcome by multiplying the function $i(\Delta E)$ by an appropriate factor. It is also proven that the evaluation of B_a and B_c depends on the choice of the scheme adopted to compute the polarization resistance. The analysis of some experimental curves concerning the behaviour of iron in H_2SO_4 and HCl solutions at different temperatures was performed using their analytical representation with a polynomial of the fourth degree. The best-fitting, which faithfully represented the experimental data over the ΔE interval $[-50, 50]$ mV, was used also for the computation of R_p. This procedure has shown that, independently of the choice of the initial values and of any graphic comparison, the method proposed provides correct information when I_c is greater than about 0.140 $mAcm^{-2}$. The method, however, may not be effective when I_c is less than 0.140 $mAcm^{-2}$. In the last cases the numerical sequences used for the computation of B_a and B_c may have an oscillating behaviour, even if the experimental values of $i(\Delta E)$ are multiplied by a constant.

Key terms: corrosion monitoring, Tafel slopes, mathematical models, numerical methods.

Introduction

Besides a rigorous control of the solution chemistry and of the preparation of the specimen surface, ensuring reproducibility of the polarization curves, the study of the kinetics of a corrosion process requires, in general, a careful choice of the electrochemical technique and the mathematical method to be used for the analysis of the experimental data. Our experience concerning the behaviour of iron in inhibited and uninhibited acid solutions[1–4] has shown that the choice of the technique to be used for performing the polarization curves is determinant when the aim of the study is to obtain a reliable representation of the dissolution kinetics.

Experimental results show, in fact, as can be seen, for instance, in Ref. 5, that the direct (I_g) and the electrochemical (I_e) determinations of the corrosion current density for iron in 0.5 m H_2SO_4 solutions containing n-decylamine usually differ and exhibit a random scattering around the straight line $I_e = I_g$. Moreover, the data of Ref. 4 show that potentiodynamic curves are liable to yield greater discrepancies if the potential sweep rate is not selected properly.

Besides simplifying processing procedures and allowing an accurate check to be made on the validity of the analytic model, the availability of numerical methods for computing the corrosion current density and the Tafel slopes permits the optimization of measurements and does not compel one to polarize the system under investigation irreversibly.

This is very important, for instance, when the corrosion rate is monitored using direct determinations of the corrosion current density by means of polarization curves carried out at periodical intervals[1]. In this case the system should not be excessively perturbed so that, at the end of each single measurement, it can revert to its free corrosion state in a comparatively

short time. The quick recovery of the free corrosion state is an essential condition for studying the free evolution of a process.

The graphic analysis of a corrosion process requires that the response of the system be examined over such a potential interval that will reveal the presence of the Tafel straight lines. The widths of the anodic and cathodic intervals can, however, be reduced if use is made of the method of successive approximations introduced by Rocchini[6]. The main advantage of this numerical technique is that it eliminates any arbitrariness in the choice of the anodic and cathodic zones where the Tafel law is thought to be valid.

The problem of the numerical analysis of polarization curves has gained further importance with the development and introduction of some computerized systems in the field of corrosion. In fact, this approach allows more accurate measurements to be made and permits the production and storage of a great number of experimental data. Once the polarization curve has been performed, a key point is the possibility of processing the data with a prefixed model without having to check the geometrical shape of the polarization curves.

The CORFIT method[7], which was proposed by Mansfeld soon after the introduction of Barnartt's three-point method[8], is the first attempt to analyze an experimental polarization curve by a non-linear global technique using the Tafel slopes as unknown parameters. However, some preliminary applications of this technique performed in our laboratory revealed the existence of convergence and reliability problems.

Yet, after the introduction of the analysis method described in Ref. 9 and based on the use of two parameters, it was decided to examine Mansfeld's method more closely and endow it with a convergence criterion while evaluating the influence of the polarization resistance[10] on the computation of the electrochemical parameters. This approach differs from Jensen and Britz's view[11] because its aim is not to compare the different methods quoted in the literature or to classify them according to their success in analyzing a polarization curve generated numerically by a fixed procedure.

General Considerations

The basic advantage of a numerical method is the simplicity of its formulation because it permits the introduction of a small number of unknowns. The simplicity of the schematization also helps to assign a precise physical significance to the parameters to be determined and makes their calculation more reliable. The effectiveness of the application, therefore, depends on the physicochemical characteristics of the system under investigation.

In other words, it is not fair to speak of the failure of a method if this is used taking no account of the conditions the response of a real system must satisfy. This applies particularly to problems of the kind mentioned in Ref. 11 for which a preliminary check on the geometrical shape of the curve is advisable in order to determine the validity of the Tafel law.

In the present study, whose principal aim is an improvement of Mansfeld's method[7], the mathematical treatments are based, for simplicity, on the current–voltage characteristic

$$i(\Delta E) = I_c[\exp(\alpha\Delta E) - \exp(-\beta\Delta E)], \qquad (1)$$

where I_c denotes the corrosion current density and ΔE is the potential difference with respect to the mixed potential E_m. The quantities α and β are linked to the anodic (B_a) and cathodic (B_c) Tafel slopes by the relationships: $B_a = \alpha^{-1} \ln 10$ and $B_c = \beta^{-1} \ln 10$. This remark is important because it underlines that the quantities α and β must always take positive values.

In the corrosion field the law (1) describes the behaviour of systems containing only two elementary processes controlled by the activation energy. In particular, to this class belong the systems that are constituted by a metal and an inhibited or uninhibited acid solution.

It should also be noted that the geometrical shape of an experimental polarization curve may be subject to considerable distortions unless the contribution of the ohmic drop to the electrode potential is eliminated or reduced. Our experience has shown that the numerical analysis of

an experimental polarization curve containing the ohmic drop contribution generally provides wrong information[12]. Hence the effect of the ohmic drop should be carefully evaluated and removed before any numerical method is applied.

The function (1) depends on the three parameters I_c, α and β. Its reduction to two parameters was obtained by Mansfeld by introducing the polarization resistance, which, according to Bonhoeffer and Jena's definition[13], is given by

$$R_p = \frac{1}{i'(0)} \equiv \frac{1}{I_c(\alpha + \beta)} . \tag{2}$$

From equation (2), the kinetic law (1) becomes

$$i(\Delta E) = \frac{1}{R_p(\alpha + \beta)}[\exp(\alpha \Delta E) - \exp(-\beta \Delta E)] \equiv F(\Delta E, \alpha, \beta) . \tag{3}$$

The mathematical validity of this form of the current–voltage characteristic is unquestionable, as it is based on the definition of R_p. This point, as will be seen further on, is of considerable importance for a correct analysis of the experimental data.

Definition of the problem

The present mathematical treatment of Mansfeld's method follows the scheme used in Ref. 9, both formulations being based on the use of a two–parameter model. But the two sets of two non–linear equations markedly differ because of the different choice of the relationship that links I_c to α and β and permits the number of unknowns to be reduced. It needs stressing that the choice of a given scheme may imply the introduction of particular conditions that must be satisfied in order to define the analytic form of the resolving equations. In the case of the technique proposed in Ref. 9, for example, to compute the partial derivatives a distinction must be made between the anodic and the cathodic zones.

The choice of the analytic relationship between the quantities I_c, α and β is fairly important because it entails some implications on the technique adopted for performing the polarization curves. Mansfeld's method, in fact, requires an accurate evaluation of R_p, while the numerical technique proposed by Rocchini[9] does not impose this condition.

Denoting by $(\Delta E_n, i_n)$ $(n = 1, ...M)$ the M pairs of experimental points available, the values of α and β are determined by searching for the minimum of the distance $G(\alpha, \beta)$ defined by the expression

$$G(\alpha, \beta) = \frac{1}{2} \sum_{n=1}^{M} [i_n - F(\Delta E_n, \alpha, \beta)]^2 . \tag{4}$$

With reference to a previous study[9] and setting, for simplicity, $F_n = F(\Delta E_n, \alpha, \beta)$, the stationary value of the function $G(\alpha, \beta)$ is determined by searching for the roots of the set of non–linear equations

$$\begin{aligned} \frac{\partial G}{\partial \alpha} &= -\sum_{n=1}^{M} (i_n - F_n) \frac{\partial F_n}{\partial \alpha} = 0 \\ \\ \frac{\partial G}{\partial \beta} &= -\sum_{n=1}^{M} (i_n - F_n) \frac{\partial F_n}{\partial \beta} = 0 . \end{aligned} \tag{5}$$

The set of equations (5) clearly shows that the present approach is completely different from Mansfeld's original method and that the only approximation introduced concerns the determinations of its roots, which will be determined using the method of successive approximations[14].

To stress the difference in the formulation and provide some basic elements for the solution of the problem it may be useful to recall that the two partial derivatives $\partial F_n/\partial\alpha$ and $\partial F_n/\partial\beta$ are given by

$$\frac{\partial F_n}{\partial\alpha} = \frac{\Delta E_n(\alpha+\beta)\exp(\alpha\Delta E_n) - \exp(\alpha\Delta E_n) + \exp(-\beta\Delta E_n)}{R_p(\alpha+\beta)^2} \tag{6}$$

and

$$\frac{\partial F_n}{\partial\beta} = \frac{\Delta E_n(\alpha+\beta)\exp(-\beta\Delta E_n) - \exp(\alpha\Delta E_n) + \exp(-\beta\Delta E_n)}{R_p(\alpha+\beta)^2} . \tag{7}$$

Furthermore, this scheme, though providing a correct formulation, does not introduce any complexities and requires only some attention in computing the partial derivatives of higher order.

In fact, the solution of the set of equations (5), based on the method of successive approximations, necessitates a knowledge of the analytical expressions of the partial derivatives $\partial^2 G/\partial\alpha^2$, $\partial^2 G/\partial\beta^2$ and $\partial^2 G/\partial\alpha\partial\beta$, which are given by

$$\frac{\partial^2 G}{\partial\alpha^2} = \sum_{n=1}^{M}\left(\frac{\partial F_n}{\partial\alpha}\right)^2 - \sum_{n=1}^{M}(i_n - F_n)\frac{\partial^2 F_n}{\partial\alpha^2} , \tag{8}$$

$$\frac{\partial^2 G}{\partial\beta^2} = \sum_{n=1}^{M}\left(\frac{\partial F_n}{\partial\beta}\right)^2 - \sum_{n=1}^{M}(i_n - F_n)\frac{\partial^2 F_n}{\partial\beta^2} \tag{9}$$

and

$$\frac{\partial^2 G}{\partial\alpha\partial\beta} = \sum_{n=1}^{M}\frac{\partial F_n}{\partial\alpha}\frac{\partial F_n}{\partial\beta} - \sum_{n=1}^{M}(i_n - F_n)\frac{\partial^2 F_n}{\partial\alpha\partial\beta} . \tag{10}$$

Setting $V_1 = \partial G/\partial\alpha$, $V_2 = \partial G/\partial\beta$, $a_{11} = \partial^2 G/\partial\alpha^2$, $a_{12} = a_{21} = \partial^2 G/\partial\alpha\partial\beta$ and $a_{22} = \partial^2 G/\partial\beta^2$ and denoting by D the determinant of the 2×2 matrix $\|a_{pq}\|$, which is assumed to be different from zero, we can define the two numerical sequences α_n and β_n by means of the recurrence relations

$$\alpha_n = \alpha_{(n-1)} - \frac{a_{22}V_1 - a_{12}V_2}{D} \tag{11}$$

and

$$\beta_n = \beta_{(n-1)} - \frac{a_{11}V_2 - a_{12}V_1}{D} . \tag{12}$$

The two numerical sequences α_n and β_n are convergent[14] if the initial values of α and β are selected in the appropriate way. The limits for n tending to infinity of the sequences (11) and (12) give the roots of the set of equations (5).

Numerical Applications

The validity of the actual method has been verified considering some ideal cases. This is because the central problem concerns the verification of the convergence of the numerical sequences (11) and (12). Validation through the examination of ideal situations has the advantage of determining the limits of a method and can give a precise idea of its reliability when the method is applied to real cases.

Based on these considerations and on the fact that the applications of the method described in Ref. 9 had given rise to no particular problems, it was decided to determine whether the introduction of the polarization resistance entailed any restrictions or required particular precautions.

The results that will be discussed were obtained developing a suitable program, written in *basic* for IBM compatible computers and based on the use of single precision. The thirty points of the polarization curves, referring to the interval $[-73, 72]$ mV, were generated at steps of 5 mV. The values of the polarization resistance were determined using the formula (2).

The problem of convergence was tackled considering a wide variety of cases with different values for I_c, B_a and B_c, so as to ascertain if the choice of the initial values of the Tafel slopes was a critical element, if there were particular conditions to be satisfied in applying this technique and if the possible limitations could be easily singled out. This approach is a valid aid for the choice of the electrochemical systems, whose kinetics can be successfully determined through the use of the present method.

Table 1, which, for simplicity, gives the values of B_{an} and B_{cn} with three decimal digits, illustrates a case of verification of the convergence of the sequences α_n and β_n considering the function (1) with $I_c = 0.3$ mAcm^{-2}, $B_a = 70$ mV and $B_c = 135$ mV ($R_p = 66.733\ \Omega\text{cm}^2$) and using $B_a = 30$ mV and $B_c = 60$ mV as initial values.

Examination of this table shows that the convergence rapidity of the sequences B_{an} and B_{cn} is fairly high and is comparable to that obtained using Rocchini's method[9]. The attainment of the true values of B_a and B_c after eleven iterations does not concern only the case under discussion but represents a very general result confirmed by many other examples.

The result obtained shows that the intent of introducing the convergence criterion into Mansfeld's method has been achieved. This step is of great practical importance because it makes it possible to obtain results that are really significant. In fact, the use of the method is independent of the sensitivity of corrosion workers.

Another important observation concerns the choice of the initial values of B_a and B_c as a function of the value of I_c. In principle, it may be stated that, since these values can be selected in such a manner that they will not differ significantly from the correct values, they have no bearing on the success of the analysis or the convergence rapidity of the method. Yet it has been numerically demonstrated that there may exist situations where their choice is quite critical, determining the failure of the method.

The existence of these situations was ascertained by studying the convergence of the sequences (11) and (12) with constant values for B_a and B_c and varying I_c. With reference to the curves characterized by $B_a = 70$ mV and $B_c = 100$ mV and using 30 mV and 50 mV as initial values, it was observed that the sequences B_{an} and B_{cn} converged after approximately eleven iterations only when I_c was equal to or greater than 0.140 mAcm^{-2}. If I_c was equal to or less than 0.130 mAcm^{-2}, convergence was attained only when the initial values were fairly close to the true ones. With $I_c = 0.06$ mAcm^{-2}, for instance, convergence was very fast (after 6 iterations) if the initial values were equal to 65 mV and 95 mV or 75 mV and 105 mV, respectively.

However, the existence of a lower bound for I_c is irrelevant for the analysis of ideal curves. In fact, the quantity I_c appears as a factor, so that the reduction of the convergence radius can be obviated by multiplying the values of $i(\Delta E)$ by an appropriate constant. The presence of this phenomenon makes one reflect on the procedures that should be adopted for an accurate validation of numerical analysis methods.

This aspect, however, might be of considerable importance in the analysis of experimental curves because the region of the plane where the values of B_a and B_c fall cannot be determined a priori. It also confirms that Mansfeld's method cannot be used in a generalized way. Yet, it is not possible to assert that by multiplying the experimental current density values by a suitable constant experimental polarization curves will be analyzed successfully. This observation is supported by the fact that the reasons for the dependence of the convergence radius on I_c are not well known.

Effect of the Polarization Resistance

In developing the theory it has been stated that the formula (3) was obtained using the analytic expression of the quantity $i'(0)$. In practical cases, however, one ought to be more cautious and consider the possibility that the numerical analysis of a polarization curve may exhibit some peculiarities, i.e. the response of the system may differ from the ideal trend or the value obtained for $i'(0)$ may be only approximate.

From this standpoint, it may be interesting to examine the effect of the evaluation of R_p on the determination of the parameters α and β by considering some ideal cases. This step is not only of theoretical interest but also of great practical importance because the value of R_p depends on the scheme adopted for its computation. In fact, experience has shown that this quantity cannot be determined univocally.

The validity of this observation, although the use of the ratio $\Delta E/\Delta i$, with ΔE inside the interval $[-10, 10]$ mV, is frequent for the evaluation of R_p, has been confirmed by Rocchini[15], who has shown that there exist several computation procedures.

A method that is very accurate and does not require any graphic analysis of the experimental data is provided by the scheme based on the use of the first derivative $i'(0)$[16].

Our experience has shown that an accurate computation of $i'(0)$ can be made using the best fitting of the experimental data within the interval $[-50, 50]$ mV with the polynomial of the fourth degree

$$i(x) = Ax^4 + Bx^3 + Cx^2 + Dx \qquad (x = \Delta E)\,. \tag{13}$$

Actually, this statement is somewhat reductive because the polynomial (13), which generally represents the experimental data inside its validity interval satisfactorily, has been used also for the analysis of polarization curves[17,18].

The dependence of B_a and B_c on R_p has been investigated examining some ideal cases. Table 2 shows the results obtained for the curve described by $I_c = 0.2$ mAcm^{-2}, $B_a = 60$ mV and $B_c = 120$ mV. The values of R_p in the first column of the table were computed using the methods that are most commonly adopted in literature.

For a correct treatment of the problem of the reliability of the information obtained from experimental data it is essential to consider some hypothetical curves. In these cases, in fact, discrepancies can only be due to the presence of an approximate evaluation. This is particularly true of the case under discussion because the sequences B_{an} and B_{cn} corresponding to the different determinations of R_p are convergent.

Examination of the data in Table 2 shows that the cathodic slope B_c, which exhibits the greatest discrepancy at 77.83 Ωcm^2, is the most affected by the approximate evaluation of R_p, while B_a undergoes no significant variations.

Furthermore, the results obtained indicate a characteristic trend of B_a and B_c, whose values are higher than the real ones when the value of R_p is less than 86.86 Ωcm^2. Thus it may be stated that the Tafel slopes are decreasing functions of R_p.

A study has also been carried out holding the values of B_a and B_c constant, so as to determine whether the values in the second and third columns of Table 2 are dependent on the choice of I_c. The results have shown that the influence exerted by R_p depends exclusively on B_a and B_c.

The values of I_c differ but little from 0.2 mAcm^{-2} and the most significant discrepancy can be observed when R_p equals 90.81 Ωcm^2. In this case, however, it is not possible to define a characteristic trend.

Considerations on Experimental Application

Although the method was developed for the analysis of experimental polarization curves, this problem must be examined more closely in the light of the discussion of the preceding paragraph. Contrary to what happens with other numerical methods, for a successful examination of the experimental data by Mansfeld's method it is necessary that they satisfy a fundamental prerequisite.

This point is essential for the definition of the methodology that best suits Mansfeld's method, for polarization curves can be obtained adopting different procedures.

The fundamental point for the application of Mansfeld's method concerns the evaluation of R_p. In this respect, measurements should be carried out in such a way as to have a reasonable number of points around the mixed potential of the system. This step is important also because, as shown, for instance, by the formula (13) ($R_p = D^{-1}$), before evaluating the polarization resistance it is necessary to define the position of the mixed potential of the electrochemical system. Actually, it can be experimentally demonstrated that the mixed potential coincides with the free corrosion potential only in the case of pulse measurements if the system is polarized by applying each pulse after it has recovered its initial state.

The potentiodynamic curves performed, passing through $i(E_m) = 0$, from the anodic to the cathodic zone or vice versa determine, in general, a relative shift of the two potentials. The extent of this shift depends on the kinetics of the corrosion process, the potential or current sweep rate and the width of the potential interval.

This procedure is unavoidable because a fundamental prerequisite of all numerical methods is that the response of the system varies continuously in passing from the cathodic to the anodic zone or vice versa. Experience shows that the analysis of a polarization curve obtained by superimposition of the anodic and cathodic characteristics performed by different measurements may yield wrong indications or be quite impossible.

This point is very important when electrochemical measurements are performed using computerized systems because in this case a specific software should provide an answer satisfying the requirements mentioned above. This problem has been dealt with, for example, by Rocchini[19,20] in the case of potentiostatic and galvanodynamic measurements. In the latter case the measurements concern the determination of the polarization resistance and the problem has been solved by collecting the values of the electrode potential and the current only if the absolute value of the difference between two adjacent potential values is equal to or greater than 2 mV. In the case of polarization curves of potentiostatic type the situation could be more complicate. In fact, the values of the polarization potential should be defined by software so as to have a significant number of experimental points quite close to the mixed potential.

The value of the mixed potential can be determined using the technique of linear approximation and considering, for instance, the values of ΔE inside the interval $[-10, 10]$ mV. Our experience has shown that the computation of E_m using the linear approximation is always correct. By this procedure we can verify that the values of the mixed potential and the free corrosion potential are very close when the corrosion rate is rather high.

The quantity R_p can be correctly computed using the polynomial (13) and examining a ΔE interval of such width that will permit a faithful reproduction of the information contained in the experimental data. Under such conditions we can compute[18] the values of B_a and B_c which can be used as initial data for Mansfeld's method.

Results

The applications that will be examined concern the behaviour of pure iron in H_2SO_4 and HCl solutions at temperatures between 25 °C and 65 °C. The polarization curves, of galvanostatic pulse type, were best fitted using the polynomial of the fourth degree (13). Prior to the

best fitting, the values of the potential difference were corrected to eliminate the ohmic drop contribution from the electrode potential. The results thus obtained have shown that the polynomial (13) represents very faithfully the experimental curves for ΔE values inside the interval $[-50, 50]$ mV.

The method was applied examining the current density values, generated with the polynomial (13) at steps of 5 mV, inside the validity interval of the best fitting. The initial values of B_a and B_c were 30 mV and 60 mV, respectively, or were determined by the technique described in Ref. 18. The only influence due to the two choices of the initial values concerned the convergence rapidity. The numerical sequences converged more rapidly when the initial values of B_a and B_c were computed using the method of Ref. 18.

The achievement of this result is a clear indication of the effectiveness of the procedure adopted, for the best fitting with the polynomial (13) does not change the information contained in the experimental data. This observation is very important because, in principle, the best fitting can be performed using a polynomial of a higher degree and considering a wider ΔE interval so as to obtain more reliable evaluation of the Tafel slopes.

The results obtained with $R_p = D^{-1}$ are shown in Table 3 where, for simplicity, the electrochemical systems are denoted by different letters, any specification of their nature being considered unessential.

The examples given above provide a direct answer to the problem, posed by Jensen and Britz[11], of how to test the validity of a given numerical technique. The use of the best-fitting also provides a procedure for the correct processing of experimental data having a random distribution around the most probable curve.

Since a common feature of the electrochemical systems examined is that the values of I_c are greater than 0.140 $mAcm^{-2}$, it may be inferred that the present method works properly only when the corrosion rate exceeds that bound.

This observation is very important because, contrary to what happens with the method described in Ref. 18, the analysis of the behaviour of iron in 0.5 m H_2SO_4 solutions inhibited with n-octylamine and n-decylamine, where corrosion rates were of the order of 0.080 $mAcm^{-2}$, was not successful. This result gives further evidence of the limitations of Mansfeld's method.

Multiplying the experimental values of $i(\Delta E)$ by a constant has shown that the two numerical sequences have an oscillating behaviour, even though the oscillation is not significant. In any case, it is not possible to determine any objective values for the Tafel slopes because they depend on the number of iterations. Graphic comparison is not of great assistance in selecting the most reliable values. But there exist other numerical techniques that can be used to deal with these situations successfully.

However, the previous results may not be very significant because the oscillating behaviour could be due to the width of the ΔE interval which plays an important role in determining the goodness of the current information.

Conclusions

Examination of some analytical curves has confirmed the validity of this version of Mansfeld's method and has shown that the convergence criterion provides a correct computation of the values of B_a and B_c. Furthermore, from a mathematical standpoint the present approach renders this technique more rigorous. Thus it is correct to assert that, when the experimental data refer to a fairly wide ΔE interval, the result of their analysis gives faithful information, even if the shape of the polarization curve does not show the typical Tafel behaviour.

The dependence of B_a and B_c on the evaluation of R_p is a real problem but not a serious difficulty when electrochemical measurements do not represent the true evolution of a corrosion process. In any case, this problem can be solved using the best fitting of the experimental data with a polynomial that need not be of the fourth degree.

The effectiveness of the method is confirmed also by the examination of some experimental

situations concerning the behaviour of iron in H_2SO_4 and HCl solutions. The study of these cases, using the data obtained from the polynomial (13), has demonstrated that the choice of the initial values of B_a and B_c is not critical because it affects only the convergence rapidity. However, this observation is valid only when the polarization resistance is determined with the scheme of the first derivative.

Finally, the analysis of some polarization curves concerning iron in inhibited acid solutions has shown that the dependence of the convergence radius of the two numerical sequences on I_c may give rise to serious troubles when the inhibitor effectiveness is high. The same remark is also valid when a metal or alloy exhibits a high chemical stability.

References

1 G. Perboni and G. Rocchini, Proc. of the 6th European Symposium on Corrosion Inhibitors, (Ferrara, Italy, 1985), Vol. 1, p. 509.

2 G. Rocchini and G. Perboni, Corrosion Reviews, 8 1&2 (1988): p. 35.

3 G. Perboni and G. Rocchini, Proc. of the 11th International Corrosion Congress, (Florence, Italy: Associazione Italiana di Metallurgia, 1990), Vol. 3, p. 497.

4 A. Colombo, G. Perboni and G. Rocchini, Proc of the 9th Int. Cong. Metallic Corrosion, (Toronto, Canada: International Corrosion Council, 1984), Vol. 1, p. 443.

5 G. Perboni and G. Rocchini, Dechema Monograph, Vol. 101 (1986), p. 327.

6 G. Rocchini, CORROSION/91, paper No. 159 (Houston, TX: National Association of Corrosion Engineers, 1991).

7 F. Mansfeld, Corrosion, 29 (1973): p. 397.

8 S. Barnartt, Electrochim. Acta, 15 (1970): p. 1313.

9 G. Rocchini, Corros. Sci., Vol. 34, p. 583, 1993.

10 M. Stern and A. L. Geary, J. Electrochem. Soc., 104 (1957): p. 56.

11 M. Jensen and D. Britz, Corros. Sci., 32 (1981): p. 285.

12 G. Rocchini, Corros. Sci., in press.

13 K. Bonhoeffer and W. Jena, Z. Elektrochem., 59 (1951): p. 51.

14 B. Démidovitch and I. Maron, Éléments de Calcul Numérique, Mir Publishers, Moscow, 1979.

15 G. Rocchini, Corrosion, 44 (1988): p. 158.

16 G. Rocchini, Corrosion Reviews, 9 3-4 (1990): p. 353.

17 G. Rocchini, Corrosion, 43 (1987): p. 326.

18 G. Rocchini, CORROSION/88, paper No. 103 (Houston, TX: National Association of Corrosion Engineers, 1988).

19 G. Rocchini, Corrosion Prevention & Control, 39 (1992): p. 53.

20 G. Rocchini, CORROSION/93, paper No. 390 (Houston, TX: National Association of Corrosion Engineers, 1993).

Table 1
Convergence rapidity of the sequences B_{an}, B_{cn} and variation of I_c

Iteration No.	B_{an} (mV)	B_{cn} (mV)	I_c (mAcm^{-2})
1	33.136	54.817	0.13440
2	37.289	57.269	0.14698
3	42.541	62.855	0.16511
4	48.913	70.866	0.18833
5	55.935	81.388	0.21575
6	62.192	94.263	0.24385
7	66.212	108.369	0.26748
8	68.361	121.580	0.28477
9	69.530	130.938	0.29555
10	69.951	134.572	0.29954
11	69.999	134.995	0.29999
12	70.000	135.000	0.30000

Table 2
Dependence of B_a and B_c on R_p

R_p (Ωcm^2)	B_a (mV)	B_c (mV)	I_c (mAcm^{-2})
86.86	60.00	120.00	0.2000
85.81	60.56	122.20	0.2025
92.79	57.19	109.51	0.1900
84.81	61.12	124.43	0.1947
94.30	56.55	107.27	0.1800
90.81	58.06	112.67	0.1723
82.51	62.50	130.09	0.1820
77.83	65.75	144.46	0.2060

Table 3
Application of the method to experimental polarization curves

System	B_a (mV)	B_c (mV)	I_c (mAcm^{-2})	R_p (Ωcm^2)
H	89.77	90.79	0.2272	86.27
I	106.59	103.95	4.1502	5.51
L	94.68	87.11	0.8205	24.01
M	92.66	85.69	0.2344	82.47
N	114.03	76.66	26.3187	0.77
O	77.17	90.83	0.4272	42.41
P	85.05	87.06	0.2819	66.29
Q	87.61	87.46	0.1763	107.80
R	90.67	85.53	1.3415	14.25

Assessment of Corrosion of Laser Surface Alloyed Aluminum and Steel by Electrochemical Techniques

R. Li
Department of Chemical Engineering
Instituto Superior Técnico
1096 Lisboa Codex, Portugal

M. G. S. Ferreira
Department of Chemical Engineering
Instituto Superior Técnico
1096 Lisboa Codex, Portugal

A. Almeida
Department of Materials Engineering
Instituto Superior Técnico
1096 Lisboa Codex, Portugal

R.Vilar
Department of Materials Engineering
Instituto Superior Técnico
1096 Lisboa Codex, Portugal

K. G. Watkins
Dept. of Materials Science and Engineering
University of Liverpool
Liverpool L69 3BX, U. K.

W. M. Steen
Department of Mechanical Engineering
University of Liverpool
Liverpool L69 3BX, U. K.

Abstract

Laser surface treatment of metallic materials modifies the corrosion properties of the materials by alteration of the microstructure and/or composition of the surface layers of the materials. In the present paper, the corrosion properties of laser surface alloyed 7175-T7351 aluminum alloy with Cr. and St37 low carbon steel alloyed with Ni, Cr and Mo have been investigated, respectively, by d. c. and a. c. electrochemical techniques. Laser surface alloying of 7175-T7351 with Cr improves the pitting corrosion resistance of the alloy, the effect being more pronounced with increase of the Cr content in the laser alloyed layer (especially that dissolved in α-Al phase). Surface alloying of St37 with Ni, Cr and Mo produces a stainless steel with a passive behavior comparable to that of conventional stainless steels.

Key terms: laser surface alloying, stainless aluminum, stainless steel, pitting corrosion.

Introduction

Laser surface treatment is a rapidly melting and a rapidly resolidifying process which modifies both the microstructure and composition of the surface of the substrate (laser surface alloying and laser surface cladding) or microstructure only (laser surface melting); in the first case alloying elements are added, while in the second case, the process is elemental addition free during the laser process. For the high cooling rates (10^3deg./sec. to 10^7deg./sec.) achieved during the laser surface melting ,the grains in the laser melted layer are refined, the deleterious phases are reduced and elements are redistributed, thus the corrosion properties of the materials are modified. There have been a number of studies of the effect of laser surface melting on corrosion properties of stainless steels [1,2], aluminum alloys [3,4] ,and zirconium alloy [5]. Alterating both the composition and the microstructure with alloying elements addition makes laser processing a more prospective technique. With laser surface alloying (LSA), Fe-Cr

and Fe-Ni-Cr surface alloys have been produced on carbon steel [6-8] and Al-Cr and Al-Mo surface alloys have been produced on aluminum foils [9]. In the present work, the authors try to produce chromium stainless aluminum alloys on 7175-T7351 aluminum alloy (an alloy widely used in the aircraft industry) and to produce a Fe-Ni-Cr-Mo stainless steel surface alloy on St37 low carbon steel by LSA and investigate the localized corrosion behavior of these alloys in chloride solution.

Experimental

The samples used for laser processing were 7175-T7351 aluminum alloy plates (10 cm x 5 cm x 1.2 cm). The laser used in the experiments was a CO2 laser operated at 2KW. To decrease the melting point of the alloying powder, a 75%Al +25%Cr powder mixture was used as feeding powder. A computer controlled hopper powder feeder system was used to deliver the powder to the melting pool. To obtain a more uniform composition distribution in the laser alloyed layer, after laser surface alloying, the alloyed layer was remelted with the laser beam for one sample. Samples and corresponding laser processing parameters are listed in table 1. Argon was blown over the melting pool to reduce oxidation of the samples during laser surface alloying and laser remelting.

With the same hopper powder feeder system, the mixture of Ni, Cr and Mo powder was delivered to the melting pool on the surface of St37 samples during laser irradiation, producing a Fe-Ni-Cr-Mo surface alloy with 12.00wt%Ni, 14.04wt%Cr and 0.25wt%Mo.To obtain surface alloying over an extensive area, successive laser passes were done with a track overlapping of 1/3 of their width.

The polarization plots on aluminum alloys were obtained by sweeping the potential at a rate of 30mV/min., from the corrosion potential. The solution used was deaerated 0.5M NaCl.

Impedance measurements were carried out on the steel alloys using a Solartron 1250 Frequency Response Analyser and a Solartron 1286 Electrochemical Interface. The solution used was naturally aerated 0.1M NaCl.

Results and Discussion

Laser Surface Alloyed 7175-T7351 Aluminum Alloy With Cr

With laser surface alloying, microcrystalline surface layers with different chromium contents were produced on 7175-T7351 aluminum alloy plates. Samples A-1, A-2, and A-3 contain 3.17wt%Cr, 4.97wt%Cr and 5.40wt%Cr respectively. In the surface layers there are mainly two phases: a α-Al phase forming the matrix, in which Cr, Cu, Mg and Zn are dissolved, and a $CrAl_7$ phase, in which Al, Cu, Mg and Zn are dissolved; this latter one appears as dendrites dispersed in the matrix. The chemical analysis results by EDX are listed in table 2, which shows the average composition of the alloys and the composition of the two phases present.

Figure 1 presents the anodic polarization curves for 7175-T7351 as received and laser surface alloyed 7175-T7351 samples in the deaerated 3%NaCl solution. These results indicate that laser surface alloying of 7175-T7351 with chromium improves the pitting resistance of the

alloy. The higher the chromium content in the laser alloyed layer, the higher the pitting potential is.

Figure 2a shows the crystallographic pitting corrosion morphology, which evidences the tunnel propagation of the pits in the NaCl solution, on 7175-T7351 aluminum alloy as received after anodic polarization. Figure 2b shows the pitting corrosion morphology of the A-3 sample after polarization. From the figure, it is observed that the matrix phase is the preferential site for pitting attack. The pitting starts at the matrix leaving the less corroded dendrites forming a dendrite skeleton. As the pits propagate, due to the decrease of the pH inside them, the areas of the attack spread, causing also the corrosion of the dendrites and forming larger pits as indicated by the arrows.

From the Al-Cr binary diagram, at 300°C, the solid solubility of Cr in the α-Al phase is about 0.04wt% and at 400°C, the aluminum content in the $CrAl_7$ phase is about 78.15wt% [10]. Laser surface alloying is a rapidly melting and a rapidly resolidifying process. In the resolidifying process, the solid-liquid interface moves more rapidly and entraps more solute elements than in the equilibrium solidifying process, because there is less time for the diffusion of the solute elements, thus the α-Al phase entraps more chromium and the $CrAl_7$ phase entraps more aluminum making the α-Al supersaturated with chromium and the $CrAl_7$ phase supersaturated with aluminum as shown in table 2. The α-Al phase in the laser alloyed layer contains more chromium than that does in the conventional cast alloy. The supersaturated chromium in the α-Al phase and the microcrystalline structure in the laser alloyed layer are beneficial to the pitting corrosion resistance of the alloyed layer [11-14]. According to Szklarska-Smialowska's recent work [15]on the effect of alloying elements on the pitting corrosion of aluminum alloy, the Cl^- and water can penetrate the passive film through the pre-existing defects forming a pit nuclei in the passive alloy. As the applied potential increases, more Al^{3+} ions are produced by dissolution of the bulk metal and hydrolysis of the ions reduces the pH value of the solution in the pit nuclei. When the pH is low enough, the passive film in the pit nuclei is dissolved, then stable dissolution of the bulk metal occurs, giving place to pitting propagation. When chromium is present in the aluminum alloy, the CrOOH and /or Cr_2O_3 passive film formed is less soluble in acid solution than the aluminum oxide film, so a higher potential is needed to produce enough Al^{3+} ions, that by hydrolysis increase the acidity of the solution in the pit nuclei and dissolve locally the CrOOH film formed on the alloy containing chromium. The pitting potential of the alloy is thus increased by alloying with chromium. As the $CrAl_7$ phase contains more chromium than the α-Al phase, the pitting potential of $CrAl_7$ is higher than that of α-Al, thus pits initiate at the α-Al phase and then spread out forming the dendrite skeleton patterns. The higher the chromium content in the laser alloyed layer (especially that dissolved in the α-Al phase), the easier is the formation of a CrOOH film, so the pitting potential increases with Cr content.

Laser Surface Alloyed St37 with Ni, Cr and Mo

The electrochemical behavior of the Fe-Ni-Cr-Mo alloy in 0.1M NaCl solution (naturally aerated) was studied by EIS. In recent work [16], the equivalent circuit proposed by Mansfeld and his co-workers for pitting of aluminum based materials[17,18] was used for explaining the pitting of stainless steel. This circuit, as shown in figure 3, has two branches, one relating to the passive surface and another one corresponding to the pitting occurring in localized area of the surface. The circuit admits that pitting could be described at low frequencies by a

transmission line type of behavior. A good coincidence was found between the model and experimental data.

If we adopt the same model in the present study, a good pitting resistance is to be expected for the surface alloy obtained by LSA as reflected in the impedance spectra shown in figure 4. From 80hrs to 130hrs, of immersion, the impedance spectra do not change much. Both of them do not show the transmission line or the maximum of phase angle at lower frequencies which are related with the pitting process, revealing that no pitting corrosion occurred up to 130hrs of immersion in 0.1M NaCl solution.

Apart the evidence for a stainless behavior of these alloys,as found for conventional stainless steel, the refinement of the microstructure and of the sulfide inclusions as well as the reduction in their number is expected to improve the pitting resistance of these alloys relatively to their conventional counterparts.

Conclusions

Laser surface alloying of 7175-T7351 alloy with Cr leads to the formation of stainless aluminum with enhanced pitting corrosion resistance relatively to the base alloy.

The stainless steel formed via LSA from the steel substrate by adding Ni, Cr and Mo shows a passive behavior like the one found on conventional alloys with the potential advantage of reduction or refinement of the sulfide inclusions, which are one of the main causes of pitting initiation.

Acknowledgment

The authors gratefully acknowledge the support received from the E. C. under contract: BREU-CT 91-0494.

References

1. J. Stewart, D. B. Wells, P. M. Scott, A. S. Bransden, Corrosion, 46 8 (1990): p.618.
2. E. McCafferty, P. G. Moore, Fundamental Aspects of Corrosion Protection by Surface Modification, (Peninington, New Jersey, Electrochem. Soc., 1984), p. 112.
3. E. McCafferty, P. G. Moore, G. Peace, J. Electrochem. Soc., 129 1 (1982): p.9.
4. P. L. Bonora, M. Bassoli, P. L. De Anna, G. Battaglin, G. Della Mea, P. Mazzoldi, A. Miotello, Electrochim. Acta, 25 (1980): p.1497.
5. J. Rawers, W. Reitz, S. Bullard, E. K. Roub, J. Electrochem. Soc., 129 10 (1991): p. 769.
6. P. G. Moore, E. McCafferty, J. Electrochem. Soc., 128 6 (1981): p. 1391.
7. S. Chiba, T. Sato, A. Kawashima, K. Asami, K. Hashimoto, Corrosion Science, 26 4 (1986): p. 311.
8. L. Renaud, F. Fouquet, J. P. Millet , J. L. Crolet, Surf. Coat. Tech., 45 (1991): p. 449.
9. P. L. Hagans, R. L. Yates, Environmental Degradation of Ion and Laser Beam Treated Surface, (The Minerals, Metals and Materials Society, 1989), p.215.
10. K. R. Van Horn, Aluminum, Vol. One: Properties, Physical Metallurgy and Phase Diagrams, (Metals Park, Ohio, American Society for Metals, 1967): p.371.
11. W. C. Moshier, G. D. Davis, G. O. Cote, J. Electrochem. Soc. 136 2 (1989): p.356

12. G. D. Davis, W. C. Moshier, T. L. Fritz, G. O. Cote, J. Electrochem. Soc. 137 2 (1990): p. 422.
13. H. Yoshioka, S. Yoshida, A. Kawashima, K. Asami and K. Hashimoto, Corrosion Science, 26 10 (1986): p. 795.
14. D. Liu, F. Wang, Ch. Cao, H. Lou, L. Zhang, H. Lin, Corrosion, 46 12 (1990): p. 975.
15. Z. Szklarska-Smialowska, Corrosion Science, 33 8 (1992):p. 1193
16. M. A. R. Catarino, Master's dissertation, Instituto Superior Técnico, Lisboa,1993.
17. F. Mansfeld, S. Lin, S. Kim, H. Shih, Corrosion, 45 8 (1989): p. 615.
18. H. Shih, F. Mansfeld, Corrosion, 45 8 (1989): p. 610.

Table 1. Laser surface alloyed samples and corresponding processing parameters.

sample	laser surface alloying				laser remelting		
	power	spot	speed	feeder rate	power	spot	speed
A-1	2KW	1.5mm	10mm/s	0.03g/s	2KW	1.5mm	20mm/s
A-2	2KW	2mm	10mm/s	0.05g/s			
A-3	2KW	2mm	10mm/s	0.05g/s			

Table 2. Average composition of the laser surface alloys on 7175-T7351 and composition of the matrix phase and dendrite phase (wt%).

	Cr	Cu	Mg	Zn	Al
A-1(average)	3.17	1.72	0.65	3.06	91.40
A-1(matrix)	0.83	0.63	0.82	3.89	93.69
A-1(dendrite)	10.83	2.31	0.38	2.52	83.96
A-2(average)	4.97	1.62	0.73	3.41	89.27
A-2(matrix)	1.23	1.36	0.74	3.86	92.81
A-2(dendrite)	11.02	1.87	0.35	2.48	84.28
A-3(average)	5.40	1.56	0.66	3.30	89.07
A-3(matrix)	1.33	0.73	0.33	2.26	95.36
A-3(dendrite)	12.04	2.11	0.42	2.67	82.76

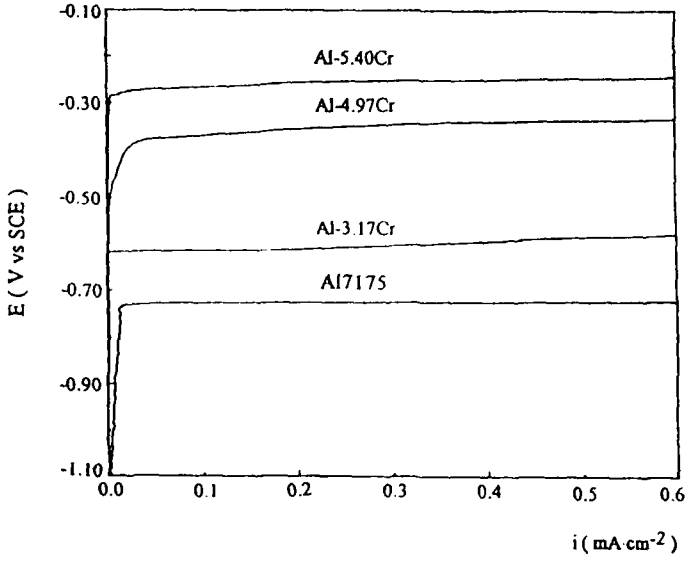

Figure 1. Anodic polarization curves of laser surface alloyed 7175-T7351 with Cr and untreated one in deaerated 0.5M NaCl.

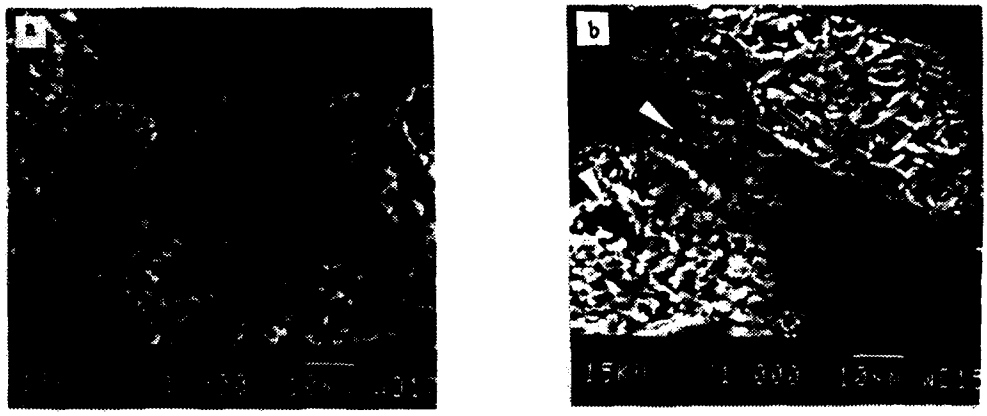

Figure 2. Scanning electron micrographs showing the pitting morphologies.
a: 7175-T7351 (as received) after anodic polarization in deaerated 3%NaCl.
b: laser chromium alloyed 7175-T7351 (A-3) after anodic polarization in deaerated 3%NaCl.

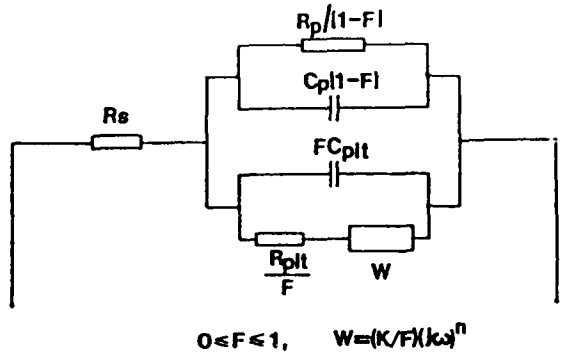

Rp: polarization resistance of the passive film,
Rpit: pitting resistance,
W: transmission line element.
Rs: solution resistance.
Cp: capacitance of the passive film,
Cpit: capacitance of the pitted area,
F: area fraction of pitted surface

Figure 3. Model for pitting corrosion[17,18].

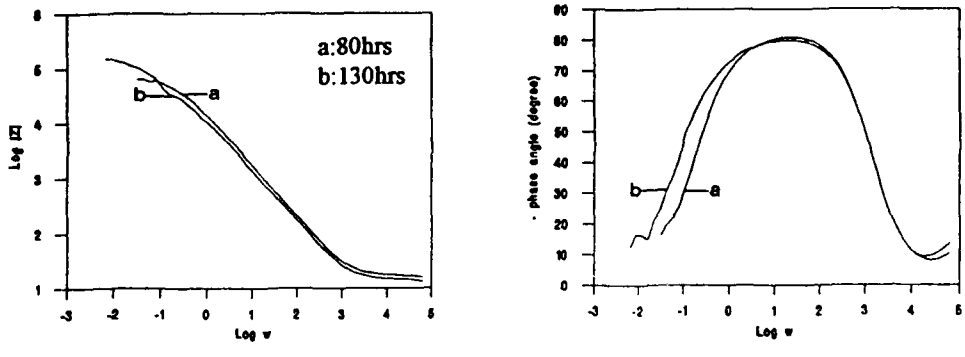

Figure 4. Bode-plots for Fe-Ni-Cr-Mo surface alloy as a function of immersion time in 0.1M NaCl.

Marine Corrosion Resistance of Aluminum and Aluminum-Lithium Alloys

P.R. Roberge
Department of Chemistry and Chem. Eng., Royal Military College
Kingston, Ontario, K7K 5L0 (Canada)

D.R. Lenard
Materials Technology Section, Defence Research Establishment Pacific
FMO Victoria, B.C., V0S 1B0 (Canada)

Abstract

Two electrochemical techniques have been used to characterize the corrosion resistance of various faces of aluminum and aluminum-lithium sheet material exposed to a synthetic marine environment. The results obtained with a new method, in which electrochemical noise was analyzed for its stochastic nature, were systematically compared to parallel measurements made with electrochemical impedance spectroscopy (EIS). The electrochemical measurements obtained with the three orthogonal faces of commercial aluminum and aluminum-lithium sheet material were also compared to the results obtained during the long term exposure of the same alloys to real sea water.

The results obtained during this extensive study indicated that short term EIS measurements can help to predict the general and localized corrosion behavior of this material when exposed to sea water. A systematic analysis of 610 fifteen minute noise records with the exponential decay analysis technique has demonstrated that the exponential decay model describes very well the potential fluctuations observed during these experiments, thereby confirming the chaotic nature of the corrosion processes in progress. The parameters revealed during the noise analysis were additionally related to the features calculated from EIS measurements or observed after long term exposure of the same alloys in a flowing sea water tank.

Key terms: marine corrosion, electrochemical impedance spectroscopy, electrochemical noise, aluminum alloys.

Introduction

The development of a special group of aluminum alloys containing lithium as one of the primary alloying elements was described as the single largest R&D effort in the history of aluminum metallurgy[1]. The main advantage of alloying lithium to aluminum used in aerospace vehicles comes from the increased modulus of elasticity and strength, which are paralleled by a unique reduction of density of the alloys. The aluminum-lithium alloys can offer substantial (≈10%) weight savings over conventional aerospace aluminum alloys such as the 2000 and 7000 series. In addition, fatigue properties and corrosion resistance of aluminum alloys are said to improve by alloying them with lithium[2]. But past experience indicates that gains in mechanical properties are often taxed by a simultaneous increase of the susceptibility to catastrophic forms of corrosion. For example, the T6 temper of Aluminum Alloy (AA) 7075 was readily adopted by aircraft designers because of its high modulus and strength. It was subsequently discovered to be highly susceptible to stress corrosion and exfoliation in the marine environment[3], at great cost to aircraft operators.

As a result of this history and because elemental lithium is extremely reactive, there has been considerable interest in the corrosion susceptibility of aluminum-lithium alloys.

A variety of accelerated corrosion tests[4-8] and standard electrochemical techniques[8-11] have been used to study the corrosion behavior of Al-Li. The resistance of aluminum alloys to stress corrosion cracking (SCC) has also been extensively studied in many laboratories around the world[4,10,12-18]. But the multitude of heat treatments which are possible, added to the variability of alloy compositions which have been studied, have resulted in an uncomfortable degree of uncertainty concerning the factors that control the initiation of localized corrosion on aluminum-lithium alloys. In order to acquire first hand experience with the behavior of these alloys in the marine environment, the Defence Research Establishment Pacific (DREP) subjected panels made from (AA)2090 and 8090 sheet, along with 2024 and 7075 sheet, to several tests involving exposure to sea water fog and full or part immersion in sea water[8]. The results of these tests were then compared with results obtained at the Royal Military College of Canada during the analysis of EIS and electrochemical noise measurements made with the same alloys exposed to synthetic sea water (3% NaCl).

Electrochemical Techniques

Electrochemical impedance spectroscopy (EIS)

Electrochemical Impedance Spectroscopy (EIS) has been successfully applied to the study of corrosion systems for almost twenty-five years. Since the early work published by Epelboin and co-workers[19] EIS has gained tremendous momentum and popularity in corrosion laboratories around the world. An important advantage of EIS over other laboratory techniques is the possibility of using very small amplitude signals without disturbing the properties being measured. EIS has also recently found its way into practical field applications[20-22] where its capability of working in difficult and changing hydrodynamic conditions can become a serious advantage once the complications of analyzing EIS results are overcome.

EIS has been shown to be a rapid, powerful and accurate method for measuring corrosion rates. But in order to access the charge transfer conductance, which is proportional to the corrosion rate at the monitored interface, the EIS results have to be understood with the help of a model of the interface. The simplest model representing such an interface must also include a capacitance which describes the capacitive charge acceptance of any metallic surface exposed to an electrolyte. The validation of this simple RC equivalent circuit model can be achieved by permuting the three data points selected to project the center of a circle in a Nyquist representation. The application of this principle to the study of various alloys exposed to aqueous environments has revealed that the non-adherence of the EIS measurements to a perfect RC model is a rich source of information[23] concerning the types of corrosion processes occurring on a metallic surface.

One omnipresent characteristic of the EIS spectra that must be addressed properly, in terms of its significance in corrosion studies, is the constant phase element (CPE) which is commonly introduced as an empirical factor in fitting procedures to describe the angle of tilt often visible in Nyquist plots. The empirical factor would then appear as an exponent β with a value between 0 and 1, which would be added to the imaginary component of an impedance frequency (ω) response $Z(\omega)$ (Eq. 1).

$$Z(\omega) = R + \frac{R_p}{1 + (j\omega R_p C_{dl})^{\beta}} \qquad (1)$$

A traditional explanation for the CPE has been surface dispersion effects[24-26] which, in the case of a corroding metal, have themselves been attributed to microscopic roughening of the surface[27-29] and more recently to typical defects produced by localized corrosion such as encountered when carbon steel[30-32] or aluminum alloys[33,34] are exposed to mildly corrosive environments.

Electrochemical noise (EN)

The most accepted technique to analyze noise data has been to transform time records in the frequency domain in order to obtain power spectra. Since noise signals can be produced by either deterministic or stochastic processes and often consist of a complex combination of these processes, a practical approach has been to correlate predominant frequencies and deconvolute unwanted signals in an iterative manner using well established mathematical functions[35].

The approach used in the present study for the analysis of voltage fluctuations has been extensively described elsewhere[36,37]. With this technique the voltage fluctuations are first transformed into individual voltage peaks as basic events. The rise time of the basic events (dV/dt) is then computed since this parameter is thought to be an important characteristic of the electrochemical systems being studied. During a second process of data transformation the probability distribution of the basic events is compared with a typical Poisson probability distribution of stochastic point processes. A measure of the goodness-of-fit is then evaluated by comparing the ideal exponential distribution to the experimental distributions observed and corresponding to individual λ_t calculated with Eq. 2 and subsequently averaged. The goodness-of-fit itself would be an expression of the difference between this average and the ideal value λ (Eq. 3).

$$\lambda_t = \frac{f(t)}{e^{-\lambda t}} \tag{2}$$

$$\text{Goodness-of fit}(\%) = \left(1 - \left|1 - \frac{\bar{\lambda}}{\lambda}\right|\right) \cdot 100\,\% \tag{3}$$

Experimental

Sea water exposure

The 76 x 76 mm panels used in the exposure tests were sheared from sheets made of Aluminum Alloys 2024-T3, 2090-T8, 7075-T6 and 8090-T851.The nominal composition of the alloys are shown in Table 1. Both surfaces of each panel were sanded with 120 grit silicon carbide abrasive paper and each panel was then fitted with two ceramic multiple-crevice washers (designed according to ASTM G78) that were held in place with a #12 stainless steel nut and bolt assembly that passed through a 6.3 mm central hole. Each bolt was fitted through plastic tubing to prevent contact with the aluminum panel. Each washer provided twelve separate sites for initiation of crevice corrosion. Each panel was suspended by way of a plastic-coated wire that was passed through a 3 mm hole that had been drilled in one corner of the specimen.

SF850 Corrosive Fog Exposure System. The exposure was conducted according to ASTM B117 with the exception that natural sea water was used to generate the fog instead of the standard sodium chloride solution.

Partial and total immersion. The remaining specimens were suspended in sea water that was drawn from the Strait of Juan de Fuca and directed through a tank measuring 16 X 62 x 177 cm.

The sea water flowed past any specimen immersed in it at a rate of 1 cm/sec and was then returned to the Strait 40 m from the intake. The water temperature in this location was within the range 7 - 11°C. One set was suspended in a single row perpendicular to the direction of flow so that one half of the specimen was under water. A second set was suspended in a single row 1 m downstream from the first so that the entire specimen was immersed.

All specimens were removed after an exposure time of four months. After the specimens were dismantled, the aluminum panels were cleaned by immersion in concentrated nitric acid. They were then rinsed with distilled water and allowed to dry after a final rinse with ethanol. Sections were cut from the panels and set in epoxy according to standard metallographic techniques in an effort to determine the depth of corrosion that had been initiated at the edges of the specimens.

Electrochemical tests

The aluminum specimens were cut to appropriate sizes for mounting in epoxy according to metallographic techniques. The samples were mounted in a manner that would expose only one face of each of three orthogonal planes that were related to the rolling direction of the sheet (the rolled surface, the long transverse edge and the short transverse edge). Prior to mounting, provisions were made for electrical connection to the unexposed part of the samples, and the edges were coated with an aluminum-vinyl anti corrosive paint to prevent crevice corrosion between the epoxy mount and the aluminum electrodes. After mounting, the specimens were polished (using 240, 400 and finally 600 grit papers) and cleaned with acetone and dichloromethane.

For each experiment, a pair of identical aluminum specimens (same alloy and same exposed face) was immersed in ~ 2 l beaker containing a solution of 3% sodium chloride. Each cell was equipped with an air purge and a saturated calomel reference electrode brought into close proximity with one electrode by a Luggin probe. The mounted specimens were separated by 2.5 mm and kept in a stable parallel position with plastic holders. EIS measurements were performed with a commercial frequency response analyzer (Solartron Model 1255) at the corrosion potential. A potentiostat was not used in these measurements. The alternating current was applied between the two aluminum electrodes and kept at a value which would not cause more than 10 mV difference (peak to peak) across the cell.

The reference electrode served to measure the corrosion potential and its fluctuations which were monitored with a sensitive multimeter (HP model 3457) through a high pass filter (1 MΩ resistor in parallel to a 1 μF capacitor) which served to increase the sensitivity even further by nulling the DC voltage component. A custom-made multiplexer controlled by a laboratory computer directed the inputs from each technique to a storage device. At the completion of these experiments, which lasted approximately two weeks, the specimens were removed and examined with both optical and scanning electron microscopy to observe any differences in corrosion morphologies.

Results and Discussion

The EIS data analysis technique mentioned earlier was used to calculate polarization resistance (R_p) values for each impedance plot gathered. These values were then converted into corrosion currents by multiplying them with a proportionality constant (B)[38] according to the Tafel extrapolation technique for measurement of corrosion kinetic parameters introduced by Stern[39] and Stern and Geary[40]. The corrosion current was itself converted into penetration rates using Faraday's law. The global equation is expressed in Eq. 4 where the corrosion rate is in mm/y

when R_p is in Ωcm^2. B is a proportionality constant for aluminum in chlorides (24 mV)[38], E.W. is the equivalent weight (9g) of aluminum (g/equiv.) and d its density ($2.7 g/cm^3$).

$$\text{Corrosion rate} = \frac{3.3 \cdot B \cdot E.W.}{R_p \cdot d} \quad (4)$$

According to the EIS polarization resistance data, which are summarized in Table 2, the 8090 alloy showed roughly equal corrosion rates for all three faces. Except for the rolled face, the corrosion rate of the 8090 alloy was substantially lower than the corresponding faces of the 2024 alloy. With the assumption that the CPE, which is directly proportional to $(1-\beta)$, increases in some manner with increased pitting, the EIS data indicated that the rolled surface of the 8090 had the lowest susceptibility to pitting, followed by the long transverse edge and the short transverse edge, which had the highest rate (Table 2). Examination of these surfaces with optical and scanning electron microscopy suggested that the correlation between the CPE and pitting rate involved the number of pits formed in any given area (pit density) rather than the pit depth. The low pitting rate suggested by EIS for the rolled surface was consistent with visual observation of the long term exposure panels. However, the approximate equivalence for all three faces was not. If the interpretation of EIS data is correct, the corrosion of the rolled surface must occur initially at this high rate, but then would fall to a much lower value over the longer term. The R_p values for the 2024-T3 alloy showed a pronounced difference in overall corrosion rate between its rolled surface and its edges, with the edges having consistently higher rates. After about 50 hours, a similar trend was observed for the CPE. These results are consistent with observations made on the long term exposure panels, which were characterized by a higher density of localized corrosion sites on the edges.

On the basis of the EIS data the conclusion would be reached that the edges of the 8090-T8 alloy had lower overall corrosion rates and were less prone to pitting than their 2024-T3 counterparts. The edges of the 8090 long term exposure panels had substantial areas where no visible corrosion had occurred. This could be consistent with the lower overall corrosion rates and lower pitting density suggested by EIS results in comparison with 2024. However, the depth of attack within each pit (Fig. 1) was as large or larger than a corresponding pit on 2024. Thus the rate of corrosion within a pit was at least as severe for 8090 as for 2024.

As was the case for the 8090 alloy, the corrosion rate determined with EIS for the rolled surface of the 7075 was approximately equal to that measured for the edges. This was not consistent with the appearance of the long term panels, which suffered more metal loss along the edges than the rolled surface. The CPE values obtained for these experiments indicated that the rolled surface of the 7075 alloy had the lowest pitting density while the long and short edges had higher rates. The higher rates reached similar and essentially constant values after 200 hours. These results did correlate very well with the long term exposure tests, in which the edges did indeed suffer much worse localized attack.

According to the EIS results the rolled surface of the 2090 alloy had a consistently lower general corrosion rate than the same surface of the 7075. This did not appear to be consistent with the long term exposure tests, in which corrosion damage seemed to be more extensive on the surface of the 2090 alloy. On the other hand the EIS data suggested that the edges of the 2090 were only slightly more corrosion resistant than the 7075 edges. Once again this did not appear to be consistent with visual observation of the long term exposure panels. In this case the edges of the

2090 panels suffered noticeably less corrosion than their 7075 counterparts. The CPE data indicated that the pit density should be lower on the rolled surface of the 2090 than the 7075 and that the pit density should be much lower on the edges of the 2090 than the 7075. These results are completely consistent with the appearance of the long term exposure panels.

In an effort to correlate the parameters calculated by the exponential decay model, 610 records of fifteen-minute data gathered during the laboratory testing of the aluminum sheet material were compared to the results obtained on the same specimens with EIS or during the long term exposure to sea water. While the agreement between the noise patterns and the model seemed to be excellent (average Goodness-of-fit = 97.2% (Eq. 3)), no simple correlation could be found between any of the calculated parameters and the general corrosion rates evaluated with EIS. Such a conclusion would confirm what others[41,42] had found previously, i.e. the degree of potential fluctuations at the corrosion potential is a relatively insensitive indication of general corrosion rates.

Fig. 2 illustrates the global behavior of the average rising time measured on all three faces of 8090-T8 sheet material for each of the noise data record gathered during the experiments, when plotted as a function of corrosion potential. These two parameters were chosen for this global representation of the results because they were thought to reflect the fundamental behavior of the equilibria being established during the continuous corrosion of aluminum specimens. It was observed that the four alloys tested behave quite differently during these two week experiments.

The predominance of the high rise time values in the anodic fraction of these plots seems to be related to the good performance of an alloy and is probably associated with the control of the corrosion processes by passivation (anodic potentials). An electrical analogy would be an open circuit situation with fast unbuffered switching of the potential. The relative fraction of slow transients was quantified (everything that is not in the left uppermost corner of Fig. 2) and these fractions were compared (Fig. 3) to the average corrosion rates measured with EIS (Table 2).

While the correlation coefficient between the two variables presented in Fig. 3 seems to be excellent ($r = 0.99$) the relation itself has to be interpreted with some caution since the time of exposure, which is not represented in these comparisons, would have a strong influence on the absolute values estimated for the predominance of fast transients which were always more prevalent during the first few days of each experiment and tapered off as exposure time progressed.

Conclusion

The long term exposure tests indicated that the rolled surfaces of the 8090-T851 sheet were more resistant to corrosion than the conventional 2024-T3 sheet. Except for some pits which developed at an air/water interface, these surfaces suffered only minor corrosion. The same tests indicated that the rolled surfaces of the 2090-T8 sheet suffered as much or even more corrosion damage than their counterparts on the 7075-T6 sheet. Some fairly deep pits occurred on the rolled surfaces of the 2090, even during the exposure to sea water fog.

The results obtained during the electrochemical testing of various faces of aluminum sheet material indicated that short term EIS measurements can help to predict the general and localized corrosion behavior of this material when exposed to sea water. In fact the prediction of the localized corrosion behavior with the CPE calculated from the EIS data seemed to agree more closely to the long term tests results than the general corrosion estimation. A systematic analysis of 610 fifteen minute noise records with the exponential decay analysis technique has also demonstrated that the

exponential decay model describes almost perfectly the potential fluctuations observed during these experiments, thereby confirming the chaotic nature of the corrosion processes in progress. The parameters revealed during the noise analysis could additionally be globally related to the features calculated from EIS measurements.

References

1. W. E. Quist and G. H. Narayanan, "Aluminum-Lithium Alloys," in A. K. Vasudevan and R. D. Doherty, Eds., Treatise on Materials Science and Technology, Academic Press, New York, 31 (1989), p. 219.
2. D.B. Williams and P.R. Howell, "The Microsstructure of Aluminum-Lithium Base Alloys," in A. K. Vasudevan and R. D. Doherty, Eds., Treatise on Materials Science and Technology, Academic Press, New York, 31 (1989). p. 364.
3. S.J. Ketcham and J.J. de Luccia, Aircraft Corrosion, AGARD Conference Proceedings No. 315 (1981).
4. C.J.E. Smith et al., "New Light Alloys," AGARD Conference Proceedings No. 444, Mierlo, Netherlands, 3-5 October 1988, p. 7-1.
5. T.S. Srivatsan, "Microstructure Compatibility of an Al-Li-Cu-Mg-Zr Alloy Exposed to Corrosive Environmenst," Report AD-A215 540, Naval Surface Weapons Center, White Oak, MD, USA (1987).
6. J. Kozol et al., "In-Service Evaluation of 2090 Aluminum-Lithium Alloy on F/A-18 Aircraft," Report AD-A248 472, Naval Air Systems Command, Washington, DC, USA (1991).
7. J.P. Moran et al., Corrosion, 43 6 (1987): p. 374.
8. D.R. Lenard, J.G. Moores. P.R. Roberge and E. Halliop, Marine Corrosion of Aluminum-Lithium Aloy Sheet, TTCP-P-TP1 Report, Defence Research Establishment Pacific, Victoria, Canada (1991).
9. R.G. Buchheit Jr., J.P. Moran and G.E. Stoner, Corrosion, 46 8 (1990): p. 610.
10. M. Habashi, Corrosion Science, in press.
11. A. Roth and H. Kaesche, "Electrochemical Investigation of Technical Aluminum-Lithium Alloys," Proceedings of Aluminum-Lithium Alloys, Williamsburg, VA, USA (1989), p. 1196.
12. R.C. Dorward, Materials Science and Engineering, 84 (1986): p. 89.
13. R.C. Dorward and K.R. Hasse, Corrosion, 44 12 (1988): p. 932.
14. B. Bavarian et al., "Localized Corrosion of 2090 and 2091 Al-Li Alloys," Proceedings of Aluminum-Lithium Alloys, Williamsburg, VA, USA (1989), p. 1227.
15. A. Buis and J. Schijve, Corrosion, 48 11 (1992): p. 898.
16. E.S.C. Chin et al., "Evaluation of 2090-T8E48 Aluminum-Lithium Plates," Report AD-A217 262, U.S. Army Materials Technology Laboratory, Watertown, MA, USA (1989).
17. C. Kumai et al., Corrosion, 45 4 (1989): p. 294.
18. T. Sheppard and N.C. Parson, Materials Science and Technology, 3 (May 1987): p. 345.
19. I. Epelboin, M. Keddam and H. Takenouti, Journal of Applied Electrochemistry, 2 (1972): p. 71.
20. V.S. Sastri and P.R. Roberge, "Monitoring Corrosion in Sour Media," Materials Performance: Sulphur and Energy, P.R. Roberge et al., Eds., The Canadian Institute of Mining, Metallurgy and Petroleum, Montreal, 1992, pp. 57-69.

21. P.R. Roberge and V.S. Sastri, CORROSION 93, Paper No. 396, (National Association of Corrosion Engineers; Houston, TX, 1992).
22. P.R. Roberge and V.S. Sastri, Corrosion Science, in press.
23. P.R. Roberge, "Analyzing Simulated Electrochemical Impedance Spectroscopy Results by the Systematic Permutation of Data Points," Electrochemical Impedance Analysis and Interpretation, D.C. Silverman and J.R. Scully, Eds., ASTM STP 1188, American Society for Testing of Materials, in press.
24. K.S. Cole and R.H. Cole, Journal of Chemical Physics, 9 4 (1941): p. 341.
25. B.W. Davidson and R.H. Cole, J. Chemical Physics, 19 12 (1951): p. 1484.
26. A.K Jonscher, Dielectric Relaxation in Solids, (Chelsea Dielectrics Press, London, U.K., 1983).
27. R. De Levie, Electrochimica Acta,, 10 (1965): p. 113.
28. P.H. Bottelbergs and G.H.J. Broers, Journal of Electroanalytical Chemistry, 72 (1976): p. 257.
29. J.B. Bates, J.C. Wang and Y.T. Chu, Solid State Ionics, 18&19 (1986): p. 1045.
30. P.R. Roberge, E Halliop, M. Asplund and V.S. Sastri, Journal of Applied Electrochemistry, 20 (1990): p. 1004.
31. P.R. Roberge, "Analyzing Electrochemical Impedance Corrosion Measurements by the Systematic Permutation of Data Points," Computer Modeling in Corrosion, R.S. Munn, Ed., ASTM STP 1154, (American Society for Testing of Materials 1992), p. 197.
32. P.R. Roberge, E. Halliop and V.S. Sastri, Corrosion, 48 6 (1992): p. 447.
33. P.R. Roberge, E. Halliop, D. Lenard and J. Moores, Corrosion Science, in press.
34. P.R. Roberge, E. Halliop, D. Lenard and J.G. Moores, "Marine Corrosion Behavior of Al-Li Alloy Sheet," 3rd. Int. SAMPE Metals and Metals Processing Conf., Toronto, October 20-22, 1992, p. M51.
35. J.S. Bendat and A.G. Piersol, Random Data: Analysis and Measurement Procedures, 2nd Ed, (John Wiley & Sons, New York, 1986).
36. P.R. Roberge, M. Farahani and K. Tomanstchger, Journal of Power Sources, 41 3 (1993): p. 321.
37. P.R. Roberge, Journal of Applied Electrochemistry, in press.
38. R. Grauer, P.J. Moreland and G. Pini, A literature review of polarisation resistance constant (B) values for the measurement of corrosion rate, (National Association of Corrosion Engineers, Houston, TX, 1982).
39. M. Stern, Corrosion, 14 (1958): p. 440.
40. M. Stern and A.L. Geary, Journal of the Electrochemical Society, 104 (1957): p. 56.
41. Lumsden, M.W. Kendig and S. Jeanjaquet, Corrosion92, Paper No. 224, (National Association of Corrrosion Engineers, Houston, TX, 1992).
42. Eden, K. Hladky and D.G. John, Corrosion86, Paper No. 274, (National Association of Corrosion Engineers, Houston, TX, 1986).

Table 1 Nominal composition of alloys tested (wt %).

Alloy	Li	Cu	Mg	Si	Fe	Mn	Zn	Zr
2024	-	3.8-4.9	1.2-1.8	0.5	0.5	0.3-0.9	0.25	-
2090	1.9-2.6	2.4-3.0	0.25	0.1	0.12	0.05	0.1	0.08-0.15
7075	-	1.2-2.0	2.1-2.9	0.4	0.5	0.3	5.1-6.1	-
8090[a]	2.35	1.23	0.67	0.02	0.03	0.001	0.02	0.11

Note a: Actual heat analysis for the specimens supplied by ALCAN

Table 2 Analyzed EIS results obtained with aluminum alloys.

Alloy	Thickness (mm)	Face	Corrosion Rate (mm/y)	β -
2024-T3	1.0	Rolled	0.05	0.81
		Long	0.16	0.77
		Short	0.22	0.75
2090-T3	1.2	Rolled	0.06	0.89
		Long	0.08	0.82
		Short	0.09	0.79
7075-T6	1.0	Rolled	0.14	0.87
		Long	0.11	0.63
		Short	0.12	0.68
8090-T8	1.5	Rolled	0.05	0.93
		Long	0.04	0.87
		Short	0.03	0.81

Table 3 Results of sea water exposure.

Alloy	Fog		Immersion		
			Partial		Total
	general	crevice	general	interface	
2024-T3	pitting	6 sites	severe pitting	severe pitting	severe pitting
2090-T3	few deep pits	none	"poultice"	severe	scattered pits
7075-T6	pitting	1 site	"poultice"	severe	scattered pits
8090-T8	minor	1 site	minor	few deep pits[a]	minor

[a] Figures 1a and 1b.

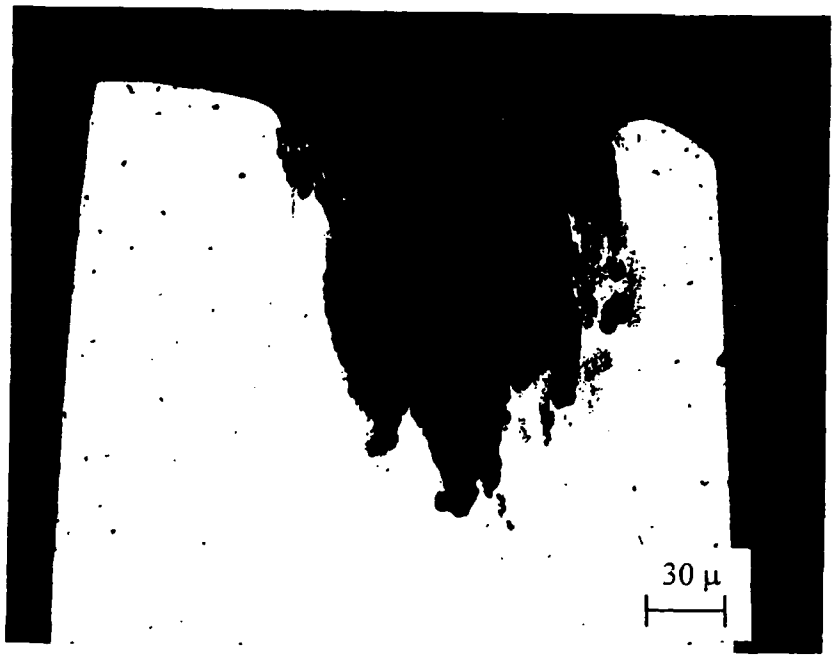

a)

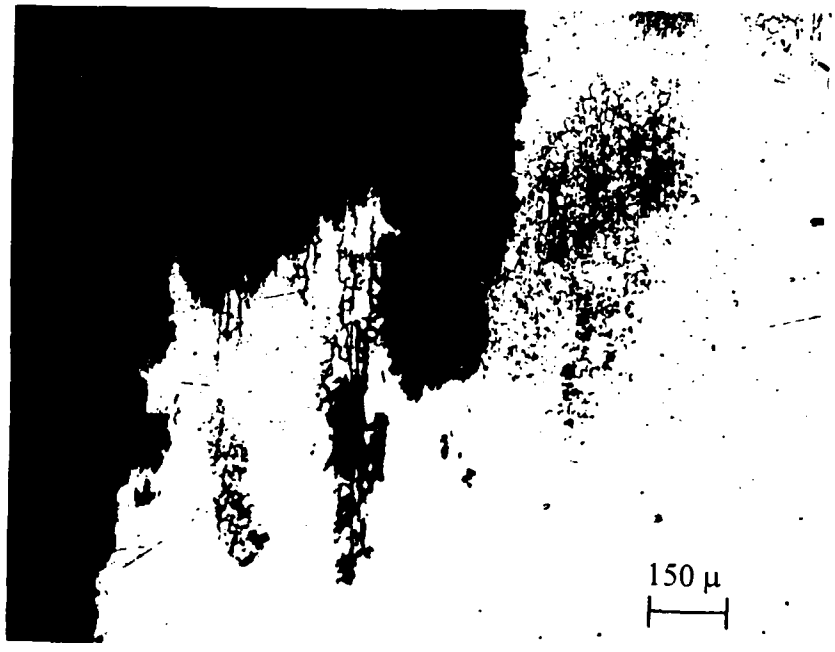

b)

Fig. 1 Metallograph of a section through an edge of the 8090 panel immersed in sea water during four months. a) at 64x and b) at 320x to illustrate the intergranular nature of the corrosion attack.

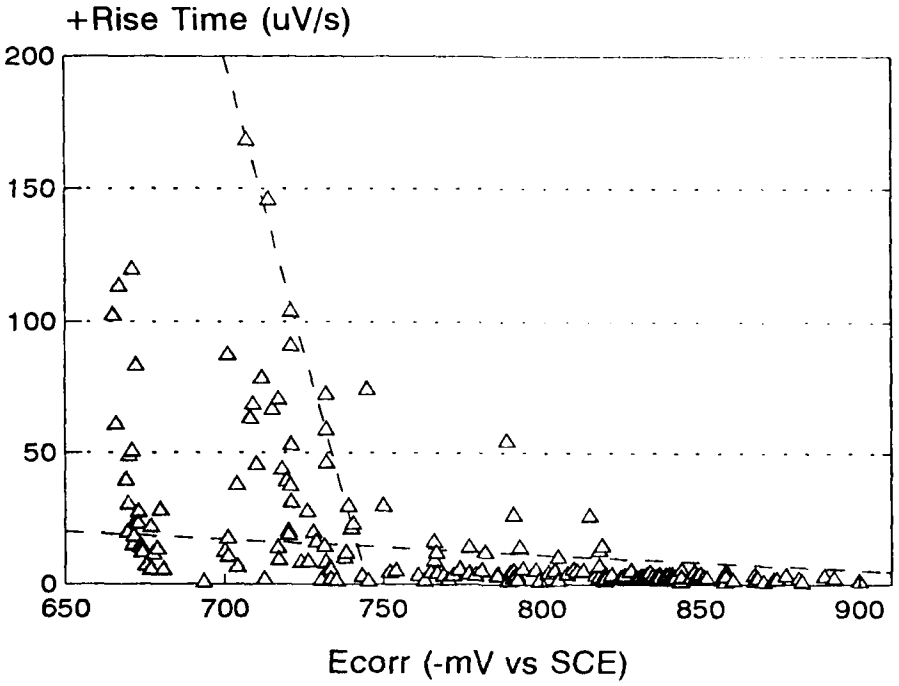

Fig. 2 Positive rise time calculated for each of 128 noise records gathered during the laboratory testing of 2090-T3 sheet material as a function of the corrosion potential.

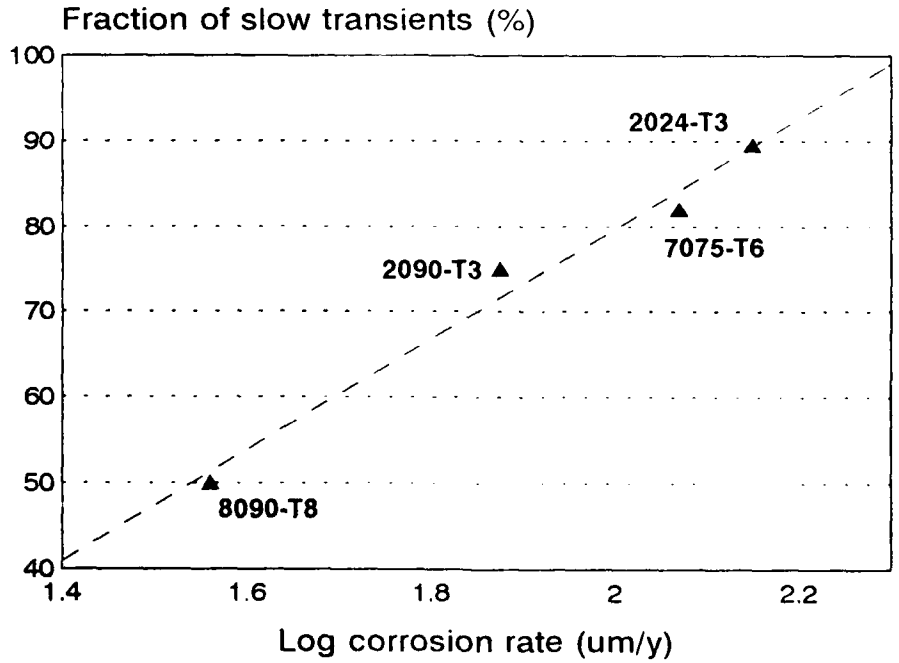

Fig. 3 Fraction of slow potential transients as a function of average corrosion rates.

Measuring Corrosion Resistance of Stainless Steels Using the "Avesta Cell" - Experiences and New Applications

Poul-Erik Arnvig
Avesta Sheffield AB, Research & Development
S-774 80 Avesta, Sweden

Ralph M. Davison
Technical Marketing Resources, Inc.
3209 McKnight East Drive, Pittsburgh, Pennsylvania 15237, USA

Abstract

The development of the new electrochemical testing device for pitting studies is reviewed. The device is commonly called the Avesta cell, and permits extremely accurate determination of critical pitting temperatures on surfaces without risk of interference from crevice corrosion where the device touches the test specimen. The cell uses a very slow flow of distilled water through the crevice that must inherently exist from such a contact, thereby preventing establishment of a local corrosive environment and so inhibiting crevice corrosion.

Investigations have demonstrated that the sensitivity of tests done with this device is sufficient to readily identify variations of corrosion resistance among different heats of the same nominal grade and even among different depths within a single plate. The sensitivity is due partly to the prevention of crevice corrosion and partly to the use of a definition of a critical pitting temperature (CPT) demanding a measurement that is completely without interference from crevice corrosion.

The CPT is defined as the lowest temperature at which pitting initiation occurs on the test specimen during a dynamic anodic polarization scan. By definition the CPT is therefore independent of the electrochemical potential applied to the test specimen. Furthermore the reproducibility of this CPT is exceptional compared to the generally accepted stochastic nature of the pitting initiation process.

In an ongoing program the authors have sought to monitor the results of other laboratories using this device or modifications of the device using the same principle to avoid crevice corrosion. Experience of these other laboratories is reviewed. With simple adaption, the test device may be applied to irregularly shaped surfaces, thereby permitting direct electrochemical testing of practical surface conditions, including welds.

The test device has shown extraordinary versatility and reproducibility in its applications in the laboratory. Data are presented for a wide range of austenitic and duplex stainless steels. Alternative pitting characterization techniques are discussed in relation to the applicability of the Avesta cell. The described device is in no way restricted by patent. Use of the test cell and further development are encouraged. The cell is available from multiple sources, and drawings are available as a basis for independent construction.

Key terms: stainless steel, pitting corrosion, critical pitting temperature, corrosion testing

Introduction

The Avesta cell - A fundamental problem during testing of various stainless steels with regard to pitting corrosion has always been the unwanted simultaneous occurrence of crevice corrosion. The crevice corrosion occurs due to masking of the specimen which is applied to obtain a well defined surface area for testing and/or to mask the electrical wire connection between sample and potentiostat.

The prevention of crevice corrosion during electrochemical testing of stainless steels has been addressed in various ways. Lacquering[1,2] of the specimen is perhaps one of the best known techniques, but to obtain a reasonable safe "crevice-free" lacquering a considerable amount of care and tideous work is required. Often some percentage of the total number of tests has been discarded due to crevice corrosion, but this inefficiency has in general been accepted[2] as unavoidable.

Other methods[3] of avoiding crevice corrosion have involved the application of a very high pressure between the masking and the specimen and at the same time a rather complicated mounting process of the specimen has had to be adopted - as is also the case with the ASTM G61 electrode holder, which virtually has been designed (unintentionally) to create crevice corrosion.

In recent years the use of the Avesta cell[4,5,6] has become more and more widespread all over the world as a simple and effective tool for electrochemical testing of stainless steels. It is even being offered for sale by several companies involved in supplying equipment for corrosion testing. The popularity of the cell can mainly be attributed to

- a very simple and fast mounting of the test specimen allowing actual surfaces of the test specimen to be tested one at a time (i.e., the surface that will be exposed to an operating environment)

and

- complete avoidance of crevice corrosion during testing.

In figure 1 the Avesta cell design is shown. The cell consist of a double walled glass chamber to facilitate heating by an external recirculating heating bath, and various inlets and connections for temperature measurement, counter- and reference electrodes, and gas bubbling.

The fundamental principle of the cell is the use of distilled water for continuous rinsing of the crevice between the gasket and the specimen - as illustrated in figure 2.

The distilled water is pumped into a circular chamber in the base plate of the cell, with a very low flow, typically 4-5 ml/hour. A small ring of ordinary filter paper is used to ensure a steady and even flow of distilled water out of the crevice into the test chamber. The flow of distilled water is further adjusted by the pressure applied to the sample from the bottom screw.

The only preparation of the test specimen necessary before testing is to cut it to a practical size that can be fit under the cell, and to perform the usual cleaning of the test surface.

Initially[4,5,6] the cell was mainly applicable for flat specimens, but as will be shown below the cell can - with simple adaptions - be used for irregular surfaces, including welds. The main aim of the applications, where the cell has been used, has been to *rank* different types of stainless steels in various environments. It should be noted that ranking involves a relative comparison of materials under standardized conditions, which together with practical experiences and other data can make the basis for the selection of a material for a specific application.

The objective of this paper is to discuss the applicability of the cell for different electrochemical pitting characterization techniques, based on a discussion of fundamental phenomenological factors and the experimental parameters affecting these factors.

Pitting characterization

Pitting Potential - The traditional method of characterizing the pitting susceptibility of stainless steels has been to measure the pitting potential[7], E_b, and/or the repassivation potential[8], E_{rp}, based on a polarization curve obtained in a chloride-containing solution[2,9,10,11,12,13] - see figure 3.

The pitting potential is defined as the electrochemical potential above which pitting occurs and the repassivation potential is the potential below which a propagating pit repassivates. For practical reasons these potentials are often defined on the basis of a critical anodic current density (i_c), typically 10-100 $\mu A/cm^2$ - see figure 3.

Some problems arise when using the pitting potential as a *ranking* parameter for the pitting susceptibility of stainless steels.

The highly corrosion resistant stainless steels may not pit at all in the chosen solution at the specific test temperature, or the solution at the chosen temperature may be so aggressive that steels with low pitting resistance will pit immediately after immersion in the solution. In both cases a ranking based on a measurable and quantitative parameter is only possible for a limited number of different stainless steels with relatively similar pitting susceptibility, i.e. within a fairly small variation in alloying elements.

Secondly, the pitting potential is a stochastic parameter[14]. This means that in spite of a careful experimental technique including "crevice-free" specimen mounting, the pitting potential will still vary within a certain interval from test to test - thereby making the assessment of small differences in pitting susceptibility impossible without a large number of experiments and proper statistical evaluation.

Critical Pitting Temperature (CPT) - It is well known that temperature has a significant effect on the pitting susceptibility of a stainless steel. Based on both chemical and electrochemical experiments, Brigham & Tozer[15,16] investigated the pitting potential's variation over a very broad range of temperatures in chloride solutions with fairly low pH.

The general picture of the pitting potential as a function of temperature found by Brigham and Tozer[15] is shown in figure 4. The fundamental finding was a critical temperature, below which no pitting occurred *regardless* of the electrochemical potential. This temperature was termed the "Critical Pitting Temperature" and was used for ranking of a wide range of stainless steels. The final testing to obtain a ranking order was performed in a solution of 10% $FeCl_3 \cdot 6H_2O$, which, due to the oxidative power of the solution, forces the corrosion potential of the stainless steel up into the potential range where pitting is potential independent.

The main advantage of this CPT was the wide range of stainless steels that could be ranked *quantitatively* by *one* parameter.

An interesting point in the original papers by Brigham & Tozer[15,16] is the fact that the experimental data only partly showed the existence of the sudden drop in the pitting potential at a specific temperature. The actual existence of a well-defined critical pitting temperature was based on extrapolation of various data.

Experimental documentation of this "potential-independent" CPT was first shown by Qvarfort[17], who showed that the drop from transpassive potentials to pitting potentials occurred within 1 °C in chloride solutions with varying pH on austenitic, non-welded stainless steel specimens. The accuracy of these measurements was based on the use of the Avesta cell.

The method used by Qvarfort to document the existence of the CPT was to determine the pitting potential and repassivation potential from a polarization curve at different temperatures. Plotting these potentials versus the temperature for a specific stainless steel shows the sudden drop of several hundred mV (depending on the chloride concentration) from the transpassive potential range, when the temperature is at or above the CPT. The full experimental procedure has been presented elsewhere[17].

The complete avoidance of crevice corrosion is necessary in this procedure, especially because the transpassive potential may be "artificially" lowered due to the occurrence of crevice corrosion close to the transpassive potential.

It is important to note that the "Avesta cell CPT" as introduced by Qvarfort[17] is fundamentally the same as the one introduced by Brigham & Tozer[15], which is widely used today, when determining the CPT of a stainless steel in the $FeCl_3$ solution defined in the ASTM G48 standard[1].

Examples of Avesta cell CPT's for the full scale of austenitic stainless steels, including standard grades type 304 (UNS S30400) and 316 (UNS S31600), the highly corrosion resistant type 904L (UNS N08904) and the superaustenitic grades Avesta Sheffield 254 SMO® (UNS S31254) and Avesta Sheffield 645 SMO™ (UNS S32654) are shown in figure 5. The last mentioned stainless steel, S32654, is a newly developed steel[18] with extremely high nitrogen content combined with high chromium and molybdenum content. For comparison Avesta cell CPT's for the two duplex stainless steels Avesta Sheffield SAF 2304® (UNS S32304), Avesta Sheffield 2205 (UNS S31803) and the superduplex stainless steel, Avesta Sheffield SAF 2507® (UNS S32750) are also shown in figure 5. The nominal content of the main alloying elements are shown in table 1. For further discussion of these data see "Applications" below.

As can be seen, with the help of the Avesta cell and the potential-*independent* CPT definition, it is possible to rank - quantitatively - an extremely wide range of stainless steels with regard to differences in pitting susceptibility. Only S32654 has a pitting resistance fully beyond the ranking range (CPT range: 2-95°C) attainable with the Avesta cell and a 1M NaCl (3.5%(w/w) Cl^-) solution, whereas S31254 and S32750 have CPT's ranging from just below 95°C to above 95°C.

Another definition of CPT that has been commonly referenced was presented by Bernhardsson et al[19]. It is based on a potentiostatic technique, where the temperature is raised in steps at a constant potential until pitting occurs - see figure 7.

The fundamental difference between this CPT definition and the Avesta cell CPT (originally Brigham & Tozer[16]) is however, that the CPT defined by Bernhardsson may be determined at a potential below the "pitting" line - see figure 4. In cases where such a potential has been chosen, the procedure proposed by Bernhardsson et. al. simply corresponds to determining the temperature at which the pitting potential is equal to the applied constant potential. This means, however, that the CPT found in this case has all the problems connected to the pitting potential as discussed above.

Applications

Initially the Avesta cell was developed as a tool for testing flat products. This despite the fact that, when looking at the published laboratory investigations in the literature, one gets the impression that wire (selected for convenience of corrosion testing) is a dominating stainless steel product.

---

[1] ASTM G48 does not involve the definition of a CPT, but rather only the testing for a stainless steel specimen in 10% $FeCl_3 \cdot 6H_2O$ at a certain temperature. This difference has caused considerable controversy and confusion over the years.

As has already been mentioned, the combination of the Avesta cell together with the potential-independent CPT has proved to be a powerful ranking tool - as shown in figure 5. The variations within grade as indicated in figure 5 should not be taken as based on a statistical analysis - they simply represent the maximum and minimum values found on a number of stainless steels samples taken from actual production.

The sensitivity of the Avesta cell CPT is illustrated in figure 6 and table 2. Samples from nine different heats have been investigated[20]. As can be seen from figure 6, the CPT is actually reproducible within 1°C. When comparing these variations in the CPT with the heat analysis, Alfonsson & Qvarfort[20] found that within-grade variation of the CPT could not be explained solely by the variations in the heat analysis. Microstructural variations, type of inclusions, their shape, size and distribution as well as microsegregations are also important factors influencing the CPT variation within-grade. For practical applications such differences are related to the range of within grade variations that may be encountered in service.

Also variation within a single plate can be detected with the help of the Avesta cell, because it is possible to test only a single surface, thus different sections of the plate. This application was used by Davison et al[21] to investigate plate material, type 316L, designed for improved machinability. They found that CPT could vary from 8 to 15°C depending on the section tested. Similar variations were found in other 316L plates of common production quality.

Avesta cell CPT's on welds have been published by Wallén et al[22] as part of the documentation for the development of S32654 although limitations were found in the ranking ability due to the extremely high corrosion resistance of this alloy.

Christie[10] has used the Avesta cell to rank different post-weld cleaning methods for type 317L and UNS S31803 in simulated aggressive bleach plant environment (*D*-stage) based on pitting potential measurements.

Also repassivation potentials based on the scratch technique have been measured with help of a somewhat modified Avesta cell (see below) by Onnela et al[23].

Jansen et al[24,25] have used the cell for characterization and ranking of austenitic stainless steels based on electrochemical noise measurements.

Experimental considerations

The presence of distilled water around the test area when performing electrochemical experiments with the Avesta cell naturally raises questions as to whether the measurement is affected by this.

Qvarfort[4] documented that the pitting potential in 0.63M NaCl solution was independent of the flow rate of distilled water in the range 1-12 ml/h. However Morach et al.[2] found that too tight a crevice opening could make the flow rate per area of crevice opening (height of crevice x length of crevice) so high that the specimen surface was flushed by distilled water which completely inhibited pitting. Our own experience is that too tight a crevice makes it difficult to keep an evenly distributed flow out of the crevice, which may lead to stagnant areas under the filterpaper, thus initiating crevice corrosion.

Another effect[2] attributed to the presence of distilled water is a contribution to the anodic current coming from the part of the specimen located under the filter paper - see figure 2. However, since this current corresponds to the passive current in a non-aggressive environment (distilled water), the effect will be seen only at very low current densities. This means that only the measured passive current is affected markedly, whereas the detection of pitting is unaffected. That the effect on the measured passive current is small is further documented by the fact that Jansen et al.[24,25] successfully

used the Avesta cell to characterize different stainless steels by measuring current spikes coming from pit initiation and repassivation in the passive region.

The dilution of the chloride solution due to the addition of distilled water has been shown by Qvarfort[4] to be insignificant for determining the pitting potential in NaCl solution of 0.1M or higher concentrations.

The original design of the Avesta cell does not involve any mechanical stirring of the solution. However, gas bubbling (N_2) is applied instead. Experiments in our lab have shown that especially the temperature on the specimen is affected by the degree of stirring. Although no actual threshold with regard to the gas flow has been found, a gas flow around 150-200 ml/min through a glass fritte has shown to give reproducible results (which has been used for all CPT's determined in our laboratory), whereas a flow around or below 25 ml/min gives a somewhat lower temperature on the specimen surface.

The actual temperature on the specimen surface compared to the solution temperature measured in the central vessel needs special attention in the case of the original Avesta cell design. This requirement is partly because of the fairly low stirring effect from the gas bubbling, which leads to a slow heat transfer from the solution to the specimen, but also because the specimen is located outside the cell - usually at room temperature. To overcome this, careful insulation of the bottom of the cell after mounting of the specimen is necessary, and calibration of the specimens surface temperature should be performed relative to the solution temperature.

Examples of measured temperatures and temperature differences while raising the solution temperature at a stepwise or constant rate are shown in figures 8-10. For the Avesta cells used in our lab, we have found a temperature difference between solution and specimen surface of less than 2°C over the whole temperature range 2-95°C, when performing a cyclic polarization of the specimen. All quoted temperatures are surface temperatures that have been obtained by calibration of the cell - a linear dependency between solution temperature and surface temperature has been found adequate to describe the system, if the cell is allowed to stand for more than 20 minutes at the test temperature before testing - see also figure 9.

Experiments with the recirculating bath having the desired temperature while the specimen is mounted, but the solution still cold, have shown, that a significant part of the heating of the specimen comes via the base of the cell from the outer heating chamber and not from the direct contact between solution and specimen - an observation that should be remembered, especially when using the Avesta cell for temperature dynamic experiments, as illustrated in figure 7.

An effective way to obtain full temperature equilibrium between the specimen and the solution would be to immerse the specimen completely. Although this is not possible in the original Avesta cell design, some modifications have been done to facilitate a full immersion.

One such modification has been published by Onnela et al.[23], and involves the mounting of the specimen in a hollow cylindrical specimen holder, which can be fully immersed in the solution (shown in figure 11) - the design was originally intended for experiments using the scratch technique. Although the design in figure 11 clearly restricts the size and form of the specimen to be tested, it still has the advantages of the original Avesta cell design including simple mounting, avoidance of crevice corrosion and testing of a single surface.

Another example where full immersion of the specimen is obtained has been developed by Mathiesen & Maahn[26,27], who have incorporated the Avesta cell principle of flushing the crevice with distilled water into the traditional electrode holder design as shown in ASTM G5. The design is shown in figure 12. The main disadvantage of this design is the use of a rod geometry for the specimen, which

means that only rod or machined thick plate specimens can be tested. A further "problem" with this traditional electrode geometry is the exposure of more than one surface of the material, thereby making differentiation of corrosion resistance between the different sections in a plate impossible.

A very effective method of minizing the temperature difference between solution and specimen would be to use a heating pad on the outside of the sample while providing for temperature monitoring and control on both the sample and the solution.

Testing of welds in the Avesta cell was first proposed by Qvarfort and Alfonsson[5] to be done by machining an annular flat around the circular unmachined test area with a diameter 0.1-0.2 mm less than the actual hole in the bottom of the Avesta cell.

However based on an idea by Agema[28], we have lately developed a method that has made it possible to test non-planar surface (welds, tubes etc.) without having to machine the specimen.

The fundamental idea is to exchange or supplement the filter paper with a thicker and more flexible material. Rings cut out from ordinary insulation material for tubes have proven to be fully adequate. Such an insulation tube has pores open in the long direction, whereas the walls on the inner side of the insulation tube have been sealed, thereby preventing distilled water from escaping. The method is illustrated in figure 13. Various samples that have been tested in the Avesta cell without any interference from crevice corrosion are shown in figure 14. For smaller variations in the surface geometry a simple planar ring as indicated in figure 13 can be used. The weld in the second row to the right in figure 14 has been tested this way. If the curvature is more significant, as for the tube and weld in the second row to the left in figure 14, the porous ring has to be cut approximately to the form of the specimen.

Although our experiences with the method still are scarce, the porous sealing seems to be simple to use and with no drawbacks. The chemical resistance of the porous material should of course be considered, but experiments with and without the "insulation" material on planar surfaces have shown no difference in the polarization curves and CPT determined in 1M NaCl solution.

Future applications (conclusion)

So far the Avesta cell as described above has been used solely for laboratory investigations where the emphasis has been on research/development. However, the operational simplicity of the cell together with today's highly automatized electrochemical equipment suggest that the cell could be used for more general testing including acceptance testing of final stainless steel end-products such as plates, sheet, strip and tubes - especially when using the Avesta cell CPT definition. This is especially so after the newly developed possibilities of testing non-planar surfaces.

Factors in favor of this approach are the extremely sharply defined potential-independent CPT, ensuring that only one specimen, in principle, is needed (although this is an extreme not recommended) to determine whether the material is above or below the CPT. Furthermore, the time involved in obtaining a single polarization curve is of the order 1-3 hours, which is much faster than the 24 hours typically used in the $FeCl_3$ test (ASTM G48, Practice A). Remembering that the definition of the Avesta cell CPT is fundamentally the same as that for $10\%FeCl_3 \cdot 6H_2O$ also speaks in favor of the Avesta cell CPT. The number of specimens that can be tested simultaneously is of course limited to the number of Avesta cells available, and for obvious reasons this will be a far smaller number than the practical number of specimens that can be tested simultaneously by simple immersion testing in $10\%FeCl_3 \cdot 6H_2O$. But the speediness with which one gets the result from the Avesta cell is still far superior to the $FeCl_3$ test.

On top of these fairly practical considerations, it should not be forgotten that the Avesta cell CPT is based on an electrochemical measurement. The polarization curve contains a lot more information than

just the pitting potential of the specimen, thereby strengthening the final evaluation of the test result compared to a simple visual examination, which always is done after pitting testing. On the other hand the need for electrochemical testing demands some fairly advanced electronic equipment, which may introduce an unwanted complexity in case of malfunction.

A final advantage of the Avesta cell compared to the $FeCl_3$ approach is the testing of a single surface avoiding all the problems associated with edge attack, that complicate the evaluation of the $FeCl_3$ test.

Another advantage of the Avesta cell is that different solutions may be used. The need for this versatility is emphasized by the development of new stainless steels such as S32654 with pitting resistance similar to nickel base alloys[18,22] like UNS N10276. Both alloys have a CPT above the boiling point in 1M NaCl solution (Avesta cell CPT) and in $10\%FeCl_3 \cdot 6H_2O$. Non-published investigations in our laboratory have indicated that bromide solutions or special chloride solutions can be used to determine an "Avesta cell CPT" for these materials.

A final "speculation" could be to develop a temperature dynamic potentiostatic method to determine the Avesta cell CPT. However such a method remains to be evaluated especially in the context of temperature equilibrium between solution and specimen as discussed above, together with an evaluation of the influence prior polarization below the CPT has on the final result.

References

1. Bombaci S.A., Taylor R.J., Corrosion **42**, 118 (1986)
2. Morach R., Schmuki P., Böhni H., Materials Science Forum, **111-112**, p. 493-506, (1992)
3. Roy D. N., Indian J. Technol., **17**, p. 319-321,(1979) August
4. Qvarfort R., Corros. Sci., **28**, 2, p. 135-140, (1988)
5. Qvarfort R., Alfonsson E., Proc. 11th Scandinavian Corrosion Congress, NKM11, Stavanger, Paper No. F-79,(1989)
6. Qvarfort R., Alfonsson E., Proc. 9th European Congress on Corrosion, Utrecht, (1989)
7. S. Brennert, J. Iron Steel Inst., **135**, p. 101, (1936); Met. Prog., **31**, p. 641, (1937)
8. M. Pourbaix, L. Klimzack-Mathieu, C. Martens, J. Meunier, C. Vanlengenhaghe, L. de Munch, J. Lareys, L. Nellmans, M. Warzee, Corros. Sci., **3**, p. 239, (1963)
9. Fielder J. W., Johns D. R., Proc. UK Corrosion 89, (1989)
10. Christie D. W., Proc. 7th Intern. Symp. on Corrosion in the Pulp and Paper Industry, Orlando, p. 87-95, (1992)
11. Szklarska-Smialowska Z., Corrosion, **27**, 6, p. 223-233, (1971)
12. Oldfield J., Int. Materials Review, **32**, 3, (1987)
13. Leckie H. P., Uhlig H. H., J. Elec. Soc., **113**, 12, p. 1262-1267, (1966)
14. Shibata T., Takeyama T., Corrosion, **33**, 7, p. 243-251, (1977)
15. Brigham R. J., Corrosion, **28**, 5, p. 177-179, (1972)
16. Brigham R. J., Tozer E. W., Corrosion, **29**, 1, p.33-36, (1973)
17. Qvarfort R., Corros. Sci., **29**, 8, p. 987-993, (1989)
18. Wallén B., Liljas M., Stenvall P., Proc. CORROSION/92-NACE, Paper No. 322, (1992)
19. Bernhardsson S., Mellström R., Brox B., Proc. CORROSION/80-NACE, Paper No. 85 Chicago, (1980)
20. Alfonsson E., Qvarfort R., Materials Science Forum, **111-112**, p. 483-491, (1992)
21. Davison R. M., Alfonsson E., Runnsjö G., Proc. CORROSION/90-NACE, Las Vegas, Paper No. 542, (1990)
22. Wallén B., Liljas M., Stenvall P., Proc. 12th Scandinavian Corrosion Congress and Eurocorr'92, Helsinki, (1992)
23. Onnela J., Forsén O., Hänninen H., Yläsaari S., Proc. 12th Scandinavian Corrosion Congress & Eurocorr '92, Helsinki, p. 151-157, (1992)
24. Jansen E. F. M., de Wit J. H. W., Proc. 12th Scandinavian Corrosion Congress & Eurocorr '92, Helsinki, p. 91-95, (1992)
25. Jansen E. F. M , Sloof W. G., de Wit J. H. W., To bee published in Proc. European Symposium on Modification of passive films and relation to the resistance to localized corrosion, Paris, (1993)
26. Mathiesen T., M.Sc. Thesis, Institute of Metallurgy, The Danish Technical University, Lyngby, Denmark, (1989)
27. Mathiesen T., Maahn E., Pamphlet in Danish, "Vejledning til Pittingelektroden", Institute of Metallurgy, The Danish Technical University, Lyngby, Denmark, (1991)
28. Agema K., KEMA, Arnhem, The Netherlands - Personal communications (1991)

Table 1 Nominal content of main alloying elements for austenitic and duplex stainless steels

UNS No.	C %	N %	Cr %	Ni %	Mo %	Others
			Austenitic stainless steels			
S30400	0.04	0.06	18.5	9	-	-
S31600	0.04	0.04	17	11	2.2	-
N08904	0.01	0.06	20	25	4.5	Cu
S31254	0.01	0.2	20	18	6.1	Cu
S32654	0.01	0.5	24	22	7.3	Cu, Mn
			Duplex stainless steels			
S32304	0.02	0.1	23	4.5	-	-
S31803	0.02	0.15	22	5.5	3	-
S32750	0.02	0.25	25	7	4	-

Table 2 Avesta cell CPT variations within grade 904L - see also figure 6. Ref. 20.

Heat No.	**CPT** °C	Si %	Mn %	Cr %	Ni %	Mo %	Cu %	N %
380124	**64**	0.35	1.57	20.16	24.78	4.30	1.51	0.035
389730	**63**	0.30	1.44	20.13	25.11	4.35	1.48	0.052
388920	**63**	0.34	1.48	19.58	24.90	4.30	1.47	0.061
388898	**62**	0.35	1.48	19.96	24.81	4.24	1.44	0.060
389339	**60**	0.38	1.46	19.83	24.96	4.34	1.50	0.061
389730-3	**63**	0.32	1.51	20.22	25.03	4.35	1.46	0.051
381197-1	**60**	0.32	1.51	19.97	24.47	4.26	1.36	0.064
382686	**59**	0.35	1.51	19.70	24.67	4.33	1.50	0.061
381254	**59**	0.36	1.46	19.89	24.96	4.27	1.45	0.062

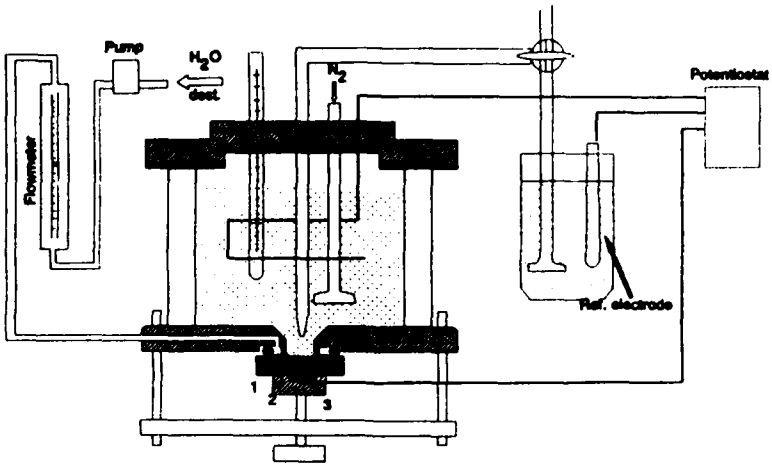

Figure 1 General design of Avesta cell set-up for electrochemical testing of stainless steels.

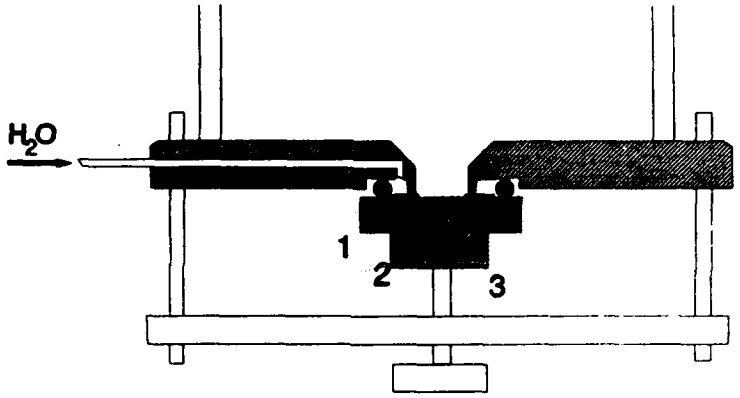

Figure 2 Crevice design at the bottom of the Avesta cell. 1) Specimen 2) Filterpaper 3) O-ring.

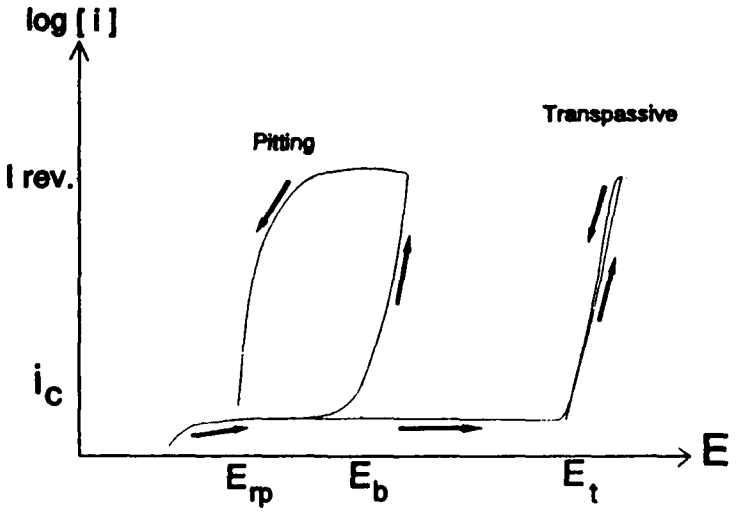

Figure 3 Polarization curve (principle). E_b: Pitting potential, E_{rp}: repassivation potential, E_t: Transpassive potential, i_c: critical current density, i-rev.: current at which scan is reversed.

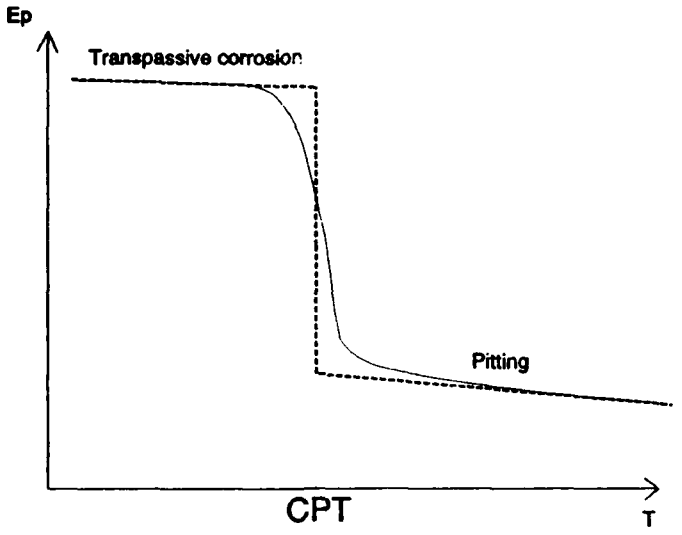

Figure 4 E_p vs. T - solid line corresponds to Brigham & Tozers[15] findings, broken line corresponds to actual relationship as argued by Brigham & Tozer[15].

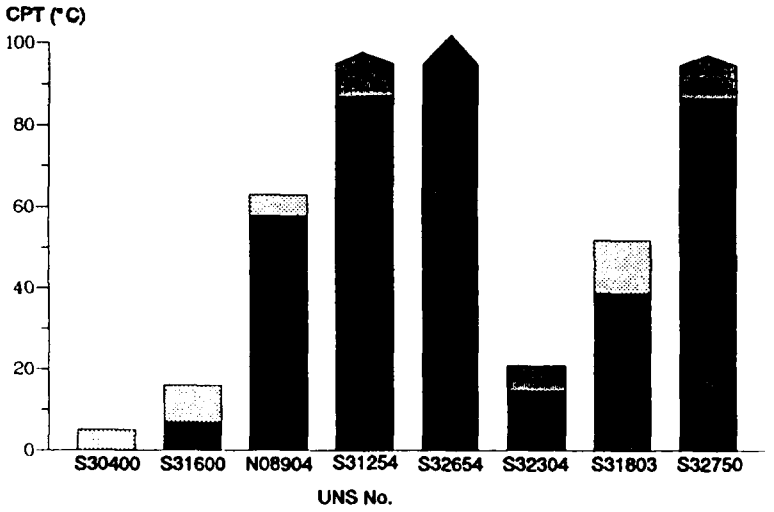

Figure 5 Avesta cell CPT's determined in 1M NaCl solution. The shaded areas indicate variations found within the same steel grade depending on the precise composition and structure of the material.

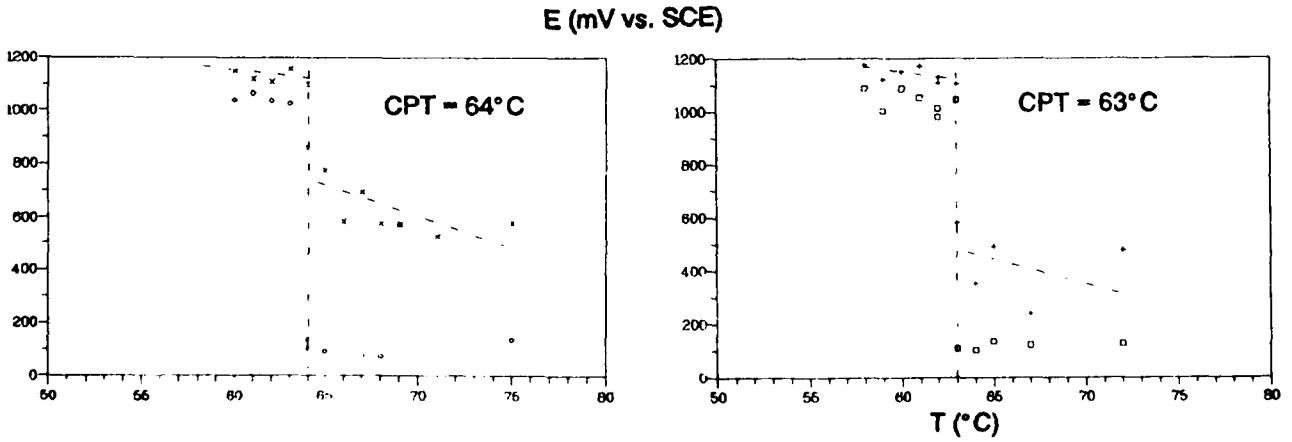

Figure 6 Determination of Avesta cell CPT for grade 904L - heat no. 380124 and 389730, table 2. x/+:E_b, pitting potentials. □/◇:E_{rp}, repassivation potentials.

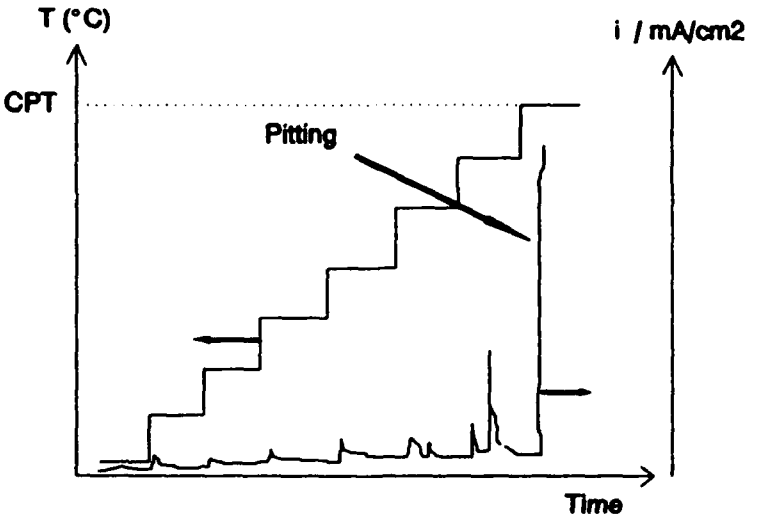

Figure 7 Determination of "CPT" at constant potential, by raising the temperature in steps and measuring the corrosion current.

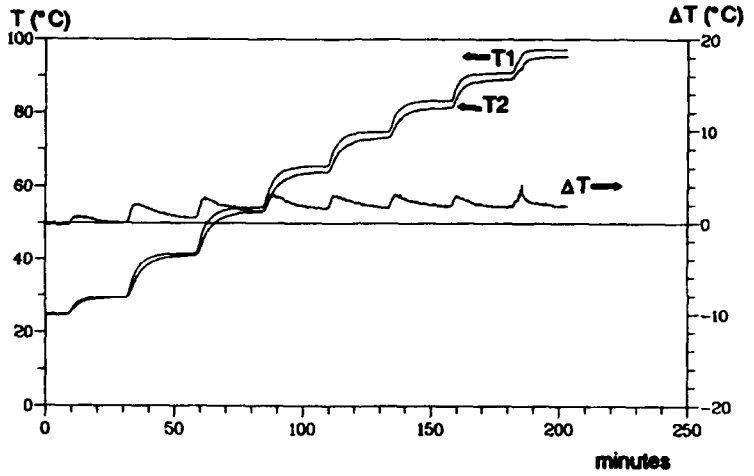

Figure 8 Temperature in solution, T1, and at specimen surface, T2, while raising the temperature in steps. ΔT=T1-T2.

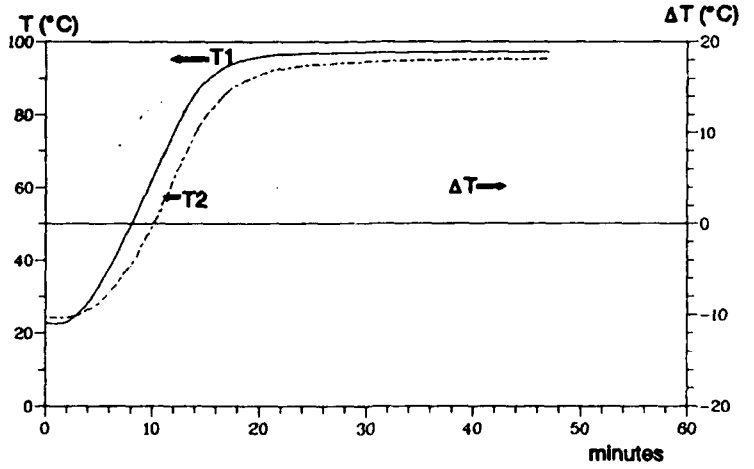

Figure 9 Temperature in solution, T1, and at specimen surface, T2, while raising the temperature fast from room temperature to max. temperature (≈97°C). ΔT=T1-T2.

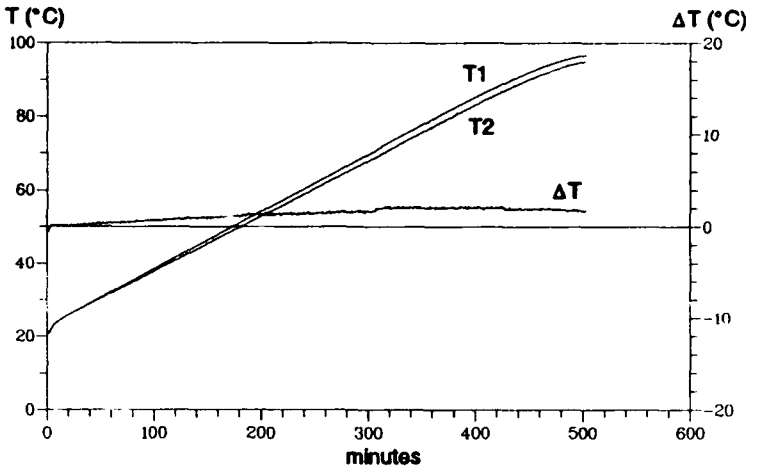

Figure 10 Temperature in solution, T1, and at specimen surface, T2, while slowly raising the temperature . $\Delta T = T1 - T2$.

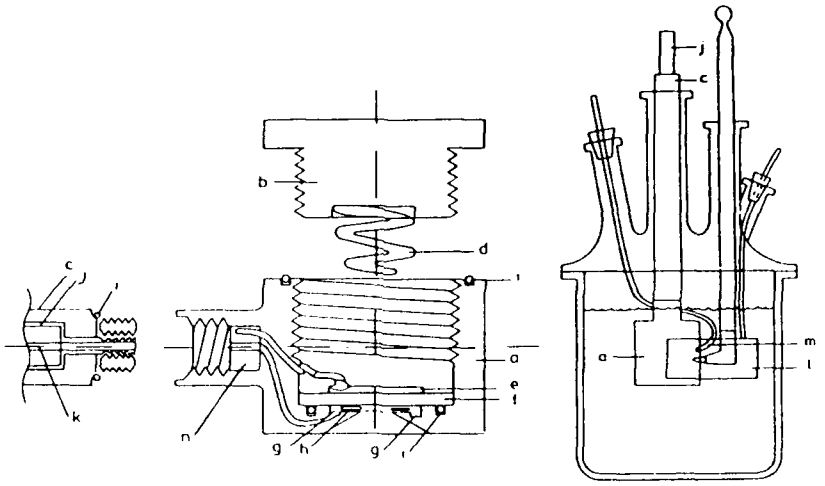

Figure 11 Schematic diagram of "Avesta cell" like electrode assembly - intended for "scratch" experiments. (a) specimen holder, (b) nut, (c) holder arm, (d) spring, (e) conduct plate, (f) specimen, (g) circular chamber, (h) filter paper, (i) O-ring seal, (j) brass tube, (k) rubber hose, (l) platinum counter electrode, (m) Luggin probe, (n) conduct plug. Ref. 23.

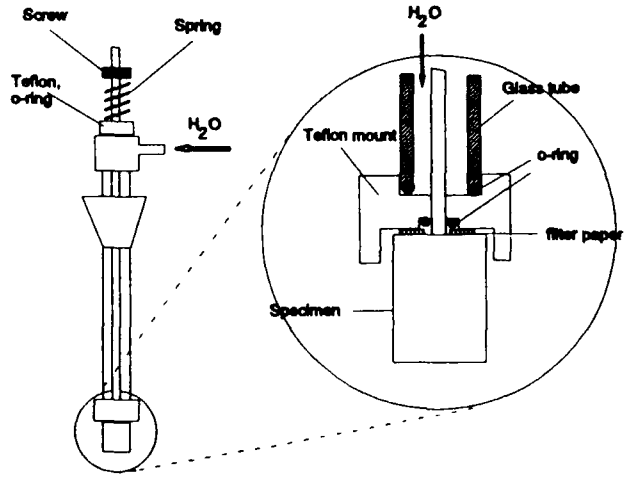

Figure 12 Modified ASTM G5 electrode holder using the Avesta cell principle of flushing the crevice with distilled water. Ref. 26,27.

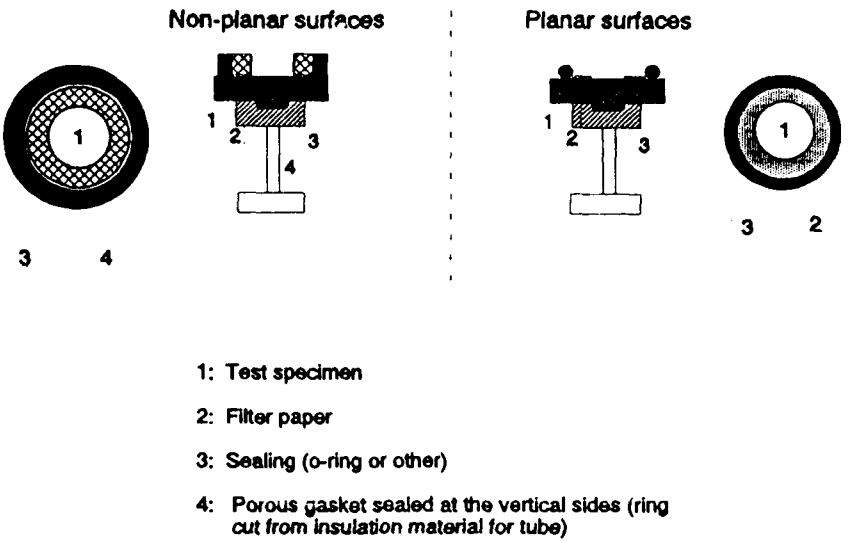

Figure 13 Sketch of sealing system for the Avesta cell for planar and non-planar surfaces.

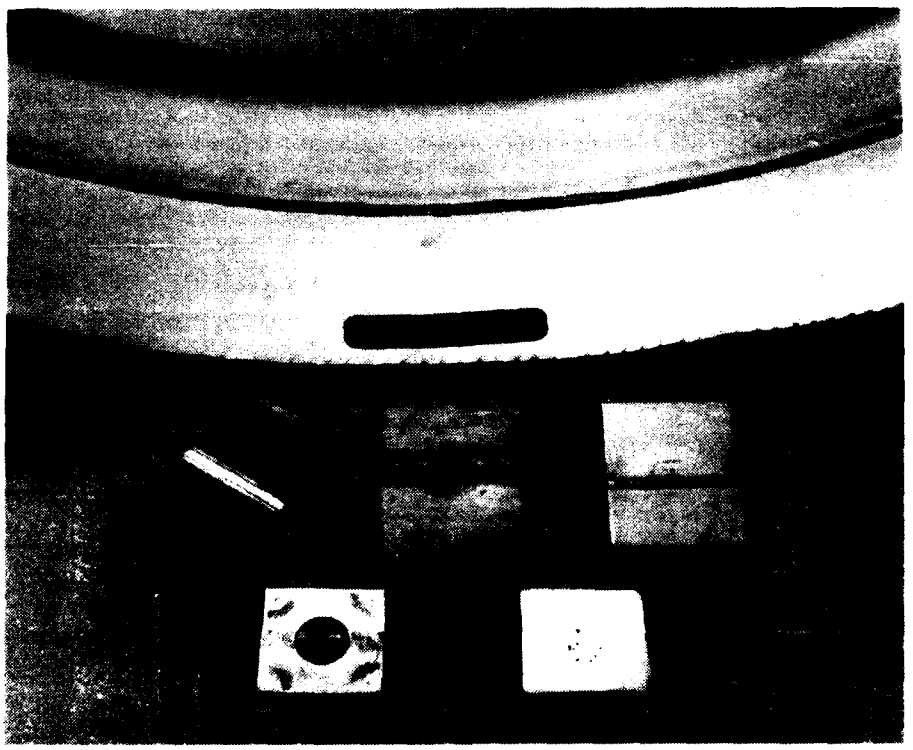

Figure 14 Samples tested in the Avesta cell. The two samples in the front line represent samples tested with filterpaper. Tube and welds in the second line have been tested by using a thick porous sealing (see figure 13).

CORROSION RESISTANCE AND BEHAVIOR OF CONSTRUCTION MATERIALS EXPOSED TO DILUTE SULFURIC ACID AT ELEVATED TEMPERATURES UNDER STATIC CONDITIONS

D. T. Nguyen
Metallurgical Engineer
National Fertilizer & Environmental Research Center
Tennessee Valley Authority
Muscle Shoals, Alabama 35660

R. D. Daniels
Professor of Metallurgical Engineering
School of Chemical Engineering and Materials Science
The University of Oklahoma
Norman, Oklahoma 73019

Abstract

Ethanol is considered a clean-burning fuel and also can be added to gasoline as an octane enhancer. Ethanol can be produced from cellulose-based materials such as crop residues, wood, forest byproducts, or waste papers by thermal-chemical hydrolysis reactions in dilute sulfuric acid at elevated temperatures. In small scale studies, highly corrosion-resistant materials such as zirconium alloys or tantalum are selected for the hydrolysis reactors. These refractory metals provide adequate corrosion performance, but their use in large scale equipment would not be practical because of their high cost. Corrosion data on high chromium-nickel stainless steels and nickel-base alloys in the hydrolysis environment are very limited. Hence, laboratory investigation has been undertaken to determine the electrochemical behavior and corrosion resistance of various construction materials in a simulated hydrolysis environment (5 wt% sulfuric acid) at temperatures ranging from 90 to 220°C under static conditions. Tests were performed in an autoclave-type electrochemical cell. The corrosion behavior of the test materials was determined using computer-controlled DC potentiodynamic polarization. Corrosion rates of the test materials were determined using AC impedance techniques.

Because of the need to limit levels of contaminants in the hydrolysis environment, only vessel materials with excellent corrosion resistance (corrosion rate of 2 mpy or less at the operating temperature) are suitable for this service. Among the stainless steels tested, only alloy N08026 (Carpenter 20Mo-6) performed satisfactory up to a temperature of 100°C. The alloy passivated spontaneously in the environment and corroded at a rate of less than 2 mpy. None of the stainless steels tested could be used at 120°C or above. A number of nickel-base alloys tested had good corrosion resistance up to 100°C, but their corrosion rate exceeded 2 mpy at higher temperatures. Zirconium alloys were satisfactory up to 180°C. Only tantalum and a tantalum-niobium alloy were satisfactory up to 220°C.

Key terms: hydrolysis environment, corrosion rates, spontaneous passivation, AC impedance tests, DC potential polarization scan tests

I. Introduction

To reduce atmosphere pollution, efforts have been made to develop cleaner burning liquid transportation fuels to partially replace or mix with gasoline. Among these, ethanol has received the most attention, and has been considered the most promising, because this alcohol can be blended with gasoline as a fuel substitute and/or an octane enhancer or it can be burned alone as a low-pollution fuel [1]. Ethanol can be produced from cellulose-based materials such as crop residues, wood, forest byproducts, or waste papers [2]. The process is carried out by chemical hydrolysis reactions in a dilute-acid environment at elevated temperatures. The feed acid may be sulfuric or hydrochloric acid. Because of lower cost, ease of handling, and availability, sulfuric acid is a more favorable reaction vehicle than hydrochloric acid.

Corrosion of construction materials for the hydrolysis reactor (hydrolyzer) is a problem because of the acid environment and elevated temperatures required for the reactions. In small scale studies, only highly corrosion-resistant materials, such as zirconium alloys and tantalum, have been selected for the hydrolysis reactors and accessories [3]. These refractory metals provide adequate corrosion performance in the hydrolysis environment, but their application is limited by their high cost and lack of availability. Currently, numerous high chromium-nickel stainless steels and nickel-base alloys are available commercially at reasonable cost. However, existing data on the corrosion resistance of these materials in the hydrolysis environment are inadequate, particularly at temperatures approaching or above the boiling point (100°C).

The objective of this study is to determine corrosion behavior of various construction materials exposed to a simulated hydrolysis environment (5 wt% dilute sulfuric acid at temperatures ranging from 90 to 220°C) by studying electrochemical potential-current relationships using DC potential scan. The general corrosion of test materials in the simulated hydrolysis environment is determined using AC impedance techniques. Results of the study provide basic information needed for proper material selection for hydrolysis reactors and associated equipment. The results also suggest that an appropriate corrosion protection should be provided, if lower corrosion resistance, but less expensive materials are considered. The materials studied include high-grade stainless steels such as N08904 (Type 904L ss), N08020 (Carpenter 20Cb-3), and N08026 (Carpenter 20Mo-6); commercially pure nickel N02200 (Nickel 200); alloy N04400 (Monel 400); alloy N01665 (Hastelloy B-2); alloy N08825 (Incoloy 825); alloy N06030 (Hastelloy G-30); alloy N08625 (Inconel 625); alloy N06022 (Hastelloy C-22); alloy N10276 (Hastelloy C-276); and refractory metals, including tantalum,

KBI-40 (a 60% Ta - 40% Nb alloy), and zirconium alloys R60705 (Zr 705) and R60702 (Zr 702). Stainless steel S31603 (Type 316L sst) was also included for comparison. Table I shows the alloy compositions, Unified Numbering System (UNS), trade name, and relative cost versus stainless steel S31603 [4]. The passivity behavior of the alloys was studied using DC potentiodynamic polarization techniques. General corrosion rates were determined using AC Impedance Spectroscopy. This technique offers many advantages such as reliable data and time saving. In addition, because it uses only a small amplitude AC signal (5 to 10 mV), the degree of disturbance to the corrosion system due to AC impedance tests is minimal, Thus, the potentiodynamic polarization scan can be performed later on the same specimen with the AC impedance testing without introducing serious error.

II. Experiment

Under conditions of high temperature and pressure, numerous difficulties arise in making electrochemical measurements. Among these are instability of the reference electrode, dissolution of the test vessel due to corrosion, current leakage, and poor pressure sealing [5]. These difficulties must be overcome or carefully controlled in order to obtain reliable and accurate data. Thus, design and fabrication of the electrochemical test cell is crucial in obtaining accurate electrochemical measurements.

The test cell consisted of a stainless steel S31603 cylinder approximately 12 in high (30.5 cm), 4 in (10.2 cm) inside diameter, and 1/4 in (0.64 cm) thick. The cell interior was lined with 1/8 in (0.32 cm) thick Teflon. The internal volume of the cell was approximately 2 liters. The cell was equipped with three identical electrode holders made of alloy S31603 sst and lined with Teflon for chemical and electrical insulation. One holder was used for the working electrode (test specimen) and located in the center of the cell. Two other holders were used for the reference and counter electrodes. These two electrodes were located at the same level, on opposite sides, and 1/2 in (1.27 cm) apart from the working electrode. All electrodes were electrically isolated from the test cell using alumina ceramics. The test cell was also equipped with a Type J thermocouple, a 2000-psig pressure gauge, and safety valves. The cell was heated using an electric furnace and the test temperature was controlled using a digital temperature controller.

Test electrodes were designed and fabricated to conform with the ASTM Standard G 3-89 [6]. All test electrodes (working, counter, and reference electrodes) consisted of a 3/8 in (0.95 cm) diameter and 0.5 in (1.27 cm) high cylindrical specimen with a total exposed area of approximately 0.82 in² (5.3 cm²). The surface of the electrodes was machined to a 600-grit surface finish. The counter and reference electrodes were made of platinum. Before a new test was begun, the exposed surfaces of these electrodes were renewed by grinding on 600-grit silicon paper and then cleaned ultrasonically in acetone to remove imperfections or deposits due to corrosion from previous tests. The tests (DC potentiodynamic and AC impedance) were conducted in accordance with ASTM Standard G 3-89. A 1-liter volume of fresh test solution was used for each test . The test solution was made using 98 wt% reagent sulfuric acid and distilled water to obtain a concentration of 5 percent by weight (wt%). After ultrasonic cleaning in acetone, the test specimen, counter, and reference electrodes were installed into the electrode holders and then immersed in the test solution. The entire test cell was heated at an average rate of 1.5°C/minute. During the test, the thermocouple was located at approximately the same level in the test cell as the test electrodes to ensure that the test temperature was uniform between these electrodes. The test temperature was controlled within ± 3°C from the temperature setpoint. After the test temperature was reached, the test specimen was allowed to stabilize in the test solution for at least 30 minutes. The AC impedance test was then conducted for approximately 3 minutes. Next, the potentiodynamic polarization test was performed on the same specimen.

The AC impedance test was conducted using an EG&G Princeton Applied Research Model 378 Electrochemical System and Model 388 AC Impedance Software. The test system consisted of a Solartron Model 1225 High-Frequency (HF) Response Analyzer, an EG&G Princeton Applied Research Model 273 Potentiostat, and a personal computer. During the test, the specimen surface was excited using an alternate cosine voltage with an amplitude of 5 to 10 millivolts (mV) and a frequency spectrum of from 0.1 hertz (Hz) to 100 kiloHertz (KHz). Tests were performed repeatedly for five cycles. Test results are average data of these five test cycles. The test results were presented in the form of Nyquist plot (-Z'' vs. Z'), and Bode magnitude plots (log Z vs. log f), and Bode phase plots (log f vs. log f) in which Z is impedance of the corrosion system and f is signal frequency. The polarization resistance, R_p, which is inversely proportional to the corrosion rate, was determined from the diameter of the Nyquist semicircle. Th corrosion current density and corrosion rate of the test specimen were calculated from the value of R_p by thefollowing equations:

$$i_{cor}(\mu A/cm^2) = 1x10^6 \cdot B_a \cdot B_c / [2.3 \cdot (B_a + B_c) \cdot R_p \cdot A] \quad (1)$$

$$Rate(mpy) = 0.13 \cdot EW / (d \cdot i_{cor}) \quad (2)$$

Where i_{cor} is corrosion current density, $\mu A/cm^2$; R_p is polarization resistance, ohm; B_a and B_c are Tafel slopes, mV; d is alloy density, g/cm^3; mpy is mils (0.001 in) per year; A is exposure area of the specimen, m^2; EW is equivalent weight, g/eq. Approximate values of B_a and B_c were selected to be equal to 100 mV for all test materials, the corrosion rate could be calculated from the value of R_p using the following relationship:

$$Rate\ (mpy) = 2826 \cdot EW / (d \cdot A \cdot R_p) \quad (3)$$

Following AC impedance tests, anodic polarization tests were performed by scanning the surface potential of the test specimen from about -250 mV to 1600 mV versus the corrosion potential, Ecor, (or to a current density of 10^4 $\mu A/cm^2$) at a scan rate of 0.17 mV/s (0.6 V/hour). The test was conducted using an EG&G Princeton Applied Research Model 273 Potentiostat and EG&G Princeton Applied Research Model M342C Electrochemical Software in conjunction with a personal computer. Test data are presented in the form of specimen surface potential E (mV) versus specimen current density i ($\mu A/cm^2$) in semi-log scale. Passivity and corrosion behavior of the test materials were determined using the values of the corrosion potential, E_{cor}; the primary passivation potential, E_{pp}; the breakdown potential, E_b; the critical passivation current density, I_c; the passive current density, i_p, and the shape of the anodic polarization curve.

III. Results

Tables II and III give the results of the AC impedance and DC potentiodynamic polarization tests. AC impedance test data include R_p (polarization resistance) and calculated corrosion rates in mils/year (mpy). The passivation behavior of the test materials is given in the terms of E_{cor} (corrosion potential), i_c (critical passivation current density), i_p (passive current density), E_{pp} (primary passivation potential), and E_b (breakdown potential). The test potential was measured relative to an in-situ platinum electrode (mV/Pt) and current density was measured in μA/cm². Figures 1 to 4 show the anodic polarization of the test materials at various temperatures. Figure 5 shows the equivalent circuit models of various corrosion mechanisms on the test metal exposed to the test solution. Figures 6 to 12 show AC impedance plots of representative materials.. Due to severe corrosion, tests were not performed on alloys S31603 and N02200 at temperatures above 120°C and on other stainless steels and nickel- based alloys at temperatures above 140°C.

A. Stainless Steels

AC impedance test results revealed severe corrosion of alloy S31603 at all test temperatures. Corrosion increased to excessively high levels with increase in temperature. The metal corroded at 79 mpy at 90°C, at 100 mpy at 100°C, and at 1000 mpy at 120°C. Observation of the potentiodynamic polarization test showed stable passivation of alloy S31603 at 90 and 100°C. The critical current, i_c, of S31603 was approximately 800 and 400 μA/cm² at 90 and 100°C, while the passive current density , i_p, was about 2.5 μA/cm² at both temperatures. The primary passivation potential, E_{pp}, was approximately -750 mV/Pt at 90°C and -712 mV/Pt at 100°C. The breakdown potential, E_b, was approximately 90 mV/Pt at 90°C and 263 mV/Pt at 100°C. At 120°C, passivation was not stable, because i_c and i_p were high, 4,000 and 10 μA/cm², respectively. The passive range was narrow.

Due to higher chromium and nickel content, alloy N08904 showed better corrosion resistance and more stable passivation than alloy S31603. The results of the AC impedance tests showed that the metal corroded at a rate of approximately 10 mpy at 90°C, 15 mpy at 100°C, and 26 mpy at 120°C. However, the metal corroded excessively, with a rate exceeding 6,000 mpy, at 140°C. Potentiodynamic polarization results showed stable passivation at 90, 100, and 120°C. The stabilized corrosion potential was -812, -713, -337, and -383 mV/Pt at 90, 100, 120, and 140°C, respectively. The E_{pp} and E_b values were -710 and 90; -678 and 264; -325 and 300 mV/Pt; and -344 and 250 mV/Pt at 90, 100, 120, and 140°C, respectively. The i_c and i_p values at 90, 100, 120, and 140°C were 250 and 2.5; 210 and 2.5; 300 and 10; and 2000 and 100 μA/cm², respectively.

Alloy N08020 behaved similarly to alloy N08904 when exposed to 5 wt% sulfuric acid. The corrosion of the alloy increased as the test temperature was increased. At 90, 100, and 120°C, the alloy corroded at rates of 12, 19, and 51 mpy, respectively. At 140°C, the alloy corroded at a rate exceeding 5,000 mpy. Observation of the anodic polarization curves indicated that alloy N08020 exhibited stable passivation at temperatures up to 100°C. Passivation was less stable and protective when the test temperature was increased to 120 and to 140°C. The stabilized corrosion potentials of alloy N08020 were -790, -726, -388, and -329 mV/Pt at temperatures of 90, 100, 120, and 140°C. The E_{pp} and E_b values were -710 and 290, -637 and 263, -375 and 450 mV/Pt, at 90°, 100°, and 120°, respectively. The i_c and i_p values were 300 and 3.0; 300 and 2.5; and 800 and 15 μA/cm² at 90, 100, and 120°C, respectively. At 140°C, there was no clear passivation of alloy N08020. The i_p value was extremely high, 1,000 μA/cm². The E_{pp} and E_b values coul not be identified on the anodic polarization curves.

Among the stainless steels tested, only alloy N08026 showed excellent corrosion resistance at 90 and 100°C. General corrosion of the test metal calculated from the AC impedance data was approximately 0.4 and 1 mpy at 90 and 100°C, respectively. As test temperature was increased to 120 and 140°C, general corrosion of alloy N08026 increased significantly to 10 and 261 mpy, respectively. Similar to general corrosion, the passivation of alloy N08026 was strongly affected by test temperatures. The passivation was stable and spontaneous at 90°and 100°C; however, passivation was less stable and protective at 120 and 140°C. The metal corroded in the passive range when exposed to 5 wt% sulfuric acid at 90 and 100°C, because the corrosion potential was more active than E_{pp}. The E_{cor}, Epp, and E_b values of alloy N08026 were -610, -660, and 290 mV/Pt at 90°C; -626, -637, and 36 mV/Pt at 100°C; -389, -450, and 300 mV/Pt at 120°C; and - 344, -450, and 250 mV/Pt at 140°C. The i_c and i_p value also increase as temperature was increased. At 90°C, i_c could not be determined due to spontaneous passivation and E_{pp} was more active than the low end of the test range. At 100, 120, and 140°C, i_c and i_p values were 10 and 2 μA/cm²; 900 and 10 μA/cm²; and 800 and 20 μA/cm², respectively.

B. Nickel and Nickel-base Alloys

Nickel N02200 (commercially pure nickel, Nickel 200) was selected for testing, because of its good corrosion resistance in reducing environments. AC impedance tests showed that corrosion of N02200 was high in 5 wt% sulfuric acid at all test temperatures. Corrosion rate increased to excessively high values when test temperature was increased. Metal N02200 corroded at rates of approximately 12, 88, and 166 mpy at 90, 100, and 120°C, respectively. Nickel did not passivate in the test solution. Active behavior was a characteristic of nickel corrosion. Alloy N04400 (30% Cu-70% Ni) is also a common corrosion-resistant material used in reducing environments. In this test series, the metal showed excellent corrosion resistance when exposed to 5 wt% sulfuric acid at 90°C with at a rate of only 2 mpy. Increase in the test temperatures accelerated general corrosion of alloy N04400 in the test solution. The metal corroded at rates of 4, 16, and 674 mpy when temperature was increased to 100 , 120, and 140°C. Similar to metal N02200, alloy N04400 did not passivate in 5 wt% sulfuric acid.

When exposed to reducing environments, alloy N10665 (28% Mo-69% Ni alloy) has shown superior corrosion resistance at temperatures up to the boiling point. AC impedance test results showed that alloy N10665 corroded at rates of 1 and 2 mpy in 5 wt% sulfuric acid at 90 and 100°C, respectively. When the temperature was increased to 120 and 140°C, the metal corroded at rates of 15 and 299 mpy, respectively. Because no chromium is present, alloy N10665 did not passivate in 5 wt% sulfuric acid at any test temperature. The metal exhibited active dissolution behavior.

The test results on alloys N08825 and N06030 indicated that Ni-Cr-Mo-Fe alloys exhibited excellent corrosion resistance when tested at temperatures of 90 and 100°C. These alloys corroded at rates of less than 1 mpy. However, general corrosion increased significantly when the test temperature was increased above 100°C. Alloys N08825 and N06030 corroded at rates of 9 and 8 mpy at 120°C and at rates of 296 and 91 mpy at 140°C, respectively. Anodic polarization showed that both alloys N08825 and N06030 passivate spontaneously and stably in 5 wt% sulfuric acid at temperatures up to 120°C. Observation of anodic polarization indicate that alloy N08825 corrodes in the passive range at 90 and 100°C, while alloy N06030 corrodes in the passive range to 120°C. The corrosion potential of these materials was more noble than E_{pp}. At 120°C, alloy N08825 corroded in the active range because the corrosion potential was more active than E_{pp}. At 140°C, corrosion of both alloys N08825 and N06030 occurred in the active range. Because of low iron and high molybdenum content, alloy N06030 exhibits more stable passivation and corrosion resistance than alloy N08825 in 5 wt% sulfuric acid. The E_{pp} values of alloys N08825 and N06030 could not be determined because they were more active than the low end of the potential scan at temperatures of 90 and 100°C, respectively. At 120 and 140°C, the E_{pp} of alloys N08825 and N06030 was -275 and -375 mV/Pt. Both metals had the same E_b of 290 and 363 mV/Pt at 90 and 100°C, respectively. At 120 and 140°C, the E_b values of alloy N08825 were approximately 600 and 300 mV/Pt, respectively, while E_b values of alloy N06030 were 500 and 100 mV/Pt, respectively. Similar to general corrosion behavior, i_c and i_p of both test alloys increased with the temperature. The i_p values of alloy N08825 were 2.5, 3, 10, and 100 μA/cm² at 90, 100, 120, and 140°C, respectively. The i_p values of alloy N06030 were 1.5, 1.0, 9, and 60 μA/cm² at 90, 100, 120, and 140°C, respectively. Due to spontaneous passivation at 90°C, the i_c values of both alloys N08825 and N06030 could not be determined. At 100°C, the i_c of alloy N08825 was 170 μA/cm², while the i_c of alloy N06030 was still not evident at 100°C. At 120 and 140°C, the i_c values of alloy N08825 were 100 and 400 μA/cm² and the i_c values of alloy N06030 were 105 and 1,000 μA/cm², respectively.

In the AC impedance tests, all three alloys N08625 (22% Cr-9% Mo-5% Fe-62% Ni), N06022 (22% Cr-10% Mo-2% Nb-3% W-53% Ni), and N10276 (16% Cr-16% Mo-5.5% Fe-4% W-57% Ni showed excellent corrosion resistance to 5 wt% sulfuric acid solution at 90 and 100°C. Corrosion rates of these test alloys were approximately 0.1 to 0.3 mpy. These alloys passivated spontaneously in the test solution at both 90 and 100°C. The passive current density of alloys N08625, N06022, and N10276 did not exceed 2.5 μA/cm². All three alloys corroded in the passive range. Corrosion increased significantly when the test temperature was increased to 120 and 140°C. Corrosion rates measured using AC impedance tests were 11 and 59 mpy for alloy N08625 at 120 and 140°C, respectively, 7 and 129 mpy for alloy N06022 at 120 and 140°C, and 6 and 147 mpy for alloy N10276 at 120 and 140°C. Passivation of these test metals shifted in the direction favoring increased corrosion. The i_p of alloys N08625, N06022, and N10276 shifted from values as low as 1.0 to 3.0 μA/cm² at 90 and 100°C, to the values as high as 10, 20, and 8 μA/cm² at 120°C, and to values as high as 50, 100, and 300 μA/cm² at 140°C. Both Epp and Eb shifted greatly with increase in temperature. At 90°C, the E_{pp} of alloys N08625, N06022, and N10276 was more active than the low end of the test range . At 100°C, the E_{pp} of alloys N06022 and N10276 was still undetectable, but the Epp value of alloy N08625 was approximately -637 mV/Pt. At 120 and 140°C, the E_{pp} values of alloys N08625, N06022, and N10276 were -200, -500, -350 mV/Pt; and 0, -275, and -250 mV/Pt, respectively. Similarly, the E_b values of alloys N08625, N06022, and N10276 were 290, 190, and 240 mV/Pt at 90°C. At 100°C, the E_b values of alloy N08625, N06022, and N10276 were 313, 363, and 363 mV/Pt. At 120°C and 140°C, the E_b values of N08625, N06022, and N10276 were 600, 550, and 400 mV/Pt; and 400, 600, and 400 mV/Pt, respectively.

C. Refractory Metals

Zirconium alloys R60705 and R60702 showed excellent corrosion resistance in 5 wt% sulfuric acid over a wide temperature range. Alloy R60705 corroded at rates less than 1 mpy up to 140°C. The alloy corroded at rates of 1 and 2 mpy at 160 and 170°C, respectively. The corrosion rate of alloy R60705 increased to 4 , 5, 7, 13, and 20 mpy when temperature was increased to 180, 190, 200, 210, and 220°C, respectively. Due to lower impurity content, Alloy R60702 showed superior corrosion resistance over alloy R60705. The alloy corroded at less than 1 mpy at temperatures up to 170°C. The alloy corroded at rates of approximately 2 and 3 mpy at temperatures of 180 and 190°C. Corrosion rate of alloy R60702 increased to 4, 6, and 7 mpy when the test temperature was increased to 200, 210, and 220°C.

AC impedance test results showed that KBI-40 (40% Nb-60% Ta) exhibited excellent corrosion resistance to 5 wt% sulfuric acid at test temperatures up to 200°C. KBI-40 corroded at rates less than or equal to 1 mpy at temperatures up to 200°C. The corrosion rate of KBI-40 increased slightly to 2 to 3 mpy at temperatures ranging from 210 to 220°C. Of all materials tested, tantalum exhibited the best corrosion performance in 5 wt% sulfuric acid. Tantalum maintained an extremely low general corrosion rate . At temperatures up to 200°C, the corrosion rate of tantalum did not exceed 0.1 mpy. Corrosion of tantalum increased slightly at temperatures of 210 and 220°C. The corrosion rate was approximately 1 mpy.

DC potential polarization results indicated that the passivation of all four refractory metals, alloys R60705, R60702, KBI-40, and tantalum was stable and spontaneous in 5 wt% sulfuric acid at all test temperatures. The corrosion of these alloys occurred completely within the passive range. The corrosion potential of these metals was always more noble than the E_{pp}. The i_p values of alloy R60705 were between 1.5 to 3.5 μA/cm² at the test temperatures up to 170°C. The i_p values of R60705 increased to 5, 15, 30, 100, and 100 μA/cm² when temperature was increased to 180, 190, 200, 210, 220°C, respectively. The ip values of alloy R60702 were less than 3 μA/cm² at temperatures below 170°C, and 3, 5, 8, 10, and 10 μA/cm² when temperature was increased to 180, 190, 200, 210, and 220°C, respectively. The i_p values of tantalum were less than or approximately 1 μA/cm² at temperatures below 200°C, and 2 to 3 μA/cm² at 200 to 220°C, respectively. The ip values of KBI-40 were less than or approximately 2 μA/cm² at temperatures below 190°C, and 3, 5, 8, and 10 μA/cm² at 190, 200, 210, and 220°C, respectively. In the potential range tested, the Eb values could not be detected at temperatures up to 190°C on alloy R60705 and 702, up to 200°C on KBI-40 and tantalum. At temperatures above 200°C, the Eb values of these refractory metals were found on the anodic polarization curves, but were as high as 1400 to 1700 mV/Pt. Similar to the values of E_b , the Epp of these alloys could not be detected in the test range. Because the passivation of these metals was stable and spontaneous, the i_{pp} values for these alloys could not be detected on the anodic polarization curves at any test temperature.

IV. Discussion

Due to the severe conditions in the hydrolysis reactors, the presence of heavy-metal ions may inhibit or impair the internal chemical reaction kinetics [3]. More specifically, soluble chromium has been found to accelerate degradation of glucose in hot acidic solution. Moreover, contamination of hydrolysis residues by heavy metals may lead to serious environmental problems. Therefore, severe corrosion of the hydrolysis reactor metal is unacceptable. Thus, selection of materials for the hydrolysis reactors should be limited to metals with excellent corrosion resistance, i.e., with general corrosion rates of 2 mpy or less. For passive metals, th passivation should be stable (low critical and passive cerrent density) and spontaneous (metal corrodes in the passive range or corrosion potential must be more noble than the Epp). The passive current density should be equivalent to a corrosion rate not exceeding 2 mpy.

A. Stainless Steels

At 90° and 100°C, the results of the AC impedance tests showed that alloys S31603, N08904, and N08020 have a poor to fair corrosion resistance. These alloys are unsatisfactory for hydrolysis service at these temperatures. Potentiodynamic polarization analysis revealed that all of these stainless steels tested passivate stably in 5 wt% sulfuric acid solution over a wide potential range, approximately 900 mV, and at low passive current densities, 3 μA/cm² or less. Thus, an average corrosion rate of less than 2 mpy is achieved if these metals remain in the passive range. However, the passivation of these stainless steels was not spontaneous. These alloys corroded in the active range, because the most stable corrosion potential, the potential recorded after the stabilization, was more active than the primary passive potential. In addition, several corrosion potentials were indicated by the shape of the polarization curves (Fig. 1). This indicated that these stainless steels would corrode preferentially in the active or active-passive range. Passive corrosion is obtained on these stainless steels only when they are potentiostatically polarized to a corrosion potential into the passive range. The initial current density required for complete polarization must exceed the alloy i_c, but the current density required to maintain passivation is equal to i_p. This technique is known as anodic protection. Examination of the anodic polarization curves showed that a higher initial current density is required for alloy S31603 than for alloys N08904 and N08020 in order to achieve the anodic protection. Because of its higher molybdenum content, alloy N08026 showed superior corrosion resistance compared to alloys S31603, N08904, or N08020. At 90 and 100°C, the resistance to general corrosion alloy N08026 was excellent. The alloy corroded at very low rates, 0.1 at 90°C and 1 mpy at 100°C. The alloy exhibited stable passivation at a low passive current density, 1.5 to 2.0 μA/cm² . Because the corrosion potential was more noble than the primary passive potential, N08026 passivated spontaneously and corroded in the passive range. No corrosion protection is needed for N08026 at temperatures near the boiling point. At 120°C, all four stainless steels corroded at excessive rates. No alloy of this class is satisfactory for hydrolysis service. Although passivation was observed on these test alloys, the passive and critical current densities were high, and the passivation range was narrow. Thus, anodic protection would be difficult and uneconomical under these conditions.

The results of AC impedance analysis revealed that all stainless steels tested corroded under activation control kinetics. AC impedance Nyquist plots of the corrosion system contained only one semicircle (Figure 6). The AC impedance Bode plots also showed this evidence (Figure 6). The electrical model of the equivalent circuit for the corrosion interface should consist of a single RC-parallel component in series with the ohmic resistance. The parallel resistance is the polarization resistance, R_p, and the capacitance is the double layer capacitance, C_d, of the electrode interface. Typical circuit model of the corrosion system for the stainless steels tested is shown in Figure 5a.

B. Nickel and Ni-Cu Alloy

Without addition of alloying elements, alloy N02200 (commercial pure nickel) showed fair corrosion resistance in 5 wt% sulfuric acid at 90°C and poor corrosion resistance at 100 and 120°C. Thus, alloy N02200 is unsatisfactory for hydrolysis service at temperatures near or above 90°C. Because of the high copper content, corrosion performance of alloy N04400 (30%Cu-70%Ni alloy) is better than nickel in 5 wt% sulfuric acid. Monel showed excellent resistance at 90°C. However, corrosion of alloy N04400 increased as temperature increased. Corrosion resistance of alloy N04400 shifted from excellent (2 mpy) at 90°C, to good (4 mpy) at 100°C, to fair (16 mpy) at 120°C, and to poor (674 mpy) at 140°C.

Potentiodynamic polarization test results indicate that neither alloy N02200 nor alloy N04400 shows passivity. Both anodic and cathodic polarizations of alloy N02200 and alloy N04400 exhibited classic Tafel behavior. At all test temperatures, an almost vertical-slope segment was observed on the cathodic polarization curves of alloy N04400, but no similar segment was seen on alloy N02200 (Figures 1 and 2). This behavior indicates that diffusion of cathodic species is a rate controlling step in the corrosion of alloy N04400, but not in N02200. Transport of reactant species through the thick film of corrosion products was attributed to diffusion. The increase of alloy N02200 and alloy N04400 corrosion with temperature was also evidenced by shifting of the alloy polarization curves in the direction of increased current density as the test temperatures was increased.

The AC impedance analysis showed that both N02200 and N04400 corroded with one corrosion system controlled by activation kinetics. This is indicated by single semicircle in Nyquist plots (Figure 7). AC impedance equivalent circuit model for alloy N02200 and alloy N04400 are also shown in Figure 6a. In contrast to the DC potentiodynamic polarization tests, no evidence of diffusion was found in the corrosion of alloy N04400 using the AC impedance tests at any test temperature (Figure 7). In DC polarization tests, significant potential shift is involved. As a result, the rate of consumption of cathodic species is high. Thus, diffusion is normally required to replenish the reaction species. If such diffusion is slow, it becomes the controlling process in the course of corrosion. A small variation of the cathodic current density creates a large shift of the surface potentials at cathodic sites. As a result, a high slope segment is normally observed on the cathodic polarization scan. Because AC impedance tests are performed normally with very low amplitude signals, only very minor potential shifts from the steady-state potential are involved. Thus, the consumption rate of cathodic species is less severe and transport corrosive species may not be the controlling process. If diffusion is a primary consideration under conditions of free corrosion (corrosion occurring at the corrosion potential), such as when corrosion occurs

underneath heavy deposits of corrosion products where transport of oxygen to the corrosion sites is the controlling step, then diffusion is likely to be found in both the DC potential polarization and AC impedance tests. The negative impedance observed on N04400 at the high frequencies when tested at 140°C indicated the corrosion cell behaved as an inductance circuit (Figure 7). The inductance behavior may be caused by the deposit of thick scales on the electrode surface under conditions of severe corrosion.

C. Ni-Mo Alloy

Only alloy N10665 (28% Mo-69% Ni alloy) is available as a commercial alloy in this class. Process experience indicated that Alloy N10665 has excellent resistance to corrosion in reducing acids such as hydrochloric and dilute sulfuric acids at moderate temperatures [7]. The AC impedance test showed that alloy N10665 had excellent corrosion resistance to 5 wt% sulfuric acid at 90 and 100°C. Corrosion rates were 1 to 2 mpy. The corrosion rate increased significantly to 15 and 299 mpy when temperatures were increased to 120 and 140°C. Similar to test results on N02200 and N04400, alloy N10665 did not passivate in the 5 wt% sulfuric acid solution. The anodic polarization curves exhibited a classical Tafel relationship. An increase in alloy N10665 corrosion was evidenced by shifting of the alloy polarization curves in the direction of increased current density. Only one semicircle was observed on the Nyquist plots of alloy N10665 at temperatures below 140°C. At 140°C, the AC Impedance data points diverged and scattered randomly. This was attributed to the rapid change of the corrosion potential and the instability of the corrosion system at high temperatures.

D. Ni-Cr-Mo-Fe Alloys

The two representative alloys of this class selected for testing were alloy N08825 (22% Cr-29% Fe-3% Mo-42% Ni) and alloy N06030 (30% Cr-15% Fe-5.5% Mo-43% Ni). With higher chromium and lower iron content, alloy N06030 is expected to corrode less severely than alloy N08825 in the 5 wt% sulfuric acid solution. At 90°C, both materials exhibited excellent resistance to corrosion. Examination of anodic polarization curves showed stable passivation of alloys N06030 and N08825, with low passive current densities, 1.5 and 2.5 $\mu A/cm^2$, respectively (Fig. 1). Both alloys passivated spontaneously and corroded in the passive range when tested at 90°C because the corrosion potential was more noble than the primary passivation potential, Epp. The Epp was not found in the anodic polarization measurements for either alloys at 90°C because it was more active than the low end of the test range. The breakdown potential of both alloys was approximately 290 mV/Pt. Similar results were observed when these alloys were tested at 100°C. Both test materials showed excellent corrosion resistance with corrosion rates of less than 1 mpy. Stable passivation was also found in both test materials with low passive current densities, 3 $\mu A/cm^2$ for alloy N08825 and 1 $\mu A/cm^2$ for alloy N06030. Both alloys had a breakdown potential of 363 mV/Pt.

Corrosion increased significantly when the alloys were tested at 120°C. Both alloys N06030 and N08825 showed fair corrosion resistance with corrosion rates of 8 to 9 mpy. Although passivation was still observed on these alloys, it was less stable and protective because the passive current density was relatively high, 9 to 10 $\mu A/cm^2$ (Fig. 2). The corrosion potential of alloy N08825 became more active than the Epp. This indicated that corrosion of the alloy shifted completely to the active region. At 120°C, corrosion of alloy N06030 still remained in the passive range. Since, the corrosion potential was more noble than Epp. However, the corrosion rate was high because alloy N06030 passivated at a high passive current density. Moreover, the corrosion potential of alloy N06030 was only slightly more noble than the Epp, approximately 45 mV. Thus, alloy N06030 could easily corrode in the active or active-passive region. General corrosion of both alloys N08825 and N06030 was high at 140°C. The rates were in the hundreds of mpy. Passivation of these two alloys was unstable and unprotective. The passive range was narrow and i_c was exceedingly high, approximately 50 $\mu A/cm^2$ for alloy N06030 and 100 $\mu A/cm^2$ for alloy N08825.

The AC impedance data indicated that N06030 and N08825 corroded by activation- controlled kinetics at most test temperatures. The Nyquist plot of the test materials had only one semicircle which corresponds to one RC-parallel circuit (Fig. 8). An exception was the corrosion of alloy N06030 at 120°C. The AC impedance Nyquist plot consisted of two semicircles (Fig. 8). One semicircle appeared in the high frequency band while the other one appeared in the low frequency band. When the corrosion potential of a passive alloy approaches the primary passivation potential, the alloy may corrode in the active-passive region. As a result, more than one electrically stable corrosion system can occur on the same electrode surface. Thus, multiple semicircles are likely to be found in the Nyquist plots. Attributed to the difference in electrochemical behavior, each corrosion system responds to a specific frequency range. The corrosion system with fast kinetics appears at the high frequencies while a corrosion system with a low corrosion rate appears at the low frequencies. Figure 5c shows a composite circuit model of the corrosion system with multiple mechanisms such as those observed on alloy N06030 at 120°C. At higher test temperatures, the rapid change of the corrosion potential caused AC impedance measurements at the low frequencies to be highly unstable. This behavior explains the dispersion of data points in both the Nyquist and Bode plots at high temperatures (Fig. 8).

E. Ni-Cr-Mo Alloys

Alloys N08625 (22% Cr-5.0 Fe-9% Mo-4% Nb-62% Ni) , N06022 (22% Cr-10% Mo-2% Nb-3% W-53% Ni), and N10276 (16% Cr-5.5% Fe-16% Mo-4% W-57% Ni) were selected in this class of alloys. In the chemical process industry, these alloys have shown excellent corrosion resistance to various acid environments [7]. Similar to results of the Ni-Cr-Mo-Fe alloys, these test materials exhibited excellent corrosion resistance at temperatures approaching 100°C. The alloys corroded at rates less than 1 mpy. AC impedance analysis showed that corrosion resistance of these alloys shifted to fair and to unsatisfactory as test temperatures were increased to 120 and 140°C, respectively.

Potentiodynamic polarization tests showed that the Ni-Cr-Mo-W alloys passivated in the same manner as the Ni-Cr-Mo-Fe alloys in 5 wt% sulfuric acid. Passivation was stable and occurred spontaneously in 5 wt% sulfuric acid at 90 and 100 °C (Fig. 1). The passive current density of these alloys was low, 1.5 to 2.5 $\mu A/cm^2$. As test temperature increased, passivation of these alloys shifted toward conditions favorable for higher corrosion rates. Passivation was neither stable nor protective at 120°C, because the values of

i_{pp} and i_c are high. The i_c values of these alloys were approximately 4 to 5 times higher than those observed at 90° and 100°C. At 140°C, the i_p values of all three alloys were unacceptably high, 50 μA/cm² and higher. Therefore, anodic protection would not be feasible under these conditions.

AC impedance spectroscopy data on alloys N08625, N06022 and N10276 indicated that the Nyquist plots consisted of one semicircle at most test temperatures. Thus, the equivalent circuit of the corrosion system for these alloys consists primarily of one RC-parallel circuit, and activation-control is the primary kinetic mechanism. The exceptions were the corrosion of alloy N08625 at 120°C. The Nyquist plot consisted of two semicircles (Fig. 9). This behavior indicates that two stable corrosion systems are present. Thus, the equivalent circuit model consists of two RC-parallel circuits in series as shown in Figures 5c.

F. Zirconium Alloys

Tests were conducted on two zirconium alloys R60705 and R60702. R60705 grade contains approximately 91 wt% zirconium (Zr), 4.5 wt% hafnium (Hf), and 3 wt% manganese (Mn). Zirconium 702 is purer and contains approximately 95 wt% Zr, 4 .5 wt% Hf, and no Mn. Because of its purity, R60702 normally exhibits better corrosion resistance than R60705 in most corrosive environments. However, R60705 is slightly less expensive than R60702. Generally, zirconium alloys are excellent corrosion-resistant materials when exposed to reducing environments, particularly hydrochloric acid and sulfuric acid solutions.

AC impedance tests revealed that both zirconium alloys showed excellent corrosion resistance to the 5 wt% sulfuric acid solution at temperatures up to 170°C. The corrosion rate was less than 1 mpy. Impedance of both alloy corrosion systems was extremely high, over several kiloohms. At 180°C, alloy R60702 still showed excellent resistance to general corrosion in the 5 wt% sulfuric acid solution. The corrosion rate was approximately 2 mpy. Corrosion resistance of alloy R60702 was good at 190 and 200°C and was fair at 210 and 220°C. Corrosion of alloy R60705 increased significantly at temperatures above 170°C. The alloy showed good corrosion resistance (4 mpy) at 180 and 190°C but only fair resistance (7 mpy) at 200°C, and poor resistance at 210 and 220°C (13 and 20 mpy, respectively).

Potentiodynamic polarization tests revealed that passivation of zirconium alloys was stable and spontaneous over a wide range of applied potential (Figures 1 to 3). The corrosion potential of both alloys was more noble than Epp at all test temperatures. Strong and protective passivation of the alloys was also demonstrated by the fact that Epp and Eb values were completely beyond the test range and could not be determined at temperatures below 200°C (Fig. 3). In addition, passive current density was low at most test temperatures, less than 3 μA/cm² . At test temperatures of 200°C and above, Epp became visible on the anodic polarization curves; however, it was as high as 1400 mV/Pt. Passivation of all alloy R60705 became less protective at 190° and 220°C. Passive current density increased as temperature was increased. Although corrosion of alloy R60705 increased significantly with test temperatures, particularly above 180°C, corrosion still occurred in the passive range. No active or active-passive corrosion region was found on the anodic polarization of alloy R60705 for the temperatures tested.

Similar to alloy R60705, stable passivation occurred for alloy R60702 at all test temperatures (Figures 1 to 3). The passive current density was as low as 1 μA/cm² at temperatures below 180°C. At test temperatures 180°C and above, the passivation of alloy R60702 shifted in the direction of increasing corrosion. The passive current density increased from 2 to 3 μA/cm² as temperature was increased from 170° to 180°C, then increased to 5, 8, 10, and 10 μA/cm² as test temperature increased to 190°, 200°, 210°, and 220°C, respectively. The corrosion resistance of alloy R60702 was better than that of alloy R60705 at all test temperatures.

Because of their corrosion rate at low temperatures, the impedance of zirconium alloys was extremely high. Thus at low temperatures, the Nyquist plots obtained by AC impedance Spectroscopy showed only about one quadrant of a circle (Figures 10 and 11). At temperatures above 180°C, the Nyquist plots were more complete. At most test temperatures, Nyquist plots for alloy R60702 consisted of only one semicircle as observed on stainless steels and nickel alloys (Fig. 11). This indicates that only activation controlled kinetics were involved in the corrosion process. Figure 5a shows the circuit model of the R60702 corrosion. Similarly, Nyquist plots of alloy R60705 below 200°C consisted of only one semicircle indicating activation-controlled kinetics. At 200°C, corrosion of alloy R60705 shifted to multiple systems and the Nyquist plot consisted of two semicircles. At 210 and 220°C, a straight-line segment was observed in addition to the semicircle resulting from the infinite diffusion-controlled kinetics (Fig. 11). Thus, infinite-diffusion was involved in alloy R60705 corrosion mechanism. The equivalent circuit model of alloy R60705 corrosion at 210 and 220°C consists of an diffusior impedance together with the RC-impedance of activation control at 210 and 220°C (Fig. 5b).

G. *Tantalum and Nb-Ta Alloy*

Tantalum and tantalum alloys are considered the best corrosion-resistant materials for exposure to both oxidizing and reducing mineral acids over a wide ranges of concentration and temperatures. However, high costs have limited their use. Tantalum has been used only in severe conditions for which there were no suitable alternative metals. Among the commercial Ta alloys, KBI- 40, an alloy containing 60% Ta and 40% Nb, is considered a superior corrosion-resistant material for many environments. AC impedance measurements showed that Ta has excellent corrosion resistance to 5 wt% sulfuric acid at temperatures up to 220°C. The polarization resistance extrapolated from AC impedance data in many thousands of ohms. Tantalum exhibited complete stability and spontaneous passivation without evidence of breakdown over a wide range of potentials. Except at 210 and 220°C, the passive range was so large that neither primary nor breakdown potentials of tantalum were observed on the anodic polarization curves. The corrosion potential of tantalum was more noble than Epp, so that tantalum corroded in the passive range at all test temperatures. Temperature had negligible on the passive current density of tantalum up to 190°C. The passive current density was 1 μA/cm² or less. At 200, 210 and 220°C, i_p increased slightly to approximately 3 μA/cm²; however, the metal remained in stable and spontaneous passivation.

AC Impedance tests for KBI-40 also showed excellent corrosion resistance in the 5 wt% sulfuric acid solution up to 200°C with a corrosion rate of less than 1 mpy. The corrosion rates were 3 and 2 mpy at 210°C and 220°C, respectively. Potentiodynamic polarization tests showed that passivation of KBI-40 was stable up to 200°C. At higher test temperatures, the anodic polarization curves of KBI-40 shifted toward increasing the passive current density. The passive current density shifted from 2 to 5 $\mu A/cm^2$ when the test temperature was increased from 190 to 200°C. At 210 and 220°C, the passivation of KBI-40 was less protective, because the passive current density increased to 8 and 10 $\mu A/cm^2$, respectively.

Similar to the zirconium alloys, the impedance of the tantalum and KBI-40 corrosion systems was extremely high at low ranges of test temperature. Within the selected frequency range, only a portion of the Nyquist semicircle was obtained at low temperatures. The complete Nyquist plot was only found at high temperatures. From the shape of the Nyquist plots, it is indicated that tantalum and KBI-40 corroded with only one corrosion system consistent with activation-controlled kinetics. At most test temperatures, the Nyquist plot revealed only one semicircle. The typical equivalent circuit model of tantalum and KBI-40 corrosion is shown in Figure 5a.

H. AC Impedance Techniques vs. DC Potential Polarization Scan Techniques

It is considered that the corrosion current densities, i_{cor}, of a spontaneously passive metal (a metal that corrodes in the passive range) is equal to the passivation current density, i_p [8]. The current densities of general corrosion obtained from the AC impedance tests are lower than those derived from the passive current density by a factor of 1 to 20 (Tables II and III). This may be explained by the fact that the selected scan rate of 0.17 mV/s (0.6 V/hr) for the DC potential polarization scan tests may be high for the electrochemical measurements at the conditions of elevated temperature. Because the selected scan rate is faster than the recovery rate, it is difficult for the corrosion system to achieve complete relaxation. As consequence, current densities measured in the DC potential scan tests are normally higher than actual current density measured under equilibrium conditions or complete steady-state. In AC Impedance tests, only low-amplitude signals in the 5 to 10 mV range were used. The degree of disturbance to the corrosion system from its equilibrium is minimal and shifting of the electrode potential was less severe. Therefore, current density obtained from the AC Impedance tests is closer to the steady-state current densities than those obtained in the potential scan tests. In addition, the rapid change of the corrosion potential with time at high temperatures affects significantly to the stability of the measured electrochemical systems. It takes less than 5 minutes to complete an AC impedance test, while a DC potential polarization scan test takes approximately 1 to 3 hours to finish. Thus, AC impedance technique is considered more stable and reliable method to determine general corrosion rate than using DC potential polarization scan. Therefore, to quantify a corrosion system at high temperatures, the AC impedance techniques offer several advantages over the DC potential scan such as time saving, stability, and reliability. However, DC potential polarization scan techniques is still reliable method to determine the behavior of a corrosion system.

V. Conclusions

A. Stainless Steels

At 90 and 100°C, strong evidence of stable passivation is observed on stainless steels S31603, N08904, and N08020; however resistance to general corrosion is fair to poor when exposed to 5 wt% sulfuric acid. If these alloys are selected, additional corrosion protection is advised to protect these stainless steel from excessive corrosion. Alloy N08026 shows excellent corrosion resistance to 5 wt% sulfuric acid at temperatures to 100°C. The alloy exhibits a stable and spontaneous passivation. At 120°C and above, all stainless steels exhibit unstable and unprotective passivation. These alloys are unsatisfactory for service with the dilute sulfuric acid in this temperature range.

B. Nickel, Ni-Cu and Ni-Mo Alloys

Alloy N02200 exhibits unsatisfactory corrosion resistance due to high corrosion rates in 5 wt% sulfuric acid at temperatures of 90°C and above. Alloy N02200 does not passivate under any test conditions. Alloy N04400 exhibited excellent corrosion resistance at 90°C and good corrosion resistance at 100°C. At temperatures above 100°C, the alloy corroded severely. Alloy N10665 shows excellent corrosion resistance to 5 wt% sulfuric acid at temperatures up to 100°C. However, corrosion resistance of alloy N10665 is inadequate in 5 wt% sulfuric acid at temperatures of 120°C and above. The alloy corroded at excessive rates. Similar to the behavior of alloy N02200, no passivation was observed on alloys N04400 and N10665 in 5 wt% sulfuric acid at any test temperature.

C. Ni-Cr-Mo-Fe and Ni-Cr-Mo-W

These alloys showed excellent corrosion resistance in 5 wt% sulfuric acid at temperatures up to 100°C. All test alloys corroded at rates of less than 2 mpy. At 120°C, these alloys corroded at rates exceeding 5 mpy. At temperatures of 140°C and higher, these alloys are unsatisfactory for service with the dilute sulfuric acid. These alloys show stable and spontaneous passivation at temperatures to 100°C. At 120°C and above, the passivation is unstable and unprotective. Because of high critical and passive current densities, application of anodic protection is not recommended for these nickel-base alloys at temperatures of 120°C or above.

D. Zirconium Alloys

Zirconium alloys R60705 and R60702 show excellent corrosion resistance in 5 wt% sulfuric acid up to 170° and 180°C, respectively. Zirconium alloy R60705 has good corrosion resistance at temperatures of 180° and 190°C; however, the corrosion resistance of R60705 declined to fair at temperature of 200°C and above. Zirconium alloy R60702 showed good corrosion resistance at temperatures of 190 and 200°C, but only fair corrosion resistance at 210 and 220°C. R60705 shows stable and spontaneously passivation up to 170°C. The passivation was less protective at 180°C and above. Alloy R60702 exhibits stable and spontaneous passivation up to 190°C. At temperatures of 200°C and above, passivation is less protective.

E. Tantalum and Nb-Ta alloy

Tantalum has excellent corrosion resistance at all test temperatures. The corrosion rate of Ta does not exceed 0.1 mpy at test temperatures up to 200°C and approximately 1 mpy at 210° and 220°C. Tantalum also passivated stably and spontaneously at all test temperatures. The KBI-40 (40% Nb- 60%Ta alloy) showed results similar to those obtained on tantalum. The alloy corroded at rates of 1 mpy or less at temperatures up to 200°C. KBI-40 shows good to excellent corrosion resistance at 210°C and 220°C. The alloy passivated stably and spontaneously up to 200°C. At temperatures of 210° and 220°C, stable passivation is still observed, but the less protection due to passive current density is somewhat high (5 to 10 $\mu A/cm^2$).

F. AC Impedance Techniques vs. DC Potential Scan Techniques

If passive current density is considered to represent the corrosion rate of the alloys that passivate spontaneously, the corrosion rates measured from AC impedance technique are lower than those obtained from the DC potential polarization scan tests by a factor of 1 to 20. To quantify a corrosion system at high temperatures, the AC impedance techniques offer several advantages over the DC potential scan such as time saving, stability, and reliability. However, DC potential polarization scan techniques is still a good method to determine the behavior of a corrosion system.

VI. References

1. J. C. Roetheli, J. E. Jordan, and C. E. Madewell, Biomass Fuels Progress Report, Tennessee Valley Authority, Muscle Shoals, Alabama, April 1984.

2. L. H. Weiss, R. L. Mednick, Technology and Economic of Ethanol Production via Fermentation, Uniscience Series, Chem System Inc., Terry Town, New York, 1983.

3. J. D. Wright, High-Temperature Acid Hydrolysis of Cellulosis for Alcohol Fuel Production, Solar Energy Research Institute (SERI), U.S. Department of Energy, 1983.

4. Muscle Shoals Corrosion Laboratory , Cost of Construction Materials for Chemical Plants, Mt , Files of Materials and Cost, National Fertilizer & Environmental Research Center, Tennessee Valley Authority, Muscle Shoals, Alabama.

5. M. G. Fontana and G. W. Staehle, Advances in Corrosion Science and Technology, Volume 1, Plenum Press, New York City, New York, 1970.

6. ASTM, Standard Practice for Conventions Applicable to Electrochemical Measurements in Corrosion Testing, ASTM G 3-81, Anual Book of ASTM Standards, Volume 03.02, Section 3, ASTM Philadelphia, 1992.

7. ASM, Corrosion, Metals Handbook, Volume 13, 9th Edition, 1985,

8. E. L. Liening, Electrochemical Corrosion Testing Techniques, Process Industries Corrosion: The Theory and Practice, NACE, Houston, Texas, 1986.

Table 1

Major Alloy Compositions of Construction Materials Exposed to 5 wt% Sulfuric Acid at Elevated Temperatures and Static Conditions

Matls tested	Trade Name	Composition, wt%											Cost ratio[a]
		C	Cr	Fe	Mn	Mo	Nb	Ni	Si	Ta	Zr	Other	
S31603	Type 316L	0.03	18	Bal.	2.0	3.0	-	12	1.0	-	-	-	1.0
N08904	Type 904L	0.02	23	Bal.	2.0	5.0	-	28	1.0	-	-	2.0Cu	1.4
N08020	Carp 20Cb-3	0.07	21	Bal.	2.0	3.0	1.0	38	1.0	-	-	4.0Cu	2.2
N08026	Carp 20Mo-6	0.03	26	Bal.	1.0	6.0	-	37	0.5	-	-	4.0Cu	2.3
N02200	Nickel 200	-	-	-	-	-	-	100	-	-	-	-	1.5
N04400	Monel 400	-	-	-	-	-	-	70	-	-	-	30Cu	2.0
N10665	Hast. B-2	0.01	1.0	2	-	28	-	Bal.	0.1	-	-	-	7.0
N08825	Incoloy 825	0.05	22	29	-	3.0	-	42	0.5	-	-	2Cu,1Ti	2.3
N06030	Hast. G-30	0.03	30	15	-	5.5	0.8	43	1.0	-	-	2.5W	5.0
N08625	Inconel 625	0.10	22	5	-	9.0	4.0	62	0.5	-	-	-	2.3
N06022	Hast. C-22	0.01	22	-	-	10	2.0	53	-	-	-	3.0W	6.0
N10276	Hast. C-276	0.01	16	5.5	-	16	-	57	0.08	-	-	4.0W	6.0
R06702	Zr 705	0.05	<.2	<.2	-	-	-	-	-	-	95	4.5Hf	4.6
R06705	Zr 702	0.05	<.2	<.2	3.0	-	-	-	-	-	91	4.5Hf	4.6
-	KBI-40	-	-	-	-	-	40	-	-	60	-	0.3W	50.0
-	Tantalum	-	-	-	-	-	-	-	-	Bal.	-	-	120.0

a: Relative cost ratio versus stainless steel S31603, Material Files, Muscle Shoals Corrosion Laboratory, National Fertilizer & Environmental Research Center, Alabama.

Table II

Results of Electrochemical Tests on Various Materials Exposed to 5 wt% Sulfuric Acid at 90, 100, and 120°C Under Static Conditions

Matls tested	R_p Ohms	i_{cor} $\mu A/cm^2$	Cor.Rate mpy	E_{cor} mV/Pt	i_c $\mu A/cm^2$	i_p $\mu A/cm^2$	E_{pp} mV/Pt	E_b mV/Pt
At 90°C								
S31603	19	204	79	-864	800	2.5	-750	90
N08904	39	25.4	10	-812	250	2.5	-710	190
N08020	126	30.8	12.0	-790	300	3.0	-710	290
N08026	3,500	1.1	0.4	-610	150	1.5	-660	290
N02200	139	22.9	12.0	-808	-b	-b	-b	-b
N04400	998	3.9	2.0	-761	-b	-b	-b	-b
N10665	2,000	2.0	1.0	-679	-b	-b	-b	-b
N08825	7,600	0.5	0.2	-571	-c	2.5	-c	290
n06030	41,000	0.1	<0.0	-521	-c	1.5	-c	290
N08625	6,900	0.6	0.2	-566	-c	3.0	-c	290
N06022	17,500	0.2	0.1	-542	-c	2.0	-c	190
N10276	12,000	0.3	0.1	-617	-c	1.0	-c	240
R60705	23,000	0.2	0.2	-637	-c	1.0	-c	-c
R60702	78,000	0.1	<0.1	-597	-c	1.0	-c	-c
KBI-40	41,000	0.1	0.1	-663	-c	1.0	-c	-c
Ta	100,000	0.0[a]	<0.1	-658	-c	1.0	-c	-c
At 100°C								
S031603	15	258.8	100.0	-790	400	2.5	-712	263
N08904	100	38.8	15.0	-713	210	3.0	-678	163
N08020	80	48.5	19.0	-726	300	2.0	-637	263
N08026	2,300	1.7	1.0	-626	10	2.0	-637	363
N02200	19	204.3	88.0	-769	-b	-b	-b	-b
N04400	480	8.1	4.0	-703	-b	-b	-b	-b
N10665	900	4.3	2.0	-706	-b	-b	-b	-b
N08825	5,000	0.8	0.3	-526	170	3.0	-612	363
N06030	27,000	0.1	0.1	-535	-c	1.0	-c	363
N08625	6,000	0.6	0.3	-539	10	2.5	-637	313
N06022	18,000	0.2	0.1	-509	-c	2.0	-c	363
N10276	6,400	0.6	0.3	-512	-c	1.5	-c	363
R60705	25,000	0.2	0.1	-734	-c	1.0	-c	-c
R60702	33,000	0.1	0.1	-662	-c	1.5	-c	-c
KBI-40	51,000	0.1	0.1	-590	-c	1.0	-c	-c
Ta	63,000	0.0[a]	<0.0	-691	-c	1.0	-c	-c
At 120°C								
S31603	2	2,588	2.0	-289	4000	10.0	-250	300
N08904	60	4.7	26.0	-337	300	15.0	-325	400
N08020	30	129.4	51.0	-388	800	15.0	-375	450
N08026	160	24.3	10.0	-389	900	10.0	-450	300
N02200	10	338.2	166.0	-410	-b	-b	-b	-b
N04400	105	37.0	16.0	-265	-b	-b	-b	-b
N10665	120	32.4	15.0	-473	-b	-b	-b	-b
N08825	163	23.8	9.0	-309	100	10.0	-275	600
N06030	180	21.6	8.0	-329	105	9.0	-375	500
N08625	135	28.8	11.0	-250	200	10.0	-200	600
N06022	212	18.3	7.0	-289	2000	20.0	-500	550
N10276	270	14.4	6.0	-285	500	8.0	-350	400
R60705	9,000	0.4	0.4	-343	-c	2.5	-c	-c
R60702	11,500	0.3	0.3	-522	-c	2.5	-c	-c
KBI-40	22,500	0.2	0.1	-487	-c	2.0	-c	-c
Ta	22,000	0.2	0.1	-545	-c	1.5	-c	-c

a: Less than 0.1
b: No passivation observed.
c: Outside measured range of potential.
d: Can not determined

Table III

Results of Electrochemical Tests on Various Materials Exposed to 5 wt% Sulfuric Acid at 140 to 220°C Under Static Conditions

Matls tested	R_p Ohms	i_{cor} $\mu A/cm^2$	Cor.Rate mpy	E_{cor} mV/Pt	i_c $\mu A/cm^2$	i_p $\mu A/cm^2$	E_{pp} mV/Pt	E_b mV/Pt
At 140°C								
N08904	0.23	16,578	6,646	-383	2000	100	-400	400
N08020	0.30	12,940	5,121	-329	-[d]	1000	-[d]	600
N08026	6	669	261	-344	800	20	-450	250
N04400	3	1,553	674	-266	-[b]	-[b]	-[b]	-[b]
N10665	6	645	299	-267	-[b]	-[b]	-[b]	-[b]
N08825	5	746	296	-318	400	100	-100	300
N06030	16	243	91	-398	1000	50	-350	100
N08625	26	149	59	-306	100	50	0	400
N06022	12	323	129	-378	1000	100	-275	600
N10276	11	353	147	-336	2000	300	-250	400
R60705	12,000	0.4	0.4	-325	-[c]	3.5	-[c]	-[c]
R60702	16,000	0.3	0.2	-548	-[c]	2.5	-[c]	-[c]
KBI-40	25,000	0.2	0.1	-229	-[c]	2.0	-[c]	-[c]
Ta	27,000	0.2	0.1	-542	-[c]	2.0	-[c]	-[c]
At 160°C								
R60705	3,300	1.2	1.0	-728	-[c]	3.0	-[c]	-[c]
R60702	10,000	0.4	0.4	-872	-[c]	2.0	-[c]	-[c]
KBI-40	6,000	0.6	0.5	-589	-[c]	1.5	-[c]	-[c]
Ta	42,000	0.1	0.1	-450	-[c]	1.0	-[c]	-[c]
At 170°C								
R60705	1,540	2.5	2.0	-612	-[c]	3.0	-[c]	-[c]
R60702	5,200	0.8	0.7	-504	-[c]	2.0	-[c]	-[c]
KBI-40	4,300	0.9	0.6	-578	-[c]	2.0	-[c]	-[c]
Ta	30,000	0.1	0.1	-677	-[c]	1.0	-[c]	-[c]
At 180°C								
R60705	850	4.6	4.0	-805	-[c]	5.0	-[c]	-[c]
R60702	1,800	2.2	2.0	-781	-[c]	3.0	-[c]	-[c]
KBI-40	4,500	0.9	0.6	-765	-[c]	2.0	-[c]	-[c]
Ta	22,000	0.2	0.1	-641	-[c]	1.0	-[c]	-[c]
At 190°C								
R60705	810	4.8	5.0	-726	-[c]	15.0	-[c]	-[c]
R60702	1170	3.3	3.0	-570	-[c]	5.0	-[c]	-[c]
KBI-40	8500	0.7	0.3	-631	-[c]	3.0	-[c]	-[c]
Ta	46000	0.1	0.1	-542	-[c]	1.0	-[c]	-[c]
At 200°C								
R60705	750	5.2	7.0	-359	-[c]	30.0	-[c]	1,400
R60702	1,009	3.8	4.0	-345	-[c]	8.0	-[c]	1,400
KBI-40	2,100	1.9	1.0	-279	-[c]	5.0	-[c]	-[c]
Ta	35,000	0.1	0.1	-432	-[c]	2.0	-[c]	-[c]
At 210°C								
R60702	680	5.7	6.0	-376	-[c]	10.0	-[c]	1,400
R60-40	1,000	3.9	3.0	-368	-[c]	8.0	-[c]	1,600
KBI-40	1,000	3.9	3.0	-368	-[c]	8.0	-[c]	1,600
Ta	7,500	0.5	0.4	-587	-[c]	3.0	-[c]	1,700
At 220°C								
R6005	190	20.4	20.0	-402	-[c]	100.0	-[c]	1,400
R6002	0	6.5	7.0	-343	-[c]	10.0	-[c]	1,250
KBI-40	1,600	2.4	2.0	-291	-[c]	10.0	-[c]	1,600
Ta	3,300	1.2	1.0	-247	-[c]	3.0	-[c]	-[c]

a: Less than 0.1
b: No passivation observed.
c: Outside measured range of potential
d: Can not determined

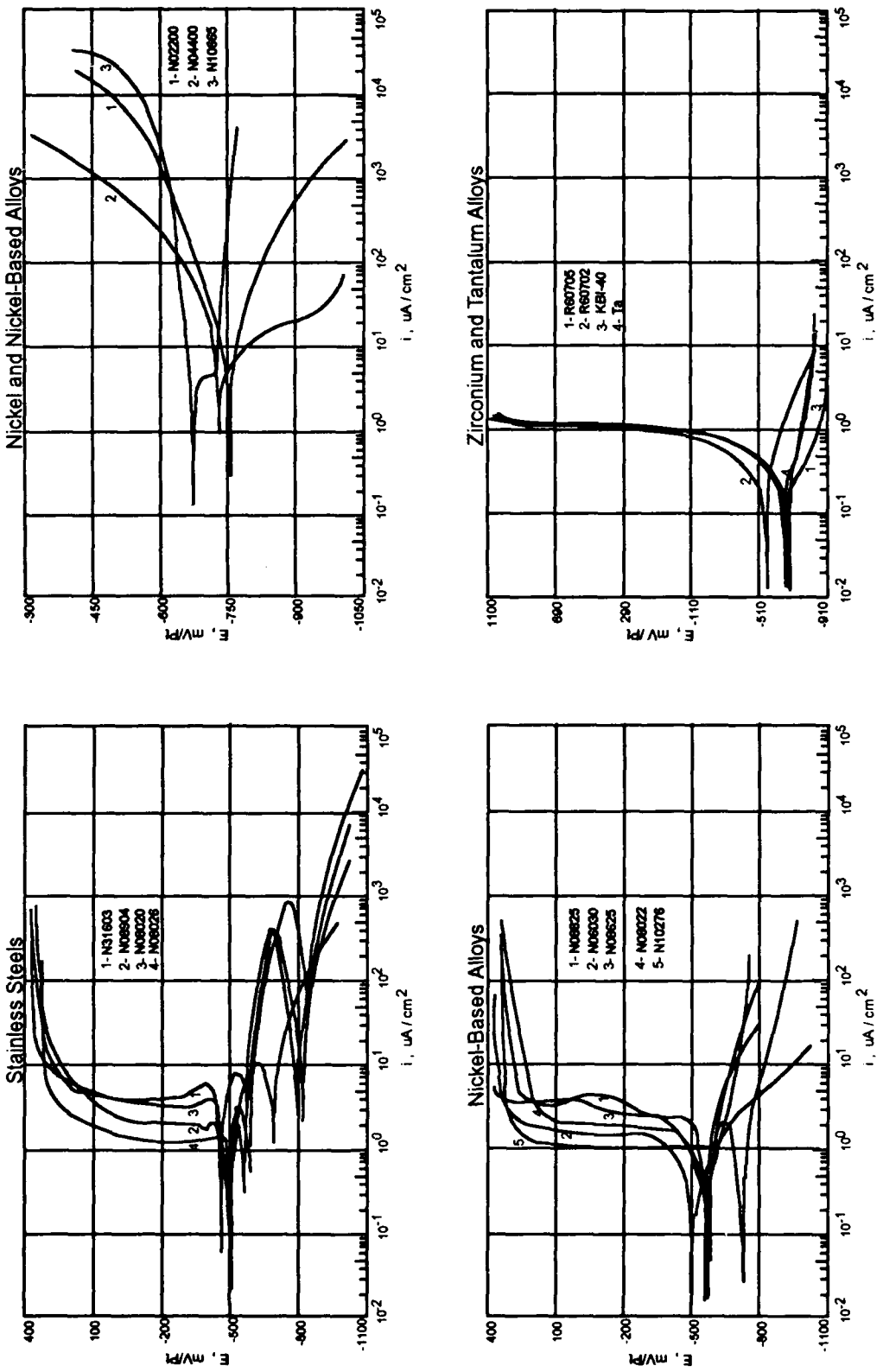

Figure 1 - Potentiodynamic polarization of Test Materials Exposed to 5 wt% Sulfuric Acid at 90°C Under Static Conditions. Test at Scan Rate of 0.17 mV/s.

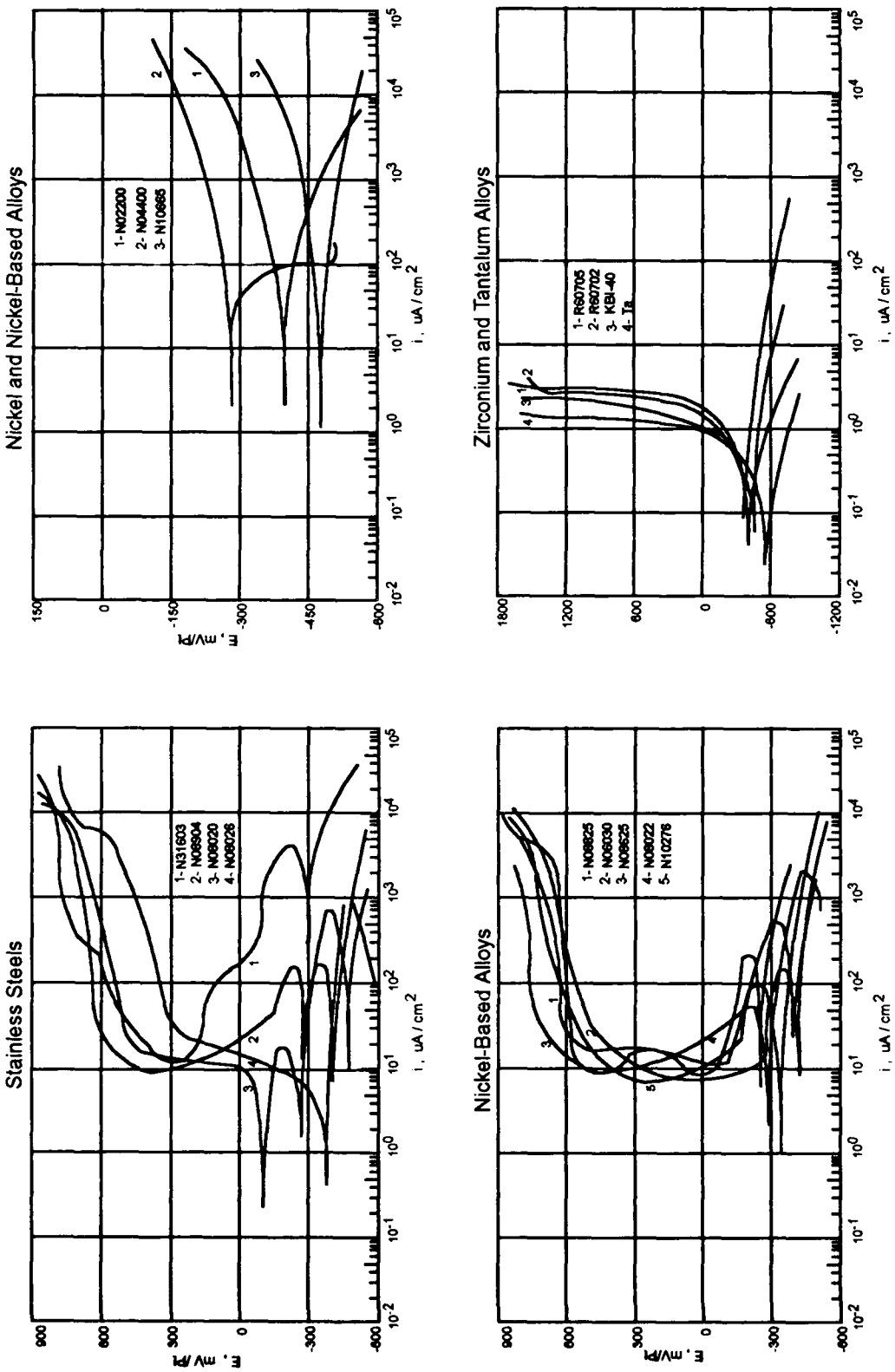

Figure 2 - Potentiodynamic polarization of Test Materials Exposed to 5 wt% Sulfuric Acid at 120°C Under Static Conditions. Test at Scan Rate of 0.17 mV/s.

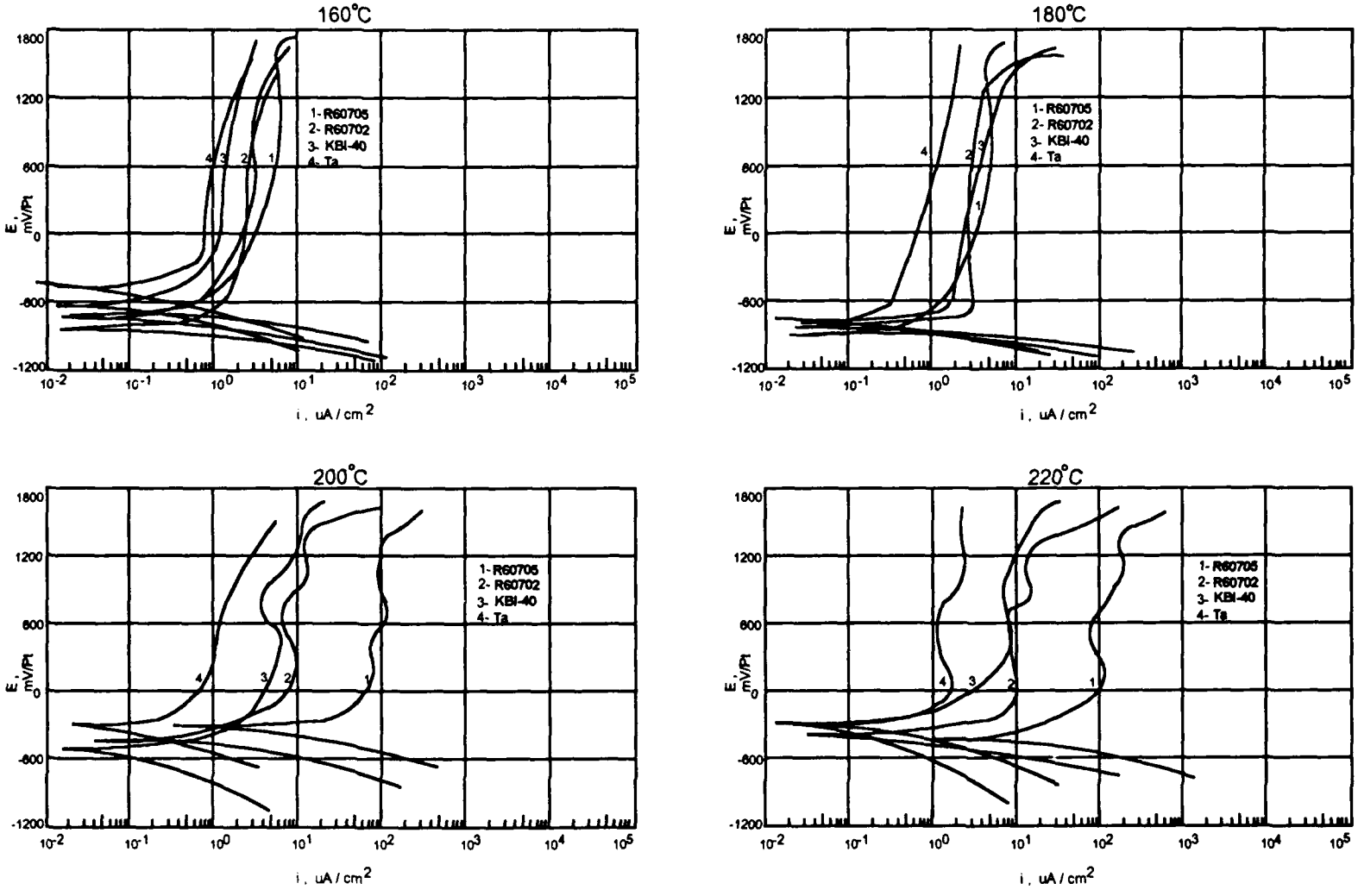

Figure 3 - Potentiodynamic polarization of Refractory Metals Exposed to 5 wt% Sulfuric Acid at at Various Temperatures Under Static Conditions. Test at Scan rate of 0.17 mV/s.

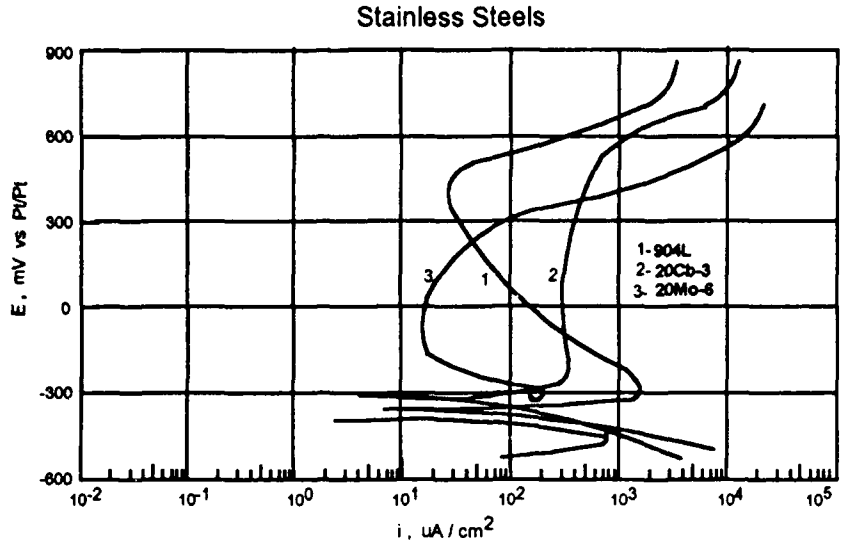

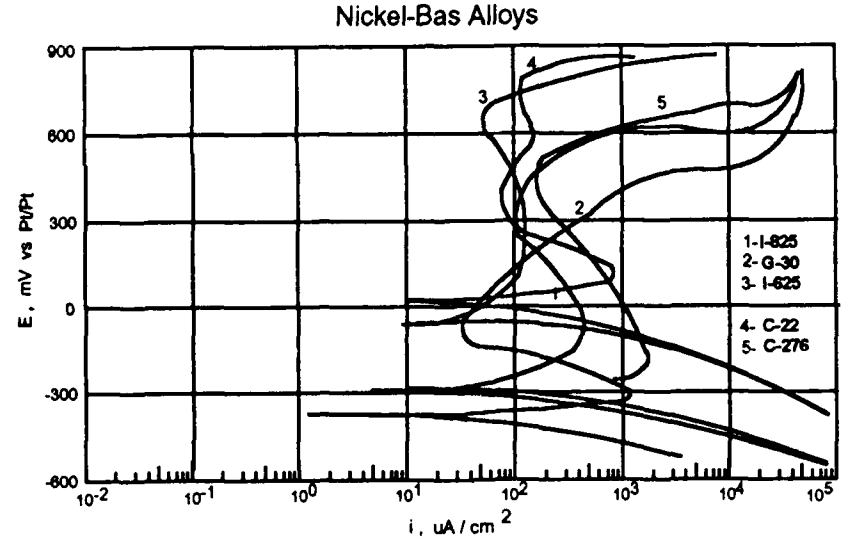

Figure 4 - Potentiodynamic polarization of Test Materials Exposed to 5 wt% Sulfuric Acid at 140°C Under Static Conditions. Test at Scan Rate of 0.17 mV/s.

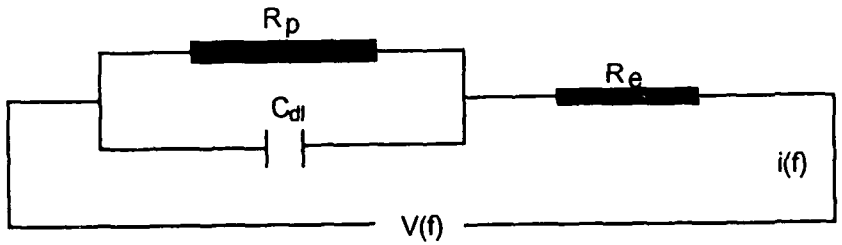

5a) Activation-Controlled Kinetics

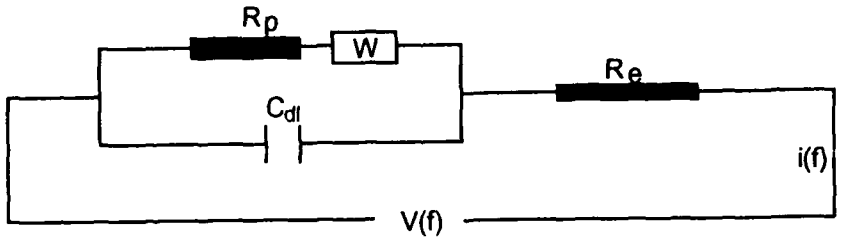

5b) Diffusion-Controlled Kinetics

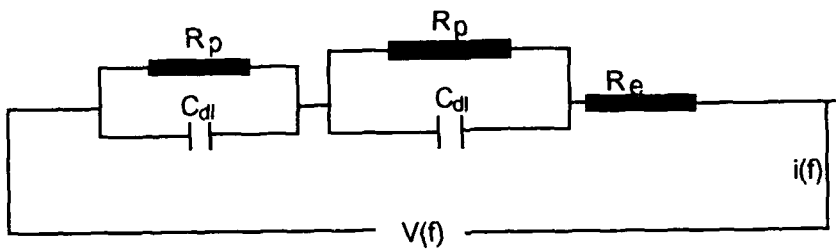

5c) Complex Activation-Controlled Kinetics

Where:

R_p	- Polarization Resistance Reciprocal to Corrosion Rate
C_{dl}	- Double Layer Capacitance
W	- Diffusion Impedance
R_e	- Ohmic or Electrolyte Resistance
V(f)	- Applied AC Voltage
i(f)	- Measured AC Current

FIGURE 5

Equivalent Circuit Model of Metals Corroded in Aqueous Environment.

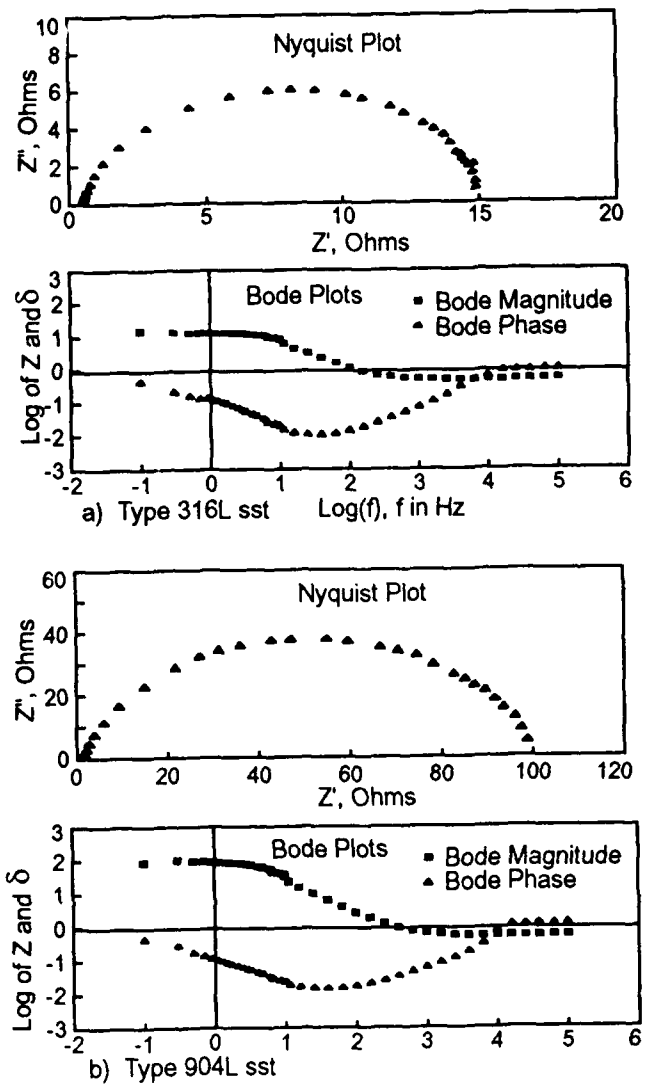

FIGURE 6

AC Impedance Plots of Types 316L and 904L at 100 C °

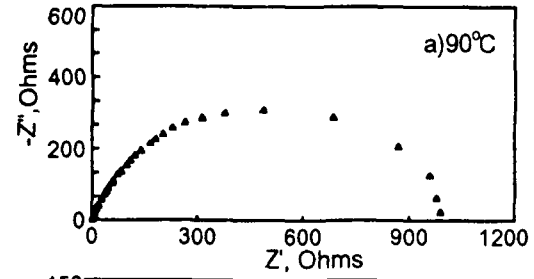

FIGURE 7
AC Impedance Nyquist Plots of Monel 400

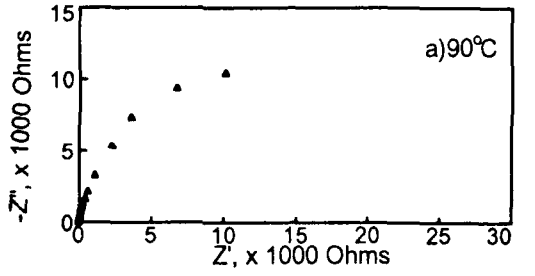

FIGURE 8
AC Impedance Nyquist Plots of Hastelloy G-30

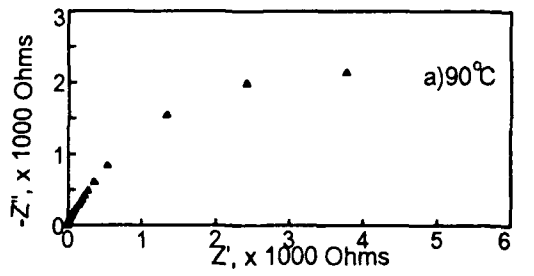

FIGURE 9
AC Impedance Nyquist Plots of Inconel 625

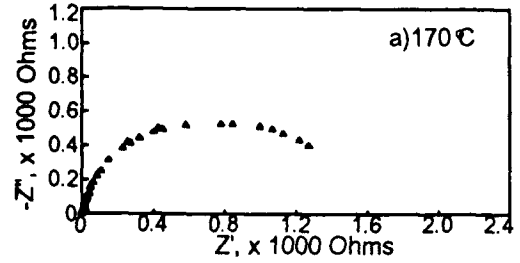

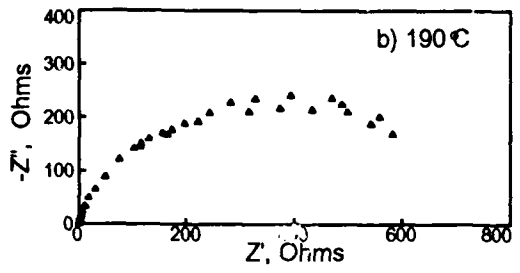

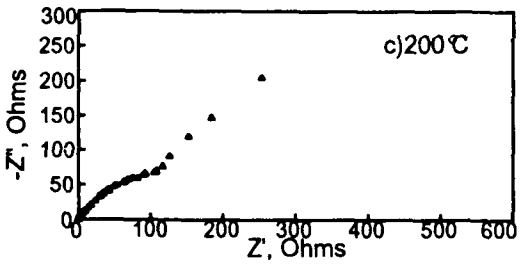

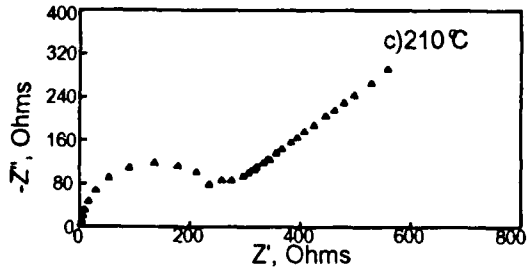

FIGURE 10
AC Impedance Nyquist Plots of Zr 705

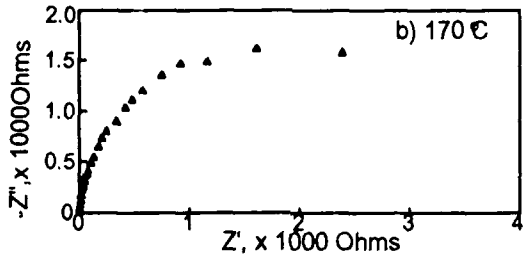

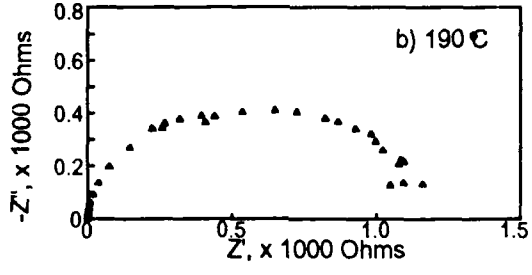

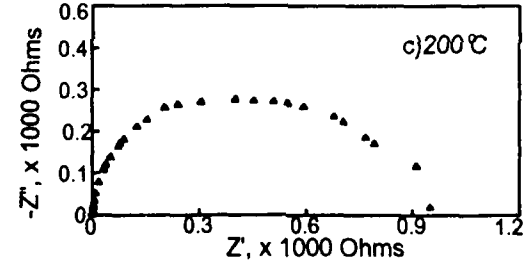

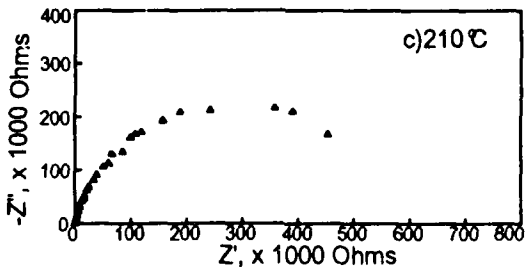

FIGURE 11
AC Impedance Nyquist Plots of Zr 702

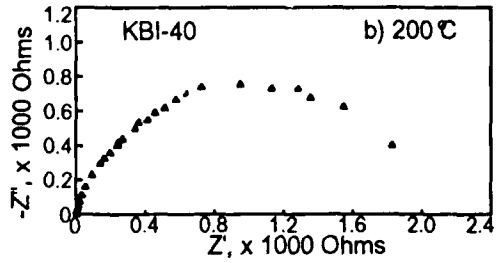

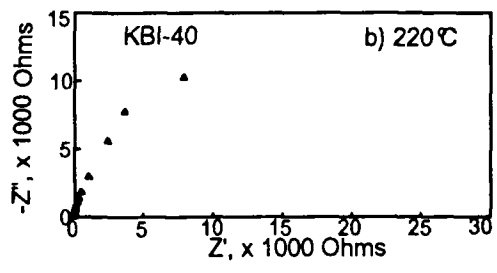

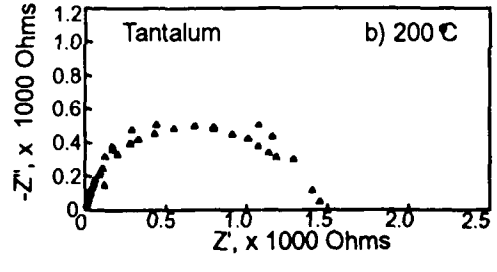

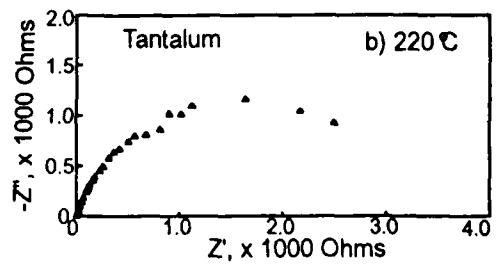

FIGURE 12
AC Impedance Nyquist Plots of Ta and KBI-40

Crack Initiation and Growth of Sensitized Type304 Stainless Steel in NaF Solution

Toshio Shibata and Takumi Haruna
Department of Materials Science and Processing,
Faculty of Engineering,
Osaka University
2-1 Yamada-oka Suita Osaka 565 Japan

Takahiro Oki
Yokkaichi Complex,
Tosoh Co. Ltd.
1-8 Kasumi Yokkaichi Mie 510 Japan

Abstract

Intergranular stress corrosion cracking, IGSCC, of sensitized Type304 stainless steel in NaF solution has been investigated. The whole IGSCC process including crack initiation and growth during a slow strain rate test, SSRT, was observed and recorded with a CCD camera and video system. Effects of NaF concentration, temperature and applied potential on the number of cracks, crack generation time, crack growth rate and K_{ISCC} were analyzed. It was concluded that the most important factor influencing the maximum stress obtained by SSRT was crack initiation, not the crack growth rate.

Key items intergranular stress corrosion cracking, slow strain rate test with CCD camera system, K_{ISCC}, crack growth rate, crack generation time, maximum stress, NaF concentration, temperature, applied potential.

Introduction

Sensitized Type304 stainless steel has been known to suffer IGSCC in wet environments containing fluoride ion, but few studies on the IGSCC of this system have been made[1-7]. These reports revealed that the IGSCC does not occur with solution-annealed stainless steel, and the highest susceptibility of the IGSCC exists at a NaF concentration of about 10^3 ppm. IGSCC occurs at ambient temperature and the susceptibility increases with increase in temperature to 353 K. In the vicinity of 0 mV_{SCE}, the sensitized steel has the highest susceptibility to IGSCC.

We have also studied the IGSCC behavior of sensitized Type304 stainless steel in NaF aqueous solution using SSRT[8]. It was found that the crack region depended on both NaF concentration and temperature as shown in Figure 1[8], which successfully coincided with the region measured by using U-bend tests[5]; IGSCC susceptibility evaluated by maximum stress changed with NaF concentration, test temperature and applied potential. Such tendencies were similar to other reports[1-7].

Although important information on the IGSCC of this system has been obtained, there is no detailed analysis about the contribution of the crack behavior to IGSCC susceptibility evaluated by the maximum stress. Therefore, the present work aims to observe crack initiation and growth on the specimen surface in-situ during SSRT, and to obtain the information about which factor of crack initiation or growth is important in determining IGSCC susceptibility.

Experimental procedure

Tensile plate specimens, schematically illustrated in Figure 2, were cut from Type304 stainless steel sheet which had the chemical composition shown in Table 1. The specimens were annealed at 1323 K for 3.6 ks followed by quenching in water. Thereafter they were sensitized at 923 K for 86.4 ks and then quenched in water. The degree of sensitization for the specimen evaluated by the electrochemical potentiokinetic reactivation method[9] was from 30 to 35 %. The specimen was mechanically polished with emery paper to #6/0 immediately before the SSRT started.

Figure 3 is a schematic drawing of the SSRT system with CCD camera used[10]. SSRT was carried out at a fixed strain rate of 8.64×10^{-7} s^{-1}. The CCD camera system, which has a high depth of focus, is mounted on a X-Z stage controlled by a personal computer, and the whole edge side of the gauge length region of the specimen can be directly observed and recorded every 7.2 ks during SSRT. From the observation, the length of each crack was measured as a function of test time with a precision of about 20 μm, from which the crack generation time and K_{ISCC} relating to crack initiation, and crack growth rate were analyzed. Since cracks always generated at the edge of the specimen and grew in the normal direction relative to the tensile as mentioned below, K_{ISCC} was calculated by using the equation for a single-notched specimen. At the same time, load and corrosion potential were monitored. In the case of potential-controlled SSRT, the polarization current was measured. The potential was measured or applied against an Ag/AgCl(3.3 kmol·m^{-3} KCl) reference electrode and was expressed without correction.

The test conditions were changed as follows; NaF concentration was from 10^1 to 8.4×10^3 ppm, temperature from 303 to 368 K and applied potential from -200 to 200 mV.

Experimental results

I. Evaluation of SCC susceptibility by SSRT

Figure 4 shows stress–strain curves and corrosion potentials depending on the concentration of NaF at 323 K. The highest SCC susceptibility evaluated by fracture strain or maximum stress is easily found at 10^3 ppm NaF. However, the maximum stress can not provide any information about the contribution of crack initiation or growth to the whole process. Therefore, the crack growth process during SSRT was directly observed in order to evaluate crack initiation and growth separately. It was found that cracks generated at random sites along the edges of the specimen and at random times, as shown in Figure 5, under any conditions. The length of each crack was measured as a function of time. The results, as shown in Figure 6, indicate that the crack generation time and the crack growth rate changed with NaF concentration as well as temperature and applied potential. Accordingly, it could be discussed which factor of crack initiation or growth was predominant to decide the SCC susceptibility evaluated by the maximum stress. Before turning to the discussion, the effects of temperature and applied potential, as well as NaF concentration, on crack generation time, K_{ISCC} and crack growth rate were analyzed statistically.

II. Crack generation time

Statistical distribution of crack generation time could be analyzed by using Weibull probability, because crack generation takes place at the weakest site on the surface, and then its generation time should obey for statistical law of the extreme value distribution for the smallest. Figure 7 (a), (b) and (c) show the distributions of crack generation time plotted on Weibull probability paper depending on NaF concentration, temperature and applied potential, respectively. Change in NaF concentration gave relatively small changes in the shape of the distribution, which was clearly seen by a slope of a line on probability paper. However, the distribution shifted to the shortest time at 10^3 ppm NaF. Increase in temperature gave almost no change in the shape but the location shifted to shorter times. As to applied potential, the slope of the distribution was the steepest and the location shifted to the shortest times at 0 to 100 mV.

III. K_{ISCC}

K_{ISCC} was calculated by the equation for a single-notched specimen, as stated before, but the validity of the equation was not checked for such small crack size of 50 μm that was detected in this study. Our previous study[10] analyzed K_{ISCC} for the small crack generated from the small round pit of a similar size on annealed Type304 stainless steel in 20 mass% NaCl containing

thiosulfate ion and found that K_{ISCC} thus obtained coincided with what was reported by Mukai et al.[11] for the long crack length. Then K_{ISCC} calculated in this study could provide the approximate value for the small crack generated on the same material as Type304 stainless steel.

Since K_{ISCC} is also considered to obey the extreme value distribution for the smallest, the distributions of K_{ISCC} was plotted on Weibull probability paper as shown in Figure 8 (a), (b) and (c). The slope and the location of the distribution changed with changing NaF concentration, temperature and applied potential. In the case of NaF concentration, the shape showed almost no change and the location shifted to the lowest values at 10^2 to 10^3 ppm NaF. Increase in temperature gave the shape almost no change but the location shifted to lower K_{ISCC}. In the potential-controlled SSRT, the slope became the steepest and the location shifted to the lowest K_{ISCC} at 0 to 100 mV.

IV. Crack growth rate

Crack length did not always change linearly with time, but could be seen as a straight line during the initial stages of crack growth. Thus, the crack growth rate was calculated from the slope of the initial stage of crack growth. The crack growth rate thus determined is also statistical variate and its distribution should obey the extreme value distribution for the largest, because the largest value of the crack growth rate determines the total failure of the specimen. The distributions of the crack growth rate plotted on Gumbel probability paper were shown in Figure 9 (a), (b) and (c). It is interesting that the slope changes with NaF concentration, temperature and also applied potential. The NaF concentration of 10^3 ppm gave the steepest slope (i.e. the narrowest shape) and the lowest location of the distribution. While, corresponding to an increase in temperature, the shape became broader and the location shifted to a faster rate. Change in applied potential induced almost no change in the shape and the location shifted to the slowest rate at 100 mV.

Discussion

As mentioned above, crack behavior, i.e., crack generation time, K_{ISCC} and crack growth rate, were found to be influenced by NaF concentration, temperature and applied potential. The SCC susceptibility evaluated by the maximum stress should naturally relate with all factors of crack behavior. Therefore, it is discussed in the following which factor of crack initiation or growth controlled the maximum stress.

I. NaF concentration

Figure 10 shows the effect of NaF concentration on such various factors

as the maximum stress, corrosion potential region during SSRT, the mean and the minimum value of K_{ISCC}, the mean and the maximum value of the crack growth rate, the shortest crack generation time, and the final number of cracks. The maximum stress as an index of SCC susceptibility in SSRT showed a minimum at 10^3 ppm NaF. However, the minimum of K_{ISCC} which is important to SCC showed almost no change with changing NaF concentration except for 8.4 x 10^3 ppm. In addition, the mean and the maximum of crack growth rate showed a minimum at 10^3 ppm NaF. Thus, SCC susceptibility evaluated by the maximum stress had no relation to both K_{ISCC} and the crack growth rate. On the other hand, the crack generation time showed the strong dependence on NaF concentration, with a minimum value at 10^3 ppm NaF. Furthermore, the largest number of cracks was found at the same concentration. The shortest time for crack generation and the largest number of cracks seemed to be quite favorable for accelerating IGSCC initiation. Consequently, it was concluded that SCC susceptibility evaluated by the maximum stress, depending on NaF concentration, was mainly controlled by crack initiation, especially crack generation time and the number of cracks.

II. Temperature

Figure 11 shows the effect of temperature on the same factors as in Figure 10. The maximum stress decreases with increase in temperature. Correspondingly, K_{ISCC} decreased and the crack growth rate increased with increase in temperature. Moreover, crack generation time decreased and the final number of cracks increased with increase in temperature except for 369 K. Consequently, all of the factors were concluded to contribute to change the maximum stress by SSRT.

Since the crack growth rate increased with increase in temperature, crack growth was thought to be controlled by a thermal activation process. Accordingly, the mean of the crack growth rate with a scatter band was plotted as a function of the reciprocal of absolute temperature, as shown in Figure 12. This figure showed that crack growth rate obeyed the Arrehnius relation, and the activation energy calculated from the slope was about 23 $kJ \cdot mol^{-1}$. This activation energy could be compared with what is obtained from the analysis of polarization curves. Polarization curves of unloaded samples measured at various temperatures are shown in Figure 13. Corrosion potentials during SSRT shown in Figure 11 were in the active region close to the passive region on the polarization curves. An Arrehnius plot of current density at −200 mV, which was equal to corrosion potential during SSRT, provided an activation energy of about 20 $kJ \cdot mol^{-1}$. Good agreement between these two energies suggests that crack growth rate is controlled by the mass transfer process of dissolved ions.

III. Applied potential

Figure 14 shows the effect of applied potential on the same factors as in Figure 10. The maximum stress minimized at 0 to 100 mV. It was interesting to note that the minimum of K_{ISCC} was almost constant value beyond 0 mV, although the mean value of K_{ISCC} showed a similar trend as the maximum stress. It should be, however, emphasized that the minimum value of K_{ISCC} is more important than the mean value because the minimum K_{ISCC} decides the first crack initiation. The crack growth rate decreased with increase in applied potential. Thus both of K_{ISCC} and the crack growth rate were found to give almost no effect on the maximum stress. On the other hand, crack generation time was found to be the shortest at 100 mV although the final number of cracks increased with increase in applied potential. Consequently, the maximum stress by SSRT depending on applied potential was controlled by only crack generation time.

It could be concluded that decrease in maximum stress observed during SSRT was more closely related to the crack initiation rather than the crack growth rate.

Summary

* IGSCC of sensitized Type304 stainless steel in NaF aqueous solution was successfully investigated in relation to the point of crack behavior during SSRT by direct observation with a CCD camera system,
* The maximum stress obtained by SSRT was sensitive to NaF concentration and it was the lowest at 10^3 ppm NaF. The maximum stress was found to be controlled by crack generation time and the number of cracks rather than crack growth rate.
* The maximum stress decreased with increase in temperature from 303 to 369 K. The same accelerating effect of temperature was found for such various factors as K_{ISCC}, crack growth rate, crack generation time and the number of cracks.
* The maximum stress was the lowest at 0 to 100 mV, and was controlled by crack generation time.
* In conclusion, crack initiation was found to be more important than crack growth rate, affecting the maximum stress during SSRT for sensitized Type304 stainless steel in NaF aqueous solution.

Reference

1. D. E. Hetzel, Metal Progress, 125–3 (1984): p.73.
2. C. T. Ward, D. L. Mathis and R. W. Staehle, Corrosion, 25 (1969): p.394.

3. G. J. Theus and J. R. Cels, Corrosion Problem in Energy Conversion and Generation (Princeton, NJ: The Electrochemical Society, 1974), p.384.
4. G. J. Theus and R. W. Staehle, Stress Corrosion Cracking and Hydrogen Embrittlement of Iron Base Alloys, (Houston, TX: National Association of Corrosion Engineers, 1977), p.845.
5. M. Takemoto, T. Shinohara and M. Shirai, Boshoku Gijutsu, 36 (1987): p.210.
6. M. Takemoto, T. Shinohara and M. Shirai, Materials Performance, 24 (1985): p.26.
7. F. Zucchi, G. Trabanelli and G. Demertzis, Corrosion Science, 28 (1988): p.1.
8. T. Shibata, T. Oki and T. Haruna, Zairyo-to-Kankyo, 42 (1993): p.15.
9. JIS G-0591.
10. T. Shibata and T. Haruna, Zairyo-to-Kankyo, 41 (1992): p.809.
11. Y. Mukai and M. Murata, Quarterly J. Japan Weld. Soc., 48 (1979): p.937.

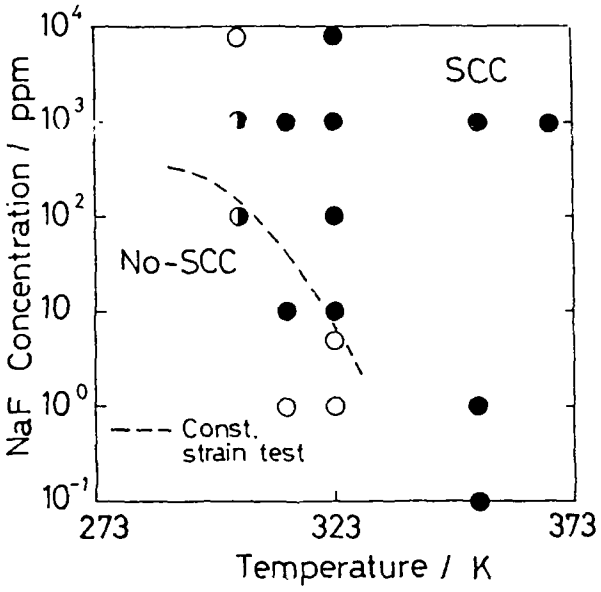

Figure 1
IGSCC susceptibility – NaF concentration – temperature diagram for sensitized Type304 stainless steel[8].

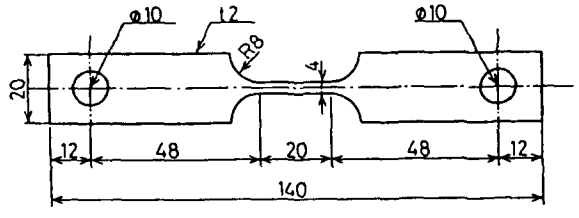

Figure 2
Shape and size of tensile specimen in mm.

Table 1
Chemical composition of Type304 stainless steel in mass%.

C	Si	Mn	P	S	Ni	Cr	O	N	Mo	Cu
0.05	0.55	0.98	0.026	0.008	9.38	18.39	--	--	0.12	0.05

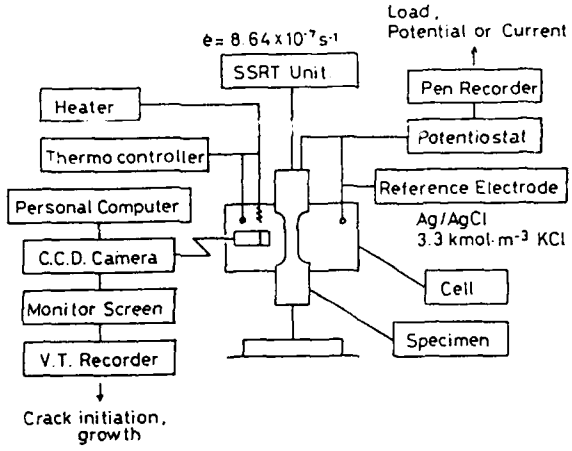

Figure 3
Schematic drawing of a slow strain rate test system attached with CCD camera and VTR.

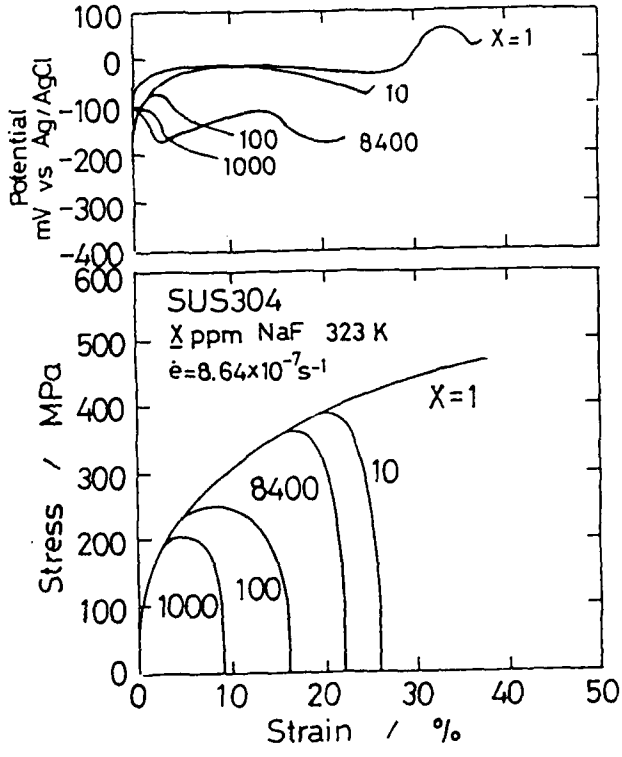

Figure 4
Stress–strain curves and corrosion potentials at various concentrations of NaF at 323 K.

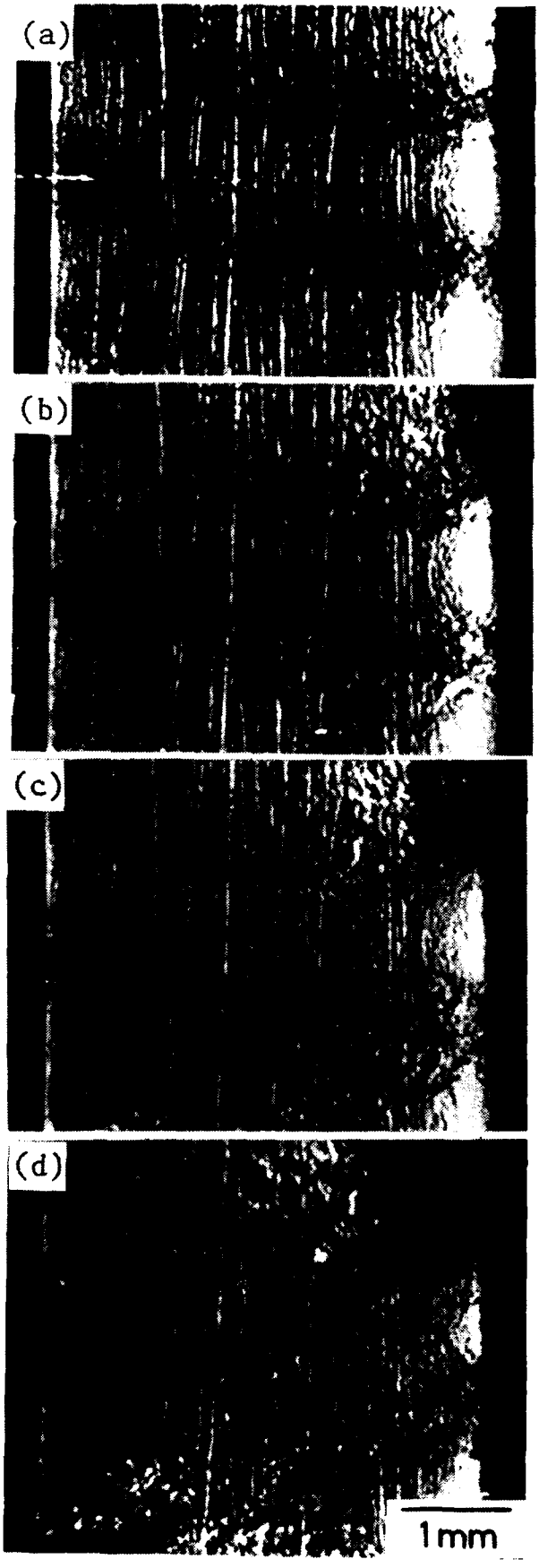

Figure 5 Typical process of crack initiation and growth during SSRT under the condition of 10^3 ppm NaF and 323 K; at strain of (a) 3.0, (b) 4.2, (c) 5.4 and (d) 9.0%.

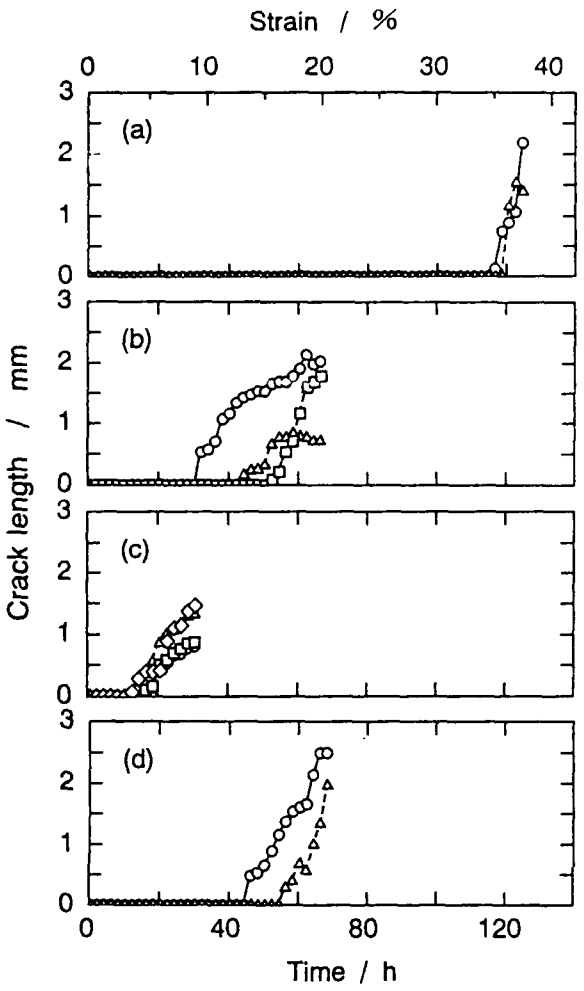

Figure 6
Change in length of each crack with test time during SSRT at 323 K and (a)10, (b)10^2, (c)10^3 and (d)8.4 x 10^3 ppm NaF. [The different symbols refer to different cracks in the same test piece.]

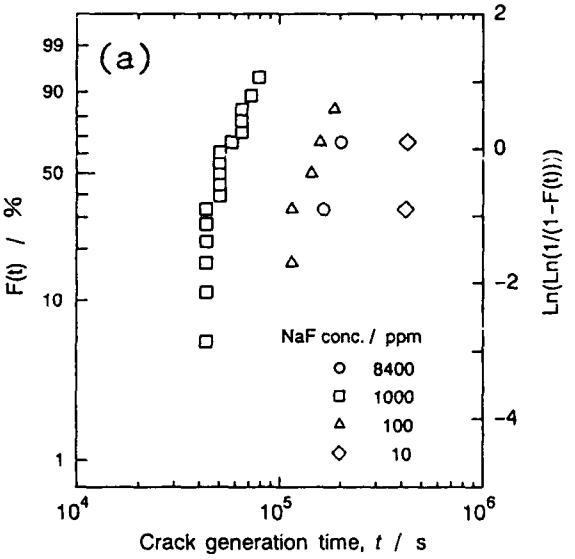

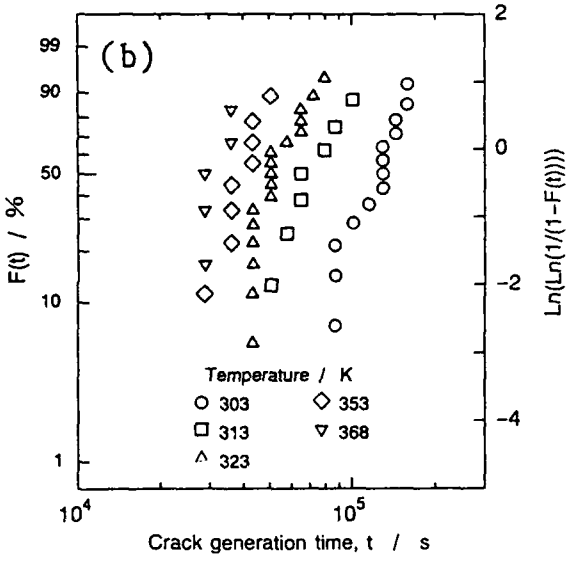

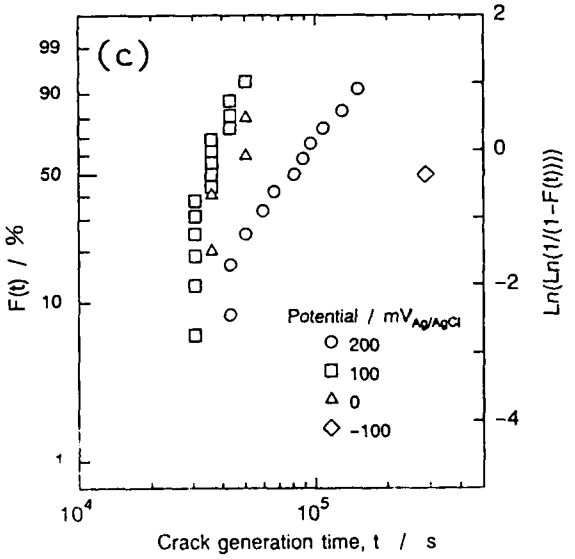

Figure 7
Weibull distributions of crack generation time depending on (a)NaF concentration, (b)temperature and (c)applied potential.

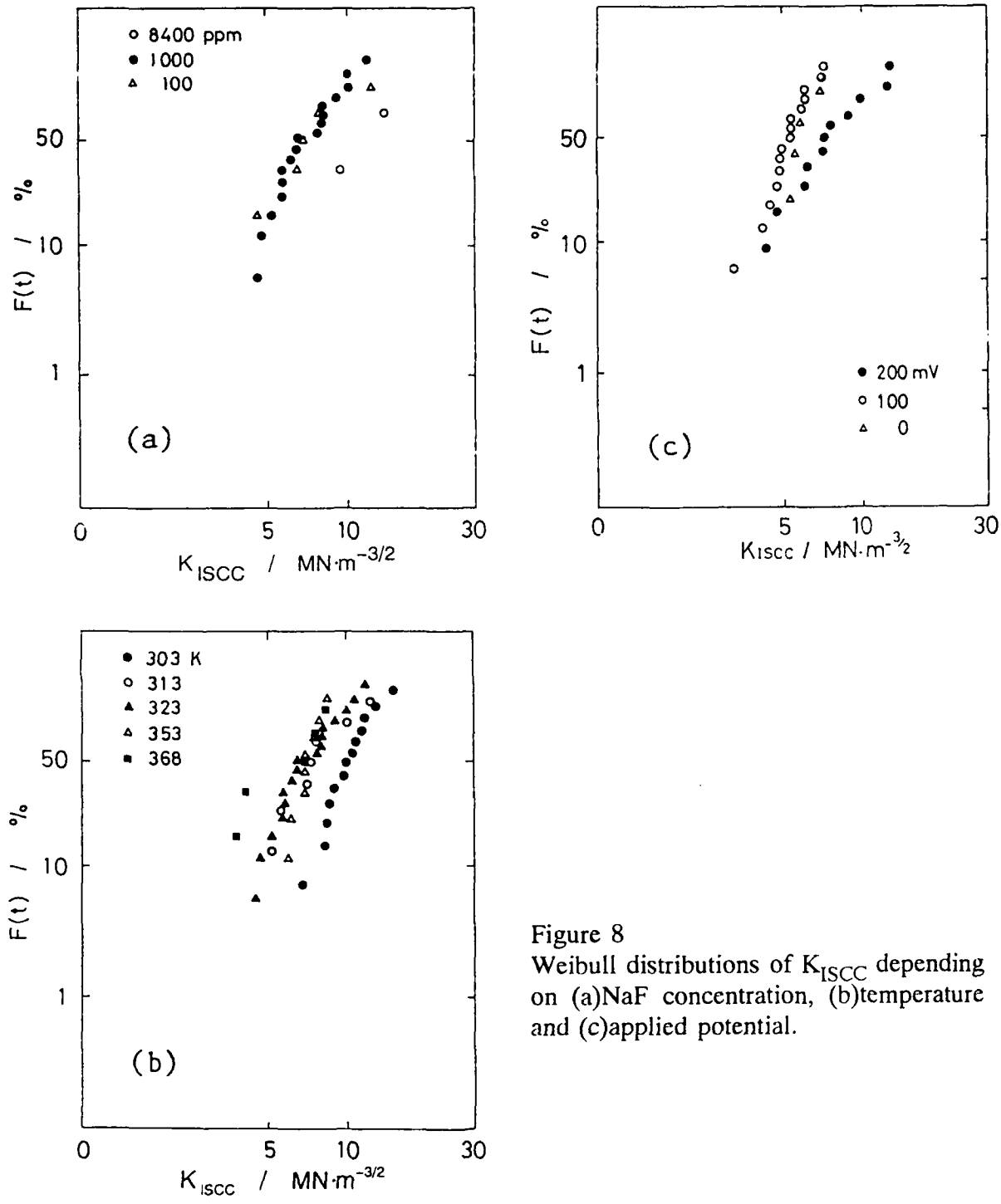

Figure 8
Weibull distributions of K_{ISCC} depending on (a)NaF concentration, (b)temperature and (c)applied potential.

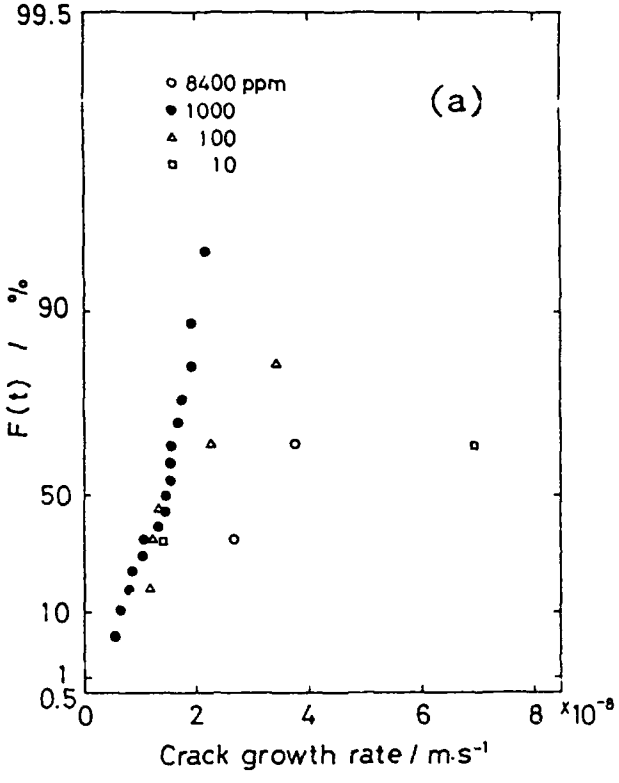

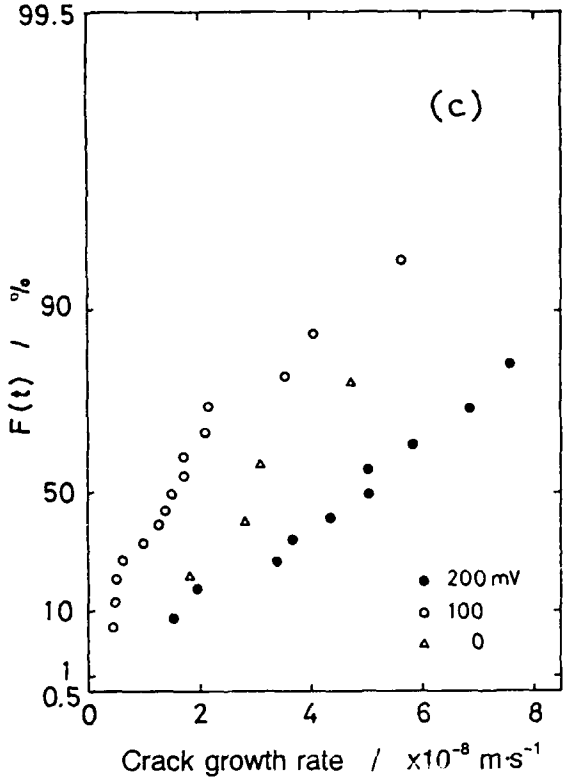

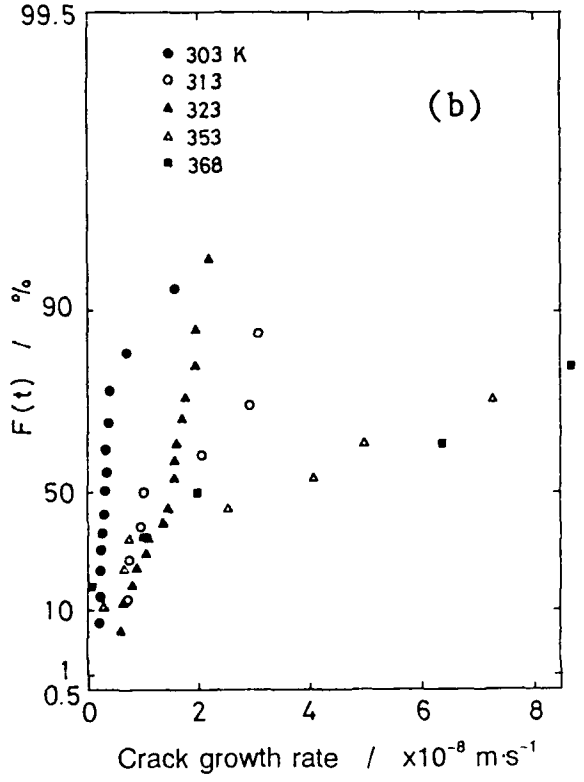

Figure 9
Gumbel distributions of crack growth rate depending on (a)NaF concentration, (b)temperature and (c)applied potential.

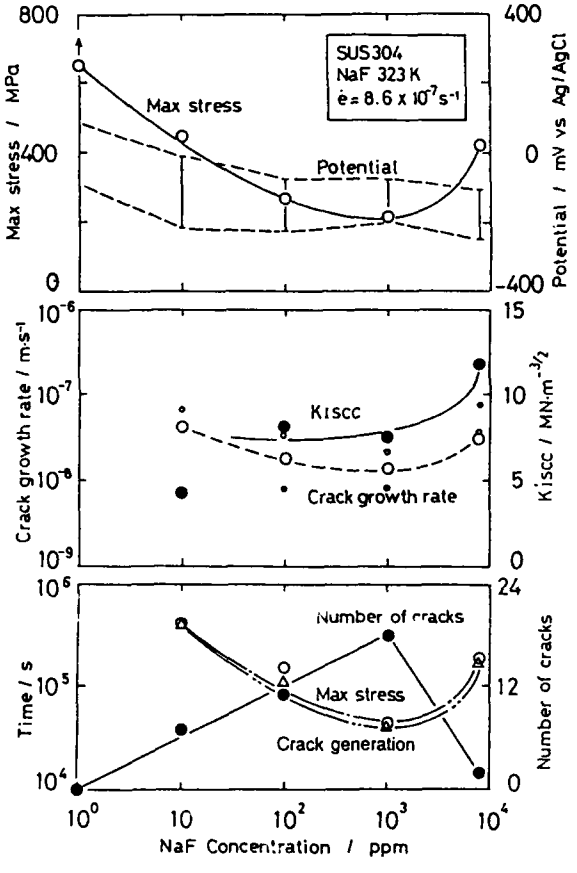

Figure 10
Effect of NaF concentration on the maximum stress, corrosion potential region, the mean (large closed mark) and the minimum (small closed mark) of K_{ISCC}, the mean (large open mark) and the maximum (small open mark) of the crack growth rate, the shortest crack generation time, and the final number of cracks.

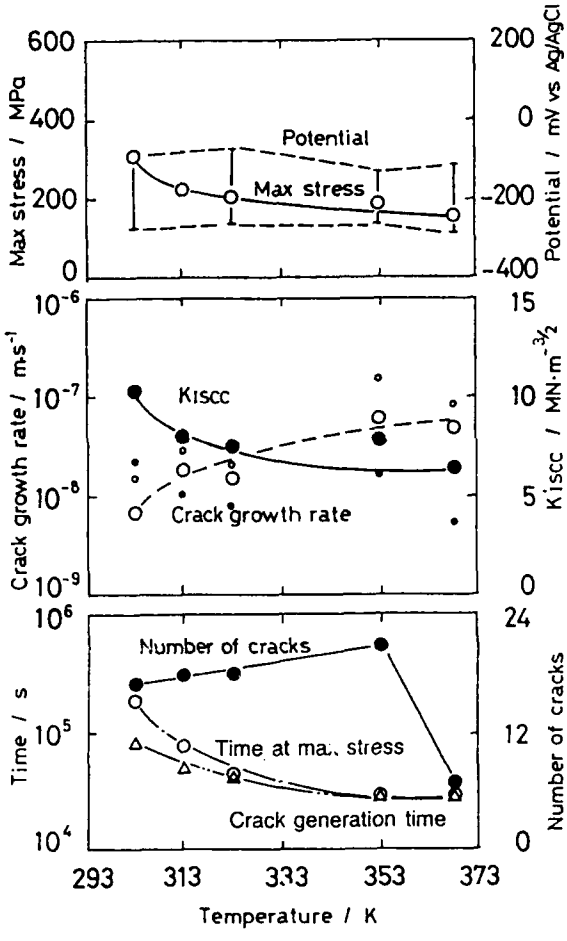

Figure 11
Effect of temperature on the maximum stress, corrosion potential region, the mean (large closed mark) and the minimum (small closed mark) of K_{ISCC}, the mean (large open mark) and the maximum (small open mark) of the crack growth rate, the shortest crack generation time, and the final number of cracks.

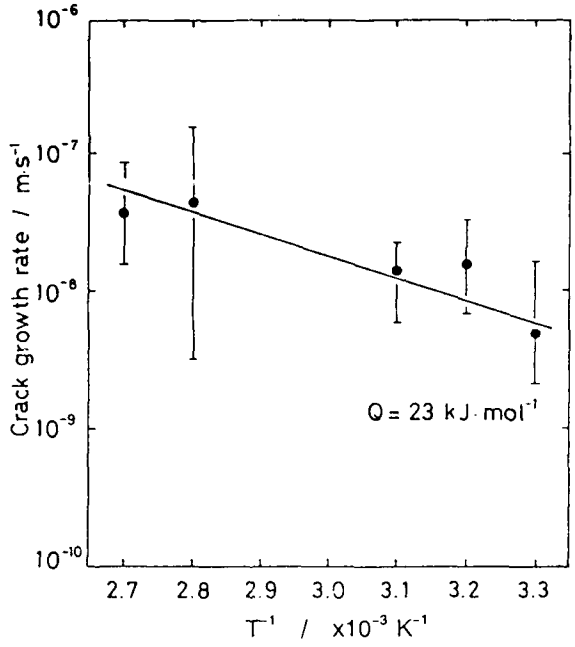

Figure 12
Arrehnius plot to the mean of the crack growth rate at 10^3 ppm NaF.

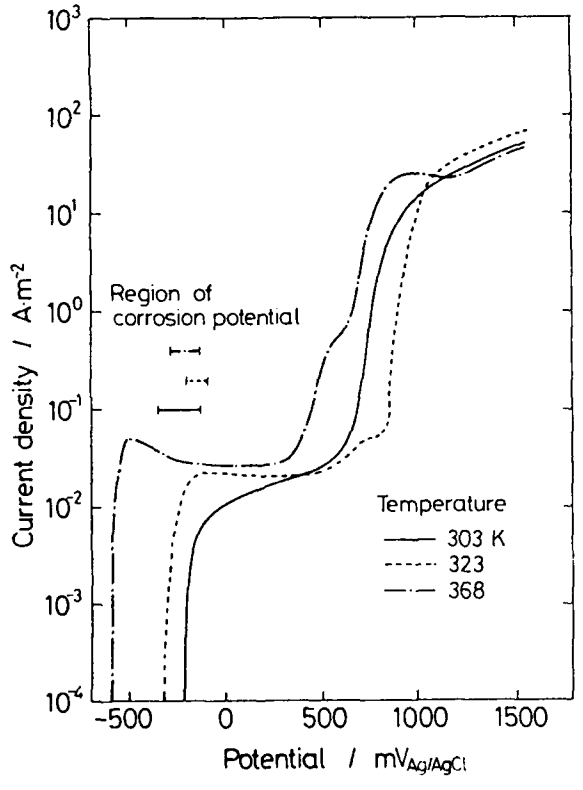

Figure 13
Polarization curves of not-loaded specimen at various temperatures.

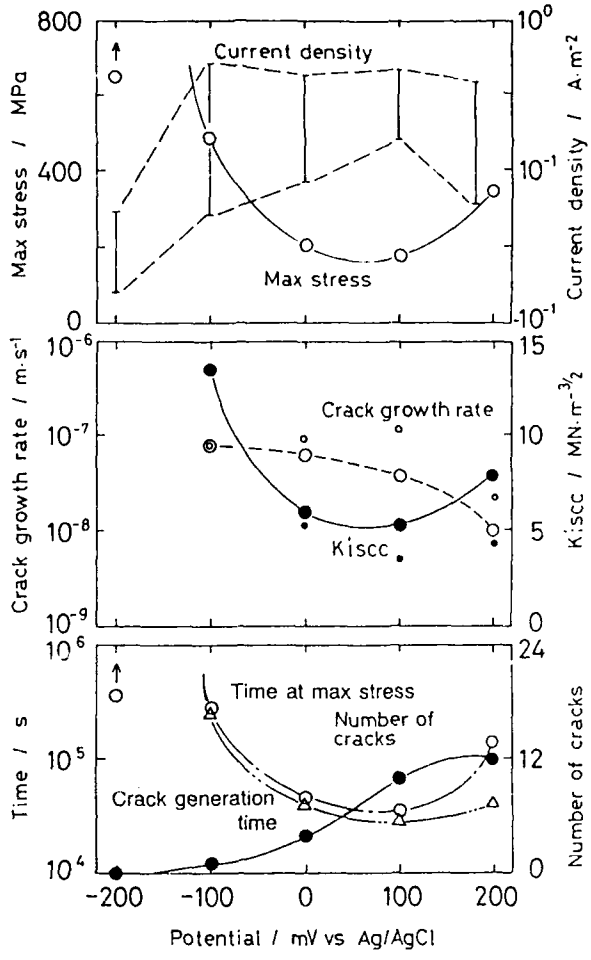

Figure 14
Effect of applied potential on the maximum stress, corrosion potential region, the mean (large closed mark) and the minimum (small closed mark) of K_{ISCC}, the mean (large open mark) and the maximum (small open mark) of the crack growth rate, the shortest crack generation time, and the final number of cracks.

Localized Corrosion Problems in Austenitic Stainless Steel Feedwater Heater Tubing

G. R. Wood
American Electric Power Service Corporation
1 Riverside Plaza
Columbus, OH 43215

Abstract

SCC susceptibility and the threshold stress for crack initiation was evaluated for several grades of welded, small diameter, austenitic stainless steel tubing used in high pressure feedwater heaters in response to a series of tube failures in newly installed heaters. Stress corrosion cracking tests were performed using ASTM G36 and a dilute chloride, wet/dry test intended to model the condensing steam environment of the heaters. The investigation determined threshold stress values for promoting crack initiation which were used to specify replacement tubing. High tensile residual stresses introduced by roller straightening operations were shown to cause cracking. Stretch straightening proved to be an effective alternative to roller straightening since lower residual stresses were produced in the OD fibers of the tubing. This fact was born out by abrasive air jet, hole-drilling residual stress measurements and corrosion tests. Time to failure versus residual stress data was developed for roller and stretch straightened tubing.

Introduction

A series of failures of high pressure feedwater tubes in six newly installed heaters at three fossil-fired generating plants prompted an investigation of the stress corrosion cracking (SCC) resistance of the ASTM A688 type 316N stainless steel tubing used in the heaters. Previous operating experience with type 304N tubing in subcritical steam plant heaters did not give any indication that the nitrogen strengthened grades were unsuitable for this service. Type 316N was chosen for the new heaters to take advantage of the higher allowable operating stresses for this material. The failures were of great concern to AEP since a program to replace retired heaters with new heaters tubed with type 316N was well underway when stress corrosion cracking failures began to occur.

Failure analyses were performed on samples of the ex-service tubing to identify crack morphology, sample for any corrodents known to produce cracking and to measure residual stress present in the tubing. Previous industry experience in nuclear and fossil steam plants has shown that reducing the tensile stress below a threshold value by a change in design or processing method, eliminating or reducing the severity of the corrosive environment and changing to a less susceptible material to be the most effective methods for preventing SCC. (1, 2, 3) Where large scale replacement of susceptible material was not possible, *in- situ* heat treatments to

reduce tensile residual stresses and/or remove sensitized regions were employed.

This investigation attempted to identify the source of the responsible corrodent and the mechanism by which cracking occurred. The differences in residual stress magnitudes related to methods of manufacture was explored as well as measurement acuity with the "split ring" residual stress test. Exposure tests in boiling magnesium chloride and dilute sodium chloride were used to check the threshold stress for SCC and to determine if a difference in resistance to SCC existed among candidate tubing materials such as 304N, 316N and 304L processed with two different mechanical straightening methods.

Presented in this paper are the results of the failure analysis, residual stress measurement trials, the exposure tests to boiling magnesium chloride and a wet/dry cell exposure to dilute sodium chloride, and the most likely causes of failure with recommendations for their avoidance.

Failure Analysis of Ex-service Tubing

All of the failures had occurred in the desuperheating zone of the heaters without exception (See figure 1). In this zone, the extraction steam first enters the heater at start-up, resulting in the evaporation of condensate and subsequent concentration of any condensate species onto the tube surfaces. Metal temperatures during operation are approximately 600°F. Cracks which had not penetrated the wall were detected by eddy current whereas through-cracks were detected as leaks during *in-situ* hydrostatic testing. Time-to-failure ranged from as short as four months at one plant to three years of service at the other two plants. In four feedwater heaters from two plants, the cracking was found to be transgranular as shown in figure 2. At the other plant, the cracking had initiated in an intergranular manner with a transition to transgranular cracking in some cases. These failures were coincident with tube support locations. (See figures 3a and 3b). The weld did not appear to be associated with the cracking in any way.

EDS spectra recorded during SEM fractography of the crack surfaces showed measurable chlorine in two cases. A typical spectra is shown in figure 4. Residual stress measurements were made using the "split ring" technique in which the change in diameter, as measured before and after the tube is split longitudinally, is used in an elastic formula to determine the average residual stress. The tube is split opposite to the weld seam. Values determined for all samples examined are listed in Table 1. As shown, the Mitchell plant tubing had the highest average values. This is also the plant which experienced the shortest time-to-failure. Tests to determine if the tubing has been sensitized were conducted in accordance with ASTM A262 Practice E. No evidence of sensitization was found.

It was concluded that stress corrosion cracking had occurred in the subject heaters. Chlorides were thought to have assisted the cracking processes in concert with the high tensile residual stresses believed to have been created by a roller straightening operation applied to the tubing after the annealing heat treatment. The differences in levels of residual stress by straightening method was reserved for further study. The appropriate replacement grade of tubing was thought to be ASTM A688 type 304N since many of AEP's subcritical steam plant heaters contained this material. The decision was deferred until further testing could be performed as described later.

Test Procedures

The exposure tests in boiling magnesium chloride were conducted in accordance with ASTM standard practice G36 with the exception that the test specimens were not placed in the flask under external load. The stress in the test specimen was the residual stress from manufacturing. The procedure was as follows; first a residual stress measurement was made using the "split ring" technique on a 2 inch piece of tubing. A second 2 inch piece was placed in boiling magnesium chloride for 48 hours after which visible dye penetrant was used to detect any cracking. Roller straightened type 316N and stretch straightened type 304L and 304N were tested by this method. It became apparent that only specimens with zero tensile residual stresses or stresses at magnitudes lower than those achievable by low temperature stress relief could survive boiling magnesium chloride.

A wet/dry exposure test was developed which would be less severe than G36 but involve the continuous localized enrichment of chlorides on the surface of tubing specimens under tensile residual stress. For this test a residual stress measurement was made as before by the split ring technique. Then an adjacent piece of tubing was placed in a stand with a cartridge heater inside the tube. The temperature on the surface of the tube was stabilized at 200°F while 3.5% sodium chloride solution was continuously dribbled on the OD surface at 4 drops/min. Inspection by stereomicroscopy followed by metallography was used to confirm cracking. As before, low temperature stress relief heat treatments were used to incrementally reduce the tensile residual stress. When cracking occurred, it was usually under the dried salt cake at the edges of the splash zone. Roller and stretch straightened 304L, 316N and 304N were all tested using the procedure with time to crack versus residual stress data the final product.

During the course of this study, some questions arose over the accuracy of the residual stress measurement made by the split ring technique. It was observed that errors could be made in estimating the diameter measurements in the ten-thousandth of inch range which effected the value of residual stress significantly. Therefore an air abrasive milling/hole drilling experiment was conducted to check the value of residual stresses in the outer fibers of the tube wall. The air abrasive technique uses an entrained abrasive

in an 80 psi air jet to drill a hole in the center of a small strain gage rosette. By drilling in .005 inch increments the strain in the outer fibers determined to a depth of .040 inch. For this test, as-received roller straightened type 316N, stretch straightened 304N and stress relieved type 316N samples were used. These same samples were later exposed in the 3.5% sodium chloride wet/dry test cell.

Test Results

The results from the ASTM G36, boiling magnesium chloride exposure tests are depicted graphically in figure 5. As shown none of the roller straightened type 316N tubing survived 48 hours without cracking with the exception of the specimens having no tensile residual stress. The same was true of the type 304L, which even though it was stretch straightened, had fairly high stresses. A limited amount of thin-walled 304L prevented a more detailed study. The thermal stress relief applied to the tubing was effective in reducing the tensile residual stresses incrementally however, the amount of reduction could not be controlled precisely. Therefore future work in this area calls for a different test procedure using loading from the ID side of the tube and heating from the OD. The stretch straightened type 304N did not crack after 48 hours due to the low tensile and in some cases compressive residual stress in the tube. This fact coincides with the service experience to date. Of all the heaters recently installed in AEP power plants (13 total), only one has tubing which was stretch straightened. This one heater has not had a tube leak. However, any heaters having roller straightened begin to show leaks either immediately or after approximately three years in operation.

The residual stress measurement method comparison trials gave relatively close agreement. Table 2 shows the results. This means that measurements taken with the "split ring" method and used in the subsequent time-to-failure plots is reasonably accurate of the true average residual stress. One source for error in the split ring test is the presence of saw burrs or deformation from the cut-off saw on the edges of the sample. Careful cutting and removal of the burrs is required.

The results from the sodium chloride exposure tests are plotted in figure 6. As shown, both the 304N and 316N samples approach run out at a residual stress value of 8 ksi. A typical indication of cracking is shown in figure 7. The crack morphology was transgranular as expected in a chloride environment. The surface condition of the tubing played a role in these tests. Laps and other crevice type defects served as locus of cracking when the tube sample was oriented with the laps in the splash zone. See figure 8. All tubing used in this test was in the bright annealed condition. Thermal stress relief was performed in an argon atmosphere furnace in order to avoid changes in surface chemistry affecting the results. Both materials used in this test appear to have similar time to cracking under residual tensile hoop stress. The data generated needs to be extended beyond the 1000 hour life

point. Further testing is planned for longer exposures and other austenitic materials of choice for feedwater heater such as non nitrogen strengthened grades. The orders for replacement tubing used to rebuild the failed heaters specified a maximum tensile residual hoop stress of 8 ksi based on the results of these tests and industry consensus on the effects of the straightening process.

Closure

The best corrosion testing cell available for testing feedwater heater tubing materials is a feedwater heater itself. However, economics and the ability to control and monitor results preclude this option. Tests such as ASTM G36 produce results in a short time but the aggressive environment does not match the wet/dry interface and pH conditions of the heater. The sodium chloride test cell used in this work also does not precisely match the heater conditions but it did provide a wet/dry condition allowing for slow enrichment of chlorides, a pH (6.8) similar to the heaters and results within a reasonable time frame. It is believed that this same wet/dry condition causing local enrichment of chlorides is chiefly responsible for the service failures occurring in the desuperheating zone of the heater. Plant chemists report water chemistry within normal operating parameters and chloride levels in the parts per billion range. Therefore it would seem that the environment is being controlled as well as possible. It is however a possibility that in the case of the Mitchell Plant failures contamination prior to service may have occurred but this cannot be conclusively proven. Control of the residual stresses in the tubing remains the most effective method of avoiding stress corrosion cracking. Roller straightening was discovered to produce unacceptably high tensile hoop stresses in the tubing. Stretch straightening produces lower tensile hoop stresses and in some cases the residual stress was compressive. (4) Use of compressive stresses to control stress corrosion cracking has been documented. (5)

Acknowledgements

The author wishes to thank AEP management for permission to publish these results as well as J. M. Hare for the failure analyses, graphics and valued criticism during the course of this project. Thanks are also due M. E. Baker of AEP's Environmental Lab for corrosion testing and general assistance with all lab work.

References

1) ASM Handbook, 9th ed. Vol. 13. 1987

2) Desai, K., Feedwater Heater Tube Material Study, EPRI Feedwater Heater Technology Symposium Oct. 1992

3) Maurer, J. R. and Pepin J. J., The Application of an Advanced Fe-Ni-Cr-Mo-N Austenitic Alloy for Feedwater Heaters, ibid

4) Roth, R. Plymouth Tube Co., Manager of Technical Services, Personal Communication

5) Jones, R. H. ed. Stress Corrosion Cracking ASM 1992

TABLE 1
Split Ring Residual Stress Measurements
From Cracked Ex-Service Tubes (KSI)

Cardinal Unit 1	+ 12.8
Muskingum River Unit 5	+ 13.1, + 13.2, + 12.3
Mitchell Unit 1	+ 17.0, + 14.2, + 14.3, + 17.6, + 16.3, + 26.0

TABLE 2
Comparison of Residual Hoop Stress Values
Measured by Split Ring and Hole Drilling (KSI)

	Split Ring	Hole Drilling
Type 304N, Stretch	+ 8.2	+ 8.7
Type 316N, Rotary With Stress Relief	+ 11.3	+ 11.8
Type 316N, Rotary As Received	+ 17.3	+ 15.2

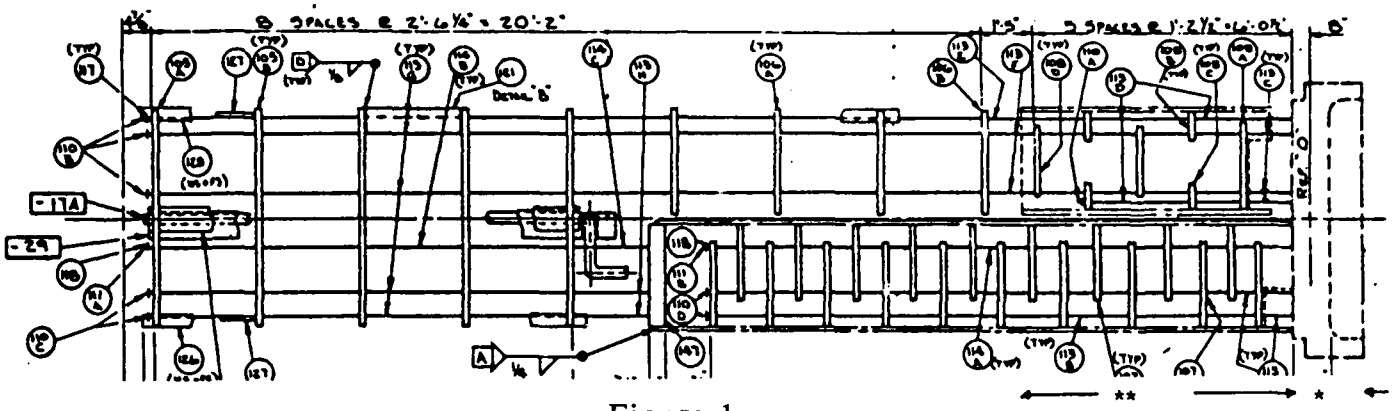

Figure 1

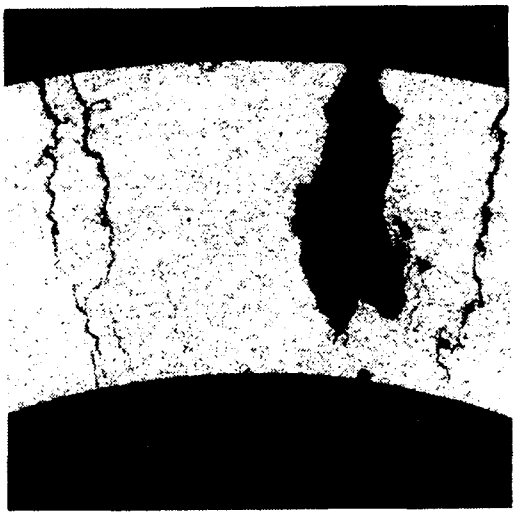

Figure 2

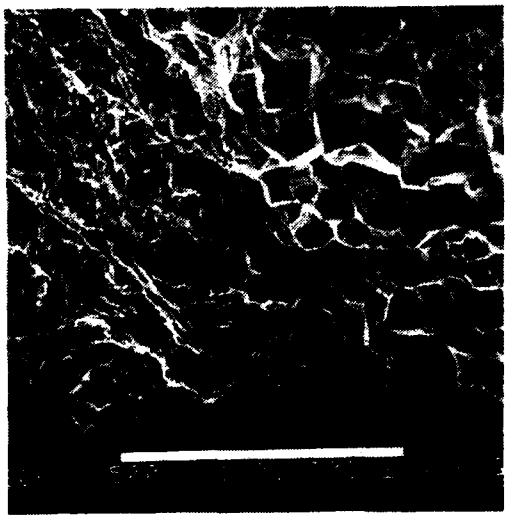

Figure 3a

Figure 3b

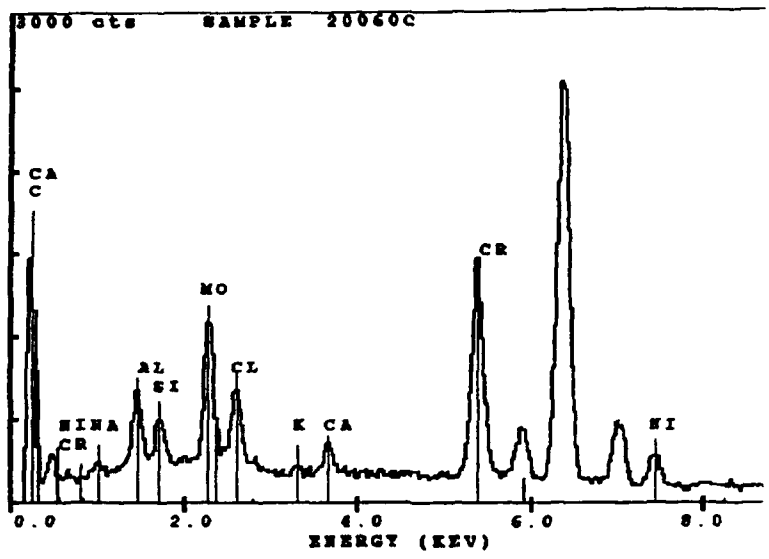

Figure 4

48 HOUR EXPOSURE TO MAGNESIUM CHLORIDE VS. RESIDUAL STRESS

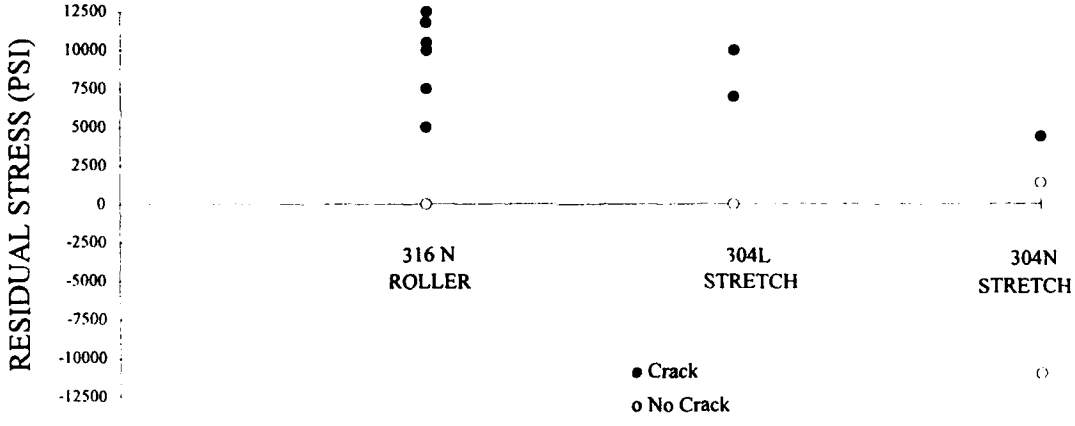

Figure 5

RESIDUAL STRESS VS. TIME TO CRACKING IN NaCl

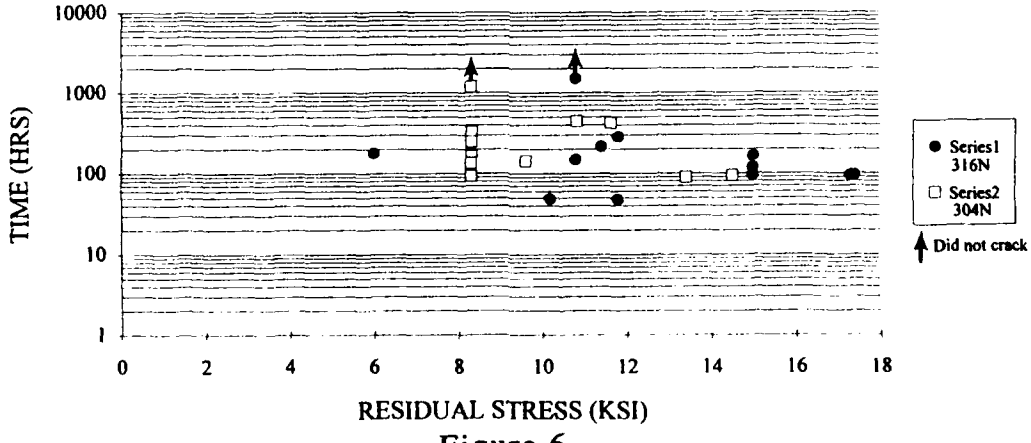

Figure 6

Figure 7

Figure 8

Stress Corrosion Cracking of Sensitized Type 316 Austenitic Stainless Steel in Pure Sulfuric Acid Solution

Rokuro Nishimura
Material Engineering Division,
Government Industrial Research Institute, Chugoku
Hiro-suehiro 2-2-2, Kure, Hiroshima 737-01, Japan.

Achmad Sulaiman
Research and Development Centre for Metallurgy,
Kompleks PUSPIPTEK, serpong, Tangerang, Indonesia.

Abstract

The stress corrosion cracking (SCC) of a commercial austenitic stainless steel type 316 has been investigated as a function of sensitizing temperature (800 K to 1300 K, 86.4 ks) in 0.82 kmol/m^3 pure sulfuric acid solution by using a constant load method. As for three parameters (time to failure, t_f, steady state elongation rate, $\dot{l}_{ss}$ and transition time, t_{ss}) obtained from corrosion elongation curve (elongation vs. time), it is found that the stress vs. three parameters curves for the sensitized specimens are divided into three regions that are dominated by either stress, SCC or corrosion. In the SCC-dominated region, the logarithm of $\dot{l}_{ss}$ is a linear function of the logarithm of t_f irrespective of sensitizing temperature. This result shows that the steady state elongation rate becomes a useful parameter for prediction of t_f as well as the case of the solution annealed specimen. However, the slope of the linear function depends upon the sensitizing temperature and becomes smaller than that of the solution annealed specimen over the whole sensitizing temperature. Furthermore, it is found that the most severe sensitization takes place at a sensitizing temperature of 900 to 950 K, at which temperature the slope of the linear function shows a minimum and the value of t_{ss}/t_f a maximum. The effect of sensitization on SCC and a SCC mechanism are qualitatively inferred.

Key words: stress corrosion cracking, prediction, steady state elongation rate, corrosion elongation curve, austenitic stainless steel, sensitization, sulfuric acid.

1. Introduction

The stress corrosion cracking (SCC) of the austenitic stainless steels (type 304 and type 316), which were solution annealed at 1373 K for 3.6 ks and then water quenched, has been investigated as functions of stress and environmental factors (pH, solution temperature, anion concentration, anion species) by using a constant load method[1-2]. From the results obtained, it has been found that a steady state elongation rate ($\dot{l}_{ss}/ms^{-1}$) obtained from a corrosion elongation curve (elongation vs. time) becomes a relevant parameter both for the prediction of time to failure and for the criterion on the assessment of SCC susceptibility for type 304 and type 316 austenitic stainless steels. Recently, it was found that the characteristics of the

steady state elongation rate can be applied to SCC of type 430 ferritic stainless steel[3] in acidic chloride and sulfate solutions by using a constant load method. On the basis of such a characteristic of $\dot{l}_{ss}$, we can estimate a threshold stress and critical values of the environmental factors such as pH, solution temperature and anion concentration for SCC. Specifically, whether a threshold stress exists or not should not be judged from whether specimens are broken or not, but by using other parameters such as t_{ss}/t_f, where t_{ss} is the transition time. However, the application of the parameter ($\dot{l}_{ss}$) for the prediction and the assessment was limited to only the solution annealed materials in earlier work.

Of the three factors (material, environment and stress) that are necessary for the occurrence of SCC of materials, an effect of the material (or metallurgical) factor, such as thermal history, on SCC still remains unclear in our studies. Specifically, it is important to clarify an effect of sensitization on SCC, since sensitization of materials is well known to show a detrimental effect on SCC and corrosion behavior[4-7]. Therefore, the purpose of the present paper is to elucidate whether the use of $\dot{l}_{ss}$ on SCC prediction described above can be applied to austenitic stainless steel type 316 that is sensitized at various temperatures.

2. Experimental

The specimens used were a commercial type 316 austenitic stainless steel (yield strength: 333 MPa and ultimate tensile strength: 647 MPa) with a gauge length of 25.6 mm and 1 mm in thickness as shown in Figure 1. The chemical composition (mass %) was as follows: C 0.054, Si 0.67, Mn 1.38, P 0.030, S 0.005, Ni 11.16, Cr 17.21, Mo 2.21. The specimens were solution annealed at 1373 K for 3.6ks under an argon atmosphere and then water quenched, which are called solution annealed specimens. Further the solution annealed specimens were sensitized at a temperature in the range of 800 K to 1300 K for 86.4 ks (24 h) under an argon atmosphere and then water quenched. Prior to the experiments, the sensitized specimens were polished to 1000 grit emery paper, degreased with acetone in an ultrasonic cleaner and washed with distilled water. After the pretreatment, the specimens were immediately set into a SCC cell. The solution used was 0.82 kmol/m^3 H_2SO_4 solution and was prepared from distilled water and guaranteed grade reagents. The test temperature was 323 and 353 ± 0.5 K. All experiments were carried out under open circuit conditions.

A lever-type constant load apparatus (lever ratio 1:10) to which three specimens can be separately and simultaneously attached was used with a cooling system on the top to avoid evaporation of the solution during experiments. The specimens were insulated from rod and grip by surface oxidized zirconium tube. A change in elongation of the specimens under the constant stress condition was measured by an inductive linear transducer with an accuracy of ± 0.01 mm.

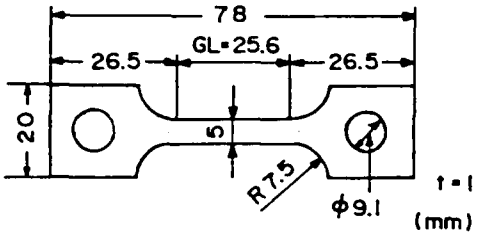

Figure 1--- geometry of the specimen.

3. Results

3.1 Corrosion Elongation Curve

Whenever a constant load method is used for SCC experiments, an elongation versus time curve can be always obtained, which is called a corrosion elongation curve. Figure 2 shows

a schematic representation of a corrosion elongation curve, which consists of three regions up to failure with an initial sudden rise of elongation; primary, secondary and tertiary regions. From this curve, we can get three parameters that are important to understand SCC behavior of materials; the steady state elongation rate ($\dot{l}_{ss}$) in the secondary region, the transition time (t_{ss}) between the secondary and tertiary regions, and the time to failure (t_f). The transition time is the time when the elongation starts to deviate from linearity in the secondary region. If there is no failure within a laboratory time scale ($< 10^7$ s), however, the tertiary region does not appear in the corrosion elongation curve, so that only $\dot{l}_{ss}$ can be obtained.

Figure 3 shows representative examples of the corrosion elongation curves for type 316 in 0.82 kmol/m^3 sulfuric acid solution. It is confirmed that the corrosion elongation curves experimentally obtained have the same shape as that in Figure 2. As a result, the three parameters described above can be obtained.

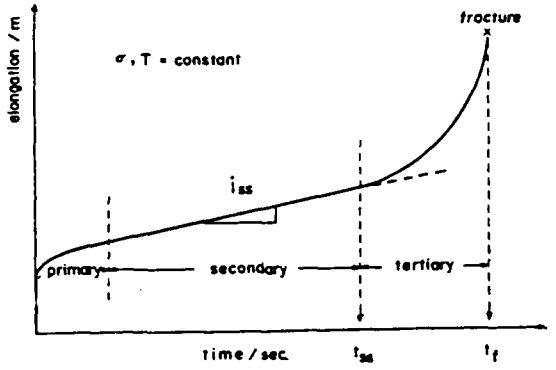

Figure 2--- Schematic representation of the corrosion elongation curve, where t_f is time to failure, t_{ss} the transition time between the secondary and tertiary regions, and $\dot{l}_{ss}$ the steady state elongation rate.

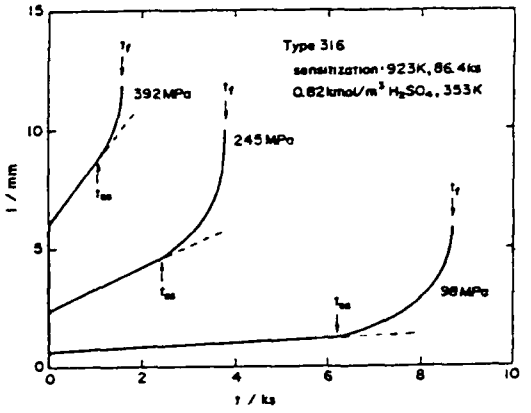

Figure 3--- Representative examples of corrosion elongation curves.

3.2 Stress Dependence of the Three Parameters ($\dot{l}_{ss}$, t_f and t_{ss})

3.2.1 Sensitizing Temperature

The three parameters obtained from the corrosion elongation curve were investigated as a function of stress for the sensitized type 316 in 0.82 kmol/m^3 H_2SO_4 solution at 353 K. Figure 4 shows representative examples of the stress vs. log t_f relationships for the specimens sensitized at 923 K and 1123 K for 86.4 ks, where the dashed line in Figure 4 is the result for the solution annealed specimen under the same experimental conditions. The relationships for the sensitized specimens are divided into three regions, as well as that for the solution annealed specimen, which are designated by arabic numerals 1 to 3 in the figure. As for the specimen sensitized at 923 K, it is clearly found that t_f becomes drastically shorter than for the solution annealed specimen. In addition, the stresses between both regions 1 and 2, and regions 2 and 3 become smaller than those for the solution annealed specimen. On the other hand, the result for the specimen sensitized at 1123 K is close to that for the solution annealed specimen. However, the stress between regions 1 and 2 is larger than that for the solution annealed specimen, while the stress between regions 2 and 3 is still smaller

than that for the solution annealed specimen.

Figure 5 shows the relationships between stress and log $\dot{I}_{ss}$ for the sensitized specimens (923 K and 1123 K), where the dashed line is the result for the solution annealed specimen. It is found that the relationships are also divided into three regions corresponding to those in Figure 4. Figure 6 shows the relationships between stress and the ratio of t_{ss} to t_f for the sensitized specimens, where the dashed line is the result for the solution annealed material. The values for the sensitized specimens in region 2 are constant independent of stress, but are slightly larger than that for the solution annealed specimen. In addition, the value for the specimen sensitized at 923 K is larger than that for the specimen sensitized at 1123 K. On the other hand, the values in regions 1 and 3 are larger than that in region 2. Thus the stress dependencies of three parameters for the sensitized specimen are found to show similar behavior to those for the solution annealed specimen, although the stresses between regions 1, 2 and 3, and the value of t_{ss}/t_f are dependent upon sensitizing temperature. With regard to the other sensitized specimens, their stress dependencies of three parameters are similar to that for the sensitized specimens (923 K and 1123 K, 86.4 ks).

Figure 7 shows the relationship between t_f (at a stress of 400 MPa) and sensitizing temperature. It is clear that t_f is short at a sensitizing temperature of 850 to 1100 K in comparison to that for the solution annealed specimen (indicated by the open triangle). In addition, Figure 8 shows the relationship between t_{ss}/t_f, in the SCC-

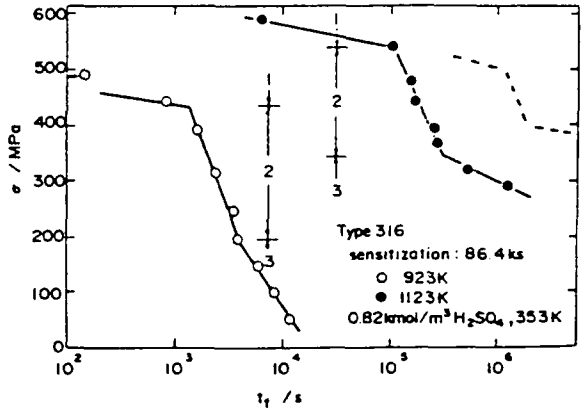

Figure 4--- Relation between stress and log t_f for sensitized type 316 in 0.82 kmol/m^3 H_2SO_4 solution at 353 K. The dashed line is the result for the solution annealed type 316.

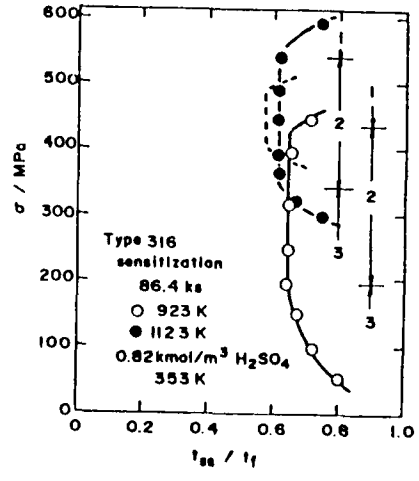

Figure 6--- Relation between stress and t_{ss}/t_f for sensitized type 316 in 0.82 kmol/m^3 H_2SO_4 solution at 353 K. The dashed line shows the result for the solution annealed type 316.

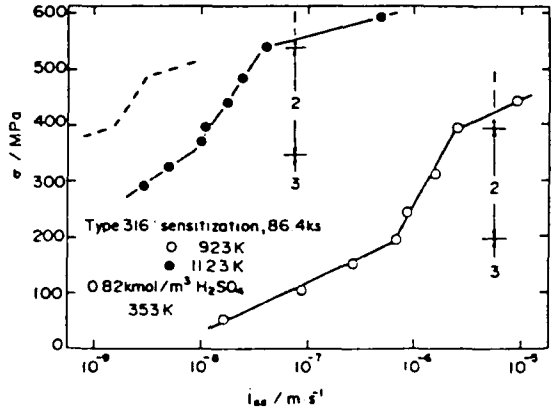

Figure 5--- Relation between stress and log $\dot{I}_{ss}$ for sensitized type 316 in 0.82 kmol/m^3 H_2SO_4 solution at 353 K. The dashed line is the result for the solution annealed type 316.

dominated region, and sensitizing temperature. The value becomes larger than that for the solution annealed specimen over the whole sensitizing temperature range and becomes a maximum at a sensitizing temperature of 900 to 950 K. The results shown in Figures 7 and 8 indicate that the most severe sensitization takes place at a temperature of 900 to 950K.

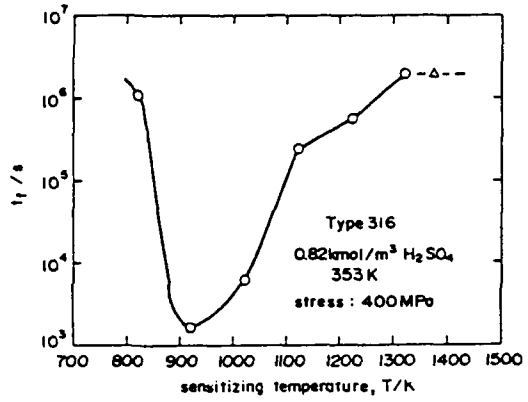

Figure 7--- Relation between t_f at a stress of 400MPa and sensitizing temperature.

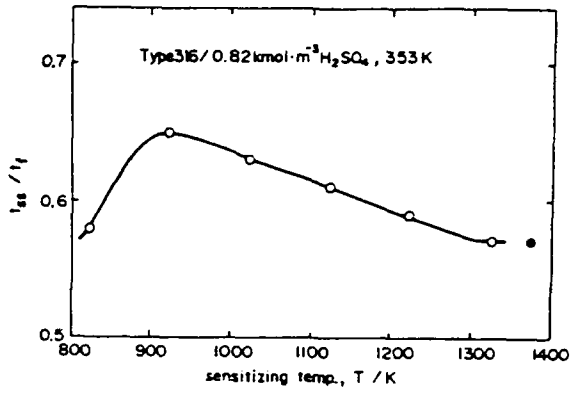

Figure 8--- Relation between t_{ss}/t_f and sensitizing temperature.

3.2.2 Solution Temperature

In the previous section, the specimen sensitized at 923K showed that the stress between regions 1 and 2 is smaller than that for the solution annealed specimen, while the specimen sensitized at 1123K had a larger stress than that for the solution annealed specimen. Therefore, we need to check whether the stress between regions 1 and 2 becomes larger or smaller than that for the solution annealed specimen for a different SCC test temperature. Figures 9 and 10 show the relationships between stress and t_f / $\dot{l}_{ss}$ for the specimen sensitized at 923K at a test temperature of 323K, where the dashed line shows the results at a test temperature of 353K. The relationships are also divided into three regions, and the stress between regions 1 and 2 at 323K is larger than those at 353K and for the solution annealed specimen, whereas the stress between regions 2 and 3 is independent of solution temperature. Figure 11 shows the relationship between stress and the value of t_{ss}/t_f. The value in region 2 is found to be constant independent of stress and test temperature. Thus test temperature affects only the stress between regions 1 and 2.

Figure 12 shows the maximum and minimum stresses in region 2 as a function of sensitizing temperature, where the solid circles in Figure 12 stand for those of the solution annealed specimen. In addition, Figure 12 also shows the result for

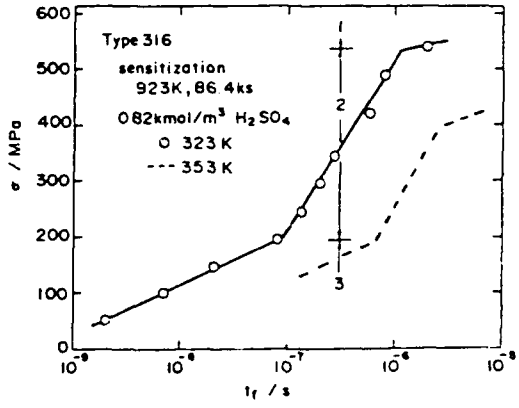

Figure 9--- Relation between stress and log t_f for sensitized type 316 in 0.82 kmol/m^3 H_2SO_4 solution at 323 K. The dashed line is the result at 353K.

the sensitized specimen (923 K, 86.4 ks) at a test temperature of 323 K (the dashed line). As for a test temperature of 353K, the maximum stress for the sensitized specimens in the range of 850 to 1100 K is smaller than that for the solution annealed specimen, while the maximum stress at a sensitizing temperature of 1100 to 1250 K is slightly larger than that for the solution annealed specimen. The maximum stress at the other sensitizing temperatures is almost the same as that for the solution annealed specimen. However, as the test temperature becomes lower, the maximum stresses for the specimens sensitized at 850 to 1100K tend to become larger than that for the solution annealed specimen. On the other hand, the minimum stress becomes smaller than that for the solution annealed specimen at a sensitizing temperature of 850 to 1250 K. Thus the decrease in the maximum stress takes place at a sensitizing temperature of 850 to 1100K when the test temperature is 353K, but not at 323K.

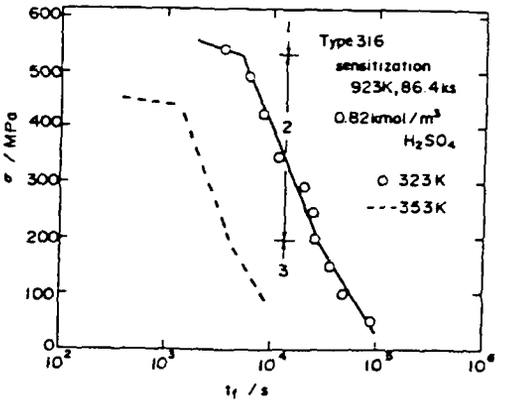

Figure 10--- Relation between stress and log $\dot{t}_{ss}$ for sensitized type 316 in 0.82 kmol/m^3 H_2SO_4 solution at 323 K. The dashed line is the result at 353K.

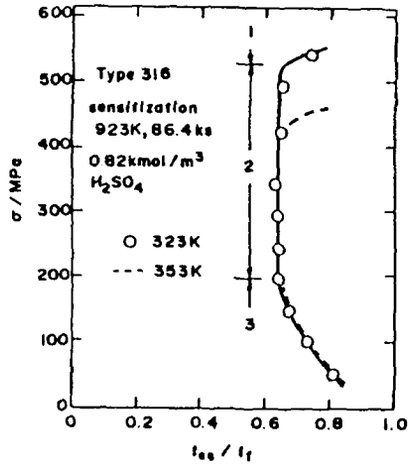

Figure 11--- Relation between stress and t_{ss}/t_f for sensitized type 316 in 0.82 kmol/m^3 H_2SO_4 solution at 323 K. The dashed line is the result at 353K.

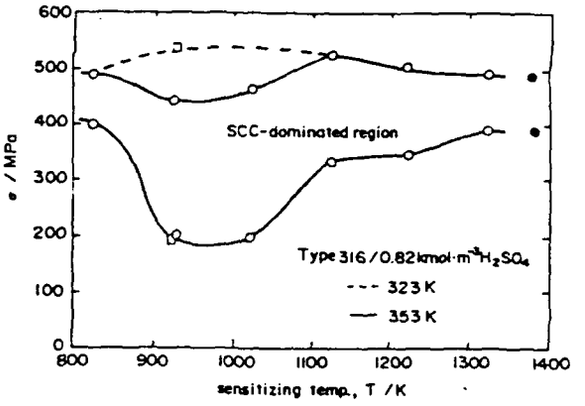

Figure 12--- Maximum and minimum stresses in region 2 (SCC-dominated region) as a function of sensitizing temperature.

3.3 Fracture Appearances

The fracture appearance of the solution annealed specimen was of a transgranular mode in the SCC-dominated region in 0.82 kmol/m^3 H_2SO_4 solution. On the other hand, with the sensitized specimens, Figure 13 shows the fracture appearance (a) of the sensitized specimen (923 K, 86.4 ks) is entirely intergranular, which is the same as that of the specimen sensitized at 1023 K for 86.4 ks. However, the sensitized specimens treated 823 K (86.4 ks) is predominantly transgranular (b). The same fracture appearance was obtained for

specimens sensitized at a sensitizing temperature above 1123 K and below 823 K. Consequently, the fracture appearances of the specimens sensitized at temperatures of 850 to 1100K only display the intergranular mode.

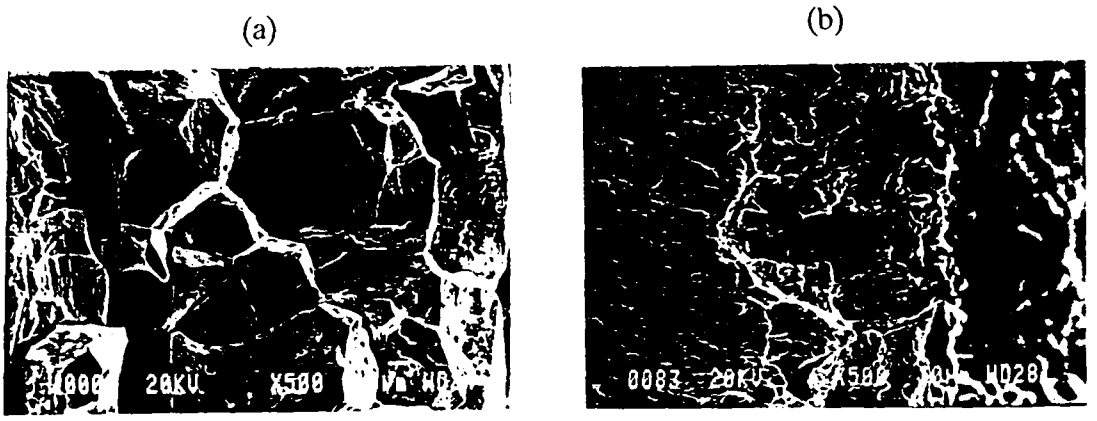

Figure 13--- The representative fracture appearances of the sensitized type 316, where (a) 923 K, 86.4 ks, x 500 and (b) 823 K, 86.4 ks, x 500.

4. Discussion

4.1 Meaning of Three Regions (1 to 3)

Consider qualitatively the meaning of each region obtained in the relationships between the three parameters and stress for the sensitized specimens. With regard to region 3, the corrosion rates of the sensitized specimens can be estimated from the weights before and after the SCC experiments, both with and without applied stress. The corrosion rates of the sensitized specimens in region 3 were almost the same as those obtained without applied stress, as was the case for the solution annealed specimen[1]. Therefore, it can be concluded that fracture in region 3 occurs by reduction in cross sectional area caused by general corrosion and this region is called a corrosion-dominated region. In contrast to region 3, region 1 is considered to correlate with mechanical fracture, in which stress plays a major role. In this case, the reduction in cross sectional area is caused by a high applied stress, so that region 1 is called a stress-dominated region. Finally, region 2 is the SCC-dominated region in which stress and corrosion show a synergistic effect on fracture for the sensitized and solution annealed specimens. In the SCC-dominated region, the value of t_{ss}/t_f always holds constant with a fixed value irrespective of stress, although it depends upon sensitizing temperature. On the other hand, the values of t_{ss}/t_f in the corrosion- and stress-dominated regions becomes close to unity. Hence the value of t_{ss}/t_f is a good indicator to distinguish between these regions.

From the above consideration, it can be understood that the minimum stress between the SCC-dominated and corrosion-dominated regions corresponds to a threshold stress below which no SCC takes place. The existence of the threshold stress cannot be determined by only t_f, especially in the cases of marked sensitization and/or aggressive solutions such as HCl[1]. The magnitude of I_{ss} and the value of t_{ss}/t_f must be taken into consideration to determine the existence of a threshold stress. As for the reduction in the maximum stress in

the SCC-dominated region, on the other hand, a further experiment must be conducted to clarify the behavior.

4.2 A Parameter for Prediction of Time to Failure

As already reported, in the case of the solution annealed type 304 and type 316 austenitic stainless steels, the steady state elongation rate becomes a useful parameter for prediction of time to failure, from the fact that log $\dot{l}_{ss}$ shows a linear function with log t_f in the SCC-dominated region, irrespective of stress and environmental factors such as pH, solution temperature and anion species. Therefore the same procedure is applied to the present results for the sensitized specimens.

Figure 14 shows representative examples of the relationships between log $\dot{l}_{ss}$ and log t_f (stress: variable) for the specimens sensitized at 923 K (323 and 353K) and 1123K, which are replotted from Figures 3, 4, 9 and 10. It was found that the relationship in the SCC-dominated region is a good straight line with a slope smaller than that (−2) for the solution annealed specimen. Such a straight line can be applicable to the relationships for sensitized specimens, although their slopes depend upon the sensitizing temperature. In addition, the slope of the straight line for the specimen sensitized at 923K is independent of test temperature. Hence we can draw the following general equation for the sensitized specimens,

$$\log \dot{l}_{ss} = -B \log t_f + C \qquad (1)$$

where the slope, B, depends upon sensitizing temperature and C is a constant depending on environmental factors and sensitizing temperature. Figure 15 shows the slope (B) of the linear relationship between log $\dot{l}_{ss}$ and log t_f as a function of sensitizing temperature. It is clear that the slope is smaller than that for the solution annealed specimen over the whole sensitizing temperature range, showing a minimum at a sensitizing temperature of 900 to 950 K.

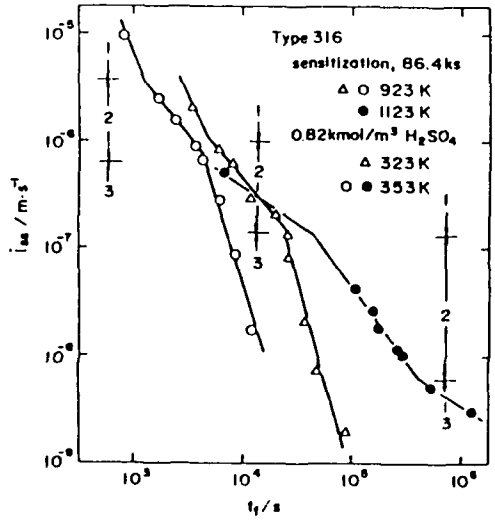

Figure 14--- Relation between log $\dot{l}_{ss}$ and log t_f for the sensitized type 316 (923K and 1123K, 86.4 ks) as a function of stress.

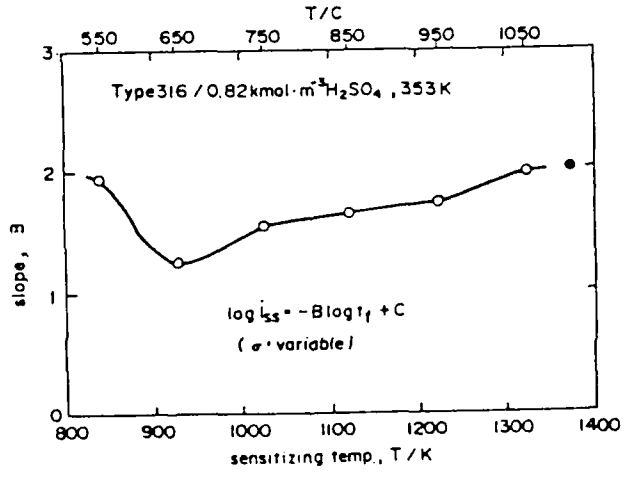

Figure 15--- Relation between the slope of the linear function (log $\dot{l}_{ss}$ vs. log t_f) and sensitizing temperature.

The above linear equation shows that $\dot{l}_{ss}$ is a useful parameter for prediction of time to failure even for the sensitized specimens, because $\dot{l}_{ss}$ can be obtained at a time within 10 to 20% of the time to failure from the corrosion elongation curve. Hence the steady state elongation rate is a parameter for prediction of time to failure for sensitized specimens as well as the solution annealed specimen.

4.3 An Implication of SCC Mechanism

With regard to the solution annealed specimens (type 304 and type 316), as already reported[1,2], three regions in the corrosion elongation curve are considered to correspond to crack nucleation and propagation periods on a SCC process, respectively. In the nucleation period (the primary region), the increase in elongation is caused by creep in the bulk[5] and the nucleation of cracks takes place at slip steps, at which preferential dissolution occurs in aggressive solutions such as HCl. In the steady propagation period (the second region), the steady state elongation rate ($\dot{l}_{ss}$) can be related to a propagation rate of the cracks, since the elongation rate is directly connected to the time to failure as presented in eq(1). However, whether or not SCC takes place depends upon the order of magnitude of $\dot{l}_{ss}$, because when $\dot{l}_{ss}$ is of the order of 10^{-10} m/s and less, no SCC occurs within a laboratory time scale ($<10^7$ seconds). The terminal propagation period (the tertiary region) shows that the rapid increase in elongation starts to lead to failure. In this region, as a crack propagates, an effective reduction in cross sectional area occurs and as a result a final mechanical failure takes place. Once this region starts, SCC always occurs. Therefore this region is called the propagation period of SCC. The fracture appearances of the solution annealed specimens show a transgranular mode, so that the emergence of the slip steps plays an important role in the SCC behavior of the solution annealed specimen.

On the other hand, in the case of the sensitized specimens, it is well recognized that the precipitation of chromium carbides occurs at the grain boundaries by sensitization, which leads simultaneously to the formation of chromium depletion areas along the grain boundaries. As the chromium depletion areas are sites for preferential corrosion, they act as crack nucleation sites, instead of the slip steps. Furthermore, the present results show that the corrosion elongation curve for sensitized specimens is almost the same shape as that for the solution annealed specimen, and the curve consists of three regions. This means that the SCC process of the sensitized specimens is identical with that of the solution annealed specimens described above. The difference is that the propagation of the cracks in the steady propagation period is along the grain boundaries. Consequently, the fracture appearance is of an intergranular mode, especially at a sensitizing temperature between 850 and 1100 K. This temperature range is in agreement with that of the sensitization based on the chromium depletion model[5].

In addition, at a sensitizing temperature above 1100 K and below 850 K, the sensitization affects slightly the slopes and t_{ss}/t_f as shown in Figures 8 and 15, but little intergranular mode appears. Briant, et al[7] pointed out that solute segregation such as phosphorous and sulfur at grain boundaries takes place even for a solution annealed specimen as well as a sensitized specimen. At these sensitizing temperatures, therefore, we might need to consider the solute segregation model.

5. Conclusions

The SCC characteristics of the sensitized specimens in pure sulfuric acid solution are

summarized as follows,

(1) The stress-three parameter ($\dot{l}_{ss}$, t_f and t_{ss}/t_f) curves are divided into three regions, that is, the stress-dominated, SCC-dominated and corrosion-dominated regions, respectively.

(2) The value of t_{ss}/t_f in the SCC-dominated region is smaller than that of the solution annealed specimen over the whole sensitizing temperature, but it is independent of stress in the SCC-dominated region and test temperature.

(3) The logarithm of $\dot{l}_{ss}$ and t_f obtained as a function of stress is a good straight line with a slope of less than -2 for the solution annealed specimen.

(4) From (3), the steady state elongation rate becomes a parameter for prediction of time to failure.

(5) The fracture mode becomes predominantly intergranular at a sensitizing temperature between 850 and 1100 K.

References

(1) R. Nishimura and K. Kudo, Corrosion, 45, 308(1989).
(2) R. Nishimura, Corrosion, 46, 311(1990).
(3) R. Nishimura, Corrosion, 48, 882(1992).
(4) R.L. Cowan, II and G.M. Gordon, Stress Corrosion Cracking and Hydrogen Embrittlement of Iron Base Alloys, Eds., R.W. Staehle, J. Hochman, R.D. McCright and J.E. Slater, National Association of Corrosion Engineers (NACE), p.1023, 1977.
(5) R.L. Cowan II and C.S. Tedmon, Jr, Intergranular Corrosion of Iron-Nickel-Chromium Alloys, p.312, 1973, Advances in Corrosion Science and Technology, Vol.3, Eds., M.G. Fontana and R.W. Staehle.
(6) G.E. Dieter, Mechanical Metallurgy (second edition), p.195, 1976, McGrAW-HILL.
(7) R.A. Mulford, E.L. Hall and C.L. Briant, Corrosion, 39, 132(1983).

The influence of H^+ and Cl^- on SCC of austenitic 304SS in acidic chloride solutions at ambient temperature

Z. Fang
Dept of Surface Sci & Corros Engin
Beijing Univ of Sci & Tech
Beijing, 100083
China

R. Z. Zhu
Dept of Surface Sci & Corros Engin
Beijing Univ of Sci & Tech
Beijing, 100083
China

Y. S. Wu
Dept of Surface Sci & Corros Engin
Beijing Univ of Sci & Tech
Beijing, 100083
China

Abstrsct

The susceptibility to SCC of austenitic 304SS in acidic chloride solutions at ambient temperature has been examined by the slow strain rate test (SSRT) method. H^+ and Cl^- ions are important in causing SCC and changing the type of corrosion. The acidity range susceptible to SCC is 0.01--1.2M H^+. Cl^- ion has a dual function in the process of SCC, ie: romoting the formation of a layer of adsorptive product film on the metal surface and damaging the perfectness of the film for the local enrichment of Cl^- ion. There are both competition and coordination roles between H^+ and Cl^- in causing SCC. With the results of AC impedance measured during SSRT at various elongations and the chemical composition of the surface film analyzed by XPS, it is proposed that the formation and subsequent rupture of the surface film enriched in Cr and Ni is a prerequisite for SCC.

Key terms: austenitic 304SS, stress corrosion cracking, acidic chloride solution, formation of surface films.

Introduction

The stress corrosion cracking (SCC) of austenitic stainless steels in chlorides can even occur in the active state, which is different from the SCC of this kind of material in the passive state and is rarely studied because it is widely considered that the overall corrosion of austenitic stainless steels in hydrochloride is serious and the development of local corrosion impossible. But the SCC of austenitic stainless steels in chlorides at ambient temperature caused by active corrosion has been reported recently[1,2].

The work of Bianchi[3] shows that transgranular stress corrosion cracking of austenitic stainless steel type 304 can occur in hydrochloric acid solution at ambient temperature. The range of acidity causing SCC is 0.3--1.0 MHCl concentration. Torchio's work[4] demonstrates that SCC of the type AISI 304 stainless steel in chlorides

containing HCl at 25°C occurs in solutions of wide acidity range. S. M. Dai[5] gives results showing that the acidity range causing SCC of the austenitic stainless steel 0Cr18Ni9 in mixed solutions of HCl + NaCl is 0.07--1.5 MH^+.

On the basis of above mentioned work, this paper is aimed at understanding the action of H^+ and Cl^- in the process of SCC of austenitic stainless steels in the active state at ambient temperature and discussing the mechanism of SCC of austenitic stainless steels in the active state.

Experimental Method

Type 304 steel having the following chemical analysis was employed: 18.13Cr, 9.30Ni, 0.18 C, wt%. The material was solution annealed at 1050°C for 30 min and water quenched.

The exposed aera of cylindical specimens in the stress corrosion tests was Ø3.5X25mm. In order to avoid any possible notch effects, the test part of the specimens was electropolished beforehand in a solution of:1000ml H_3PO_4 + 500ml H_2SO_4 + 500ml H_2O at 50-60°C.

The slow strain rate test (SSRT) technique was used to impose stress on the test specimens. The AC impedance of a test specimen at different elongation in SSRT was measured by 1286 Electrochemical Interface and 1250 Frequency Response Analyzer. The chemical composition of the surface film on the test specimen in the active corrosion state was analyzed by XPS.

Experimental Results

1 Stress corrosion tests

The stress-time curves for 304SS in solutions of 3.0M Cl^-+ 0.5M H^+, 3.0M Cl^-+ 0.1M H^+ and in air were shown in Fig. 1. It can be seen from this figure that the maximum stress, elongation and the area enclosed by the curves of the specimens in HCl + NaCl medium are smaller than for the specimen in air. Therefore it can be concluded that 304SS is susceptible to SCC in a HCl + NaCl medium at ambient temperature and the susceptibility to SCC is enhanced by increase of the concentration of H^+.

Fig. 2 shows the effect of concentration of H^+ and Cl^- on time to failure of the specimens. At lower concentration of Cl^- (1.0M), the time to failure is shortened with the increase of H^+ concentration. At a higher concentration of Cl^- (5.0M), the time to failure goes through two stages, first decreasing and then increasing. At a certain concentration of H^+, the effect of Cl^- concentration on the time to failure is complicated. For lower H^+ concentrations (<0.2M), the time to failure is shortened with the increase of Cl^- concentration. For higher H^+ concentrations, it changes reversely. The effects of H^+ and Cl^- concentration on elongation and reduction in area are similar to that on time to failure. It can be seen from the SSRT results that the effects of H^+ and Cl^-on the susceptibility to SCC in the system "304SS/HCl+NaCl" are interralated, and the concentration of H^+ and Cl^- are important factors in the susceptibility to SCC. Fig.3 gives a corrosion type diagram for 304SS in solutions of HCl+ NaCl. From Fig. 3 it can be seen that there exists an acidity range susceptible to SCC for the system "304SS / HCl+NaCl". The

acidity range susceptible to SCC widens with increase of the total concentration of Cl^- and the minimum concentration of H^+ causing SCC is decreased.
When the concentration of Cl^- is fixed, the corrosion type changes markedly with the increase of H^+ concentration. In weak acidity, there is only even general corrosion, but as the acidity is increased, pitting, stress corrosion cracking and uneven general corrosion appear successively.

2 The measurement of AC impedance

The AC impedance of 304SS in solution of $1.5MCl^-+1.0MH^+$ at different elongations in the SSRT process was measured. Fig.4 shows the AC impedance diagrams after elongations of 0%, 8%, and 17% respectively. At 0%, the diagram is of semicirclar shape; the reaction resistance is 10.4 Kohm•cm^2. When the elongation attained 8% and 17%, the real parts at low frequency region contracted and the reaction resistance decreases markedly, to 0.5 Kohm•cm^2 and 0.3 Kohm•cm^2 respectively. This indicates that the stress promotes active corrosion of the metal.

Under our experimental conditions, the formation of an oxide on the metal surface can be excluded, but a stain on the metal surface could clearly be seen. It can be inferred that there is a corrosion product film forming on the metal surface. If this is so, the AC impedance diagram should be characterized by a porous film. These types of diagram would take different shapes with the changes of reaction resistance and interface capacity. The contraction of the real part at the low frequency region on the AC impedance diagram shown in Fig. 4 may be caused by the formation of an adsorptive product film on the metal surface.

3 Analysis of the surface film

The distributions of elements in the 304SS surface layer was analyzed by XPS after immersion in solution of $1.5MCl^-+ 0.5MH^+$ for two days. The results show that in the surface layer, Fe takes form of Fe and Fe^{2+} ion, Cr exsists as Cr and Cr_2O_3, Ni as Ni, Ni_2O_3 and $Ni(OH)_2$; Cl also appeared in the surface layer.

Table 1 gives the content of Fe, Cr, Ni and Cl at different depths from the surface. It can be seen that Cr, Ni and Cl are concentrated in the very thin surface film(<60 Å).

On the basis of these results and reference to former works[6,7] on the metal dissolution process, it can be considered that the dissolution of 304SS in HCl +NaCl contains the following three kinds of composites: $(MOH)_{ads}$, $(MCl)_{ads}$, and $(MOHCl)_{com}$, where M refers to Fe, Cr and Ni metal elements. In addition Cr and Ni ions hydrolyses and form Ni_2O_3 and Cr_2O_3. These composites form the surface film. This surface film enriched in Cr and Ni plays a certain protective role on metal, which is one of the essential conditions for the occurance of SCC of 304SS in active state. The cracks nucleate on film rupture and active points.

Discussion

The occurrence of SCC in austenitic 304SS in solutions of HCl+NaCl is closely related with the concentrations of H^+ and Cl^-. There exsists a range of H^+ concentration and a critical Cl^- concentration susceptible to SCC (Fig. 3) and it is suggested that Cl^- has a dual nature in the process of SCC: the increase of Cl^- concentration is favorable for the adsorptive process and the adsorptive product film can be formed on the metal surface

which can protect the base metal from corrosion. On the other hand, the adsorption of Cl^- can damage the perfectness and the electrochemical evenness of the surface film. Richter's [8] measurements by
radioisotope showed that Cl^- ions distribute uniformly on the whole surface of austenitic stainless steel, but Cl^- ion is highly concentrated in the area suffering from local corrosion, which also illustrates the dual action of Cl^- ion.

With the increase of H^+ concentration, the corrosion type of the material changes markedly at a certain Cl^- concentration. The material is susceptible to SCC within a certain range of H^+ concentrations. The lower critical concentration of H^+ is the turning point of the austenitic stainless steel from the passive to the active state and the upper critical concentration of H^+ is where competition between local corrosion and uneven general corrosion occurs. The lower and upper critical concentrations of H^+ susceptible to SCC change with the total concentration of Cl^-.

The action of H^+ and Cl^- on SCC in the active state is both competitive and coordinative. H^+ is one of the prerequisite environmental conditions, since with the existence of H^+can SCC in the active state occur. Cl^- ion has a dual action of both promoting the formation of an adsorptive product film which protects the base metal from corrosion and ruptures the surface film. The coordination action can be illustrated from curves of critical H^+ concentration susceptible to SCC shown in Fig. 3. The reason for the lower and upper H^+ concentrations decreasing with increase of Cl^- ion concentration is that the Cl^- ion can enhance the activity of H^+.

Conclusions

1 SCC in the system "austenitic 304SS / HCl + NaCl" can occur at ambient temperature and the diagram of "[Cl^-]-[H^+]-SCC" is obtained.
2 There exsits a definite range of acidity susceptible to SCC for the system "austenitic 304SS / HCl+NaCl". This acidity range depends upon concentration of Cl^- ion.
3 Cl^- ion has a dual function in the process of SCC, ie: promoting the formation of a layer of adsorptive product film on the metal surface and damaging the perfectness of the film for the local enrichment of Cl^- ion.
4 There are both competition and coordination roles between H^+ and Cl^- in causing SCC.
5 With the results of the AC impedance measurement, and XPS analysis, the surface film formed in solutions of HCl+NaCl at ambient temperation is enriched in Cr, Ni and Cl and exhibits a moderately protective role.

References

1 G. Herbsleb u. F. Theiler, Werkst. u. Korros., 40 8(1989): p. 467
2 "Corrosion problems of the stainless steel tube in Weihe engineering", Technique proc., 1990
3 G. Bianchi and F. Mazza: "Extended Abstracts 5th Int. Congr. Met. Corros.", (NACE, Houston, Texas, 1974), p. 380
4 S. Torchio, Corros. Sci., 20, 4(1980): p. 555
5 S. M. Dai and H. Liang, Proc.: 9th Int. Congr. Met. Corros., (1984): p. 216
6 D. R. Macfarlane and S. I. Smedley, J. Electrochem. Soc., 133 11(1986): p. 2240
7 P. Q. Zhang, Doctor thesis of Beijing Univ. of Sci. & Tech. (1991): p. 32
8 M. Richiter u. A. Walter, Werkst. u. Korros., 39, 8(1988): p. 355

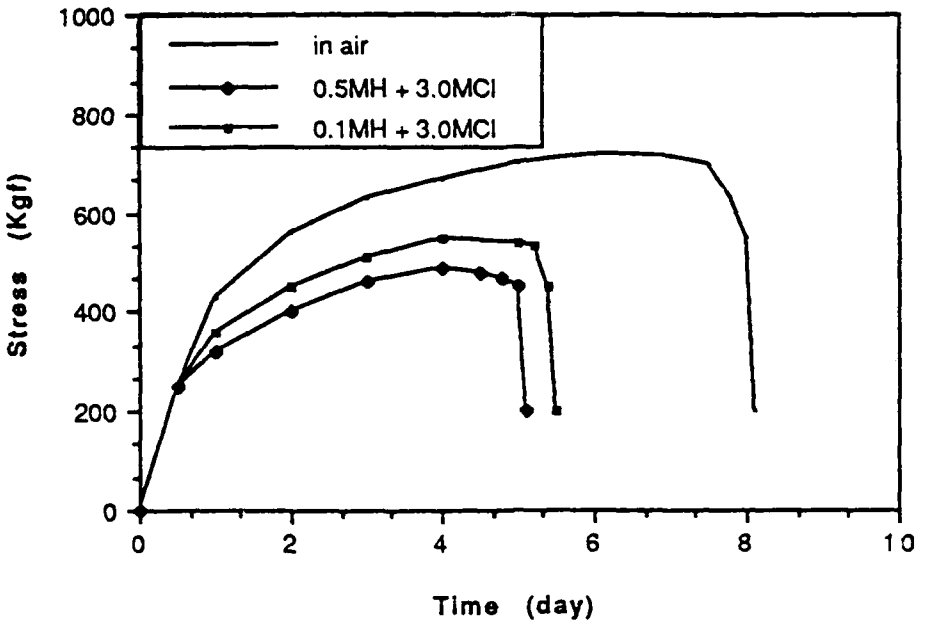

Fig. 1 Stress-Time curves for the system "304SS / HCl+NaCl" by SRRT.

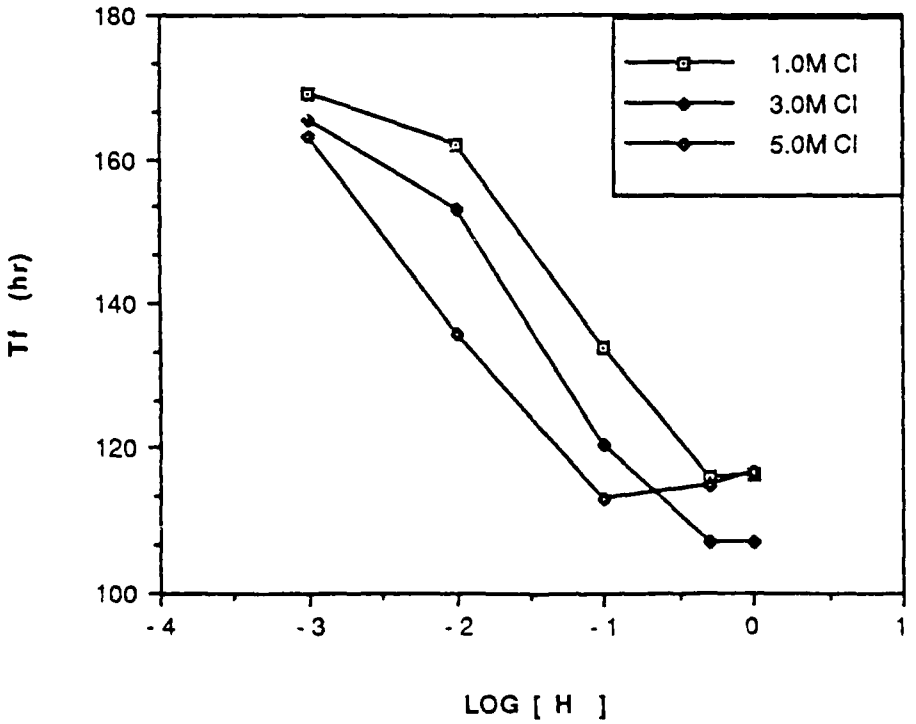

Fig. 2 The effect of H^+ and Cl^- concentration on time to failure of specimens by SSRT.

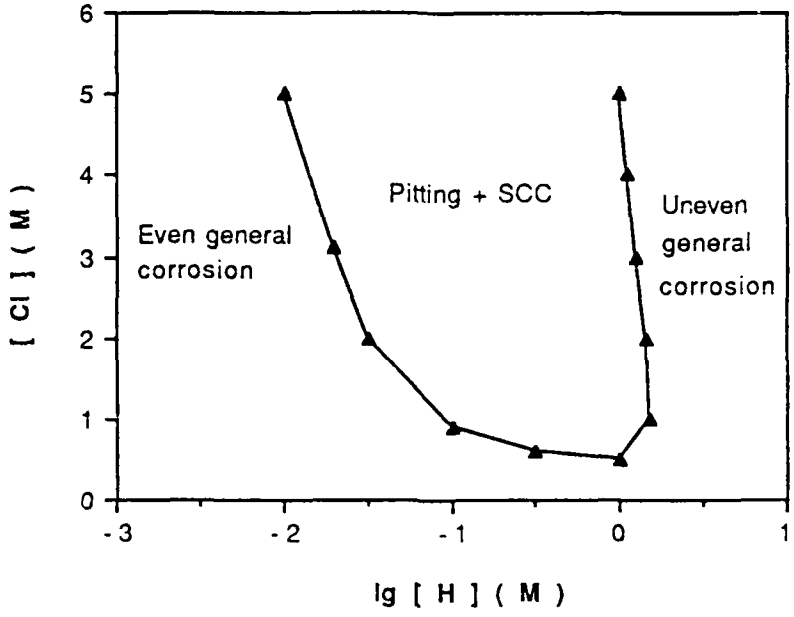

Fig. 3 [Cl^-]-[H^+]-SCC diagram of system "304SS/HCl+NaCl" by SSRT.

Table 1 Content of Fe, Cr, Ni and Cl in the surface layer of 304SS after immersion for 2 hours in a solution of 1.5M Cl^- + 0.5M H^+ at 25°C (at. %)

depth(Å)	Fe	Cr	Ni	Cl
20	45.56	27.32	8.48	18.63
30	44.60	30.52	5.87	18.01
60–70	75.65	20.85	3.50	0

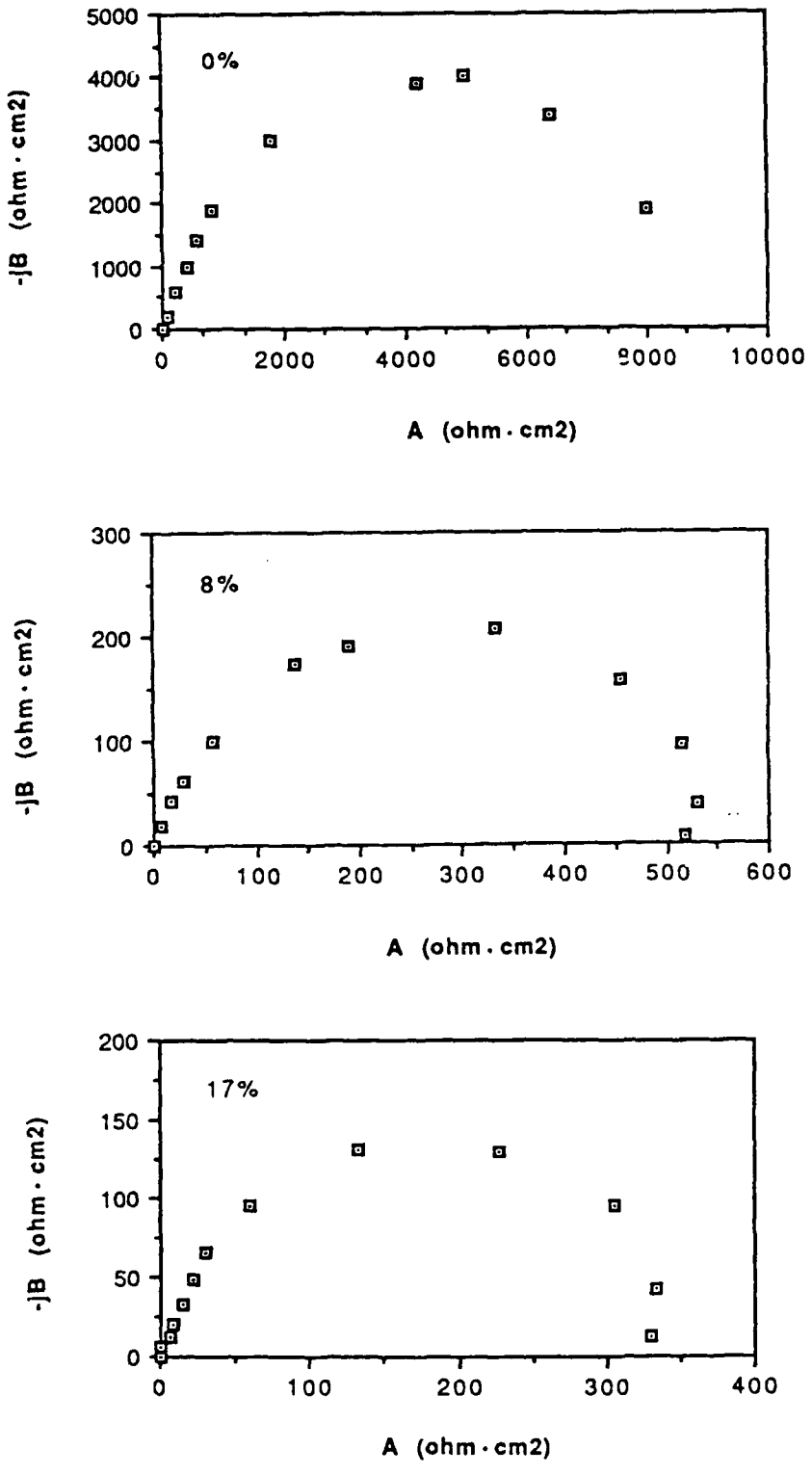

Fig. 4 AC impedance diagrams for 304SS in solution of $1.5MCl^{-}+1.0MH^{+}$ at different elongations by SSRT.

Differentiation Between Sulphide Stress Corrosion Cracking in 13%Cr and Duplex Stainless Steels

J. C. Barker, J. Yu, R. Brook
Dept. of Engineering Materials
University of Sheffield, UK

Abstract

Sulphide stress corrosion cracking tests have been performed on a 13%Cr stainless steel and a duplex stainless steel. Important differences were found between the cracking behaviour of the two steels in hydrogen sulphide solutions. Their susceptibility to cracking is discussed in terms of threshold stress-intensity (K_{1scc}) and crack growth rate. The role of hydrogen charging, both at the crack-tip and in the bulk material, has been investigated by tests on coated specimens and by measurement of fracture toughness after pre-charging.

This work summarizes and develops further the analysis of the results achieved recently at the University of Sheffield with the support and co-operation of the National Physical Laboratory, UK and BP International Limited.

Key terms: sulphide stress corrosion cracking, 13%Cr stainless steel, duplex stainless steel.

Introduction

As existing oil and gas fields are gradually depleted, further production places greater and greater demands on the use of materials. The occurrence of so-called sour wells, containing hydrogen sulphide, becomes more likely as new wells are drilled deeper, and as existing wells tend to sour with age due to the practice of injecting surface waters[1]. Higher pressures, stresses and temperatures are also associated with deep wells, and hence the use of corrosion resistant alloys (CRA) is becoming increasingly common[2].

Martensitic stainless steels have been used to resist CO_2 corrosion for many years and also find applications in sour service as downhole and wellhead equipment, and downhole tubulars. Duplex stainless steels, which comprise a dual-phase microstructure of ferrite and austenite, have in recent years been used for similar applications[3,4].

Laboratory evaluation of the resistance of CRA's to sulphide stress corrosion cracking (SSCC) in H_2S-environments has predominantly been by ranking tests on plain specimens. However, a fracture mechanics approach to testing is considered more suitable for predicting in-service failure because the stress-corrosion threshold stress-intensity, K_{1scc}, can be substituted in stress-intensity relations for tubular goods[5]. Hence, this paper compares and contrasts the response of a 13%Cr stainless steel and a duplex stainless steel to fracture mechanics-based SSCC tests.

Experimental Procedures

Materials

The test materials were AISI 410 (UNS S41000) 13%Cr stainless steel and Uranus B50 (UNS S32404) duplex stainless steel, supplied in the form of 77 mm diameter round bars. Their compositions are listed in Table 1.

The 13%Cr steel was heat treated by hardening (2 hrs, 980°C, oil quench) followed by double tempering (3 hrs, 680°C, air cool then 1 hr, 650°C, air cool), giving a 0.2% proof stress of 580 MPa. Its

microstructure comprised mainly of tempered martensite with occasional globular carbides; the mean prior-austenite grain size was 30 μm.

The duplex steel was tested as-received in a hot-rolled condition, with a 0.2% proof stress in the range 700–800 MPa. Quantitative image analysis showed almost equal areas of ferrite and austenite phases[6].

Environmental Conditions

The test environments were variations on the standard NACE test solution[7]; 5 wt% NaCl acidified to pH 2.6 by 0.5 wt% acetic acid, deaerated and saturated with H_2S at room temperature. For tests at the lower H_2S concentrations of 20 and 200 ppm, argon was mixed with the H_2S gas in calibrated proportions of flow rate. The H_2S concentration was analysed at appropriate intervals by iodimetric titration[8]. For tests at elevated temperature, a hotplate with temperature control unit was added and vaporized water was replaced from a reservoir of deionized water.

A recirculating gas/solution control loop was used, based on one designed by the National Physical Laboratory[9], to minimize environmental variations (such as the notorious pH drift[10,11]), and to allow solution to flow past the specimens. The solution was circulated by pump at a controlled rate of about 1 mm/s through the test cells.

SSCC Testing

The standard double cantilever beam (DCB) specimen was mainly employed as it is the only fracture mechanics-based specimen recommended in NACE TM0177-90[7]. It is wedge-loaded to give a constant displacement (strain). On crack arrest, K_{1scc} is calculated by:

$$K_{1scc} = \frac{Pa(2\sqrt{3} + 2.38h/a)}{Bh^{3/2}} \left[\frac{B}{B_n}\right]^{0.577} \quad (1)$$

where P is lift-off load (measured after test), a is crack length, B is specimen thickness, B_n is web thickness, h is half-height and 0.577 is the side groove correction exponent, after Heady[10]. Specimens of optional thickness 12.7 mm were used. Where necessary, for specimens with noncoplanar crack fronts, B_n was replaced in the above equation by B_n', the crack front width. A significant non-conservative error has been observed when, in accordance with TM0177-90, the web thickness is still used to calculate K_{1scc} for cracks which deviate into the side-grooves[12].

Standard ISO compact tension (CT) specimens of width, w = 25.4 mm were also tested which, under constant load, give K_{1scc} by increasing K_1[13]. All the specimens were machined with the notch and crack parallel to the longitudinal (rolling) direction. Fatigue pre-cracking was carried out as specified in the relevant standards. For DCB specimens, the pre-crack extended at least 5 mm beyond the notch, and for CT specimens, the initial a/w was 0.3.

Crack growth was monitored for one DCB specimen in each test cell by means of the four-point probe direct current potential drop (DCPD) technique calibration of Yu *et al*[14]. The crack growth rate, da/dt, was then plotted against K_1 (by load-line *displacement*) as described previously[15].

In order to identify the effects of bulk- and crack tip-hydrogen charging on K_{1scc}, a silicone rubber coating was applied to some DCB specimens, exposing only selected areas as follows (Fig. 1)[6]:

1. fully coated (FC)
2. coated, except side-groove roots (ESGR)
3. coated, except side-grooves (ESG)
4. only side-grooves coated (OSG)

It must be emphasized that the pre-crack was exposed to the solution in *all* cases. The coating was applied following wedge loading, and the specimens were only exposed to solution after the silicone rubber had cured (24 hrs).

Fracture Toughness Determination

Compact tension specimens of width 25.4 mm were exposed to standard NACE solution and then, within 30 mins of their removal, fracture toughness (K_{1C}, or K_Q if invalid) was determined according to BS 5447:1977[16], using a clip gauge to measure crack opening displacement. In contrast with SSCC tests on CT specimens, the pre-crack length a/w was 0.45-0.55.

Discussion of Results

Threshold Stress Intensity, K_{1scc}

Double cantilever beam tests in recirculated, standard NACE solution (H_2S-saturated to 2700 ppm at room temperature) gave K_{1scc} values of 15–17 $MPam^{1/2}$ for 13%Cr steel, compared to 25–26 $MPam^{1/2}$ for the duplex steel, *ie.* the 13%Cr steel was more susceptible to SSCC despite having a higher fracture toughness in air ($\geq$87 $MPam^{1/2}$, *c.f.* $\sim$ 55 $MPam^{1/2}$ for the duplex alloy)[6].

The K_{1scc} of the S32404 duplex steel was low compared to previously reported results by Cigada *et al*[17], who found the K_{1scc} of a 22Cr-5.5Ni-3Mo duplex steel (of different cold-worked conditions) in standard NACE solution to be 43–50 $MPam^{1/2}$, using WOL specimens. Whether such a significant difference is due to materials condition or testing methodology needs to be further explored.

When tested in modified NACE environments of 20 and 200 ppm H_2S, both steels were still susceptible to SSCC, although their K_{1scc} values were now higher, and the 13%Cr steel remained the more susceptible of the two[15]. Neither steel was found to crack in H_2S-free solution (5% NaCl, acidified to pH 2.1 by 1% acetic acid), for applied stress intensities of up to 65 $MPam^{1/2}$ (13%Cr) and 54 $MPam^{1/2}$ (duplex)[6]. In Fig. 2 , K_{1scc} is represented as a function of H_2S concentration, and data is also included for one specimen tested in static solution with 180 ppm H_2S [15]. The K_{1scc} of the 13%Cr steel becomes lower than that of the duplex steel somewhere between 0 and 20 ppm H_2S.

It must be noted that the K_{1scc} values for the duplex steel at 20 ppm H_2S are not valid according to the NACE standard as the stress-corrosion cracks did not extend 2.5 mm beyond the pre-crack. However, it is difficult to obtain a valid K_{1scc} for this particular alloy-environment system due to the relatively small difference between K_{1c} and K_{1scc}.

Test Duration

In standard NACE DCB testing, *ie.* H_2S-saturated solution at room temperature, the recommended minimum test duration for low alloy steels is two weeks[7], and often cracking may cease within two days[10]. However, for stainless steels the NACE standard recommends at least 30 days (720 hrs) duration, but notes that a longer duration may give a lower "threshold". In principal, the duration of DCB tests is governed by the time taken to ensure that the threshold stress intensity for SCC has been attained. It is thus clearly controlled by the crack growth rate, as well as by the stress intensity both as applied at the start of the test (K_{1i}), and as ultimately determined by the material's response to the specific environment *ie.* K_{1scc} itself. The duration of SSCC tests on stainless steels has been shown to be strongly dependent on test environment[15], but also shows a metallurgical dependence.

In the present work, DCPD monitoring enabled testing to continue until crack growth reached a satisfactorily low level (in general, 10^{-7} mm/s). The stress-intensity over time of the two stainless steels is shown in Fig. 3, for tests in 20 and 200 ppm H_2S [15]. It should be noted that in such environments it is quite common for appreciable cracking to occur even after 1000 hrs or more. A dramatic example of this is the case of the 13%Cr specimen in 20 ppm H_2S in which growth was monitored for almost 2500

hrs and K_1 was seen to drop by approximately 15 MPam$^{1/2}$ in the period beyond 720 hrs. For all tests in various solutions at room temperature it can be said that, in general, the 13%Cr steel took the longer time to reach its threshold due to its higher susceptibility. However, the influence of applied K_1 must also be considered, and hence for the test in 200 ppm H_2S solution it is the duplex steel with its lower growth rate which took longer to reach its threshold.

For the purposes of carrying out normal, unmonitored DCB tests, it is important to have an appreciation of the variation of test duration with alloy-environment system in order to prevent premature test termination and consequently, a non-conservative error in K_{1scc}.

Crack Growth Rate, *da/dt*

The crack growth tendencies of DCB specimens showed a metallurgical dependence, as well as an environmental dependence. Of the two steels, the 13%Cr steel always had a higher maximum *da/dt* for the same environment, as can be seen in Fig. 4 for saturated H_2S [15].

From the curves of *da/dt* against (decreasing) K_1 it can be seen that crack growth in the 13%Cr steel, in particular, was intermittent. This implies either that,

(a) for a given stress-intensity, hydrogen up-take in the crack-tip region must reach a critical concentration before the crack front advances; but it subsequently slows down or stops upon entering a region of lower hydrogen content, or that

(b) growth rate is hindered as the crack front deviates away from the central plane to a plane of lower K_1, and increases once more as it returns towards the central position (evidence of crack deviation within the side-grooves has been presented previously[12]), or

(c) both.

The *da/dt* of 13%Cr DCB specimens was relatively low initially, despite the maximum applied stress-intensity being at the start of the test. As the test progressed, crack growth accelerated and (intermittently) reached a maximum *da/dt*, before decreasing (also intermittently) as the K_1 approached the threshold. The nature of crack growth in S41000 appears to reflect a dynamic balance between the build-up of hydrogen in the steel, up to saturation, and the gradual decrease in K_1 with increasing crack length as the test progresses. Further evidence of the influence of time dependent hydrogen entry on this steel's *da/dt* was given previously by comparison of crack behaviour in constant strain DCB tests (K_1 decreasing) and constant load CT tests (K_1 increasing)[6]. For stress intensities in the region of the K_{1scc}, the DCT specimen, which had been exposed to the solution for a much longer time, experienced higher growth rates than those of the CT specimen.

Crack propagation in the duplex steel seemed less intermittent and did not show a markedly slow start to cracking *i.e.* maximum growth rates were attained at a very early stage of testing. It could be the case that crack deviation within the side-grooves is the predominant reason for intermittent cracking in this steel, and that bulk hydrogen charging plays a limited role in its cracking mechanism.

Response to Pre-charging

The fracture toughness of the 13%Cr steel was initially quite high (K_Q in air $\geq$ 87 MPam$^{1/2}$), and fracture was totally ductile. As can be seen in Fig. 5, K_{1c} / K_Q dropped sharply after 2 days pre-exposure to saturated NACE solution, with increasingly brittle fracture, until totally brittle fracture occurred after 30 days exposure ($K_{1c} \sim 50$ MPam$^{1/2}$)[6]. The time dependence of K_{1c} / K_Q for S41000 in NACE solution may have important implications in the methodology of SSCC testing, and it appears to confirm the influence of time dependent hydrogen entry on cracking, as suggested by the *da/dt* vs K_1 curves.

It was also shown that during SSCC tests on CT specimens of the same steel in the same solution, that K_{1c} (measured at the point where unstable crack propagation started, for a test which lasted more than

a month due to step-wise loading) was only 35 $MPam^{1/2}$ [6], *ie.* much lower than that of the specimens pre-charged and tested in air. Therefore crack-tip stress appears to have an influence on hydrogen uptake.

The K_{1C} (in air) of the S32404, uncharged, was low ($\sim$ 55 $MPam^{1/2}$) but there was no discernible reduction in fracture toughness by pre-charging in NACE solution for up to 44 days. The absence of embrittlement was further verified by other workers at the University of Sheffield using various hydrogen charging methods. Compact tension specimens were cathodically charged in NACE solution[18] and in 0.5 M H_2SO_4 with 1 g/l thiourea[19], while others were exposed to H_2S-saturated NACE solution at 50°C[18,19], yet there was still no discernible decrease in fracture toughness. These data are also included in Fig. 5.

As for the explanation for the absence of bulk embrittlement in the duplex steel, it must be noted that hydrogen generation and transport are limited, compared to S41000. The duplex specimens in all SSCC tests remained bright and shiny, unlike the 13%Cr with its copious black corrosion product, and hence less hydrogen was available from corrosive reactions at the surface of S32404. Even if hydrogen was available from the environment (*e.g.* from low pH solutions), its entry into the duplex steel would be limited by both the protective surface film, and by the low diffusion coefficient, which has been reported to be two orders of magnitude lower for a 44.8% austenite duplex stainless steel (4.17×10^{-10} cm^2/s)[20] than for S41000 in NACE solution (3.0×10^{-7} - 7.6×10^{-8} cm^2/s)[21]. However, S32404 was found to be susceptible to SSCC and so there may be strain induced hydrogen charging in the region of the crack-tip.

Influence of Coating

The application of silicone rubber coating suppressed the SSCC susceptibility of 13%Cr DCB specimens, increasing K_{1scc} from 15–17 $MPam^{1/2}$ (uncoated) to nearly three times higher when fully coated, as in Table 2 [6]. Crack paths remained intergranular, despite the reduction in susceptibility. The free corrosion potential was not influenced by coating.

The K_{1scc} of S41000 decreased in the following order for the various covers of coating:

$$FC > ESGR > OSG > ESG > uncoated$$

ie. whenever the exposed area was reduced, or the distance of bulk hydrogen diffusion was increased, the susceptibility of 13%Cr steel to bulk embrittlement was suppressed. The former case is illustrated by the K_{1scc} decreasing:

$$FC > ESGR > ESG$$

In support of the latter case, although the specimen with only its side-grooves (OSG) coated had a larger exposed area than that of the specimen with exposed side-grooves (ESG), its K_{1scc} was higher because the hydrogen had to diffuse further to reach the crack tip region.

One DCB specimen of S32404 was tested fully coated but no suppression of SSCC susceptibility was evident. This appears to confirm the absence of bulk charging in this alloy-environment system, and that the possible influence of hydrogen is confined to the exposure of solution at the crack *tip*, under stress.

Fractography

As has already been mentioned, fracture of S41000 in air is totally ductile. In support of the above evidence of hydrogen embrittlement, sub-critical crack growth was predominantly by intergranular fracture in the tested environments of 20–2700 ppm H_2S, pH 2.6, at room temperature, although some transgranular "tearing" was also found at the lower H_2S concentrations. A typical fracture surface is shown in Fig. 6, for saturated H_2S. Fracture morphology appeared to be unaffected by coating.

Understanding of the SSCC fracture mechanism in S32404 is made more complex by the duplex nature of the microstructure. Its light grey-brown fracture surface was visibly distinct from the still shiny outer

surfaces. The crack mainly propagated through the ferrite phase in a transgranular manner, but also along the boundaries between the two phases (Fig. 7). As shown previously[6], on encountering an austenite grain, the crack front changes direction by either moving into the ferrite or along the boundary. Some preferential dissolution occurs by corrosive reactions, but it is not certain whether it is the austenite which dissolves, or rather the austenite grain boundaries; and whether the dissolution is part of the cracking process, or occurs after cracking. Barteri *et al*[22] postulated a mechanism for SSCC in duplex steels based on dissolution of austenite leading to cleavage of ferrite (for high constant load, at 80°C).

Effect of Temperature

In DCB tests on S32404, the K_{1scc} was found to be higher in H_2S-saturated solution (1300 ppm) at 50°C (31–36 $MPam^{1/2}$)[6] than in both 200 ppm and saturated H_2S solutions at room temperature (25–26 $MPam^{1/2}$)[6,15], *ie.* for constant displacement DCB tests, the effect of raising the temperature is to decrease the SSCC susceptibility. However, constant load tests, on CT specimens of the same steel, evaluated K_{1scc} at 50°C in H_2S-saturated solution to be 23–24 $MPam^{1/2}$, and displayed a more brittle fracture surface, which suggests that the effect of raising temperature may be to raise susceptibility. This is in keeping with the majority of the literature[3,4,22–24], where the "susceptibility" of duplex steel is generally reported to increase with temperature in this range, often reaching its peak at 60–80°C, although this trend may vary with materials' condition.

Further tests have confirmed that the lower susceptibility of the duplex DCB specimens at 50°C is reproducible. Fig. 8 presents crack growth data for a specimen which was gradually approaching a threshold at 50°C (K_{1scc} estimated to be 33.9 $MPam^{1/2}$, using a by DCPD); crack growth accelerated considerably when the solution was subsequently allowed to cool to 22°C, whilst maintaining the H_2S concentration at 1300 ppm[15].

Clearly the K_{1scc} of S32404 at 50°C is dependent on test methodology, and hence caution must be exercised in the interpretation of SSCC tests on duplex stainless steels. It might be interesting to investigate whether the apparent influence of temperature on this steel's susceptibility is strain-rate dependent.

The susceptibility of a 13%Cr DCB was not found to be significantly affected on lowering the temperature from 50°C [15]. It is generally believed that the degree of hydrogen embrittlement in martensitic stainless steels decreases with increasing temperature[4].

Conclusions

Both S41000 and S32404 stainless steels suffered sulphide stress corrosion cracking in laboratory test environments based on NACE solution, but the difference in their behaviour was not merely in terms of susceptibility, and can be distinguished as follows:

1. The K_{1scc} of S41000 was lower than that of S32404 in solutions containing H_2S from 20 ppm to saturation, at room temperature, despite the former steel having the higher K_{1C} in air.
2. The duration of DCB tests was usually longer for the 13%Cr steel, but this may not always be the case due to the influence of K_{1i}. In low-H_2S environments, specimens of this steel can still suffer appreciable cracking after a number of months.
3. Crack growth in DCB tests was intermittent, but more so for the 13%Cr steel. Furthermore, the start of cracking in this steel was also delayed, which reflects the influence of bulk hydrogen charging.
4. Bulk hydrogen charging was shown to decrease the fracture toughness of S41000, and this effect was enhanced by the conjoint action of stress. The influence of bulk embrittlement on sub-critical crack growth was confirmed by exposing selected areas of DCB specimens.
5. By contrast, S32404 could not be charged sufficiently to observe bulk embrittlement, and when only the crack-tip of a DCB specimen was exposed to solution, the susceptibility was unaffected; this infers that SSCC in this steel occurs predominantly by crack tip localized processes.

6. The lower susceptibility of S32404 DCB specimens at 50°C, with respect to room temperature, was shown to be reproducible. Their susceptibility was regained when the solution was allowed to cool down; this interesting effect was not observed in S41000 steel.

Acknowledgement: The authors wish to thank Prof C.M. Sellars for provision of research facilities in the Dept. of Engineering Materials and gratefully acknowledge the collaboration of Dr. A. Turnbull (NPL) and Dr. M. B. Kermani (BP). Financial support was also given to J.C.B. by the Science and Engineering Research Council, UK and BP.

References

1. R. A. King, R. G. Miller, The Chemical Engineer(UK), 438 (1987): p. 38.

2. M. Barteri, L. Scoppio, A. Tamba, "Application of Corrosion Resistant OCTG in Oil and Gas Production", Proceedings of 11th ICC, Vol. 4 (Florence, Italy, 1990), p. 471.

3. R. D. Kane, Stainless Steels '84 (London, UK : Institute of Metals, 1985), p. 429.

4. NACE Technical Committee Report 1F192, "Use of Corrosion Resistant Alloys for Resistance to Environmental Cracking in Oilfield Environments" (Houston, TX : National Association of Corrosion Engineers, 1992).

5. M. B. Kermani, R. G. MacCuish, Society of Petroleum Engineers, Vol. Δ, SPE 20457 (Richardson, TX, 1990), p. 525.

6. J. Yu, R. Brook, R. B. Hutchings, A. Turnbull, "Stress-Corrosion of Stainless Steels in Sour Marine Environments", Proceedings of Life Prediction of Corrodible Structures, 3rd NACE International Relations Committee Symposium, Cambridge, UK , 1991, paper no. 48 (Houston, TX : National Association of Corrosion Engineers, 1993).

7. NACE Standard TM0177-90, Laboratory Testing of Metals for Resistance to Sulfide Stress Cracking in H_2S Environments (Houston, TX : National Association of Corrosion Engineers, 1990).

8. API Recommended Practice for Analysis of Oil-Field Waters, API RP 45, 2nd Edition (Washington, DC : American Petroleum Institute, 1968).

9. M. Saenz de Santa Maria, A. Turnbull, Corrosion Science, 29 1 (1989) : p. 69.

10. R. B. Heady, Corrosion, 33 3 (1977) : p. 98.

11. D L. Sponseller, Corrosion, 48 1 (1992) : p. 159.

12. J. Yu, R. Brook, R. B. Hutchings, A. Turnbull, "Stress-Corrosion Testing of AISI 410 Stainless Steel in Sour Environments Using Side-Grooved DCB Specimens", Proceedings of Life Prediction of Corrodible Structures, 3rd NACE International Relations Committee Symposium, Cambridge, UK, 1991, paper no. 46 (Houston, TX : National Association of Corrosion Engineers, 1993).

13. ISO 7539-6 : 1989(E), "Corrosion of Metals and Alloys - Stress Corrosion Testing - Part 6: Preparation and Use of Pre-Cracked Specimens" (Switzerland : International Organization for Standardization, 1989).

14. J. Yu, J. C. Barker, R. Brook, "The Optimization of Crack Length Measurement by DCPD in DCB Specimens", ISOPE-93, Singapore (Golden, Colorado: International Society of Offshore and Polar Engineers, 1993).

15. J. C. Barker, J. Yu, R. Brook, M. B. Kermani, "Some Environmental Aspects of Sulphide Stress Corrosion Cracking in Stainless Steels", ibid.

16. BS 5447 : 1977, "Methods of Test for Plain Strain Fracture Toughness (K_{1C}) of Metallic Materials" (London, UK : British Standards Institution, 1977).

17. A. Cigada, T. Pastore, P. Pedeferri, B. Vicentini, Corrosion Science, 27 10/11 (1987) : p. 1213.

18. J. Philiber, J. Electrochem. Soc. , 139 2 (1992) : p. 51C.

19. A. T. Hassan, "Effects of Hydrogen on Stainless Steel for Offshore Use", MMet thesis (University of Sheffield, UK, 1992).

20. J. H. He, "Diffusion of Hydrogen in ($\alpha + \gamma$) Duplex Phase Stainless Steel", PhD thesis (Hsing Hua University, China, 1988).

21. A. Turnbull, M. Saenz de Santa Maria, N. D. Thomas, Corrosion Science, 29 1 (1989) : p. 89.

22. M. Barteri, F. Mancia, A. Tamba, G. Montagna, Corrosion Science, 27 10/11 (1987) : p. 1239.

23. K. van Gelder, J. G. Erlings, J. W. M. Damen, A. Visser, ibid. : p. 1271.

24. A. Miyasaka, K. Denpo, H. Ogawa, Corrosion, 45 9 (1989) : p. 771.

Table 1: Compositions of S41000 and S32404 steels, in mass%.

	C	Si	Mn	S	P	Cr	Ni	Fe	Mo	Co	Cu
S41000	0.13	0.33	0.40	0.006	0.02	13.20	0.38	bal.	0.03	0.02	0.06
S32404	0.018	0.91	0.61	0.001	0.026	21.67	6.24	bal.	2.50	-	1.07

Table 2: Coated and uncoated DCB specimens exposed to standard NACE solution for 1080 hrs.

	Coating	E_{corr} mV(SCE)		K_{1i}	K_{1scc}
		initial	final	$MPam^{1/2}$	$MPam^{1/2}$
S41000	FC	-	-	58.2	44.4
	FC	-664	-658	49.3	48.4
	ESGR	-664	-652	40.5	35.1
	OSG	-659	-651	53.0	33.0
	ESG	-663	-654	38.2	20.9
	None	-665	-648	40.1	15.2
	None	-	-	55.9	17.1
	None	-	-	44.3	15.2
S32404	FC	-528	-514	56.4	25.2
	None	-520	-511	52.0	25.7
	None	-	-	55.0	25.3

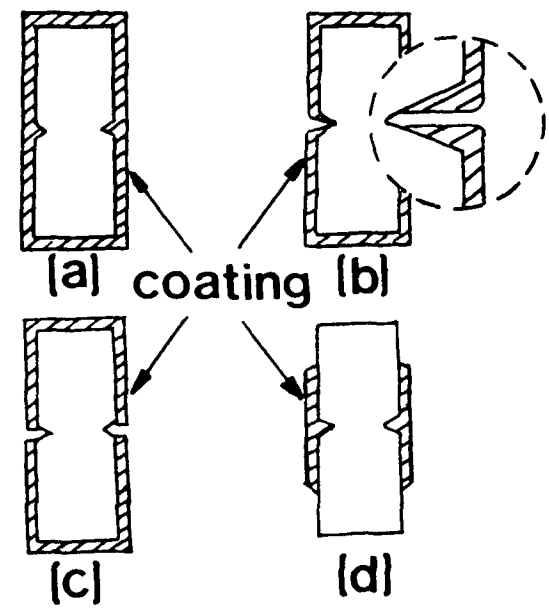

Figure 1: Schematic diagram of coated DCB specimens in cross-section; (a) FC, (b) ESGR, (c) ESG, (d) OSG.

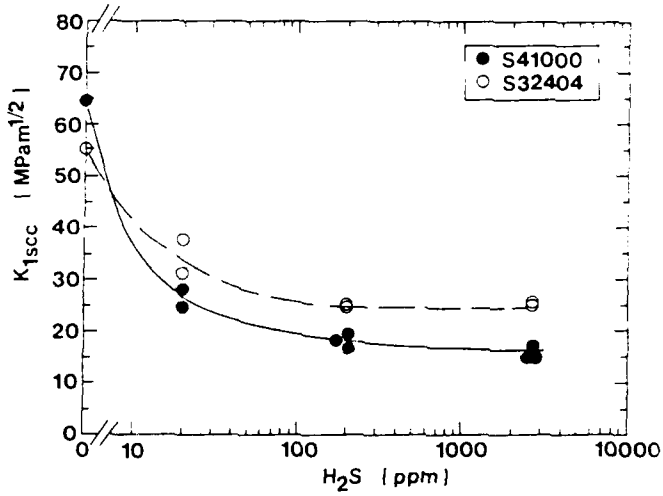

Figure 2: The K_{1scc} of DCB specimens as a function of H_2S concentration; where K_{1scc} at 0 ppm H_2S is represented by the highest K_1 applied without cracking for S41000, and by K_{1C} for S32404.

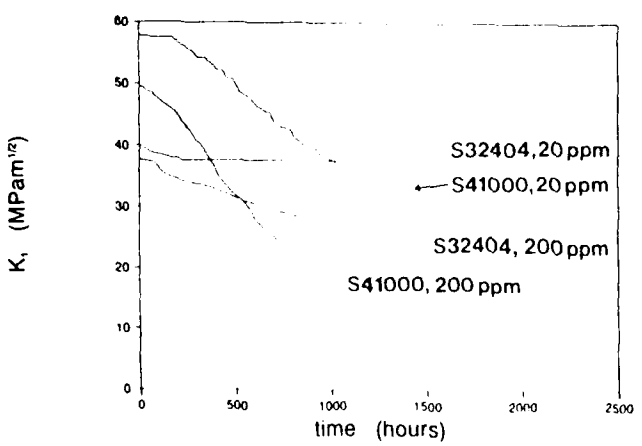

Figure 3: Stress-intensity as a function of time, for DCB specimens in 20 and 200 ppm H_2S .

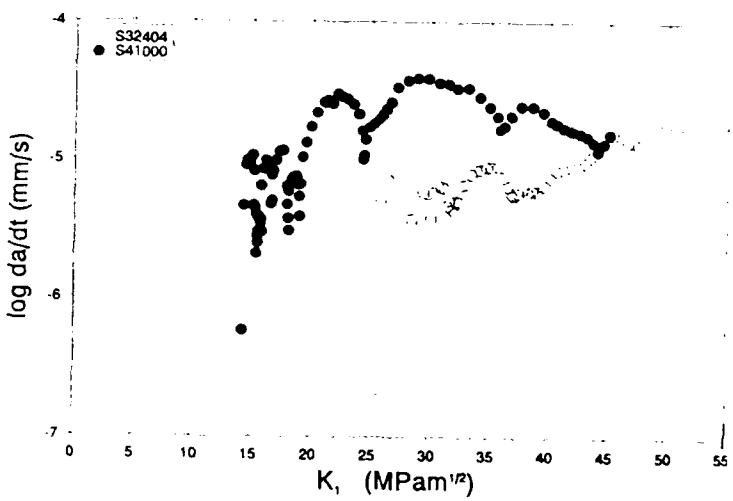

Figure 4: Crack growth rate as a function of stress-intensity, for DCB specimens in saturated H_2S.

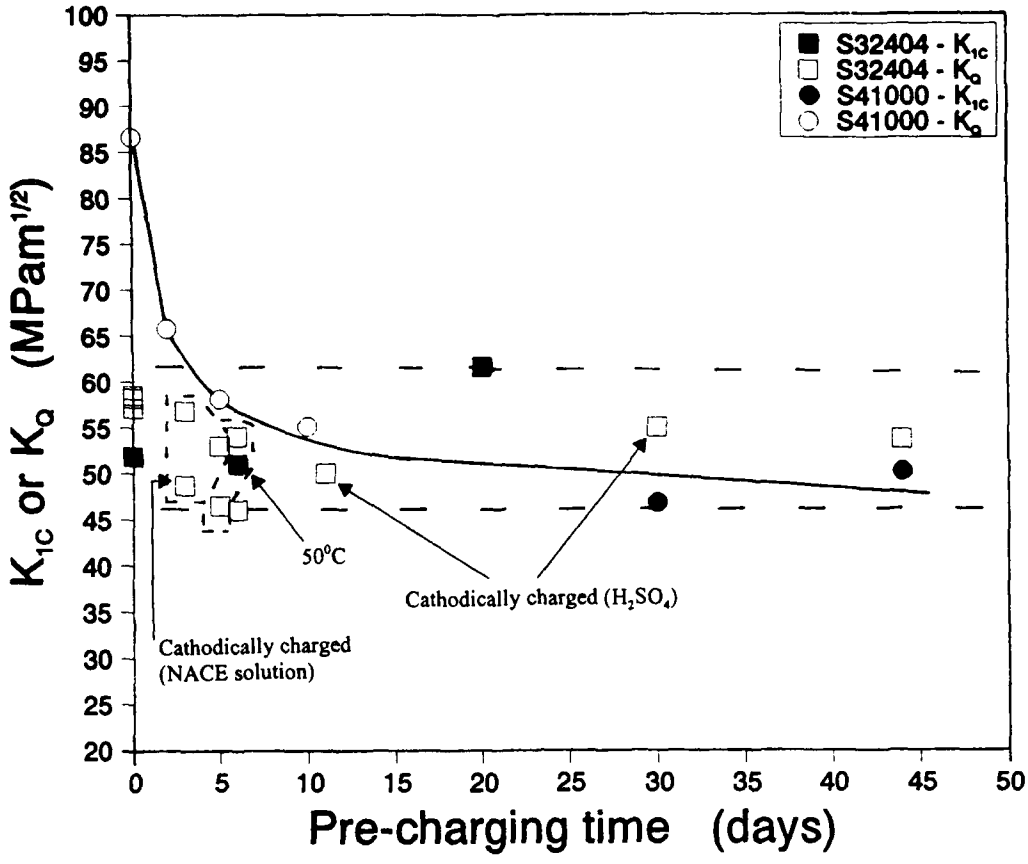

Figure 5: Fracture toughness as a function of pre-charging time, for CT specimens exposed to standard NACE solution unless otherwise stated.

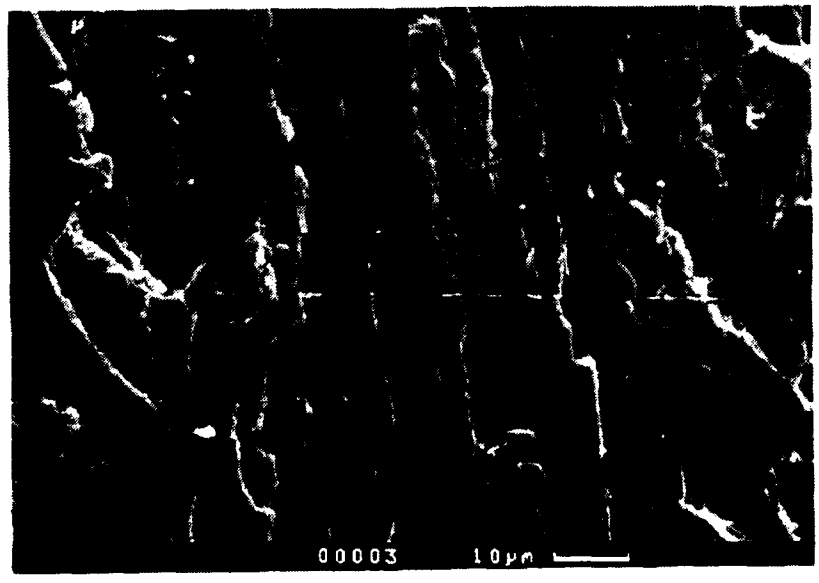

Figure 6: SEM fractograph from an S41000 DCB specimen tested in saturated H_2S.

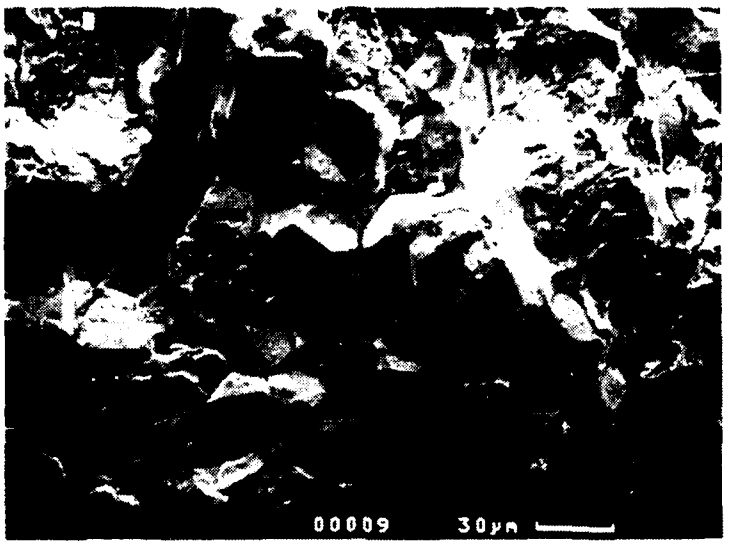

Figure 7: SEM fractograph from an S32404 DCB specimen tested in saturated H_2S.

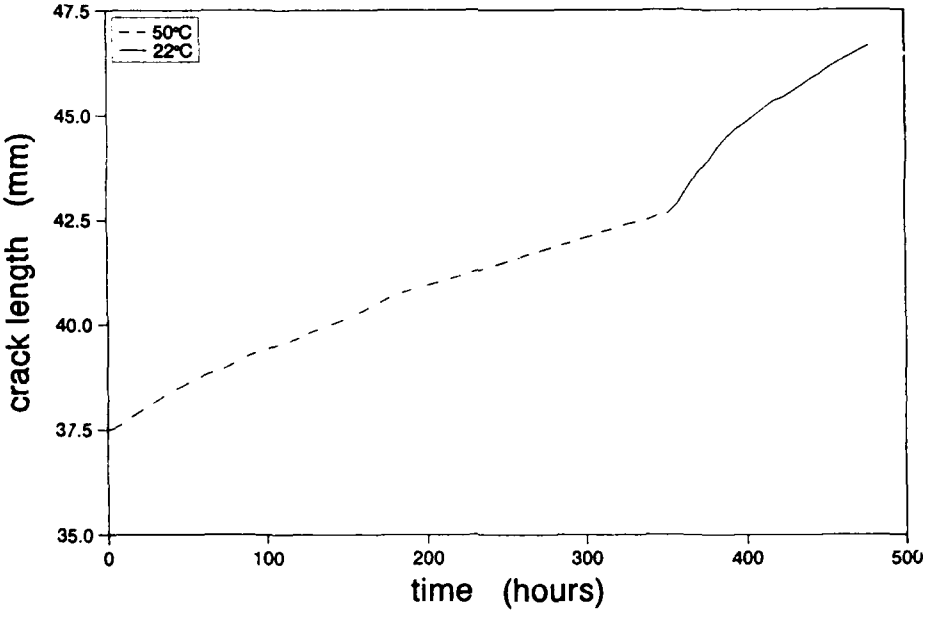

Figure 8: The effect of lowering solution temperature on crack growth in an S32404 DCB specimen.

Stress Corrosion Cracking of 321 Stainless Steel Single Crystal Under Mode II Loading

Li-Jie Qiao
Department of Materials Physics
University of Science and Technology Beijing
Beijing, 100083, P. R. China

Dong-ling She
Department of Materials Physics
University of Science and Technology Beijing
Beijing, 100083. P. R. China

Wu-yang Chu
Department of Materials Physics
University of Science and Technology Beijing
Beijing, 100083, P. R. China

Chi-Mei Hsiao
Department of Materials Physics
University of Science and Technology Beijing
Beijing, 100083, P. R. China

Abstract

SCC of 321 stainless steel(SS) single crystal was studied under mode II loading in a 42% boiling $MgCl_2$ solution. The results showed that SCC initiated at the maximum normal stress site, while no SCC occurred at the maximum shear stress site. Although there were slip lines around the maximum normal stress site, SCC in general, did not occur along the slip lines. Some micro-cracks could be observed on the slip lines, which inclined about 20 degrees to the slip line, but did not propagate. The slip lines could appear owing to heat activation when a polished constant displacement specimen was heat at 150°C for 2 hrs. The slip lines appeared during heating were polished before SCC experiment, SCC still initiated at the maximum normal stress site while no slip step emerged on the specimens. These results are conflict with the "slip - dissolution" model of SCC. The SCC mechanism of austenitic stainless steel may be relative with stress concentration due to dislocation pile-up instead of slip steps. The normal stress plays a important part in the SCC.

Key terms: stress corrosion cracking, austenitic stainless steel, single crystal,

Introduction

The mechanism of stress corrosion cracking(SCC) for austenitic stainless steel(ASS) in boiling $MgCl_2$ solution has been widely studied[1]. Some experimental results support the theory of the anodic dissolution mechanism of SCC instead of the hydrogen induced cracking(HIC).[2-5]

Despite numerous researches, there are conflicting views on the mechanism of the anodic path dissolution of SCC.[1] It is considered that the function of stress is to induce dislocation slip disrupting the surface film, so that the crack can propagate via the anodic path dissolution of fresh metal, SCC should initiate along the maximum shear stress plane because slip is induced by shear stress. However, SCC under mode III loading propagated along maximum normal stress plane, where there was no shear stress[4]. Under mode II loading, SCC initiated at maximum normal stress, too[5].

For mode II notch specimen, the calculation via the finite element method showed that the maximum normal stress site was different from the maximum shear stress site, as shown in Fig. 1. The maximum shear stress site is located at $\theta = 80°$, point A in Fig. 1, and its direction is $\alpha=5°$. The maximum normal stress σ_{max} is located at $\theta = -110°$ and the direction is $\alpha = 10°$, point B in Fig. 1. Therefore, the role of normal stress and shear stress in SCC can be distinguished according to the site of the crack initiation.

Experimental Procedures

321 ASS single crystal made by melt method was used in the present study. The mode II notched specimen and gripping arrangement for shear test are shown in Figure 2. The radius of the notch is 0.1 mm and the specimen thickness is 2 mm. All specimens were annealed in an argon atmosphere at 1050 °C and then cooled in air. The SCC test was conducted in boiling 42% $MgCl_2$ solution (143 °C). Scanning electron microscope(SEM) was used to examine nucleation site and propagation direction of SCC and dislocation slip step emergence.

Experimental Results and Discussions

1. Relationship Between a Crack Nucleation and Component of Stress

SCC of the single specimen under mode II loading initiated at the maximum normal stress site, $\theta = -110°$ rather than at maximum shear stress site, as shown in Fig. 3. The crack propagated along direction of slip line at first stage, and then along normal stress plane. The specimen no longer is mode II type as soon as the SCC propagated from the notch. Therefore, only the crack nucleation rather than propagation can be investigated under mode II loading. The site of the crack initiation always located at the maximum normal stress site for all specimens with different crystalline plane specimens. This appears to show that normal stress plays a main part during SCC.

2. Relationship Between SCC and Slip Line

The nucleation of a crack was not relative with slip line. Although there exist slip lines around the maximum normal site, SCC did not occur near the slip lines, as shown in Figure 3. SCC propagated across the slip lines rather than along them. A lot of microcracks on the slip lines were observed with SEM. The cracking inclined about 20° to the slip line and these microcracks would be corroded to pits with time increasing and did not propagate during SCC because of the short range of pile-up stress, as shown in Figure 4. If slip lines appeared during heating were polished before SCC experiment, SCC still initiated at the maximum site while no slip step emergence on the specimens. Those results are conflict with the "slip - dissolution" model of SCC. The SCC mechanism of austenitic stainless steel maybe relative with stress concentration due to dislocation pile-up, but not with slip steps. The normal stress plays a important part in SCC.

The "slip-dissolution" model cannot explain the direction of a crack propagation and the site of the nucleation. The model considered that the role of stress only induced dislocation slip and formed stage emergence on a specimen surface. The slip emergence and anodic dissolution were regarded as separated steps. Synergistic action of stress and anodic dissolution was negatived. In facts, the dislocation play two parts in SCC. One is that dislocation slip generates steps disrupting surface film. As a result, bare fresh metal is objected to corrosion. The another is that dislocations pile up and result in high local stress, which makes atoms easier be corroded. Only the former role of a stress was considered in the most of SCC mechanisms. Synergistic action of the stress with electronic chemical medium should be paid more attention to explain the mechanism. The effect of stress on anodic dissolution current can be expressed as following:[7]

$$i_\sigma = i_0 \exp [M\sigma^2 / 2E\rho RT] \qquad (1)$$

where M stands for element weight, σ for stress, E for Young' modulus, ρ for density, R for gas constant and T for absolute temperature, i_σ and i_0 for anodic current with and without stress σ, respectively. Usually, elastic limit stress of whole specimen is small. It has little effect on anodic dissolution. When dislocations pile up at a barrier, local stress concentration owing to a crack and/or dislocation pile-up, however, is much higher than yield stress, maybe near to cohesive strength. For example, the transmission electron microscope (TEM) *in situ* observation for ASS showed that a crack tip might be still sharp after dislocations were emitted from the crack tip and dislocation-free zone(DFZ) formed. So that the local stress concentration in the DFZ was high enough to equal to the cohesive strength σ_{th}.[8] It can make anodic dissolution current increase extremely and satisfy the need of SCC speed.

Acknowledgment

The project was supported by the National Natural Science Foundation of China.

References

1. C.J. Theus, R.W. Staeahle, Stress Corrosion Cracking and Hydrogen Embrittlement of Iron Base Alloys, N. Staehle et al eds., NACE, Houston, Texas, 1977, P.845.
2. W.Y. Chu, H.L. Wang, C.M. Hsiao, Corrosion, Vol.40(1984), P.487.
3. W.Y. Chu, J. Yao, C.M. Hsiao, Corrosion, Vol.40(1984), P.302.
4. L.J. Qiao, W.Y.Chu, C.M. Hsiao, Corrosion, Vol.43(1987), P.479.
5. L.J. Qiao, W.Y.Chu, C.M. Hsiao, and J.D. Lu, Corrosion, Vol.44(1988), P.50.
6. A.N. Stroh, Advance in Physics, Vol.6(1957), P.418.
7. S.W.Jr. Dean, Stress Corrosion - New Approaches, ASTM STP 610, 1976, P.308.
8. Q.Z. Chen, W.Y. Chu and C.M. Hsiao, Science in China, In press.

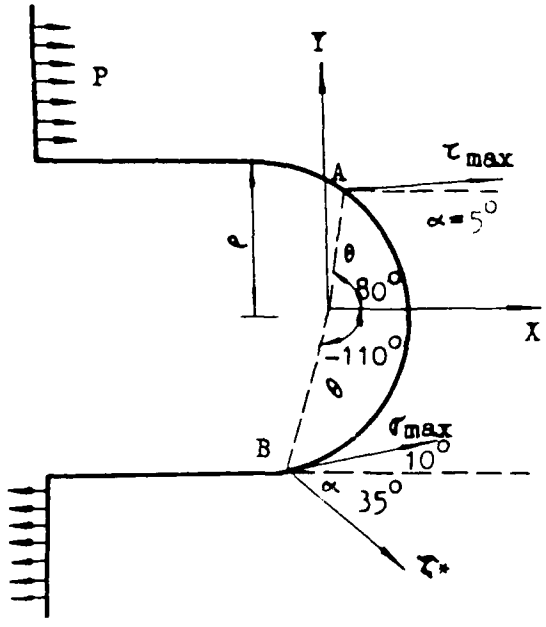

Fig. 1 - The sites and directions of the maximum stress components

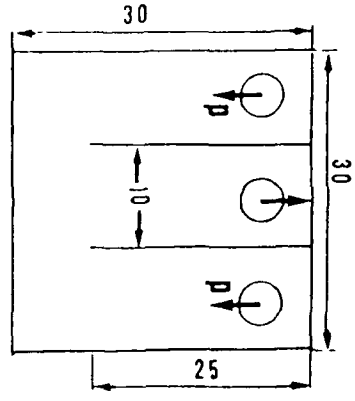

Fig. 2 - Mode II notch specimen

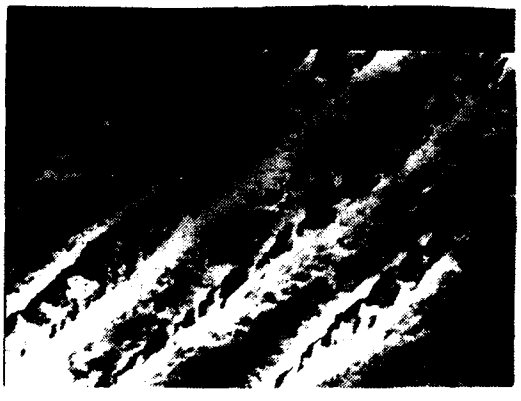

Fig. 3 - SCC initiation and slip lines around the maximum normal stress site

Fig. 4 - The SCC microcracks and pits on slip lines

Effect of Heat Treatment on Stress Corrosion Cracking Behavior of 40CrMnSiMoVA Steel

Shi Jin
Corrosion and Protection Research Laboratory
Northwestern Polytechnical University
Xi' an, Shaanxi, The People' s Republic of China

ShiJie Li
Corrosion and Protection Research Laboratory
Northwestern Polytechnical University
Xi' an, shaanxi, P. R. China

XiaoKun Liu
Corrosion and Protection Research Laboratory
Northwestern Polytechnical University
Xi' an, Shaanxi, P. R. China

Abstract

The effects of heat treatments on stress corrosion cracking (SCC) behaviors of new type low alloy ultra-high strength steel 40CrMnSiMoVA ($\sigma_b = 1830 \sim 1974$MPa, $\sigma_{0.2} = 1372 \sim 1583$MPa, $\delta = 11.5 \sim 15.2\%$, $K_{IC} = 54 \sim 66$MPa $\sqrt{m}$) in 35℃ 3.5% NaCl solution and its mechanism are investigated using BL-WOL specimens. The SCC characteristic parameters of 190°、280°、300° and 310℃ isothermally quenched and 260℃ 4 hr tempered steels are measured. The data show that the threshold values K_{ISCC} of four different heats of steels are almost the same (from 12.95 to 14.20 MPa $\sqrt{m}$), about one fifth to one fourth of K_{IC} values, which indicates that 40CrMnSiMoVA steel is quite sensitive to SCC. However, the crack growth rates in K-independent region Ⅱ $(da/dt)_Ⅱ$ are significantly different from each other. In 35℃ 3.5% NaCl solution at E_{corr} (−630mV, SCE) $(da/dt)_Ⅱ$ of steels of four heats mentioned above are 10.52, 4.20, 0.24 and 1 mm/hr respectively. The Heat 3(300℃ isothermal quenching)shows the best resistance to SCC among different heats and $(da/dt)_Ⅱ$ is only about one fortieth of that for Heat 1— conventionally used 190℃ isothermal quenching. Metallographic examinations show that the SCC susceptibility of 40CrMnSiMoVA is mainly related to microstructural compositions of steel. Both bainitic and quasi-bainitic structures which are main compositions of Heat 3 and 4 demonstrate much lower crack propagation rate than martensitic 40CrMnSiMoVA (Heat 1 and Heat 2). In addition, the content of retained austenite which usually enhances the resistance to SCC is higher in heat 3 than in others. Both fracture mechanics properties and SEM fractographic analyses indicate that the 40CrMnSiMoVA steel is relatively susceptible to SCC even under improved heat treated condition.

Introduction

40CrMnSiMoVA steel is one of main structural steels in China because of its high strength ($\sigma_b = 1830 \sim 1974$MPa, $\sigma_{0.2} = 1372 \sim 1583$MPa, $\delta = 11.5 \sim 15.2\%$, $K_{IC} = 54 \sim 66$MPa $\sqrt{m}$) and Ni-free composition. However, serious cracking problems often occurred to this steel during manufacturing and operating processes. According to failure analyses, it is considered that the conventional heat treatment which makes this steel have low impact toughness, ductility, and high notch sensitivity promotes cracking. Nevertheless, our preliminary investigation showed that its

high susceptibility to stress corrosion cracking (SCC) was also one of the main causes of such cracking[1]. It is well known that both the mechanical properties and the susceptibility to SCC of high strength steel are significantly influenced by heat treatment[1,3]. And it is usually adopted that SCC susceptibility can be reduced with higher tempering and aging temperatures. In view of the fact that the isothermal quenching has been the conventional heat treatment for this steel, the objective of this paper is to try to enhance the SCC resistance of 40CrMnSiMoVA steel by changing the temperatures of isothermal quenching without obvious reduction of its mechanical properties and to investigate the mechanisms of SCC failure.

Experimental Materials And Methods

The SCC behaviors of 40CrMnSiMoVA steel were investigated using BL-WOL type of plane-strain precracked specimens. All specimens were made from the vacuum arc remelted 40CrMnSiMoVA steel. Its composition and microstructures were examed and qualified before machining. The composition of this steel is listed in Table 1.

After re-forging from Φ100mm rods, the wrought plates were heat-pretreated, machined, isothermally quenched and tempered, then ground to the given size. The BL-WOL specimens were 25.50 $\pm$0.01mm in thichness, 63.0$\pm$0.1 in width and 82.0$\pm$0.01mm in length, and in TL orientation. 1.5$\sim$2mm precracks were made using high frequency fatigue test machine. Four heats of specimens including 190°、220°、300° and 310°C isothermally quenched then 260°C 4hr tempered steels were investigated. The technological parameters of heat treatment, mechanical properties and microstructures for each heat are given in Table 2.

35°C、3.5%NaCl solution was used as the corrosion environment for SCC testing. The crack growth rates of all specimens were measured at corrosion potencial ($E_{corr}=-630$mV, SCE) using a microscope of low magnification. Both optical and scanning electronic microscope (SEM) were used for fractographic examination.

Results And Discussion

SCC Behavior

The stress corrosion crack propagation data obtained from four heats of specimens mentioned in Table 2 in 35°C 3.5% NaCl solution at E_{corr} are shown in Table 3 and Fig1-4. The datum of 180°C isothermal quenched heat in Fig. 3 is get from reference[4].

It can be seen from Fig. 1-4 and Table 3 that the threshold values of stress intensity factors K_{ISCC} of four different heats of steels are almost the same (from 12.95 to 14.20 MPa $\sqrt{m}$), about one fifth to one fourth of their K_{IC} values, which demonstrates that 40CrMnSiMoVA steel is quite sensitive to SCC. However, the crack growth rates in K-independent region Ⅱ $(da/dt)_Ⅱ$ are significantly different from each other. In 35°C 3.5% NaCl soultion at E_{corr} $(da/dt)_Ⅱ$ of steels of four heats mentioned above are 10.52, 4.20, 0.24 and 1mm/hr respectively. The heat 3 (300°C isothermal quenching) shows the best resistance to SCC among different heats and its $(da/dt)_Ⅱ$ is only about one fortieth of that for heat 1 (conventionally used 190°C isothermal quenching).

The temperature of isothermal quenching seems to be the main factor influencing the SCC behavior of 40CrMnSiMoVA steel. Below 300°C the K_{ISCC} slightly but $(da/dt)_Ⅱ$ significantly reduced with

increasing temperature. Further enhancing isothermal quenching temperature, however, even at 310℃ for only 9 minutes, both K_{ISCC} and $(da/dt)_I$ increased immediatedly, as shown in Fig. 3.

Fractographic Examination

The appearences of all heats of specimens show the stress corrosion cracks propagating perpendicularly to the direction of applied stress and without branching. However, the shapes of stress corrosion crack tips on fractured planes of specimens of different heats after testing are different: Heat 2 (280℃ isothermal quenching) produced almost a level tip, i. e. the tongue shape wasn' t apparent; heat 3 and Heat 4 (310℃ isothermal quenching) formed "M" shape tips; and heat 1 made an inverted tongue shape of crack tip. It means that the cracks propagate faster on the side surface than in the subsurface layer and even than in the central part of BL-WOL specimens for Heat 1,3,4, or at an equal rate for Heat 2. In view of the effect of the occlusive cell (electrochemistry) and the effect of plane-strain load(fracture mechanics) to different extent for different heats on cracking (central part of specimen should crack faster)[5], according to the macro-fractographic morphology of crack growth, it is considered that the SCC mechanism of 40CrMnSiMoVA steel in aqueous solution involves a combined action of anodic dissolution at crack tip and hydrogen assisted cracking rather than purely hydrogen embrittlement.

Microfractographic examinations show almost the same SCC characteristic for specimens of all heats. The stress corrosion cracks propagate mainly along the grain bondaries and the transgranular failure can also be observed. The intergranular failure fraction on the fracture surface increases with decreasing the K_I value, as shown in Fig. 5.

Discussion

It is generally considered that the K_{ISCC} of a given steel in a specific corrosion environment is dependent on its yield strength σ_s level, and the higher the σ_s, the lower the K_{ISCC}. However, this is not the case for 40CrMnSiMoVA steel. As shown in Fig. 6, the K_{ISCC} of 40CrMnSiMoVA slightly increases with its yield strength.

It is well known that the effects of heat treatment on high strength steel are related to both yield strength and the microstructures. The microstructures of a given steel may be quite different while the yield strengths reach the same level using different heat treatments. However, the difference of microstructure may influence the SCC behavior significantly[3,6].

Therefore, it is unreasonable to relate the K_{ISCC} to purely strength effects. Although the K_{ISCC} of Heat 3 (300℃) lower than Heat 1 (190℃) a little, the crack propagation rate in K-independent region $(da/dt)_I$ of the former is markedly lower than that of the latter. The influence of microstructures on SCC characteristics of high strength steel has long been discussed[3,6,7]. Martensite plate boundaries and transformation twins usually favorate formation of easy paths for crack propagation. For a given steel, the K_{ISCC} values may be similar at the same yield strength level whether the steel is in martensitic or bainitic condition. However, the $(da/dt)_I$ is lower for bainitic steel compared to martensitic one[3].

The fraction of the microstructural composition of different heats of 40CrMnSiMoVA steel are given in Table 4. The microstructure of Heat 3 (300℃) is basically bainite or quasi-bainite (with film-type retained austenite between ferrite plates or quasi-plates), however, Heat 1 (190℃) is

mainly in martensitic plates condition. It is obvious that just the microstructural differences cause the significant changes in stress corrosion growth rate for different heats. Our experimental results have demonstrate in turn that the SCC resistance of bainite is higher than that of martensite, especially at high stress level.

Table 4 and Fig. 7 indicate that the retained austenite content and the transformation amount from retained austenite into untempered martensite induced by mechanical deformation are different for differnt heats. The existence of retained austenite is generally Known to enhance SCC resistance, but the untempered martensite is just an opposite[3]. These factors also influence the SCC behaviors. In addition, the transformation amount of retained austenite (A_R) into tempered martensite (M) may also affect the SCC characteristics owing to the volume-change induced stress (Fig. 8). The highest content of retained austenite after tempering and mechanical deforming and the lowest tempering transformation amount of $A_R \rightarrow$ M of heat 3 (300℃), which means that A_R of Heat 3 has high thermal and mechanical stabilities, are also considered to be related to improving the SCC behaviors of 40CrMnSiMoVA steel.

Conclusion

1. The temperature of isothermal quenching influences the SCC behaviors of 40CrMnSiMoVA steel significantly. The stress corrosion crack propagation rates in K-independent region of 190°、280°、300° and 310℃ isothermal quenched and then 260℃ 4hr tempered 40CrMnSiMoVA steel in 35℃ 3.5%NaCl are 10.52、4.20、0.24 and 1.0mm/hr respectively. The K_{ISCC} values of different heats, however, are almost the same (from 12.95 to 14.20 MPa $\sqrt{m}$).

2. Microstructural change is the main cause of changing the SCC characteristics of 40CrMnSiMoVA steel. The bainitic conditon, the high content of retained austenite, and the high thermal and mechanical stabilities of retained austenite of 300℃ isothermally quenched steel compaered to 190℃ isothermally quenched one are considered to be the factors reducing the stress corrosion crack growth rate of steel.

3. The SCC mechanism of 40CrMnSiMoVA steel in aqueous solution involves combined action of anodic dissolution at the crack tip and hydrogen assisted cracking.

4. 300℃ isothermal quenching has improved not only the SCC behaviors but also the general mechanical properties of 40CrMnSiMoVA steel (enhancing ductility, impact toughness and fracture toughness without significant reduction of strength). It is suggested that the conventional 190℃ isothermal quenching technology should be substituted by 300℃ isothermal quenching.

References

1. S. Jin, X. Liu, Corrosion Cracking, (Salt Lake City, Utah, American Society for Metals, 1985), p. 69.
2. S. Jin, X. Liu, Journal of Northwestern Polytechnical University, 7,2(1989). pp. 223-232.
3. G. Sandoz, Stress Corrosion Cracking in High Strength Steels and in Titanium and Aluminium Alloys, (Washington, D.C., Naval Research Laboratory, 1972), pp. 117-118.
4. F. Xu et al, Stress Corrosion Cracking Testing Method and Data Collection. (Beijing, Beijing Institute of Aeronautical Materials, 1984), pp. 80～81.
5. S. Jin, S. Li, Journal of Chinese Society of Corrosion and Protection, 9,4(1989), pp. 303-

304.
6. I. M. Berstein et al, Hydrogen Embrittlement and Stress Corrosion Cracking, (Metals Park, OH, American Society for Metals, 1984), pp. 135-152.
7. A. W. Thompson et al, Advances in Corrosion Science and Technology, 7, (Houston, TX, National Association of Corrosion Engineers, 1980), pp. 53-176.
8. R. Tas, D. Chen, Graduate student Theses, Northwestern Polytechnical University, 1987, p. 37, p. 67.

Table 1. Chemical Composition of 40CrMnSiMoVa

Alloy Element	C	Cr	Mn	Si	Mo	V	P	S
Content(%wt.)	0.41	1.47	0.97	1.20	0.53	0.11	0.014	0.002

Table 2. Mechanical Properties And Microstructure of 40CrMnSiMoVA

Heat No.	Isothermal Geat*	E GPa	σ_b MPa	$\sigma_{0.2}$ MPa	δ %	ψ %	K_{IC} MPa $\sqrt{m}$	Micro-structure**	Grain size
1	190℃,60′	195.18	1937.7	1582.7	11.92	46.5	60.90	$M+B_L+(M-A)+A_R$	7
2	280℃,60′	195.68	1877.7	1429.8	11.50	46.0	54.25	$M+B_L+(M-A)+A_R$	7
3	300℃,60′	195.68	1830.6	1378.8	15.17	50.7	64.60	$M+B_U+B_L+(M-A)+A_R$	7
4	310℃,9′	195.68	1878.7	1372.0	11.80	46.6	66.03	$M+B_U+B_L+(M-A)+A_R$	7

* Specificaiton: 920℃,20′ -Isothermal heated-cooled in 60℃ water-Tempered at 260℃, 4hrs.

* * M—Martensite; B_L, B_L—Upper, Lower bainite; M-A—Martensite-austenite island; A_R—Retained austenite.

Table 3. Stress Corrosion Cracking Behavior of 40CrMnSiMoVa In 3.5%NaCl

Heat No.	Temperature (Isothermal) ℃	K_{ISCC} MPa $\sqrt{m}$	(da/dt), mm/hr	Number of specimens
1	190	14.17	10.52	3
2	280	13.90	4.2	3
3	300	12.95	0.24	3
4	310	13.90	1.00	3

Table 4. Microstructural Component of 40CrMnSiMoVA

Heat No.	Temperature (Isothermal) ℃	Before Tempering %			After Tempering %		After 0.2% Mechanical Deformation %	
		M	B	A_R	A_R	$A_R \rightarrow M$ Transformation	A_R	$A_R \rightarrow M$ Transformation
1	190	85.1	3	11.9	7.8	34	6.9	12
2	280	—	—	12.1	9.2	24	7.8	15
3	300	9.3	79.4	11.3	9.2	19	8.4	8

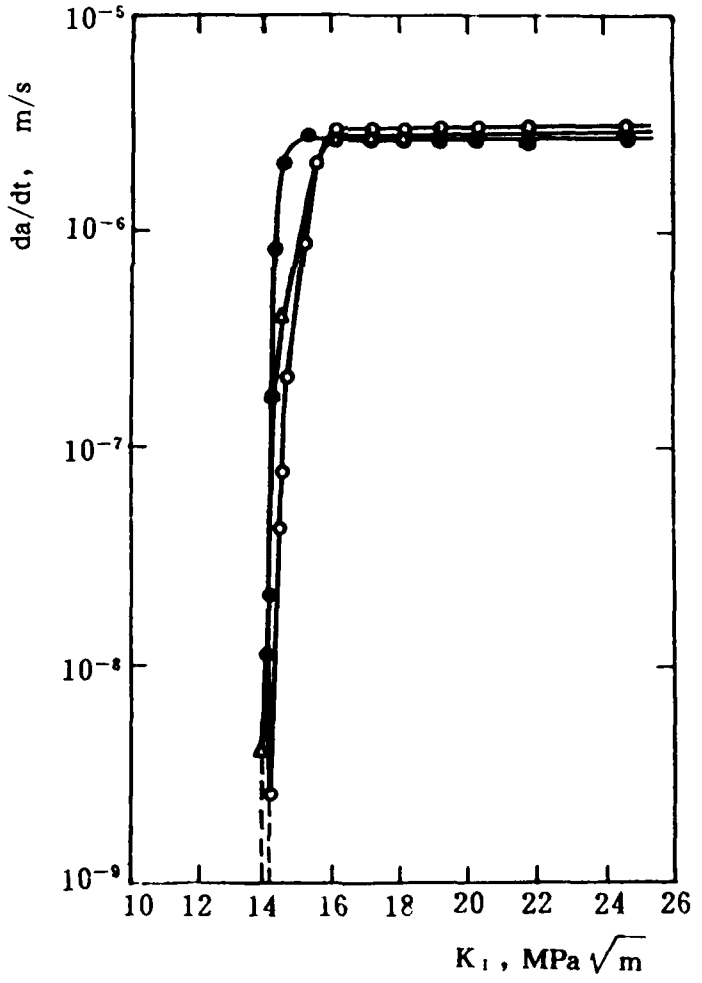

Fig. 1 Stress corrosion crack propagation behavior of 190℃ isothermally quenched and tempered 40CrMnSiMoVA steel in 35℃, 3.5% NaCl solution.

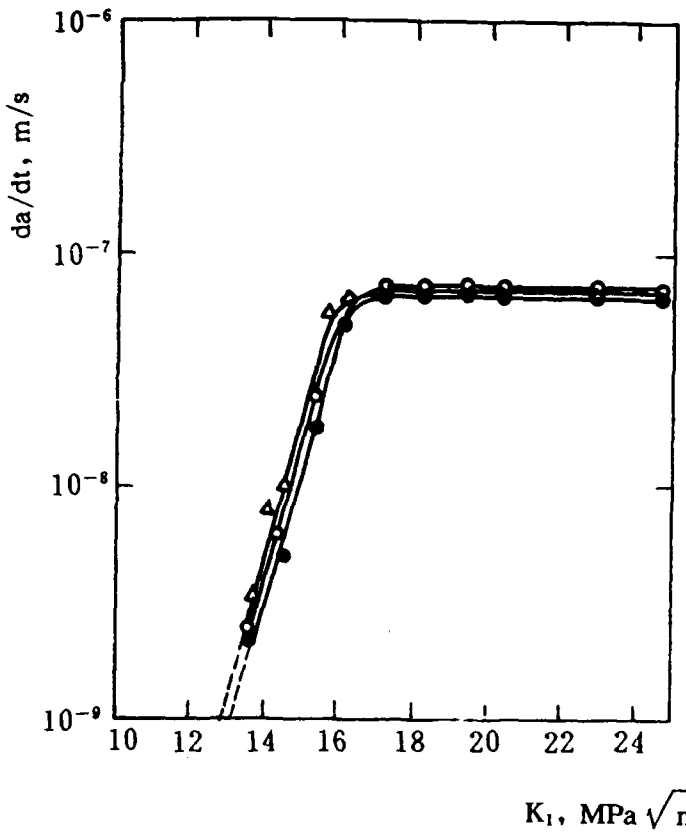

Fig. 2 Stress corrosion crack propagation behavior of 300℃ isothermally quenched and tempered 40CrMn SiMoVA steel in 35℃, 3.5% NaCl solution

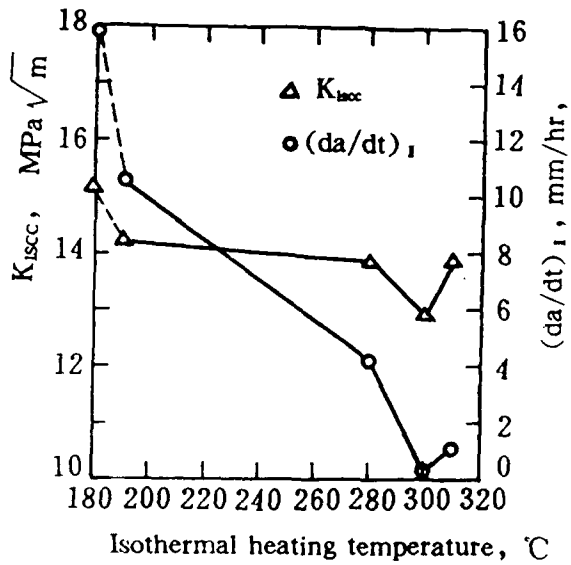

Fig. 3 Effect of isothermal heating temperture on SCC behaviors 40CrMn SiMoVA steel in 35℃, 3.5%NaCl solution.

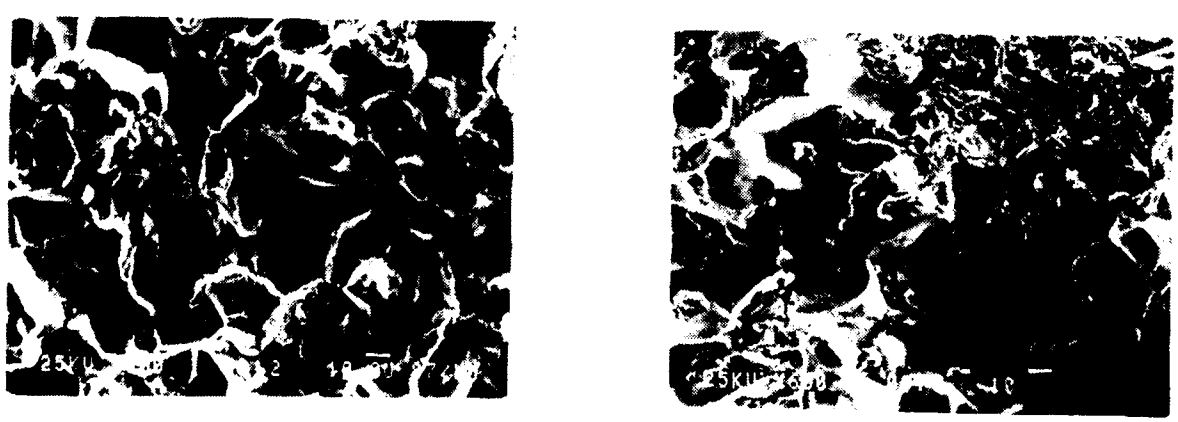

a. Low K_I region

b. Crack-arrest region

Fig. 5 SEM Microfractographic morphology of fracture surface of 40CrMnSiMoVA BL-WOL Specimen failured in 35℃ 3.5% Nacl solution (×600)

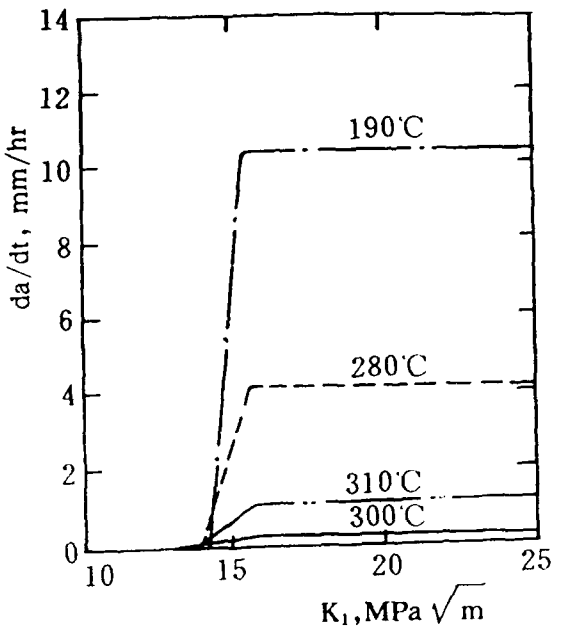

Fig. 4 Effect of isothermal heating temperature on crack growth of 40CrMnSiMoVA steel in 35℃, 3.5% NaCl solution

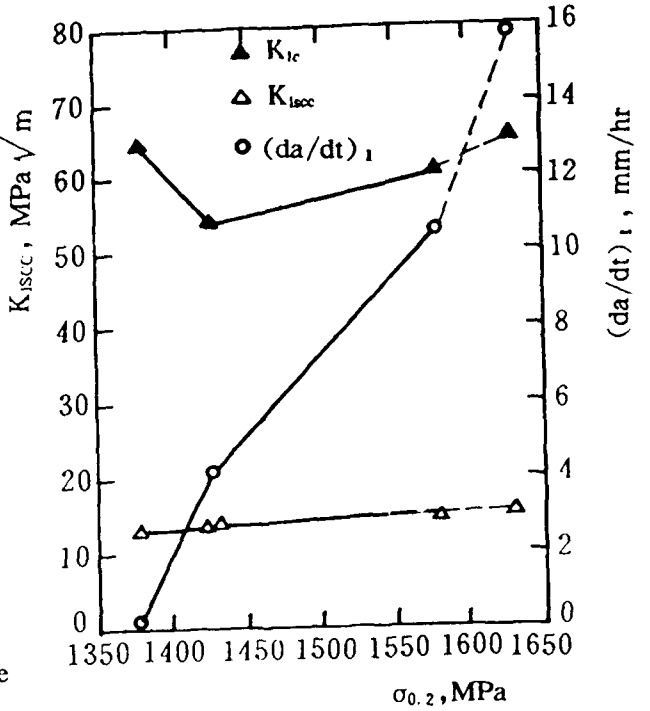

Fig. 6 Relation ship between SCC behaviors and yield strength of 40CrMnSiMoVA

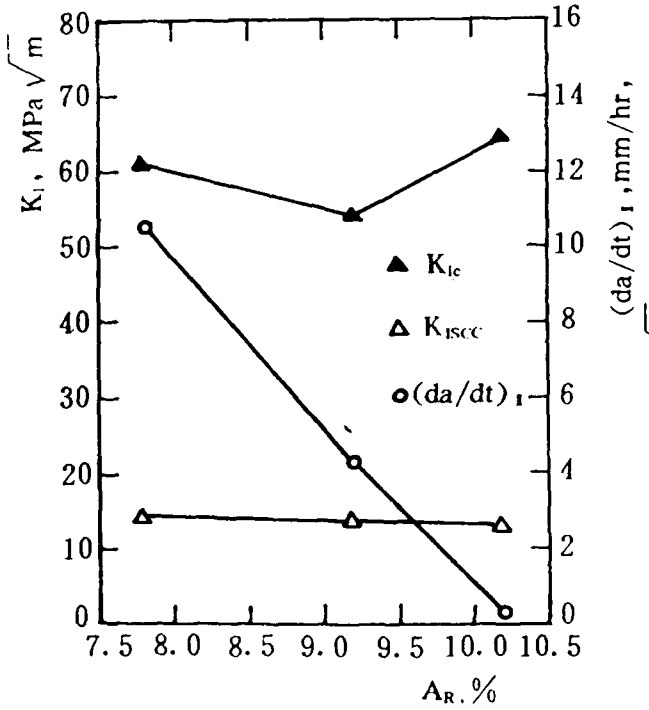

Fig. 7 Effect of retained austenite amount on scc behavior and K_{Ic} of 40CrMnSiMoVA

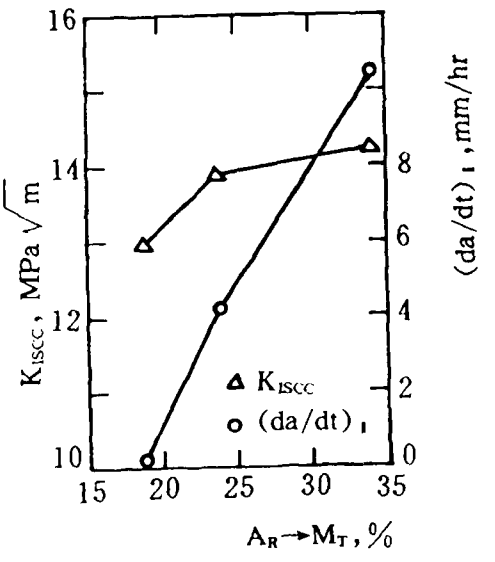

Fig. 8 Effect of transformation of $A_R \rightarrow M$(tempered) on SCC behavior of 40CrMnSiMoVA.

Corrosion Kinetics within Pits or Stress Corrosion Cracks of 1Cr13 Martensitic Stainless Steel

Youping Liu
Beijing Institute of Chemical Technology
Beijing, 100029,P.R.China

Yanqing Cen
Beijing Institute of Chemical Technology
Beijing, 100029,P.R.China

Jingyi Zuo
Beijing Institute of Chemical Technology
Beijing, 100029,P.R.China

Abstract

Electrochemical impedance spectra, potentiodynamic polarization curves and corrosion rates etc. of 1Cr13 steel in simulated occluded solutions at different stages were determined experimentally. A critical pH value about 3.7 was found on the "corrosion rate / pH" curve, the E / pH diagram and the electrochemical impedance spectra, below which the corrosion rate inside OCC increased rapidly. A potential / pH diagram depicting kinetic as well as thermodynamic behaviours within pits or cracks of 1Cr13 steel was constructed with the experimental data. Chemical and Electrochemical states, corrosion velocities and hydrogen evolution rates of occluded cell at different stages were presented on this E / pH diagram. It was found that the Nyquist plots with pH below the critical value were very different from those with higher pH values. In the former case, the passive film on the pit bottom or crack tips ruptured completely, accompanied with the sudden drop of potential and the occurrence of hydrogen evolution reaction.

Key terms: occluded cell corrosion, E / pH diagram, EIS, 1Cr13 steel, kinetics

I. Introduction

The key to pitting or stress corrosion cracking is the occluded cell within pits or cracks[1]. Since the actual cracks or pits are too narrow to be studied efficiently, Zuo et al developed a series of convenient and effective methods to study the behaviours inside pits or cracks[2], and verified the accelerating effect of occluded cell in "18–8 stainless steel / Cl^-" system. 1Cr13 martensitic stainless steel is also sensitive to localized corrosion when it is used in neutral chloride solutions. Recently, we determined the chemical compositions of occluded cell solution at different propagation stages for "1Cr13 steel / 0.5M NaCl" system and found that the pH value inside the occluded cell could drop down to about 3.45[3]. In this paper , the simulated occluded solutions at different stages were prepared to determine the corrosion rates, polarization curves, electrochemical impedance spectra and to construct the experimental potential / pH diagram depicting behaviours within pits or crscks of 1Cr13 steel. The equivalent circuits and kinetic models of occluded cell in different stages were also discussed.

II. Experiments

A. Preparation of specimens

1Cr13 martensitic stainless steel used was in the solution treated condition. Its chemical compositions(wt%) were as follows: C, 0.13; Cr, 11.77; Si, 0.58; Mn, 0.70; P, 0.024; S, 0.002; Fe, bal. The dimensions of the specimens were 2 × 15 × 20mm. All the surface of the specimens were polished with 700# abrasive paper finally, rinsed with distilled water and degreased with acetone.

B. Simulated occluded solutions

The test solutions were simulated occluded solutions of 1Cr13 steel / 0.5M NaCl system, with different pH values, Cl^- and metallic ions concentrations, determined previously by sending a given anodic current to occluded specimens and analyzed the occluded solution at different time intervals[3]. The compositions listed in table 1 represent the actual solution inside occluded crack tip or pit bottom at different stages of propagation.

A.R. salts and distilled water were used to make up the above 8 kinds of solutions. The pH of each solution was adjusted by HCl or NaOH to the value as listed. The solutions were deaerated by passing in nitrogen gas during the tests.

C. Determination of corrosion rate with weight loss tests

Weight loss tests were carried out in above 8 kinds of simulated occluded solutions at 90℃ with a test period of 50 hours. The corrosion rate / pH curve was obtained.

D. Measurement of open–circuit potential / time curves

The open–circuit potentials of 1Cr13 steel in occluded solutions were determined. The open–civcuit potential / time curves with different pH values were obtained. The tests lasted about 24 hours.

E. Determination of potentiodynamic polarization curves

Polarization scans were performed in a Model 350A Corrosion Measurement System, using a scan rate of 20mV / minute. Before tests began, nitrogen gas was released into the occluded solutions for 5 minites, then, the specimens were polarized cathodically to remove the passive oxide films. Cathodic polarization scans started from free potential to about −1000mV(SCE), and anodic ones from free potential to 300mV(SCE).

F. Determination of upper immunity potential

The corrosion rates of 1Cr13 steel in simulated occluded solutions were determined at different potentials. The potential corresponding to 10^{-7} A / cm^2 at "corrosion rate(current) / potential" curve was adopted as the upper immunity potential.

G. Measurement of electrochemical impedance spectra

The electrochemical impedance spectra of 1Cr13 steel in simulated occluded solutions were measured in a M378 Electrochemical Impedance Measurement System. The amplitude of AC voltage signal was ± 10mV. The frequency was from 100KHz to 0.05Hz. All the spectra were determined at open–circuit potentials.

The data obtained from the above experiments were used to construct the experimental E / pH diagram depicting the behaviours of occluded all corrosion of 1Cr13 steel.

Ⅲ. Results and Discussion

A. Corrosion rates and critical pH value of 1Cr13 steel in simulated occluded solutions of different stages.

The relationship between corrosion rate and pH value of occluded solution was found in Fig.1. It was shown that the corrosion rate increased with the decrease of pH value. In the corrosion rate / pH curve, there is an obvious breakpoint—critical pH value (pH = 3.7) below which the occluded cell corrosion rate increased rapidly.

B. Open–circuit potential / time curves

Fig.2 showed the potential–time curves of 1Cr13 steel in simulated occluded solutions of different pH value. The potential of specimens in solution with a pH value between 7 and 3.92 were in a range from −460 to −520mV(SCE). When the pH value of the occluded solution decreased down to or below 3.67, the potential of specimens dropped down to a value lower than −600mV(SCE). These potential / time curves confirmed the existance of a critical pH

value between 3.92 and 3.67 at which the electrochemical state of occluded cell changed.

C. Potentiodynamic polarization curves

Anodic and cathodic polarization curves of 1Cr13 specimens in four kinds of simulated occluded solutions at different stages were shown in Fig.3. It was indicated by anodic polarization curves that the effect of passivity diminished with pH dcreasing, e.g. the critical current density for passivity increasing, the passive region becoming larger and the rupture potential becoming more negative. When the pH value of the occluded solution decreased down to 3.67 or less, the passive region in the polarization curve disappeared entirely. The cathodic polarization curves showed that the process of hydrogen evolution was enhanced as the pH value decreased.

D. Experimental potential / pH diagram

The experimental potential / pH diagram shown in Fig.4 was constructed by superimposing the above polarization curves, potential / time curves and immunity border line etc. The diagram was divided by thick solid lines into four zones: corrosion, immunity, passivity and pitting. The kinetic curves presenting corrosion velocity and hydrogen evolution rate were also superimposed on this E / pH diagram with the thin solid lines and thin dotted lines respectively. The construction of kinetic lines were based on the following procedures: (1) The potentiostatic weight–loss tests were performed to get the corrosion rate (current density) / potential curves of different pH values (Fig.5 was an example). So the isocorrosion rate curves in the corrosion zone of the E / pH diagram were obtained. The isocurrent line of $10^{-7}A / cm^2$ was adopted as the border line between corrosion and immunity zones. (2) The isocurrent lines above the passivity zone were composed of the data of anodic polarization curves. The oxidation rates were approximately equal to the applied current as the potential shifted to more positive values. (3) The isocurrent lines of hydrogen evolution were obtained by using the Tafel extrapolation method of cathodic polarization curves.

Fig.4 is useful to describe the electrochemical states and occluded reactions in different stages of pitting or cracking propagation of 1Cr13 stainless steel. It is also useful in depicting the corrosion velocity and hydrogen evolution rate of occluded cell at fixed potential and pH value and in interpreting the reason for the existance of accelerating effect inside pits or cracks. More accurate critical pH value corresponded to the intersection of line E_p and line E_{oc}. Above the critical pH value, the occluded cells were in passive state, occluded reactions were dominated by macro–cell composed of pits and external surface (i.e. the oxygeon concentration difference cell). When the pH value of the occluded solution decreased down to the critical value, the potential of the occluded cells dropped down into the "corrosion" zone, a passive–active transition and an accelerating corrosion effect occurred at crack tips or pit bottom. And the hydrogen evolution reaction became a dominating factor of the occluded cell corrosion.

E. Electrochemical impedance spectra

Nyquist plots of 1Cr13 steel in the occluded solutions of different pH values were shown in Fig.6. It was indicated that the resistance of the occluded reaction was reduced gradually with a pH decreasing. The spectra at pH values below the critical value were semicircles at a range of the test frequencies. When the pH value of the solution was above the critical value, the spectra at low frequencies were deflected from the semicircles at high frequencies. The critical pH value could also be obtained from the above electrochemical impedance spectra. The break point of the $1 / R_r$–pH curve as shown in Fig.7 was agreement with that of corrosion rate–pH curve(Fig.1).

The equivalent circuit of the occluded cell based on plot e or f could be presented with Fig.8. The anodic reactions inside the occluded cell were active dissolution of crack tips or pit bottom when the pH value of the occluded solution decreased bolow the cditical value. And the dissolution rate was dominated by the hydrogen evolution reaction within occluded cells. The mathematical expression of Fig.8 was as follows:

$$Z_{(\omega)} = R_l + \frac{1}{\frac{1}{R_r} + j\omega C_d} \tag{1}$$

A similar shape of Nyquist plots of 1Cr13 steel in the occluded solution with a pH value above the critical value appeared as plot d (pH = 3.92) in Fig.6. The dimensions of each plot depended upon the pH value and Cl^- concentration of each solution. The equivalent ciruit of the occluded cell at a pH value above the critical value could be supposed as shown in Fig.9. R_{r1} referred to the reaction resistance of the passive alloy, not including Cl^- effects. C_a was the electric capacity caused by non–Faraday absorption of Cl^-. R_{r2} represented the effects of the absorption of Cl^- on the reaction resistance of the passive alloy. Fig.9 could be expressed in the following formula:

$$Z_{(\omega)} = R_l + \frac{1}{\frac{1}{R_{r1}} + \frac{1}{R_{r2} + \frac{1}{j\omega C_a}} + j\omega C_d} \tag{2}$$

Supposing $a = \omega R_{r2} C_a$, formula (2) could be sorted out as

$$Z_{(\omega)} = R_l + \frac{1}{\frac{1}{R_{r1}} + \frac{a^2}{(1+a^2)\cdot R_{r2}} + j\omega(C_d + \frac{C_a}{1+a^2})} \tag{3}$$

If $\omega >> \frac{1}{R_{r2} C_a}$, i.e. a >> 1, formula (3) could be simplified as formula (4).

$$Z_{(\omega)} = R_l + \frac{1}{\frac{1}{R_{r1}} + \frac{1}{R_{r2}} + jwC_d} \tag{4}$$

The Nyquist plot corresponding to formula(4) was a circle with a diameter of $R_{r1} // R_{r2}$.

The diameter of the impedence circle at lower frequencies, $R_{r1} // (R_{r2} + \frac{R_{r2}}{a^2})$, increased as the frequency decresed. The shift of spectra at lower frequencies were interpreted qualitatively as that shown in Fig.10. Point a, b and c corresponded to the impedance at frequency ω_1, $\omega_2$and $\omega_3(\omega_1 > \omega_2 > \omega_3)$respectively.

The primary factor affecting R_{r1} in Fig.9 was the pH value of the occluded solutions. R_{r2} depended on Cl^- concentration. R_{r1} and R_{r2} decreased with the acidification of the occluded solution and the migration of Cl^- into the occluded cells, i.e. the effect of passivating of the occluded cell was weakened as pH value decreased and Cl^- concentrated. Above electrochemical impedence spectra were helpful to understand the kinetics and the critical pH value of the occluded cell corrosion. However, fruther and thorough analyses were still needed.

IV. Conclusions

A. The corrosion rates of 1Cr13 steel in simulated occluded solutions at different stages were determined. A critical pH value about 3.7 was found in t" "corrosion rate / pH curve", the "potential / time" curves, the anodic polarization curves, the ε / pH diagram and in the electrochemical impedance spectra. When the pH value of the occluded solution decreased below the critical value, the corrosion rate inside the occluded cell increased rapidly.

B. A potential / pH diagram depicting kinetic and thermodynamic behaviours within pits or cracks of 1Cr13 steel was constructed. The chemical and electrochemical states, the corrosion velocity and the hydrogen evolution rates of the occluded cells at different stages were presented on this E / pH diagram.

C. The electrochemical impedance spectra of 1Cr13 steel in the occluded cell solutions with a pH value higher than the critical value were quite different from those with a pH value lower than the critical pH value. It was found that there existed a passive film on the pit bottom or crack tips when the pH value of the occlucdc solution was above the critical value. The passivity of occluded cells was weakened and the reaction resistance was reduced with the decreasing of pH value and the concentration of Cl^-. When the pH value of the occluded solution decreased below the critical value, the crack tips or pit bottom dissolved actively and the occluded cell was dominated by the hydrogen evolution reaction within pits or cracks.

References

1. M.G.Fontana, N.D.Greene, Corrosion Engineering (1967): pp42–43, 51–52.
2. J.Zuo, Y.Liu et al, Extracts of Scientific Lectures, (ACHEMASIA'92, Beijing, 1992): pp168–170.
3. Y.Liu, X.Liu, J.Zuo, Corrosion Science and Protection Technique (in Chinese), 4 3 (1992): pp168–173.

Table 1. Solution compositions of the simulated occluded cell in different stages(Anodic current density: 1mA / cm^2) Bulk solution: 0.5 mol / l NaCl, 50℃; Specimen: 1Cr13 steel

No.	Time hr	pH	Cl^- mol / l	Fe g / l	Cr g / l
1	0	7.00	0.500	/	/
2	1	4.90	0.515	0.353	0.037
3	2	4.35	0.530	0.691	0.070
4	5	4.18	0.561	1.315	0.117
5	7	3.92	0.606	2.142	0.222
6	10	3.67	0.650	2.970	0.328
7	20	3.48	0.727	6.820	0.690
8	31	3.45	0.923	13.98	1.424

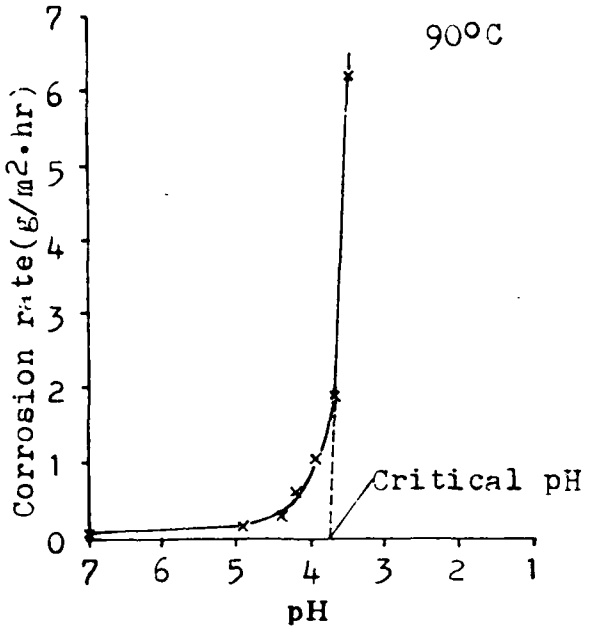

Figure 1. The effects of pH changes on the corrsion rate in occluded cells of 1Cr13 steel.

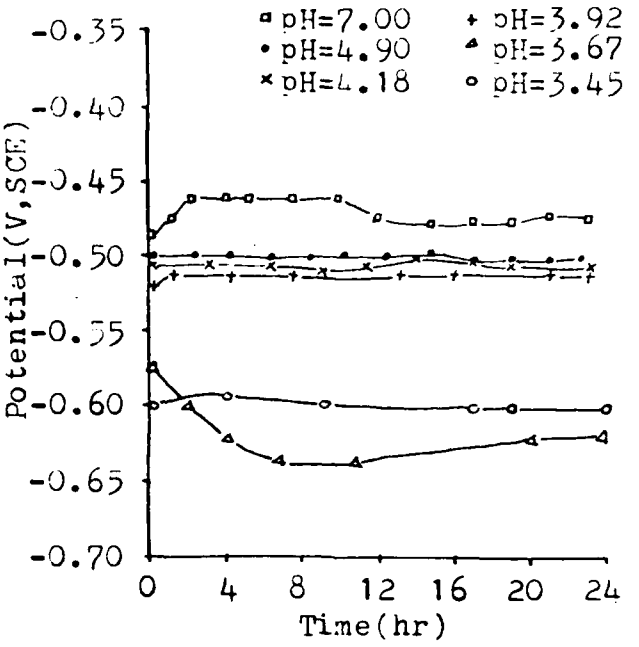

Figure 2. Open-circuit potential / time curves for 1Cr13 steel in different OC solutions(90℃).

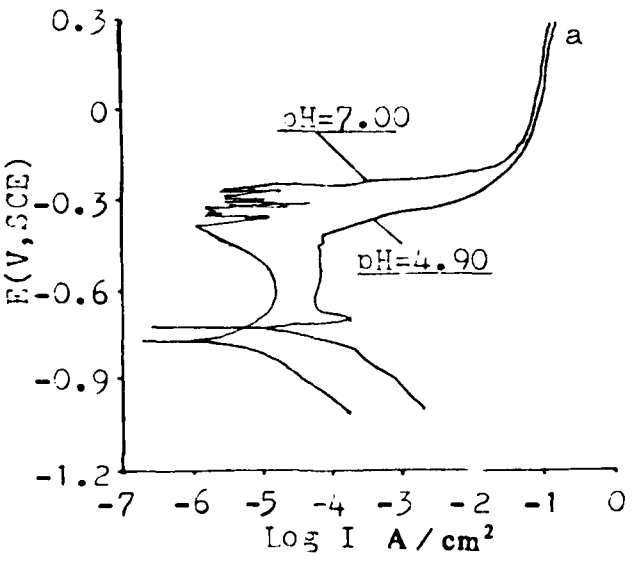

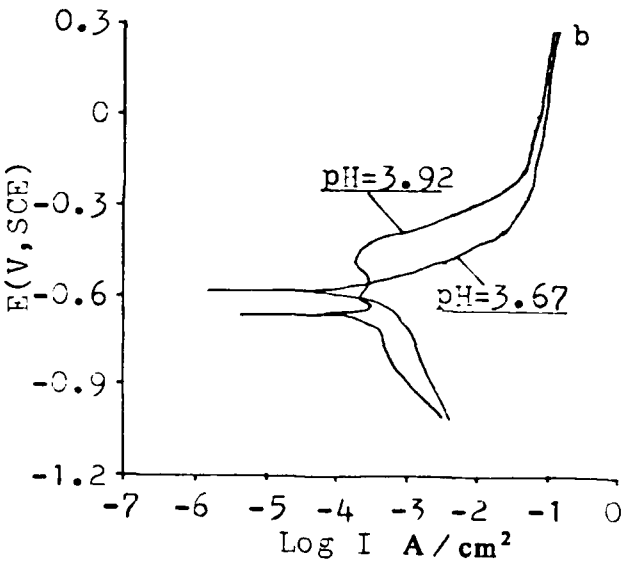

Figure 3. Potentiodynamic polarization curves for 1Cr13 steel in different OC solutions(90℃). Scan rate: 20mV / minute.

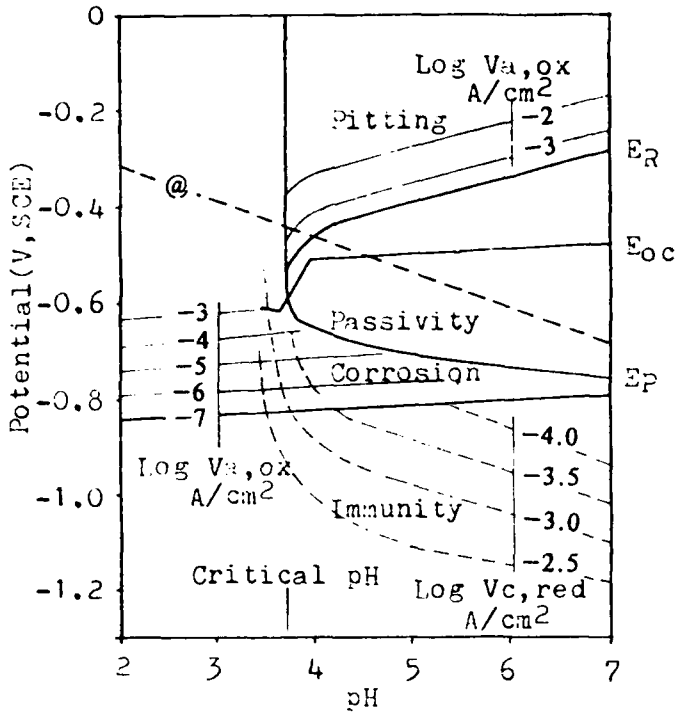

Figure 4. Experimental potential / pH diagram depicting kinetic and thermodynamic behaviours of occluded cell for 1Cr13 steel / Cl^- system(90℃).
E_R: Rupture potential(or pitting potential)
E_p: Passivation potential
@: Hydrogen equilibrium line
$V_{a,ox}$: Oxidation currents on the specimen
$V_{c,red}$: Reduction currents for hydrogen evolution
E_{oc}: Open–circuit potential relating to the initially passivated specimen

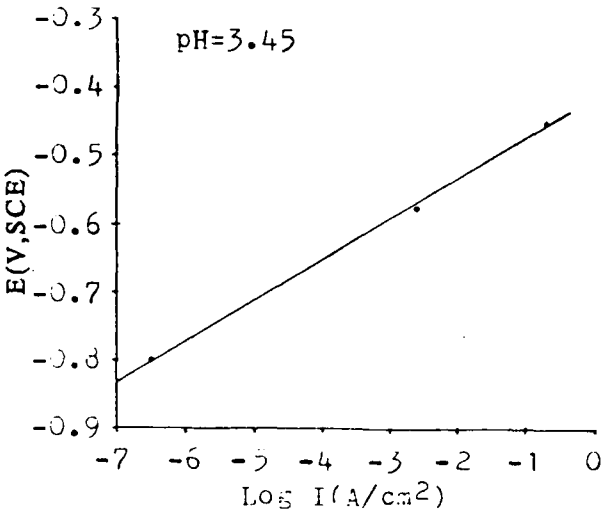

Figure 5. Example for determination of upper immunity potentials corresponding to corrosion current of 10^{-7}A / cm^2.

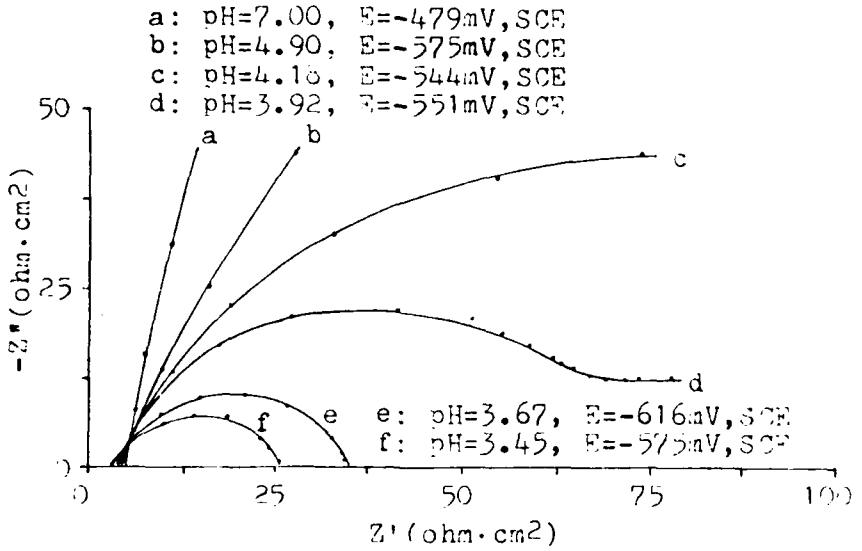

Figure 6. Electrochemical impedance spectra for 1Cr13 specimens in different occluded solutions(90℃)

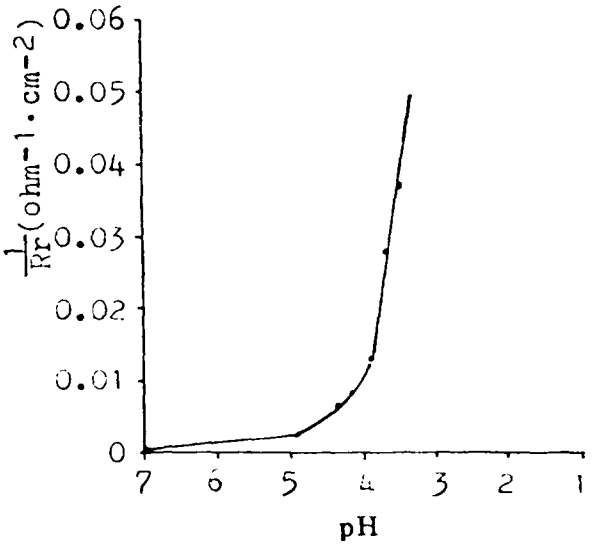

Figure 7. The effects of pH changes on reaction resistance(R_r) of occluded cell corrosion for 1Cr13 steel / Cl^- system(90℃)

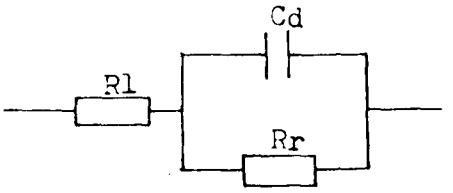

Figure 8. Equivalent circuit of Z based on plot e or f in figure 6 with a pH below the critical value

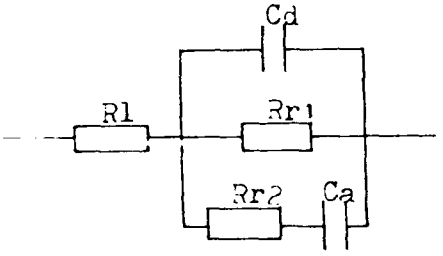

Figure 9. Equivalent circuit of Z based on plot d or b, c in figure 6 with a pH above the critical value

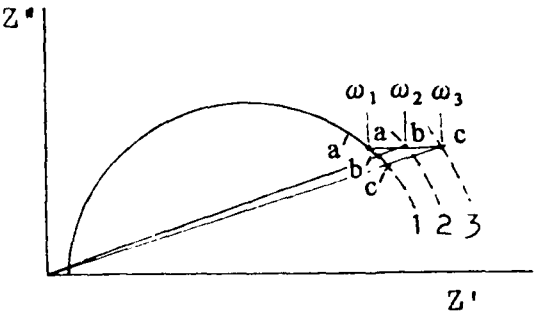

Figure 10. Schematic for qualitative interpretation of plot d on figure 6.

Investigation of Mechanical and Environmental Effects on the Occluded Cell within Stress Corrosion Cracks of 1Cr13 Martensitic Stainless Steel

Youping Liu
Beijing Institute of Chemical Technology
Beijing, 100029, P.R.China

Fang Chi
Beijing Institute of Chemical Technology
Beijing, 100029, P.R.China

Jingyi Zuo
Beijing Institute of Chemical Technology
Beijing, 100029, P.R.China

Abstract

Specimens stressed at yielding point and artificial occluded solutions were tested to simulate the mechanical and environmental states within stress corrosion cracks for "1Cr13 steel / Cl^-" system and to determine corrosion rates as well as electrochemical behaviours of crack tips at different propagating stages. A critical pH value (about 4.1 at 90℃) was found from the "corrosion rate / pH" curve, "potential / time" curves, and potential / pH diagrams, below which the passive–active transition occurred at crack tips and corrosion rate increased rapidly. Stress caused the passivating effect of cracks diminishing. It also caused the corrosion rate and the critical pH value rising. The experimental potential / pH diagrams depicted the mechanical and environmental effects on occluded cell within cracks of 1Cr13 stainless steel.

Key terms: stress corrosion crack, 1Cr13 steel, occluded cell

I. Introduction

Both Cr18Ni9 and Cr13 stainless steels are sensitive to stress corrosion cracking(SCC) in aqueous solutions containing Cl^-. The susceptibility of the former is higher than that of the latter. The comparison of the chemical and electrochemical states of crack tips for these two kinds of steels would be important to perfect the theory of corrosion and to develope the new alloys resisting SCC.

The chemical and electrochemical as well as mechanical states of crack tips are very different from those of the external surface . Scientists have done much about the electrochemistry of SCC of Cr18Ni9 steel[1,2]. Yet few or unsystematic studies were made on the behaviour of crack tips for Cr13 steel. The composition and pH value of occluded solution within cracks at different propagating stages were determined with the simulated occluded cell for 1Cr13 steel / Cl^-system[3]. This paper presents the mechanical and environmental effects on kinetic as well as thermodynamic behaviours of crack tips of 1Cr13 martensitic stainless steel.

II. Experimental

A. Material and Specimens

1Cr13 martensitic stainless steel used was in the solution treated condition, with yielding point of about 450MPa and the chemical compositions(Wt%) as follows: C, 0.13; Cr, 11.77; Si, 0.58; Mn, 0.70; P, 0.024; S, 0.002; Fe, bal.

Conventional tensile specimens (Fig.1) used in tests were polished with 700# abrasive paper finally, rinsed with distilled water and degreased with acetone. The surface of the specimens were shielded with polytetrafluoroethylene and silicon rubber ribbon except the central part(20mm) which was exposed to solutions. Stress about 455MPa was applied to specimens during the tests to simulate the yielding state of crack tips.

B. Test solutions.

The test solutions were simulated occluded solutions of 1Cr13 steel / 0.5M NaCl system, with different pH values, Cl^- and metallic ions concentrations. The solution compositions are listed in Table 1, representing the actual solution inside occluded crack tips at different stages of crack propagation.

A.R. salts and distilled water were used to make up the above 8 kinds of solutions. The pH value of each solution was adjusted by HCl or NaOH to the value as listed. The solutions were deaerated by passing in nitrogen gas during the tests.

C. Test Procedures

1. Determination of corrosion rate with linear polarization technique.The tensile specimen and a solution container with a volume of 200 ml were fixed in a SCC test apparatus of constant load. The initial stress applied to the specimens was about 455 MPa, approximately equal to their yield stress. Reference electrode, Pt electrode, nitrogen inlet and outlet, heater and thermostat etc. were included in the container. Linear polarization was carried out to determine the corrosion rate of stressed 1Cr13 specimens in simulated occluded solutions at 50℃ and 90℃ respectively.

2. Measurement of open-circuit potential / time curves.The open-circuit potential of stressed specimens in simulated occluded solutions of different pH value, Cl^- and metallic ions concentrations were determined. Both stress and pH effects on the potential / time curves were indicated. The measuring lasted about twenty-four hours.

3. Determination of potentiodynamic polarization curves.Polarization scans were performed in a Model 350A Corrosion Measurement System, using a scan rate of 20mV / minute. Before the scans began, nitrogen gas was released into the occluded solutions for 5 minutes and the specimens were polarized cathodically to remove the passive oxide films. Cathodic plarization scans began from free potential to about −1000 mV(SCE), and the anodic ones from free potertial to 300mV(SCE).

Ⅲ. Results and Discussion

A. Influences of stress and occluded solution on the corrosion rate of crack tips of 1Cr13 steel

The corrosion rates of stressed 1Cr13 steel specimens in the simulated occluded solutions of different pH value were shown in Fig.2. There was a same tendency of increasing corrosion rate as the pH value decreased down inside cracks at 50℃ and 90℃ respectively. When the pH value of occluded solution was above 4.1, the corrosion rate was low. But the corrosion rate increased rapidly as pH decreased down below 4.1 at 90℃ . There existed a critical pH value below which accelerating corrosion effect occurred, corresponding to the break point of the corrosion rate / pH curves(about 4.1 at 90℃ , 3.7 at 50℃). Compared with unstressed conditions, the accelerating process of yielding crack tips started in solution of higher pH value, i.e. stress was another important factor of accelerating corrosion. In addition, increasing temperature was also a factor of increasing corrosion rate. Of all the influencing factors, the acidification of occluded solution within cracks was the most dominating one.

B. Open-circuit potential / time curves

The open-circuit potential / time curves of stressed 1Cr13 steel specimens in occluded solutions at 50℃ were shown in Fig.3. The potential of the specimen in solution with a pH value higher than 3.92 dropped down to about −620mV(SCE) at the start of loading, then increaced in positive direction and became stable at about −490～−520mV(SCE) finally. The open-circuit potential in solution with a pH value lower than 3.67 lay in a range of about −640～−650mV(SCE) at the end of the tests. There was a significant transition of electrochemical state of crack tips in solution with a pH value from 3.92 to 3.67. This transition was in agreement with the breakpoint of corrosion rate / pH curve of the same temperature. The potential / time curves of 90℃ as shown in Fig.4 were also divided into two groups. The potential of specimen in solution with a pH value higher than 4.18 maintained at about −550mV(SCE) at the end of tests. But when pH value decreased down below 3.92, the potential of the specimen were between −640 and −650mV(SCE) finally. The critical pH value obtained from corrosion rate / pH curve at 90℃ in Fig.2 lay in a range from 3.92 to 4.18. These potential / time curves will be discussed in the following paragraphs.

C. Potentiodynamic polarization curves

The potentiodynamic curves of stressed 1Cr13 steel specimens in simulated occluded solutions at 50℃ and 90℃ were shown in Fig. 5 and 6 respectively. The passivity of the stressed specimens diminished with pH decreasing or temperature increasing. The passivating effects were also weakened by stress, i.e. the passivity region became smaller, the primary passive potential became more positive and the critical anodic current density for passivity became higher. When the solution pH decreased to 3.45, the passive region in polarization curve disappeared entirely. Cathodic polarization curves showed that the hydrogen evolution rate increased as pH value decreased.

D. Experimental potential / pH diagrams

Fig.7 and 8 were E / pH diagrams which were constructed with above electrochemical data to present the kinetic and thermodynamic behaviours of crack tips for "1Cr13 steel / Cl^-" system. The E_{oc} line indicating the state of crack tip at different stages was composed of the stable values of the potential / time curves of different pH value. The intersection of the E_{oc} and E_p lines corresponded to the exact critical pH value, above which the cracks were in passive state. When the pH value of the occluded solution decreased below the critical value, the crack tip was transformed into active state, and the corrosion velocity and hydrogen evolution rate increased rapidly. The potential / time curves shown in Fig.3 and 4 could be explained as follows: At the beginning of loading, the strain rate was so high that the passive film on the surface of the specimen could not be repaired promptly, so the potential of the specimens droped quickly. After a few ninites, the strain of the specimen became constant, and the passive film on specimens were repaired gradually in the solution with a pH value above the critical value. The higher the pH value was, the faster the repairing rate of passive film and the increasing rate of potential were. Below the critical pH value, the specimen was in active state. Its potential changed insignificantly during the tests.

The isocurrent lines of corrosion rate or hydrogen evolution rate were also superimposed on the E / pH diagrams. An arbitary criterion of the corrosion rate lower than $10^{-7}A / cm^2$ was adopted as immunity. The border line between "corrosion" and "immunity" regions was composed of the data obtained in the way as shown in Fig.9. The immunity potential of the stressed specimen was lower than that of unstressed one, but the difference between them was only within a range of

10mV.

The temperature effects on SCC could be seen by comparing Fig.8 to Fig.7. The temperature increasing from 50℃ to 90℃ made the "passivity" and "immunity" zones smaller and the "corrosion" zone larger in E / pH diagrams. It also caused the critical pH value and corrosion rate rising. All these changes indicated that the higher the temperature was, the material would be more sensitive to SCC.

The effect of stress on cracks at different stages could be summarized as follows: Stress caused the initiation of cracks easier by lowering the rupture potential. When the pH value of occluded solution was higher than the critical value, Stress caused the passivity of passive cvack tips diminished. At the critical pH value, the acidic occluded solution and stress had a cooperative effect on the passive–active transition of crack tips. Below the critical pH value, the crack tip was in active state, stress accelerated the occluded cell corrosion by lowering the activating energy of the alloy.

Ⅳ. Conclusions

A. A critical pH value about 4.1 at 90℃ existed within stress corrosion cracks of "1Cr13 steel / Cl^-" system. When the pH value of occluded solution decreased below the critical value, the passive–active transition occurred at crack tips, accompanied with the sudden drop of potential and the rapid increasing of corrosion velocity as well as the hydrogern evolution rate.

B. The corrosion rate of crack tips at a pH value below the critical value was about two decades higher than that of the external surface of 1Cr13 steel. Both acidification of occluded cell solution and the stress were the essential factors of accelerating corrosion of crack tips. The environmental effect is more important.

C. The changes of localized environment and stress caused the effect of passivity of alloy diminished. They had a cooperative effect on the passive–active transition of crack tips at the critical pH value. Stress caused the critical pH value rising.

D. The effects of temperature on SCC were interpreted from the experimental E / pH diagrams presenting the kinetic as well as thermodymic behaviours of OCC. The higher the temperature was, the smaller the passivity and immunity zones in the E / pH diagram were and the higher the critical pH value and corrosion rate of OCC were.

References

1. M.Pourbaix, Proc. Intern. Symp. Corrosion Science and Engineering, Vol.1, pp307–314(Brussels, 1989).
2. J.Y.Zuo, Y.P.Liu et al, Extracts of Scientific Lectures, ACHEMASIA'92, PP168–170(Beijing,1992).
3. Y.P.Liu, X.X.Liu and J.Y.Zuo, Corrosion Science and Protection technique, in Chinese, 4 3 (1992): pp168–173.

Table 1. Solution compositions of the simulated occluded cell in different stages(Anodic current density: 1mA / cm^2)
Bulk solution: 0.5 mol / l NaCl, 50℃; Specimen: 1Cr13 steel

No.	Time hr	pH	Cl^- mol / l	Fe g / l	Cr g / l
1	0	7.00	0.500	/	/
2	1	4.90	0.515	0.353	0.037
3	2	4.35	0.530	0.691	0.070
4	5	4.18	0.561	1.315	0.117
5	7	3.92	0.606	2.142	0.222
6	10	3.67	0.650	2.970	0.328
7	20	3.48	0.727	6.820	0.690
8	31	3.45	0.923	13.98	1.424

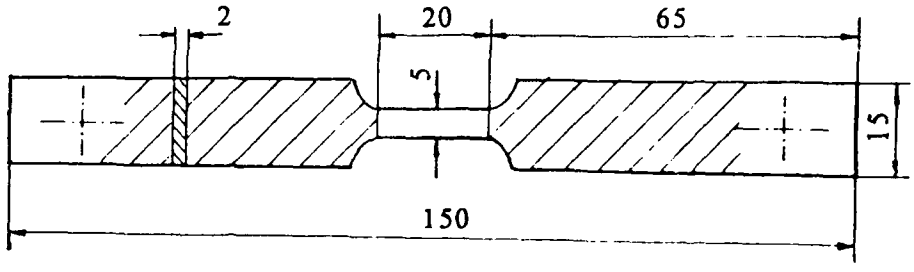

Figure 1. Schematic of the tensile specimens

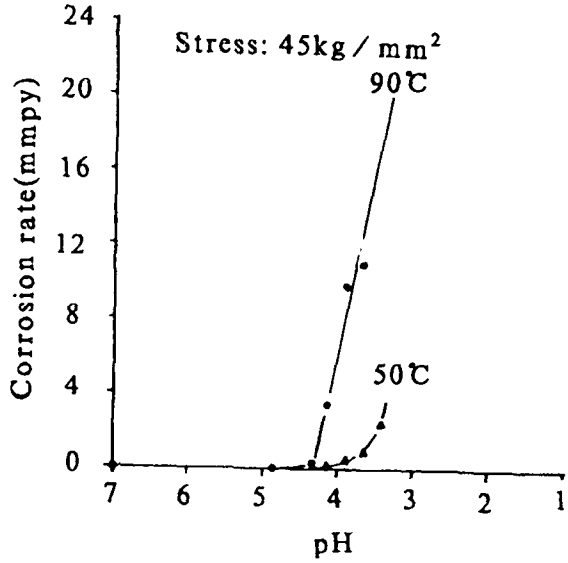

Figure 2. Changes of corrosion rate of stressed 1Cr13 steel with pH value of occluded solution

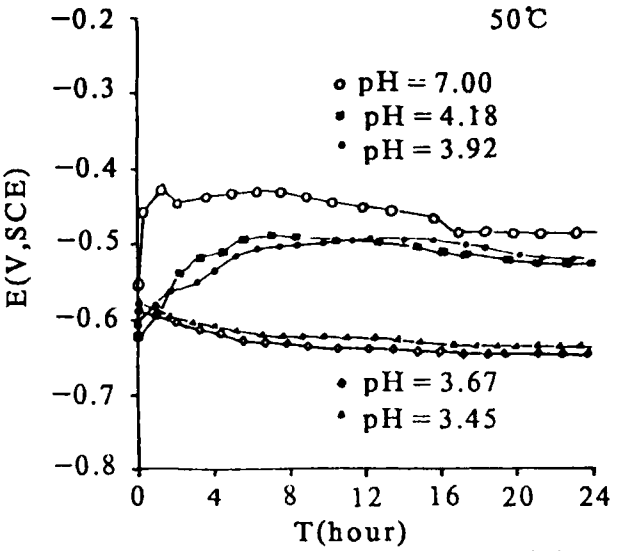

Figure 3. Open-circuit potential / time curves of stressed 1Cr13 steel in occluded solutions

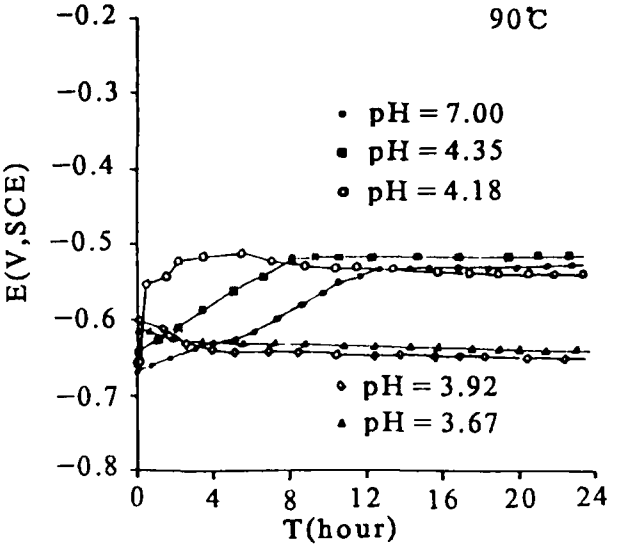

Figure 4. Open-circuit potential / time curves of stressed 1Cr13 steel in occluded solutions

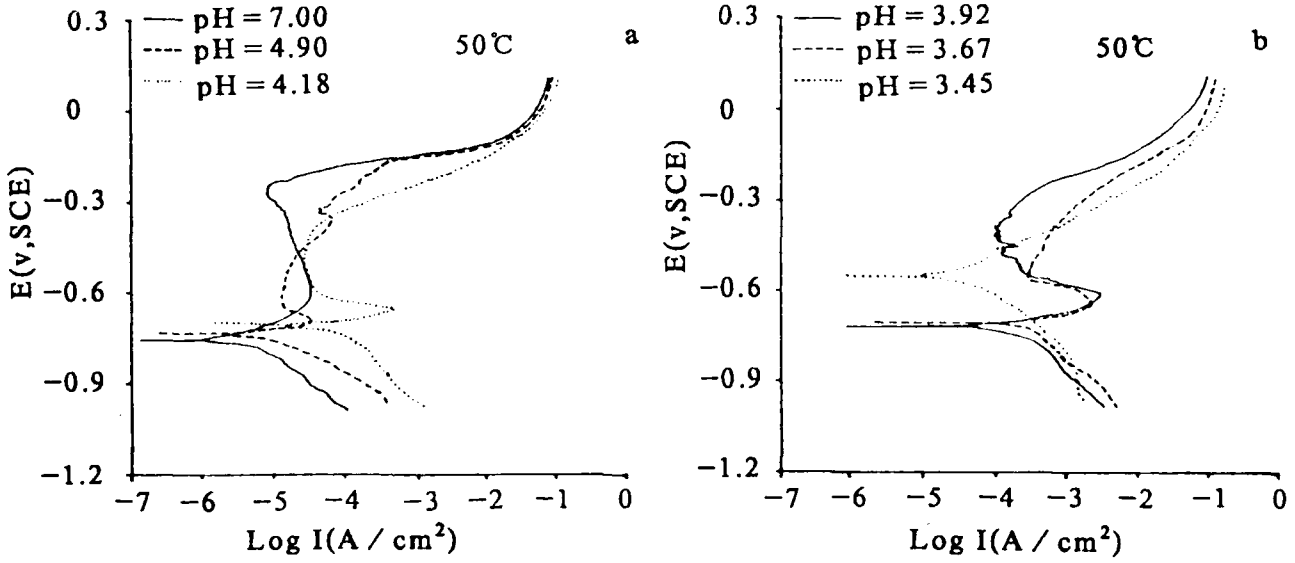

Figure 5. Potentiodynamic polarization curves of stressed 1Cr13 steel in different occluded solutions(50℃)

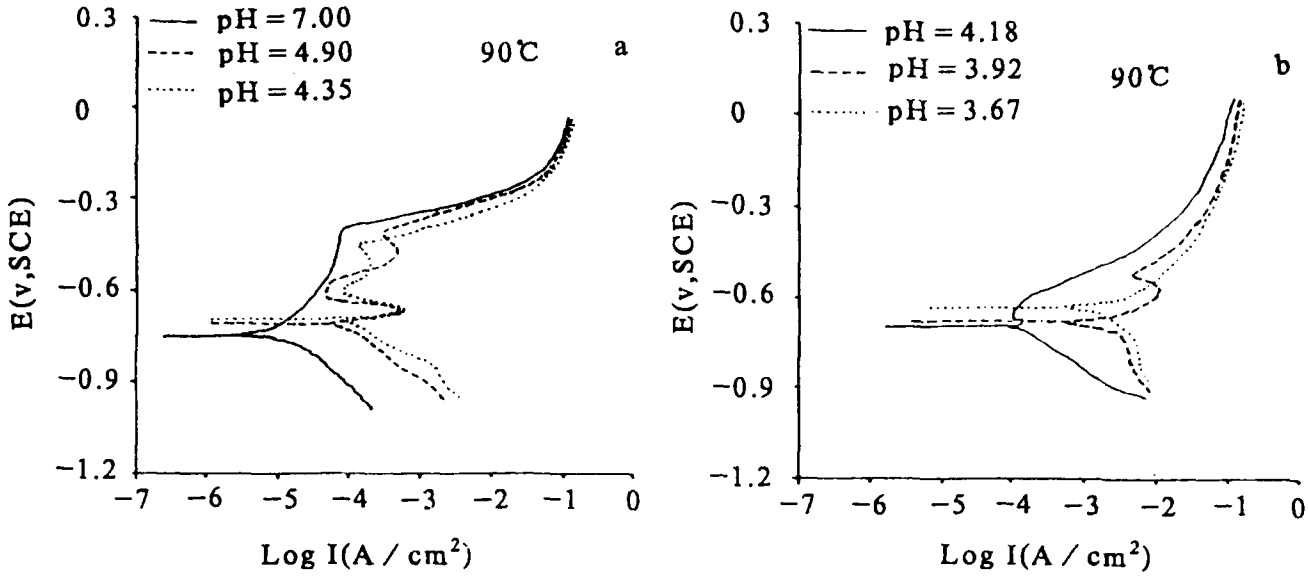

Figure 6. Potentiodynamic polarization curves of stressd 1Cr13 steel in different occluded solutions(90℃)

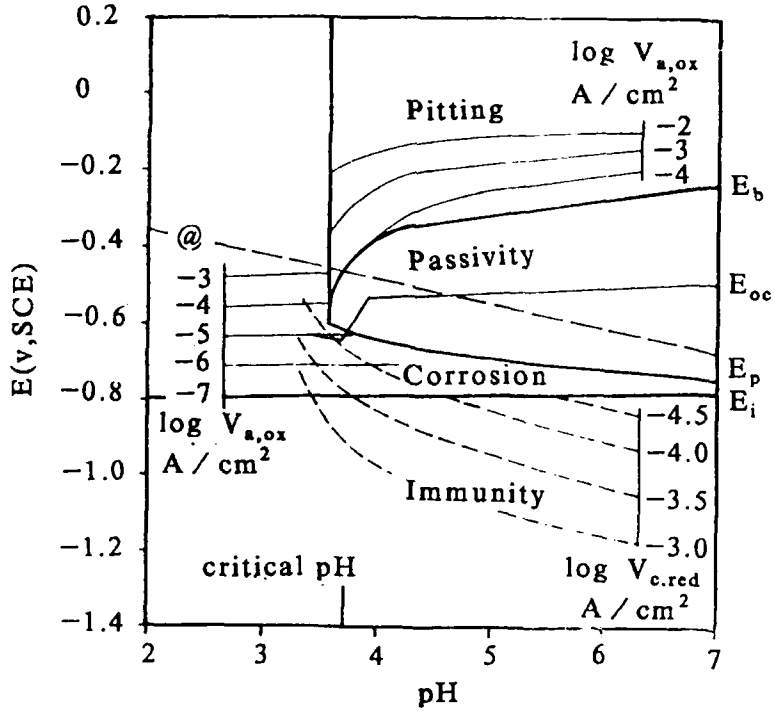

Figure 7. Experimental potential / pH diagram depicting kinetic and thermodynamic behaviours of crack tips for 1Cr13 steel / Cl^- system(50℃)

$V_{a,ox}$: Oxidation currents on the specimens

$V_{c,red}$: Reduction currents for hydrogen evolution

E_{oc}: Stable open-circuit potential of stressed specimen in occluded solutions

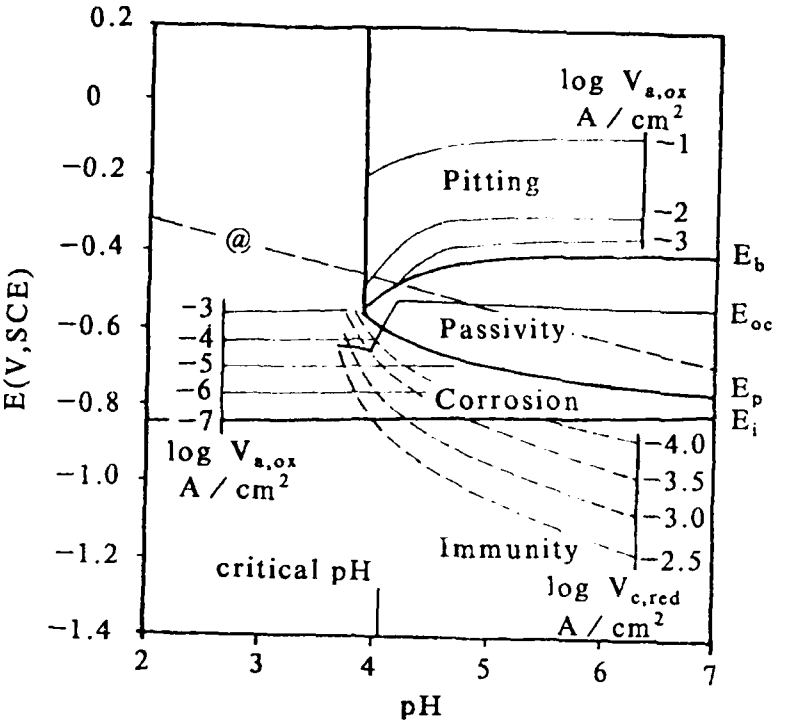

Figure 8. Experimental potential / pH diagram depicting kinetic and thermodynamic behaviours of crack tips for 1Cr13 steel / Cl^- system(90℃)

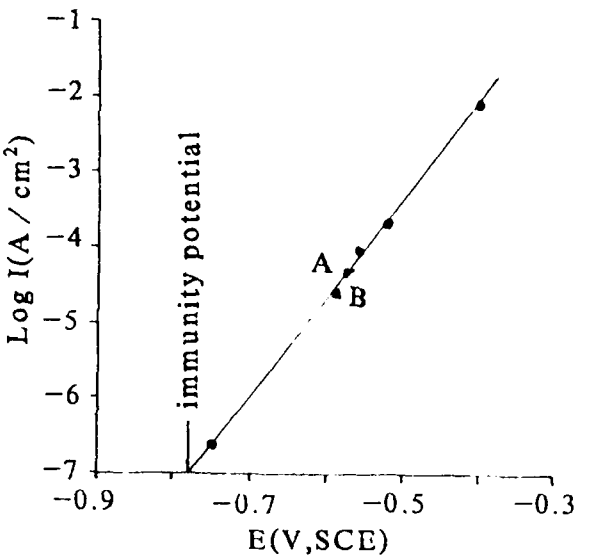

Figure 9. Example for determination of upper immunity potential corresponding to corrosion rate of 10^{-7}A / cm^2

• from weight loss tests with unstressed specimens

A from linear polarization test with unstressed specimen

B from linear polarization test with stressed specimen

12th International Corrosion Congress
September 19-24, 1993
Houston, Texas USA

A Fully-Plastic Micro-Cracking Model For T-SCC in Planar-Slip Materials

William F. Flanagan
Min Wang
Mengke Zhu
Barry D. Lichter

Vanderbilt University
Nashville TN 37235 USA

Abstract

It has been confirmed that T-SCC can be discontinuous under slow strain-rate testing, at least for samples which deform by planar slip (i.e., those which have low stacking-fault energy). Interpretation of the load and current transients shows that the crack velocity is on the order of 100μm/s, depending on the environment, too slow to be explained by a running brittle crack, and too fast to be explained by Faradaic dissolution. Support of such an interpretation is given by the agreement between predictions of crack area by mechanical analysis of the load transients with that predicted by analysis of the current transients; and the agreement of these predictions with the resulting crack-advance distance determined from fractography. Such agreement follows if the assumption is made that cracking is fully plastic, that is, that deformation accompanies cracking such that the uncracked portion of the specimen is maintained at the flow stress.

I. Introduction

Transgranular stress-corrosion cracking (T-SCC) in materials exhibiting planar slip (i.e., in materials having low stacking-fault energy) has been shown to be discontinuous [1-7]. The fracture surfaces match, and consist of micro-cracks on the order of 1μm in size which gives a "cobblestone" appearance. The details of this cracking is sensitive to the imposed potential and to the crack-growth direction [4,5,8-10]. It has been shown in experiments on single crystals that crack blunting can occur when the crack-growth direction is such that the crack tip is roughly coplanar with the active slip planes, and this results in "crack arrests" which are spaced on the order of 50-200μm apart [4,5,8]. In this case, continued fracture requires that the crack be renucleated [3], but such renucleation may require times on the order of minutes, and is highly sensitive to the corrosion potential [2,4,8,9]. T-SCC is also discontinuous on a microscale, where the combined effects of the ubiquitous ligaments, which control the

COD, and the corrosive environment, which affects the value of K_{IC}, lead to discrete micro-crack advances [5]. This results in an effective velocity between renucleation events which is too large for Faradaic dissolution to be rate-controlling, as claimed by classical slip-dissolution models [11], and too small for a single unstable crack growth event to have occurred, as claimed by proponents of various versions of the film-induced cleavage model [6,7]. Moreover, the latter models are also excluded in accounting for micro-crack advances, since they depend on diffusional processes (to form films or dealloyed layers) which can not operate during the microcracking events [4,12]

Thus, average crack-growth rates for T-SCC can be very small, as low as 0.1μm/s, when macro crack-arrests occur, this being determined mainly by the time required for crack renucleation. On the other hand, the instantaneous crack-growth rates are found to be several orders of magnitude higher, and describe the overall crack-growth rate in the absence of crack arrests, or that rate which occurs discontinuously between crack arrests. By analysis of simultaneous current and load transients which accompany such instantaneous crack growth in experiments on oriented single crystals, we have been able to determine the instantaneous velocity and the prevailing stress state accompanying such crack growth.

II. Data Analysis

The data for the following calculations come from the slow-strain-rate tests performed on Cu-25Au single crystals which undergo $\{110\}\langle 00\bar{1}\rangle$ cracking (resulting in periodic "crack arrests") in 0.6 M sodium chloride solution [8]. The specimens were masked with MICCROSTOP, except at the crack-initiation site, and enclosed in a corrosion cell mounted on an APPLIED TEST SYSTEMS universal tensile testing machine. The tests were performed at constant displacement rates such that the overall strain-rate of the specimen was about $\sim 10^{-6}$ s^{-1}. The imposed potential was controlled with a THOMPSON low-noise potentiostat. Both the current-signal output from the corrosion cell through the potentiostat and the load-signal output from the tensile machine were detected, triggered, and simultaneously recorded on a NICOLET digital oscilloscope. The time resolution per data point was chosen to be 50ms.

After crack initiation, serrated load drops were observed and these were correlated with current transients: every unique load drop coincided with a current transient, as seen in Fig. 1, and a one-to-one correspondence was found between the major crack arrests on the fracture surface, the major shear bands on the side surface of the specimen ([11] Fig.27, and [13] Fig. 7), and the load-drop/current-transient pairs. These load drops and current transients could be caused by either crack advance or deformation, both of which produce new area.

III. Evaluation of Data

Fig. 2 shows, at high resolution, a typical load-drop/current-transient curve taken at a potential of 380 mV(s.c.e.), which was chosen as representative and used for the following calculations. Two approaches were used for analyzing the initial portion of the data: the Brittle Crack Analysis assumes that the corrosion crack initiates (renucleates) and grows with no accompanying deformation, until gross crack-blunting slip is generated, resulting in a sudden, large load drop which reduces the stress in the remaining uncracked cross-section of the sample to the yield stress; the Fully Plastic Analysis assumes that deformation accompanies crack growth at all times, maintaining the stress in the remaining uncracked cross-section of the sample at the yield stress.

A. Brittle Crack Analysis

The Brittle Crack Analysis associates the small load drop which occurs over time prior to the major load drop (i.e., AB in Fig. 2) with a relatively slow (but microscopically discontinuous [4,5]) elastic crack advance, and then associates the subsequent major load drop (BC in Fig. 2) with abrupt plastic deformation, i.e., nucleation of a shear band. This sudden deformation relaxes the high built-up stress resulting from the reduction in cross section as the crack grows, and arrests and subsequently blunts the crack. When this happens, the stress intensity at the crack tip is reduced to the yield stress, and the lagging portion of the crack continues to grow minimumly, only up to the slip band, accompanied by continuing deformation (CD in Fig. 2). The load /current data of Fig. 2 corresponds to the middle of the overall test (F_o = 97N, whereas F_{max} = 174N), when the crack had gone about half way through the specimen (F_o/F_{max} = 0.56).

It is assumed that t_o is the starting time for the initiation of cracking, chosen to be that moment when the load starts to drop and/or the current starts to rise, and that F_o is the corresponding load at that time. This occurs at point A in Fig. 2.

As the renucleated crack grows, the total change in cross-head displacement (ΔU_t) at any time $t > t_o$, is obtained from consideration of the elastic deformation of the machine (ΔU_m), the elastic deformation of the sample (ΔU_e), the plastic deformation of the sample (ΔU_p) and the elastic relaxation due to the crack opening (ΔU_c):

$$\Delta U_t = \Delta U_m + \Delta U_e + \Delta U_p + \Delta U_c \qquad (1)$$

In particular, the displacement (ΔU_c) due to the presence of the crack is a function of the load F, the crack length C, and the width W of the specimen, and is given by Tada et al. [13] as:

$$\Delta U_c = \frac{4F(1 - \nu^2)C}{A\,E}\, f\left(\frac{C}{W}\right) \qquad (2)$$

where,

$$f\left(\frac{C}{W}\right)=\left(\frac{C}{W}\right)\frac{1}{\left(1-\frac{C}{W}\right)^2}\left(0.99-\frac{C}{W}\left(1-\frac{C}{W}\right)\left(1.3-1.2\frac{C}{W}+0.7\left(\frac{C}{W}\right)^2\right)\right) \quad (3)$$

and $\nu = 0.3$ is Poisson's ratio, and
$E = 1.1 \times 10^{11}$ N/m^2 is Young's modulus for Cu-Au alloy.

These equations are accurate to better than 1% for any C/W. However, they assume that only elastic deformation occurs, and so they rigorously apply only to the case of continuous elastic cracking, without shear-band formation. The use of these equations should lead to an overestimate of the displacement due to a given crack length, but in the absence of an analytical solution which explicitly takes the shear band into account, we have assumed that this will not lead to too large an error. (At present we are engaged in an FEM analysis of this problem.) For this special case of discontinuous crack advance, there are two options for choosing the factors C and W:

Case I: Assume the pre-existing crack (C_o) is completely blunted by the shear band and that ΔC is small compared to the original crack opening displacement (COD). Then, at least initially, the crack can be represented by a crack increment ΔC acting on a specimen of width W_o-C_o, and the component of displacement due to crack growth (ΔU_c) is a consequence of the new crack (ΔC) acting on the remaining cross section (W_o-C_o). Thus:

$$\Delta t\,\dot{V} = K_m\,\Delta F + \frac{l_o\,\Delta F}{A_o\,E} + \frac{4\,F\,\Delta C\,(1-\nu^2)}{(W_o-C_o)\,E} f\left(\frac{\Delta C}{(W_o-C_o)}\right) \quad (4)$$

where $\dot{V}$ is the cross head velocity, t is the time, and K_m is the machine compliance which was experimental determined to be 3.0×10^{-7} m/N.

Case II: Assume that ΔC is comparable to the pre-existing crack opening displacement (COD), in which case W_o should be used as the effective specimen width, and the elastic displacement due to the growth, ΔU, of the crack involves the whole crack ($C_o+\Delta C$). Thus:

$$\Delta U_{(\Delta C)} = U_{(C_o+\Delta C)} - U_{(C_o)} \quad (5)$$

and equation (4) becomes:

$$\Delta t\,\dot{V} = K_m\Delta F + \frac{l_o\Delta F}{A_oE} + \frac{4(1-\nu^2)}{A_oE}\left[F(C_o+\Delta C)\,f\left(\frac{C_o+\Delta C}{W_o}\right) - F_oC_of\left(\frac{C_o}{W_o}\right)\right] \quad (6)$$

In the third region of the load drop, following the abrupt drop in load, the stress at the crack tip is relaxed to the yield

stress, and cracking now occurs at this reduced stress level. For this case, the crack distance C is simply given by:

$$\frac{\Delta C}{W} = (1-\frac{F}{F_{max}}) \qquad (7)$$

Figs. 3a and 3b show crack-distance/time curves calculated from the data for the two different cases respectively. The extent of cracking associated with the initial load drop (AB in Fig. 2) is calculated according to the assumptions of case I to be very much greater than that observed on the fracture surface, and the velocity predicted is therefore too high. Because of this, Case I is dismissed as inappropriate and will not be considered in the following discussion. The predicted crack advance according to the assumptions of case II is more compatible with experimental observations of the fracture surface, and will be considered further.

B. Fully Plastic Analysis

The Fully Plastic Analysis considers that the load drop at all times is a consequence of both cracking and deformation, and that ~1μm crack advances are accompanied by mini-shear bands so that the stress level in the uncracked cross section of the specimen is maintained at the yield stress. It is presumed that these bands are ineffective in blunting the entire crack front sufficiently to arrest it, because the slip produced occurs either ahead of or behind the other micro-crack tips. Blunting sufficient to cause crack arrest requires large (broad) shear bands, which we presume are a result of dislocation sources away from the crack tip becoming activated when ΔC becomes large enough to raise the "global" K_{IC} to the critical value K_D required to operate such sources [5]. Nevertheless, the total crack advance is always proportional to the drop in the load (c.f. equation (7). The resulting calculation of crack-distance vs time is shown as one of the curves in Fig. 4: the instantaneous crack grows slowly at first, then increases its velocity rapidly to 50 μm/s, and then slows down again.

This analysis requires dislocations to be continually emitted from sources located near the tip of the crack during its growth. The component of the cross-head displacement due to deformation can be obtained from equation (1) assuming the slip-step of magnitude $S = U_p/\sin\Psi$ is produced on the surface by such plasticity. The total number of dislocations swept out of the surface is calculated to be about 12x10*3, corresponding to a slip step magnitude S of 2.8μm. It is observed, from intersection of the shear band with slip lines on the side surface of the specimen [9(Fig. 13)], that the slip step magnitude S caused by the passage of dislocations is equal to or less than 5 μm at a potential of 450 mV (s.c.e.), in rough agreement with the calculations.

C. Relationship Between Current and Crack Velocity

The current signal results from the dissolution of the more active copper atoms. For the current or load transients observed in slow-strain-rate tests, the time involved is very much larger than the transient time for dissolution from an exposed surface [4,12], and hence the current (i.e., the time rate of charge transfer) should be a direct measure of the rate of area production, without the complication of convoluting the crack velocity and the "passivation" rate. For example, scribing experiment [10,12,14] indicate that a fresh surface of a sample exposed to the solution results in a current pulse which decays very quickly, to (1/e) of its maximum value in less than 10ms and essentially to background level in less than 100ms. Experiments have shown that the integrated charge from such exposed surfaces corresponds to the order of a monolayer of dissolution [4,12]. Since the slow-strain-rate cracking experiments involve data recorded with a time resolution of 50ms, it is therefore reasonable to assume that this total charge is passed "immediately", i.e., within the time elapsed between readings. Therefore the rate of production of new surface in such measurements, due to both cracking and deformation, is directly proportional to the measured current, and further, the time-integrated current charge in these experiments directly corresponds to the area created. In summary, assuming the current is independent of the nature of its formation (i.e., whether the surface formed is the result of a "brittle" crack, or a slip-step arising from deformation), then the time integral of the current would be proportional to the area of the newly exposed surface, and the incremental area of crack advance at any time would be proportional to the magnitude of the current at that time.

A plot of current as a function of time is given in Fig. 2, and implies that the rate of area production, i.e., crack-growth rate, goes through a maximum. Thus:

$$\Delta C \propto A(t-t_o) = M \int_{t_o}^{t} \left(I(\tau) - \left[I_o + B \int_{t_o}^{\tau} \left(I(\xi) - I_o \right) d\xi \right] \right) d\tau \qquad (8)$$

where the bracketed term accounts for background current, I_o being the initial background current with the inner integral involving the variable ξ approximately accounting for the increase in this background current as the crack area increases, and M and B are scale factors.

One of the curves in Fig. 4 shows the integral of the current as a function of time. Comparing this to the extent of crack growth based on predictions from the load drop, assuming no accompanying plasticity (Brittle Crack Analysis)(Fig. 3b), we find that there is disagreement in the initial curvature of the two curves. In contrast to this, the predictions assuming that crack growth is accompanied by plasticity (Fully Plastic Analysis) show agreement in this respect. In fact, by adjusting the scale for the current-integral/time plot so that it conforms to load-drop

predictions by use of the scale factor M, and by choosing the background current I_o and parameter B appropriately, good agreement is obtained between the measured current and the results of calculations from the load drops (Fig. 4).

Tables I and II summarizes results of calculations from a series of current and load transients obtained at 380 and 450mV(s.c.e.) respectively, assuming fully plastic behavior. The values of ΔC are in substantial agreement with measured crack-arrest distances.

IV. Discussion

The correlation of the measured current with predictions from changes in the measured load, using the Fully Plastic Analysis, indicates that T-SCC is accompanied by plastic deformation to the degree that the remaining crack-reduced cross section is maintained at the yield stress.

The brittle-cracking process is thought to occur by the almost-simultaneous occurrence of numerous micro-cleavage events [4,5]. For each cleavage event, the stress intensity increases at the crack tips as cracking proceeds, and this could stimulate the nucleation of dislocations at the crack tip or activate nearby dislocation sources, leading to slip that reduces the local stress back to the yield stress. Thus, T-SCC may be viewed as alternative (or simultaneous) processes of cleavage and deformation.

From the macroscopic perspective, the flow stress is maintained constant at the yield stress in the uncracked region of the sample. As the crack propagation rate increases (as evidenced by an increase in the current during the early stage of propagation) more and more dislocations will be emitted in order to adjust the stress level around the crack tip, and those that intersect the surfaces of neighboring cracks that have grown ahead will produce new surface, in the form of slip steps, in contact with the solution in the crack. When the macro crack has grown to the point where an external source is activated, gross slip occurs, blunting the crack and causing arrest. Slip will continue at the arrested crack-tip because of the constant imposed strain rate, coarsening the shear band that corresponds to the crack-arrest marking on the fracture surface. Thus, the combination of these coarse slip lines, and the fine slip lines between the pairs of coarse slip bands, on the side surface of the experimental sample provide the evidence that plasticity is occurring during the growth of the crack (i.e., discontinuously during propagation of the micro-cleavage cracks).

From a fracture mechanics perspective, at a major crack arrest, the shear band has reduced the stress intensity factor to unity. As the crack renucleates, supposedly by a dislocation pile-up mechanism [3], this stress intensity factor grows rapidly to a value consistent with the applied load and the total crack length. This build-up is responsible for the eventual operation of a

dislocation source and the resulting crack-arresting shear band. Such a shear band may form slightly ahead of most of the growing crack tip, and as a consequence would tend to shield that portion of the crack front which has not yet reached it. In this way, we would expect the crack velocity to decrease as the crack nears the shear band, as is seen in Fig. 5, which shows the crack velocity as a function of crack advance, calculated from the data in Figs. 2 and 4.

V. Conclusions

1. The mechanism of T-SCC is cleavage cracking accompanied by plasticity. This may be explained in terms of a model which predicts the nucleation of cracks at Lomer-Cottrell locks and their propagation by corrosion-assisted cleavage.

2. The stress in the remaining un-cracked portion of the specimen is maintained at a constant yield stress during cracking because of the plastic accommodation. There is a linear relationship between the crack advance and the amount of accommodating slip.

3. The crack velocity varies from 1 to 50μm/s for an imposed potential of 380mV(s.c.e.).

References

[1] D. V. Beggs, M. T. Hahn, E. N. Pugh, Hydrogen Embrittlement and Stress-Corrosion Cracking, American Society for Metals, Metals Park, Ohio (1984) p. 181.

[2] B. D. Lichter, W. F. Flanagan, J. B. Lee and M. Zhu, Environment-Induced cracking of Metals, (Eds.) M. B. Ives and R. P. Gangloff, pp. 251-9, National Association of Corrosion Engineers, Houston, Texas, 1990.

[3] W. F. Flanagan, P. Bastias and B. D. Lichter, Acta Metall. Mater., Vol. 39 (1991) pp. 695-705.

[4] B. D. Lichter, M. Bhatkal, W. F. Flanagan, Parkins Symposium on Fundamental Aspects of Stress-Corrosion Cracking, (Eds.) S. Bruemmer and E. I. Meletis, pp. 279-302, The Minerals, Metals and Materials Society, Warrendale, PA, (1992).

[5] W. F. Flanagan, Lijun Zhong and B. D. Lichter, Quasi-Brittle Fracture Symposium, Metall. Trans., vol. 24A (1992) pp. 553-559.

[6] K. Sieradzki and R. C. Newman, Philos. Mag., Vol. 51 (1985) pp. 95-132.

[7] K. Sieradzki and R. C. Newman, J. Phys. Chem. Solids, Vol.48 (1987) pp. 1101-1113.

[8] M. Zhu, Ph. D Thesis, Vanderbilt University (1990)

[9] L. J. Zhong, M. S. Thesis, Vanderbilt University (1992)

[10] J. B. Lee, Ph. D Thesis, Vanderbilt University (1990)

[11] F. A. Champion, Symposium on Internal Stress in Metals and Alloys, p. 468, Inst. of Metals, London, 1948; H. L. Logan, J. Res. Nat. Bur. Standards, 48 (1952) 99-105; R. M. Latanision, Atomistics of Fracture, (Eds.) R. M. Latanision and J. R. Pickens, pp. 3-38, NATO Conference Series VI, vol. 5, Plenum Press, New York, 1983.

[12] R. M. Bhatkal, M.S. Thesis, Vanderbilt University (1991)

[13] H. Tada, P. C. Paris, and G. R. Irwin, The Stress Analysis of Cracks Handbook, pp. 2.10-2.12, Del Research Corp., St. Louis, MO, 1985.

[14] J. B. Lee, W. F. Flanagan and B. D. Lichter, Wear-Corrosion Interactions in Liquid Media, (Eds.) A. Sagues and E. I. Meletis, pp.19-35, The Minerals, Metals and Materials Society, Warrendale, PA, (1991)

TABLE I

POLARIZATION POTENTIAL 380 mV (s.e.c.)						
F_o/F_{max} $=1-C/W_o$	0.661	0.556	0.437	0.421	0.412	0.393
ΔC (μm)	95.03	43.06	58.71	48.58	52.45	43.65
V_{max} ($\mu m/s$)	50.53	42.03	30.35	29.35	19.50	14.99
I_o (μm)	5.30	4.75	4.45	4.45	4.40	4.40
B	0.02	0.02	0.02	0.02	0.02	0.02
M	22.5	35	22	23	18	19

TABLE II

POLARIZATION POTENTIAL 450 mV (s.e.c.)						
F_o/F_{max}	0.656	0.617	0.576	0.539	0.505	0.474
ΔC (μm)	117.72	124.33	113.95	103.67	97.91	75.69
ΔX (μm)	102.9	139.7	110.3	117.6	88.2	73.5
V_{max} ($\mu m/s$)	431.89	479.41	420.00	408.13	399.74	303.30

ΔC is the crack distance predicted from current transient, ΔX is the crack advance observed on fracture surface, V_{max} is the calculated maximum velocity , and I_o, B, and M (where given) are the values of curve-fitting constants , all shown as a function of F_o/F_{max}, which is linearly related to the crack size C.

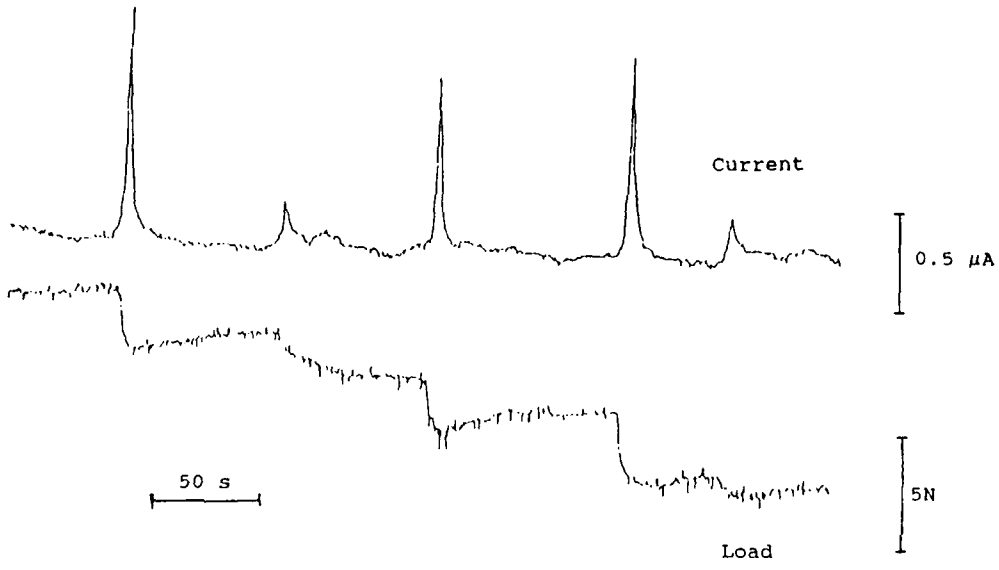

Fig. 1 A portion of the load/current curve as a function of time for a Cu_3Au single crystal tested at 380mV(s.c.e.) in 0.6M NaCl solution at a contant cross-head displacement.

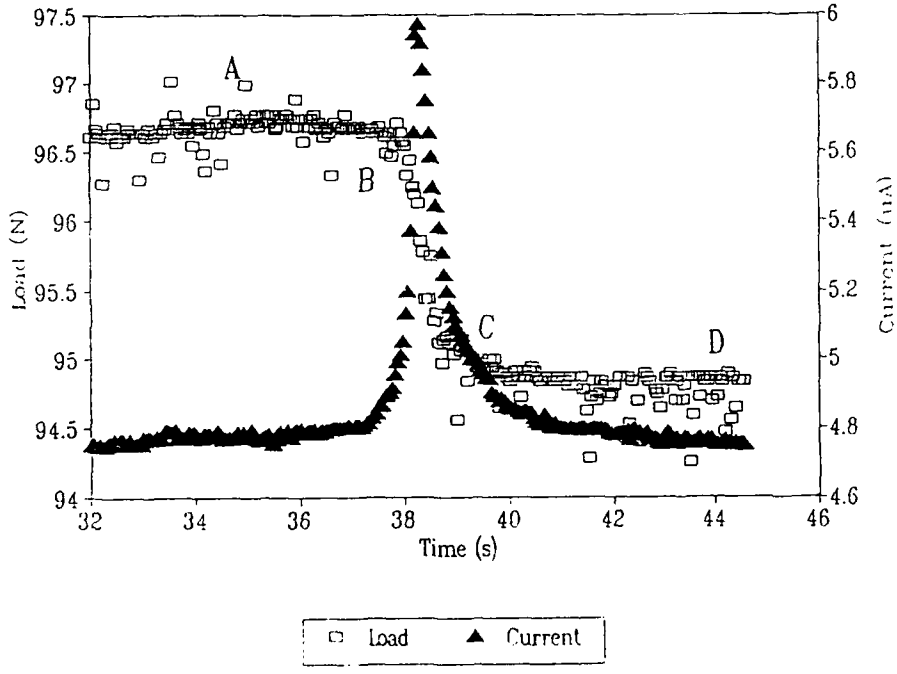

Fig. 2 Load-drop/current-transient curves at F_o/F_{max} = 0.56 at a potential of 380mV(s.c.e.).

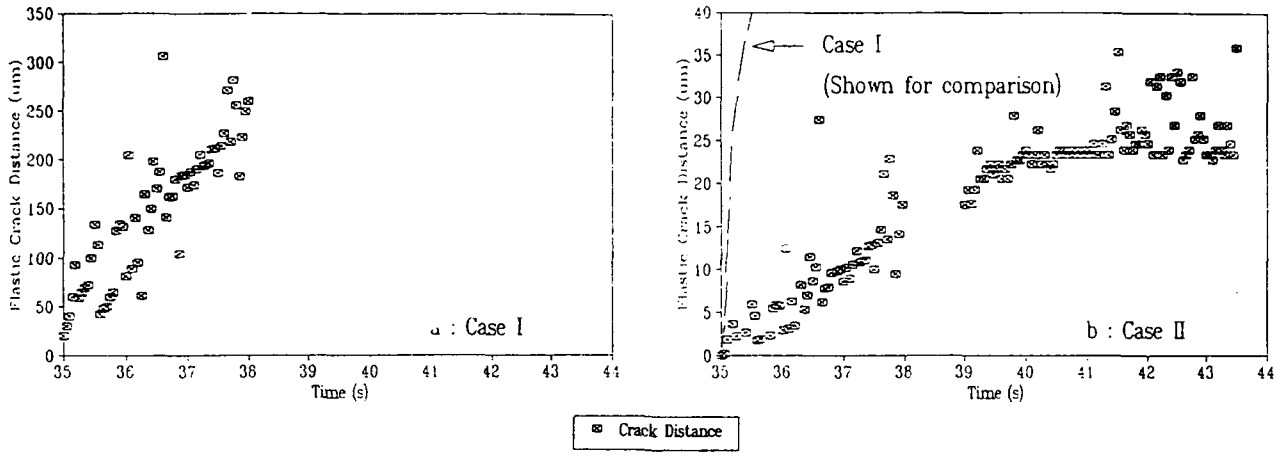

Fig. 3 Calculated brittle crack advance without accompanying deformation: (a) Case I where $\Delta C/(W_o-C_0)$ is used for C/W in equation (2) ff; (b) Case II where $(C+\Delta C)/(W_o)$ is used for C/W in equation (2) ff.

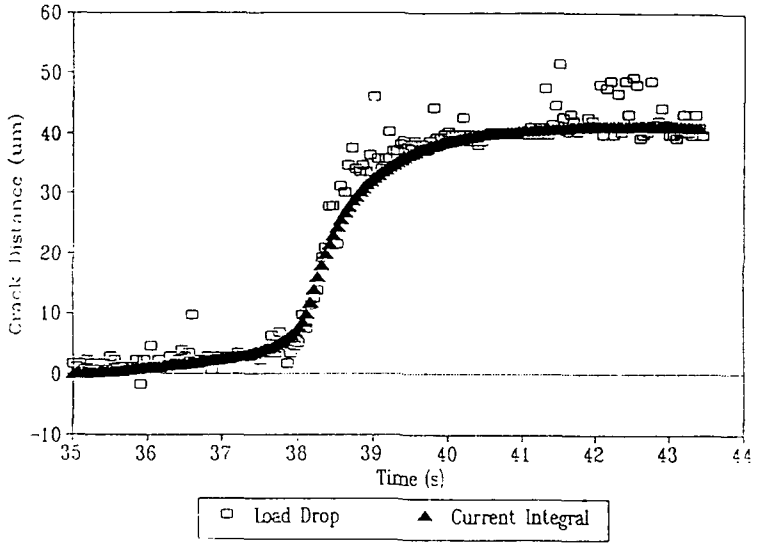

Fig. 4 Crack distance as a function of time predicted from the load drop and from the current integral, showing agreement between the two methods. $(F/F_{max})=0.56$

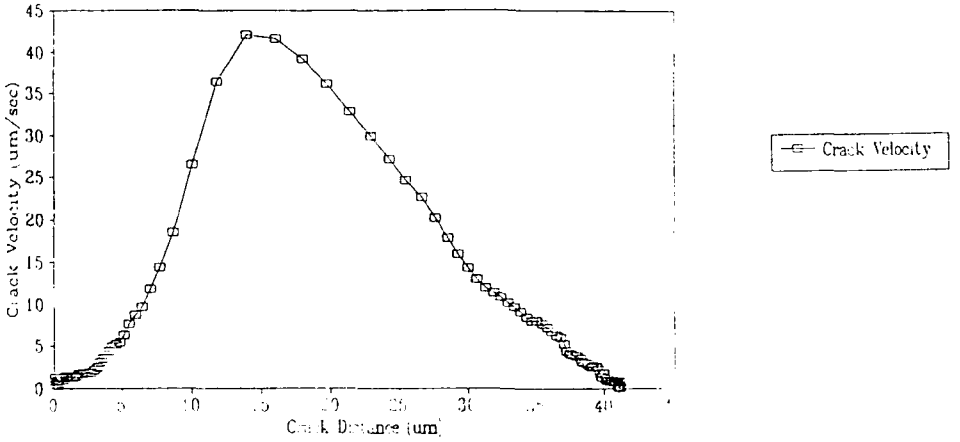

Fig. 5 Crack velocity as a function of crack advance.

Improved Stress Corrosion Performance for Alloy 718 via Melt Practice and Heat Treatment Variation

M. T. Miglin, J. V. Monter and C. S. Wade
Babcock & Wilcox, a McDermott Co.
1562 Beeson St.
Alliance, OH 44601

J. L. Nelson
Electric Power Research Institute
3412 Hillview Ave.
Palo Alto, CA 94303

ABSTRACT

Stress corrosion cracking (SCC) tests were conducted using alloy 718 in various melt practice and heat treatment conditions. Fatigue-precracked, 12.5-mm-thick compact fracture specimens were subjected to a constant extension rate of 1.3×10^{-9} m/s in a 360°C buffered aqueous environment. Crack growth rate was measured during testing using a reversing DC potential drop technique. Results in the form of SCC crack growth rate versus applied stress intensity demonstrate that the SCC resistance of alloy 718 can be improved by changes in melt practice and heat treatment. The SCC resistance of electroslag remelted (ESR) material is optimized by applying a high-temperature solution anneal followed by aging below the temperature region in which δ precipitates.

Keywords: stress corrosion cracking, light water reactor, pressurized water reactor, alloy 718, nickel-base alloy, spring, bolt, Ni-Cr-Fe alloy, K_{ISCC}, K_{IEAC}, SCC, IGSCC, PWR, LWR

INTRODUCTION

Alloy 718, a Ni-Cr-Fe superalloy, is increasingly used in light-water reactors (LWRs) for core internals requiring high strength, relaxation resistance, and corrosion resistance. Typical PWR primary-side applications for alloy 718 include bolts and springs. Service failures of alloy 718 in PWR applications have been attributed to intergranular SCC and high-cycle fatigue. Replacement of failed in-core components can require costly shutdowns, which prompted sponsorship of a program by the Electric Power Research Institute (EPRI) to improve performance of alloy 718 by optimizing the melt practice, heat treatment, and alloy chemistry.

Melt practice, heat treatment and alloy chemistry interact to determine the SCC resistance of alloy 718. Melt practice affects the degree of niobium segregation, which in turn affects the response of the material to heat treatment. Highly segregated alloy 718 is susceptible to forming Laves phase, which is deleterious to SCC performance, in the niobium-rich regions. Melting and thermomechanical processing practices for alloy 718 have been reviewed by Loria.[1]

Alloy 718 components for the nuclear industry are usually fabricated from vacuum-induction-melted, electroslag-remelted (VIM/ESR) rolled barstock or plate. The ESR process produces better chemical homogeneity and cleanliness than the older vacuum-arc-remelting (VAR) process, and ESR ingots are more easily worked. Further improvements in cleanliness are provided by a triple-melt process (VIM/ESR/VAR) used for space shuttle applications. Additional newer melting practices include electron-beam, cold-hearth refining (EBCHR), plasma-melt refining (PMR) and vacuum-arc, double-electrode refining (VADER) processes, but with higher cost and more limited availability.[1]

Heat treatment has been shown to significantly affect SCC resistance.[2] For reactor applications, alloy 718 is usually given one of several similar heat treatments originally developed for aerospace applications. These heat treatments produce room-temperature yield strengths near 1200 MPa, and are designed for maintaining roughly 85% of room-temperature yield strength over extended exposures at 650°C. However, heat treatments designed for microstructural stability at high temperatures may not provide optimal stress corrosion resistance in the 290 to 360°C aqueous environments typical of nuclear service.

Alloy 718 has an austenitic matrix hardened by precipitation of face-centered-cubic γ' [$Ni_3(Ti,Al)$], and by body-centered-tetragonal γ'' [$Ni_3(Ti,Al,Nb)$]. When alloy 718 is heat treated near 950°C for aerospace applications, δ [Ni_3Nb] precipitates rapidly, stabilizing the grain boundaries for increased creep resistance. Alloy 718 also forms Laves [A_2B], a nonequilibrium phase that precipitates if the local concentration

of niobium is high, as well as MC-type carbides and carbonitrides and M_6C carbides.[3-5] A time-temperature-transformation diagram for alloy 718 is given in Figure 1. Earlier work on this program demonstrated that a heat treatment which avoided the temperature range for delta precipitation produced improved SCC resistance.[2]

The SCC test matrix reported below emphasizes the effects of melt practice and heat treatment of alloy 718 on SCC resistance in the PWR primary-side environment. It is part of a larger program to evaluate the influence of melt practice, thermomechanical processing, and alloy chemistry. Constant displacement rate K_{ISCC} tests were performed using three heats of alloy 718, one given conventional VIM-ESR processing, one triple-melted (VIM-ESR-VAR) heat, and a third heat produced by the EBCHR process.

The constant-displacement-rate K_{ISCC} test used for this work is similar to that described by Mayville, et al.[6] and Dietzel, et al.[7] There are numerous methods of conducting K_{ISCC} tests,[6-9] none of which are standardized. The constant-displacement-rate (sometimes called rising-load) test method was chosen because it generates results in a short time. This method produces a curve of SCC growth rate versus applied stress intensity in as little as three weeks using a single compact fracture specimen, rather than in many months using several specimens with self-loaded or dead-weight-loaded test methods.

EXPERIMENTAL PROCEDURES

The test materials include one heat of direct-age-processed VIM-ESR 718 meeting AMS 5662F, chemistry only (designated ESR-DA for direct age); one heat of triple-melted VIM-ESR-VAR 718 meeting AMS5664B (designated TM for triple melt), and one heat of EBCHR material. Chemical compositions of the three heats are reported in Table 1, and heat treatment and hardness data are given in Table 2. Where available, the ultimate tensile strength is also listed.

The single heat treatment which is the same for all three melt practices is the AERO heat treatment, which provided the best SCC performance earlier in this program.[2] The CONV (for conventional) heat treatment is common between the ESR and the triple-melt heats. The CONV heat treatment is commonly found in nuclear power plants and jet engine service, for which it was designed. The remaining heat treatments, which were applied to the ESR heat, were intended to elucidate the effects of the various precipitation hardening steps, in the peak-hardness and overaged conditions, on the SCC resistance of alloy 718. The 1093°C solution anneal was chosen because this is the lowest temperature that left no evidence of prior grain boundaries, and hence prior grain boundary precipitates, as determined by light microscopy.

Several aging treatments were applied in combination with the

1093°C anneal. The overaged (OA) conditions were developed based on experience with alloy X-750, a γ'-hardened Ni-Cr-Fe alloy which is used for similar nuclear applications as alloy 718. For alloy X-750, overaging the γ' precipitates improves the SCC resistance. When γ' is overaged, it becomes incoherent relative to the gamma matrix. As an incoherent precipitate, it cannot be cut by dislocations but must be bypassed, increasing the difficulty of slip step formation. This may retard SCC by slowing the slip step formation and dissolution process. The OA-A and OA-C conditions were designed to overage γ' and γ'' without producing δ, and the OA-D condition to overage δ, γ' and γ''.

The specimens listed in Table 2 were 12.5-mm-thick compact fracture specimens fabricated in the L-C orientation according to the ASTM test for plane-strain fracture toughness of metallic materials (E399-83). The specimens were precracked by fatigue loading in air, with the final stress intensity range below 20 Mpa$\sqrt{m}$ for each specimen. Five specimens were loaded simultaneously in a specially designed loading device, as described in reference 2. The loading fixture is affixed to an autoclave mounted in a load frame with a screw-driven actuator. The autoclave was continuously refreshed with 360°C PWR primary-side water, as specified in Table 3. A constant displacement rate of 1.3×10^{-9} m/sec was applied to all specimens for the entire test duration. This displacement rate was chosen based on a displacement rate matrix conducted for alloy 718 in the PWR primary-side environment by Miglin and Nelson.[10]

Crack length was monitored throughout each test using the reversing DC potential drop technique and a current of 10 A.[11] Current was carried by leads connected to the center top and center bottom of the specimen with threaded fasteners. Potential was measured using leads spot-welded diagonally across the crack mouth. Load was monitored with a load cell and displacement with a displacement transducer mounted on the load rod. For each specimen, a record of load, crack length, and displacement versus time is generated during the test, and converted to a graph of crack growth rate versus stress intensity, as described in reference 2.

RESULTS

Post-test fractographic examination confirmed that crack propagation in all specimens occurred by intergranular SCC, except for four specimens, DA-ANN, TM-AERO, DA-OA-C and DA-2Age, which did not undergo SCC. Test results for the remaining specimens listed in Table 2 are given in Figures 2 through 8 as plots of SCC crack growth rate versus applied stress intensity factor, K_I. No data are available for the EBCHR-AERO specimen because of experimental difficulties. However, fractographic examination revealed intergranular crack propagation.

DISCUSSION

These results demonstrate that the SCC resistance of alloy 718 in the PWR primary-side environment is affected by melt practice and heat treatment. Surprisingly, there were no striking differences in tramp element content among the three heats, except for a low cobalt content for the triple-melt heat, and a low phosphorus content for the EBCHR heat. Comparison of the three melts in the AERO heat treatment condition shows no SCC for the triple melt heat, and similar SCC susceptibility for the ESR and EBCHR heats, as determined by fractographic examination using a scanning electron microscope (SEM). While the superior performance of the triple melt heat may be a result of the extra melting step, it may also result from lower strength. The R_c hardness of the TM-AERO specimen is 10 points lower than the hardness of the DA-AERO or EBCHR-AERO specimens. The lower hardness is likely a result of fewer inclusions available for retarding grain growth during annealing.

Comparison of the triple melt and ESR heats in the CONV condition (see Figure 3) indicates no significant effect of melt practice on SCC resistance in this highly susceptible heat treatment condition. The CONV condition has copious grain boundary δ resulting from the one hour exposure at 954°C, which may overwhelm the effects of differences between the ESR and VIM-ESR-VAR melt practices. It should be noted, however, that both of these heats are clean relative to other commercially available material. Cleanliness has been shown to affect SCC resistance amongst dirtier heats even in conventionally heat treated material.[8]

A significant influence of heat treatment on SCC performance is readily apparent. Careful comparison of the test results points to the involvement of grain boundary precipitates in the SCC of alloy 718. The annealed (DA-ANN) specimen did not undergo SCC, indicating that susceptibility to SCC is caused by a phenomenon occurring during precipitation hardening. The DA-1Age specimen (718°C/8h) was aged in the γ' + γ'' region without crossing the δ curve as it is drawn on Fig. 1. (However, without a detailed metallographic exam, it cannot be concluded that the material is free from δ phase.) The DA-1Age specimen underwent SCC. Lengthening the exposure at 718°C to 50h creates the DA-OA-A (718°C/50h) condition and improves the K_{ISCC} value, even though DA-OA-A ages into the δ precipitation region. Adding to OA-A an additional 50h treatment at 663°C creates OA-C (718°C/50h + 663°C/50h), which showed no SCC.

It appears that a short aging treatment at 718°C creates susceptibility, which is reduced by further exposure at the same temperature, or at a lower temperature. Comparison of DA-1Age (718°C/8h) with HEA (718°C/8h + 663°C/8h) and AERO (718°C/8h +

621°C/8h) reinforces this observation, because both HEA and AERO have higher K_{ISCC} values. Avoiding 718°C altogether is effective in reducing SCC susceptibility, as is evidenced by the DA-2Age (663°C/100h) specimen, which showed no SCC.

It is possible that SCC susceptibility is produced by short exposures at 718°C due to formation of δ phase or its precursor, and that further exposure at 718°C or at lower temperatures reduces susceptibility by a competing mechanism, such as overaging of γ'. It is likely that δ is deleterious for SCC performance, because specimen OA-D (788°C/16h + 718°C/50h + 663°C/50h) was aged at the nose of the δ curve and produced very poor SCC resistance, in agreement with earlier results. Because there are two or three precipitate types forming simultaneously in each of these heat treatments, it is impossible to determine from hardness measurements whether a single precipitate type is in the overaged condition. Again, a detailed microstructural examination would be needed.

A mechanistic understanding of the SCC behavior of Ni-based alloys in PWR primary-side environments would be an invaluable guide in further improving the SCC performance of alloy 718. Hwang, et al.[13] contend that there is a galvanic effect between the less noble grain boundary precipitates and the more noble surrounding matrix, and that SCC occurs by dissolution of the grain boundary precipitates. Hydrogen may also play a role in the SCC of alloy 718, with the precipitates acting as hydrogen traps. Even at 360°C, hydrogen embrittlement is possible in alloy 718 in the PWR primary-side environment.[8]

The above results are important for application of alloy 718 in corrosive environments. The CONV condition is most commonly used, but produces poor SCC resistance. Improvement can be obtained by switching to the OA-A or the AERO condition with only slight reduction in material hardness.

Future work will include microstructural characterization, and determination of tensile properties at room temperature and at 360°C. The effects of variations in alloy chemistry will also be explored by testing several experimental alloys recently developed by Collier, et al.[14] to have low δ and high γ' content.

CONCLUSIONS

From the work presented here, the following conclusions can be drawn regarding SCC of alloy 718 in constant-displacement-rate (1.3×10^{-9} m/sec) K_{ISCC} tests in 360°C PWR primary water:

1. Annealing temperature affects the K_{ISCC} value and SCC growth rate for alloy 718. Material given a high-temperature anneal (1093°C) performs better than material annealed at a lower temperature (954°C) when both are given the same commonly used two-step aging treatment (718°C/8h + 621°C/8h/AC).

2. Aging treatment affects the SCC resistance of alloy 718. Material given a high temperature anneal (1093°C) followed by two-step aging for long times (718°C/50h + 663°C/50h) produced no SCC under the test conditions, despite a Rockwell C hardness of 42. Material given the same anneal and a single lengthy age (663°C/100h) had a somewhat lower Rockwell hardness (37 R_C) and produced no SCC under the test conditions.

3. Triple-melted (VIM-ESR-VAR) alloy 718 has better resistance to SCC than material produced by the ESR or EBCHR processes when all are given an SCC-resistant heat treatment (1093°C/1h/WQ + 718°C/8h + 621°C/8h/AC), but with much lower hardness (by 10 R_C). When in a more susceptible heat treatment condition (954°C/1h/AC + 718°C/8h + 621°C/8h/AC), no effect of melt practice is observed for the melt practices tested.

4. Aging material at the nose of the precipitation curve for δ degrades SCC performance, while long-time aging at lower temperatures improves SCC performance.

ACKNOWLEDGMENTS

The authors would like to acknowledge Teledyne-Allvac and Special Metals for donation of test materials, and the Univ. of Texas at Austin for supplying material donated by the Nippon Mining Co. They also thank E.A. DeStephen for conducting the experiments. This work was funded under EPRI project RP3154-3.

REFERENCES

1. E.A. LORIA, The Status and Prospects of Alloy 718, *J. of Metals*, July, 1988, pp. 36-41.

2. M. T. MIGLIN, J. V. MONTER, C. S. WADE, and J. L. NELSON, Effect of Heat Treatment on Stress Corrosion of Alloy 718 in Pressurized-Water-Reactor Primary Water, *Proc. Fifth Int'l. Symp. on Environmental Degradation of Materials in Nuclear Power Systems--Water Reactors*, ANS, LaGrange Park, IL, 1992, pp. 279-286.

3. C.T. SIMS, A Perspective of Niobium in Superalloys, *Niobium, Proceedings of the International Symposium*, H. Stuart, Ed., AIME, 1982, pp. 1169-1220.

4. J.F. BARKER, E.W. ROSS, and J.F. RADAVICH, Long Time Stability of Inconel 718, *J. of Metals*, January 1970, pp. 31-41.
M. D. Boldy, unpublished results, Teledyne-Allvac (1991).

5. J.F. RADAVICH, Metallography of Alloy 718, *J. of Metals*, July, 1988, pp. 42-43.

6. R.A. MAYVILLE, T.W. WARREN, and P.D. HILTON, *J. of Testing and Evaluation*, Vol. 17, No. 4, July 1989, pp. 203-211.

7. W. DIETZEL and K.-H. SCHWALBE, *Materialprufung*, Vol. 28, No. 11, Nov. 1986, pp. 368-372.

8. B.P. MIGLIN, M.T. MIGLIN, J.V. MONTER, T. SATO, and K. AOKI, *Proceedings of the Fourth International Symposium on Environmental Degradation of Materials in Nuclear Power Systems^FWater Reactors*, NACE, Houston, 1990, pp. 11-32 - 11-44.

9. R.W. JUDY, JR., W.E. KING, JR., J.A. HAUSER II, and T.W. CROOKER, Naval Research Laboratory Memorandum Report No. 5896, Dec. 30, 1986.

10. M.T. MIGLIN and J.L. NELSON, *Superalloy 718, 625 and Various Derivatives, TMS-AIME*, E.A. Loria, Ed., TMS, Warrendale, Pa., 1991, pp. 695-704.

11. K.-H. SCHWALBE and D. HELLMANN, *J. of Testing and Eval.*, Vol. 9, No. 3, 1981, pp. 218-220.

12. M. D. BOLDY, Unpublished results, Teledyne-Allvac (1991).

13. I.S. HWANG, R.G. BALLINGER, AND J.W. PRYBYLOWSKI, *J. Electrochem. Soc.*, Vol. 136, No. 7, July 1989.

14. J. P. COLLIER, S. H. WONG, J. C. PHILLIPS, and J. K. TIEN, *Metall. Trans. A.*, Vol. 19A, No. 7, July 1988, pp. 1657-1666.

Table 1
Alloy 718 Chemical Composition
(percent by weight)

Heat	Ni	Cr	Fe	Ti	Al	Nb+Ta	Mo	Mn	Si	C	S	Co	B	Cu	P
VIM-ESR	51.5	17.6	Bal.	1.05	0.55	5.21	2.92	0.08	0.09	0.04	0.0004	0.32	0.004	0.05	0.005
VIM-ESR-VAR	54.1	17.9	Bal.	0.98	0.46	5.40	2.94	0.05	0.06	0.03	0.0007	0.09	0.0026	0.06	0.010
EBCHR	53.1	17.9	18.5	1.02	0.50	5.32	3.01	0.01	0.12	0.03	0.0005	0.35	0.004	0.08	0.001

Table 2. Heat Treatments*

Heat	Specimen ID	Hardness, R_C (UTS, MPa)	Heat Treatment
ESR-DA	DA-CONV	44 (~1400)	982°C/1h/AC + 718°C/8h + 621°C/8h/AC
	DA-AERO	41 (1314)	1093°C/1h/WQ + 718°C/8h + 621°C/8h/AC
	DA-ANN	49 R_A	1093°C/1h/WQ
	DA-1Age	37	1093°C/1h/WQ + 718°C/8h/AC
	DA-2Age	37	1093°C/1h/WQ + 663°C/100h/AC
	DA-HEA	38	1093°C/1h/WQ + 718°C/8h
	DA-OA-A	39	1093°C/1h/WQ + 718°C/50h/AC
	DA-OA-C	42	1093°C/1h/WQ + 718°C/50h + 663°C/50h/AC
	DA-OA-D	40	1093°C/1h/WQ + 788°C/16h + 718°C/50h + 663°C/50h/AC
TM	TM-CONV	44	954°C/1h/WQ + 718°C/8h + 621°C/8h/AC
	TM-AERO	31	1093°C/1h/WQ + 718°C/8h + 621°C/8h/AC
EBCHR	EBCHR-AERO	40	Same

* Unless otherwise indicated, the cooling rate between heat treatment steps is 55°C/h.

Table 3
Primary Water Specifications

Dissolved Oxygen	$\leq$ 0.01 ppm
Boric Acid	5700 ppm ($\pm$500 ppm)
Lithium	2 ppm
pH	6.5 ($\pm$0.5)
Conductivity	<20 μmhos/cm
Dissolved Hydrogen	15-50 Std cc/kg H_2O
Chloride	<0.1 ppm
Fluoride	<0.1 ppm

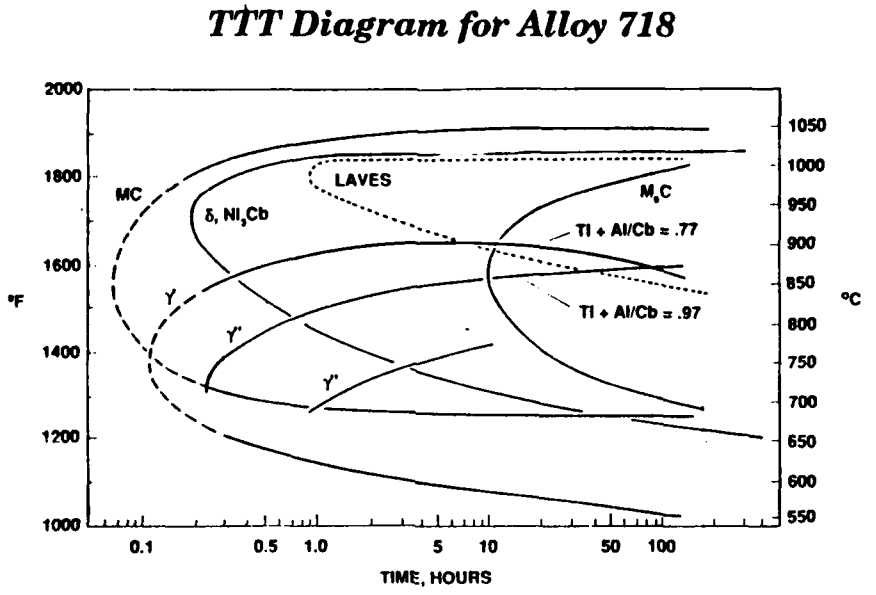

Figure 1 Time-temperature-transformation diagram for alloy 718.[3]

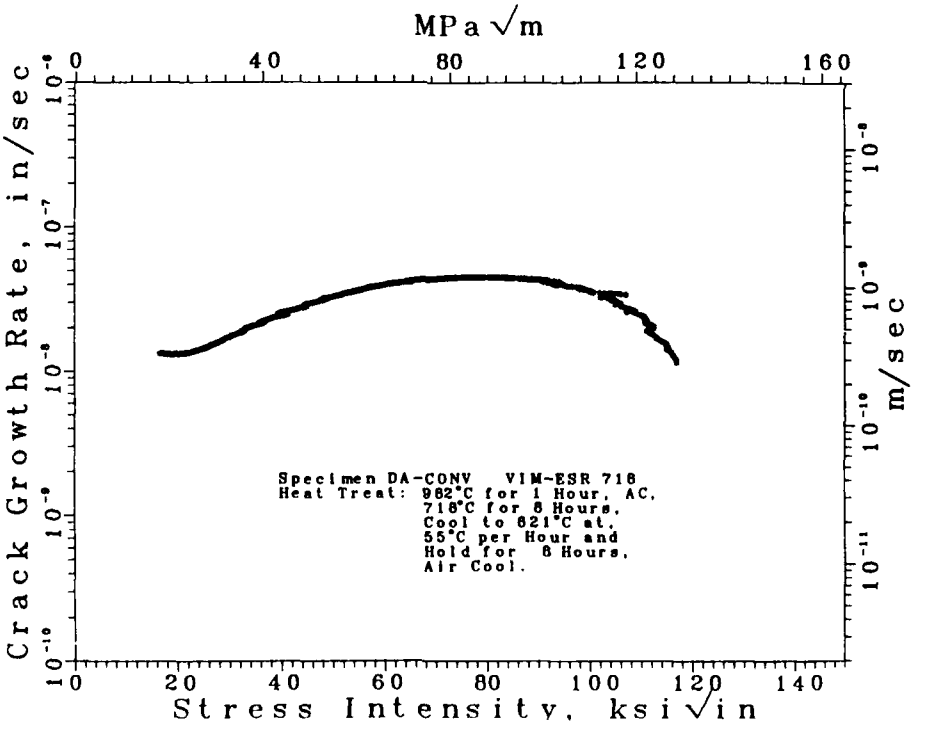

Figure 2 Crack growth rate versus applied stress intensity results for specimen DA-CONV.

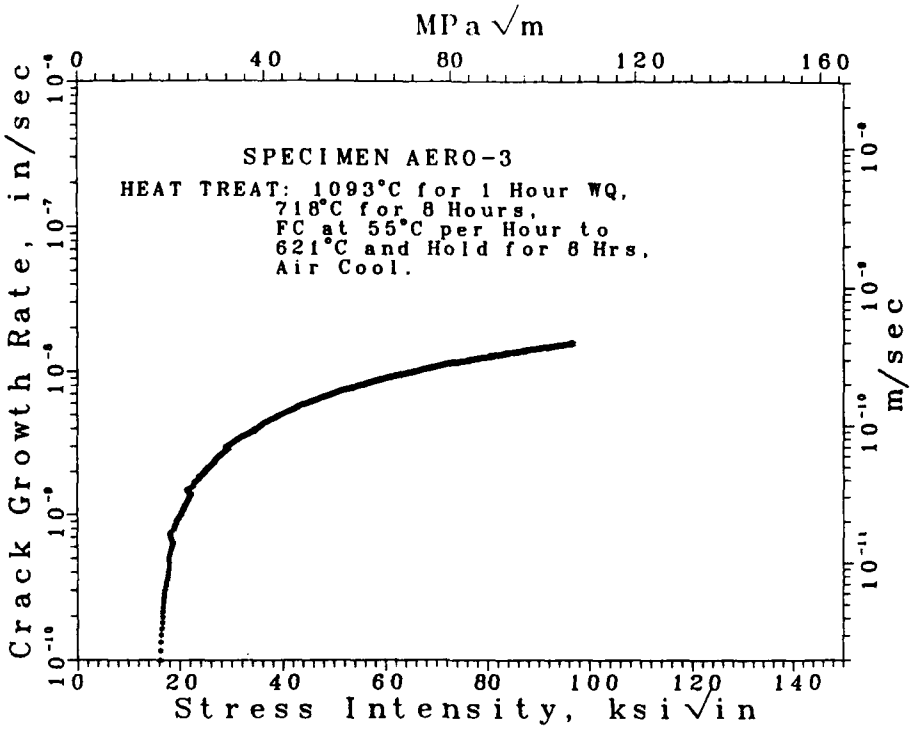

Figure 3

Crack growth rate versus applied stress intensity results for specimen DA-AERO.

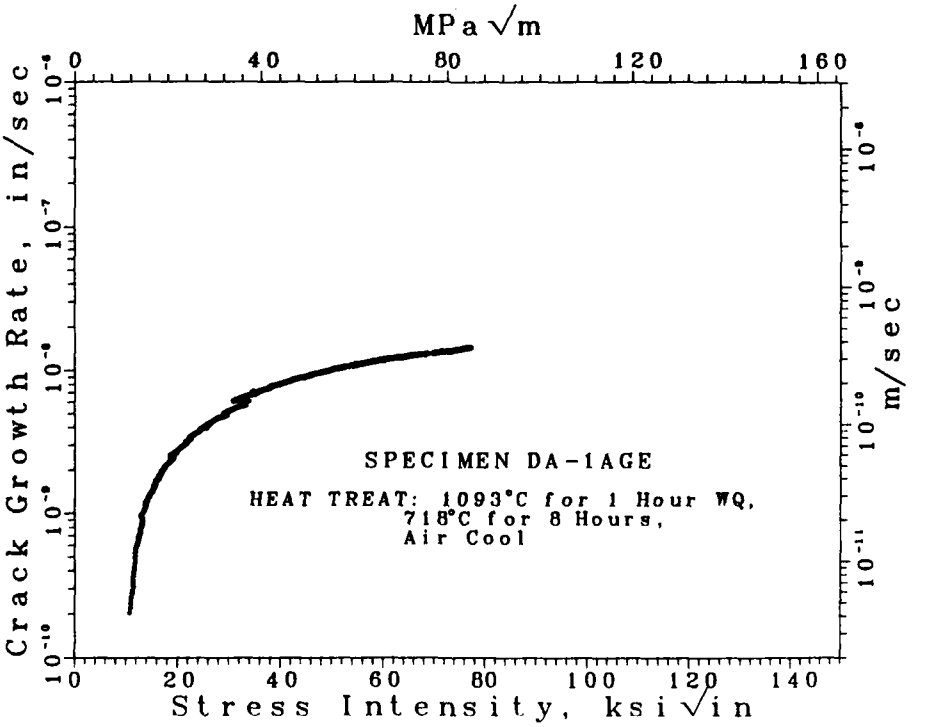

Figure 4

Crack growth rate versus applied stress intensity results for specimen DA-1Age.

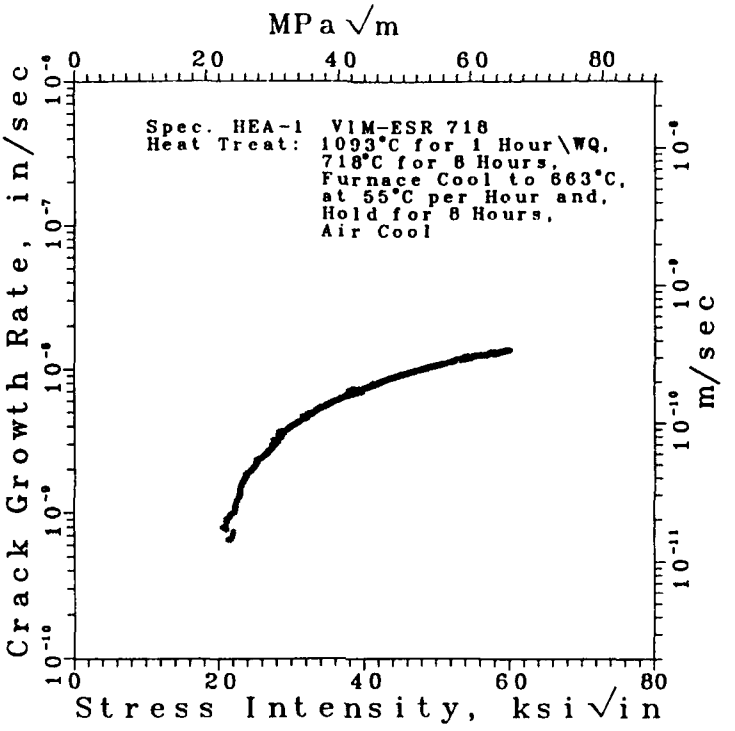

Figure 5

Crack growth rate versus applied stress intensity results for specimen DA-HEA.

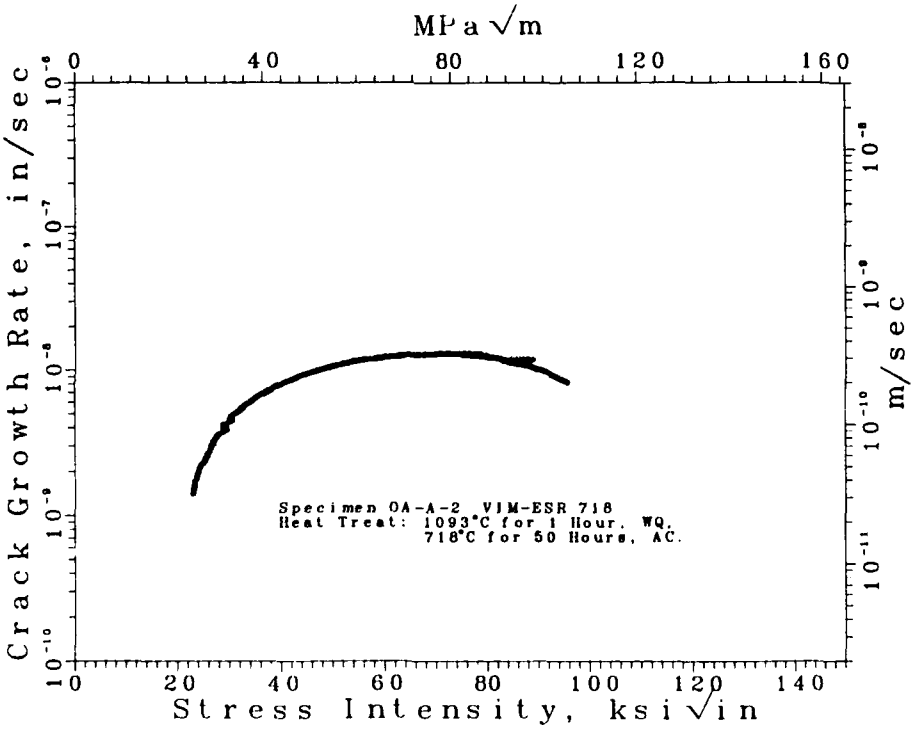

Figure 6

Crack growth rate versus applied stress intensity results for specimen DA-OA-A.

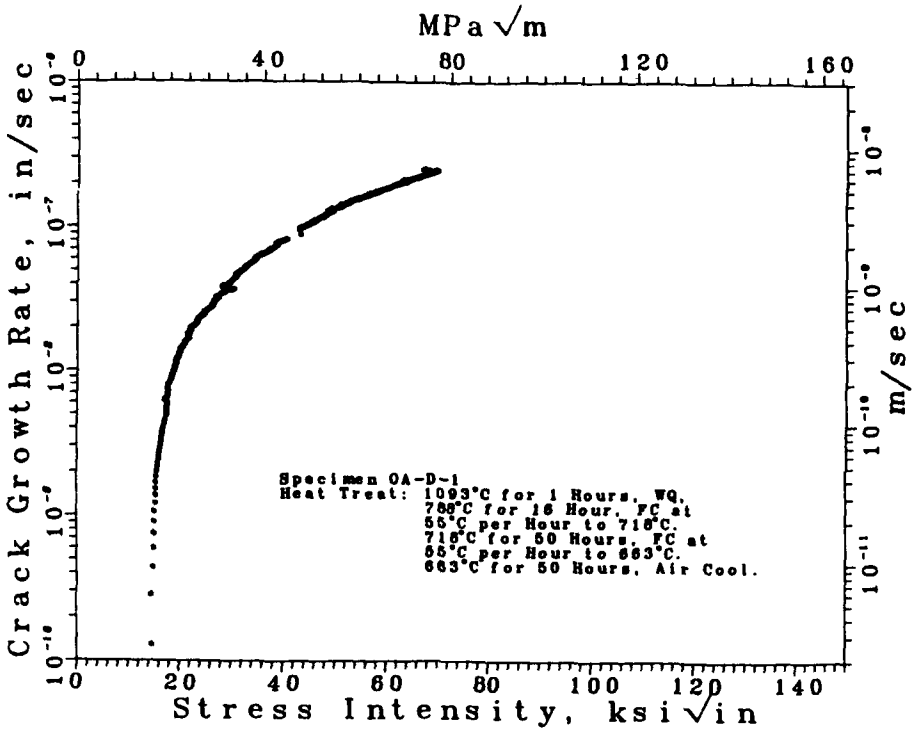

Figure 7

Crack growth rate versus applied stress intensity results for specimen DA-0A-D.

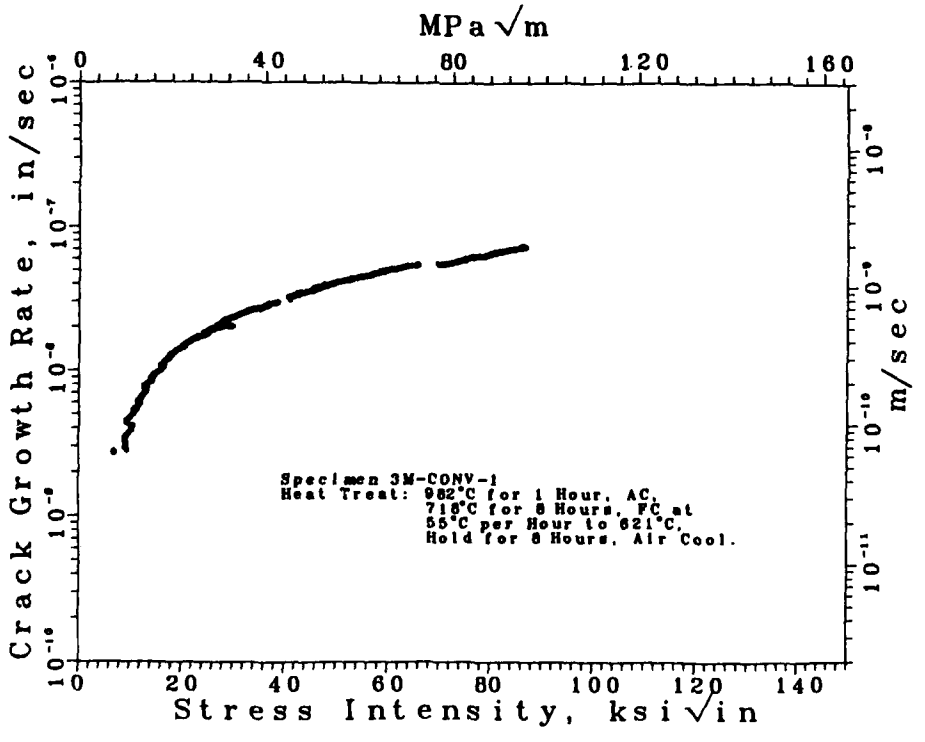

Figure 8

Crack growth rate versus applied stress intensity results for specimen TM-CONV.

Competition Between Anodic Dissolution And Hydrogen Effects During Stress Corrosion Cracking of a 7150 Aluminium Alloy

D.Najjar, O. Moriau, R. Chieragatti, T. Magnin
Université de Lille I. Laboratoire de Métallurgie Physique, URA CNRS 234,
59655 VILLENEUVE D'ASCQ Cedex, FRANCE

T.J. Warner
Pechiney Centre de Recherches de Voreppe
BP 27-38340 VOREPPE, FRANCE

Abstract

A study has been conducted to understand the mechanisms of stress corrosion cracking (SCC) of a commercial 7150 aluminium alloy in an aerated 3% sodium chloride solution. The SCC of this high strength alloy has been characterized for a temper corresponding to the maximum strength (T651) and for overaged tempers (T7651, T7451) using the slow strain rate technique (SSRT).

For aluminium alloys, two basic mechanisms are cited to explain SCC : anodic dissolution and/or hydrogen embrittlement (decohesion and/or enhanced localized plasticity). This study aims to differentiate between these two mechanisms using a slow strain rate test at different potentials.

Different strain rates varying from 4.10^{-7} s^{-1} to 7.10^{-5} s^{-1} have been used. Elongations, chosen as the criterion of SCC susceptibility, obtained at free potential or at a cathodic potential were compared to laboratory air ones. Scanning Electron Microscopy (SEM) studies have been carried out on fracture surfaces in order to distinguish the different effects of anodic dissolution and hydrogen embrittlement according to the applied electrochemical potential. Particular attention has been paid to the interactions between cracks initiating at the surface during the slow strain rate test and hydrogen produced by the cathodic reaction.

The relative influence of anodic dissolution and hydrogen effects are then discussed.

Introduction

Aluminium alloys, and in particular the high strength Al-Zn-Mg(-Cu) alloys of 7XXX series, are susceptible to SCC. Two basic mechanisms have been evolved to explain SCC : anodic dissolution and/or hydrogen embrittlement[1-9]. But up today, there is no consensus on the precise mechanism of Al-Zn-Mg(-Cu) alloys.

Various experimental techniques have been developed to study SCC[10-12] including the SSRT developed by Parkins[13-15]. This technique allows the control of the strain rate which is known to be a major parameter in SCC. Another advantage of this technique is that SCC can be approached from a damage or mechanistic point of view, which is of great importance for both engineers and researchers.

This study aims to differentiate between anodic dissolution and hydrogen embrittlement of a commercial 7150 Al-Zn-Mg-Cu high strength aluminium alloy in an aerated 3% sodium chloride solution using the SSRT. Potential changes during the test allow to study of the relative influence of anodic dissolution and hydrogen effects as a function of surface damage. SCC will be approached from mechanistic point of view and SEM investigations are systematically correlated with mechanical/electrochemical tests.

Key terms: 7XXX high strength aluminium alloy, stress corrosion cracking, anodic dissolution, hydrogen embrittlement.

Experimental

Material

The material examined was a commercial 7150 Al-Zn-Mg-Cu high strength aluminium alloy containing in weight percent: Zn 6.07 , Mg 2.35 , Cu 2.12 , Zr 0.1 , Cr 0.01 , Fe 0.07 , Si 0.044 , Mn 0.016 , Ti 0.03 , Al bal. The material was provided by Pechiney in the form of smooth tensile specimens. These specimens, with a gage length and a diameter of 15 and 4 mm respectively, were machined from 36 mm thick rolled plates. Their tensile axis was parallel to the short transverse direction which is the most susceptible orientation to SCC at free potential. The microstructure (*Figure 1*) was of flat pancake shaped grains, elongated in the rolling direction, containing an unrecrystallized subgrain structure as well as small recrystallized grains. This microstructure contains also (Al,Cu) constituent particules with Fe and Si.

Three tempers have been studied, one corresponding to the maximum strength (T 651 : UTS=570 MPa), the other ones to overaged tempers (T 7651 : UTS=525 MPa, T 7451 : UTS=500 MPa).

Experimental Procedure

Slow strain rate tests have been conducted on an electromechanical machine with strain rates varying from 4.10^{-7} s^{-1} to 7.10^{-5} s^{-1}. Elongation to fracture has been chosen as criterion for SCC susceptibility.

For each temper, elongations obtained in an aerated 3% sodium chloride solution (pH= 6.5) at free or at cathodic potential (E_K= -1.1 V/SCE) were compared to laboratory air ones. In such a solution the free potential is very close to the pitting one. In every case, the specimen has been pre-immersed during 15 min to achieve a stabilization of the electrochemical potential. To differentiate between anodic dissolution and hydrogen embrittlement mechanisms, a new method is proposed for the slow strain rate test. The specimen is strained at free potential until 0.75 % plastic strain amplitude (called transition plastic strain amplitude). Then a cathodic potential (E_K= -1.1 V/ECS) is applied until failure occurs. During the first part of the test, anodic dissolution and hydrogen embrittlement can operate simultaneously at free potential until the transition plastic strain amplitude is achieved. At such a plastic strain, corrosion-deformation interactions were sufficient to produce a significant surface damage which will be described later. This was verified with an interrupted test and controlling the general surface damage with a SEM.

During the application of the cathodic potential, the cathodic reaction will be highly localized at sites where surface damage took place at free potential. So the severity of hydrogen entry is likely to be enhanced and hydrogen embrittlement to be favoured[16].

To identify which mechanisms are concerned in each case, SEM investigations have been carried out to analyse and compare differences on fracture surfaces.

Results

Mechanical Properties

Mechanical properties are given according to the environment and the electrochemical potential for an applied strain rate $\dot{\varepsilon} = 4.10^{-7}$ s^{-1}. Elongations to fracture are summarized on *Figure 2* . For a strain rate $\dot{\varepsilon} = 7.10^{-5}$ s^{-1}, all tempers are resistant to SCC.

At free potential, SCC susceptibility decreases as : T651 > T7651 >T7451. Even though only one test has been carried out for each case, the same classification has been obtained by M. Reboul and coworkers[17] on the same alloy using alternate immersion static time to failure experiments (ASTM G47). At cathodic potential (E_K= -1.1 V/SCE), whatever the temper, little effect has been observed on the elongation compared to air. That is not to say that no surface damage exists resulting from hydrogen embrittlement but that another damage process (necking) emphasized by a tensile test may screen its effect on macroscopic elongation.

For overaged tempers (T7651, T7451), however, elongation is further reduced compared to elongation at free potential if the specimen is strained according to the scheme proposed for the new method and described in the experimental procedure part (see *Figure 2*). This result must be emphasized. For the T651 temper, the elongation at free potential is too low to perform such a test.

Fractography

Whatever the temper and the electrochemical potential, only a small fraction of the fracture surface is affected by SCC. This fraction is localized near the external surface where corrosion-deformation interactions take place. Nevertheless, such damage does not necessarily ring the entire circumference of the specimen. The centre of the specimens consists of dimpled and smooth regions characteristic of purely mechanical ductile failure. This kind of bulk damage is similar to that observed on the total surface of a specimen tested in air *(Figure 3)* and may interfer with surface damage to cause the failure.

Only near surface damage which is directly associated with corrosion-deformation interactions and SCC mechanisms will be considered hereafter.

Free potential. For the most susceptible temper (T651), the top face damage consists of pits but a crack with smooth regions can be seen on the fracture surface *(Figure 4)*. A specimen which has been immersed at free potential for 2 hours without stress shows that constituent particles (Al,Cu,Fe) and (Al,Cu) as well as grain boundary zones are sites of localized attack. For the overaged tempers, surface damage *(Figure 5)* consists mainly of cracks originating from large pits. These pits and cracks show important anodic dissolution. Particles in pits and a geometrical aspect produced by anodic dissolution may be noted *(Figure 5c)*.

Nevertheless, anodic dissolution is always accompanied by a cathodic reaction of equal intensity. For the overaged tempers, a cathodic reaction associated with the anodic one is observed to be mainly localized on the surface sample around pits which is typical of galvanic corrosion.

Cathodic Potential (E_K= -1.1 V/SCE). At this potential, whatever the temper, there are small pits (perhaps due to the pre-immersion period or to sites of hydrogen attack) and many cracks on the top surface samples. These cracks are localized near the fracture surface where deformations are high at the end of the tensile test. The presence of such cracks does not greatly affect the elongation value. The fracture surface shows many small cracks which are brittle in appearance with particles. One of them can be observed on *Figure 6*. Cleavage-like features are observed *(Figure 6b)* similar to those detected by A.W. Thompson, I.M. Bernstein and coworkers [18,19] for different Al-Zn-Mg(-Cu) alloys (commercial 7075 and 7050 alloys and a 7075 equiaxed one) using a test for which specimens were simultaneously plastically deformed and cathodically charged (Straining Electrode Test). In their work, the crack path was demonstrated to be transgranular and brittle in nature by fracture surface matching. These cleavage-like features have been also reported by J. Nelson and E.N. Pugh[20] and N.J.H. Holroyd and D.Hardie[8] for 7XXX series specimens tested in moist air where hydrogen embrittlement is possible.

Free Potential+Cathodic Potential. This test has been performed to differentiate between anodic dissolution and hydrogen embrittlement mechanisms. It favours hydrogen discharge and hydrogen embrittlement in the bulk of the specimen by a localization of the cathodic reaction at the preexisting crack tip. These preexisting cracks, originating mainly from large pits, were produced at free potential even at such a low transition plastic strain of 0.75 % *(Figure 7)*. Moreover, the crack tip environment contains certainly a large amount of H^+ because of $Al(OH)_3$ precipitation on the mouth of the crack. So the reduction of H^+ is favoured at the crack tip and highly localized when the subsequent cathodic potential is applied.

On fracture surfaces *(Figure 8)*, regions of highly anodic dissolution associated with pits or cracks are observed near the external surface of the specimens. Below these domains, an other kind of region with brittle appearance that can be associated with hydrogen embrittlement is observed. These two kind of regions are similar to those observed above for tests totally conducted either at free or at cathodic potentials respectively.

Discussion

The slow strain rate technique allows to approach SCC from different point of view. Whatever the criterion chosen to describe SCC susceptibility for a tensile test, fracture of specimens in a corrosive environment occurs as a consequence of multiple damage processes. Multiple damage processes for such a test consist of mainly: nucleation, growth and coalescence of microvoids (bulk damage) and a surface damage produced by corrosion-deformation interactions (pits, crevices, cracks). This concept of distributed damage has been described by A.W. Thompson[21] for a simple tensile test and can be naturally applied for SCC tests which magnify the role of surface damage. So the macroscopic results obtained with SSRT allows to classify the materials according to their SCC susceptibility but the usual concept of fracture by crack motion is uncertain in presence of multiple damage[21]. Nevertheless, corrosion-deformation interactions always take place at the surface and the fractography analysis is complementary with slow strain rate tests, providing data to approach SCC mechanisms.

A common feature of passive alloys susceptible to SCC is the creation of a defect with two distinct phases: an incubation and a propagation steps. Most of the existing models describe the propagation phase but a slow strain rate test includes both phases. During the incubation time, the stability of the passive layer is necessarily affected. Instabilities are due to mechanical, metallurgical and electrochemical interactions that create perturbations of the potential distributions close to the surface-film interface. So the passive film is disrupted and such events induce obviously a stochastic aspect for the incubation time and the time to failure. Film rupture has been associated in several models[22-24] with the emergence of slip steps for certain metal/environment couples. In these cases, the protective film reforming kinetics is the rate determining step of crack growth. The presence of defects in the film must also be taken into account because of the limited resistance of the film/defects interfaces under stress or of the electrochemical potential gradient from each part of the interface in a corrosive solution.

For 7150 alloy tested in an aerated 3% sodium chloride solution, extensive pitting occurs at free potential (which is close to the pitting one) on constituent particles (Al,Cu,Fe) and (Al,Cu) as well as in grain boundary zones. Pits (or sites of hydrogen attack) are also observed at a cathodic potential (E_K= -1.1 V/SCE). So the film is always disrupted in such corrosive solution during the slow strain rate test whatever the electrochemical potential. Such a disruption allows corrosion-deformation interactions between the exposed metal and the corrosive environment, in particular, anodic dissolution and hydrogen ingress and subsequent embrittlement.

At free potential, for all tempers, large pits (degenerating into cracks) and cracks are observed on the top surfaces of the specimens as a consequence of rapid and localized anodic dissolution of the metal. However, hydrogen effects cannot be eliminated because a cathodic reaction of high intensity must balance the anodic one. The nature and the localization of this(these) cathodic reaction(s) in an aerated chloride solution which participates in the mechanical/electrochemical process for such an aluminium alloy are difficult to determine exactly because of the precipitation of $Al(OH)_3$. This gelatineous white layer covers pits or cracks isolating them partially from the bulk environment. Thus, bulk and crack tip environments are certainly very different. Then, both oxygen reduction on the top surface and hydrogen reduction at a crack tip can occur simultaneously. Nevertheless, experimental evidence of hydrogen effects is in fact difficult to obtain because of the high intensity of the anodic reaction. Bare aluminium is dissolved and the characteristic brittle features due to possible hydrogen effects on the fracture surface may be unavoidably attacked by the corrosive environment during the test.

At a cathodic potential (E_K= -1.1 V/SCE), hydrogen discharge is favoured on the specimen free surfaces. Pits and cracks are observed on the top surface. On fracture surfaces, it can be seen that hydrogen embrittlement produces cracks for which the path was demonstrated to be transgranular and brittle in nature. Particles surrounded by traces of anodic dissolution are often observed within these cracks. This surprising result seems to indicate that, even at a cathodic potential, anodic dissolution can operate locally. Hydrogen-related fracture occurs when the hydrogen concentration reaches a critical value.

Decohesion and enhanced localized plasticity due to the presence of hydrogen at the crack tip are the most common mechanisms which can explain such brittle crack propagation[25]. While such a fracture is associated with little macroscopic deformation, it is necessarily accompanied with some localized plastic deformation. Thus, the decohesion model is based on the Griffith equation in which a plastic term must be introduced whatever the mechanical test. So as stated by Oriani[26], this latter is complementary with the enhanced localized plasticity model rather than competitive. The major difficulty is in fact to know how hydrogen is transported in the material to traps where hydrogen concentration reaches a critical value causing embrittlement. Is it by random walk diffusion through the lattice, pipe diffusion, grain boundary diffusion or by an enhanced diffusion process (due to either stresses and plastic strain which exist at a crack tip causing lattice dilatation or the dislocation transportation) in low diffusivity metals as aluminium alloys?

It has been now recognized that no material is totally resistant to SCC. In our study, the new test that we proposed indicates that overaged tempers, which are less susceptible at free potential and non susceptible at a cathodic potential (E_K= -1.1 V/SCE) can be embrittled by hydrogen localization in a preexisting defect. The preexisting defects have been created first by straining the sample until a 0.75% plastic strain amplitude. Such defects can be also created in another way, in fatigue for example. With such a test, hydrogen can be transported deeper into the sample than with a simple cathodic tensile test. Hydrogen discharge is localized at the defect tip (pits or cracks) and enhanced hydrogen embrittlement is promoted affecting not only the microscopic characteristics but also the macroscopic properties.

Conclusion

SCC mechanisms of a 7150 Al-Zn-Mg-Cu alloy in an aerated 3% NaCl solution can be related to both anodic dissolution and hydrogen embrittlement. Their relative influence depends on the electrochemical potential which is applied and on the temper of the alloy, in all probability.

This study clearly emphasized the role of surface sample defects suchs as pits and small cracks on the SCC damage mechanisms. Hydrogen produces a brittle fracture and hydrogen embrittlement is enhanced with prior pitting or surface damage.

The new SCC test with potential changes is very relevant means of studying the relative influence of anodic dissolution and hydrogen effects.

References

1 - E.H. Dix, Transactions ASM 42 (1950): p 1057.

2 - A.J. Sedriks, P.W. Slaterry, E.N. Pugh, Transactions ASM 62 (1969): p 815.

3 - D.O. Sprowls, R.H. Brown, Fundamental Aspects of Stress Corrosion Cracking, (Houston, TX: National Association of Corrosion Engineers, 1969): p 466.

4 - P. Doig, J.W. Edington, Metallurgical Transactions 6A (1975): p 943.

5 - R.J. Gest, A.R. Troiano, L'Hydrogène dans les Métaux, Editions Science et Industrie, (Paris, France: 1972): p 427 ; Corrosion 30 (1974): p 247.

6 - M.O. Speidel, Metallurgical Transactions 6A (1975): p 631.

7 - W. Gruhl, Zeitschrift für Metallkunde 75 (1984): p 819.

8 - N.J.H. Holroyd, D. Hardie, Corrosion Science 21 (1981): p 129.

9 - N.J.H. Holroyd, Environment Induced Cracking of Metals, (Houston, TX: National Association of Corrosion Engineers, 1989): p 311.

10 - The Slow Strain Rate Technique, G. Ugiansky, J. Payer Editors, ASTM STP 665 (1979).

11 - D. Desjardins, M. Puigalli, F. Vaillant, Matériaux et Techniques Special, Corrosion Sous Contrainte, (1988): p 7.

12 - C. Lemaitre, Corrosion Sous Contrainte: Phénoménologie et Mécanismes, Editions de Physique, (Bombannes, France: 1990): p 467.

13 - R.N. Parkins, Fundamental Aspect of Stress Corrosion Cracking (Houston, TX: National Association of Corrosion Engineers, 1969): p 361.

14 - R.N. Parkins, The Slow Strain Rate Technique, G. Ugiansky, J. Payer Editors, ASTM STP 665 (1979): p 5.

15 - R.N. Parkins, Corrosion Science 20 (1980): P 147.

16 - T. Magnin, C. Dubessy, P. Rieux, Aluminium alloys, Vol II, E. Starke , T. Sanders Editors, (Charlottesville, U.S.A: 1986): p 1177.

17 - M. Reboul, T. Magnin, T.J. Warner, The 3rd International Conférence on Aluminium Alloys, (N.T.H. Trondheim, Norway : 1992): p 453.

18 - J. Albrecht, I. M. Bernstein, A. W. Thompson ; Metallurgical Transactions 13A (1982): p 811.

19 - D.A. Hardwick, A.W. Thompson, I.M. Bernstein : Metallurgical Transactions 14A (1983): p 2517.

20 - J.L. Nelson, E.N. Pugh, Metallurgical Transactions 6A (1975): p 1459.

21 - A.W. Thompson, Chemistry and Physics of Fracture, G.M. Latanision, R.H. Jones Editors, (1987): P129.

22 - D.A. Jones, Environment-Induced Cracking of Metals, (Houston, TX: National Association of Corrosion Engineers, 1989): p 265.

23 - F.P. Ford, Corrosion Sous Contrainte: Phénoménologie et Mécanismes, Editions de Physique (Bombannes, France: 1990): p 307.

24 - T. Magnin, Corrosion Sous Contrainte: Phénoménologie et Mécanismes, Editions de Physique (Bombannes, France: 1990): p 345.

25 - R.N. Parkins, Environment-Induced Cracking of Metals, (Houston, TX: National Association of Corrosion Engineers, 1989): p 1.

26 - R.A. Oriani, Environment Induced Cracking of Metals, (Houston, TX: National Association of Corrosion Engineers, 1989): p 439.

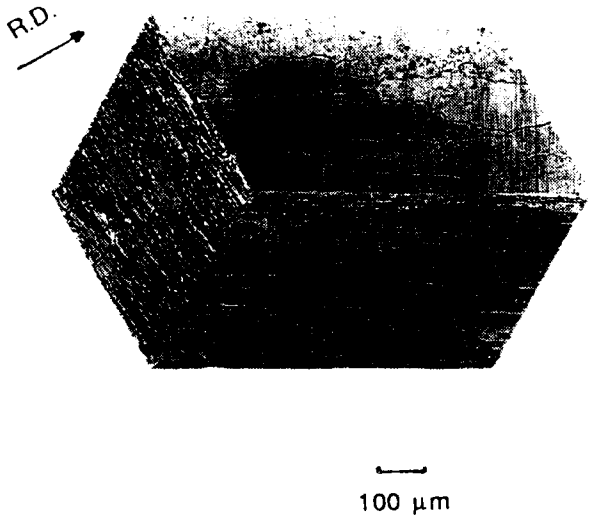

Figure 1 :
Grain structure of the 7150 alloy.

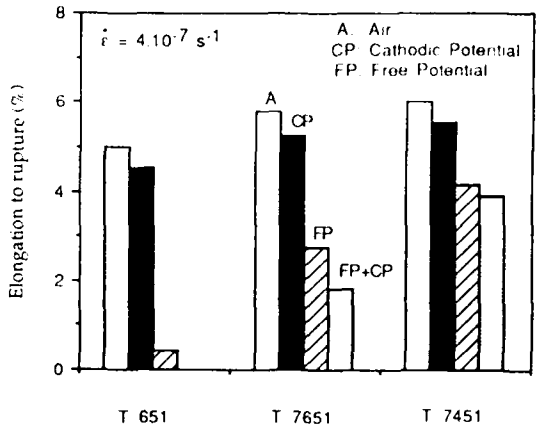

Figure 2 :
Elongation to fracture versus temper for various environments and electrochimical potentials.

Figure 3 :
SEM fractograph showing the general aspect of fracture surface for a specimen strained in air (T7651 temper). Dimpled and smooth regions in the rolling direction are observed whatever the temper.

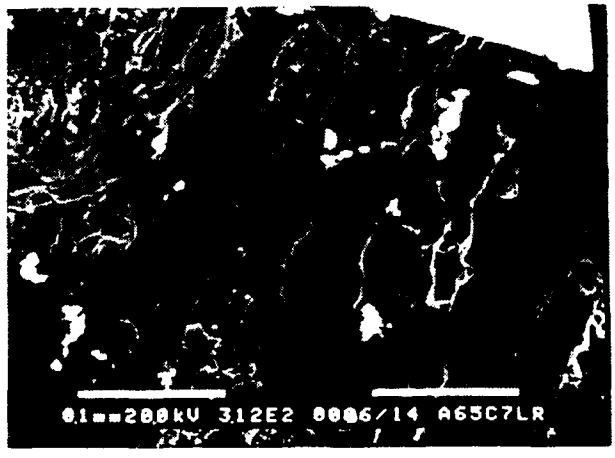

Figure 4 :
SEM fractograph of the main crack with smooth regions for T651 temper at free potential in an aerated 3% NaCl solution.

a)

b)

c)

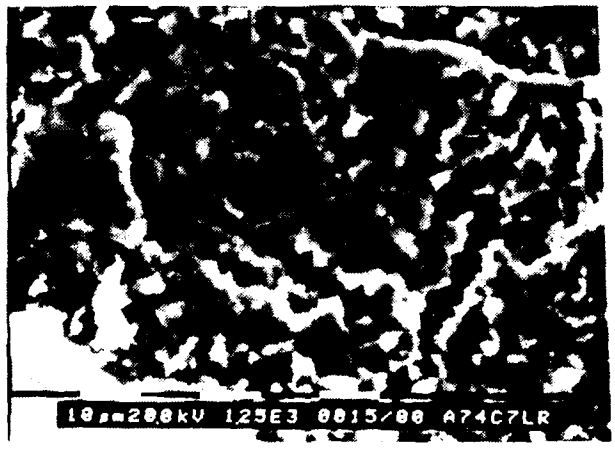

Figure 5 :
SEM of fracture surface near the external surface for T7451 temper at free potential in an aerated 3% NaCl solution:

a) Crack originating from a pit containing a particle.
b) Other kind of crack showing an important anodic dissolution.
c) Magnification of the geometrical aspect created by the important anodic dissolution.

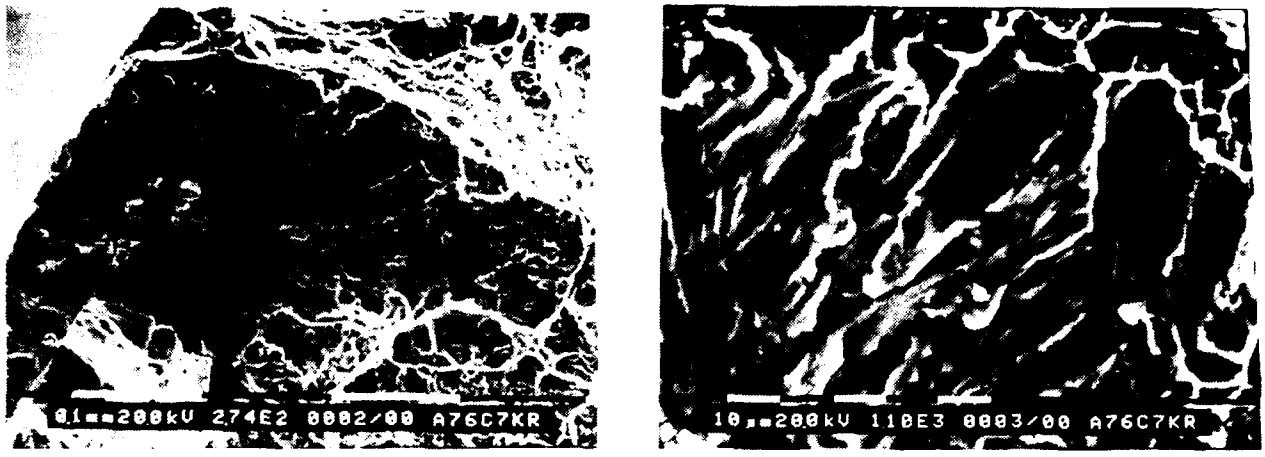

a) b)

Figure 6 :
SEM of fracture surface near the external surface for T7651 temper at a cathodic potential E_k= -1.1 V/ECS in an aerated 3% NaCl solution :

a) Crack with brittle appearance and containing a particle.
b) Magnification of the brittle facets.

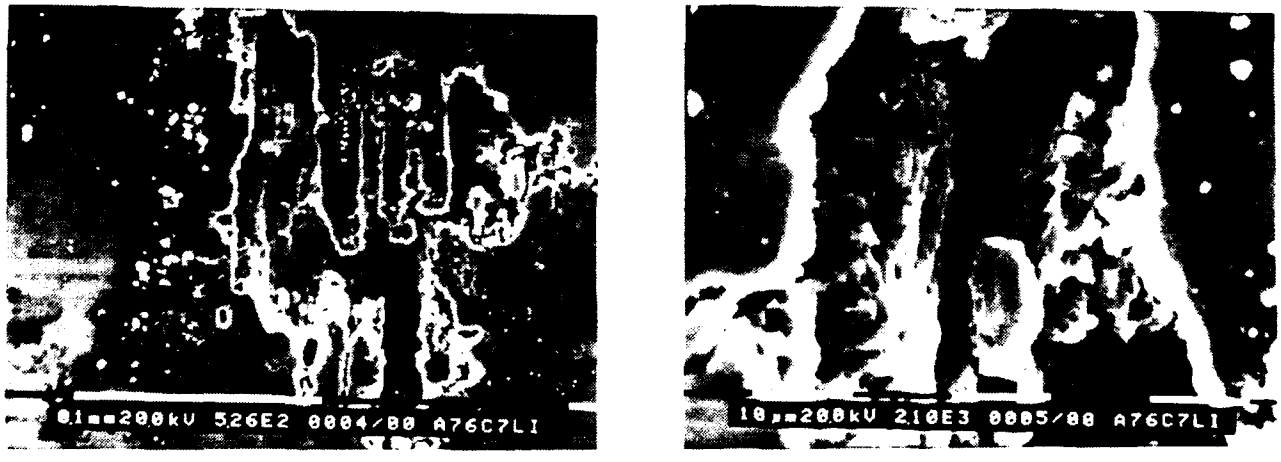

a) b)

Figure 7 :
SEM of surface damage obtained at the transition plastic strain for T7651 temper at free potential in an aerated 3% NaCl solution :

a) Crack perpendicular to the tensile axis.
b) Magnification of the crack.

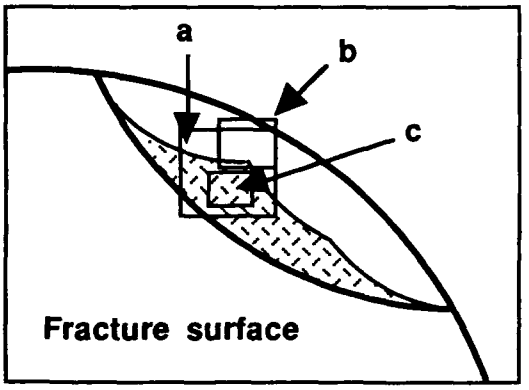

A

B

C

Figure 8 :
SEM fractographs of fracture surface for T7451 temper at free potential until 0.75 % plastic strain and subsequent cathodic potential.
a) Typical crack for this test with important anodic dissolution nearby the external surface followed by a region with brittle appearance.
b) Magnification of the region with important anodic dissolution.
c) Magnification of the region with brittle appearance.

Specific Features of Electrochemical Behavior and Stress Corrosion of Aluminium-Lithium Alloys

V.S. Sinyavsky
All-Russia Institute of Light Alloys
121596, Moscow, Gorbunova st. 2, Russia

A.M. Semenov
All-Russia Institute of Light Alloys
121596, Moscow, Gorbunova st. 2, Russia

V.D. Valkov
All-Russia Institute of Light Alloys
121596, Moscow, Gorbunova st. 2, Russia

V.V. Ulanova
All-Russia Institute of Light Alloys
121596, Moscow, Gorbunova st. 2, Russia

Abstract

By the present time, a number of industrial alloys based on Al-Li-Cu, Al-Li-Mg, Al-Li-Cu-Mg systems have been developed. Some of them are beginning to find use in the designs of modern aircraft. However, the corrosion and electrochemical properties of these alloys still remain to be studied. In particular, there are no data on the effects of electrochemical characteristics on the corrosion properties of Al-Li alloys. This impedes their application in a large measure. And this is the subject of this work.

The present paper deals with studies of pressed strips produced from Al-Li, Al-Li-Cu, Al-Li-Mg, Al-Li-Cu-Mg alloys, establishes the basic regularities of corrosion and electrochemical behavior of these alloys, defines their electrochemical characteristics and shows their relation to the corrosion properties.

The carried out corrosion and electrochemical tests formed the basis for recommending the optimization of the chemical composition and conditions for heat treatment of alloys.

Key words: corrosion cracking, layer corrosion, corrosion potential, pitting initiation potential, repassivation potential, corrosion rate in terms of mass loss.

INTRODUCTION

By the present time, a number of industrial alloys based on Al-Li-Cu, Al-Li-Mg, Al-Li-Cu-Mg systems have been developed. Some of them are beginning to find use in the designs of modern aircraft. However, the corrosion and electrochemical properties of these alloys still remain to be studied. In particular, there are no data on the effects of electrochemical characteristics on the corrosion properties of Al-Li alloys. This impedes their application in a large measure.

In the 1950-s, in his study G.V. Akimov [1], who investigated the electrochemical behavior of solid solutions based on aluminium, also including Al-Li alloys in NaCl solution, showed a slight shift towards the negative side of the potential without cleaning and, on the contrary, towards the positive side upon cleaning of the surface in electrolyte of the electropositive component (in this case aluminium E = -1.667 V) when alloyed by electronegative lithium (E = - 3.045 V). The author explains this by the probable conversion of the electrochemical properties of lithium in a solid solution. Thus, lithium added to aluminium has anomalous electrochemical properties which is supported by our investigations. Lately, much consideration has been given to Al-Li alloys [3-6]. However, there are few studies dealing with electrochemical characteristics. Thus, Dorward's paper [7] considers the problems of reduced corrosion resistance of Al-Li-Cu alloy system. This is attributed to the precipitation of anodic $T_1(Al_2LiCu)$-phase along grain boundaries. In paper [8] the low corrosion resistance of sheets of alloy 1420 of Al-Li-Mg system after quenching in water and ageing at 120oC for 12 h is attributed the precipitation of anodic phase $S(Al_2MgLi)$. Meanwhile, the electrochemical characteristics obtained in this work lead to the conclusion that the process of anodic dissolution is the main factor in the mechanism of corrosion resistance contrary to the authors' opinion. Comparative investigations of the electrochemical characteristics of sheets produced from 2091 and 2024 alloys enabled the authors of paper [9] to claim that the corrosion properties of these alloys are similar.

Thus, the relation of the electrochemical parameters and corrosion characteristics of aluminium-lithium alloys, especially under stressed conditions, is still to be clarified. And this is the subject of the present paper.

Material and Methods

The objective of this study was to investigate pressed strips of various system alloys. The chemical composition of these alloys are presented in Table 1. The tests for resistance to stress corrosion cracking (SCC), exfoliation corrosion(EC) and intercrystalline corrosion (ICC) were carried out in accordance with ISO 9591, CD 11881, CD 11846.
The structure was investigated by using NEOPHOT-2 AND JEM-100CX microscopes at 100 kV.

Electrochemical studies were carried out in a three-electrode glass electrochemical cell, the reference electrode was of chlorine silver, platinum wire was used as an auxiliary electrode. Electrochemical characteristics: corrosion potential (Ecor), pitting initiation potential (Ep.i.), repassivation potential (Er.p.), current density in passive region (ip.r.) were determined by polarization diagrams.

Results and Discussion

Corrosion and mechanical tests (Table 2) showed that binary Al-Li alloys at a selected ageing temperature of 170°C are aged slowly. The alloy with lithium content of 0.8%, which hardly changes its mechanical properties during artificial ageing, appears to be an exception.

Pressed strips of the investigated alloys are noted for their high resistance to local corrosion types: SCC, EC and ICC. When tested for SCC, the specimens of all the alloys are not destroyed for 90 days at a stress of 0.75 and even 0.9 of the yield point. At the same time all the alloys are insensitive either to layer (2-nd point for all ageing regimes) or intercrystalline corrosion.

Dependence of corrosion rate in terms of mass loss (Fig. 1 scc 1) on lithium concentration in the alloy is defined in a complex way. Up to the concentration not surpassing the ultimate solubility of lithium in aluminium (Al - 0.8% Li), the corrosion rate shows a drastic increase, 30 times as high as compared to aluminium from $\Delta M=0.0004$ $g/m^2 \cdot h$ for Al to $\Delta M=0.0120$ $g/m^2 \cdot h$ for Al-0.8% Li alloy (for 720 hours of tests). This is related to the selective corrosion of lithium from solid solution - Al-0.8% Li alloy. Selective corrosion of lithium was first discovered in our investigation jointly with the Karpov Research Institute for Physicochemical Investigations [9]. Further increase in lithium concentration by 3 times (Al-2.3% Li) does not lead to any changes in the corrosion rate in terms of mass loss (Fig. 1. cr. 1).

Fig. 1 scc. 2 shows that when 0.8% Li is introduced into aluminium, the corrosion potential becomes 18 mV more negative. With increasing lithium content to 2.3% the shift reaches 0.15 V. However, as seen from Table 3.2, pitting initiation potential also becomes more negative (from - 0.425 V for pure aluminium to -0.478 V for alloy 3, which equals 0.053 V).

The polarization diagrams of alloys 1 and 3 obtained by different techniques: 1) anodic polarization from corrosion potential (Fig. 2 a,) and 2) preliminary cathodic polarization to potential -1.6 V (standard hydrogen electrode) and then anodic polarization (Fig. 2 b,) shows that irrespective of the method for obtaining the polarization curve, the pitting initiation potentials practically coincide. However, the value of current density in the passive region for Al-2.3% Li alloy surpasses the indicated parameter by 15 times as compared to Al-0.8% Li , although in the first method of plotting the curve the current density is identical for both

alloys. The repassivation potential depends on the polarization method to a greater extent. This parameter as well as the difference between the repassivation potential and pitting initiation potential unambiguously show that the alloys with a greater lithium concentration are characterized by lower passivating ability (Fig. 2 b, than the alloys with a lower content of this component. At the same time, with increase of lithium concentration to 2.3% in the alloy the value of Ecor - Ep.i. also rises from 0.073 V (0.8% Li) to 0.169 V (2.3% Li), i.e. 2.3 times (Table 3). The latter points to the fact that with increase of lithium content in the alloy the probability of pitting corrosion should drop. However, the data of Table 3 and Fig. 2 show that the repassivation potential is located between the corrosion and pitting initiation potential, except for alloy N 1 (in this case the corrosion potential is equal to the repassivation potential). Proceeding from the nature of alloy (lithium is the most negative element in the periodic table and electrochemical tests (Table 3, Fig. 2) it would be possible to suggest that with increase in lithium concentration in the alloy the corrosion rate in terms of mass loss will also rise. This is evidenced by an increase in the value Er.p. - Ep.i. with a rise of lithium concentration in the alloy, as well as by displacement of the corrosion potential towards the negative side. However, actually corrosion rate does not rise (Fig. 1, cr. 1, pt.II). The latter apparently results from from the fact that at a concentration exceeding 1.3% (Al - 1.9% Li and Al - 2.3% Li) lithium is contained not only in solid solution, but also in the precipitations of anodic O (Al3Li) phase (Fig. 3 b). At the same time the particles of O-phase act as electrochemical protectors of the matrix.

Fig. 3 shows that semifinished products have non-recrystallized structure with precipitation of strengtheningphase (Al3Li). Moreover, the boundary regions do not differ from the grain body in anything (for all the investigated alloys). No differences emerge even after artificial ageing at 170oC for 144 h. Thus, there is no electrochemical heterogeneity between the grain body and the boundary due to the uniform distribution of anodic O -phase. This is supported by the absence of intercrystalline corrosion and layer corrosion for the investigated semifinished products of Al-Li alloys. As far as corrosiion cracking is concernend, the semifinished products of binary aluminium - lithium alloys are not susceptible to this type of corrosion for two reasons: first, there is no electrochemical heterogeneity between the grain body and the boundary and, second, there seems to be no localization of stresses at grain boundaries.

Thus, the corrosion resistance of Al-Li alloy system is formed under the influence of two counteracting factors. On the one hand, with increase in lithium content the resistance to pitting corrosion and potentially corrosion resistance rise. On the other hand, the capacity for self-passivation of such alloys falls and this potentially reduces the corrosion resistance.

Alloying Al-Li systems by magnesium to 2.8% promotes further increase in the values TS and YS (up to 420 and 320 MPa, respectively) and has no marked effect on the resistance to local corrosion types, although in this case the corrosion rate in terms of mass loss rises twice as much (Table 4).

An increase in magnesium concentration to 5.2% leads under certain conditions of heat treatment (quenching in water) to the emergence of sensitivity to local corrosion types - SCC, EC. In combination of corrosion and mechanical properties as well as technologically, in metallurgy the alloys with a low content of magnesium (<3.0%) are superior to the alloys containing up to 5.2% of magnesium. At the same time, it was shown (Table 5) that the use of nonconventional artificial ageing "AS35" that we developed leads to a considerable rise in the resistance of alloys with 5.2% Mg to SCC and EC. Another technique which considerably enhances resistance to SCC, EC and the stability of obtained properties is "double quenching" [11], the use of which produces semifinished products with a high level of corrosion and mechanical properties. The threshold level of stresses at SCC - σ_{scc} = 250 MPa in transverse and σ_{scc} = 125 MPa in short transverse directions, respectively (Table 5). Studies of electrochemical characteristics showed that Al-Li-Mg system alloys have rather negative values of corrosion , pitting initiation and repassivation potentials Table 6), which with decrease in Mg concentration are displaced towards the positive side. No marked changes in the electrochemical characteristics were observed with variation heat treatment conditions. Consequently, it should be noted that the electrochemical factor plays a certain role rather than primary one in the mechanism underlying the SCC of Al-Li-Mg system alloys.

The introduction of copper into Al-Li alloys in the condition aged for the highest strength leads to a considerable growth of strength characteristics (by 180 MPa), has no noticeable influence on the resistance to EC, is conducive to a decrease in the resistance of semifinished products to SCC, ICC and a considerable rise in the corrosion rate in terms of mass loss by 10-15 times (Table 7). The electrochemical characteristics in this case are greatly displaced towards the positive side.

The additional alloying of such systems by magnesium exerts a complex influence on the corrosion characteristics . The addition of magnesium into Al-Li-Mg alloy in the amount of 0.2-0.4% exercises a positive effect on the resistance to SCC (Fig. 5, cr. 3) and practically changes no resistance to EC (Fig. 5, cr 2). Further increase in magnesium concentration (to 1%) in the alloys under consideration leads to a considerable drop of their resistance to local corrosion types and corrosion rate in terms of mass loss ΔM. Al-Li-Cu-Mg alloys are markedly inferior to Al-Li-Cu alloys with a small addition of Mg in these indices. With increase in Mg concentration the electrochemical characteristics are displaced towards the negative side (Table 8). At the same time, it should be noted that the capacity for selfpassivation falls. Apparently, an increase in the resistance to SCC in the case of alloying by

small additions of Mg (0.2-0.4%) can be explained by the action of two factors: decrease in electrochemical heterogeneity shown by displacement of corrosion potential towards the negative sidewith increase in magnesium concentration in the alloy and change in the nature of plastic deformation inside the grains. A drastic fall of all corrosion properties with increase in magnesium concentration is most likely related to the emergence in the structure of new phase components, such as S'(Al_2CuMg) phase, as described in paper [12].

A considerable influence on the corrosion characteristics of Al-Li-Cu-Mg alloys is exerted by copper to magnesium ratio in them. Corrosion tests showed that the alloy with copper to magnesium ratio equal to 2.0 and and a sum of 2.1% have a low resistance to SCC and EC (Table 9). Quite different results were obtained for the alloy with the same sum, but a lower copper to magnesium ratio equal to 0.5. Such alloy is insensitive EC (2-nd point irrespective of the composition of test solution), has a relatively high threshold level of stresses in the case of SCC (σ_{scc} > 125 MPa) and practically unsusceptible to ICC - the depth of subgrain corrosion is not in excess of 0.05 mm. These alloys possess a high resistance to general corrosion in terms of mass loss. Corrosion rate based on six-month tests equals only 0.009 g/m2·h (Table 9). This allows Al-Li-Cu-Mg alloys with a ratio of Cu/Mg=0.5 and the total content of these components 2.1% to be referred to a group of stable alloys.

Consideration of the obtained electrochemical characteristics makes it possible to establish quite definitely their relation with the corrosion properties of the investigated alloys (Table 10). Indeed, the alloy with increased corrosion properties (with Cu/Mg=0.5 and Cu+Mg=2.1) is characterized by the most negative values of corrosion (Ecor = -0.701 V) and repassivation (-0.483 V) potentials as well as by the least difference between the repassivation and pitting initiation potentials (Er.p.-Ep.i. = 0.071 V), the greatest difference between the corrosion potential and pitting initiation potential (Ecor - Ep.i.= 0.289 V).

Investigation of the dependence of pitting initiation potential on chlorine ion concentration in solution (Table 11) shows that linear dependence Ep.i. on chlorine ion concentration holds true for all the alloys. This is evidenced by a high correlation factor (0.991 - 0.999). However, for alloy N 10 (Table 1) the prelogarythmic coefficient is 1.5 times lower than for other alloys, i.e. the capacity of this alloy for pitting initiation is lower than that of alloy N9 (Table 1).

The established regularities can be explained from the viewpoint of a dislocation-electrochemical model of corrosion cracking. Studies of the structure showed that semifinished products of Al-Li-Cu-Mg alloys have non-recrystallized structure consisting of three structural components: solid solution, precipitations of strengtheninganodic (Al3Li)-phase and S'(Al_2CuMg)-phase, which unlike -phase is precipitated at dislocations or at grain and subgrain boundaries. Such structure is characteristic of alloys N9-10.

Therefore, a drastic increase in the resistance to SCC and EC with decrease in copper to magnesium ratio seems to result from a reduction in the volume fraction of S'(Al_2CuMg)-phase. This statement follows from the fact that binary aluminium-lithium alloys, in which under similar conditions of artificial ageing (170°C, 4-144 h) only precipitations of strengthening (Al_3Li)-phase are present, appear to be corrosion resistant. The negative influence of S'phase is related to the formation of electrochemical heterogeneity along the grain boundaries apparently due to the depletion of boundary zones in copper. The higher corrosion resistance of alloys with a lower copper to magnesium ratio is supported by changes in the electrochemical characteristics, specifically by more intensive selfpassivation and more extensive range of resistance potentials to pitting, as evidenced not only by a higher value of (Ec - Ep.i.) as compared to alloy N9, but also by a low prelogarythmic factor indicating that the resistance to pitting initiation for alloys with a copper to magnesium ratio equal to 0.5 is 1.5 times higher than for alloy N9.

CONCLUSIONS

1. Binary Al-Li alloys with lithium content up to 2.3% were found to have high resistance to local corrosion types - SCC, EC, ICC. This arises from the absence electrochemical heterogeneity. Lithium added to aluminium was shown to have anomalous electrochemical behavior (corrosion potential slightly shifts towards the negative side) and the difference between the corrosion and pitting initiation potentials considerably rises.

2. The addition of magnesium to Al-Li alloy in the amount up to 3% exerts a favorable effect on the corrosion and mechanical characteristics of such alloys. The corrosion properties of alloys containing more than 3% of magnesium (5.2%) are low and they can be enhanced by using heat treatment technique ("ASS35") that we have developed.

3. The addition of copper (2.8%) to binary alloys leads to higher strength characteristics, at the same time, they begin to show susceptibility to local types of corrosion. This results from an increasing role of the electrochemical factor in the mechanism of SCC, EC due to the emergence of new structural components - $T_1(Al_2CuLi)$ located at the grain and subgrain boundaries.

4. A small addition of magnesium (0.2 - 0.4%) to Al-Li-Cu alloys improves not only their strength characteristics, but also raises the resistance to SCC with EC and ICC remaining invariable. Further increase in Mg concentration in the alloy to 1% leads even to a greater rise of strength characteristics, however the resistance to SCC and EC drastically drops. The corrosion rate in terms of mass loss also grows.

5. The Cu/Mg ratio and sum of these components in Al-Li-Cu-Mg alloys were found to have the decisive influence on their corrosion resistance. The alloy with a Cu/Mg ratio of 0.5 and their sum equal to 2.1% is noted for high corrosion characteristics. The electrochemical factor plays the principle role for the alloys of this system.

REFERENCES

1. Akimov G.V. Teoriya i metody issledovaniya metallov (Theory and Methods of Investigating Metals), Akademizdat, 1945
2. Sinyavsky V.S., Semenov A.M., Valkov V.D., Samarina M.V. Aluminium-Lithium, ed. Peterson and Winken P. - Y (Germany 1992), pp. 719-724
3. Niskanen P., Sanders T.H., Marek M., Rinker I.G. - Aluminium-Lithium Alloys. (Proceedings of the First International Al-Li Conference, Ed. by Sanders T.H. and Starke E.A. AIME, 1981), O. 347-376
4. Christodolou L., Struble L., Pickens J.R. - Aluminium-Lithium Alloys II, (Proceedings of the Second International Al-Li Conference, Ed. by Starke E.A. and Sanders T.H. AIME, 1983), pp. 561-579
5. Ahmad M. and Ericsson T. - Aluminium-Lithium Alloys III, (Proceedings of the International Al-Li Conference, Ed. by Starke E.A. and Sanders T.H., AIME, 1985), p. 309-515.
6. Buchheit R.G., Stoner G.E.(Proceedings of the Fifth International Al-Li Conference Williamsburg, Virginia, 1989), p. 1347.
7. Dorward R.C. and Hasse K.R. Corrosion 1988 vol. 44, N 12, p. 932-941.
8. Batrakov V.P., Karimov S.A., Komissarov V.S. - Zashchita Metallov (Metal Protection), 1981, vol. 17, N 6, p. 627-637.
9. Kolotyrkin Ja.M., Sinyavsky V.S., Kiselev V.D., Semenov A.M., Knyazheva V.M. Aluminium-Lithium ad. Peterson and Winken P.-Y(Germany 1992) pp. 843-847
10. Sinyavsky V.S., Valkov V.D., Semenov A.M. - in Metallovedenie legkikh splavov VILS (Physical Metallurgy of Light Alloys of VILS), 1989, p. 78.
12. Harris S.I., Noble V., Dinsdale. Journal de physique colloqe C3, suppliment au N9, Tome 48, septembre 1987.

Table 1

Chemical composition of investigated alloys*

	Content of components in % by mass			
	Li	Cu	Mg	Zr
1	0.8	–	–	0.10
2	1.9	–	–	0.10
3	2.3	–	–	0.10
4	2.0	2.8	–	0.11
5	2.0	2.8	0.2	0.11
6	2.0	2.8	0.4	0.10
7	2.0	2.8	0.7	0.11
8	2.0	2.8	0.1	0.10
9	2.0	1.4	0.7	0.11
10	2.0	0.7	1.4	0.10
11	2.0	–	2.8	0.11
12	2.2	–	5.2	0.12

* Concentration of Fe and Si was maintained at 0.06% and 0.05, respectively, for all alloys.

Table 2

Mechanical properties of pressed strips of Al-Li alloys depending on ageing conditions

Alloy No and Li % in alloy	Ageing conditions	Mechanical properties		
		TS MPa	YS MPa	δ %
1	Natural ageing 1 month	101	93	28.4
	170 C, 4 h	113	101	26.6
0.8%Li	170 C, 16 h	123	102	29.6
	170 C, 144 h	126	102	25.0
2	Natural ageing 1 month	193	158	17.2
	170 C, 4 h	300	255	9.2
1.9%Li	170 C, 16 h	335	278	8.8
	170 C, 144 h	359	308	7.2
3	Natural ageing 1 month	223	191	10.0
	170 C, 4 h	332	270	5.2
2.8%Li	170 C, 16 h	362	296	5.2
	170 C, 144 h	388	316	5.2

Table 3

Electrochemical characteristics of binary Al-Li alloys; ageing at 170°C for 16 h

Alloy	-Ec, V	-Ep.i., V	-Er.p., V	Ec-Ep.i	Er.p.-Ep.i	ip.i. A/cm²
A995	0.498	0.425	0.540	0.073	0.115	15
N1	0.516	0.440	0.518	0.076	0.078	23
N2	0.625	0.474	0.602	0.151	0.128	21
N3	0.647	0.478	0.625	0.169	0.147	20

Table 4

Corrosion and mechanical properties of pressed strip of alloys 2, 11 and 12 ageing 170° C for 16 h.

Alloy No.	Mech properties			SCC tests 3% NaCl σ_{scc} in MPa	Tests for EC resistance		Corrosion rate in terms of mass loss ΔM g/m² h
	TS MPa	YS MPa	δ %		2S	4S	
2	335	278	8.8	σ_{scc}=0.9YS	A	A	0.120
11	386	335	4.6	σ_{scc}=225	A	A	0.220
12	482	427	9.7	σ_{scc}<50	B	B	0.280

Table 5

Corrosion and mechanical properties of sheets of alloy 12 depending on heat treatment conditions

Quench. condi-tions	Ageing condi-tions	Mechanical properties MPa			SCC tests σ_{scc} in MPa transverse direction	Resistanc tests	
		TS	YS	δ%		EC	ICC
460°C для water	"AS535"	515	352	7.5	σ_{scc}>0.75YS	A	abs
"DZ"	120°C,12h	484	331	9.3	σ_{scc}>0.75YS	A	abs

Table 6

Electrochemical characteristics of alloys 2, 11, 12; standard hydrogen electrode

Alloy No	Heat treat.	-Ec V	-Ep.i. V	-Er.p. V	Ec -Ep.i V	Er.p. -Ep V	ip.i A/cm²
2	Quench. 525 C+ ageing 170 C, 16 h	0.625	0.474	0.602	0.151	0.128	21
11	Quench. 465 C+ ageing 170 C 16 h	0.730	0.487	0.589	0.243	0.102	27
12	"AS535"	0.789	0.529	0.641	0.260	0.112	32
	"DZ"	0.809	0.545	0.647	0.264	0.102	36

Table 7

Corrosion and mechanical properties of pressed strips of alloys N2 and 4; ageing 170, 16 h

No	Mechanical properties			SCC tests short transverse direction	EC resistance			ICC test
Alloy	TS	YS	δ%		2S	3S	4S	h in mm
2	335	278	8.8	σ_{scc}=0.9YS	A	A	A	abs.
4	483	458	8.8	σ_{scc}=75 MPa	A	B	A	0.090

Table 8

Electrochemical characteristics of pressed strip depending on Mg concentration in alloy, ageing 170o C, 16 h (normal hydrogen electrode)

No Alloy	-Ec. V	-Ep.i.V	-Er.p.V	Ec-Epi. V	Erp-Epi V	ipi A/cm2
4	0.455	0.355	0.550	0.100	0.195	50
5	0.478	0.376	0.625	0.102	0.249	51
6	0.494	0.380	0.650	0.114	0.270	50
7	0.503	0.390	0.662	0.113	0.272	50
8	0.520	0.390	0.671	0.130	0.281	54

Table 9

Corrosion and mechanical characteristics of pressed strips depending on Cu/Mg ratio and sum of Cu+Mg; ageing 170o C, 16 h.

No Alloy	Cu/Mg; (Cu+Mg)	Mech. proper-ties MPa			SCC tests ST σ_{scc} in MPa	EC	ICC h in mm	Corr. rate M g/m2 · h
		TS	YS	δ%				
9	2.0; 2.1	431	378	4.2	σ_{scc}<<50	B	0.040	0.018
10	0.5; 2.1	407	360	4.1	σ_{scc}>125	A	0.026	0.009

Table 10

Electrochemical characteristics of alloys of Al-Li-Cu-Mg alloys, ageing 170° C, 16 h, standard hydrogen potential

No Alloy	-Ec. V	-Ep.i.V	-Er.p.V	Ec-Epi. V	Erp-Epi V	ipi A/cm2
9	0.599	0.396	0.488	0.203	0.092	32
10	0.701	0.412	0.483	0.289	0.071	30

Table 11

Dependence of pitting initiation potential on chlorine ion concentration, ageing 170° C, 16 h; standard hydrogen potential

Alloy No	Regression equation	Correlation factor
9	- Ep.i. = -0.422-0.8812g C cl-	0.999
10	- Ep.i. = -0.429-0.0581g C cl-	0.991

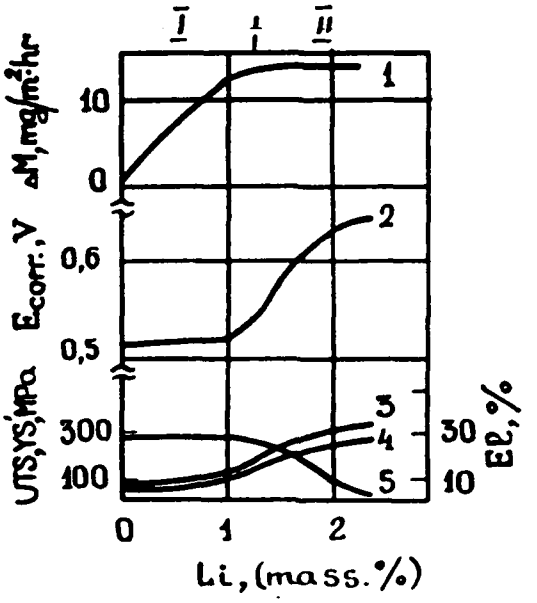

Fig. 1. Change in corrosion rate in terms of mass loss (1), in corrosion potential (2), mechanical characteristics of Al-Li alloys (3 - TS, 4 - YS, 5 - δ) depending on lithium concentration in alloy; pressed strip 10 x 100 mm in crosssection, quenching in water from temperature 525° C, ageing at 170°C for 16 h.

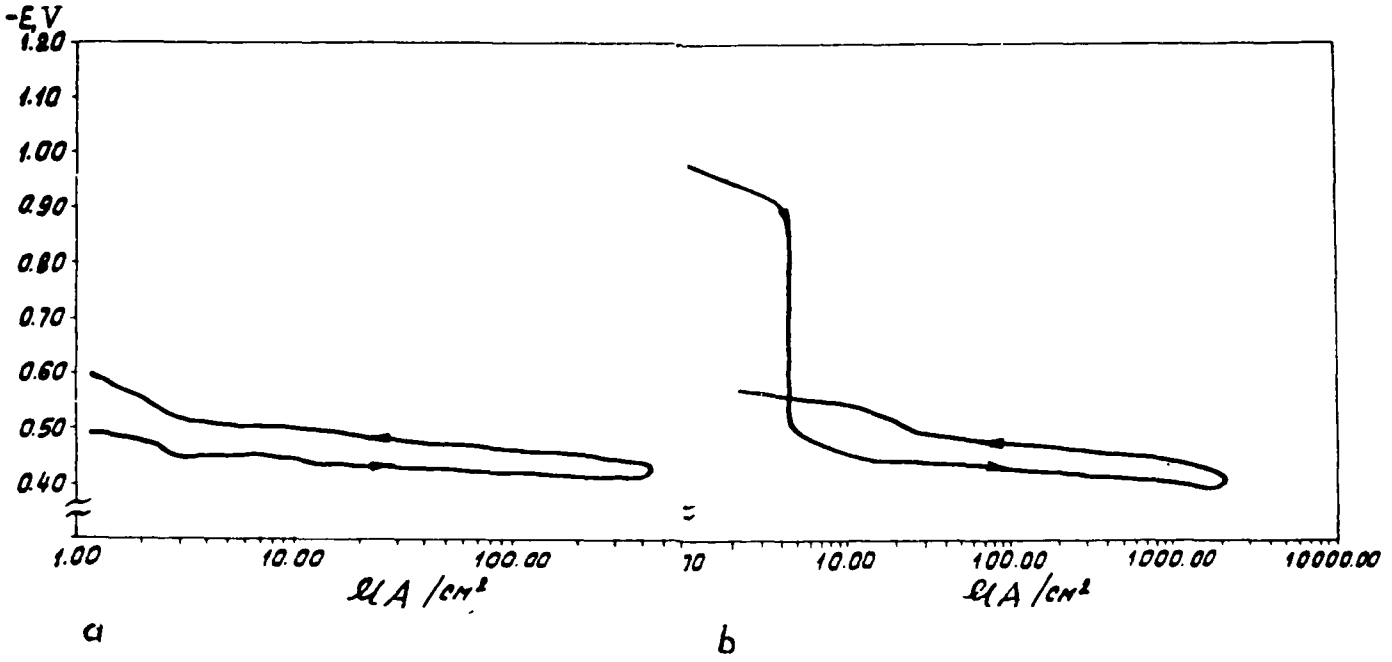

Fig. 2. Polarization diagrams of alloys N1 -a), b) and N3 c), d) constructed by different methods a, c - from corrosion potential; b, d - preliminary cathodic polarization to potential -1.6 V (standard hydrogen electrode); pressed strip 10 x 100 mm in cross-section; quenching from 525° C in water, ageing at 170° C for 16 h.

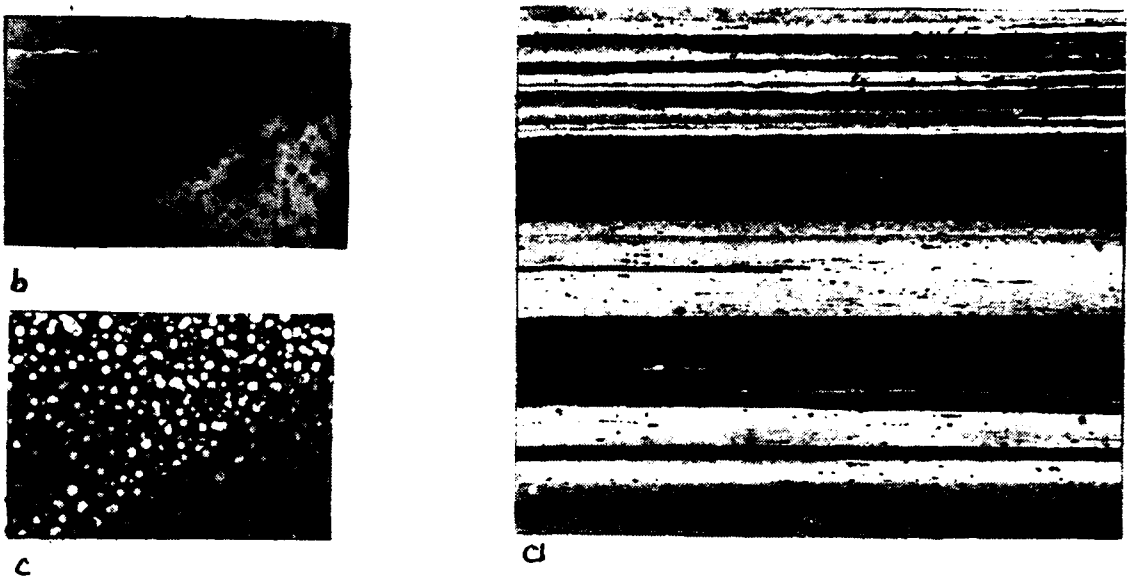

Fig3.Stucture of pressed strips of binary Al-Li alloys:
a-longitudinal direction,electropolishing
b-light colored representation
c-dark-colored representation of the same region

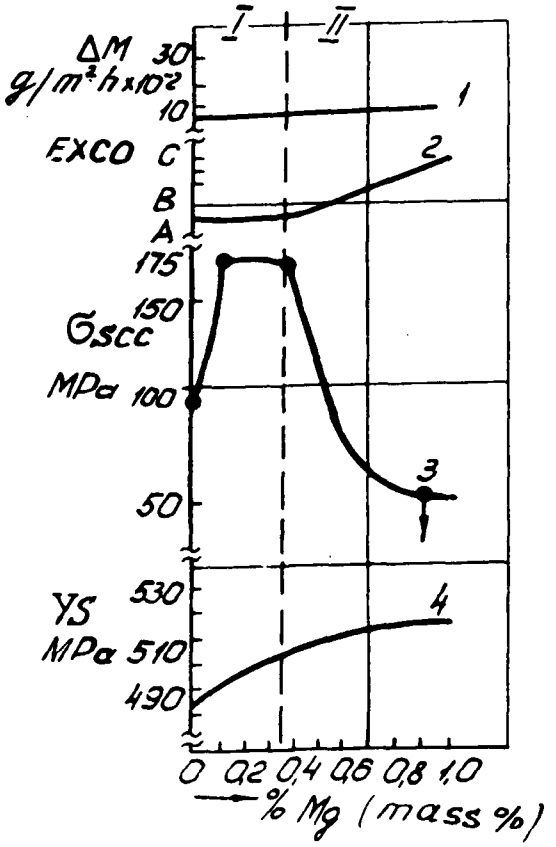

Fig.4 Effects of adding magnesium on corrosion M(1) EC(2) Oscc(3) and YS (4) properties of Al-2.0%Li-2.8%Cu; quenching from 525 C in water, aging 170 C,16 hr.

The Cathodic Corrosion of TiAl and Effect of Hydrogen

Ke-Wei Gao
Jian-Wen Jin
Li-Jie Qiao
Wu-Yang Chu
Chi-Mei Hsiao
Dept. of Materials Physics
Univ. of Science and Technology, Beijing
Beijing, 100083, China

Abstract

The titanium aluminide TiAl could undergo severe corrosion during cathodically charging with hydrogen in various aqueous solutions and molten salt at 160°C, called it as cathodic corrosion. The phenomena and mechanism of the cathodic corrosion has been investigated. The results showed that the rate of the cathodic corrosion under a constant potential was much higher than that of the anodic dissolution under the same potential difference. The rate of the cathodic corrosion under a constant current increased linearly with increasing of the current, and had the maximum value in the $0.5MH_2SO_4$ solution, the minimum one in the Na_2SO_4 solution, and the former was ten times higher than the latter. Local hydride formation disrupting the surface film during the cathodic polarization was key step, the mechanism of dissolution of the alloy during cathodic polarization in the H_2SO_4 solution, however, was different with that in the NaOH and Na_2SO_4 solutions. Experiment showed that hydrogen dissolved in the specimen could accelerate the cathodic corrosion.

Introduction

Our experiment showed that when TiAl was electrolyticly charged with hydrogen in various aqueous solutions or fused salt, the alloy, as a cathode, sustained severe corrosion. As a result, it is not able to investigate the susceptibility of hydrogen induced cracking during dynamically charging of TiAl alloy yet.

Kaesche found that the dissolution rate of a pure Al during cathodic polarization because of the increase of PH value of the solution around the Al specimen as cathode and called it cathodic corrosion[1]. Pourbaix called one kind of corrosion, in which the potential was in the corrosion area of the potential-PH figure, as cathodic corrosion[2]. The cathodic corrosion of an alloy, however, should be different with that of pure metal. The cathodic corrosion of the TiAl can not be explained based on the potential-pH figures of Ti and Al or the alkalification of the solution on interface caused by cathodic polarization, for the TiAl did not suffer corrosion in alkaline solution in the open circuit potential. For titanium aluminides, the terminal solubility of hydrogen in matrix in equilibrium with the hydride at room temperature was very low[3,4],

so that virtually all hydrogen thermally charged was precipitate as hydride upon cooling. Examination of the charged and cooled TiAl alloy revealed very extensive hydride formation[4-6], broadly comparable to that in Ti_3Al+Nb material[3,7]. Recent work showed that hydrogen atoms could enter into the interstitial sites in TiAl and a tetragonal hydride $(TiAl)H_X$ formed during cathodic charged at room temperature[8]. Is it possible that the cathodic corrosion of TiAl is due to local hydride formation disrupting the surface? Our experiment, however, indicated that Ti_3Al+Nb and Ti_3Al, which could also form hydride after thermal charging and cooling or during cathodic charging at room temperature, has not cathodic corrosion. Therefore, at least the cathodic corrosion of TiAl can not be completely due to hydride formation. The purpose of this work is to investigate the cathodic corrosion in various medium, e.g., acid, alkaline and salt solutions and molten salt and the effect of hydrogen out it, then to see if any obtained results can provide insight into the mechanism of the cathodic corrosion.

Experiment Procedures

The TiAl material used in this paper had the following composition (in atomic%):Al=49.5, Fe=0.16, O=0.12, N=0.005, H=0.14, balance Ti. It was in the form of a cast and homogenized ingot. The thin specimens with thickness of 0.8mm were sealed in evacuated tubes and heat treated at 1250°C followed by air cooling, then annealed at 900°C for 2 hours to stabilize the microstructure. The microstructure of all specimens was on equiaxed grains of single-phase γ[9]. After heat treatment, all specimens were graund , polished and then ultrasonically cleaned in acetone.

The rate of corrosion was measured based on the weight loss of the specimen, determined by an analytical balance with a sensitivity of 10^{-4}g. The weight of the specimen was about 1g, thus the error in weight was less than 10^{-2}%.

The tests of the cathodic corrosion carried out in acid solutions of pH=0.2($0.5MH_2SO_4$), 2($0.5MNa_2SO_4+H_2SO_4$) and 2.5($H_2SO_4+CS_2$); alkaline solution of pH=13(0.5MNaOH); salt solution of pH=6($0.5MNa_2SO_4$) and the molten salt at 160°C (50%$NaHSO_4$+50%$KHSO_4$), respectively. The pH value of the solutions would increase slightly during cathodic corrosion, e.g. from 0.2 to 0.3 in the $0.5MH_2SO_4$ solution and from 6 to 7 in the $0.5MNa_2SO_4$ solution, etc.. Pt was chosen as anode.

In order to investigate the influence of hydrogen on the cathodic corrosion, hydrogen recombination poison As_2O_3 (250mg/l) was added in the Na_2SO_4 solution with pH=6, resulting in increase of the hydrogen concentration on the surface and in the interior of the specimen during cathodic corrosion, i.e. the cathodic charging. In addition, the variation of the cathodic corrosion rate with the time of charging with hydrogen in the molten salt, i.e., the amount of hydrogen had been investigated.

The corrosion product on surface of the specimen was analyzed by the method of X-ray Photoelectron Spectroscopy (XPS). The matters fallen into the solution during cathodic corrosion in the alkaline solutions and the hydride formed during cathodic charging have been determined by X-ray diffraction.

Experiment Results

1. Polarization curve and corrosion rate

The corrosion rate of the TiAl alloy immersed in solutions with pH from 0.2 to 13 for 225hrs were listed in table 1. It was indicated that the observable corrosion occurred only in the acid solution with pH < 2 in the open circuit condition.

The polarization curves in the $0.5MH_2SO_4$, $0.5MNa_2SO_4$ and 0.5MNaOH solutions were measured using potentiostatic method, as shown in Fig.1.

Table 1. The corrosion rate of TiAl in different aqueous solutions

pH	Solution	Corrosion rate mg/cm^2, h
0.2	$0.5MH_2SO_4$	0.43
2	$0.5MNa_2SO_4+H_2SO_4$	0.01
2.5	$H_2SO_4+CS_2$	0
6	$0.5MNa_2SO_4$	0
13	0.5MNaOH	0

2. Anodic dissolution and cathodic corrosion under the constant potential

Under the condition of constant potential, the variation of the rate of anodic dissolution and cathodic corrosion in the $0.5MH_2SO_4$ solution of pH=2 with potential difference was shown in Fig.2. It was indicated that the rate of the cathodic corrosion was 3-8 times higher than that of anodic dissolution under the same potential difference. The rate of the cathodic corrosion increased rapidly with the increment of the applied potential difference while the rate of anodic dissolution approached saturation quickly. On the other hand, severe corrosion pits appeared under the anodic polarization, in contrast with the general corrosion under the cathodic corrosion.

3. Cathodic corrosion under constant current

The rate of the cathodic corrosion in the $0.5MH_2SO_4$ solution increased linearly with increasing the cathodic current and it was also true even in the alkaline and salt solutions, as long as the cathodic current was higher than a critical value, as shown in Fig.3. Fig.3 indicates that the rate of cathodic corrosion is the lowest in the salt solution with pH=6, the highest in the H_2SO_4 solution and the latter is ten times larger than the former in the same current.

4. Effect of hydrogen on the cathodic corrosion

Adding the hydrogen recombination poison As_2O_3 of 250mg/l into the $0.5MNa_2SO_4$ solution, the rate of the cathodic corrosion would evidently increase, as shown in Fig.4.

During cathodic corrosion or called as cathodic charging in the molten salt at 160°C under constant current, the specimens as cathode were taken out to weigh per hour and then put into the electrolyte immediately or after polished the surfaces to remove the film, the variations of the weight loss with the time of charging with hydrogen were obtained, as shown in Fig.5. From Fig.5, the weight loss per area $\Delta w/A$ and the rate of cathodic corrosion V could be got as follows:

$\Delta w_1/A=0.118t-0.011t^2+0.006t^3$ $v_1=0.118-0.022t+0.018t^2$ with surface film

$\Delta w_2/A=0.483t-0.064t^2+0.011t^3$ $V_2=0.483-0.128t+0.033t^2$ without surface film

The rate of cathodic corrosion in the molten salt increases with increasing time of cathodic charging. That is to say that the rate of cathodic corrosion increases with the increment of the hydrogen concentration in the specimen. Fig.5 also shows that the rate of cathodic corrosion in the molten salt will increase when the surface film or corrosion product was removed.

5. Affirmation of the corrosion products

During the cathodic corrosion in the salt or alkaline solutions, a lot of small pieces fell into the solution, which were white, then changed quickly into black. They were affirmed as the mixture of Ti_2O_3 and $(TiAl)H_X$ based on X-ray diffraction, as shown in Fig.6.

There was, however, no any precipitate during the cathodic corrosion in the acid solution. While dropping NaOH into the acid solution after the cathodic corrosion, white precipitate appeared first and then dissolved by shaking the solution. It means that there should be Al^{3+} ion in the solution after cathodic corrosion in the H_2SO_4 solution. The corrosion solution would become red after adding H_2O_2 and adding excessive amount of NaOH into the solution produced white precipitate. This means that there is also TiO^{2+} ion in the H_2SO_4 solution after cathodic corrosion because

$TiO^{2+} + H^2O_2 \rightarrow [TiO(H_2O_2)]^{2+}$ $TiO^{2+} + 2OH^- + H_2O \rightarrow Ti(OH)^-_4$

where $[TiO(H_2O_2)]^{2+}$ is red and $Ti(OH)_4$ is white precipitate.

Analysis by XPS showed that there were Ti^{4+} and Al^{3+} ion on the surface of the specimen after cathodic corrosion in the H_2SO_4 solution, as shown on Fig.7.

X-ray diffraction results for the sample before and after cathodic corrosion in $0.5MH_2SO_4$ solution was identical with Figure 1 in Ref.[8], which revealed that a hydride phase $(TiAl)H_X$

was formed during cathodic corrosion, i.e., cathodic charging.

A shining and reflective surface film existed on the specimen after cathodic corrosion in the molten salt, which consisted of Ti^{4+}, Al^{3+} ion and metal Al based on the analysis of XPS.

Discussion

1.The cause of cathodic corrosion

These were oxide films on the surface of the TiAl alloy and the outer layer was TiO_2, the inner one was mixture of TiO_2 plus Al_2O_3[10]. The surface film was stable and there was no corrosion in the aqueous solution with $pH \geq 2$ and in the molten salt at 160°C. Because hydrogen atoms could enter into the interstitial sites in TiAl and a tetragonal hydride $(TiAl)H_{0.5}$ formed during cathodic charging at room temperature, resulting in a large volume expansion[8], the local hydride formation would disrupt the oxide film on the surface.

The fresh metal will expose to the solution after the oxide film was disrupted by hydride formation and then Ti and Al in the alloy will react with the H^+ ion during the cathodic polarization, i.e.,

$$Ti + 3H^+ \text{--> } Ti^{3+} + 3H \qquad Al + 3H^+ \text{--> } Al^{3+} + 3H \qquad (1)$$

Ti^{3+} is very easy to be hydrolysis into TiO^{2+}, i.e.,

$$4Ti^{3+} + 2H_2O + O_2 \text{--> } 4TiO^{2+} + 4H^+ \qquad (2)$$

As a result, the alloy is dissolved and cathodic corrosion occurs.

Table 2. The amount of H^+ in various reaction during cathodic corrosion in $0.5MH_2SO_4$ solution

i mA/cm^2	Δg/st $mg/cm^2.h$	$[H^+]_i$ $mg/cm^2.h$	$[H^+]^{\bullet}_{TiAl}$ $mg/cm^2.h$	$[H^+]_{TiAl}$ $mg/cm^2.h$	pH	$-\Delta[H^+]$ $mg/cm^2.h$
0	0.43	0	0.04	0.03	0.21	0
187	3.53	6.96	0.31	0.29	0.25	0.34
244	5.25	9.13	0.48	0.40	0.30	0.51
514	8.34	19.13	0.74	0.62	---	---

During the cathodic polarization in the salt or alkaline solutions if the cathodic current is larger than a critical value, a enough high atomic hydrogen concentration gradient can also be

established on the surface resulting in local hydride formation disrupting the oxide films. The pH value near the surface of the specimen as a cathode increases evidently in consequence of reaction of Eq.(1), and then the Al in the alloy will be dissolved preferably in the solution with local alkalinity, as follows

$$Al + 4OH^- \dashrightarrow Al(OH)_4 + 3e \qquad (3)$$

Because of the preferable dissolution of Al and the hydride formation, Ti and hydride as a small piece would peel off in the solution and Ti was oxidized as Ti_2O_3 during the cathodic polarization in the salt and alkaline solutions, as shown in Fig.6.

During the cathodic corrosion in the acid solution, one part of H^+ ion would react with TiAl and the other would contribute to cathodic current. The amount of H^+ ion forming cathodic current per time and reaction area, designated as $[H^+]_i$, could be obtained based on the reaction of $H^+ + e \rightarrow H$, which is listed in third column of Table 2. According to the equivalent law, the amount of H^+ ion per time and reactive area necessary to dissolve the alloy, designated as $[H^+]^*_{TiAl}$, could be estimated from Eq.(1) and has been listed in 4th column of Table 2. The hydrolysis of Ti^{3+} will result in increase of concentration of H^+ ion. Combining Eq.(2) with Eq.(1), we can get

$$Ti + 2H^+ + 0.5H_2O + 0.25O_2 \dashrightarrow TiO^{2+} + 3H^+ \qquad (4)$$

The real amount of H^+ ion necessary to dissolve TiAl alloy, designated as $[H^+]_{TiAl}$, which is less than $[H^+]^*_{TiAl}$ because of the hydrolysis of Ti^{3+}, has been calculated, as listed in 5th column of Table 2. It shows that $[H^+]_{TiAl}$ is one order of magnification lower than $[H^+]_i$. Based on the Table 2, $[H^+]_{TiAl} = \alpha[H^+]_i$ where $\alpha = 0.04$. Because $H_2O \dashleftarrow\dashrightarrow H^+ + OH^-$, where $[H^+] = [H^+]_{TiAl} + [H^+]_i$ ignoring the effect of polarization, OH^- ion in the solution during cathodic corrosion was inevitably excess, and the pH value of the whole solution would increased. The larger the cathodic current was, the higher the $[H^+]_{TiAl}$ and then the pH value of the solution, which has been proven by our experiment. The pH values of the acid solution after cathodic corrosion for 24 hours under various constant currents were measured and shown in Table 2 too. The amount of H^+ ion consumed during the cathodic corrosion for 24 hours, designated as $\Delta[H^+]$, could be calculated according to the difference of the pH value, the volume of the solution and the area of the specimen, as listed in the last column of Table 2. Comparing $\Delta[H^+]$ with $[H^+]_{TiAl}$, it can be seen that $\Delta[H^+]$ calculated on the difference of the pH value in the solution is near to $[H^+]_{TiAl}$ calculated on Eq.(1) and Eq.(2) by using the weight loss. Consequently, the dissolution reaction of the TiAl alloy should occur according to Eq.(1) during the cathodic corrosion in the acid solution.

2. Accelerate role of hydrogen on cathodic corrosion

A part of atomic hydrogen generated during the cathodic polarization would enter into the surface layer and diffuse into the specimen. The atomic hydrogen dissolved in the specimen will change

the energy of the system resulting in an acceleration of the cathodic corrosion. The rate of the cathodic corrosion in the specimen containing hydrogen v(H) could be obtained as follows[11]

$$v(H)=v_0\exp[-(\Delta E-T\Delta S)/RT] \qquad (5)$$

where v_0 stands for the rate of the cathodic corrosion of the specimen without hydrogen, ΔE and ΔS for the change of the internal energy and entropy induced by hydrogen, respectively.

Calculation showed that when hydrogen concentration c=1atom%, $v(H)/v_0=1.25$[11]. Although the solubility of hydrogen in the TiAl alloy was lower[4], the instantaneous concentration of hydrogen on the surface of the specimen should be very high during the dynamic charging with hydrogen, i.e., the cathodic corrosion. It means that hydrogen can increase the dissolution rate during dynamic charging with hydrogen, i.e., the cathodic corrosion. It has been proved that hydrogen could accelerate anodic dissolution of the austenitic stainless steel[11]. Fig.(4) indicates that the rate of cathodic corrosion in the Na_2SO_4 solution with As_2O_3 is 1.8 times higher than that without As_2O_3, which is higher than the calculated value 1.25[11]. It means that hydrogen increases the dissolution rate by some other methods except for changing the internal energy and entropy.

Hydrogen dissolved in the metals could increase the mobility of metal atoms resulting in accelerating order-disorder transformation[12]. It is evidently that the increase of the mobility of the metal atoms, particularly on the surface, must accelerate the dissolution of the metal. Since the corrosion is a process of charging with hydrogen, the rate of the cathodic corrosion should increase with the increase of the charging time because of the increase of hydrogen concentration in the specimen, which has been confirmed in the Fig.5.

The severe cathodic corrosion occurred in various solution and the molten salt for the titanium aluminide TiAl, for another titanium aluminide Ti_3Al, however, there was no cathodic corrosion in any aqueous solution and molten salt, for the Ti-24Al-11Nb alloy, a slightly cathodic corrosion occurred only in the $0.5MH_2SO_4$ solution. The reason may be due to the difference of the oxide films on the surface for the different titanium aluminides. Maybe, the oxide film of Ti_3Al can not be disrupted by the local hydride formation.

Conclusions

1. The titanium aluminide TiAl can undergo severe corrosion during cathodically charged with hydrogen in various aqueous solution and the molten salt , called it as cathodic corrosion.

2. The rate of the cathodic corrosion had the maximum value in the acid solution and the minimum in the salt solution; the former was ten times larger than the later in the same current.

The mechanism of the cathodic corrosion in the acid solution was different with that in the alkaline or salt solution.

3. The rate of cathodic corrosion under a constant potential was much higher than that of anodic dissolution under the same potential differences. The rate of the cathodic corrosion under constant current increased linearly with increasing the current.

4. The atomic hydrogen dissolved in the specimen could accelerate the cathodic corrosion.

References

[1] H. Kaesche, Z. Phys. Chem, 34(1962), p.87.

[2] M. Pourbaix, Lectures on Electrochemical Corrosion, Plenum press, New York-London, 1973, p.8.

[3] W. Y. Chu, A. W. Thompson and J. C. Williams, Acta Metall. Mater., 40(1992), p.455.

[4] W. Y. Chu, A. W. Thompson, Scri. Metall. Mater., 25(1991), p.2133.

[5] D. Legzdian, I. M. Robertson and H. K. Birnbaum, J. Mater. Res., 6(1991), p.1230.

[6] D. E. Matejczyk and C. G. Rhodes, Scri. Metall. Mater., 24(1991), p.1369.

[7] W. Y. Chu, and A. W. Thompson, Metall. Trans.A, 23A(1992), p.1299.

[8] J. Gao, Y. B. Wang, W. Y. Chu, C. M. Hisao, Scri. Metall. Mater., 27(1992), p.1219.

[9] K. W. Gao, W. Y. Chu, Y. B. Wang, C. M. Hsiao, Scri. Metall. Mater., 27(1992), p.555.

[10] Y. Umakshi etal, J. Mater. Sci., 24(1989), p.1599.

[11] L. J. Qiao, W. Y. Chu, J. M. Xiao, Science in China, 35A(1992), p.505.

[12] W. Y. Chu and A. W. Thompson, Scripta Metall, 25(1991), p.2133.

[13] H. Noh, T. B. Flanagan, M. H. Ransick, Scripta Metall, 26(1992), p.353.

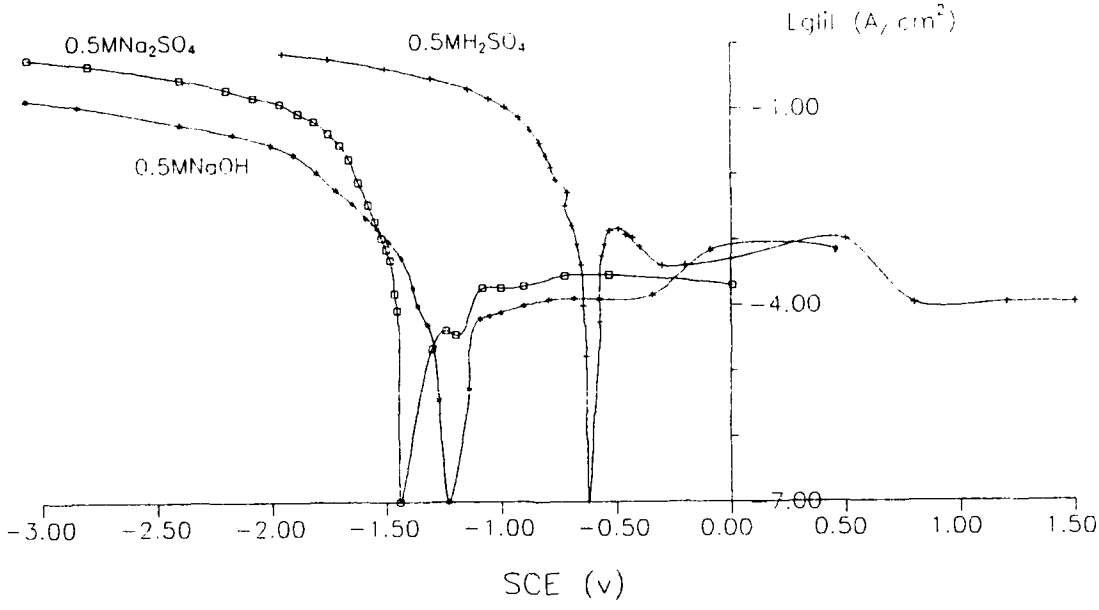

Fig.1 Polarization curves of TiAl in $0.5MH_2SO_4$, 0.5MNaOH and $0.5MNa_2SO_4$, respectively.

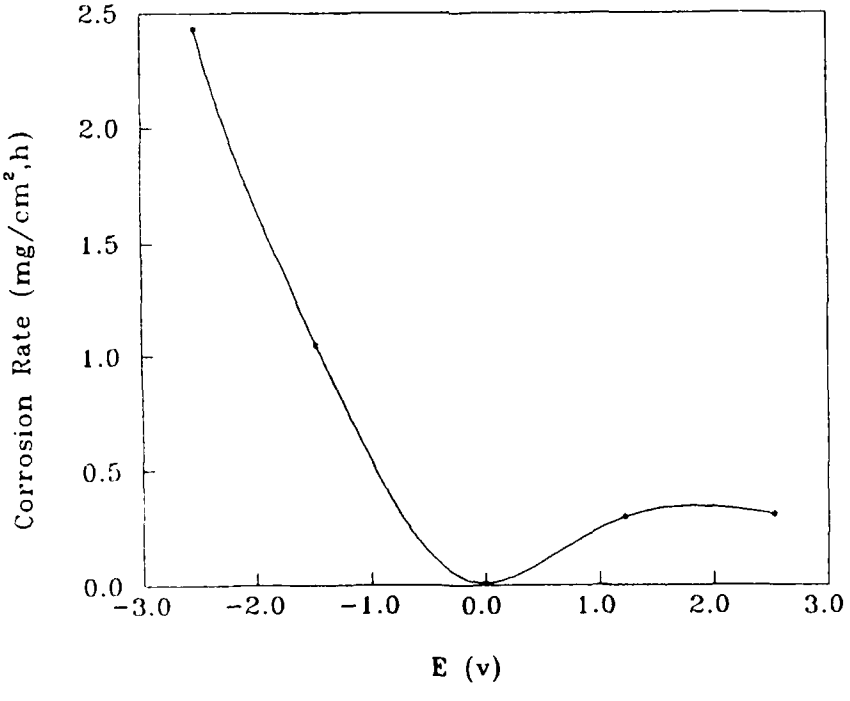

Fig.2 Variation of the anodic dissolution and cathodic corrosion of TiAl with the applied constant potential ($0.5MNa_2SO_4+H_2SO_4$, PH=2, t=24 hours)

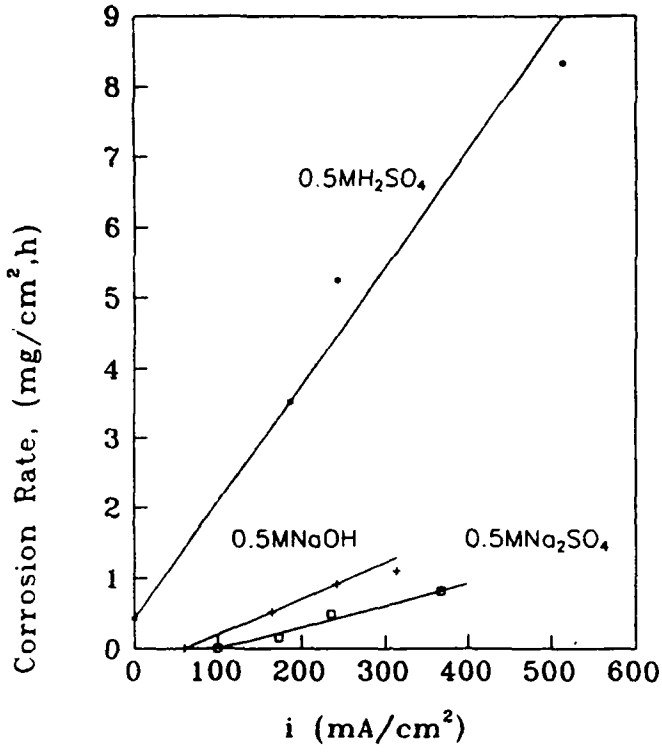

Fig.3 Rate of cathodic corrosion vs. current density under constant current condition in H_2SO_4,NaOH and Na_2SO_4 solution, respectively.(t=25 hours)

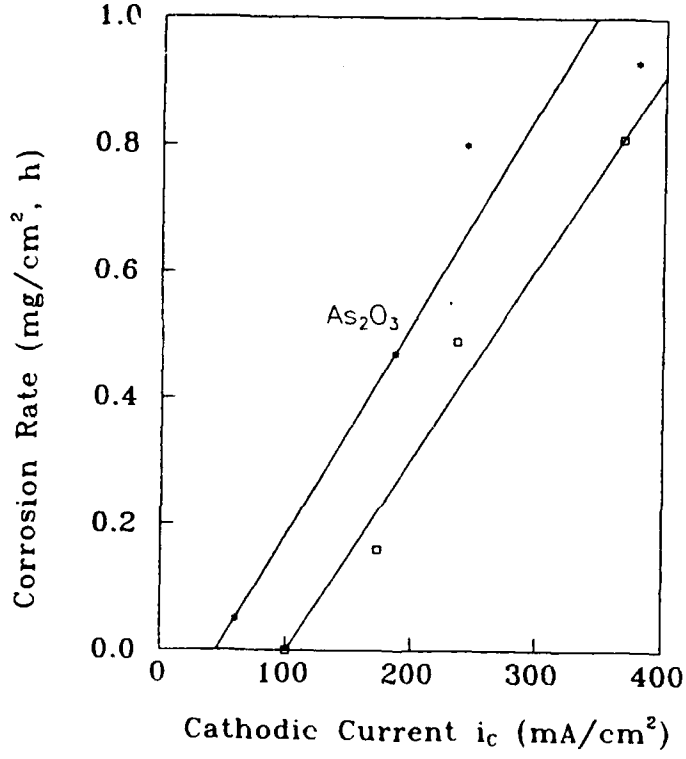

Fig.4 Effect of poison As_2O_3 on the rate of cathodic corrosion in Na_2SO_4 solution with PH=6 under constant current (t=70 hours)

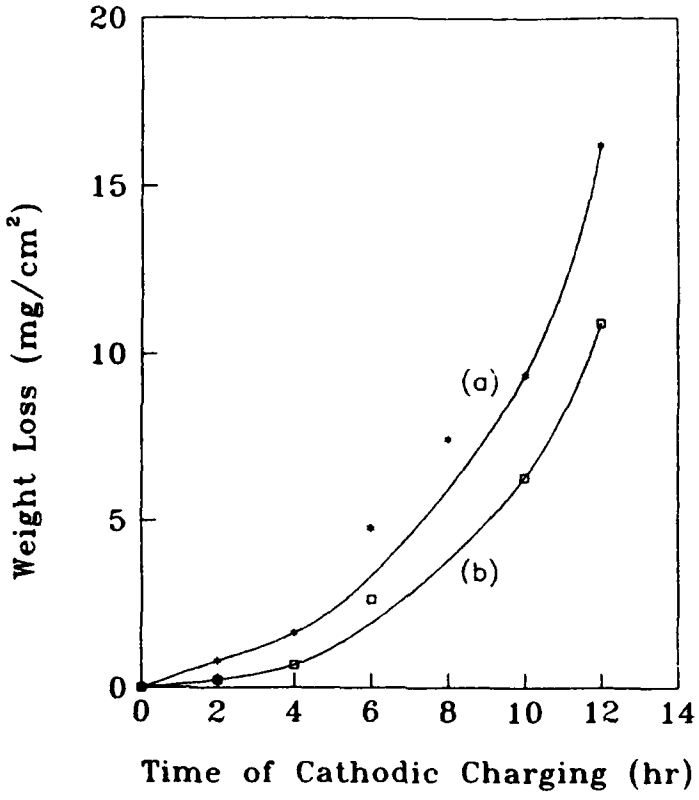

Fig.5 Variation of weight loss under cathodic corrosion in a fused salt at 160°C with the charging time (i=30mA)
(a) With original surface
(b) With surface polished after cathodic corrosion

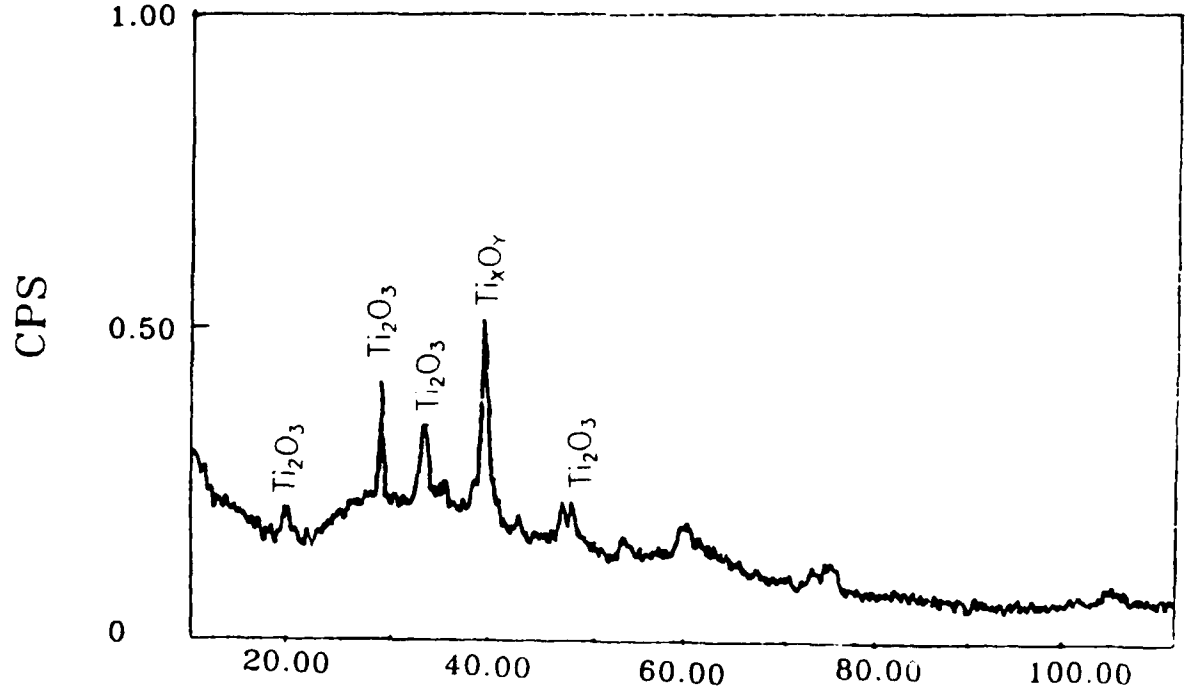

Fig.6 X-ray diffraction of corrosion produce during cathodic corrosion in 0.5MNaOH solution

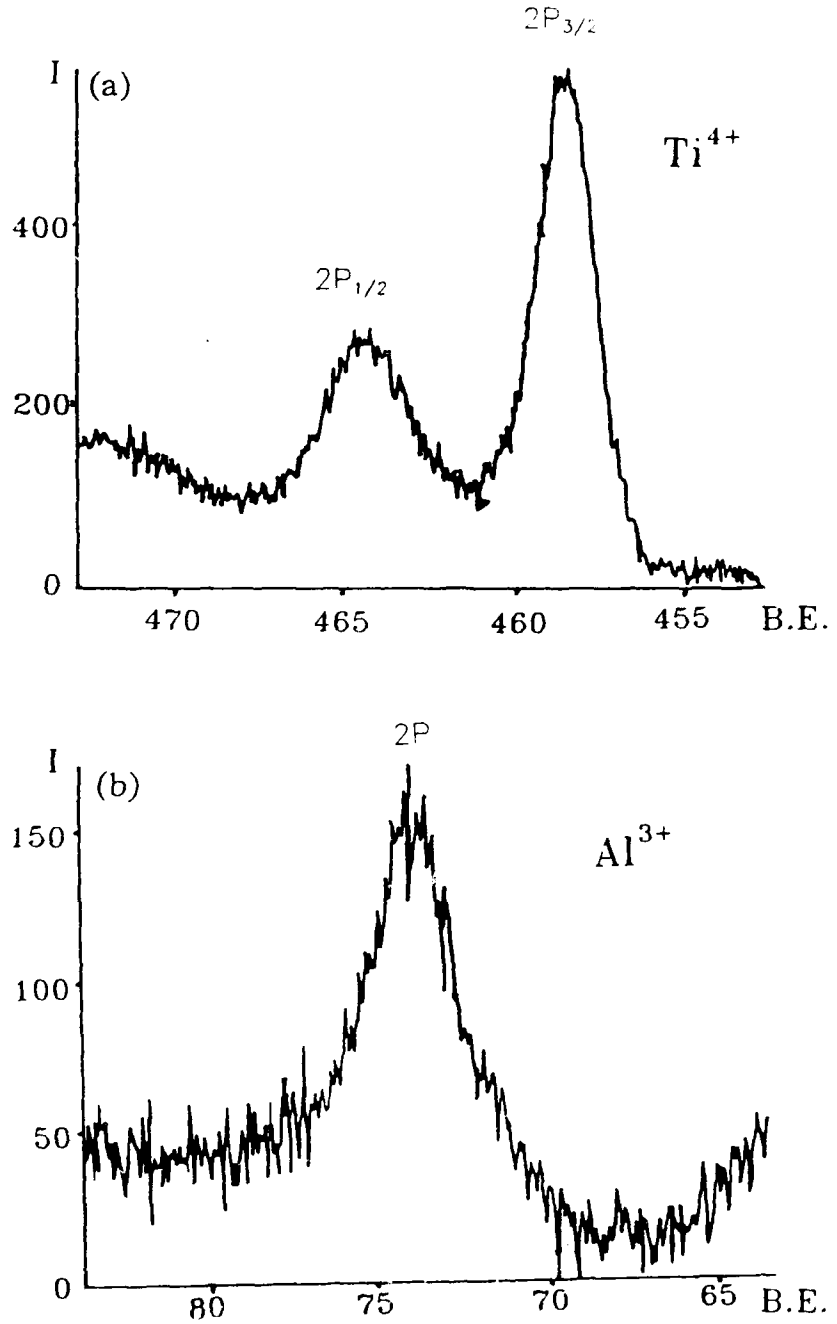

Fig.7 Element analysis by XPS on the surface layer after cathodic corrosion in the H_2SO_4 solution

USING REAL-TIME HOLOGRAPHY TO MONITOR STRESS CORROSION CRACKING INITIATION

V. H. Desai
Material Science and Engineering Program
Mechanical Engineering Department
University of Central Florida
Orlando, Florida

E. L. Principe
Engineering Mechanics Department
Pennsylvania State University

Lily Qian-Falzone
Mechanical Engineering Department
University of Central Florida
Orlando, Florida

F. A. Moslehy
Mechanical Engineering Department
University of Central Florida
Orlando, Florida

ABSTRACT

Stress corrosion cracking (SCC) has long been a topic under extensive study due to its unpredictable nature and catastrophic effects. In this paper, technique based upon coherent optical methods, namely real time holographic interferometry (RTHI) as means of monitoring the initiation of SCC is described. The advantage of this technique includes high sensitivity and the ability to conduct testing in-situ in a non-invasive manner. By using RTHI, the initiation activity of SCC could be observed before the crack is microscopically noticeable. The method is capable of detecting stress corrosion crack initiation and in conjunction with laser speckle photography can provide an excellent means of monitoring crack propagation.

INTRODUCTION

Stress corrosion cracking occurs when a susceptible alloy under stress (typically much below the yield stress limit) is exposed to a specific environment. Due to its rapid growth rate and hard to detect nature, SCC often goes undetected until it is too late. Virtually all alloys are susceptible to SCC in a specific environment producing brittle cleavage-like cracking in an otherwise ductile material[1]. Although SCC is one of the most intensely studied problems in corrosion, the mechanism which governs its behavior is still not fully understood. The complex interaction between the material, environment and the stress field during its progress makes SCC one of the hardest problems to study. For justifiable reasons, more effort and funds have been expended on stress corrosion than on all other forms of corrosion combined[2].

The susceptibility of an alloy to SCC depends upon its resistance to crack initiation and propagation. Many alloys, such as titanium in chloride environments, are resistance to SCC by virtue of the long incubation time, t_i, required to initiate the crack while the crack propagation is quite rapid[3]. It would be of interest to determine what effect the microstructure or the environment or the stress field has on t_i. However, the sensitivity of the technique determining the t_i decides the accuracy of the results. More sensitive the technique, sooner we would be able to detect the crack after it has initiated. Conventional techniques usually report crack initiation long after it had occurred, therefore these data could not be considered as actual initiation data[4]. Real time holographic interferometry enable us to visually observe the initiation taking place as it happens, and the resolution of the technique could be as good as 0.3 micrometer (micron) with He-Ne laser used in this experiment. Although this is not the very first attempt to apply holography to SCC, there are only two other known documented previous studies[5,6]. This work further explored the approach Vest first implemented.

Another coherent optical technique used in conjunction with RTHI is the laser speckle photography (LSP). While RTHI is primarily sensitive to out-of-plane components of the surface displacements, LSP is yields in-plane surface displacement components. This technique could be used to monitor advancing crack front to determine the crack width, and to calculate the stress field state surrounding the crack tip. Therefore, used in conjunction, LSP and RTHI are complementary in SCC characterization studies.

Holography is a technique for recording and reconstructing coherent light waves[7]. Using holographic interferometry, one can produce a three-dimensional lensless reproduction of an original object. The fact that holograms are created using coherent laser light allows sensitive measurement to be made of the relative motion between the original object and the reconstructed virtual image. This is accomplished by observing and interpreting the resulting interferometric fringes superimposed on the images. The dark and light bands formed correspond to displacement which are multiples of half the wave length of the laser light. Schematic of the real-time holographic interferometry setup is shown in figure 1.

Laser speckle pattern is created as a result of constructive and destructive interference occurring across the optically rough surface of the object. They serve as a "finger print" describing the surface state of the specimen. The pattern is imaged on high resolution glass plate. In double exposure laser speckle photography, the speckle pattern is recorded for the same specimen in a different state for each of the two exposures. The specklegram consists of a set of identical speckle pairs separated spatially a distance proportional to the local in-plane displacement. When a laser is shone through the specklegram it produces young's fringes. The interspacing and direction of fringes determine the magnitude and direction of in-plane displacement. Hybrid analysis can then be utilized to determine stress field at advancing crack front.

EXPERIMENTAL SETUP

The primary material selected for this study is 70/30 α brass. The material allows easy cracking at ambient conditions in ammoniacal solution thus simplifying experimental setup. Also, the microstructure of the alloy remains single alpha phase throughout a wide range of temperature, so that the grain size can be easily adjusted by simply heat treating the material. For this study, heat treatment was performed at a temperature of 750 C with times ranging from four to twenty-four hours. It is highly unlikely that hydrogen embrittlement could play a role based on thermodynamics consideration alone. Brass undergoes SCC in both the trans and intergranular mode and that a careful selection of the environment would force it to crack in one mode or the other[8]. Thus both modes of propagation and the effect of grain size can be studied in this system quite readily.

The specimens were made into four-point-bend (FPB) configuration. A starter notch was cut on one side of it using a fine blade jeweler's saw. Thus a high stress concentration point is manually created where SCC is most likely to initiate.

The specimens were stressed using a manual screw-driven load frame. The loading system was setup on a research series Newport vibration isolation table to satisfy the high stability requirement for holography. (figure 2) A static load was then applied. After the relaxation period which typically lasted 2 hours, the electrolyte was introduced through a thin tube to the highly stressed crack tip. Testing was continued until a "through the thickness" crack resulted. This was determined by examining the degree of fringe localization which become apparent during the testing. Video tape recordings were made of the crack growth which illustrate the evolution and character of the dynamic fringe patterns.

Double exposed images of a laser speckle surface at two different state were filmed on a high resolution glass plate. Young's fringes were then created by shinning a unexpended laser beam through a interested point on the grass plate. Using point wise filtering, the in-plane displacement of the surface could be calculated from these young's fringes. These displacement data were then input into a finite element analysis program, the region of interest around the crack was partitioned and treated as a separate domain

The domain was then modeled by 143 finite elements. This study is classified as hybrid analysis, and the stress field around the cracked region was calculated using this method.

RESULTS AND DISCUSSION

The initiation of SCC is represented by the localization of fringes around the crack tip. It is difficult to appreciate the power of real-time holography through presentation of still images. The strength of the technique lies in its ability to visualize minute changes while being subjected to SCC. The images presented here are meant to provide a feel for the type of observations which can be made using this sensitive technique.

Shown in figure 3 is an image of specimen SPC3I having an initial load of 120 lbs. After an exposure time of 1 hour and 52 minutes. Localization of fringes has just begun to occur around the area of the crack tip. After a period of 5 hours and 20 minutes a new hologram was made and definite signs of initiation become evident. (Figure 4) This specimen was removed and examined using both optical and scanning electron microscopy (SEM) and no surface crack was visible. The sample was then pulled apart and the fracture surfaces were examined. It was observed that SCC fracture had occurred within the thickness of material and had progressed within 10 micron of the surface but had not yet become a through and through crack. These observations clearly establish the superior sensitivity of RTHI in detecting SCC initiation.

Figure 5 shows specimen SPC4I (initial load 160 lbs) after only a period of 2 hours and 5 minutes. This image was captured after initiation and it can be observed that the point of fringe localization has moved away from the starter notch. This specimen was permitted to continue cracking. Figure 6 shows the same specimen after 6 hours and 15 minutes. Although it has been over 4 hours later and load was still close to 160 lbs., the crack has not propagated much further than is shown in figure 5. Figure 7 shows this specimen after 10 hours and 20 minutes of exposure. The fringes have localized at the new position of the crack tip and the crack path is also visible.

During these tests, the fringe patterns would "flex" and "yawn" routinely in a somewhat energetic manner. It is felt that these fringe behaviors were indicative of the cracking process itself and were not due to external influences such as air currents, external vibration, or rigid body motion. Some period of growth were more active than others and the rate at which the fringe growth occurred was linked to the rate at which the crack propagated.

It is also possible to observe the difference in rates of initiation for specimens with different metallurgical properties. Figure 8 shows specimen SPC8I after only 15 minutes of exposure. Although the crack path is not yet visible, the fringe localization has already moved off from the starter notch. While the load on this specimen is only 85 lbs., the material was cold worked and is the probable cause for this rapid initiation.

A summary of the tests results showing the initiation time as a function of the initial

applied load in shown in figure 9. The purpose of these tests was primarily to demonstrate the feasibility of applying RTHI to initiation studies. The graph shows the expected trend with a reasonable degree of confidence. The sample SPC5I was locally cold worked in a region above the starter notch and subsequent study of the fracture surface showed that propagation had preferentially progressed in this area. Specimen SPC8I was uniformly cold worked to approximately 40% reduction.

Significantly, it was noticed that in the case of α-brass the fringe fluctuation began almost immediately following introduction of the electrolyte. This observation strongly suggests that, at least for this system, there is no real incubation time for the events responsible for the crack initiation. This observation was very consistent and is likely an important conclusion drawn from this work with respect to initiation behavior.

In-plane displacements occurred during crack propagation were measured by LSP around the crack region. These displacement values were used as input data for the Finite Element Model (FEM) on prescribed boundary nodes. Typical stress distribution is displayed in Figure 10. This figure represents the stress developed in the region surrounding the crack during 390 second of crack growth. Thus by repeating the process of displacement measurement and FEM computation, a sequence of stress distribution for each duration of crack growth can be computed. Thus, a complete stress history associated with crack propagation can be obtained.

CONCLUSION

Real time holographic interferometry has proven to be an effective, sensitive tool to detect the initiation of SCC at its very early stage. The technique is preformed real time, in-situ and in a non-intrusive manner.

A crack as small as 10 micron has been detected by RTHI. Therefore, actual initiation time data can be recorded rather than the initiation time plus time lag for detectable crack growth as is done in conventional techniques. In conjunction with LSP, the technique is useful in detecting and monitoring SCC. The technique's sensitivity lends itself to be utilized for a mechanistic study on SCC propagation.

REFERENCES

1. E. N. Pugh, "Progress Toward Understanding the Stress Corrosion Problem", Corrosion, 517-26, 41, 1985.

2. M. G. Fontana, Corrosion Engineering, McGraw-Hill, New York (1986)

3. V. H. Desai, "Stress Corrosion Cracking Studies of Surfical Implant Alloys",

Doctoral Dissertation, The Johns Hopkins University, July 1984.

4. R. Balboian, D. Sheldon, eds. "Corrosion Testing and Evaluation ASTM STP 1000: Silver Anniversary Volume", :39 Philadelphia, Pa., 1990.

5. C. M. Vest, "Holographic Interferometry in Material Testing," Nondestructive Testing, 351-74, Vol. 3, 1972.

6. V. O. Magnitskii, F. M. Mustafa-Zade, "Study of Cast Chromium-Nickel Steel by Holographic Interferometry," Azerb. Neft.Khoz. 10, 63-66, 1979.

7. C. M. Vest, Holographic Interferometry, John Wiley & Sons,Inc, New York 1979.

8. U. Bertocci, E. N. Pugh, "SCC of Brass in Aqueous Ammonia in the Absence of Detectable Anodic Dissolution", *Corrosion*, 40, 439-40, 1984.

9. V. Desai, F. Friedersdorf, T. Shaw, "Study of Transgranular Stress Corrosion Crack Propagation in Austenitic Steel by Load-Pulsing Method", NACE: Proceedings of the First International Conference on Environment-Induced Cracking of Metals in Kohler, 1988.

10 J. A. Beaver, E. N. Pugh, "The propagation of Transgranular Stress Corrosion Crack in Admiralty Metal", Metal, Trans. A., 11A:809, 1980

ACKNOWLEDGEMENT

We acknowledge the partial support of this project from NASA, Kennedy Space Center through a grant.

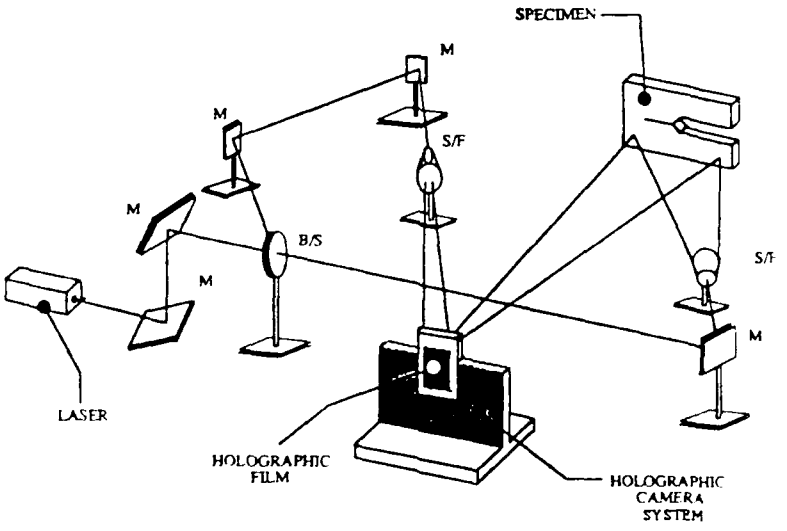

Figure 1 Schematic of basic holography setup.

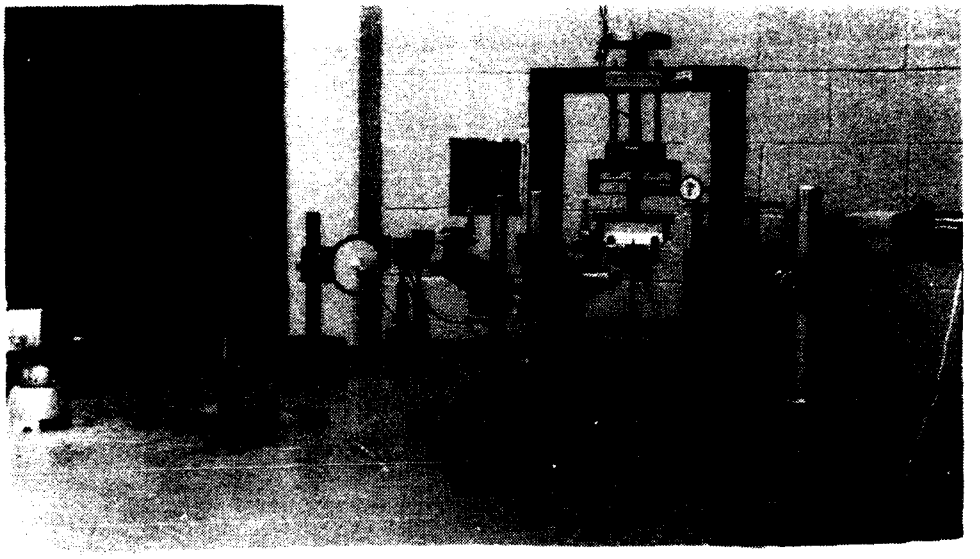

Figure 2 Picture of the Actual Holography Table Setup

Figure 3 Specimen SPC3I after 1 hr. 52 min.

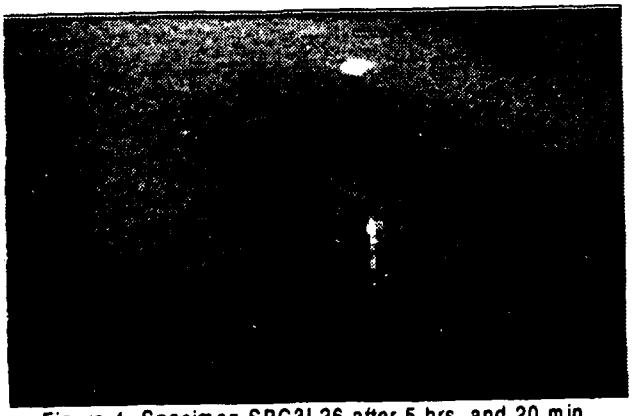

Figure 4 Specimen SPC3I 26 after 5 hrs. and 20 min.

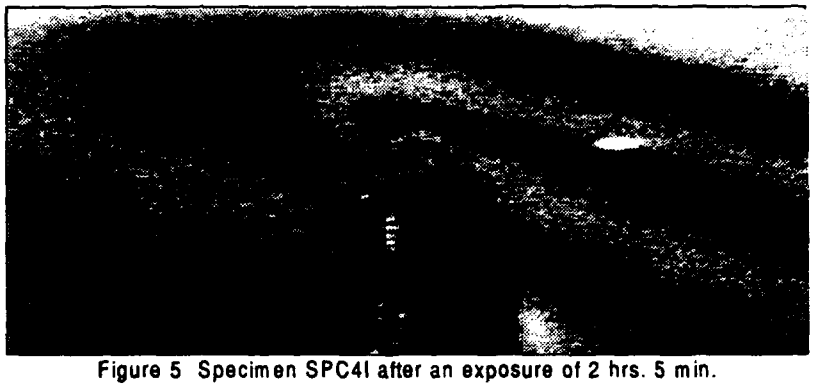

Figure 5 Specimen SPC4I after an exposure of 2 hrs. 5 min.

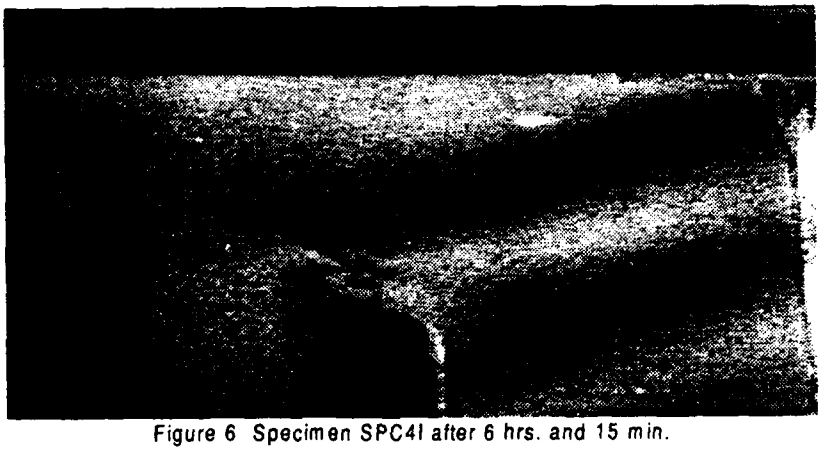

Figure 6 Specimen SPC4I after 6 hrs. and 15 min.

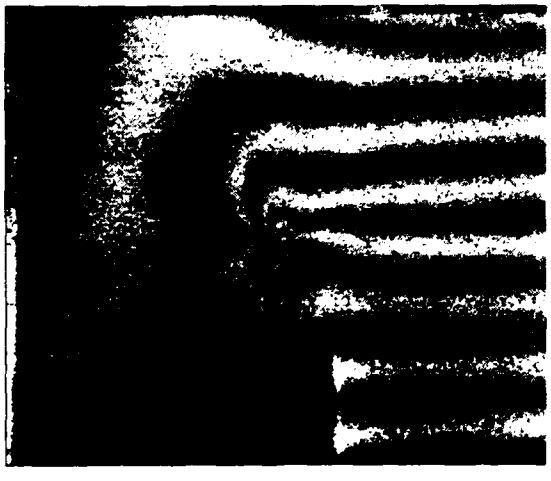

Figure 7 Specimen SPC4I after an exposure of 10 hrs. 20 min.

Figure 8 Specimen SPC8I after only 15 min. of exposure.

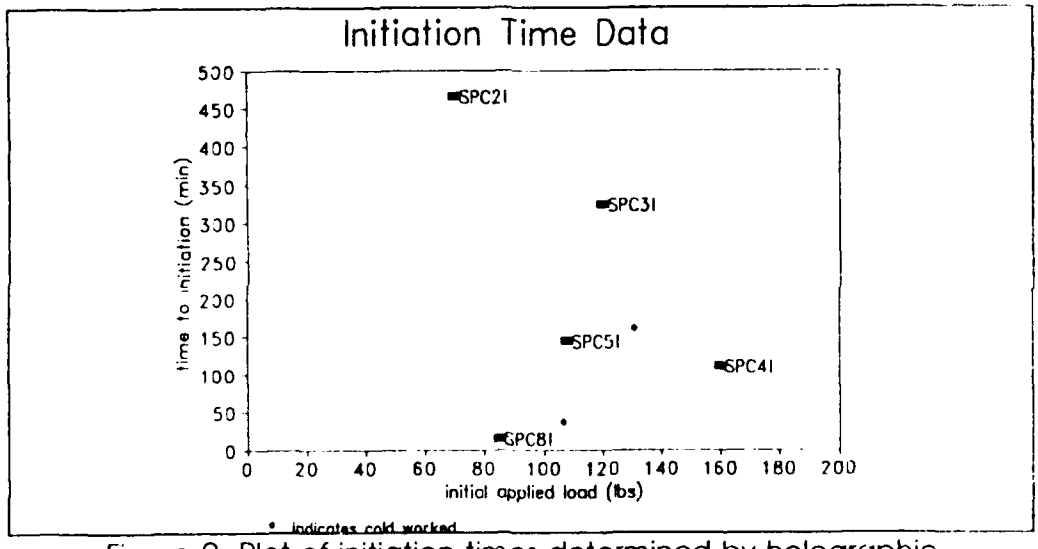

Figure 9 Plot of initiation times determined by holographic interferometry.

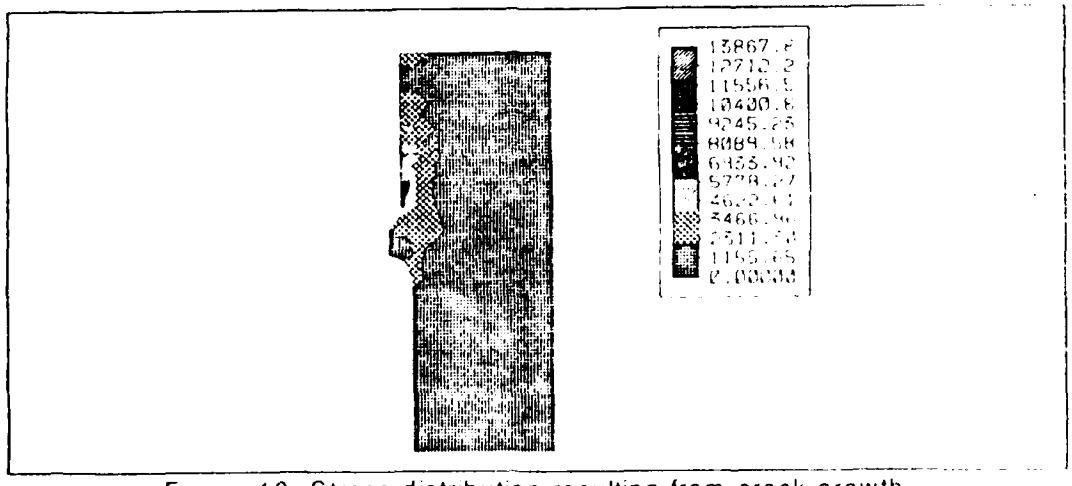

Figure 10 Stress distribution resulting from crack growth

Pre-crack Fatigue Damage and Crack Initiation Under Corrosion Fatigue Conditions

Jane M. Seidel
Materials Engineering Department
Rensselaer Polytechnic Institute
Troy, New York 12180-3590

David J. Duquette
Materials Engineering Department
Rensselaer Polytechnic Institute
Troy, New York 12180-3590

Abstract

Cyclic deformation experiments were performed on polycrystalline nickel at constant strain amplitudes in dry air, and 0.5 N H_2SO_4 at potentials corresponding to the open circuit corrosion potential, at the active-passive transition and in the passive regime. Virtually no change in hardening rate and only slight differences in saturation stress level were observed. Active dissolution of the nickel surfaces resulted in an increase in the cumulative plasticity, preferential attack of the grain boundaries and intergranular crack initiation. At low strain amplitudes, crack initiation and propagation were transgranular in air, at the corrosion potential and in the passive regime. At higher strain amplitudes, cracking occurred in a mixed mode for these environments. Current densities associated with applied potentials fluctuated with each strain cycle. These observations are explained by a model which suggests a strong degree of synergism between local strain events and the environment.

Key terms: nickel, corrosion fatigue, crack initiation, cyclic deformation

Introduction

It is widely accepted that the most damaging effect on engineering components in corrosion fatigue is caused by the interactions between the corrosive environment and cyclic loading [1]. Aggressive environments have been reported to affect different fatigue phenomena such as hardening rate, strain localization, as well as crack nucleation and propagation. On the other hand, cycling can accelerate the corrosion rate through preferential dissolution, pitting attack and film rupture. These interactions ultimately cause the premature failure of the components.

Because crack nucleation is usually a surface related phenomenon, aggressive aqueous solutions, which react with the surface of metals and alloys, often play a significant role in the fatigue crack initiation process. A number of mechanisms have been proposed to explain the reduction of fatigue life in an aggressive environment. These include: pitting [2-4], preferential dissolution [5-10], film rupture [11,12], and surface energy reduction (sometimes called the Rebinder effect) [13]. It is generally accepted that corrosion fatigue processes are so complicated that no single model can completely explain all corrosion fatigue phenomena [14].

It has been shown that cyclic deformation (under load control) of polycrystalline copper during controlled dissolution results in an increase in both the number and height of persistent slip bands (PSB's), as well as in PSB broadening when compared to specimens cyclically deformed in laboratory air [15-16]. Under these conditions, crack initiation and early propagation were confined to grain boundaries. These results have been attributed to a synergistic corrosion-deformation process. According to this model, the preferential deformation associated with near grain boundary regions is further enhanced by surface dissolution, confining the majority of the crack initiation event to the grain boundaries. Once cracking initiates, the generation of new slip bands at the crack tip leads to preferential crack extension in the grain boundary. Thus, surface dissolution causes an alteration in both crack initiation and propagation to an intergranular mode, where only transcrystalline crack initiation and propagation are observed in air.

In order to examine the generality of these results and the validity of the model which has been proposed, a series of corrosion fatigue experiments was undertaken. Additionally, it was decided to examine a different material, nickel, which has similar fatigue deformation characteristics to copper, but exhibits electrochemical passivity in specific potential ranges. This allowed a study of the effect of thin surface films as well as active dissolution of surfaces under conditions of controlled total strain.

Experimental Procedure

Strain-controlled, low cycle fatigue experiments were performed on polycrystalline nickel of 99.99% purity (major impurities: 0.01% carbon, 0.004% tungsten). Polycrystalline specimens were machined from a plate to a square gauge cross section of 4.0 mm and a 10 mm gauge length. The specimens were annealed at 800 °C for 1 hour in an argon atmosphere. The resultant microstructure consisted of an equiaxed grain size of approximately 200 um. Prior to testing, the specimen gauge surfaces were mechanically ground through 600 grit, followed by electropolishing in 50% H_2SO_4 solution at 5 volts for 5 to 8 minutes. The yield stress of the nickel was 40 MPa, while the ultimate tensile strength was 320 MPa.

Total strain-controlled cyclic deformation experiments were conducted in a closed-loop servohydraulic machine in 1.0 Hz with a fully-reversed triangular wave form.

For corrosion fatigue studies, a solution of 0.5 H_2SO_4 was recirculated from a reservoir through an environmental cell which surrounded the specimen. The cylindrical body of the cell was constructed of Plexiglas and included a platinum counter electrode. The cell was hermetically sealed using O-rings. A saturated calomel reference electrode (SCE) was connected to the specimen by means of a salt bridge leading to an external volume of H_2SO_4 solution. Argon was used to deaerate the solution for at least 12 hours prior to testing, and deaeration was continued throughout the experiment.

Experiments were conducted in laboratory air and in 0.5 N H_2SO_4 as a function of applied potential. Specimens were tested at the free corrosion potential of -275mV vs. SCE, at a potential corresponding to the maximum current density measured during cyclic loading (+75mV vs. SCE), and at a potential in the passive regime (+800mV vs. SCE). Polarization curves were measured for static as well as cyclic conditions.

Metallograhic cross sections were examined to determine crack initiation and propagation paths.

Results

Figure 1 shows a typical hysteresis loop obtained in the saturation range of hardening under total strain control of 0.5% (+/- 2.5 x 10^{-3}). Also shown in Figure 1 is a hysteresis curve for the sample after the load was reduced by 5%. At this stage the test was arbitrarily interrupted, and crack "initiation" was defined, since the drop in load was associated with cracking. Figure 2 shows that cyclic deformation of the nickel results in a marked shift in the corrosion potential. However, during cyclic hardening the corrosion potential is essentially constant, the decrease in potential occurring only when stress saturation is reached. Figure 3 shows a comparison of the electrochemical polarization curves for the nickel under a no load condition and during cyclic deformation after stress saturation was reached. These data show that strain cycling results in a reduction in the critical current density, a narrowing of the active-passive transition potential range and a small reduction in the passive current density. Also, cyclic deformation resulted in instabilities or "noise" in the passive current density regime. Based on the polarization results obtained under conditions of cyclic deformation, fatigue tests were performed at the corrosion potential, the potential corresponding tc the critical current density (+ 0.075V vs. SCE) and at a potential in the passive current density regime (+ 0.800V vs. SCE). Figure 4 shows the cyclic hardening curves for each of these environmental conditions, compared to cyclic hardening curves obtained in dry laboratory air. These data indicate that none of the environmental conditions had any appreciable effects on the cyclic hardening behavior of polycrystalline nickel.

Polycrystalline specimens were also cycled to failure during exposure to the same environments. These results are summarized in Table I. At a total strain range of 0.5%, fatigue life in air and in the solution at the open circuit potential were identical. However, in the passive regime the number of cycles to failure was reduced by approximately 25%, and under actively dissolving conditions, the sample life was reduced by approximately 50%. Additionally, longitudinal cross sections of failed specimens tested at a strain range of 0.5% showed that cracking occurred intergranularly in the solution at the potential of maximum dissolution, whereas crystallographic transgranular cracks were observed under the other environmental conditions.

Several experiments were also conducted at a higher strain range of 1.0%. These results (also given in Table I) show that the higher strain caused a shift in the crack path from entirely transgranular, to a mixed mode of intergranular at the surface and transgranular several grains below the surface, for all of the conditions examined. A similar effect was reported by Laird and Smith for polycrystalline nickel tested in laboratory air at high applied strain ranges [17].

The effect of cyclic straining on the current density was investigated by maintaining constant potentials of + 800mV vs. SCE (passive) and + 75mV vs. SCE (active). In the passive case (Figure 5), the current density increased upon application of the cyclic

strain and continued to increase during rapid hardening. At stress saturation the current density approached a steady state value. However, once slip band cracks formed, the stress began to decrease and the current density increased. The current density fluctuated with each strain cycle and exhibited a maximum corresponding to the peak in the tensile quarter cycle, and a minimum corresponding to the peak in the compressive quarter cycle.

Figure 6 shows that, under conditions of active dissolution, the current density decreased upon initiation of cycling and continued to decrease during hardening, reaching a minimum as saturation was approached. During the saturation stage, the current density again approached a steady state value. Upon the initiation of cracking, a more rapid increase in the current density was observed. The current density cycled with strain in a similar manner to that observed in the passive regime, exhibiting a maximum at the peak of the tensile quarter cycle and a minimum at the peak of the compressive quarter cycle.

Figure 7 shows secondary cracks in cross sections of nickel samples cyclically deformed to failure at a total strain range of 0.5%. In air and at the free corrosion potential, multiple transgranular cracks are formed, initiating in slip bands at the surface. At the potential corresponding to the critical current density, however, cracking is entirely intergranular. In the passive regime cracks are again transgranular, initiating at persistent slip bands. Figure 8 shows that, at a total strain range of 1%, crack initiation and initial propagation are mixed transgranular and intergranular in air and in the passive regime. Under active dissolution conditions, however, cracking is entirely intergranular, and occurs at multiple initiation sites.

Table I summarizes the observations described above, and shows that, in air and in a 0.5 N H_2SO_4 solution at the corrosion potential, the number of cycles to crack initiation (N_i), the number of cycles to failure (N_f) and the cracking mode are essentially unchanged. Cyclic deformation in the passive regime results in reduction in both N_i and N_f., although the crack mode is of the same character. Active general dissolution of the surface, on the other hand, results in a marked reduction in both N_i and N_f and the crack mode changes from either transgranular (for small applied strain ranges) or mixed (for large applied strain ranges) to a totally intergranular mode.

Discussion

Exposure of pure polycrystalline nickel to an aqueous 0.5 N H_2SO_4 environment under free corrosion conditions during fatigue does not appreciably alter the fatigue behavior from that developed in air. Specimens cyclically deformed at the open circuit potential exhibit a similar hardening rate, saturation stress, cumulative plasticity, fatigue life, surface deformation structure, and crack path as specimens tested in an air environment. In deaerated acid solutions, the corrosion potential of polycrystalline nickel corresponds to a negligible corrosion rate [18]. Thus, in solution at the free corrosion potential, the specimen is subjected to a very mildly aggressive environment which is not hostile enough to have any impact on fatigue behavior. This supports the hypothesis suggesting that a critical corrosion rate is required to effectively reduce fatigue resistance [4].

On the other hand, the cyclic deformation and fatigue resistance of polycrystalline nickel is affected by exposure to conditions of both active dissolution and passivity. Active dissolution results in increased cumulative plasticity, intergranular crack initiation and propagation, and a reduction in fatigue life, whereas slip band cracking and slightly reduced fatigue life are observed when the metal is passive.

These results can be explained by a mechanism of preferential dissolution at regions of strain localization on the metal surface. This model is based on the fact that slip bands and grain boundaries are known to be regions of high dislocation density. The high energy strain field associated with dislocations favors preferential dissolution at slip bands and at grain boundaries. During fatigue, the cyclic strain, accommodated by the to-and-fro motion of PSB's, provides a continuous source of fresh metal to the environment for further dissolution, resulting in simultaneous strain localization and dissolution localization.

In polycrystalline materials subjected to cyclic deformation, the strain accommodation is partitioned between long, relatively straight persistent slip bands in the grain bodies, and persistent slip bands near the grain boundaries. Because of the complex stress and strain states which exist at grain boundaries, the persistent slip band pattern can be expected to be more complex, involving more slip systems than that in the grain bodies. Further, the PSB density can be expected to be larger, and the corresponding slip step offsets less intense. Thus, under conditions of active dissolution, those regions of highest strain, at the grain boundaries, are preferentially dissolved. This dissolution, in turn, results in the removal of barriers to further slip, effectively enhancing the localization of both deformation and further dissolution [7]. The results of these interactions are grain boundary crack initiation and propagation. It is interesting to note that in this study and in that of Laird and Smith [17], increasing the applied strain range resulted in intergranular initiation of fatigue cracks. Thus, the effect of dissolution of the metal during cyclic deformation is equivalent to increasing the applied strain range. This observation supports the hypothesis that simultaneous dissolution and cyclic deformation results in enhanced local plasticity. The observation that active dissolution also results in enhanced cumulative plasticity also lends considerable support to this concept. The apparent small increase in the saturation stress which develops under active dissolution conditions may be attributed to the increased stress required to sustain the increase in the density of active PSB's at the grain boundaries.

If the metal is passive, rupture of the passive film is required in order for the solution to interact with the metal. When rupture of the passive film does occur, large amounts of current (and associated metal dissolution) are passed as the surface attempts to re-passivate. In this case, the PSB's which are active in the body of the grains are fewer, but more intense than those which occur at the grain boundaries. Thus, it is these PSB's which rupture the passive film, and are preferentially corroded leading to further strain localization which enhances subsequent PSB activity at the metal surface. The result of these interactions is premature crack initiation at those slip bands which rupture the passive film and a concomitant reduction in fatigue resistance.

The observation that the corrosion potential remains essentially constant during rapid hardening and decreases markedly at stress saturation lends further support to the concept that emerging metal associated with slip bands is in an activated state. At

saturation only PSB's are mobile and constitute a small fraction of the total surface area. Thus the effective or relative anodic surface area is reduced, and the effective or relative cathodic surface area is enhanced, leading to an active shift in the corrosion potential.

Strong support for a model of local enhancement of both dissolution and plasticity is also provided by the observations of current fluctuations during cycling, and by the shift of the corrosion and active-passive potentials in the active direction. Under conditions of active dissolution (at the active-passive transition potential), there is an apparent decrease in the measured current density from the beginning of cycling, which does not increase until active cracks have formed. An examination of the polarization curves for nickel in sulfuric acid also indicates that the active-passive transition region of the curve is narrow with respect to potential, and is shifted in the active direction with the onset of cyclic deformation (Figure 3). The active shift in the active-passive transition potential indicate that the active slip bands become the only regions of the metal surface which undergo active dissolution, while the majority of the surface act is passivated. During the rapid hardening period the number of active slip bands is reduced until a stable number of PSB's is reached (at saturation). Thus, the surface area of active metal reaches a constant value and the current density stabilizes. For polycrystalline nickel under conditions of active dissolution, however, intergranular cracks form shortly after saturation is reached, effectively increasing the active surface area, resulting in an increase in the current density. The hysteresis in the current which is observed between the tensile and compressive cycles can be attributed to the lack of complete reversibility of the PSB's. The tensile quarter cycle exposes more fresh metal than does the compressive quarter cycle. Similarly, once cracks have formed, the tensile cycle exposes fresh metal, while the compressive cycle closes cracks.

Under passive conditions, the current density monotonically increases with increasing numbers of cycles. During rapid hardening, the increased current density can be associated with the multiplication of slip lines and the corresponding movement of dislocations that break through the passive film. This enhances the activity of the specimen surface and increases the number of active sites. Upon reaching saturation, the movement of dislocations is localized into PSB's. The number of active sites is reduced and correspondingly, the dissolution rate increases more slowly, as the metal surface attempts to re-passivate. With continued cycling, PSB's are preferentially attacked and eventually cracks develop within the PSB's. At this point, the corrosion rate increases more rapidly due to the increase of exposed metal surface available at the crack surfaces. As in the case of active dissolution, the current density parallels the strain cycle. The tensile portion of the cycle corresponds to a maximum in current density as slip steps rupture the passive film and increase the total surface area of exposed metal. In compression, slip is reversed along slip planes and partial re-passivation occurs. This reduces the amount of exposed metal surface available for corrosion, and therefore, the current density is reduced relative to that which occurs in tension. Similar observations of current fluctuations in the passive regime have been reported by Magnin and his co-workers for ferritic stainless steels [19], and by Pyle and his co-workers for austenitic stainless steels [20].

Conclusions

1. The fatigue behavior of polycrystalline nickel exposed to an aqueous 0.5 N H_2SO_4 solution under free corrosion conditions does not differ from the fatigue response that is observed in air.

2. Cyclic deformation of polycrystalline nickel in a 0.5 N H_2SO_4 solution at a passive potential results in preferential attack and cracking of PSB's, and reduced fatigue life.

3. The fatigue response of polycrystalline nickel tested in 0.5N H_2SO_4 solution under active conditions is characterized by an increase in cumulative plasticity, intergranular cracking, and a reduced number of cycles to crack initiation and failure.

4. The crack path shifts from a transgranular mode to an intergranular mode as the environment becomes more aggressive or as the applied strain range is increased.

5. For applied potential experiments, the current density fluctuates with the strain cycle developing a maximum in tension and a minimum in compression. Crack formation results in an increase in both the tensile and compressive current densities.

These results support a model of synergistic interaction between cyclic deformation and corrosion.

Acknowledgments

One of the authors (Jane M. Seidel) would like to acknowledge the generous financial support provided in the form of fellowships from the Office of Naval Research and W.R.. Grace.

References

1. P.O. Gilbert, Metall. Rev.,1 (1956): p379.

2. D.J. McAdam, Jr. and G.W. Geil, Proc. ASTM, 41 (1928): p696.

3. D.J. McAdam, Jr., Proc. ASTM, 31 (1931): p259.

4. D.J. Duquette and H.H. Uhlig, Trans. ASM, 61 (1968): p449.

5. U.R. Evans and M. Simnad, Proc. Roy. Soc., 188A (1947): p72.

6. R.W. Revie and H.H. Uhlig, Acta Met., 22 (1974): p619.

7. H.N. Hahn and D.J. Duquette, Acta Met., 26 (1978): p79.

8. D. Whitwham and U.R. Evans, J. Iron and Steel Inst., 165 (1950): p79.

9. D.J. Duquette and H.H. Uhlig, Trans. ASM, 62 (1969): p839.

10. B. Yan, Ph.D. Thesis, University of Pennsylvania, (1984).

11. B.H. Gough and D.G. Sopwith, Proc. Roy. Soc., A135 (1932): p92.

12. S.R. Ortner, Ph.D. Thesis, University of Pennsylvania, (1985).

13. E.K. Venstrem and P.Q. Rebinder, Z. Fiz. Khim., 26 (1952): p12.

14. D.J. Duquette and C. Laird, Corrosion Fatigue: Chemistry, Mechanisms and Microstructure, (Houston, TX: National Association of Corrosion Engineers, 1972), p88.

15. H.N. Hahn and D.J. Duquette, Met. Trans., 10A (1979): p1453.

16. H. Masuda and D.J. Duquette, Met. Trans., 6A (1975): p87.

17. C. Laird and G.C. Smith, Phil. Mag., 8 (1963): p1945.

18. C. Garcia and D.J. Duquette, Corrosion of Nickel-Base Alloys, (Metals Park, OH, American Society for Metals, 1985), p127.

19. T. Magnin and L. Coudreuse, Mat. Sci. and Eng., 72 (1985: p25.

20. T. Pyle, V. Rollins and D. Howard, J. Electrochem. Soc., 122 (1975): p1445.

Table I Fatigue and Corrosion Properties of Polycrystalline Nickel

Environment	Strain Range	N_i (x 10^{-3})	N_f(x10^{-3})	Cracking Mode
Air	0.5%	19	35	T/G
Free Corrosion	0.5%	15	35	T/G
Active	0.5%	9	16	I/G
Passive	0.5%	11	26	T/G
Air	1.0%	5.5	10	Mixed
Active	1.0%	0.7	1.5	I/G
Passive	!.0%	4	9	Mixed

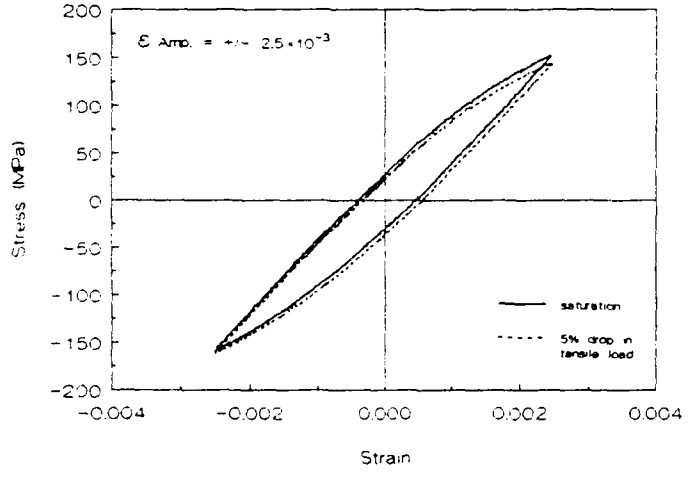

Figure1 Hysteresis loops measured at stress saturation and after a 5% drop in stress for polycrystalline nickel, in air

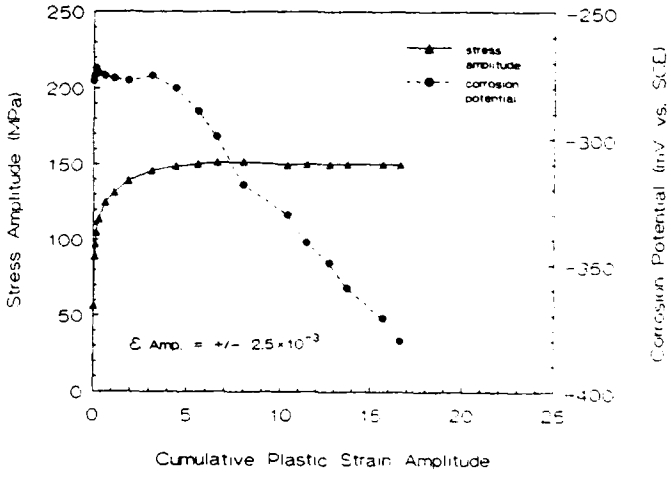

Figure 2 Variation of stress amplitude and corrosion potential vs. cumulative strain amplitude for nickel in 0.5N H_2SO_4

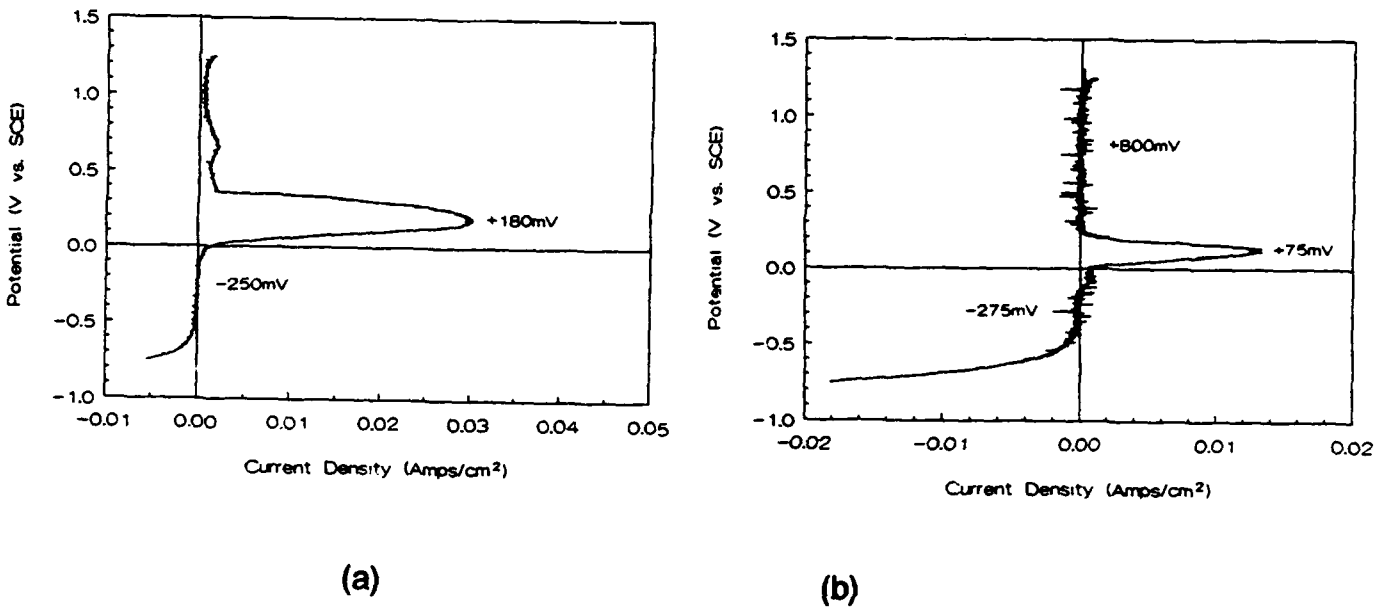

Figure 3 Polarization curves for nickel in 0.5N H_2SO_4 (a) no load (b) at stress saturation

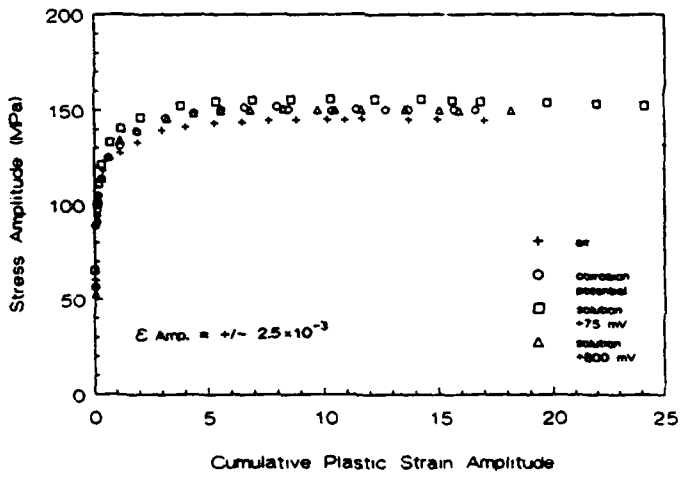

Figure 4 Cyclic hardening curves for nickel as a function of test environment

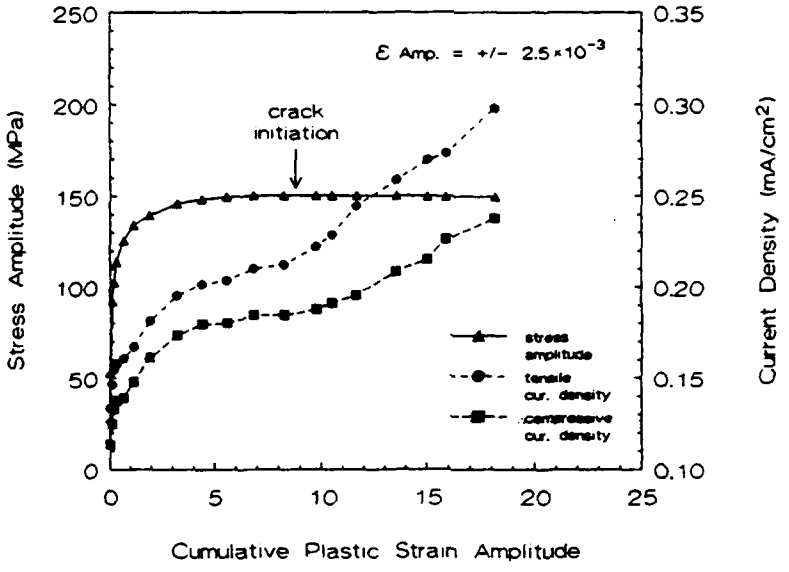

Figure 5 Variation of stress amplitude and tensile and compressive current densities vs. cumulative plastic stain amplitude for nickel in 0.5N H_2SO_4 at + 800 mV vs SCE

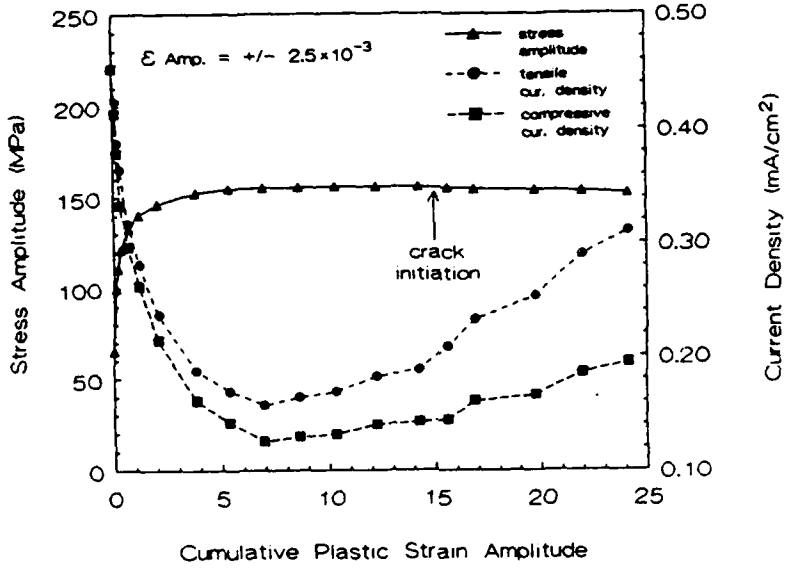

Figure 6 Variation of stress amplitude and tensile and compressive current densities vs. cumulative plastic strain for nickel in 0.5N H_2SO_4 at +75 mV vs. SCE

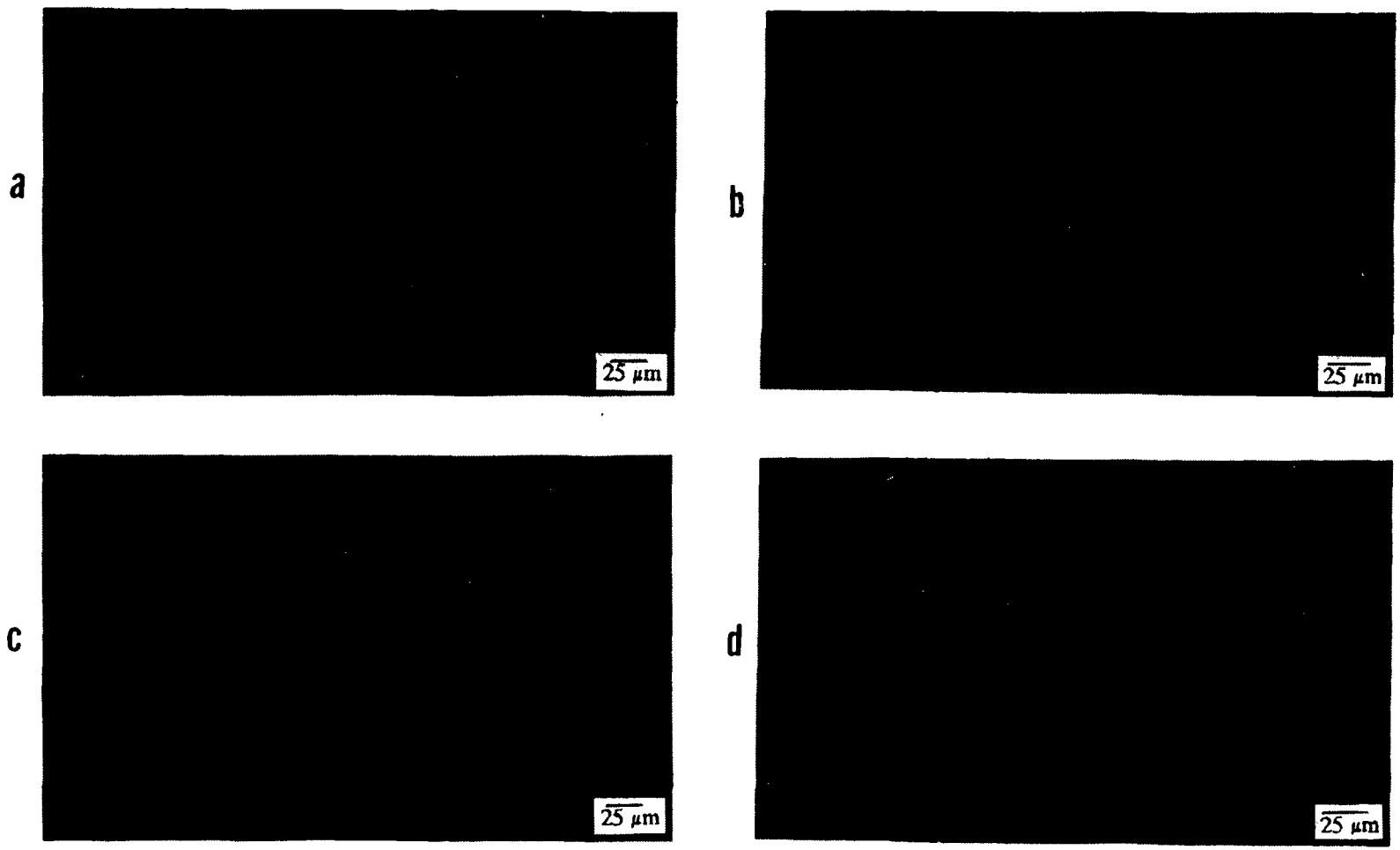

Figure 7 Longitudinal cross-sections of nickel cycled to failure at a total strain range of 0.5% (a) air (b) at the corrosion potential (c) at +75mV vs. SCE and (d) at +800mV vs. SCE in 0.5N H_2SO_4 solution

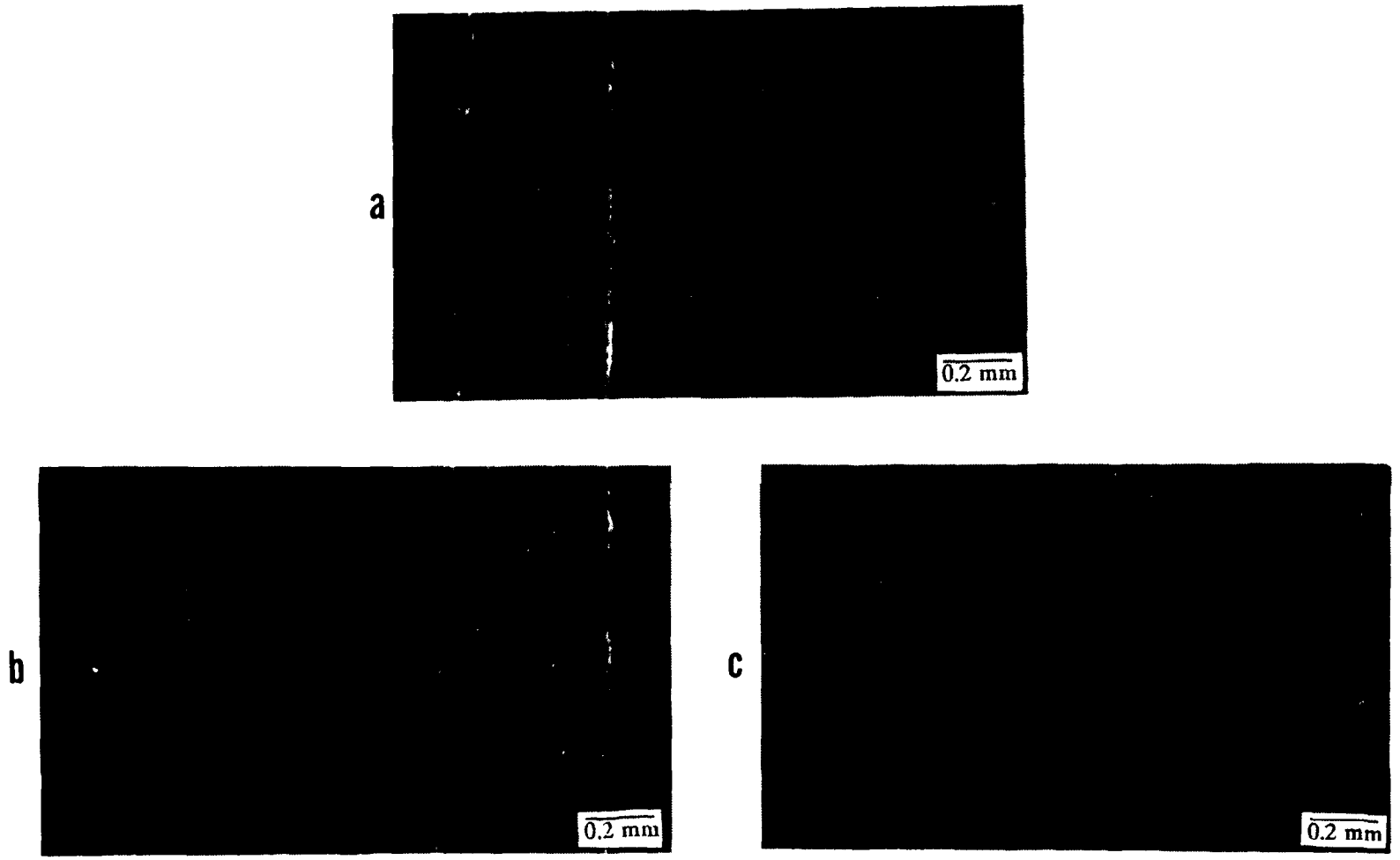

Figure 8 Longitudinal cross-sections of nickel cycled to failure at a total strain range of 1% (a) air (b) at +75 mV vs. SCE and (c) at +800 mV vs. SCE, in 0.5N H_2SO_4 solution

CORROSION FATIGUE OF MARINE STRUCTURAL STEELS IN SALINE ENVIRONMENTS

M B Kermani and F Abbassian
BP Group Research & Engineering, Sunbury-on Thames, Middlesex, England

ABSTRACT

Offshore oil and gas exploration and production structures are subjected to cyclic loading due to the action of wind, current and waves. This cyclic loading together with the corrosiveness of the environment, makes an understanding of the corrosion fatigue behaviour of the materials used in such structures vital to their safe design and operation. In this context, corrosion fatigue crack propagation rates of a marine structural steel (BS 4360 - Grade 50D) was determined in aerated 3.5% NaCl solution using compact tension specimens. It has been demonstrated that the presence of saline environments increases the crack propagation rates over the values measured in air by a factor of 2-4. The degree of this enhancement was found to be dependent on both the stress intensity range and the cathodic protection level. This influence is explained on the basis of the build up of hydrogen at the tip of the advancing crack and the effective strain rate in developing freshly created metal. The observation of brittle fracture and acceleration in fatigue crack growth rate are consistent with a hydrogen embrittlement mechanism resulting from the presence of cathodically evolved hydrogen. The implication of cathodic protection on fatigue life has been addressed by the application of fracture mechanics approach to a typical welded tubular Y-joint. The acceleration in crack propagation rate resulted in a substantial decrease in the predicted life of tubular joints.

KEYWORDS: Cathodic Protection, Corrosion Fatigue, Fatigue Life Prediction, Fracture Mechanics, Offshore Structures, Remnant Life Assessment

INTRODUCTION

Many large marine, fixed gas and oil production platforms are constructed from low strength structural steels. These structures are subject to cathodic protection in order to prevent their general corrosion. Maintenance of such structures and their long term integrity require the ability to understand the effect of cathodic protection on their mechanical performance and a full knowledge of fracture mechanics. The fatigue performance of these C-Mn steels in saline solutions has been the object of intensive studies in the recent years [1-6]. In these studies, the principal emphasis has been placed upon the role of environmental and mechanical parameters on fatigue crack growth rates [1,3]. The loss in ductility [2] and the enhanced crack growth increments [3-6] have been attributed to a hydrogen embrittlement mechanism.

While some attention has been given to the effect of cathodic potential level, there has been little understanding of the fatigue behaviour of marine structural steels exposed to saline environments over a wide range of cathodic potentials. This motivated the current work to study the environmental cracking behaviour of a typical steel used in the manufacturing of offshore structures. The work was extended to a fatigue assessment of a typical Y-joint under long term wave loading. A comparison was made between the remaining life of a typical Y-joint obtained from the fatigue crack growth rate data generated in the present study and those recommended by the UK Department of Energy.

The results presented, in addition to assisting the recognition of the cracking mechanism of C-Mn steels, provide significant practical implications through distinguishing the effective level of cathodic protection to eliminate detrimental side effects of overprotection [2].

EXPERIMENTS

The fatigue crack growth rate (FCGR) data were produced for a low carbon/manganese marine structural steel rolled plate. The steel conformed to BS 4360 Grade 50D showing a pearlitic/territic banded microstructure. The chemical composition and mechanical properties are summarised in Table 1. Additional details of the materials properties are given elsewhere [2].

Compact tension (CT) fatigue specimens, 12.5 mm thick and 50mm wide, were used to generate FCGR. The specimen geometry was in accordance with ASTM E647- 83 requirements and is shown in Figure 1. Majority of the specimens were taken from the centre of each plate in a way that the fatigue crack propagated perpendicular to the rolling direction.

Constant amplitude loading was applied to the CT specimens by means of a servo-hydraulic testing machine at an R ratio (P_{min}/P_{max}) of zero. The fatigue machine had a horizontal actuator which enabled the specimen grips and clip gauge to be isolated from the environment. Principally, a sinusoidal waveform was used for all the experiments.

Crack lengths were determined by monitoring the specimen compliance and fatigue crack growth rates (FCGR) were calculated using the method described in ASTM E- 647-83. Measurements of crack length, a, and number of applied cycles, N, were converted to values of crack growth rate per cycle (da/dN), by means of a computer program based on a seven data point polynomial method (ASTM E647-83).

Reference crack data were determined in laboratory air at either 0.1 Hz or 0.4Hz and comparative tests were carried out in solution at 0.1Hz either freely corroding or at various cathodic potentials. The latter frequency was selected to closely simulate the North Sea wave spectra. The cyclic frequency has been shown to have a strong influence on FCGR in corrosive environments [3]. Corrosion fatigue studies were carried out in continuously aerated 3.5% NaCl solution at various levels of cathodic potentials. Full details of the experimental procedures are described elsewhere [7].

Detailed examination of the fracture surfaces was carried out at 2mm intervals along the crack face using both scanning electron microscope (SEM) and transmission electron microscope (TEM). The SEM provided an overall picture of the fracture mode while examination of two stage plastic/carbon replicas using TEM revealed the finer details of the fracture morphology.

CRACK GROWTH RATE DATA

The fatigue crack propagation data were analysed and presented in the conventional manner relating fatigue crack growth rate per cycle (da/dN) to crack tip stress intensity range (ΔK) on a double logarithmic scale. The results carried out in laboratory air are presented in Figure 2.

Calculated values of the Paris constant (C) (Eqn 2) and the Paris exponent (m) are given in Table 2, which includes the regression coefficient (R_c). Clearly, the correlation falls into two regions; at lower ΔK values there is a steeper relationship with an exponent value of 3.16 followed by an exponent value of 2.51 at higher ΔK values. The mean value of m is 3.09. The Paris exponent values are in close agreement with the values reported by others for a similar grade of steel [3,4].

FCGR in aerated 3.5% NaCl solution of specimens in freely corroding conditions and under a -1000 mV (with reference to saturated calomel electrode, SCE) cathodic potential are presented in Figure 3. Extracted Paris constants from Figure 3 are tabulated in Table 3 for freely corroding and cathodically protected specimens. These results indicate that the FCGR are accelerated by the environment and also by the application of cathodic potentials.

The trends of FCGR with potential are not immediately clear from Figure 3. In order to obtain a clearer comparison of the effect of potential, FCGRs were calculated from respective Paris equation at three values of ΔK. These stress intensity ranges were selected arbitrarily, reflecting, low, medium and high ΔK values. The data are presented in Figure 4a. The normalised crack growth rates (calculated by dividing the values obtained in the environment by the corresponding air value), were also determined and are presented in Figure 4b. This indicates that the rates of corrosion fatigue crack growth in 3.5% NaCl solution are on average 2-4 times greater than the corresponding FCGR in air irrespective of the potential.

Fractographic Features

Generally, a straight crack front was observed which indicated uniform through thickness crack propagation. Beachmarks were observed on macroscopic examination of the fracture face. A macrograph example of a fracture face produced in air is shown in Figure 5. Detailed fractography of fracture faces produced in air often displayed typical ductile striation patterns. SEM and TEM examples are shown in Figures 6a and 6b, respectively. The latter showing detailed topographic features of ductile striations which were not apparent on the SEM micrographs. Secondary cracking was prevalent on the fracture surfaces, particularly in the higher ΔK ranges, an example is shown in Figure 7 taken at a ΔK of 31 MN/m3/2.

Corrosion fatigue testing in 3.5% NaCl solution resulted in a complex mixture of fracture modes. In this case, the fracture surface consists of many relatively flat, intergranular and transgranular cleavage facets distributed within a matrix of ductile striations. The former brittle facets predominated at low ΔK ranges whereas the intermediate ΔK ranges facilitated the occurrence of transgranular cleavage levels, although the extent of each was found to be dependent on the level of cathodic protection.

Figure 8a illustrates the overall appearance of the mixed mode fracture. The cleavage facets are usually confined to a single ferrite grain and grow initially on a number of parallel planes. However, these eventually link up and the steps formed by the successive coalescence of cleavage cracks on parallel planes form typical river patterns. An example of this cleavage fracture is given in Figure 8b. Many of the cleavage facets displayed brittle striations which were aligned normal to the river markings. These features are illustrated in Figure 8b and clearly demonstrate that the cracks propagate discontinuously across the facets.

FATIGUE PERFORMANCE EVALUATION

There are two methods of predicting corrosion fatigue endurance of tubular welded joints. The first is the stress life (S-N) approach where the number of cycles to failure at a given operating stress is determined from an S-N curve usually obtained experimentally. The second approach makes use of fracture mechanics techniques to perform cyclic crack growth analyses. However, the data derived from the latter approach can be used to generate a corresponding S-N curve, on the basis of which cumulative fatigue damage assessment can be made. A brief description of these methods follows.

S-N Approach

S-N approach is widely used in fatigue life assessment of tubular joints particularly during the design stage. This method is based on empirically derived relationship between applied hot-spot stress range (S) and elapsed cycles to failure (N). The main disadvantage of this approach is that it fails to distinguish between crack initiation and its stable growth and as such cannot address fatigue assessment of joints which contain cracks. This is due to the fact that the recommended S-N curves are based on tests carried out on uncracked specimens and do not include the effect of existing cracks on fatigue life.

S-N curves relates hot spot stress rang ($\Delta\sigma$) with the number of cycles to failure (N) and is represented by the following relationship.

$$N = G\ \Delta\sigma^{-m} \tag{1}$$

where G is a constant and the exponent m for mild steel in air is $\equiv 3.00$. G can vary with weld details and the environmental parameters.

Fracture Mechanics Approach

Since its introduction as a method of characterising fatigue behaviour in the 1960's, linear elastic fracture mechanics (LEFM) is increasingly being incorporated into many engineering codes of practice. Conventionally, offshore structures have been designed on the basis of fatigue design S-N curves for welded joints such as those published by the UK Department of Energy [10]. However, the application of fracture mechanics to offshore structural design has been increasingly acknowledged [6]. This has been based on the recognition that fatigue life is controlled by crack growth and incorporates the influence of environmental variables on FCGR.

In contrast to S-N approach, LEFM approach, assumes that a defect of certain size exists in the component and considers the growth rate of the crack during all stages of its stable propagation. This makes the fracture mechanics approach very suitable in situations where the total fatigue life is dominated by crack growth and also for the assessment of defects discovered in service.

FCGR are normally approximated in the form of the well know Paris equation [8]. This relates da/dN and ΔK by an equation of the type:

$$da/dN = C\ \Delta K^{m} \tag{2}$$

where ΔK is the range of the crack tip stress intensity factor defined by:-

$$\Delta K = Y\ \Delta\sigma\ (\pi a)^{1/2} \tag{3}$$

where Y is a geometrical factor and a is crack length. The fatigue life is obtained by integrating this equation between an assumed initial crack size (a_i) and a final size at failure (a_f).

FATIGUE LIFE ASSESSMENT: Application to a Y-Joint

The influence of cathodic protection on fatigue life of tubular joints in an offshore jacket was demonstrated on a typical Y-joint shown in Figure 9. The overall fatigue assessment methodology is illustrated by the flow chart in Figure 10. Details of the approach adopted in this study are outlined in the Appendix. The primary steps are briefly described as follows:-

Long term wave loading spectra was represented by an exceedance relationship (Eqn A.1) indicating the number of waves exceeding a given wave height, H, during N_o cycles. For a given wave height and wave period, the wave loading on the structure was then determined from Morison's equation. In practice, all the significant wave directions should be considered and the fracture mechanics analysis should be performed accordingly.

Nominal loads in the braces are usually obtained from a global structural analysis of the jacket. This often requires using finite element method with members modelled as rigidly connected beam elements. The effect of local joint flexibility can also be included [9]. Member loads-wave/height relationships can then be represented by a power law through which the exceedance of the member load ranges are represented by the Weibull distribution (Eqn A.2). In the present fatigue evaluation, the typical values (listed in Table 4) were used for the axial load, in-plane and out-of-plane bending moment ranges in the brace. Where required, the contribution of dynamic loadings can be incorporated into the analysis, particularly when the natural period of the structure is close to the wave period.

The potential crack locations (hot spots) are usually in the welded region around the chord/brace intersection. To obtain the local stress range at the hot spots, stress concentration factors (SCFs) had to be determined (Eqn A.3a, b). For complex joints, a finite element analysis of the joint represented by shell elements is often required. However, in the case of the simple Y-joint used in the present study, semi-empirical equations recommended in reference [10] were employed. The exceedance of hot spot stresses were then obtained (Eqn A.4).

The stress intensity factor was then required in order to relate crack intensity to hot-spot stress which in general depends on crack geometry and loading mode. For complex weld intersections, it is necessary to carry out a local stress analysis of weld cross section at crack location under hot spot stresses using a finite element solution. However, for simple cases such as the Y-joint, classical solutions or semi-empirical formulae exist such as that described by Eqn (A.5).

Crack Growth Analysis

Fatigue cracks often initiate around the weld toe and usually in the chord due to its higher local stresses. Two hot-spot locations were considered, namely the crown and the saddle. A surface crack of depth 0.5mm was assumed to exist in the chord at these locations. The parameters used in the study are listed in Table 4.

For a crack having an initial depth a_i, Eqn (A.8) represents an implicit relationship between instantaneous crack depth, a, and the elapsed stress cycle, N. This relationship, calculated from the FCGR data in Tables 2 and 3 is shown in Figure 11 for the saddle and the crown crack under the three conditions of (i) in air, (ii) freely corroding and (iii) cathodically protected. The elapsed cycle corresponding to a through thickness crack ($a = T_c$) was defined as the remaining fatigue life of the joint. Figure 11 shows that saddle represent a lower fatigue life than the crown. This is due to relatively higher levels of hot spot stresses at the saddle. It is noted that a high proportion of the fatigue life is spent during the early stages of crack growth. These results also show that cathodic protection reduces fatigue life of the joint by some 8-10 times when compared with the values obtained in air. However, this apparently large reduction in remnant life of the joint based on the FCGR data should be considered with cautious. In a more realistic environmental conditions of sea water, formation of a calcareous deposit has a strong influence on FCGR.

The influence of initial crack depth, a_i, on fatigue life was obtained from Eqn (A.9) by putting $a = a_f = T_c$. The results are shown in Figure 12 for the three exposure conditions. It is seen that fatigue life is progressively decreases with increasing initial crack size, a_i, and that small initial crack sizes has a limited effect in reducing the remaining life.

Equivalent S-N Curves

From material's crack growth rate data, an equivalent S-N curve was obtained relating the hot-spot stress range, $\Delta\sigma_{hs}$, to cycle to failure, N_f, using Eqn (A.6) by substituting T_c for a. The difference between such S-N curve and one which is obtained directly by cyclic fatigue tests on tubular joints is that the former incorporates an initial crack depth size. Using the FCGR data in Tables 2 and 3 and appropriate crack intensity parameters Yo, p and q for a Y-joint, the equivalent S-N curves are plotted in Figure 13. Included in this Figure are the UK Department of Energy (DOE) recommended design S-N curves or freely corroding and in sea water with adequate cathodic protection [17,18]. These S-N curves are corrected for chord wall thickness effect and taken to be two standard deviations below the mean. In this recommendation, the S-N curve for tubular joints with adequate protection is assumed to be the same as those in air.

Cumulative Damage

The cumulative fatigue damage for variable amplitude fatigue loading was obtained by means of the linear fatigue damage model of Miner-Palmgren rule [12] using the equivalent stress concept (Eqn A.8) as discussed in the Appendix (Eqns A.10 and A.11). The results are shown in Figure 14 illustrating the increase in cumulative damage ratio, D, as a function of elapsed stress cycles. A comparison between Figures 11 and 14 demonstrates the equivalence between crack growth and S-N approaches: it is noted that the elapse cycles at $a = T_c$ in Figure 11 coincides with elapsed cycles at $D = 1$ on Figure 14 indicating that the two approaches give identical predictions on total cycles to failure.

DISCUSSION

The adverse influence of cathodic potentials on fatigue crack growth rates presented in this study can be explained on the basis of a hydrogen embrittlement (HE) mechanism. Hydrogen enters the cathodically polarised steel during exposure, particularly at potentials more negative than about -900 mV_{SCE} where hydrogen evolution is the dominant cathodic reaction [2]. At the free corrosion potential, the evidence also points to a dominant influence of HE, although in these circumstances dissolution at the crack tip may be thermodynamically possible. The observation of brittle fracture and the increase in FCGR produced by environmental changes (Figures 3 and 8) are all consistent with such a view.

It is speculated that the two competing processes at the crack tip are (i) hydrogen build-up or its availability and (ii) the effective crack tip strain rate in developing freshly created metal. Hydrogen entering the metal lattice builds up to a concentration sufficient to induce brittle cleavage fracture over a distance ahead of the crack tip, the extent of which is determined by the local effective strain rate. At higher stress intensity ranges, the crack growth rate tends towards the behaviour in air (Figure 3). Figure 4 shows that, on a comparative basis crack propagation rate peaks at low ΔK ranges and where the dominant cathodic reaction becomes hydrogen evolution. The peak in FCGR could correspond to situations where crack tip strain rate is compatible to the extent of hydrogen entry within the crack tip region. Therefore, at an appropriate combination of these two competing processes, large acceleration of crack growth rate occurs (Figure 4).

There appears to be a degree of difference between the fatigue crack growth rates produced in the current study using a 3.5% NaCl solution and those generated by others [3,4] in natural seawater. The difference is attributed to the nature of saline solution employed: in natural seawater, the introduction of cathodic potentials leads to the formation of calcareous deposit which in turn suppresses crack growth. This in turn would affect the cumulative fatigue damage assessment that showed alarmingly low fatigue lives in the presence of cathodic protection.

Fatigue fracture surfaces produced in air displayed typical ductile striation patterns (Figure 6). It was observed that the introduction of a saline solution results in a complex mixture of fracture modes, including intergranular and transgranular brittle type fracture (Figure 8). These fracture surfaces generally consist of many relatively flat transgranular facets, with superimposed brittle striations, distributed within a matrix of ductile striation.

It is interesting to note that the equivalent S-N curves for both conditions of freely corroding and in air are seen to be close to the UK Department of Energy recommended design curves (Figure 13). However, the equivalent S-N curve for cathodically protected conditions falls substantially below the corresponding air curve and also below that of freely corroding. It should be emphasised that the crack growth rate data are based on a limited number of tests with limited associated statistical analysis. Furthermore, in the presence of the actual sea water, formation of calcareous deposit may have a beneficial effect on improving the crack growth rates. These parameters can in turn influence the corresponding equivalent S-N curves with resultant improved fatigue lives.

The UK Deprtment of Energy S-N data (Figure 13) using smooth specimens shows that the presence of seawater approximately halves the fatigue life, compared with the air value and that the application of normal levels of cathodic protection restores the corrosion fatigue life to that of the air value [1,17,18]. In contrast, this study has shown that the presence of saline environments increases the crack growh rate by a factor of 2-4 compared to air data (Figures 3 and 4) with a significant influence on the fatigue life (Figures 11 and 13). In this case the application of normal cathodic protection did not restore the air properties and overprotection resulted in further marked increase in the crack growth rates (Table 3). This observation is supported by others using a similar material in seawater [3,4]. These contradictory observations can be explained by the underlying geometrical and electrochemical effects. These effects are associated with the retardation of crack initiation and propagation of very short cracks (<0.5mm) in the presence of corrosive environments which has a beneficial effect on S-N curves. During the crack propagation stage (for crack length >1 mm), however, cathodic protection and overprotection accelerates crack growth rate.

This enhanced fatigue crack growth rate can have a significant effect on the fatigue life of offshore installations. The fracture mechanics assessment outlined in this work indicates that for a typical Y-joint under a representative variable amplitude wave loading, the fatigue life reduces by an order of magnitude (Figure 11). Since the conventional way of fatigue design of offshore installations is based on S-N data, the practical implications of these conclusions are considerable. This is particularly true in situations where cathodic protection levels on offshore structures and pipelines are more negative than the nominal, optimum potentials.

CONCLUSIONS

1. Fatigue crack growth rate increases by a factor of 2-4 compared with air values on the introduction of saline environments in conditions of freely corroding or with cathodic protection.

2. In contrast with the current industry's belief, "adequate" cathodic protection does not restore the fatigue properties.

3. Fatigue assessment of a typical Y-joint indicates that the implication of enhanced crack growth rate can result in an order of magnitude shorter lives.

4. Fatigue cracking of structural steels in air propagates by a ductile striation formation mechanism. The introduction of saline environment combined with cathodic protection results in a complex fracture mode comprising of intergranular, transgranular and ductile striations.

5. An appropriate combination of crack tip strain rate and cathodic potential results in large acceleration of crack growth rates.

ACKNOWLEDGEMENT

The authors wish to thank BP Exploration Frontier International for provision of support and permission to publish this paper.

REFERENCES

1. Procter, R P M, Cathodic Protection Theory and Practice - The Present Status, Coventry, Paper No 18 (1982).

2. Kermani, M B and Procter, R P M, The American Society of Mechanical Engineers, 8th International OMAE Conference, eds. M M Salama et al, Vol III, p 447 (1989).

3. Scott, P M, Thorpe, T W and Silvester, D R V, Corr. Sci., 23, p 559, (1983).

4. Thorpe, T W, Scott, P M, Rance, A and Silvester, D, Int. J. Fatigue, 5, No 3, p 123 (1983).

5. Proceeding of an International Conference on Fatigue and Crack Growth in Offshore Structure", eds. W D Dover, G Glinka and A G Reynolds, Inst. of Mechanical Engineers (1986).

6. Dover W D and Austin J A, Presented at the meting of the Institute of Marine Engineers and Marine Technology Directorate, November, (1992).

7. Kermani M B and Abbassian F, 12th International Corrosion Congress, 19-24 September, Houston (1983).

8. Paris P C, Erdogan, F, "A Critical Analysis of Crack Propagation Laws", Trans. ASME, Journal of Basic Engineering, Vol 85, pp 528-534 (1963)

9. Node Flexibility and Its Effect on Jacket Structures: a pilot study on two-dimensional frames, Under Water Engineering Group (UEG) Publication, Report UR22, CIRIA (1984).

10. Design of Tubular Joints for Offshore Structures, Vol 1,2,3, Under Water Engineering Group (UEG) Publication, Report UR33, UEG/CIRIA (1985).

11. de Kazinczy, F, 1954, A Theory of Hydrogen Embrittlement, J. I. S. I., Vol 177, pp 85-92.

12. Miner M A, "Cumulative Damage in Fatigue", Transactions of ASME, Journal of Applied Mechanics, Vol 67, pp A159-A164 (1945)

13. Turnbul A and Saenz de Santa Maria, M, Metall. Trans. 19A, p 1795 (1988).

14. Fatigue Handbook, Offshore steel structures, Edited by A. Almar-Naess, Tapir, 1985.

15. Morlet, J G, Johnson, H H and Troiano, A R, 1958, J.I.S.I., Vol. 189, p 37 (1958).

16. Dover, W D, Dharmavasan, S, "Fatigue Fracture Analysis of T and Y Joints, OTC 4404, presented at the 14th Annual Offshore Technology Conference, Houston, Texas, 1982.

17. "Offshore Installation: Guidance on Design and Construction", UK Department of Energy, HMSO (1984)

18. Background to the New Fatigue Design Guidance for Steel Welded Joints in Offshore Structures", UK Department of Energy, London (1984).

APPENDIX

FATIGUE ASSESSMENT APPROACH

This Appendix outlines the fatigue assessment methodology adopted in the fracture mechanics evaluation.

Long Term Wave Loading History

Long term wave loading history is described by the following simplified exceedance distribution giving the number of waves, N, exceeding a given wave height, H:

$$H = H^{*} \left(1 - \frac{\log N}{\log N_{o}}\right) \qquad (A.1)$$

where H^{*} is the maximum expected wave height during the design life of the structure and No is the total number of applied wave cycles during the period considered.

Nominal Member Forces

The nominal member forces are calculated by means of a global structural analysis of the jacket under applied load using finite element analysis. Based on the structural analysis results, the relationship between member loads and wave height at a given location in the jacket, can often be represented by a power law, i.e. member load $\propto H^{1/h}$. The corresponding long term nominal member load ranges at a joint can then be represented by an appropriate Weibull distribution [14]:

$$\Delta\underset{\sim}{F} = \Delta\underset{\sim}{F}^{*} \left(1 - \frac{\log N}{\log N_{o}}\right)^{1/h} \qquad (A.2)$$

where ΔF is the vector representing nominal forces and moments in a given member, ΔF^{*} is member load vector corresponding to the maximum expected wave height, H^{*}, and h is Weibull parameter. h in general depends on location of the joint and the type of structure.

Local Stress Range at Hot Spots

For each potential crack location (the hot spots) around the weld toe, the long term distribution of relevant stress ranges was obtained by multiplying the nominal member stresses by the corresponding stress concentration factors (SCFs). In the case of a Y-joint, under the axial load range (ΔP_a) and in-plane and out-of-plane moment ranges (ΔM_{ipb}, ΔM_{opb}), the peak hot-spot stress ranges ($\Delta\sigma^{*}_{hs}$), at the saddle and crown are given by:

<u>At saddle:</u>

$$\Delta\sigma^{*}_{hs} = SCF_{a} \frac{\Delta P^{*}_{a}}{A_{b}} + SCF_{opb} \frac{\Delta M^{*}_{opb}}{Z_{b}} \qquad (A.3a)$$

At crown:

$$\Delta\sigma^{*}_{hs} = SCF_{a} \frac{\Delta P^{*}_{a}}{A_{b}} + SCF_{ipb} \frac{\Delta M^{*}_{ipb}}{Z_{b}} \qquad (A.3b)$$

where A_b and Z_b are the cross-sectional area and elastic section modulus of the brace, respectively, and SCF_a, SCF_{ipb}, and SCF_{opb} are the corresponding stress concentration factors.

SCFs were obtained via parametric equations recommended in [10] which are based on experimental data on Y-joints. Note that SCF_a is in general different for the saddle and for the crown. The long term distribution of hot spot stress can then also be described by a Weibull distribution:

$$\Delta\sigma_{hs} = \Delta\sigma^{*}_{hs} \left(1 - \frac{\log N}{\log N_{o}} \right)^{1/h} \qquad (A.4)$$

In the above calculation, the effect of mean stress and hence the residual stresses in the weld zone have not been taken into account.

Fatigue Crack Growth Analysis

For constant amplitude fatigue cycles, the crack depth growth as a function of elapsed cycles can be obtained from crack growth rate data by substituting Eqn(3) for ΔK in Paris Law Eqn(2) and integrating from a_i, the initial crack depth, to a, the current crack depth.

The proportionality factor, Y, which takes account of weld geometry and crack details, is in general related to chord thickness and crack size:

$$Y = Y_{o} T_{c}^{p} a^{-q} \qquad (A.5)$$

The parameters Y_o, p and q were obtained from the experimental studies on Y joints reported in [16]. It has been shown that, for a given joint type, Y_o, p and q depend on stress distribution around the weld toe and hence the mode of loading. However, in the present study, average values of these parameters have been used. The current crack depth, a, as a function of elapsed cycles, N, is then given by:

$$N = \frac{\left(a^{\xi} - a_{i}^{\xi} \right)}{\pi^{m/2} \xi C Y_{o}^{m} T_{c}^{pm}} \Delta\sigma_{hs}^{-m} \qquad (A.6)$$

where C and m are Paris constants and

$$\xi = 1 + \frac{2q-1}{2} m \qquad (A.7)$$

The above equation does not address the variations in the crack aspect ratio which occurs during fatigue crack growth. However, experimental observations have indicated that crack depth, a, is the principal parameter in cyclic crack increment.

For a variable amplitude fatigue loading, the crack growth analysis can most conveniently be performed through the equivalent stress concept. It can be shown that [14] the fatigue life corresponding to a variable amplitude stress range, described by Weibull distribution (Eqn A.4), is identical with an equivalent constant amplitude stress, $\Delta\sigma_{eq}$. This is given by:

$$\Delta\sigma_{eq} = \frac{\Gamma(1+m/h)^{1/m}}{(\ln N_o)^{1/h}} \Delta\sigma^*_{hs} \qquad (A.8)$$

where Γ is gamma function. The corresponding crack growth equation can be obtained by substituting the above equation for $\Delta\sigma_{hs}$ in [A.6]:

$$N = \frac{(a^{\xi} - a_i^{\xi})}{\pi^{m/2} \xi C Y_o^m T_c^{pm}} \frac{(\ln N)^{m/h}}{\Gamma(1+m/h)} \Delta\sigma^{*-m}_{hs} \qquad (A.9)$$

where a is the current crack depth and N is the corresponding elapsed cycles of variable amplitude fatigue stress.

It should be emphasised that equivalent stress approach ignores the possible interaction effect between variable amplitude cycles, but structural steels show minimum interaction dependent tendency.

S-N Approach

When adopting the S-N approach to fatigue assessment under variable amplitude loading, the equivalent stress (Eqn A.8) can be used directly in the S-N Eqn(1) to obtain cycles to failure, N_f:

$$N_f = G \frac{(\ln N)^{m/h}}{\Gamma(1+m/h)} \Delta\sigma^{*-m}_{hs} \qquad (A.10)$$

For N cycles of applied variable amplitude loading, the cumulative damage ratio, D, can then be obtained via Miner-Palmgren rule [12]:

$$D = \frac{N}{N_f} = \frac{N}{G} \frac{\Gamma(1+m/h)}{(\ln N)^{m/h}} \Delta\sigma^{*m}_{hs} \qquad (A.11)$$

where N_f refers to the number of cycles to failure corresponding to N cycles of applied variable amplitude fatigue stress.

A comparison between the S-N and fracture mechanic approaches can be made by revisiting Eqn(A.6). This equation, which was obtained from the integration of crack growth rate equation, represents an equivalent S-N relationship when current crack depth, a, reaches a_f, the crack depth at failure (or crack depth at the onset of unstable fracture). In the fatigue assessment of tubular joints, a_f is often taken as the chord thickness, T_c. Since the high proportion of fatigue life is expended during the early portion of the crack growth (see Figure 12), an exact knowledge of a_f is not essential.

It should be noted that if constant G in Eqn(A.10) is put equal to that obtained from the equivalent S-N relationship (A.6) with $a=a_f$, then the cycles to failure N_f obtained from Eqn(A.10) becomes identical to

the number of cycles predicted by Eqn(A.9) which are required to extend the crack depth to af. Furthermore, from Eqn(A.11), this number of cycles correspond to a cumulative damage ratio D=1. This reiterates the equivalence of the S-N approach to that of fracture mechanics, as would be expected when the S-N curve is deduced from crack growth rate data.

NOMENCLATURE

a	crack depth
a_f	final crack depth
a_i	initial crack depth
A_b	brace cross-sectional area
C	Paris constant
D	cumulative damage ratio
D_b	brace diameter
D_c	chord diameter
G	S-N constant
h	Weibull parameter
H	wave height
H^*	maximum expected wave height
K	stress intensity factor (= $Y \sigma(\pi a)^{1/2}$)
m	Paris exponent
M_{ipb}	brace in-plane moment
M_{opb}	brace out-of-plane moment
N	number of elapsed stress cycles
N_f	number of stress cycles to failure
N_o	number of stress cycles during the design life of the structure
p	exponent in stress intensity factor, Eqn(A.5)
P_a	brace axial force
P_{min}	minimum load cycle
P_{max}	maximum load cycle
q	exponent in stress intensity factor, Eqn(A.5)
R	stress ratio
R_c	regression coefficient
T_c	chord thickness
T_b	brace thickness
Y	stress intensity proportionality factor
Y_o	multiplier in stress intensity factor, Eqn(A.5)
Z_b	brace elastic section modulus
Γ	gamma function
$\Delta\sigma$	stress range
ξ	constant defined by Eqn (A.7)
σ_{hs}	hot-spot stress

TABLE 1

CHEMICAL COMPOSITION AND MECHANICAL PROPERTIES OF GRADE 50D STEEL

CHEMICAL COMPOSITION (wt%)								CARBON Eq.	MECHANICAL PROPERTIES		
C	Si	Mn	Nb	V	S	P	Fe		σ_{upp} (MPa)	UTS (MPa)	Elongation (%)*
0.041	0.26	1.56	0.04	0.04	0.005	0.003	Bal.	0.335	379	528	29.1

*: Elongation to fracture over a 25mm gauge length

TABLE 2

PARIS CONSTANTS OF GRADE 50D STEEL IN AIR

ΔK ($MPm^{1/2}$)	C	m	R_c
Low	3.9×10^{-12}	3.16	0.9870
High	4.4×10^{-11}	2.51	0.9980
Mean Value	5.1×10^{-12}	3.09	0.9980

TABLE 3

PARIS CONSTANTS AT DIFFERENT ENVIRONMENTAL CONDITIONS (Aerated 3.5% NaCl Solution)

Cathodic Potential (mV_{SCE})	C	m	R_c
Open Circuit	2.72×10^{-11}	2.94	0.977
-800	7.5×10^{-11}	2.66	0.993
-850	8.5×10^{-10}	1.93	0.992
-900	1.33×10^{-9}	1.85	0.989
-1,000	1.1×10^{-10}	2.46	0.999

TABLE 4

DEFINITION OF PARAMETERS USED

Parameter	Description
Join Geometry	Shown in Figure 10
Crack Length	Initial, a_i = 0.5 mm Final, a_f = 38 mm
Crack Growth Parameters	Tables 2 and 3
Stress Intensity Parameters	Y_o = 0.7 p = 0.43 q = 0.33
Stress Concentration Factors	SCF_a (Saddle) = 5.57 SCF_a (Crown) = 3.87 SCF_{opb} (Saddle) = 4.75 SCF_{ipb} (Crown) = 2.19
Nominal Brace Load Rang	ΔP^*_a = 1.6 x 10^6 N ΔM^*_{ipb} = 0.8 x 10^5 Nm ΔM^*_{opb} = 0.5 x 10^5 Nm
Weibull Exponent	h = 0.85
Load Cycles	N = 5.26 x 10^6 per year (average wave period of 6 a few)

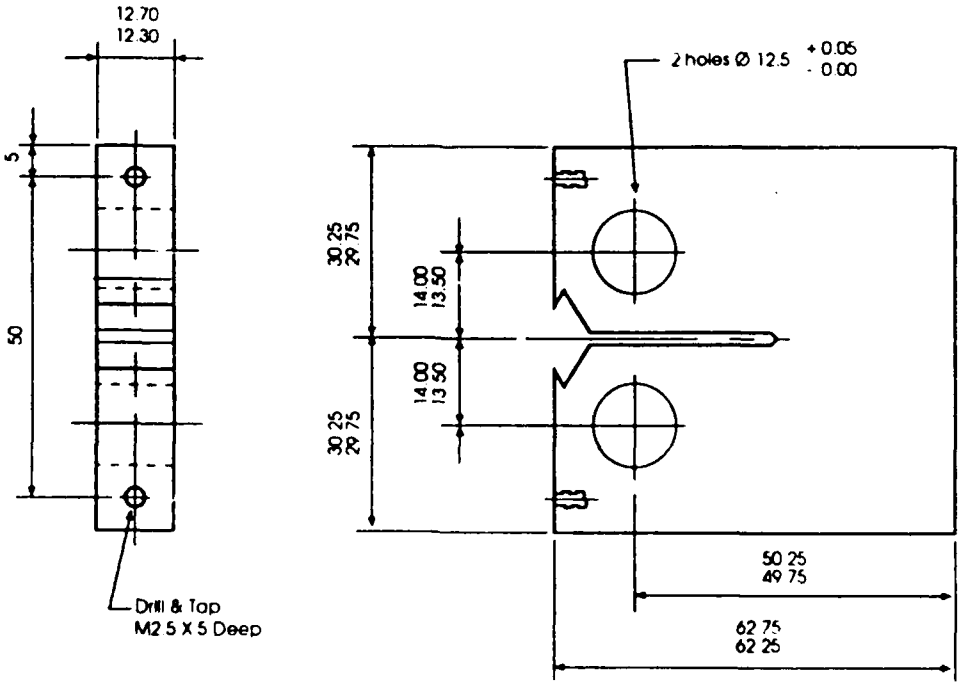

Figure 1. Compact tension specimen (Note: all dimensions are in mm).

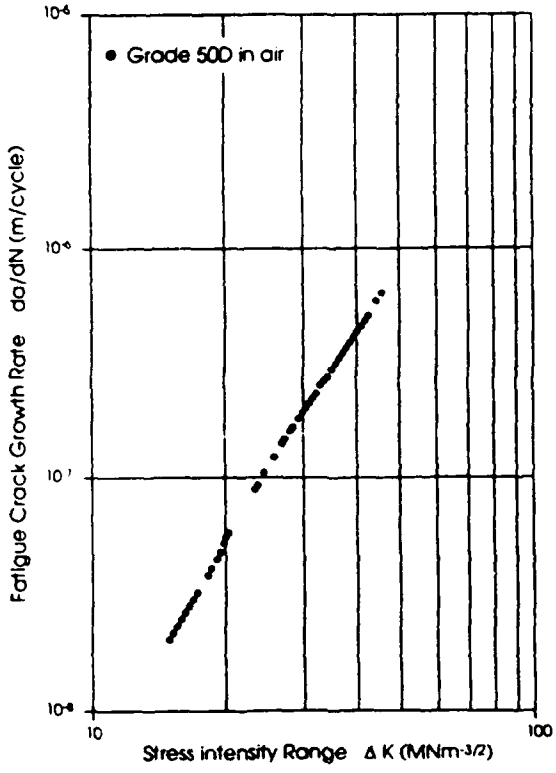

Figure 2. Fatigue crack growth rate data for Grade 50D steel in air.

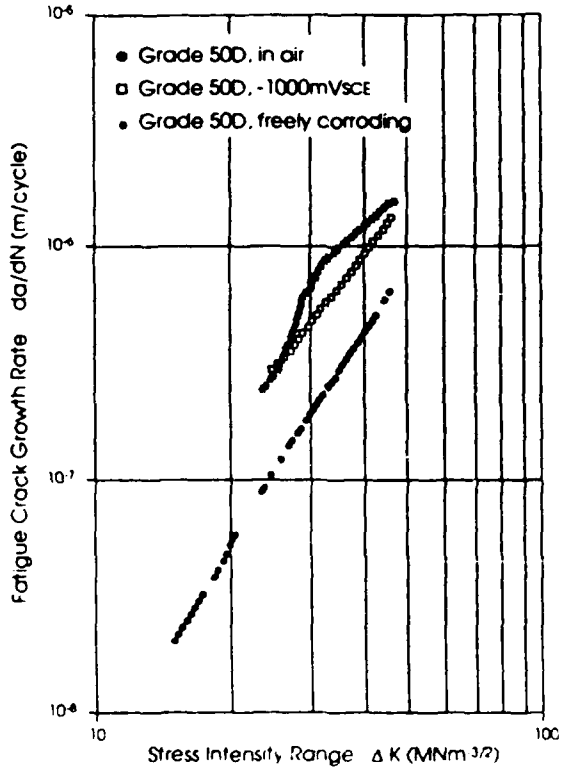

Figure 3. Fatigue crack growth rate data for Grade 50D steel in aerated 3.5% NaCl solution.

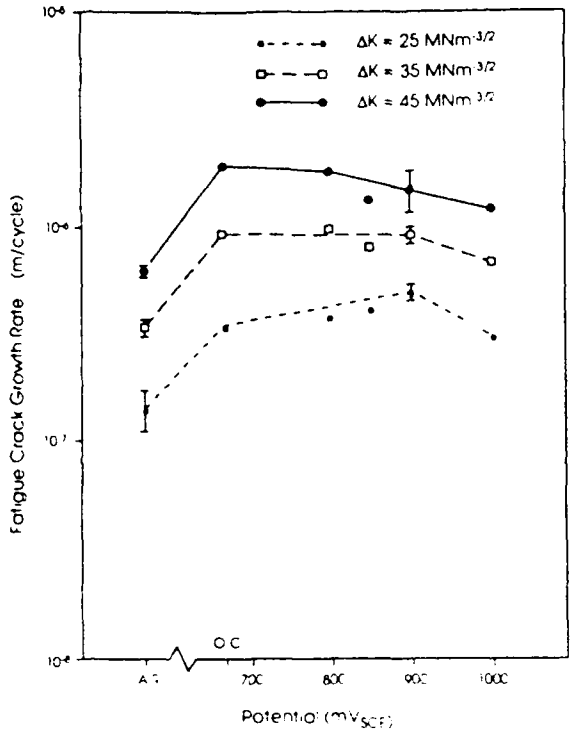

Figure 4a

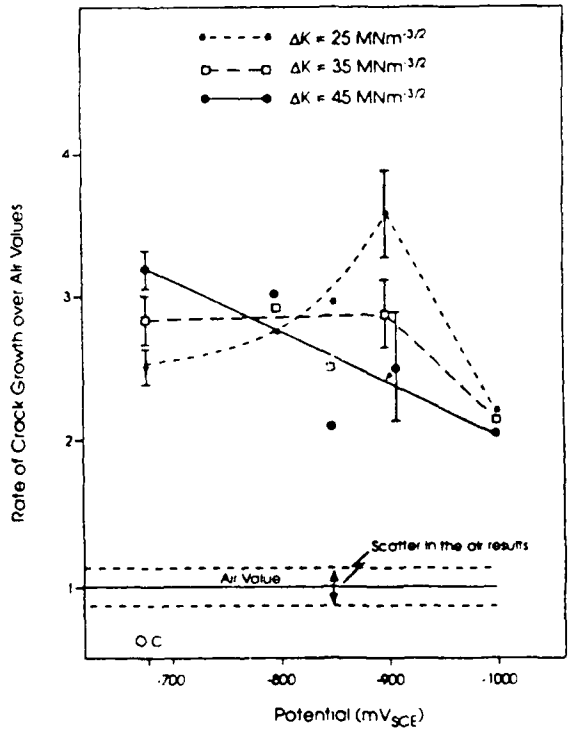

Figure 4b

Figure 4. Variation of fatigue crack growth rate with cathodic potential for grade 50D steel at three different ΔK ranges, (a) actual data and (b) normalised data.

Figure 5. Fracture surface of a specimen produced in air showing a straight crack front and macroscopic beach marks.

Figure 6a

Figure 6b

Figure 6. Typical fatigue ductile striations on fracture of Grade 50D steel tested in air, (a) SEM micrograph and (b) TEM micrograph both taken at similar magnifications.

Figure 7. Fracture surface at a high ΔK region showing separated striations.

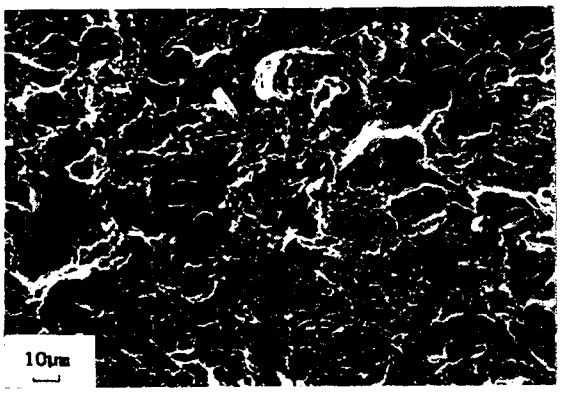

Figure 8a

Figure 8b

Figure 8. Fracture surface of Grade 50D steel tested in 3.5% NaCl solution cathodically polarised at -1000 mV_{SCE} showing a predominantly transgranular cleavage fracture, (a) an overall SEM view and (b) detailed TEM brittle striations.

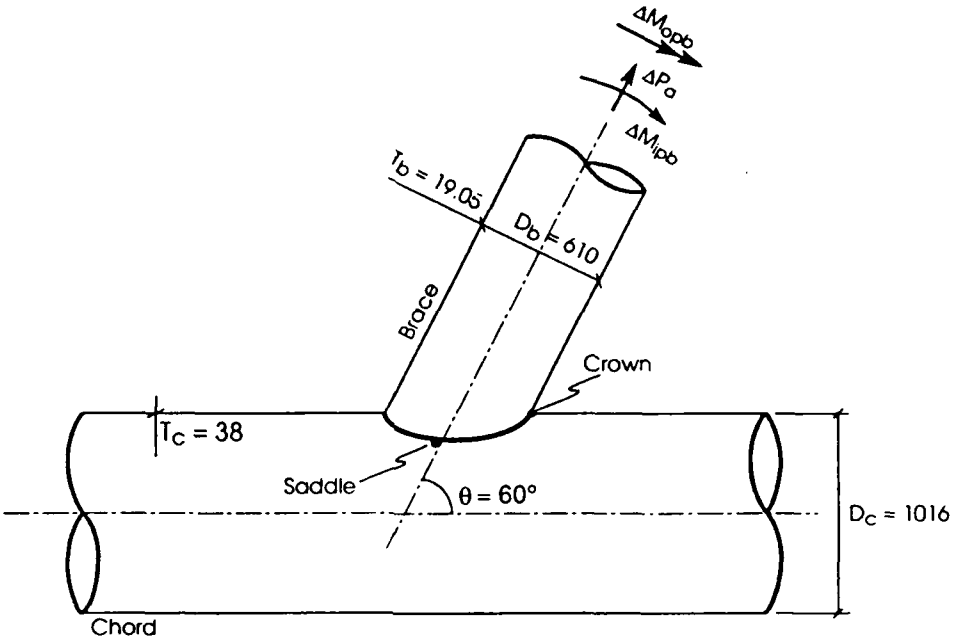

Figure 9. Geometry of the Y-joint with the nominal brace loading (Note: all dimensions are in mm).

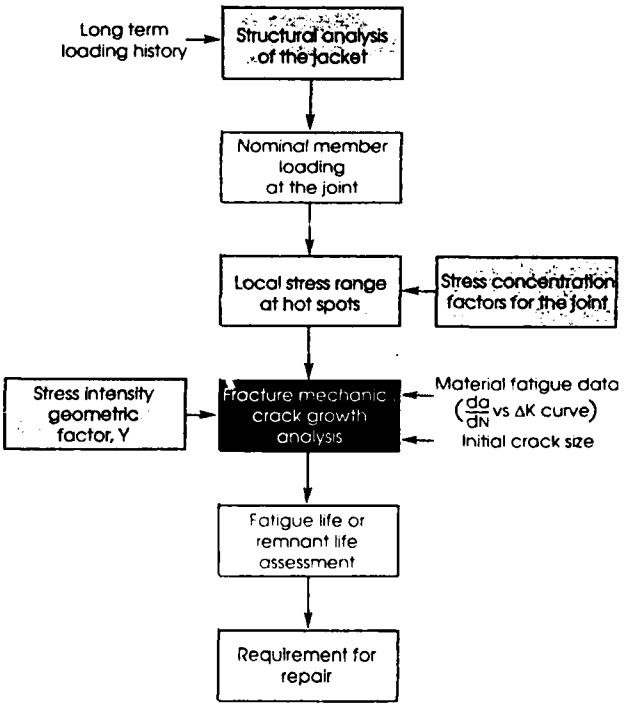

Figure 10. Fatigue assessment methodology.

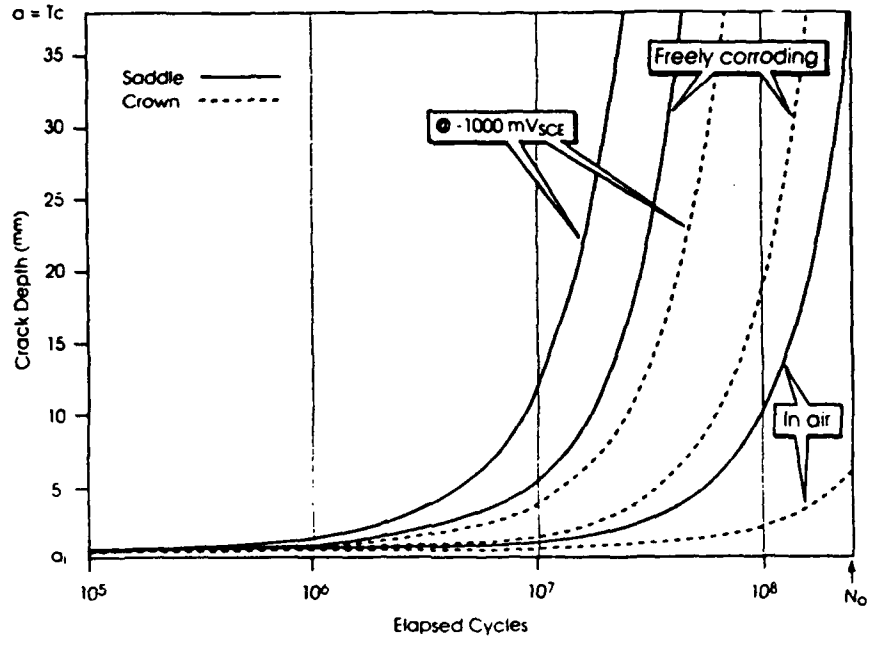

Figure 11. The variation of crack depth growth with elapsed cycles (a_i = 0.5 mm).

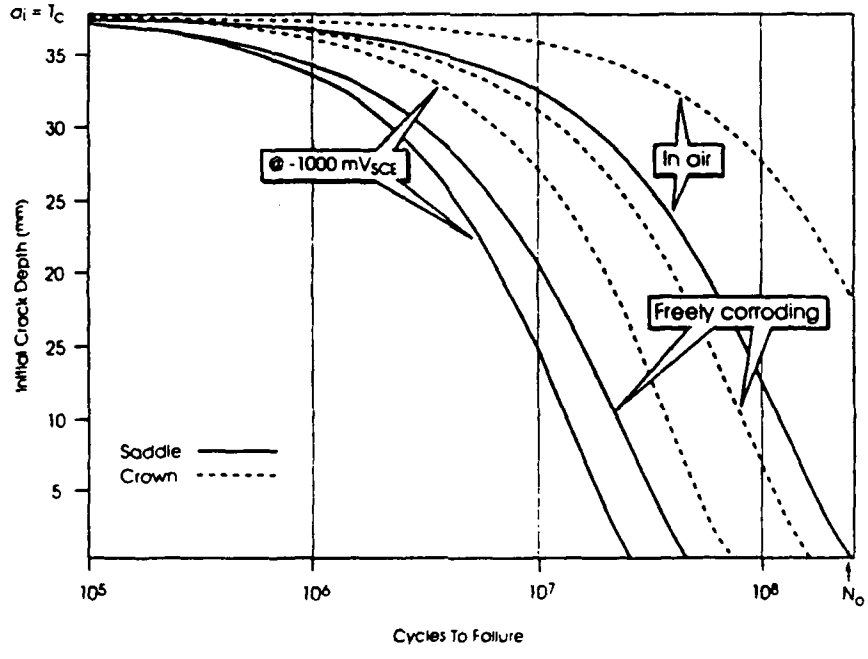

Figure 12. The influence of initial crack depth on elapsed cycles to failure (a_f = 38 mm).

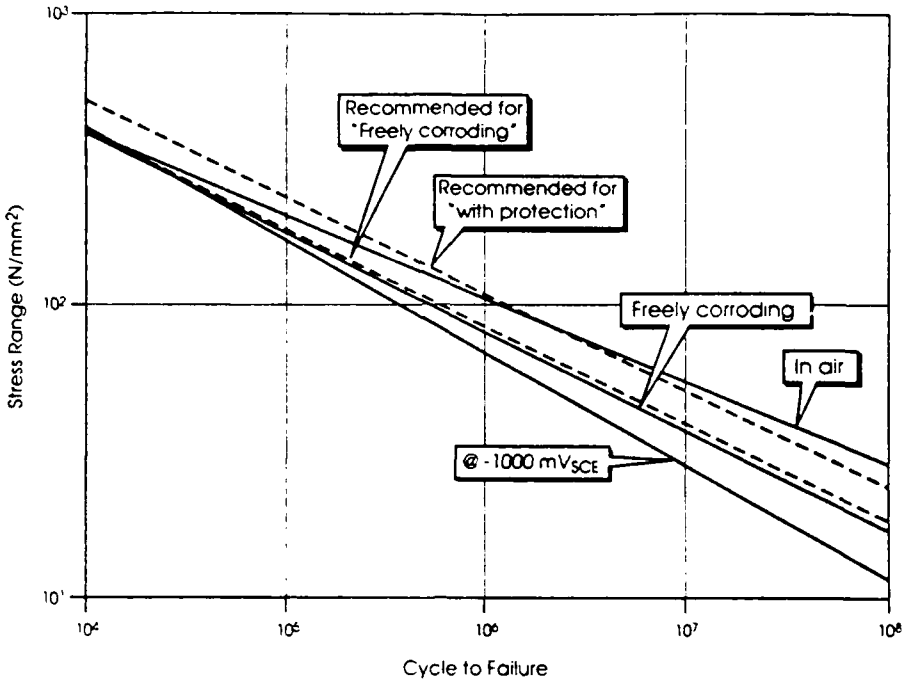

Figure 13. The S-N curves (a_i = 0.5mm, a_f = 38 mm).

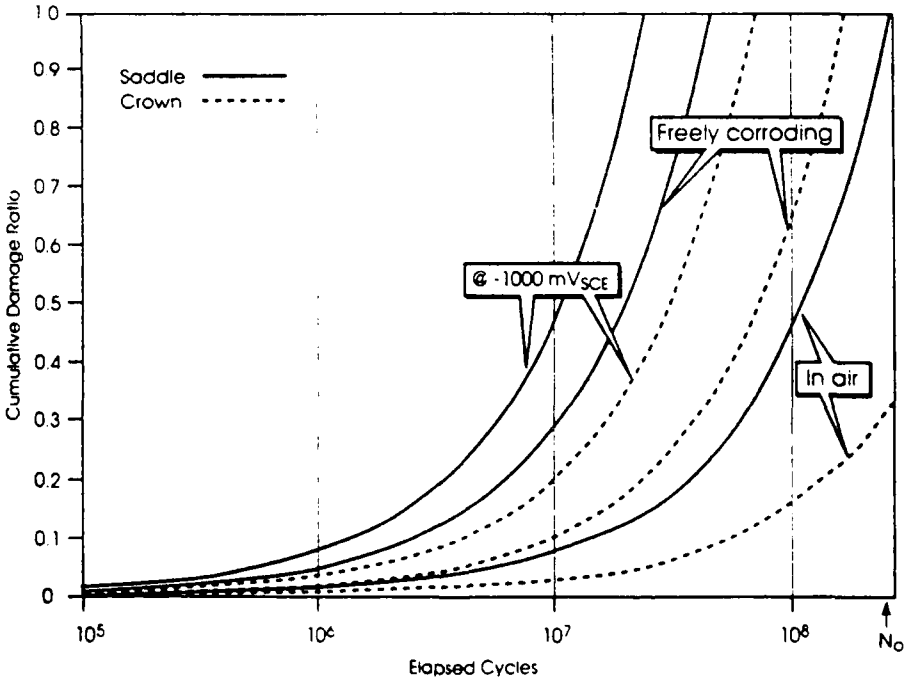

Figure 14. The variation of cumulative fatigue damage ratio with elapsed cycles.

CORROSION FATIGUE PROPAGATION OF HIGHER YIELD STRENGTH OFFSHORE STRUCTURAL STEEL IN ARTIFICIAL SEAWATER

J. Yu, R. Brook
Dept. of Engineering Materials
University of Sheffield, S1 3JD, UK;

I. Cole
CSIRO, Australia;

D. Morabito, G. Demofonti
CSM, Rome, Italy.

Abstract

Corrosion fatigue propagation of a higher yield strength offshore structural steel ($\sigma_y > 400\ MPa$) was studied using compact tension specimens in $10°C$ artificial seawater at a frequency of 0.35Hz. The effects of cathodic protection potential and stress intensity ratio (R) on the susceptibility to the corrosion fatigue were investigated. The corrosion fatigue propagation rate was significantly accelerated by increasing R ratio from 0.1 to 0.7. The effect of potential is dependent on applied stress intensity range (ΔK) and R ratio. Cathodic over-protection at -1.10 V ($Ag/AgCl$) speeded up the crack propagation rapidly with increasing ΔK.

The results are compared with previous data from the traditional BS4360:50D offshore structural steel ($355\ MPa \leq \sigma_y \leq 390\ MPa$). It is suggested that up-grading the yield strength of offshore structural steels may not necessarily increase the susceptibility to corrosion fatigue. The threshold stress intensity range (ΔK_{th}) was estimated by extrapolation and its rationality in relation to the mechanisms is discussed.

KEY WORDS: corrosion fatigue, offshore structural steel, cathodic protection, crack propagation.

1. Introduction

Modern offshore technology shows a strong trend to employ structural steels of much lower carbon equivalent value (CEV) but with higher strength to meet the demand of modern platform design and the exploitation of increasingly inaccessible fuel reserves[1,2]. This trend will continue to increase in the next decade and perhaps for the foreseeable future. Techniques such as roller quench and tempering (RQT) and thermally controlled-mechanical processes (TCMP) have replaced simple rolling and normalization. The existing data on corrosion fatigue for the "traditional" steels, which should be regarded as inferior to modern steels[3], needs to be augmented to assure the safety and integrity of modern offshore structures. Hence the present work, aimed at providing a further understanding of the corrosion fatigue of a novel offshore structural steel with low CEV but higher yield strength.

It has been realized that in welded structures, small sharp defects are unavoidable and , particularly in an aggressive environment, act as sites for the initiation and sub-critical growth of cracks; the life time of the offshore structure is therefore predominantly concerned with fatigue-controlled crack propagation[4]. For this realistic reason, the present investigation is focussed on the fatigue crack propagation rate, da/dN, as a function of the stress intensity range at the crack tip, ΔK, based on linear elastic fracture mechanics (LEFM). Particular attention has been paid to the effects of cathodic protection and stress intensity ratio, R, on such propagation. These two variables, related respectively to environment and mean stress intensity, are among the most important factors affecting the mechanisms of fatigue crack propagation[5][6].

2. Experimental Method

2.1 Material

Table 1 lists the chemical composition of CSM355 steel tested, together with that of a traditionally used, standard BS355D steel[7] (frequently represented previously in the literature as BS4360 Grade:50D[8]) for comparison. A tentative calculation[1] by the traditional equation[9].

$$CEV = C + \frac{Mn}{6} + \frac{Cr + Mo + V}{5} + \frac{Ni + Cu}{15} \tag{1}$$

shows that the CEV for CSM355 is approximately 0.32, which easily meets the maximum CEV of 0.43 allowed for structural steels with good weldability; the CEV of BS355D is just in the range between 0.43 and 0.45 according to the minimum and maximum compositions specified by BS7191[7].

If using the equation suggested recently by Uwer and Degenkolbe[2],

$$CEV = C + \frac{Mn + Mo}{10} + \frac{Cr + Cu}{20} + \frac{Ni}{40} \tag{2}$$

the CEV of CSM355 is 0.21, being 0.12 below that of BS355D. The CEV values calculated using both equations are also listed in Table 1.

It is noted that the composition of the present steel is very close to that used quite recently by Kermani and Proctor[10] in their slow-strain rate tests. However, the yield strength of CSM355, *ie.* 410 (longitudinal direction) to 417 (transverse direction) MPa, was beyond the upper bound of yield strength 390 MPa allowable for conventional BS355D or BS4360:50D steel. The heat-treatment and mechanical properties for the steels are given in Table 2.

Fig.1 shows the microstructure of CSM355 in three dimensions, as revealed by optical metallography. The steel is mainly composed of ferrite with less than 10% of pearlite, as assessed by quantitative image analysis, and has a slight preferred orientation in the rolling direction, L. This latter observation agrees with the insignificant dependence of strength on orientation, as shown in Table 2. The average grain size of the ferrite was about 10 μm (ASTM Grain Size No.10[11]).

2.2 Specimen

The form and dimensions of compact tension (CT) specimen are given in Fig.2. The positions of DC input leads and two pairs of potential output leads, *ie.* V_x and V_y, for using four-probe direct current potential drop (DCPD) to measure the crack growth [12] [13] are also indicated in the diagram.

The stress intensity range, ΔK_1, for CT specimens was calculated using the following equations [14].

$$\Delta K_1 = \frac{\Delta P}{B\sqrt{w}} Y \tag{3}$$

$$Y = \frac{2 + a/w}{\sqrt{(1 - a/w)^3}} [0.886 + 4.64(a/w) - 13.32(a/w)^2 + 14.72(a/w)^3 - 5.6(a/w)^4] \tag{4}$$

where ΔP is load amplitude, a is crack length, B and w are specimen thickness and width respectively. This equation is considered to be accurate within $\pm 0.5\%$ over the range $0.2 \leq a/w \leq 1.0$[14]. In the present work ΔK_1 is simply represented by ΔK. The specimens were machined in the TS orientation, with the notch parallel to the short transverse direction.

2.3 Environment

Artificial seawater to ASTM standard[15] was used throughout the work. Before each test the pH was adjusted to $8.1 - 8.2$, using $0.1N\ NaOH$ solution. For each test, 10 *litres* of aerated solution was used and recirculated at a flow rate of about 3 mm/s over the specimen surface. During the test the temperature of the solution was kept constant at $10 \pm 0.5°C$. Temperature was monitored in both cell and reservoir, to ensure that the solution passed the specimen at the desired temperature.

Where the effect of cathodic protection was studied, the potential was applied by a potentiostat with respect to the potential of a $Ag/AgCl$ reference electrode.

[1]The accuracy of this equation has not been verified for carbon steels with C less than 0.17%. However, the comparison is worthwhile to distinguish between the qualities of these two steels.

2.4 Testing Facilities

The cells were made of perspex and were suitable for fully aerated solutions. The solution was pumped into the bottom of the middle cell and overflowed into the outer jacket from which it drained, allowing total immersion of the specimen in the solution. Platinum counter electrodes were located on both lateral sides of the specimen when constant potentials were tested. The grips and pins were also made of CSM355 steel, identical to the specimen. Nevertheless, acetate sheet was used to insulate the loading pins from the specimen holes, to assure the accuracy of crack growth measurement using DCPD method. The sealing between the lower grips and cell was achieved by double Viton rings.

Corrosion fatigue tests were conducted on a cam-driven, constant amplitude (sine wave) EMEC machine of 20 KN capacity, modified for corrosive marine environment testing at a low frequency. The desired load range and load ratio are achievable by adjusting the top loading bar in conjunction with an appropriate eccentric ratio of the cam. The adjustment can be controlled manually or automatically through a stepper-motor. The load was continuously monitored by load cell.

Computerized data acquisition system was used. Four data channels are allocated to record the experimental data for each testing rig; two channels are for DCPD output, one channel for load and one channel for corrosion potential. The recording speed is 255 $points/s$.

2.5 Corrosion Fatigue Testing

Specimens were fatigue precracked in laboratory air on a servo-hydaulic fatigue machine at a frequency of 30 Hz and R ratio of 0.1. The precrack length giving $a/w = 0.3$ was adopted for all tests. The maximum stress intensity factor for the last 0.5 mm of fatigue crack extension was controlled to below 10 $MPam^{1/2}$.

The electrical leads for measurement of potentials, including both DCPD and corrosion potential leads, were spot-welded while the constant current input leads were screwed to the specimen. The joint point and exposed part of leads were carefully coated with silicon-rubber. Before test, the specimens were cleaned, by wiping, using acetone followed by 1-1-1 trichloroethane.

Once the solution reached the desired temperature, the valves to the corrosion cells were opened to start the test. When tested at controlled potential, a constant potential was applied as soon as the specimen was totally immersed in the solution. Before the application of load, all the specimens were precharged in the solution for six days with or without applied potential according to the environmental conditions required.

After precharging, load was applied to start the corrosion fatigue tests. The "increasing ΔK" method was employed for tests, as recommended by the standard for measuring the crack propagation rate greater than $10^{-9} m/cycle$[16] [17]. For the tests with R ratio of 0.7, this loading method was used throughout the test, as the K_{max} initially applied for corrosion fatigue at $R = 0.7$ was always well above the final K_{max} of fatigue precracking. However, for tests at $R = 0.1$, in order to avoid any possible effect of the pre-crack tip in retarding propagation of the corrosion fatigue crack, a K_{max} 30% higher than the maximum stress intensity in the final stage of precracking was applied initially to the specimen at the start of the corrosion-fatigue test. If this initial stress intensity range caused immediate crack propagation, ΔK was decreased until $da/dN < 10^{-8}$ $m/cycle$. The rate of ΔK decrease, C, was greater than -0.08 mm^{-1}, where,

$$C = \frac{dK}{Kda} \tag{5}$$

During crack propagation, the increase of ΔK was controlled by the increment of crack length while ΔP (the load range) and R were kept constant.

The loading frequency for corrosion fatigue was 0.35 Hz throughout the work. It has been shown[18][19][21][22] that the difference in crack growth rate between the loading frequencies of 0.1 and 0.35 Hz does not exceed a factor of two. Such a difference is no more than the normal data scatter band for data when measuring fatigue crack growth rates greater than $10^{-8} m/cycle$[17].

During the test, the calcareous scales on the specimen was removed daily. The potential and temperature were monitored continuously. The pH of the solution was checked at appropriate intervals and the solution was renewed weekly.

The measurements and testing data were validated according to the specifications of ASTM E 647 [17]. A da/dN vs ΔK plot was computed from the data using a seven-point incremental polynomial curve fitting method, as recommended by the Standards[16] [17].

3. RESULTS

3.1 Effect of Potential at $R = 0.7$

Figure 3 shows the effect of potential on da/dN vs ΔK determined at R ratio, 0.7. Since the specimens at high R ratio were subjected to a high K_{max}, the linear elastic fracture mechanics validity limit (LEFMVL) of ΔK, *ie.* $15 MPam^{1/2}$, is indicated in the figure. Strictly speaking, linear elastic fracture mechanics is only valid for ranges of ΔK below the limit. The criteria for defining the true limit of tested specimens follows the recommendation by ASTM Standard E647[17]:

$$W - a \geq \frac{4}{\pi}\left(\frac{K_{max}}{\sigma_y}\right)^2 \tag{6}$$

where W and a are the specimen width and crack length respectively, $K_{max} = \Delta K/(1-R)$, and σ_y is the yield strength ($410\ MPa$) for the present steel.

The results show that the effect of potential is ΔK dependent. At relatively lower ΔK, cathodic over-protection at $-1.10\ mV$ suppressed da/dt. However, da/dN at $-1.10\ V$ increased rapidly as ΔK increased, and exceeded da/dN at the other two potentials when ΔK was over 11 $MPam^{1/2}$. The effect of potential became less significant just before unstable crack propagation took place.

The tests of $R = 0.7$ were terminated when unstable crack propagation took place. Therefore, the provisional fracture toughness, K_Q, was calculated by

$$K_Q = \frac{\Delta K_{insta}}{1-R} \tag{7}$$

where ΔK_{insta} is the ΔK at which the crack growth becomes unstable.

The effect of potential on K_Q is shown in Table 3. The result at free corrosion potential is just in the range of K_Q measured by Webster *et al.* for rolled BS4360:50D plate in air ($67 - 83\ MPam^{1/2}$)[23]. Moreover, at $-1.10\ V$, the effect of bulk hydrogen charging in lowering the fracture toughness[13] appears appreciable. It is also noted that in wet H_2S environment, the K_Q of rolled BS4360:50D plate, determined by Webster *et al.*[23], is $60 - 62\ MPam1/2$, which is identical to the K_Q of the present steel at $-1.10\ V$.

3.2 Effect of Potential at $R = 0.1$

Fig.4 shows the effect of potential on corrosion-fatigue crack propagation at $R = 0.1$. All the data presented in the diagram satisfy the requirements of linear elastic fracture mechanics.

Comparing the results between the two R ratios, three general observations are noted below:

- at both R ratios, crack growth at $-1.10\ V$ increased rapidly as ΔK increased, reaching the highest da/dN at high ΔK;
- in the low range of ΔK (near the threshold region), the most susceptible crack propagation at $R = 0.1$ occurred at the free corrosion potential(F.C.P), compared with $-0.85V$ under $R = 0.7$;
- for a given potential, tests at $R = 0.7$ always showed more susceptibility to corrosion-fatigue propagation than tests at $R = 0.1$.

(The last observation will be depicted more clearly in the next section in conjunction with detailed data analysis of the individual da/dN curves).

The free corrosion potential measured for CSM355 steel exposed to ASTM seawater was about $-0.68\ V$ $(Ag/AgCl)$ at the beginning of immersion, and then dropped to a fairly stable level of $-0.74\ V$ in about two days. Fatigue loading at the different R ratios did not seem to have any discernible effect on the change of F.C.P. Within a week, the pH of the solution remained in the range of 8.1 to 8.2 at all potentials applied, before the renewal of the solution.

3.3 The Effect of R Ratio on Crack Growth

Although the results at different R ratios are already included in the previous diagrams showing the effect of potential, clearer views of the effect of R ratios in individual potentials are helpful to analyse the results further. Figs.5–7 present the da/dN vs ΔK curves of two R ratios in the form respectively at F.C.P., $-0.85\ V$ and $-1.10\ V$. In these figures, the solid lines are drawn by the regression of at least five data points based on the Paris Relationship[24],

$$da/dN = C\Delta K^m \tag{8}$$

where, C and m are constants. The details of the constants are given in the following equations with corresponding range of ΔK based on the present experimental data:

Potential (Ag/AgCl)	R	Range of ΔK $(MPam^{1/2})$	$da/dN = C\Delta K^m$ $m/cycle$
F.C.P	0.7	$7.7 < \Delta K \leq 9.6$	$da/dN = 2.51 \times 10^{-31}\Delta K^{22.7}$
		$9.6 < \Delta K \leq 20.4$	$da/dN = 2.02 \times 10^{-12}\Delta K^{3.91}$
	0.1	$7.8 < \Delta K \leq 12.2$	$da/dN = 9.05 \times 10^{-22}\Delta K^{12.4}$
		$12.2 < \Delta K \leq 27.9$	$da/dN = 3.97 \times 10^{-12}\Delta K^{3.48}$
$-0.85V$	0.7	$7.4 < \Delta K \leq 20.0$	$da/dN = 6.55 \times 10^{-11}\Delta K^{2.67}$
	0.1	$10.0 < \Delta K \leq 33.0$	$da/dN = 1.20 \times 10^{-12}\Delta K^{3.40}$
$-1.10V$	0.7	$6.2 < \Delta K \leq 11.6$	$da/dN = 7.74 \times 10^{-19}\Delta K^{10.2}$
		$11.6 < \Delta K \leq 17.3$	$da/dN = 4.38 \times 10^{-9}\Delta K^{1.31}$
	0.1	$13.6 < \Delta K \leq 24.0$	$da/dN = 9.40 \times 10^{-25}\Delta K^{12.4}$
		$24.0 < \Delta K \leq 35.6$	$da/dN = 4.61 \times 10^{-10}\Delta K^{1.98}$

From the diagrams, it appears that the effect of R ratio on the corrosion fatigue for a given ΔK becomes more pronounced as the applied potential becomes more negative, in terms of both the near threshold region and the crack propagation rate.

The primary objective of the present task is to study crack propagation, for which attention has been paid mainly to crack growth rates greater than $10^{-8}\ m/cycle$. Neverthless, the threshold stress intensity range, ΔK_{th}, has been assessed tentatively by extrapolating the data down to $da/dN = 10^{-10}\ m/cycle$. The effects of potential and R ratio on ΔK_{th} are shown in Fig.8. The rationality of the assessment will be discussed later.

It is also noted that in Fig.7, the data produced by two different R ratios at $-1.10\ V$ all seem to possess a small inflection on their da/dN curves. Alternatively, a possible propensity of da/dN as a function of ΔK is marked by broken (dashed) lines. This may be more than an interesting coincidence, given by different loading ratios, and might conceal some effect of environment. If this were to be true, the ΔK_{th} would be defined by the broken lines instead of the intercept of the solid lines based on Paris Relationship. However, until the results have been reproduced, more conservative data are preferred currently for discussion.

The fractographic examinations showed the crack paths under all tested conditions to be transgranular; brittle fracture surfaces, associated with fatigue striations, were observed. There was no distinctive effect of potential, or of R ratio, on the crack morphology. Secondary cracks were frequently found.

4. DISCUSSION

4.1 Crack Propagation Rate

A general comparison shows that the whole range of crack propagation rates of CSM355 steel determined so far are similar to that of BS4360:50D steels summarized in the review by Gangloff[6], despite the

differences in loading frequency, steel composition and seawater. To further confirm the similarity, Fig.9 compares the present results of da/dN vs ΔK at the free corrosion potential with curves (the solid lines in the diagram) calculated based on Thorpe's simple model[25] for BS4360:50D welded joints in natural seawater subjected to loading at $1Hz$ and various R ratio. The details of Thorpe's model for free corrosion condition are given below[2]:

Range of ΔK ($MPam^{1/2}$)	$da/dN = C\Delta K^m$ $m/cycle$
$\Delta K < 11.8 - 5.2R$	0
$\Delta K > 11.8 - 5.2R$	if $R < 0.5$: $da/dN = (1+2R)5.8 \times 10^{-12}\Delta K^{3.2}$
$\Delta K > 11.8 - 5.2R$	if $R > 0.5$: $da/dN = 1.54 \times 10^{-11}\Delta K^{3.3}$

Taking the possible scatter in data into account, both results agree well with each other, although the steels, loading frequencies and (even) seawaters are different.

In order to understand the effect of cathodic protection, the normalized crack propagation rate as a function of potential is shown in Figs.10 and 11 respectively for $R = 0.1$ and 0.7. The normalization was made by taking the crack propagation rate at $-0.85\ V$ as unity. The stress intensity ranges for the comparison are 22 $MPam^{1/2}$ for $R = 0.1$ and 12 $MPa^{1/2}$ for $R = 0.7$. Consideration is given to the crack propagation stage where the environment played a relatively important role in crack growth, and also to the valid stress intensity range of LEFM especially for $R = 0.7$.

At $R = 0.1$, cathodic protection with applied potential of $-0.85\ V$ has a beneficial effect on the reduction of crack growth rate. This analysis is in agreement with the results of BS4360:50D steel in seawater at $20°C$, subjected to stress intensity range in the range from 20 to 30 $MPam^{1/2}$ at a loading frequency of $f = 0.1\ Hz$ and $R = 0.1$[6][19].

However, at $R = 0.7$, the susceptibility to corrosion fatigue in terms of relative crack growth rate is enhanced by cathodic protection at $\Delta K = 12\ MPam^{1/2}$; data from the more negative potential results in faster crack growth in that ΔK range. Although there is no comparable data available for $R = 0.7$, the present results can reasonably be explained in terms of the effect of hydrogen on the acceleration in crack propagation at high K_{max}. A simple calculation gives a K_{max} of 40 $MPam^{1/2}$ at $R = 0.7$ which is much greater than the K_{max} of 24 $MPa^{1/2}$ for $\Delta K = 22MPam^{1/2}$ at $R = 0.1$. It is not surprising that hydrogen embrittlement will become more effective at high stress intensities, even if the potential of $-0.85\ V$ for normal cathodic protection is applied. This also accounts for the fact that regardless of R ratio, the crack growth rate due to corrosion-fatigue at the cathodic over-protection potential ($-1.10\ V$) always developed rapidly as the stress intensity range increased (see Figs.3 and 4). In a dry hydrogen atmosphere, Cotterill and King reported[26] that for BS4360:50E steel, there is little contribution of hydrogen to fatigue crack growth at values of ΔK below 20 $MPam^{1/2}$ at $R = 0.1$ and $f = 0.1\ Hz$; the great enhancement of crack growth by hydrogen was observed at high ΔK range. This supports the present argument.

4.2 Threshold Stress Intensity Range

The data published for ΔK_{th} of offshore structural steels are quite controversial. It is now well accepted that the results are strongly dependent on test methodology[3][17][27]. To detect a reliable threshold value, a load shedding/ΔK decrease method at a certain rate of $d\Delta K/Kda$ is suggested[17][27]. The threshold should be defined at sufficiently low da/dN ($< 10^{-10}\ m/cycle$), but several months, at least, are needed to obtain such data[3].

It has been admitted already that the extrapolation used in the present work is approximate. Nevertheless, it is interesting to see that the ΔK_{th} estimated is not far beyond the range of the threshold stress intensity range of BS4360:50D in seawater reported by a number of workers[3][28][29][30], as shown from

[2]Thorpe also proposed a model for da/dt vs ΔK at $-0.85\ V$ ($Ag/AgCl$), but the comparison is hindered because of inconsistencies contained within the expressions given in Reference [25] (Table 1, page 6).

Fig.12. More interestingly, Fig.8 exhibits quite regular effects of potential on the ΔK_{th}. Little effect of R ratio on the threshold can be detected at free corrosion potential. When the potential goes more negative, the threshold increases almost linearly with the decrease in potential at $R = 0.1$ whereas a reversal of this trend is observed at $R = 0.7$. It is difficult to reach a conclusion based on these extrapolations. If the results are reproducible, they might presumably reflect the cracking behaviour characteristic of stress-corrosion fatigue[31][32] (including the contribution of hydrogen); the lesser significance of mean stress intensity on the crack initiation mainly by localised dissolution at free corrosion potential, and the greater significance of mean stress intensity on hydrogen-induced, stress-dominated crack initiation at cathodic potentials as shown in Fig.8 are appropriate to that mechanism. This explanation is also supported by the crack-tip electrochemistry of BS4360:50D under corrosion fatigue, studied by Turnbull[33]. In addition, the fatigue threshold stress intensity of offshore structural steels are always reported to be higher in seawater than in air[6][27], which is an important feature of stress-corrosion fatigue. At the same R ratio but different potential, the competition of localized dissolution and hydrogen embrittlement, in conjunction with the effective stress intensity range, might control the threshold. Kermani and Procter[10] produced additional evidence from slow strain rate tests which supports the hydrogen embrittlement of BS4360:50D steel in 3.5% $NaCl$ solution under cathodic protection, finding that the ductility of the steel decreased considerably below a cathodic potential of $-0.85\ V\ (SCE)$.

4.3 The Effect of Effective Stress Intensity Range

It is well known that the effects of R ratio on fatigue crack propagation are mainly attributable to crack closure, by which the effective stress intensity range is reduced; a low R ratio will result in more effective crack closure. Therefore, the reduced susceptibility of crack propagation at lower R and at all applied potentials is not surprising. In addition to R ratio, the effective stress intensity range also depends strongly upon crack geometry[34] and micro-roughness[35][36]. In corrosion-fatigue, the situation becomes more complicated as corrosion products would enhance the crack closure while the maximum stress intensity may play more roles in environment-induced cracking. For a certain R ratio, the relative contributions of crack closure and maximum stress intensity factor to the corrosion fatigue crack propagation have not been fully analysed.

5. Conclusions

The following conclusions are drawn from the results of corrosion fatigue tests for CSM355 steel in ASTM artificial seawater at $10°C$, subjected to two R ratios (0.1 and 0.7), three potentials (F.C.P., -0.85 and -1.10 V (Ag/AgCl)), at a loading frequency of 0.35 Hz.

1. In general sense, the corrosion-fatigue propagation of CSM355 steel does not show a radical difference from that of traditional BS355D (BS4360:50D) steels. It is suggested that increasing the strength of offshore structural steel may not necessarily exacerbate its susceptibity to corrosion fatigue in seawater.
2. High $R = 0.7$ ratio shows more susceptibility to corrosion-fatigue crack propagation.
3. The effect of potential on crack propagation rate is influenced by ΔK range. Normal cathodic protection is beneficial at low ΔK and low R ratio. At both R ratios, crack growth at the cathodic over-protection potential, $-1.10V$ increases rapidly as ΔK increases.
4. The crack growth rates, provisional fracture toughness and extrapolated threshold stress intensity ranges of CSM355 steel are in similar ranges to the corresponding data available from BS355D (BS4360:50D).
5. The corrosion-fatigue data produced at a loading frequency of $0.35Hz$ are comparable with those at $0.1 - 0.167\ Hz$.

Aknowledgement: The authors thank Professor C. M. Sellars for the provision of research facilities in the Dept. of Engineering Materials, University of Sheffield and are grateful to CSM, Rome for their financial support and permission to publish this work.

References

[1] J Billingham, "Materials for Offshore Structures", Metals and Materials, August, pp.472-478, (1985).

[2] D.Uwer and J.Degenkolbe, "Recent Trends in the Development of Offshore Steels", Proceedings of the First International Offshore and Polar Engineering Conference, Edinburgh, UK, 11-16 August, (1991), pp.190-199.

[3] H.G.Morgan, "The determination of Fatigue Thresholds and Short Crack Growth Behaviour in Structural Steel to BS4360:50D in Air and Seawater", UK AEA Report, ND-R-985(S), (1985),OTO, HMSO.

[4] J.V.Sharp, "The Use of Steel and Concrete in the Construction of North Sea Oil Production Platform", Journal of Materials Science, 14, pp.1773-1799, (1979).

[5] D.M.Shuter, "A Prediction Methodology for Fatigue Crack Propagation," Proceedings of the First International Offshore and Polar Engineering Conference, Edinburgh, UK, 11-16 August, (1991), pp412-419.

[6] R.P.Gangloff, "Corrosion Fatigue Crack Propagation in Metals ", Proceedings of the First International Conference on Environment-Induced Cracking of Metals, Eds. R.P.Gangloff and M.B.Ives, October 2-7, (1988), The American Club, Koler, Wisconsin, USA, NACE, pp.55-109.

[7] BS7191:1989, British Standard Specification for Weldable Structural Steels for Fixed Offshore Structures.

[8] BS4360:1986, Specification for Weldable Structural steels.

[9] Institute of Welding, Technical Report 1967, IIW Doc.IW-535-67.

[10] M.B.Kermani and R.P.M.Procter, "Environmental Cracking of Cathodically Protected Marine Structural Steels in a Saline Environment", Proceedings of Eighth International Conference on Offshore Mechanics and Arctic Engineering, *Vol.III, Eds. M.M.Salama, N.V.Bangaru, R.Denys*, H.C.Rhee and M.Toyod, Book No.10285C, (1989), pp.447-459.

[11] George E.Dieter, "Mechanical Metallurgy", MacGRAW-HILL KOGAKUSHA, LTD. Second Edition, p.199; or: "Metals Handbook", American Society for Metals, Metals Park, Ohio, 1948.

[12] L.N.McCartney, P.E.Irving, G.T.Symm, P.M.Cooper and A.Kurzfeld, "Measurement of Crack Lengths in Compact Tension and Single Edge Notch Specimens Using a New Electrical Potential Calibration", NPL Report, DMA(B)3, February, (1977).

[13] J.Yu, R.Brook, R.B.Hutchings and A.Turnbull, "Stress-Corrosion of Stainless Steels in Sour Marine Environments ", Paper No. 48, NACE Conference on Life Prediction of Corrodible Structure, 23-26 September (1991), Cambridge, UK.

[14] BS 6980:Part6:1990; ISO 7539-6:1989(E), Corrosion of Metals and Alloys-Stress Corrosion Testing-part 6: Preparation and Use of Pre-Cracked Specimens.

[15] ASTM D1141-86, Standard Specification for Substitute Ocean Water.

[16] BS 6835:1988, British Standard Method for Determination of Rate of Fatigue Crack Growth in Metallic Materials.

[17] ASTM E647-88, American Standard Test Method for Measurement Fatigue Crack Growth.

[18] H.G.Morgan and T.W.Thorpe, "An Introduction to Crack Growth Testing in the UKOSRP and Its Relevance to the Design of Offshore Structure", Fatigue in Offshore Structural Steels, Thomas Telford Ltd, London, (1981), pp.25-43.

[19] P.M.Scott, T.W.Thorpe, D.R.V.Silvester, "Rate-Determining Processes for Corrosion Fatigue Crack Growth in Ferritic Steels in Seawater", Corrosion Science, 23, pp.559-575, (1983).

[20] P.M.Scott and D.R.V.Silvester, Interim Technical Report, UKOSRP, 3/02, Department of Energy, HMOS, London, (1977).

[21] P.M.Scott and D.R.V.Silvester, UK Offshore Steels Research Project Interim Technical Report 3/03 (1975), OT-R-7732, Technical Report Centre, Orpington, Kent,(1975).

[22] P.M.Scott and D.R.V.Silvester, UK Offshore Steels Research Project Interim Technical Report 3/03 (1977), OT-R-7731, Technical Report Centre, Orpington, Kent,(1977).

[23] S.E.Webster, I.M.Austen, W.J.Rudd, Fatigue, Corrosion Fatigue and Stress Corrosion of Steels for Offshore Structures, Final Report, British Steel Corporation, Swinden Laboratories, ECSC. Agreement No. 7210, KG/801.

[24] P.C.Paris and F.Erdogan, "A Critical Analysis of Crack Propagation Laws", Journal of Basic Engineering, Trans. ASME, Vol.85, pp.528-534, (1963).

[25] T.W.Thorpe, A Simple Model of Fatigue Crack Growth in Welded Joints, Offshore Techninology Report, OTH 86 225, HMSO, London, (1986).

[26] P.J.Cotterill and J.E.King, Int. J. Fatigue, 13, 6, pp.447-452, (1991).

[27] D Taylor, A Compendium of Fatigue Thresholds and Growth Rates, (1985), EMAS.

[28] T.W.Thorpe and A.Rance, Corrosion Fatigue Crack Growth in BS4360 Grade 50D Structural Steel in Seawater under Narrow Band Variable Amplitude Loading, Offshore Technology Report, London, HMSO, (1986).

[29] I.M.Austen, W.J.Rudd and E.F.Walker, "Factors Affecting Corrosion Fatigue and Stress Corrosion Crack Growth in Offshore Steel", Proceedings of International Conference on Steel in Marine Structures, Paris, October (1981).

[30] E.Bardal, T.Barge, M.Grovlen, P.J.Haggensen and B.M.Forre, "Measurements of Very Low Corrosion Fatigue Crack growth Rates in Structural Steel in Artificial Seawater", Proceedings of International Conference on Fatigue Thresholds, Stockholm, June 1981, Eds. C.J.Beevers, EMAS (1982).

[31] I.M.Austen, E.F.Walker, Fatigue 84, pp.1457-1469.

[32] I.M.Austen and E.F.Walker, "Quantitative Understanding of the Effects of Mechanical and Environmental Variables on Corrosion Fatigue Crack Growth Behaviour", IMechE, C98/77, pp.1-10, (1977)

[33] A.Turnbull, "Crack-Tip Electrochemistry in Relation to Corrosion Fatigue of Offshore Structural Steels in Seawater-Technical Summary and Implications", OTH 90 325, Heath and Safety Executive-Offshore Technology Report, UK.

[34] Hein-Peter Stüwe, Reinhard Pippan and Guo Xin Shan, "On the Geometry of Fatigue Crack Closure", Steel Research, 63, No.8, pp.368-370, (1992).

[35] S.Suresh, "Fatigue Crack Deflection and Fracture Surface Contact: Micromechanical Models", Metallurgical Transactions A, Vol.16A, February, pp.249-260, (1985).

[36] S.Suresh, "Crack Growth Retardation due to Micro-Roughness: A Mechanism for Overload Effects in Fatigue", Scripta Metallurgica, Vol.16, pp.995-999, (1982).

Table 1: Chemical composition (wt.%) and carbon equivalent value (CEV) of CSM355 steel in comparison with the specification of standard BS355D (BS4360:50D) steel.

Element	CSM355	BS355D
C	0.053	0.180
Mn	1.44	$\leq$1.50
Si	0.29	0.10/0.50
P	0.010	0.040
S	$\leq$0.001	0.040
Ni	0.30	-
Cr	$\leq$0.01	-
Mo	$\leq$0.005	-
V	$\leq$0.01	0.003/0.10
Nb	$\leq$0.021	0.003/0.10
Ti	0.034	-
Al	0.039	-
Cu	$\leq$0.01	-
N	0.005	-
O	0.0012	-
CEV(Eq.1)	0.32	0.43/0.45
CEV(Eq.2)	0.21	0.33

Table 2: Comparison of heat-treatment and mechanical properties between CSM355 and BS355D steel. The data are obtained from 50 mm thick plate.

Steel	CSM355	BS355D
Heat-treatment	accelerated cooling after controlled rolling	normalized after rolling
$\sigma_y(MPa)$	410 (longitudinal) 417 (transverse)	355-390
$\sigma_{uts}(MPa)$	508 (longitudinal) 510 (transverse)	490-640
Elongation(%)	32 (longitudinal) 31 (transverse)	20 (min.)
Charpy V-notch impact at $20°C$ (J/cm^2)	300	50 (min.)

Table 3: The effect of potential on the provisional fracture toughness, K_Q, of CSM355 steel exposed to ASTM seawater; the true R ratio used for calculation was 0.69.

Potential (V) $(Ag/AgCl)$	ΔK_{insta} $(MPam^{1/2})$	K_Q $(MPam^{1/2})$
F.C.P	21.7	70.0
-0.85	20.7	66.8
-1.10	18.6	60.0

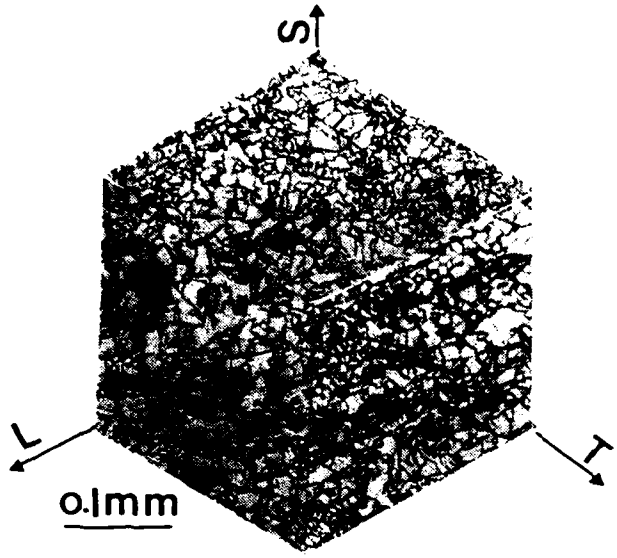

Figure 1. Optical metallograph of CSM355 steel in three dimensions; sample etched.

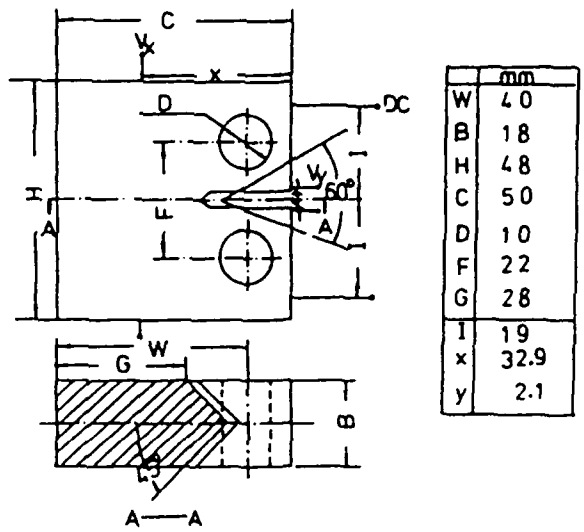

Figure 2. Specimen dimensions and DCPD lead positions.

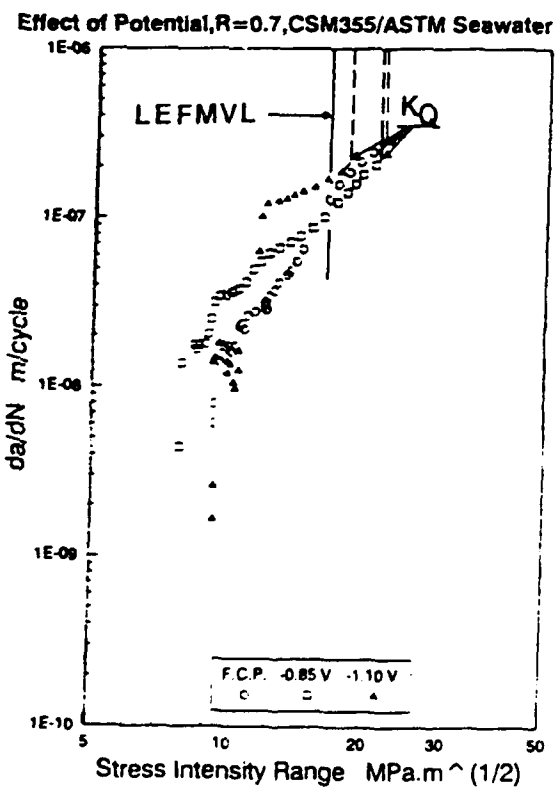

Figure 3. Effect of potential on da/dN vs ΔK, at $R = 0.7$ and $f = 0.35\ Hz$.

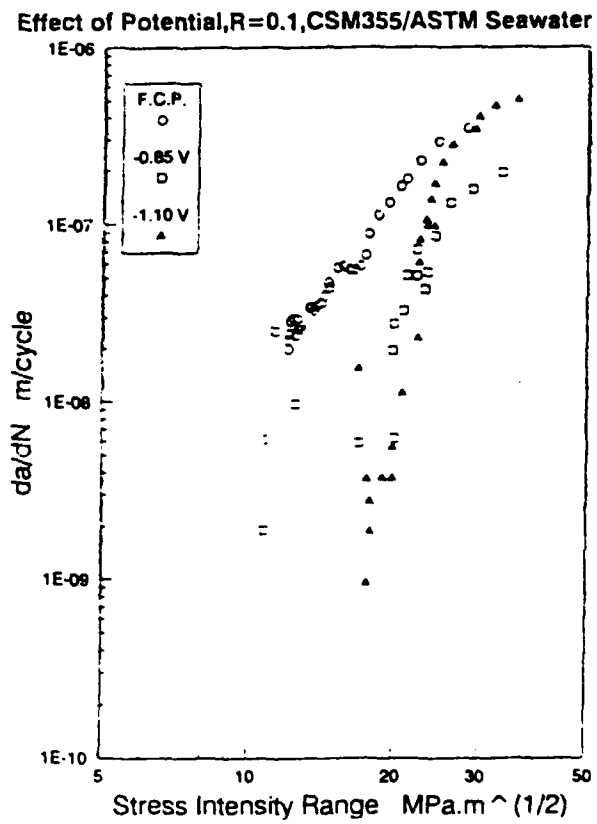

Figure 4. Effect of potential on da/dN vs ΔK, at $R = 0.1$ and $f = 0.35\ Hz$.

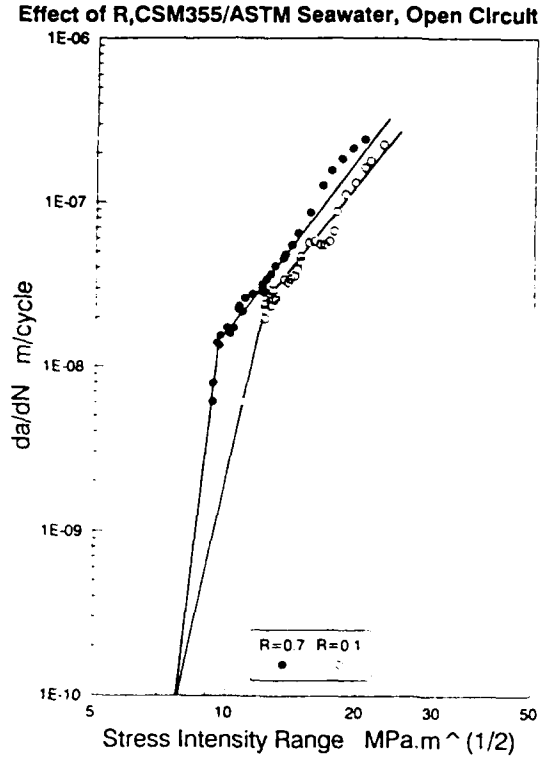

Figure 5. Effect of R ratio on da/dN vs ΔK, at free corrosion potential and $f = 0.35\ Hz$.

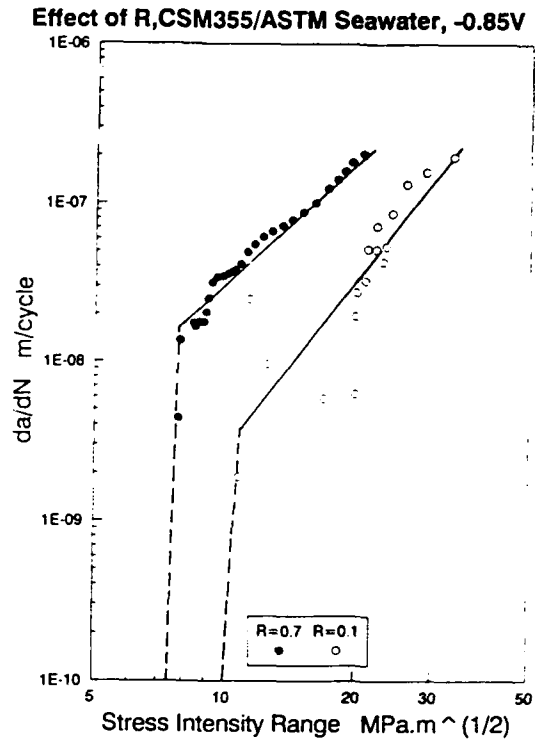

Figure 6. Effect of R ratio on da/dN vs ΔK, at $-0.85V$ and $f = 0.35\ Hz$.

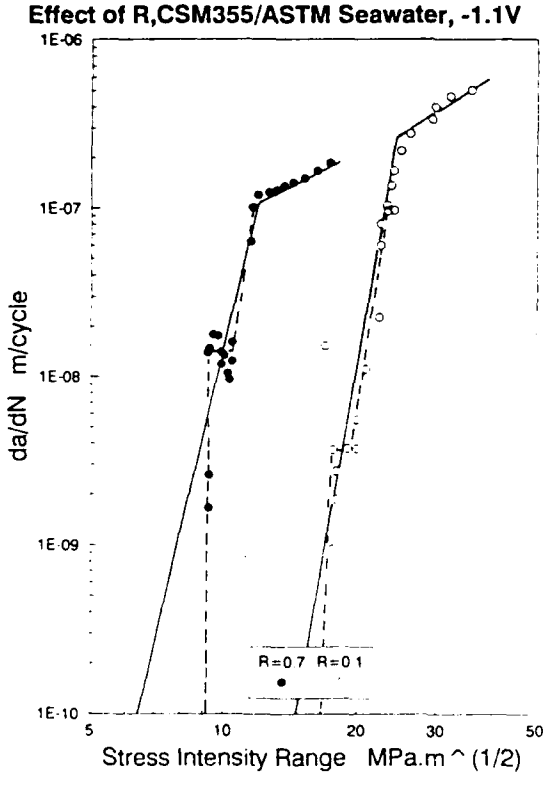

Figure 7. Effect of R ratio on da/dN vs ΔK, at $-1.1V$ and $f = 0.35 Hz$.

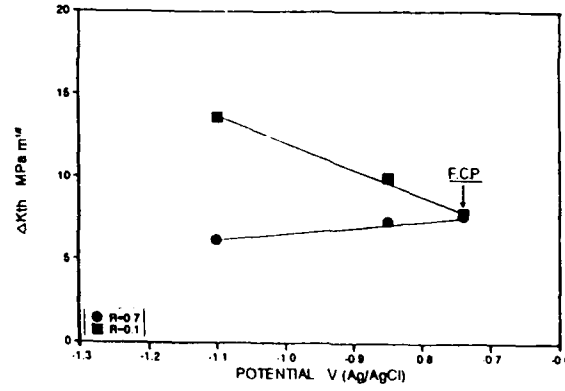

Figure 8. Effect of potential and R ratio on $DeltaK_{th}$ of CSM400 steel.

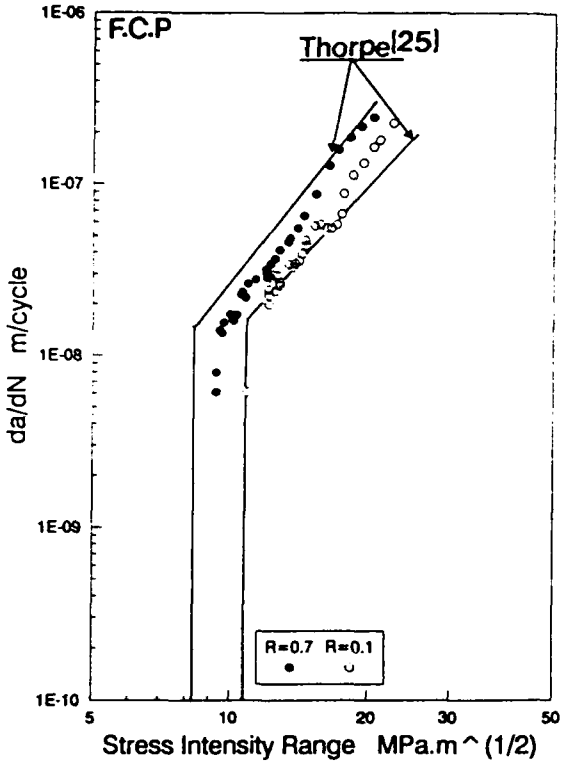

Figure 9. Comparison between the present results and Thorpe's model[25] for BS4360:50D welded joint subjected to a loading frequency of $0.1Hz$ in seawater at free corrosion potential.

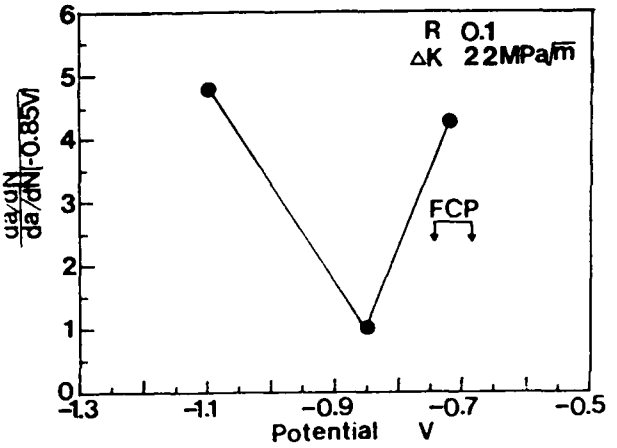

Figure 10. Normalized crack growth rate as a function of potential; $R = 0.1$, $\Delta K = 22MPam^{1/2}$.

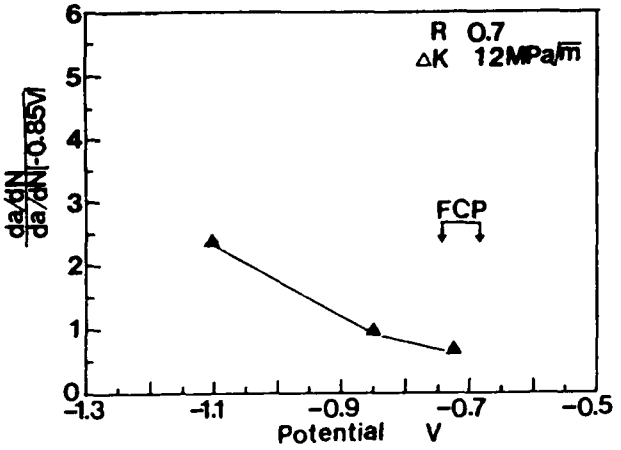

Figure 11. Normalized crack growth rate as a function of potential; $R = 0.7$, $\Delta K = 12MPam^{1/2}$.

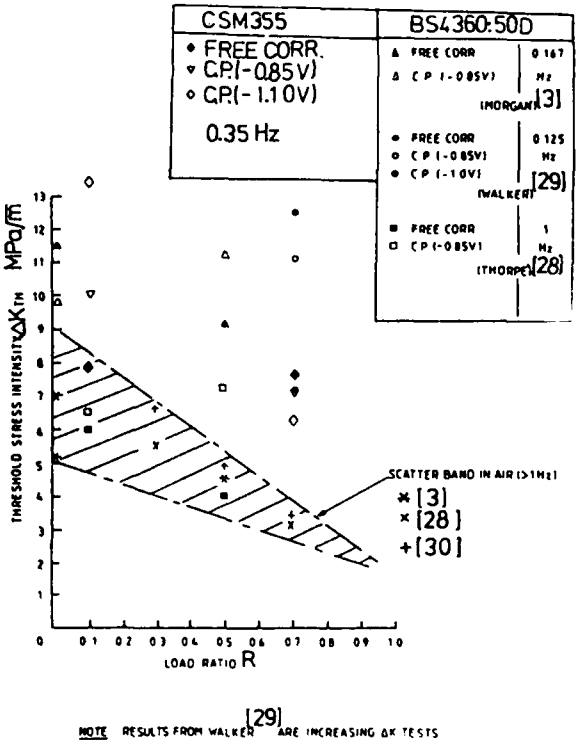

Figure 12. ΔK_{th} of CSM355 steel, obtained from the present results, in comparison of published data for BS4360:50D steel.

Corrosion Fatigue in Fossil-Fueled Boilers

G. I. Ogundele
Ontario Hydro
700 University Avenue
Toronto, Ontario
Canada

E.T.C. Ho
Ontario Hydro
700 University Avenue
Toronto, Ontario
Canada

D. Sidey
Ontario Hydro
700 University Avenue
Toronto, Ontario
Canada

Abstract

Corrosion fatigue of waterwall tubing in fossil-fueled boilers is a significant problem. As part of a wide-ranging study into the phenomenon, laboratory tests to reproduce the failures typically observed in the field were performed with the objective of defining the critical environmental parameters controlling tube life.

The laboratory tests involved the use of full size carbon steel tubing material produced to meet the specification SA 210-A1, which is widely used for waterwall and economizer tubes. The rationale for this test approach is that it provides an actual boiler tube condition in terms of geometry, waterside surface, microstructure, and cracking orientation. A recirculating autoclave loop system was developed to perform the tests under carefully controlled water chemistry and stressing conditions. Results have shown that cracking morphology similar to those found in field failures can be reproduced. Dissolved oxygen and pH are the environmental factors that have the largest influence on corrosion fatigue behavior of the steel.

This paper presents a review of field observations of a number of boiler tube failures, current research efforts to generate similar failure mode to provide a root cause of corrosion fatigue in boiler tubes, and a discussion on the possible mechanisms to explain the corrosion fatigue process.

Key terms: corrosion fatigue, crack initiation, dissolved oxygen, pH, mechanisms, power plant, carbon steel

Introduction

In thermal generating stations, low or medium carbon steels are used for steam generating waterwall and economizer tubes. These materials, subjected to intense operating conditions of high pressure and high temperature, are expected to display adequate mechanical strength and acceptable corrosion resistance to attain reasonable operating efficiency and reliability of the boilers[1]. Waterwalls, be they of membrane or tangent tube construction, are large structures with numerous constraining attachments. At start-up and shutdown, mechanical strains in tube walls are very significant and, in the presence of any constraint, low-cycle fatigue damage is likely to occur[2]. Moreover, these boilers may experience problems resulting from enhanced corrosion processes which occur during start-ups. This simultaneous application of low-cycle fatigue and corrosion processes would result in corrosion fatigue cracking. Corrosion fatigue, if not controlled, leads inevitably to boiler tube failures. Boiler tube failures in fossil-fueled power

plants have resulted, typically in an annual plant availability loss of 4% in North America; corrosion fatigue is responsible for a significant proportion[3].

The corrosion fatigue process involves two principal aspects - crack initiation and crack propagation. Crack initiation entails cyclic plastic deformation followed by initiation of one or more micro cracks and coalescence of micro cracks to form one or more macroscopic cracks[4]. The initiation aspect is further complicated by the environmental influence. Of immediate practical need to address any corrosion fatigue damage in boiler tubes is for data generation relating crack initiation to the usual mechanical loading parameters in realistic boiler water chemistry environments[2]; currently, such data appear to be non-existent.

This paper presents (a) a review of some field observations based on metallurgical failure analysis on a number of tubes removed from operating boilers, (b) current research efforts to generate a failure mode similar to those observed in the field, and (c) a discussion on the possible mechanisms to explain the corrosion fatigue process.

Field Observations

The characteristic features of corrosion fatigue failures are normally obtained through metallurgical failure analysis performed on tubes removed from boilers. The tubes either leaked or were suspected to contain some sort of damage detected during non-destructive examination. The procedure typically involves visual and metallographic examinations, microstructural characterization, fractographic examination and chemical analysis.

Figure 1 shows examples of cracking in boiler tubes due to corrosion fatigue. The inside surface and cross-section of a header vestibule attachment are shown in Figures 1 (a) and 1 (b). The cracking was caused by high hoop stresses and upsets in water chemistry. Figure 1 (c) shows axial cracking in a thick wall section, economizer feed water elbow, caused by thermal stress-induced fatigue and enhanced by corrosion. The bulge profile along the length of the crack was probably caused by corrosion. Figure 1 (d) shows a crack in an economizer tube hairpin bend. The failure location on the hairpin bend coincided with regions of the highest tensile elastic hoop stress with combined residual and elastic stresses that were produced during tube fabrication, ovality conditions at the U-bend area, and boiler operating conditions. Figure 2 shows the morphology of cracks in a waterwall tube that suffered corrosion fatigue and was then repaired by weld overlay. The cracks initiated from the waterside surface, propagated through the boiler tube and the weld repair. This crack path suggests that the repair did not remove all the previous damage. It is probable that conditions promoting corrosion fatigue existed even after returning the component back into service.

The fracture surface of a field produced crack revealed multiple semi-elliptical shapes indicating several initiation sites. Scanning electron microscopy examination of a region on the fracture surface of a field sample is shown in Figure 3. As expected, the structure of the fracture surface has been modified by severe corrosion attack.

Examination of the crack morphologies in Figures 1 and 2 indicates that the cracks initiated from the bottom of pits or directly from the waterside surface. The waterside surface of boiler tubes is microscopically "rough" from manufacture and, with extended plant operation, the boiler water environment would facilitate the growth of any generic discontinuities on the waterside surface. In this respect, information on crack initiation phenomena can be gleaned from the assessment of the conditions of the inside surface of waterwall and economizer tubes. As part of understanding boiler tube failures, Ontario Hydro conducts, quite routinely, the characterization of waterside surface conditions to assess the impact of, for example, chemical cleaning and lay-up conditions on boiler tube integrity. Figure 4 shows a series of pits which originated from the waterside surface of tubes obtained from operating boilers. The pits appear round, dish-like, sharp, and elongated. The inside surface of the pits are filled with oxide scale. The scales normally consist of a typical double layer morphology which includes an inner protective magnetite layer. In some cases active pits are observed with no oxide scale coverage.

From the above examples and others published elsewhere[1,2] corrosion fatigue damage in boiler tubes is characterized by multiple cracks which initiate and grow from the waterside surface. Ultimately, one crack becomes dominant and causes a throughwall crack[1]. The cracks are commonly longitudinal with respect to the tube axis, which is

normal to the maximum tensile hoop stresses; but cracks may occur in any orientation, depending on the local stress pattern. The loading on boiler tubes includes complex interaction of thermal stresses, system forces, and residual stresses. The cracking locations in waterwalls and economizers are somewhat associated with complex tube geometry and attachments such as at windbox casings, buckstay corners, tie-bar supports, sootblower and hairpin bends.

Having recognized the principal features in field-generated corrosion fatigue cracks, there was a need to develop a laboratory test program whereby corrosion fatigue cracking can be realistically generated under controlled conditions in a section of boiler tubing. The required test technique, including the choice of specimen geometry, should attempt to reproduce the above characteristics in order to provide a root cause of corrosion fatigue damage in boiler tubes.

Current Research Efforts

Specimen Design

The material was taken from a commercial heat, grade SA210-A1, carbon steel tubing commonly used in drum type boilers. The chemical composition in weight percent was 0.17 C, 0.62 Mn, 0.013 P, 0.013 S, 0.21 Si, 0.044 Mo, 0.16 Cr, 0.13 Ni, 0.17 Cu, 0.015 Al, <0.005 V, <0.005 Ti, remainder Fe. The microstructure of the steel in orthogonal directions, shown in Figure 5, indicates the usual ferrite-pearlite aggregate with non-degenerated pearlite. The mechanical properties at 274°C were: 0.2% yield strength equals 298 MPa and tensile strength equals 603 MPa. The test specimen is shown in Figure 6. No machining of the inside surface or thermo-mechanical treatment was done on the material before testing.

Environmental Controls and Mechanical Loading

The test electrolyte was prepared from reagent grade chemicals and deionized water. Tests were conducted at *different levels of dissolved oxygen (<10 to 1000 ppb) and pH (6.5 and 9).* The chloride and sulfate ion concentrations were kept constant at a nominal concentration of 600 ppb. The solutions were well controlled within ±10% of the nominal concentration values.

The specimen was held between loading grips as shown in Figure 7. The grips were designed to facilitate cyclic compression of the tubular specimen between specified minimum and maximum loads using an MTS servohydraulic closed loop system. This arrangement produced tensile stresses on the inside surface of the tube at the lower adapter position. Finite element analysis of this loading arrangement agrees well with those determined using strain gauges. The experiments were conducted under load control from 25 kN to 100 kN at a cycle frequency of 0.0005 Hz using an inverted haversine waveform. The maximum inside surface stress was determined to be 520 MPa which is well into the plastic regime of the material. Since the test conditions were expected to produce a wide range of fatigue cycles to cause cracking, the parameter effects were evaluated by comparing the damage produced in the specimens after about the same number of cycles, 1000 to 1125.

Test Apparatus

A schematic of the recirculating flow loop system is shown in Figure 8. The loop is equipped with sufficient instrumentation to facilitate on-line measurements of dissolved oxygen, pH, conductivity, pressure, temperature and flow rate. Heating of the sample was achieved by the hot electrolyte leaving the water heater. The test temperature was 274°C, loop pressure was 15 MPa (2200 psi) and the solution flow rate was 10 l/h. The fatigue loading was started after establishing a steady state in the test conditions. The flow loop system is discussed in detail elsewhere[5].

Results

A typical inside surface of a laboratory specimen after testing is shown in Figure 9 (a). Metallographic polishing of the cross-section shows multiple cracks extending into the metal from the waterside surface as revealed in Figure 9 (b). The cracks appear to have originated from the bottom of pits or surface irregularities. The fracture surface of a laboratory generated crack also revealed typical semi-elliptical shape. Scanning electron microscopy examination

of the fracture surface is shown in Figure 10. The fracture surface was slightly covered by corrosion products. These characteristics compare well with field produced cracks presented earlier.

The extent of cracking after testing was assessed using metallographic sectioning and measuring the depth of the cracks. On the effect of dissolved oxygen at pH 9, the longest cracks were 5.6 mm and 0.07 mm for 1000 ppb and 10 ppb levels respectively. This is in agreement with the data in Figure 11 where the number of cycles required to initiate cracks decreased as the dissolved oxygen content was increased[5]. The effect of pH was examined at two levels of 6.5 and 9. The amount of dissolved oxygen was reduced to approximately 10 ppb in these tests. The longest cracks were 1.5 mm and 0.07 mm for pH 6.5 and pH 9 respectively. Thus, lowering the pH has a detrimental effect on the corrosion fatigue cracking of the boiler tube in deaerated water.

Generally, the laboratory test technique produced the desired result which is the generation of corrosion fatigue cracks comparable with those found in the field samples. The possible corrosion fatigue cracking mechanisms are discussed, in part, on the basis of the above results.

Mechanisms of Corrosion Fatigue of Boiler Tube Failures

One of the basic requirements for the attainment of high corrosion resistance on boiler tubes is the possession of high thermodynamic stability of oxide film on the waterside surface in the service environment. For carbon steel in high temperature water the corrosion resistance is largely dependent upon the formation and maintenance of a protective layer of magnetite, Fe_3O_4[1,2]. The magnetite is formed at high temperatures on the steel surface during operation through a complex reaction represented by

$$3Fe + 4H_2O \rightarrow Fe_3O_4 + 8H^+ + 8e^- \quad [1]$$

Because corrosion fatigue cracks are typically filled with oxides, then oxide formation, stability, and destruction either by chemical attack or by mechanical straining are involved in the corrosion fatigue process. In this respect, the chemical and mechanical properties of the oxide film are crucial in governing the process of crack initiation; for example, by influencing the tendency to pitting and the geometry of the pits formed when the substrate alloy is subjected to strains[6-8].

Several theories have been proposed to explain the mechanism of corrosion fatigue for carbon steel in high temperature water. These are pitting, film rupture/destabilization, strain induced corrosion cracking, and hydrogen embrittlement models. Details of these mechanisms have been reviewed in previous publications4,[9-16]. They are briefly discussed below with respect to crack initiation in boiler tubes and on the basis of the present preliminary experimental observations.

Pitting Corrosion Model

In this model, pitting, as a form of surface reaction, serves to accelerate the corrosion fatigue crack initiation process through a purely mechanical notch effect. Pits develop under cyclic loading over a range of chemical and electrochemical conditions. The localization of surface energy at slip steps and persistent slip bands as a result of cyclic loading will in turn change the corrosion kinetics[13].

The formation of pits can be explained through electrochemical viewpoint. The schematic in Figure 12 represents a typical anodic dissolution process. The active-passive illustration is characteristic of the formation of an oxide film on the metal surface and is a few Angstroms thick. The constitution of this film is complex and could not be considered a simple layer of oxides or hydroxides with a fixed composition. The composition largely depends on the metal and the nature of the electrolyte. In region I of Figure 12, pits may form and grow to a critical depth and shape. That is, cracks may begin through notch effect and stress concentration. The strain at a pit may be higher than those nominally imposed on the bulk surface. Also pits form occluded cells and serve to concentrate the aggressive species in the local environment[14,17]. In region II, repassivated pits can be preferred areas of stress concentration. Cracks may initiate for a given plastic deformation in the vicinity of the pits depending on the

amplitude of the applied stress. Non-metallic inclusions or other heterogeneities in the metal may play an important role.

Müller[11] presented a theoretical evaluation of corrosion fatigue crack initiation controlled by pitting corrosion. He showed that the number of cycles to initiate a corrosion fatigue crack is a function of the loading frequency, incubation time for pit nucleation and critical pit depth. The critical pit depth is, in turn, dependent on the applied stress range, cyclic yield strength, specimen geometry, and fatigue crack growth threshold stress intensity factor.

Although corrosion fatigue cracks in many material/environment systems do not initiate at pits, the morphology of the majority of the cracks observed both in the field and in the laboratory strongly suggests that crack formation occurred from the bottom of pits. This makes the pitting corrosion model attractive and worthy of consideration. What is required at this stage is the modelling of the numerous inherent discontinuities in as-manufactured boiler tubes and stressing and environmental conditions experienced by boiler tubes to determine the time required to generate a pit (or multiple pits) that is large enough to cause a corrosion fatigue crack to initiate. Moreover, there is no universal definition of the aspect ratio a pit transforms to the description of a crack which may vary with the detailed geometry of the features being studied[17]. Attempts have been made in this direction for various systems[11,18].

Film Rupture/Destabilization Model

In this model, crack initiation is linked to the local rupture effect of passive film due to cyclic plastic deformation[13]. The various stages of the rupture mechanism is shown in Figure 13. During fatigue loading, cracks generally initiate at either persistent slip bands (PSBs) or are associated with intrusions/extrusion bundles and grow into the metal or alloy along slip bands. In the presence of an aggressive environment, slip bands are preferentially corroded in contrast to the surrounding matrix.

The surface oxide layers which form on many metals and alloys can act as barriers to dislocation activity. Under passive corrosion conditions, the passive layer has to be penetrated by slip steps, to form corrosion fatigue cracks. In this case, depending on the applied stress range, crack initiation is controlled by the repassivation kinetics of the material and also by a critical notch depth[11]. The kinetics of electrochemical reactions are sensitive to localized deformation processes, which are in turn alloy composition and applied strain rate sensitive[19]. At low dissolution rates, the environmental effect will be to dull the relief created on the surface by the localization of the cyclic plastic deformation which will not lead to fast initiation of cracks. At high dissolution rates or in the presence of thin oxide film, the barriers to slip are reduced, slip localization is favored and PSB spacing increases. When the PSB spacing is increased by environmental effects, each PSB carries a larger local plastic strain leading to accelerated crack initiation. Additionally, the environment alters the stability of near surface matrix dislocation structures causing the matrix dislocations to be transferred more easily into the PSB, further accelerating the formation of PSBs[4].

It is important to note that the dominance of mechanical parameters on crack initiation do not occur in all metal/environment systems. It is probable that a critical applied stress in conjunction with a critical corrosion rate promotes the surface film rupture mechanism micro-crack initiation[4].

Strain Induced Corrosion Model

There are several variations to this model. This model is similar in many respect to the film rupture model[4,19,20,21]. One school of thought is presented schematically in Figure 14. Localized rupture of the protective film due to discontinuous plant operation leads to pitting. Crack initiation from the pits may then occur due to the application of fatigue loading of appropriate magnitude[9].

Another view of this model suggests dissolution of emerging slip bands[4]. Dissolution effectively unlocks otherwise blocked slip processes, accelerates extrusion-intrusion formation, and accordingly promotes premature crack initiation. According to the authors, the difference between strain induced corrosion cracking (SICC) and film rupture model is that SICC is operative when the metal is in an active corrosion state (region V in Figure 13) while film rupture is dominant when the metal is in a passive state (region III)[4].

Hydrogen Embrittlement Model

The hydrogen embrittlement model suggests that the degradation of material properties in an environment is due to the absorption of hydrogen. The loss of ductility due to absorbed hydrogen has been demonstrated for many alloy systems, including carbon and low alloy steels. Hydrogen produced as a result of the half-reaction of the corrosion process (reduction of H+ or dissolved oxygen) can be absorbed in the steel structure leading to embrittlement. The source of the hydrogen in power generating systems are corrosion reactions represented by the overall reaction

$$3Fe + 4H_2O \rightarrow Fe_3O_4 + 4H_2 \quad [2]$$

The hydrogen is produced through an intermediate reaction step. In occluded cells, the pH can drop locally on the surface in a neutral solution through a mechanism of metallic cation hydrolysis given by the reaction

$$M^{n+} + nH_2O \rightarrow M(OH)^n + nH^+ \quad [3]$$

In either case, the embrittling effect of the hydrogen is possible only if the release and adsorption are located on the cracks. Hydrogen absorption into the material is promoted by certain chemical species, such as sulfides[20]. Note that the absorption of hydrogen into the steel is only possible when a critical surface concentration is attained. The integrity of the passive film is also important in this case because when localized depassivation occurs due to localized plastic deformation, the relevant cathodic reaction can be triggered. Whatever the exact corrosion reaction occurring, nearly all corrosion reactions of carbon steel in water involve hydrogen generation as the cathodic reaction.

Discussion

The laboratory program identified oxygen as the single largest factor affecting corrosion fatigue of boiler tubing. The role of oxygen in the corrosion fatigue process is not clear but it has been proposed that it accelerates the corrosion reactions by increasing the cathodic reaction rate, and altering the composition of the oxide film formed on the metal surface. Moreover, dissolved oxygen (a) reacts with the metal surface to affect slip behavior and (b) alters adsorption processes on the metal surface[4]. Also, high dissolved oxygen may polarize the metal surface to regions on the anodic polarization curve (region I in Figure 12) favouring the formation of pits.

Experiments have also shown, however, that the structure, composition and morphology of oxide formed on carbon steel in water are controlled by temperature and dissolved oxygen content of the water[22,23]. Magnetite layers which form below approximately 230°C seem to have only a limited protective effect because of the initially precipitated ferrous (II) hydroxide[21]. High levels of dissolved oxygen lead to the formation of double-layered or mixed-films of magnetite, hematite and ferric oxides/hydroxides on low alloy steel surfaces. Because of its reduced ductility in comparison with magnetite, an outer hematite-containing film may very well lead to crack initiation upon straining[9]. Mixed films on unstrained steel surface has been studied by Mabuchi et. al.[22]. It is probable that under the test conditions used in this investigation (dissolved oxygen 1000 ppb, temperature 274°C, pH 9) the oxide scale consisted of an inner layer of compact magnetite and an outer layer of hematite.

The results also show that corrosion fatigue was accelerated by reduction of the solution pH in deaerated waters. This can be explained via electrochemical viewpoint by examining the combined influence of oxygen and pH. The type of oxide formed in aqueous systems is a function of the electrochemical potential of the material. The potential is in turn controlled by the oxygen content of the water[7]. The stable oxide species, under the present experimental conditions, can be identified on a potential-pH map (also known as a Pourbaix diagram)which shows that corrosion fatigue occurs most readily outside of the magnetite Fe_3O_4 stability region.

Clearly, the formation, stability and destruction of the oxide scale formed on waterside surfaces of boiler tubes are crucial in maintaining the integrity of the tubes. The effects of dissolved oxygen on modifying the composition of the oxide film appear to support a variety of mechanisms for corrosion fatigue crack initiation. The morphology of the field and laboratory cracks supports the pitting corrosion and film rupture models.

Summary

A recirculating autoclave loop system has been developed to perform corrosion fatigue tests under carefully controlled water chemistry and stressing conditions. The results show that crack morphology similar to those found in field failures can be reproduced. Dissolved oxygen and pH are the environmental factors that have the largest influence on corrosion fatigue behavior of the steel. From the results, it is apparent that: (a) high dissolved oxygen may readily lead to early initiation of corrosion fatigue cracks and (b) corrosion fatigue can be accelerated by reduction of the solution pH in deaerated waters.

It is concluded that oxide destabilization and repassivation, occurring either sequentially or concurrently, is the mechanism leading to corrosion fatigue. The bulk of evidence points to the pitting corrosion and film rupture/destabilization models as being the mechanism responsible for corrosion fatigue in power plants.

Acknowledgment

The authors are grateful to EPRI under contract RP1890-5 for the support of this work. Comments by W.H.S. Lawson and D. McNabb are appreciated. The authors are also grateful to R.E. Irwin for his diligent effort in the development of the test facility and conducting the experiments and to A.V. Manolescu for providing some of the micrographs.

References

1. M.D.C. Moles and H.J. Westwood, Proc. Int. Conf. on Materials to Supply the Energy Demand, Harrison, B.C. Can. ASM, (1980): p. 515.

2. H.J. Westwood and W.K. Lee, J. Mater. Eng. 9, (1987): p. 163.

3. R. B. Dooley, "Boiler Tube Failures - A Perspective and a Vision", Int. Conf. on Boiler Tube Failures in Fossil Plants, EPRI, San Diego, CA. November 5-7, 1991.

4. T.S. Srivatsan, T. S. Sudarshan, J. of Materials Science, 23, (1988): p. 1521.

5. Corrosion Fatigue Boiler Tube Failures in Waterwalls and Economizers - Volume 2: Laboratory Corrosion Studies, EPRI TR-100455, Project 1890-05, (July 1992).

6. M. Schutzë, Int. J. Pressure Vessel & Piping 47, (1991): p. 293.

7. G. Ward, B.S. Hockenhull, P. Hancock, P., Met. Trans., 5, (1974): p.1451.

8. V.I. Nikitin, E.V. Kiseleva, A.M. Gvozd, Soviet Mat. Sci., 14, 5, (1978): p. 464.

9. J. Hickling, D. Blind, Nuclear Engineering and Design, 91, (1986): p. 305.

10. L.D. Paul, M.T. Miglin, and W.A. VanDerSluys, CORROSION/92, paper no. 156 (Houston, TX: National Association of Corrosion Engineers, 1992).

11. M. Müller, Met. Trans. A, 13A, (1982): p. 649.

12. F.P. Ford, P. Combrade, Proc. 2nd IAEA Specialists' Meeting on Subcritical Growth, Sendai, Japan, (1985).

13. T. Magnin, Momoires et Etudes Scientifiques Revue de Metallurgies, LS7857/7Feb90/js, (1983).

14. B.N. Leis, R. Rungta, M.E. Mayfield, J.A. Beavers, ASTM STP 801, (1983): p. 197.

15. L.D. Paul, G.I. Ogundele, E.T.C. Ho, Int. Conf. on Boiler Tube Failures in Fossil Plants, EPRI, San Diego, CA. November 5-7, (1991).

16. G.I. Ogundele, D. Sidey, Proc. Fatigue 93, Montreal Canada, May 3-7, (1993).

17. J. Congleton, I.H. Craig, R.A. Olieh, R.N. Parkins, ASTM STP 801, (1983): p. 367.

18. D.W. Hoeppner, ASTM STP 675, pp. 841, 1979.

19. R.P. Gangloff, D.J. Duquette, Chemistry and Physics of Fracture, Martinus Nijhoff Publishers, Boston, (1987): p. 613.

20. J. Hickling, NUREG/CP-0112, ANL-90/22, Vol.II, Proc. 3rd IAEA Specialists' Meeting on Subcritical Crack Growth, Moscow, May 14-17, (1990).

21. W. Schoch, H. Spahn, Corrosion Fatigue: Chemistry, Mechanics and Microstructure, (Houston, TX: National Association of Corrosion Engineers, 1971). p. 5.

22. K. Mabuchi, Y. Horii, H. Takahashi, M. Nagayama, Corrosion, 47, 7, (1991): p. 500.

23. J.R. Park, D.D. Macdonald, Corrosion, 45, 7, (1989): p. 563.

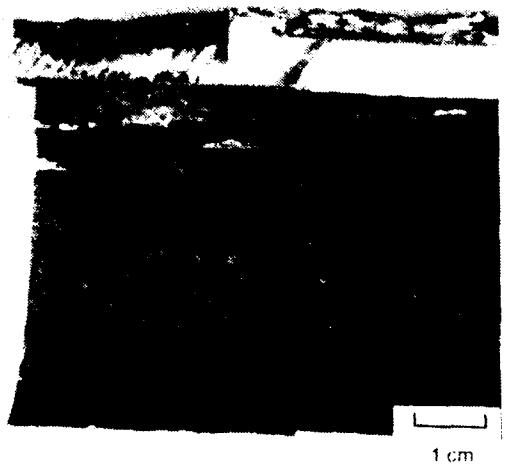

(a) Inside surface of a boiler tube

(b) Cross-sectional view of the boiler tube in (a)

(c) Crack morphology in an elbow

(d) Crack morphology in a hairpen bend

Figure 1 Examples of Corrosion Fatigue Cracking in Boiler Tubes

(a)

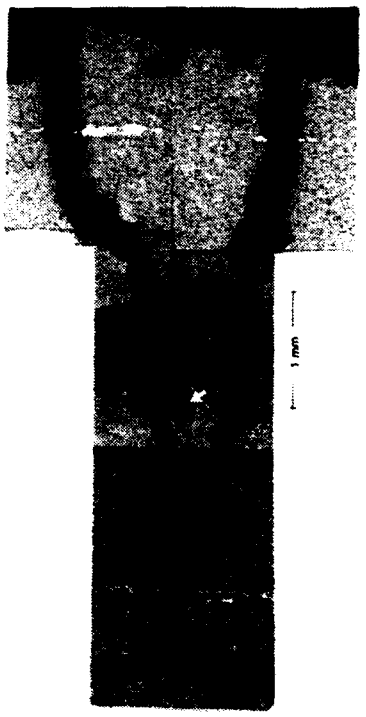

(b)

Figure 2. Crack Morphology in a Waterwall Tube.
a) Note the severe corrosion on the crack walls
b) Arrowed is the weld-parent metal interface

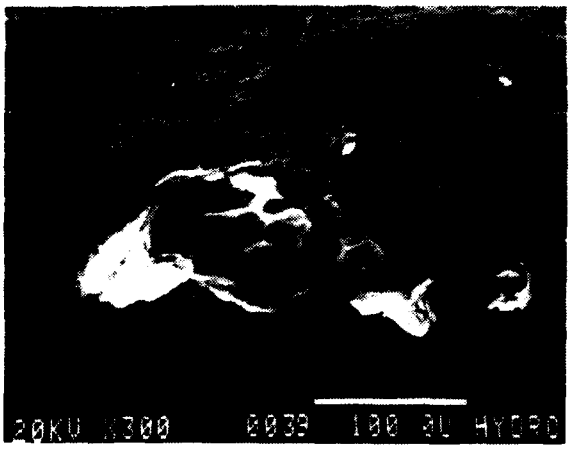

(a) Crack initiation region

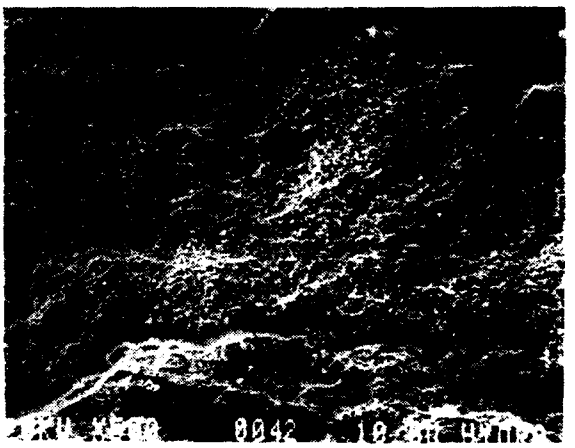

(b) Region further into the crack

Figure 3. Scanning Electron Micrograph
of a fracture surface of a field sample

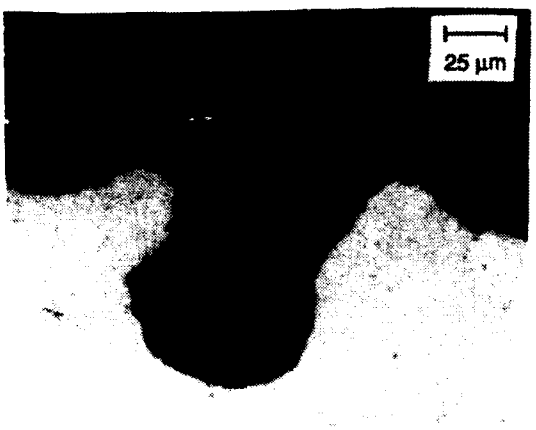

(a)

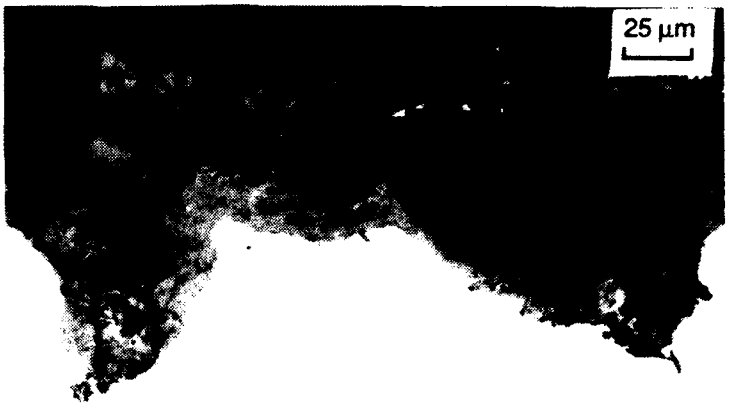

(c)

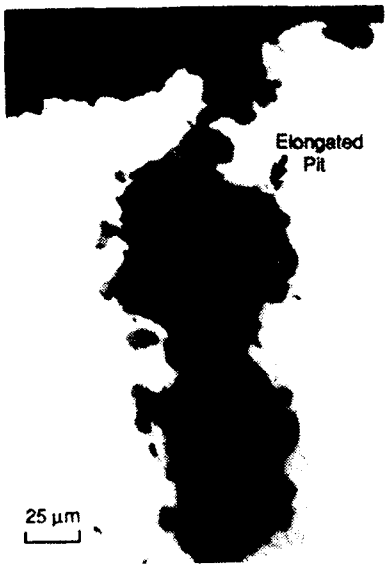

(b)

Figure 4. Cross-Section of Waterside Surfaces
(a) pitted surface of an economizer tube
(b) An elongated pit in a waterwall tube
(c) pitted surface

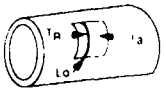

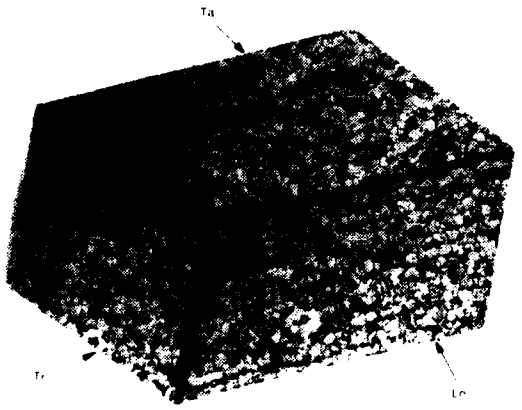

Figure 5. Microstructure of the Test Material

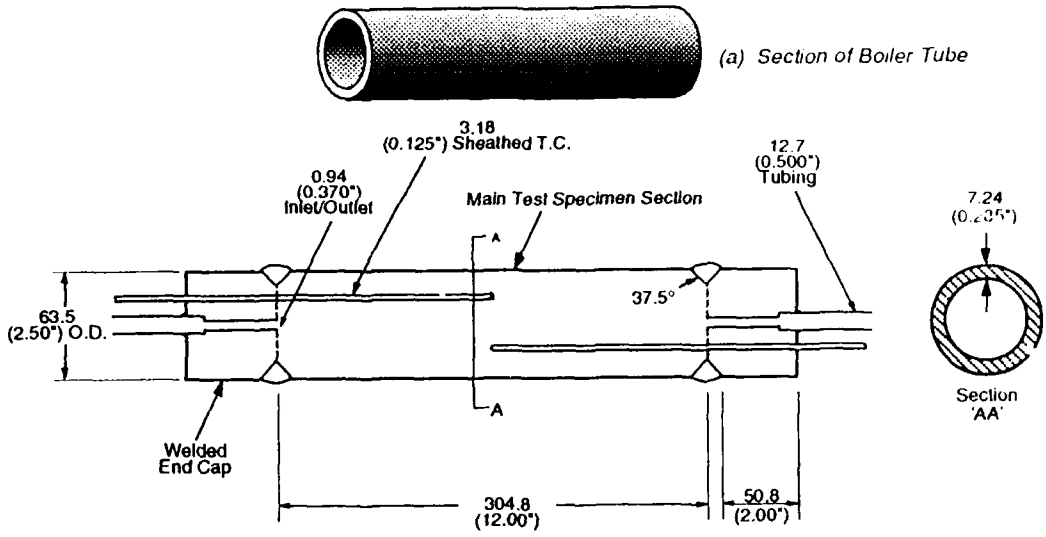

Figure 6. Schematic of boiler tube sample for corrosion fatigue tests (dimensions in mm (inches))

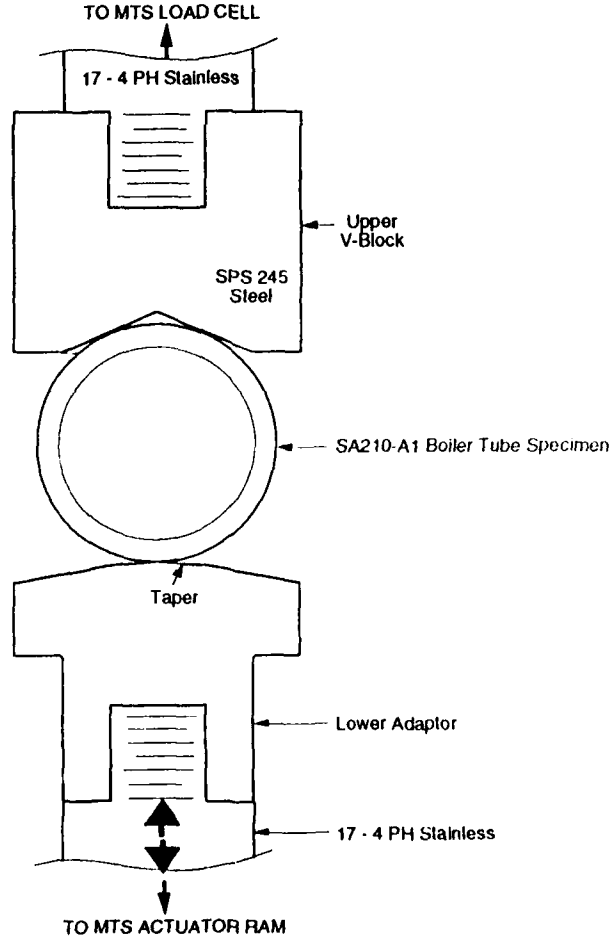

Figure 7. Schematic of specimen and grips assembly for the plain tube geometry and tapered lower compression adaptor

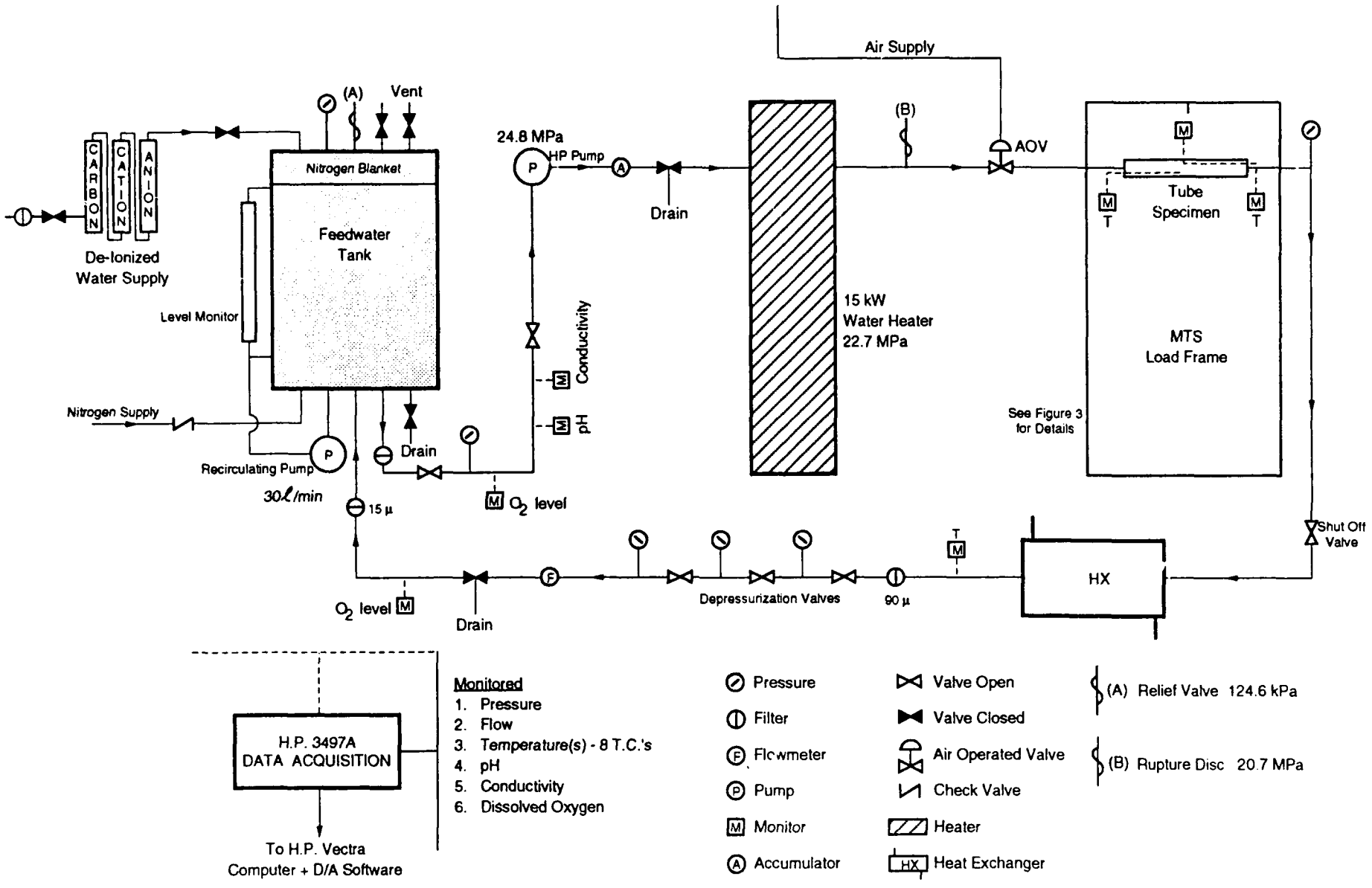

Figure 8. Schematic of the recirculating flow loop system for corrosion fatigue tests

(a) Inside surface

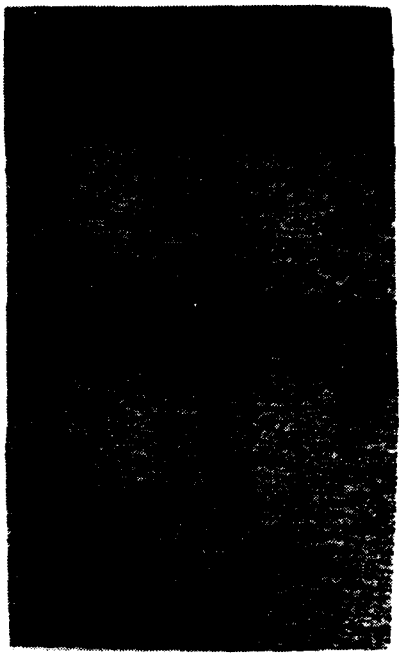

(b) Cross-sectional view

Figure 9 Laboratory produced corrosion fatigue cracks in a boiler tube

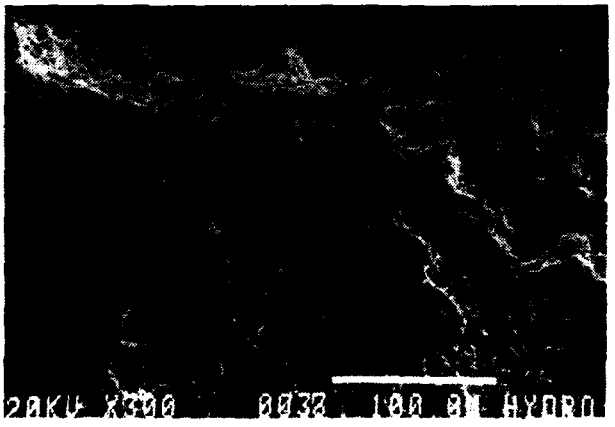

(a) Fracture surface morphology near the initiation site

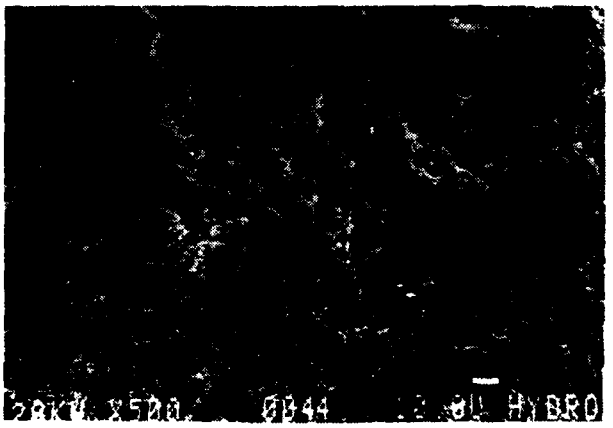

(b) Region on the surface further away from the initiation site

Figure 10. Scanning electron micrograph of the fracture surface of a laboratory sample

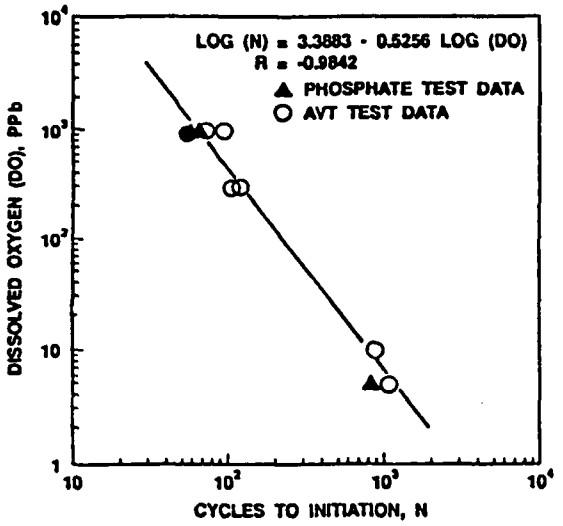

Figure 11. Number of cycles to initiate cracks in 274°C boiler water as a function of dissolved oxygen (5)

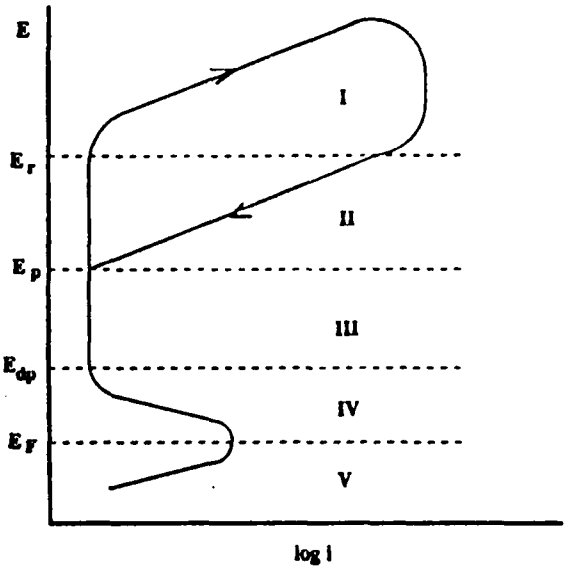

Figure 12 Schematic of current density-potential anodic polarization curve

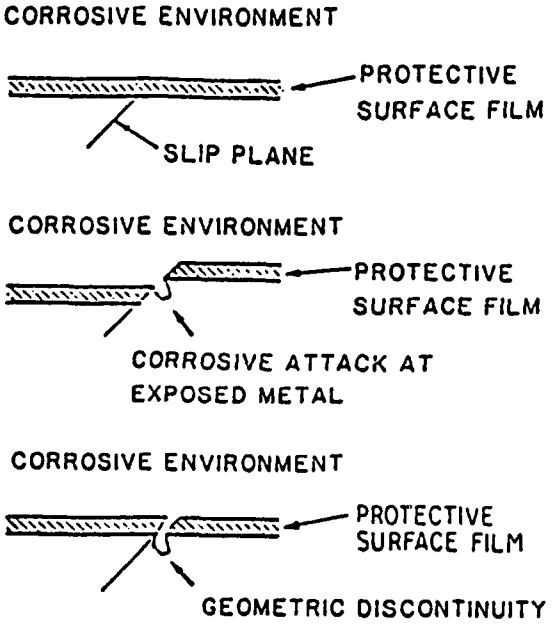

Figure 13. Mechanism of surface film rupture for environmentally enhanced crack initiation (4)

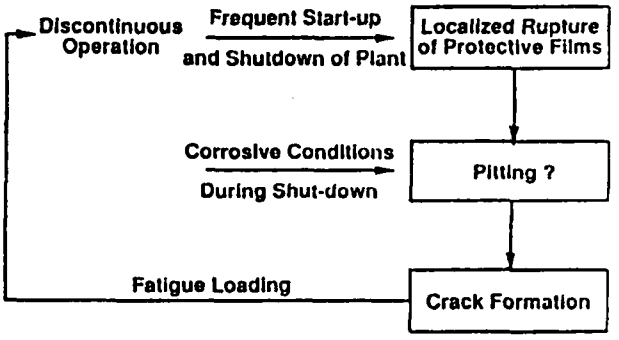

Figure 14. Mechanism of stress induced corrosion cracking (9)

Influence of Surface Microcracks on The Corrosion Fatigue Mechanisms of Ferritic and Austenitic Stainless Steels

T. Magnin
Université de Lille 1, Laboratoire de Métallurgie Physique, URA CNRS 234
59655 VILLENEUVE D'ASCQ Cedex, FRANCE.

Abstract

Corrosion fatigue mechanisms of ferritic and austenitic stainless steels are studied. The aim of this paper is to present new results on the influence of surface microcracks which form during low cycle fatigue tests on the corrosion fatigue damage accumulation. The density of microcracks, their influence on the stability of the passive layer, their ability to micropropagation and coalescence at specimen surface and their influence on hydrogen absorption are analysed and taken into account to modelize the corrosion fatigue lifetimes.

Numerical simulations are proposed to integrate the role of surface microcracks on the corrosion fatigue damage evolution of austenitic stainless steels in Cl^- solutions.

Introduction

Corrosion fatigue (CF) mechanisms of ferritic (Fe-26 Cr-1 Mo) and austenitic (316 L) stainless steels in Cl^- solutions have been shown to be closely related to localized corrosion-deformation interactions[1,2]. Crack initiation and early crack propagation mechanisms have been proposed : the slip dissolution model[3], the restricted slip reversibility model[4], the adsorption induced plasticity model[5] and the hydrogen enhanced decohesion model[6].

Nevertheless, it has been shown in low cycle fatigue and corrosion fatigue that a large density of short cracks can form very early at the specimen surface[2]. Their influence must be taken into account on both the stability of the surface film (and relative localized corrosion effect) and on the mechanical surface damage (micropopagation and coalescence).

Thus the aim of this paper is to analyse the CF damage of ferritic and austenitic stainless steels in a 3 % NaCl solution, taking into acount the role of these surface microcracks at the mesoscopic scale of the grain size. Il will be shown that CF damage can be quantified using numerical simulations of the evolution of surface microcracks which play a significant role on CF damage mechanisms, particularly in low cycle fatigue.

The surface Microcracking process

Figure 1 shows the cyclic behaviour of four different fcc and bcc single phased polycristalline materials strained in air at a prescribed plastic strain amplitude $\Delta\varepsilon p/2 = 2 \times 10^{-3}$ and strain rate $\dot{\varepsilon} = 10^{-2}s^{-1}$. Even if the materials exhibit a quite different cyclic properties (in stress levels, fatigue lifetimes, dislocation behaviour), a kind of homologous behaviour can be established looking at the evolution of the microcracking process. For the applied plastic strain, the first surface microcracks form very early at about 0.1 Ni,where Ni is the number of cycles corresponding to a fast 1 % decrease of the saturation stress (Ni = 0.9 N failure). These first microcracks (type I) have a surface length less than one grain size ($l < 50\mu m$ for the 316 L alloy). At about 0.3 Ni, type II cracks ($1 < l < 3$ grain sizes, Figure 2) form and correspond to the crossing of the microstructural barriers which are the grain boundaries. At about 0.5 Ni, type III cracks ($3 < l < 10$ grain sizes) form and at N = Ni, one or two long surface cracks induce the final propagation and fracture of the specimen. It has been observed[7] that 80 % of the fatigue life is controlled by the evolution of surface cracks the depths of which are less than one or two grain sizes, and the densities of which can reach 50 per mm^2. Thus the main part of the low cycle fatigue damage is controlled by the statistical evolution of a large population of surface cracks which can interact, coalesce and propagate at the specimen top face. Coffin-Manson laws can be evaluated from this evolution using the standard laws of statistical physics[7].

In a 3 % NaCl solution (pH 6.5) at free potential, the low cycle fatigue lifetimes of the austenitic and ferritic stainless steels are reduced by a factor two. This reduction can be, in this case, directly related to the acceleration of the surface microcracking process as shown on Figure 3 for the ferritic stainless steel. The number of type I cracks and their kinetics of formation increase in the aqueous solution. The crossing of the grain boundaries is facilitated, which leads to a reduction of the fatigue lifetime even if the general features of the evolution of type I, II and III cracks at free potential are homologous to air.

It must be emphasized that at cathodic potentials, for the ferritic alloy, as soon as the first microcracks are mechanically formed by fatigue, the damage process is very accelerated, the densities of surface microcracks decrease and a rapid failure is observed. This last effect has been related to hydrogen embrittlement which is very rapid as soon as microcracks are formed, leading to hydrogen entry. This close relation between microcracks (or defects) and hydrogen entry is very important is many hydrogen sensitive alloys during SCC and CF.

The influence of surface microcracks on the electrochemical reactions and on the depassivation process is clearly shown on figure 4 for the austenitic 316 L alloy in a 3 % NaCl solution. During the first cycles, the potential cyclically evolves and its mean value strongly decreases, which corresponds to the formation of numerous slip lines at the specimen surface. Then the average potential raises slowly when the localization of the plastic strain occurs in intense slip bands, which decreases the number of

depassivation events. Then the average potential starts to decrease rapidly till rupture. This may be associated with the nucleation of type I microcracks and the beginning of type II cracks formation. At about 50 % of the fatigue lifetimes, a secondary repassivation peak appears, corresponding to the formation of type III microcracks with a more marked opening-closing process. This sensitive electrochemical method is very useful to follow the interactions between microcracks and the electrochemical behaviour at the specimen surface and to follow the damage process.

Numerical Simulations of the CF damage

The experimental data reported above clearly show that the fatigue and CF damages of the ferritic (Fe-26 Cr-1 Mo) and austenitic (316 L) stainless steels can be modelled by the behaviour of surface cracks populations. 2D Monte-Carlo type numerical simulations can be proposed, as described in detail elsewhere[8,9] for fatigue in air. They consider both the growth of individual surface cracks generated at random and the interactions and coalescence of these cracks for transgranular cracking. The grains are represented by hexagons, which are divided in 36 squares (Figure 5), inside which the slip planes are indicated ((111) for the 316 L alloy). The orientation of the slip planes is defined in relation with the stress axis.

The software includes the nucleation of microcracks, their micropropagation and their coalescence at the specimen surface. At the beginning, a random number is generated in the range 0 to 1 for each undamaged square. When this number is higher than the nucleation threshold (defined by the operator, according to the plastic strain amplitude and ajusted from experiments), cracking occurs in the square. Then the nucleated microcracks propagate through the grain from square to square. A propagation threshold is calculated from the nucleation threshold, increasing with the misfit between the easy cracking direction of the crack tip square and the easy cracking direction of the tested square. The microcracks are blocked to grain boundaries, and a new propagation threshold must be calculated. It depends on the interactions with other microcracks of other grains by two ways : (i) overlapping or influence of plastic zones which can increase the individual propagation rate of the considered microcracks ; (ii) direct coalescence, related here to the Ochi criterion[10]. This effect of coalescence is illustrated by the Figure 6 : it increases the crack velocity. Nevertheless the influence of overlapping of plastic zones on the individual growth of microcracks is quite important in the acceleration of damage, particularly for corrosion fatigue (because corrosion decreases the threshold value at grain boundaries).

The new propagation threshold value PT is calculated as follows :

$$PT = NT + f(\text{crystallographic misfit}, l, \Delta\varepsilon p) - g(l, \Delta\varepsilon p) - h(\text{sampling number}, \Delta\varepsilon p),$$

where the various functions f, g and h refer, respectively, to (i) the relative resistance of grain boundaries, (ii) to the effect of microcrack lengths l and (iii) to the current percentage of fatigue lifetime. The parameter termed "misfit" is related to the difference between the two cosines of the angles between the intense slip bands and the loading axis.

When type III cracks form and propagate perpendicularly to the loading axis, the surface crack propagation is $dl/dN = l \times Ln(1 + y)$, where y is a very small number (1.2×10^{-4} for $\Delta\varepsilon p/2 = 4 \times 10^{-3}$). This law results from experimental observations[8].

These growth rates are functions of the plastic strain range similarly to the type of equations originally proposed by Tomkins[11] : $dl/dN = A\ \Delta\varepsilon p^{\beta}$, where A = 6.67 and β = 1.148 for type I microcracks, A = 757.83 and β = 1.968 for type II microcracks.

Figure 7 compares the experimental observations and the numerical simulations of the evolution of surface microcracks populations in fatigue and in C F for the autenitic 316 L alloy at $\Delta\varepsilon p/2 = 4 \times 10^{-3}$. A very good correlation is found between the simulations and the experiments for both the microcrack densities and the damage. It confirms that corrosion affects mainly the number of nucleation sites, the surface micropropagation threshold (particularly to cross grain boundaries), the kinetics of propagation and then the crack velocity at the surface and the final fracture.

Concluding Remarks

Different mechanisms have been proposed for corrosion fatigue damage, such as the slip dissolution model, the restricted slip irreversibility model and the hydrogen enhanced brittle fracture models. They are great interest and they must be completed by the modelization of the localized crack tip chemistry. Moreover such mechanisms describe the local corrosion fatigue damage (microscopic scale).

In the present paper, the interest to take into account the mesoscopic scale (the grain size) to quantify and modelize the low cycle corrosion fatigue damage is quite clear. It is based on the statistical evolution of a population of surface microcracks in fatigue and corrosion fatigue. The notion of microstructural barrier (grain boundaries for instance) is emphasized and the effect of anodic dissolution is then essential to accelerate the crossing of these barriers and the kinetics of the surface crack evolution. Moreover the interaction of these surface microcracks with the surface film and the hydrogen entry is also emphasized. These results clearly shows that it is necessary to take into account both the microscopic and the mesoscopic scales to analyse and quantify the low cycle corrosion fatigue damage of single phased materials.

References

1 - T. Magnin, L. Coudreuse, J.M. Lardon, Basic Questions in Fatigue, (ASTM STP 924, Vol. II., 1988), p. 128.

2 - T. Magnin, Environment Assisted Fatigue, (EGF, P. Scott and R.A. Cottis Ed., MEP, 1990), p. 409.

3 - O. F. Devereux, A.J. Mc Evily, R.W. Staehle, Corrosion Fatigue, (Houston, TX : National Association of Corrosion Engineers, 1972).

4 - C. Fong, D. Tromans, Metall. Trans. 19 A (1988) : p 2765.

5 - S.P. Lynch, Acta Met., 36 (1988) : p 2639.

6 - W. Gerberich, Corrosion Deformation Interactions (Editions de Physique, T. Magnin and J.M. Gras Ed. , 1993), to be published.

7 - T. Magnin, Scripta Met. et Mat., 26 (1992) : p 1541.

8 - T. Magnin, A. Bataille, C. Ramade, ECF8 (EMAS, D. Firrao Ed., Vol III, 1990) : p 1330.

9 - A. Bataille, T. Magnin, K.J. Miller, Short fatigue cracks (ESIS 13, K.J. Miller Ed., MEP, 1992) : p 115.

10 - Y. Ochi, A. Ishii, J.K. Sasaki, Fat. Fract. Eng. Mater. Struct., 8 (1985) : p 327.

11 - B. Tomkins, Phil. Mag, 18(1968) : p 1041.

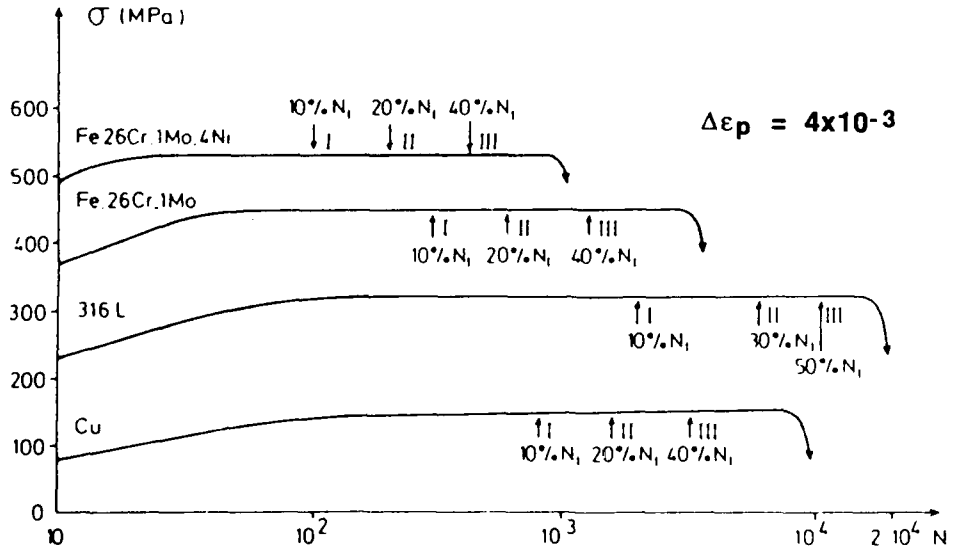

Figure 1 : Microcracking process of four fcc and bcc materials at $\Delta\varepsilon p/2 = 2 \times 10^{-3}$ and $\dot{\varepsilon} = 2 \times 10^{-3}\ s^{-1}$.

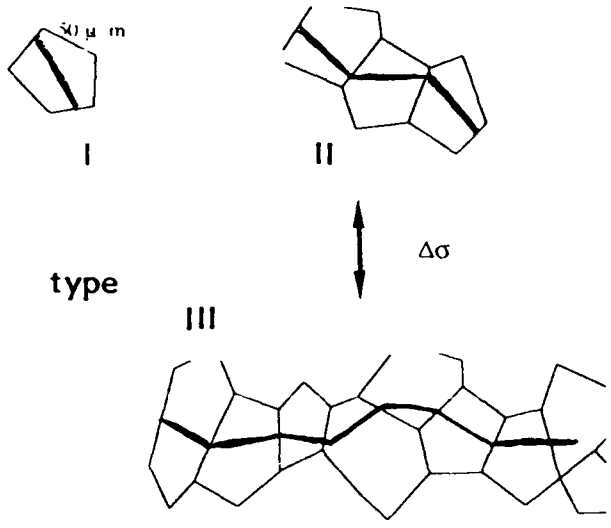

Figure 2 : Définition of type I, II and III microcracks for transgranular cracking.

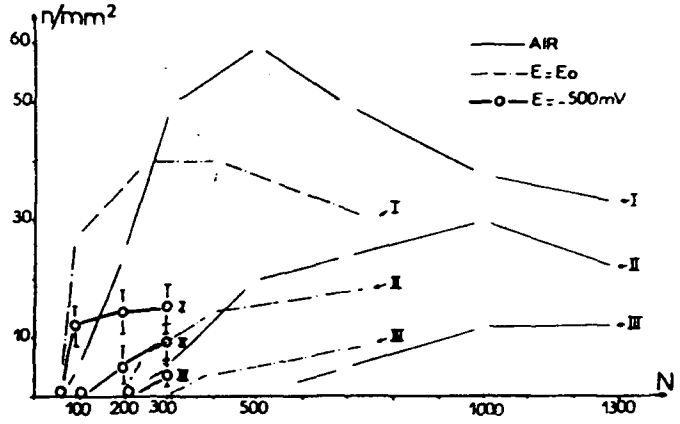

Figure 3 Evolution of surface microcracks for the Fe - 26 Cr - 1 Mo alloy at $\Delta\varepsilon p/2 = 4 \times 10^{-3}$ and $\dot{\varepsilon} = 2 \times 10^{-3}\ s^{-1}$.

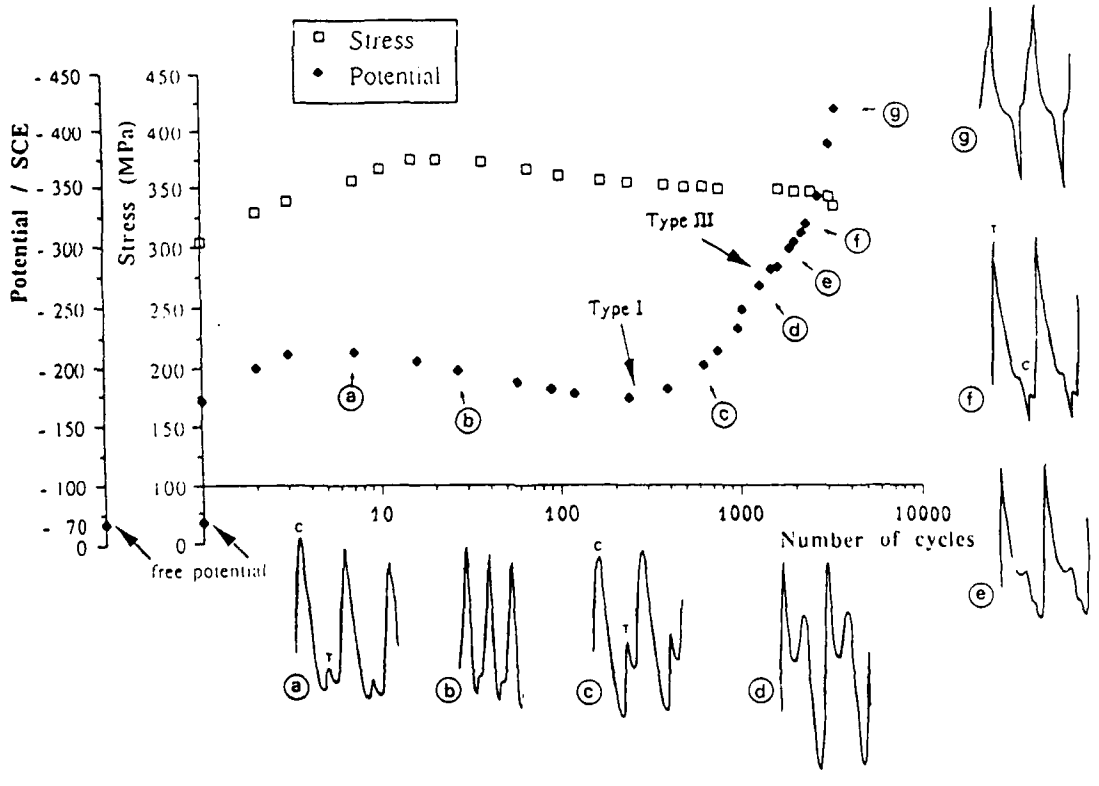

Figure 4 : Simultaneous evolution of the cyclic stress σ, the average potential and the shape of the cyclic current transients for a 316 L alloy in 30 g/l NaCl, $\Delta\varepsilon p/2 = 4 \times 10^{-3}$, $\dot{\varepsilon} = 10^{-2}\ s^{-1}$.

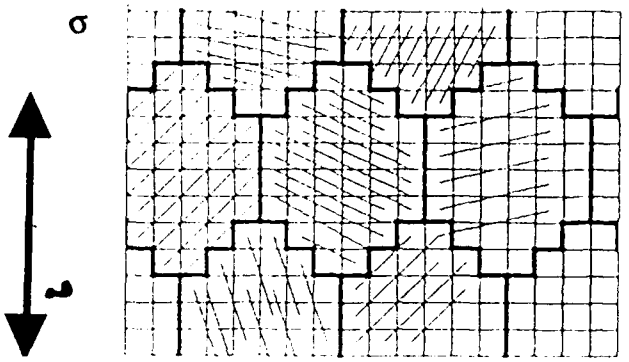

Figure 5 : A schematic of model grains for numerical simulations.

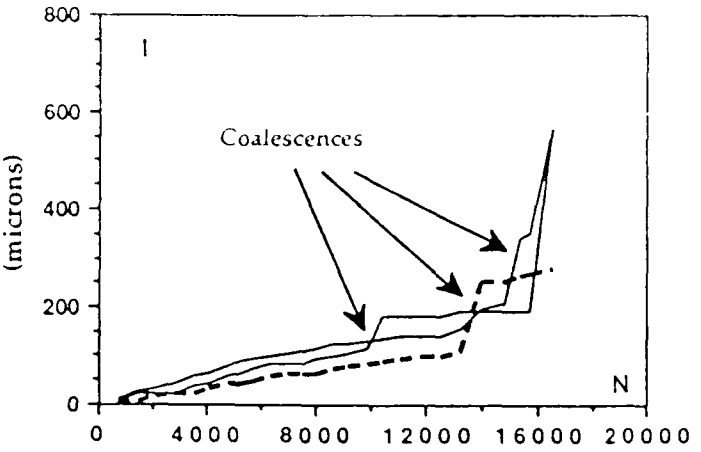

Figure 6 : Effect of coalescence on the evolution of the surface length of cracks.(316 L at $\Delta\varepsilon p/2 = 2 \times 10^{-3}$).

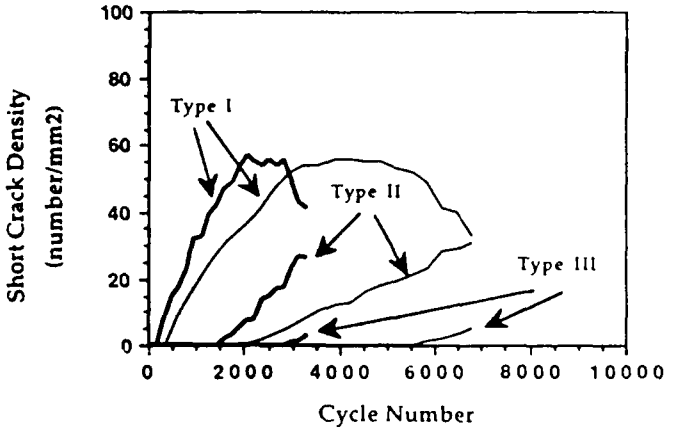

(a)

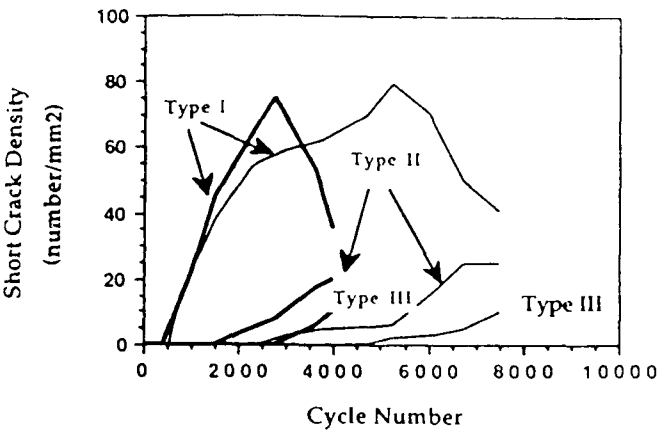

(b)

Figure 7 : Experimental observations (a) and numerical simulations(b) of the evolution of surface microcracks population in fatigue (fine lines) and CF (black lines). 316 L alloy at $\Delta\varepsilon p/2 = 4 \times 10^{-3}$, $\dot{\varepsilon} = 2 \times 10^{-3}\ s^{-1}$.

INFLUENCE OF APPLIED POTENTIAL ON CORROSION FATIGUE LIFE AND CRACK CHEMISTRY OF LOW CARBON STEEL

HAN En-Hou
Corrosion Science Laboratory
Institute of Corrosion and Protection of Metal,
Academia Sinica, Shenyang 110015,
P.R.China

HAN Yumei
Corrosion Science Laboratory
Institute of Corrosion and Protection of Metal,
Academia Sinica, Shenyang 110015,
P.R.China

KE Wei
Corrosion Science Laboratory
Institute of Corrosion and Protection of Metal,
Academia Sinica, Shenyang 110015,
P.R.China

ABSTRACT

Electrode potential and pH within growing corrosion fatigue cracks and at crack tip for different polarized potentials on SM50B-Zc steel and in 3.5% NaCl solution were measured by means of a new technique. There existed higher potential drop and lower pH value in corrosion fatigue cracks, and some cathodic polarization potentials which seem as if reasonable was detrimental to structure with deeper crack, and only higher cathodic polarization potentials may protect corrosion fatigue crack. Adequate anodic polarization will impose beneficial restrictions on longer crack growth. The reasons of different effects of various polarization potentials in different material-environment systems were discussed.

Key terms: corrosion fatigue; fracture chemistry; polarization; electrode potential; crack tip; cathodic protection; stress corrosion cracking

INTRODUCTION

Cathodic protection was usually used to prolong the life of structure serving in corrosive environment, which will be valid to structure with no cracks. It has been studied widely whether cathodic potential can also extend corrosion fatigue (CF) life of structure with cracks in different material-environment systems. In 1983, Brown reviewed

systematically this problem [1]. In the recent years, some new results [2~5]have been obtained from research on various material–environment systems. It has been found that the optimum cathodic protection potentials were different in various systems, and the effects of polarization potentials in various systems were different, for example for structure with cracks, sometimes, cathodic potential was detrimental and anodic potential can delay CF cracks growing. There have been no identical views about these.

The potential drops φ and potential distribution within crack, crevice and at crack tip after polarization have been noted for several years. Pickering and co–workers [6~8]studied systematically ohmic potential drops for crevice corrosion; Ateya and Pickering, Galvele, Doig and Flewitt predicted φ in stress corrosion crack [9~11], Parkins and co–workers measured φ in simulated stress corrosion cracks and actual fatigue cracks [12]. Turnbull and Ferriss predicted φ in CF crack of structural steel in sea water with a model and measured a few fixed situation [13]. All of these results have played an important role on studying reasons causing φ in crevice and crack, and on choosing the optimum protection potential.

The objectives of the present work were to give specific experimental data in chemistry and eletrochemistry parameters within CF crack and their variation at CF crack tip with CF crack propagating, and to try to illustrate effects of polarization potential on CF life in different systems using an unified principle and to explore the method for deterimining the optimum protection potential for structure with cracks.

EXPERIMENTAL METHOD

All fatigue tests were performed at 294K, a frequency of 7.9Hz, stress ratio 0.625 and sinusoidal loading waveform on servo–hydraulic fatigue testing machine in 3.5%NaCl solution, circulated continuously at 5ml / s in a 3 liter plexiglas test chamber. Compact tension specimens, 34mm thick and 100mm, machined in the LT orientation (i.e., the crack growth was along with the rolling direction), were used, as shown in Fig.1. The specimens were pre–cracked 5.5mm in air at 20 Hz frequency by a load shedding procedure, then immersed in solution to pre–crack about 0.5mm at the test frequency and load again. The material tested was SM50B–Zc steel of chemical composition (wt%) 0.19 C, 0.38 Si, 1.34 Mn, 0.013 P, 0.0084 S, with yield and tensile strengths of 345.52 MPa and 525.78 MPa, respectively, an elongation to fracture of 28.0 percent.

The painted specimen was insulated from testing machine, and drilled a hole through the center of its thickness in crack growth direction. A micro–electrode (thin tube) was inserted into the hole to measure pH value and electrode potential within crack and at crack tip (Fig.2). The potential was measured by a potentiostat, saturated calomel electrode(SCE) located 30mm from the crack mouth and two platinum counter electrodes positioned 10mm from each side of the working electrode specimen.

A antimony electrode was installed in the appropriate position of the tube made from dielectric elastic material, connected a conducting wire with one side. And the other side of tube was filled with salt bridge liquid. The antimony electrode was separated from salt bridge liquid by insulating materials. Four very small holes were made on the tube wall at the head of antimony electrode and of salt bridge respectively, and their diameters were made as small as possible. The expected positions of small holes were controlled by moving the tube when pH and electrode potential were measured within the crack and at the crack tip with crack growth.

CF crack length was measured using compliance technique. Stress intensity factor and crack growth rate were calculated according to national standard GB 6398–86.

RESULTS AND DISCUSSIONS

The variation of electrode potential and pH at CF crack tip during fatigue loading, had something to do with frequency, stress ratio, stress intensity factor and material–environment systems. In the test, all pH and electrode potential in the paper were the mean value in a cycle since the variations of pH and electrode potential at each cycle were smaller than 0.03 units and 2 mV respectively.

1 Under Open Circuit

Under open circuit, the electrode potential within CF crack was always lower than that in bulk solution, and decreased monotonously with crack depth (Fig.3). The electrode potential and pH at crack tip decreased with crack growing (Fig.4, 5). One of the fundamental results, that potential at crack tip was made negative progressively and the local environment was acidated, made the local fresh surface at crack tip as an anode and some hydrogen entering into material at crack tip, where dissolution rate was faster relatively, therefore CF growth rate was faster than that in air(Fig.6).

2 Difference of Electrode Potential and pH at the Crack tips between CF and Stress Corrosion Cracking (SCC)

By stopping alternating load while remaining mean load to measure potential and pH at crack tip during SCC, both the pH and potential rose again gradually with the advance of time in contract with that during CF, and reached some stable values in enough time depending on crack depth in a certain system (Fig. 7) . This meant the fresh surface at crack tip was formed faster in CF than in SCC although pumping effect in CF crack accelerated the exchange of internal ions and external ions.

3 Under Cathodic Polarization

Under cathodic polarization, a large amount of hydrogen ions combined as hydrogen molecules at crack tip where acidity of local solution was very low. Though bulk metal was polarized cathodically, the material within crack and at crack tip have not been polarized enough, the local electrode potential will be higher therein than on surface (Fig.3, 5). The difference between them will be much obvious with cathodic polarization potential increasing. As polarization potential was not very low (such as −820 mV,(SCE)), because of bulk metal as a big anode providing a large amount of electrons, the positive potential drop in crack made local corrosion potential at crack tip not too lower than free corrosion potential of material in solution, and higher than non−corroded potential of material in solution. In this circumstance, hydrogen formed at crack tip entered less into material and dissolution volume was smaller at crack tip in about neutral local environment. So the crack growth rate was slower than that under open circuit (Fig.6).

When polarization potential was very low such as −1200 mV (SCE) which was usually thought as reasonable to protect cathodically CF crack growth, because the lower actual potential at crack tip than free corrosion potential and the difference of hydrogen concentration between in local crack tip environment and in bulk solution, increased hydrogen ability to enter into material, crack growth rate was faster than that under open circuit (Fig.6). The appearances of hydrogen embrittlement were observed in their fracture surface.

4 Under Anodic Polarization

Under anodic polarization potential (−470 mV (SCE)), the potential in crack and at crack tip were lower than that in bulk solution (Fig.3, 5). For shorter cracks because hydrogen ions concentration was higher in local acidic environment at crack tip than under free corrosion state, local anodic dissolve rate was not very low. Along with crack length increasing, the potential at crack tip reached gradually free corrosion potential, and dissolve rate at crack tip decreased gradually while no more hydrogen entered into material(Fig.6). So anodic polarization potential will play an protective effect on material in some conditions.

5 Reason for changed potential and pH

Since a certain extent of surface film was always formed on fresh surface of SM50B−Zc steel in 3.5% NaCl solution, dissolution rate of metals will be decreased. The material at crack tip, as be sharpened and blunted repeatedly under alternating load in grate strain and strain rate field was always in active corrosion state at relatively higher frequency. So the dissolution rate of crack tip material was higher and the unstable passivation film formed on crack tip surface was thinner even if under unloading. The smaller distance

to crack mouth and the more effective corrosion passivation were, the smaller the dissolve rate was. This meant that the diffuse potential drop was formed because the difference of reaction kinetics between at crack tip and in other region of crack produced the differences among the solution compositions in various regions. Since current flowing in solution can produce ohmic potential drop, the larger current produced under polarization potential will cause larger ohmic potential drop. And the higher the polarization potential was, the larger the ohmic potential drop was. Advection induced by the cyclic displacement of the crack walls can change above–mentioned potential levels. So it were chemical and electrochemical reactions, diffusion potential drop, ohmic potential drop and advection that caused φ in CF crack.

6 Role of φ, ΔpH in CF

CF crack growth rate depended on local chemical and electrochemical conditions, local material properties and local mechanical behavior at crack tip. The effect of polarization potential was to decrease absorption and promot hydrogen entering into material. This has been proved by results of strain electrode in imitating crack tip environment and mechanical condition [14, 15], and the results of analyzing hydrogen concentration on CF fracture surface [16]. φ and ΔpH at crack tip provided condition of absorption, increasing dissolve rate at crack tip and promoting hydrogen to enter into material.

7 Difference of φ, ΔpH among Systems

The factors affecting φ, ΔpH were mechanics, material, environment and crack geometry. All of stress ratio decreasing, frequencies decreasing and ΔK increasing made φ, ΔpH increasing. The φ, ΔpH became larger as the crack length was longer, the specimen was thicker, the crack open angle was larger, the conductivity of solution was lower, and the applying potential deviated further from free corrosion potential.

8 Determination of the optimum Protection Potential

The the optimum protection potential was determined based on reducing corrosion rate and hydrogen content at crack tip for structural with cracks. Since loading and material–environment were usually definite, electrode potential should be controlled to make φ close to zero while making electrode potential deviate no far from the line at which hydrogen discharge became possible, and making pH close to alkalinity as possible at crack tip. Thus electrode potential controlled will change with crack length because φ, ΔpH were different along with crack length. Based on two dimensional mathematical models [17]calculating potential, pH within CF cracks and at crack tip under open circuit, the model of calculating potential, pH in crack and at crack tip under polarization have been exploring, and by which the optimum protection potential will

be obtained.

CONCLUSIONS

1. There was larger electrode potential drop and pH drop in CF crack. Under free corrosion, both the potential and pH were lower at crack tip than that in bulk solution. And the cooperation of local dissolution and hydrogen discharge at crack tip accelerated crack growth.
2. Under cathodic polarization, the potential drop in crack was larger as crack length was longer, and potential at crack tip didn't reach applied polarization potential level. The increasing of local hydrogen discharge promoted crack growing. The CF life was extended when crack length was smaller or under not too low cathodic polarization.
3. Anodic polarization accelerated smaller CF crack growth rate and may reduce crack growth rate in a certain level for longer CF crack .
4. The potential drop and pH drop within crack were the most important two factors affecting CF life in different applied potential.

ACKNOWLEDGMENTS

This research was supported financially by National Natural Science Foundation of China, by Post–doctoral Science Foundation of China, and by Liaoning Doctoral Natural Science Foundation. The authors gratefully acknowledge this support.

REFERENCES

1. B. F. Brown, Corrosion Fatigue: Mechanics, Metallurgy, Electrochemistry, and Engineering, ASTM STP 801, (Philadelphia, PA: American Society for Testing and Materials, 1983), p.508
2. J–B. Buh, W–T. Tsai, J–T. Lee, and H. Chang, Corrosion, 46 12 (1990): p.983
3. J. A. Todd, P. Li, G. Liu and V. Raman, Scripta Metallurgica, 22 6 (1988): p.745
4. T. Misawa, Corrosion Engineering, (in Japanese) 38 5 (1989): p.274
5. K. Komai and M. Noguchi, Bulletin Jappan Soc. Mech. Engrs., (in Japanese), A52 480 (1986), p.1770
6. H. W. Pickering, advances in Localized Corrosion. (Houston, TX: NACE–9,1990), p.77
7. Yuan Xu and H. W. Pickering, Critical Factors in Localized Corrosion, (Pennington, NJ: Electrochem. Soc., 1992), p.389
8. K. Cho and H. W. Pickering, ibid, p.407
9. B. G. Ateya and H. W. Pickering, J. Electrochem. Soc., 122 (1975): p.1018
10. J. R. Galvele, ibid, 123 (1976): p.464
11. P. Doig and P. E. J. Flewitt, Met. Trans. A, 9A (1978): p.357
12. R. N. Parkins, I. H. Craig and J. Congleton, Corr. Sci., 24 (1984): p.709

13. A. Turnbull and D. H. Ferriss, ibid, 26 (1986): p.601
14. KE Wei and HAN En-Hou, Proc. 6th National Conference on Fatigue (Invited Lecture, in Chinese, 1993).
15. HAN En-Hou, HAN Yumei and KE Wei, Proc. National Youth Conf. on Fatigue (in Chinese, 1992), p.36
16. HAN En-Hou, CUI Guangchun and XU Hao, Proc. CMRS'90, (Elsevier Science Publishers, 1990), 5 p.299
17. HAN En-Hou and KE Wei, Corr. Sic., (to be published in 1993)

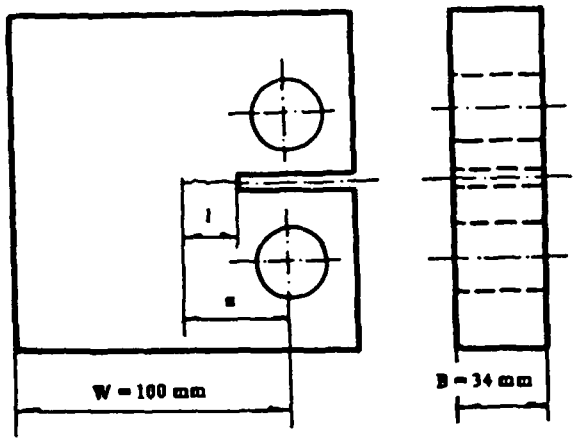

Fig.1 Geometry of specimen

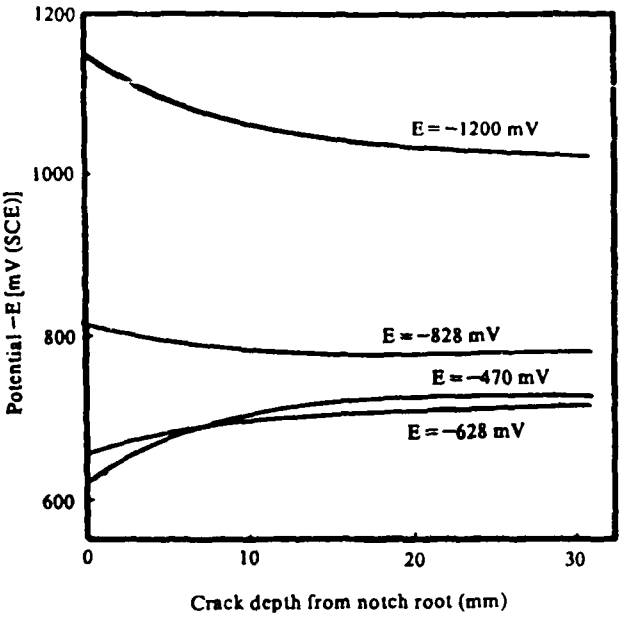

Fig.3 Distribution of pH and potential within corrosion fatigue crack for a given crack length

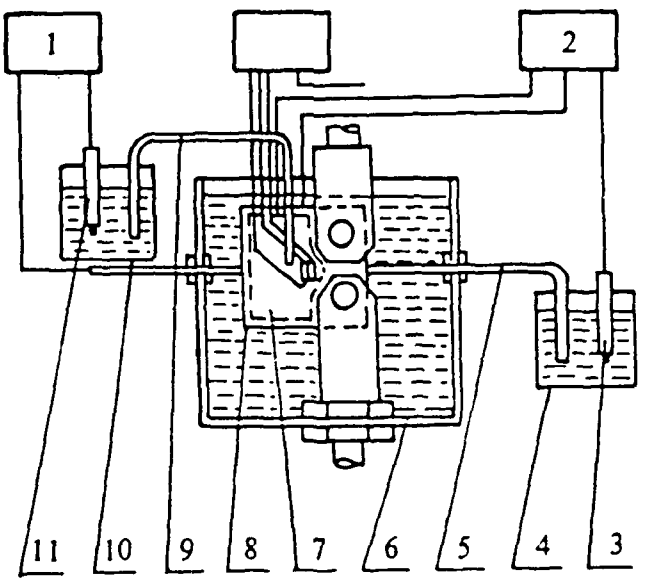

1 pH meter 2 potentiostat 3 saturated calomel electrode
4 container a 5 micro−electrode 6 test chamber
7 Pt electrode 8 specimen 9 salt bridge
10 container b 11 saturated calomel electrode

Fig.2 Schematic of measuring pH and potential at crack tip

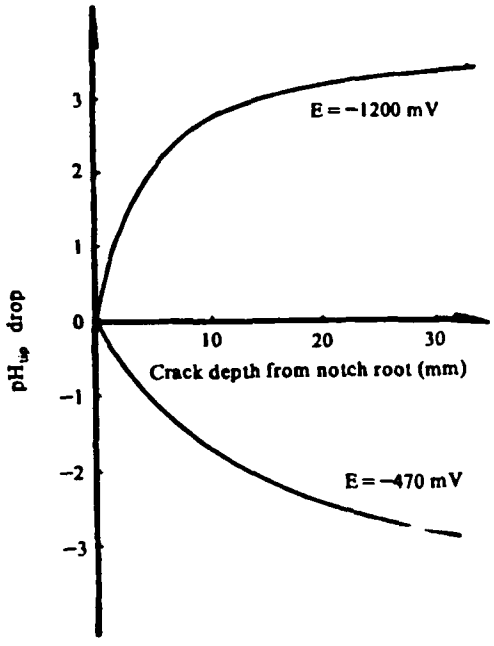

Fig.4 pH drop at growing corrosion fatigue crack tip

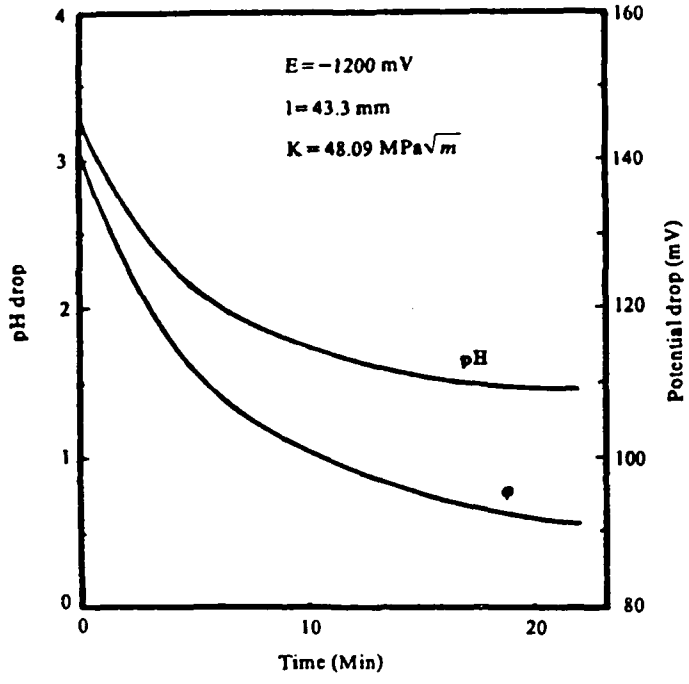

Fig.7 Variation of pH drop and potential drop at crack tip with time after a pause in cyclic loading

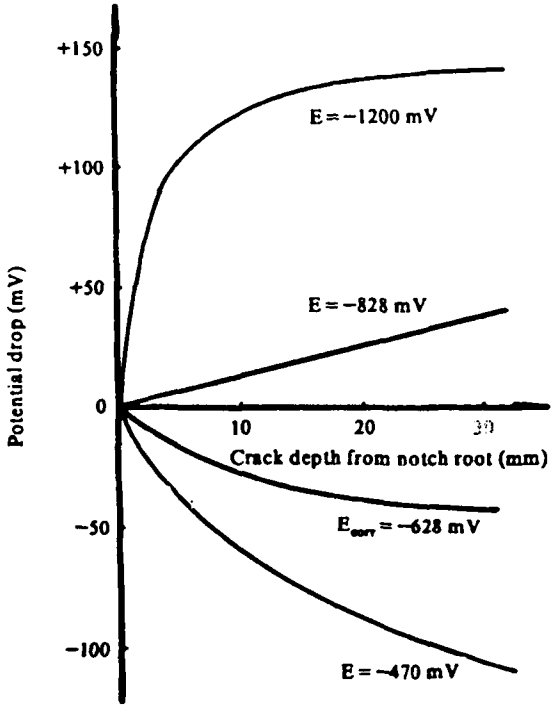

Fig.5 Potential drop at crack tip for a growing corrosion fatigue crack

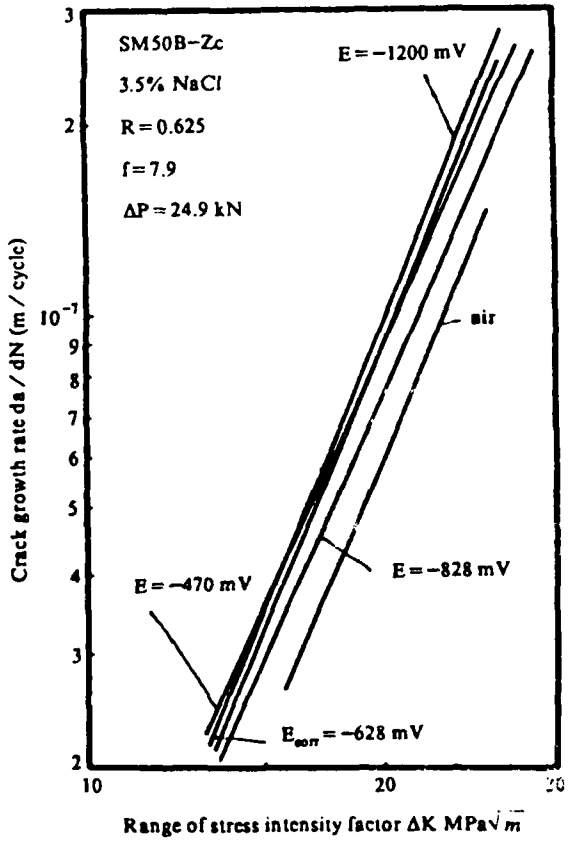

Fig.6 Effect of polarization potential on crack growth rate